Graduate Texts in Physics

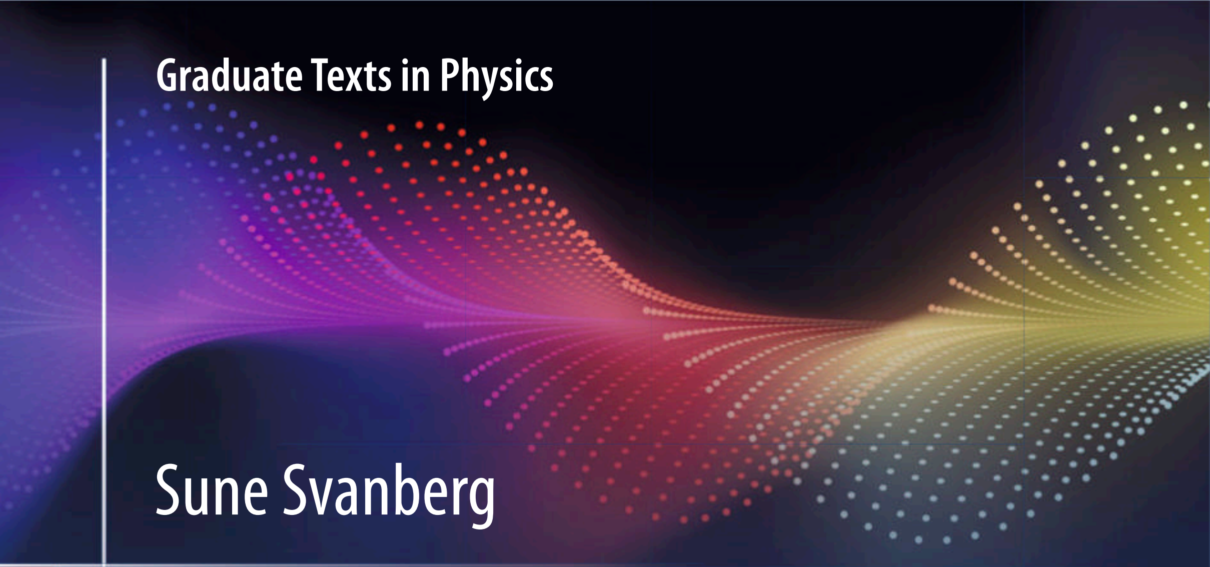

Sune Svanberg

Atomic and Molecular Spectroscopy

Basic Aspects and Practical Applications

Fifth Edition

Springer

Graduate Texts in Physics

Series Editors

Kurt H. Becker, NYU Polytechnic School of Engineering, Brooklyn, NY, USA

Jean-Marc Di Meglio, Matière et Systèmes Complexes, Bâtiment Condorcet, Université Paris Diderot, Paris, France

Sadri Hassani, Department of Physics, Illinois State University, Normal, IL, USA

Morten Hjorth-Jensen, Department of Physics, Blindern, University of Oslo, Oslo, Norway

Bill Munro, NTT Basic Research Laboratories, Atsugi, Japan

Richard Needs, Cavendish Laboratory, University of Cambridge, Cambridge, UK

William T. Rhodes, Department of Computer and Electrical Engineering and Computer Science, Florida Atlantic University, Boca Raton, FL, USA

Susan Scott, Australian National University, Acton, Australia

H. Eugene Stanley, Center for Polymer Studies, Physics Department, Boston University, Boston, MA, USA

Martin Stutzmann, Walter Schottky Institute, Technical University of Munich, Garching, Germany

Andreas Wipf, Institute of Theoretical Physics, Friedrich-Schiller-University Jena, Jena, Germany

Graduate Texts in Physics publishes core learning/teaching material for graduate- and advanced-level undergraduate courses on topics of current and emerging fields within physics, both pure and applied. These textbooks serve students at the MS- or PhD-level and their instructors as comprehensive sources of principles, definitions, derivations, experiments and applications (as relevant) for their mastery and teaching, respectively. International in scope and relevance, the textbooks correspond to course syllabi sufficiently to serve as required reading. Their didactic style, comprehensiveness and coverage of fundamental material also make them suitable as introductions or references for scientists entering, or requiring timely knowledge of, a research field.

Sune Svanberg

Atomic and Molecular Spectroscopy

Basic Aspects and Practical Applications

Fifth Edition

Springer

Sune Svanberg
Department of Physics
Lund University
Lund, Sweden

ISSN 1868-4513 ISSN 1868-4521 (electronic)
Graduate Texts in Physics
ISBN 978-3-031-04775-6 ISBN 978-3-031-04776-3 (eBook)
https://doi.org/10.1007/978-3-031-04776-3

Originally published as volume 6 in the series: Springer Series Atoms Plasmas

1st–4th editions: © Springer-Verlag Berlin Heidelberg 1991, 1992, 2001, 2004
5th edition: © The Editor(s) (if applicable) and The Author(s), under exclusive license to Springer Nature Switzerland AG 2022
This work is subject to copyright. All rights are solely and exclusively licensed by the Publisher, whether the whole or part of the material is concerned, specifically the rights of translation, reprinting, reuse of illustrations, recitation, broadcasting, reproduction on microfilms or in any other physical way, and transmission or information storage and retrieval, electronic adaptation, computer software, or by similar or dissimilar methodology now known or hereafter developed.
The use of general descriptive names, registered names, trademarks, service marks, etc. in this publication does not imply, even in the absence of a specific statement, that such names are exempt from the relevant protective laws and regulations and therefore free for general use.
The publisher, the authors, and the editors are safe to assume that the advice and information in this book are believed to be true and accurate at the date of publication. Neither the publisher nor the authors or the editors give a warranty, expressed or implied, with respect to the material contained herein or for any errors or omissions that may have been made. The publisher remains neutral with regard to jurisdictional claims in published maps and institutional affiliations.

This Springer imprint is published by the registered company Springer Nature Switzerland AG
The registered company address is: Gewerbestrasse 11, 6330 Cham, Switzerland

To Katarina, Emilie, Kristina,
and the memory of my Parents
Soli Deo Gloria

Preface to the Fifth Edition

Eighteen years have elapsed since the publishing of the fourth edition of the book, and clearly much has happened in the field of Atomic and Molecular Spectroscopy at this time. Thus, there was a very urgent need for an updated edition, which has now been filled. Many new techniques have been introduced both regarding basic aspects and practical applications—both areas have been addressed in the present quite substantially revised edition. Further, the formation of images based on multi-spectral recordings of objects is more emphasized in this edition, since such aspects constitute a very important part of spectroscopic practical applications.

Based on his 50-year experience in lecturing spectroscopy and its interdisciplinary applications, and having personally worked with a large number of techniques from X-rays to radio waves, and covering basic and applied aspects, certain pedagogical "tricks" and parallels were developed, and have to some extent been incorporated in this edition, hopefully of help for the reader to better understand the phenomena and their interrelations. The field of spectroscopy is full of fascination, and the author's wish is to convey it to the reader. Hopefully, this new edition will serve a good purpose for students on the Master's or PhD level, while also others, including seniors, might find it useful for an overview with many new references. Since each chapter is reasonably self-contained, certain chapters can be selected for a course focusing on specific aspects of spectroscopy.

The author is most grateful for the fruitful collaboration with numerous colleagues and students through the years.

Special thanks go to Dr. Zachary Evenson of Springer-Nature for organizing the publication of this new edition.

Lund, Sweden
March 2022

Sune Svanberg

Preface to the Fourth Edition

The present book – *Atomic and Molecular Spectroscopy – Basic Aspects and Practical Applications* – has been developed over a long time. The Third Edition, which appeared in 2001, was fully revised and updated to the state of the field at that time. The book appeared in hard cover well suited for individual and library use. However, the book is basically a text, also well suited as a base for a course on the topic. A lower-cost paper-back edition better serves such purposes, as did the Second (paper-back) Edition of the book. The Fourth Edition presented has now been corrected for misprints and contains some additional text. A number of important literature references up until mid-2003 have been added to provide a fully updated account of the dynamic field of Atomic and Molecular Spectroscopy.

Lund, October 2003 Sune Svanberg

Preface to the Third Edition

Atomic and molecular spectroscopy – both in its basic and in its applied aspects – is in a dynamic state of development. It continues to provide new fascinating possibilities for a deeper understanding of the fundamental properties of the building blocks of matter and their interaction with electromagnetic irradiation. It generates new possibilities for practical applications in industry, chemistry, astronomy, geosciences, biology, medicine and information technology.

Ten years after the appearance of the first edition there was a need for a thorough revision of the book, again bringing it up to the leading edge in the new millennium. This has led to a considerable extension of the material and thus of the size of the book. As previously, the focus has been on the physical understanding of the processes and phenomena, and on providing a broad overview of the possibilities of atomic and molecular spectroscopy. Thus, the mathematical description is frequently superficial – for the benefit of students and scientists in other natural sciences without a rigourous physics background. My belief is that the physical (and intuitive) understanding, when possible, is also the most important aspect for the hard-core physicist. The reader will find ample references to textbooks, review articles and research papers providing all the details on almost any topic in the field, and the reference list was, with considerable effort, updated till mid-2000 and in some cases till early 2001. This could still mean that important references are lacking, and I apologize to the authors for unfortunate omissions.

The reader who already knows the previous editions will notice that new material is added, particularly in the following fields: clusters, satellite remote sensing, astrophysical applications, the generation of ultrafast and ultraintense laser radiation, diode laser spectroscopy, ultrafast spectroscopy, femtochemistry, high-power laser–matter interaction, laser cooling and trapping, Bose–Einstein condensation, and lasers in environmental and medical research. Thus, it is felt that the book provides a rather extensive overview of the major spectroscopy fields.

In order to improve the usefulness of the book as a text for a course on the topic at the pre- or postgraduate level, a section of questions and exercises has been added. The material is presented following the chapters, and, in addition, material connecting wider areas is supplied. A detailed subject index is also provided, helping the reader to easily find an entry to the introduction of a subfield and references to the relevant literature.

The author benefited a lot from the interaction with students and colleagues when developing this book. He is very grateful for comments and corrections.

Finally, I would like to thank Gertrud Dimler, Adelheid Duhm and Claus Ascheron at Springer-Verlag for their professional work, and Helmut Lotsch for his encouragement throughout this book project.

Lund, June 2001 Sune Svanberg

Preface to the First Edition

Atomic and molecular spectroscopy has provided basic information leading to the development of quantum mechanics and to the understanding of the building blocks of matter. It continues to provide further insight into the statics and dynamics of the microcosmos, and provides the means for testing new concepts and computational methods. The results of atomic and molecular spectroscopy are of great importance in astrophysics, plasma and laser physics. The rapidly growing field of spectroscopic applications has made considerable impact on many disciplines, including medicine, environmental protection, chemical processing and energy research. In particular, the techniques of electron and laser spectroscopy, the subjects of the 1981 Nobel prize in physics, have contributed much to the analytical potential of spectroscopy.

This textbook on *Atomic and Molecular Spectroscopy* has been prepared to provide an overview of modern spectroscopic methods. It is intended to serve as a text for a course on the subject for final-year undergraduate physics students or graduate students. It should also be useful for students of astrophysics and chemistry. The text has evolved from courses on atomic and molecular spectroscopy given by the author since 1975 at Chalmers University of Technology and at the Lund Institute of Technology. References are given to important books and review articles which allow more detailed studies of different aspects of atomic and molecular spectroscopy. No attempt has been made to cover all important references, nor have priority aspects been systematically considered.

It is assumed that the reader has a basic knowledge of quantum mechanics and atomic physics. However, the completion of a specialized course on atomic and molecular physics is not required. The present treatise (disregarding Chap. 4) is not particularly mathematical, but emphasizes the physical understanding of the different techniques of spectroscopy. In the course given by the author, the time for solving calculational problems has been reduced to allow a more complete overview of the field in the time available. Particular emphasis has been given to technical applications. However, by increasing the allotted problem-solving time or by omitting certain areas of spectroscopy, a more problem-oriented course can easily be taught based on this book. In his courses, the author has combined lectures with a number of 5-hour laboratory experiments (performed on research equipment) and a number of 1-2 hour visits to local research groups in physics, chemistry and astronomy.

Part of the material is reworked from the Swedish textbook *Atomfysik* by I. Lindgren and S. Svanberg (Universitetsförlaget, Uppsala 1974). The author is very grateful to his teacher Prof. I. Lindgren for contributions and support through the years. He would also like to thank many colleagues, including Prof. D. Dravins, Dr. Å. Hjalmarsson, Prof. I. Martinson, Prof. J. Nordgren, Prof. C. Nordling, Dr. W. Persson, Prof. A. Rosén, Prof. H. Siegbahn and Dr. C.-G. Wahlström for valuable suggestions and corrections.

Special thanks are due to Mrs. C. Holmqvist for typing numerous versions of the manuscript and Dr. H. Sheppard for correcting the English and assisting with the figures. Mr. Å. Bergqvist and Mr. G. Romerius helped by drawing some of the figures. Finally, the kind help and support of Dr. H. Lotsch of Springer-Verlag is gratefully acknowledged.

Lund, September 1990 Sune Svanberg

Contents

1 Introduction 1
- 1.1 Spectroscopy and Multi-spectral Imaging 5
- 1.2 Some Fundamentals of Quantum Mechanics 9

2 Atomic Structure 15
- 2.1 One-Electron Systems 15
- 2.2 Alkali Atoms 16
- 2.3 Magnetic Effects 18
  - 2.3.1 Precessional Motion 18
  - 2.3.2 Spin–Orbit Interaction 20
- 2.4 General Many-Electron Systems 21
- 2.5 The Influence of External Fields 28
  - 2.5.1 Magnetic Fields 29
  - 2.5.2 Electric Fields 33
- 2.6 Hyperfine Structure 35
  - 2.6.1 Magnetic Hyperfine Structure 35
  - 2.6.2 Electric Hyperfine Structure 37
- 2.7 The Influence of External Fields (hfs) 39
- 2.8 Isotopic Shifts 42

3 Molecular Structure 45
- 3.1 Electronic Levels 45
- 3.2 Rotational Energy 48
- 3.3 Vibrational Energy 51
- 3.4 Polyatomic Molecules 52
- 3.5 Clusters 53
- 3.6 Other Molecular Structures 54

4 Radiation and Scattering Processes 55
4.1 Resonance Radiation 55
4.2 Spectra Generated by Dipole Transitions 66
4.2.1 Atoms 67
4.2.2 Molecules 70
4.3 Rayleigh and Raman Scattering 76
4.4 Raman Spectra 79
4.4.1 Vibrational Raman Spectra 79
4.4.2 Rotational Raman Spectra 80
4.4.3 Vibrational–Rotational Raman Spectra 81
4.5 Mie Scattering 81
4.6 Atmospheric Scattering Phenomena 83
4.7 Comparison Between Different Radiation and Scattering Processes 88
4.8 Collision-Induced Processes 89
4.9 Quantum Optics and Quantum Information 89

5 Spectroscopy of Inner Electrons 93
5.1 X-Ray Spectroscopy 93
5.1.1 X-Ray Emission Spectroscopy 95
5.1.2 X-Ray Absorption Spectroscopy 101
5.1.3 X-Ray Imaging Applications 103
5.2 Photoelectron Spectroscopy 109
5.2.1 XPS Techniques and Results 110
5.2.2 Chemical Shifts 113
5.3 Auger Electron Spectroscopy 116

6 Optical Spectroscopy and Multispectral Imaging 121
6.1 Light Sources 122
6.1.1 Line Light Sources 122
6.1.2 Continuum Light Sources 131
6.1.3 Synchrotron Radiation 133
6.1.4 Natural Radiation Sources 137
6.2 Spectral Resolution Instruments 140
6.2.1 Prism Spectrometers 140
6.2.2 Grating Spectrometers 143
6.2.3 The Fabry–Pérot Interferometer 147
6.2.4 The Fourier Transform Spectrometer 154
6.3 Detectors 157
6.4 Optical Components and Materials 165
6.4.1 Interference Filters and Mirrors 165
6.4.2 Absorption Filters 169
6.4.3 Polarizers 172
6.4.4 Optical Materials 174
6.4.5 Influence of the Transmission Medium 175

- 6.5 Optical Methods of Chemical Analysis ... 181
  - 6.5.1 The Beer–Lambert Law ... 181
  - 6.5.2 Atomic Absorption/Emission Spectrophotometry ... 185
  - 6.5.3 Burners, Flames, Sample Preparation and Measurements ... 190
  - 6.5.4 Modified Methods of Atomization ... 191
  - 6.5.5 Multi-element Analysis ... 194
  - 6.5.6 Molecular Spectrophotometry ... 195
  - 6.5.7 Raman Spectroscopy ... 198
- 6.6 Optical Remote Sensing ... 199
  - 6.6.1 Atmospheric Monitoring with Passive Techniques ... 201
  - 6.6.2 Land and Water Measurements with Passive Remote Sensing Techniques ... 209
- 6.7 Astrophysical Spectroscopy ... 216

7 Radio-Frequency Spectroscopy ... 231
- 7.1 Resonance Methods ... 232
  - 7.1.1 Magnetic Resonance ... 232
  - 7.1.2 Atomic-Beam Magnetic Resonance ... 233
  - 7.1.3 Optical Pumping ... 241
  - 7.1.4 Optical Double Resonance ... 245
  - 7.1.5 Level-Crossing Spectroscopy ... 248
  - 7.1.6 Resonance Methods for Liquids and Solids ... 255
- 7.2 Microwave Radiometry ... 264
- 7.3 Radio Astronomy ... 267

8 Lasers ... 275
- 8.1 Basic Principles ... 275
- 8.2 Coherence ... 278
- 8.3 Resonators and Mode Structure ... 279
- 8.4 Fixed-Frequency Lasers ... 284
  - 8.4.1 The Ruby Laser ... 284
  - 8.4.2 Four-Level Lasers ... 286
  - 8.4.3 Pulsed Gas Lasers ... 290
  - 8.4.4 The He–Ne Laser ... 292
  - 8.4.5 Gaseous Ion Lasers ... 293
- 8.5 Tunable Lasers ... 295
  - 8.5.1 Dye Lasers ... 295
  - 8.5.2 Colour-Centre Lasers ... 305
  - 8.5.3 Tunable Solid-State Lasers ... 306
  - 8.5.4 Tunable CO_2 Lasers ... 307
  - 8.5.5 Semiconductor Lasers ... 308
- 8.6 Nonlinear Optical Phenomena ... 313

8.7 Ultrashort and Ultra-High Power Laser Pulse Generation 327
8.7.1 Short-Pulse Generation by Mode-Locking 328
8.7.2 Generation of Ultra-High Power Pulses 333

9 Laser Spectroscopy 339
9.1 Basic Principles 339
9.1.1 Comparison Between Conventional Light Sources and Lasers 339
9.1.2 Saturation 340
9.1.3 Excitation Methods 341
9.1.4 Detection Methods 342
9.1.5 Laser Wavelength Setting 344
9.2 Doppler-Limited Techniques 347
9.2.1 Absorption Measurements 347
9.2.2 Intracavity Absorption Measurements 348
9.2.3 Absorption Measurements on Excited States 349
9.2.4 Level Labelling 351
9.2.5 Two-Photon Absorption Measurements 352
9.2.6 Opto-Galvanic Spectroscopy 352
9.2.7 Single-Atom and Single-Molecule Detection 357
9.2.8 Opto-Acoustic Spectroscopy 358
9.3 Optical Double-Resonance and Level-Crossing Experiments with Laser Excitation 360
9.4 Time-Resolved Atomic and Molecular Spectroscopy 366
9.4.1 Generation of Short Optical Pulses 366
9.4.2 Measurement Techniques for Optical Transients 367
9.4.3 Background to Lifetime Measurements 372
9.4.4 Survey of Methods of Measurement for Radiative Properties 374
9.4.5 Quantum-Beat Spectroscopy 380
9.5 Ultrafast Spectroscopy 385
9.5.1 Ultrafast Measurement Techniques 387
9.5.2 Molecular Reaction Dynamics (Femtochemistry) 391
9.5.3 Coherent Control 393
9.6 High-Power Laser-Matter Interactions and Applications 395
9.6.1 Above Threshold Ionization (ATI) 395
9.6.2 High Harmonic Generation 397
9.6.3 Attosecond Generation and Spectroscopy 403
9.6.4 X-Ray Laser Pumping 403
9.6.5 Broadband X-Ray Generation 406
9.6.6 Relativistic Effects and Laser Accelerators 409
9.6.7 Laser-Nuclear Interactions and Laser-Driven Fusion 410

9.7 High-Resolution Laser Spectroscopy 412
9.7.1 Spectroscopy on Collimated Atomic and Ionic Beams 412
9.7.2 Saturation Spectroscopy and Related Techniques 419
9.7.3 Doppler-Free Two-Photon Absorption 430
9.7.4 Precision Laser Spectroscopy on Hydrogen 431
9.7.5 Emergence of the Laser Frequency Comb Technique 435
9.8 Cooling and Trapping of Ions and Atoms 439
9.8.1 Introduction 439
9.8.2 Ion Traps 442
9.8.3 Basic Laser Cooling in Traps 444
9.8.4 Trapped Ion Spectroscopy 446
9.8.5 Atom Cooling and Trapping 447
9.8.6 Atom Optics 451
9.8.7 Bose–Einstein Condensation and “Atom Lasers” 452
9.8.8 Ultracold Fermionic Gases 453

10 Applications of Laser Spectroscopy 455
10.1 Diagnostics of Combustion Processes 455
10.1.1 Background 455
10.1.2 Laser-Induced Fluorescence and Related Techniques 458
10.1.3 Raman Spectroscopy 464
10.1.4 Coherent Anti-Stokes Raman Scattering 465
10.1.5 Velocity Measurements 469
10.2 Laser Remote Sensing of the Atmosphere 472
10.2.1 Optical Heterodyne Detection 474
10.2.2 Long-Path Absorption Techniques 476
10.2.3 Lidar Techniques 480
10.3 Laser-Induced Fluorescence and Raman Spectroscopy in Liquids and Solids 498
10.3.1 Hydrospheric Remote Sensing 499
10.3.2 Vegetation, Cultural Heritage, and Fauna Monitoring 502
10.3.3 Food and Pharmaceutical Spectroscopy 506
10.3.4 Monitoring of Surface Layers 506
10.4 Laser-Induced Chemical Processes 509
10.4.1 Laser-Induced Chemistry 511
10.4.2 Laser Isotope Separation 512
10.5 Spectroscopic Aspects of Lasers in Medicine 517
10.5.1 Thermal Interaction of Laser Light with Tissue 517
10.5.2 Photodynamic Tumour Therapy 519
10.5.3 Tissue Diagnostics with Laser-Induced Fluorescence 524
10.5.4 Scattering Spectroscopy 531
10.6 Closing Remarks 545

Questions and Exercises 549

References 561

Index 671

Chapter 1
Introduction

By *spectroscopy,* we usually mean experimental charting of the energy-level structure of physical systems. For that purpose, the transition processes, spontaneous or induced, between different energy states are studied, and spectroscopy therefore normally means the analysis of various types of radiation—electromagnetic or particle emission. Spectroscopic investigations can be of a fundamental or an applied nature. Experimentally determined energy levels, transition probabilities, etc. are employed in fundamental spectroscopy for obtaining an understanding of the studied systems using adequate theories or models. Usually, certain primary quantities (wavelengths, intensities, etc.) are measured in spectroscopic investigations. These quantities are then used to evaluate more fundamental quantities. This process is schematically illustrated in Fig. 1.1.

Quantities, such as wavelengths and transition probabilities, determined using spectroscopy for atoms and molecules, are of direct importance in several disciplines such as astrophysics, plasma-, and laser physics. Here, as in many fields of applied spectroscopy, spectroscopic information can be used in various kinds of analysis. For instance, optical atomic absorption or emission spectroscopy is used for both qualitative and quantitative chemical analysis. Other types of spectroscopy, e.g. electron spectroscopy methods or nuclear magnetic resonance, also provide information on the chemical environment in which a studied atom is situated.

Tunable lasers have had a major impact on both fundamental and applied spectroscopy. Applied laser spectroscopy includes, among many other things, remote sensing of the environment, medical applications, combustion diagnostics, laser-induced chemistry, and isotope separation.

Dynamic properties of atomic and molecular systems can be studied by time-resolved spectroscopy. Such studies presently range from the second- to the attosecond timescale. The availability of reasonably compact high-power lasers has allowed a quickly expanding research activity in ultra-intense laser–matter interaction, also offering many new challenges for theory.

© The Author(s), under exclusive license to Springer Nature Switzerland AG 2022

S. Svanberg, *Atomic and Molecular Spectroscopy*, Graduate Texts in Physics,
https://doi.org/10.1007/978-3-031-04776-3_1

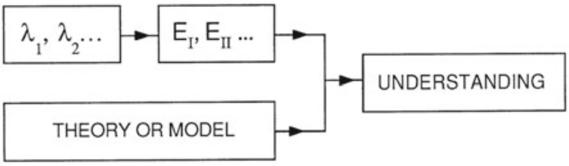

Fig. 1.1 The spectroscopic process [1]

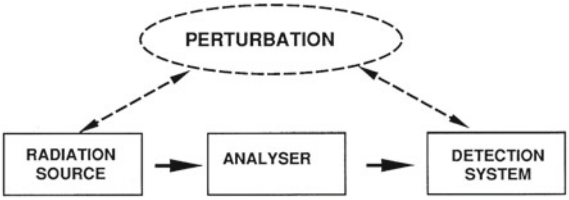

Fig. 1.2 Basic arrangement of a spectroscopic set-up [1]

Tunable lasers have also enabled the strongly expanding field of quantum information, where the concept of entanglement, an integral part of quantum mechanics, has obtained a fundamental role in quantum computing, storage, and even teleportation.

In principle, a setup for spectral studies consists of three components: a radiation source, an analyser, and a detection system. The system under investigation is in many modern techniques subjected to different types of static or oscillatory fields, and the influence of these fields on the system is studied in order to obtain a more complete picture of the system. Resonance methods in the radio-frequency domain have historically been of special importance, since they provide high accuracy in the determination of small energy splittings. The basic arrangement of a spectroscopic set-up is shown in Fig. 1.2.

The choice of spectroscopic method is primarily determined by the energy range of the phenomenon to be studied. The spectral ranges that are of interest in atomic and molecular spectroscopy are shown in Fig. 1.3. The energy ranges for different types of structures and transitions are also indicated. Using the simple relations

$$\begin{array}{cccc} \Delta E = h\nu, & \lambda = c/\nu, & 1/\lambda = \nu/c, & \nu = c(1/\lambda), \\ \text{Energy} & \text{Wavelength} & \text{Wavenumber} & \text{Frequency}, \end{array} \tag{1.1}$$

(h: Planck constant; c: velocity of light) an energy interval ΔE can be uniquely expressed in eV (energy), nm (1 nm = 10 Å) (wavelength), cm^{-1} (wavenumber), or Hz (frequency). Conversion factors between different units are given in Table 1.1. The general field of scientific unit conversion is treated in [2, 3]. The conversion factors are clearly connected to the unit definitions and the values of the fundamental constants [4, 5].

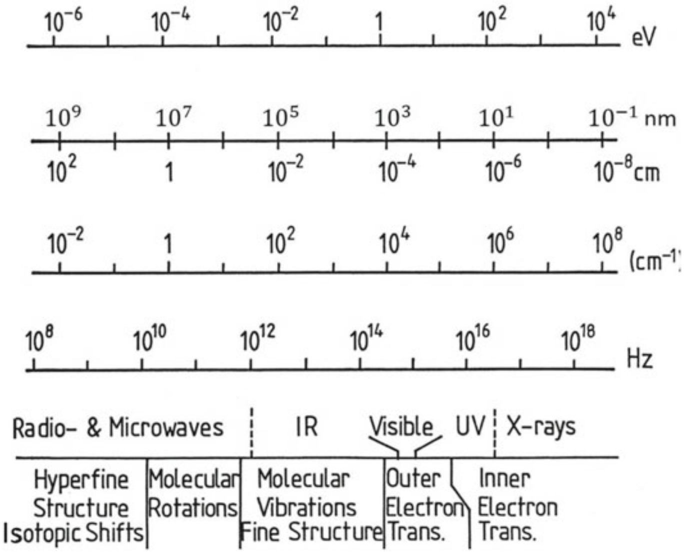
10⁻⁶ 10⁻⁴ 10⁻² 1 10² 10⁴ eV
10⁹ 10⁷ 10⁵ 10³ 10¹ 10⁻¹ nm
10² 1 10⁻² 10⁻⁴ 10⁻⁶ 10⁻⁸ cm
10⁻² 1 10² 10⁴ 10⁶ 10⁸ (cm⁻¹)
10⁸ 10¹⁰ 10¹² 10¹⁴ 10¹⁶ 10¹⁸ Hz
Radio- & Microwaves
IR
Visible
UV
X-rays
Hyperfine Structure Isotopic Shifts
Molecular Rotations
Molecular Vibrations Fine Structure
Outer Electron Trans.
Inner Electron Trans.

Fig. 1.3 Energy scales and spectroscopic phenomena

Table 1.1 Conversion factors between different energy units

Unit	Joule	cm^{-1}	Hz	eV
1 J (1 J)	1	5.03378×10^{22}	1.50919×10^{33}	6.24150×10^{18}
1 cm^{-1}	1.98658×10^{-23}	1	2.99792×10^{10}	1.23992×10^{-4}
1 Hz	6.62608×10^{-34}	3.33565×10^{-11}	1	4.13567×10^{-15}
1 eV	1.60218×10^{-19}	8.06502×10^{3}	2.41799×10^{14}	1

The choice of the unit depends, to a great extent, on the energy region and traditional factors:

X-ray region	keV
Visible and UV regions	nm, (in solid-state physics: eV)
Infrared region	µm, cm^{-1}, (cm^{-1} is in older literature called Kayser)
Radio-frequency region	MHz, cm^{-1}

It is practical to memorize the following approximate relations:

$$1\,\mathrm{eV} \longleftrightarrow 8000\,\mathrm{cm}^{-1} \longleftrightarrow 1200\,\mathrm{nm};\ \text{i.e. } 2\,\mathrm{eV} \longleftrightarrow 600\,\mathrm{nm};\ \text{visible light}$$
$$1\,\mathrm{cm}^{-1} \longleftrightarrow 30\,\mathrm{GHz},$$
$$kT \text{ at } T = 300\,\mathrm{K} : kT_{300} \sim 1/40\,\mathrm{eV}$$

(k is the Boltzmann constant, and T is the absolute temperature).

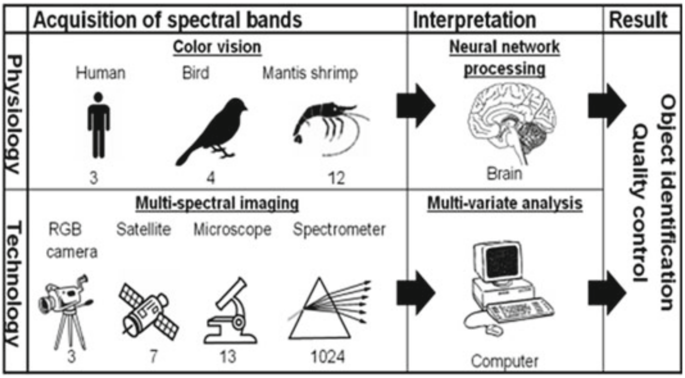
Acquisition of spectral bands
Interpretation
Result
Physiology
Color vision
Human
Bird
Mantis shrimp
3
4
12
Neural network processing
Brain
Technology
Multi-spectral imaging
RGB camera
Satellite
Microscope
Spectrometer
3
7
13
1024
Multi-variate analysis
Computer
Object identification
Quality control

Fig. 1.4 Acquisition of multi-spectral information for extraction of meaningful information from images. The cases of physiological data recording followed by brain processing, as well as the technological approach with image recording in multiple spectral bands, followed by computer image analysis are illustrated ([6]; reproduced with permission from AIP Publishing)

Transitions between inner electron orbitals normally occur in the keV range (X-rays), while the energies for transitions between outer orbitals are in the eV region (visible or near-UV and IR regions). The fine structure of atoms is of the order of 10^{-3} eV ($\sim$10 cm^{-1}) and hyperfine structures are typically about 10^{-6} eV ($\sim$300 MHz). Molecular vibrational energy splittings are of the order of 10^{-1} eV, while rotational splittings are typically 10^{-3} eV. Of course, these energies vary widely, and the above values are given only to provide the first estimate of typical orders of magnitude.

If spectroscopy is performed in many spatially related points, simultaneously or sequentially, thus collecting the optical "fingerprints" characterizing an object, we obtain a multi-spectral image, where after image processing objects can be identified and discerned based on their spectroscopic properties. This extension of spectroscopy to *multi-spectral imaging* (sometimes called *hyperspectral imaging*) is illustrated in Fig. 1.4, where the technological approach is illustrated in the lower row, while the physiological counterpart (human apprehension) is illustrated in the upper row. The number of spectral bands utilized varies from 3 for humans up to a dozen for certain animals, while in man-made devices up to thousands of spectral bands may be used. The spectral information is then digitally processed into meaningful information, e.g. by using multi-variate statistical and other methods [7–9], while a "trained" brain in an unprecedented way can perform the same task, but clearly, with much less endurance.

1.1 Spectroscopy and Multi-spectral Imaging

We will introduce spectroscopy and multi-spectral imaging by choosing some simple illustrations from the optical range. Details will be described later. We will start by showing in Fig. 1.5 a number of emission spectra, which were recorded by a compact fibre-coupled spectrometer with digital read-out from a charge coupled device (CCD)

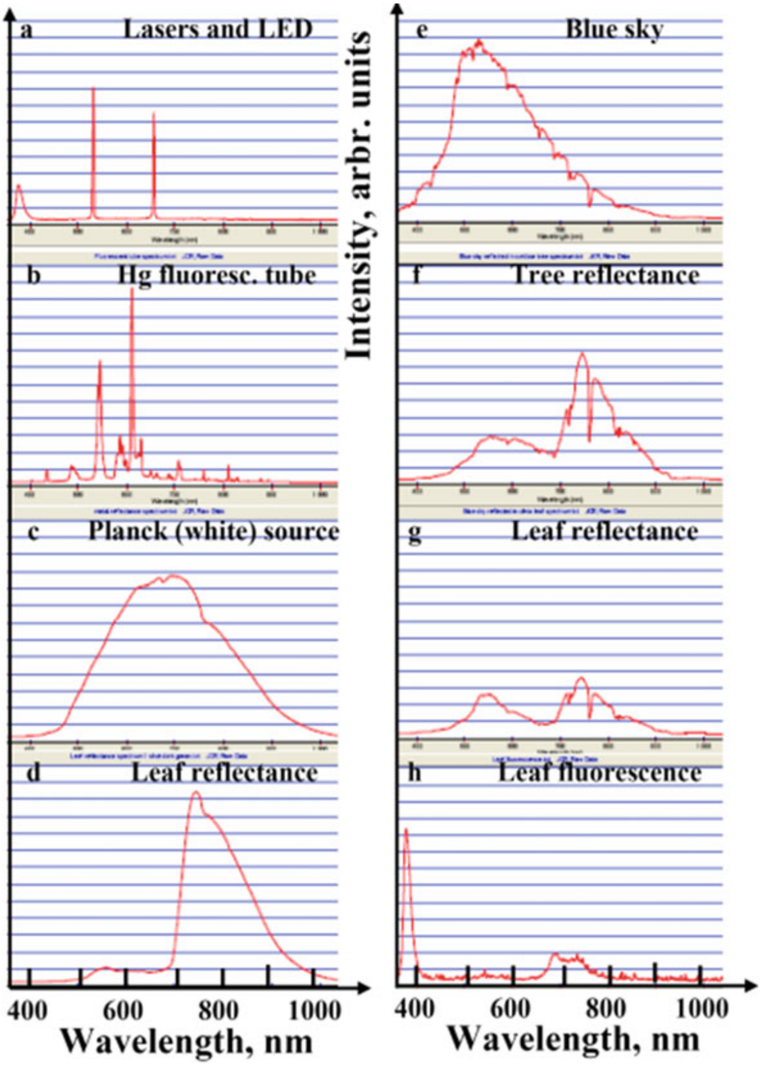

Fig. 1.5 Spectra recorded by a fibre-coupled, compact digital spectrometer. **a** Green and red laser pointer, and violet LED, **b** fluorescent discharge lamp tube, **c** Planck radiator, **d** reflection of Planck radiator lamp from a green leaf, **e** blue sky, **f** skylight reflection from a distant green tree, **g** skylight reflection from a close-by green leaf and **h** chlorophyll fluorescence induced by a violet LED

or complementary metal oxide semiconductor (CMOS) detector (Sect. 6.3) directly to a computer screen. The spectroscopic recordings provide a fingerprint identification of the substance under study. If it is not a point source, it will anyway pertain to a particular part of the source, from which the spectrum is recorded.

The sharp emission from a red and a green laser pointer, as well as the broader, but well-localized emission of a light-emitting diode (LED) are shown in (a), while the atomic line emission due to mercury in the discharge in a fluorescence tube for illumination is shown in (b). In contrast, the emission from a hot wire (Planck radiator) is in (c) shown to be very broad. If such radiation impinges on a leaf from a green plant, the near-infrared spectral parts are reflected strongly as seen in (d), since chlorophyll absorbs visible light, but slightly less in the green spectral region, which gives the leaf its green colour. By directing the receiving fibre towards the blue sky, a likewise broad spectrum is obtained, (e), reflecting the Planck radiation from the hot solar surface, but with sharp absorption lines also visible, which in part are due to terrestrial atmospheric gas absorption (oxygen, water vapour), but in certain cases are due to absorption in colder outer layers of the sun (Fraunhofer lines). When such light falls on vegetation (a distant tree, towards which the fibre is pointed, (f), or a close-by green leaf, (g), spectra similar to the one in (d) are observed, but with a particularly strong molecular oxygen 760 nm absorption line (the Fraunhofer A-line) now clearly emerging. Finally, by illuminating a leaf with violet light from the LED (with spectrum also shown in (a)) the chlorophyll fluorescence light is observed in the near-IR spectral region, (h).

The basic idea behind *multi-spectral imaging* is given in Fig. 1.6. Light is collected from all points of a rectangular area. Within the area, there is a specific region, where the spectral fingerprint is different from the other points within the rectangle. A schematic emission spectrum from a point within the rectangle is shown, where emission peaks (of different intensities) occur for wavelengths λ_1, λ_2, λ_3, and λ_4. Then, the full image scene can be recorded, as spectrally filtered in the four wavelength bands, to produce 4 monochromatic images, where the specific region occurs with varying contrast with regard to the surrounding image elements (pixels). In order to compress the whole information into an understandable single image, a contrast

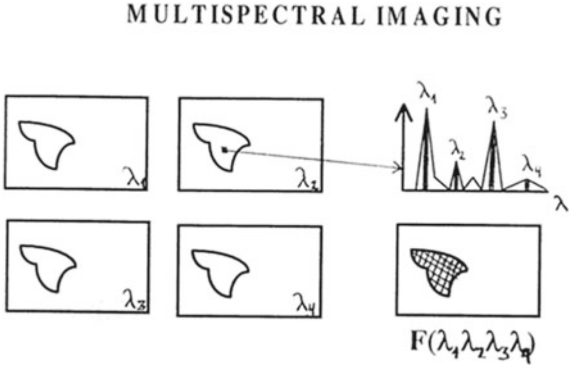

Fig. 1.6 The principle of multi-spectral imaging, for the case of 4 selected spectral bands chosen in the full spectrum. By forming a contrast function F using the recorded intensities in each pixel, an area with specific spectral fingerprint (e.g. a cancer tumour) can be identified after thresholding

function, F, is designed in an optimum way to take all the spectral differences into account. The idea is that the region of interest would attain higher F-values than the surrounding pixels. Then a threshold T can be appropriately chosen, and all pixels with $F > T$ are displayed, identifying the area looked for. Such an area could, for example, be the localization of a cancer tumour as surrounded by normal tissue, now producing useful information from an advanced instrument to a user, who is unfamiliar with spectroscopy.

Designing the function F so that it does not have a unit (such as [m] or [W/cm^2]) has many advantages, since it becomes independent of many factors, which are hard to control (Sect. 10.5.3). The simplest example of a *dimensionless quantity* is a ratio, A/B. More complex ratios are $(A - kB)/C$, where k is a constant, $(A - B)/(C - D)$ or AB/CD. Here, A, B, C, and D are spectral intensities measured in the same spectrum. Since a dimensionless quantity does not contain any unit (it is only sensitive to the *shape* of the spectral signature, not to its *intensity*), it becomes immune to

- variations in the angle of incidence of the radiation (surface topography);
- variations in distance from the object pixels to the detector;
- variations in intensity of illumination over the image;
- intensity fluctuations in the illumination source;
- variations in wavelength-independent absorption factors, etc.

The procedure of extracting useful information from large amounts of spectroscopic data in order to achieve, e.g. object identification, is further illustrated in Fig. 1.7.

Here, we want to distinguish objects/pixels Y from objects/pixels X (e.g. damaged trees from normal trees in satellite imagery, or cancer from normal tissue in close-range investigation) using different types of spectral information. For example, the fluorescence spectra, induced by a UV laser, can be used. Alternatively, the reflectance spectra (the "colour") can be recorded using sunlight illumination. The objects Y and X can also be characterized by the rate at which excited molecules decay, i.e. the temporal fall-off of the fluorescence intensity can be studied and expressed in one or more lifetime values τ_i. Contrast functions F (or f) can then be constructed, incorporating in principle all types of spectral information. A plant physiologist or a pathologist would then identify the Y:s and X:s with their standard methods, and the mean value M of the selected contrast functions and the standard deviations σ_Y and σ_X for the two classes can be calculated. We have

$$M_X = \frac{\sum_{i=1}^{n} x_i}{n}, \tag{1.2}$$

etc. where n is the number of measured samples with results x_i, and

$$\sigma_X = \sqrt{\frac{\sum_{i=1}^{n} (x_i - M_X)^2}{n - 1}} \tag{1.3}$$

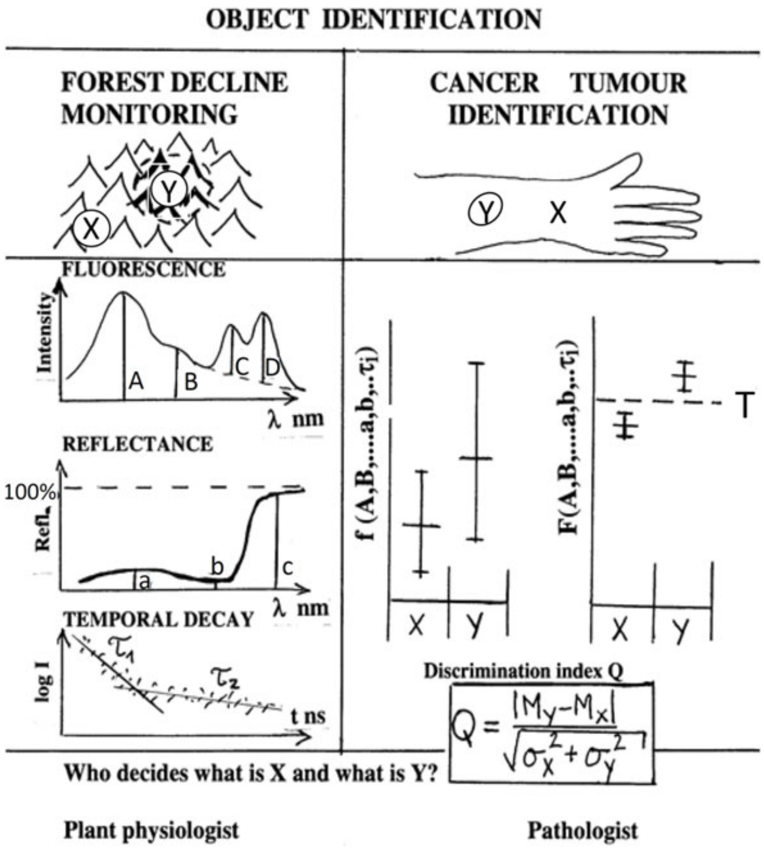
OBJECT IDENTIFICATION
FOREST DECLINE MONITORING
CANCER TUMOUR IDENTIFICATION
X
Y
Y
X
FLUORESCENCE
Intensity
A
B
C
D
λ nm
REFLECTANCE
100%
Refl.
a
b
c
λ nm
TEMPORAL DECAY
log I
τ1
τ2
t ns
f (A,B,....a,b,..τi)
X
Y
F(A,B,....a,b,..τi)
T
X
Y
Discrimination index Q
Q = |My-Mx| / √(σX² + σY²)
Who decides what is X and what is Y?
Plant physiologist
Pathologist

Fig. 1.7 Object identification in spectroscopy and multi-spectral imaging

is the standard deviation having the same unit/dimension as M.

The important question is then, whether it is possible to set a threshold value T in such a way that the two classes are clearly distinguished (as indicated on the right-hand side of Fig. 1.7), which is related to the value of the *Discrimination Index* Q, defined as

$$Q = \frac{/M_X - M_Y/}{\sqrt{(\sigma_X^2 + \sigma_Y^2}}. \tag{1.4}$$

A contrast function F is better than another one f (it has a better *Quality*) if it has a higher (*q*uality) Q value. That means that the mean values M have a large separation in terms of the typical error bars for the two groups. Thus, in principle it would be possible to let a computer try a lot of (dimensionless) contrast functions on recorded data and decide which one is the best to separate the two groups.

The procedure indicated is a possible and conceptually easy-to-grasp methodology. As a matter of fact, advanced multi-variate methods from statistical mathematics have, as already mentioned, been developed and are able to pursue segmentation of complex spectral data without any human intervention (see, for example, [7–9]). As an example, in *principal component analysis (PCA),* a complex spectrum of an object can be expanded (expressed) in principal component basis spectra, which mathematically are orthogonal (like basis/Eigenfunctions are in quantum mechanics; Sect. 1.2). The procedures are mostly performed using matrix algebra, and very advanced computer programs are commercially available to pursue segmentation and classification.

Digital image processing mostly relates to spatial aspects with image rectification and enhancement, information compression, and pattern recognition [10, 11]. Such procedures can be much enhanced by incorporating the spectroscopic aspects available in multi-spectral imaging.

After this brief introduction to the concepts of spectroscopy and multi-spectral imaging, we will now successively systematically deal with the different elements of importance. As a background to atomic and molecular spectroscopy, a survey of atomic and molecular structure is given in Chaps. 2 and 3. Based on the experience of the author, some students of spectroscopy/readers of this book may not have the expected background in quantum mechanics, while still learning a lot regarding the many spectroscopic approaches presented. Therefore, a very brief introduction to some basic concepts of quantum mechanics is given below in Sect. 1.2, preceding Chaps. 2 and 3 in this edition of the book, to provide a better foundation for the contents of these chapters. This introduction intends to convey a brief idea about the concepts, even if it clearly by no means suffices as a basis for the formal theory of these chapters, and in particular not for the first part of Chap. 4, which is the most mathematical one in the book. That chapter deals with the fundamental radiative and scattering processes that are encountered in spectroscopy. However, the author believes that even if the details are not comprehended, the reader can appreciate the general ideas, and on this basis continue grasping the practicalities of spectroscopy. Chapter 5 is devoted to the study of inner electrons, while the techniques of basic and applied optical spectroscopy are treated in Chap. 6. Multi-spectral imaging is then also emphasized in this context. The precision methods of radio-frequency spectroscopy are described in Chap. 7. Finally, the last three chapters deal with lasers and their numerous applications to fundamental and applied spectroscopy.

1.2 Some Fundamentals of Quantum Mechanics

Quantum mechanics, as developed by *W. Heisenberg, E. Schrödinger, P. Dirac* (Nobel Prizes in Physics (NP) in 1932, 1933, and 1933, respectively), and others during the first half of the twentieth century mathematically describes the machinery in the micro-cosmic world of, for example, atoms, molecules, and solids, and has with its further refinements attained an astonishing perfection in describing physical phenomena. Classical mechanics, a field which has been well understood for a long time, describes large-scale phenomena such as the path of a stone which is thrown, or the launching of a satellite into an orbit around the earth. The negatively charged electron, moving around a positively charged proton (the nucleus) representing the most simple atom, hydrogen, can in a simple-minded picture be seen as a small orbiting satellite. The attractive forces follow very similar laws in both cases—so what is the difference? We will start our discussion with some very simple arguments.

The energy of the satellite is the sum of the potential (position) energy and the kinetic (motion) energy, which relates to its velocity. Depending on the launching velocity, a continuous range of energies, corresponding to increasing orbit radii can be obtained (Fig. 1.8a). In the hydrogen atom, the orbiting electron can be seen as a matter wave with a *de Broglie wavelength* λ_{dB}, which depends on the velocity v and the particle mass m [12]:

$$\lambda_{dB} = \frac{h}{mv}. \tag{1.5}$$

Here, h is the Planck constant. Since the mass is very small (e.g. in comparison to that of the satellite), the wavelength becomes appreciable. A possible velocity and thus energy state must correspond to a standing wave, i.e. the "orbit" must correspond to an integer number of matter wavelengths. Thus, only specific energies are possible for the electron, as indicated in Fig. 1.8b. We obtain a quantized system.

The origin of quantization taking the behaviour of waves into account can be further illustrated by the oscillation of a guitar string (Fig. 1.8c). If the string, of specific thickness/mass and tension, is brought to the side and then is released, a large number of oscillation frequencies could potentially have resulted. The string

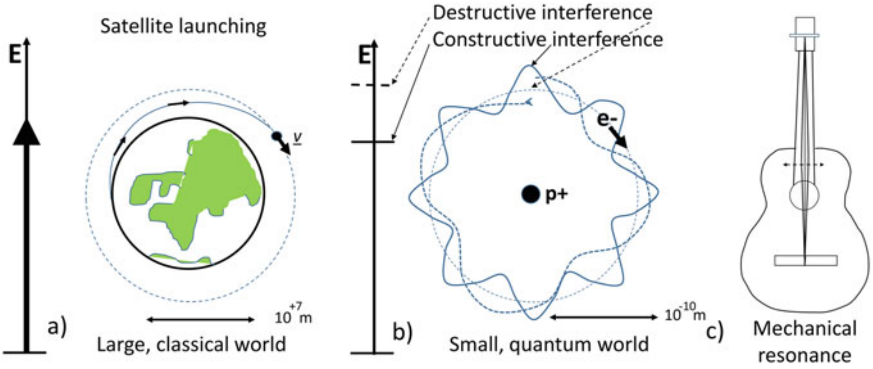

Fig. 1.8 Interacting systems: **a** a satellite orbiting the earth in the "large world" under the influence of gravitational attraction, depending on the launching velocity (above a minimum speed of about 8 km/s); the energy of the orbiting satellite can attain a continuous range of energies as indicated. **b** An electron orbiting a nucleus in the "small world" under the influence of electrostatic attraction. The electron, because of its wave nature and being subject to interference, can only be in "orbits" with discrete velocities, and thus discrete energies. **c** Guitar string oscillation only at fixed frequency

may "try" them all, but will very quickly "realize" that only the frequency corresponding to a standing wave (constructive interference) can be supported—even this large-scale system becomes quantized! Here, we deal with mechanical standing waves. An organ pipe can also only support specific standing acoustic waves. The quantum–mechanical de-Broglie waves are clearly of different origin, and the picture in Fig. 1.8b is extremely simplified, but can serve the purpose of illuminating the origin of quantization. The wave nature of systems as large as the C_{60} molecule [13] and certain very large complexes such as $C_{284}H_{190}F_{320}N_4S_{12}$, containing up to 810 atoms [14], has been experimentally demonstrated.

We illustrated in Fig. 1.8b that only energies corresponding to a standing wave can be supported—the wave returns onto itself in phase—constructive interference. This observation immediately leads to a further fundamental conclusion, which is sometimes expressed as the *Heisenberg uncertainty relation*: For the lowest state, which basically has an infinite lifetime, the energy, and thus the matter wavelength, must be extremely well defined, because of the many possible revolutions, leading to that even the slightest phase mismatch would ultimately work itself up to complete destructive interference. In contrast, a higher, excited state, which would exist for only a few nanoseconds before the electron returns to its lower state, could be less well-defined in energy and thus have slight phase mismatches, which would not be a problem for the existence of the state, since it would anyway persist only for a few non-perfect classical orbits. Thus, excited states are broadened in energy and the shorter the lifetime, the larger the broadening.

The particle–wave dualism, present for small particles, such as electrons, is also present in the same way for photons. Depending on the type of experiment performed, one or the other aspect is manifested as illustrated in Fig. 1.9. A light wave with a well-defined wavefront is shown in Fig. 1.9a falling in towards two slits, and the wave is propagating, according to Huygen's principle, in circular patterns, and interference,

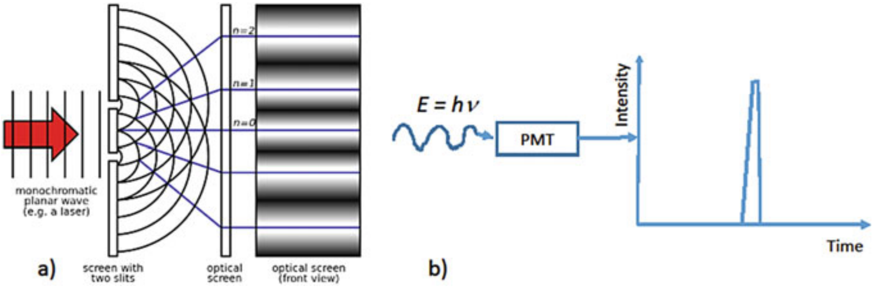

Fig. 1.9 The particle–wave dualism for photons. **a** Young's double-slit experiment clearly illustrates the wave nature of light—well-defined interference fringes are formed. *Source* https://commons.wikimedia.org/w/index.php?title=File:TwoSlit_Experiment_Light.svg&oldid=491041868 **b** A photomultiplier tube (PMT) records the arrival of individual light quanta by producing distinct electrical pulses

causing bright and dark fringes, occurs on a recording plate. This is the famous *Young double-slit experiment*.

In another experiment, shown in Fig. 1.9b, extremely weak light is impinging on a sensitive light detector, such as a photomultiplier tube (Sect. 6.3), and each photon gives rise to a discrete pulse, due to the released electrical charge. Interestingly, if the light intensity in the Young double-slit experiment is reduced to the single-photon detection case, the same interference pattern will occur in the statistical average [15].

Mathematically, energy structures in the micro-world are governed by the *Schrödinger equation*, which in a quantum–mechanical way basically describes the well-known truth that the total energy of a simple system, such as the ones shown in Fig. 1.8b, is equal to the sum of the kinetic energy and the potential energy:

$$\frac{1}{2m}p^2 + V(r) = E. \tag{1.6}$$

Here, $V(r)$ in a simple system, such as the hydrogen atom, is the Coulomb potential, which varies only with the distance r, and not with the polar angles ϕ and φ:

$$V(r) = -\frac{e^2}{4\pi\varepsilon_0 r}. \tag{1.7}$$

$p = mv$ is the linear momentum and m and v are the particle mass, and velocity, respectively. The quantum–mechanical expression is written as

$$\left[-\frac{\hbar^2}{2m}\varDelta + V(r)\right]\varPsi = E\varPsi. \tag{1.8}$$

Here, p has been replaced by a quantum–mechanical so-called *operator* $\boldsymbol{p}$, which is based on

$$p_x = i\hbar\frac{\partial}{\partial x} \tag{1.9}$$

and

$$\varDelta = \frac{\partial^2}{\partial x^2} + \frac{\partial^2}{\partial y^2} + \frac{\partial^2}{\partial z^2} \quad (\mathit{Laplace\ operator}). \tag{1.10}$$

The Schrödinger equation is mathematically a partial differential equation, which has a number of solutions, with corresponding *eigenvalues* E, which are the possible discrete energies of the system. The function $\varPsi$, on which the total operator (the *Hamiltonian*) acts, is called the *wave function*, and for each possible solution E_i, there is a corresponding wave function, called the *eigenfunction* $\varPsi_i$.

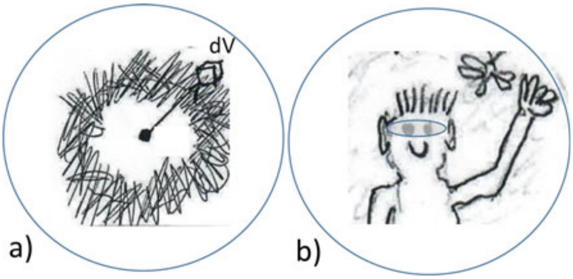

Fig. 1.10 **a** Probability interpretation of the wave function, describing where the electron might be located. **b** Mechanistic parallel to the probability interpretation for the case of catching a mosquito

It can be shown that when the potential energy only depends on r, i.e. $V(r)$, the solution of the Schrödinger equation can be separated into a radial part (only dependent on r) and an angular part (only dependent on the polar angles θ and φ).

$$\Psi(r, \Theta, \varphi) = P_n(r) Y_{lm}(\theta, \varphi), \tag{1.11}$$

where n, l, and m specify the function and are called quantum numbers.

The wavefunction has a very special and deep interpretation in terms of the probability to find the particle, i.e. the electron, somewhere around the nucleus, as shown in Fig. 1.10a.

The probability P to find the electron in the volume element dV is given by

$$P = |\Psi|^2 dV. \tag{1.12}$$

Thus, the higher the absolute value of the wave function is in a particular region, the larger the probability is to find the electron there. Clearly, the electron must be somewhere, so the integral over the whole space is equal to 1:

$$\int |\Psi|^2 \, dV = 1. \tag{1.13}$$

The situation is similar to the case depicted in Fig. 1.10b, where a blindfolded person tries to catch with his hand a single mosquito circulating around his head. It must be somewhere, but with a higher probability closer to the head.

It can be shown that for a given value of the principal quantum number n, the corresponding angular wave functions for the limited number of matching l and m values fulfil the relation

$$\sum\nolimits_{l,m} \left|Y_{l,m}(\theta, \varphi)\right|^2 = Const. \tag{1.14}$$

meaning that a spherically symmetric angular distribution results for the sum of the electrons having the same value on n. A simple illustration for the case of two distributions is shown in Fig. 1.11. The probability is the same in different directions

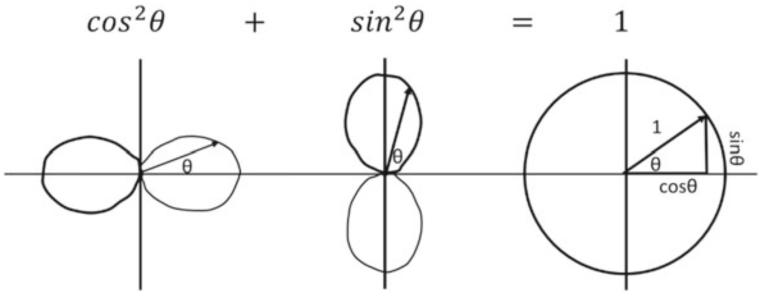

Fig. 1.11 Illustration in two dimensions of how two different angular probability distributions can add up to a distribution, which is symmetric. The extension is the occurrence of spherically symmetric closed shells, explaining the periodic system of the atoms

around the centre. As we will see in Chap. 2, this leads to the formation of closed, spherically symmetric electron subshells for a certain number of electrons, and a great simplification in understanding atoms is obtained, including the explanation of the existence of a periodic system of the atoms.

Chapter 2
Atomic Structure

A brief account of the energy-level structure of atomic systems as described by quantum mechanics will be given in this chapter. The atomic structures that are explored with the spectroscopic techniques discussed in this text will be described. The reader is referred to standard textbooks on atomic physics and quantum mechanics for a more complete treatment [16–46].

2.1 One-Electron Systems

In hydrogen and hydrogen-like systems, a single electron moves around the nucleus of charge Ze at a distance r in a *central field*, and its potential energy is given by

$$V(r) = -\frac{Ze^2}{4\pi\epsilon_0 r}. \tag{2.1}$$

The simplest case of hydrogen, with $Z = 1$, was already treated in the introduction to quantum mechanics in Sect. 1.2. The Hamiltonian, describing the total energy of the single-electron system is

$$\mathcal{H}_0 = \frac{1}{2m}\boldsymbol{p}^2 + V(r) \tag{2.2}$$

($\boldsymbol{p}$ is the momentum operator, m is the electron mass) and the energy eigenvalues are obtained by solving the Schrödinger equation, as already discussed above

$$\left[-\frac{\hbar^2}{2m}\Delta + V(r)\right]\psi = \mathrm{E}\psi \tag{2.3}$$

© The Author(s), under exclusive license to Springer Nature Switzerland AG 2022

S. Svanberg, *Atomic and Molecular Spectroscopy*, Graduate Texts in Physics,
https://doi.org/10.1007/978-3-031-04776-3_2

(Δ is the Laplace operator, and $\hbar = h/2\pi$). The eigenvalues depend only on the principal quantum number n and are independent of the azimuthal quantum number l and its projection m

$$E_\mathrm{n} = -hc\mathrm{Ry}\frac{Z^2}{n^2}(n = 1, 2, 3, \ldots), \tag{2.4}$$

where Ry is the Rydberg constant

$$\mathrm{Ry} = \frac{me^4}{4\pi(4\pi\epsilon_0)^2 c\hbar^3}. \tag{2.5}$$

However, the l and m values specify the wavefunctions, and thus the probability distributions for finding the electron, and the states are labelled according to

$$\begin{array}{llllll} l = 0 & 1 & 2 & 3 & 4 & 5 \\ s & p & d & f & g & h. \end{array}$$

If relativistic and quantum electrodynamic (QED) effects are considered, the far-reaching degeneracy for hydrogen-like systems is lifted. The simple energy-level diagram of hydrogen is shown in Fig. 2.1.

Besides hydrogen, hydrogen-like ions [47] and positronium (positron + electron) and muonium (proton + muon) [48–50] have been much studied since they constitute good testing grounds for advanced theories.

2.2 Alkali Atoms

Alkali atoms have a single electron outside a spherically symmetric inner electron cloud (core, as described by Eq. 1.14). The field in which the outer electron moves is not Coulombic, but is still essentially central. The energy for such a system can be written as

$$E = -\frac{hc\mathrm{Ry}}{n_\mathrm{eff}^2}, \tag{2.6}$$

where $n_\mathrm{eff} = n - d$ is called the *effective quantum number* and d the *quantum defect*. The s electrons may penetrate into the core (they can even be found at the surface, or even inside the nucleus), thus experiencing an increased force from the less shielded nucleus, which results in a stronger binding. This behaviour is reflected in the quantum defect, which for s electrons is about 2. For high-l orbits (*non-penetrating electrons*), the quantum defect approaches zero, and the situation is hydrogen-like.

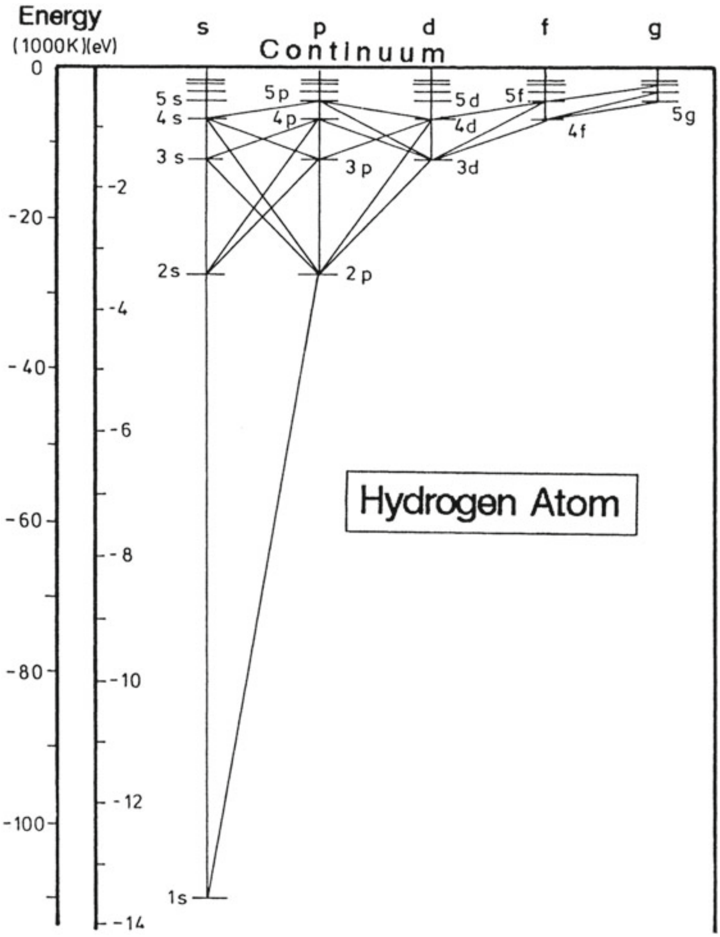
Energy
(1000K)(eV)
s
p
d
f
g
Continuum
0
-20
-40
-60
-80
-100
-2
-4
-6
-8
-10
-12
-14
5s
4s
3s
2s
1s
5p
4p
3p
2p
5d
4d
3d
5f
4f
5g
Hydrogen Atom

Fig. 2.1 Energy level diagram of the hydrogen atom [1]

These effects are illustrated in the case of sodium in Fig. 2.2. The 5g, 5f, and 5d levels are basically at the hydrogen position, while the 5p electron partially dives into the core electron cloud and is less shielded; binding stronger to the central charge. The 5s electron is even more strongly pulled down in the central potential.

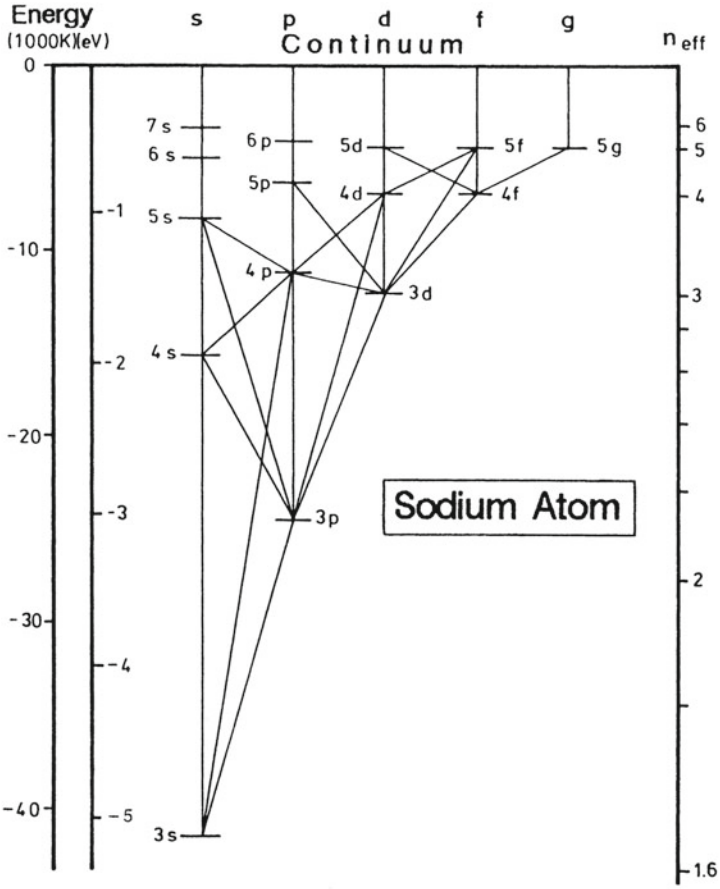
Energy
(1000K)(eV)
s
p
d
f
g
Continuum
n eff
0
-10
-20
-30
-40
-1
-2
-3
-4
-5
7 s
6 s
5 s
4 s
3 s
6 p
5p
4 p
3p
5d
4d
3d
5f
4f
5g
Sodium Atom
6
5
4
3
2
1.6

Fig. 2.2 Energy level diagram of the sodium atom [1]

2.3 Magnetic Effects

2.3.1 Precessional Motion

An angular momentum vector $\boldsymbol{L}$, associated with a magnetic moment $\boldsymbol{\mu}_{\mathrm{L},}$ will precess in a magnetic field, as illustrated in Fig. 2.3. We frequently encounter this phenomenon in the description of atomic and molecular processes. To demonstrate the phenomenon, imagine magnetic poles q in analogy with the electrical case of positive and negative charges, for which we have the same mathematical description. We then have the mechanical moment $\boldsymbol{M}$ defined as

$$|\boldsymbol{M}| = q\,B\frac{d}{2}\sin\,\theta + q\,B\frac{d}{2}\sin\theta = q\,B\,d\sin\theta, \tag{2.7}$$

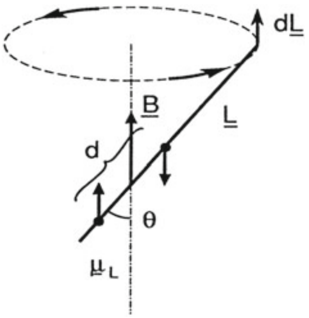

Fig. 2.3 Precession of an angular momentum vector and an associated magnetic moment in the magnetic field

that is

$$\boldsymbol{M} = \boldsymbol{\mu}_L \times \boldsymbol{B} \text{ with } |\boldsymbol{\mu}_L| = qd. \tag{2.8}$$

But

$$\boldsymbol{\mu}_L = -g\mu_\mathrm{B}\boldsymbol{L}, \tag{2.9}$$

where μ_B is the *Bohr magneton* and g is a positive constant of proportionality. The minus sign is due to the electron having a negative charge. (Throughout this book we use dimensionless angular momentum vectors. μ_B has the dimension of a magnetic moment.) The classical mechanical laws of motion then yield

$$\frac{\mathrm{d}\boldsymbol{L}}{\mathrm{d}t} = \boldsymbol{M} = -g\mu_\mathrm{B}\boldsymbol{L} \times \boldsymbol{B}. \tag{2.10}$$

Thus

$$\mathrm{d}\boldsymbol{L} = -(g\mu_\mathrm{B}\boldsymbol{L} \times \boldsymbol{B})\mathrm{d}t, \tag{2.11}$$

showing that the tip of $\boldsymbol{L}$ moves perpendicularly to both $\boldsymbol{L}$ and $\boldsymbol{B}$, i.e. $\boldsymbol{L}$ precesses *around* $\boldsymbol{B}$ with an angular frequency $\omega = g\mu_\mathrm{B}B$.

The magnetic precession has many similarities with the mechanical precession of a small toy gyro, which has been spun up to high speed and placed on a support. Instead of just falling down due to the gravitational force, it precesses around the direction of the gravitational force. Likewise, instead of aligning itself with the magnetic field (which a compass needle would do), the atom, seen as a small magnet, importantly associated with angular momentum, precesses around the field direction.

2.3.2 Spin–Orbit Interaction

The electron has a spin angular momentum $\boldsymbol{s}$ and an associated magnetic moment $\boldsymbol{\mu}_{\mathbf{s}}$, i.e.

$$\boldsymbol{\mu}_s = -g_s \mu_{\mathrm{B}} \boldsymbol{S}. \tag{2.12}$$

Again, the minus sign is due to the electron having a negative charge. As the electron moves in the electric field of the nucleus, it is subject to a magnetic field $\boldsymbol{B}_l$, which is proportional to the angular momentum $\boldsymbol{l}$ of the electron (Fig. 2.4). The electron magnet then has an orientational energy E_{so} in the field equal to the force qB times the distance $(1/2)d\ \cos\theta$, that each magnetic "pole" q has been displaced in the field; i.e. $2qb(1/2)d\cos\theta$,which can be written as a scalar product

$$E_{\mathrm{so}} = -\boldsymbol{\mu}_{\mathbf{s}} \cdot \boldsymbol{B}_l = \zeta \boldsymbol{l} \cdot \boldsymbol{s}, . \tag{2.13}$$

where ζ is a constant of proportionality, and the energy zero point is defined for $\boldsymbol{\mu}_s$ and $\boldsymbol{B}_l$ being perpendicular. $\boldsymbol{l}$ and $\boldsymbol{s}$ couple and precess about their mutual resultant $\boldsymbol{j}$ with a frequency proportional to the strength of the field. We have

$$\boldsymbol{j} = \boldsymbol{l} + \boldsymbol{s}. \tag{2.14}$$

For the corresponding quantum numbers describing the length of the vector (e.g. $|\boldsymbol{j}| = [j(j+1)]^{1/2}$, dimensionless angular momentum; the normally occurring $h/2\pi$ in the length expression of an angular momentum vector is included in ζ !), we have

$$\begin{aligned} s &= 1/2, \\ l &= 0, 1, 2, \ldots, \\ j &= l \pm 1/2. \end{aligned}$$

Using the vector cosine theorem

$$\boldsymbol{j}^2 = (\boldsymbol{l} + \boldsymbol{s})^2 = \boldsymbol{l}^2 + \boldsymbol{s}^2 + 2\boldsymbol{l} \cdot \boldsymbol{s}$$

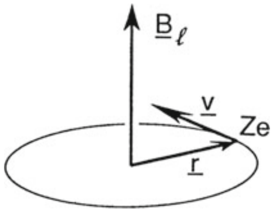

Fig. 2.4 Magnetic field associated with orbital motion [1]

Table 2.1 Fine-structure splittings in ^2P states of the alkali atoms (cm^{-1})

n	Na	K	Rb	Cs
3	17			
4	5.6	58		
5	2.5	19	238	
6	1.2	8.4	78	554
7	0.7	4.5	35	181
8	0.4	2.7	19	83
9		1.7	11	45
10		1.2	7	27

we obtain

$$E_{\text{so}} = \zeta[j(j+1) - l(l+1) - s(s+1)]/2. \tag{2.15}$$

Here we have inserted the "quantum-mechanical squares" or, to use a more modern term, used first-order perturbation theory. The so-called *fine-structure splitting* between the two possible j levels is given by

$$\Delta \mathrm{E}_{\text{so}} = \zeta(l + 1/2). \tag{2.16}$$

ζ is found to be a positive quantity and scaling as $1/n_{\text{eff}}^3$ in a simple calculation. The high-j level then has higher energy than the low-j level. This is found to be true for p-states of alkali atoms, and in Table 2.1, some experimentally determined fine-structure splittings are given. *Level inversion* sometimes occurs for $l > 1$, i.e. the high-j level has the lower energy. This is due to *core polarization*. The outer electron polarizes the closed shells so that a dominating, oppositely directed magnetic field contribution is obtained from these shells. The origin is the quantum-mechanical phenomenon of an exchange interaction only between electrons with the same spin state, leading to an imbalance between electrons in the otherwise closed shells. The level ordering for the alkali atoms doublets is indicated in Fig. 2.5.

2.4 General Many-Electron Systems

The structure of the general many-electron system with i electrons is obviously much more difficult to calculate. As a starting point, the following approximate Hamiltonian is used:

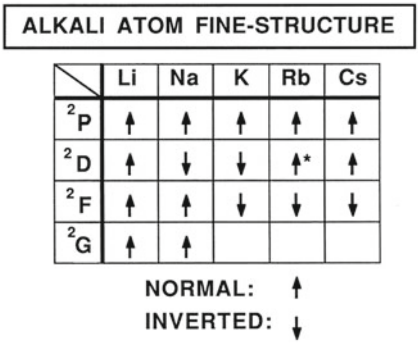

ALKALI ATOM FINE-STRUCTURE

	Li	Na	K	Rb	Cs
^{2}P	↑	↑	↑	↑	↑
^{2}D	↑	↓	↓	↑*	↑
^{2}F	↑	↑	↓	↓	↓
^{2}G	↑	↑			

NORMAL: ↑
INVERTED: ↓

Fig. 2.5 Level ordering in alkali atom doublet series. (The asterisk* indicates that the lowest member of the Rubidium series is inverted)

$$\mathcal{H} = \sum_i \left(\frac{1}{2m} \boldsymbol{p}_i^2 - \frac{Ze^2}{4\pi\epsilon_0 r_i} \right) + \sum_{i<j} \frac{e^2}{4\pi\epsilon_0 r_{ij}} + \sum_i \zeta_i(r_i) \boldsymbol{l}_i \cdot \boldsymbol{s}_i \qquad (2.17)$$

Here r_{ij} is the distance between the electrons i and j. As an approximation to (2.17), we assume that every electron moves independently of the other electrons in an average field, generated by the nucleus and the other electrons (the *independent particle model*). The field is assumed to be *central* (dependent only on r). This is the *central-field approximation*. The assumption of a central field combined with the *Pauli exclusion principle* results in a shell structure for the electrons and successively heavier elements can be constructed using the building-up principle (the total energy is minimized). The atom can be characterized by its *electron configuration*; e.g. for the lowest state of sodium, we have

$$1s^2 2s^2 2p^6 3s.$$

The ground configurations of the atoms are listed in Table 2.2. Obviously, the field in atoms is only approximately central. Besides a *central* part, the electrostatic repulsion between electrons causes a *non-central* contribution, which can be treated as a perturbation. The spin–orbit interaction must also be taken into account. If the non-central electrostatic part strongly dominates over the spin–orbit interaction, the latter is neglected as a first approximation. A coupling between the individual angular momenta is then obtained

$$\boldsymbol{L} = \sum_i \boldsymbol{l}_i, \ \boldsymbol{S} = \sum_i \boldsymbol{s}_i. \qquad (2.18)$$

Depending on which values are possible for the corresponding quantum numbers L and S for a certain configuration, a number of electrostatically split *terms* are obtained. Such terms are designated

Table 2.2 Ground configurations of atoms [16]

Atomic number Z	Element		Shells												LS configuration of the ground state	First ionization potential [eV]	
			K $n=1$	L $n=2$		M $n=3$			N $n=4$			O $n=5$					
			s	s	p	s	p	d	s	p	d	s	p				
1	Hydrogen	H	1												$^2S_{1/2}$	13.60	
2	Helium	He	2												$^1S_0$	24.58	
3	Lithium	Li	2	1											$^2S_{1/2}$	5.39	
4	Beryllium	Be	2	2											$^1S_0$	9.32	
5	Boron	B	2	2	1										$^2P_{1/2}$	8.30	
6	Carbon	C	2	2	2										$^3P_0$	11.26	
7	Nitrogen	N	2	2	3										$^4S_{3/2}$	14.54	
8	Oxygen	O	2	2	4										$^3P_2$	13.61	
9	Fluorine	F	2	2	5										$^2P_{3/2}$	17.42	
10	Neon	Ne	2	2	6										$^1S_0$	21.56	
11	Sodium	Na	2	2	6	1									$^2S_{1/2}$	5.14	
12	Magnesium	Mg	2	2	6	2									$^1S_0$	7.64	
13	Aluminium	Al	2	2	6	2	1								$^2P_{1/2}$	5.98	
14	Silicon	Si	2	2	6	2	2								$^3P_0$	8.15	
15	Phosphorous	P	2	2	6	2	3								$^4S_{3/2}$	10.55	
16	Sulphur	S	2	2	6	2	4								$^3P_2$	10.36	
17	Chlorine	Cl	2	2	6	2	5								$^2P_{3/2}$	13.01	
18	Argon	Ar	2	2	6	2	6								$^1S_0$	15.76	
19	Potassium	K	2	2	6	2	6		1						$^2S_{1/2}$	4.34	
20	Calcium	Ca	2	2	6	2	6		2						$^1S_0$	6.11	
21	Scandium	Sc	2	2	6	2	6	1	2						$^2D_{3/2}$	6.56	Transition elements
22	Titanium	Ti	2	2	6	2	6	2	2						$^3F_2$	6.83	
23	Vanadium	V	2	2	6	2	6	3	2						$^4F_{3/2}$	6.74	
24	Chromium	Cr	2	2	6	2	6	5	1						$^7S_3$	6.76	
25	Manganese	Mn	2	2	6	2	6	5	2						$^6S_{5/2}$	7.43	
26	Iron	Fe	2	2	6	2	6	6	2						$^5D_4$	7.90	
27	Cobalt	Co	2	2	6	2	6	7	2						$^4F_{9/2}$	7.86	
28	Nickel	Ni	2	2	6	2	6	8	2						$^3F_4$	7.63	
29	Copper	Cu	2	2	6	2	6	10	1						$^2S_{1/2}$	7.72	
30	Zinc	Zn	2	2	6	2	6	10	2						$^1S_0$	9.39	
31	Gallium	Ga	2	2	6	2	6	10	2	1					$^2P_{1/2}$	6.00	
32	Germanium	Ge	2	2	6	2	6	10	2	2					$^3P_0$	7.88	
33	Arsenic	As	2	2	6	2	6	10	2	3					$^4S_{3/2}$	9.81	
34	Selenium	Se	2	2	6	2	6	10	2	4					$^3P_2$	9.75	
35	Bromine	Br	2	2	6	2	6	10	2	5					$^2P_{3/2}$	11.84	
36	Krypton	Kr	2	2	6	2	6	10	2	6					$^1S_0$	14.00	
37	Rubidium	Rb	2	2	6	2	6	10	2	6		1			$^2S_{1/2}$	4.18	
38	Strontium	Sr	2	2	6	2	6	10	2	6		2			$^1S_0$	5.69	
39	Yttrium	Y	2	2	6	2	6	10	2	6	1	2			$^2D_{3/2}$	6.38	Transition elements
40	Zirconium	Zr	2	2	6	2	6	10	2	6	2	2			$^3F_2$	6.84	
41	Niobium	Nb	2	2	6	2	6	10	2	6	4	1			$^6D_{1/2}$	6.88	
42	Molybdenum	Mo	2	2	6	2	6	10	2	6	5	1			$^7S_3$	7.13	
43	Technetium	Tc	2	2	6	2	6	10	2	6	6	1			$^6D_{9/2}$	7.23	
44	Ruthenium	Ru	2	2	6	2	6	10	2	6	7	1			$^5F_5$	7.37	
45	Rhodium	Rh	2	2	6	2	6	10	2	6	8	1			$^4F_{9/2}$	7.46	
46	Palladium	Pd	2	2	6	2	6	10	2	6	10				$^1S_0$	8.33	
47	Silver	Ag	2	2	6	2	6	10	2	6	10	1			$^2S_{1/2}$	7.57	
48	Cadmium	Cd	2	2	6	2	6	10	2	6	10	2			$^1S_0$	8.99	
49	Indium	In	2	2	6	2	6	10	2	6	10	2	1		$^2P_{1/2}$	5.79	
50	Tin	Sn	2	2	6	2	6	10	2	6	10	2	2		$^3P_0$	7.33	
51	Antimony	Sb	2	2	6	2	6	10	2	6	10	2	3		$^4S_{3/2}$	8.64	
52	Tellurium	Te	2	2	6	2	6	10	2	6	10	2	4		$^3P_2$	9.01	
53	Iodine	J	2	2	6	2	6	10	2	6	10	2	5		$^2P_{3/2}$	10.44	
54	Xenon	Xe	2	2	6	2	6	10	2	6	10	2	6		$^1S_0$	12.13	

(continued)

Table 2.2 (continued)

Atomic number Z	Element		Shells												LS configuration of the ground state	First ionization potential [eV]	
			N $n=4$				O $n=5$				P $n=6$			Q $n=7$			
			s	p	d	f	s	p	d	f	s	p	d	s			
55	Cesium	Cs	2	6	10		2	6			1				$^2S_{1/2}$	3.89	
56	Barium	Ba	2	6	10		2	6			2				$^1S_0$	5.21	
57	Lanthanum	La	2	6	10		2	6	1		2				$^2D_{3/2}$	5.61	Rare earths
58	Cerium	Ce	2	6	10	2	2	6			2				$^3H_4$	5.6	
59	Praseodymium	Pr	2	6	10	3	2	6			2				$^4I_{9/2}$	5.46	
60	Neodymium	Nd	2	6	10	4	2	6			2				$^5I_4$	5.51	
61	Promethium	Pm	2	6	10	5	2	6			2				$^6H_{5/2}$		
62	Samarium	Sm	2	6	10	6	2	6			2				$^7F_0$	5.6	
63	Europium	Eu	2	6	10	7	2	6			2				$^8S_{7/2}$	5.67	
64	Gadolinium	Gd	2	6	10	7	2	6	1		2				$^9D_2$	6.16	
65	Terbium	Tb	2	6	10	9	2	6			2				—	5.98	
66	Dysprosium	Dy	2	6	10	10	2	6			2				$^5I_8$	6.8	
67	Holmium	Ho	2	6	10	11	2	6			2				$^4I_{15/2}$		
68	Erbium	Er	2	6	10	12	2	6			2				$^3H_6$	6.08	
69	Thulium	Tm	2	6	10	13	2	6			2				$^2F_{7/2}$	5.81	
70	Ytterbium	Yb	2	6	10	14	2	6			2				$^1S_0$	6.22	
71	Lutetium	Lu	2	6	10	14	2	6	1		2				$^2D_{3/2}$	6.15	Transition elements
72	Hafnium	Hf	2	6	10	14	2	6	2		2				$^3F_2$	5.5	
73	Tantalum	Ta	2	6	10	14	2	6	3		2				$^4F_{3/2}$	7.7	
74	Tungsten	W	2	6	10	14	2	6	4		2				$^5D_0$	7.98	
75	Rhenium	Re	2	6	10	14	2	6	5		2				$^6S_{5/2}$	7.87	
76	Osmium	Os	2	6	10	14	2	6	6		2				$^5D_4$	8.7	
77	Iridium	Ir	2	6	10	14	2	6	9						$^2D_{5/2}$	9.2	
78	Platinum	Pt	2	6	10	14	2	6	9		1				$^3D_3$	9.0	
79	Gold	Au	2	6	10	14	2	6	10		1				$^2S_{1/2}$	9.22	
80	Mercury	Hg	2	6	10	14	2	6	10		2				$^1S_0$	10.43	
81	Thallium	Tl	2	6	10	14	2	6	10		2	1			$^2P_{1/2}$	6.11	
82	Lead	Pb	2	6	10	14	2	6	10		2	2			$^3P_0$	7.42	
83	Bismuth	Bi	2	6	10	14	2	6	10		2	3			$^4S_{3/2}$	7.29	
84	Polonium	Po	2	6	10	14	2	6	10		2	4			$^3P_2$	8.43	
85	Astatine	At	2	6	10	14	2	6	10		2	5				9.5	
86	Radon	Rn	2	6	10	14	2	6	10		2	6			$^1S_0$	10.75	
87	Francium	Fr	2	6	10	14	2	6	10		2	6		1		4	
88	Radium	Ra	2	6	10	14	2	6	10		2	6		2		5.28	
89	Actinium	Ac	2	6	10	14	2	6	10		2	6	1	2			Actinides
90	Thorium	Th	2	6	10	14	2	6	10		2	6	2	2			
91	Protactinium	Pa	2	6	10	14	2	6	10	2	2	6	1	2			
92	Uranium	U	2	6	10	14	2	6	10	3	2	6	1	2			
93	Neptunium	Np	2	6	10	14	2	6	10	4	2	6	1	2			
94	Plutonium	Pu	2	6	10	14	2	6	10	6	2	6		2			
95	Americium	Am	2	6	10	14	2	6	10	7	2	6		2			
96	Curium	Cm	2	6	10	14	2	6	10	7	2	6	1	2			
97	Berkelium	Bk	2	6	10	14	2	6	10	8	2	6	1	2			
98	Californium	Cf	2	6	10	14	2	6	10	10	2	6		2			
99	Einsteinium	Es	2	6	10	14	2	6	10	11	2	6		2			
100	Fermium	Fm	2	6	10	14	2	6	10	12	2	6		2			
101	Mendelevium	Md	2	6	10	14	2	6	10	13	2	6		2			
102	Nobelium	No	2	6	10	14	2	6	10	14	2	6		2			
103	Lawrencium	Lw	2	6	10	14	2	6	10	14	2	6	1	2			
104	Kurchatovium		2	6	10	14	2	6	10	14	2	6	2	2			
105	Hahnium		2	6	10	14	2	6	10	14	2	6	3	2			

$$^{2S+1}X.$$

The quantity $2S + 1$ is called *multiplicity*. In analogy with the one-electron case, we have

$$\begin{aligned} L &= 0\ 1\ 2\ 3\ 4 \\ X &= S\ P\ D\ F\ G. \end{aligned}$$

This type of coupling is called *LS coupling*.

The spins of two electrons can be arranged such that $S = 0$ (singlet state) or $S = 1$ (triplet state). The energy-level diagram for helium is shown (ground configuration $1s^2$) in Fig. 2.6. The alkaline-earth atoms Be, Mg, Ca, Sr, and Ba in their ground configuration all have two s electrons in the outer shell, and thus have similar energy-level diagrams. As an example, the energy-level diagram for calcium is given in Fig. 2.7. Zn, Cd, and Hg also have similar energy-level schemes as they also have two electrons in the outer shell.

Coupling the individual orbital and spin angular momenta to the resultants $\boldsymbol{L}$ and $\boldsymbol{S}$ is more complicated for atoms with more electrons in the outer shell. For electrons of the same type (e.g., p electrons), it is important to distinguish between *equivalent* electrons (n quantum numbers also the same) or *non-equivalent* electrons. The Pauli principle strongly reduces the number of possible states in the former case. The *LS* terms obtained for different electron configurations are listed in Table 2.3.

The description *LS* coupling may be somewhat confusing as there is primarily no spin–orbit interaction. However, we can now introduce this interaction as an additional, small perturbation. Through this perturbation, $\boldsymbol{L}$ and $\boldsymbol{S}$ couple to produce a resulting $\boldsymbol{J}$. As magnetic fields and magnetic moments can be associated with both $\boldsymbol{L}$ and $\boldsymbol{S}$, there should, according to Sect. 2.3.1, be a precession of $\boldsymbol{L}$ about $\boldsymbol{S}$ and of $\boldsymbol{S}$ about $\boldsymbol{L}$. As none of the vectors is fixed in space, a precession about the resultant $\boldsymbol{J}$ occurs as shown in Fig. 2.8. For the corresponding J quantum number, we have the relation

$$J = L + S, L + S - 1, \ldots\ldots. |L - S|. \tag{2.19}$$

In analogy with the one-electron case, we have

$$E_{\mathrm{so}} = A(L, S)[J(J + 1) - L(L + 1) - S(S + 1)]/2. \tag{2.20}$$

We have the *Landé interval rule* for the interval ΔE_{so}

$$\Delta E_{\mathrm{so}(J,J-1)} = AJ. \tag{2.21}$$

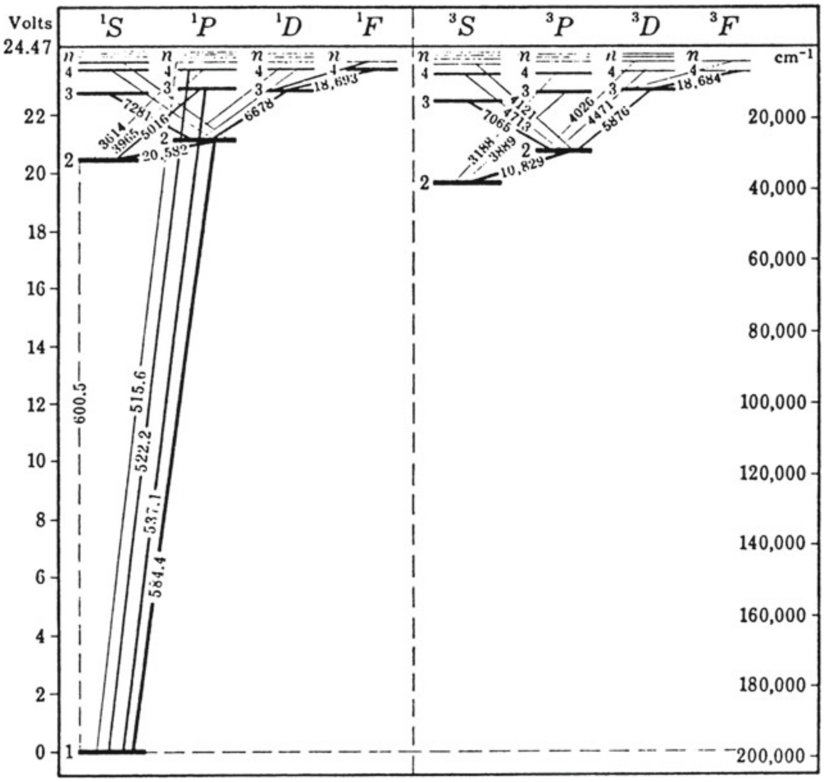
Volts
24.47
22
20
18
16
14
12
10
8
6
4
2
0
^1S
^1P
^1D
^1F
^3S
^3P
^3D
^3F
n
4
3
2
1
cm^{-1}
20,000
40,000
60,000
80,000
100,000
120,000
140,000
160,000
180,000
200,000
7281
3614
3965
5016
20,582
6678
18,693
600.5
515.6
522.2
537.1
584.4
4121
4713
7066
3188
3889
10,829
4026
4471
5876
18,684

Fig. 2.6 Energy level diagram for the helium atom [21]. Transition wavelengths are given in Ångström (1 Å = 0.1 nm)

The resulting energy levels for the case of two equivalent *p* electrons in *LS* coupling are shown in the left-hand part of Fig. 2.9.

If, contrary to what was assumed above, the spin–orbit interaction dominates over the non-central electrostatic interaction, we obtain primarily a coupling between the orbital and spin angular momenta of the individual electrons

$$\boldsymbol{j}_i = \boldsymbol{l}_i + \boldsymbol{s}_i \tag{2.22}$$

We talk about *jj coupling* in this case. If the weaker electrostatic interaction is then applied, the individual $\boldsymbol{j}_i$ momenta couple to form a resultant $\boldsymbol{J}$. The resulting energy-level diagram is quite different compared to the case of *LS* coupling (i.e. there is no interval rule). In the right-hand part of Fig. 2.9, the *jj* structure for two equivalent *p* electrons is shown. There is generally *LS* coupling in the outer shells of light elements, whereas *jj* coupling is typically exhibited by the inner shells of heavy atoms. In general, the situation is an inter-mediate one of the two cases described and *intermediate coupling* arises. By experimentally determining the relative positions of the

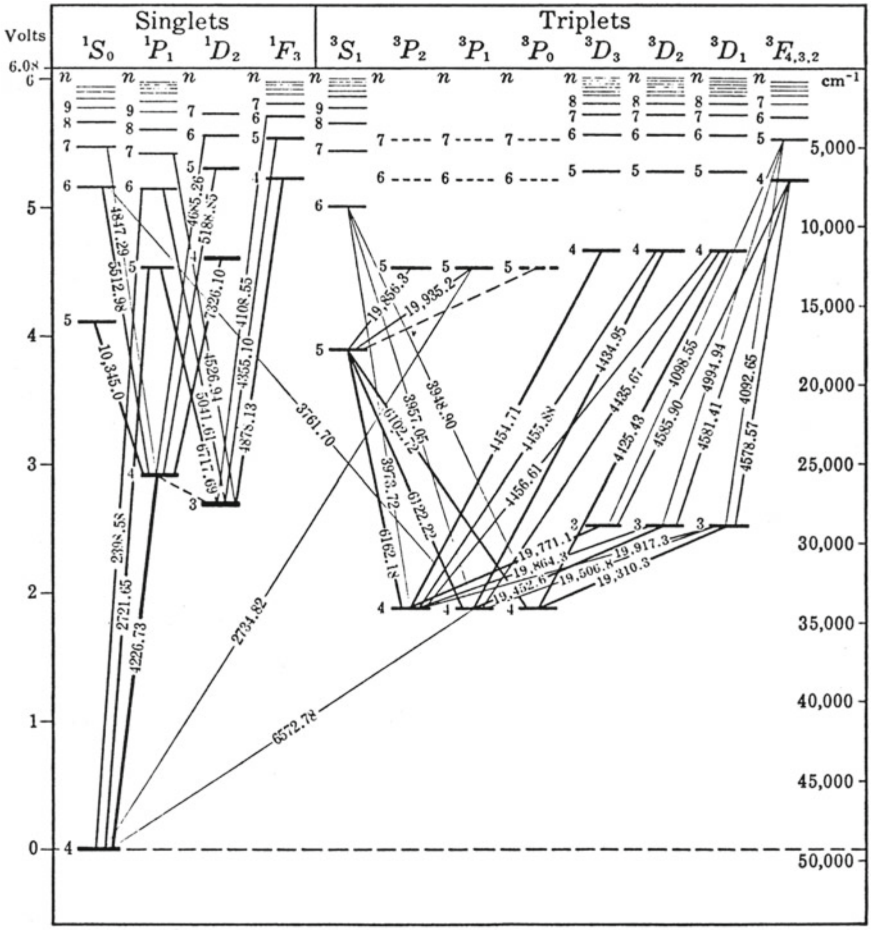
Volts
Singlets
Triplets
$^1S_0$
$^1P_1$
$^1D_2$
$^1F_3$
$^3S_1$
$^3P_2$
$^3P_1$
$^3P_0$
$^3D_3$
$^3D_2$
$^3D_1$
$^3F_{4,3,2}$
n
cm^{-1}
6.08
6
5
4
3
2
1
0
5,000
10,000
15,000
20,000
25,000
30,000
35,000
40,000
45,000
50,000
4847.29
5512.98
10,345.0
4685.26
5188.85
7326.10
4108.55
4355.10
4526.94
5041.61
6717.69
4878.13
2398.58
2721.65
4226.73
3761.70
2734.82
6572.78
19,856.3
19,935.2
3948.90
3957.05
6102.72
3973.72
6122.22
6162.18
4454.71
4455.88
4456.61
4434.95
4435.67
4425.43
4098.55
4585.90
4994.94
4581.41
4092.65
4578.57
19,771.1
19,864.3
19,917.3
19,506.8
19,452.6
19,310.3

Fig. 2.7 Energy level diagram for the calcium atom [21]. Transition wavelengths are given in Ångström (1 Å = 0.1 nm)

energy levels of a given configuration using spectroscopy, the coupling conditions can be investigated. The energy-level diagrams and level designations of atoms and singly and multiply ionized atoms have been determined in a process that is still continuing. A lot of this material is collected in [51–58]. Theoretical calculations, employing *self-consistent field* methods, and other advanced techniques for describing the basic atomic energy-level structure, have been described in [22, 59–65]. The energy-level structure for atoms with two outer electrons is frequently parametrized using the so-called *multichannel quantum defect theory* (MQDT) [66–71].

Table 2.3 Examples of *LS* terms for some configurations. The designation ^{1}D(2) means that there are two ^1D terms [21]

Electron configuration	Terms
Equivalent	
s^2	^1S
p^2	^1S,^1D, ^3P
p^3	^2P, ^2D, ^4S
p^4	^1S, ^1D, ^3P
p^5	^2P
p^6	^1S
d^2	^1S, ^1D, ^1G, ^3P, ^3F
d^3	^2P, $^2D(2)$, ^2F, ^2G, ^2H, ^4P, ^4F
d^4	$^1S(2)$, $^1D(2)$, ^1F, $^1G(2)$, ^1I, $^3P(2)$, ^3D, $^3F(2)$, ^3G, ^3H, ^5D
d^5	^2S, ^2P, $^2D(3)$, $^2F(2)$, $^2G(2)$, ^2H, ^2I, ^4P, ^4D, ^4F, ^4G, ^6S
Non-equivalent	
$s\ s$	^1S, ^3S
$s\ p$	^1P, ^3P
$s\ d$	^1D, ^3D
$p\ p$	^1S, ^1P, ^1D, ^3S, ^3P, ^3D
$p\ d$	^1P, ^1D, ^1F, ^3P, ^3D, ^3F
$d\ d$	^1S, ^1P, ^1D, ^1F, ^1G, ^3S, ^3P, ^3D, ^3F, ^3G

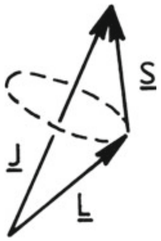

Fig. 2.8 Precession of ***L*** and ***S*** about ***J***

2.5 The Influence of External Fields

Since the particles making up the atoms have magnetic moments, and since the charged electrons describe "orbits" around the nucleus, the atom as a whole has magnetic properties (has a resulting magnetic moment) and is influenced by external magnetic fields. In the same way, the negatively charged electron cloud will be displaced with regard to the positive nuclear charge (will obtain an electric dipole moment) under the influence of an external electric field, and then get orientational energy in that field.

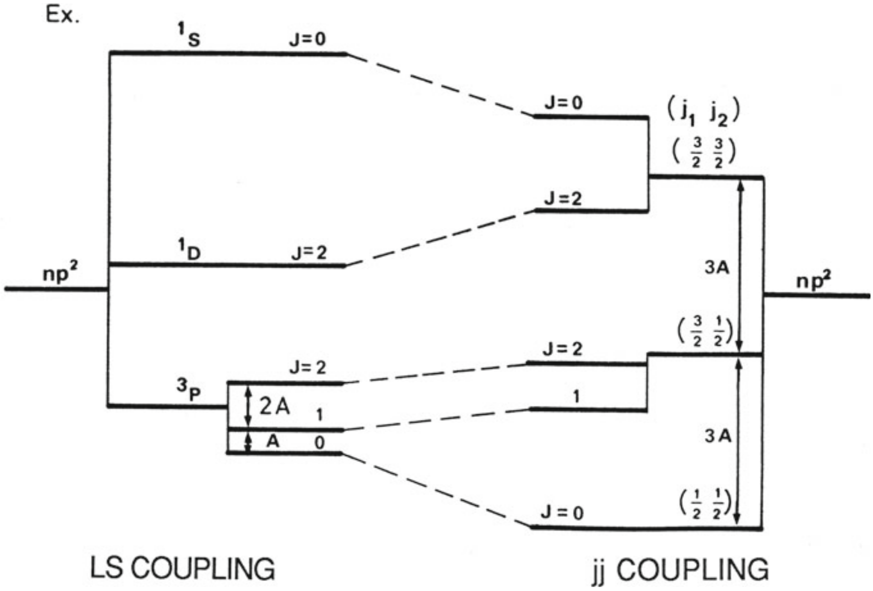

Fig. 2.9 Coupling conditions for two equivalent *p* electrons [1]

2.5.1 Magnetic Fields

First, consider an atom with only one electron outside the closed shells. The atom is situated in a homogeneous magnetic field $\boldsymbol{B}$**,** which is *weak*. The meaning of the word “weak” will be clarified later. Associated with the orbital and spin motions, there are magnetic moments; see (2.9), i.e.

$$\boldsymbol{\mu}_{\mathrm{s}} = -g_s \mu_{\mathrm{B}} \boldsymbol{s}, \tag{2.23}$$

$$\boldsymbol{\mu}_l = -g_l \mu_{\mathrm{B}} \boldsymbol{l}. \tag{2.24}$$

It has been found that $g_s = 2$ (apart from a 0.1% correction due to quantum electrodynamics) and $g_l = 1$. The spin–orbit interaction causes a precession of $\boldsymbol{s}$ and $\boldsymbol{l}$ about $\boldsymbol{j}$**,** which results in a magnetic moment $\boldsymbol{\mu}_j$ precessing around $\boldsymbol{j}$ with a time-averaged value $\langle \boldsymbol{\mu}_j \rangle$ and in the opposite direction to $\boldsymbol{j}$**.** As shown in Fig. 2.10, the averaged moment will now precess slowly around an external field $\boldsymbol{B}$ which may be generated, for example, by fixed coils. Clearly, there is a back-action on the coils like in the spin–orbit coupling, but since the coils are heavy and fixed, the coils do not precess! In the vector model, we can project the contribution of $\boldsymbol{\mu}_j$ in the $\boldsymbol{j}$ direction

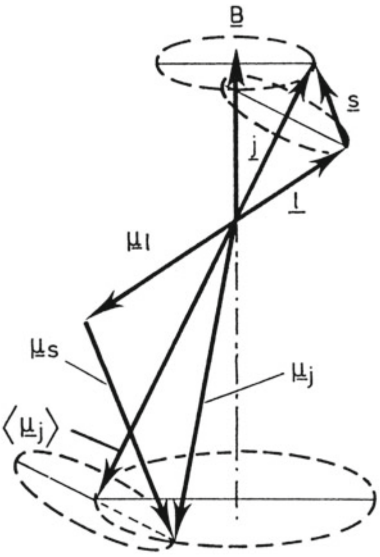

Fig. 2.10 Vector model for the Zeeman effect [1]

$$\langle \boldsymbol{\mu}_j \rangle = -\mu_{\mathrm{B}} \frac{3\boldsymbol{j}^2 - \boldsymbol{l}^2 + \boldsymbol{s}^2}{2\boldsymbol{j}^2} = -\mu_{\mathrm{B}} g_j \boldsymbol{j} \tag{2.25}$$

$$g_j = 1 + \frac{j(j+1) - \ell(\ell+1) + s(s+1)}{2j(j+1)} \text{ (Landé formula).} \tag{2.26}$$

To obtain these expressions, we have utilized the relations

$$\boldsymbol{l} \cdot \boldsymbol{j} = \left(\boldsymbol{j}^2 + \boldsymbol{l}^2 - \boldsymbol{s}^2\right)/2 \tag{2.27}$$

and

$$\boldsymbol{s} \cdot \boldsymbol{j} = \left(\boldsymbol{j}^2 - \boldsymbol{l}^2 + \boldsymbol{s}^2\right)/2, \tag{2.28}$$

and have inserted the “quantum-mechanical squares”. For the orientational energy E_{m} in the external field, we then obtain

$$E_{\mathrm{m}} = -\langle \boldsymbol{\mu}_j \rangle \cdot \boldsymbol{B} = \mu_{\mathrm{B}} B g_j m_j, \tag{2.29}$$

where the effect is seen in the *space quantization* m_j ($m_j = j, j - 1, \ldots -j$). The equidistant splitting of the m_j sublevels described by (2.29) is called the *Zeeman effect*. The Zeeman effect is obtained in magnetic fields of sufficiently low strengths so that the orientational energy E_{m} of the atom in the external field is negligibly small compared with the internal orientational energy, the spin–orbit interaction energy.

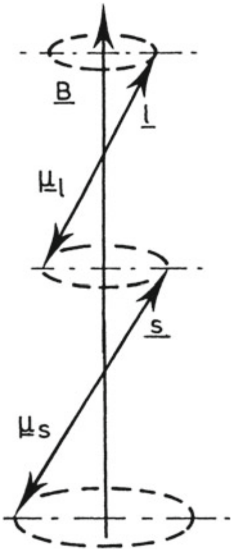

Fig. 2.11 Vector model for the Paschen–Back effect

The coupling between $\boldsymbol{l}$ and $\boldsymbol{s}$ remains strong in such cases. According to (2.10) and (2.29), the precession velocity is proportional to the coupling energy. Another way of expressing the Zeeman effect condition is then to state that the precession movement about the external field is very slow compared with the internal ($\boldsymbol{j} = \boldsymbol{l} + \boldsymbol{s}$) precession velocity. If we have the opposite condition, i.e. a *strong* field, more energy is associated with the individual coupling of $\boldsymbol{\mu}_l$ and $\boldsymbol{\mu}_s$ to the external field $\boldsymbol{B}$ than with the internal coupling. The coupling between $\boldsymbol{l}$ and $\boldsymbol{s}$, therefore, breaks up, and $\boldsymbol{l}$ and $\boldsymbol{s}$ precess independently about the field with separate space quantizations (Fig. 2.11). This is called the *Paschen–Back effect*. For this condition, we have

$$E_{\mathrm{m}} = \mu_{\mathrm{B}} B(m_l + g_s m_s) + \zeta m_l m_s, \tag{2.30}$$

where ζ is the fine-structure interaction constant from (2.13). Of course, all intermediate situations are also possible and the mathematical treatment then becomes more complicated. Still restricting ourselves to cases with only one outer electron, a general expression for the magnetic field dependence of the sublevels of a fine-structure doublet can be given, which describes the Zeeman, Paschen–Back, and the intermediate field regions (the *Breit–Rabi formula* for the fine structure)

$$E\left(J, m_j\right) = -\frac{\Delta E_{\mathrm{so}}}{2(2\ell+1)} + \mu_{\mathrm{B}} B m_j \pm \frac{\Delta E_{\mathrm{so}}}{2}\sqrt{1 + \frac{4m_j x}{2\ell+1} + x^2} \tag{2.31}$$

with

$$x = (g_s - 1)\frac{\mu_B B}{\Delta E_{\rm so}} \quad \text{and} \quad \Delta E_{\rm so} = (\ell + 1/2)\zeta$$

The plus sign corresponds to the sublevels originating in the higher J level.

The magnetic field behaviour of a ^2P state with a fine-structure splitting ΔE of 110 cm^{-1} is shown in Fig. 2.12. The energies are linear functions of the field B in the Zeeman region, (where $E_{\rm m} \ll 110$ cm^{-1}, which is also the case in the Paschen–Back region (where $E_{\rm m} \gg 110$ cm^{-1}), which is not fully reached in the figure. For the quantum numbers m_j in the Zeeman region and m_l and $m_{\rm s}$ in the Paschen–Back region, we have $m_j = m_l + m_{\rm s}$ (as $j_z = l_z + s_z$ is a constant of motion). This relation in connection with the *non-crossing rule* (levels with the same $m_j = m_l + m_{\rm s}$ cannot cross) prescribes which Zeeman level should be connected to which Paschen–Back level. (The non-crossing rule can be understood considering the signs of the second-order perturbation terms in the description of the behaviour of the energy levels.) Equation (2.31) describes how sublevels with the same m_j value mix, resulting in nonlinear field dependencies. As the $m = 3/2$ and $-3/2$, levels have no mixing partner, they remain linear in the magnetic field. (The expression under the square root becomes $(1 \pm x)^2$.)

A similar description can be given for the magnetic field influence for many-electron systems. We have for the Zeeman effect

$$E_{\rm m} = g_{\rm J}\mu_{\rm B} m_J B. \tag{2.32}$$

The Landé formula for g_J, (2.26), in the many-electron case is only valid for pure LS coupling. For jj coupling of two electrons, the following expression for the g-factor can be derived:

$$\begin{aligned} g = {} & \frac{J(J+1) + j_1(j_1+1) - j_2(j_2+1)}{2J(J+1)} g_1 \\ & + \frac{J(J+1) + j_2(j_2+1) - j_1(j_1+1)}{2J(J+1)} g_2. \end{aligned} \tag{2.33}$$

Here, g_1 and g_2 are g-factors for electrons 1 and 2, respectively, according to the Landé formula (2.26). By measuring the g-factors for all states of a given configuration, it is possible to determine the degree of intermediate coupling, i.e. to determine the coefficients c_i in the expansion $\psi' = \sum c_i \psi_i(LS, (jj))$ of a real state ψ' in pure LS, or jj states, Ψ_i.

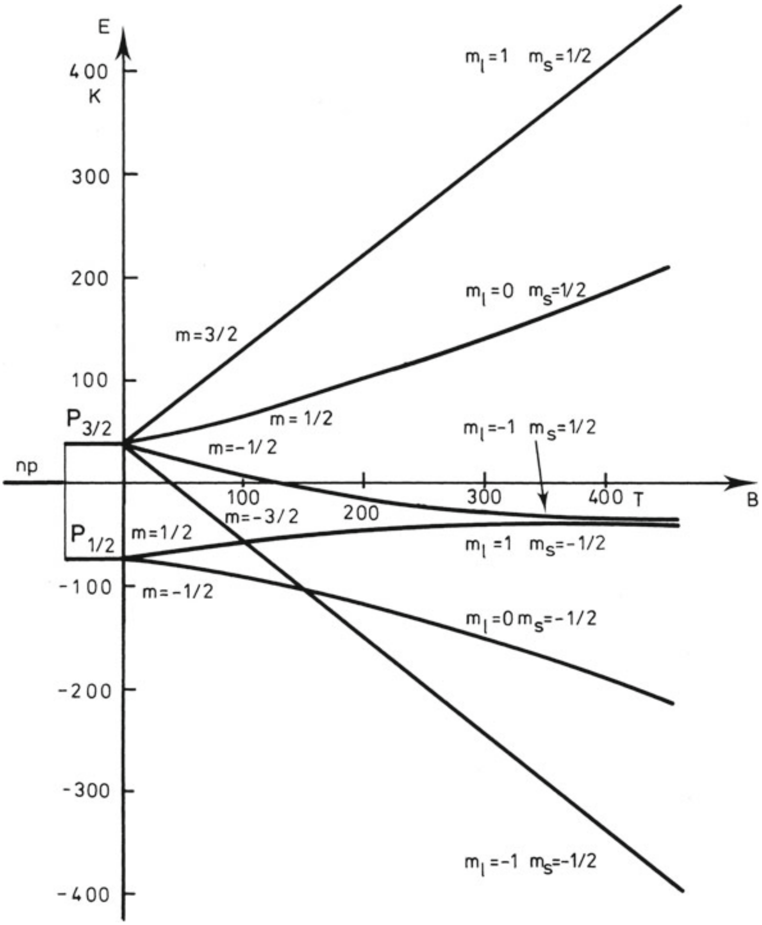

Fig. 2.12 Energy level diagram for a ^2P state with fine-structure splitting 110 cm^{-1} [1]

2.5.2 Electric Fields

An atom becomes *polarized* in a homogeneous electric field $\boldsymbol{\mathcal{E}}$, i.e. the centre of the electronic cloud no longer coincides with the nucleus. The field induces an electric dipole moment $\boldsymbol{d}$, which is proportional to the field

$$\boldsymbol{d} = \alpha \boldsymbol{\mathcal{E}}. \tag{2.34}$$

The orientation energy of the induced dipole is given by $E_e = -\boldsymbol{d} \cdot \boldsymbol{\mathcal{E}}$, in analogy with the magnetic case. This so-called *Stark effect* thus generally increases as the square of the applied electric field strength. Special conditions prevail for hydrogen and hydrogen-like systems due to the level degeneracy, and hence a *linear* Stark effect is obtained. It can be shown for the normal quadratic case that a common displacement of all sublevels (the *scalar* effect) is obtained, as well as a differential displacement, depending on the $m^2{}_j$ value (the *tensor* effect). We have, for a fine-structure level with quantum number J

$$E_s = -\frac{1}{2}\left(\alpha_0 + \alpha_2 \frac{3m_J^2 - J(J+1)}{J(2J-1)}\right)\mathcal{E}^2, \tag{2.35}$$

where α_0 and α_2, being the *scalar* and *tensor polarizability constants*, respectively, can be determined experimentally and calculated theoretically. There is only a scalar effect for $J = 0$ or 1/2, for which the formula breaks down. The Stark effect can be seen as an admixture of other states into the state under study. Perturbing states are those for which there are allowed electric dipole transitions (Sect. 4.2) to the state under study. Energetically close-lying states have the greatest influence. A theoretical calculation of the constants α_0 and α_2 involves an evaluation of the matrix elements of the electric dipole operator (Chap. 4). Investigations of the Stark effect are therefore, from a theoretical point of view, closely related to studies of transition probabilities and lifetimes of excited states. (Sects. 4.1 and 9.4). An example of the Stark effect is given in Fig. 2.13; different aspects of this phenomenon have been treated in [72].

Highly excited atoms with large principal quantum numbers n (*Rydberg atoms*) [73–77] are very sensitive to electric fields since they have large α_0 and α_2 values. Clearly, the loosely bound outer electron is strongly influenced by an electric field. If the field strength is sufficiently high, the electron can be swept away (*field ionization*). The critical field for Rydberg atoms for field ionization is proportional to n^{-4}. Whereas ground-state atoms can be field-ionized only at field strengths of the order of some MV/cm, an atom in an $n = 30$ state only requires a few V/cm. The phenomenon of field ionization is illustrated by a potential diagram in Fig. 2.14, showing the possibility of electron tunnelling through the potential barrier and the conversion from bound to unbound states. The reader is referred to [78–80] for a more detailed discussion of field ionization. It should be noted that (2.35) is valid

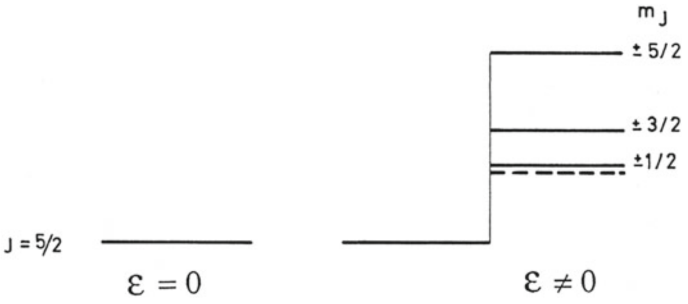

Fig. 2.13 Stark effect for a $J = 5/2$ state

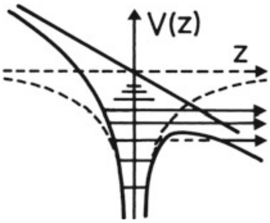

Fig. 2.14 Atomic field ionization

only for low electric field strengths far from the region of field ionization. Stronger fields must be handled with a different mathematical approach [81].

2.6 Hyperfine Structure

Hyperfine structure (hfs) in optical spectra was discovered independently by A. Michelson, Ch. Fabry, and A. Pérot at the end of the nineteenth century. The effect is explained by the presence of nuclear magnetic and electric moments, interacting with the electronic shell.

2.6.1 Magnetic Hyperfine Structure

Associated with its spin angular momentum $\boldsymbol{I}$**,** a nucleus has a magnetic dipole moment $\boldsymbol{\mu}_{\boldsymbol{I}}$

$$\boldsymbol{\mu}_I = g_I \mu_{\mathrm{N}} \boldsymbol{I} = g'_{\boldsymbol{I}} \mu_{\mathrm{B}} \boldsymbol{I}. \tag{2.36}$$

In this expression, which is analogous to (2.9), (2.23), and (2.24), the *nuclear magneton* $\mu_{\mathrm{N}} = \mu_{\mathrm{B}}/1836$, and $g_{\mathrm{I}}\left(g'_{\mathrm{I}}\right)$ is a constant of proportionality with positive or negative sign. At the site of the nucleus, the electron shell exhibits an effective magnetic field $\boldsymbol{B}_{\mathbf{J}}$ directed along the atomic "axis of rotation" $\boldsymbol{J}$, i.e.

$$\boldsymbol{B}_J = k\boldsymbol{J}. \tag{2.37}$$

There will be a magnetic coupling (orientational energy) between the nucleus and the electron shell, and the interaction is, in analogy with the fine-structure case (2.13), described by

$$H_{\mathrm{mhfs}} = a\boldsymbol{I} \cdot \boldsymbol{J} \tag{2.38}$$

Fig. 2.15 Coupling of angular momentum vectors

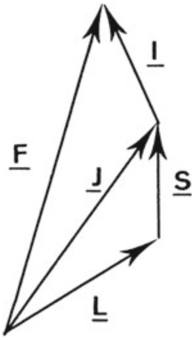

with

$$a = -k g_I \mu_{\mathrm{N}}. \tag{2.39}$$

Note that the *magnetic dipole interaction constant a* is a product of a nuclear quantity g_I, which is proportional to the moment, and an electronic quantity k, which is proportional to the internal magnetic field strength. $\boldsymbol{I}$ and $\boldsymbol{J}$ precess about their resultant $\boldsymbol{F}$**,** as shown in Fig. 2.15. We have

$$\boldsymbol{F} = \boldsymbol{I} + \boldsymbol{J}, \qquad F = I + J, I + J - 1, \ldots |I - J|. \tag{2.40}$$

The energy contribution is calculated from (2.38) in the same way as the spin–orbit interaction (2.15)

$$E_{\mathrm{mhfs}} = \frac{a}{2}[F(F+1) - I(I+1) - J(J+1)]. \tag{2.41}$$

In analogy with the fine-structure case (2.16), the Landé interval rule is also valid for the magnetic hyperfine structure

$$\Delta E_{mhfs}(F, F-1) = aF. \tag{2.42}$$

Hyperfine structures for two cases are displayed in Fig. 2.16, one for the case of a positive a value ("*normal*" structure) and one for the case of a negative a value (*inverted* structure). Clearly, both signs can occur, since the sign of the g_I factor varies for different nuclei. The sign of k can also vary due to the electronic core polarization effects; Fig. 2.5. We also note in passing, that for the electronic Zeeman effect, the g_J factor is intrinsically negative due to the negative charge of the electron. However, by convention, a minus sign is artificially inserted in (2.25) and also in (2.23) and (2.24), to force the g_J factor to become positive. Since both signs are intrinsically possible for the nuclear g_I factor, that convention is removed in this case.

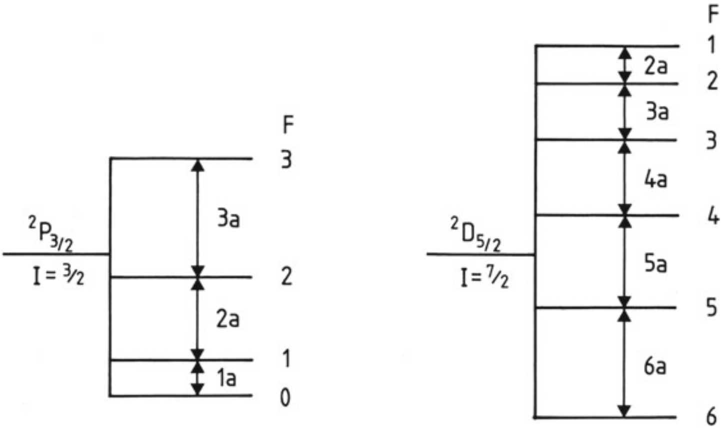

Fig. 2.16 Examples of magnetic hyperfine structure

The magnetic dipole interaction constant a can frequently be determined accurately with precise methods which will be discussed in Chaps. 7 as well as 9. As we have mentioned, it represents a quantity in the field of atomic as well as nuclear physics. If the nuclear moment is known, the measurement yields an experimental value of the magnetic field at the nucleus that can be compared with the results of atomic calculations. The field is then measured with a calibrated probe. If, on the other hand, the field can be calculated reliably, information on unknown nuclear moments can be obtained. The hyperfine structure will be particularly large if the atom contains an unpaired s electron, giving rise to the *Fermi contact interaction*, caused by the large probability of the s electron being found inside the nucleus.

The field strength at the nucleus is of the same order of magnitude as that exerted on the electron in its spin–orbit interaction. Since typical magnetic moments for nuclei are about 1000 times smaller than corresponding moments for the electron shell ($\mu_B/\mu_N = 1836$), the magnetic hyperfine structure is correspondingly smaller compared with the fine structure. (Angular momenta are similar, but nuclei are much heavier—thus the electric charges rotate slowly and less magnetism is generated). As mentioned in Chap. 1, typical hyperfine splittings are of the order of 10^{-6} eV ($\sim 10^{-2}$ cm^{-1}).

2.6.2 *Electric Hyperfine Structure*

In the same way as to how a magnetic dipole acquires orientational energy in a magnetic field, a non-spherically symmetric charge distribution will also acquire such energy in an electric field gradient (Fig. 2.17).

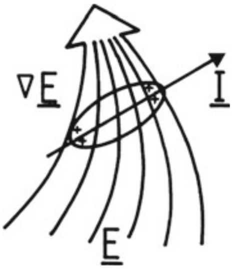

Fig. 2.17 Orientation energy of an electric quadrupole in an electric field gradient

Atomic nuclei can be stretched like cigars (prolate shape) or compressed like discs (oblate shape). The deformation is described by the *electric quadrupole moment* Q (prolate: $Q > 0$; oblate: $Q < 0$). The principal interaction is, of course, the normal electrostatic (Coulomb) force on the charged nucleus (*monopole* interaction). The differential interaction, which depends on the structure of the nucleus and on the variation of the field across its finite extension, is of course very much smaller (*quadrupole* interaction). It gives rise to an electric hyperfine structure. The energy contribution depends on the direction of the nuclear spin in relation to the electric field gradient. The electric hyperfine interaction is described by

$$E_{\text{ehfs}} = b\frac{(3C/4)(C+1) - I(I+1)J(J+1)}{2I(2I-1)J(2J-1)} \tag{2.43}$$

with

$$C = F(F+1) - I(I+1) - J(J+1) \quad \text{and} \quad b = \frac{\text{e}^2}{4\pi\epsilon_0}q_J Q. \tag{2.44}$$

In analogy with the magnetic dipole interaction constant a, the *electric quadrupole interaction constant b* is a product of a nuclear quantity Q, the electric quadrupole moment, and an electronic quantity q_{J}, which is proportional to the electric field gradient. Thus, with the b factor experimentally determined, information on the nucleus *or* the electronic shell can be obtained. The electric hyperfine structure is of the same order of magnitude as the magnetic one, but generally somewhat smaller. It exhibits itself as a deviation from the Landé interval rule. Two examples of the combined action of magnetic and electric hyperfine structures are shown in Fig. 2.18.

If the nucleus has no spin, i.e. $I = 0$, there is neither a magnetic nor an electric hyperfine structure. Only a magnetic interaction is possible for $I = 1/2$, whereas the occurrence of the electrical hyperfine structure requires $I \geq 1$ and $J \geq 1$. Hyperfine structure and the determination of nuclear moments have been discussed in [82]. Extensive data on nuclear moments have been listed in [83, 84]; hfs data for the extensively studied alkali atoms have been compiled in [85] and the theoretical aspects of atomic hyperfine interactions have been covered in [86–91].

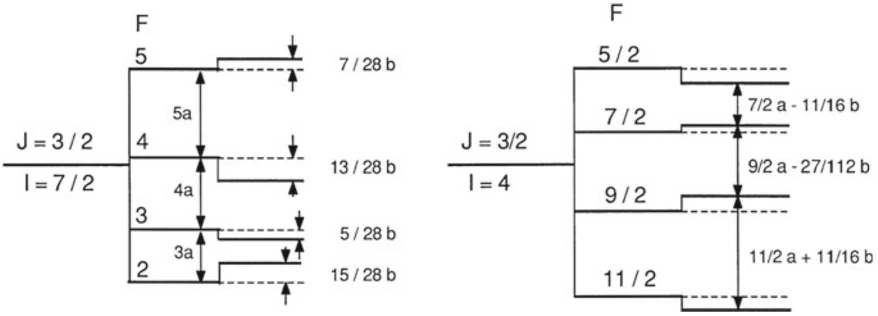

Fig. 2.18 Examples of magnetic and electric hyperfine structure for J = 3/2 states and different nuclear spins (could be ^{133}Cs with I = 7/2, and ^{40}K with I = 4)

We will finish this section with some general comments on angular momenta and the coupling of angular momenta into a new, resultant angular momentum. Since the size of angular momentum is quantized, the length of the corresponding vectors is also quantized and given by $(q(q+1))^{1/2}$, where q is the angular momentum quantum number, which can only have integer or half-integer values. Since a valid result of the coupling of two quantum-mechanical angular momenta must again be a quantum-mechanical angular momentum, with a length again restricted by the just given expression, it is clear that the coupling can only result in a very limited number of angles between the two participating vectors. This is the origin of the rules for possible values for a resulting angular momentum quantum number (see, e.g. (2.19) and (2.40)).

2.7 The Influence of External Fields (hfs)

In a weak external magnetic field ***B***, there will be a splitting of magnetic sublevels for the hyperfine structure (hfs) case as for the previously discussed case, where the influence of the nucleus was omitted. However, also in the hyperfine structure case, the electronic shell is responsible for the interaction. Because of the coupling between ***I*** and ***J***, these vectors precess about ***F***. Thus, the direction in relation to ***B*** of the electronic magnetic moment, which is associated with ***J***, is influenced. The situation is illustrated in Fig. 2.19.

As the nuclear magnetic moment is negligibly small in comparison with that of the electronic shell, the direct interaction of the nuclear moment with the field is normally negligible. The coupling in the inner, extremely strong field (the magnetic hyperfine coupling) is, however, much larger, and as a matter of fact, the *Zeeman effect for the hyperfine structure* demands that the external interaction is negligible compared with the internal one. Using the vector model, we obtain, as in the fine-structure case

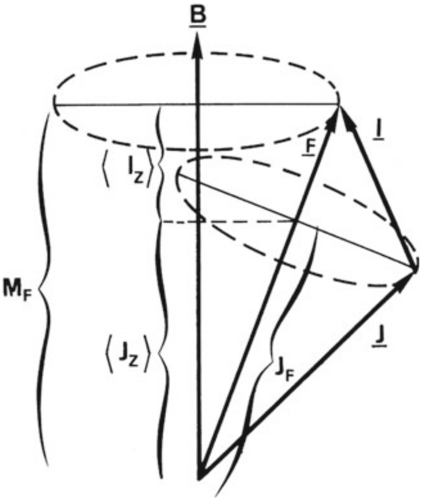

Fig. 2.19 Vector diagram for the Zeeman effect of the hyperfine structure [1]

$$E_{\mathrm{m}} = \mu_{\mathrm{B}} B g_J \frac{F(F+1) - I(I+1) + J(J+1)}{2F(F+1)} M_F = \mu_{\mathrm{B}} B g_F M_F . \tag{2.45}$$

In the presence of hyperfine structure, g_F now takes the place of g_J in describing the "gear ratio" between the magnetic energy contribution and field strength. Although the *electronic* magnetic moment is the important factor in action, its influence is modified by the nuclear coupling, resulting in a different angle of $<\boldsymbol{\mu}_J>$ with respect to the magnetic field. If J and g_J are known, a measurement of g_F gives information on the nuclear spin I.

In strong magnetic fields, the *Paschen–Back effect for the hyperfine structure* will result. As for the fine-structure case (2.30), the mathematical expression is simple, i.e.

$$E_{\mathrm{m}} = \mu_B B\big(g_J M_J - g_I' M_I\big) + a M_I M_J . \tag{2.46}$$

The calculation is more complicated in *intermediate fields*. For I or $J = 1/2$, the *Breit–Rabi formula* can be expressed in analogy with the fine-structure case; see (2.31). For $J = 1/2$, we have

$$E(F, M_F) = -\frac{\Delta E}{2(2I+1)} - g_I' \mu_{\mathrm{B}} B M_F \pm \frac{\Delta E}{2}\sqrt{1 + \frac{4 M_F x}{2I+1} + x^2} \tag{2.47}$$

with

$$x = \big(g_J + g_I'\big)\frac{\mu_{\mathrm{B}} B}{\Delta E} \quad \text{and} \quad \Delta E = \left(I + \frac{1}{2}\right) a .$$

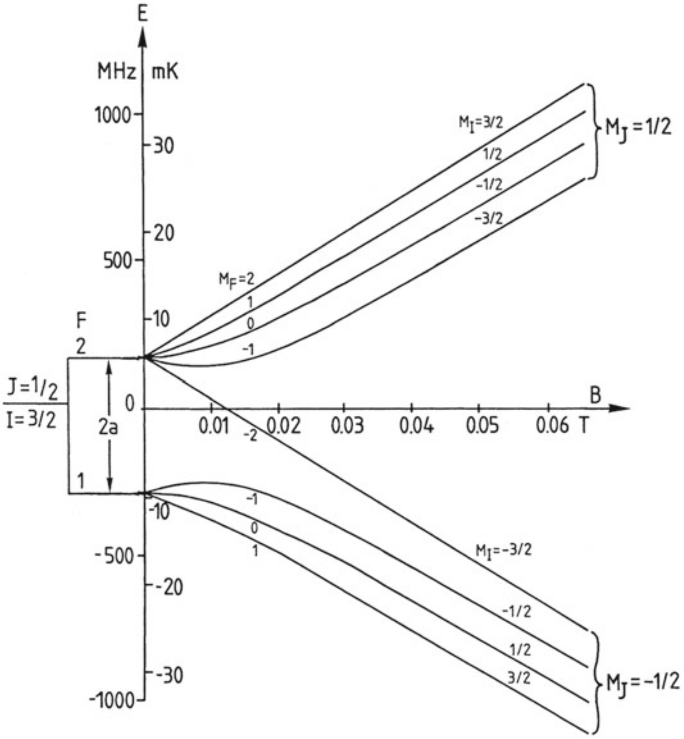

Fig. 2.20 Breit–Rabi diagram for an alkali state with $J = 1/2$ and $I = 3/2$. (Ground state of ^{39}K) [1]

Here, the plus sign refers to the higher F value. The dependence of the sublevels on the magnetic field for a $J = 1/2$, $I = 3/2$ state is shown in Fig. 2.20.

The Zeeman and Paschen–Back regions can be identified and the relevant quantum numbers M_F, M_I, and M_J, are indicated ($M_F = M_I + M_J$). The $M_F = \pm 2$ levels have no mixing partner and proceed linearly into the Paschen–Back region.

A computer calculation, in which the quantum-mechanical energy matrix is *diagonalized*, is required for the general case. Atoms with hfs in external magnetic fields have been discussed in [82]. Hyperfine structures are normally given in MHz. Using this unit for energy and expressing B in Gauss (10^{-4} T), μ_B/h has the numerical value of 1.400 (MHz/G).

In the presence of an external electric field, a Stark effect for the hyperfine structure occurs. The theory which applies to this situation has been given in [92, 93].

2.8 Isotopic Shifts

Isotopes with $I = 0$ have no hyperfine structure, but in transitions between energy levels in a mixture of $I = 0$ isotopes of the same element, a line structure may still be obtained. This effect is called the *isotopic shift*. It has two origins and a distinction is made between the *mass effect* and the *volume effect*. The mass effect can be divided up into the *normal* and the *specific* mass effects. The normal mass effect is due to the movement of the nucleus, which is due to the fact that it is not infinitely heavy. For hydrogenic systems, it is possible to take this into account by using the *reduced mass* μ instead of m

$$\mu = \frac{mM}{m + M} \tag{2.48}$$

(m: electron mass, M: nuclear mass). For a transition in hydrogenic systems, one finds that the mass shift between two isotopes of mass M and $M + 1$ decreases with M according to

$$\Delta v \propto M^{-2}. \tag{2.49}$$

The specific mass effect is due to the interactions (correlations) between the different outer electrons. The mass effect is very prominent for hydrogen/deuterium, but is quickly reduced for heavier elements. For such elements, the volume effect becomes important. It is particularly prominent when the electron configuration contains unpaired s electrons. The nucleus has a charge density ρ_{n} over a finite volume. The s electron with a charge probability distribution $\rho_e(r)$ can penetrate the nucleus and is then no longer under the influence of the pure Coulomb field. A nucleus of mass M has a smaller radius r than one with the mass $M + \Delta M$, and thus the potential begins to deviate from a Coulombic one at smaller values of r. The situation is illustrated in Fig. 2.21. There will be an energy shift described by

$$\Delta E = \int_0^{r_0} \rho_e(r) 4\pi r^2 \delta V(r) \mathrm{d}r. \tag{2.50}$$

Studies of the volume effect yield information on the charge distribution in the nucleus. Hyperfine structure and isotopic shifts are of the same order of magnitude. Isotopic shifts can be studied in the visible region as well as in the X-ray region. Particularly prominent isotopic shifts are obtained for muonic atoms, in which, for example, a μ meson ($m_\mu = 209 m_{\mathrm{e}}$) has taken the place of an electron. The classical radius of the orbit is reduced by a factor of 209, and thus the nuclear influences are much greater than those pertaining to the electrons. Isotope shifts and their interpretation have been discussed in [94–98].

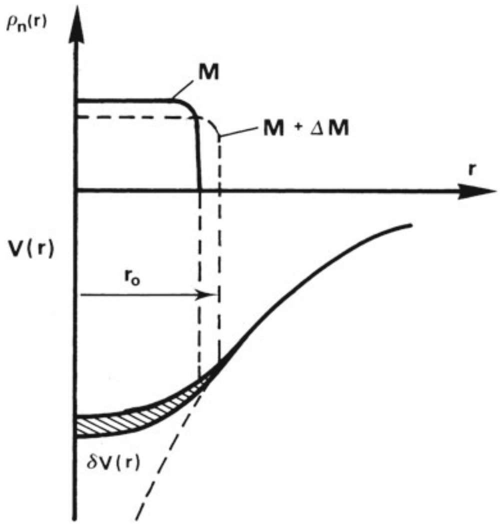

Fig. 2.21 The origin of the volume isotopic shift

Different aspects of current atomic physics research are covered in the proceedings of a series of international atomic physics conferences [99–125]. Further reviews may be found in [126, 127].

Chapter 3
Molecular Structure

A molecule is formed by the binding of two or more atoms in such a way that the total energy is lower than the sum of the energies of the constituents. The bonds are normally of *ionic* or *covalent* nature. Particularly weak bonds occur in *van der Waals* molecules. The energy-level diagrams of molecules are significantly more complicated than those of atoms since, apart from energy levels corresponding to different electronic arrangements, there are also different states corresponding to vibrational and rotational motion. The structure is schematically shown in Fig. 3.1. This chapter will mainly be concerned with *diatomic* molecules, which are the easiest ones to describe. However, we will also briefly present more complex systems, including fullerenes, nanotubes, and graphene.

For a more detailed description of molecular structure and molecular spectroscopy, the reader is referred to Refs. [128–152].

3.1 Electronic Levels

In the mathematical treatment of atoms, it has been found that the interactions, especially electron–electron interactions, are rather complicated. Theoretical studies of molecules are even more complicated than those of atoms because we do not have any given centre but many centres, one for each atom in the molecule. As for atoms, the theoretical treatment of molecules starts with the Schrödinger equation and, as in the case of atoms, it is useful to consider the independent-particle model. In this approximation, one assumes that each electron moves independently of the others in the field generated by the nuclei and the other electrons. The central field approximation is then a natural further step for an atom. However, as there are many centres in a molecule, such a model does not apply here. In order to facilitate the calculations, one generally tries to utilize other symmetry properties of the molecule. In the treatment of diatomic molecules, we have *cylindrical symmetry* and it is then possible

© The Author(s), under exclusive license to Springer Nature Switzerland AG 2022

S. Svanberg, *Atomic and Molecular Spectroscopy*, Graduate Texts in Physics,
https://doi.org/10.1007/978-3-031-04776-3_3

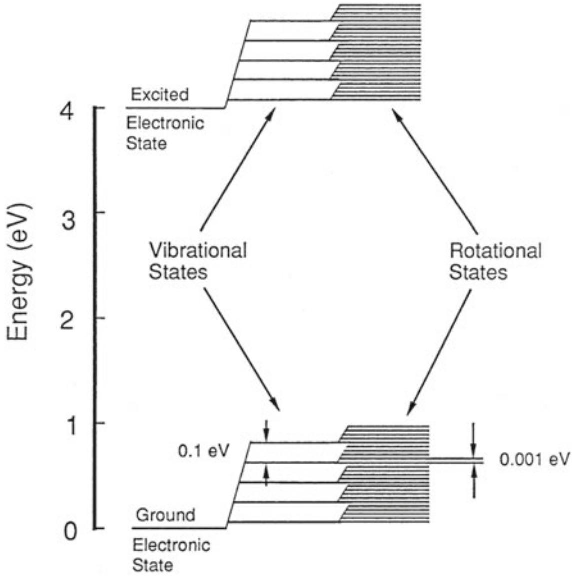

Fig. 3.1 Schematic molecular energy-level diagram with electronic, vibrational, and rotational levels

to separate the Schrödinger equation into equations corresponding to different absolute values of the angular momentum projection onto the symmetry axis. Electronic orbitals denoted by σ, π, δ, … are obtained corresponding to the m_l values 0, 1, 2, … (m_l is the quantum number for the orbital angular momentum projection). In molecules with two atoms of the same kind (homo-nuclear molecules), there is a centre of symmetry. The states are further classified for such molecules by indicating the parity of the wavefunction: even, g (German "gerade") or odd, u (German "ungerade"), e.g. σ_g, σ_u, π_g, π_u, …

Electrons are much lighter than nuclei and move much faster. Thus, the electrons can adjust to the movement of the nuclei, which means that the electronic states are at any moment essentially the same as if the nuclei were fixed. This is the basis of the *Born–Oppenheimer approximation*, which assumes fixed nuclei. The wave function can be expressed as a product of an electronic wave function with the nuclei assumed fixed and a nuclear wave function describing the relative nuclear motion. Energy eigenvalues for the electronic Schrödinger equation, solved for different nuclear separations, form a potential, that is inserted into the nuclear Schrödinger equation together with the nuclear repulsion term.

In order to further describe the molecular wavefunctions or the molecular orbitals, Linear Combinations of Atomic Orbitals (LCAO) are normally used (*LCAO method*). Such a method of solution is possible since the directional dependence of the spherical-harmonic functions for the atomic orbitals can be used. Pauli's principle can be applied to the single-electron molecular orbitals, and by filling the states with the available electrons, the molecular electron configurations are attained. The coupling of the angular momenta of the open shell then gives rise to molecular terms.

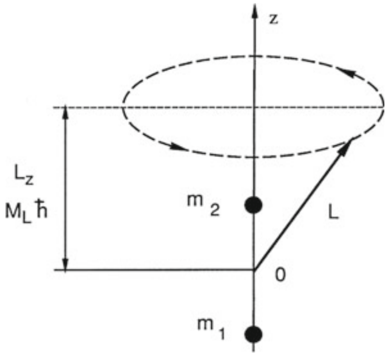

Fig. 3.2 Precession of ***L*** in a diatomic molecule

The total angular momentum of the electrons in a molecule is not a constant of motion, since the electrons do not move in a central field. The coupling of angular momenta for the electrons will, therefore, be different from the atomic case.

Let us consider a diatomic molecule which has an axial symmetry with regard to the axis through the two nuclei (i.e. cylindrical symmetry). Only the component of the electron orbital angular momentum L_z along the symmetry axis will be a constant of motion. The total angular momentum $\boldsymbol{L}$ will precess about the symmetry axis, as shown in Fig. 3.2.

The projected component is characterized by the quantum number M_L

$$M_L = L, L-1, \ldots . - L. \tag{3.1}$$

However, since the internuclear field is of electric nature rather than magnetic, the energy is not changed for the exchange $M_L \rightarrow -M_L$. (Compare the Stark effect with the Zeeman effect). Since the field is very strong, the energy separation between states with different $M_L$values is quite substantial. The absolute value for $M_L$is designated Λ

$$\Lambda = |M_L|, \quad \Lambda = 0, 1, 2, \ldots, L. \tag{3.2}$$

The states are given the following symbols

$$\begin{array}{lcccc} \Lambda = & 0 & 1 & 2 & 3 \\ & \Sigma & \Pi & \Delta & \Phi. \end{array}$$

The states are doubly degenerate apart from Σ states because of the $M_L \leftrightarrow -M_L$symmetry.

The resulting spin quantum number S of the electrons is also needed to characterize the molecular states. In diatomic molecules with $\Lambda > 0$, $\boldsymbol{S}$ precesses about the internuclear axis and can have $2S + 1$ well-defined projections. The quantum

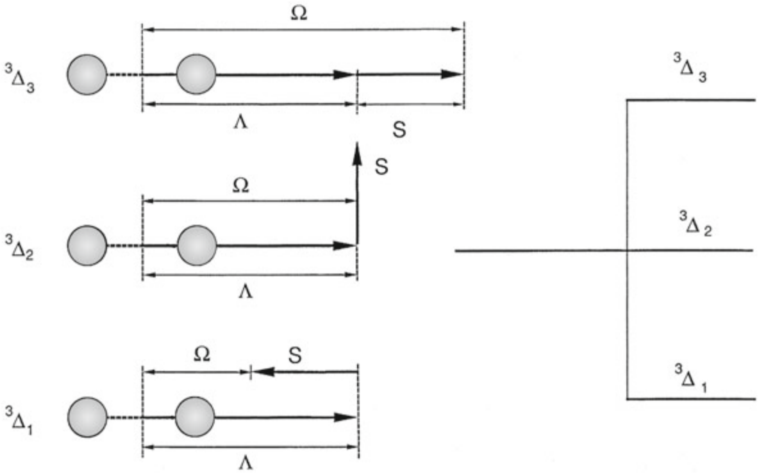

Fig. 3.3 Term splitting for molecules

number for S_z is called Σ. As for the atomic case, the *multiplicity*, $2S + 1$, is placed as an index of the Λ symbol, e.g. $^3\Pi$, $^1\Delta$.

The total electronic angular momentum along the internuclear axis is designated Ω and is obtained from Λ and Σ

$$\Omega = \Lambda + \Sigma, \Lambda + \Sigma - 1, |\Lambda - \Sigma|. \tag{3.3}$$

For $\Lambda > 0$, the $(2S + 1)$ values of Ω with different energies are obtained. In Fig. 3.3, the possible states for $\Lambda = 2$ and $S = 1$ are shown.

The strength and type of bonding between two atoms depend on the tendency of the participating atoms to donate, attract, and share electrons. The variation of the electronic energy with the bond length r between the nuclei is schematically shown in Fig. 3.4 for the OH (heteronuclear) and O_2 (homonuclear) molecules. The curve with the lowest energy corresponds to the ground state, while the other curves represent different electronic states, which may also be unbound. The ground state is designated *X*, and the excited states are conventionally called *A*, *B*, *C,* etc.

3.2 Rotational Energy

Consider a rotating diatomic molecule, as shown in Fig. 3.5, with the atomic masses m_1 and m_2 at distances r_1 and r_2 from the centre of gravity. The moment of inertia with respect to the rotational axis is *I*. We have

$$r = r_1 + r_2.$$

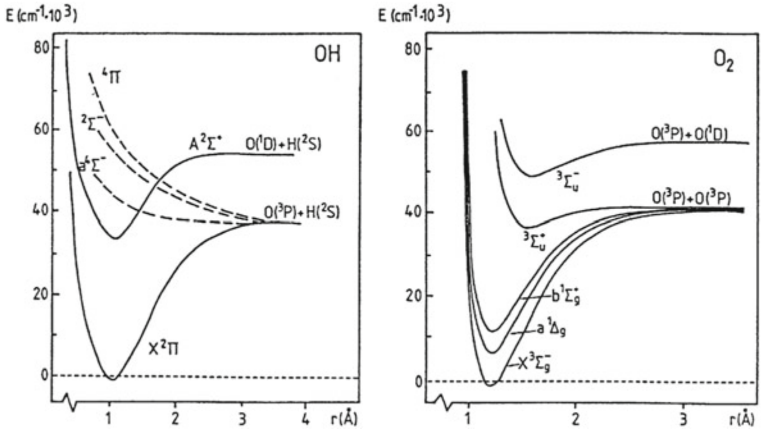

Fig. 3.4 Energy level diagram for OH (*left*) and O_2 (*right*)

Fig. 3.5 Rotation of a diatomic molecule

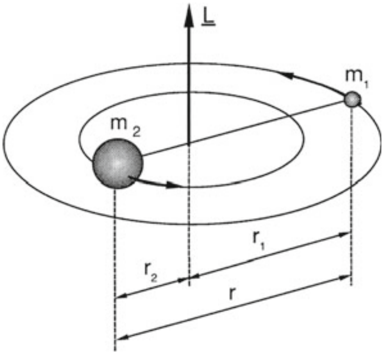

$$m_1 r_1 = m_2 r_2,$$
$$I = m_1 r_1^2 + m_2 r_2^2.$$

We then obtain

$$I = \frac{m_1 m_2}{m_1 + m_2}(r_1 + r_2)^2 = \mu r^2, \tag{3.4}$$

where μ is the reduced mass. The angular momentum $\boldsymbol{L}$ and the energy E are given by

$$\left.\begin{aligned} \boldsymbol{L} &= I\omega/\hbar \\ E &= I\omega^2/2 \end{aligned}\right\} \Rightarrow E = \frac{\boldsymbol{L}^2\hbar^2}{2I},$$

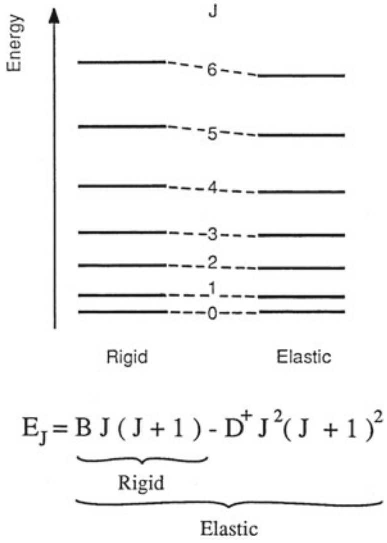

Fig. 3.6 Rotational levels for a rigid rotator (*left*) and an elastic rotator (*right*)

where ω is the angular frequency vector. Quantum mechanically, $\boldsymbol{L}$ is given by

$$|\boldsymbol{L}| = \sqrt{J(J+1)},\ J = 0, 1, 2, \ldots \tag{3.5}$$

and thus the quantized energy of the rotator is given by

$$E_J = J(J+1)\hbar^2/2I = BJ(J+1). \tag{3.6}$$

This energy expression leads to energy levels such as those shown in Fig. 3.6.

If the rotator is not completely rigid, it is slightly extended in higher rotational states. Then I will increase and $E_J$will decrease. This results in a successive downward movement of the upper energy levels. The elastic rotator is described by

$$E_J = BJ(J+1) - D^+J^2(J+1)^2. \tag{3.7}$$

Here D^+ is a positive constant and $D^+/B \ll 1$. The modified rotational levels are also included in Fig. 3.6. The energy separation between rotational levels is of the order of 10^{-3} eV.

There is a coupling between the angular momentum of the electrons and the molecular rotation in molecules with an open electron shell. The situation is described by the *Hund coupling cases* a, b, c or d. (This complication, which sometimes leads to the absence of the first rotational levels, will not be treated in this book.) The coupling between $\boldsymbol{L}$ and $\boldsymbol{J}$ can lead to a splitting of each J level into two states (Λ doubling), breaking the $M_L$degeneracy.

3.3 Vibrational Energy

The potential energy of a diatomic molecule depends on the internuclear distance r. A typical potential curve is shown in Fig. 3.7. The so-called *Morse potential* is often used

$$V(r) = D\big(1 - \mathrm{e}^{-\alpha(r-r_0)}\big)^2. \tag{3.8}$$

Here r_0 corresponds to the bottom of the potential curve and D is the dissociation energy. One atom oscillates with regard to the other one in this potential. A Taylor expansion of $V(r)$ close to $r = r_0$

$$V(r) = D\alpha^2(r - r_0)^2 + \dots \tag{3.9}$$

shows that the bottom of the potential curve may be approximated by a parabola and the molecule is then called a *harmonic oscillator*. The classical vibrational frequency ν_c is then given by

$$\nu_\mathrm{c} = \frac{1}{2\pi}\sqrt{\frac{k}{\mu}}, \tag{3.10}$$

where μ is the reduced mass and k is the force constant (defined by the force expression $F = -k(r - r_0)$. Thus, $k = 2D\alpha^2$ according to Eq. (3.9)). Quantum mechanically, we have

$$E_v = (v + 1/2)h\nu_c, \quad v = 0, 1, 2, \dots \tag{3.11}$$

Fig. 3.7 Vibrational potential and energy levels

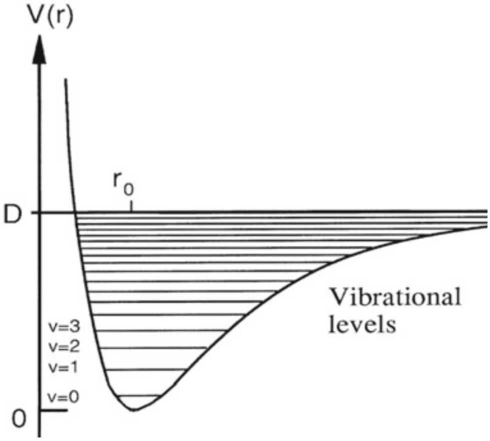

leading to *equidistant* vibrational levels and the presence of a *zero-point energy* $h\nu_c/2$. This is in accordance with the Heisenberg uncertainty relation, which states that the product of the uncertainty in the position and in the velocity has a finite value. If the lowest state would be at the bottom of the parabola, there would be no uncertainty in position, no movement, and thus no uncertainty in the velocity, which would violate the uncertainty principle. It is fascinating to note how quantum mechanics is fully self-consistent, while it is not so evident how in the formalism the non-zero result is enforced! The harmonic oscillator model for higher-lying vibrational levels is obviously not valid, since the higher terms of $V(r)$ become important. The energy eigenvalues for a non-harmonic oscillator are given approximately by

$$E_v = (v + 1/2)h\nu_c - (v + 1/2)^2\chi_e h\nu_c. \tag{3.12}$$

Here x_e is a small positive constant. Increasingly closer-lying energy levels are obtained, developing into a continuum at $E = D$. The separation between low-lying vibrational levels is typically 0.1 eV.

3.4 Polyatomic Molecules

While the energy-level structure of diatomic molecules can be divided up reasonably easily, the degree of complexity is greatly increased for polyatomic molecules. Such molecules have several nuclear distances, several force constants, several dissociation energies, etc. which must normally be determined simultaneously. While for diatomic molecules, it is possible to start from empirical regularities in the spectra and arrive at a theoretical interpretation, such a procedure is difficult for polyatomic molecules. Instead, it is more advantageous to first develop the theory and then use the theory to interpret the observed spectra. An important point to consider is the *shape* of the molecule, i.e. the internal arrangement of the atoms, as certain qualitative features are associated with a certain shape. The study of *symmetry properties* is thus very important in the understanding of complicated molecules [153–156]. The symmetry is described in group theory in terms of *point groups*. For example, carbon tetrachloride CCl_4, which has a tetrahedral structure, belongs to a point group called T_d.

The vibrational motion of a polyatomic molecule is described by *fundamental frequencies (modes)*, corresponding to different types of vibration. Every atom has 3 degrees of freedom (the 3 dimensions of space) leading to 3 N degrees of freedom for an N-atomic molecule. Of these degrees of freedom, three describe rotation around a centre of mass, which does not correspond to any vibrational motion. A further three degrees of freedom describe a translational motion that does not either give rise to any vibrational movement. Thus, in general, an N-atomic molecule has $3N - 6$ vibrational modes. For a *linear* molecule, there is one more mode ($3N - 5$) because only two independent rotational movements exist. The different vibrational modes in the molecule represent stretching, where the distance between the atoms in the

Fig. 3.8 Stretching and bending modes for the molecular groups

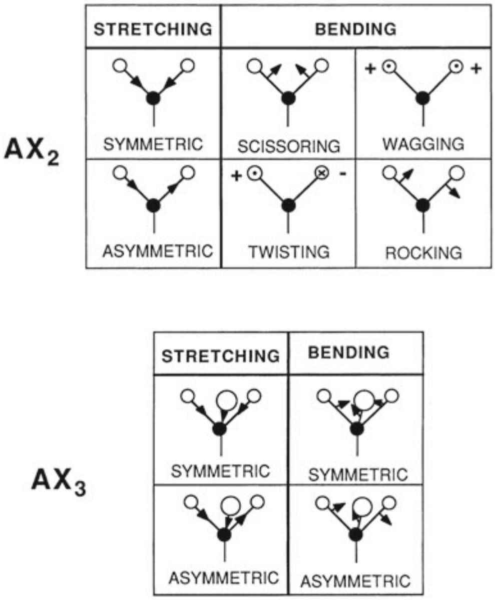

molecule is changed, or bending, where the angle between the atoms in the molecule is changed. Examples of stretching and bending modes for AX_2 and AX_3 molecular groups are given in Fig. 3.8.

The possibilities of understanding even complicated molecular structures have much improved with advanced theoretical development. The result is the firm establishment of *quantum chemistry* as a discipline, comprising many advanced theoretical approaches [157–166], and culminating in the award of the Nobel prize in chemistry in 1998 to *W. Kohn* and *J. A. Pople.*

3.5 Clusters

Clusters are polyatomic molecules, generally consisting of atoms of the same kind. Many elements spontaneously evaporate as molecules, e.g. arsenic (As_4), tellurium (Te_2), and Bi (Bi_x). If an element is evaporated into a supersonic jet of inert gas, e.g. by laser ablation, clusters are formed in the rapidly expanding and adiabatically cooling gas [167–173]. Mass spectrometric studies can be performed to show the distribution of masses in the cluster formation. In studies of carbon, it was found that C_{60} and C_{70} were overabundant. It has been shown (Nobel prize in chemistry 1996 to *R. F. Curl Jr.*, *H. Kroto*, and *R. E. Smalley*) that C_{60} corresponds to a particularly symmetric arrangement of the atoms in the form of a soccer ball (20 hexagons, 12 pentagons) as shown in Fig. 3.9, where also carbon cluster mass spectra for different running conditions are shown. The symmetric structure is normally referred to as *buckminster*

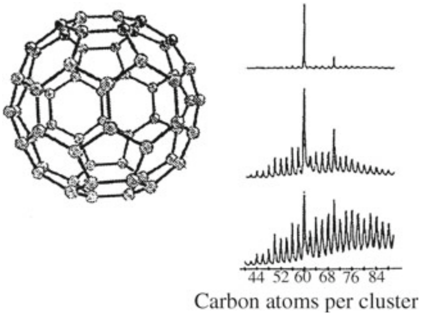

Fig. 3.9 Carbon cluster mass spectra and the structure of C_{60} [173]

fullerene (after R. Buckminster Fuller, an American architect who constructed a dome of this shape for the 1967 Montreal World Exhibition). The structures are cage-like, and other atoms can be trapped inside, giving rise to *endohedral fullerenes*. Clusters and fullerenes have very interesting physical and chemical properties, which are much studied. They may become of great technological use for catalysts, lubricants, etc. It has been shown that more complicated structures can be obtained with carbon atoms, such as tubes [174–181]. Complex molecules of these kinds are of considerable interest in nanometer technology. As earlier mentioned, even for a comparatively massive particle such as $C_{60,}$ it has been possible to show that it possesses a wave nature [182].

Related to fullerenes and nanotubes, a flat carbon structure, called *graphene* has also been generated and extensively studied [183–189]. *A. Geim and K. Novoselov* were awarded the Nobel Prize in physics for the discovery of graphene [190, 191].

3.6 Other Molecular Structures

Apart from the energy-level structures discussed above, molecules exhibit both the Zeeman and Stark effects. Further, hyperfine structure and isotopic shifts also occur. The occurrence of isotopic shifts is particularly simple to understand considering the substantially altered values of the reduced mass found in the vibrational and rotational energy expressions.

Chapter 4
Radiation and Scattering Processes

After the brief survey of atomic and molecular energy structures in Chaps. 2 and 3, we will now consider radiation and scattering processes by which atoms and molecules change their energy state. The processes are accompanied by the absorption or release of radiation, giving rise to spectra. These spectra can be used to clarify the structure of atoms and molecules as well as for a wealth of analytical purposes. We will first consider the case of transitions at a frequency corresponding to given energy separations (resonance radiation) and then discuss the Rayleigh, Raman, and Mie scattering. A detailed presentation of the theory of radiation and scattering processes can be found in [192–211]. Several of the books on atomic, molecular, and quantum mechanics, cited earlier, also discuss this topic in more detail.

4.1 Resonance Radiation

The following section, which largely follows Ref. [1], requires some knowledge of quantum mechanics. A reader with limited exposure to the formal theory could move directly to the paragraph starting immediately before Fig. 4.3 and still have a working knowledge of resonance radiation.

Consider an atomic or molecular system with energy levels E_k subject to a time-dependent perturbation $\mathcal{H}'$, e.g. the oscillating electric field of incoming monochromatic light (Fig. 4.1). We will in this section consider in what state E_n a system, initially in a given state E_i, will be found after having interacted with an electromagnetic field for a time t. We start with the time-dependent Schrödinger equation

$$i\hbar \frac{\partial \Psi(\mathrm{t})}{\partial t} = \left(\mathcal{H}_0 + \mathcal{H}'\right)\Psi(\mathrm{t}). \tag{4.1}$$

© The Author(s), under exclusive license to Springer Nature Switzerland AG 2022

S. Svanberg, *Atomic and Molecular Spectroscopy*, Graduate Texts in Physics,
https://doi.org/10.1007/978-3-031-04776-3_4

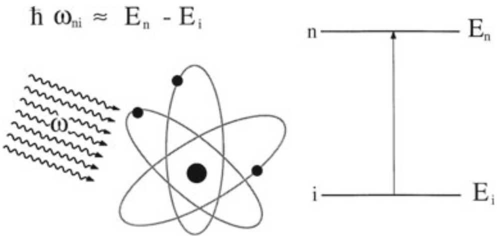

Fig. 4.1 Interaction between electromagnetic radiation and an atom

The time-independent eigenfunctions of $\mathcal{H}_0$ (describing the non-perturbed system) and the eigenvalues E_k are assumed to be known:

$$\mathcal{H}_0\psi_{\mathrm{k}}^0 = \mathrm{E}_{\mathrm{k}}\psi_{\mathrm{k}}^0. \tag{4.2}$$

The eigenfunctions are supposed to be normalized and those with the same eigenvalues have been orthogonalized. These eigenfunctions have the time dependence

$$\Psi_k^0(t) = \psi_k^0 \exp(-\mathrm{i}\omega_k t) \tag{4.3}$$

with $\omega_k = E_k/\hbar$. Since the functions constitute a complete system, an arbitrary time-dependent function can be expanded according to

$$\Psi(t) = \sum_k c_k(t)\Psi_k^0(t) = \sum_k c_k(t)\psi_k^0 \exp(-\mathrm{i}\omega_k t) \tag{4.4}$$

Inserting this expression into the Schrödinger Eq. (4.1), we obtain

$$\mathrm{i}\hbar\sum_k \frac{\mathrm{d}c_k}{\mathrm{d}t}\exp(-\mathrm{i}\omega_k t)\psi_k^0 = \mathcal{H}'\sum_{\mathrm{k}} \mathrm{c}_{\mathrm{k}}\exp(-\mathrm{i}\omega_{\mathrm{k}} t)\psi_{\mathrm{k}}^0 \tag{4.5}$$

Multiplication by Ψ_n^{0*} and integration yield

$$\frac{\mathrm{d}c_n}{\mathrm{d}t} = -\frac{\mathrm{i}}{\hbar}\sum_k \exp(\mathrm{i}\omega_{nk}t)\langle\psi_n^0|\mathcal{H}'|\psi_k^0\rangle$$

with

$$\omega_{nk} = \omega_n - \omega_k = \frac{1}{\hbar}(E_n - E_k).$$

The set of Eqs. (4.5), written for the various values of n, constitutes a set of coupled linear differential equations. The coupling between these equations arises solely from the existence of the perturbation $\mathcal{H}'$, which has non-zero off-diagonal elements in the matrix of $\mathcal{H}'$, formed with the Ψ_k^0 basis functions. Assume that the system is in an eigenstate of $\mathcal{H}_0$, say E_i, at $t = 0$. Thus, with the probability interpretation of the wave function, we have

$$c_i(0) = 1, \quad c_k(0) = 0, \quad k \neq i. \tag{4.6}$$

The first-order result is now obtained by integration of (4.5), using the condition (4.6) in the integral also for $t > 0$, i.e.

$$c_n(t) = -\frac{\mathrm{i}}{\hbar}\int\limits_0^t \exp\left(\mathrm{i}\omega_{ni}t'\right)\left\langle n\left|\mathcal{H}'\right|i\right\rangle \mathrm{d}t', n \neq i, \tag{4.7}$$

where $|i\rangle$ abbreviates $\left|\psi_i^0\right\rangle$ and correspondingly for $\langle n|$ The transition probability from state i to state n is then $|c_n(t)|^2$. In order to calculate this quantity, we must consider the time-dependent perturbation $\mathcal{H}'$ more explicitly.

We start by considering a one-electron system influenced by an electromagnetic field. This field can in a source-free region be expressed by the magnetic vector potential $\boldsymbol{A}$, fulfilling the condition $\boldsymbol{\nabla} \cdot \boldsymbol{A} = 0$ according to the Lorentz condition $\boldsymbol{\nabla} \cdot \boldsymbol{A} + c^{-1}\partial\varphi/\partial t = 0$. The Hamiltonian of the system is

$$\begin{aligned} \mathcal{H} &= \frac{1}{2m}(\boldsymbol{p} + e\boldsymbol{A})^2 + V(r) \\ \mathcal{H} &= \frac{1}{2m}(-i\hbar\boldsymbol{\nabla} + e\boldsymbol{A})^2 + V(r), \end{aligned} \tag{4.8}$$

where $V(r)$ is the static potential. But $\boldsymbol{\nabla} \cdot (\boldsymbol{A} f) = (\boldsymbol{\nabla} \cdot \boldsymbol{A}) f + \boldsymbol{A} \cdot (\boldsymbol{\nabla} f) = \boldsymbol{A} \cdot (\boldsymbol{\nabla} f)$, since $\boldsymbol{\nabla} \cdot \boldsymbol{A} = 0$ according to the Lorentz condition, i.e. $\boldsymbol{A}$ and $\boldsymbol{\nabla}$ commute. Thus,

$$\mathcal{H} = \underbrace{-\frac{\hbar^2}{2m}\boldsymbol{\nabla}^2 + V(r)}_{\mathcal{H}_0} \underbrace{- \mathrm{i}\frac{\hbar e}{m}\boldsymbol{A} \cdot \boldsymbol{\nabla} + \frac{e^2}{2m}\boldsymbol{A}^2}_{\mathcal{H}'}. \tag{4.9}$$

For weak fields, the last quadratic term can be neglected (it is important for two-photon transitions; see Sect. 9.1.3). If the radiation is of frequency $\omega, \boldsymbol{A} = \boldsymbol{A_0}\cos\omega t,$ and the quadratic term is neglected, then

$$\mathcal{H}' = -\mathrm{i}\frac{\hbar \mathrm{e}}{\mathrm{m}}\boldsymbol{A} \cdot \boldsymbol{\nabla} = \mathrm{C}\cos\omega \mathrm{t} \tag{4.10}$$

with

$$C = -\mathrm{i}\frac{\hbar e}{m}\boldsymbol{A}_0 \cdot \boldsymbol{\nabla}. \tag{4.11}$$

Using the Eulerian formula cos $x = \left(e^{ix} + e^{-ix}\right)/2$, Eq. (4.7) now becomes

$$c_n(t) = -\frac{1}{2\hbar}\langle n|C|i\rangle\left(\frac{\exp[\mathrm{i}(\omega_{ni} - \omega)t] - 1}{\omega_{ni} - \omega} + \frac{\exp[\mathrm{i}(\omega_{ni} + \omega)t] - 1}{\omega_{ni} + \omega}\right). \tag{4.12}$$

The case when $\Delta\omega = \omega_{\mathrm{ni}} - \omega$ is close to zero is of special interest. This is when the irradiation frequency ω is close to the energy difference between states i and n. Then the second term in (4.12) can be neglected and, again using an Eulerian formula, $\left(e^{ix} - e^{-ix}\right)/2i = sin\, x$, the first term becomes

$$c_n(t) = -\frac{\mathrm{i}}{2\hbar}\langle n|C|i\rangle \mathrm{e}^{\mathrm{i}\Delta\omega t/2}\frac{\sin(\Delta\omega t/2)}{\Delta\omega t/2}t. \tag{4.13}$$

The time-dependent probability of an $i \rightarrow n$ transition is thus

$$|c_n(t)|^2 \propto \left(\frac{\sin(\Delta\omega t/2)}{\Delta\omega t/2}\right)^2 t^2. \tag{4.14}$$

The transition probability is plotted in Fig. 4.2 as a function of $\Delta\omega$ for a given value of t. The function has a prominent maximum for $\Delta\omega = 0$, i.e. when the photon energy of the radiation field exactly matches the energy difference between the final and initial states.

$$\hbar\omega = \hbar\omega_{ni} = E_n - E_i. \tag{4.15}$$

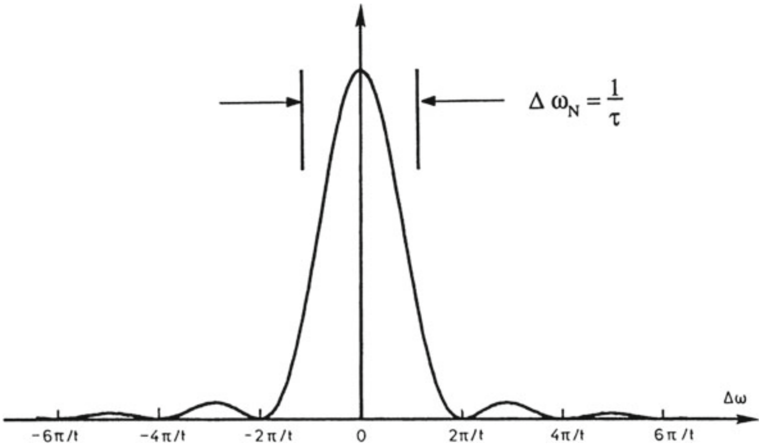

Fig. 4.2 Transition probability for absorption and stimulated emission [1]

This condition is called *resonance*. We have assumed that a transition to a state with higher energy occurs, i.e. *absorption* of radiation. However, exactly the same result is obtained if

$$\hbar\omega = \hbar\omega_{in} = E_i - E_n, \tag{4.16}$$

where the final state n is below the initial state. In this case, the first term in (4.12) is neglected instead of the last. The situation where the perturbation causes the system to emit a photon of the same energy as that of the incoming photons is called *stimulated emission*. From completely equivalent mathematics, it follows that the probabilities for absorption and stimulated emission are the same. Furthermore, a stimulated photon is emitted in the same direction and the wave has the same phase as that of the incoming photon (coherence). This can be seen in a semiclassical picture of these radiative processes where the two processes are considered essentially equivalent. The coherence properties of the stimulated photon result in a strengthening of the incoming beam, a process that is the exact counterpart of the attenuation of a well-defined beam by absorption processes in a non-scattering medium. In both cases, the directional and coherence properties are retained. We will consider later which process dominates.

According to (4.14), the maximum transition probability ($\Delta\omega = 0$) is proportional to t^2, where t is the time during which the system is subject to perturbation. This seems unphysical; one would expect the transition probability to increase linearly with t. However, we must consider that the energy levels are not infinitely sharp, but have a certain width, associated with the natural lifetime (τ) of the state. This point will be considered later in this chapter (See also the discussion following Fig. 1.8!). If the perturbation is applied for a time $t \gg \tau$, the resonance curve of Fig. 4.2 will be much narrower than this level width. The maximum value of the curve then has no significance; instead, the area below the curve yields the transition probability. Since the half-width of the curve is proportional to t^{-1} and its maximum value to t^2 (the internal shape being independent of t), the area under the curve is proportional to t, as expected. This is called the *Fermi Golden Rule*.

At this point, we should recall that a prerequisite for any process to take place at all is that the matrix element $\langle n|C|i\rangle$ in (4.12) is non-zero. We will now consider this matrix element more closely, namely

$$\langle n|C|i\rangle = -\mathrm{i}\frac{\hbar \mathrm{e}}{m}\langle n|\boldsymbol{A}_0 \cdot \nabla|i\rangle. \tag{4.17}$$

Transitions involving outer electrons normally occur in the optical or UV region, which means that the wavelength of the radiation ($\lambda > 100$ nm) is much greater than the dimensions of the atom (~0.1 nm). Thus, the spatial variation of the amplitude over the atom can be neglected and we can write

$$\langle n|C|i\rangle = -\mathrm{i}\frac{\hbar \mathrm{e}}{m}\boldsymbol{A}_0\langle n|\nabla|i\rangle. \tag{4.18}$$

Using the relations

$$\mathrm{i}\frac{\hbar(\mathrm{d}\boldsymbol{r})}{\mathrm{d}t} = [\boldsymbol{r}, \mathcal{H}_0]$$

and

$$\boldsymbol{p} = m\frac{\mathrm{d}\boldsymbol{r}}{\mathrm{d}t} = -\mathrm{i}\hbar\boldsymbol{\nabla}$$

we obtain

$$\boldsymbol{\nabla} = -\frac{m}{\hbar^2}[\mathcal{H}_0, \boldsymbol{r}]$$

and thus

$$\langle n|\boldsymbol{\nabla}|i\rangle = -\frac{m}{\hbar^2}\langle n|\mathcal{H}_0\boldsymbol{r} - \boldsymbol{r}\mathcal{H}_0|i\rangle = -\frac{m}{\hbar^2}(E_n - E_i)\langle n|\boldsymbol{r}|i\rangle.$$

Here, the Hamiltonian operator $\mathcal{H}_0$, being Hermitian, acts to the left in the first term and to the right in the second term. We then obtain

$$\langle n|C|i\rangle = \mathrm{i}e\omega_{ni}\boldsymbol{A}_0 \cdot \langle n|\boldsymbol{r}|i\rangle. \tag{4.19}$$

Thus, we have shown that the transition probability $|\mathrm{c}_n(t)|^2$ is proportional to the square of the matrix element between the initial and final state, Eq. (4.13), formed with the atomic *electric dipole operator*

$$\boldsymbol{p} = -\mathrm{e}\boldsymbol{r}. \tag{4.20}$$

So far we have treated absorption and stimulated emission of radiation. However, it is well known that an atom can emit radiation even when it is not externally perturbed, i.e. *spontaneous emission*. It is not possible to treat this process fully here, since consideration of the quantization of the electromagnetic field as described by *quantum electrodynamics* (QED) is necessary.

According to QED, a coupling between the atom and the "vacuum state" of the field is responsible for the emission. This is related to the lowest energy state of the quantum–mechanical harmonic oscillator being non-zero (3.11)—the electromagnetic field being represented by an ensemble of harmonic oscillators can never be shut off completely!

A simple relation, following the arguments of Einstein in 1917, will be derived between the probabilities for spontaneous and stimulated emission and absorption of radiation using well-known statistical distribution laws. Consider a system such as that illustrated in Fig. 4.3 with two energy levels, E_1 and E_2, populated by N_1

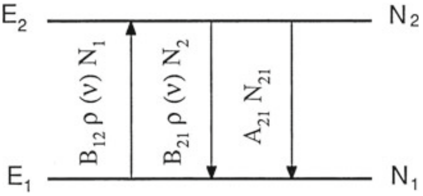

Fig. 4.3 Radiative processes connecting energy levels E_1 and E_2

and N_2 atoms, respectively. Three radiative processes can occur between the levels, as discussed above. In the figure, the processes are expressed using the so-called *Einstein coefficients*, B_{12}, $B_{21,}$ and A_{21}, which are defined such that the rate of change in the population numbers is

$$\frac{\mathrm{d}N_1}{\mathrm{d}t} = -\frac{\mathrm{d}N_2}{\mathrm{d}t} = -B_{12}\rho(\nu)N_1 + B_{21}\rho(\nu)N_2 + A_{21}N_2, \tag{4.21}$$

where $\rho(\nu)$ is the energy density of the radiation field per frequency interval, and $\nu = (E_2 - E_1)/h$. At equilibrium, we have

$$\frac{\mathrm{d}N_1}{\mathrm{d}t} = \frac{\mathrm{d}N_2}{\mathrm{d}t} = 0 \tag{4.22}$$

yielding

$$\rho(\nu) = \frac{A_{21}}{B_{12}(N_1/N_2) - B_{21}}. \tag{4.23}$$

We now assume the system to be in thermodynamic equilibrium. The distribution of the atoms is governed by Boltzmann's law

$$\frac{N_1}{N_2} = \exp\left(\frac{h\nu}{kT}\right), \tag{4.24}$$

where T is the absolute temperature of the system and k is the Boltzmann constant. By identifying the expression for ρ given above with the Planck radiation law

$$\rho(\nu) = \frac{16\pi^2\hbar\nu^3}{c^3}\frac{1}{\exp(h\nu/kT) - 1} \tag{4.25}$$

we obtain the following relations between the three coefficients

$$B_{12} = B_{21}, \tag{4.26}$$

$$\frac{A_{21}}{B_{21}} = \frac{16\pi^2\hbar\nu^3}{c^3}. \tag{4.27}$$

The first relation shows that the probabilities for absorption and stimulated emission are the same for a transition between states 1 and 2. This is in accordance with the result obtained above using formal quantum mechanics. Note that the result (4.26) is independent of the strength of the radiation field. It was in discussions of this kind that A. Einstein, in 1917, found it necessary to introduce the concept of stimulated emission in order to obtain agreement with the statistical laws known at that time [212].

From (4.13), (4.19), and (4.27), the spontaneous transition probability between the states i and k is found to be

$$A_{ik} = \frac{32\pi^3}{3}\frac{\nu^3}{4\pi\epsilon_0\hbar c^3}|\langle i|e\mathbf{r}|k\rangle|^2. \tag{4.28}$$

The most important result here is that this transition probability is determined by the same matrix elements as the induced transitions. Thus, there are common *selection rules* for all three types of transitions. These rules tell under what circumstances the matrix element is non-zero, in turn reflecting the mathematical properties of the angular part $Y_{lm}(\theta, \varphi)$ of the wave functions of the states involved.

So far we have only treated electric dipole radiation. In a more detailed treatment, the radiation field can be described by electric and magnetic "*multipole fields*", i.e. magnetic dipole radiation, electric quadrupole radiation, etc. Magnetic dipole radiation is analogous to electric dipole radiation and it depends on the magnetic dipole moment of the atom

$$\boldsymbol{\mu}_J = -\mu_\mathrm{B}\sum_i (\boldsymbol{l}_i + 2\boldsymbol{s}_i) = -\mu_\mathrm{B}(\boldsymbol{L} + 2\boldsymbol{S}). \tag{4.29}$$

If electric dipole radiation is allowed, i.e. if the matrix element of $\boldsymbol{r}$ between the two states is non-zero, this type of radiation strongly dominates over the other types. If, however, an electric dipole transition is not allowed, other types of radiation become important.

The total spontaneous transition probability per unit time for an atom, in a specific state i, can be expressed as

$$A_i = \sum_k A_{ik}, \tag{4.30}$$

where the summation is over all levels of the atom having energies less than E_i and A_{ik} is the spontaneous transition probability for a single process. (As an analogy, we may consider a barrel full with water, where the water escape rate depends on the sum of the escape rates for all holes in the bottom). This means that the number of atoms, N, in a certain state i will decrease exponentially with time

$$N = N_0 \exp(-t/\tau_i) \tag{4.31}$$

with

$$\tau_i = 1/A_i. \tag{4.32}$$

Here, we have assumed that the considered level is not re-populated by decay from higher lying levels.

On average, the time elapsed before an atom in the upper state decays to another state is

$$\bar{t} = \frac{\int_0^\infty t \exp(-t/\tau)\mathrm{d}t}{\int_0^\infty \exp(-t/\tau)\mathrm{d}t} = \tau \tag{4.33}$$

and therefore τ is called the *mean lifetime*. It is also possible to calculate the *variance* Δt of the lifetime of the atom in the state of interest

$$(\Delta t)^2 = \frac{\int\limits_0^\infty (t-\tau)^2 \exp(-t/\tau)\mathrm{d}t}{\int_0^\infty \exp(-t/\tau)\mathrm{d}t} = \tau^2. \tag{4.34}$$

Thus, the "uncertainty" in the lifetime is also equal to τ. The corresponding uncertainty (ΔE) in an energy determination of the level must fulfil the Heisenberg uncertainty relation

$$\Delta E \cdot \Delta t \geq \hbar/2. \tag{4.35}$$

Here, mathematically the uncertainties are *variances*. The minimum value of this product yields the minimum energy uncertainty which can never be surpassed

$$\Delta E_{\mathrm{min}} = h\Delta \nu. \tag{4.36}$$

We find that the so-called *natural radiation width* (in frequency units) is given by

$$\Delta \nu_{\mathrm{N}} = 2\Delta \nu = 1/2\pi\tau. \tag{4.37}$$

It is interesting to compare this "microscopic" treatment of radiative processes with the "macroscopic" treatment of classical physics. In the latter view, the atom is considered as an exponentially damped harmonic oscillator generating the oscillating electric field (Fig. 4.4)

$$\mathcal{E} = \mathcal{E}_0 \mathrm{e}^{-\mathrm{t}/2\tau} \cos(2\pi \nu_0 \mathrm{t}). \tag{4.38}$$

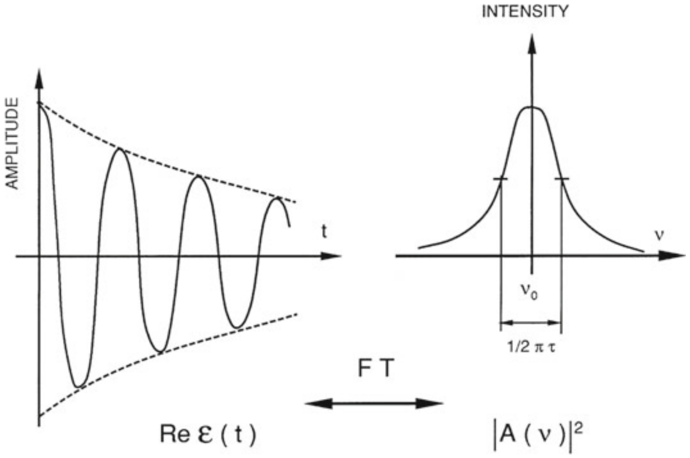

Fig. 4.4 Semiclassical picture of a radiating atom [1]

Because the oscillation is damped, the frequency cannot be infinitely sharp. A Fourier analysis allows a determination of the frequency distribution giving rise to this special time dependence for the oscillation. In the Fourier analysis, it is convenient to work with the complex function

$$\mathcal{E}(\mathrm{t}) = \mathcal{E}_0 \mathrm{e}^{-\mathrm{t}/2\tau} \mathrm{e}^{\mathrm{i}2\pi\nu_0 \mathrm{t}}, \tag{4.39}$$

the real part of which is the function given in (4.38). The *amplitude* distribution is described by the Fourier transform

$$\begin{aligned} A(\nu) &= \frac{1}{2\pi} \int\limits_0^\infty \mathcal{E}_0 \mathrm{e}^{t/2\tau} \mathrm{e}^{\mathrm{i}2\pi(\nu_0 - \nu)t} \mathrm{d}t \\ &= \frac{\mathcal{E}_0}{2\pi} \frac{-1}{\mathrm{i}2\pi(\nu_0 - \nu) - 1/2\tau}. \end{aligned}$$

The intensity distribution is $|A(\nu)|^2$:

$$\begin{aligned} |A(\nu)|^2 = A(\nu)A^*(\nu) &= \frac{\mathcal{E}_0^2}{4\pi^2} \left[4\pi^2(\nu - \nu_0)^2 + 1/4\tau^2\right]^{-1} \\ &= \frac{\left(\mathcal{E}_0^2 \tau^2\right)}{\pi^2} \left[1 + \left(\frac{\nu - \nu_0}{1/4\pi\tau}\right)^2\right]^{-1}. \end{aligned} \tag{4.40}$$

This is a Lorentzian curve with a full width at half-maximum of $\Delta\nu = (2\pi\tau)^{-1}$. This classical approach thus yields the same radiative width as quantum mechanics.

The broadening of the transition due to the finite lifetime of the excited state is called the *homogeneous* broadening in contrast to *inhomogeneous* broadening, which will be discussed in Chap. 6.

At the end of this section, we would like to mention two kinds of phenomena that can influence the natural radiative lifetime. The first one is the *ambient black-body radiation* which, even at room temperature, can have a substantial effect on the lifetime of highly excited, normally long-lived, states. Such states are connected to nearby levels by microwave electric dipole transitions. The substantial black-body radiation in this wavelength region can induce transitions through absorption or stimulated emission, thus effectively reducing the lifetime of the investigated state. The effects can be quite drastic and can only be eliminated by cooling the atomic environment to low temperatures [213–215].

The second phenomenon is of a much more fundamental nature and can be understood in the more detailed treatment of the interaction between matter and light provided by the quantum electrodynamic (QED) theory. As we have seen above, it is frequently sufficient to treat the light/matter interaction by quantizing the matter (atoms/molecules) and to consider the light as an electromagnetic field from which absorption can occur only in quantized energy units (photons). However, many aspects require a more rigorous treatment, where the electromagnetic field is also quantized. We have already discussed the case of spontaneous emission, which can be seen as due to an interaction of the atom with the lowest (vacuum) state of the quantized field. The field can be seen as an ensemble of harmonic oscillators, but the harmonic oscillator has a non-zero lowest state; see Eq. (3.11). Thus, it is normally not possible to completely shut off the field—the perturbation that causes the change in quantum states.

Based on the theory of spontaneous emission, there is now a possibility of influencing the natural lifetime of an excited state by manipulating the quantized field ground state. This can be done by placing an atom in a cavity whose dimensions are too small to support the vacuum mode of the field (“turning off the vacuum”), leading to a prolonged excited-state lifetime [216–219]. In the same way, the vacuum mode can be enhanced by using a cavity tuned to resonance with an atomic microwave transition, resulting in an increased spontaneous emission rate and a decreased lifetime [220]. The *Lamb shift*, which is a pure quantum electrodynamical effect, is also influenced by a cavity.

The quantized nature of the field and its fundamental interaction with atoms lead to many further interesting non-classical phenomena, which are treated in a field referred to as *quantum optics*. The field also comprises emerging practical applications such as *quantum computing* and *quantum cryptography*. We will discuss this field later in Sect. 4.9.

4.2 Spectra Generated by Dipole Transitions

A spectrum is generated by transitions between different energy states according to certain selection rules. The selection rules for allowed transitions essentially reflect the requirement of conservation of angular momentum for the atom/molecule–photon system. Considerations of symmetry for the wave functions describing the states involved are also important. The establishing of selection rules for electric dipole transitions is according to (4.13) and (4.19) equivalent to a determination of the conditions under which the matrix element $\langle n|\mathbf{r}|i\rangle$ is non-zero. Since $\boldsymbol{r}$ is an odd operator, we can immediately state that the two considered states must be of *opposite parity*.

The selection rules will not be derived here, but stated with some comments. The rules mathematically reflect the properties of the spherical harmonics $Y_{lm}(\theta, \varphi)$, which appear in (1.8) and (1.11).

We will present how spectra are generated by allowed transitions between energy levels described in Chaps. 2 and 3. It is best to treat atoms and molecules separately, but first some general features will be discussed in connection with Fig. 4.5.

The spectra of atoms and molecules resulting from absorption or emission can be studied. In *absorption*, a wavelength continuum is used, from which certain wavelengths are absorbed. *Emission* spectra may be generated in a discharge in a light source where the excited levels are populated by, for example, electron collisions. If atoms or molecules are irradiated by the light of a wavelength that corresponds to the energy of an allowed transition from the ground state, there will be a *resonance absorption* of photons followed by the release of *resonance radiation* in the decay back to the original level. If the decay occurs to levels above the ground state, the emitted light is called *fluorescence light*, having a longer wavelength. We say that the fluorescence is *Stokes-shifted* with regard to the excitation wavelength.

A special type of emission, *phosphorescence*, can be obtained from certain molecules that are excited from the ground state to a higher lying state in the normal

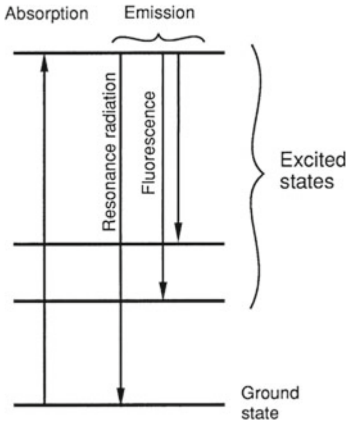

Fig. 4.5 Terminology for radiative processes

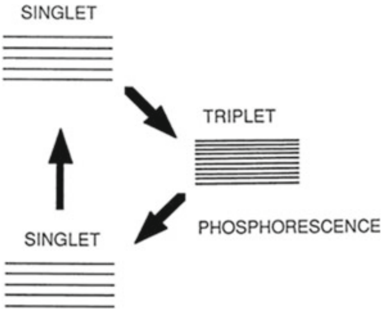

Fig. 4.6 The phosphorescence phenomenon

way. If the molecules make transitions to a lower lying state of another multiplicity, for example, through collisions, the molecules can accumulate here for a long time, since the transition to the ground state is normally radiatively forbidden (Fig. 4.6). In phosphorescing substances, the state is not depopulated through radiationless transitions and therefore an extremely long lifetime is obtained (seconds or more), and weak light will be emitted long after the excitation has been terminated.

4.2.1 Atoms

For one-electron systems, we have the following selection rules:

$$\Delta l = \pm 1, \tag{4.41}$$

$$\Delta j = 0, \pm 1.$$

The transition energies for hydrogen, and systems with similarity to hydrogen, are obtained from (2.4) and (2.6) as the Balmer and the Rydberg formulae, respectively. Thus, for hydrogen,

$$\frac{1}{\lambda} = R_y\left(\frac{1}{n^2} - \frac{1}{m^2}\right) \; Balmer\ formula. \tag{4.42}$$

With $n = 1, 2, 3\ldots$ and m as increasing interger, we obtain the Lyman (ultraviolet), Balmer (visible), Paschen (infrared), etc. series of hydrogen spectral lines, respectively. For the more general case we have:

$$\frac{1}{\lambda} = R_y\left(\frac{1}{(n-d_1)^2} - \frac{1}{(m-d_2)^2}\right) \; Rydberg\ formula \tag{4.43}$$

For many-electron systems, we have

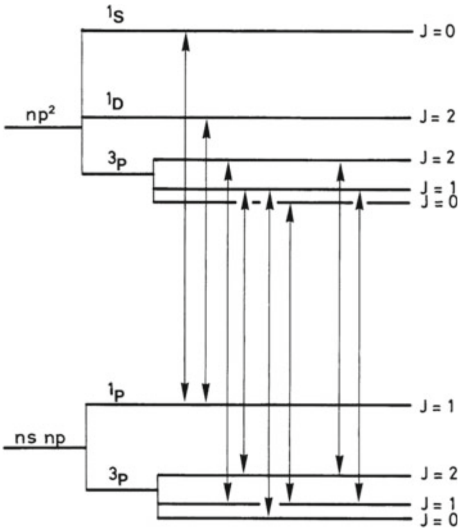

Fig. 4.7 Allowed electric dipole transitions between a p^2 and an *sp* configuration [1]

$$\Delta J = 0, \pm 1 \quad 0 \nleftrightarrow 0 \quad \text{forbidden}\,. \tag{4.44}$$

In pure *LS* coupling, we also have

$$\Delta L = 0, \pm 1 \quad 0 \nleftrightarrow 0 \quad \text{forbidden},$$

$$\Delta S = 0 \tag{4.45}$$

Allowed transitions between a p^2 and an *sp* configuration are indicated in Fig. 4.7 as an example.

Transitions in the H, Na, He, and Ca atoms are indicated in Figs. 2.1, 2.2, 2.6, and 2.7, respectively.

Even at small deviations from *LS* coupling, transitions between states of different multiplicity (*intercombination lines*) are observed. Such lines are indicated for the Ca atom in Fig. 2.7 and are weak because of the long excited-state lifetime. However, such very week transitions, which have very narrow linewidths, are very interesting for the construction of ultra-stable atomic clocks (see Sect. 9.7), which could approach an accuracy of 1: 10^{17}. Suitable atomic lines being considered include "forbidden" transitions in ^{87}Sr and ^{199}Hg atoms and in ^{27}Al, ^{171}Yb, and ^{199}Hg ions.

In the presence of hyperfine structure, there is a further selection rule:

$$\Delta F = 0, \pm 1 \quad 0 \nleftrightarrow 0 \quad \text{forbidden}. \tag{4.46}$$

So far we have only considered transitions of outer electrons giving rise to lines in the IR, visible, and UV spectral regions. If a vacancy is created in an inner shell, de-excitation occurs by successive transitions inwards by electrons from outer shells

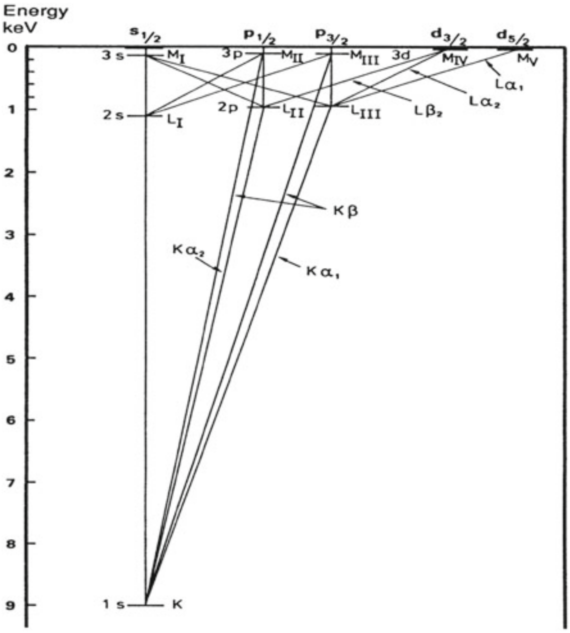

Fig. 4.8 X-ray transitions in the copper atom [1]

(Chap. 5). Level and transition designations for the inner shells of the copper atom are given in Fig. 4.8.

So far we have not discussed the selection rules for the M (sometimes written m) quantum number. M describes projections of the *resulting* angular momentum of the atom, which can be $\boldsymbol{J}$ or $\boldsymbol{F}$. The rule is

$$\Delta M = 0, \pm 1. \tag{4.47}$$

The different values of ΔM correspond to different *angular distributions* of the radiation and to different *polarization conditions*. For $\Delta M = 0$, only the z-component of $\boldsymbol{p} = -e\boldsymbol{r}$ contributes and the radiation can be compared to that of a classical dipole oscillating along the direction of the magnetic field (quantization axis). The radiation then has an intensity that is proportional to $\sin^2\theta$, θ being the angle between the field and the direction of radiation. As for the polarization, the electrical vector oscillates in the plane defined by the field and the direction of the radiation. (The magnetic vector is perpendicular to the electric one and both vectors are perpendicular to the direction of propagation.) In a similar way, it is found that the $x \pm iy$-components in a coordinate system representing the vector $\boldsymbol{r}$ as $(x + iy, x - iy, z)$ are responsible for $\Delta M = \pm 1$ transitions corresponding to an electric dipole rotating in the x–y-plane, i.e. perpendicularly to the field direction. The intensity is, in this case, proportional to $\left(1 + \cos^2\theta\right)$, and the radiation is generally elliptically polarized. In the z-direction, it is circularly polarized and in the x–y-plane linearly polarized. The radiation that

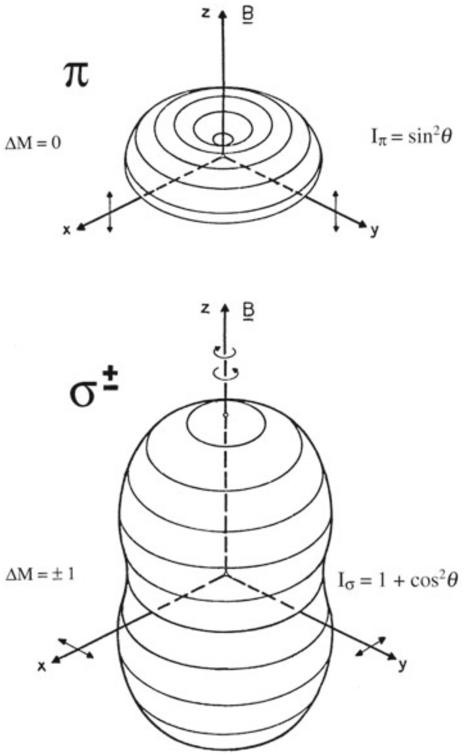

Fig. 4.9 Intensity distributions for π and σ radiation. The marks on the coordinate axes indicate the oscillation direction of the electric field vector [1]

corresponds to $\Delta M = 0$ is called π radiation and for $\Delta M = \pm 1$ the term σ radiation is used. The intensity and polarization distributions are illustrated in Fig. 4.9.

We have discussed above the distribution of the emitted radiation. Clearly, the process is reversible and the given angular distributions then give the relative probability of absorption by a lower energy state atom of a photon, incoming from a certain direction and with a given polarization.

Radiative transitions in atoms and selection rules have been discussed in more detail in the atomic physics books referred to in Chap. 2.

4.2.2 Molecules

Classically, light is emitted by a system only if its electric dipole moment is changed. This rule is also valid quantum mechanically and is of special importance in the consideration of the radiative properties of molecules. We will first treat rotational and vibrational transitions within a given electronic molecular state. Primarily, we only consider $^1\Sigma$ states for which the complications, discussed at the end of Sect. 3.2, do not occur since the rotational angular momentum is the only form of angular momentum present.

Rotational Transitions. A diatomic molecule with two different kinds of atoms has a permanent dipole moment in the direction of the symmetry axis. If the molecule rotates, the dipole should classically emit radiation (see also Fig. 4.9). Quantum mechanically, radiation occurs when the rotation is changed. For the rotational quantum number J, which was defined in Chap. 3, we have

$$\Delta J = \pm 1. \tag{4.48}$$

Like for atoms, the rule reflects the mathematical properties of the spherical harmonics $Y_{lm}(\theta, \varphi)$, which describe the rotational motion, and also reflects the fact that a photon carries an angular momentum of $1\hbar$. Using the energy expression (3.6) for rotational levels we have

$$\nu_{J+1\leftrightarrow J} = \frac{2B}{h}(J+1), \quad J = 0, 1, 2, \ldots \tag{4.49}$$

Thus, we obtain equidistant rotational lines in the far IR (~1000 μm) as illustrated in Fig. 4.10.

If we take the elasticity of the molecule into account (3.7), we obtain

$$\nu_{J+1\leftrightarrow J} = \frac{2B}{h}(J+1) - \frac{4D^+}{h}(J+1)^3. \tag{4.50}$$

Vibrational Transitions. If the molecule has a permanent dipole moment at the equilibrium distance (r_0 in Fig. 3.7), this moment will vary periodically during vibration. Classically, radiation will then be emitted. If a diatomic molecule has a

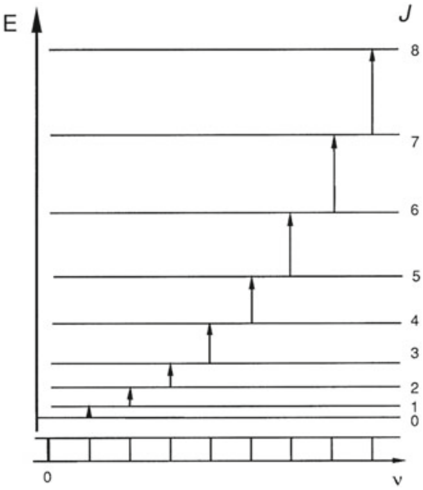

Fig. 4.10 Rotational transitions in a diatomic molecule

harmonic oscillatory movement, we obtain the quantum–mechanical selection rule

$$\Delta \upsilon = \pm 1. \tag{4.51}$$

Since the energy levels of the harmonic oscillator are equidistant, only one IR vibrational line (∼10 μm) is obtained. If the potential deviates from the harmonic oscillator, transitions with $\Delta \upsilon = \pm 2$, $\Delta \upsilon = \pm 3$, etc. can also occur. These transitions, which are generally weak, are called overtones (harmonics). As for rotational motion, molecules of the type O_2 and N_2 (i.e. homonuclear molecules) do not exhibit electric dipole vibrational lines, since no dipole moment exists. However, quadrupole- and pressure-induced transitions of homonuclear molecules can be observed faintly.

Vibrational–Rotational Spectra. If there were no interaction between rotational and vibrational motion, the energy of a rotating vibrator would simply be the sum of its rotational and vibrational energies according to the above expressions. However, the moment of inertia of the molecule is influenced by molecular vibration during rotation. The vibrational energy is much greater than the rotational energy and we can use the mean value of r^2 (see (3.4) and (3.6)) during the vibration to calculate an effective rotational constant B′, which is slightly lower than the one corresponding to the equilibrium separation. Writing the energy of a molecular level as

$$E = (\upsilon + 1/2)h\nu_c + B'J(J+1) \tag{4.52}$$

and using the selection rules $\Delta \upsilon = \pm 1$, $\Delta J = \pm 1$, we obtain the absorption spectrum

$$\Delta E = h\nu_c \begin{cases} +2B'(J+1) & J \to J+1 \quad J = 0, 1, \ldots \quad \text{(R branch)} \\ -2B'J & J \to J-1 \quad J = 1, 2, \ldots \quad \text{(P branch)} \end{cases} \tag{4.53}$$

Lines corresponding to the upper expression form the so-called *R branch*, while the lower expression yields the *P branch*. The transitions are indicated for a simple case in Fig. 4.11. Note that there is no line at $\Delta E = h\nu_c$, since $\Delta J = 0$ is forbidden for diatomic molecules. As a matter of fact, the value of B' will decrease for higher vibrational states. By designating the rotational constants for the two states B' and B'' (upper and lower states, respectively), we obtain

$$\Delta E = h\nu_c \begin{cases} +2B' + (3B' - B'')J + (B' - B'')J^2 \\ J \to J+1 \quad J = 0, 1, \ldots \text{(R branch)} \\ \quad -(B' + B'')J + (B' - B'')J^2 \\ J \to J-1 \quad J = 1, 2, \ldots \text{(P branch)} \end{cases} \tag{4.54}$$

Both branches can be represented by a single formula

$$\Delta E = h\nu_c + (B' + B'')m + (B' - B'')m^2 \tag{4.55}$$

Fig. 4.11 Vibrational–rotational spectrum when the rotational constant B is the same in both vibrational states

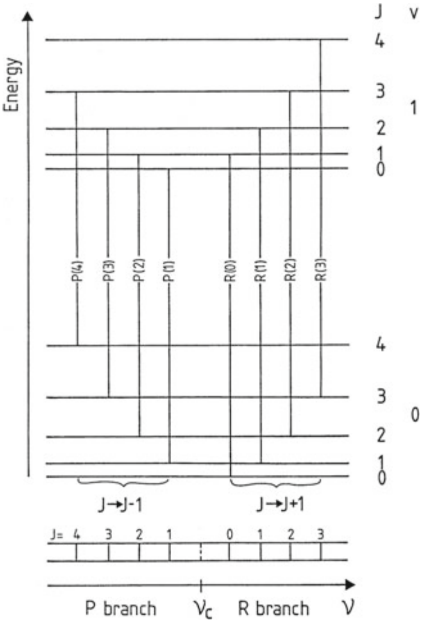

with

$m = 1, 2, 3\ldots$ for the R branch.

and

$m = -1, -2, -3\ldots$ for the P branch.

Since $B' < B''$, because of the averaging over r^2 in the asymmetric Morse potential (see Fig. 3.4 and (3.8)), this formula shows that the distance between lines becomes successively smaller in the R branch, while there is a corresponding increase in the P branch, as illustrated in Fig. 4.12.

For sufficiently high values of *J,* there can be an inversion of the R branch, giving rise to the formation of a *bandhead*. Since the *B* values differ still more between states belonging to different electronic levels, bandheads are more frequently observed in spectra obtained in electronic transitions. Equation (4.55) represents a parabola, and a diagram like the one given in Fig. 4.13 is called a *Fortrat parabola*. Depending on the relative sizes of B' and B'', the parabola has its vertex towards higher or lower frequencies. If $B' < B''$, the band is said to be *shaded to the red*, whereas if $B' > B''$, it is *shaded to the violet*. We note that many lines fall at basically the same wavelength, at and close to the bandhead, which leads to a strong observed signal intensity. The phenomenon is similar to what is observed for the rainbow (Sect. 4.6).

The population of different vibrational levels is given by the Boltzmann distribution. Thus, only the state with $\upsilon = 0$ is well populated for molecules with a large separation between the vibrational levels, e.g. N_2 and O_2. The distribution for a molecule with a small value of $h\nu_c/kT$ is shown in Fig. 4.14.

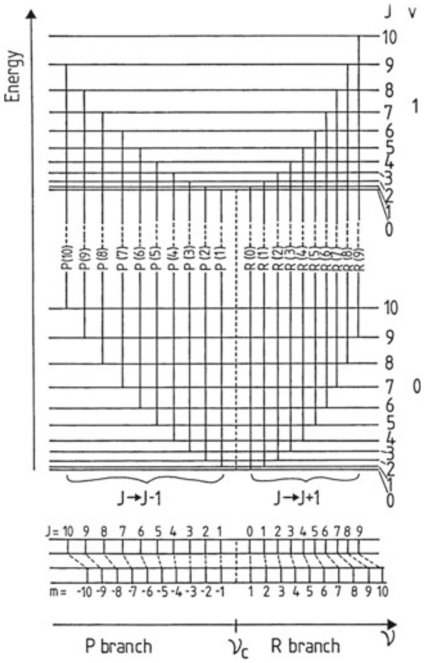
Energy
J v
10
9
8
7
6
5
4
3
2
1
0
1
0
P(10) P(9) P(8) P(7) P(6) P(5) P(4) P(3) P(2) P(1)
R(0) R(1) R(2) R(3) R(4) R(5) R(6) R(7) R(8) R(9)
J→J-1
J→J+1
J= 10 9 8 7 6 5 4 3 2 1 0 1 2 3 4 5 6 7 8 9
m= -10 -9 -8 -7 -6 -5 -4 -3 -2 -1 1 2 3 4 5 6 7 8 9 10
P branch
ν_c
R branch
ν

Fig. 4.12 Vibrational–rotational spectrum when the rotational constant B is smaller in the upper vibrational state

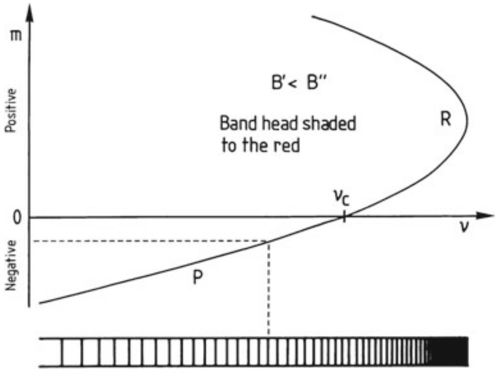
m
Positive
0
Negative
B′< B″
Band head shaded to the red
R
ν_c
ν
P

Fig. 4.13 The Fortrat parabola

The intensity distribution *within* a vibrational–rotational band is also determined by the Boltzmann distribution. It is then necessary to take the $2J + 1$ magnetic sublevels of a rotational level into account. The distribution factor is

$$N_J \propto (2J + 1)\mathrm{e}^{-BJ(J+1)/kT}. \tag{4.56}$$

This distribution for the HCl molecule ($B = 10.44\ \mathrm{cm}^{-1}$) is shown in the left part of Fig. 4.15 for room temperature. This distribution leads to a somewhat higher intensity of the R branch compared with the P branch, which is also illustrated in

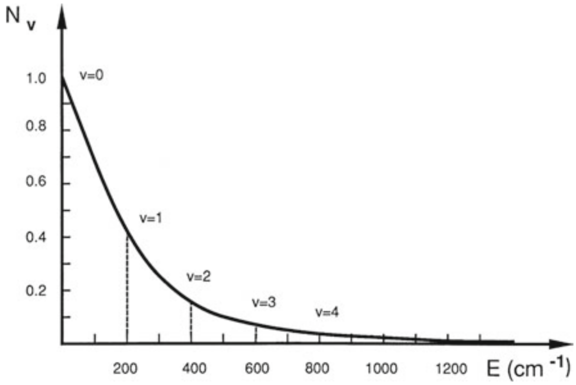

Fig. 4.14 Population distribution on different vibrational levels of I_2 [221]

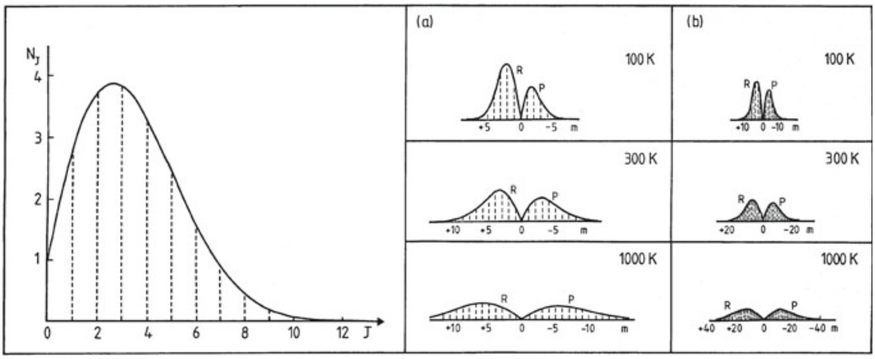

Fig. 4.15 Population distribution on different rotational levels and resulting spectra for different temperatures, **a** $B = 10.44\ \mathrm{cm}^{-1}$ and **b** $B = 2\ \mathrm{cm}^{-1}$ [221]

the figure for two molecules with large and small B values, respectively. As seen in Fig. 4.11, an R-branch transition always starts with a lower and better populated rotational level than the matching P-branch transition. The population dependence can be utilized for spectroscopic temperature measurements.

Electronic Transitions—The Franck–Condon Principle. Vibrational and rotational spectra are related to the movements of the atomic nuclei of the molecule. In transitions between different electronic configurations, much higher energies are involved (∼ eV, visible, or UV region). Normally a transition in the electronic shell is accompanied by transitions between different vibrational and rotational levels of the molecule. Therefore, *bands* are also obtained in the visible region. The intensities of the components of the observed vibrational structure are explained by the *Franck–Condon principle*. Electronic transitions in molecules occur so quickly that the nuclei do not change their relative positions in vibrational motion. Some cases are illustrated in Fig. 4.16. In part (a) of the figure, the equilibrium distances of the two

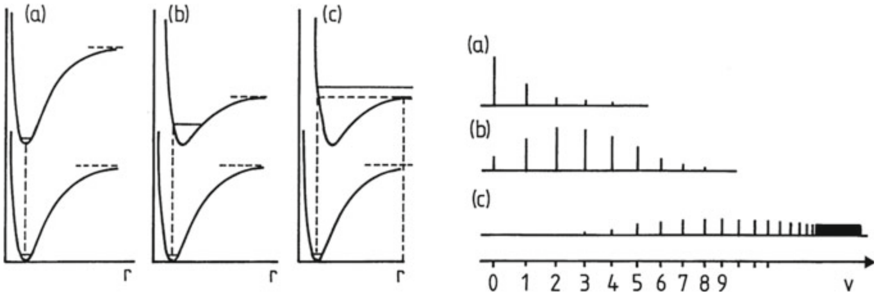

Fig. 4.16 Illustration of the Franck–Condon principle and resulting spectra [221]

potential curves are the same. Primarily, we then obtain a $\upsilon = 0 \rightarrow \upsilon = 0$ transition in absorption since the relative positions and velocities of the nuclei are not changed. In (b), transitions occur primarily from the $\upsilon = 0$ level to a level with higher υ, since the wave function in the excited state has a maximum at the classical turning point. In (c), dissociation also occurs, resulting in a continuum in the absorption spectrum. Typical spectra are also shown beside the potential curves.

The transition back to the ground state from an excited electronic state can occur in several ways. Transitions can occur by the direct emission of a photon. De-excitation can also occur through successive transitions via the vibrational levels in the excited electron configuration and only after that be followed by a return to the ground state. The light is then shifted towards red compared with the excitation wavelength (*Stokes shifting*). This can be observed, for example, in organic dye molecules.

While $\Delta J = 0$ is forbidden in a pure rotational–vibrational transition, this type of transition is allowed in connection with electronic transitions (still not for $^1\Sigma - {}^1\Sigma$ transitions). The new selection rule gives rise to a *Q branch*, in addition to the R and P branches.

Molecular spectra have been discussed in more detail in the molecular physics books referred to in Chap. 3.

4.3 Rayleigh and Raman Scattering

As shown in Sect. 4.1, resonant transitions can be obtained if an atomic or molecular system is irradiated by light with an energy corresponding to the energy separation between two levels. Even if the light is not of a resonant frequency, weak scattering effects are still obtained, so-called the *Rayleigh* and *Raman scattering*. This scattering can be explained classically as well as quantum mechanically. Detailed descriptions of these phenomena and their utilization can be found in [205–211].

If a molecule is subject to an electric field $\mathcal{E}$, an electric dipole moment $\boldsymbol{P}$ is induced in the molecule (see the Stark effect), i.e.

$$\boldsymbol{P} = \alpha \boldsymbol{\mathcal{E}}. \tag{4.57}$$

Generally, $\boldsymbol{P}$ is not directed along $\boldsymbol{\mathcal{E}}$, since the molecule is frequently asymmetric and α is then replaced by a *polarization tensor*. For an oscillating field

$$\boldsymbol{\mathcal{E}} = \boldsymbol{\mathcal{E}}_0 \sin(2\pi \nu t) \tag{4.58}$$

the polarization will vary at the frequency ν, resulting in a re-radiation of light of the same frequency. This *Rayleigh scattering* is *elastic* in nature. The total radiated energy I from an oscillating dipole is from the electromagnetic theory given by

$$I = \frac{2}{3c^3} \overline{\left(\frac{\mathrm{d}^2 P}{\mathrm{d}t^2} \right)^2} \tag{4.59}$$

where the bar denotes time averaging. Equations (4.59) and (4.58) yield

$$I = \frac{16\pi^4 c}{3\lambda^4} \alpha^2 \mathcal{E}_0^2. \tag{4.60}$$

Here, we have used the relation $\overline{(\sin^2 2\pi \nu t)} = 1/2$. As can be seen, the Rayleigh scattering strongly increases with diminishing wavelength.

If a molecule vibrates, its polarizability varies. Further, the polarizability depends on the orientation of the molecule with regard to the field, as mentioned in connection with the introduction of the polarizability tensor. Thus, the polarizability of the molecule varies as it rotates. We can then state

$$\alpha = \alpha_0 + \alpha_{\mathrm{lv}} \sin(2\pi \nu_{\mathrm{vibr}} t) \quad \alpha_{\mathrm{lv}} \ll \alpha_0 \tag{4.61}$$

for the vibrational motion and

$$\alpha = \alpha_0 + \alpha_{\mathrm{lr}} \sin(2\pi 2\nu_{\mathrm{rot}} t) \quad \alpha_{\mathrm{lr}} \ll \alpha_0 \tag{4.62}$$

for the rotational motion, where the variation occurs at twice the rotational frequency ν_{rot}. This is due to the fact that the polarizability is the same for opposite directions of the field. We note that there is a connection between this factor of 2 and the $\pm m$ energy degeneracy for the Stark effect (2.35), and the molecular term splitting (3.2). If an external oscillating field of frequency ν is applied, there will be a coupling between the applied and the internal oscillation. This coupling becomes evident if (4.61) or (4.62) is inserted into $|\boldsymbol{P}| = \alpha |\boldsymbol{\mathcal{E}}|$ and the simple trigonometric relation $2 sin\alpha sin\beta = cos(\alpha - \beta) - cos(\alpha + \beta)$ is applied.

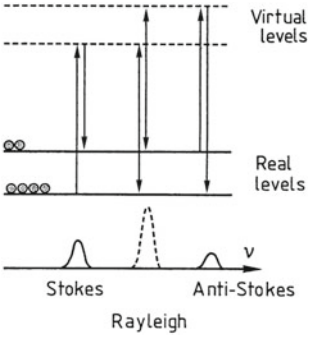

Fig. 4.17 Raman scattering

For vibrational motion

$$P = \alpha_0 \mathcal{E}_0 \sin(2\pi \nu t) + (1/2)\alpha_{1v}\mathcal{E}_0 \\ [\cos 2\pi(\nu - \nu_{\text{vibr}})t \quad - \cos 2\pi(\nu + \nu_{\text{vibr}})t] \tag{4.63}$$

for rotational motion

$$P = \underset{\substack{\uparrow \\ \text{Rayleigh}}}{\alpha_0 \mathcal{E}_0 \sin(2\pi\nu t)} + (1/2)\alpha_{1r}\mathcal{E}_0 \, [\underset{\substack{\uparrow \\ \text{Stokes}}}{\cos 2\pi(\nu - 2\nu_{rot})t} - \underset{\substack{\uparrow \\ \text{Anti - Stokes}}}{\cos 2\pi(\nu + 2\nu_{rot})t}] \; . \tag{4.64}$$

Thus, a sideband is obtained on both sides of the Rayleigh line. The sidebands are shifted from the Rayleigh frequency by the vibrational frequency and twice the rotational frequency, respectively. The down- and upshifted components are called the *Stokes* and the *anti-Stokes* lines, respectively, and their strength is generally $\sim 1/1000$ of the strength of the Rayleigh line. The phenomenon is called the *Raman effect* and was first observed experimentally in 1928 by the Indian scientist *C.V. Raman* (Nobel prize in Physics 1930). The Raman effect represents *inelastic scattering*. In the quantum–mechanical theory of the Raman scattering, *virtual* levels are introduced which mediate the scattering (Fig. 4.17).

In the interaction with a molecule, an amount of energy can be emitted or absorbed by the molecule, corresponding to a change in the frequency of the scattered light quantum. From (4.63) and (4.64), it is evident that the Raman effect occurs only when the polarizability is changed in the process ($\alpha_1 \neq 0$). The Raman scattering increases for shorter wavelengths and also exhibits resonances when real levels are approached.

4.4 Raman Spectra

When a molecular gas is intensely irradiated with monochromatic light, usually from a laser, a spectrum of Raman lines is generated close to the strong elastic Rayleigh component.

4.4.1 Vibrational Raman Spectra

For the Raman effect, vibration in a harmonic oscillator potential leads to the same selection rule as for the normal IR spectrum

$$\Delta \upsilon = \pm 1. \tag{4.65}$$

Thus, a Stokes and an anti-Stokes component are obtained, shifted by a frequency ν_c from the Rayleigh line. At normal temperatures, most of the molecules are in the lowest state ($\upsilon = 0$) and a few are in the $\upsilon = 1$ state. The intensity of the Stokes line, corresponding to the transition 0 → 1, is thus much greater than that of the anti-Stokes line (1 → 0). In the quantum–mechanical picture, the intensities reflect the populations of the levels. On the other hand, the classical picture falsely predicts components of equal intensity. By comparing the intensities of the Stokes and the anti-Stokes components, the temperature can be determined, for example, in a flame. Because of the non-harmonicity of the vibrational potential, the spacing between the vibrational levels is not constant. This results in the occurrence of separated Stokes components originating from different vibrational levels. Utilizing the components from higher levels (*hot bands*), the temperature can conveniently be determined as illustrated in Fig. 4.18.

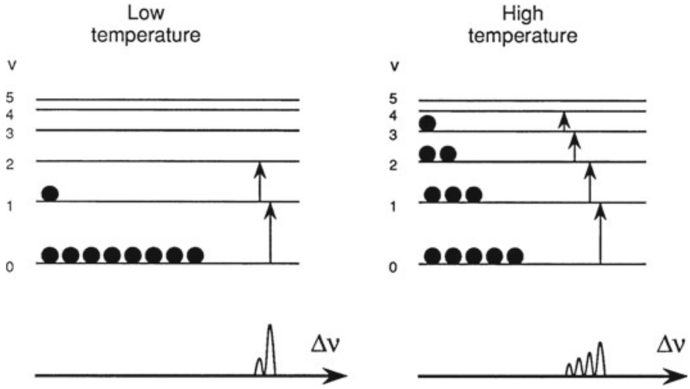

Fig. 4.18 The occurrence of vibrational "hot bands" in the Raman spectra

Diatomic molecules with identical atoms do not exhibit any IR spectrum because of the absence of a permanent dipole moment. They are, however, *polarizable* and the Raman effect is then observed. The separation between the lowest vibrational levels is for most diatomic molecules so large, that only the Stokes line can be observed at room temperature. However, anti-Stokes lines can be observed for most polyatomic molecules which exhibit lower vibrational frequencies.

4.4.2 Rotational Raman Spectra

While the vibrational Raman effect has the same selection rule as the IR transitions, different rules apply for the rotational Raman effect (compare with the classical picture!)

$$\Delta J = \pm 2. \tag{4.66}$$

Since several rotational levels with different J values are frequently populated, the rotational Raman spectrum consists of several lines. $\Delta J = 0$ corresponds to the Rayleigh line. The Stokes and anti-Stokes branches of equidistant lines corresponding to $\Delta J = \pm 2$ are obtained. The branches are called S and O for $\Delta J = +2$ and $\Delta J = -2$, respectively. Utilizing (3.6), we have

$$\nu_{J+2\leftrightarrow J} = \frac{4B(J+3/2)}{h}. \tag{4.67}$$

An example of the rotational Raman effect is shown in Fig. 4.19.

Fig. 4.19 Rotational Raman spectrum

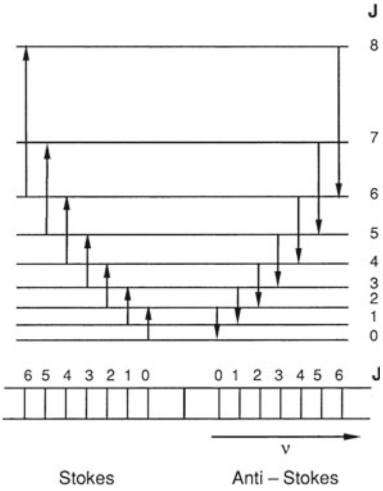

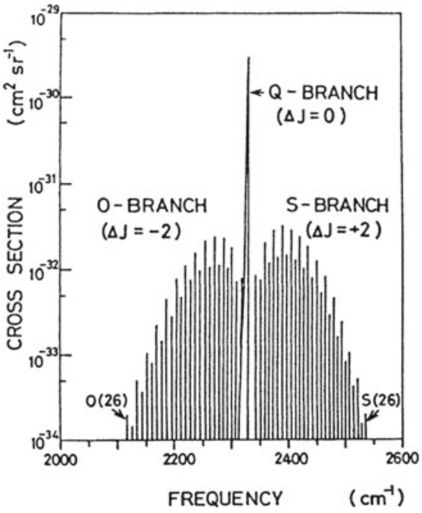

Fig. 4.20 Vibrational–rotational Raman spectrum of N_2 [222]

4.4.3 *Vibrational–Rotational Raman Spectra*

As for dipole transitions, we obtain a combined vibrational–rotational spectrum for Raman scattering. Such a Raman band contains three branches, S, Q ($\Delta J = 0$), and O. Since the rotational constants for the vibrational levels with $\upsilon = 0$ and 1 are almost identical, the lines of the Q branch occur almost on top of each other and can frequently not be resolved. Because of this, a very strong central line occurs. The S and O branches are much weaker since the components are spread out. These branches correspond to the R and P branches in IR spectra, with the difference that the separations in the Raman spectrum are twice as large. An example of a Raman spectrum is given in Fig. 4.20. The intensity distribution, previously discussed for IR transitions, is illustrated.

As we have seen, the IR and Raman spectra frequently yield the same information. Raman spectra can, in many respects, be considered as IR spectra which have been moved into the visible region employing a visible excitation line as an off-set. However, IR and Raman spectra also complement each other, as different transitions can sometimes be observed.

4.5 Mie Scattering

We discussed the Rayleigh scattering in Sect. 4.3. It occurs when a light wave induces a varying polarization in molecules. The wavelength is larger than the molecular diameter in this case. When light falls on particles of a size considerably exceeding the light wavelength, again elastic scattering is observed. This type of scattering was investigated as early as 1908 for the case of spherical particles by G. Mie. The *Mie scattering* has been discussed in detail in Ref. [199]. The probability (cross-section) for the Mie scattering is a complicated function of wavelength λ, particle radius r, index of refraction, and absorption

$$\sigma_{\text{Mie}} = f(x, m_{\text{rel}}), \tag{4.68}$$

where

$$x = \frac{2\pi r}{\lambda}, \quad m_{\text{rel}} = m_1/m_2, \tag{4.69}$$

and m_1 is the complex index of refraction ($m_1 = n - ik$) for the particles and m_2 is the corresponding quantity for the surrounding medium. For air, $m_2 \sim 1$. σ_{Mie} oscillates rapidly as a function of the parameter x due to interference effects related to surface waves on the particles. The oscillations are smeared out for natural particle distributions in the atmosphere and the scattering intensity varies only slowly with the wavelength. The intensity increases towards shorter wavelengths, but only quite weakly. The Mie scattering from particles is normally more important than the Rayleigh scattering from molecules in the lower atmosphere. In contrast to the Rayleigh scattering, which has a $(1 + cos^2\theta)$ angular dependence, the Mie scattering is pronounced in the forward direction and even more for larger scattering particles. These aspects are illustrated in Fig. 4.21. The angular dependence of the Rayleigh scattering from an unpolarized beam can be understood as the average of a dipole radiation pattern $sin^2\theta$ perpendicular to the symmetry axis, yielding persistently the value of 1 in the direction of the rotation axis, but the mean value of $sin^2\theta$ (equal to 0.5) in the perpendicular direction, where the light will also be fully polarized, perpendicularly to the direction of the incoming light.

The atmospheric visibility is determined by the Mie scattering. The visibility would be hundreds of kilometres in the absence of particles in the lower atmosphere. A relatively simple relation between the visibility and the effective Mie-scattering cross-section exists.

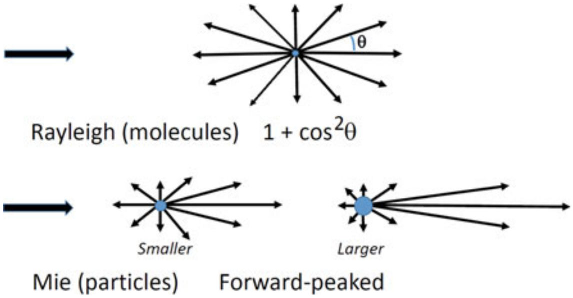
θ
Rayleigh (molecules) 1 + cos²θ
Smaller
Larger
Mie (particles) Forward-peaked

Fig. 4.21 Angular scattering patterns for the Rayleigh and Mie scattering

The Mie scattering can be used to monitor particles in ambient air and water (Sect. 10.2.3). It is also useful in the laboratory. Measurements in the direction of the probing beam are called *turbidimetry* while measurements in other directions are called *nephelometry*. (Greek nephele = cloud). Particle sizes and shape parameters can be determined from the angular and polarization distributions, at least under favourable conditions [223–225]. Scattering phenomena play a very important part in light propagation through turbid media, such as biological tissue (Sect. 10.5).

4.6 Atmospheric Scattering Phenomena

The wavelength dependence of the Rayleigh scattering is responsible for the blue of the clear sky and the red of the setting sun. The sun emits essentially "white" light. Blue light is scattered more effectively than red and so red light is transmitted better when the angle at which the sun shines is small (long path length through particle-rich layers). These well-known atmospheric scattering phenomena are illustrated in Fig. 4.22. The sky radiation is partly polarized depending on observation angles. If the sun is at the zenith, the highest degree of polarization occurs at 90° around the horizon, where the light is horizontally polarized (up to 80%). Even if the sun is hidden by clouds, the skylight is partially polarized, a fact which is used for orientation by many insects. It is even speculated that Vikings on their long sea voyages 1000 years ago took advantage of the polarization of the sky by observing it through a doubly refringent natural crystal (a "sunstone").

Clouds illuminated by sunlight are whitish, reflecting the very slow wavelength dependence of the Mie scattering on wavelength. Observing the sun disc through

Fig. 4.22 The occurrence of blue sky and red sunset

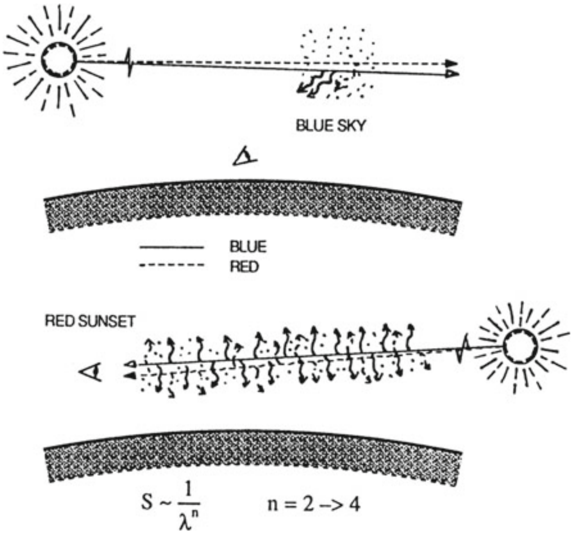

thin clouds or light fog results in a strong whitish halo of light around the sun caused by the forward-scattered light of Mie origin.

Another well-known atmospheric feature is the *rainbow*. This phenomenon can be explained in detail using the Mie-scattering theory. However, the general principles of the rainbow can be described considerably more simply. As early as in the seventeenth century, R. Descartes explained the most important points of the rainbow phenomenon. The normal, most intense rainbow (the *primary* rainbow) is formed by the rays of the sun being reflected once in the interior of water droplets, as illustrated in Fig. 4.23. The colours occur (starting at the outside) in the order red, orange, yellow, green, blue, indigo, and violet. Often, a weaker, *secondary* rainbow can be observed outside the primary rainbow. This is formed by light, which has been reflected twice in the interior of the droplets, and the colours occur in the reverse order. The angle of deflection for a ray impinging on a drop depends, according to the Snell refraction law (Sect. 6.2.1, and Fig. 6.20), on the index of refraction and the parameter of incidence b, which is the vertical distance between the incoming ray and an axis drawn through the centre of the drop parallel to the incoming beam (Fig. 4.23). Parallel light rays impinging on a drop are refracted and scattered in many directions because all parameters of incidence are represented and because of partial reflection from the drop surface. Thus, at first sight, one might think that all colours would smear into white light. However, a strong concentration of intensity in a particular direction is obtained for a particular colour. Rays with zero parameter of incidence are reflected, retracing their path and giving a deflection angle of 180°. For increasing values of b, the angle of deflection θ decreases to a certain value, $\theta = \theta_r$, from which it slowly increases again for increasing values of b, as illustrated in Fig. 4.24. Around θ_r the variation of θ with b is slow and all rays with a parameter of incidence close to b_r leave in a narrow angular range, resulting in a high intensity. For water droplets, θ_r (the rainbow angle) is 138° for red light and 140° for blue light. This wavelength dependence due to dispersion (the wavelength dependence of the water index of refraction n) is the origin of the rainbow, in combination with the fact that a comparatively large fraction of the area of the raindrop, exposed to the sun, results in rays going in the same direction for each colour, while the remaining fraction results in rays going in widely varying directions, leading to smearing. The secondary rainbow, corresponding to two inner reflections, can be explained in the same way. A high light intensity is obtained around 130°. Somewhat un-poetically, the rainbow touching the ground is not a *location*, it is an *angle!*

The maybe unexpected aggregation of intensity in connection with the formation of the rainbow also brings to mind the phenomenon of the formation of bandheads in molecular spectroscopy (Fig. 4.13). Another somewhat related association, which can be made, is the observation that if flash photographs are taken at random of a clock pendulum in a dark room, most of the pictures will show the pendulum close to its turning points, where it spends most of the time. (In the quantum–mechanical treatment of the harmonic oscillator, the square of the wave function (1.12) has maximum values (high probability) at the classical turning points (Fig. 3.7).) Another related observation is that the length of the day changes very little around the summer and winter solstice and very quickly at the spring and autumn equinox.

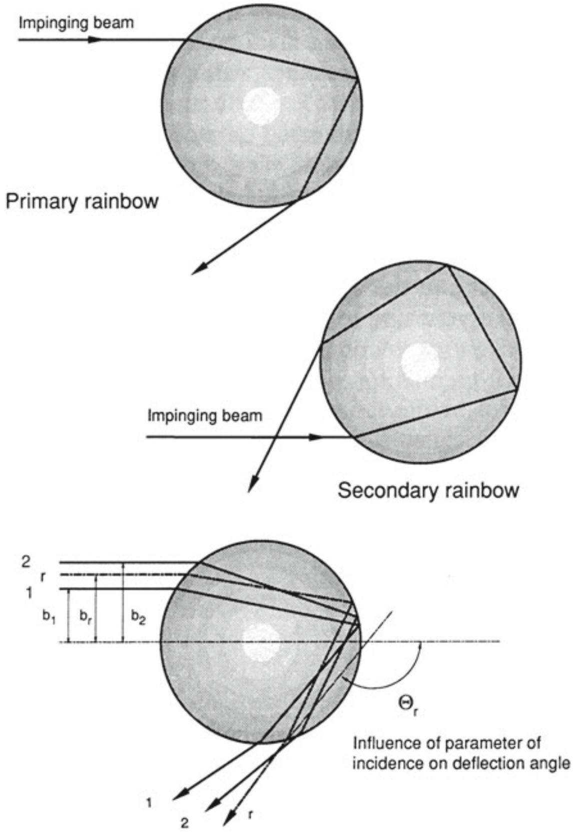
Impinging beam
Primary rainbow
Impinging beam
Secondary rainbow
2
r
1
b_1
b_r
b_2
Θ_r
Influence of parameter of incidence on deflection angle
1
2
r

Fig. 4.23 Reflection and refraction in raindrops

Returning to atmospheric optics, in the range of angles between the two rainbows, there will be no rays corresponding to one or two reflections. Therefore, the sky brightness is reduced. This darker region is called *Alexander's dark band* (Greek philosopher, 200 B.C.). The strong darkening of the sky outside the primary rainbow is clearly seen in the photographs in Fig. 4.24.

On the inner bright side of the primary rainbow (close to the violet primary band), a number of extra bands often occur, alternating in colour between green and pale red. These extra bands are caused by interference between rays with b values slightly higher and slightly lower than b_r being deflected in the same direction (cf. Young's double-slit experiment). Since the interference effect is due to differences in the path length through the drop, the appearance of extra bands depends on the drop size. Frequently the bands are most visible below the top of the primary rainbow. The raindrops are smallest at high altitudes and increase in size as they fall. The interference effect is smeared out for large drops.

The scattered light in rainbows is almost fully polarized since the angle of incidence for the internal reflection is close to the Brewster angle ($\tan\theta = n$).

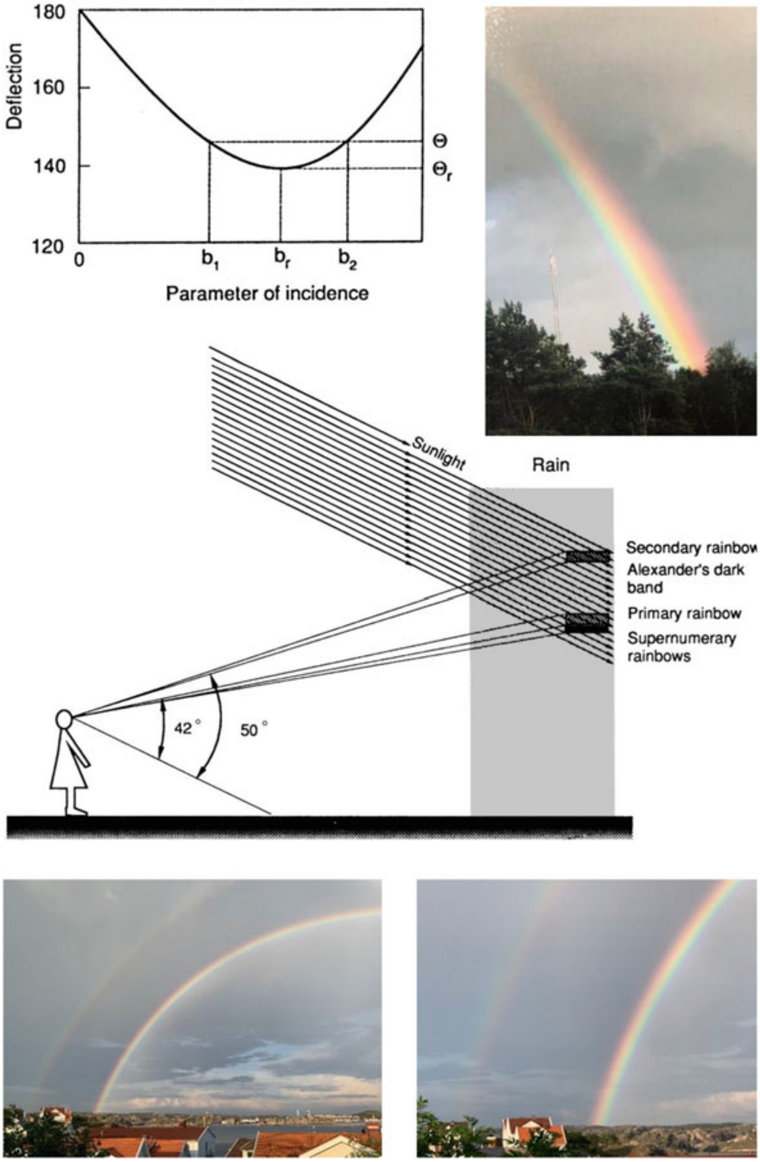
180
160
140
120
Deflection
Θ
Θr
0
b1
br
b2
Parameter of incidence
Sunlight
Rain
Secondary rainbow
Alexander's dark band
Primary rainbow
Supernumerary rainbows
42°
50°

Fig. 4.24 Dependence of deflection angle on the parameter of incidence (*above*) and observation angles for the rainbow (*below*). The manifestation of the dark band of Alexander is clearly seen in the inserted rainbow photographs, as well as the appearance of a second rainbow (bottom) (Photographs towards the coastal village of Rönnäng, taken from the island of Klädesholmen, Sweden)

The angle of observation for a rainbow is shown in Fig. 4.24. A rainbow is circular due to the spherical symmetry of the drops. From an aeroplane, in principle, a complete rainbow can be seen centred around the shadow of the aeroplane.

The rainbow phenomenon has been discussed in [226]. Other phenomena such as atmospheric haloes, mirages, and the "green flash" have been treated in [227–239]. A large class of rare phenomena are due to scattering and refraction in high-altitude ice crystals, while other ones are due to ray bending in the air, where large temperature gradients cause changes in its refractive index. An example of a mirage (from Latin *mirus*: astonishing) is shown in Fig. 4.25. There also the origin of the "green flash" is shown. Because of strong temperature and associated density gradients close to the horizon, over the sea or in the desert, the sun disc appears at slightly different heights over the horizon for different colours due to the prism action. When the dominant red and yellow light is blocked by the horizon, only the blue and green light at the edge of the sun disc can reach the eye. Since the blue light is mostly scattered away, a green, rather than a blue flash appears exactly when the last rays are emitted. Mirages and green flashes can also be caused by more complex atmospheric structures.

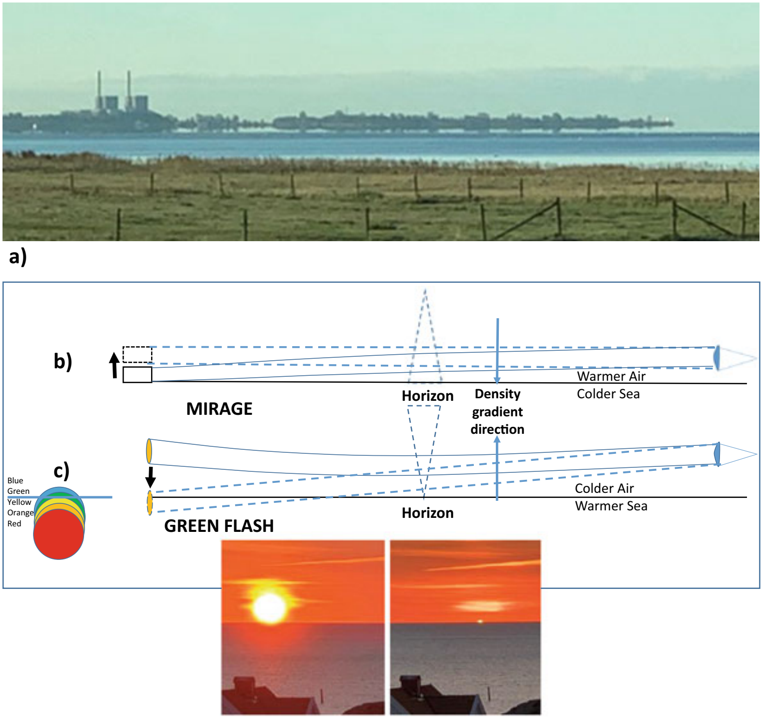

Fig. 4.25 **a** Mirage observed at the decommissioned Barsebäck nuclear plant on the West coast of Sweden. **b** Prism action in the air due to temperature differences in the sea and the atmosphere cause structures to appear lifted up in the air, causing the mirage. **c** Origin of the green flash. The photos show the situation when the green flash can occur

For completeness, we will also discuss two further atmospheric emission phenomena, of quite different origins—the *auroral* emission and *lightning*. Spectacular night-time light emissions observable in clear weather sometimes appear in the sky in ring-shaped areas close to the northern and southern magnetic poles of the earth (*aurora borealis* and *aurora australis*, respectively). The emission is due to atomic and molecular excitations at very high altitudes, due to the impact of electrons and protons, which are ejected from the sun; in particular abundantly when eruptions, solar flares, occur. The most common green-yellowish emission is due to the oxygen atom at typical heights of 100–140 km. Strong emission at 557.7 nm occurs from an upper state, with a natural lifetime of 0.7 s. Quenching by collisions (See also Sect. 10.1.2) does not occur at the low pressures, where the free oxygen atoms are formed, following UV-light splitting of O_2 molecules—part of the ozone formation process; see Sect. 6.4.5. Dark red emission (two lines around 630 nm) can also be related to oxygen atoms (at even higher heights due to even more long-lived, and thus more quenching-prone, atoms. Numerous weak violet and blue emission lines due to N_2, and N_2^+ molecular ions occur from 85 km and upwards [240, 241].

The collisional excitation mechanisms responsible for the aurora have a counterpart at much lower atmospheric heights, where high-voltage electrical discharges between clouds or between clouds and the ground result in bright lightning. Voltage differences of typically 10^8 V give rise to few cm diameter discharge channels, carrying currents typically above 10^4 A for tens of μs. The whitish light mostly contains spectral lines due to neutral and in particular ionized nitrogen atoms, while also lines from neutral and ionized oxygen appear, as well as the Balmer H-α (656 nm) and H-β (486 nm) lines of hydrogen (4.42) (from dissociated water) are observed [242, 243].

4.7 Comparison Between Different Radiation and Scattering Processes

The cross-sections for different radiation and scattering processes are compared in Table 4.1. Of course, the strength varies considerably for a particular process, but the numbers give an indication of the relative strengths. Resonance absorption and the associated fluorescence process (electric dipole radiation) are the strongest processes. Strong fluorescence only occurs at low pressures at which collisional processes can be neglected. At atmospheric pressure, the return to the lower state usually occurs through collisional processes (*quenching*); see (10.1.2). The fluorescence intensity can then be reduced by a factor of 10^3–10^5. The Rayleigh scattering is generally 10^{10} times weaker than resonance absorption. The Raman scattering is a further factor of 10^3 weaker. The strength of the Mie scattering varies strongly with the particle size.

Table 4.1 Comparison between different radiation and scattering processes

Process	Cross-section σ (cm^2)
Resonance absorption	10^{-16}
Fluorescence	10^{-16}
Fluorescence (quenched)	10^{-20}
Rayleigh, scattering	10^{-26}
Raman scattering	10^{-29}
Mie scattering	10^{-26}–10^{-8}

4.8 Collision-Induced Processes

In this chapter, we have dealt with the radiative transfer of atoms and molecules between different energy states rather extensively. However, transitions can also be induced by collisions. Extensive information on the static and dynamic properties of atoms and molecules can be obtained from collision physics. Although this book is centred on the spectroscopy of atoms and molecules, the importance of collisional physics should be clearly pointed out. For studies of these aspects, the reader is referred to [244–249].

4.9 Quantum Optics and Quantum Information

The field of quantum optics and quantum information is one of the fastest developing ones in modern physics. Many phenomena studied heavily rely on the concept of *entangled states,* which is at the basis of quantum mechanics. A system can be in a superposition of states, which leads to non-classical aspects such as non-locality or "action" at a distance. Famous examples are the studies performed by *J. Clauser, A. Aspect, A. Zeilinger,* and others [250–256] regarding the coupling between photon polarization in cascade decays of atoms, where a measurement of the polarization of the first photon will determine the polarization of the second photon, even if it is detected at a far distance from the first one. Results are expressed in terms of violation of the *Bell Inequality* [257, 258], which had its origin in the famous paradox by Einstein–Podolsky–Rosen (*The EPR Paradox*) [259]. This non-locality property of quantum mechanics has now been demonstrated in experiments, where the detectors are separated by huge distances [256, 260, 261]. Many efforts have been made to close possible "loop holes" in the measurements, i.e. the remote possibility that there could have been some pre-determined "agreement" between the observed events. Entangled states were already very early discussed in quantum mechanics related to the *Schrödinger cat paradox*, where the cat presumably could be in a superposition of being alive or dead. The 2022 Nobel Prize in Physics was given to Clauser, Aspect and Zeilinger (www.nobel prize.org/uploads/2022/10/popular-physicsprize2022-2.pdf)

Entangled states also allow computing tasks, which in principle can be solved much faster than what a conventional computer can do, since holistic operations not only involving sequential execution of elementary operations on information bits can be performed, but now involving *qubits*. One such task is the factorization of large integer numbers [262]. Very recently, a problem was solved by an elementary quantum computer more than 10^9 times faster than what would have been needed by the best super-computers [263]. Here, superconducting qubits were employed, while other approaches include cooled and trapped particles [264–267] (Sect. 9.8) and spectral hole-burning in rare-earth-element crystals [268, 269].

A very important aspect of the use of entangled states is to achieve completely secure *cryptography*, e.g. for bank transfers, etc. An encryption key can be transferred between a sender and a recipient, without running the risk of being intercepted by an eavesdropper. This has been demonstrated even over very long distances [270–274], and commercial equipment is available.

Teleportation is perhaps the most intriguing aspect of entangled states in quantum communication. In contrast to the perception in science fiction contexts, quantum teleportation means the transfer of the information, unlimited by space and time, enabling the construction of a true replica of an object. Such teleportation has been achieved for small objects on the atomic scale [275–277].

The first observation of the non-classical properties of light was made in the *Hanbury Brown* and *Twiss experiment* [278], which sought to deduce the size of a star from studies of intensity fluctuations in the light. They studied the correlation between intensity fluctuations at two spatially separated detectors. The experiment lead to an increased interest in the quantum–mechanical coherence properties of light. It was shown that partially coherent light exhibits a bunching effect, i.e. photons are not detected equally spread in time [279]. This could be understood from the quantum field theory of light [280, 281]. The theory also predicted *photon anti-bunching* in the interaction with atoms. This phenomenon in light interaction with a single atom has been observed [282–284] and can be understood in terms of *shelving* (See Sect. 9.8.4). Because of the finite lifetime of an atom in an excited state, there must be some time separation between two emitted photons. A Nobel Prize in Physics in 2005 was given to *R. Glauber* for his theoretical description of the quantum theory of optical coherence [285].

Further interesting quantum-optical experiments have been pursued using a single atom in a cavity of extremely high Q-value (wall reflectivity). Single-atom maser action has been achieved and detailed studies of the interaction between the atom and the field have been pursued [286–291]. Single-atom laser action in the visible spectrum has been observed in later studies [292, 293]. Other experiments have focused on the light field. It has become possible to count the number of photons in a high-finesse cavity without destroying them. Atoms were laser-excited into high Rydberg states, and microwave transitions to neighbouring Rydberg states were observed. The Nobel Prize in Physics in 2012 was given to *S. Haroche* and *D.J. Wineland* [294, 295] for enabling the measurement and manipulation of individual quantum systems.

A further aspect of the quantized electromagnetic field is the possibility of generating light in a *squeezed* state [296–304]. Coherent light can be described as radiation with equal variance (uncertainty) in space and momentum corresponding to a minimum uncertainty state according to the Heisenberg relation. It can also be expressed in a similar manner in terms of intensity and phase. The accuracy of optical measurements is limited by the variances. However, a reduced variance in one observable can be compensated by an increase in the other one, still compatible with the uncertainty principle. This is achieved for squeezed light, for which the phase can be measured more accurately than primarily expected, at the expense of an increased intensity uncertainty. Squeezed light has been generated in many ways, maybe most conveniently in the optical parametric generation process (Sect. 8.6). It might have important applications for optical communication and has recently been used in precise interferometric measurements of extremely small displacements, such as those in gravity-wave detection interferometers [304–306]. Squeezed light significantly can increase the detectivity in the huge Michelson interferometers used in the LIGO and VIRGO gravitational wave laboratories, where such waves from colliding binary black holes were first detected [307, 308], while still not using squeezed light (see also Sect. 6.2.4).

The literature in the field of quantum optics and quantum information is very extensive. Some material is given in [309–323].

Chapter 5
Spectroscopy of Inner Electrons

We will discuss spectroscopic methods that involve inner electrons in this chapter [324–327]. Such electrons are much more strongly bound than outer electrons and the interaction energies become correspondingly high. Two kinds of methods are used to study inner electrons; those that are based on absorbed or emitted X-ray radiation (*X-ray spectroscopy*) and those dealing with energy measurements on emitted photoelectrons (*photoelectron spectroscopy* (XPS or ESCA)).

5.1 X-Ray Spectroscopy

When a solid is bombarded by electrons at an energy of few keV or more, X-rays are emitted. The radiation consists of a continuous part (*Bremsstrahlung; German for "breaking radiation"*) and a discrete (*characteristic*) part. The Bremsstrahlung is generated by the charged electrons that undergo deceleration and a change in direction of motion when interacting with the atoms of the sample. This is related to Eq. (4.59). The maximum energy of the X-ray quanta corresponds to a full conversion of the kinetic energy of the incoming electrons. The discrete radiation is a line spectrum that is characteristic for the material and, as for optical radiation, it is caused by spontaneous transitions between atomic states. As a result of electron bombardment, an electron can be knocked out of an inner shell of the atom. The atom is then in a state of high excitation and a transition to a state of lower energy quickly occurs through an electron from an outer shell falling into the vacancy to fill the hole. Thus, the electron hole is seen to move outwards towards outer shells. A series of emission lines, corresponding to the particular atomic energy losses, is obtained. The processes are illustrated in Fig. 5.1, in which energy levels corresponding to an electron vacancy in the K, L, M, N, etc. shell (see also Table 2.2) are indicated, and emission lines corresponding to transitions between such states are shown. The transitions are denoted $K\alpha$, $K\beta$, $K\gamma$, etc., corresponding to the movement of the electron hole from the K shell to the L, M, etc. shell. Correspondingly, $L\alpha$, $L\beta$, etc.

© The Author(s), under exclusive license to Springer Nature Switzerland AG 2022

S. Svanberg, *Atomic and Molecular Spectroscopy*, Graduate Texts in Physics,
https://doi.org/10.1007/978-3-031-04776-3_5

lines are emitted when an L-shell vacancy is filled. If fine structure is also considered, energy levels are given a further index L_I, L_{II}, L_{III}, etc. and emission lines a further specification $K\alpha_1$, $K\alpha_2$, etc. as already indicated in Fig. 4.8, in which the more commonly used convention of negative level energies was used. As an example, an X-ray emission spectrum from molybdenum excited by 35 keV electrons is shown in Fig. 5.2 with the continuum Bremsstrahlung and the most energetic characteristic lines.

X-rays were discovered by *K. Röntgen* in 1895 [328, 329] and awarded with the first Nobel Prize in Physics in 1901. The rays were shown to be electromagnetic radiation with a wavelength comparable to the distance between crystal planes

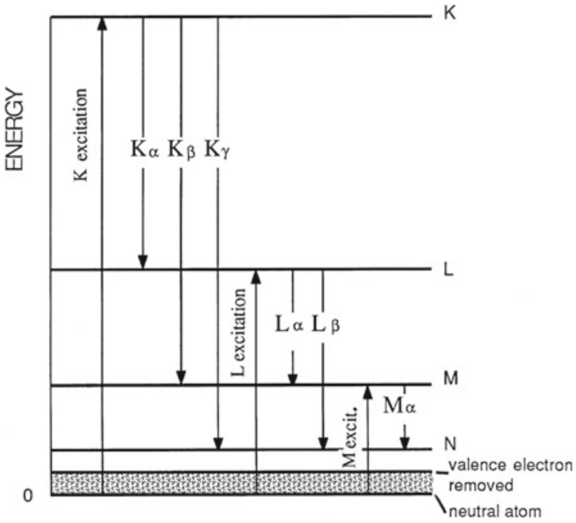

Fig. 5.1 Inner electron energy levels and corresponding X-ray transitions

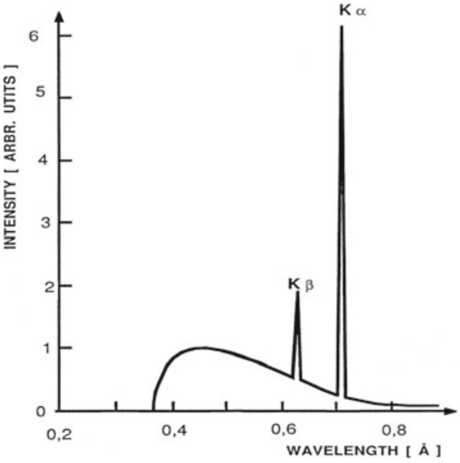

Fig. 5.2 X-ray emission spectrum from molybdenum, obtained for an acceleration voltage of 35 kV. The continuum radiation (Bremsstrahlung) as well as characteristic lines are shown

Fig. 5.3 Diagram illustrating Moseley's law

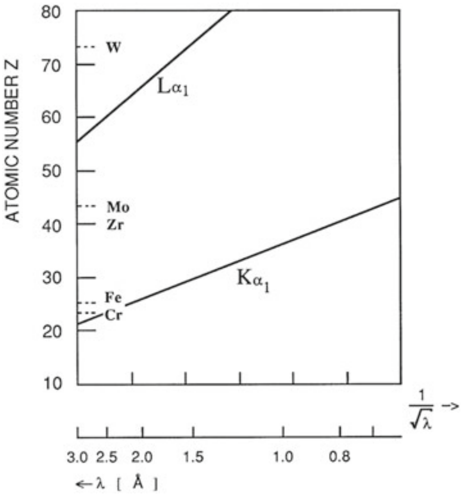

($\sim$0.1 nm) in investigations by *K. von Laue* and *W.H.* and *W.L. Bragg*, father and son (1913); they were awarded with the Nobel Prize in Physics in 1915; the latter being the youngest one to receive the prize; 25 years old. More detailed studies of X-ray spectra were performed by H. Moseley (fallen at the battle of Gallipoli, 1915), and high-precision techniques were introduced by M. Siegbahn (Nobel Prize in Physics 1924). The atomic X-ray investigations have resulted in a very thorough charting of the energy levels of inner electrons.

The energy levels in the inner electron shells are comparatively little affected by the chemical environment of the atoms. Thus, a spectral analysis of the characteristic X-ray emission is well suited for elemental analysis. The relation between the wavelength λ of a particular X-ray line and the nuclear charge Z of the corresponding atom is given by *Moseley's law*

$$1/\sqrt{\lambda} = C(Z - \sigma). \tag{5.1}$$

Here C and σ are constants characterizing a particular spectral series. Moseley's law can be derived from the simple Bohr atomic model (Sect. 2.1 and 2.4; 4.42) taking shielding into account. A Moseley diagram for $K\alpha$ and $L\alpha$ emission is shown in Fig. 5.3. Using such a diagram the identification of different elements in a sample is greatly facilitated.

5.1.1 X-Ray Emission Spectroscopy

X-ray emission can be induced in different ways. We have already mentioned the use of energetic electrons. Alternatively, heavier charged particles can be used. It is also possible to create an inner shell vacancy by irradiating the sample with X-ray radiation. We are then dealing with an inner shell photoelectric effect. The characteristic radiation following X-ray absorption is referred to as *X-ray fluorescence* following the terminology in the optical spectral region. The energy (wavelength) of the X-ray quanta can be determined in two basically different ways. Measurement systems are referred to as being *wavelength-dispersive* or *energy-dispersive*. In the former type of instrument an X-ray spectrometer using a crystal for the wavelength analysis is used. A diagram of a wavelength-dispersive X-ray fluorescence system is shown in Fig. 5.4. An X-ray tube with an anode (also called "anti-cathode") of tungsten or sometimes chromium, gold, or rhodium is used for exciting X-ray fluorescence in the sample. Parallel beams from the sample are directed towards the flat crystal at an angle of incidence θ with the aid of a collimator. The analysing crystal has been cut to have its crystal planes, separated by d, parallel to the crystal surface. The detector of the spectrometer is placed behind a collimator to receive radiation that has been deflected by 2θ from the original direction. When using the spectrometer, the crystal is turned by a motor at a constant angular velocity at the same time as the detector arm is moved at twice the angular velocity. Radiation quanta can pass into the detector when the *Bragg relation* is fulfilled (Fig. 5.4).

$$2d \sin\theta = k\lambda. \tag{5.2}$$

NaCl ($d = 0.56$ nm) or LiF ($d = 0.4$ nm) are frequently used as crystals. The X-rays bundles are collimated using systems of thin metal plates (thickness: 50 μm) arranged parallel to each other at small separations (0.5 mm). The divergence can in this way be limited to one degree or less. An example of an X-ray fluorescence spectrum of an alloy sample is shown in Fig. 5.5.

A curved crystal can be used: this will cause radiation diverging from an entrance slit to be focused towards an exit slit with a strong intensity advantage. Curved crystals

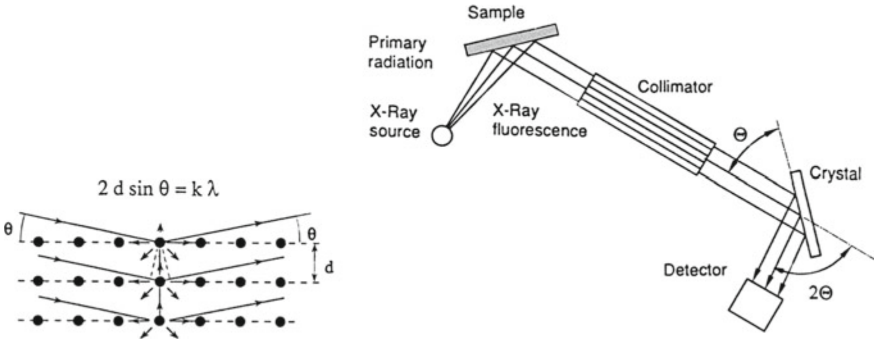

Fig. 5.4 Illustration of Bragg diffraction (*left*) and a wavelength-dispersive X-ray fluorescence spectrometer (*right*)

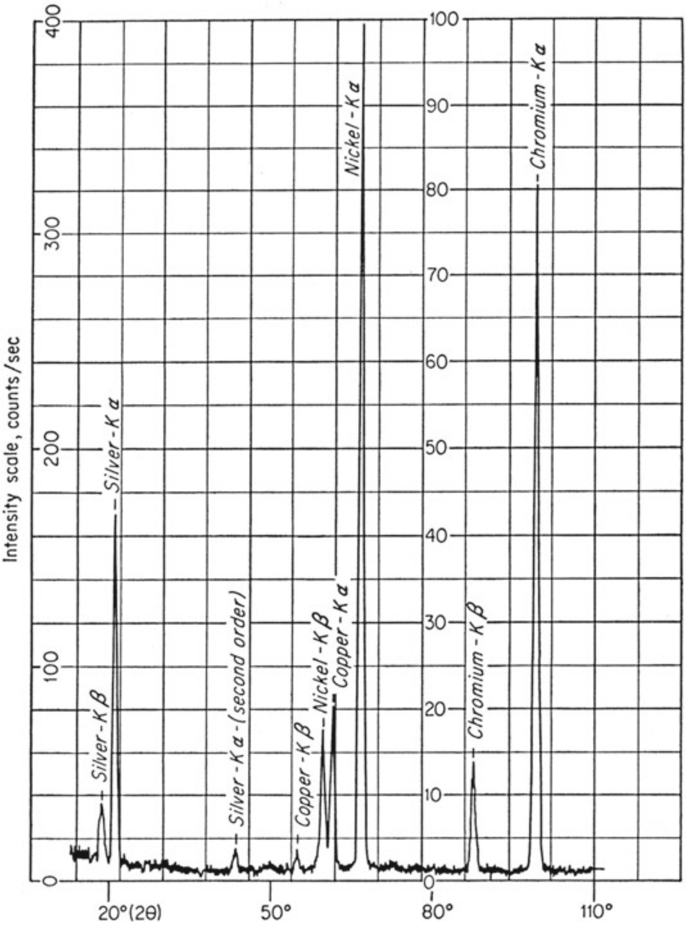

Fig. 5.5 X-ray fluorescence spectrum of chromium–nickel plating on a silver–copper base. The recording was taken with a wavelength-dispersive spectrometer [330]

of alkali halides or mica can be used. X-ray spectrometers, where the diffracting crystals operate in transmission (*Laue*) geometry instead of in reflectance (*Bragg*) geometry, can also be constructed. Different spectrometers and techniques for the X-ray region are discussed in [330–344]. An example of a recording of the Ta Kα,β lines, recorded with a Laue spectrometer, is shown in Fig. 5.6 [333]. The X-rays were generated by focusing a high-power laser beam onto a rotating tantalum disc (see also Sect. 9.6.4). Because of the widespread use of synchrotron radiation (Sect. 6.1.3) at short wavelengths, an advanced technology for X-ray monochromators (selecting a narrow band out of a continuum) has been developed.

A Geiger counter, a proportional counter or a scintillation counter, can be used for X-ray detection. The two former types are gas-filled. The incoming X-rays cause

Fig. 5.6 Recording of the K α,β lines from tantalum [333]

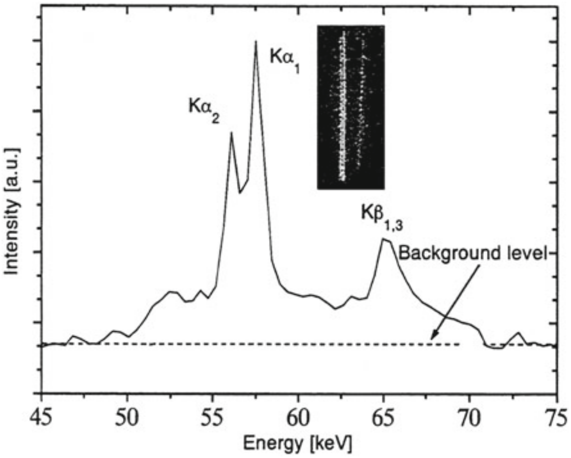

the formation of ions which are then detected. Such detectors are mostly used for long-wavelength radiation (λ > 0.2 nm).

Scintillation counters in which X-ray-induced light flashes in sodium iodide crystals are detected by a photomultiplier tube (Sect. 6.3) are used for X-rays of shorter wavelengths. Imaging X-ray detectors are also available as discussed below in connection with X-ray imaging. Such detectors are of course very useful for efficient simultaneous spectroscopic recording of a specific X-ray wavelength region.

Fluorescence spectrometers are widely used in the metal industry. Frequently, parallel spectrometers are employed. Such an instrument actually consists of a number of crystal spectrometers, each set for a particular emission line. The spectrometers are arranged around the sample, which is irradiated by an X-ray tube. One of the spectrometers is set for a standard sample that is contained in the sample holder. In this way the intensity of the X-ray tube can be monitored. Frequently, a measurement is terminated when a preset number of counts for the reference sample has been obtained. The corresponding number of counts from the other detectors can then be directly used for a parallel assessment of the elemental composition of the sample. With a sequential spectrometer, a number of selected elements are measured sequentially by turning the crystal and the detector to preset positions. With computer steering the measurement process is automatic. This type of instrument is well suited for varying types of analysis, whereas parallel spectrometers are more suited to continuous control operation of, for example, a steel mill in near-real time.

As was mentioned above, X-ray analysis can also be performed using an *energy-dispersive* system. No analysing crystal is needed in this case. Instead the radiation falls directly on an energy-dispersive detector. Normally, a lithium-doped silicon detector (Si(Li)) is used, which yields voltage pulses that are proportional to the energy of the X-ray quanta. The pulses are sorted according to their amplitude (energy) in a multi-channel analyser using an Analogue-to-Digital Converter (ADC).

Gradually, the full spectrum emerges on the system display. The linewidth obtained with a Si(Li) detector is about 150 eV. Partly overlapping lines can be deconvoluted using computer analysis. It should be noted that an energy-dispersive system of this kind automatically permits multi-element analysis.

It might be expected that the intensity of a spectral line from a sample would be directly proportional to the amount of the corresponding element in the sample. In practice the intensity can deviate considerably from the expected linear relation due to absorption in the matrix material and multiple scattering processes. However, it is possible to correct for such effects and very reliable quantitative analyses can be performed. X-ray fluorescence measurements on alloys have an elemental sensitivity of about 10 ppm (ppm: parts per million, $1:10^6$). The typical penetration depth of the radiation in the metal is about 1 μm, and thus, primarily, the surface is analysed. X-ray emission techniques have been discussed in [338–340].

As we have already mentioned, characteristic X-rays can also be induced using accelerated heavy particles such as protons. This technique is called PIXE (*Particle-Induced X-ray Emission*) [345–349]. The cross-section for the creation of an inner shell vacancy is very high using protons at an energy of a few MeV, and therefore a sensitivity much better than that typical for X-ray fluorescence is obtained. Most elements except the very light ones ($Z < 14$) can be detected in concentrations below 1 ppb (parts per billion: $1:10^9$). Also, the continuous Bremsstrahlung is strongly reduced by employing heavy protons instead of easily deflectable electrons. Using a specially focused proton beam (microbeam), quantities of an element as low as 10^{-18} g can be detected. As an example of a PIXE spectrum, illustrating the use of an energy-dispersive Si(Li) detector, a spectrum of sea water is shown in Fig. 5.7, with characteristic lines for different elements identified.

By using a highly focused proton beam which is scanned over a sample, it is possible to produce elemental imaging of a microscopic specimen, in which the spatial intensities of individual X-ray emission lines are displayed. Clearly, there are many applications of this micro-probe technique to medical, toxicological, environmental, semiconductor, and forensic science monitoring. An example of an elemental PIXE image is shown in Fig. 5.8, showing the distribution of different elements in a human hair strand.

X-ray analysis using different excitation and detection techniques has wide applications in fields ranging from biology and medicine to archaeology and forensic science. One interesting area of application is the measurement of heavy metals in particulate air pollution [351–353]. Airborne particles can be collected in different size fractions using special devices called cascade impactors. The particles deposited on the foils are then analysed. Small particles with diameters less than 2.5 μm are particularly important, since they follow inhaled air down into the alveoles of the lung. The human uptake of metals due to general air pollution or due to special working environments (e.g., inhalation of fumes by welders) can be investigated with samples of blood serum.

Our discussion of X-ray emission spectroscopy has so far mainly been focused on the analytical capabilities of systems with moderate resolution. Clearly, X-ray emission spectroscopy is also a field of active basic research, particularly in the soft

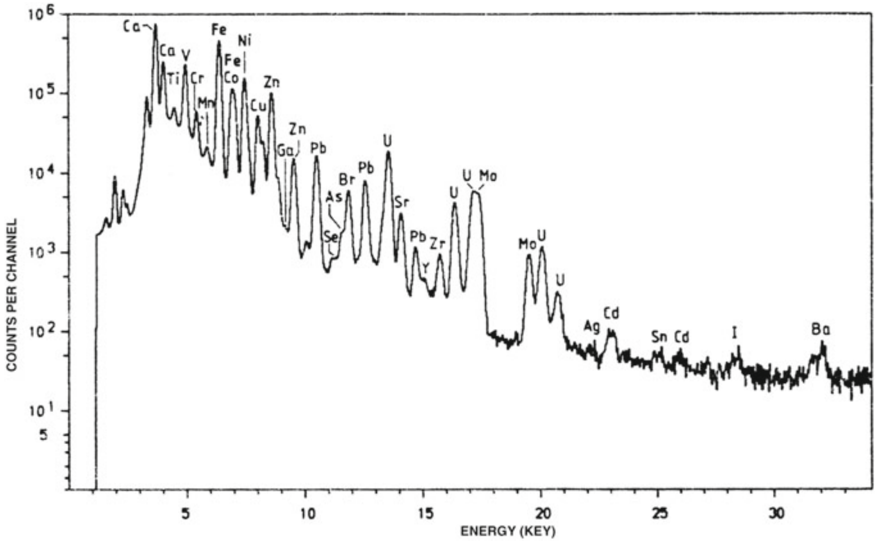

Fig. 5.7 PIXE spectrum of Arctic sea water. An energy-dispersive detector system was utilized [345]

X-ray region. Here dipole transitions between well-defined inner orbitals and more diffuse (perturbed) valence orbitals are studied, yielding valuable information on the latter orbitals. It is clearly desirable to increase the resolution as much as possible in such measurements. Wavelength-dispersive instruments are then mandatory. Above 3 nm, two orders of magnitude better resolution than in energy-dispersive systems is attainable. Special organic crystal materials with a large crystal plane separation, such as potassium hydrogen ftalate ($d = 2.7$ nm) and lead stearate ($d = 10$ nm), can be used for soft and ultra-soft X-ray wavelengths. If the wavelength is not too short the best choice is frequently to use a concave grating at grazing angle of incidence (see also Sect. 6.2.2). Ion-etched holographic X-ray gratings can have an efficiency exceeding 10%. Traditionally, photographic plates were used and provided parallel detection of many lines. They have been replaced by electronic multichannel techniques for X-ray spectra recording (see also Fig. 6.42). If the entrance slit, the plate and a grating with a radius of curvature r are placed on a circle of radius $r/2$ (the *Rowland circle*), sharp spectral lines are obtained without using any collimators (Fig. 6.27).

As an example of a spectrum obtained with a 10 m instrument (grating radius 10 m) a recording of the carbon K emission line from the CO_2 molecule is shown in Fig. 5.9. As can be seen, the high resolution reveals a clear structure due to molecular vibration. Through careful analysis of a spectrum of this kind it is possible to evaluate the C−O bond length very accurately in the core-ionized molecule. It turns out that the bond length is shortened by about 2% when the $1s$ core vacancy has been formed in the carbon atom. It is also possible to evaluate the natural lifetime of the C $1s$ state from the linewidth (Sect. 9.4.4). The lifetime is of the order 10^{-14} s. Atomic structure research using X-ray emission spectroscopy has been discussed in [354–359].

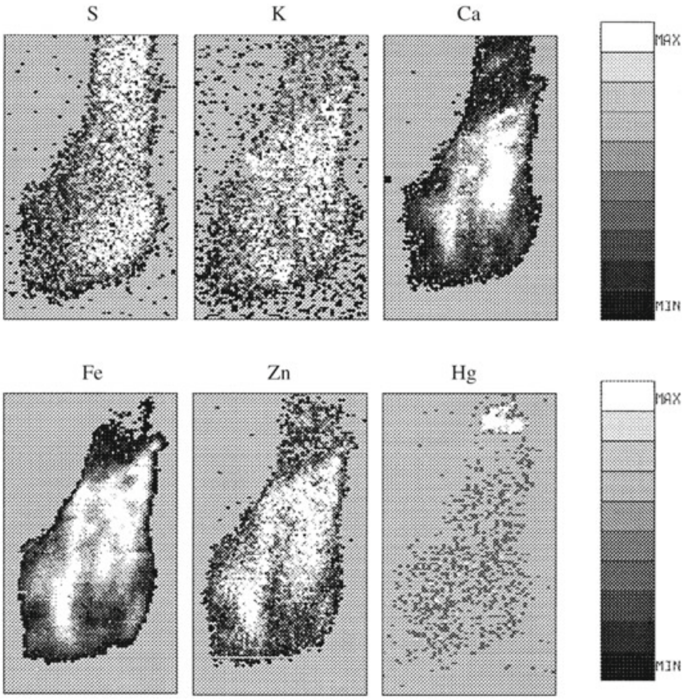

Fig. 5.8 Distributions of different elements in a human hair strand (with root) obtained with the PIXE microbeam technique. The beard hair belonged to the famous astronomer Tycho Brahe (1546–1601), and was retreaved at the opening of his tomb in the Tyn cathedral in Prague. Note the uptake of mercury shortly before the death of the bearer [350]

5.1.2 X-Ray Absorption Spectroscopy

We have seen how measurements of X-ray emission lines have an important analytical potential and also yield fundamental information on the structure of atoms and molecules. An emission line yields information on the *difference* in binding energy between two electronic states. However, from a theoretical point of view the *absolute* binding energies are of even greater interest. In order to determine such energies, *absorption* of X-rays, rather than emission, has to be studied. An X-ray continuum is used for such purposes, and the sample absorption as a function of the wavelength is measured. If the energy of the X-ray photons is sufficiently high, an inner electron can be excited to an unoccupied state, either in the discrete or in the continuous part of the spectrum. In the latter case an electron has been released from the system (photoemission). The available empty discrete levels (the excited valence-electron states) are closely spaced in a region of a few eV and converge at the ionization limit. The absorption is strongly increased for increasing X-ray energies at the energy at which an additional, more strongly bound electron is released. An *absorption edge* is observed, from which the approximate binding energy is obtained.

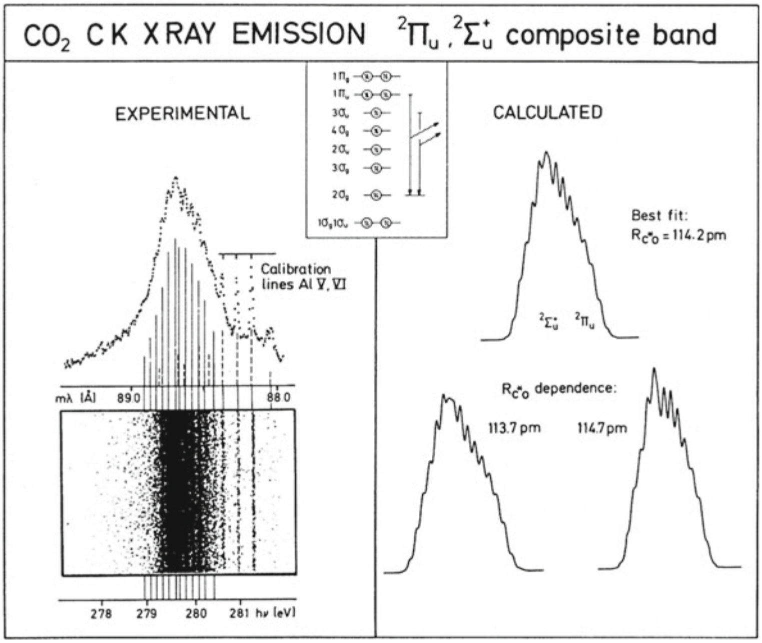

Fig. 5.9 The carbon K emission spectrum from the CO$_2$ molecule. To the left the photographic plate and a corresponding densitometer trace are shown. Calculated spectra are shown to the right, illustrating the sensitivity of the spectrum to the C–O bond length [354]

The thresholds for photoemission from deeper and deeper shells are reached for increasing photon energy and additional contributions to the total absorption are obtained, resulting in a number of edges, as illustrated in Fig. 5.10. Apart from the edges there is a general fall-off in absorption due to a ν^{-3} dependence of the absorption coefficient. The absorption edges exhibit fine structure corresponding to the fine structure of the core states (Sect. 5.1). However, even the K edge exhibits a structure, as shown in Fig. 5.11, which is due to discrete levels close to the series limit. The position of the edges also depends slightly on the chemical composition of the studied material (chemical shifts, Sect. 5.2.2). The shifts are of the order of a few eV, and the difference in position of the edge for a solid and free atoms can be expected to be of the same order of magnitude. A measurement on a solid is in relation to the Fermi level and thus a correction for the work function must be applied in order to allow a comparison with measurements or calculations for free atoms. The different effects discussed above result in an uncertainty of at least 5 eV for atomic binding energies obtained from X-ray absorption data. However, since binding energies are frequently of the order of keV or larger, this uncertainty is frequently of less importance. X-ray absorption data are available for most elements in the solid state. High-resolution measurements of the edge structures are pursued using synchrotron radiation (Sect. 6.1.3). Such measurements are referred to as EXAFS (Extended X-ray Absorption Fine Structure) studies or NEXAFS (Near-Edge X-ray

Fig. 5.10 X-ray absorption spectrum with absorption edges

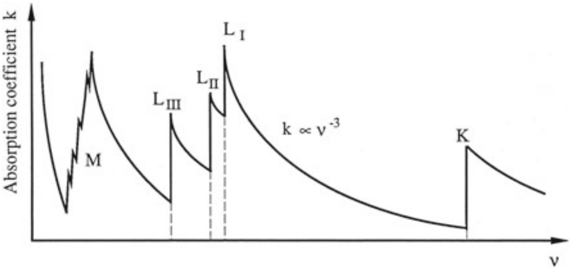

Fig. 5.11 Fine structure at a *K* absorption edge, observed at high resolution (EXAFS spectrum). [Adapted from a figure by C. Nordling]

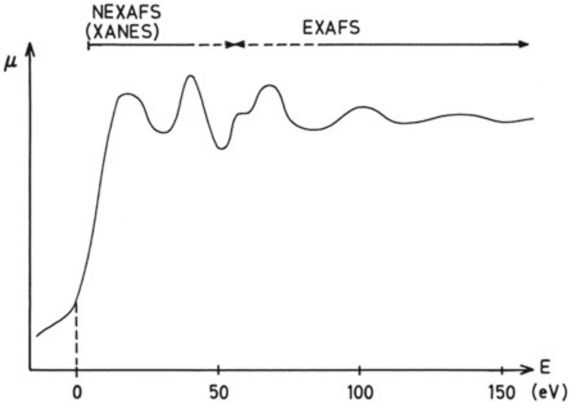

Absorption Fine Structure)—also termed XANES for X-ray Absorption, Near-Edge Structure—depending on how far from the edge one records and analyses the X-ray absorption spectrum. Information on distances to neighbouring atoms from the studied atoms is obtained from EXAFS spectra.

X-ray absorption and EXAFS spectroscopy has been discussed in [360–363]. Most X-ray spectroscopic studies are currently performed at synchrotron radiation facilities (Sect. 6.1.3).

5.1.3 X-Ray Imaging Applications

Medical Imaging. X-ray absorption is extensively used in medical diagnostic imaging. Different aspects of diagnostic radiology are covered in Refs. [364–366]. The energy of the exciting electrons in the X-ray tube (determining the high-energy cut-off; see Fig. 5.2) needed for different medical applications depends on the tissue thickness and is typically 20 keV for mammography and 60 keV for chest radiography. Soft X-ray radiation, which would otherwise be strongly absorbed in the superficial layers, is filtered away by means of an aluminium or copper filter. Bones appear as shadows since they contain heavier elements, primarily calcium, which absorb more strongly. Historically, X-ray film was used for the recording but have been replaced by image plates with much better sensitivity. The image information stored in metastable states of certain rare-earth salts is read out with a focused laser beam inducing blue optical fluorescence, and a digitized image is obtained, which allows efficient processing and storage. The dynamic range (the ability to reproduce both very weak and very strong signals) is increased by a factor 100 over photographic film (see also Sect. 6.3). The quality of X-ray recordings is impaired by Compton-scattered X-ray photons, which give rise to a diffuse background on the plate. It can be reduced by introducing channeled plates in the ray path so that only non-scattered rays can pass. As discussed in Chap. 9, gated viewing can be introduced to restrict detection to non-scattered photons emerging from a ps laser-driven X-ray source.

In order to enhance certain structures in the body, contrast agents (biocompatible compounds of higher-Z materials) are used. Thus, barium sulphate is normally administered orally to enhance gastro-intestinal radiography. A further very important agent is iodine, which when injected as an organic compound into blood vessels can yield an enhanced contrast for radiography, e.g., of the coronary arteries providing the heart muscle with its blood supply. An example of medical recordings before and after the administration of iodine is shown in Fig. 5.12, where the vessels alone are shown by subtracting two images [367].

Blood vessels can be monitored even more efficiently and using lower doses of X-rays if narrow-band radiation, provided from a synchrotron (Sect. 6.1.3) is used. X-rays are applied just above the K-absorption edge of iodine (33.2 keV) and then immediately below the same edge, resulting in two images [369–371]. By subtracting or dividing the two images, which can be recorded in a swift sequence after the contrast agent has been supplied, the vessels appear very clear in this differential absorption scheme. The same philosophy of differential absorption is also used in imaging of air pollutants using laser radar techniques (Sect. 10.2.3). In both cases, division of the data curves/images has the advantage of providing dimensionless data, which are immune to distance, variations in illumination, etc. (See also Sects. 1.1 and 10.5.3).

A further, much employed differential absorption X-ray imaging method is Dual X-ray energy Absorptiometry (DXA). Here, two different X-ray energies (or energy distributions) are used, as obtained, e.g., by changing the X-ray tube voltage from 70 to 140 kV. The absorption coefficient of muscle and bone (or iodine contrast agent) varies with X-ray photon energy (is reduced for higher energies). Moreover, and critically important in connection with DXA, the ratio between the absorption coefficients also changes with energy (i.e., the coefficients have different dependencies on energy). This means that when imaging a scene containing muscle as well as bone at the two tube voltages, it is possible to match the measured intensities for muscle in the two images, by multiplying one of the images by a certain factor. On subtraction, the muscle pixles would now be zero, which is not the case for the bone pixels, which now appear isolated. The new bone image, which is free from influence from the soft tissue, can now be used for calculating the density of the bone. This

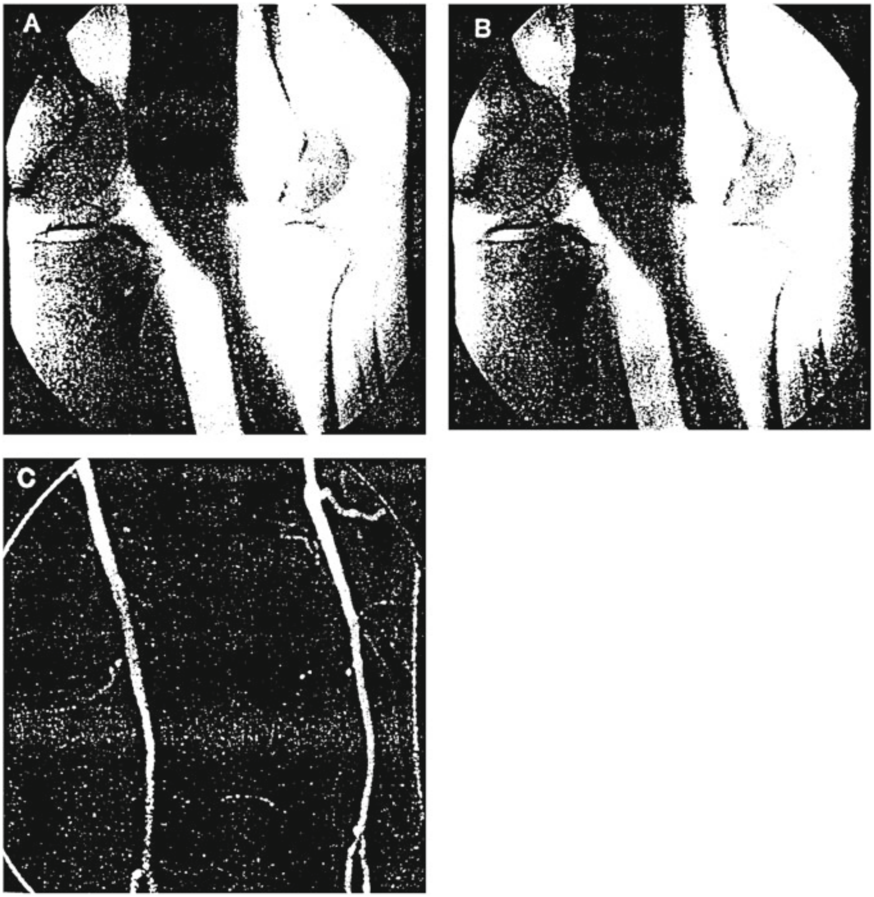

Fig. 5.12 Medical imaging with a contrast agent. **a** before contrast injection; **b** after contrast injection; **c** subtracted images [367]

is very important in the diagnosis of the common disease of osteoporosis in elderly, which is characterized by loss of bone [372].

Only "line-of-sight" information is obtained in X-ray transillumination recordings. In order to obtain three-dimensional data it is possible to make the transilluminations in many different directions (projections). The basic idea of absorption tomography is illustrated in Fig. 5.13a. An absorbing object (X-ray, or light absorption) is illuminated from different directions, and the shadows are recorded. It can be intuitively concieved that it should be possible to figure our the shape of the object if a sufficient number of projections is recorded. Mathematical algoritms based on Fourier or Radon transforms can be used to automatically perform the tomographic reconstruction [366, 373, 374]. A modern medical computerized tomograph (CT) X-ray scanning machine is shown in Fig. 5.13b.

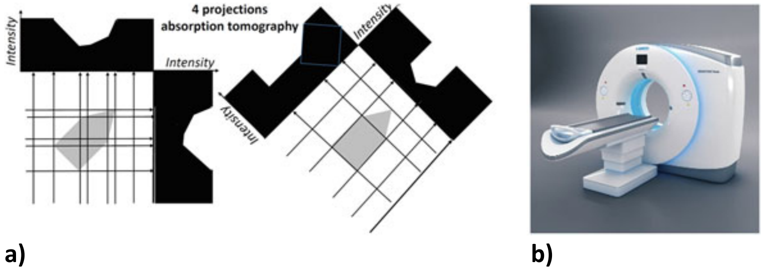

Fig. 5.13 **a** Principle of absorption tomography performed by observing the "shadows" of an object in different projections (adopted after H. Hertz). **b** Medical computerized tomography (CT) scanner for full-body imaging (*Courtesy* Siemens Healthcare GmbH)

High-energy photons are also used in nuclear medicine, but now not X-rays originating in inner electronic shell processes or Bremsstrahlung, but rather γ -rays due to decay of radioactive nuclei are used. *Single-photon emission computed tomography (SPECT),* also called *scintography,* is such a technique [375–377]. Short-lived radioactive isotopes, frequently produced in cyclotrons in connection to the hospital, are used for γ-ray imaging of organs after intravenous injection of a compound containing the radioactive nucleus. So called gamma cameras with collimators making the detection highly directional are used to generate the images. The gamma camera can be rotated, and from the recordings a tomographic emission image of the organ can be generated. Important isotopes are ^{123}I (159 keV, 13 d half-life; thyroidea monitoring) and ^{99}Tc (141 keV, 6 d half-life; dynamic monitoring of uptake of specific substances into which the isotope has been incorporated). Scintograms using Tc^{99} showing metastases to the skeleton are presented for two patients in Fig. 5.14 (front and back recordings). A further method is *positron emission tomography (PET)* [378–381]. PET works in a similar way as SPECT. Positron-emitting radioactive nuclei, in particular ^{15}O, ^{11}C, ^{13}N, and ^{18}F, which have short half-lives (2–110 min) are used in this case, and thus they must be produced by a local cyclotron. The most commonly used isotope is ^{18}F, which has a half-life of 110 min. It is incorporated into fluoro-deoxy-glucose (FDG). Glucose demand is enhanced in malignant tumours, which have a very strong metabolism. Positrons decay by combining with electrons within one ns. Two 0.511 MeV quanta are emitted in opposite directions (annihilation radiation). The fact that a decay always leads to two oppositely emitted quanta can be utilised for the localisation of the source. The patient is surrounded by nuclear detectors, and coincidences of events detected in oppositely positioned detectors are recorded. By tomographic inversion it is possible to map out the area containing the isotope. PET is of great importance for the study of brain and heart conditions.

Returning to X-rays, high-power laser radiation focused to a very small spot on a high-Z material, such as tantalum, can be used to generate X-rays with energies reaching up to the MeV regime and with extremely short temporal duration [382–388]. (See Fig. 5.6 and Sect. 9.6.5). Such radiation has also been considered

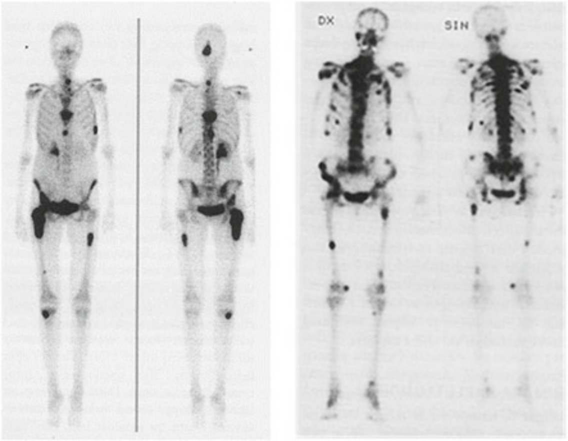

Fig. 5.14 SPECT images (front and back recordings) of two patients reveiling tumor metastases using the isotope Tc^{99} (Courtesy: Dr. Eva Brun, Division of Oncology, Lund University)

for biological and medical imaging. New possibilities of magnification radiography [384], single-shot ultrafast (1 ps) imaging [385, 386], differential imaging [389], and rejection of Compton-scattered, image-blurring photons [390, 391] have been explored.

A large amount of data on the structure of complex organic molecules has been obtained in X-ray diffraction studies on crystalline samples [392–394]. Recently, X-ray pulses have been used for time-resolved diffraction studies, allowing dynamic processes to be investigated [395]. Experiments, where short-time laser pulses and synchrotron radiation are combined provide additional information [396, 397]. Free-electron lasers (FELs) (Sect. 6.1.3) provide very high X-ray pulse energies in the fs domain enabling unprecendented studies of complex molecular structure and dynamics [398].

X-Ray Microscopy. The resolution of a microscope is limited by diffraction of the radiation used in the instrument. The resolution is inversely proportional to the wavelength, and thus it is attractive to go to the X-ray region for obtaining high resolution [399–404]. A particularly interesting region for X-ray microscopy is the so-called water window ($2.4\,\text{nm} < \lambda < 4.4\,\text{nm}$), corresponding to the wavelength region between the K absorption edges of oxygen and carbon (Fig. 5.15). By choosing the soft X-ray wavelength in this window a natural contrast between water and proteins (containing carbon) is obtained, allowing efficient microscopy of living cells/tissue, and the need for differential imaging using two wavelengths is reduced (see above). As a radiation source for X-ray microscopy, high-intensity pulsed-laser irradiation of liquid micro-droplets seems to be particularly promising [405–407], yielding sharp K-line emission, which can be focused by a microzone plate (Fig. 5.15). X-ray microscopy has lower resolution compared to electron microscopy [408–410] but has the big advantage of allowing fresh, living sample cells to be used in contrast to the need for drying and metal-film coating of the cells. Phase-contrast X-ray microscopy is also a method of increasing importance [344], and also here laser-produced X-rays can

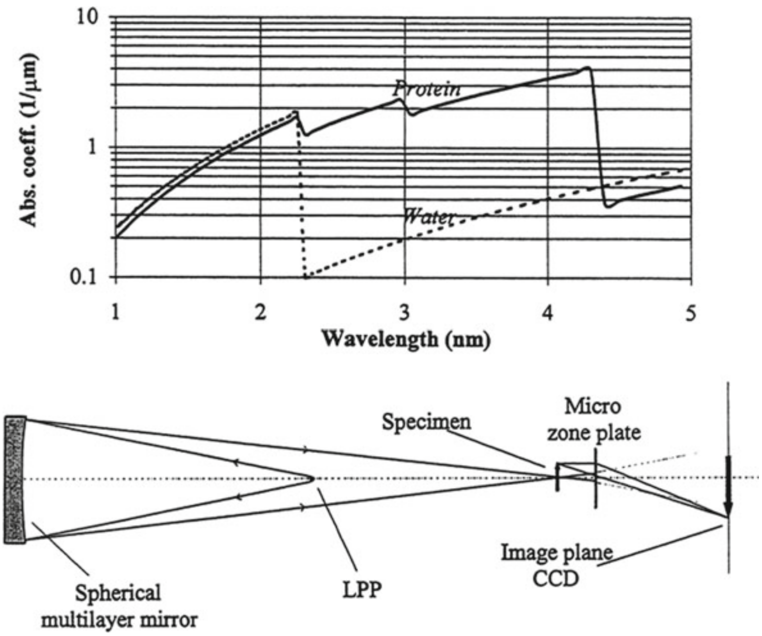

Fig. 5.15 The water window for soft X-ray microscopy, and a set-up for X-ray microscopy. LPP: laser-produced plasma [405]

be used. Of special interest is the generation of so called *betatron radiation*, when a high-power laser beam is used to accelerate electrons, which then upon bending generate X-rays [411, 412] (See also Sect. 9.6.6).

X-Ray Lithography. Lithography is used for patterning, e.g., in the microelectronics industry [413, 414]. X-ray lithography offers the potential advantage over ultraviolet lithography by providing higher resolution, again for reasons of reduced diffraction. In *proximity X-ray lithography,* a mask is placed just above the substrate (resist), generally consisting of *poly-methyl-meth-acrylate (PMMA)*. An X-ray reflecting optical system is used instead in *projection X-ray lithography*. Reasonable reflectivities in the soft X-ray region for perpendicularly incident rays can be achieved using Mo/Si multilayers. X-rays are produced by synchrotrons or from laser-produced plasmas. Short wavelength lithography has important applications for high-density electronics and nano-fabrication [415]. EUV lithography at 13.5 nm is replacing 193 nm technology based of ArF excimer lasers (see Sect. 8.4.3). The soft-X-ray intense radiation is frequently produced by focusing high-energy laser pulses on small droplets of molten tin, produced in a similar way as the ink-jet in a printer [416, 417], as discussed above.

5.2 Photoelectron Spectroscopy

We described in the previous section how X-ray absorption measurements can be used to obtain information on energy levels in atoms. An electron can be released in the absorption process, and an alternative way of obtaining energy-level information is therefore to study the energies of the emitted electrons (photoelectrons). This technique was applied as early as in the beginning of the twentieth century, but the instruments used had such a low resolution that little information was obtained. At the same time the optical and X-ray methods of spectroscopy were developed to higher and higher precision and there was little interest in electron spectroscopy for a long time. However, having developed high-precision beta spectrometers for nuclear physics, *K. Siegbahn* and co-workers applied the techniques for atomic electron spectroscopy. Their doubly focusing iron-free spectrometer with two coaxial coils was found to be very well suited to the analysis of X-ray excited photoelectron spectra, and the first results were reported in 1957. This was the starting point for a new type of spectroscopy called XPS (*X-ray Photoemission Spectroscopy*) or ESCA (*Electron Spectroscopy for Chemical Analysis*). This field of research has since developed very rapidly. The Nobel Prize in Physics was awarded to K. Siegbahn in 1981 for his contributions to XPS/ESCA [418]).

The principle of XPS is very simple, as illustrated in Fig. 5.16. Using a characteristic X-ray line from an X-ray tube, an electron is ejected from an inner shell in a sample atom, and its kinetic energy E_{kin} is then the difference between the photon energy $h\nu$ and the binding energy E_{B} of the electron:

$$E_{\text{kin}} = h\nu - E_{\text{B}}. \tag{5.3}$$

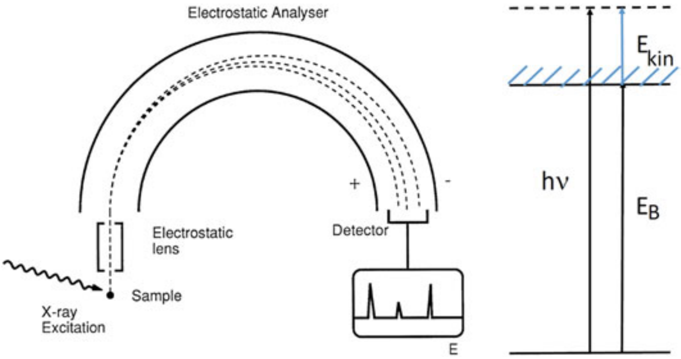

Fig. 5.16 The principles of XPS. The photoelectrons emitted from the sample with kinetic energy corresponding to the excess energy available are analysed for energy in an electrostatic spectrometer [1]

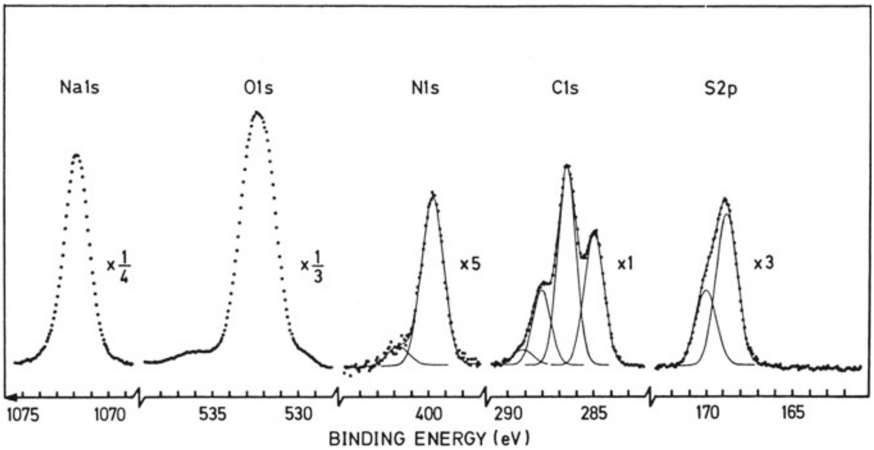

Fig. 5.17 XPS spectrum of a complex organic molecule (heparin) [419]

(The recoil energy of the atom can normally be disregarded.) The binding energy of the electron is defined as the energy difference between the final and initial states

$$E_B = E_{\text{ion}} - E_{\text{atom}}. \tag{5.4}$$

By analysing the emitted electrons it is possible to determine the binding energies of electrons in different shells. This has been done for most elements, and the results are in general more reliable than those obtained by X-ray absorption. In Fig. 5.17 the different peaks obtained in measurements on a complex organic molecule are shown. From the recording the binding energies of $1s$ and $2p$ electrons in several light atoms can be deduced. Initially, electron spectroscopy measurements were only made on solids, and uncertainties similar to those discussed in connection with the X-ray absorption technique occurred. However, it is also possible to perform measurements on free atoms and molecules with a corresponding increase in accuracy in binding energy determinations. This is important for comparisons with theoretical calculations, which can presently be performed very accurately.

Electron spectroscopy has been discussed in detail in [418–427].

5.2.1 XPS Techniques and Results

Presently, electrostatic energy analysers have fully replaced magnetic ones, since the former have many practical advantages. An electrostatic analyser consists essentially of two concentric cylindrical capacitor electrodes that produce a well-defined radial electric field (Fig. 5.16).

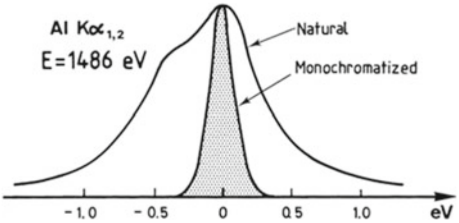

Fig. 5.18 Line profile of the $K\alpha$ line of Al, with and without monochromatization [428]

The resolution of an instrument will be limited by the monochromaticity of the exciting X-ray radiation. Frequently, the K emission from aluminium at 1486 eV is used. The natural radiation width of the line is about 1 eV and the line is broadened by unresolved fine structure (the overlapping $K\alpha_1$ and $K\alpha_2$ components). *X-ray monochromatization* by filtering out a narrow spectral region can be accomplished by placing the X-ray anode, a spherical single-crystal analyser and the sample on a *Rowland circle* (Fig. 6.27). For a certain angle between the three objects, the Bragg relation will be fulfilled only for a specific wavelength. Since both the anode and the sample have a finite size the monochromatization has limitations. A typical effect of monochromatization is shown in Fig. 5.18. Although a linewidth below the natural one has been achieved this does not violate the Heisenberg uncertainty relation, since it is still not possible to measure the $K\alpha$ photon energy of Al with a higher precision than before.

It is possible to increase the resolution further for solid samples by compensating for the finite extension of anode and sample by constructing the spectrometer with a certain dispersion. This is illustrated in Fig. 5.19. If the anode has a certain size, the Bragg relation will be fulfilled at slightly different wavelengths for different parts of its surface. These different wavelengths will be focused at slightly different parts on the sample, resulting in slightly different emitted electron energies from different parts of the sample. By making modifications in the design of the spectrometer, these electrons can be focused to the same point in the detector plane for a given setting of the spectrometer. Unfortunately, this technique does not work for gases which are of particular interest, since the surface of the sample is no longer restrained to the Rowland circle. Instead a *fine-focusing technique* has been developed in which the extension of the X-ray source has been strongly reduced by focusing the exciting electron beam onto a very small surface. In order to avoid overheating, the anode must then be rotated at high speed. The fine-focusing technique provides the most efficient monochromatization in work with gaseous, liquid, and solid samples. Monochromatized radiation from synchrotrons is presently widely used in XPS studies (Fig. 6.15) [429]. Outer shells can be investigated using special short-wavelength lamps, e.g., strong He lamps emitting the $1s2p$ -$1s^2$ resonance line at 58.4 nm (21.2 eV) [430].

In order to be able to measure many electron lines simultaneously a multichannel detector is frequently placed in the detector plane instead of using a detector behind an exit slit. The electrons then impinge on a micro channel plate (see also Fig. 6.42), in which electron multiplication occurs due to secondary emission by the inner wall material in the densely packed tubes in the plate. The original electron line image in

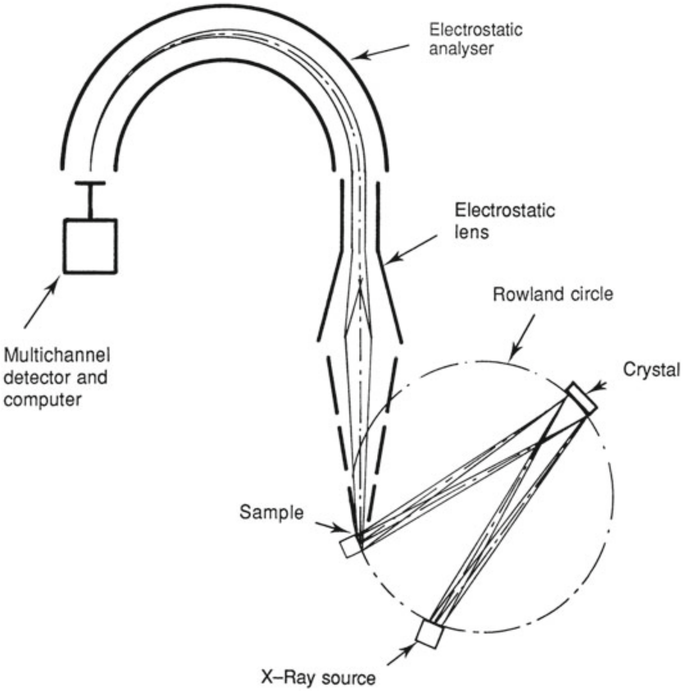

Fig. 5.19 An ESCA instrument with X-ray monochromatization and dispersion compensation [1]

the focal plane of the spectrometer is amplified and, by using two channel plates in series, an electron multiplication of 10^8 can be obtained. The electron showers are converted into optical signals on a phosphor screen which is viewed by a diode array (Fig. 6.42).

As an example of an atomic photoelectron spectrum a recording for mercury is shown in Fig. 5.20, in which all populated levels in the N, O, and P shells ($n = 4$, 5, and 6) can be observed. The common level designations from X-ray spectroscopy (Sect. 5.1; Fig. 4.8) have been used. Thus N_I corresponds to the 4s level, N_{II} and N_{III} are the $4p_{1/2}$ and $4p_{3/2}$ fine structure levels, N_{IV} and N_V are the $4d_{3/2}$ and $4d_{5/2}$ levels, etc. It can be clearly seen how the spin–orbit interaction decreases with increasing principal quantum number, as for alkali atom valence-electron excited states (Table 2.1). An enlarged section of the spectral region to the left of the N_{VI} and N_{VII} lines (the $4f_{5/2}$ and $4f_{7/2}$ levels) is also included, revealing many weak components. Some of these are referred to as *shake-up lines*. At the same time as a photoelectron is ejected, an outer electron can be excited, resulting in a lower photoelectron energy than otherwise, i.e., corresponding to a line for a higher binding energy. The presence of shake-up lines is a fundamental quantum–mechanical phenomenon. The wave function $\left|\psi^0_{N-1}\right\rangle$ for the system with a newly created inner shell vacancy can be expanded in the wave function system for the ordinary ion system that is obtained after the relaxation of the electronic shell.

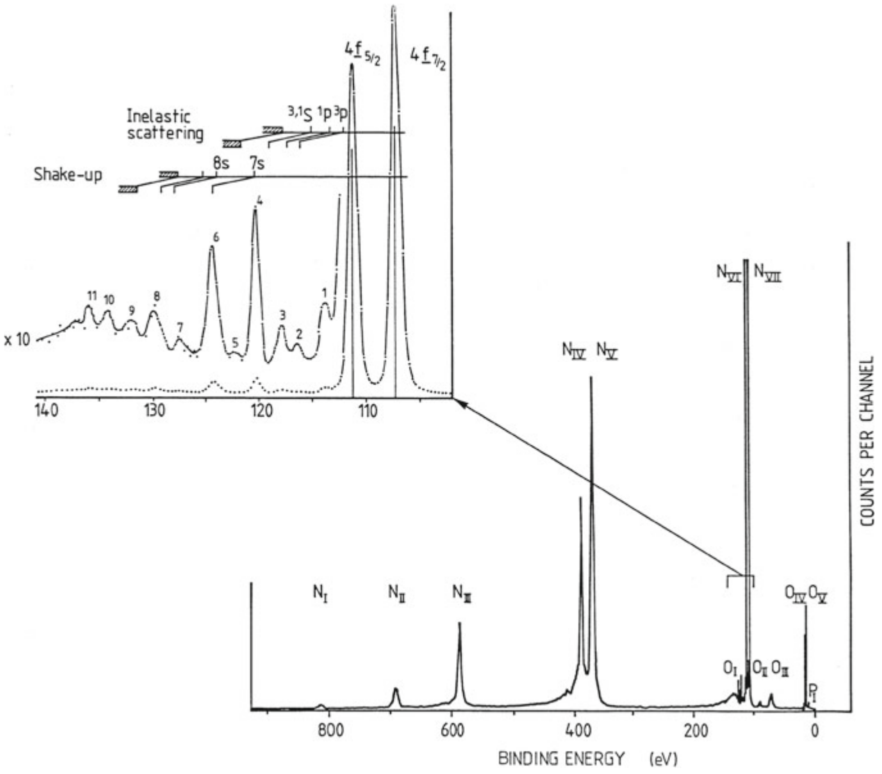

Fig. 5.20 ESCA spectrum of atomic mercury exhibiting shake-up lines [431]

The intensity I_i of a shake-up line, corresponding to the state $\left|\psi^i_{N-1}\right\rangle$ of the ion is given by

$$I_i \propto \left|\left\langle \psi^0_{N-1} \middle| \psi^i_{N-1} \right\rangle\right|^2. \tag{5.5}$$

A sulphur L-shell XPS spectrum showing valence orbitals of the SF_6 molecule is shown in Fig. 5.21. An ultra-soft X-ray emission spectrum for the same molecule is also included. The figure illustrates how the different selection rules for X-ray emission and XPS lead to complementary information for the interpretation of the valence orbital structure of the molecule.

5.2.2 Chemical Shifts

We will in this section discuss an aspect of electron spectroscopy that is of great importance because of its applications: the presence of *chemical shifts* in the binding

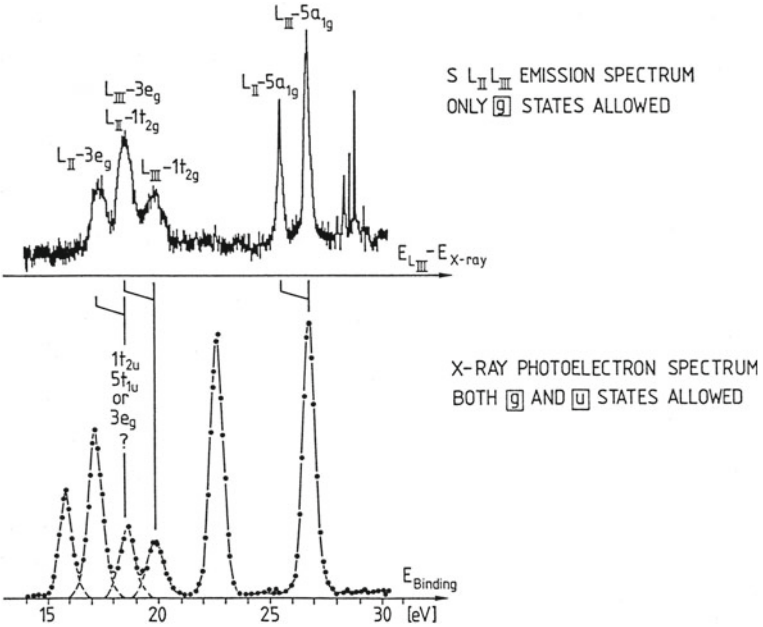

Fig. 5.21 Comparison between an X-ray emission spectrum and an XPS spectrum for SF_6, illustrating different selection rules [356]

energies. Such shifts, which have already been mentioned in connection with X-ray absorption spectroscopy (Sect. 5.1.2), constitute a source of error in the determination of binding energies, but also provide rich information on the atomic chemical environment. It is found that when the binding energy of a particular inner orbital is studied in different chemical environments, a variation (chemical shift) of typically a few eV is found. This is illustrated in Fig. 5.22 for the case of acetone. Whereas the $1s$ electron for oxygen only shows one distinct binding energy, the corresponding electronic state for carbon gives rise to a split line with a 1:2 intensity relation between the two components. The double line reflects the different positions of the three carbon atoms in the acetone molecule; one related to a double bond to oxygen and two equivalent positions in CH_3 groups. For comparison, the corresponding lines in the CO_2 molecule are included in the figure showing still other shifts. Chemical shifts are evident in the already shown Fig. 5.17, where different positions of the carbon atom in the molecule are reflected in the spectrum particularly clearly. An illustrative example is given for the case of the ethyltrifluoroacetate molecule in Fig. 5.23, featuring four equally strong carbon $1s$ lines corresponding to four different chemical environments. By comparing experimentally determined chemical shifts with theoretical calculations, valuable information on the molecular structure is obtained and at the same time the reliability of different theoretical models can be tested. The shift of the inner energy levels is not due to a deformation of the corresponding orbitals but rather to a change in the electrical potential in the inner part due to the change in the outer orbitals. Detailed calculations using molecular self-consistent-field approaches yield good agreement with experiments. In a simpler approach, the molecule is represented by ions with specific "effective" charges. Using atomic calculations the shift of inner levels can be obtained as a function of this charge. Comparisons with experimentally determined shifts give a description of the charge distribution in the molecule.

As we have pointed out, the presence of chemical shifts has resulted in important applications for electron spectroscopy. Since the positions of the lines depend on the

Fig. 5.22 Spectra of the acetone and the carbon dioxide molecules, illustrating chemical shifts [432]

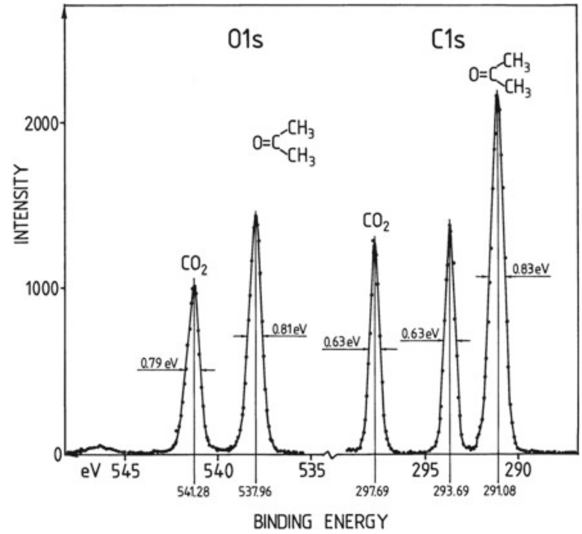

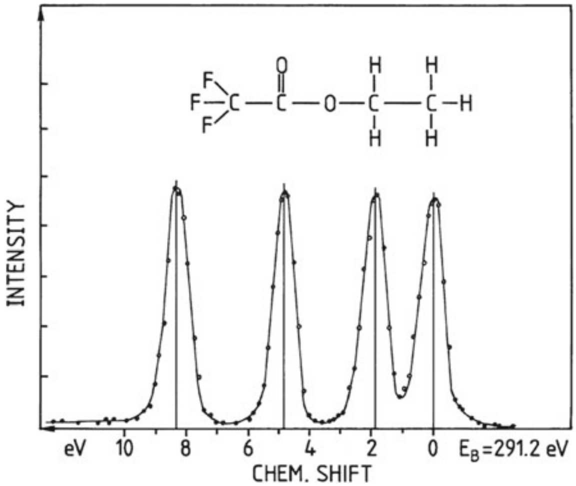

Fig. 5.23 1*s* electron lines for carbon in ethyltrifluoroacetate [432]

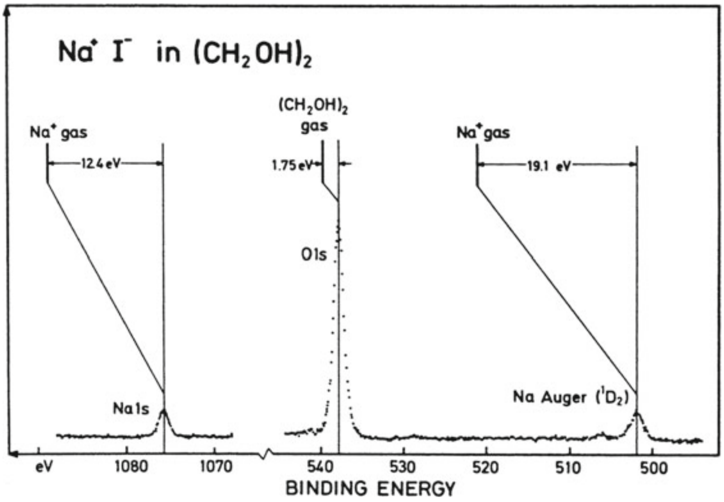

Fig. 5.24 Electron spectrum of a solution of Na^+I^- in glycole. Solvation shifts with respect to the gas phase line positions are observed [433]

chemical composition, the method can be used for qualitative as well as quantitative chemical analysis. One of the commonly used names for the XPS method, ESCA (*Electron Spectroscopy for Chemical Analysis*), focuses on this aspect.

One can also use the shift between free atomic or molecular species and the condensed phase to study cohesive properties. An example for a liquid phase system is shown in Fig. 5.24, regarding the photoelectron spectrum of a NaI solution. In this case the free-ion/dissolved-ion shift can be related to the energy of dissolution of the ion in the solution (solvation energy), providing information on the solution structure [433].

In the study of condensed phase samples it is the outermost layers which are probed in the photoelectron experiments (down to 1 nm below the surface). The *surface sensitivity* is illustrated in Fig. 5.25 for the case of slow oxidation of a potassium surface. Peaks due to potassium oxide and physisorbed O_2 occur. A further example of surface studies is shown in Fig. 5.26, which shows ESCA spectra for a clean gold foil and for a gold foil contaminated by a faint fingerprint from a finger that had previously been in contact with silicone oil. Surface monitoring has been discussed in [435, 436].

5.3 Auger Electron Spectroscopy

As described above, in normal photoelectron spectroscopy the energy of the ejected electrons varies according to the energy of the exciting X-ray quanta; see (5.3). However, an emission of electrons with a kinetic energy that does not depend on the

Fig. 5.25 ESCA surface sensitivity illustrated by progressing oxidation of a potassium surface. $1L$ corresponds to 10^{-6} torr·s of O_2 exposure [434]

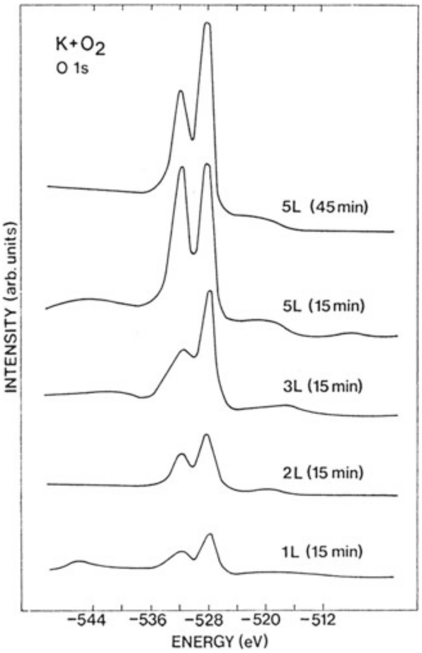

Fig. 5.26 ESCA surface sensitivity illustrated by spectra from a clean and a contaminated gold surface [437]

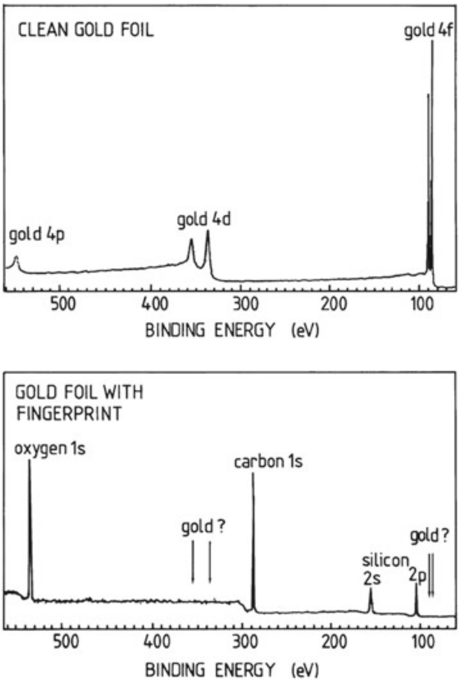

excitation energy is also observed. This process is called the *Auger effect* (P. Auger, 1923). The energy that would normally be emitted as, for example, a $K\alpha$ quantum is instead used to release an outer electron, which emerges with a kinetic energy E_{kin} determined by the $K\alpha$ energy $E_{K\alpha}$ and the binding energy of the outer electron E_{B}:

$$E_{\mathrm{kin}} = E_{K\alpha} - E_{\mathrm{B}}. \tag{5.6}$$

The process is illustrated in Fig. 5.27 for the case of a KLL Auger process, corresponding to the primary removal of a K electron, the infall of an L electron into the hole and the ejection of a further L electron. Clearly, the Auger electron energy must also depend on the coupling of the two holes in the final state. Corresponding Auger spectra from Mg and MgO are shown in Fig. 5.28. The influence of the hole coupling is shown as well as the chemical shift between the metal and the oxide. Additional peaks in the Mg spectrum are due to volume plasmons (a solid-state phenomenon).

Auger electrons can be emitted if the inner-shell vacancy is created by the absorption of an X-ray quantum or by electron bombardment. However, in the latter case an electron continuum due to the scattered electrons tends to mask the frequently weak Auger lines in the case of solid samples. Spectral derivation techniques can then be used to enhance the signals. The background is weak and causes no problems for gases.

The probability of Auger-electron emission dominates over the emission of characteristic X-rays for light elements, while the opposite conditions prevail for heavy elements.

The Auger technique is comparatively simple, and it has the same surface sensitivity as XPS. Because of this, Auger spectroscopy is frequently used as a diagnostic tool, e.g., for controlling the cleanliness of a surface in connection with surface physics investigations. A particularly valuable technique is scanning Auger spectroscopy, which can provide surface images with a resolution of 200 nm [438, 439].

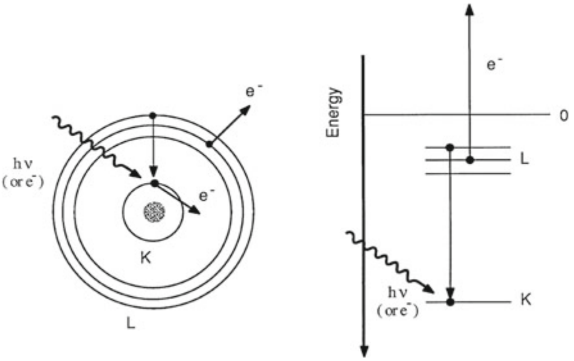

Fig. 5.27 Illustration of the Auger process (KLL Auger process)

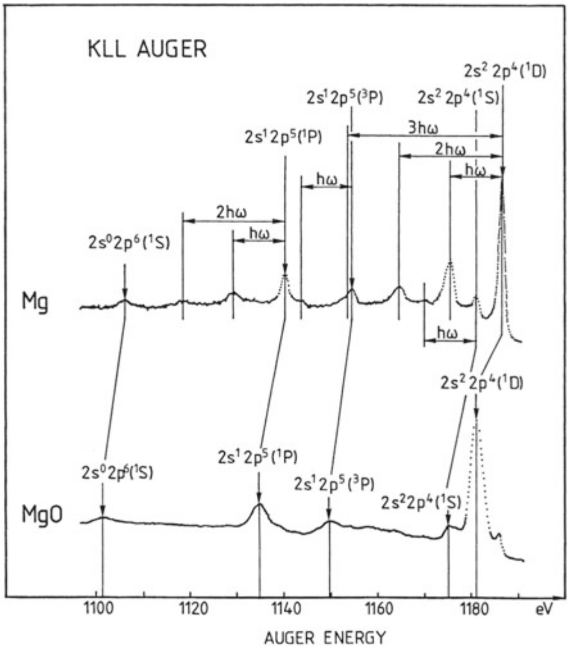

Fig. 5.28 Auger electron spectra for Mg and MgO (solids) illustrating the influence of chemical shifts and electron hole coupling. Additional peaks $n\hbar\omega$ are due to volume plasmons [436]

Chapter 6
Optical Spectroscopy and Multispectral Imaging

The method of spectroscopy, using a suitable light source and a spectral apparatus for radiation analysis, has its natural field of application in the determination of the general energy-level structure in the energy range corresponding to UV, visible, and IR light. The energy-level scheme for atoms and ions of many different charge states has been established from spectral analysis in different wavelength regions, as discussed in Chap. 2. Many of the observed spectral lines are listed in standard monographs [440–446]. Hyperfine structure can also be studied in many cases using high-resolution instruments. The first observations of hyperfine structure in optical spectra were made at the end of the nineteenth century by A. Michelson (1891) and by Ch. Fabry and A. Pérot (1897). An interpretation of the structure was put forward at the end of the 1920's. The optical method for studies of hyperfine structure is particularly suitable when unpaired *s*-electrons are present (large hyperfine structure). A large number of nuclei have been studied with regard to nuclear spin and moments through the years. Many radioactive isotopes have also been studied using very small samples. Although the classical optical method has low accuracy, compared with resonance methods (Chap. 7) or laser techniques (Chap. 9), its field of application is wide. A very large number of excited levels can be studied through the structure in the large number of lines emitted by a light source. The structure in spectral lines, connecting a ground state or a well-populated metastable state with higher-lying, short-lived states, can also be studied in absorption experiments, in which the atomic absorption in a continuous spectral distribution is recorded. The techniques of classical optical spectroscopy have been covered in [447–450].

There are numerous applications of optical spectroscopy. Many optical methods for analysis exist regarding industry, environment, and medicine. Measurements can also be performed at a distance, by remote sensing. Satellites provide global coverage of, e.g., earth resources. Also, most of our knowledge in astronomy stems from optical spectroscopy. Remote sensing and astronomy also provide ample examples of spectroscopy in numerous adjacent points—multispectral imaging.

© The Author(s), under exclusive license to Springer Nature Switzerland AG 2022

S. Svanberg, *Atomic and Molecular Spectroscopy*, Graduate Texts in Physics,
https://doi.org/10.1007/978-3-031-04776-3_6

6.1 Light Sources

Many different types of light sources (lamps) have been developed for atomic spectroscopy investigations. If the radiation from the source is to be analysed directly, the lamp should, of course, contain the atomic species for which the emission spectrum is to be studied. Such light sources are designated *line light sources*. If the light source is to be used for excitation of atoms that are to be studied with some spectroscopic method, any light source yielding a sufficient intensity at the excitation wavelength can be used: accidental coincidences between lines from different elements can, for example, be used. Close-lying lines can cause confusion in spectral analysis and have therefore been listed [451]. However, such perfect coincidences are rare, considering that the lines normally have to overlap within 0.001 nm. In certain experiments (e.g., in absorption experiments) *continuum light sources*, which do not produce any characteristic line spectrum, can be used. However, such light sources generally yield too low an intensity per spectral interval to be useful for excitation purposes, unless the absorption bands are broad. The opposite is true for the third main group of light sources, *lasers*. Here, the intensity per spectral interval is many orders of magnitude higher than that which is obtained from line sources. Initially, only laser transitions in fixed-frequency lasers [452, 453], or accidentally coincident lines could be employed. However, tunable lasers of many types subsequently became available, making more general applications of the unique properties of laser light possible in spectroscopy. Lasers will be discussed in Chap. 8.

6.1.1 Line Light Sources

The accuracy of a spectroscopic measurement is determined by the sharpness of the lines to be measured. The experimentally recorded width of the lines is due to two contributions: the primary width (from the source) and the instrumental width of the spectral apparatus used. We will first consider the factors contributing to the primary line width of the light source. These broadening factors are also relevant in absorption experiments. We have already dealt with the *natural radiation width* (*homogeneous broadening*) of energy levels in Chap. 4. This width is for most light sources small compared with the *Doppler broadening*. Because of the varying velocities and directions of movement for the atoms under study, light within a certain frequency interval can be emitted or absorbed, as illustrated in Fig. 6.1.

Doppler broadening is an example of *inhomogeneous* broadening, in which different atoms contribute to different parts of the line profile. Light of frequency ν_0, emitted from a source moving with a thermal velocity υ, towards ($\upsilon > 0$) or away ($\upsilon < 0$) from an observer is recorded with a frequency shift $\Delta\nu$ given by

$$\Delta\nu/\nu_0 = \upsilon/c. \tag{6.1}$$

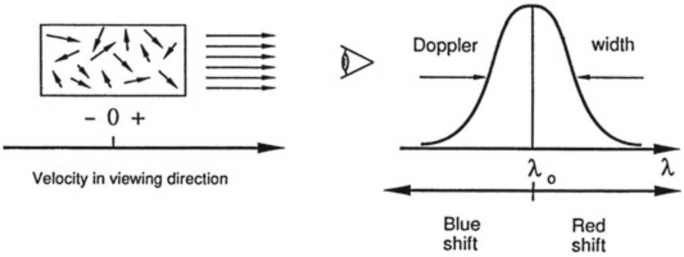

Fig. 6.1 The origin of Doppler broadening of a spectral line

This expresses the *Doppler effect.*

In a light source or in an absorption cell the velocities of the atoms follow a Maxwell distribution and the number of atoms with velocity components between υ and $\upsilon + d\upsilon$ in the direction of observation is

$$\mathrm{d}N = Nf(\upsilon)d\upsilon, \tag{6.2}$$

where $f(\upsilon)$ is the distribution function for the particular velocity component υ:

$$f(\upsilon) = \sqrt{\frac{M}{2\pi RT}}\exp\left(-\frac{M}{2RT}\upsilon^2\right). \tag{6.3}$$

Here N is the total number of atoms, M is the atomic weight, and R is the general gas constant. The light power emitted in the frequency interval ν to $\nu + \Delta\nu$ is denoted by P_ν dν. This power is proportional to the number of light-emitting atoms in this band, i.e., the atoms with a velocity component υ between υ and $\upsilon + d\upsilon$, hence

$$\upsilon = c\frac{\nu - \nu_0}{\nu_0} \quad \text{and} \quad \mathrm{d}\upsilon = c\frac{\mathrm{d}\nu}{\nu_0}, \tag{6.4}$$

and

$$P_\nu \mathrm{d}\nu = KNf\left(c\frac{\nu - \nu_0}{\nu_0}\right)c\frac{\mathrm{d}\nu}{\nu_0}, \tag{6.5}$$

resulting in

$$P_\nu = K'f\left(c\frac{\nu - \nu_0}{\nu_0}\right) = K''\exp\left(-\frac{M}{2RT}c^2\frac{(\nu - \nu_0)^2}{\nu_0^2}\right). \tag{6.6}$$

K, K', and K'' are constants of proportionality. Equation (6.6) describes a Gaussian with a half-intensity at $e^{-x^2} = 1/2$, i.e., when

$$\delta\nu = \nu - \nu_0 = \frac{\nu_0}{c}\sqrt{\frac{2RT}{M}\ln 2}. \tag{6.7}$$

The full-width at half-maximum (FWHM), the *Doppler width*, is then

$$\Delta\nu_{\mathrm{D}} = 2\delta\nu = \frac{2\sqrt{2R\ln 2}}{c}\nu_0\sqrt{\frac{T}{M}}. \tag{6.8}$$

The value of the constant is $7.16 \times 10^{-7}\ \mathrm{K}^{-1/2}$. As an example, for $\lambda = 500$ nm, $T = 500$ K and $M = 100$ the Doppler broadening is

$$\Delta\nu_{\mathrm{D}} = 7.16 \times 10^{-7}\frac{3 \times 10^8}{5 \times 10^{-7}}\sqrt{5} = 960\ \mathrm{MHz} \longleftrightarrow 0.001\ \mathrm{nm}.$$

A general rule, which may easily be memorized, is that the typical Doppler width in the visible range for typical light sources is about 0.001 nm or 1000 MHz. In the IR region the width is, of course, proportionally smaller, i.e., about 50 MHz at 10 μm.

If the atoms under study undergo frequent *collisions*, the spectral lines will be broadened. With increasing pressure, *Lorentz broadening* (due to collisions between different kinds of atoms) and *Holtsmark broadening* (due to collisions between the same kind of atoms) will be more and more prominent. These two broadening mechanisms are generally treated together as pressure broadening. The collisional width, $\Delta\nu_{\mathrm{coll}}(P,T)$, of the resulting Lorentzian curve is about 0.5–5 GHz at atmospheric pressure and room temperature. The width can be calculated for any temperature and pressure, if the reference value $\Delta\nu_{\mathrm{coll}}(P_0,T_0)$, for a given pressure P_0 and a given temperature T_0 is known, by using the relation

$$\Delta\nu_{\mathrm{coll}}(P,T) = \Delta\nu_{\mathrm{coll}}(P_0,T_0)\frac{P}{P_0}\sqrt{\frac{T_0}{T}}. \tag{6.9}$$

Clearly, Doppler and collisional broadening are present at the same time, which leads to a composite lineshape obtained by convolving the two line shapes into a *Voigt line profile*. Since the collisional broadening measured in frequency is independent of the frequency itself, while Doppler broadening is not, collisional broadening dominates in the IR region, while the opposite is frequently true at short emission wavelengths.

If collisions with electrons and ions occur, as in discharge lamps, *Stark broadening*, due to the strong electrical fields experienced by the atoms during collisions, will also contribute to the total line broadening.

Line broadening mechanisms and resulting lineshapes have been discussed in [454–458].

A number of line light sources have been schematically depicted in Fig. 6.2. With a *DC gas discharge* between two electrodes the spectra of most gases can be conveniently produced. The discharge current is generally low, about 100 mA. Considerably stronger currents are used in DC *arcs*. The cathode contains the atomic species for which the spectrum is to be produced. Atoms are brought into the arc, which is burning between the anode and the cathode in an inert-gas atmosphere, through sputtering. This type of lamp has been extensively used for studies of the strengths of spectral lines (transition probabilities) [459, 460].

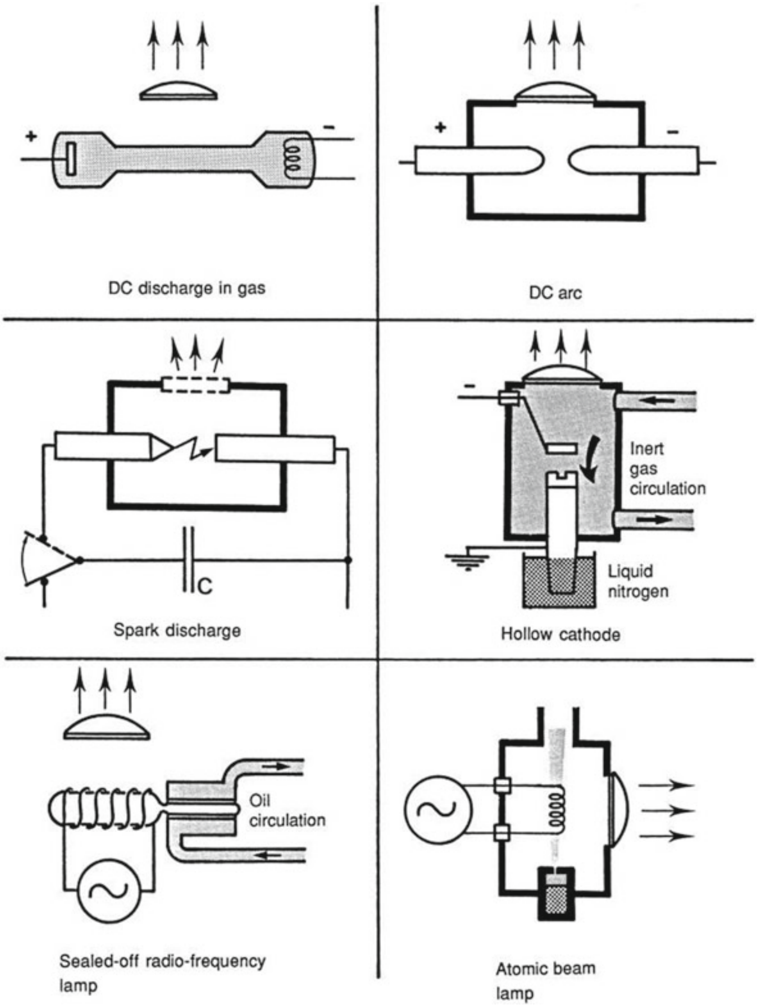
+
−
DC discharge in gas
+
−
DC arc
C
Spark discharge
−
Inert
gas
circulation
Liquid
nitrogen
Hollow cathode
Oil
circulation
Sealed-off radio-frequency
lamp
Atomic beam
lamp

Fig. 6.2 Line light sources of different constructions [1]

The *hollow cathode* is a very useful light source, which produces comparatively narrow spectral lines. A dc discharge of typically 10 to 500 mA runs in an inert-gas atmosphere (pressure: 1–5 torr; 133–667 P) between a ring-shaped anode and the cathode, which is made of the element to be studied. A hole, with a typical depth and diameter of 5 mm, is drilled in the cathode. Because of the field distribution around the hole the discharge will run down into the hole. Atoms are sputtered into the discharge through the ion bombardment, and the atoms are excited in the discharge. Intense light emission is obtained from the hole. By cooling the hollow cathode with liquid nitrogen, the Doppler width, which is the dominating source of broadening, can be further reduced (Schüler hollow cathode).

In an electric *spark discharge* considerably higher excitation energies are obtained than in the light sources described earlier. A large capacitor ($\sim 0.5\ \mu F$) is discharged through a spark gap between two electrodes of the element to be studied. Sometimes a piece of insulating material is placed between the electrodes to guide the spark (*sliding spark*). Highly ionized atoms with more than 10 electrons removed can be obtained and the corresponding spectra studied. The intermittent light emission from the spark was traditionally studied with spectrographs with photographic recording, since the photographic plate is a perfect light integrator. The blackening of photographically recorded plates could conveniently be recorded with photoelectrical methods (microdensitometer). Clearly, Charged Coupled Devices (CCDs) or Complementary Metal Oxide Semiconductors (CMOS) detectors (Sect. 6.3) fill the same function as plates and in a much more convenient arrangement.

A sealed *radio-frequency discharge lamp* can be used for most elements which develop a sufficient vapour pressure ($>10^{-3}$ torr, 0.13 P) within the temperature range, in which glass or quartz vessels can be employed (below 1000 °C). The lamp vessel is sealed under high vacuum after a small amount of the element of interest has been brought into it by heating a lump of the material that is kept in a sidearm of the vacuum manifold. The sealed lamp vessel is placed in an RF coil inside an oven, and an RF power of typically 100 W is applied. This kind of lamp is frequently used for alkali atoms. At the low temperatures needed in these cases, the metal vapour pressure can be accurately regulated by circulating oil around a cold finger on the lamp vessel, which is kept at a slightly higher temperature. The coldest point on the vessel will determine the metal vapour pressure.

In the *atomic-beam lamp*, an atomic beam is excited in an RF coil, and light emitted at right angles to the atomic beam is collected. In this way the Doppler broadening of the emission lines will be much reduced. The same principle for linewidth reduction is used in absorption measurements, in which absorption from a continuous wavelength distribution by atoms is recorded at right angles to the collimated beam. The resulting Doppler width when atoms with a preferred direction of motion are used can be calculated in a similar way as for the case with evenly distributed directions of motion. In practical cases, linewidths of tens of MHz are obtained in optical absorption measurements on atomic beams, at thermal velocities (a few hundred m/s).

A special type of light emission is obtained from a *laser-produced plasma* [461–466]. Here the beam from a high-power laser is focused onto a small spot on the surface of a metallic substrate. Typically, a Nd:Glass laser (Chap. 8) is used with a pulse energy of about 10 J and a pulse length of a few ns. (We will in Sect. 10.2.3.1 discuss a similar technique, *laser-induced break-down spectroscopy (LIBS)*, however utilizing laser pulses with much lower energy). Plasma temperatures as high as 10^6–10^7 K can be obtained. The ionization occurs very quickly, and the low states of ionization do not have time to radiate. The maximum state of ionization (up to 60 electrons removed) can be varied by changing the pulse energy and focusing. The laser-produced plasma spectrum is easier to interpret than the spectrum from a spark, where a large number of ionization stages simultaneously yield spectral lines. In particular, if a high-Z target material is used, a strong soft X-ray continuum will also be obtained. This radiation is comparable to that produced by an electron synchrotron (Sect. 6.1.3). Such short-wavelength radiation is very useful both for spectroscopic investigations and for technical applications such as X-ray microscopy and lithography in connection with semiconductor circuit production (see Sects. 5.1.3 and 9.6.5).

In laser-driven fusion research, high-power beams are made to impinge on small targets of deuterium and tritium [467–470]. It is also possible to study highly ionized spectra from other plasma generators used in fusion research, such as *Tokamak* machines. A smaller plasma light source is the *theta pinch*, where a strong current pulse in a one-turn coil excites and contracts the plasma. Spectral analysis of the plasma light serves as an important diagnostic tool in fusion research machines [471–475].

Finally, the *beam-foil light* source and its applications will be described. These techniques were introduced in 1963 by *Kay* and *Bashkin* [476, 477]. The principles of beam-foil spectroscopy are illustrated in Fig. 6.3. Ions of the element to be studied are produced with a well-defined energy (velocity) in an ion accelerator. The ions (with a typical velocity of 10^6 m/s) pass a 50 nm thick carbon foil, in which very abrupt excitation occurs (the passage time is $\sim 10^{-14}$ s). Ions of different charges are formed. An electron can also be picked up, and a neutral atom is then formed. The excited states will decay after passing through the foil, and the corresponding spectrum can be recorded with a spectrometer. Because of a certain lateral scattering in the foil and since a finite solid angle must be used for the detection of the photons, the Doppler broadening for the fast particles will be large, typically a few 0.1 nm. The linewidth can, however, be reduced using special imaging techniques (refocusing) [478]. A typical beam-foil spectrum is shown in Fig. 6.4.

Since the velocity of the particles is known, a well-defined timescale is obtained after the foil and the decay can be observed directly. The foil is normally moved back and forth in such measurements, while the detection system remains fixed. A certain energy loss and velocity spread (straggling) is obtained as the ions pass through the foil and these small effects can be studied if an electrostatic velocity analyser is placed after the foil, as is illustrated in the Fig. 6.3. Lifetimes of excited states of atoms and ions can be conveniently measured with the beam-foil method. Since the excitation process is not selective, the decay curve must be carefully analysed so that cascade decays from higher-lying states can be identified and corrected for [480, 481]. Lifetime measurements using the beam-foil technique are illustrated in

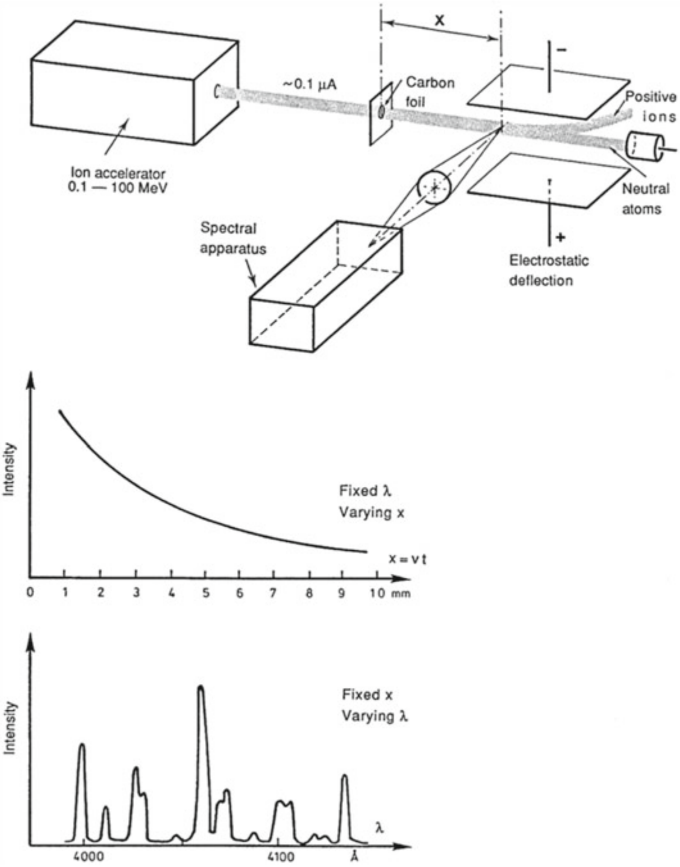
x
~0.1 μA
Carbon foil
Positive ions
Neutral atoms
Ion accelerator 0.1 — 100 MeV
Spectral apparatus
–
+
Electrostatic deflection
Intensity
Fixed λ
Varying x
x = vt
0 1 2 3 4 5 6 7 8 9 10 mm
Intensity
Fixed x
Varying λ
λ
4000
4100
Å

Fig. 6.3 Principles of beam-foil spectroscopy [1]

Fig. 6.5. The beam-foil method yields low signal strengths, since the particle density in the beam is typically 10^5 ions/cm^3. Ion accelerators in different energy ranges can be used: from mass separators yielding 100 keV energy to heavy ion accelerators yielding particle energies up to 300 GeV. Atoms ionized 90 times have been observed. In order to determine which lines belong to a certain ionization state, a strong electric field can be applied, which deflects the beam according to the charge states of the ionic beam constituents.

As a result of the abrupt foil excitation, atoms and ions can be excited into a quantum–mechanical state that is a coherent superposition of eigenstates. By "coherent" we mean in this context that a well-defined relation exists between the phase factors of the different eigenstates. If the sublevels are not equally populated but a certain degree of "alignment" is brought about, some components of the light from the decaying, abruptly excited state will be modulated at frequencies that correspond to the energy splittings between the substates. Such an alignment can be obtained in

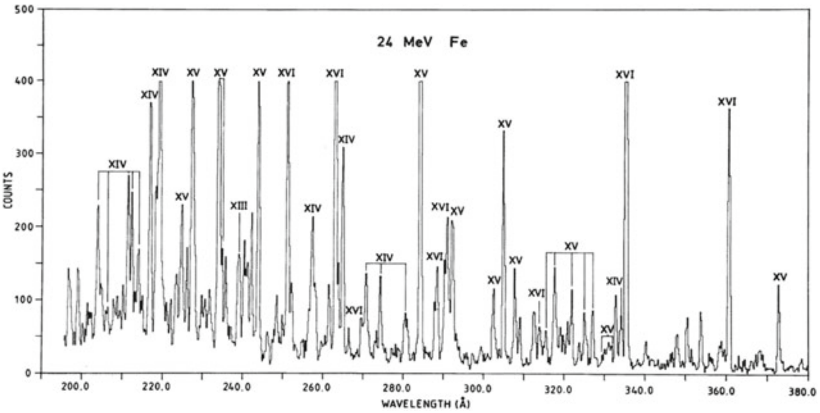

Fig. 6.4 Example of a beam-foil spectrum obtained using an accelerated iron-ion beam (1 Å = 0.1 nm) [479]

Fig. 6.5 Examples of decay curves obtained with beam-foil spectroscopy [482]. Curve *a* presents the decay of a Be I level unaffected by cascades. In (*b*) a level in C II is repopulated by a short-lived level, while in (*c*) a level in BII is repopulated by a longer-lived level. τ_f denotes the half-life of the level feeding the level of interest

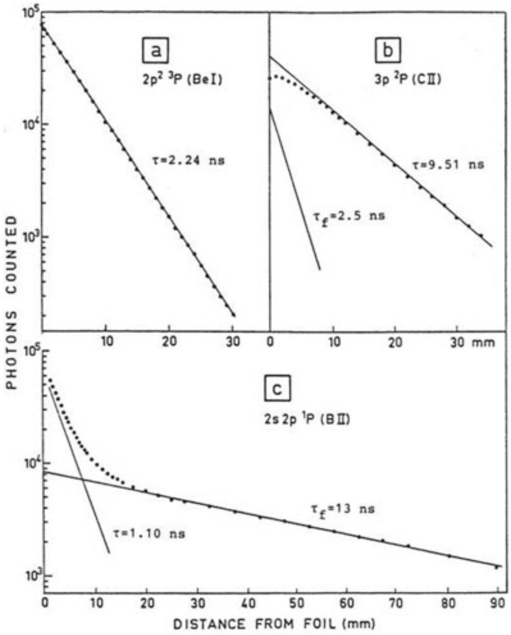

the beamfoil excitation process, especially if the symmetry is broken by inclining the foil with respect to the ion beam [483]. This so-called *quantum-beat spectroscopy*, which was treated theoretically for the beam-foil case in [484], is very useful for measuring fine- and hyperfine- structure separations. The technique is illustrated by a fine-structure determination for ^{4}He in Fig. 6.6. An example of hyperfine structure quantum beats is given in Fig. 6.7. We will return to quantum-beat experiments in Sect. 9.4.5, where the more well-defined case of optical (laser) excitation is discussed.

As we have seen, the beam-foil light source offers many possibilities for studies of spectra, lifetimes and level separations, and extensive data have been collected [487–489]. Comprehensive reviews of the field of beam-foil spectroscopy have been written [490–494].

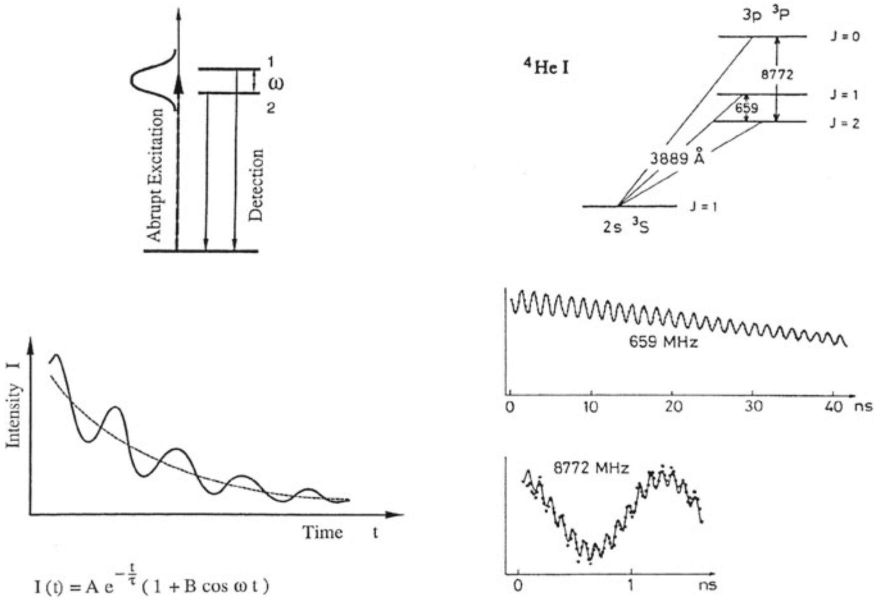
1
ω
2
Abrupt Excitation
Detection
Intensity I
Time t
I (t) = A e^{-t/τ} (1 + B cos ω t)
⁴He I
3p ³P
J = 0
8772
J = 1
659
J = 2
3889 Å
J = 1
2s ³S
659 MHz
0 10 20 30 40 ns
8772 MHz
0 1 ns

Fig. 6.6 Principle of quantum beats (*left*) and illustration of fine-structure quantum beats in ^{4}He (*right*) [485]

Fig. 6.7 Fourier analysis of hyperfine-structure quantum beats in the $1s2p\ ^3P_{1,2} \rightarrow 1s2s\ ^3S_1$ decay of Be III [I(^{9}Be) = 3/2] [486]

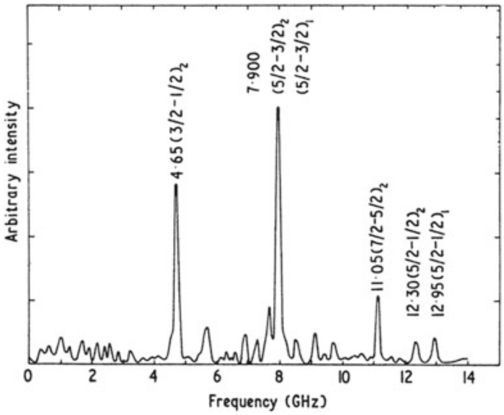

6.1.2 Continuum Light Sources

The *black-body emitter* is the simplest type of continuum light source. The radiation from a heated tungsten ribbon approaches that of a Planck emitter. However, for a given temperature, only about 30% of the power emitted by a truly black body is obtained (emissivity: 30%). The highest temperature attainable in this way is 3400 K. Normally, the working temperature for a tungsten lamp is about 2900 K. Such a lamp is useful in the wavelength region 320 nm to 2.5 μm. Planck radiation diagrams for certain characteristic temperatures are shown in Fig. 6.8, which also illustrates the displacement of the wavelength of maximum emission towards shorter wavelengths with increasing temperature (the Wien displacement law: $\lambda_{\max} \propto T^{-1}$). For the IR region a so-called *Nernst glower* is frequently used. This consists of a heated rod of sintered cerium and zirconium oxides (1500–2000 K).

During recent years, white light LED (light emitting diode) lamps have largely replaced normal Planck-radiation lamps as light sources for illumination. This development came about through the development of very efficient blue LEDs based on GaN semiconductor materials, which was awarded the 2014 Nobel Prize in Physics to *I. Akasaki, H. Amano, and S. Nakamura* [495–497] (see also Sect. 8.5.5). The primary emission is at about 460 nm, and part of the blue light is converted to longer wavelengths by a strongly fluorescent material surrounding the diode. A typical spectrum is shown in Fig. 6.9 [498]. The red, green, and blue light components are weighted in such a way that the human eye experiences the light as white. Clearly, the light appearance may be changed from a more "warm" to a more "cold" type by

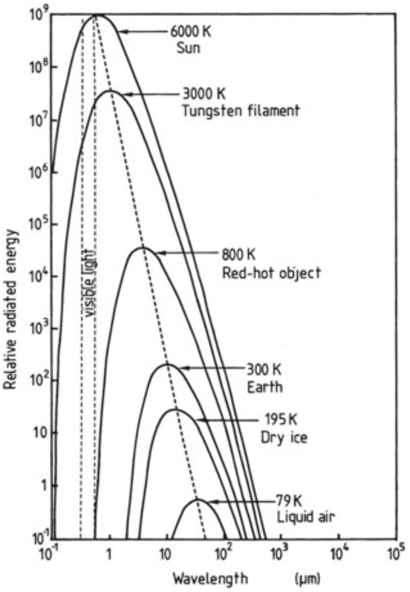

Fig. 6.8 Planck radiation diagrams for different temperatures

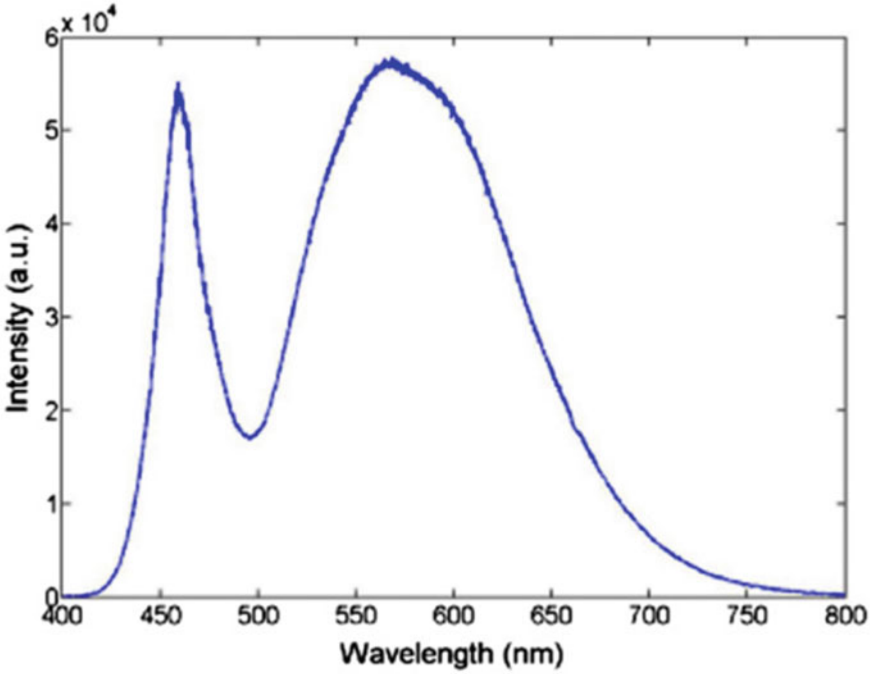

Fig. 6.9 Spectral distribution from an LED lamp ([498]; reproduced with permission from Wiley)

changing the weight between the primary blue light and the induced fluorescence. LED lighting technology is discussed in [499–501].

The blue LEDs used in the new illumination lamp technology is a specific embodiment of the general principle of LEDs, which are now available over a very wide range of wavelengths, as determined by the band gap of the semiconductor material used in the fabrication. The LED spectral width is typically 30 nm. The emission spectra of different LEDs are shown in Fig. 6.10.

Lamps utilizing a gas discharge are frequently used in the UV and visible regions. In a *deuterium lamp* at a pressure of some tens of torrs, the spectral lines are broadened to a continuum-like spectrum with only certain peaks remaining. The practical region of use is 180–380 nm. Lamps with much higher pressures can also be used. In *xenon* and *mercury lamps* pressures of tens of atmospheres are often used. Spectral distributions of gas-filled lamps are presented in Fig. 6.11. Such lamps use a discharge arc, emitting isolated spectral lines as well as a continuous background from the plasma containing free electrons and ions. Although the total output power from a continuum source of this kind can be very high (>1 kW), the power within a region corresponding to an individual atomic absorption line (0.001–0.005 nm) is always small.

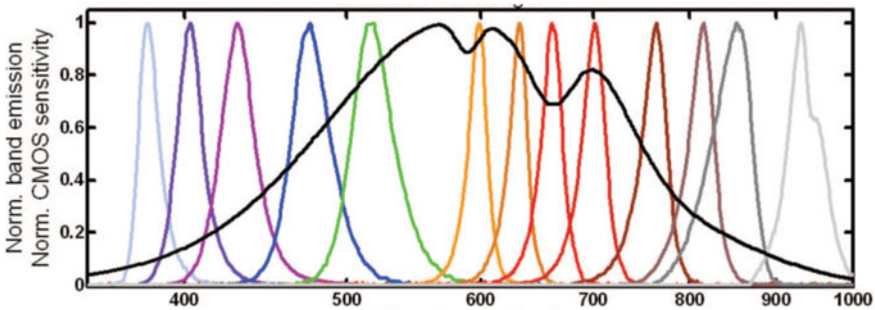

Fig. 6.10 Emission of 13 different LEDs. The sensitivity curve for a CMOS detector is also included (black curve) ([502], reproduced with permission from AIP Publishing)

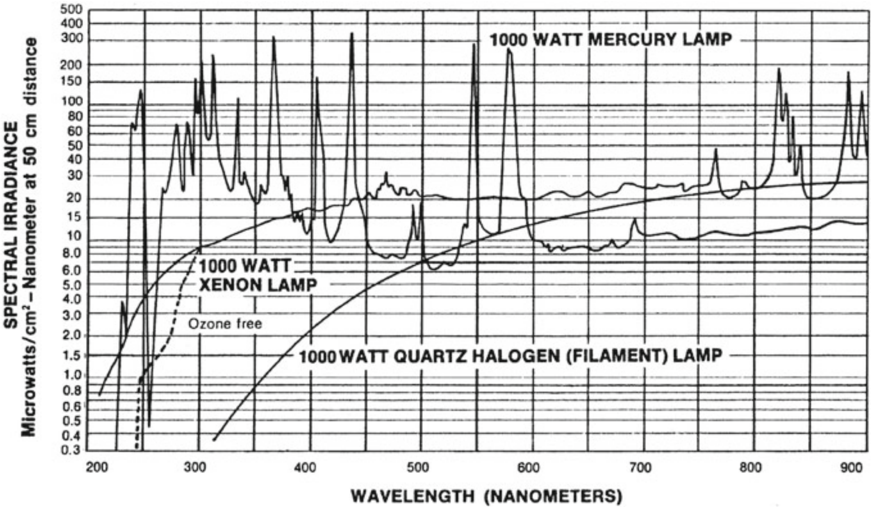

Fig. 6.11 Spectral distributions from some gas-filled lamps (Courtesy: Oriel Corp., Stratford, CT, USA)

6.1.3 Synchrotron Radiation

During the latest decades *electron synchrotrons* have been increasingly used as sources of continuum radiation. Originally, the radiation was obtained "parasitically" from machines that were constructed for nuclear physics experiments. Today large synchrotrons used for elementary particle physics have synchrotron radiation as an unwanted loss mechanism. However, an increasing number of machines, dedicated solely for light generation, have been built. Because of the strong centrifugal acceleration ($\sim 10^{16}$ g for electrons with a velocity close to c in an orbit of 1 m radius), the electrons will emit radiation. At low velocities the emission pattern is a

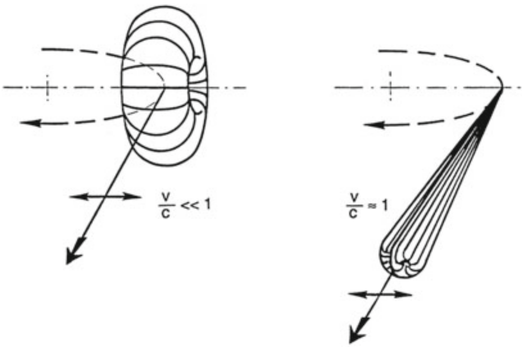

Fig. 6.12 Generation of synchrotron radiation [504]

normal $\sin^2\theta$ dipole distribution with the orbit radius as the symmetry axis (Fig. 6.12). Because of relativistic effects the emission characteristics will be strongly peaked in the momentary flight direction of a high-speed electron [503–506]. The opening angle of the emission cone is inversely proportional to the electron energy and is typically a small fraction of a degree. The light is linearly polarized. The total power P of the synchrotron radiation increases as the fourth power of the electron energy E

$$P[\mathrm{W}] = 88.5\frac{I[\mathrm{mA}](E[\mathrm{GeV}])^4}{R[\mathrm{m}]}, \tag{6.10}$$

where I is the electron beam current and R is the radius of the electron orbit. Classically, the frequency of the radiation emitted by a circulating electron would be the inverse of the period of revolution and would be typically 10 MHz. However, because of relativistic effects, overtones of very high orders are emitted at high powers. Because of the short time for the radiation lobe of an individual electron to sweep over the detector and fluctuations in energy and orbit position, the frequency distribution is smeared out into a continuum which extends down to very short wavelengths. A synchrotron radiation source is normally classified by its *characteristic wavelength* λ_c.

$$\lambda_c[\mathrm{\AA}] = 5.6\frac{R[m]}{(E[GeV])^3} \tag{6.11}$$

The maximum of the intensity distribution is close to λ_c. The characteristic wavelength for typical, large machines is around 1 nm. It is possible to express the distribution of any electron synchrotron radiation in normalized intensity units using the characteristic wavelength as the wavelength unit. The universal distribution function is shown in Fig. 6.13.

In order to achieve high radiation intensities, *electron storage rings* are used. The layout of such a ring is shown in Fig. 6.14. In these rings, which are pumped by (filled from) an electron accelerator, circulating currents of the order of 1 A can be

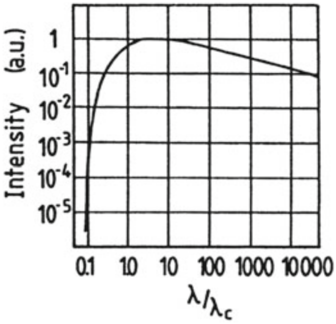

Fig. 6.13 Universal intensity distribution function for synchrotron radiation

obtained. Using radio-frequency fields, sufficient energy is delivered to the electrons to compensate for the radiative losses. (Compare with the Bohr atomic model!) In the ring the electrons are arranged in circulating bunches. Thus, the emission as seen by a user who is placed tangentially to the orbit will be pulsed with a pulse width in the subnanosecond region and a repetition rate of the order of MHz to GHz. Thus, time-resolved experiments can be performed [507–511]. Data for a number of facilities producing synchrotron radiation are given in Table 6.1. With synchrotrons of resonable sizes the intensity per Doppler width that is achievable is comparable to that which is obtained from efficient line light sources. However, the intensity increases towards the extreme UV (XUV) and X-ray regions, where no comparable continuum light sources exist.

The performance of syncrotrons and storage rings can be further enhanced by using *wigglers* or *undulators* [512–514]. A number of local, sharp bends in the electron beam are made in the former type of system, using strong magnets In this way a local emission of still shorter wavelength can be obtained; see (6.11). An undulator is a periodical structure of magnets on a straight part of the electron path between the large bending magnets of the machine, where the electrons are bent back and forth resulting in particularly strong radiation in narrow wavelength bands (fundamental band and high overtone bands) and in a well-defined direction. By introducing suitable mirrors, or achieving sufficient amplification, laser action can be achieved in a so-called *Free-Electron Laser* (FEL) [515–521].

Several FELs are now operating producing tuneable radiation from the IR to the XUV spectral regions (See, e.g.; Table 6.2). Coherent light generation from an undulator is possible without using laser mirrors employing the *optical klystron* process [522, 523]. In very long undulators with exceedingly high electron-beam quality the *SASE* (Self-Amplified Spontaneous Emission)-*FEL* operation is possible [524–526]. Such devices, e.g., the XFEL facilty at DESY (Hamburg), and the LCLS XFEL (Stanford) can produce ultra-intense coherent radiation down to the 10 nm range and possibly lower. The *Inverse Free-Electron Laser* (IFEL) action [527] can be used to accelerate electrons using intense laser beams. A more common method to accelerate electrons by ultra-intense laser light is by the so called wake-field acceleration process (see Sect. 9.6.6).

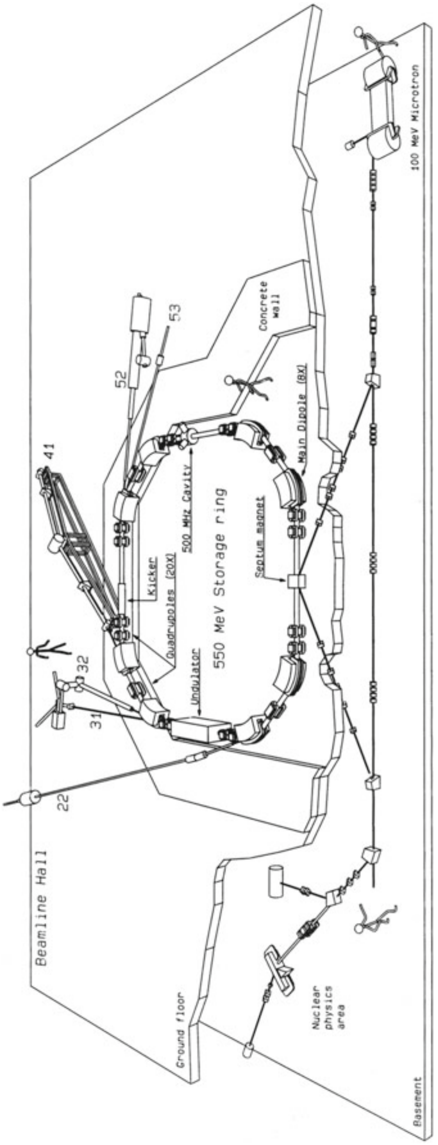
100 MeV Microtron
Concrete wall
Main Dipole (BX)
53
52
41
500 MHz Cavity
550 MeV Storage ring
Septum magnet
Kicker
Quadrupoles (20X)
Undulator
32
31
22
Beamline Hall
Ground floor
Nuclear physics area
Basement

Fig. 6.14 Layout of the now decommissioned MAX storage ring (Lund), shown to illustrate the general lay-out of a system for the generation of synchrotron radiation (Courtesy: P. Röjsel, MAX-Lab.)

Synchrotron radiation has many applications in a large number of scientific and industrial areas: physics, chemistry, biology, medicine, and electronics. With regard to atomic and molecular spectroscopy, synchrotron radiation is particularly applicable for X-ray and photoelectron studies. It is necessary to have monochromatized photons in most experiments. This can be accomplished using specially designed monochromators capable of handling the intense radiation. An arrangement for ESCA studies (Sect. 5.2) using synchrotron radiation is shown in Fig. 6.15. Another

Table 6.1 Data for some synchrotron radiation facilities

Facilities	E [GeV]	Circumference [m]
MAX IV (Lund)	3.0	528
Bessy II (Berlin)	1.7	240
ALS (Berkeley)	1.9	197
Elettra (Trieste)	2.4	259
Photon Factory (Tsukuba)	2.5	189
SPEAR II (Stanford)	3.0	234
ESRF (Grenoble)	6.0	844
APS (Chicago)	7.0	1104
Soleil (Paris)	2.7	354
Spring-8 (Riken)	8.0	1436
SSRF (Shanghai)	3.5	432
Petra III (DESY)	6.0	2304
NSLS II (Brookhaven)	3.0	792

Table 6.2 Free-electron laser facilities (partial list)

Facilities	Wavelength range
FLASH (Hamburg)	Soft X-ray
XFEL (Hamburg)	X-rays
FERMI (Trieste)	100–4 nm
LCLS (Stanford)	6.2–0.13 nm
FHI (Berlin)	3–60 μm
FELIX/FLARE/FELICE (Nijmegen)	3–1500 μm

important area in which synchrotron radiation can be applied is EXAFS (Extended X-ray Absorption Fine Structure spectroscopy, Sect. 5.1.2). A spectrum can be recorded in typically 1/1000 of the time needed when a conventional X-ray source is used. X-ray FELs have become particularly useful for studying diffraction patterns of complex molecules that give their unperturbed imprint before being disintegrated by the high intensity pulse [529]. Synchrotron radiation and its applications have been discussed in [530–536].

6.1.4 *Natural Radiation Sources*

We will also consider some natural radiation sources in connection with continuum light sources. The sun is clearly our most powerful radiation source and, apart from a large number of absorption and emission lines, it essentially radiates like a Planck radiation source at a temperature of 6000 K (Fig. 6.16). Amazingly, the total energy hitting the Earth in one hour corresponds to the total energy consumption of the world

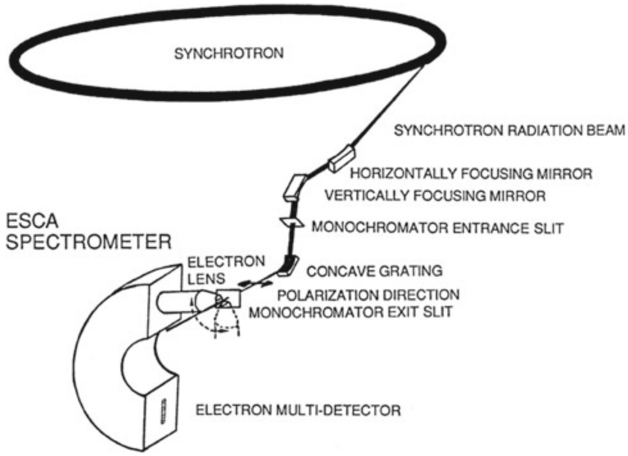
SYNCHROTRON
SYNCHROTRON RADIATION BEAM
HORIZONTALLY FOCUSING MIRROR
VERTICALLY FOCUSING MIRROR
ESCA SPECTROMETER
MONOCHROMATOR ENTRANCE SLIT
ELECTRON LENS
CONCAVE GRATING
POLARIZATION DIRECTION
MONOCHROMATOR EXIT SLIT
ELECTRON MULTI-DETECTOR

Fig. 6.15 XPS (ESCA) arrangement at a synchrotron radiation source [528]

Fig. 6.16 Spectral distribution of sunlight outside the atmosphere [537]

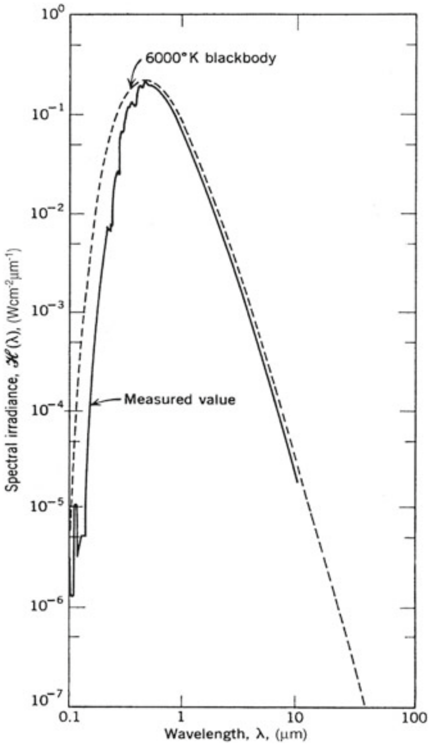

in 1 year! (This is sometimes taken as a strong argument for developing photovoltaic solar energy).

The moon exhibits a similar spectral distribution, although about 10^6 times weaker. (The enormous difference in intensity tells us something about the huge dynamic range of the human eye!). The clear sky also yields a continuum-like distribution (Fig. 6.17). The distribution from the sun is enhanced towards the blue region because of the strong wavelength dependence of Rayleigh scattering. Further, there is a general $\sim$ 300 K radiation in the IR region due to the thermal emission of the atmosphere. The spectral distribution of the night sky is determined by scattered starlight, galactic light and zodiacal light (Fig. 6.18).

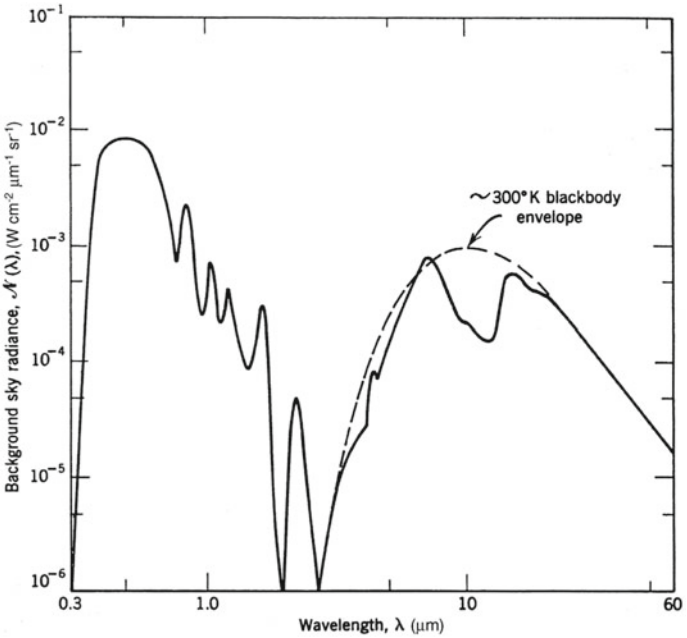

Fig. 6.17 Spectral distribution of the blue sky [538]

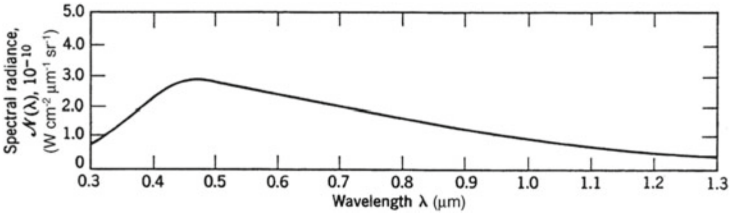

Fig. 6.18 Spectral distribution of the night sky [538]

6.2 Spectral Resolution Instruments

Spectral resolution instruments of different kinds are used for resolving the different wavelength components of light. Important factors of merit for such devices are resolving power and light transmission. The resolving power $\mathcal{R}$ is defined by

$$\mathcal{R} = \frac{\lambda}{\delta\lambda}, \tag{6.12}$$

where $\delta\lambda$ is the resulting linewidth of the spectral apparatus when using monochromatic light of wavelength λ.

We will describe four types of instruments: prism and grating instruments, the Fabry–Pérot interferometer and the Fourier transform spectrometer. A large number of varieties of these different types are used in spectroscopic research and various applications. Spectroscopic instruments have been discussed in [447, 539–541].

6.2.1 *Prism Spectrometers*

Names such as spectrometer, spectroscope, spectrograph, or monochromator are used for basically the same types of instrument, which are, however, applied in different ways. The principle of a prism spectrograph is illustrated in Fig. 6.19. Different wavelengths are refracted in different directions at the entry and exit of the prism material, which has a wavelength-dependent index or refraction n. If α is the angle of incidence and β is the refraction angle (both calculated from the normal to the surface) we have $sin\alpha = n\ sin\beta$ (the *Snell refraction law*). The origin of refraction is that the speed of light is reduced by a factor of n when light propagates in a transparent material. Thus, in order to ascertain constructive interference of different Huygens partial waves originating at each considered surface point, the direction of the outcoming beam must be changed as illustrated in Fig. 6.20a.

The resolving power $\mathcal{R}$ is determined by the dispersion, dn/dλ, and the length of the prism base b

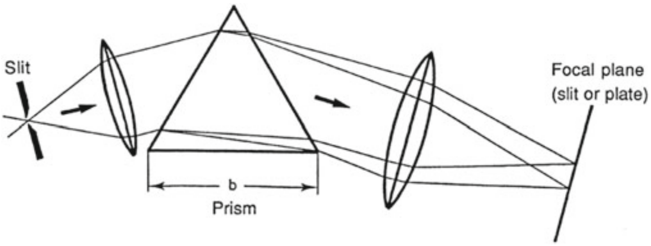

Fig. 6.19 Principle of a prism spectrograph [1]

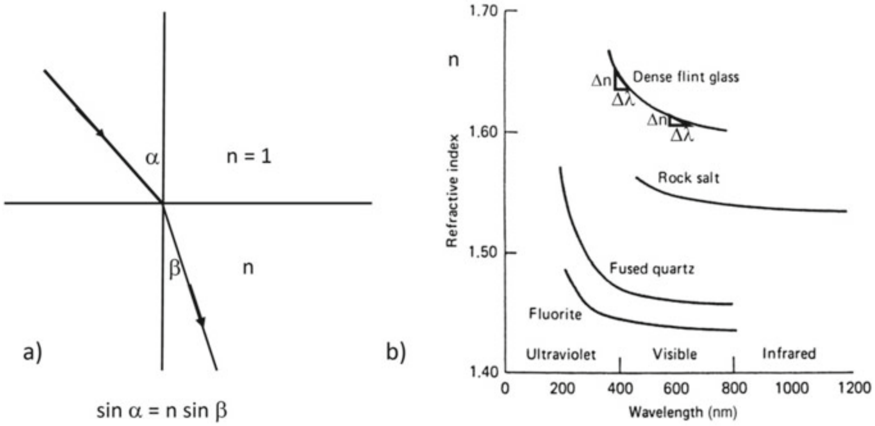

Fig. 6.20 **a** The Snell law of diffraction **b** Dispersion of various prism materials (modified from [542])

$$\mathcal{R} = \frac{\lambda}{\delta\lambda} = b\frac{\mathrm{d}n}{\mathrm{d}\lambda}. \tag{6.13}$$

If the prism is made of flint glass ($\mathrm{d}n/\mathrm{d}\lambda = 1200\ \mathrm{cm}^{-1}$ at $\lambda \sim 500$ nm) and has a base length of 5 cm, then the resolving power $\mathcal{R}$ will be 6000. For practical reasons the size of the prism must be limited and thus this type of spectrograph will necessarily have a relatively low resolution. The finite width of the slits used will clearly reduce the theoretical resolving power given above. Since the dispersion of a prism strongly increases towards shorter wavelengths, the resolution obtainable with a prism instrument will vary with the wavelength. The dispersions of different prism materials are shown in Fig. 6.20b. Figure 6.21 displays the slit width necessary to achieve a 1 nm band pass for a typical prism spectrometer.

Commercial instruments frequently use a so-called *Littrow* mount. Here a Littrow prism with a 30° angle and one surface silvered, as shown in Fig. 6.22, is used for increased dispersion. Arrangements with lenses or mirrors can be used for collimating the incoming light onto the prism and for focusing the refracted beams towards the imaging detector or the exit slit. Actually, a spectrum can be seen as a sequence of sharp images of the entrance slit, one image for each small spectral interval.

Prisms of different kinds can be used to deflect or deviate a beam of light. They can invert or rotate images, and they can be used for separation of different states of polarization. Some prisms that are frequently used in optical and spectroscopic systems will be discussed here. Illustrations are found in Fig. 6.23.

A *right-angle prism* using total internal reflection off the uncoated hypotenuse deviates a beam by 90°, if it impinges perpendicular to one of the entrance surfaces. This type of prism is very useful for deviating high-power laser beams.

In the *Amici (roof) prism*, the hypotenuse in the right-angle prism is replaced by two internal reflector surfaces oriented at 90° to each other (a “roof”). This prism

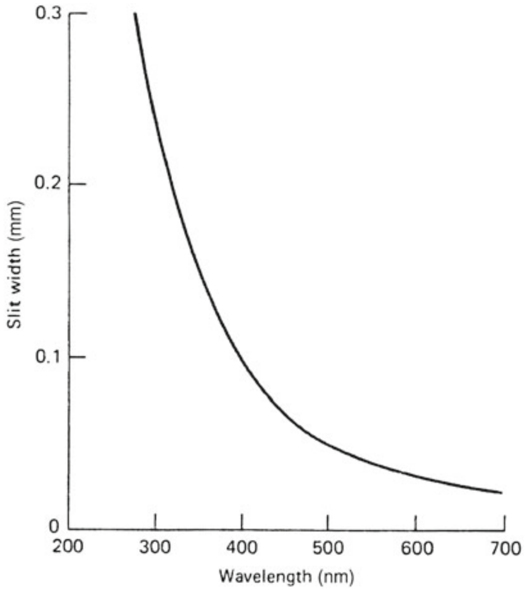

Fig. 6.21 Diagram showing the slit width required to achieve a constant band pass of 1 nm from a prism spectrograph [542]

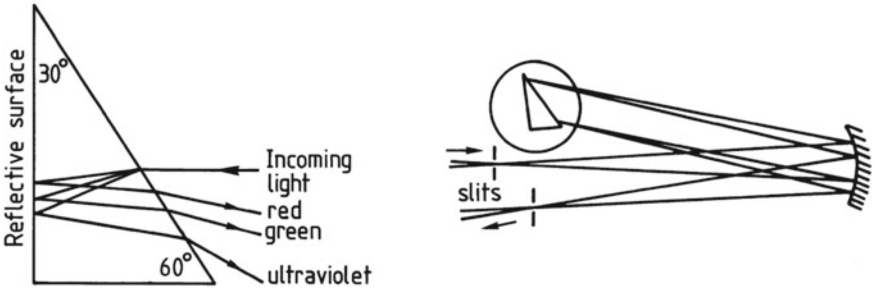

Fig. 6.22 Littrow prism and Littrow prism mount

also deflects a beam by 90° but at the same time rotates the image by 180°. The *penta-prism* deflects the incoming beams by 90° *regardless* of the angle of incidence and does not invert or reverse the image. This prism does not operate on total internal reflection but requires a mirror coating on two faces.

The *Pellin–Broca* prism also deviates beams by roughly 90° but is a dispersive prism, frequently used to separate laser beams of different colours after nonlinear frequency conversion (Sect. 8.6) (see Fig. 10.4 for an application example). By combining four Pellin–Broca prisms, beam separation with maintained direction of propagation for the selected wavelength component can be achieved. In the *straight-view prism* colour dispersion in the forward direction is instead accomplished. The

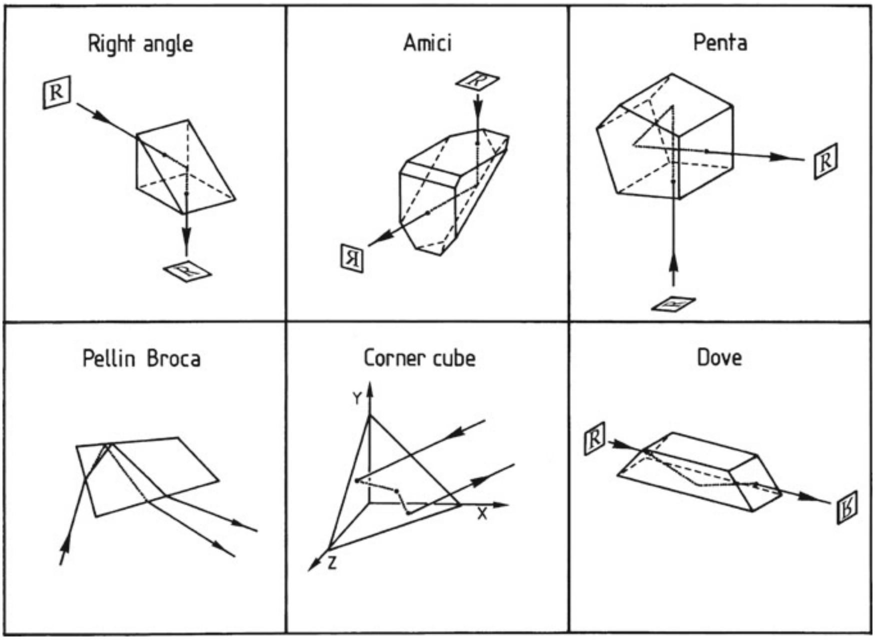

Fig. 6.23 Prisms frequently used in optical and spectroscopic systems (After material from Melles Griot)

Dove prism also transmits light in the forward direction but without dispersion. It has the important property of rotating the image (at twice the angular rate of the prism). An application example is shown in Fig. 10.26b, where a Dove prism ensures that the imaged horizon is always kept horizontal when the folding mirror of a lidar system is rotated. A *corner-cube prism*, with three orthogonal total internal reflection faces, acts as a *retroreflector*. A beam entering the corner cube will, after 3 reflections, be sent in the opposite direction regardless of the angle of incidence. The explanation can, when restricting ourselves to the two-dimensional case (flat geometry), easily be understood. Frequently, corner cube reflectors are made from 3 first-surface mirrors rather than from solid glass or quartz.

6.2.2 Grating Spectrometers

A reflection grating is used for the spectral separation in a grating spectrometer. The basic arrangement is shown in Fig. 6.24a. As is illustrated in Fig. 6.24b, constructive interference is obtained for the Huygens partial waves emerging from the different lines/groves, when the optical path difference is an integer number (m) of wavelengths for diffraction at adjacent lines, as expressed by the grating equation

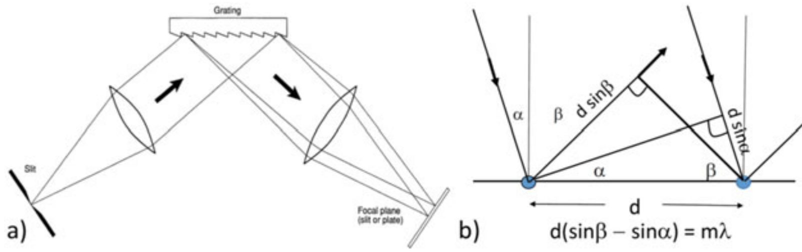

Fig. 6.24 **a** Principle of a grating spectrograph, **b** The grating equation

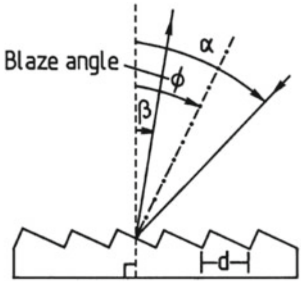

Fig. 6.25 Blaze angle of a grating

$$m\lambda = d(\sin\beta - \sin\alpha). \tag{6.14}$$

Here d is the line separation and α and β the angles of incidence and reflection, respectively. The resolving power $\mathcal{R}$ of the grating is determined by the total number of illuminated lines N and by the diffraction order m, i.e.,

$$\mathcal{R} = \frac{\lambda}{\delta\lambda} = N \cdot m. \tag{6.15}$$

Thus, a 10 cm grating with 3000 lines/cm has a resolving power of 30,000 in the first order.

Gratings were first made by J. Fraunhofer in 1823. Traditionally, a grating was ruled in a surface layer of aluminum on a substrate by means of a diamond tip. The ruling is performed with high-precision ruling machines, which are interferometrically controlled. *Replica gratings* which are the ones that are marketed, are manufactured by a casting procedure. Nowadays, *holographic gratings* are much being used. These gratings are produced by recording interference fringes from two crossed laser beams. An Ar^+ laser acting on photoresist can be used. A density of up to 6000 lines/mm can be attained.

The intensity that is diffracted at a certain wavelength depends on the shape of the lines. Ruled gratings are made with a certain *"blaze" angle*, chosen according to which wavelength region is to be enhanced through reflective action (Fig. 6.25). The efficiency of a grating can be up to 70% at the blaze angle for a certain order.

It is also possible to produce gratings with a blaze by the holographic process. So-called ghost lines can appear in mechanically ruled gratings due to periodical errors in the mechanical feeding of the machine. Such lines do not result from holographic gratings, which also have a lower level of diffusely scattered light (stray light). While the first diffraction order is normally used in small spectrometers, higher diffraction orders are frequently used in large research instruments.

One drawback of grating spectrometers is that for a certain grating setting a series of wavelengths (λ_0, $\lambda_0/2$, $\lambda_0/3$, …) is diffracted in the same direction (overlapping orders). The problem can be eliminated using filters or a pre-monochromator. An especially high resolution, but also many overlapping orders, is obtained with an *Echelle* grating (Fig. 6.26). Such gratings operate at such a high angle that the steep side of the line is utilized. Echelle gratings have comparatively few lines/mm but operate at a very high diffraction order. A resolving power approaching 10^6 can be achieved with grating instruments. Grating characteristics are discussed in [543, 544].

Grating spectrometers are, in general, equipped with mirrors instead of lenses. Some common arrangements are shown in Fig. 6.27. Instruments for the visible region frequently make use of the *Ebert* or the *Czerny–Turner* arrangement. A grating in a Littrow mount is frequently used for tuning pulsed dye lasers (Sect. 8.5.1). By using concave gratings, fabricated by holographic techniques, the need for collimating and focusing mirrors is eliminated. Modern compact optical spectrometers are frequently of this kind, also featuring fibre-optical input coupling and direct computer read out from a CCD or CMOS detector, which can have read out rates in the kHz range. A photograph of a compact, fiber-coupled grating spectrometer is shown in Fig. 6.28a. The spectra shown in Fig. 1.5 were recorded with such a device. An even smaller spectrometer is shown in Fig. 6.28b.

Sometimes an arrangement utilizing the *Rowland circle* are used. The entrance slit, the grating, and the spectral image are all on a circle which has a diameter equal to the radius of curvature of the concave grating. For the very short wavelengths that are obtained in spectra from highly ionized atoms or in X-ray spectra, a *grazing angle of incidence* is used to minimize the absorption losses in the grating.

The beam leaving a monochromator always contains small amounts of radiation at wavelengths other than the selected one. This *stray light* is due to reflections and scattering from different parts of the monochromator. The amount of stray light can be much reduced by using a *double monochromator* which consists of two

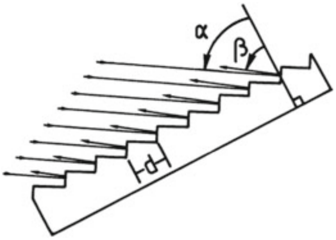

Fig. 6.26 Echelle grating

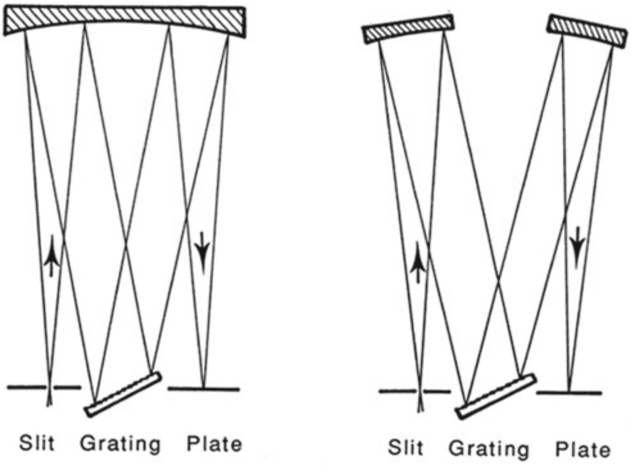
Slit
Grating
Plate
Slit
Grating
Plate

Ebert – Fastie *Czerny–Turner*

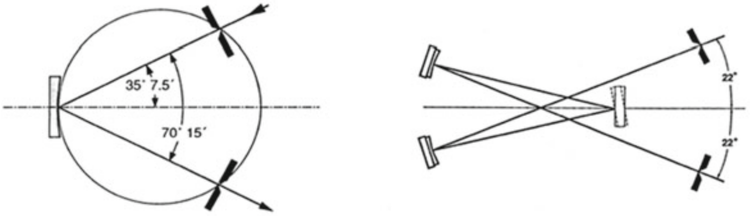
35° 7.5′
70° 15′
22°
22°

Seya–Namioka *Criss–crossed Czerny–Turner*

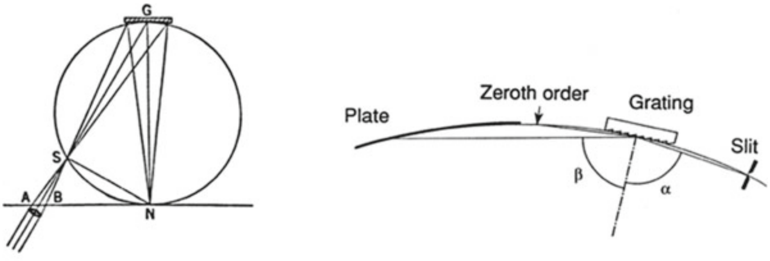
G
S
A
B
N
Plate
Zeroth order
Grating
Slit
β
α

Rowland arrangement *Grazing incidence*

Fig. 6.27 Some common arrangements for grating spectrometers

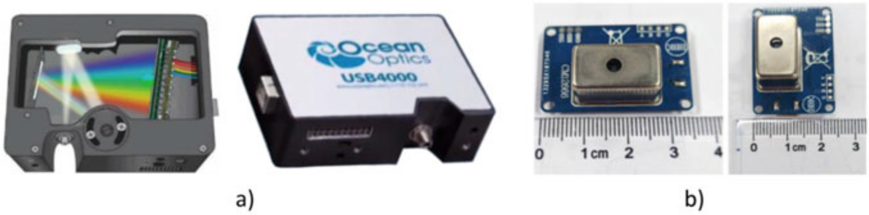

Fig. 6.28 **a** Compact USB spectrometer with fiber coupling. The largest measure is 90 mm. The spectral coverage is 360 nm–1000 nm and the spectral resolution is typically 10 nm (Courtesy: Ocean Optics, DBA Ocean Insight), **b** Mini-spectrometer from Hamamatsu, mounted on an external circuit board. The spectral resolution is about 10 nm (Courtesy: Hamamatsu)

adjacent single monochromators connected only through a common intermediate (exit/entrance) slit. Stray light can also be largely eliminated by spatially tagging the intensity over the entrance slit [545]. As already noted, a spectrum is a sharp image in the focal plane of the entrance slit, recorded for each spectral line. Thus, at the detector, only light, which exhibits the corresponding spatial modulation as at the slit should be recorded. Straylight moves around in the spectrometer and has lost the specific spatial imprint. This can be seen as an example of spatial lock-in detection (normally, lock-in techniques are used in spectroscopic work in the temporal or frequency domains, as will be further explained below in connection with Fig. 6.68). Examples of spatial lock-in approaches can be found in connection with combustion spectroscopy [546, 547], where also the SLIPI (Structured Light Illumination Planar Imaging) approach has been introduced [548]. A further technique, denoted FRAME (Frequency Recognition Algoritm for Multiple Exposures) [549] also uses structured illumination for tagging different wavelength components in an image. Chosing different directions of the stripes in the illumination, different colours can be tagged to be isolated in the Fourier plane of the image, although they are all mixed in the simultaneous recording of all colours in a single original frame. A further example, now in the context of close-range scattering elimination, was recently demonstrated [550]. Here, the useful information in an image, which in the relevant application cases cannot be tagged or modulated, is instead isolated by tagging the disturbing background, which is accessible.

6.2.3 The Fabry–Pérot Interferometer

The Fabry–Pérot interferometer was introduced by C. Fabry and A. Pérot in 1896. The interferometer consists of two flat, parallel mirrors with high reflectivity and low absorption. Light impinging on the interferometer will undergo multiple reflections between the mirrors whereby part of the light is transmitted (Fig. 6.29). The different components of the transmitted light will interfere at infinity, but the interference pattern can be imaged on a screen or a detector using a lens. According to the Fermat

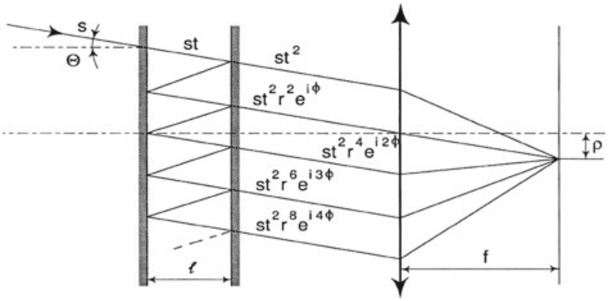

Fig. 6.29 Ray tracing in a Fabry–Pérot interferometer [1]

principle the relative phases of the different rays will not be changed by their passage through the lens. For the analysis we introduce the following symbols pertaining to light *intensity*:

R: reflectivity of a mirror layer,
T: transmission of a mirror layer,
A: absorption of a mirror layer, with the relationship

$$R + T + A = 1. \tag{6.16}$$

For the *amplitudes*, the corresponding quantities are r, t, and a, i.e.,

$$r^2 = R, \quad t^2 = T, \quad a^2 = A. \tag{6.17}$$

Further, we introduce

ℓ: distance between the layers, n: index of refraction between the layers,
θ: angle of incidence of the light,
f: focal length of the lens,
λ: wavelength of the incoming monochromatic light,
ϕ: phase shift between two successively emerging rays, and
s, S: amplitudes.

We will first calculate the optical path difference $\varDelta$ (the *retardation*) between two successive rays making use of Fig. 6.30, namely

$$\varDelta = 2n\ell\cos\theta. \tag{6.18}$$

Constructive interference requires

$$\varDelta = m\lambda, \tag{6.19}$$

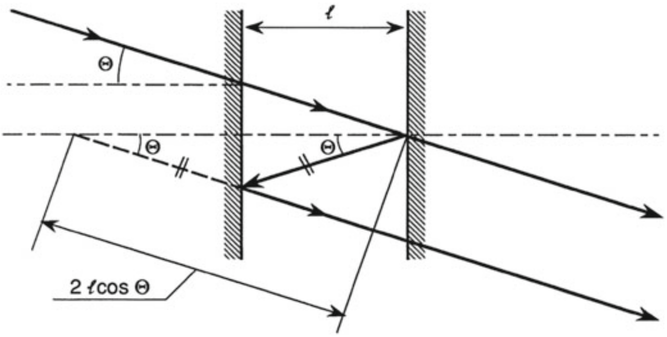

Fig. 6.30 Evaluation of the retardation [1]

where m is normally a large integer ($m \sim 10^4$). All rays that are incident on a conical surface are equivalent. Thus we will obtain a system of rings on the screen. The radius of a ring is denoted by ρ. For small angles we have $\cos\theta = 1 - \theta^2/2$ and $\theta = \rho/f$, which together with (6.18) and (6.19) yields

$$2n\ell\left(1 - \rho^2/2f^2\right) = m\lambda, \quad \text{and}$$

$$\rho = f\sqrt{(2n\ell - m\lambda)/n\ell}. \tag{6.20}$$

Thus, for the case when constructive interference occurs on the symmetry axis (the square root is zero for $m = m_0$), rings with $m = m_0 - 1, m_0 - 2, \ldots$ will have radii proportional to $\sqrt{1}, \sqrt{2}, \sqrt{3}$, etc.

We shall now study the intensity distribution in more detail. Using Fig. 6.29 we find that the total transmitted amplitude S for the case of $a = 0$, i.e., $t^2 = 1 - r^2$, is given by the geometrical series

$$S = st^2\left(1 + r^2 e^{i\phi} + r^4 e^{i2\phi} + r^6 e^{i3\phi} + \ldots.\right) = \frac{s\left(1 - r^2\right)}{1 - r^2 e^{i\phi}}, \tag{6.21}$$

where the phase shift ϕ is given by

$$\phi = \frac{\Delta}{\lambda} 2\pi = \frac{\Delta}{c} 2\pi\nu. \tag{6.22}$$

From the amplitude S we obtain the corresponding intensity I

$$I = |S|^2 = \frac{s^2\left(1 - r^2\right)^2}{1 - r^2\left(e^{i\phi} + e^{-i\phi}\right) + r^4}.$$

But $(e^{i\phi} + e^{i\phi})/2 = \cos\phi = 1 - 2\sin^2(\phi/2)$. With $s^2 = I_0$ we then have

$$I = I_0\left(1 + \frac{4r^2}{\left(1 - r^2\right)^2}\sin^2\phi/2\right)^{-1}.$$

Finally, if the absorption in the layers is considered we obtain

$$I = \left(\frac{T}{1 - R}\right)^2 I_0\left(1 + \frac{4R}{(1 - R)^2}\sin^2\phi/2\right)^{-1}. \tag{6.23}$$

This is called the *Airy distribution* and is illustrated in Fig. 6.31. The maximum intensity

$$I_{\max} = I_0\left(\frac{T}{1 - R}\right)^2 \tag{6.24}$$

is obtained for $\phi = 0, 2\pi, \ldots$, while the minimum intensity

$$I_{\min} = I_0\left(\frac{T}{1 + R}\right)^2 \tag{6.25}$$

is obtained for $\phi = \pi, 3\pi, \ldots$ etc.

The separation between maxima is called the *free spectral range*. In frequency units it is given by

$$\Delta\nu_{\mathrm{fsr}} = \frac{c}{\Delta} = \frac{c}{2n\ell\cos\theta} = \frac{c}{2n\ell}. \tag{6.26}$$

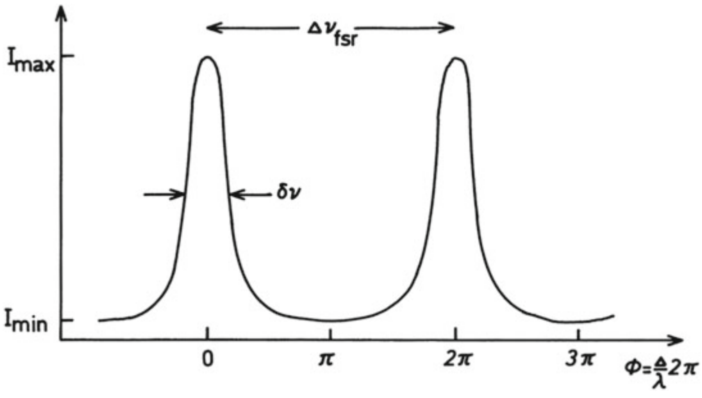

Fig. 6.31 Airy distribution from a Fabry–Pérot interferometer [1]

The half-width of a transmission peak is

$$\delta\nu = \frac{c}{\pi}\frac{1-R}{\Delta\sqrt{R}} \quad \text{(for large values of } R\text{)}. \tag{6.27}$$

The ratio between these two quantities is called the *finesse* N and is determined only by the reflectivity R of the layers

$$N = \frac{\Delta\nu_{\mathrm{fsr}}}{\delta\nu} = \frac{\pi\sqrt{R}}{1-R}. \tag{6.28}$$

The resolution of the Fabry–Pérot interferometer is

$$\mathcal{R} = \frac{\lambda}{\delta\lambda} = \frac{\nu}{\delta\nu} = \frac{\nu}{\Delta\nu_{\mathrm{fsr}}}\frac{\Delta\nu_{\mathrm{fsr}}}{\delta\nu} = \nu\frac{2n\ell}{c}N. \tag{6.29}$$

The variable ϕ in the Airy function is

$$\phi = \frac{2n\ell\cos\theta}{\lambda}\cdot 2\pi. \tag{6.30}$$

Thus, for a given wavelength λ we can run through the transmission curve in Fig. 6.31 by varying θ, n, or ℓ.

In a photographic or CCD recording, the ring system is recorded as a function of θ. For a photoelectric recording $\theta = 0°$ is chosen by placing a small hole on the symmetry axis, and the intensity of the central spot is recorded with a photomultiplier tube. Now either ℓ or n is changed. The Fabry–Pérot interferometer normally consists of two flat quartz substrates with reflective coatings and the substrates are precisely separated by Invar spacers. n can then be varied by changing the gas pressure in the Fabry–Pérot housing (pressure scanning). Alternatively, the spacing can be varied by using piezoelectric crystals in the mounts of one of the plates.

As an example, we will consider a Fabry–Pérot interferometer which has a mirror separation of 1 cm (air). The coatings have a reflectivity of 98%. We then have $\Delta\nu_{\mathrm{fsr}} = c/2\,l = 15$ GHz, $N \cong 150$, and $\delta\nu = 100$ MHz. If the interferometer is used at 500 nm $\leftrightarrow 6 \times 10^{14}$ Hz, then $\mathcal{R} = 6 \times 10^{6}$. Clearly, for such an interferometer, the width of the spectral line from the light source is a limiting factor.

Because of small imperfections and the finite size of the circular aperture the practically achievable resolution is frequently reduced. Because of its high resolution, the Fabry–Pérot interferometer has been much used for measuring hyperfine structure and isotope shifts. The spectral line of interest is then first selected by a monochromator or an interference filter. First, a free spectral range of sufficient width to accomodate all the spectral components of the line is chosen to allow the correct order of components to be determined. Then the plates are moved further apart, resulting in an increased resolution but also the inclusion of overlapping orders.

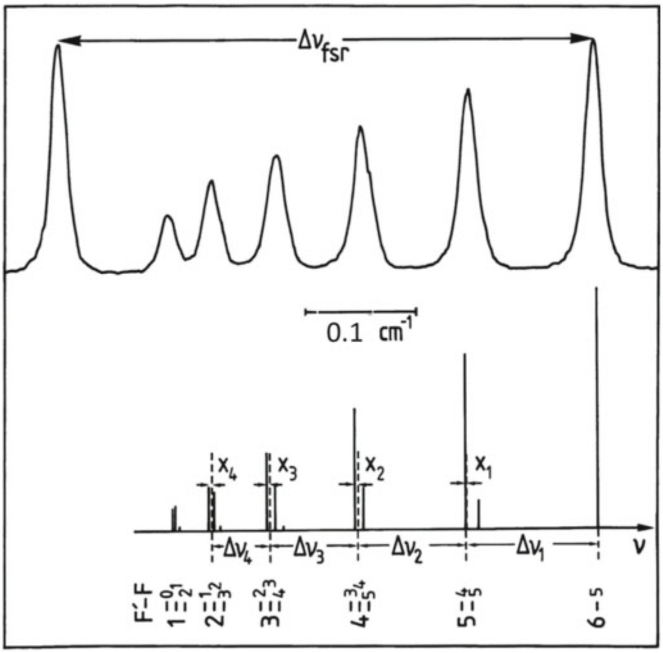

Fig. 6.32 Examples of a Fabry–Pérot recording obtained by pressure scanning. The hyperfine structure of ^{55}Mn ($I = 5/2$) in a $J = 7/2 \leftrightarrow 5/2$ transition at 539.5 nm has been recorded with an instrumental free spectral range of 15 GHz [551]

All hyperfine components have their own Airy functions, which are shifted with respect to each other. The Fabry–Pérot pattern repeats itself with a period of the free spectral range, which is used for the frequency calibration. An example of a Fabry–Pérot recording is given in Fig. 6.32. The Fabry–Pérot interferometer was discussed in [552, 553].

Interferometers with spherical mirrors can also be used. A frequently used arrangement is employed in the *confocal* interferometer, where the mirror separation ℓ equals the radius r of the mirrors (Fig. 6.33). The name of this interferometer reflects the fact that the focal length f of a mirror of radius r is $f = r/2$. In a confocal interferometer a light ray makes two double passes between the mirrors before the primary and the reflected beams again coalesce at the second mirror and can interfere.

Since this corresponds to a planar interferometer with double the mirror separation the free spectral range for a confocal interferometer is given by

$$\Delta\nu_{\mathrm{fsr}} = \frac{c}{4n\ell}. \tag{6.31}$$

This interferometer is a special case of the *multi-pass interferometer*, where N double passes between the mirrors occur before interference. For such an interferometer we have

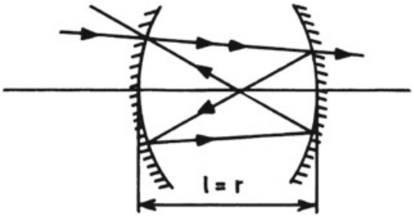

Fig. 6.33 Confocal interferometer [554]

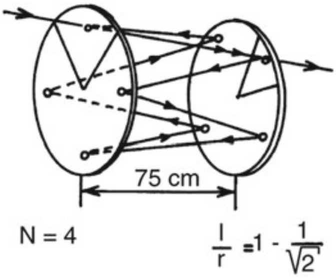

Fig. 6.34 Multi-pass interferometer for $N = 4$ [554]

$$\Delta\nu_{\mathrm{fsr}} = \frac{c}{N \cdot 2n\ell}. \tag{6.32}$$

It can be shown that the mirror radius and the mirror separation must fulfil the relation

$$r = \ell[1 - \cos(\pi/N)]^{-1}. \tag{6.33}$$

For $N = 2$ we have the special case of the confocal interferometer. As an example, we can choose a multi-pass interferometer with a mirror separation of 0.75 m operating with $N = 4$ (Fig. 6.34). We find $r = 0.75/(1 - 1/\sqrt{2}) = 2.56$ m. The free spectral range for this device is $\Delta\nu_{\mathrm{fsr}} = c/4 \cdot 2 \cdot 0.75\ \mathrm{m} = 50$ MHz.

Multi-pass interferometers are frequently used for monitoring laser beams of a very sharp frequency. A small free spectral range can be obtained without using a very long interferometer. Using special multilayer techniques it has become possible to produce coatings with a reflectivity of 99.97 percent, resulting in a finesse of the order of 10^4 ("supercavity"). Clearly, such instruments have important applications for ultra-stable lasers and precision metrology. Recently, a new way to achieve even sharper Fabry-Pérot resonances has emerged using so called "slow-light effects"; see Sect. 9.5.3.

6.2.4 The Fourier Transform Spectrometer

The Fourier transform spectrometer (FTS) is a dual-beam interferometer, which is most frequently of the Michelson type (Nobel Prize in Physics to *A.A. Michelson* in 1907, and related to the non-observation of differences in measurements separated by half a year, leading to the falsification of the Ether theory—describing electromagnetic wave propagation through a fictive medium, the Ether) as shown in Fig. 6.35. If the arms of the interferometer have equal lengths, the path difference between the two interfering beams would be 0. Then all wavelengths passing the interferometer show constructive interference, a fact, which is utilized in optical coherence tomography (OCT); see Sect. 10.5.4.3). If the mirror is moved $\Delta/2$, an optical path difference of Δ is introduced. For the case of monochromatic radiation and equally intense beams the intensity at the detector will be

$$I(\Delta) = I_0 \cos^2(\phi/2) \tag{6.34}$$

with

$$\phi = \frac{\Delta}{\lambda} 2\pi = \frac{\Delta}{c} 2\pi \nu. \tag{6.35}$$

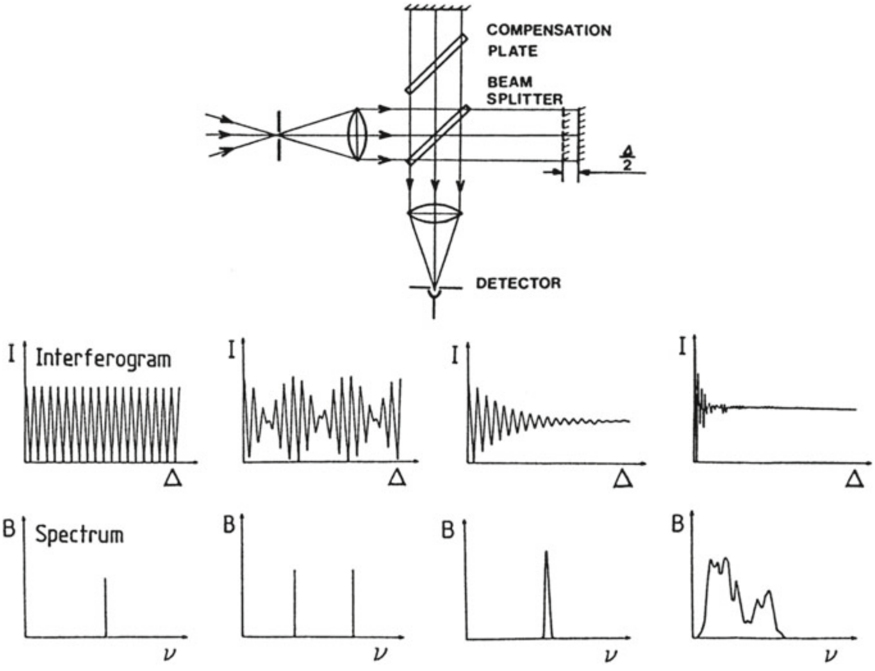

Fig. 6.35 Fourier transform spectrometer and basic signals (Courtesy: Ulf Litzén)

If the light source emits a spectrum $B(\nu)$ we then obtain

$$\begin{aligned} I(\Delta) &= \int_0^\infty B(\nu)\cos^2\left(\frac{\Delta}{c}\pi\nu\right)\mathrm{d}\nu \\ &= \frac{1}{2}\int_0^\infty B(\nu)\left[1+\cos\left(\frac{\Delta}{c}2\pi\nu\right)\right]\mathrm{d}\nu. \end{aligned} \tag{6.36}$$

The part of the above expression that depends on Δ is called the *interferogram*

$$J(\Delta) = \frac{1}{2}\int_0^\infty B(\nu)\cos\left(\frac{\Delta}{c}2\pi\nu\right)\mathrm{d}\nu. \tag{6.37}$$

The spectrum $B(\nu)$ can be calculated from the interferogram $J(\Delta)$ as its Fourier cosine transform.

$$B(\nu) \propto \int_0^\infty J(\Delta)\cos\left(\frac{\Delta}{c}2\pi\nu\right)\mathrm{d}\Delta. \tag{6.38}$$

The corresponding calculation (fast Fourier transformation; FFT) is conveniently performed on a computer [555–557] and special, very fast processors have been constructed. In practice, the movable mirror can only be moved a limited distance (<1 m) and therefore the integration must be performed over a finite interval. Such a limited integration gives rise to side maxima on the spectral lines. By using a mathematical trick, which involves the multiplication of the integrand in (6.37) by a particular function, the unwanted maxima can be suppressed. However, this procedure, which is called *apodization*, gives rise to broader spectral lines. The interferogram has many similarities to a *hologram*. Every part of it contains information on the whole structure, but a high resolution is obtained only when a large part of it is utilized. One of the great advantages of Fourier transform spectroscopy is that all spectral lines are recorded at the same time (the *multiplex* or *Felgett advantage*). Unless photographic or array detector recording is used, the earlier mentioned types of spectral apparatus only collect information at a particular wavelength at any time. In the IR region, where cheap imaging detectors are not available, Fourier instruments are particularly valuable. Further, a Fourier transform spectrometer has a comparatively high light collecting efficiency, since it does not require narrow slits for the above-mentioned reasons (the *Jaquinot advantage*). Instruments of this kind have a very good signal-to-noise ratio and instruments with a resolution of $\mathcal{R} = 10^7$ can be constructed. The movement of the mirror is normally controlled by fringes from a

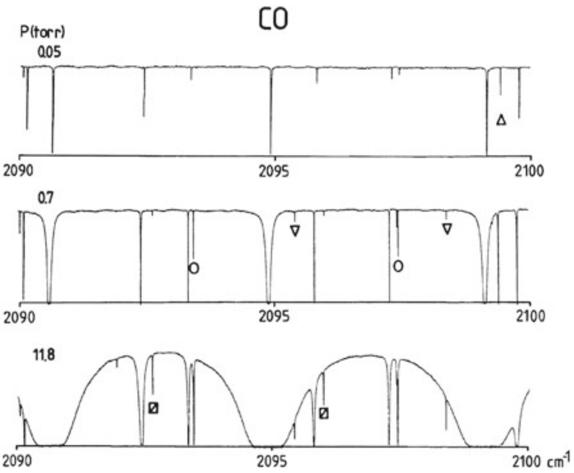

Fig. 6.36 Fourier-transform spectrometer recording for a gas containing different isotopic species of CO at increasing pressures [558]

HeNe laser. Examples of FTS spectra are shown in Fig. 6.36. Interferometers and interferometry have been discussed in [559–563].

Extremely large interferometers (arm lengths above 4 km) are used in the gravitational wave laboratories LIGO and VIRGO, where such signals were first detected from colliding binary black holes [564]. The deformation of space due to the passage of the gravitational wave, which is believed to have been generated 1.3 billion years earlier, is causing a tiny change in arm length. This achievement was awarded with the 2017 Nobel Prize in Physics to *B.C. Barish, K.S. Thorne, and R. Weiss* [565–567]. The forth-coming LISA interferometer, using three satellites in a triangular configuration with the sides 2.5 * 10^6 km long, will clearly have an extreme sensitivity [568, 569] (See also Sect. 4.9).

We will finish this section on spectral resolution instruments by some general remarks on the nature of optical resolution. It can all be seen as different aspects of the basic fact that the resolution is limited by how detailed the partial wave interfererence is, with the general feature, that sharp structures can only be built up by using a large number of partial waves, with sufficient phase difference, emerging from the optical component (Huygen´s principle). A well-known reflection of this is that for a lens, the smallest angular resolution $\delta\phi$, is given by 1.22 λ/d, where λ is the wavelength and d is the diameter of the primary imaging component. Also the prism spectrometer resolution (Eq. 6.13) depends on the prism size, b, and that of the grating spectrometer on the number of illuminated grating lines (Eq. 6.15). We observe that these observations are reflections of the same principle, which also pertains to the resolution of the Fabry-Pérot (Eq. 6.29) and the Fourier transform spectrometer. The same principles govern the sharpness of pulses in laser mode-locking (equidistant modes, which cover a large spectral region; Sect. 8.7.1) and the sharpness of a hologram (the larger the area, the sharper virtual image due to the detailed spatial interference of partial waves will be).

6.3 Detectors

Historically, the photographic plate has been an important detector of light that has been spectrally decomposed by a spectral apparatus. Photographic emulsions can still be important, e.g., for recording the emission lines from ionized atoms. As we have already mentioned, the *photographic material* has the unique property of being an integrator over the intensity fluctuations of a light source. There are many types of films for spectroscopic use. In Fig. 6.37 regions of sensitivity for some emulsions are shown. The information stored on a plate can be sensed by a *microdensitometer* and transferred to a recorder. For the evaluation of emission spectra, reference lines from a different light source are frequently exposed on the same plate. A *comparator* is used to determine the relative positions of the lines on the plate.

Clearly, photographic films are since long obsolete, also for their use in medical X-ray imaging, where they are largely replaced by image plates, as discussed in Sect. 5.1.3.

Optical radiation is frequently detected by semiconductor photodiodes. A semiconductor material with a p–n junction is used. Incoming photons cause electron–hole pairs, which are separated and a current is detected. Common materials used in semiconductor photodiodes are silicon, germanium, and InGaAs, and the corresponding spectral response curves are shown in Fig. 6.38. The detectors can be operated in two modes, the *photovoltaic* mode, when no voltage is applied over the p–n junction, and the *photoconductive* mode, when a reverse bias voltage is applied. The former mode is also the common one used in large-area applications for solar energy harvesting, where silicon panels have long been applied [571, 572], but are now being challenged by cheaper materials, based on, e.g., perovskites ($CaTiO_3$) [573, 574]. The

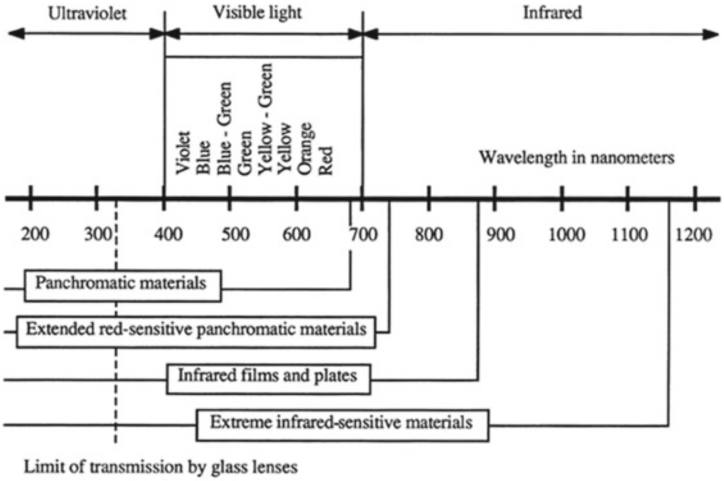
Ultraviolet
Visible light
Infrared
Violet
Blue
Blue - Green
Green
Yellow - Green
Yellow
Orange
Red
Wavelength in nanometers
200
300
400
500
600
700
800
900
1000
1100
1200
Panchromatic materials
Extended red-sensitive panchromatic materials
Infrared films and plates
Extreme infrared-sensitive materials
Limit of transmission by glass lenses

Fig. 6.37 Sensitivity regions for photographic emulsions [570]

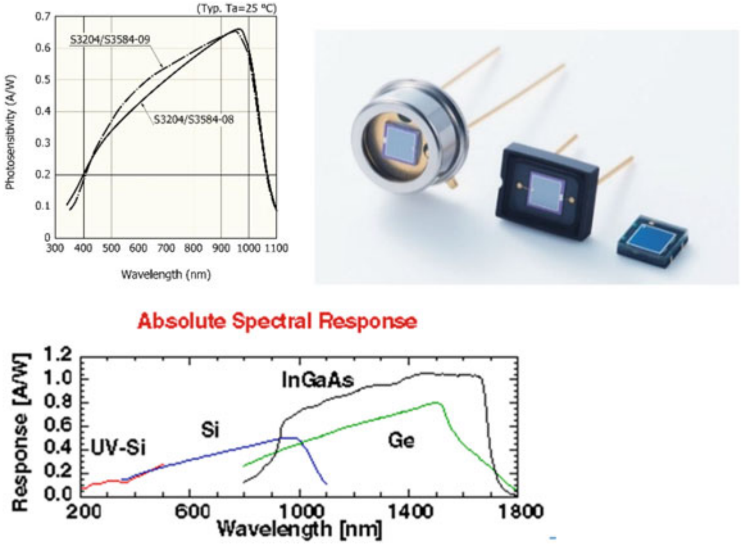

Fig. 6.38 **a** Typical silicon photodiode spectral response (Courtesy: Hamamatsu), **b** Photos of typical silicon photodetectors (Courtesy: Hamamatsu), **c** Comparison between Si, Ge and InGaAs spectral responses (Courtesy: NIST)

photoconductive operation mode allows a faster temporal response, at the expense of a higher noise level.

In the visible or the UV region a *Photomultiplier Tube* (PMT) is normally used. A PMT is an amplifying photocell. The light falls on a photocathode from which electrons are released due to the photoelectric effect. The electrons are accelerated through a chain of secondary electrodes, dynodes, that are held at increasingly higher potential. The dynodes, which are normally covered with CsSb, release secondary electrons and an avalanche amplification is obtained. A current that can be more than 10^6 times stronger than the primary photocurrent is obtained from the collecting anode. A PMT and its electrical supply are shown in Fig. 6.39. A number of cathode materials with different spectral sensitivities can be chosen. The sensitivity is frequently expressed as the *quantum efficiency*, which is the number of photoelectrons (< 1) that on the average can be obtained per incoming absorbed photon. Two common materials are Na_2KSbCs ("trialkali") and AgOCs. The so called ERMA cathode materials provide an approximatively flat spectral response out to 0.9 μm. Recently, PMT operation has been extended out to 1.6 μm using InP/InGaAs, although with very low quantum efficiency. Curves for a number of materials are shown in Fig. 6.40.

In many cases it is important to minimize the *dark current* of the PMT. The number of thermally released electrons can be reduced by cooling. No further improvement is obtained below −30 °C for most materials, except for red-sensitive materials, for

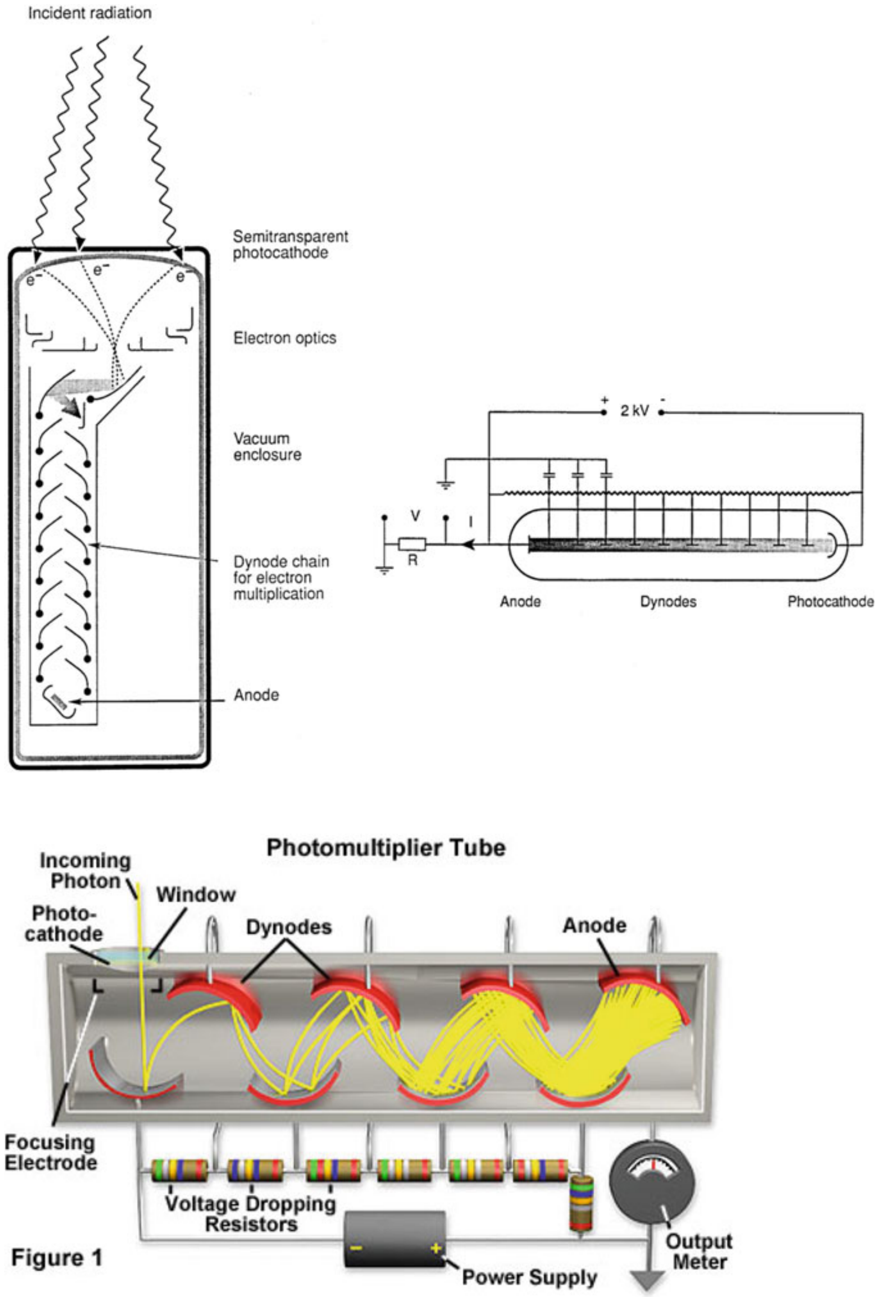
Incident radiation
e⁻
e⁻
e⁻
Semitransparent photocathode
Electron optics
Vacuum enclosure
Dynode chain for electron multiplication
Anode
+ 2 kV -
V
I
R
Anode
Dynodes
Photocathode
Photomultiplier Tube
Incoming Photon
Window
Photo-cathode
Dynodes
Anode
Focusing Electrode
Voltage Dropping Resistors
-
+
Power Supply
Output Meter
Figure 1

Fig. 6.39 Construction of a photomultiplier tube and its high-voltage supply (Lower part: Courtesy: Olympus)

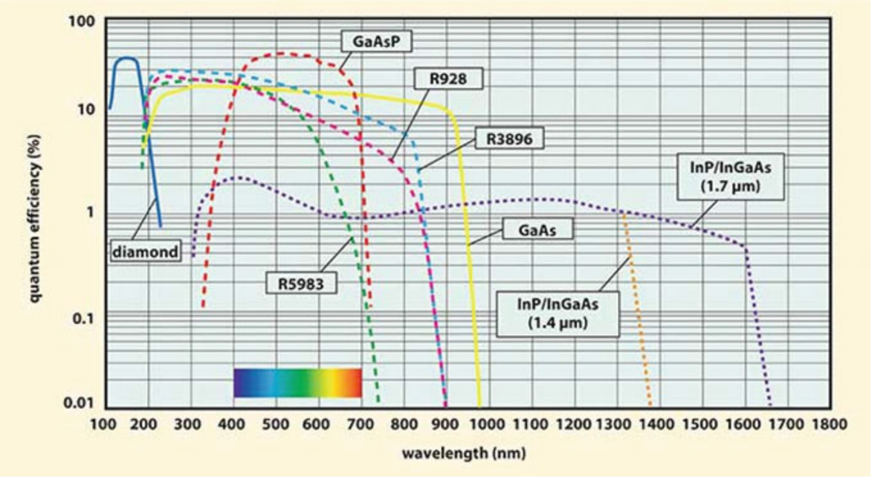

Fig. 6.40 Quantum efficiency curves for various photocathode materials (Courtesy: Laurin Publishing Co; https://www.photonics.com/Articles/Photomultipliers_Low-Light_High-Speed/a25145)

which dry ice (222 K) or liquid nitrogen (77 K) cooling is advisable. The dark current in PMTs can be reduced by a factor of 10 or more by cooling.

Semiconductor detectors based on silicon, germanium, or GaSbAs can be operated in the *avalanche photodiode* (APD) mode. Then a high voltage is applied over the p–n junction, and primary absorbed photons can give rise to an avalanche of electron resulting in strong charge amplification. This type of operation can be particularly valuable for single-photon counting. The detectors are then called *SPAD* (single-photon avalanche diode) units [576, 577].

No detectors of the PMT type exist for the IR region. Other types of detectors are instead used. A *thermocouple* can be a useful detector at long wavelengths. It measures heat, and the junction between two different metallic materials generates a week (Seebeck) voltage. A *bolometer* is a resistance thermometer with a platinum wire or a thermistor as a sensor. Certain crystals are *pyroelectric*, i.e., they give rise to an electrical potential between opposite surfaces when heated. Lithium niobate is used for such purposes. *Photoconducting detectors* are particularly useful in the IR region. Especially common is the *lead sulphide (PbS) cell*, which operates at room temperature, but with a very slow ($\sim$ ms) response time. Detectors made of *indium arsenide* (InAs) or *indium antimonide* (InSb) are considerably faster and are frequently cooled to liquid nitrogen temperatures (77 K). Further down in the IR region, e.g., around 10 μm, cooled *mercury cadmium telluride* (HgCdTe) detectors are used. Sensitivity curves for different detector materials are shown in Fig. 6.41.

Since the internal low-noise amplification of PMTs has no counterpart in the IR region (except possibly for the case of *avalanche diodes*) one has to rely on low-noise electronic amplification. Noise is normally a greater problem in the IR region than

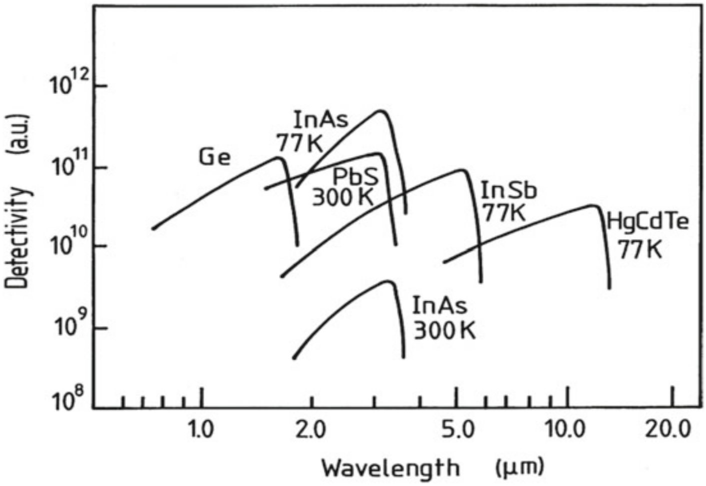

Fig. 6.41 Sensitivity curves for infrared detector materials

in the visible region. One remedy in the IR region is to use *heterodyne detection*, as described in Sect. 10.2.1. Optical detectors have been discussed in [577–582].

We shall conclude this section on detectors by briefly describing *array detectors,* which combine the advantages of the integration and multiplexing characteristics of the photographic plate, as well as the electronic read-out of the PMT. A large number of light-sensitive elements (256, 512, or 1024) are closely arranged in a row in these solid-state devices. Each one corresponds to one channel of a multichannel analyser, in which a certain number of counts is stored, proportional to the intensity of the impinging light. If the array of detectors is arranged in the focal plane of a spectrograph, the spectrum is immediately obtained in the multichannel analyser (Optical Multichannel Analyser, OMA). A linear diode array can consist of, for example, 512 optical diodes, each 50 μm wide and 2.5 mm high. The elements then form an "electronic photographic plate" of size 25 × 2.5 mm^2. In order to attain a higher light sensitivity the array can be placed behind an *image intensifier tube*, which is based on a microchannel plate [583]. The arrangement is shown in Fig. 6.42. The spectrum illuminates a photocathode in which electrons are released. The electrons are sucked into the narrow channels of the microchannel plate. The channels are covered with a material emitting secondary electrons and multiplication occurs as the electrons pass along the channel, propelled by an applied electric field. The showers of electrons, that are spatially arranged corresponding to the primary spectrum, impinge on a phosphor screen that produces an amplified image of the original spectrum. The light is then transferred to the diode array with retained spatial information, sometimes employing bunches of optical fibres. An amplification of more than 10^4 can be obtained. The high voltage for the channel-plate operation can be pulsed rapidly, and thus the whole detector assembly can be gated to be sensitive

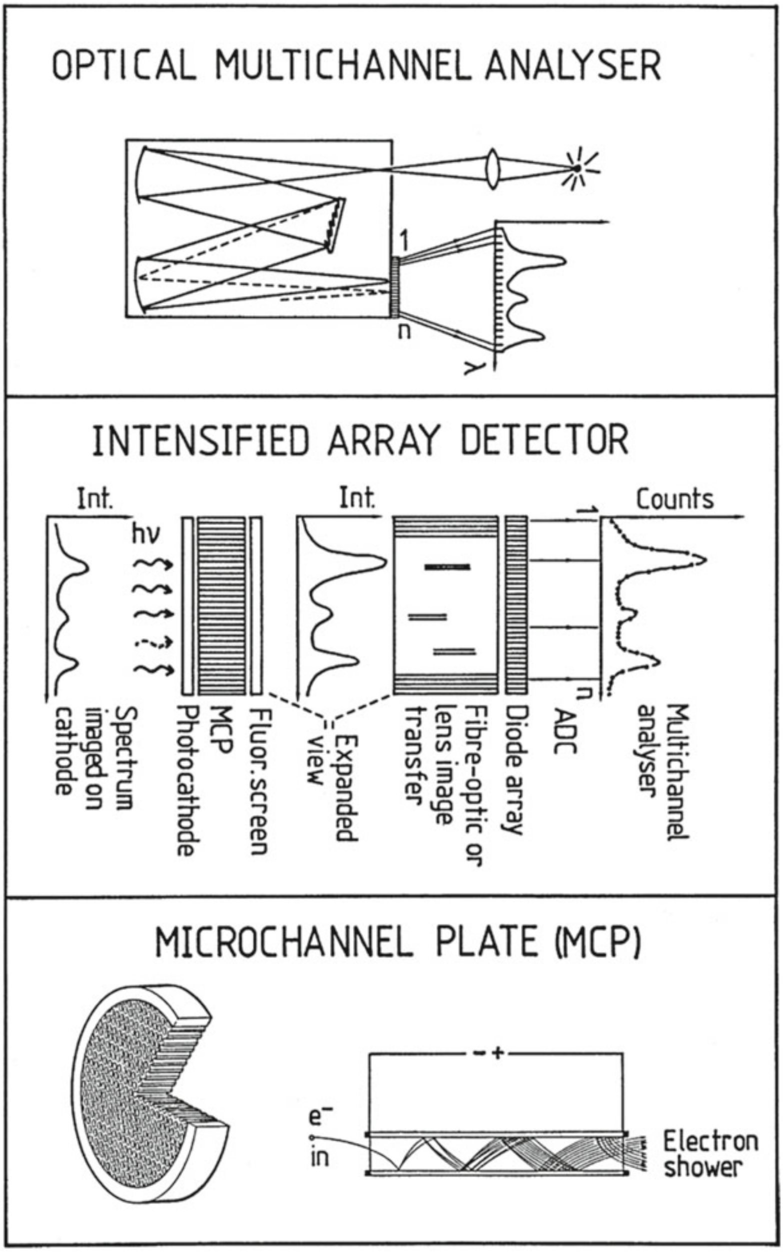
OPTICAL MULTICHANNEL ANALYSER
1
n
λ
INTENSIFIED ARRAY DETECTOR
Int.
hν
Int.
1
n
Counts
Spectrum imaged on cathode
Photocathode
MCP
Fluor. screen
Expanded view
Fibre-optic or lens image transfer
Diode array
ADC
Multichannel analyser
MICROCHANNEL PLATE (MCP)
− +
e⁻ in
Electron shower

Fig. 6.42 Optical multichannel analyser with microchannel-plate image intensifier

during time intervals down to 1 ns. This type of operation is of great interest, e.g., for background rejection in connection with spectroscopy using short laser pulses.

Detectors of the type just discussed are frequently two-dimensional and are then used for imaging. We will discuss spectroscopic applications of such imaging later. The field of solid-state array detectors is rapidly developing. The CCD (Charge Coupled Device) technology was first introduced for astronomy applications but has now penetrated numerous areas. CCDs come in many different sizes; they may, e.g., have 512 × 512 separate light-sensitive pixels. The charge collected on each light-sensitive element is read out using *shift registers* like a stream of sequential data, which is then sorted into digital bins in the computer memory. The 2009 Nobel Prize in Physics was awarded to *W.S. Boyle and G.E. Smith* for the invention of the CCD [584, 585]. Only the light intensity recorded is of interest for spectroscopy (black-and-white recording), while for use in a digital camera clearly colour sensitivity is also important.

This can be achieved using a *Bayer colour filter*. Here 4 pixles with filters (2 green, 1 blue, and 1 red), corresponding to the human retina sensitivity (see below) are used for forming one spatial element. When detecting spectral or image information with a CCD, light can be allowed to charge up the detector element during a certain time (integration on the detector) before the data are read out using the shift register.

During recent years a further class of multi-element imaging detectors have emerged, the CMOS (complementary metal–oxide–semiconductor) sensors. A comparison between CCDs and CMOS sensors shows that the former ones have higher sensitivity and larger power consumption, but higher production costs than the latter ones, which are used, e.g., in smart-phone cameras. The sensitivity range goes from about 400 nm to 1000 nm for CCD as well as CMOS devices. Using InGaAs as the semiconductor material, the spectral range for array detectors can be extended out to 1.7 μm, and to 3.5 μm with InAs. Clearly, such detectors strongly benefit from cooling. Photographs of such near-IR devices are shown in Fig. 6.43.

In particular, imaging spectrometers can be constructed, in which different spatial locations along a line across the object are imaged along the entrance slit. In the perpendicular direction the spectrum can be dispersed, and thus the full spectrum in each point along the chosen line is recorded on a two dimensional detector. This

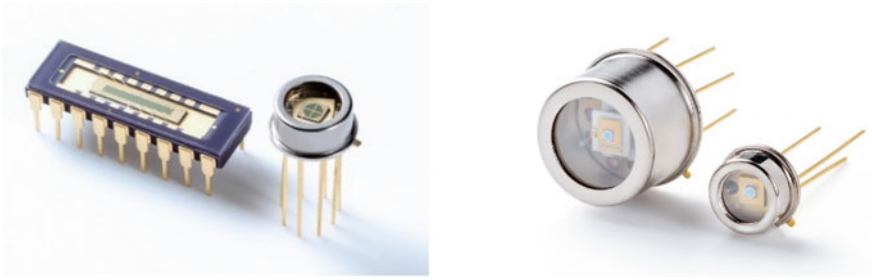

Fig. 6.43 InGaAs array detector (0.9–1.7 μm) and InAs detector (1.2–3.5 μm) (Courtesy: Hamamatsu)

technology is used, for example, in “push-broom” remote-sensing systems installed in airplanes or satellites (Sect. 6.6.2). There are also many utilizations in biophotonics (Sect. 10.5) and in connection with lidar techniques utilizing fluorescence and Raman scattering (Sect. 10.3.2).

A further application of such two-dimensional detectors is to provide simultaneous spectral and temporal resolution for an object. In such a system the detector is placed in the focal plane of a streak camera (Sect. 9.5.1) preceded by a spectrometer.

Imaging electro-optic detectors have been discussed in [586–590].

The human eye is a very-high-resolution detector, which is highly integrated with the brain to perform real-time object detection and identification, as already discussed in Chap. 1. A cross section of the eye is given in Fig. 6.44 (left). The high acuity part of the retina is the approximatively 1.5 mm diameter *fovea* (“yellow spot”), where some 5 million colour-sensitive *cone* receptors capture the scene. The spectral response of the three types of cones is given in Fig. 6.44 (right). There is a considerable overlap between the curves, but the brain still manages to separate a huge number of colors and hues based on the detailed weighting av the RGB (red–green–blue) responses. More spread across the retina are the 100 million, much more light-sensitive *rod* receptors, which, however, do not distinguish colours. The corresponding response curve peaks in around 500 nm. Thus, at low-ambient-light conditions all objects are only vaguely seen (by the rods) on a grey-scale. Human vision is treated in [591, 592].

Enhanced *night vision* is obtained using an image intensifier tube, where the input photocathode side of the tube is placed in the image plane of the light-collecting optics, and an eyepiece lens is used to observe the thousand-fold intensified image on the phosphor side of the tube. Clearly, any colour perception is lost in the process, and images appear green, since that is the colour of the most efficient phosphors.

However, there is a way to achieve “*colour night vision*” [593, 594], if blue, green, and red filter sectors are used in two synchronously rotated filter wheels placed on either side of an image-intensifier tube, which has been equipped with a special broad-band (“white”) phosphor. This phosphor is similar to that used in

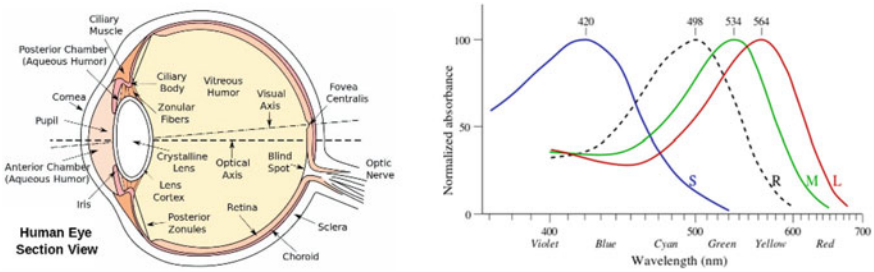
Ciliary Muscle
Posterior Chamber (Aqueous Humor)
Cornea
Pupil
Anterior Chamber (Aqueous Humor)
Iris
Ciliary Body
Zonular Fibers
Vitreous Humor
Visual Axis
Fovea Centralis
Crystalline Lens
Lens Cortex
Optical Axis
Blind Spot
Optic Nerve
Posterior Zonules
Retina
Sclera
Choroid
Human Eye Section View
420
498
534
564
100
50
0
Normalized absorbance
S
R
M
L
400
500
600
700
Violet
Blue
Cyan
Green
Yellow
Red
Wavelength (nm)

Fig. 6.44 (Left) Cross-section through the human eye (https://upload.wikimedia.org/wikipedia/commons/thumb/f/f5/Eyesection.svg/512px-Eyesection.svg.png) and spectral response of the three types of cones and for the “color-blind” rods shown in a dashed line (right) https://upload.wikimedia.org/wikipedia/commons/3/32/Opsin_Absorption_Spectra.png fluorescent lamp tubes, where the strong UV mercury line radiation from the emitting vapour is converted into white light [595, 596]. The three different colours are now intensified separately. For example, when the red-transmitting filter sector is in front of the cathode, the red parts of the image are intensified into a white image, which is observed through a red-transmitting filter. In the same way, the blue and green parts of the object are intensified (with colour preserved!). If the filter wheels rotate fast enough, the brain will see the full colour image without flickering. By proper adjustment of sensitivities and filter transmissions the normal colours are seen, since moon- or star-light basically has a very similar spectral distribution as the sun- or day-light (Fig. 6.18). In principle, the same result is obtained if filtered images are recorded by a black-and-white CCD detector and then co-processed digitally into a colour TV image.

We will finish this section on detector technology by recalling some new developments in X-ray imaging as discussed in Sect. 5.1.3. Traditionally, photographic films, which are blackened by the high-energy X-ray quanta, have been used in medical radiology. A much higher sensitivity is obtained using *image plate technology* [597]. Instead of the silver bromide grains the "emulsion" contains microscopic crystals of certain rare-earth salts. The absorbed energy of the X-ray quantum transfers the rare-earth ion into a long-lived metastable state and a "latent" image is formed. The image information is sequentially read out with a scanned and focused He–Ne laser beam, transferring the metastable ions into a higher, short-lived state from which blue fluorescence light is emitted in the decay. A digitized image is obtained, which allows efficient processing and storage. By proper light treatment the plates can be again prepared with the ions in the proper state to allow repeated use of the same image plate.

CCD detectors can also be used for X-ray imaging, e.g., for dental applications [598, 599].

6.4 Optical Components and Materials

6.4.1 Interference Filters and Mirrors

Filters of different kinds are employed to select a certain spectral region. Relatively narrow spectral regions can be isolated using an *interference filter*. Such a filter for a wavelength λ is, in its simplest form, a Fabry–Pérot interferometer with a mirror separation of $\lambda/2$. Transmission maxima are also obtained for the wavelengths $\lambda/2$, $\lambda/3$, $\lambda/4$, etc. Filters for the short wavelength region, $\lambda < 240$ nm, are frequently made in this way with partially reflecting metal layers on each side of a $\lambda/2$ dielectric layer. Transmission maxima at shorter wavelengths are effectively absorbed by the substrate material (e.g., quartz; see below). The absorption of the metal layers reduces the transmission of the filter. Because of this, *multiple dielectric layers* are used almost exclusively at longer wavelengths. In order to achieve a high reflectivity and low absorption, many layers of thickness $\lambda/4$ with alternating high and low refractive indices (e.g., ZnS, $n = 2.3$ and MgF_2, $n = 1.35$) are used [600]. The number of layers used determines the sharpness of the filter. The centre wavelength is determined by the thickness of the spacer layer. By using two or more filters of this kind in series (multicavity filter), with coupling layers to reduce reflection losses, sharper filters can be constructed. Suppression of transmission maxima at shorter wavelengths can easily be achieved by combining the interference filter with a high-pass coloured glass filter (Sect. 6.4.2). Unfortunately, there are no simple efficient low-pass filters for suppressing long wavelengths. If such suppression is required a filter with *induced transmission* can be used. Such a filter, which is a hybrid between a metal-dielectric-metal filter and an all-dielectric filter, is characterized by the absence of long-wavelength transmission. In order to obtain a sharp interference filter with complete suppression outside the passband it can be necessary to combine a multicavity filter, an induced transmission filter, and a high-pass coloured glass filter to form an integrated composite filter. Examples of individual transmission curves are shown in Fig. 6.45.

The transmission maximum of an interference filter is shifted towards shorter wavelengths if it is used at an inclined angle. The new transmission wavelength λ_θ is related to the nominal wavelength λ_0 by

$$\lambda_\theta = \lambda_0 \frac{\sqrt{n^2 - \sin^2\theta}}{n}. \tag{6.39}$$

Here θ is the angle of incidence and n is the refractive index of the spacer layer. As an example, for $\theta = 10^\circ$, $n = 1.45$ and a filter wavelength of 600 nm, we obtain $\Delta\lambda_\theta = \lambda_0 - \lambda_\theta \sim 4$ nm. This means that if a filter is used in a converging or diverging beam of light, the transmission profile is somewhat shifted towards shorter wavelengths. For a cone of light with an angle at the apex of 2θ the effective shift is about $\Delta\lambda_\theta/2$.

Tunable narrow-band filter action can be obtained by placing a liquid crystal between polarizers. The action is similar to that of the Lyot filter used, e.g., in dye laser tuning (Sect. 8.5.1; Figs. 8.23 and 8.24), but now the birefringence is controlled by an electrical voltage. The wavelength region from 400 to 1100 nm can be used, and the band-pass achieved can approach 10 nm. Since such filters do not operate on interference, they are not sensitive to the angle of incidence and are useful in multispectral imaging applications [602, 603].

Mirrors are also made using multiple dielectric layers of thickness $\lambda/4$. The more layers that are added, the better the reflectivity that can be achieved in a certain wavelength region [600]. The effect of an increase in the number of layers is demonstrated in Fig. 6.46. A reflectivity better than 0.999 can be obtained using 30 layers. Clearly, thin-film techniques of this kind are of great importance for the construction of laser cavities and for interferometers with sharp frequency discrimination characteristics.

We will also briefly discuss *anti-reflection layers*. A surface without any special preparation between an external medium (frequently air), with refractive index n_0, and an optical component with refractive index n, has a reflectivity R given by

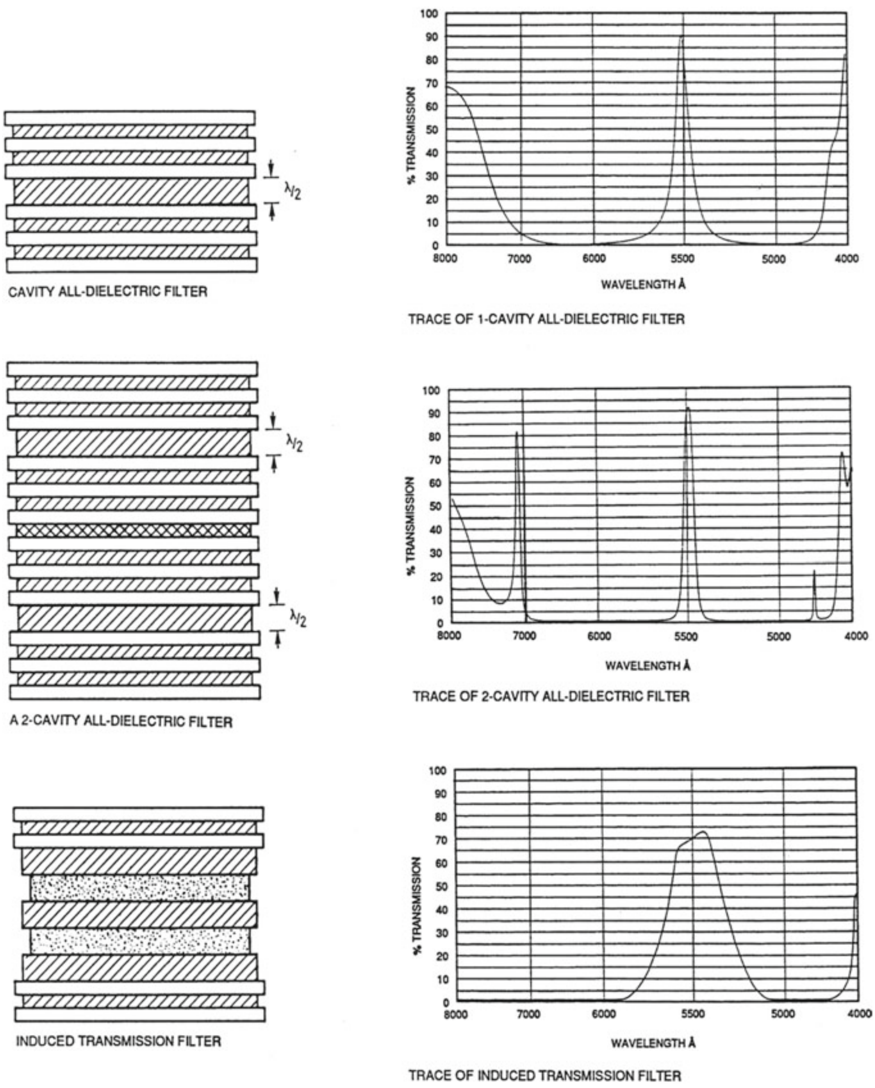

Fig. 6.45 Interference filter layers and resulting transmission curves [601]

$$R = \left(\frac{n - n_0}{n + n_0}\right)^2. \tag{6.40}$$

For a quartz–air boundary we have $R = [(1.5 - 1)/(1.5 + 1)]^2 = 4\%$. It can be shown that if a layer of refractive index n_1 and thickness $\lambda/4$ is evaporated onto the optical component the reflectivity will be zero provided that $n_1 = \sqrt{n}$. MgF_2 with $n = 1.35$ is frequently a suitable material. In order to achieve anti-reflection properties in a

Fig. 6.46 Multiple-layer mirror reflectivity [604]

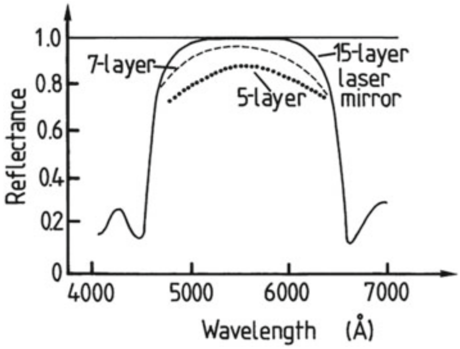

larger wavelength region, e.g., in the whole visible region, multiple-layer techniques are used, as illustrated in Fig. 6.47. Advanced anti-reflection techniques are clearly a prerequisite for the construction of modern multiple-element lenses, etc., which would otherwise be cluttered by scattered light from the many surfaces.

Mirrors that are intended to be used over a wide range of wavelengths generally consist of *metal coatings* on a substrate. A layer thickness of the order of 150 nm is adequate. Reflectivity curves for some metal coatings are shown in Fig. 6.48. Silver has a reflectivity of 96–98% in the visible and IR regions. Since a silver surface tarnishes, a protective layer of, for example, SiO is needed. Gold is a highly suitable material for the IR region. Aluminum can be used over a wide range of wavelengths from UV to IR. Aluminum coatings are especially useful far down in the UV region, i.e., 200 nm and below. The reflective properties in the UV region can be improved by using a surface layer of SiO_2 or MgF_2, which also allows the otherwise very vulnerable mirror to be cleaned. Aluminum mirrors have a limited applicability in techniques involving high-power pulsed laser beams because of the possibility of evaporation of the coating. Dielectric mirrors or totally reflecting 90° prisms are normally used in such applications.

Fig. 6.47 Action of anti-reflection coatings [604]

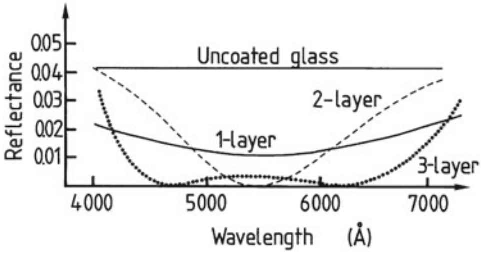

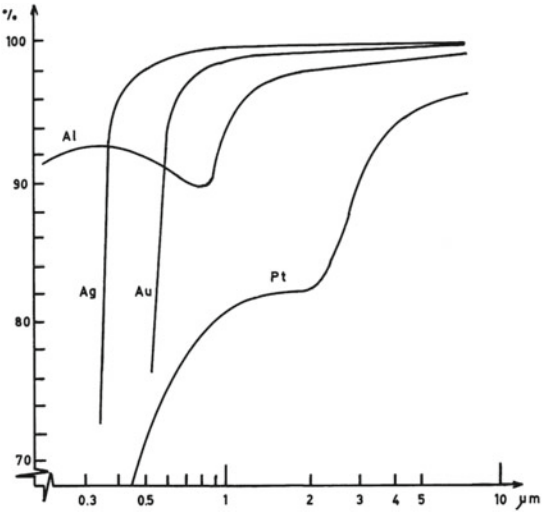

Fig. 6.48 Reflectivity of metal coatings

6.4.2 Absorption Filters

If the narrow region of transmission typical for an interference filter is not required, a simpler and much cheaper absorption filter can frequently be used. In *coloured glass filters* or plastic filters, the absorption can be caused by simple or complex ions (e.g., nickel, cobalt, neodymium, praseodymium, uranium). Semiconductor-doped glasses are used as sharp cut-off filters. Using $\mathrm{CdS}_x\ \mathrm{Se}_{1-x}$ doping the absorption edge moves downwards for increasing x-values. Such filters are very efficient for suppressing short wavelengths. Some transmission curves for coloured glass filters are given in Fig. 6.49. We note that if a high discrimination in transmission between two different wavelength regions is desirable, it is advisable to use a thicker filter. As an example, if for a filter of 1 mm thickness a transmission of 0.9 is obtained in a certain desired spectral region, and only 0.1 in another region to be rejected, the transmissions for a 2 mm thick filter would be $0.9 \times 0.9 = 0.81$ and $0.1 \times 0.1 = 0.01$, respectively. Thus, while basically still letting almost all desired light through, the undesired light is suppressed by a factor of 10 by chosing the thicker filter, and for thicker filters the discrimination is even more impressive.

Sometimes *liquid filters* consisting of a quartz cuvette filled with a particular liquid can be quite useful. Organic liquids can be used as high-pass filters with cut-offs in the UV region, where coloured glass filters cannot be used. The cut-off wavelengths are schematically given in Fig. 6.50 for a number of liquids. Water solutions of inorganic salts are also of interest. For example, a mixture of nickel sulphate and cobalt sulphate is transparent in the UV region over 230–330 nm but completely blocks the visible region. Liquid filters can be particularly valuable if large amounts of optical energy must be absorbed with associated temperature increase, which can

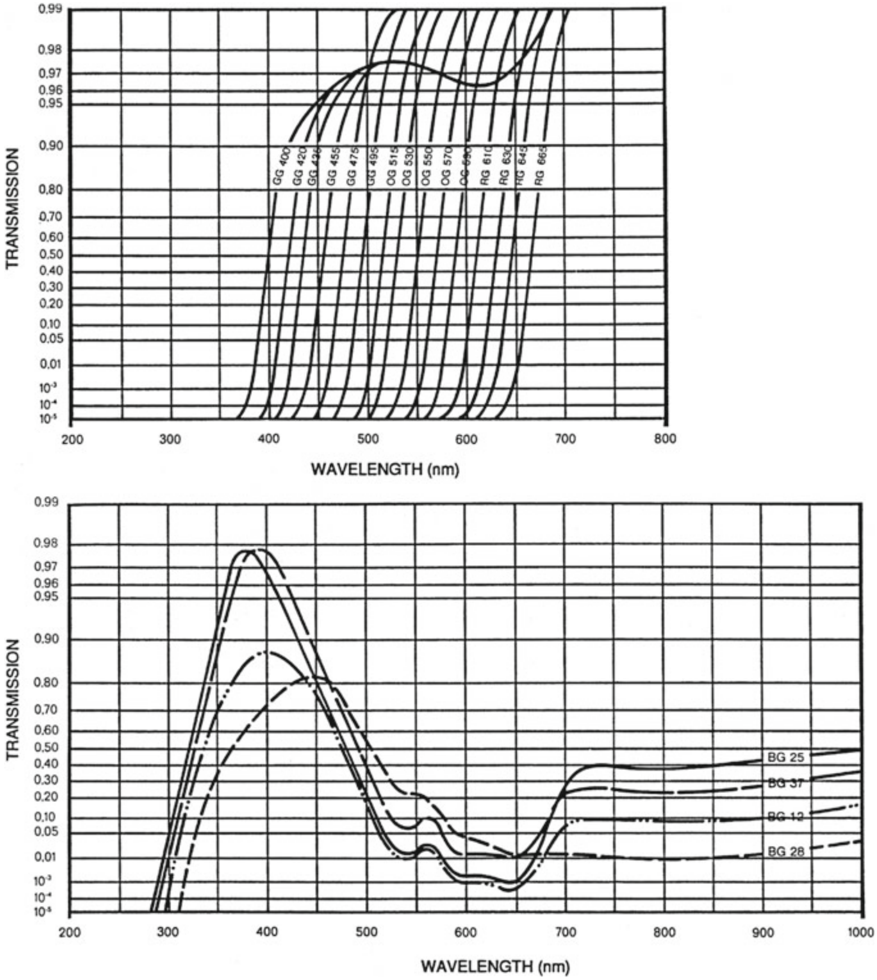

Fig. 6.49 Examples of transmission curves for coloured-glass filters (Courtesy: Schott Glaswerke)

be handled for a circulating liquid medium, but not by a coloured glass filter, which would break. Liquid filters have been discussed in [605, 606].

Absorption filters, in contrast to interference filters, can be used at any angle of incidence and can thus be used in strongly converging or diverging beams. It should be noted that certain coloured glass filters can exhibit rather strong broadband fluorescence when used to block UV light, which can sometimes cause problems. When a combination of an interference and a coloured glass filter is used, placing the interference filter in front of the fluorescing filter can improve the performance in the visible region.

Neutral-density filters are used to reduce the intensity of a light beam in a well-defined way, e.g., for testing the linearity of an optical detector. Filters of this kind

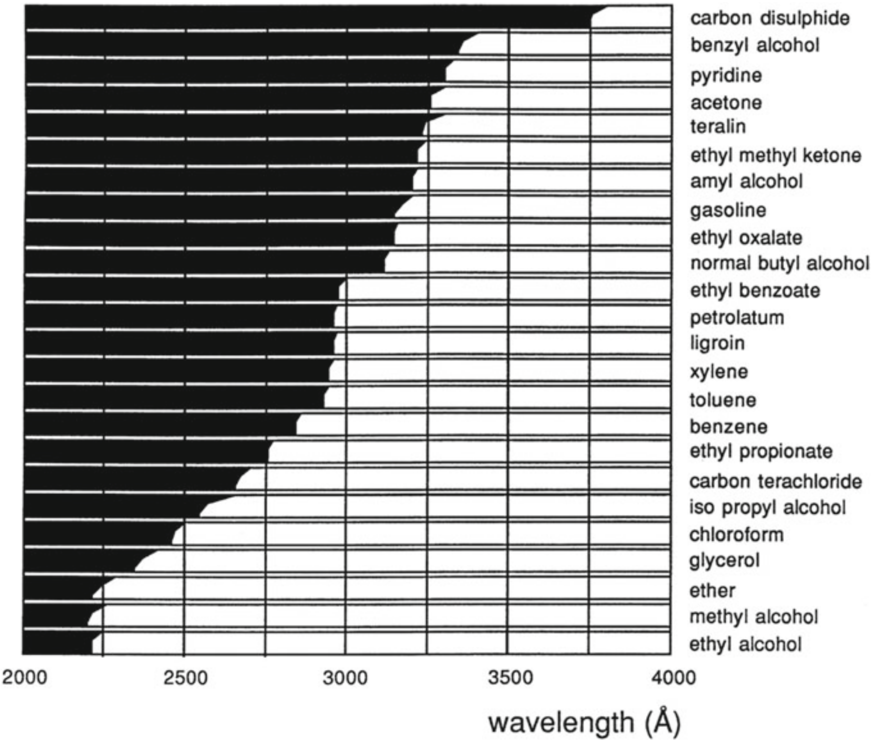

Fig. 6.50 Spectral characteristics for some liquid filters. Black indicates blocked transmission 10Å = $1nm$ [605]

should have a constant attenuation over large spectral ranges to facilitate their use. Normally, semitransparent metal films of chromium or nickel on quartz substrates are used. A filter is characterized by its transmittance T, or optical density D. D and T are related according to

$$D = \log_{10}(1/T). \tag{6.41}$$

Thus, a filter of optical density $D = 1.0$ has a transmittance T of 0.1 (10%). When two neutral density filters are combined, the transmittances are multiplied, while the optical densities are added. Pairs of D and T values are given in Table 6.3. A good rule to remember is that a $D = 0.3$ filter blocks 50% of the radiation and becomes very convenient when checking the linearity of optical detectors. For high-power laser beams, bulk absorbing glasses or combinations of inclined quartz plates (Fresnel reflection) must be used [607].

Finally in this section we would like to mention the rapidly emerging field of "smart-window" technology [608], which can provide variable optical properties for windows and mirrors. *Electrochromic films*, which change their transmission or

Table 6.3 Optical densities *D* and transmissions *T*

D	T [%]	D	T[%]
0.0	100	0.8	16
0.1	79	1.0	10
0.2	63	1.5	3.1
0.3	50	2.0	1.0
0.4	40	3.0	0.1
0.5	32	4.0	0.01

colour when an electric voltage is applied across the film, are used. WO_2 is the most commonly used material, which is influenced by ionic transport through an adjacent ionic film. Transparent electrode films attached to normal glass sheets can be made from tin-doped In_2O_3. Electrochromic windows have the potential for reducing the need for air-conditioning considerably in hot regions. A mirror preceeded by an electrochromic film will have a varible reflectivity. This technology is already commercially available in anti-glare rear mirrors for cars. The related phenomenon of *photochromism* is used in the eyeglasses, which reduces transmission when subjected to the UV part of sunlight. Materials with variable and controllable transmission are discussed in [608–611]. A somewhat related field is the one of *electronic paper* [612, 613].

6.4.3 Polarizers

Polarized light can be obtained or analysed using certain prisms or polarizing films. Reflection at a non-normal angle of incidence at the flat surface of an optical material also results in a certain degree of polarization according to the Fresnel formulae (Fig. 6.51). In particular, at the Brewster angle ($\tan\theta = n$) the reflected light is fully polarized perpendicularly to the plane of incidence (the plane containing the normal to the surface) (S-polarized light).

Light components polarized in the plane of incidence (P-polarized light) penetrate into the medium without loss. A stack of glass or quartz plates at the Brewster angle will successively reflect almost all components perpendicular to the plane of incidence, leaving a highly polarized transmitted beam.

A convenient way to attain a very high degree of linear polarization is to use prisms made of the birefringent material calcite ($CaCO_3$). The arrangements in *Glan–Taylor* and *Glan–Thompson* polarizers are shown in Fig. 6.52. Both these polarizers consist of a combination of two prisms, in the first type air-spaced, in the second case cemented. The prism angle has been chosen such that the ordinary beam is totally internally reflected and absorbed laterally in the prism, while the extraordinary beam is transmitted into the next prism and leaves it undeviated. Glan–Thompson prisms have a larger acceptance angle but cannot be used in the UV region because of

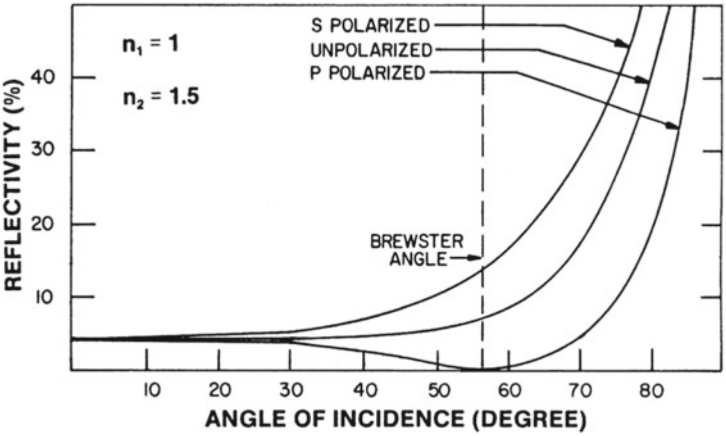

Fig. 6.51 Polarization-dependent reflectivity at an optical surface (Fresnel formulae) [604]

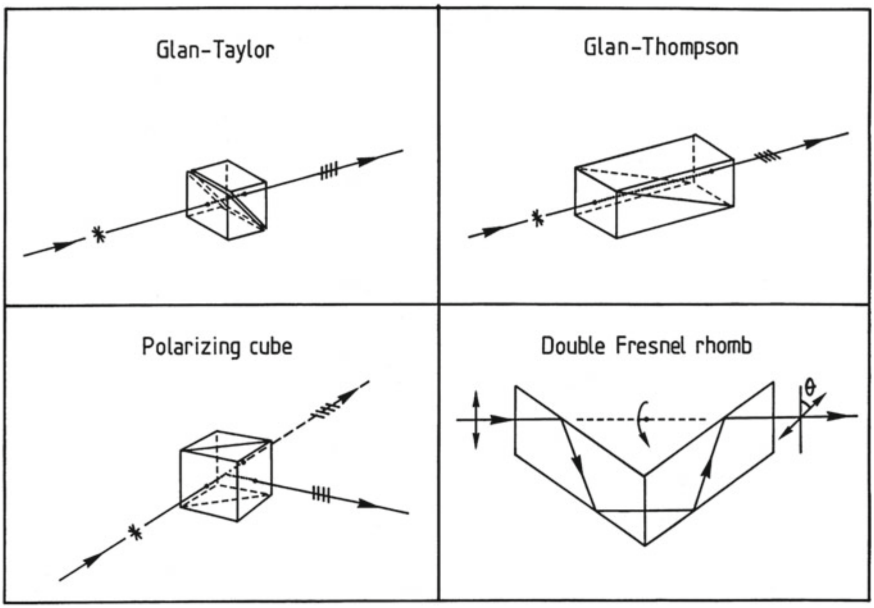
Glan-Taylor
Glan-Thompson
Polarizing cube
Double Fresnel rhomb
θ

Fig. 6.52 Polarizing prisms (After material from Melles Griot)

absorption in the optical cement. Both types of Glan prism exhibit an extinction ratio of better than 10^5 for crossed polarizers.

A *polarizing beam-splitter* is formed by combining two right-angle prisms into a cube. A special multilayer film between the prisms acts as a stack polarizer as described above. An unpolarized beam is thus divided into two perpendicular highly

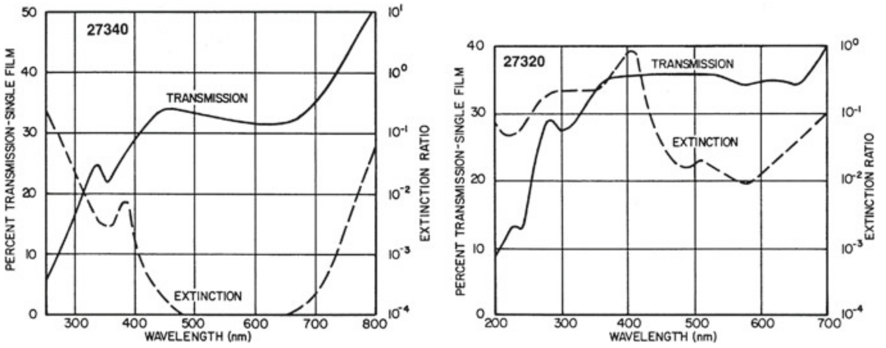

Fig. 6.53 Spectral characteristics of polyvinyl film polarizers (Courtesy: Oriel Corp., Stratford, CT, USA)

polarized components. Conversely, two polarized beams can be combined into a single beam using this type of component.

Optical retarder plates, of appropriate thicknesses, made of birefringent material, normally crystalline quartz or mica, can be used to rotate the plane of polarization for linearly polarized light or to produce circularly polarized light. To rotate linearly polarized light by an arbitrary angle, a *double Fresnel rhomb* is very useful (Fig. 6.52).

Linear polarizers can also be made of *polyvinyl film* that has been stretched so as to align long chains of molecules. Different kinds of polarizer of this type are available for wavelengths from 200 nm up to the near-IR. Examples of transmission and extinction curves are shown in Fig. 6.53.

6.4.4 Optical Materials

Optical components are manufactured from transparent materials of certain refractive indices. We have already discussed the refractive properties of glass and quartz in Sect. 6.2.1. Here we will consider the transmission properties of optical materials. Optical glass is transparent from about 350 nm to 2.6 μm [614]. This region of transmission can be extended by using quartz. Transmission curves for different qualities of quartz are shown in Fig. 6.54. As can be seen, the best quartz has a transmission down to 170 nm. However, strong absorption bands can occur in the near-IR region, particularly at 2.7 μm. These are due to the presence of water (O − H bonds) in the quartz. Water-free quartz can be used up to about 3.5 μm.

The region of UV transmission can be extended down to 125 nm using CaF_2 and to 110 nm using LiF. These materials are also transparent in the IR region out to 9 and 6 μm, respectively. At still longer wavelengths NaCl can be used. The transmission curves for these materials are shown in Fig. 6.55.

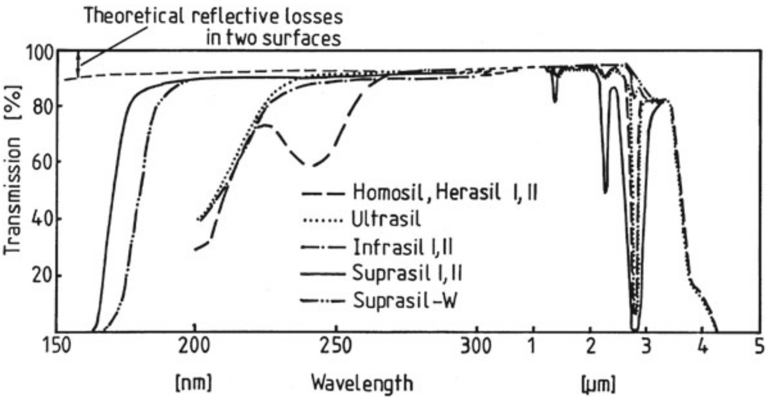

Fig. 6.54 Transmission curves for different qualities of quartz (Courtesy Heraeus Quarzglas GmbH)

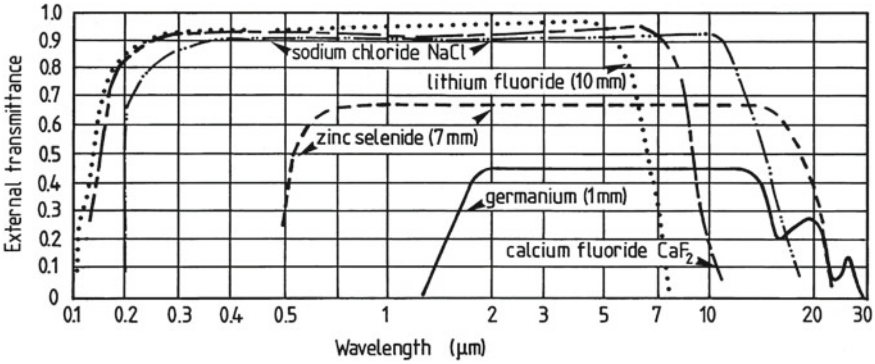

Fig. 6.55 Transmission curves for far-UV and IR-transmitting materials (After material from Oriel Corp., Stratford, CT, USA)

6.4.5 Influence of the Transmission Medium

In discussing the transmission of different optical materials we should also consider the properties of air. It is important to note that in laboratory spectroscopy oxygen, water vapour and carbon dioxide in the air strongly absorb wavelengths below 200 nm. Thus the spectroscopic equipment must be evacuated when working in short-wavelength regions (*vacuum spectroscopy*). Alternatively, for wavelengths above 145 nm the equipment can be flushed with nitrogen. Wavelengths measured in air must be corrected for the refractive index of air to yield *vacuum wavelengths*, which are those used to calculate the positions of energy levels. The wavelength corrections, $\Delta\lambda$, to be *added to an air wavelength* (15 °C, 760 torr, 101 kP) are given by the *Edlén formula* [615]

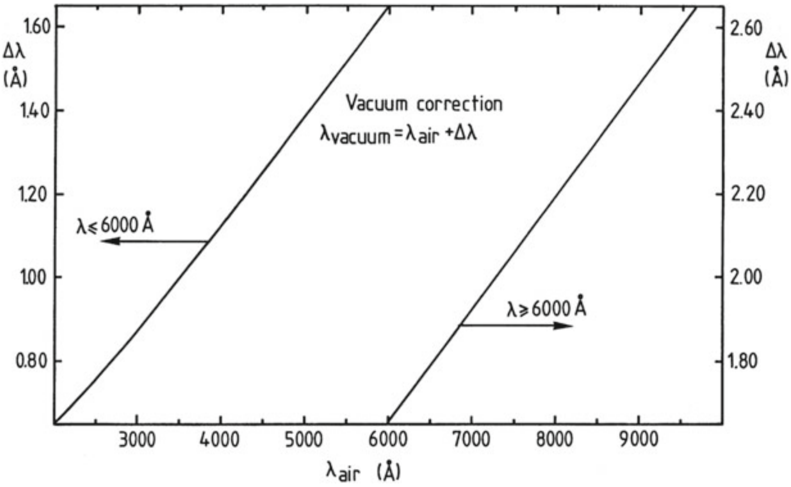

Fig. 6.56 Wavelength correction curve (10 Å = 1 nm) (Courtesy: P. Grafström)

$$\begin{aligned}
\Delta\lambda &= (n-1)\lambda_{\text{air}} > 0 \\
(n-1) &= 10^{-8}\left(8342.13 + \frac{2,406,030}{130-\sigma^2} + \frac{15,997}{38.9-\sigma^2}\right), \\
&\quad \left(\sigma = 1/\lambda, \sigma \text{ in } \mu\text{m}^{-1}\right).
\end{aligned} \tag{6.42}$$

The correction is graphically displayed in Fig. 6.56.

Air has strong absorption bands in the IR region, which are mainly due to H_2O and CO_2. The slowly increasing CO_2 content of the atmosphere will lead to a gradual heating of the atmosphere. In astronomical observations very long absorption paths through the atmosphere are obtained. The stratospheric ozone layer, at a height of about 25 km, absorbs strongly in a band around 9.5 μm. More interestingly, it absorbs all radiation below 300 nm, which is essential for shielding life from mutagenic short UV radiation. In recent years it has become obvious that a depletion of the protecting ozone layer due to human activities is going on. One area of concern is the injection of nitrogen oxides (NO_x) into the stratosphere in the form of exhaust from high-flying, Supersonic Transport (SST) aeroplanes. Tropospheric NO_x is normally washed out as acid rain. More important is the influence of freons (CFCs; chlorinated fluorocarbons), from spray cans and cooling equipment, which are inert with respect to the normal atmospheric gases. Freons diffuse into the stratosphere, where they can react with the ozone molecules.

The elucidation of the chemistry behind the ozone formation and depletion was awarded the Nobel prize in chemistry 1995 (*P. Crutzen, M. Molina* and *F.S. Rowland*). Many partial reactions are involved in the process. An important aspect is that a single chlorine atom (formed by UV splitting of the chlorinated fluorocarbon) can catalytically destroy many ozone molecules, which are primarily formed by UV splitting of O_2 into O free radicals, then to combine with O_2 to O_3. A reaction chain occurs, where the chlorine atom eliminates the ozone molecule while being integrated in a ClO radical, which is subsequently split up to free the chlorine atom. Then a new string of events leading to ozone destruction occurs:

$$\begin{aligned} 2O_2 + UV &\rightarrow O + O_3 \\ Cl + O_3 &\rightarrow ClO + O_2 \\ ClO + O &\rightarrow Cl + O_2 \end{aligned}$$

Strong regulations against freons are now being enforced (the Montreal Protocol, 1989). The natural variations in the thickness of the ozone layer are quite large and delayed the full conviction of a very dangerous trend. Since the time constants for processes of the kind discussed here are tens of years, it is important to identify trends as early as possible. A pronounced Antarctic "ozone hole" was found to be formed during the (Antarctic) spring months [616–618]. Spectroscopic ozone-layer monitoring is being performed through absorption measurements from the ground (Dobson instruments) or from satellites and balloons. Ground-based vertical lidar sounding of ozone is also a powerful technique (Sect. 10.2.3). A positive result of the Montreal protocol is now being experimentally observed. Air pollution and atmospheric chemistry in general have been discussed in [619–625].

The spectral distribution of the sun's radiation is shown in Fig. 6.57, both outside the atmosphere and at sea level with different absorption bands indicated. The vertical transmission of the earth's atmosphere, including longer IR wavelengths, is shown in Fig. 6.58. The curve for the whole atmosphere is depicted at the bottom, and individual constituent curves are included, too. These data will determine the spectral range of ground-based astronomical observations. The data in Figs. 6.57, 6.58, 6.17 and 6.8 also give insight into the origins of the *enhanced greenhouse effect*, now leading to an increased global temperature [628–633]. The sun radiation peaks in the visible region around 500 nm (Figs. 6.57, 6.8) where the atmospheric gases are transparent. Reaching ground, heating occurs and the earth surface emits thermal radiation, peaking at about 10 μm (Figs. 6.8, 6.17). Much of this radiation is reabsorbed by the atmospheric gases, which are heated and in turn radiate back to earth. Water vapour is the most prominent normal greenhouse gas. As a matter of fact, if the earth did not have an atmosphere, the average temperature on earth would be about -20 °C instead of $+15$ °C, which it is now! Apart from water vapour, CH_4 and in particular CO_2, reabsorb the thermal radiation, and are particularly important in the spectral regions, where the water vapour does not anyway block out all the radiation. The increased CO_2 concentration (which was about 280 ppm before the industrial revolution as compared to the 2021 value of 420 ppm), leads to an increased net absorption, e.g., around 4 μm, and beyond around 13 μm (see Fig. 6.58). The increasing concentration may lead to a few degrees of average temperature increase, as projected by extensive *climate forcing* modelling, also involving the influence of aerosol particles, etc. [634]. A schematic diagram illustrating the enhanced greenhouse effect is shown in Fig. 6.59. Interestingly, the extremely fundamental and threatening phenomena of ozone layer depletion and the extended greenhouse effect both have a clear background and understanding in molecular spectroscopy.

A curve for horizontal atmospheric absorption at sea level over a distance of one nautical mile (1.8 km) is given in Fig. 6.60. This curve is of interest when considering free-laser-beam optical communications or passive and active forms of atmospheric remote sensing (Sects. 6.6.1 and 10.2). The absorption properties of the atmosphere have been discussed in [636–638].

We will conclude this section by giving the transmission properties of sea water [639–641]. The absorption coefficients for different types of waters are given in Fig. 6.61 [642]. The "blue-green window" of water is clearly seen. The curves determine vertical visibility and the possibility of laser bathymetry (Sect. 10.3.1), etc. Communication with submarines is accomplished using satellite-based blue-green lasers. The only alternative for such communication purposes is the use of radio waves of extremely long wavelength (VLW).

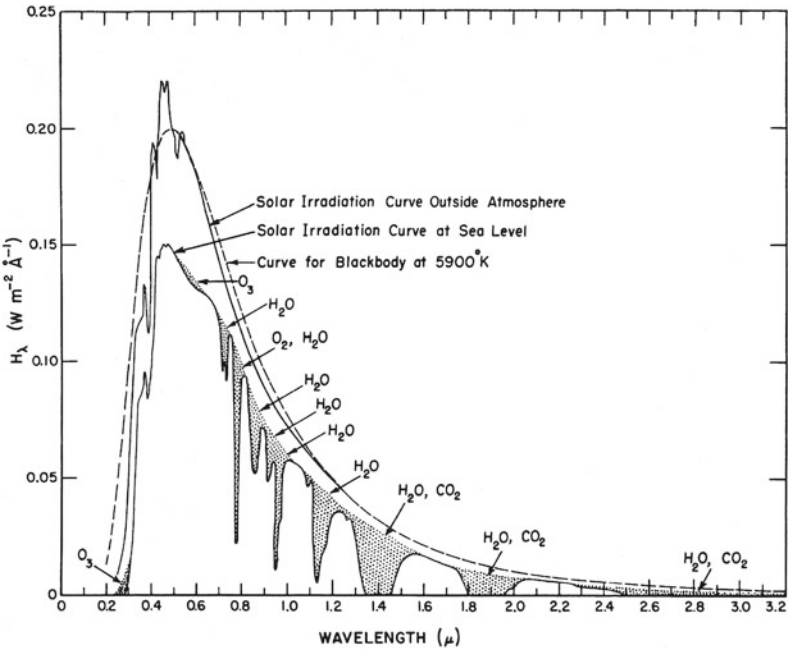

Fig. 6.57 Spectral distribution of the sun´s radiation outside the atmosphere and at sea level, with absorption bands indicated [626]

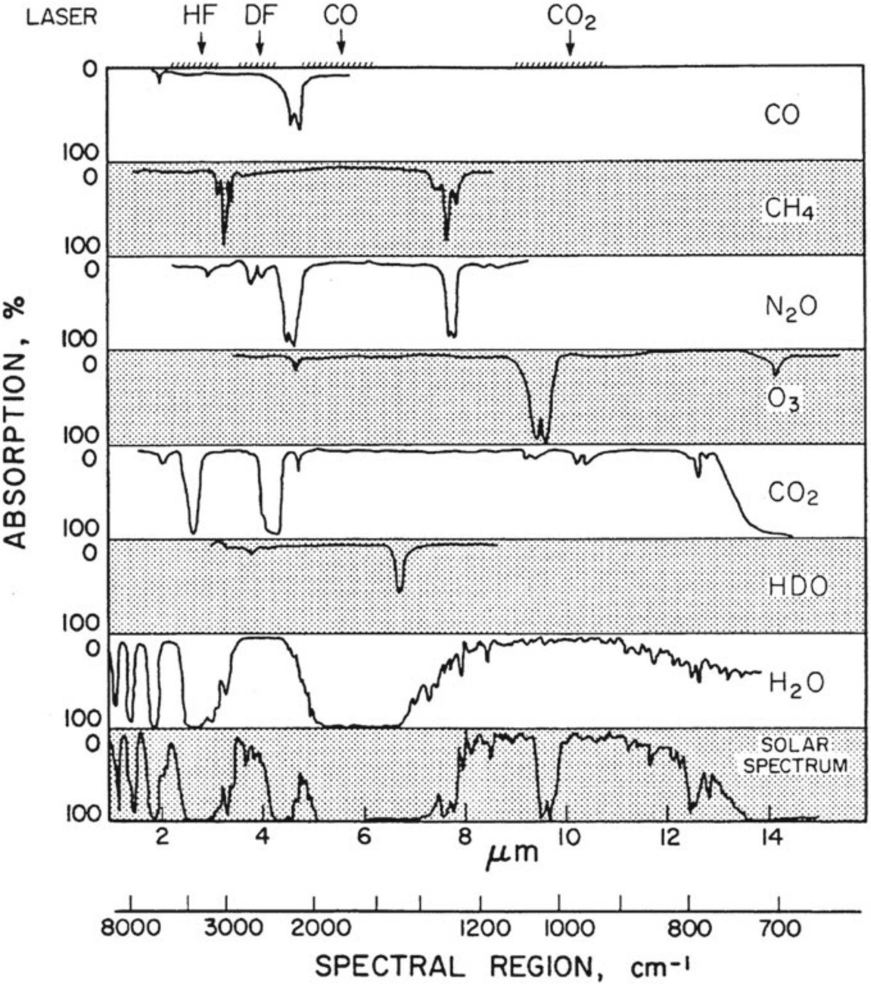

Fig. 6.58 Vertical absorption curve for the earth's atmosphere (*bottom*), and individual constituent contributions [627]

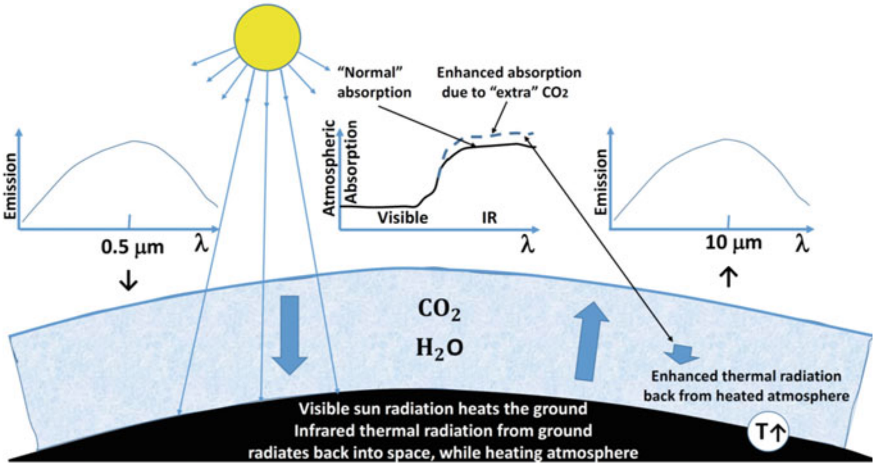
"Normal" absorption
Enhanced absorption due to "extra" CO2
Emission
0.5 µm
λ
Atmospheric Absorption
Visible
IR
λ
Emission
10 µm
λ
CO2
H2O
Enhanced thermal radiation back from heated atmosphere
Visible sun radiation heats the ground
Infrared thermal radiation from ground
radiates back into space, while heating atmosphere
T↑

Fig. 6.59 Schematic, simplified, diagram of the cause of the enhanced greenhouse effect

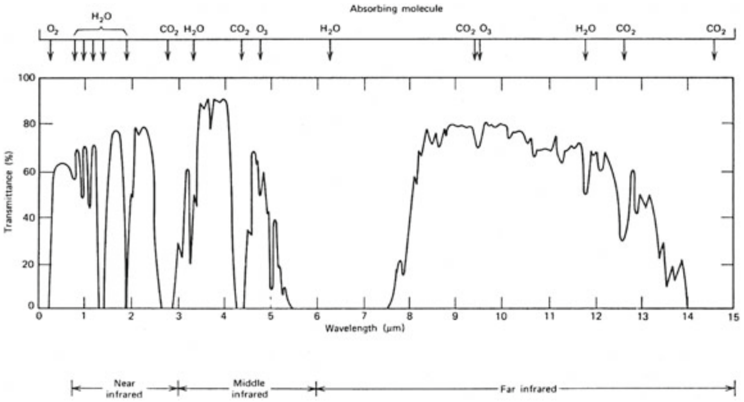

Fig. 6.60 Horizontal atmospheric absorption curve over a distance of 1.8 km at sea level [635]

Fig. 6.61 Spectral dependence of the absorption coefficient for different types of sea water (From [642], based on data from [639, 643])

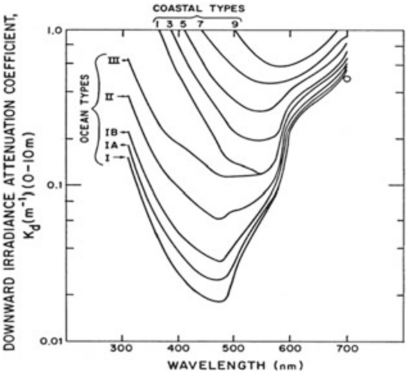

6.5 Optical Methods of Chemical Analysis

Several highly applicable methods of analysis rely on the interaction between light (UV–visible–IR) and matter. The wavelengths (energies) at which the interactions occur are characteristic for the individual substances (spectral “fingerprint”), and this forms the basis of qualitative analysis using light. Further, the intensities that are measured in such interactions are closely related to the concentration of the particular substance. Therefore quantitative analysis, which is frequently very accurate, can be performed.

The optical methods of analysis, as well as those based on X-ray transitions (Chap. 5), are of great interest for determinations of the presence and concentration of a very large number of substances. The presence of chemical elements can be determined and molecular identification can also be made. Molecular analysis can be performed by IR absorption spectroscopy and also by XPS (Chap. 5) and NMR (nuclear magnetic resonance) (Chap. 7). We will briefly describe some applications of optical analysis methods.

In the steel industry, as well as in the chemical and pharmaceutical industries, there are clearly many fields of application for analysis techniques. Determinations of haemoglobin and metal concentrations in blood and of glucose, albumin and heavy metals in urine are often performed in the field of medicine. In agriculture, it is of great interest to determine the concentration of certain trace elements in soil samples to assess the need for the addition of fertilizers. It is necessary to measure the concentrations of a large number of substances in the air and water in low concentrations in the area of environmental conservation. Low concentrations are frequently given in ppm (parts per million: 1: 10^6), ppb (parts per billion, 1: 10^9) or ppt (parts per trillion, 1: 10^{12}). Frequently, it is necessary to be able to perform the analysis on quantities as small as 10^{-15} to 10^{-20} g. Using laser-spectroscopic techniques, even single atoms can be detected (Sect. 9.2.7).

The development of analytical methods has been in progress since the beginning of the nineteenth century. J.J. Berzelius (1779–1848) determined the constituents of about 2000 chemical compounds. The periodic table of the elements was put forward by D. Mendeleyev in 1872. At that time only 67 elements were known. By 1900 the number had increased to 83. Even today the number of elements is increasing, approaching $Z = 120$, due to the possibilities at heavy-ion accelerators [644–647].

6.5.1 *The Beer–Lambert Law*

Analysis by optical techniques is frequently performed by measuring absorption. It is important to be able to correctly relate the absorption to the concentration. The relation, which is called the *Beer–Lambert* law, will now be considered. It is named after *A. Beer* and *J.H. Lambert*, who focused on different aspects of the relation. (Sometimes the name of *Bouget* is added to the name of the law, after *P. Bouger*, who was really the first one (1729) to address the issue of how light is absorbed).

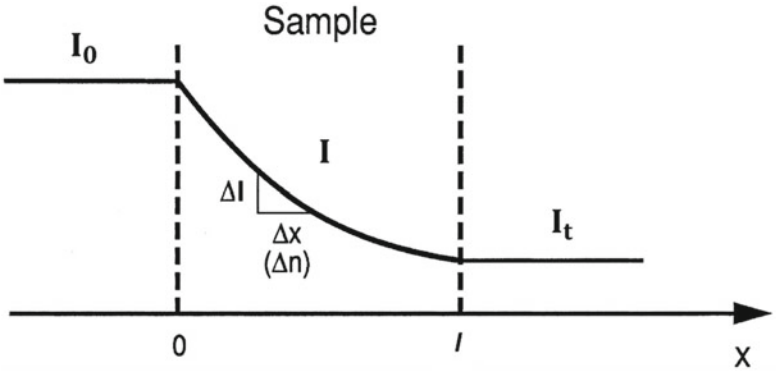

Fig. 6.62 Illustration of the Beer-Lambert law

Consider monochromatic light of intensity I_0 impinging on a sample of thickness l as illustrated in Fig. 6.62.

The sample can be a solution in a cuvette or atoms in a flame from a specially designed burner. An intensity I_t is transmitted through the sample. (We disregard possible effects from the sample confinement). We now consider the conditions over a small interval Δx in the sample. Before the considered space interval, the intensity has been reduced to I, and it will be further reduced by ΔI in the interval Δx. The fractional attenuation $\Delta I/I$ is proportional to the number of absorbers, Δn (i.e., proportional to the concentration c), in the small interval Δx

$$\frac{\Delta I}{I} = -k\Delta x = k_1 c\Delta x. \tag{6.43}$$

Here k and k_1 are constants and the assumption of a uniform concentration c (unit [1/m^3]) throughout the sample is made. The constant k_1 is normally denoted σ, the *cross-section,* with unit [m^2]. We then have $k = \sigma c$. When light passes through the sample, I changes from I_0 to I_t, n from 0 to N, and x from 0 to l. By integration we obtain

$$\int_{I_0}^{I_t} \frac{dI}{I} = -\int_0^N k dn = -\int_0^l \sigma c dx; \quad ln\frac{I_0}{I_t} = kN = \sigma cl;$$

or

$$\frac{I_t}{I_0} = e^{-\sigma cl}. \tag{6.44}$$

In passing we note that this is a similar expression as for, e.g., radioactive decay, or the time-resolved emission from an abruptly excited atomic state. As a matter of fact, all physical processes for which the probability for something to happen next, is independent of what happened before, lead to an exponential function. The expression is clearly non-linear, and is related to the obvious "non-linearity" in nature, that while the amplitude of a signal can grow to almost any value, it cannot be lower than zero! That value is approached with an exponential fall-off in the Beer-Lambert law.

We now define the *absorbance A:*

$$A = log_{10}\frac{I_0}{I_t} = 0.434 ln\frac{I_0}{I_t}. \tag{6.45}$$

Thus

$$A = k_2 c \ (k_2 \text{ is a proportionality constant}). \tag{6.46}$$

This is the essence of the *Beer–Lambert law*, stating that the absorbance is proportional to the concentration of absorbers in the sample.

The ratio I_t/I_0 is defined as the transmittance T. Thus we have

$$A = \log_{10} T^{-1} = 0.434 \ln T^{-1}. \tag{6.47}$$

We note that the absorbance A, and the optical density D, previously introduced (Sect. 6.4.2), are synonymous concepts.

When the focus is on the resulting light attenuation rather than on the specific influence of the cross-section (which is related to the transition probability) or the concentration, we instead use the *absorption coefficient k*, which actually commonly is denoted μ, with $\mu = \sigma c$. Then the Beer-Lambert law (6.44) is instead written

$$\frac{I_t}{I_0} = e^{-\mu l}.$$

This is the equation form usually used, e.g., when considering tissue optics (Sect. 10.5.4).

We will now consider the accuracy of a concentration determined by a measurement of the transmission through the sample. In analytical instruments based on absorption measurements the transmittance or absorbance value is read off directly on a scale or is given digitally. A linear scale for transmittance and a corresponding logarithmic scale for absorbance are given in Fig. 6.63 (compare with Table 6.3). From (6.46) and (6.47) we find

$$\frac{\Delta c}{c} = \frac{\Delta A}{A} = -\frac{0.43}{A}\frac{\Delta T}{T}.$$

The relative accuracy in the concentration determination $\Delta c/c$ depends on the error in reading the scale (or the error in digitizing). Clearly, a small error ΔT in the T reading results in a large uncertainty in the absorbance if T is small (then also $A \cdot T$ is small). In the same way it is important that the full-scale deflection ($T = 100\%$) is suitably set in order to be able to determine small concentrations. If we assume that the uncertainty in the full-scale setting and in measurements is the same, we obtain

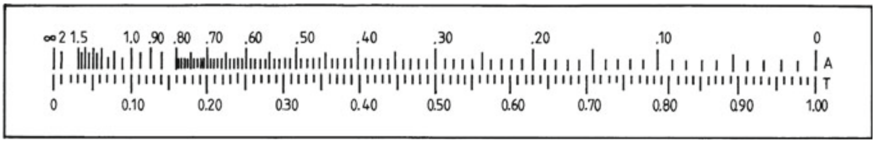

Fig. 6.63 Linear scale for transmittance and corresponding logarithmic scale for absorbance

the resulting relative concentration error by quadratic addition of the errors:

$$\frac{\Delta c}{c} = \frac{\Delta A}{A} = -\frac{0.43}{A}\sqrt{\left(\frac{\Delta T}{T}\right)^2 + \left(\frac{\Delta T}{1}\right)^2} = -\frac{0.43\sqrt{1+T^2}}{AT}\Delta T. \tag{6.48}$$

Hence, the error in the relative concentration depends on ΔT and on the factor $0.43(1 + T^2)^{1/2}/AT$. The variation in this factor as a function of A is given in Fig. 6.64. The factor is large for small and large values of A and has a minimum for $A = 0.48$. The analysis performed above reflects the almost self-evident fact that it is much more difficult to measure accurately a concentration corresponding to very little absorption or very little transmission than to measure it in a situation for which about half of the light is absorbed.

The atoms or molecules in the *ground state* are monitored in *absorption* measurements. In contrast, the *excited-state population* is monitored in *emission* studies. The excitation can be performed in many ways, thermally or in a spark discharge. The intensity of the emitted light clearly depends on the concentration of the substance. If the excitation has been brought about through irradiation with light from an external light source, *fluorescence* light is obtained. The fluorescence light intensity can be directly related to the ground-state population.

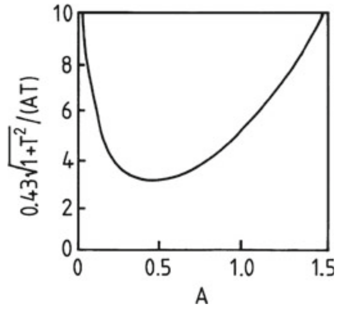

Fig. 6.64 Illustration of error distribution curve

6.5.2 Atomic Absorption/Emission Spectrophotometry

The colouring of flames when a metal salt is introduced was studied as early as in the eighteenth century. In 1860 R. Bunsen and G.R. Kirchhoff established the connections between spectral emission lines and certain elements, i.e., *flame emission spectroscopy* was first used for qualitative analysis. Since then, flame emission spectroscopy techniques have been further developed, including the construction of special burners into which the sample can be injected, and the use of electronic light-measuring equipment. The light emitted by thermally excited atoms is measured. However, only a small fraction of the atoms are excited in the flame, while most of them remain in the ground state. The Boltzmann law describes the relation between the number of excited and ground-state atoms N_{exc} and N_{gr}, respectively:

$$\frac{N_{\mathrm{exc}}}{N_{\mathrm{gr}}} = \frac{g_{\mathrm{exc}}}{g_{\mathrm{gr}}} \mathrm{e}^{-\Delta E/kT}. \tag{6.49}$$

Here g_{exc} and g_{gr} are the statistical weights of the states ($g = 2\,J + 1$ for atomic states characterized by the total electronic angular momentum quantum number J). (This is basically Eq. (4.24) but now formulated more precisely). As an example, at $T = 2500$ K we find for Na with the ground state $3\,s\,{}^2S_{1/2}$ and the first excited state $3p\,{}^2P_{1/2}$ ($\Delta E = 2.1$ eV, $g_{\mathrm{exc}} = g_{\mathrm{gr}} = 2$) that $\frac{N_{\mathrm{exc}}}{N_{\mathrm{gr}}} = 5 \times 10^{-5}$.

The accuracy and sensitivity in a measurement should be improved if the determination were instead based on the large number of ground-state atoms. Relatively speaking, the number of ground-state atoms does not change significantly for a small change in temperature, while, on the other hand, the number of excited-state atoms depends strongly on the temperature. Observations of this kind suggest the introduction of the *atomic absorption method*, which has become a very common standard method for accurate measurements of low concentrations of elements.

Atomic absorption spectroscopy differs from normal spectrophotometry (Sect. 6.5.6) in one important aspect. As we have described before (Sect. 6.1.1), the linewidth of an atomic line is a few thousands of a nm. It is therefore necessary to use a line light source, since a monochromator of reasonable dimensions cannot resolve such a line. With a continuum light source filtered by a monochromator to a passband with a width of a few nm the absorption due to the atoms in the flame would be totally negligible (Fig. 6.65). On the other hand, if a *hollow-cathode lamp* is used, the linewidths for the corresponding element match and strong absorption can be obtained. It should be noted that the Beer-Lambert law is strictly valid only if the line width of the probing light is much smaller than the width of the absorption line.

A monochromator is still necessary, even if a hollow-cathode lamp is used, in order to suppress other lines that do not originate in the ground state. The presence of such lines would clearly dilute the total light absorption by the atoms. Generally, a special hollow-cathode lamp is used for each element to be measured. In certain cases several elements can be combined in one hollow cathode. However, since the

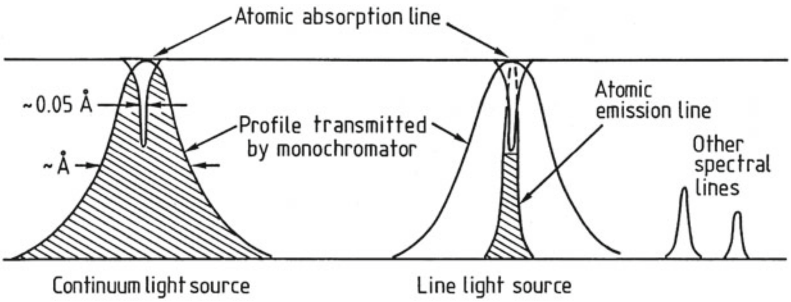

Fig. 6.65 Comparison between the use of a continuum and a line light source in atomic absorption measurements

burning time of a lamp is limited to about 1000 h, the advantage is limited. Instead, provisions for rapidly changing the lamps can be utilized. Suitable spectral lines for atomic absorption spectrophotometry are given in Table 6.4. The lines are generally strong resonance lines from the ground state and in some cases lines originating in metastable states.

Basic set-ups for atomic emission, as well as absorption spectrophotometry are shown in Fig. 6.66. In the absorption mode it is necessary to modulate the output of the lamp, either by modulating the discharge current or by using a mechanical chopper. The signal at the PMT will then consist of a DC contribution due to the thermally excited atoms emitting the line studied and an alternating current (AC) contribution due to the transmitted hollow-cathode light. By detecting the AC component with a frequency and phase-sensitive AC amplifier (*lock-in amplifier*) it is possible to study the absorption without background problems. Frequently, a dual-beam system is used (Fig. 6.67). The light is then intermittently sent through the flame (sample beam) or beside it (reference beam). The two beams are balanced on the lock-in amplifier (zero AC component) for the case of no sample injection into the flame. The presence of atoms to be measured results in an imbalance between the two beams (an AC component), the amplitude of which is proportional to the absorption. Using this method, drifts in the lamp intensity, the sensitivity of the detector and the electronic amplification can be compensated for.

Since the lock-in amplifier technique for retrieving weak signals in the presence of noise is a very common one and will occur in numerous applications described through-out this book, we will now describe the basics of this technique a bit more in detail. We will here focus on the physics aspects, rather than on the electronic techniques and circuitry to isolate and enhance the signal. Our description relates to Fig. 6.68. Generally speaking, the phenomenon we want to detect may be quite weak, and more or less buried in background noise. The fundamental idea behind the lock-in technique is then to modulate the phenomenon of interest, and detect the effect of this modulation in the total signal, by restricting the detection to the pre-selected modulation frequency, and disregarding noise, which occurs at many different frequencies. This is illustrated in Fig. 6.68a, b. Since an important part of

Table 6.4 Suitable lines for atomic absorption spectrophotometry

Element	Wavelength [nm]	Element	Wavelength [nm]
Aluminium	309.3	Neodymium	492.5
Antimony	206.6	Nickel	232.0/341.5
Arsenic	193.7	Niobium	405.9
Barium	553.5	Osmium	290.9
Beryllium	234.9	Palladium	244.8/247.6
Bismuth	223.1/306.8	Platinum	265.9
Boron	249.8	Potassium	766.5
Cadmium	228.8	Praseodymium	495.1
Calcium	422.7	Rhenium	346.0
Caesium	852.1	Rhodium	343.5
Cerium	520.0	Rubidium	780.0
Chromium	357.9	Ruthenium	349.9
Cobalt	240.7	Samarium	429.7
Copper	324.8	Scandium	391.2
Dysprosium	421.2	Selenium	196.0
Erbium	400.8	Silicon	251.6
Europium	459.4	Silver	328.1
Gadolinium	368.4	Sodium	589.0
Gallium	287.4	Strontium	460.7
Germanium	265.2	Tantalum	271.5
Gold	242.8	Tellurium	214.3
Holmium	410.4	Thallium	276.8
Indium	303.9	Thorium	371.9
Iron	248.3	Tin	224.4/233.4
Lanthanum	550.1	Titanium	364.3
Lead	217.0/283.3	Tungsten	255.1
Lithium	670.8	Uranium	358.5
Lutetium	336.0	Vanadium	318.4
Magnesium	285.2	Ytterbium	398.8
Manganese	279.5	Yttrium	410.2
Mercury	253.6	Zinc	213.9

back-ground noise has a *1/f* fall-off with frequency f, it is advantageous to choose a high modulation frequency. Then the signal of interest can be detected in a narrow band around the selected frequency f, as indicated in the b) panel. Here we have access to the full signal, but only very little of the total *1/f* noise distribution (which otherwise would drown the signal) is present—only the noise of frequency occurring accidentally at frequency f. We basically do a frequency tagging of the phenomenon

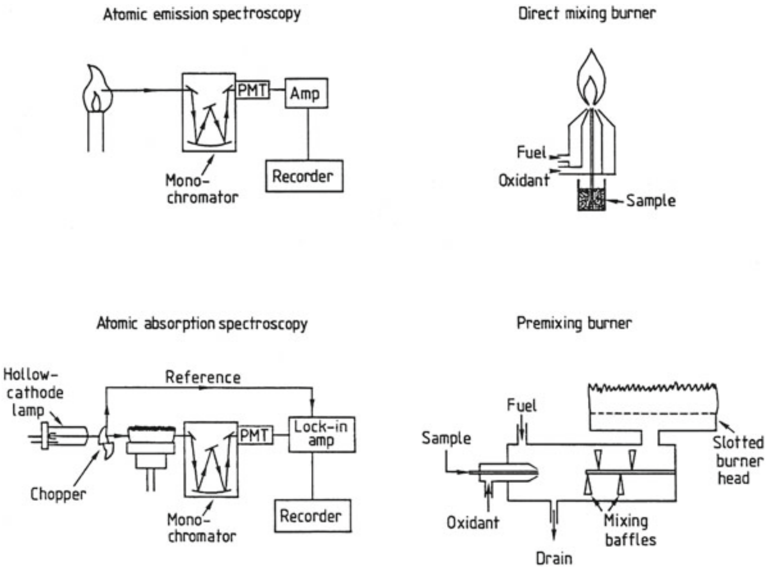
Atomic emission spectroscopy
PMT
Amp
Recorder
Mono-chromator
Direct mixing burner
Fuel
Oxidant
Sample
Atomic absorption spectroscopy
Hollow-cathode lamp
Reference
PMT
Lock-in amp
Recorder
Chopper
Mono-chromator
Premixing burner
Fuel
Sample
Slotted burner head
Oxidant
Mixing baffles
Drain

Fig. 6.66 Basic arrangements for atomic emission and atomic absorption spectrophotometry. Burner arrangements are also shown

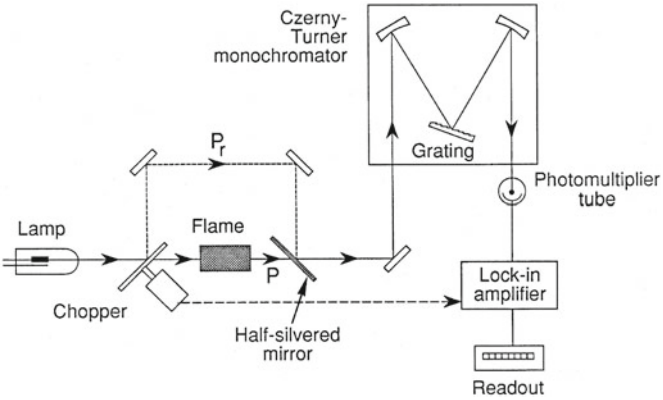
Czerny-Turner monochromator
Grating
P_r
Photomultiplier tube
Lamp
Flame
P
Chopper
Lock-in amplifier
Half-silvered mirror
Readout

Fig. 6.67 A dual-beam spectroscopic system

of interest. Already in Fig. 1.2 we introduced the option of using an agreed-on modulation or perturbation to enhance signal retrieval in the general spectroscopic process.

Panel (a) shows how the chosen frequency is generated inside the lock-in amplifier and is sent to a modulation device, which can influence either the illumination source, L, or the sample, S. We just had examples of modulation of the illumination source in connection with the flame atomic-absorption set-ups shown in Fig. 6.66 (lower

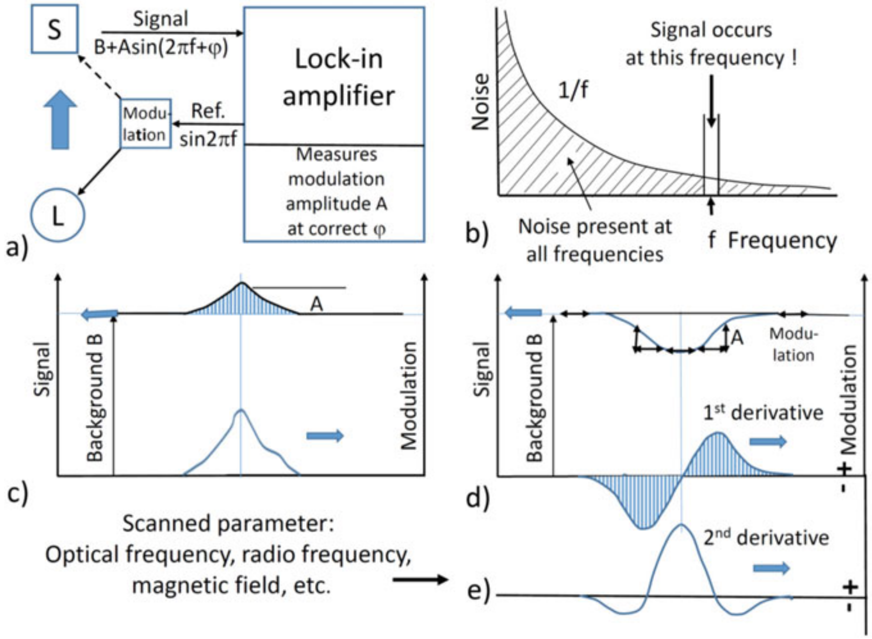
S
Signal
B+Asin(2πf+φ)
Lock-in amplifier
Modulation
Ref.
sin2πf
Measures modulation amplitude A at correct φ
L
a)
Noise
1/f
Signal occurs at this frequency !
b)
Noise present at all frequencies
f Frequency
Signal
Background B
A
Modulation
c)
Scanned parameter:
Optical frequency, radio frequency, magnetic field, etc.
Signal
Background B
A
Modu-lation
1st derivative
Modulation
d)
2nd derivative
e)
+
-

Fig. 6.68 Illustration of the operation of a lock-in amplifier. **a** The instrument generates a reference signal, which controls the modulation unit, and the modulation is imposed either on the light source L or the illuminated sample S. **b** *1/f* noise distribution and its reduction in the narrow window around the chosen modulation frequency *f*. **c** A modulation (AC) component at frequency *f*, on top of the unmodulated background B is generated in the detected signal, and the amplitude of the modulation is displayed as the output of the lock-in amplifier (bottom curve in panel (c). **d** If the controlled variable (laser frequency, magnetic field, etc.) is modulated, an AC component is generated if an intensity slope is encountered, and the modulation amplitude is recorded by the lock-in amplifier as a signal of first derivative character. Since the modulation phase is switched by 180 degrees on passing the center of the detected resonance feature, the amplitude will change sign (bottom curve in panel (d)). **e** If the signal response is non-linear, modulation will also occur at the double frequency (*2f*), then generating a signal, which resembles the second derivative of the original signal

left) and Fig. 6.67. The light of the hollow-cathode lamp is chopped on and off at the frequency f, and by this tagging the intensity of this light can then be isolated from the heavy light background B from the flame, which has no modulation. The modulated light will have a particular and constant phase shift φ with regard to the reference signal, which is generated by the lock-in amplifier. This phase-shift is specific for the set-up and phenomenon studied, and the lock-in amplifier, in addition to isolate the signal with the correct frequency, also is set to amplify the signal with the correct phase—again, noise has random phases, and is again discriminated against. The lock-in amplifier can thus be seen as a frequency- and phase-sensitive amplifier.

The modulation can also be performed directly in the illuminated sample. This is done, e.g., in connection with radiofrequency spectroscopy (Chap. 7), where the influence of a radiofrequency field on the fluorescence from atoms is studied when the rf power is periodically switched on and off, then changing the angular distribution of the light, which results in an AC component. When the radiofrequency is swept through the atomic resonance corresponding to, e.g., a fine- or hyperfine structure splitting, a modulation in the fluorescence light is only seen on-resonance—otherwise the light is not modulated. This is illustrated in panel (c). The amplitude of the modulated light (i.e., the output signal from the lock-in amplifier) is then plotted as a function of frequency to show the resonance curve, peaking at a specific frequency and having a half-width related to the excited-state lifetime.

We may also modulate the frequency of a tunable laser to observe the modulation when passing through a weak absorptive feature of a gas, as discussed in Sects. 10.2.2 and 10.5.4.5, or we may modulate a magnetic field when ramping up the field to pass through atomic coherence phenomena called level-crossings, as discussed in Sect. 7.1.5. Now we refer to panel (d). The modulation of the parameter swept (laser frequency, or magnetic field) will result in no induced modulation in the output signal, as long as there is no slope of the measured intensity. However, at resonance, the symmetric dip in the intensity will result in a derivative-shaped AC component due to the modulation, and the signal will change sign (corresponding to a phase shift of 180°) on passing through the central frequency (positive and negative slope, respectively). Finally, if the signal response to the modulation is non-linear, we may also observe a modulation signal at the double modulation frequency ($2f$), and now it will have a shape resembling the second deriviative of the original curve ("the slope of the slope") as shown in e). We will frequently see examples of this line shape in connection with diode laser spectroscopy, presented in Chap. 10. It should be noted, that perfect derivative shapes are only obtained for infinitely small modulations (Cf. $\Delta y/\Delta x \rightarrow dy/dx$). However, then the induced modulation (the useful signal we want to detect) will also disappear!

6.5.3 Burners, Flames, Sample Preparation and Measurements

Two types of burners are used for flame spectrometry—direct-mixing burners and premixing burners. The gas and the oxidant are mixed immediately before ignition at the burner mouth in the former type. The sample, which is kept as a water solution, is sucked into the flame through a thin tube. In contrast, in premixing burners the gases are mixed in a chamber into which the sample solution is also sprayed. The latter type of burner normally has a slit-shaped head of about 10 cm in length, yielding a long absorption path through the laminar flame obtained with this type of burner. Any gas mixtures can be used in direct-mixing burners while only gas combinations with a burning velocity slower than the gas flow velocity out of the burner can be used in premixing burners to avoid flash-back. This eliminates the hot acetylene/oxygen flame (3100 °C), while acetylene/air (2200 °C) and acetylene/N_2O

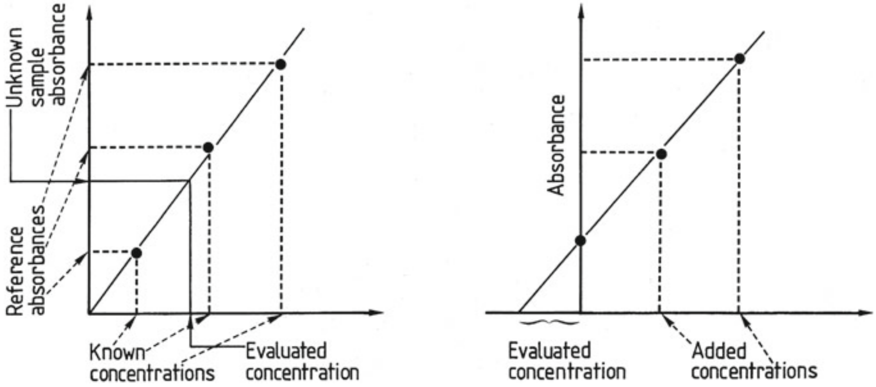

Fig. 6.69 Illustration of concentration evaluations using standard solutions and the standard-addition method

(2800 °C) can readily be used. The small sample droplets are dried in the flame and then the salt particles are dissociated into free atoms. The flame temperature must be chosen in a trade-off between the desired high degree of molecular dissociation and undesired atomic ionization, the latter leading to a reduction in the signal. Practical measurements are performed with water solutions containing the sample which has been dissolved, sometimes using an acid. The measurements are performed by comparing the sample solution with standard solutions of known concentrations. Using a number of such standards a calibration curve, which should exhibit linearity in absorbance versus concentration, see Eq. (6.46), is obtained. Another possibility is to add known amounts of an element to the sample solution and observe the increase in absorbance ("standard addition method"). Sensitivities obtained are frequently in the ppb region. The use of these techniques is illustrated in Fig. 6.69.

6.5.4 *Modified Methods of Atomization*

In burners of the types discussed above only about 20% of the solution is atomized while the rest is lost due to the formation of large droplets that are drained away. Further, the concentration in the flame at any one time is low because of the continuous aspiration of the sample solution. A number of techniques have been developed, in which the whole sample is vaporized, at the same time yielding a stronger, transient absorption peak. In the *graphite oven* technique, the sample is injected into an electrically heated graphite tube through which inert gas is flowing, as indicated in Fig. 6.70. The heating is performed in three steps. First the sample is dried at a low temperature. Then it is ashed at a higher temperature and is finally evaporated as the heating current is further increased. The measurement is performed during the third stage while the vaporized sample remains in the oven.

Fig. 6.70 Graphite oven vaporization of analytical samples

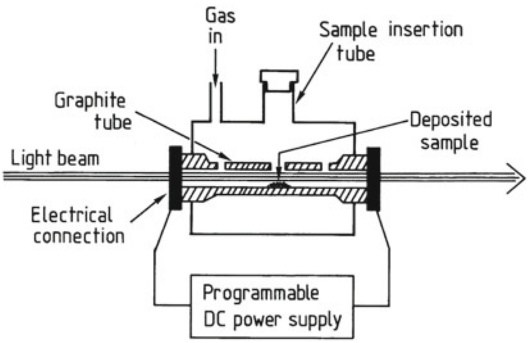
Gas in
Sample insertion tube
Graphite tube
Deposited sample
Light beam
Electrical connection
Programmable DC power supply

As compromises between flame and flameless atomization techniques, the Delves cup and sample boat methods have been developed (Fig. 6.71). In the first of these two techniques the sample is kept in a small cup made of nickel. It is introduced into the flame of an ordinary atomic absorption slit burner. The sample is vaporized and the vapour passes through a hole into a nickel tube that is mounted horizontally in the flame above the cup. The whole sample is used for the measurement and is present at the same time in the light path. In the sample boat technique, the sample is placed in an elongated "boat" made of tantalum. The sample is brought into the flame just below the light path and an absorption peak is recorded for a short time. The modified methods of atomization discussed above allow the detection limit for many elements to be lowered by 1–4 orders of magnitude.

Atomic absorption and emission techniques have been discussed in [648–651].

An interesting variety is used for measuring low concentrations of atmospheric atomic mercury. Since background concentrations are as low as few ng/m^3, (on the ppt level) a large volume of air is pumped through a plug made of gold film to produce a large area, on which all mercury is amalgamated. The plug is then transiently heated and the "puff" of mercury gas is then recorded by absorption of the 253.7 nm $^3P_1$–$^1S_0$ line emitted from a mercury lamp, or, more frequently, by observing mercury fluorescence as excited by the mercury lamp. It may be easier to observe a weak fluorescence arising from a zero back-ground, instead of detecting a minute intensity

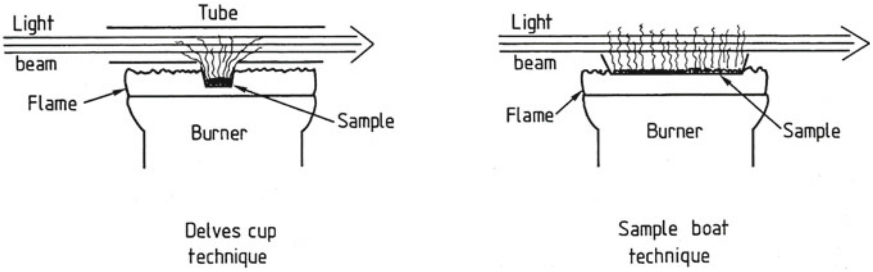
Light beam
Tube
Flame
Burner
Sample
Delves cup technique
Light beam
Flame
Burner
Sample
Sample boat technique

Fig. 6.71 Delves cup and sample-boat arrangements

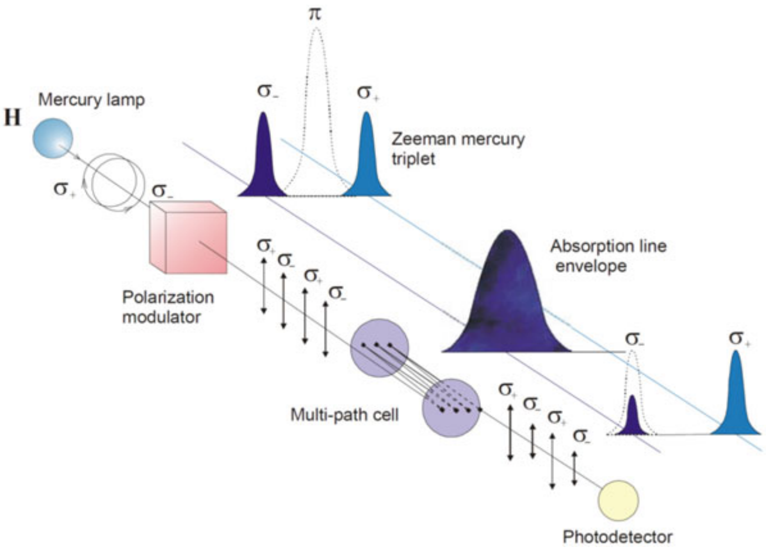

Fig. 6.72 Operation principle of a mercury gas analyzer based on the Zeeman modulation technique. A mercury lamp, emitting the 253.7 nm $^3P_1$–$^1S_0$ line is placed in a strong permanent magnetic field, and two Zeeman-shifted line components are differentially absorbed by the gas sample under study (Courtesy: LUMEX, St. Petersburg)

reduction due to absorption. Calibration is provided by instead pumping gas from a container containing some liquid mercury of precisely known temperature, where the known saturation pressure of the metal has been established (precision reading of a curve of the type shown in Fig. 7.2).

In a further, extremely sensitive approach, the Zeeman effect is used to modulate the mercury line absorption [652]. The principle is illustrated in Fig. 6.72. A mercury lamp, containing a separated isotope of mercury, with a large isotope shift (Sect. 2.8) is placed in a strong magnetic field so the mercury emission line 6s6p $^3P_1$–6s^2 $^1S_0$ is split up in three components corresponding to $\Delta M = 0, \pm 1$, i.e., a π, a σ^+, and a σ^- component. In one of the magnetic poles there is a hole, where only the σ components can emerge, in the magnetic field direction (see Figs. 4.9 and 7.10). Because of the large isotopic shift with regard to the main, pressure-broadened composite mercury absorption line (see also Fig. 10.22), one of the σ components of the lamp, passing through the multi-pass absorption cell is, due to the Zeeman shift, moved into mercury gas absorption, while the other component falls outside the composite absorption line. The two σ line components are emitted with equal intensity from the lamp, so in the absence of mercury in the cell the detector sees equal intensities for the two σ components. However, this is not the case if mercury is present. In order to allow the detector to monitor the two components separately, a polarization modulator (a quarter-wave plate placed before a rotating linear polarizer) is inserted in the illumination beam. A frequency and phase-sensitive (lock-in) amplifier (Fig. 6.68) is used to detect minor modulation of the intensity due to the gas absorption. The measurement approach is of the gas correlation type, which is further discussed in Sect. 6.6.1.

6.5.5 *Multi-element Analysis*

It is frequently desirable to be able to determine the concentration of several elements simultaneously. Atomic absorption is then impractical, since different hollow-cathode lamps are required. Clearly, the atomic emission method is more suitable. However, a drawback with this technique is that thermal excitation in a flame is relatively poor, but alternative methods of excitation can be used. For a long time arcs or sparks have been used in metallurgical analysis. In this case the sample, which must be solid, forms one of the electrodes.

In order to eliminate the drawback of being limited to solid samples, a different type of excitation source, the *Inductively Coupled Plasma (ICP)* source, has been developed. The working principle for this source is illustrated in Fig. 6.73. Three concentric quartz tubes carry flowing gases. An inductance coil fed by an RF generator is placed around the upper end of the outer tube. In the oscillating field argon gas flowing out between the outer and middle tube will be ionized and forms a plasma at a temperature in the 5,000–10,000 K range. Some argon gas also flows between the inner and middle tubes to stabilize the plasma and prevent it from coming into contact with the inner tubes. When the sample is introduced, as fine droplets in the argon stream through the inner tube, complete atomization and efficient thermal excitation are obtained in the hot plasma.

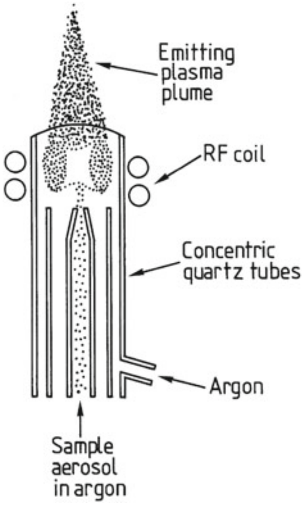

Fig. 6.73 Principle of the inductively coupled plasma source

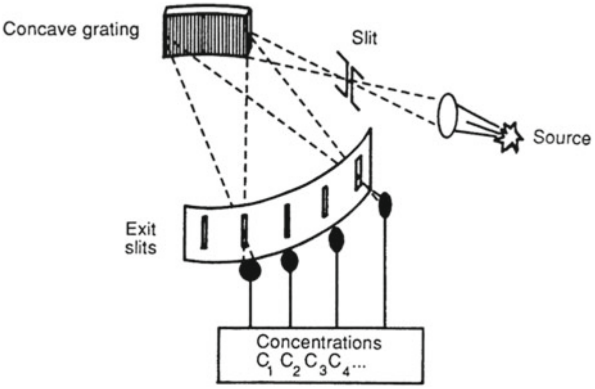

Fig. 6.74 System for multi-element analysis

The light emitted from the excitation source is dispersed and recorded by multiple photodetectors placed behind suitably located exit slits (Fig. 6.74). Fibre-optical techniques can also be used to collect light at a suitable location in the spectrometer focal plane for transmission to a battery of PMTs. Calibration can be provided using standard solutions or standard electrodes. Using a computer-controlled data collection system the concentrations of the selected elements can be printed out shortly after the introduction of the sample. A complete system frequently incorporates means for automatic sample exchange.

6.5.6 Molecular Spectrophotometry

The absorption of a molecular sample (gas, liquid or solid) can be measured in a spectrophotometer as a function of the wavelength. The absorption normally occurs in bands that are not too narrow and therefore a continuum light source can be used in connection with a spectral resolving apparatus, which is normally a grating monochromator but can also be a Fourier transform spectrometer [653, 654]. Spectrophotometers based on grating monochromators are frequently of the dual-beam type, with one beam passing the sample cell and the other one a reference (empty) cell of the same type before the transmitted intensities are compared at the detector. The layout for such an instrument is shown in Fig. 6.75.

Instruments are normally designed for the UV/visible region or the IR region. Tungsten or deuterium lamps (Sect. 6.1.2) are used in the former types of instruments while, for example, a Nernst glower, is employed in the IR region. Correspondingly, PMTs or PbS cells are used as detectors.

The sample to be studied in the spectrophotometer can be solid, liquid or gaseous. Liquids are investigated in cells or cuvettes made of quartz ($\lambda < 3\ \mu m$) or NaCl ($3\ \mu m < \lambda < 15\ \mu m$). The cell walls and the solvent will affect the measurements, and to

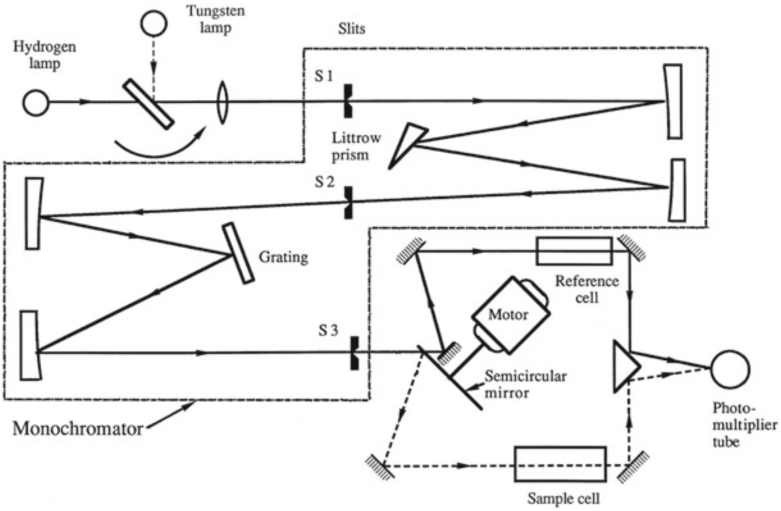

Fig. 6.75 Spectrophotometer of the dual-beam type [650]

correct for these effects a reference cell of the same kind filled with the same solvent but without the sample molecules is used.

The transmittance can then be written

$$T = \frac{I_{solution}}{I_{solvent}} \cong \frac{I}{I_0} \tag{6.50}$$

Commonly used solvents are carbon disulphide CS_2 (7.5–16 μm) and carbon tetrachloride CCl_4 (2.5–7.5 μm). If highly absorbing solvents are used the length of the cell must be kept short, e.g., 0.01 mm. Solids that cannot be dissolved are ground into fine particles (<2 μm) that are suspended in an oil.

Most inorganic and organic compounds in the liquid or solid phase give rise to broad absorption peaks. Exceptions are ions of the lanthanides and actinides that have sharp, well-defined peaks in the UV and visible regions. The peaks are due to transitions of the optically active 4*f* or 5*f* electrons that are shielded by external electrons (see Table 2.2, Sects. 4.9 and 8.4.2). Gaseous samples investigated in multipass cells give very sharp absorption features with corresponding demands on spectral resolution. An especially valuable device for gas studies is the *White cell* [655, 656], for which multiple reflections can be used to achieve an effective absorption path of more than 100 m even if the physical length of the cell is only 1 to 2 m. The optical arrangement in a White cell is illustrated in Fig. 6.76.

Extended path lengths for absorption spectroscopy can also be obtained by using more undefined scattering in an *integrating sphere* with highly reflecting walls [658,

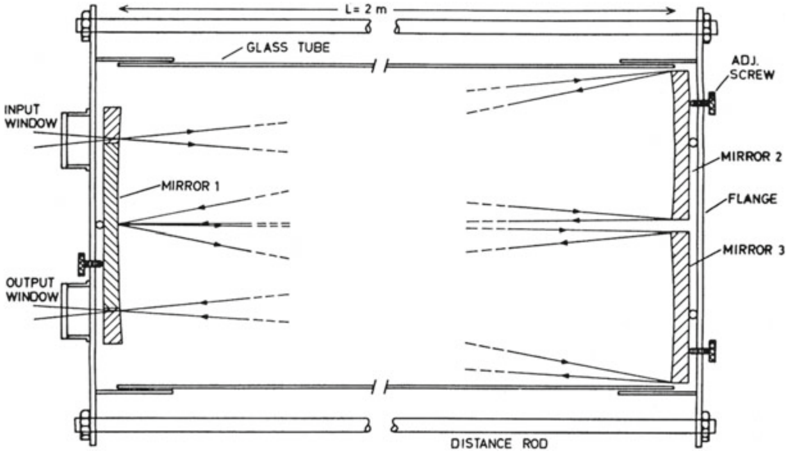

Fig. 6.76 Optical arrangement for a White cell [657]

659] or by using a strongly scattering porous medium, where a very long effective pathlength can be achieved in gas in scattering media absorption spectroscopy (GASMAS) experiments [660, 661], to be further discussed in Sect. 10.5.4.5.

Spectrophotometry in the UV/visible/IR regions can be used for qualitative as well as quantitative analysis. Qualitative analysis is performed by empirically comparing measured spectra with reference spectra that have been catalogued for a large number of compounds [662–666]. Multi-variate methods are convenient in the disentanglement for complex spectra containing multiple species [667, 668]; see also Sect. 10.3.2. For quantitative analysis the same principles as those used in atomic absorption spectrometry are utilized. The structures observed in the IR region are due to vibrational transitions. These give rise to rather sharp spectral features, even for liquids and solids, in comparison with those obtained for normal electronic transitions observed in the UV/visible regions. The rotational motion is quenched and thus only broadened vibrational transitions are observed. In a complicated molecule many fundamental frequencies, corresponding to different atomic groups, are obtained (Sect. 3.4). This facilitates the identification of substances. Examples of characteristic frequencies are given in Table 6.5. Small shifts occur in the characteristic group frequencies related to how large the rest of the molecule is. The concept of reduced mass here comes to mind (Sect. 2.8). As an analogy, we may consider a dog waving its tail! The process will react back on the body; to different extent depending on the relative weight of the body and the tail. Two examples of IR absorption spectra are given in Fig. 6.77.

Table 6.5 Characteristic bond-stretching vibration frequencies of certain molecular groups

Group	Wave number [cm^{-1}]	Group	Wave number [cm^{-1}]	Group	Wave number [cm^{-1}]
≡C−H	3300	>N−H	3350	≥C−C≤	900
=C−H	3020	>C=O	1700	≥C−F	1100
		−C≡N	2100	≥C−Cl	650
≥C−H	2960	−C≡C−	2050	≥C−Br	560
−O−H	3680(gas) 3400(liquid)	>C=C<	1650	≥C−I	500

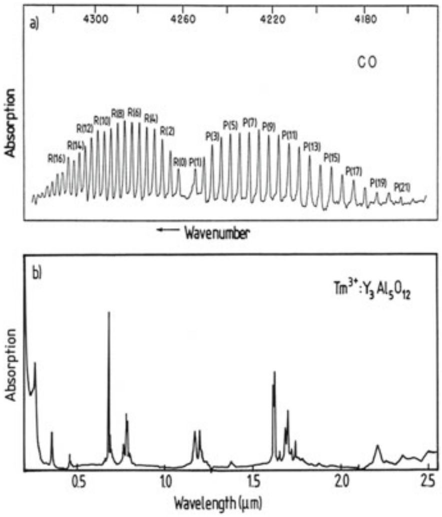

Fig. 6.77 Two examples of IR absorption spectra: **a** carbon monoxide gas [669]; **b** thulium ions in a crystalline matrix [670]. This is a good example of the appearance of sharp spectral lines in condensed matter, caused by the shielding of the optically active 4f electrons in rare-earth atoms (Table 2.2)

6.5.7 *Raman Spectroscopy*

As we have previously noted, Raman spectroscopy is complementary to IR spectroscopy. A special feature of Raman spectroscopy is that molecules without a dipole moment can be investigated, e.g., H_2, N_2, and O_2. In early Raman spectroscopy measurements a strong Hg lamp was used as a light source. An Ar^+ laser (Sect. 8.4.5) with an output power of several watts in a single line (normally 514.5 or 488.0 nm) has been common in commercial instruments, while now being replaced by solid-state CW lasers. The light scattered from the sample is analysed with a spectrometer.

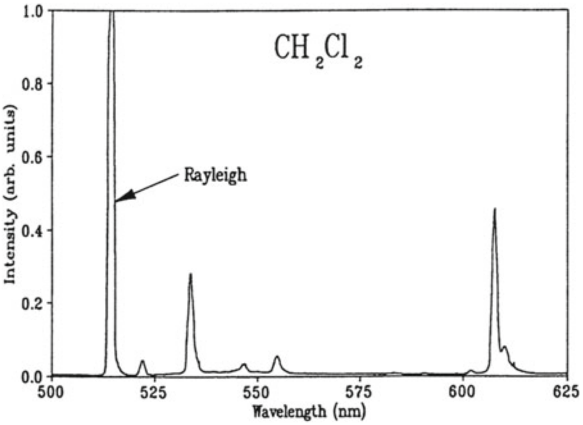

Fig. 6.78 Raman spectrum of liquid CH_2Cl_2 obtained using an argon-ion laser emitting at 515 nm [677]

Normally, a double or a triple spectrometer is used, since it is of utmost importance to suppress the intense Rayleigh-scattered light. Specifically designed dielectric-layer filters, which fully transmit the surrounding wavelengths but strongly reject the laser wavelengths (notch filters) are also very helpful in Raman spectroscopy. The polarization of the Raman-scattered light can give valuable additional information on the structure of the investigated molecules. In Raman spectroscopy it is important to work with pure substances in order to avoid the masking of weak Raman components by broadband fluorescence from impurities. (The Stokes components are on the same side of the exciting line as the red-shifted fluorescence light). Raman techniques have been discussed in [671–676].

As an example of a Raman spectrum from a liquid a recording for CH_2Cl_2 is shown in Fig. 6.78. Raman spectra for gases will be discussed in Sect. 10.1.3.

The Raman scattering can be enhanced by a factor of the order of 10^6 if the exciting line coincides with an allowed electronic transition (*resonance Raman effect*). Several types of *coherent Raman spectroscopy* [678] have been introduced in recent years, e.g., *coherent anti-Stokes Raman spectroscopy* (CARS) (Sects. 8.6 and 10.1.4) and *Raman gain spectroscopy*. Raman spectroscopy has attained a strong position also in biomedical diagnostic research, as further discussed in Sect. 10.5.3.

6.6 Optical Remote Sensing

We have in the previous section described how optical spectroscopy can be used to analyse samples in the laboratory. We will now describe how spectroscopy can provide information on the environment by performing measurements at a distance. *Remote sensing* is a general term used for techniques by means of which information on physical or chemical conditions at a spatially remote location can be gained using suitable equipment. The possibility of quickly changing the object of study

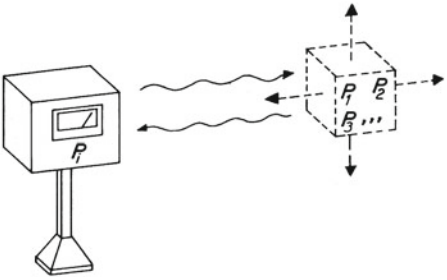

Fig. 6.79 Principle of remote sensing [679]

is included in the concept of remote sensing. The principle of remote sensing is illustrated in Fig. 6.79. By means of electromagnetic waves, the remote-sensing equipment (generally called the *sensor*) is in contact with the spatially separated measurement volume, which is characterized by parameters P_1, P_2, $P_{3,}$ etc. Using the sensor, the value of a certain parameter, P_i, in the measurement volume can be read off. The measurement process involves an analysis of the radiation reaching the sensor from the object and can be characterized as a type of applied molecular spectroscopy [680].

Remote sensing can be performed using *passive* or *active* techniques. While changes in the spectral distribution of the background radiation (e.g., sunlight) are analysed using passive techniques, changes in the radiation transmitted by the equipment, due to interactions with the measurement volume, are studied in active techniques. These concepts can be illustrated by a simple example:

In colour photography of a sunlit object the absorption and reflection properties (the colour) of the object can be assessed knowing the spectral composition of the sun radiation and the colour sensitivity of the film or digital detector. The image constitutes a remote sensing recording using passive techniques. If instead the object had been photographed in a dark room using a flashlight with a certain spectral distribution (frequently simulating that of sunlight), an active recording would have been obtained. This example illustrates that remote sensing is a very general concept. The information obtained can be of different kinds: geometrical information (maps), natural resources, meteorological information or concentrations of atmospheric pollutants.

Remote-sensing systems can be mounted on different platforms depending on the type of measuring task. A sensor mounted on a satellite can have global coverage. Many of the numerous satellites that orbit the earth are equipped with sensors for monitoring meteorological conditions, earth resources or for military surveillance. Examples of series of satellites transmitting their information to ground-receiving stations via microwave links are TIROS, LANDSAT, SPOT, IRS etc. Airborne sensors or mobile land systems can be used for regional remote sensing. Finally, fixed systems are suitable for monitoring urban or industrial areas.

Different passive and active remote-sensing techniques are illustrated in Fig. 6.80. The selective reflection of solar radiation from the earth's surface, the absorption or the thermal emission of the atmosphere can be studied with passive techniques. Active

Fig. 6.80 Passive and active remote sensing techniques [681]

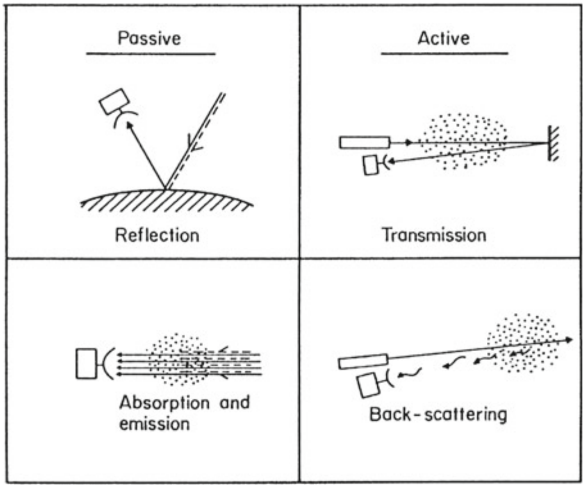

techniques frequently make use of laser or microwave radiation. The transmission or scattering of such radiation can yield information on the atmosphere or the land and sea surface.

6.6.1 Atmospheric Monitoring with Passive Techniques

Some passive atmospheric monitoring techniques will be discussed here, while active techniques for such purposes will be described in Chap. 10. The general principle of passive atmospheric monitoring is illustrated in Fig. 6.81. The absorption of the sun's or sky's radiation, caused by atmospheric constituents, can be measured using a suitable spectrometer. The observed frequencies of absorption are used for gas identification, and the strengths of the absorption lines determine the concentration of absorbing molecules according to the Beer–Lambert law (Sect. 6.5.1). If the absorption coefficient $\sigma(\nu)$ of the gas is known from laboratory measurements, the total number of absorbing molecules can be determined from the ratio between the received radiation intensity $P_t(\nu)$ and the original intensity $P_0(\nu)$. If $N(r)$ is the molecular concentration at the range r we have

$$\frac{P_t(\nu)}{P_0(\nu)} = \exp\left[-\sigma(\nu)\int_0^\infty N(r)\mathrm{d}r\right]. \tag{6.51}$$

Thus, range-resolved concentrations cannot normally be obtained using passive techniques since the path of absorption is undefined. If there is a temperature inversion in the atmosphere, no mixing occurs through the inversion layer and a value for the

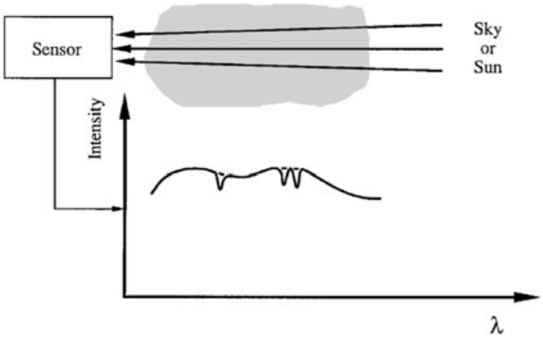

Fig. 6.81 Principle of passive atmospheric monitoring [681]

average concentration up to the inversion layer can be obtained in vertical measurements. Using satellites, absorption measurements can be made at sunrise and sunset through varying thicknesses of the atmosphere (“limb” absorption) (Fig. 6.82). By carefully measuring the line shape of absorption lines it is possible to determine a vertical concentration profile through a deconvolution procedure, taking the pressure broadening (Sect. 6.1.1) at different heights into account [682, 683] (Sect. 10.2.1). Grating, Fourier transform or heterodyne spectrometers can be used to analyse the spectral distribution. Ground-based monitoring against the sun or moon disc can also be performed [684].

Satellites have been extremely useful in studying the development of the ozone holes in polar regions (see Sect. 6.4.5). Apart from limb absorption measurements, direct observation of light backscattering from the atmosphere in combination with extensive modelling can be used. Gases such as CH_4 and NO_2 can also be monitored on the global scale. Methane emissions, e.g., from rice paddies in South East Asia are important in global warming assessment. Nitrogen dioxide is closely connected to car traffic. Interestingly, and also astonishing, such mappings reveil weakly activities, which clearly are related to the occurrence of the “week-end”, which is different for different religions (Sunday, Friday, and Saturday for Christians, Muslims and Jews, respectively). Data of this kind are shown in Fig. 6.83 [685, 686].

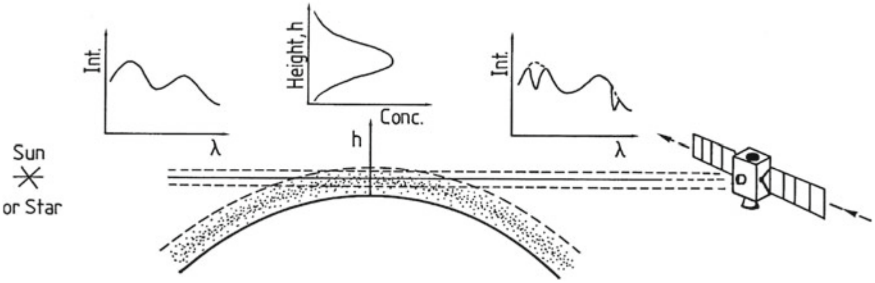

Fig. 6.82 Limb absorption measurements from a satellite

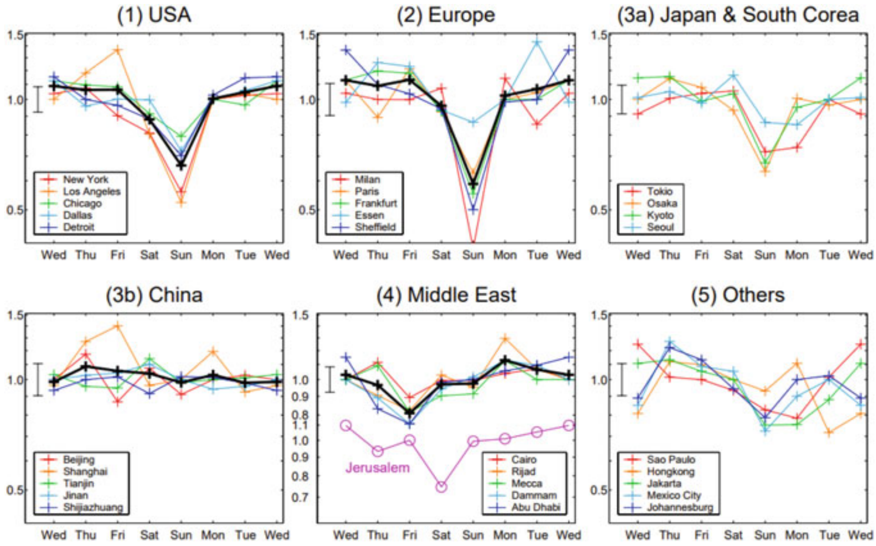

Fig. 6.83 Concentration of NO_2 on different weekdays for different regions as measured with the GOME satellite ([685], reproduced under the Creative Commons Attribution 4.0 License, CC BY 4.0)

A special problem in optical atmospheric monitoring is the ever-present turbulence of the air that makes the recorded light intensity vary substantially(hence the “twinkling” of the stars). However, the amplitude of such fluctuations is negligible for frequencies above 100 Hz. This observation calls for the registration of certain small wavelength regions with peaks and valleys in a time of the order of 10 ms, if small net absorptions are to be detected. This can be performed by exchanging the fixed exit slit of the spectrometer for a rotating disc with radial slits scanning the spectrum in front of a sufficiently large detector surface (e.g., a 5 cm diameter PMT). To ensure a good signal-to-noise ratio thousands of individual scans can be added in a computer, allowing absorption features as small as 0.01 percent to be detected. With such a sensitivity not only common air pollutants can be detected but also the presence of various low-concentration atmospheric radicals such as HONO and NO_3. This technique is normally combined with the use of a distant artificial continuum light source such as a high-pressure xenon lamp (Sect. 6.1.2). The technique is then normally referred to as *doas* (*d*ifferential *o*ptical *a*bsorption *s*pectroscopy) [687–693]. The same effect can be obtained by simultaneously recording a high-resolution spectrum and a low-resolution (normalizing) spectrum using a spectrometer with dual output slits and then dividing one signal by the other [694]. A doas set-up for urban pollution monitoring is shown in the upper part of Fig. 6.84 and its use for sulphur dioxide measurements is illustrated in four panels in the middle part of the figure [691]. In panel (a) the spectral distribution of a xenon lamp 2 km away is recorded in the wavelength region 280–320 nm after the light has passed through the city atmosphere. The small absorption features around 300 nm are magnified in panel

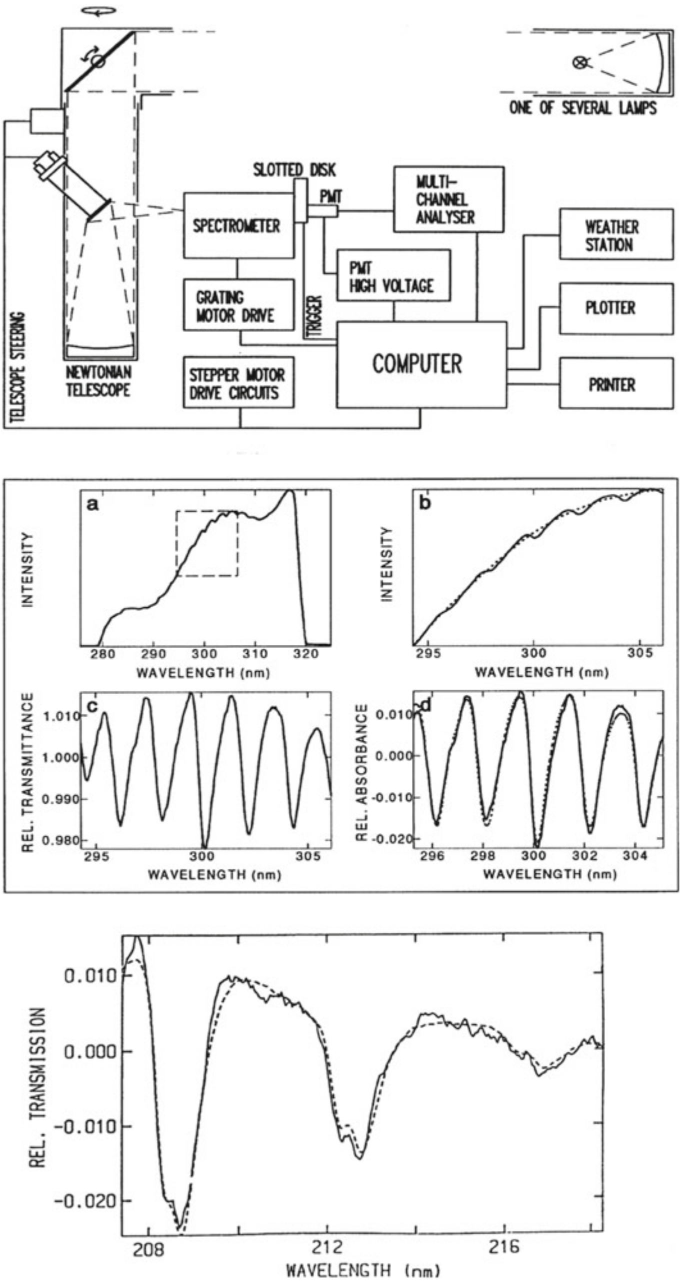
ONE OF SEVERAL LAMPS
SLOTTED DISK
PMT
MULTI-CHANNEL ANALYSER
SPECTROMETER
WEATHER STATION
PMT HIGH VOLTAGE
GRATING MOTOR DRIVE
TRIGGER
PLOTTER
COMPUTER
PRINTER
STEPPER MOTOR DRIVE CIRCUITS
NEWTONIAN TELESCOPE
TELESCOPE STEERING
a
INTENSITY
280 290 300 310 320
WAVELENGTH (nm)
b
INTENSITY
295 300 305
WAVELENGTH (nm)
c
REL. TRANSMITTANCE
1.010 1.000 0.990 0.980
295 300 305
WAVELENGTH (nm)
d
REL. ABSORBANCE
0.010 0.000 -0.010 -0.020
296 298 300 302 304
WAVELENGTH (nm)
REL. TRANSMISSION
0.010 0.000 -0.010 -0.020
208 212 216
WAVELENGTH (nm)

Fig. 6.84 *Top*: Set-up for doas spectroscopy. *Middle*: Measurement example with signals due to an average concentration of 4 ppb of SO_2 over 2000 m [691]. *Bottom*: Atmospheric NH_3 spectrum recorded with a doas system over a 265 path 2 m above a meadow in a rural area [690]

(b), where a 5th order polynomial (not being able to follow the fast undulations) is also fitted to the spectrum. In panel (c) the atmospheric spectrum is divided by the fitted curve to give a spectrum normalized to the case of a lamp with equal and constant intensity spectral distribution. Finally, in panel (d) a laboratory spectrum for sulphur dioxide (dashed curve) is fitted and we observe an almost perfect fit in a logarithmic representation. An average mixing ratio of 4 ppb is evaluated. In the lower part of the figure experimental doas data for ammonia are shown [690]. Again, a laboratory spectrum has been fitted. The NH_3 molecule absorbs at around 210 nm, where the lamp intensity is quite low and where atmospheric scattering also strongly attenuates the beam.

The doas technique can also be employed using sky radiation (scattered sunlight) as the (passive) light source. In Fig. 6.85 the vertically recorded sky spectrum at the side (b) and below (a) the volcanic plume of Mt. Etna is shown [695], together with a (logarithmic) curve obtained when dividing the two curves by each other. The SO_2 spectral signature clearly emerges as demonstrated by the almost perfect fit to a laboratory spectrum (see also Fig. 6.84 (*middle*)). Since the atmospheric scattering is complex and occurs not only above the plume but also inside and below, the calculation of the gas column involves some corrections (see also Sect. 10.2.3.1). A complex Fraunhofer line pattern intermingled with major atmospheric species absorption features is shown in Fig. 6.85. The cut-off towards shorter wavelengths at about 300 nm due to the stratospheric ozone! It should be noted that with the improvement of CCD/CMOS imaging detectors, “flying-slit” arrangements can be replaced.

Instruments called *correlation spectrometers* can also be used for passive gas analysis. In these systems a spectrum stored in the instrument is compared (correlated) with the spectrum of the incoming light and a signal that is proportional to the number of absorbing molecules of a particular kind is generated. The correlation can be performed in different ways. In a dispersive, photoelectrically recording spectrometer a metal mask with slits made for the lines of a particular gas can be vibrated back and forth in the image plane and the AC component of the transmitted intensity can be recorded (Fig. 6.86). If the light does not exhibit the particular lines there will be no correlation, but if the lines are present, systematic increases and decreases in the transmitted intensity are obtained when the mask is moved, and the signal is picked up by a lock-in amplifier (Fig. 6.68). The mask pattern can be made as concentric rings deposited on a round quartz disc that is rotated in the focal plane. For half the circumference the pattern is slightly displaced from the expected spectral lines [696].

In a different type of instrument a gas cell is instead used for the correlation [697–700]. A *gas correlation spectrometer* is shown in Fig. 6.87. The incoming light is alternatingly sent through a cell containing the gas to be studied at such a high concentration that little or no light can pass at the absorption wavelengths, and through an empty reference cell. For the case of no external gas a gray wedge (continuously graded neutral density filter) is adjusted so that equal intensities are obtained through both spectrometer channels in a particular passband isolated by a filter. Now, if an external pollution cloud is present, the signal through the gas

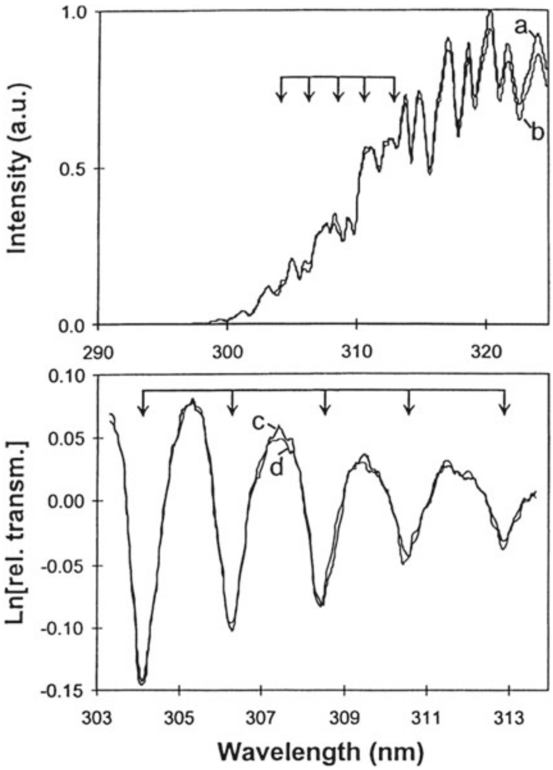

Fig. 6.85 Passive doas recording using blue sky radiation as the illumination source. Sky spectra recorded through the volcanic plume of Mt. Etna (**a**) and at the side of the plume (**b**) are shown together with a divided spectrum (**c**) clearly showing the SO_2 signature matching the calibration spectrum (**d**) [695]

correlation cell is not affected, since no higher absorption than full absorption, already accomplished, can be obtained. On the other hand, the light through the reference channel is reduced due to the absorption lines of the cloud. Thus an imbalance is recorded at the initially balanced lock-in detector (Fig. 6.68). For calibration purposes a cell with a known (concentration × length)-value can be inserted in the light path in front of the correlation spectrometer.

The gas correlation concept can be extended to the case of imaging, where images are recorded both through a gas cell and directly [701–703]. By subtracting or dividing the images pixel by pixel, only the areas of the scene affected by specific gas absorption will be separated out. Since most gases have their absorption in the IR region, an IR camera operating in a scanning mode with a single detector ("thermovision") or with an IR CCD is employed (Sect. 6.3). It should be noticed that the gas cell provides a "holistic" perfect match to the spectrum of the gas to be studied, and that all pixels in the image are simultaneously "processed", with no additional complexity over a single-channel recording.

Application in the gas and petroleum industry are relevant, e.g., detecting gas leaks at refineries or at oil platforms to avoid explosions.

The background distributed radiation source (the sky, walls, ground or an artificial heat blanket) must have a different temperature than the gas to be imaged (see also

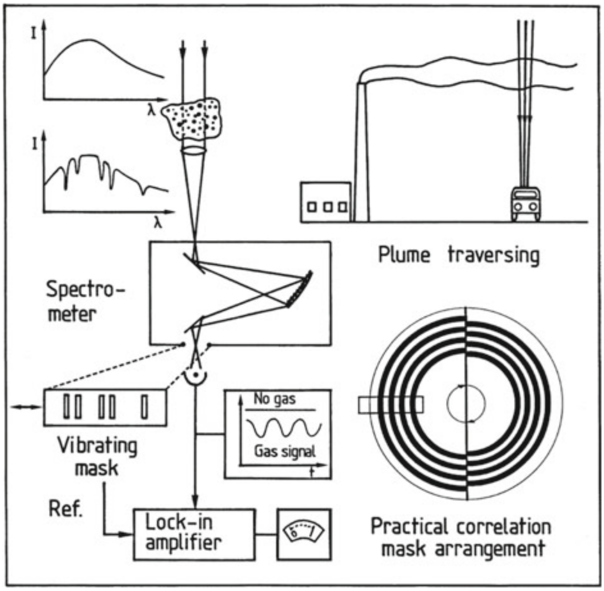
I
λ
I
λ
Plume traversing
Spectro-meter
No gas
Gas signal
t
Vibrating mask
Ref.
Lock-in amplifier
Practical correlation mask arrangement

Fig. 6.86 Principle of a dispersive mask correlation spectrometer

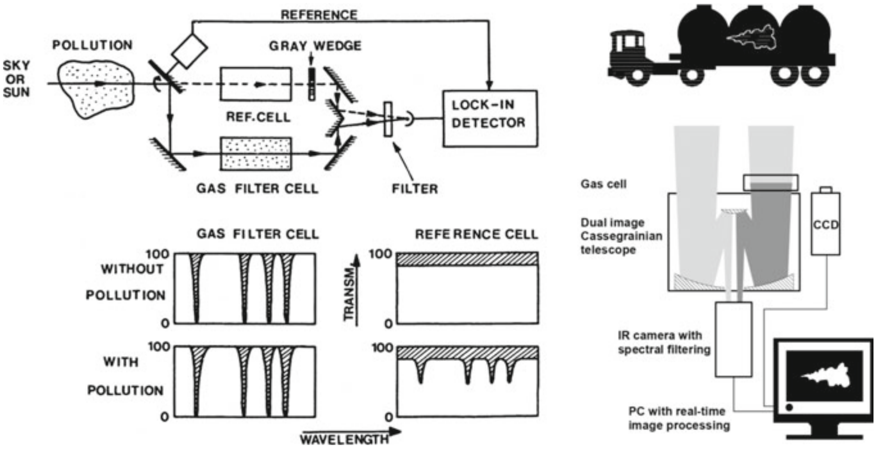
REFERENCE
POLLUTION
SKY OR SUN
GRAY WEDGE
REF.CELL
LOCK-IN DETECTOR
GAS FILTER CELL
FILTER
GAS FILTER CELL
REFERENCE CELL
100
WITHOUT POLLUTION
0
TRANSM.
100
0
100
WITH POLLUTION
0
100
0
WAVELENGTH
Gas cell
Dual image Cassegrainian telescope
CCD
IR camera with spectral filtering
PC with real-time image processing

Fig. 6.87 Principle of a gas correlation spectroscopy [681], and imaging ([702], reproduced with permission from OPTICA)

Fig. 7.30 and [704]). Techniques, where the target gas is actively illuminated with a scanned infra-red laser beam have also been developed [705].

A correlation set-up can also be achieved by modulating the absorption spectrum of the gas in a reference cell. Then the optical path does not need to be divided into two paths, but the external gas can be observed through the modulated cell

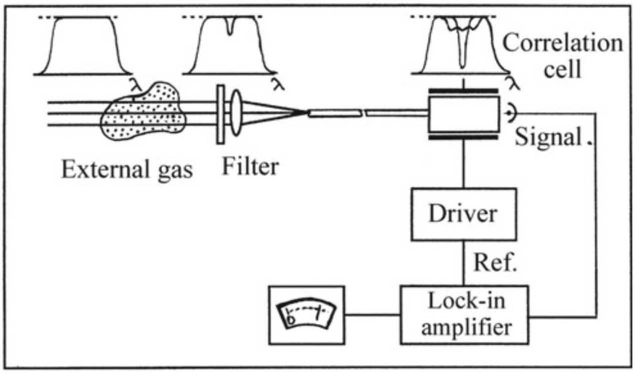

Fig. 6.88 Illustration of modulated gas-correlation spectroscopy for the case of a fibre-optic gas monitoring system. Here the gas correlation cell is modulated, rather than the illumination source, as was the case in Fig. 6.72

as indicated in Fig. 6.88. This can be performed using pressure, Stark or Zeeman modulation. The modulation at the detector in the presence of the selected gas in the measurement volume is caused by a decreased absorption in the modulation cell, where the perturbation broadens the line, thus reducing the blocking capacity of the cell for the unmodulated gas absorption profile. The use of Zeeman modulation in a correlation scheme for atomic mercury detection was discussed in connection with Fig. 6.72.

A further means of broadband monitoring of gas absorption is to place the measurement cell inside one of the arms of a Michelson interferometer, which for the case of the absence of the trace gas in the cell is adjusted close to the equal armlength setting for a minimum signal transmission to the detector (Note; exactly equal armlengths lead to a maximum signal as utilized in optical coherence tomography (OCT; see Sect. 10.5.4.3). This is possible in a comparatively large wavelength range, selected by a filter placed after the lamp. If the gas absorptive components are present in the cell, light at the absorbing wavelengths is not cancelled out by exact interference at the detector, and the spectral signal appears in "emission" from a zero background, although it is a weak absorption signal. Changes in index of refraction, etc., normally only cause a small effect in these measurements, which rely instead on the optical absorption imbalance between the arms. Related gas correlation techniques are presented in [706–708]. A laser variety of balanced Michelson interferometry has also been demonstrated with sensitive methane monitoring as an example [709].

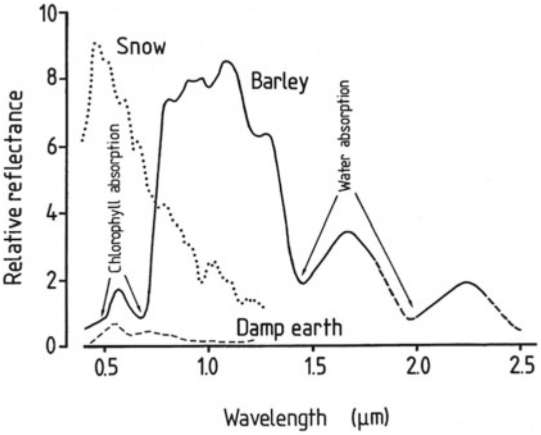

Fig. 6.89 Reflectance curves for different ground surfaces (After L. Wastensson)

6.6.2 Land and Water Measurements with Passive Remote Sensing Techniques

The reflective properties or the IR thermal emission are normally used in passive monitoring of land or water surfaces. In earth resource monitoring the selective reflection properties of different types of materials, exposed to sunlight, are used. Some reflectance curves are shown in Fig. 6.89.

Multi-spectral aerial photography historically represents the simplest type of reflective remote sensing. A number of aligned identical cameras equipped with different filters, were activated at the same time. This technique produced images directly and could be used to monitor land vegetation, and oil, algae and turbidity in water. The sensitivity of photographical materials only extends into the near-IR region, which limited the possibility of discriminating between different materials, while solid-state detectors (Sect. 6.3) widely extend the capability.

Many substances and materials have characteristic spectral signatures in the IR region, which together with the visible region can now easily be covered by electro-optical recordings. As a general-purpose technique in wide wavelength regions, *Multi-Spectral Scanning* (MSS) performed from an aeroplane or a satellite, can be used. The principle of this historically important technique is illustrated in Fig. 6.90.

Different points on the earth's surface are sensed sequentially using a scanner mirror placed in front of a light-collecting telescope ("*whisk-broom*" *sensor*). As the sensor platform moves forward, a certain strip ("swath") on the surface is covered. The radiation is divided up into different wavelength bands that are recorded in parallel detectors. After digitizing, the information is stored on a recorder or transmitted to a receiving station on the ground. American LANDSAT satellites were early launched and operate from a height of about 700 km and have a swath of about 185 km. The surface reflectivity is sensed in 7 bands centred at 0.49, 0.56, 0.66, 0.83, 1.65, 2.25 and 11.45 µm. The spatial resolution is 30 × 30 m^2. The wavelength bands (excluding the thermal 11.45 µm band, denoted band 6) are shown in

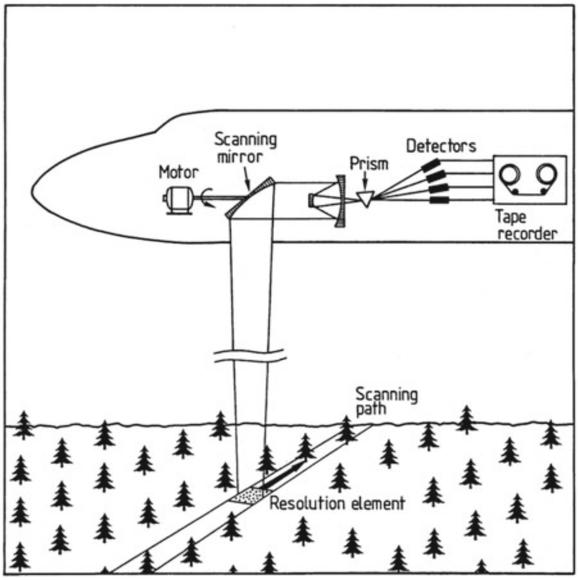
Scanning mirror
Motor
Prism
Detectors
Tape recorder
Scanning path
Resolution element

Fig. 6.90 Multi-spectral scanning of the earth's surface (whisk-broom sensor)

Fig. 6.91, superimposed on reflectance spectra from leaves (green, yellowing and senescent). The spectral bands in the middle infrared (MIR) region are selected to prevent interference from the strong atmospheric absorption bands due to CO_2 and H_2O (See Fig. 6.57).

Receiving stations are distributed around the globe. The digital data must first be rectified to a normal map grid to eliminate the influence of the observation angle and

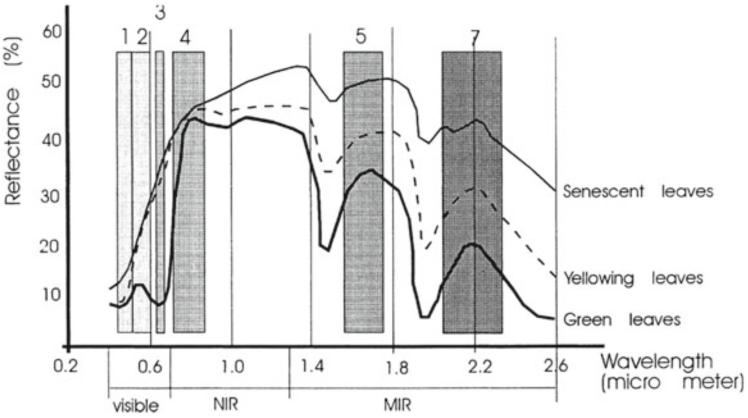

Fig. 6.91 Spectral bands for the LANDSAT Thematic Mapper sensor superimposed of typical reflectance spectra of leaves in different seasonal stages (Courtesy: L. Olsson, Lund University)

also be spectrally corrected for atmospheric influence, the latter also being a very important and complex procedure. Packages of data preprocessed in this way, called "*scenes*", covering a surface of 185 × 185 km^2, for example, are made available to users. Image processing can then be performed with advanced interactive computer systems. A classification of the information in a scene can be made using stored spectral signatures. Thus maps can be produced showing, for example, different kinds of crops identified by their specific spectral signatures. Present trends in digital image processing include an increasing utilization of the geometrical line and granulation patterns (texture). This field is developing very rapidly.

Two-dimensional detectors are nowadays frequently used to combine spatial and spectral information ("*push-broom sensors*", also denoted imaging spectrometers; see also Sect. 6.3). This concept is illustrated in Fig. 6.92. For each signal integration on the detector, the spectral data along a swath perpendicular to the satellite flight direction are collected as adjacent columns on the two-dimensional detector. At the next signal integration the satellite has moved forward and data for the next section on the ground is collected. This type of technology is used on most satellites, and early on the French SPOT satellites, which have a spatial resolution of about 10 × 10 m^2. Sensor systems with very high spectral resolution and many spectral bands have also been developed, e.g., the SeaWIFS (Sea-viewing WIde Field-of-view Sensor) on board the SeaSTAR satellite. Airborne sensor systems with a hundred closely spaced spectral channels are also operational, performing *hyperspectral imaging*. Figure 6.93 shows a satellite map of the southern part of Sweden, where the multi-spectral data has been processed to show forest coverage.

Generally speaking, processed satellite maps showing various aspect of earth resource utilization are being produced based on the spectral information available from the sensors. Calibration is frequently achieved by *ground truth* recordings of verified spectral signatures recorded in the field. Detailed information on different types of crops, etc., can be obtained by extensive spectral analysis, combined with multi-variate statistical techniques. Satellites are also extremely valuable in the monitoring of the oceans. As an example, Fig. 6.94 shows the occurrence of algal blooms in the Baltic Sea.

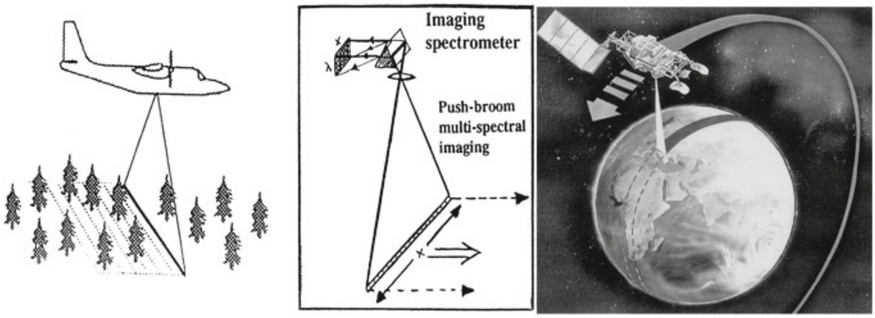

Fig. 6.92 Principle of a push-broom multispectral sensor, in airplane installation (left) and on a polar satellite (right; Courtesy: Swedish Space Corporation)

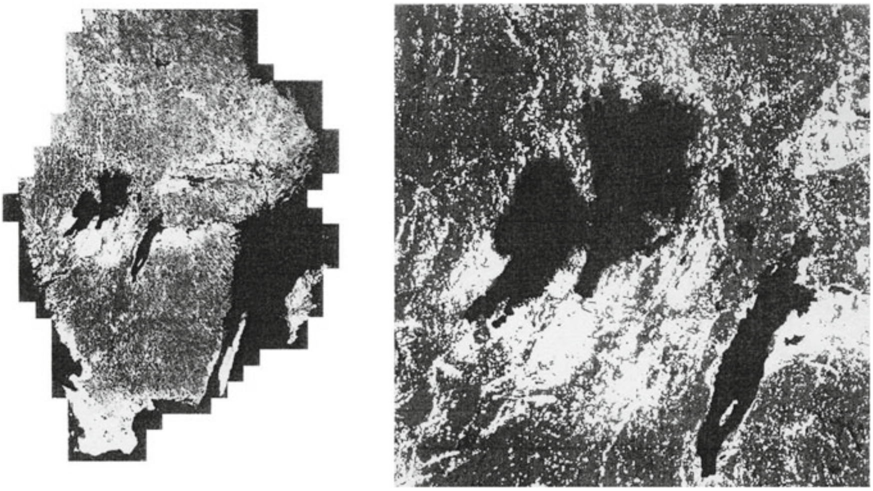

Fig. 6.93 Forest coverage map for southern Sweden, processed from LANDSAT and SPOT satellite imagery. A magnification of the great lakes area is included. Forest pixels are dark in the pictures (Courtesy: Swedish Space Corporation)

IR measurements for assessing surface temperature are of interest in many contexts. One application is to monitor heat plumes in water adjacent to nuclear power plants. A dramatic example of this concept is shown in Fig. 6.95, documenting the 1986 Chernobyl reactor accident in Ukraine as detected by the SPOT and LANDSAT satellites. The accident is manifested in the major change in the distribution of heated water before and after the accident and in the occurrence of a hot spot (one pixel) marking the reactor building.

By monitoring temperature inertia in a diurnal cycle, information on different types of rocks, for example, can be obtained from the heat dynamics. At close range, such techniques can be used to detect buried land mines, where the soil above the mine has different thermal inertia than that of the surrounding soil [710–712].

Thermal imaging is quite useful in remote sensing, but also has many other applications. Thus, “thermovision” cameras can be used to find heat leaks from houses in cold regions, or leaks in city heating networks laid down under the streets. The techniques also have applications in finding “cold-solder” joints on printed-circuit boards (joint heating) and have been investigated for tumour localization (tissue temperature rise).

A final example of monitoring from space is given in Fig. 6.96, documenting the tsunami disaster, which struck South East Asia on December 26, 2004 and killing about 230,000 people. Recordings shows the area at Bandar Aceh, Sumatra, Indonesia, before and after the strike. Generally speaking, satellite recordings separated by given time intervals, are extremely useful in documenting global changes, including the increasing deforestation, e.g., in the Amazonas, and the increased desertification in the African Sahel region, south of Sahara. Clearly, the images must be

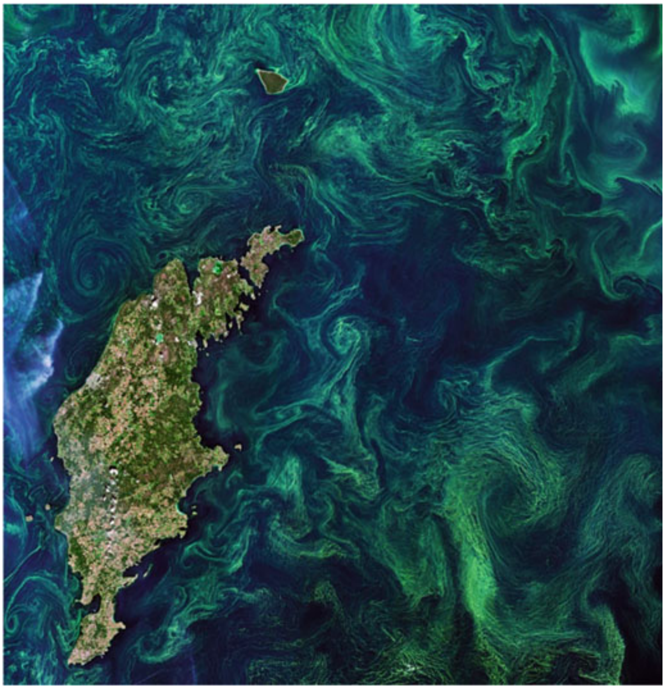

Fig. 6.94 Satellite image of algal blooms in the Baltic Sea east of the Swedish island of Gotland. The processed image is from Sentinel-2 Satellite data, recorded on July 19, 2019. The satellite carries a push-broom imager with 13 spectral bands, and has a swath of 290 km (contains Copernicus Sentinel data (2019), processed by ESA, CC BY-SA 3.0 IGO)

processed for the same geometry, with higher precision, the finer details the study addresses.

Techniques and applications of multi-spectral analysis from space have been discussed, for example, in [713–719].

Strongly related to satellite remote sensing we will here add some comments about the enabling launching technology of satellites and spacecrafts. Using the laws of mechanics, we can calculate that in order for an object to go into orbit (meaning that it falls towards the ground at the same rate as the ground is curving away!) a *flight velocity* of about 8 km/s is required. However, an orbit very close to the ground is impossible due to atmospheric friction. At a height of 800 km the drag due to the residual atmospheric density starts to become insignificant. It is easy to conceive that it is favourable to perform a satellite launch using staged rockets, so that only a small mass has to be accelerated to the ultimate speed. Thus, a first stage consuming most of the fuel has the largest weight and overcomes most of the gravitational pull. It is then decoupled from the rest of the rocket and falls to the ground. A second, and possibly a third stage, are then ignited to increase the speed of the pay-load. These latter propulsion stages also fall to the ground and a final

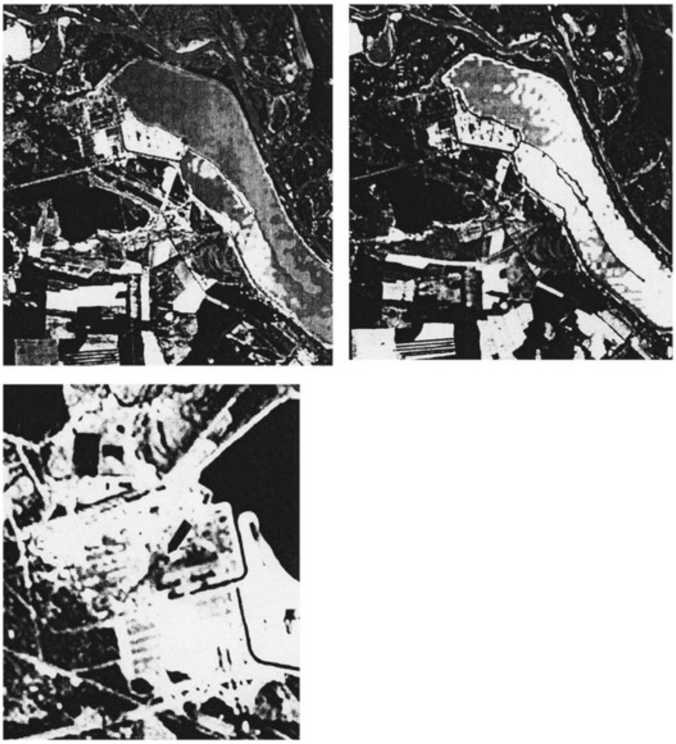

Fig. 6.95 Processed SPOT images of the Chernobyl nuclear power-plant area, before and shortly after the reactor accident (April 26, 1986). *Top left*: before accident. *Top right*: after accident; cooling water stream perturbed. *Left*: magnification showing damaged reactor building as a spectral anomaly, at arrow (Courtesy: Swedish Space Corporation)

rocket engine injects the satellite into its orbit. Recently, burnt out stages can be made to safely land, allowing reuse. Rocket engines operate with different fuels and oxidants, such as kerosene and liquid oxygen, or liquid hydrogen and liquid oxygen. Catalytic explosive decomposition of a single substance, normally hydrazine, is also employed. Solid fuel booster rockets are frequently attached around the first stage to provide additional thrust. The satellite is equipped with small attitude adjustment rockets to control it. For orbit corrections, ion engines using the reactive push when charged xenon ions are electrically accelerated are sometimes used.

It is practical to launch a satellite eastward from a coast (like Cape Canaveral in Florida, or Kourou, French Guyana) to benefit from the earth rotation sling effect (0.5 km/s at the equator) and for letting the burnt-out stages fall into the sea. Russia launches from Bajkonur and China from Jiuquan, which are situated in low-populated areas. Modern earth-resource monitoring satellites are frequently launched into circular *polar* orbits at a height of 700–900 km, corresponding to a revolution time of about 100 min. Such a satellite performing push-broom scanning was schematically shown in Fig. 6.92. The sensor will cover the whole surface of

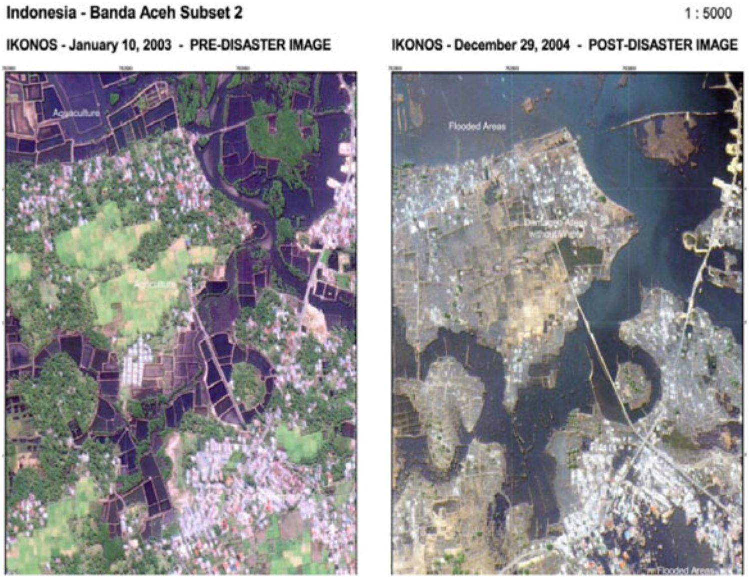
Indonesia - Banda Aceh Subset 2
1 : 5000
IKONOS - January 10, 2003 - PRE-DISASTER IMAGE
IKONOS - December 29, 2004 - POST-DISASTER IMAGE
Aquaculture
Agriculture
Flooded Areas
Damaged Areas without Water
Flooded Areas

Fig. 6.96 Satellite images of Bandar Aceh (Sumatra), before and after the 2004 tsunami catastrophy. The Ikonos satellite, which is fully stabilized with gyro fly-wheels and star trackers, was launched in 1999. It carries a 70 cm diameter telescope and provides a ground resolution down to 1 m (Courtesy: European Space Imaging/German Aerospace Center, DLR)

the earth in time periods which typically vary between 15 days and a month. The orbit is frequently arranged to be *sun synchronous,* always with a fixed position with respect to the sun. This means that when a satellite returns overhead a particular geographic location it is always at the same time of the day. In this way the ground is always observed with the same illumination angles, facilitating the comparison of data taken over time. It could be noted, that when employing polar orbit satellites, it is very advantageous to place receiving stations on the ground close to the poles (as the Swedish ESRANGE station, north of the Arctic circle), since data can then be received on every orbit in the microwave down-link.

A completely different type of satellite orbit is the *geostationary* one, where the satellite maintains its position at a given location above the equator. With an orbit time of 24 h this corresponds to a distance above the ground of about 36,000 km. This is the preferred arrangement for communication satellites, where the receiver parabolas can be mounted fixed aiming at the stationary satellite, whose small position drifts due to the irregular shape of the earth, etc., are compensated by occasionally firing small rockets on the spacecraft. A small number of geostationary satellites can provide meteorological surveillance over the whole globe [720]. As examples, the US operates the GOES satellites, Europe four METEOSAT units, while China relies on its FENGYUN (“wind and cloud”) system. Needless to say, weather forecasts have improved dramatically thanks to satellites combined with advanced digital weather modelling.

Clearly, the attitude of a satellite must be controlled very accurately to provide precision imagery of the earth´s surface, and even more, for astronomical observations (see below). This is normally performed with three-axial gyros, where flying wheels are accelerated by electrical motors and the space-craft has to turn under the reactive forces. When the wheels have accumulated a high speed they are spun-down employing small rockets to provide the breaking forces. In this way a good fuel economy can be achieved and a longer satellite lifetime.

6.7 Astrophysical Spectroscopy

In the same way as in laboratory optical analysis and in remote sensing it is possible to use characteristic wavelengths and line intensities in light from astronomical sources for qualitative and quantitative analysis of the chemical constituents of stars and other objects [721–726]. The radiation is collected with large telescopes. In this section we will give a few examples illustrating how knowledge can be obtained on astronomical objects by the analysis of electromagnetic radiation, mostly in the optical region. The "surface temperature" of a star can be determined from its spectral features. Stars are divided up into classes according to their temperature (highest → lowest): O, B, A, F, G, K and M-type stars. Some classified star spectra are shown in Fig. 6.97. Table 6.6 lists special spectral features pertaining to the different classes.

Stellar spectra normally consist of absorption lines, which occur when the intense continuum radiation from the hot interior of the star is filtered on passing through the cooler outer stellar atmosphere. Strong such absorption lines in the spectrum of our own sun are called *Fraunhofer lines*, after the German scientist who observed them as early as 1814. (In passing, we note a similar phenomenon in the emission of the high-pressure xenon-mercury lamp, as shown in Fig. 6.11, where the strong transition at 254 nm from the mercury ground state gives rise to an absorption line in the background plasma radiation!). The strength of the stellar absorption line is a measure of the abundance of the element. As a measure in the determination of the number of absorbing atoms the so-called *equivalent width* of the spectral line is

Table 6.6 Spectral features characterizing different classes of stars

O	Lines of neutral and ionized He, and of multiply ionized light elements
B	Lines of He and of singly ionized light elements. Hydrogen Balmer series appears
A	Strong hydrogen Balmer series. Neutral and singly ionized metal lines
F	Hydrogen Balmer series weaker. The Fraunhofer K and H lines due to Ca^+ become very strong
G	Lines of neutral metals dominate the spectrum. Molecular bands of CN and CH appear
K	The lines of neutral metals and the molecular bands become even stronger than in class G. Bands of TiO appear
M	TiO bands become stronger and many other molecular bands are present

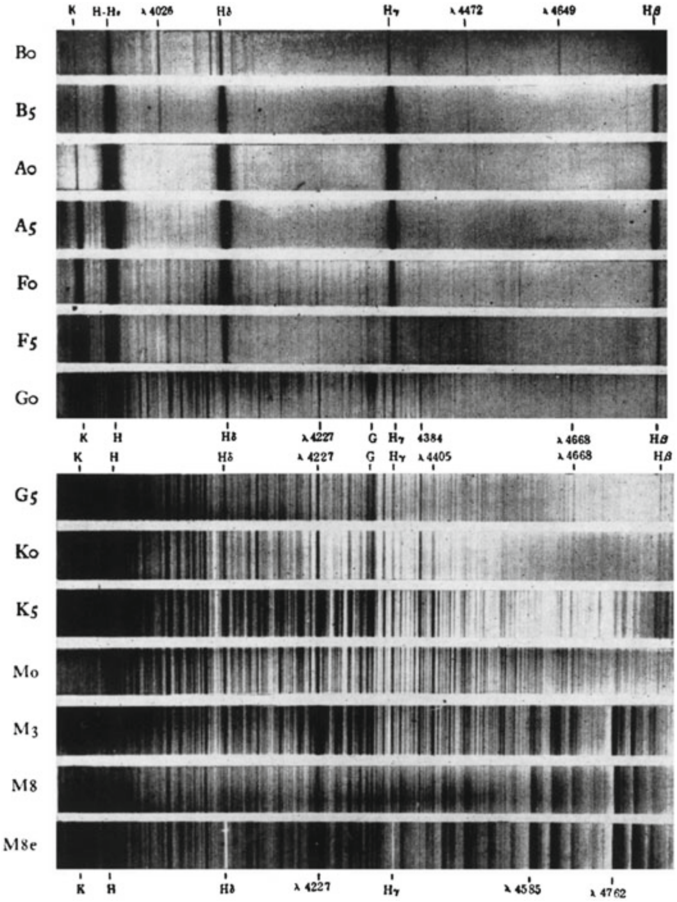
K
H-Hε
λ 4026
Hδ
Hγ
λ 4472
λ 4649
Hβ
B0
B5
A0
A5
F0
F5
G0
K
H
Hδ
λ 4227
G
Hγ
4384
λ 4668
Hβ
K
H
Hδ
λ 4227
G
Hγ
λ 4405
λ 4668
Hβ
G5
K0
K5
M0
M3
M8
M8e
K
H
Hδ
λ 4227
Hγ
λ 4585
λ 4762

Fig. 6.97 Classified star spectra [727]

used. The equivalent width is defined as the width of a square box that covers the same surface as the actual absorption profile of the line, as illustrated in Fig. 6.98. An example of an experimentally recorded stellar line is included in the figure.

The relation between equivalent width and the number of absorbing atoms is called the *curve of growth*. Clearly, the transition probability for the transition considered is of paramount importance in this context, and we will return to this point later (Sect. 9.4.3). In calculations it is necessary to assume a certain model for the stellar atmosphere. A small wavelength interval of the spectrum of the sun, recorded at a high spectral resolution, is shown in Fig. 6.99. The resonance line of Ca II is very prominent. It corresponds to the yellow sodium line at 589 nm; note, how the non-balanced nuclear charge contracts the system leading to the spectral line now appearing at 393 nm—the Na and the Ca^+ lines are here the first two members of a

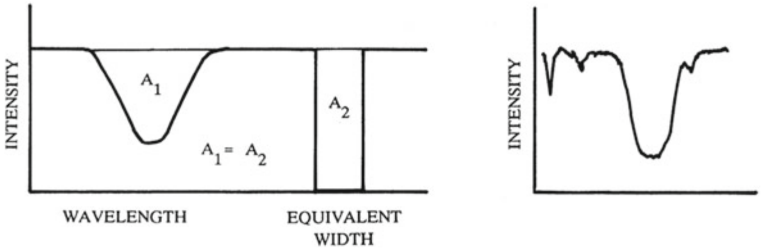

Fig. 6.98 Definition of equivalent width and an experimentally recorded spectral line, from the star Arcturus, the fourth brightest stars of the total sky, and the brightest one at Northern latitudes [728]

so called *isoelectronic sequence*. The relative abundances of the elements in the sun, as obtained using spectral analysis, are given in Fig. 6.100.

Emission lines also occur in stellar radiation, especially from hot stars, e.g., from Wolf–Rayet stars. Emission lines from very highly ionized atoms occur in the solar corona. Several of these lines that are observed in the visible or UV regions correspond to "forbidden" transitions within an ionic ground configuration. For example, the 530.3 nm line is due to 13-fold ionized iron. The coronal lines constituted a long-lasting puzzle, which was solved by *B. Edlén* [731, 732]. A very early problem

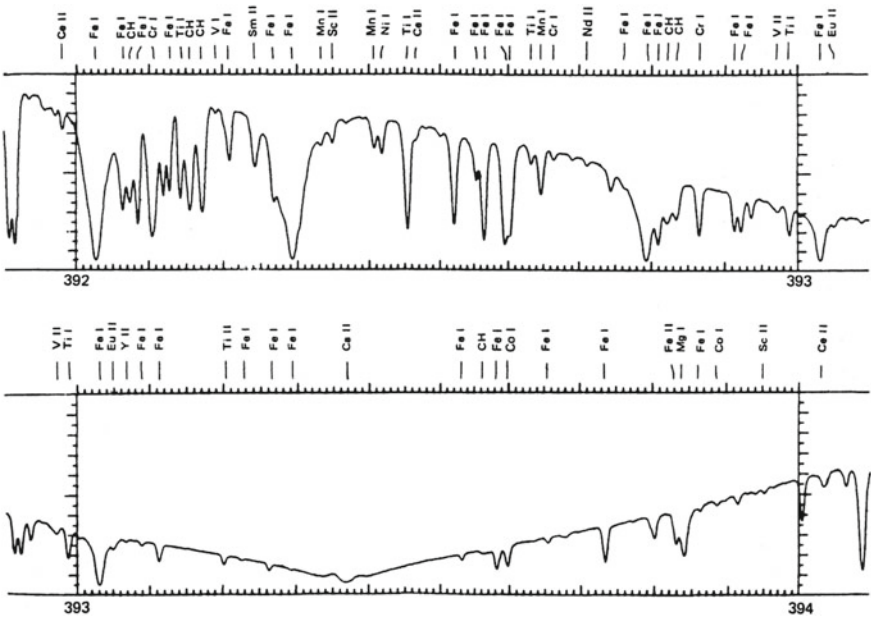

Fig. 6.99 A small interval of the sun's spectrum around the strong CaII resonance line (isoelectronic with the sodium yellow line 3p -3 s) [729]

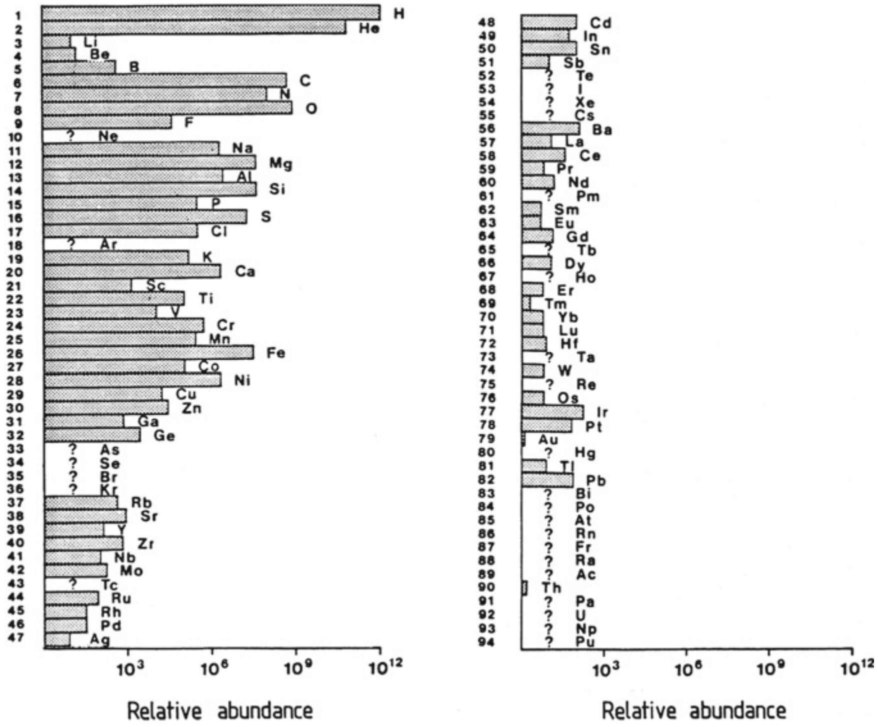

Fig. 6.100 Relative abundances of the elements in the sun, as obtained using spectral analysis [730]

was the identification of the strong He lines in the solar spectrum and first attributed to a new and at that time unknown element (named after *Helios*, Gr. for sun), later found in the laboratory. There has always been a very close interaction between astrophysics and atomic physics in terms of identifying observed lines, and evaluation of transition probabilities (see, e.g., [733] and Sect. 9.4.3).

Lines from very highly ionized atoms in general fall in the extreme UV region because of the strong excess nuclear charge (related to Eq. (2.4)). Telescopes for X-ray and short UV wavelengths have been placed on astronomical satellites that are controlled from ground observatories. Examples of early X-ray astronomy satellites are OSO (Orbiting Solar Observatory), Einstein, Exosat, IUE (International Ultraviolet Explorer) and ROSAT, while current units include the Newton, Swift and AGILE observatories [734–737]. Exploration of the sky in the IR region from space, e.g., by the Herschel satellite, is also of major interest [738].

The *Hubble Space Telescope* (HST) [739–743], which is a very powerful spaceborne astronomical facility, was launched in 1990. The high-resolution Echelle spectrometer on board the HST has provided VUV spectra, e.g., of chemically peculiar stars. Such spectra have shown an over-abundance of rare-earth elements, gold, etc. in these stars by a factor of 10^3–10^5, relative to the sun. A representative spectrum for such a star (*Chi Lupi*) is shown in Fig. 6.101, with a calculated model spectrum included as a dashed curve [744]. The best previously recorded spectrum, obtained with the IUE satellite, is also included in the figure and illustrating the benefits of a high resolution. Apart from being free of atmospheric absorption problems (Figs. 6.57, 6.58), HST also, after a service mission in 1993 to correct the faulty optics, provides extremely sharp images, not blurred by atmospheric turbulence. Actually, the HST "Deep Field" camera could see further into the universe than any other previous telescope (Fig. 6.102). It should be noted, that the exposure time for such a recording is hundreds of hours, which can be achieved by using a low-noise CCD detector while the camera is locked to the fixed position by using star-trackers on the moving platform.

The *James Webb Space Telescope (JWST)* was launched by an Ariane 5 rocket from the Kourou launching site in 2021 [746]. It works in the IR region and will greatly exceed the capability of the *Spitzer Space Telescope (SST),* which served from 2003 to 2020 [747]. The JWSP has a 6.5 m diameter telecope (compared to 2.4 m for HST). It will cover the IR range (from 0.6 - 28 μm), which will enable it to see objects even further away than what can be accomplished with the shorter wavelengths available at HST. The telescope has a large shield shadowing it from the sun and the IR detectors will operate at a temperature as low as 50 K for highest sensitivity. The telescope has started to present images of unprecedented quality.

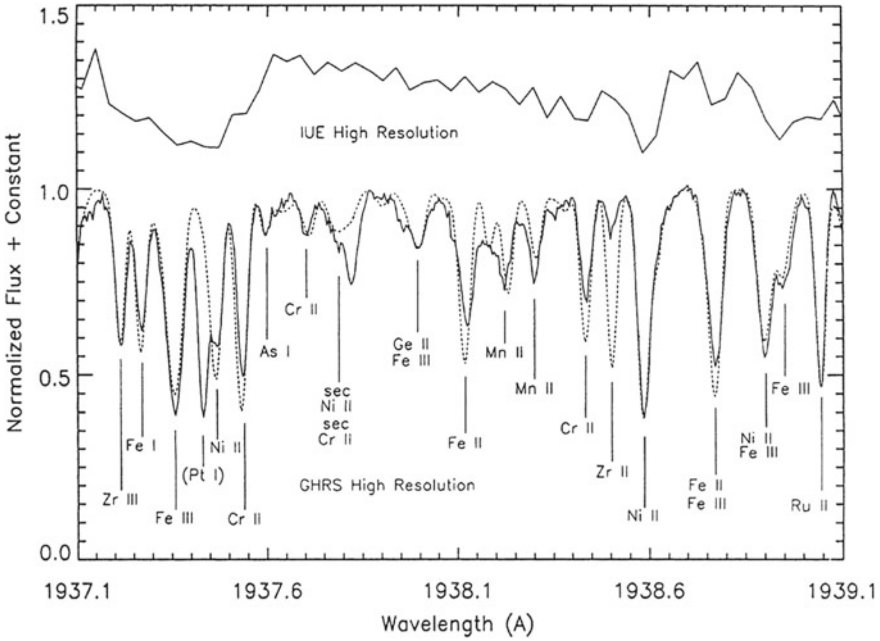

Fig. 6.101 Spectrum of the chemically peculiar star *Chi Lupi*, recorded with the Echelle spectrometer of the Hubble Space Telescope [744]

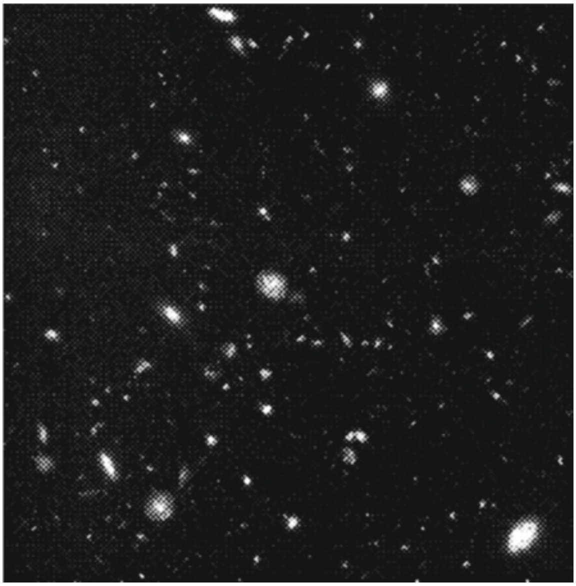

Fig. 6.102 Hubble Space Telescope "Deep Field" image of the most distant part of the universe observed so far. Each blob in the figure is a galaxy at distances ranging out to 10 billion light years [745]

While earth-bound astronomical observations are always impaired by atmospheric absorption, the detrimental effects of turbulence can be reduced by choosing telescope sites with particularly good "seeing", i.e., stable atmospheric conditions. This has lead to the selection of Chilean high-altitude desert locations, e.g., for the European Southern Observatory (ESO) at La Silla and the new *Very Large Telescope (VLT)* at Paranal. Nevertheless, there are random fluctuations in the air index of refraction. In spectral monitoring this can be handled by fast scanning or parallel (diode-array) detection, as discussed for doas applications, for example (Sect. 6.6.1). However, images will suffer blurring. The technique of adaptive optics, whereby a mirror can be deformed by actuators to compensate for turbulence [748, 749], can improve the situation considerably. A bright star must be available within the field of view, and is forced to be recorded as the point source it in fact is, by fast feed-back, adaptive regulation of the mirror surface. If this is achieved, faint and perhaps distributed objects such as remote galaxies will be able to be recorded sharply. Since bright stars are absent in most regions of the sky, a "laser guide star" formed by a strong laser beam inducing sodium fluorescence in the mesospheric sodium layer can be used as a replacement [750] (Sect. 10.2.3.1).

The VLT is a composite optical telescopes incorporating guide-star and adaptive optics techniques. Four fixed telescopes of diameter 8.2 m and four movable telescopes of diameter 1.8 m can be combined to achieve an unprecedented light collection efficiency at the same time as a spatial resolution of 0.001 arcsecond can be achieved. This corresponds to being able to resolve the two headlights of a car on earth when observered from the moon.

The *Extremely Large Telescope (ELT)* on the top of the Chilean mountain Armazones is now in a 10-year construction phase, and is planned to be completed in 2024. It will have an effective diameter of 39 m accomplished by merging 998 hexagonal mirror segments.

We will now give a few further examples of interesting observations in astrophysical spectra. Sometimes certain stellar lines appear much brighter than would be expected, considering the temperature, transition probabilities, branching ratios, etc. Such phenomena can be explained as due to accidental coincidences between broadened strong spectral lines of high-abundance elements, resonantly pumping transitions in the elements studied and causing strong fluorescence upon decay. This is the so-called *Bowen mechanism* [751, 752], and well-known examples are the 313.4, 304.7 and 344.4 nm lines in O III, pumped by the 30.38 Ly-α line of He II, and the 245.9, 249.2 and 248.1 nm lines in Fe II, pumped by the 154.8 nm line of C IV. Very recently, even optical lasing on Fe II lines around 1.7 μm has been observed in the region of the star *Eta Carinae* [753], caused by amplification of spontaneous emission in a cloud of ions. Two Fe II lines around 251 nm are pumped by the hydrogen Ly-α in a Bowen mechanism (See Fig. 6.103), and they feed two long-lived states to inversion (Sect. 8.1) leading to the near-infrared lasing.

The Doppler effect causes displaced spectral lines from objects in motion. The rotation of a star around its axis causes an extra broadening of the spectral lines, as does turbulence in the stellar atmosphere. A detailed analysis of the line profiles can clearly yield interesting information on the physical condition of the object.

Two spectra of high members of the hydrogen Balmer series (2 *s* - *np*) recorded for identical experimental conditions are shown in Fig. 6.104 for the two brightest stars, *Alpha Canis Majoris* (Sirius) and *Alpha Carinae* (Canopus). The much higher gas pressures on the dwarf star Sirius causes a smearing-out of the highest Balmer lines. In the low-pressure atmosphere of the bright giant Canopus, the Balmer series can be followed to around $n = 28$, at 366.5 nm, while for Sirius none can be identified above

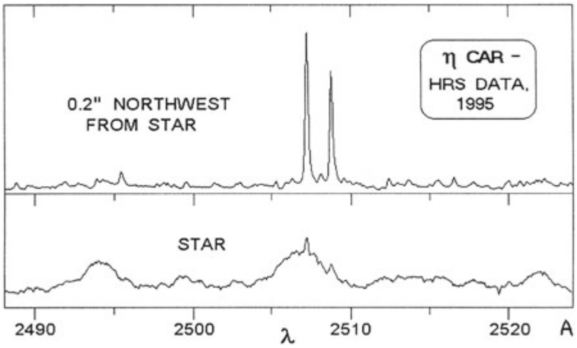

Fig. 6.103 Anomalously bright Fe II fluorescence lines at 250.6 and 250.8 nm, observed in the neighbourhood of *Eta Carinae*. The lines feed two long-lived states, which decay in lasing transitions around 1.7 μm. As a reference, the stellar spectrum, with normal intensities of the Fe II lines, is also shown [753]

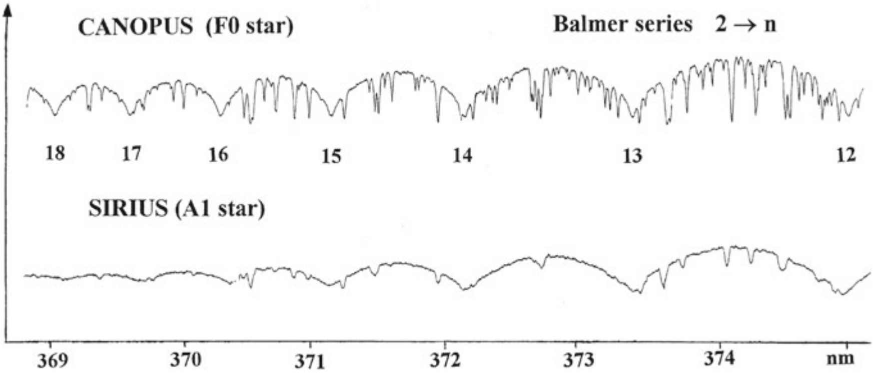

Fig. 6.104 Series of absorption lines corresponding to high Balmer series transitions for the stars Canopus and Sirius. The high Rydberg states are sensitive to collisions. Other sharper absorption lines due to transitions between low-energy states in different elements are shown superimposed on the hydrogen lines (Courtesy: D. Dravins, Lund Observatory)

$n = 18$, around 369 nm. The extent to which lines in the Balmer series can be followed is thus a spectroscopic criterion for stellar surface pressure. The temperatures of the two stars are quite similar, and the rotational broadening is only a negligible fraction of the Balmer line widths.

Distant galaxies exhibit large red shifts. Extremely large red shifts are observed for quasars [754–756]. The red shifts are interpreted in terms of radial motion. The largest equivalent velocity observed exceeds $0.9c$. A spectrum for a quasar with a velocity of $0.85c$ is shown in Fig. 6.105. It can be noted how, for example, the Lyman α line, normally at 121.6 nm, has been shifted up to 445.1 nm in the blue spectral region! The study of other extraordinary celestial objects has been further stimulated by the sudden occurrence of the 1987 supernova in the Large Magellanic Cloud, a satellite galaxy to our own [757–761]. It was the first supernova in 383 years that could be seen with the naked eye. A spectrum of the nova recorded 7 days after the explosion is shown in Fig. 6.106. The spectrum exhibits a continuum background and superimposed Balmer-α and -β lines.

The hydrogen lines are strongly broadened due to different velocities in the expanding gas shell. Note that both emission and absorption line components occur. By studying Doppler-shifted narrow absorption lines from Na and Ca II with the bright nova continuum as background it has been possible to identify more than 10 cold gas clouds moving at different speeds (see figure insert). Earlier prominent supernovae are the Johannes Kepler star of 1604 and the Tycho Brahe star of 1572. The latter one, which was observed in the Cassiopeia constellation, has later been shown to be of the 1A type, which has a standard absolute luminosity. By observing such very distant supernovae, it was shown by *S. Perlmutter*, *B.P. Schmidt* and *A.G. Riess* that the universe has an accelerating expansion, an accomplishment which was awarded with the 2011 Nobel Prize in Physics. The driving mechanism for such an acceleration is considered to be connected to the presence of *dark energy,* which by

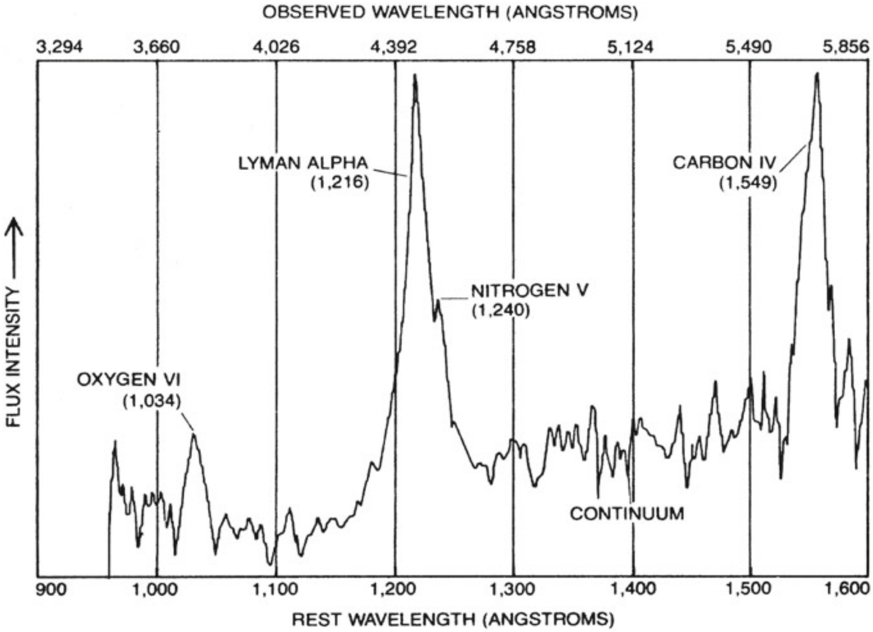

Fig. 6.105 Spectrum of a quasar exhibiting huge Doppler shifts (10 Å = 1 nm) [756] (Copyright 1982 by Scientific American, Inc. All rights reserved)

the $E = mc^2$ relation strongly dominates over normal (*baryonic) matter*, and so far unknown *dark matter* (see also discussion related to Fig. 7.35).

The Zeeman effect of spectral lines can be used to measure magnetic field strengths in the region of line formation. Clear Zeeman patterns occur in lines originating from sunspots, which are characterized by strong magnetic fields.

The study of the planetary atmospheres has become a field of increasing interest during recent years. Terrestrial observations have been complemented by recordings from spacecraft. Terrestrial IR recordings of CO_2 in the atmosphere of Venus are shown in Fig. 6.107, illustrating the increase in information content with increasing spectral resolution. As an example of a spacecraft recording, a spectrum of the atmosphere of one of the Saturn moons, Titan, is shown in Fig. 6.108. The IR recording exhibits lines from many hydrocarbons. Our knowledge of Jupiter, Saturn, Uranus, and Neptune has been vastly extended through the Voyager missions, and very detailed information on Saturn was obtained from the more recent Cassini mission [764–771]. At the return of Halley's comet in 1986, humankind had also become ready to launch a whole fleet of well-equipped scientific space vehicles towards it, including the European Giotto [772–774] (named after the artist Giotto di Bordone, who made the famous painting "The Adoration of the Magi", where a comet was depicted as the star of Bethlehem, probably influenced by the 1301 passage of the comet, which he witnessed). A $16 \times 8 \times 8$ km^3-sized comet nucleus could be photographed at close range (600 km) using Giotto's multi-colour camera. Giotto

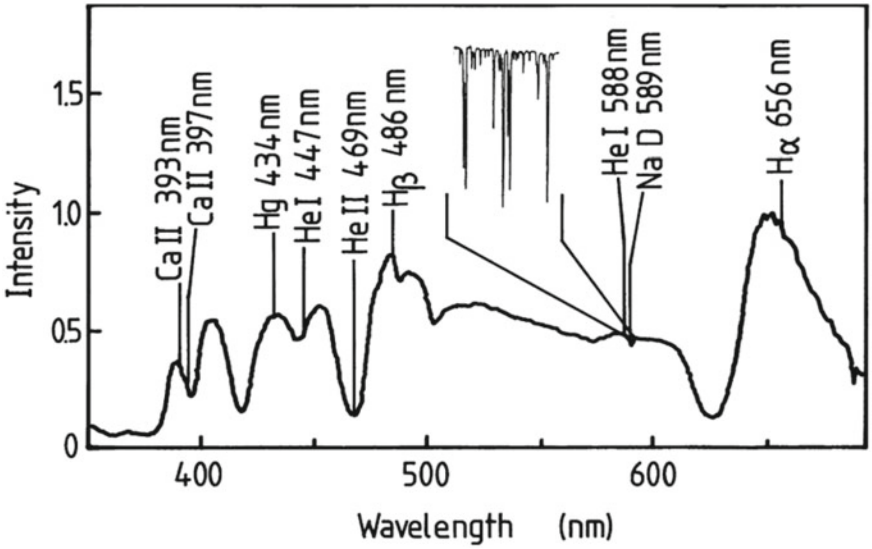

Fig. 6.106 Spectrum of the supernova 1987A in the Large Magellanic Cloud, recorded 7 days after the explosion. The prominent lines are due to the hydrogen Balmer series, Doppler-shifted and broadened due to very high expansion velocities (10,000 km/s). The Balmer-α line is partly seen also in emission. An insert shows narrow Na absorption lines due to cold gas clouds moving with different velocities along the line of sight [762]

also made a close pass-by at the comet Grigg-Sjellerup. Comet spectra are rich in molecular emission bands. A terrestrial photographic recording of a Halley's comet spectrum after the passage of the perihelium is shown in Fig. 6.109. By using a long spectrometer slit, imaging a distance of 10^5 km from the nucleus (*bottom*) through the comet tail, the strength of the emission through the comet structure could be recorded.

A very clear band-head (see also Fig. 4.13) due to the C_2 molecule appears at 473 nm. The comet, with a well-documented earlier passage in 1066 (according to the Bayeux tapestry depicting the Battle of Hastings) had its more recent passages in 1910 and as mentioned in 1986, and will again appear in 2061 (at its perihelion, closest to the sun, on July 28; 76 year periodicity), giving a new opportunity for precision studies. The Rosetta spacecraft in 2014 made a successful landing on the comet Churyumov-Gerasimenko after having orbited it for 18 months [776, 777].

A further recent achievement in astronomy is the observation of exoplanets, i.e., planets orbiting stars other than our sun. The first observation was reported in 1995 [778] by *M. Marcy* and *D. Quelot* (Physics Nobel Prize in 2019) [779, 780], who could observe the tiny periodic Doppler shift in spectral lines from the star *51 Pegasi*, which is located 50 light years away. An extremely stable and highly resolving spectrometer could be used to observe the periodic changes in radial velocity corresponding to a maximum velocity difference of about 120 m/s. The data are consistent with a planet of a mass similar to that of Jupiter, orbiting the star in 4.23 days. As a comparison,

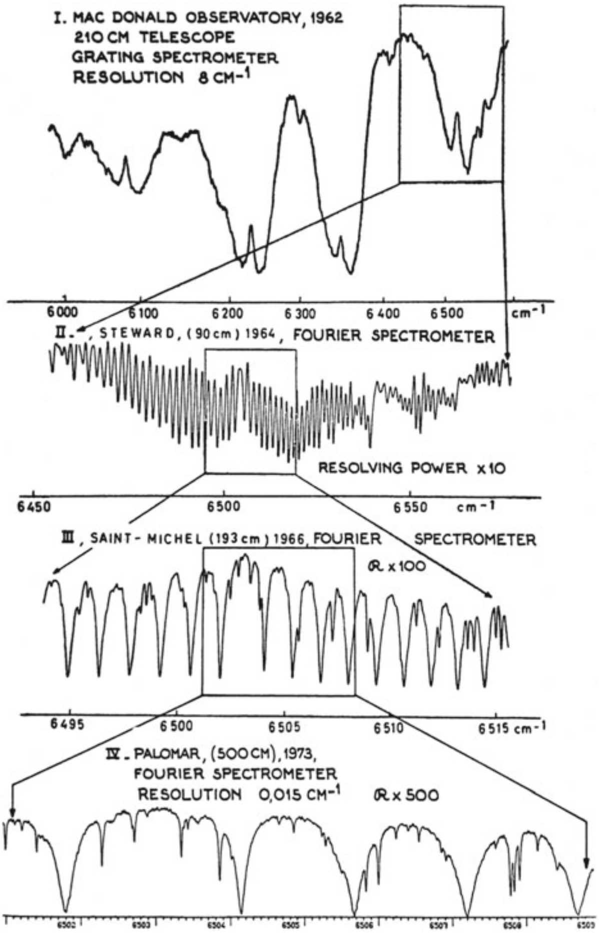

Fig. 6.107 Terrestrial recordings of CO_2 in the atmosphere of Venus illustrating the continuing refinement of the available spectral resolution [763]

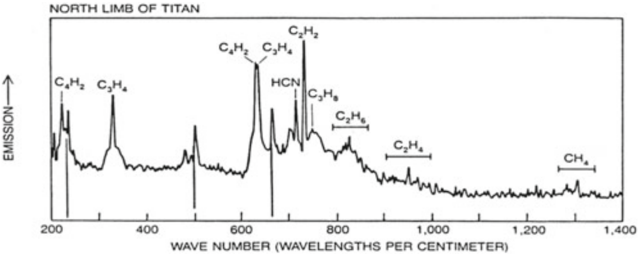

Fig. 6.108 Recording of emission bands in the atmosphere of the Saturn moon Titan, obtained by the spectrometer of the Voyager I spacecraft entering the Saturn–moon system [764] (Copyright 1982 by Scientific American, Inc. All rights reserved)

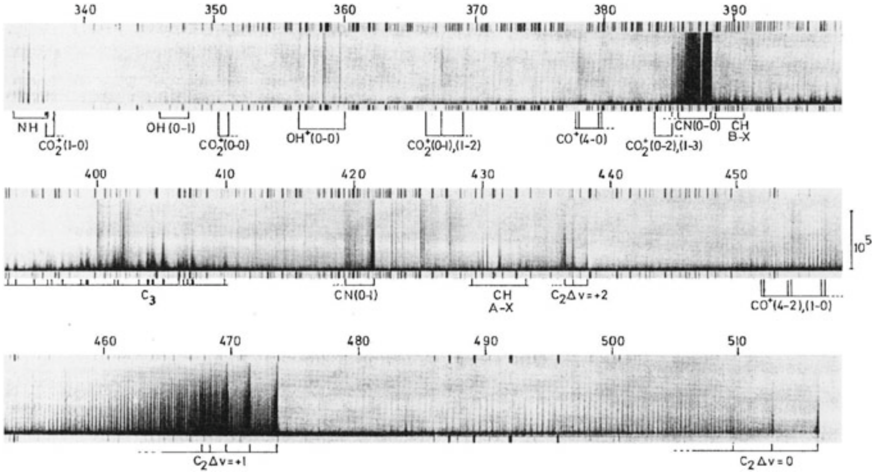

Fig. 6.109 Molecular emission spectrum from Halley's comet on its 1986 return to its perihelion [775]. Along the vertical scale the whole length of the comet tail is imaged using a long spectrometer slit. C_2, C_3 and CN bands are very prominent. Note that the C_3 emission (the "Comet" band) occurs only from a region close to the comet nucleus. It could be mentioned that at the earlier comet passage in 1910 it was already spectroscopically detected that the comet tail contained toxic CN molecules (see band at about 420 nm!). It was also realized, that the Earth would pass straight through the comet tail. Some panic reactions resulted, but because of the very dilute gas, nothing happened..... More recently, there have been considerations of an accidental terrestrial hit by a large asteroid (historical impact craters are evidenced on the surface of the Earth, and are very evident on the surface of the Moon). The orbits of a large number of minor objects in the solar system are therefore being tracked, and possible interventions to prevent an encounter are being contemplated

an observer outside our solar system would detect a corresponding solar velocity difference of 26 m/s due to the movement of Jupiter, with a period of 12 years. Using further instruments, especially the one on board the *Kepler satellite* (launched in 2009) [781], the number of detected exoplanets in 2020 exceeded 4000. The satellite utilized the other main method for detecting exoplanes - observation of star occulations - which are already well-known from the terrestrial examples of the rare Venus and Mercurius passages in front of the sun disc. Due to the close range, the planets can be physically imaged on their passage, which also cause a slight reduction of the sun total-light intensity. This effect can be observed for distant stars, the discs of which can clearly not be imaged. The light reduction is generally much less than 1 percent. As an example, a hypothetical occultation observation due to the Earth passing in front of our Sun would amount to about 0.008 percent. As a further exoplanet detection method, gravitational micro-lensing can be utilized. Much more prominent such lensing occurs for some of the galaxies recorded in Fig. 6.102. A major challenge in the study of exoplanets is to detect and analyze atmospheric gases [782, 783]. Because of the very high intensity of the central star this is a formidable task compared to the recording of the Venus and Titan atmospheric gases, as shown in Figs. 6.107 and 6.108. However, combined data from the HST and VLT have allowed the detection of water vapour at the exoplanet WASP-39b, which orbits a star similar to our own sun at 700 light years distance [784].

Related to the monitoring of exoplanets, the photographs of the “pale blue dot”, our own planet Earth, first photographed from Voyager-1 in 1990, then in connection with various planet Mars missions, and later by the Cassini spacecraft from the Saturn surrounding (Fig. 6.110] stems to thinking about our own existence among the billions of stars in each of the billions of galaxies. Clearly, the atmospheric gases of the earth would leave very clear absorptive imprints in the reflected light analyzed at high spectral resolution, and the characteristic absorption edge around 700 nm due to chlorophyll (Figs. 6.89, 6.91) would be easily detectable even at low resolution. Some thoughts about the cosmic and other perspectives are shared at www.svanberg-sweden.se.

A recent high-light in non-conventional astronomy was the observation of gravitational waves, originating from the merging of two black holes spiraling around each other, which, as earlier mentioned, resulted in the 2017 Nobel Prize in Physics [564–567]. Gravitational waves were predicted already by Einstein in 1915 as a consequence of the general theory of relativity, and should be manifested by a transient deformation of space–time. Since the effect is exceedingly weak, it for a long time seemed impossible to detect them. However, basically identical signals from two large laser-based Michelson interferometers (LIGO, Laser Interferometer Gravitational-Wave Observatory) (Sect. 6.2.4), localized in the US at Hanford and Livingston, 3000 km apart, could be observed, with a relative delay related to the observatory separations.

The two highly stabilized interferometers, with 4.2 km long perpendicular arms, and operating with extremely stable high-power CW lasers, were able to observed the minute change in the length of the arms on the passage of the wave, believed to be generated 1.3 billion years ago. The precision corresponds to a distance change measurement of 10^{-4} of the diameter of a proton. Recordings are shown in Fig. 6.111. Additional interferometers, such as VIRGO, have been added and will be added, enabling the localization of events with regard to direction. An update of the status of gravitational wave detection is given in [785].

The physical presence of black holes, i.e., ultra-massive objects with such a strong gravitational field, that radiation cannot escape, also becomes apparent in a study of star movements at the centre of our own galaxy [786], and resulted in the Nobel Prize in Physics in 2020 to *A. Ghez* and *R. Genzel*. As illustrated in Fig. 6.112, the star is completing an orbit around an invisible strong attractor in just 15 years, implying that the attractor must be a super-massive black hole.

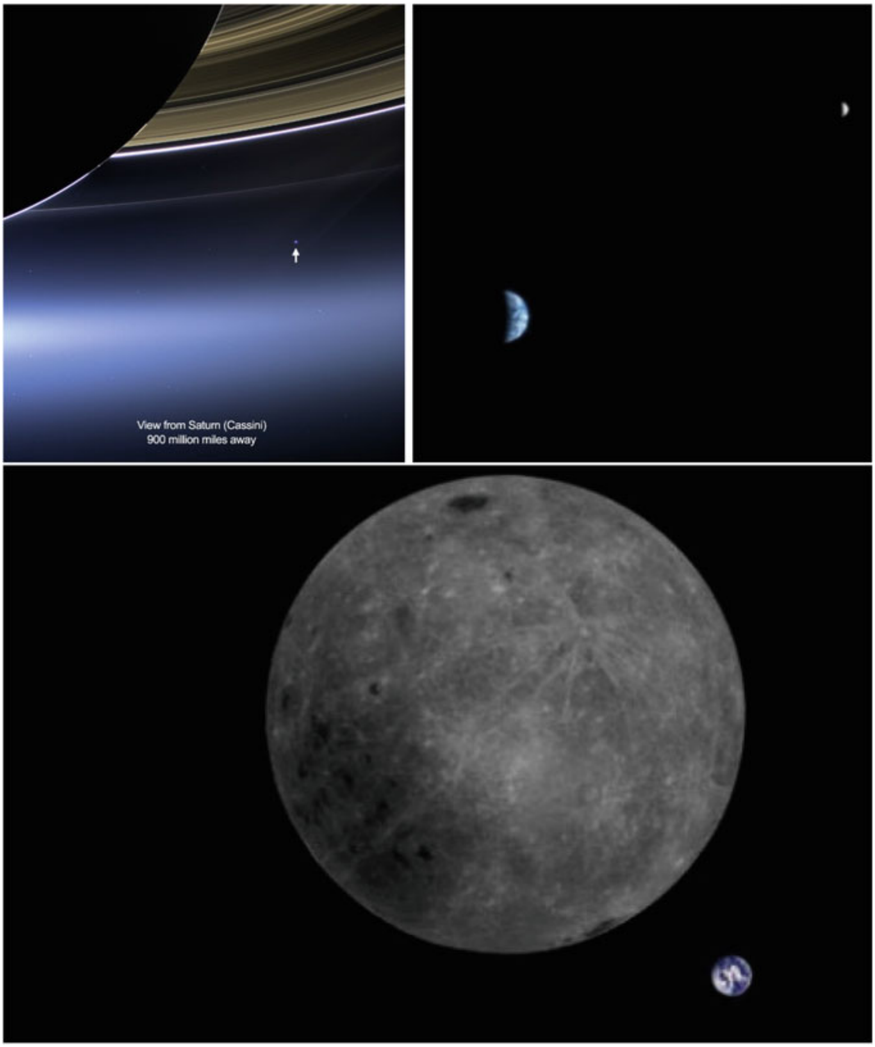
View from Saturn (Cassini)
900 million miles away

Fig. 6.110 Top left). Photograph of the Earth taken in 2013 by the Cassini spacecraft, close to Saturn (Courtesy: NASA) Top right) Mars Reconnaissance Orbiter photograph of the Earth and the Moon, taken in 2008 (Courtesy: NASA). Bottom) Photograph taken in 2018 by the Chinese Longjiang-2 lunar orbiter showing the back side of the Moon and the Earth (Courtesy: China National Space Agency)

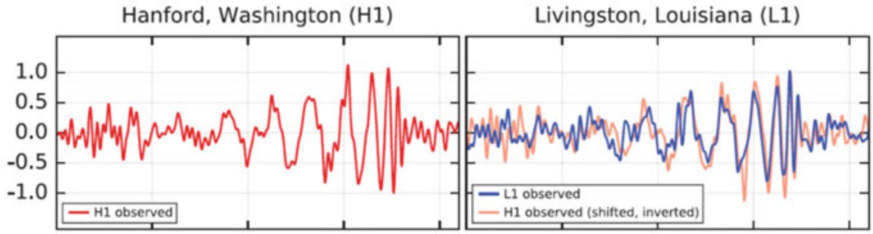

Fig. 6.111 Observation during 0.2 s at the two LIGO detectors of gravity waves generated in the merging of two black-holes, spiraling around each other at a distance of 1.3 billion light years ([564], Creative Commons Attribution 3.0 License; APS). The time difference between the recordings was about 7 ms, which combined with the base-line distance between the two laboratories (about 3000 km) gives some information of the location of the source. Combined recordings by three laboratories, as accomplished by adding the VIRGO system, could provide a full angular localization of the source

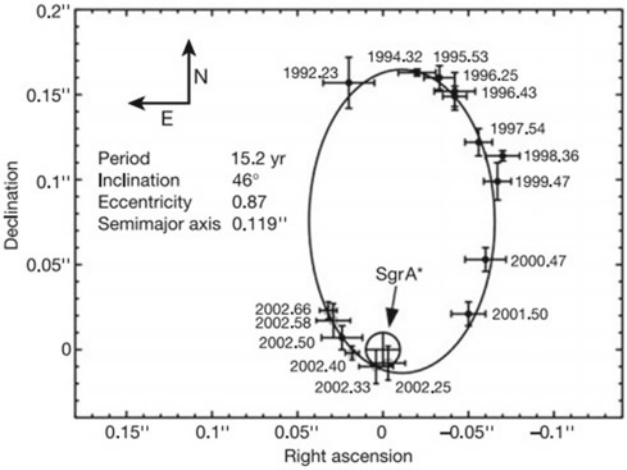

Fig. 6.112 The orbiting of a star close to the galactic centre, exhibiting a very short orbiting time ([786], reproduced with permission from Springer-Nature)

Chapter 7
Radio-Frequency Spectroscopy

Whereas the resolution in standard optical investigations of free atoms is limited by different broadening mechanisms in the light source and the spectral equipment, resonance methods yield a linewidth which is limited essentially only by the Heisenberg uncertainty relation. Two methods *Optical Pumping* (OP) and *Atomic-Beam Magnetic Resonance* (ABMR) can be utilized for investigations of ground- and metastable states. In the second method, a spatial deflection of free atoms is used, while the first method is an optical resonance method. Two additional optical precision methods are available for studies of short-lived excited states: *Optical Double-Resonance* (ODR) and *Level-Crossing* (LC) spectroscopy. Resonance techniques can also be used for investigating liquids and solids. *Nuclear Magnetic Resonance* (NMR), *Electron Spin Resonance* (ESR), and *Electron-Nuclear Double Resonance* (ENDOR) will be discussed. Nuclear magnetic resonance is also the basis for magnetic resonance imaging (MRI), which is an extremely important medical imaging modality. As the radio-frequency techniques make use of *magnetic resonance*, a general description of this phenomenon will first be given.

Radiowaves and microwaves also have several other fields of application in spectroscopy. Molecular rotational transitions correspond to this wavelength region. Radiometers can be used for passive remote sensing of, for example, temperature and air humidity, and radar systems can be utilized for active measurements of, for example, oil slicks at sea. Finally, radio astronomy is a fascinating field, yielding information also on the most remote parts of the universe.

© The Author(s), under exclusive license to Springer Nature Switzerland AG 2022

S. Svanberg, *Atomic and Molecular Spectroscopy*, Graduate Texts in Physics,
https://doi.org/10.1007/978-3-031-04776-3_7

7.1 Resonance Methods

7.1.1 *Magnetic Resonance*

We will now study the influence of a rotating magnetic field $\boldsymbol{B_1}$ on a magnetic moment $\boldsymbol{\mu_L}$, which precesses with an angular frequency ω_0 in an external magnetic field $\boldsymbol{B_0}$, as illustrated in Fig. 7.1 (see also Sect. 2.3.1). We have

$$\boldsymbol{\mu_L} = -g\mu_B \boldsymbol{L} \tag{7.1}$$

and

$$\boldsymbol{\omega}_0 = q\mu_B \boldsymbol{B_0}, \tag{7.2}$$

where $\boldsymbol{L}$ is the angular momentum vector associated with $\boldsymbol{\mu_L}$. The field $\boldsymbol{B_1}$ rotates with an angular frequency ω around $\boldsymbol{B_0}$. If ω and ω_0 are very different, the relative positions of $\boldsymbol{\mu_L}$ and $\boldsymbol{B_1}$ vary quickly and only a minor influence on $\boldsymbol{\mu_L}$ can be expected. However, if $\omega = \omega_0$, the relative positions of $\boldsymbol{\mu_L}$ and $\boldsymbol{B_1}$ are fixed and it can be seen intuitively that $\boldsymbol{B_1}$ will have a large effect on $\boldsymbol{\mu_L}$. We will now show this more rigorously. We have, see (2.10),

$$\frac{d\boldsymbol{L}}{dt} = \boldsymbol{M} = \boldsymbol{\mu}_L \times (\boldsymbol{B}_0 + \boldsymbol{B}_1), \tag{7.3}$$

and

$$\frac{\mathrm{d}\boldsymbol{\mu}_L}{\mathrm{d}t} = -\boldsymbol{\mu}_L \times (g\mu_B\boldsymbol{B}_0 + g\mu_B\boldsymbol{B}_1) = (\boldsymbol{\omega}_0 + \boldsymbol{\omega}_1) \times \boldsymbol{\mu}_L. \tag{7.4}$$

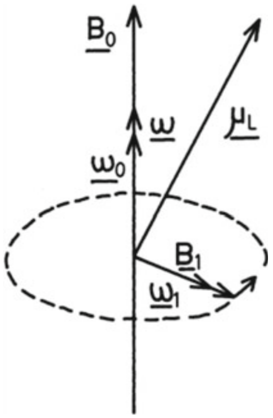

Fig. 7.1 Illustration of magnetic resonance

Here, we have defined $\boldsymbol{\omega}_1$ by the relation $\boldsymbol{\omega}_1 = g\mu_B \boldsymbol{B}_1$ in analogy with (7.2). In order to evaluate the influence of the rotating field, we now introduce a coordinate system that rotates with $\boldsymbol{B_1}$ around $\boldsymbol{B_0}$. We then have

$$\left.\frac{\mathrm{d}\boldsymbol{\mu}_L}{\mathrm{d}t}\right|_{\text{lab}} = \left.\frac{\mathrm{d}\boldsymbol{\mu}_L}{\mathrm{d}t}\right|_{\substack{\text{rel}\\ \text{rot}\\ \text{syst}}} + \left.\frac{\mathrm{d}\boldsymbol{\mu}_L}{\mathrm{d}t}\right|_{\substack{\text{rot}\\ \text{syst}}}, \tag{7.5}$$

$$(\boldsymbol{\omega}_0 + \boldsymbol{\omega}_1) \times \boldsymbol{\mu}_L = \left.\frac{\mathrm{d}\boldsymbol{\mu}_L}{\mathrm{d}t}\right|_{\substack{\text{rel}\\ \text{rot}\\ \text{syst}}} + \boldsymbol{\omega} \times \boldsymbol{\mu}_L, \tag{7.6}$$

$$\left.\frac{\mathrm{d}\boldsymbol{\mu}_L}{\mathrm{d}t}\right|_{\substack{\text{rel}\\ \text{rot}\\ \text{syst}}} = (\boldsymbol{\omega}_1 + \boldsymbol{\omega}_0 - \boldsymbol{\omega}) \times \boldsymbol{\mu}_L = (\boldsymbol{\omega}_1 - \delta\boldsymbol{\omega}) \times \boldsymbol{\mu}_L. \tag{7.7}$$

When $\delta\omega = \omega_0 - \omega = 0$, $\boldsymbol{\mu_L}$ rotates around $\boldsymbol{\omega_1}$. The projection of $\boldsymbol{\mu_L}$ on $\boldsymbol{B_0}$ then changes sign periodically and the energy increases and decreases regularly. This is the semi-classical description of *magnetic resonance*. A quantum-mechanical description corresponding to the one given for *electrical* dipole transitions can be given for these *magnetic* dipole transitions.

As we have seen, a resonance will be induced by a rotating field. However, it is easier to produce a linearly oscillating field and such a field can always be resolved into two counter-rotating components, out of which one can be made resonant. The other component is then very far from resonance and will normally have a negligible effect.

7.1.2 Atomic-Beam Magnetic Resonance

Atomic beams [787, 788] are employed in many spectroscopic techniques, e.g. in *Atomic-Beam Magnetic Resonance (ABMR)*. Such beams are generated in a vacuum system by evaporation of atoms. Vacuum techniques are discussed in [789–791]. The energy of the atoms will be of the order of *kT*, normally corresponding to thermal velocities of a few hundred m/s. The temperature needed to produce an atomic beam is determined by the vapour pressure of the element [792–794] (typically a value of 10^{-3} torr (0.13 P) is used in the evaporating oven). Vapour pressure data for different elements are given in Fig. 7.2.

The first atomic-beam experiments were performed between 1910 and 1920. In 1922, *O. Stern* and *W. Gerlach* performed their famous experiment, in which they

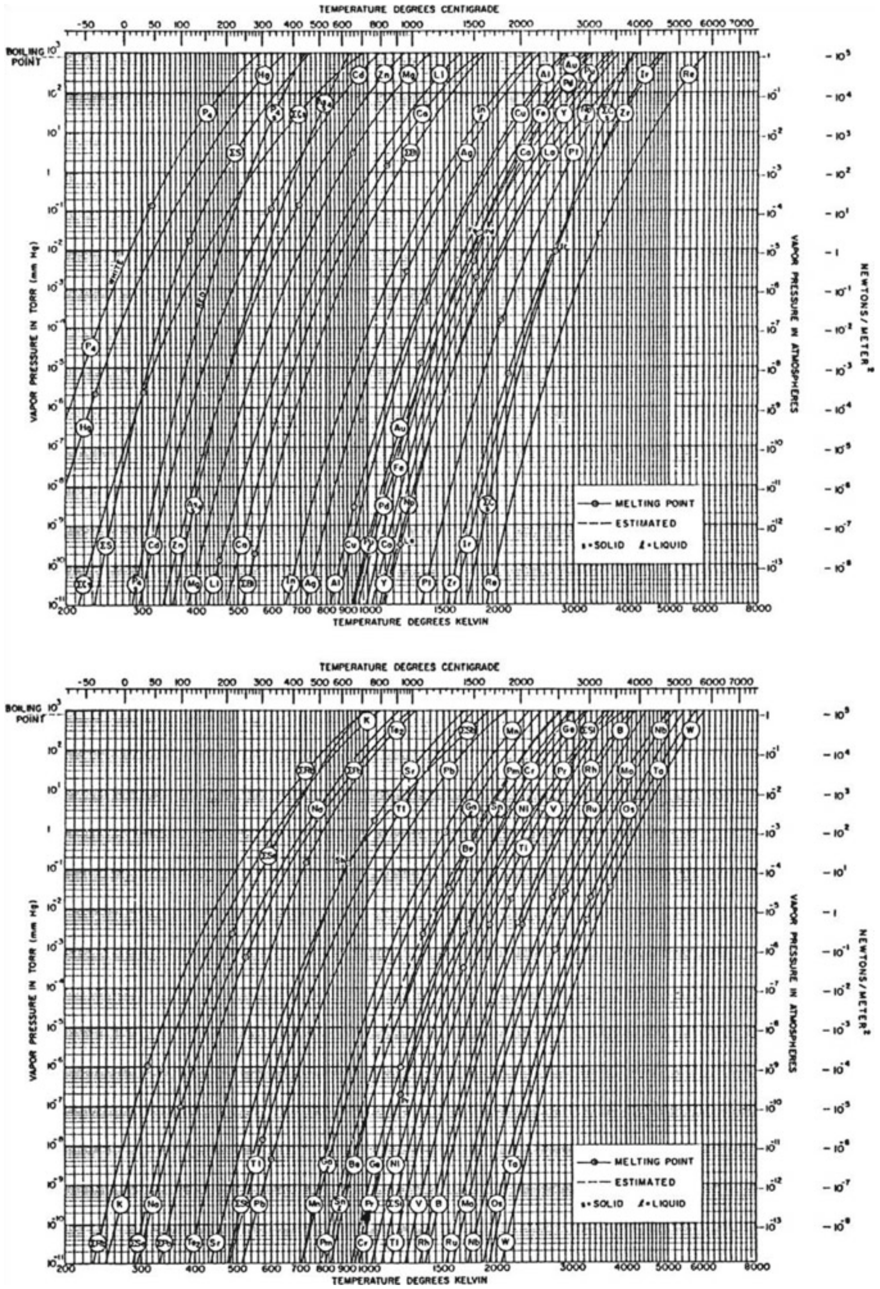

Fig. 7.2 Vapour pressure data for the elements [793]

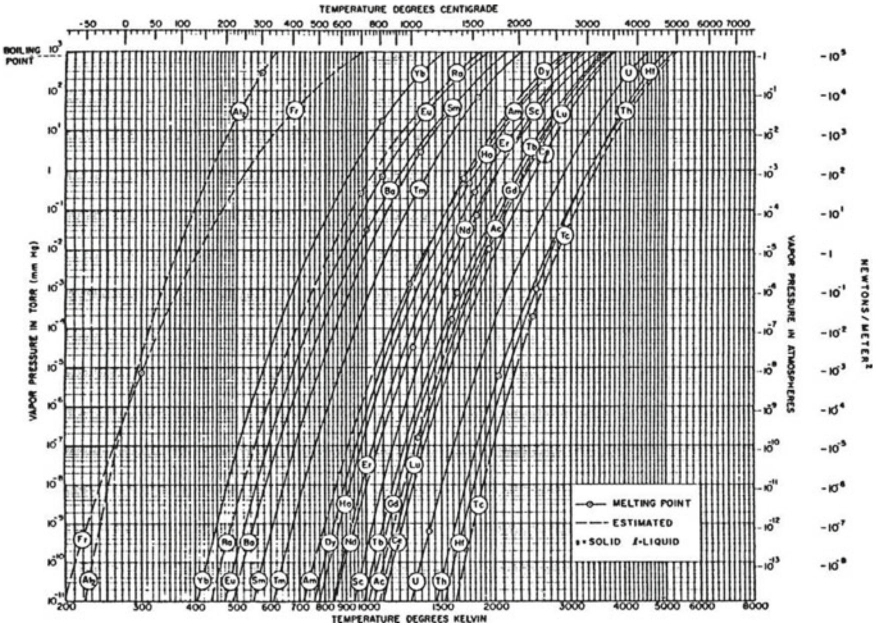

Fig. 7.2 (continued)

showed that a beam of silver atoms was divided up into two components in an inhomogeneous magnetic field [795]. This was the first direct experimental demonstration of space quantization. In order to explain the results of this experiment, we will first consider an *electric* dipole placed in an inhomogeneous *electric* field, as illustrated in Fig. 7.3. The dipole is influenced by the force

$$\boldsymbol{F} = e\mathrm{d}\boldsymbol{E}, \tag{7.8}$$

where $\mathrm{d}\boldsymbol{E}$ has the components $\mathrm{d}E_x$, $\mathrm{d}E_y$, and $\mathrm{d}E_z$.

$$\mathrm{d}E_x = \frac{\partial E_x}{\partial x}\mathrm{d}x + \frac{\partial E_x}{\partial y}\mathrm{d}y + \frac{\partial E_x}{\partial z}\mathrm{d}z = (\mathrm{d}\boldsymbol{r} \cdot \boldsymbol{\nabla})E_x. \tag{7.9}$$

Corresponding expressions are obtained for the y- and z-components. The electric dipole moment is defined as $\boldsymbol{P} = e\mathrm{d}\boldsymbol{r}$ and thus

$$F_x = (\boldsymbol{P} \cdot \boldsymbol{\nabla})E_x, \text{ etc.} \tag{7.10}$$

An analogous expression is valid for a magnetic dipole $\boldsymbol{\mu}$ in an inhomogeneous magnetic field $\boldsymbol{B}$.

$$F_x = (\boldsymbol{\mu} \cdot \boldsymbol{\nabla})B_x, \text{ etc.} \tag{7.11}$$

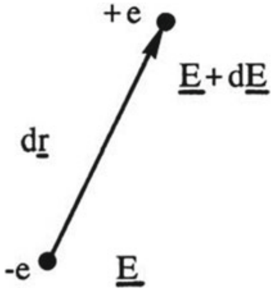

Fig. 7.3 An electric dipole in an inhomogeneous electric field

If $\boldsymbol{\mu}$ is the dipole moment $\boldsymbol{\mu}_J$ of an atom, only the force component in the direction of the field will yield a net effect due to the precessional motion.

If we choose the field direction at the atom to be the z-direction, the time-averaged value of (7.11) is reduced to

$$\langle F_x \rangle = \langle F_y \rangle = 0; \ \langle F_z \rangle = \langle \mu_{J_z} \rangle \frac{\partial B}{\partial z}. \tag{7.12}$$

In the Zeeman region for the fine structure, in which M_J is well defined, we can write

$$\langle \mu_{J_z} \rangle = -\mu_B g_J M_J, \tag{7.13}$$

i.e. the atom is influenced by a force that is proportional to M_J. Silver atoms have $J = 1/2$ in the ground state and thus the beam is separated into two components, as shown in Fig. 7.4.

If we take the coupling between $\boldsymbol{I}$ and $\boldsymbol{J}$ into account, the total magnetic moment (which is essentially due only to the electronic shell) will vary with the field strength

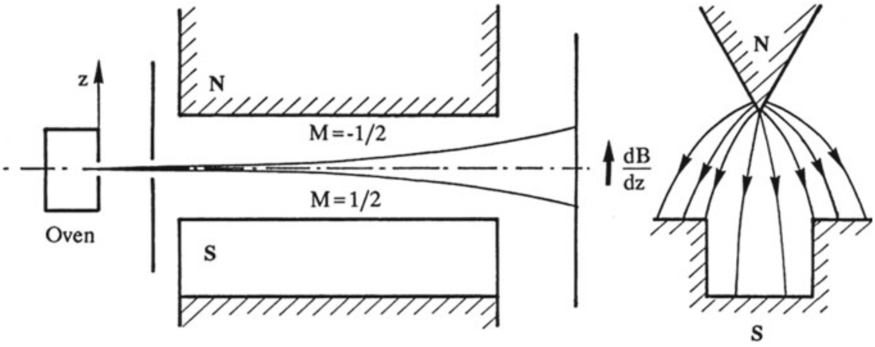

Fig. 7.4 The Stern–Gerlach experiment [1]

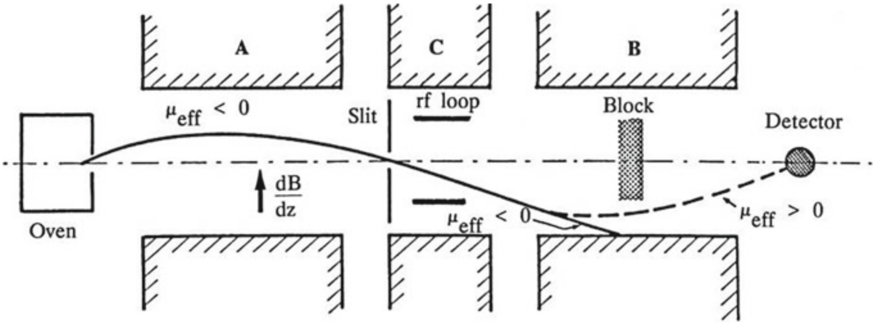

Fig. 7.5 Atomic-beam magnetic resonance apparatus (flop-in arrangement) [1]

because of the successive decoupling of $\boldsymbol{I}$ and $\boldsymbol{J}$, which occurs for increasing magnetic fields. The general expression for the force acting on an atom is

$$\boldsymbol{F} = -\boldsymbol{\nabla} W = -\frac{\mathrm{d}W}{\mathrm{d}B}\boldsymbol{\nabla} B, \tag{7.14}$$

where W is the atomic energy in the magnetic field, which depends on the absolute value of the magnetic field strength $B = |\boldsymbol{B}|$. If we compare this equation with (7.12), we can define an effective magnetic moment

$$\mu_{\text{eff}} = -\frac{\mathrm{d}W}{\mathrm{d}B} \tag{7.15}$$

and the force is still given by (7.12). Figure 2.20 shows an energy-level diagram for an atom with a hyperfine structure, subject to an external magnetic field. As can be seen, μ_{eff} varies strongly with the field for certain sublevels. For special values of the field, $\mu_{\text{eff}} = 0$ for one or several sublevels ($M_F = -1$ in Fig. 2.20). This was used by *Rabi* and co-workers for the determination of several nuclear spins and hfs constants (zero-moment method).

A great improvement in the atomic-beam technique was made with the introduction of the *Atomic-Beam Magnetic Resonance (ABMR)* technique by Rabi and co-workers in 1938 [796]. This was the first application of the magnetic resonance principle, which has subsequently been successfully used in many other cases (see below). The ABMR technique is illustrated in Fig. 7.5. An atomic beam produced by an oven passes through two inhomogeneous magnetic fields A and B, which are of the same type as those used in the Stern–Gerlach experiment. If the field gradient is directed upwards in both magnets, an atom with $\mu_{\text{eff}} < 0$ will, according to (7.12), be deflected downwards, as indicated by the full line in the figure. A magnet C is placed between the A and B magnets, generating a homogeneous field, in which an oscillating magnetic field can be applied through an RF loop. If the applied frequency corresponds to the energy difference in the C field between the originally selected state and another higher or lower state of the atom, a transition to such a state can occur through absorption or stimulated emission of the corresponding radiation. This is the resonance phenomenon discussed in Sects. 4.1 and 7.1.1. If the transition occurs to a state with $\mu_{\text{eff}} > 0$ in the B field, the atom will be deflected according to the dashed line in the figure and will hit a particle detector.

This so-called *flop-in* arrangement produces a strong increase in the signal at resonance. If the A and B fields have oppositely directed field gradients, the detector normally detects a large signal, which is decreased at resonance (*flop-out* arrangement). Note that the atoms normally experience a strong magnetic field in the A and B magnetic fields, facilitating the sign determination of μ_{eff} for the Paschen–Back region atoms.

The theoretical linewidth in resonance experiments is determined by the Heisenberg uncertainty relation. In ABMR, the width is determined by the time spent by the atoms in the oscillating field and corresponds to 10–50 kHz. The resonance frequency can therefore normally be determined to within a few kHz, whereas the accuracy in conventional optical spectroscopy is of the order of 100 MHz. In a modified method introduced by *N. Ramsey* (Nobel prize in Physics 1989) [787, 797, 798], two synchronously oscillating RF fields, widely separated in a long C field, are used to effectively increase the interaction time, and the linewidth can be reduced to a few hundred Hz, enabling extremely accurate hfs determinations. Due to the interference in the two separated interactions, fringe patterns are obtained, as illustrated in Fig. 7.6 (*Ramsey fringe method*) (see also Sect. 9.7.5 for a laser variety of the method).

The selection rules and transition probabilities for RF transitions are determined by the magnetic dipole operator for the whole system

$$\boldsymbol{\mu} = \boldsymbol{\mu}_I + \boldsymbol{\mu}_J. \tag{7.16}$$

In a weak field (Zeeman effect of the hfs), the selection rules for RF transitions are

$$\Delta M_F = 0, \pm 1, \tag{7.17}$$

$$\Delta F = 0, \pm 1, \quad F = 0 \nleftrightarrow F = 0 \quad \text{forbidden}. \tag{7.18}$$

$\Delta M_F = 0$ transitions are induced by a magnetic RF field parallel to the static field, while $\Delta M_F = \pm 1$ transitions occur for an oscillating field perpendicular to the static field. The transitions are denoted σ and π transitions, respectively.

(The magnetic field is perpendicular to the electric field; compare Sect. 4.2.1.) In a strong magnetic field (Paschen–Back effect of hfs), we have the selection rules

$$\Delta M_I = 0, \Delta M_J = 0, \pm 1. \tag{7.19}$$

This means that the RF field can flip the decoupled electronic angular momentum but not the nuclear spin.

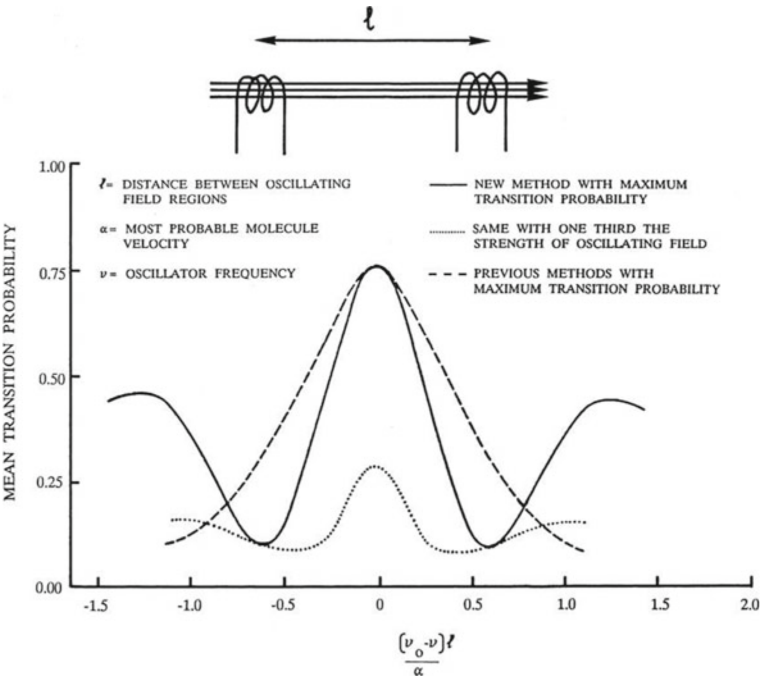

Fig. 7.6 Arrangement and signal for the Ramsey fringe technique [797]

According to (2.45), the resonance frequency for a $\Delta F = 0$, $\Delta M_F = \pm 1$ transition in a weak field is given by

$$\nu = \frac{|\Delta E_m|}{h} = \left| \frac{\mu_B B g_J}{h} \frac{F(F+1) - I(I+1) + J(J+1)}{2F(F+1)} \right|, \tag{7.20}$$

where the small contribution from the nuclear magnetic moment has been neglected. (If ν is expressed in MHz and B in Gauss (1 Gauss = 10^{-4} T), the value of μ_B/h becomes 1.400 MHz/Gauss.) The above expression is used to determine nuclear spins, I, with the ABMR method. Since I is limited to integers or half-integers, the g_J value can be determined by the same relation if an approximate value is known. A prerequisite for the detection of a resonance is that the value of μ_{eff} in strong fields is changed through the transition. (For the flop-in arrangement, the sign must also be changed.) Therefore, for $J = 1/2$, only one $\Delta F = 0$ transition can be studied (between $M_F = -1$ and $M_F = -2$ in the example given in Fig. 2.20).

F is no longer a well-defined quantum number in stronger fields. The influence of the other F states can be calculated using higher order perturbation theory or *matrix diagonalization*. The deviation from the linear expression given in (7.20) in this field region thus yields approximate information on the hfs splitting. Using the approximate value as a starting point, a search for $\Delta F = 1$ transitions in low fields can be performed. From the hfs constants a and b, the magnetic dipole moment μ_I and the electric quadrupole moment Q of the nucleus can be determined, provided that reliable theoretical calculations of the electronic magnetic field and the electric field gradient at the nucleus can be performed; see (2.39) and (2.44). If the magnetic moment has been determined by a direct method (like NMR, Sect. 7.1.6) for one isotope, it is possible to determine the corresponding moment for another isotope using the ratio between their interaction constants. According to (2.36) and (2.39), we have $a = -kg_I\mu_N$ and $\mu_I = g_I\mu_N I$. The maximum component $\mu_I = g_I\mu_N I$ is defined as the scalar dipole moment of the nucleus. For two isotopes 1 and 2, we then have

$$\frac{\mu_{I_1}}{\mu_{I_2}} = \frac{a_1}{a_2}\frac{I_1}{I_2}. \tag{7.21}$$

This relation is based on the assumption that the k value is the same for both isotopes. Since k, to a first approximation, is only related to the electronic shell, such an assumption is very reasonable. However, small differences in k can occur due to electron penetration into the nucleus (s-electrons). This results in a deviation from the relation in (7.21), or a so-called *hyperfine anomaly* [799–801]. However, this anomaly is generally less than 1%. The dipole moment of the nucleus can also be determined directly by high-precision ABMR measurement in high magnetic fields, by observing the small direct contribution from the nucleus (c.f. Eq. 2.46).

The first ABMR measurements were performed on alkali atoms, which can easily be detected using a hot wire of W, Pt, or some other material with a high work function (The Langmuir–Taylor detector). An atom with a low ionization energy is ionized with a high probability when it hits the wire, and the resulting ion current is measured. For elements with a higher ionization potential, the ionization can be accomplished through electron bombardment, but the yield is then many orders of magnitude lower. Atoms which have passed the apparatus at resonance can also be detected by observing the fluorescence light which is released upon irradiation with a laser tuned to a strong transition (Sect. 9.7.1). Radioactive isotopes can be detected with very high sensitivity by using the radioactive decay. The atoms are then collected on a foil which, after exposure, is transferred to a scintillation or the Geiger–Müller detector. For a further increase in sensitivity, focusing sextupole magnets can be used instead of the conventional A and B magnets. In a sextupole magnet, such as the one shown in Fig. 7.7, the field strength is proportional to r^2 (r is the distance from the symmetry axis), which, according to (7.14) and (7.15), means that a focusing force is obtained for $\mu_{\text{eff}} < 0$, while defocusing occurs for $\mu_{\text{eff}} > 0$. A large number of short-lived radioactive nuclei have been studied with regard to spin and moment using the ABMR method [802–804]. Such measurements are made possible by placing the ABMR apparatus online with an isotope-producing target at an accelerator facility. Nuclear spins for isotopes with a half-life shorter than 1 min can be determined.

Apart from being applied to atomic ground states, the ABMR method can also be used for investigating metastable states with a lifetime of at least a few milliseconds, a time allowing passage through the apparatus. Metastable levels not higher than

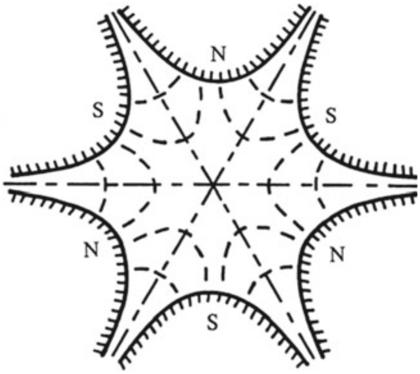

Fig. 7.7 A sextupole magnet [1]

0.5 eV above the ground state are often sufficiently populated thermally [805]. Special techniques have been developed for producing atomic beams of refractory elements such as Mo, Ta, and W [806–808]. Metastable levels can be efficiently populated with a plasma discharge in the oven [809, 810], by light irradiation, etc. It is valuable to study several states belonging to the ground configuration, allowing for a more complete analysis of the hyperfine interactions. ABMR techniques and results are discussed in [811, 812]. Atoms with $J = 0$ (diamagnetic atoms) cannot be studied by the ABMR method, since they are not deflected in inhomogeneous fields. Spin and moment determinations can then be made only after populating a state with $J > 0$.

The ABMR method has an important application as time and frequency standard. Presently, the hfs splitting between the $F = 4$ and $F = 3$ levels of the $6\,^2S_{1/2}$ ground state in ^{133}Cs in zero magnetic field is used as a frequency/time standard. This splitting has been determined to be (and then defined as)

$$\Delta v\left(^{133}\mathrm{Cs}\right) = 9,192,631,770\ \mathrm{Hz}.$$

This value agrees with the astronomical definition based on the tropical year of 1900 within the accuracy of the latter definition. The stability and reproducibility are presently about 1: 10^{14}. The Ramsey fringe technique is used to attain this high degree of accuracy. Atomic clocks operating on microwave frequencies can also be based on optical pumping (Sect. 7.1.3), hydrogen masers (Sect. 7.1.3), and fountains of cold atoms. They may in a near future be replaced by optical clocks, which by running at much higher frequencies (10^{15} Hz) could intrinsically have a much higher precision (Sect. 9.7.5).

7.1.3 Optical Pumping

Differences in population between substates are detected using different techniques in magnetic resonance experiments. The differences are created by spatially deflecting

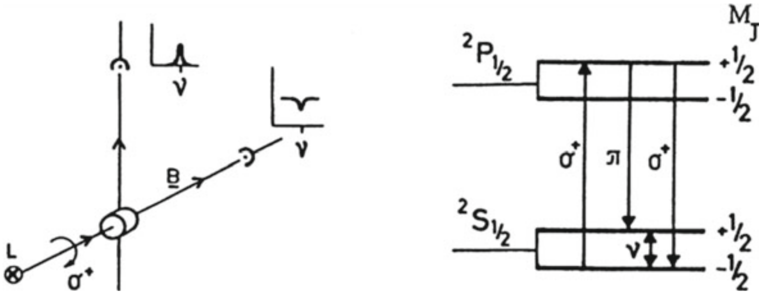

Fig. 7.8 Principles of optical pumping [1]

the atoms in the ABMR method. In 1950, *A. Kastler* showed that large differences in population between the sublevels of the ground state can be obtained using circularly polarized light [813]. (Nobel Prize in Physics for Kastler in 1966.) This results in a high sensitivity compared with the case of Nuclear Magnetic Resonance (NMR) and Electron Spin Resonance (ESR), for which methods the normal thermal population differences are used (Sect. 7.1.6). The basic principle for the Optical Pumping (OP) method is illustrated in Fig. 7.8.

Here, alkali atoms are considered with a $^2S_{1/2}$ ground state and a first excited $^2P_{1/2}$ state. First, we disregard the influence of the nuclear spin. In a weak magnetic field, both states are split into two magnetic sublevels with $M_J = \pm 1/2$. If the field is 1 Gauss (10^{-4} T), the lower of the two levels of the ground state has a thermal population excess of a few parts in 10^7. The optical pumping is performed on a low-density gas with a vapour pressure of about 10^{-6} torr (1.3 10^{-4} P) corresponding to about 10^{11} atoms/cm^3. The atoms can be considered to be free from the influence of collisions at this low pressure. For example, if we want to study sodium, a resonance cell containing sodium vapour is irradiated with a sodium lamp, preferably of the RF-discharge type (Sect. 6.1.1). Using an interference filter, the transition $3p\ ^2P_{1/2} - 3s\ ^2S_{1/2}$ at 589.6 nm (D_1 line) is selected. If the light is circularly polarized with right-hand helicity and if it is radiated along the magnetic field direction, the atoms must take up the angular momentum of the photon upon absorption. The angular momentum is directed in the light propagation direction; σ^+ excitation (Fig. 4.9). This means that the ground-state atoms with $M_J = -1/2$ are transferred to $M_J = +1/2$ ($\Delta M_J = +1$) in the excited state, from which they decay after about 10^{-8} s.

The relative probabilities for decays to the $M_J = -1/2$ and $M_J = +1/2$ levels of the ground state are 2/3 and 1/3, respectively. Atoms in the $M_J = +1/2$ state cannot be excited, since the angular moment of the photon (1 h/2π) cannot be accommodated. Thus, atoms that were originally in the $M_J = +1/2$ state remain uninfluenced, whereas the $M_J = -1/2$ atoms are pumped over into the $M_J = +1/2$ ground level after a sufficient number of excitation processes. This is equivalent to an atomic orientation. After the pumping, the gas is totally transparent to the pumping light since no absorption can occur, and a detector placed in the field direction will register a high light intensity. If an RF field, fulfilling the resonance condition for the ground state, is now applied perpendicularly to the static field direction, magnetic dipole transitions $\Delta M_J = \pm 1$ will be induced, transferring atoms into the $M_J = -1/2$ state, where they immediately start to absorb light. At the detector, a decrease in the transmitted intensity is observed. After the excitation, fluorescence light from σ and π transitions is obtained (Fig. 4.9), which can be observed by a detector placed perpendicularly to the magnetic field. The RF resonance, which often occurs at an energy of about 10^{-8} eV, thus results in a release and detection of energetic optical photons (2–3 eV in the visible region), and an extremely strong internal atomic amplification is obtained.

If we take the influence of the nuclear spin into account, we have analogous conditions. With a nuclear spin $I = 3/2$ (e.g. ^{23}Na, ^{39}K, or ^{87}Rb), the ground state has an energy-level scheme of the type illustrated in Fig. 2.20. The excited $^2P_{1/2}$ state has a Breit–Rabi diagram of essentially the same appearance as that of the ground state. When σ^+ light is radiated, the magnetic quantum number is increased by one unit in each absorption process, whereas the magnetic quantum number can remain the same or be decreased or increased by one unit in the emission process. The systematic increase in the quantum number in the absorption process results in a final accumulation of atoms in the state with the highest M_F quantum number, after a sufficient number of excitations. (Since $\Delta F = \pm 1$ transitions are also allowed, the hyperfine level groups communicate with each other.) When the $\boldsymbol{F}$ vector has been oriented in this way, there will also be a nuclear orientation due to the coupling between $\boldsymbol{I}$ and $\boldsymbol{J}$. This nuclear orientation can be used for the radioactive detection of unstable atoms [814, 815]. Oriented β-emitting nuclei will give rise to an anisotropic β-particle intensity distribution. At resonance, the orientation is lost and an isotropic angular distribution is obtained. Several short-lived isotopes have been studied with this method, particularly at online production facilities [816–818]. Here, an even more massive internal amplification occurs. The action of an RF photon of energy 10^{-8} eV will lead to the redirection of β-particles (or γ quanta) with energies in the MeV range.

If the electronic shell has no angular momentum ($J = 0$), such as in the inert gases, direct nuclear orientation is obtained by pumping. The nuclear moments can then be determined directly, as in NMR experiments (Sect. 7.1.6), but with a much higher sensitivity.

In practice, the optical pumping process is made more difficult by the possibility to leave a pumped state without being affected by an applied resonant field. This phenomenon is called *relaxation* and is primarily caused by collisions with the cell walls. By filling the cell with 10–50 torr (1.3–6.7×10^3 P) of inert gas (buffer gas), the time between wall collisions can be much prolonged due to diffusion. After collisions with inert gas atoms with spherically symmetric electron shells, the orientation of the alkali atom is maintained since the inert gas atoms cannot take up angular momentum. Alternatively, the cell walls can be covered with some suitable organic compound, such as paraffin or teflon. In this way, relaxation times longer than one second can be attained. According to the Heisenberg uncertainty principle, this corresponds to a resonance linewidth of less than 1 Hz. A large number of precision determinations

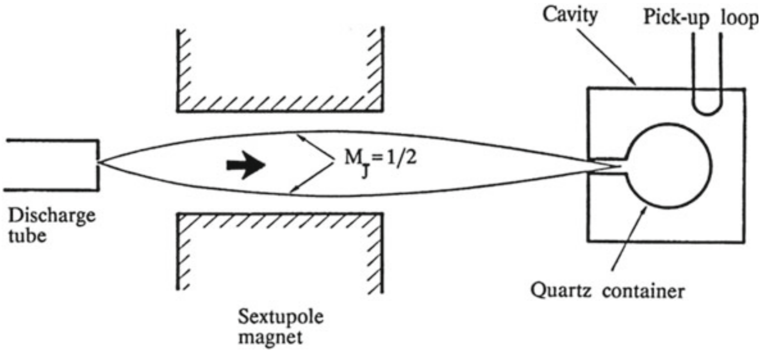

Fig. 7.9 The hydrogen maser [1]

of the hyperfine structure have been made using optical pumping. Optical pumping experiments are discussed in more detail in [819–821].

Since extremely narrow resonance lines can be obtained in optical pumping experiments, frequency standards of comparatively simple design can be achieved. The hyperfine transitions used in the atomic-beam clock are also used in the optically pumped frequency standards. However, the resonance frequency is comparatively strongly dependent on the pressure of the buffer gas [822]. It is also dependent on the intensity of the pumping light ("light shifts") [820]. Thus, it would seem that an *absolute* frequency standard of maximal precision cannot be achieved. On the other hand, optically pumped systems have proven to be very suitable for relative measurements and as *secondary* standards. By observing sharp $\Delta F = 0$, $\Delta M_F = \pm 1$ transitions, which are strongly magnetic field-dependent, fields can be measured with a very high precision. Optically pumped magnetometers can also be used at low magnetic fields in contrast to NMR devices, which require a field of a few hundred Gauss (0.02 T) to produce a measurable signal.

The *hydrogen maser* provides another way of obtaining an atomic clock [823–825]. The principle of this device is shown in Fig. 7.9. Atomic hydrogen is formed through the dissociation of hydrogen molecules in an electric discharge. A beam of hydrogen atoms is passed through a sextupole magnet. Atoms in the $M_J = +1/2$ state are then focused, while atoms with $M_J = \ - /2$ are defocused (ABMR, Sect. 7.1.2). The former atoms arrive in a quartz container inside a cavity which is tuned to the hfs separation for the ground state of hydrogen, about 1420 MHz. The cavity is subjected to a weak magnetic field, and the $M_J = +1/2$ state is then transformed into the $F = 1$ state since the nuclear spin is $I = 1/2$. Transitions to the lower state, $F = 0$, can then occur through stimulated emission (c.f. the NH_3 maser, Sect. 8.1). If there is a sufficient number of $F = 1$ atoms in the cavity, self-oscillation (maser action) occurs at a frequency corresponding to the hfs separation of hydrogen. The linewidth is influenced by relaxation processes. By coating the walls with teflon, long relaxation times can be achieved. Since buffer gas is not needed in the cavity, there are no pressure shifts. On the other hand, the resonance frequency is slightly dependent on the shape of the cavity and the wall surface, etc. However, these effects are several orders of magnitude lower than the pressure shift in optical pumping. The most accurate determination of the hfs separation in hydrogen is

$$\Delta\nu(H) = 1,420,405,751.7667 \pm 0.0009 \text{ Hz}$$

using the ABMR caesium clock as the reference. The reproducibility of the hydrogen maser does not exceed that of the ABMR Cs clock, which still constitutes the official standard. Atomic clocks, both in the microwave and in the optical region (see further Sect. 9.8.4), have been discussed in [826–837].

Accurate atomic clocks form a core ingredient for the navigational possibilities provided by satellite-based *Global Positioning System*s (GPS) [838–842]. Such systems, with full global coverage, are now operated by the US (GPS), Russia (GLONASS), EU (GALILEO), and China (BEIDOU), the rational for redundancy being that an operator at any time can switch off the access to everyone except for own use (including military). A GPS device receives the clock-controlled signals from several satellites and interpolates (basically by triangulation) the actual position of the receiver with a precision of typically few metres. Optically pumped Rb or Cs clocks, and sometimes hydrogen masers, are operated on board the satellites and are regularly calibrated towards precision terrestrial atomic clocks. It should be noted that the propagation times of the GPS signals are slightly influenced by the water vapour content of the atmosphere. High-precision data analysis yields both accurate positions and a global mapping of atmospheric water vapour, which is of the utmost interest for accurate weather prediction [843, 844]. Atomic clocks are also very important for the synchronization of radio-frequency astronomical telescopes (Sect. 7.3).

7.1.4 Optical Double Resonance

In 1949, *A. Kastler* and *J. Brossel* proposed a resonance method for excited atomic states [845]. The principles of this method are best described by discussing an explicit example. A suitable case is the very first experiment of this kind, performed by *Brossel* and *Bitter* for spin-zero mercury isotopes, as illustrated in Fig. 7.10 [846]. A resonance cell containing mercury vapour is illuminated with light from a mercury lamp and the released fluorescence light is observed. The first excited state, $6s6p\ ^3P_1$, is split up into three magnetic sublevels in an external magnetic field, while the ground state, $6s^2\ ^1S_0$, is not affected. If the electric field vector of the exciting light is parallel to the external field, only π transitions, $\Delta M = 0$, are induced (Fig. 4.9). The fluorescence light, which is emitted after about 10^{-7} s, will also be due to π transitions, with an angular distribution $I_\pi \propto \sin^2\theta$ (Fig. 4.9). Thus, no light is emitted in the field direction. By subjecting the cell to a resonant RF field, transitions to the $M = \pm 1$ levels can be induced, and σ-components ($\Delta M = \pm 1$) are now obtained in the fluorescent light. Since the σ light has an angular distribution $I_\sigma \propto$

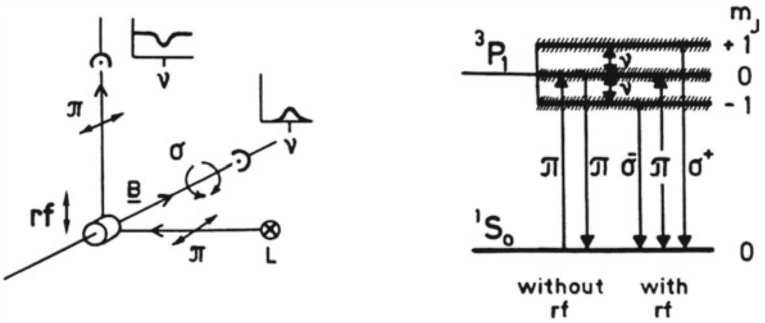

Fig. 7.10 Principles of optical double resonance [1]

$(1 + cos^2\,\theta)$ (Fig. 4.9) with maximum intensity in the field direction, the resonance can be observed as an increase in the light signal at a detector in this direction. Of course, the π emission is correspondingly decreased, and this can be observed at right angles to the field direction through a linear polarizer set to select the π-components. The width of the resonance curve will be

$$\Delta\nu = \frac{1}{\pi\tau}, \tag{7.22}$$

since the two sublevels involved both have a natural radiation width of $\Delta\nu_N = (2\pi\tau)^{-1}$. As in optical pumping, the influence of low-energy RF photons is detected using high-energy optical photons. The name double resonance indicates that both optical and RF resonances are required in the technique. Experimental information on the g_J factor and the natural radiative lifetime is obtained for the excited state in the chosen example. Examples of RF resonance in excited S states of ^{39}K are shown in Fig. 7.11 together with the corresponding Breit–Rabi diagram. In this case of hyperfine structure, the signals in the Paschen–Back region yield information on the nuclear spin ($2I + 1$ resonances), the magnetic dipole interaction constant (the signal separations are $a/\mu_B g_J$), and the Landé g_J factor (the centre of gravity of the $2I + 1$ signals corresponds to the pure electronic Zeeman effect magnetic field position). The hyperfine structure can be measured by optical double resonance, even if the magnetic field is zero. (The direction of the electric field vector of the light is then chosen as the quantization axis.) A schematic example of $\Delta F = 1$ transitions induced in zero field for the 7 $^2P_{3/2}$ state of ^{133}Cs ($I = 7/2$) is given in Fig. 7.12. The corresponding energy-level diagram can be found in Fig. 2.18 (*left*; $b(^{133}\text{Cs})$ is almost zero).

Elements with such a low vapour pressure that a sufficient atomic density cannot be obtained in a quartz resonance cell before the softening point of quartz is reached can be investigated in an atomic beam which is produced in a vacuum system (Sect. 7.1.2). A section of the beam is illuminated with light and is subject to an RF field. The intensity, or polarization distribution, of the fluorescence light is observed. The optical double-resonance technique is a very general one, allowing important information

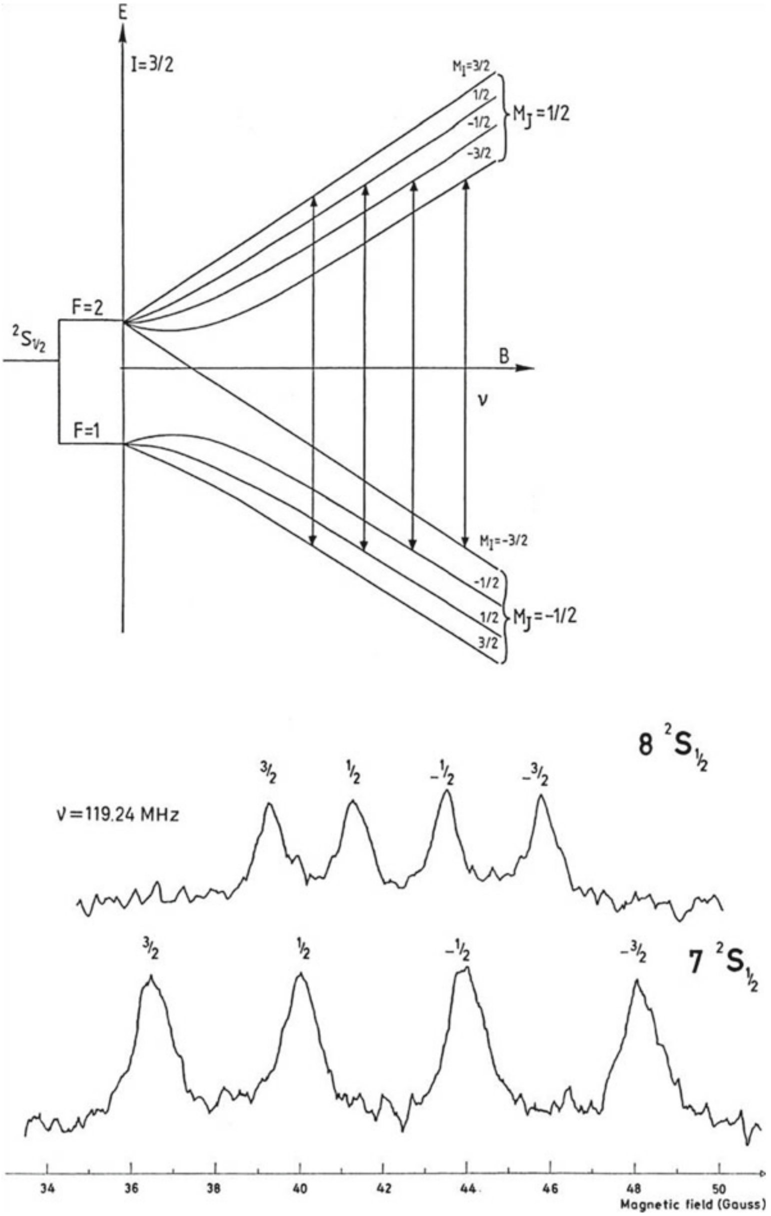

Fig. 7.11 Optical double-resonance signals in the Paschen–Back region for excited S states of ^{39}K ($I = 3/2$). Stepwise excitations from the $4\,^2S_{1/2}$ ground state via the $4\,^2P_{1/2}$ state (see Sect. 9.3) with circularly polarized light were used [847]. Note the observed and expected behaviour on promoting the electron to a higher excited $^2S_{1/2}$ state: the g_J value remains the same (as inferred from the signal centre of gravity), the lifetime becomes longer (narrower signals), and the hyperfine a-factor becomes smaller

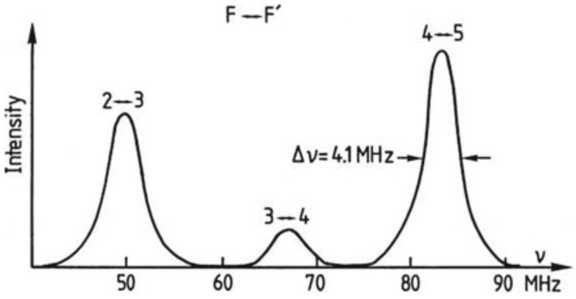

Fig. 7.12 $\Delta F = \pm 1$ ODR signals in the $7p\,^2P_{3/2}$ state of ^{133}Cs [1]

to be extracted for excited states (see also Sect. 9.3). Similar information is obtained in experiments using the level-crossing technique, which will be described next. The experimental arrangements are also quite similar.

7.1.5 Level-Crossing Spectroscopy

In the level-crossing (LC) method, interference effects in the fluorescence radiation are studied instead of RF resonances. Since the technique is very closely related to the resonance methods, we will treat it in this context. Level-crossing effects were first observed by *W. Hanle* in 1924, who studied the magnetic field dependence of mercury fluorescence light close to zero magnetic field [848]. A classical description of the effect was given. The phenomenon was investigated again in 1959 in a study of fine-structure level crossings for the $1s^2p\,^3P$ multiplet of ^{4}He, performed by *Colgrove* et al. [849].

Let us consider two magnetic sublevels belonging to an excited state of lifetime τ. In a particular field $B_{0,}$ the two levels cross. We also consider two sublevels belonging to the ground state. We assume in Fig. 7.13 that the magnetic quantum numbers M are 1 and 3 in the excited state and 2 and 3 in the ground state.

The atoms are irradiated with light that is polarized at right angles to the external magnetic field. Such light will induce σ^+ and σ^- transitions ($\Delta M = \pm 1$), as described in Fig. 4.9. First, we consider the case where the magnetic field is set far from B_0. The

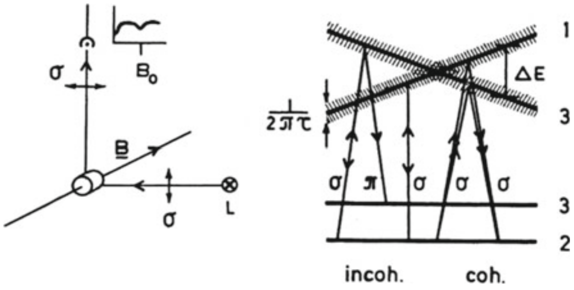

Fig. 7.13 Principles of level-crossing spectroscopy [1]

$M = 3$ level in the excited state is excited from the $M = 2$ level in the ground state, and in the decay, σ as well as π light is obtained. The $M = 1$ level can be excited from the $M = 2$ level, and σ light is emitted in the decay. The scattering processes, in which the two excited levels participate, are completely independent of each other. This is called *incoherent* scattering. In the magnetic field region in which the two excited levels overlap within their natural radiation widths $(2\pi\tau)^{-1}$, a different scattering process can occur. *Coherent* excitation of the two levels is possible from the $M = 2$ level, since every incoming photon has σ^+ ($\Delta M = +1$) as well as σ^- ($\Delta M = -1$) character. Because of the uncertainty in energy, the process is allowed in the overlap region from an energy point of view. The atom is excited into a linear superposition of the two excited substates. The difference in phase in the factors $\exp(-\mathrm{i}Et/\hbar)$ for the wave functions of the two states is

$$\Delta\phi = \frac{\Delta E t}{\hbar}. \tag{7.23}$$

Within the overlap region

$$\frac{\Delta E}{h} \leq \frac{1}{2\pi\tau} \tag{7.24}$$

the phase difference will not exceed $\Delta\phi = 1$ during the lifetime τ. Thus, a "phase memory" is retained from the excitation to the decay and we get interference between the amplitudes from the scattering processes involving the two sublevels. The total intensity of the scattered light is independent of the strength of the magnetic field, but in the overlap region, the angular distribution of the fluorescence light is changed. The detected intensity change can be used to localize the level-crossing position. Conceptually, there are many parallels between the level-crossing phenomenon and Young's double-slit experiment (Fig. 1.9). Thus, the levels correspond to the slits. There is interference only when the slits are close to each other, not when they are far apart. The total intensity is constant, and only the distribution changes. The interference effect occurs only if the two slits are illuminated coherently. There are also connections to the quantum-beat phenomenon discussed in Sect. 9.4.5.

The complete theory of resonance scattering is given by *Breit* [850] and *Franken* [851]. The *Breit formula* from 1933 gives the intensity S of emitted photons with polarization vector $\boldsymbol{e_g}$ obtained after absorption of photons with polarization $\boldsymbol{e_f}$ ($\boldsymbol{e_g}$ and $\boldsymbol{e_f}$ are unity vectors) in the interaction with an atomic system (Fig. 7.14).

If the excited state has magnetic sublevels with indices M and M' and the ground state has sublevels with indices μ, and μ', the *Breit formula* can be written

$$S = C \sum_{\substack{\mu\mu' \\ MM'}} \frac{f_{M\mu} f_{\mu M'} g_{M'\mu'} g_{\mu' M}}{1 + 2\pi i \tau (\nu_M - \nu_{M'})}. \tag{7.25}$$

Here, $f_{M\mu}$, $g_{M'\mu'}$, etc. are matrix elements of the type

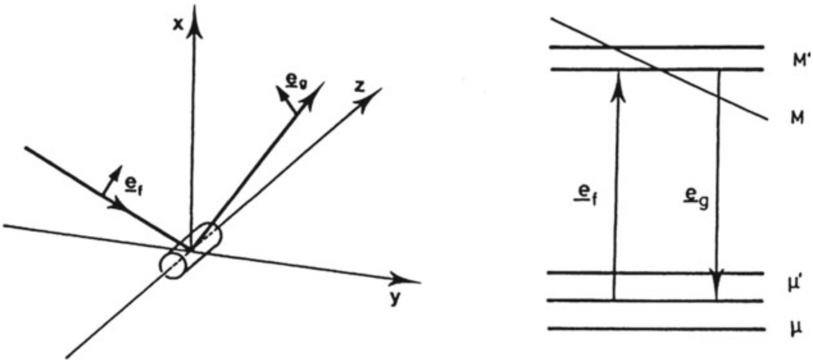

Fig. 7.14 Resonance scattering

$$
\begin{aligned}
f_{M\mu} &= \langle M | \boldsymbol{e}_f \cdot \boldsymbol{r} | \mu \rangle, \\
g_{M'\mu'} &= \langle M' | \boldsymbol{e}_g \cdot \boldsymbol{r} | \mu' \rangle,
\end{aligned} \tag{7.26}
$$

where $e\boldsymbol{r}$ is the electric dipole operator. The transition probability per time interval between sublevels with quantum numbers M and μ is proportional to $|f_{M\mu}|^2$. τ is the natural radiative lifetime for the excited state and $\nu_M - \nu_M{}'$ is the energy separation in frequency units between the sublevels with quantum numbers M and M'. The summation should in (7.25) be performed for all pairs of levels in the excited state and in the ground state. To differentiate between summations over the ground-state levels and over excited-state levels, we define

$$
K_{MM'} = \sum_{\mu\mu'} f_{M\mu} f_{\mu M'} g_{M'\mu'} g_{\mu' M}. \tag{7.27}
$$

We then have

$$
S = C \sum_{MM'} \frac{K_{MM'}}{1 + 2\pi \mathrm{i} \tau (\nu_M - \nu_{M'})}. \tag{7.28}
$$

Since the order of summation is immaterial, we can write

$$
\begin{aligned}
S &= C \sum_{MM'} \frac{1}{2} \left(\frac{K_{MM'}}{1 + 2\pi \mathrm{i} \tau (\nu_M - \nu_{M'})} + \frac{K_{M'M}}{1 + 2\pi \mathrm{i} \tau (\nu_{M'} - \nu_M)} \right) \\
&= C \sum_{MM'} \frac{1}{2} \left(\frac{K_{MM'}}{1 + 2\pi \mathrm{i} \tau (\nu_M - \nu_{M'})} + \frac{K^*_{MM'}}{1 - 2\pi \mathrm{i} \tau (\nu_M - \nu_{M'})} \right),
\end{aligned} \tag{7.29}
$$

since $f_{M\mu}{}^* = f_{\mu M}$, etc. We then have

$$S = C\sum_{MM'}\left(\frac{\mathrm{Re}\{K_{MM'}\}}{1+4\pi^2\tau^2(\nu_M-\nu_{M'})^2} + \frac{\mathrm{Im}\{K_{MM'}\}2\pi\tau(\upsilon_M-\nu_{M'})}{1+4\pi^2\tau^2(\nu_M-\nu_{M'})^2}\right). \tag{7.30}$$

Because of the selection rule $\Delta M = 0, \pm 1$, we find that $K_{MM}{}' \neq 0$ only for $|M - M'| = 0, 1$, or 2. For $|M - M'| = 0$, a level crossing cannot occur because of the non-crossing rule. Instead a related phenomenon, "*anti-crossing*", can be observed under certain circumstances [852–854]. For the arrangement shown in Fig. 7.13, it can be shown that $K_{MM'} = 0$ for $|M - M'| = 1$. If we now consider the special case where the sublevels of the excited state are linear Zeeman levels, we have $|\nu_M - \nu_M{}'| = 2\mu_B gB/h$ for $|M - M'| = 2$, yielding

$$S = C\left(\sum_M \mathrm{Re}\{K_{MM}\} + \frac{\sum\limits_{\substack{MM'\\|M-M'|=2}} \mathrm{Re}\{K_{MM'}\}}{1+(2g\mu_B\tau B/\hbar)^2} + \frac{\sum\limits_{\substack{MM'\\|M-M'|=2}} \mathrm{Im}\{K_{MM'}\}2g\mu_B\tau B/\hbar}{1+(2g\mu_B\tau B/\hbar)^2}\right). \tag{7.31}$$

The first term represents the field-independent background, the second denotes a Lorentzian (of type $1/(1 + x^2)$) with FWHM $\Delta B = \hbar/g\mu_B\tau$, and the third one describes a dispersion curve (of type $x/(1 + x^2)$) with the extrema separation $\Delta B = \hbar/g\mu_B\tau$.

This formula describes the signal around zero magnetic field, the so-called *Hanle effect*. The signal is generally a superposition of a Lorentzian and a dispersion curve on a constant background. The background corresponds to the incoherent excitation processes, in which each level scatters individually. We note that

$$K_{MM} = \sum_{\mu\mu'} \left|f_{M\mu}\right|^2 \left|G_{M\mu'}\right|^2. \tag{7.32}$$

Depending on the chosen polarization directions, $K_{MM'}$ can be made purely real or purely imaginary. It can be shown that when the polarization of the detected light is chosen to be parallel or perpendicular to the polarization of the exciting light, $K_{MM}{}'$ will be real, yielding a pure Lorentzian, whereas at 45° $K_{MM'}$ is imaginary. By changing the polarization, it is thus possible to choose the signal shape. From (7.31), it can be seen that the signal half-width depends not only on τ but also on g. The g value describes the rate of crossing and it is obvious from Fig. 7.13 that the region of level overlap depends on the crossing angle. For a general level-crossing signal in a field B_0, where B_0 is non-zero, the signal full-width at half-maximum (FWHM) of a Lorentz-shaped curve is given by

$$\Delta B = \frac{1}{\pi \tau (\mathrm{d}\nu / \mathrm{d}B)_{B_0}}. \tag{7.33}$$

The Hanle effect is, in general, much stronger than the high-field signals, since many pairs of $|\Delta M| = 2$ levels contribute to the zero-field signal.

While the level-crossing phenomenon in general requires a quantum-mechanical treatment, a simple, semi-classical model can be given for the Hanle effect. We then consider the absorbing atoms as electrical dipoles which oscillate along the horizontal axis, as shown in Fig. 7.15. Such a dipole will radiate in a $\sin^2 \theta$ pattern, where θ is measured relative to the horizontal axis. Thus, no intensity will be observed at the detector shown in the figure. If a magnetic field is applied, the atom seen as a magnetic dipole will process around the magnetic field with the Larmor frequency ω_L:

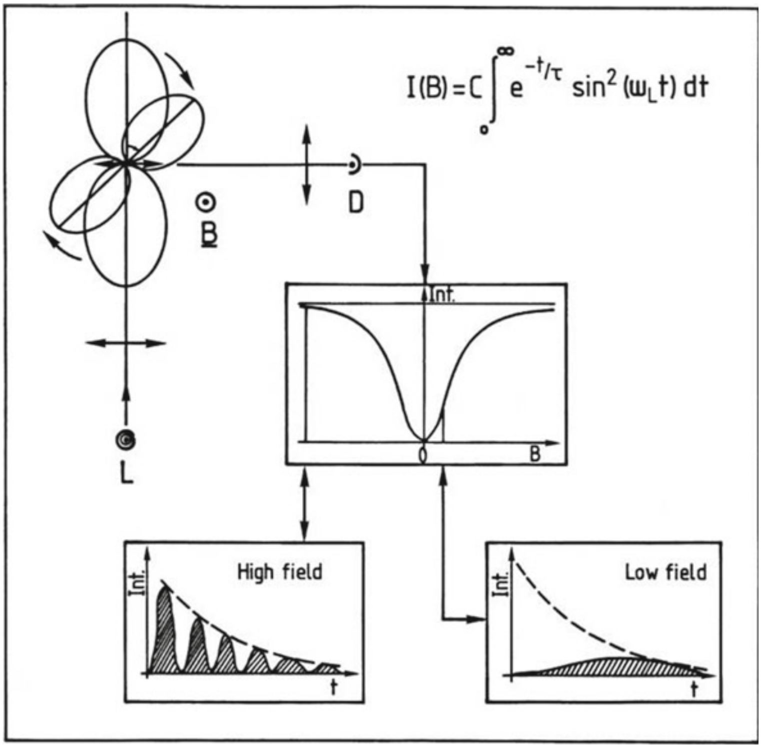
$I(B) = C \int_0^\infty e^{-t/\tau} \sin^2(\omega_L t)\, dt$
D
B
L
Int.
0
B
High field
Int.
t
Low field
Int.
t

Fig. 7.15 Semi-classical picture of the Hanle effect

$$\omega_{\mathrm{L}} = \frac{g_L \mu_B B}{\hbar}. \tag{7.34}$$

The dipole radiation pattern will then revolve and the direction θ can be replaced by $\omega_{\mathrm{L}} t$, where t is the time after the excitation. Since the dipole radiates energy, a factor $\exp(-t/\tau)$ must be added. τ is the mean lifetime of the state. In level-crossing spectroscopy, continuous excitation of dipoles occurs and the reradiated light is observed continuously. The observed intensity $I(B)$ will then be the result of an integration from 0 to infinity in time. We thus have

$$I(B) = C \int_0^\infty e^{-t/\tau} \sin^2(\omega_{\mathrm{L}} t) \mathrm{d}t, \tag{7.35}$$

where C is a constant. (If time-resolved excitation and detection are used, the rotation of the radiation lobes is actually detected; this is the Zeeman quantum-beat phenomenon (see Sect. 9.4.5)). Evaluation of the standard integral in (7.35) yields

$$I(B) = C' \left(1 - \frac{1}{1 + (2 g_L \mu_B \tau B / \hbar)^2} \right), \tag{7.36}$$

which is an inverted Lorentzian.

An example illustrating the use of the level-crossing method for the determination of hyperfine structure is given in Fig. 7.16. The state $6p\ ^2P_{3/2}$ in ^{87}Rb is studied. By employing magnetic field modulation in conjunction with lock-in detection (see Fig. 6.68d), the derivative (approximately) of the $\Delta M = 2$ level-crossing signals is recorded. Clearly, the positions of the crossings depend not only on the factors a and b but also on the g_J factor. As a matter of fact, only the ratios a/g_J and b/g_J can be determined by level-crossing spectroscopy.

Using optical double-resonance and level-crossing spectroscopy, much experimental information, particularly on hyperfine structure, has been obtained. To perform a complete hyperfine-structure analysis, it is necessary to have data for many states belonging to the same configuration. Using excitation from metastable states and utilizing a cascade population of lower states from high-lying states open up a wide field of application for these methods [856, 857]. By using tunable lasers as excitation light sources still further possibilities are created (Sect. 9.3). The consistency of theoretical calculations for evaluating nuclear moments can be tested by studying a large number of levels for the same atom. (Clearly, the nucleus can only have well-defined nuclear moments.) The influence of polarization, correlation, and relativistic effects can be investigated in this way.

As we have seen, lifetimes for excited states can be determined using optical double-resonance and level-crossing spectroscopy. The results are very reliable since these methods are subject to only small systematic errors.

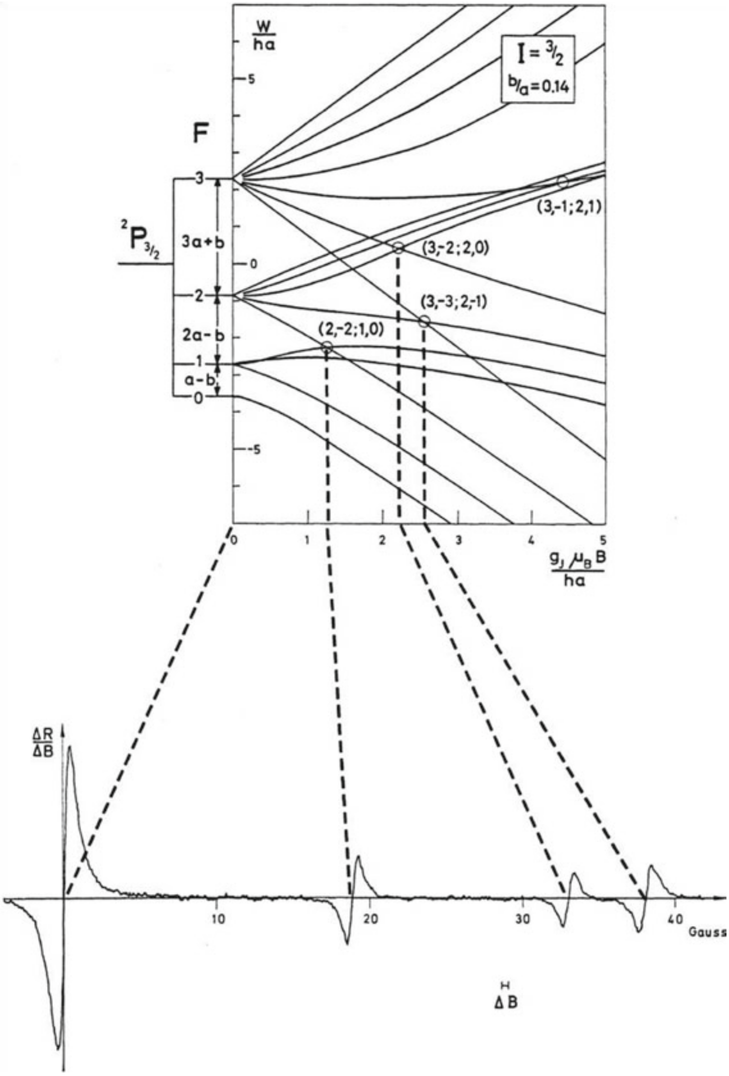

Fig. 7.16 Hfs level diagram for the $6p\,^2P_{3/2}$ state in ^{87}Rb and corresponding level-crossing signals. $\Delta M = 2$ level crossings are denoted by the symbol $(F, M; F^{'}, M^{'})$ [855]. From the energy-level diagram, it becomes clear that the level crossings move towards higher fields for larger hyperfine structures and smaller g_J factors

At the end of this section, we would like to point out that the radio-frequency methods, employing optical pumping and optical double resonance, are not Doppler-free methods in the meaning that the Doppler effect is eliminated, as is the case of the high-resolution laser spectroscopy methods (Sect. 9.7). Instead, the high resolution down to the natural radiation width is obtained because the Doppler effect is proportional to the frequency itself, and now the frequency is typically 10^8 Hz instead of 10^{15} Hz as pertaining to visible light. Thus, the Doppler effect is 10^7 times smaller, i.e. of the order of a few Hz, which is negligible compared to typical natural linewidths.

Resonance scattering by atoms has further been discussed in [858]. ODR and LC techniques were reviewed in [859–862], and extensive results for alkali metal atoms have been presented in [863].

7.1.6 Resonance Methods for Liquids and Solids

We will now discuss resonance techniques that are useful for studying liquid and solid samples. The differences in population between magnetically separated sublevels, due to the thermal Boltzmann distribution, are utilized in these methods. Magnetic field splittings are always small in comparison to kT, which is about 1/40 eV at room temperature. Thus, population differences will always be small, and the number of atoms required is much larger than for the optical resonance techniques. However, very sensitive resonance detection techniques based on RF signals have been developed. The field of resonance spectroscopy of non-gaseous media is covered in [864–871].

When sample atoms are not in a gaseous phase, coupling to the surrounding medium occurs. This has the effect that after a perturbation, e.g. an abrupt magnetic field change, a new equilibrium value $\overline{\boldsymbol{\mu}}_L$ of the macroscopic magnetization, $\boldsymbol{\mu}_L$, is reached in the sample only after a certain time, the *relaxation time* characterized by the time constant τ. The effect of the relaxation can be taken into account by adding a term $(\overline{\boldsymbol{\mu}}_L - \boldsymbol{\mu}_L)/\tau$ to (7.7). The new mathematical relations, expressed in component form, are known as the *Bloch equations*. The solution reveals that the magnetic resonance curve is a Lorentzian with a half-width inversely proportional to τ. From the equations, it also follows that, apart from fast changes of sign for $(\boldsymbol{\mu}_L)_z$ at resonance (see Eq. 7.7), there will also be a transverse macroscopic component $(\boldsymbol{\mu}_L)_\mathrm{T}$, which rotates at the resonance frequency. Here, the relaxation time τ is introduced in a vector relation and thus all components of $\boldsymbol{\mu}_L$ will have the same value of τ. However, it is generally necessary to separate the *longitudinal relaxation time* τ_1 for $(\boldsymbol{\mu}_L)_z$ and the *transverse relaxation time* τ_2 for $(\boldsymbol{\mu}_L)_{x,y}$.

Magnetic resonance is normally detected utilizing the transverse component $(\boldsymbol{\mu}_L)_\mathrm{T}$, which is formed when the resonance condition is fulfilled. A detection coil, placed at right angles to the inducing RF coil, is used in the detection method devised by *F.B. Bloch*. A sinusoidal voltage component is induced in the detection coil by the rotating magnetization. Because of the perpendicular arrangement, the driving field is not picked up. A simple measurement system based on this principle is shown in Fig. 7.17. In a different detection technique, devised by *E.M. Purcell*, a single coil is employed and a bridge circuit is used to measure the induction changes in the coil that occur at resonance. Bloch and Purcell shared the Nobel Prize in Physics in 1952.

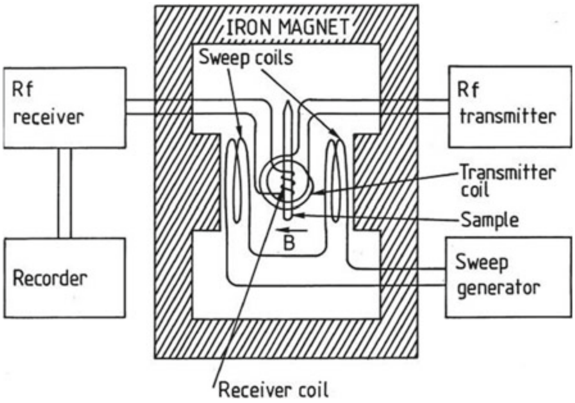

Fig. 7.17 An NMR spectrometer

Nuclear Magnetic Resonance. The nuclear magnetic resonance (NMR) technique utilizes the macroscopic magnetic moment resulting from the nuclei in the sample. In an external magnetic field B, the nuclear spin I can have $2I + 1$ different orientations. The energy E_m of a magnetic sublevel is given by

$$E_\mathrm{m} = -g'_I \mu_B B m_I. \tag{7.37}$$

A macroscopic longitudinal magnetization $(\boldsymbol{\mu}_I)_z$ due to the slightly different thermal level populations is obtained. Using an RF field, magnetic dipole transitions between the levels are induced and g_I can be measured. Since the magnetic moments of nuclei are small ($\mu_N = \mu_B/1836$), the resonance frequencies for commonly used field strengths are low. At a field of 1 T, typical for an iron magnet, resonance frequencies of a few tens of MHz are obtained. With superconducting magnetic field coils, fields of 10 T corresponding to ~500 MHz (for protons) have been attained with a corresponding increase in signal strength.

The nucleus most commonly observed is the hydrogen nucleus (proton). The proton resonance frequency is slightly dependent on the position of the hydrogen atom in the molecule. This is because a varying degree of shielding of the magnetic field occurs, depending on the properties of the neighbouring atoms. Thus, the NMR method can be used for structural determinations and chemical analysis (see also ESCA, Sect. 5.2.2, and specific vibration frequencies, Table 6.5). As an example, an NMR spectrum for ethanol C_2H_5OH is shown in Fig. 7.18. The proton resonance frequency is characteristic for each of the structural groups. At higher resolution, it is observed that the resonances are broken up into a number of separate signals. This is due to *spin–spin interactions* between the different nuclei in the molecule. Further information on the molecule can be obtained from the number of resonances and the size of splittings.

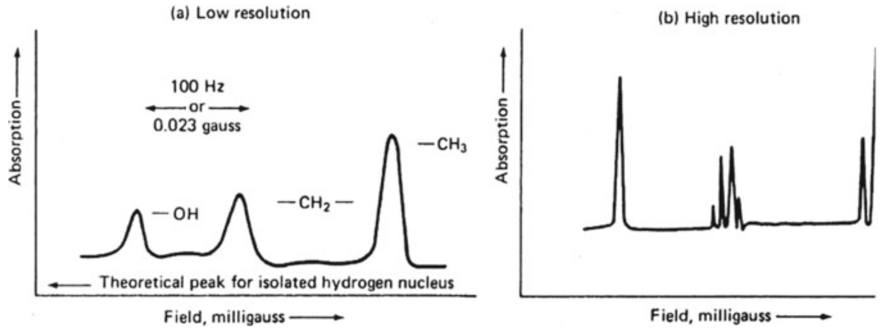

Fig. 7.18 NMR spectra of the protons in C_2H_5OH taken at low and high resolution [872]

The technique we have discussed so far is the continuous-wave (stationary) method. The frequency of the oscillator, which generates a field with an amplitude of about 10^{-7} T, is slowly swept while keeping the magnetic field constant, and the signal is recorded as a function of frequency. An NMR spectrum in the *frequency domain* is thus obtained.

Modern NMR spectroscopy frequently uses pulsed RF radiation and the observation is performed instead in the *time domain.* Pulsed NMR can be utilized in different ways. If a short pulse of high field strength B_1, ($\sim 10^{-3}$ T) and duration t_p is applied, the magnetic moments will be rotated by an angle α around B_1,

$$\alpha = g_I' \mu_B B_1 t_p, \tag{7.38}$$

and a macroscopic transverse magnetization is created for nuclei with a resonance frequency covered by the Fourier-broadened frequency distribution, $\Delta\nu$, centred around the nominal oscillator frequency ν_0 ($\Delta\nu \propto 1/t_p$). For each kind of nuclei (e.g. the protons in the ethanol molecule), a rotating macroscopic transverse magnetization will occur that will induce an oscillating voltage in the pick-up coils. The oscillation will die away with the relaxation time constant. The recorded signal is called the *Free Induction Decay* (FID) signal. Every type of nucleus covered by the pulse will give rise to separate FID signals which will interfere with each other. Using a Fourier transform, the individual Larmor precession frequencies $F(\omega)$ (resonance frequencies) can be calculated from the time-domain spectrum (the interferogram) $f(t)$:

$$F(\omega) = 2\pi \int_{-\infty}^{+\infty} f(t) \exp(-\mathrm{i}\omega t) \mathrm{d}t. \tag{7.39}$$

Clearly, this *Fourier Transform NMR* (FT-NMR) has much in common with optical Fourier transform spectroscopy (Sect. 6.2.4) and quantum-beat spectroscopy (Sect. 9.4.5), including the multiplex advantage, allowing simultaneous detection of the signals from different nuclei. In a mechanical analogy, the sharp pulse can be seen as a stroke that excites several tuning forks, which for some time ring out their eigenfrequencies. A very good signal-to-noise ratio is obtained in FT-NMR, allowing the detection of biologically less abundant nuclei with non-zero spin, e.g. ^{13}C and ^{31}P.

High-resolution NMR spectra for liquids, such as the one shown in Fig. 7.18 for ethanol, can be obtained. Sharp signals, separated due to spin–spin or quadrupole interactions, are obtained. The signals are not broadened since the molecular motion in the liquid averages out the inhomogeneities that would otherwise make the resonance frequency unsharp. This is not the case for solids, in which the constituents are fixed and yield permanent different field distributions broadening the resonance lines. A remedy for the broadening is to simultaneously apply a strong radio-frequency field that is resonant with the nuclei that are not under (resonance) investigation. These nuclei will then rotate and the spin–spin coupling to the studied nuclei will be averaged out. The technique is called *high-power decoupling*. Broadening due to coupling between nuclei of the same kind obviously cannot be eliminated in this way, but this can be accomplished instead by choosing a *magic angle* θ ($3\cos^2\theta - 1 = 0$, $\theta = 54.7°$) between an axis of rapid mechanical sample rotation and the B_0 direction (see also Sect. 9.4.5).

Many NMR techniques that utilize pairs of RF pulses or sequences of pulses have been devised for measurements of τ_1 and τ_2. The angle of rotation due to the B_1 field can be chosen by varying the length of the pulses; see (7.38). In one technique, a "90° pulse" brings the magnetization down into the x-y-plane from the initial z-direction. Because of slight inhomogeneities in the magnetic field, the individual nuclear spins will have slightly different Larmor precession frequencies, and thus the spins, which were initially aligned by the 90° pulse, will dephase leading to a decay of the AC signal picked up from the rotating transverse magnetization. However, if a "180° pulse" is applied after some time T, all the individual spins will be inverted and start precessing in the opposite direction, again with slightly different Larmor frequencies. After a time T, the individual spins will again be in phase, creating a macroscopic transverse magnetization that will result in a strong pick-up signal, a *spin echo*, which will begin to die away when the spins begin to be out of phase again. The situation is similar to that in a race between fast and slow runners, where the runners change direction at a second signal and run back to the starting line, which they will all reach at the same time. The height of the spin echo will reflect the true "dephasing time", τ_2, due to the spin–spin relaxation, which can now be measured in spite of the unavoidable field inhomogeneities. However, if a molecule moves in a liquid subject to an inhomogeneous field, the amplitude of the echo will be further reduced and diffusion coefficients or even flow velocities can be measured. The spin echo phenomenon has its counterpart in the optical region, where photon echoes can be induced by laser pulses (Sect. 9.5.3). Echo techniques have been discussed in [873, 874].

NMR techniques are used for studying the chemical composition as well as the detailed structure and bond character of molecules. Kinetic processes, such as rotations and inversions of molecules, can also be studied. NMR has found many industrial applications, especially in measurements on foodstuffs. The strength of the proton signal yields the concentration of a hydrogen-containing substance. The signal of protons in a solid matrix decays faster than that for a liquid sample. This property can be used for fast measurements of moisture content or oil assessment in seeds, etc. A recent development is the extension of NMR to the study of the three-dimensional structure of large macromolecules, which was awarded the 2002 Chemistry Nobel Prize to *K. Wüthrich* [875].

A simple technical application of NMR techniques is for magnetic field measurements. A well-defined, small probe sample, e.g. water in an RF coil is used, positioned in the unknown field, which is determined by inserting the measured frequency in (7.37). Because the population differences are due to thermal effects, fields above 0.02 T are normally necessary. This technique is also frequently used for stabilizing a magnetic field by regulating the magnetizing coil power supply using a servo-loop locked into the NMR signal.

A diagnostic application of NMR in the medical field has been made possible through the development of the *NMR imaging (tomographic) technique* [876–881], frequently referred to as MRI (*magnetic resonance imaging*). Here, the object, e.g. the head of a patient, is placed in a magnetic field that has a well-defined field gradient produced by gradient coils in the x-, y-, and z-directions. For a given oscillator frequency, the resonance condition is fulfilled only in a particular layer/slice, which can be moved in the gradient direction through the object by varying the frequency. By sequentially measuring the signals from layers at different orientations in the object, it is possible to reconstruct the proton density of the object in three dimensions by a mathematical algorithm (back-projection), similar to the one used in X-ray tomographic imaging (Computer-Aided Tomography (CAT) scanners, Sect. 5.1.3). In this way, high-resolution images can be obtained, which discriminate between different types of tissues. The diagnostic capability is much increased by using the different relaxation times in different tissues, e.g. in tumours compared with normal tissue. Rather than imaging the proton concentration, images of the local τ_1 and τ_2 values can then be made. Paramagnetic ions, such as Gd^{3+}, influence relaxation times and can be used as MRI contrast agents [882]. The 2003 Medicine or Physiology Nobel Prize was given to *P.C. Lauterbur* and *P. Mansfield* for the development of MRI imaging techniques.

An example of an early NMR tomographic image is shown in Fig. 7.19 and a corresponding X-ray tomographic image is shown in Fig. 7.20, illustrating the detection of a brain tumour with the two techniques. An MRI image with a much higher resolution is shown in Fig. 7.21.

Using pulse techniques, it is also possible to produce dynamic images of blood flow, etc. Current developments are aimed at increasing the sensitivity, e.g. by using higher fields, so that imaging of other nuclei of high medical interest but low biological abundance (^{43}Ca, ^{31}P, ^{23}Na, ^{19}F, ^{15}N, and ^{13}C) may be realized.

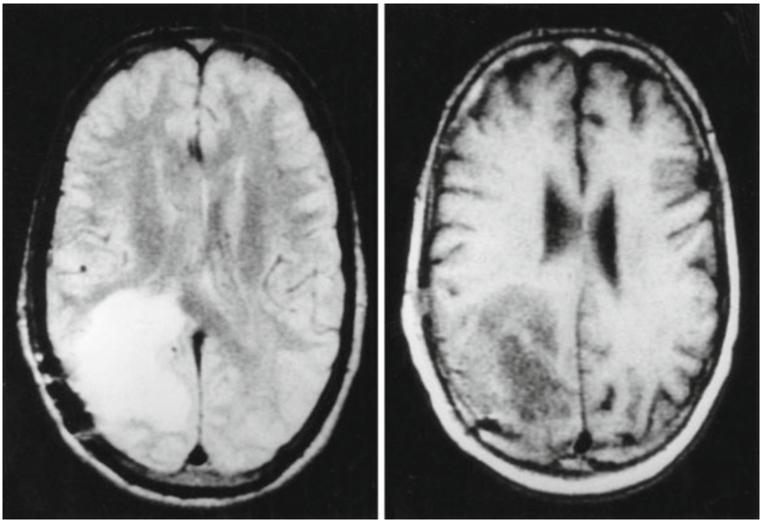

Fig. 7.19 NMR tomographic images of a human brain revealing a malignant tumour in the lower left region. The image to the *left* is τ_2 weighted while the image to the *right* is τ_1 weighted (Courtesy: O. Jarlman, Lund University)

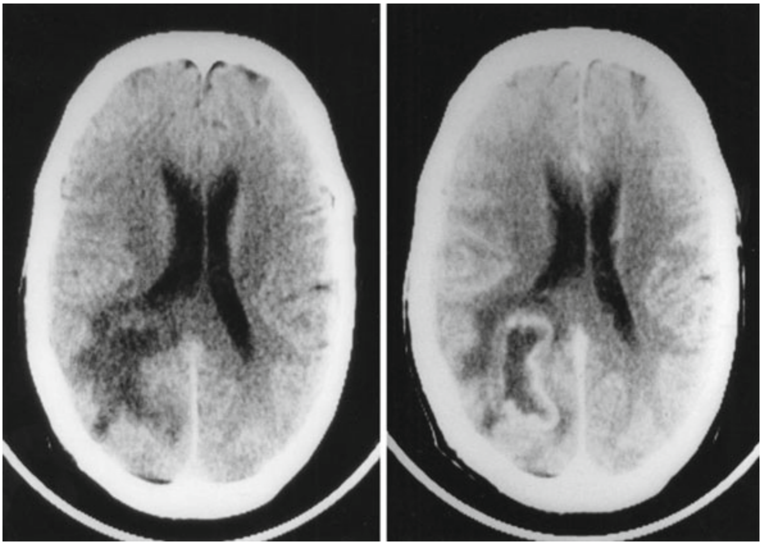

Fig. 7.20 Computerized X-ray tomographic images of the same human head as shown in Fig. 7.19. The image to the *right* is enhanced with an iodine contrast medium (Courtesy: O. Jarlman, Lund University)

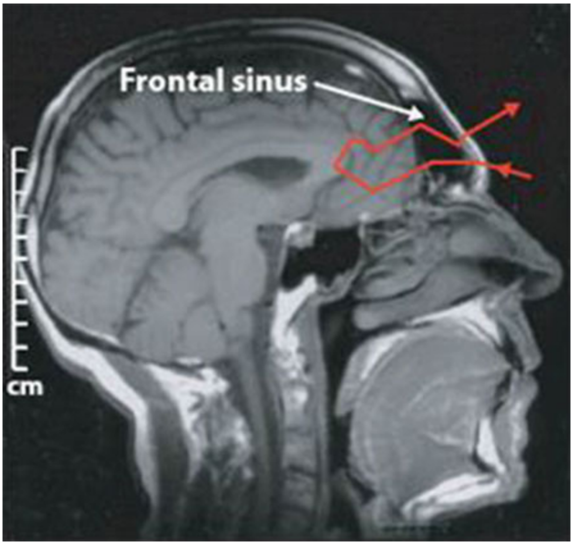

Fig. 7.21 High-resolution MRI image of a "more or less" normal human head—that of the author! The red line indicates a possible path of injected photons probing the gas in the frontal sinus with the GASMAS technique, to be discussed in Sect. 10.5.4.5

The MRI techniques have been extended to the imaging of gas filling in the lungs [883–886]. Lungs are traditionally very difficult to image. In the new technique, inert gas atoms are first polarized by optical pumping (Sect. 7.1.3). Metastable ^{3}He atoms were polarized by optical pumping on the $1s2s\ ^3S_1$–$1s2p\ ^3P_0$ transition, induced by the circularly polarized 1083 nm output from an arc-lamp-pumped LNA ($La_{1-x}Nd_xMgAl_{11}O_{19}$) laser [887]. The orientation is transferred with high efficiency to the $1s^2\ ^1S_0$ ground state by spin-exchange collisions leading to a strong orientation of the $I = 1/2$ nuclei [888]. Alternatively, rubidium atoms are first optically pumped (by a powerful diode laser), transferring their orientation to the ^{3}He nuclei in spin-exchange collisions [889, 890]. In this way, ground-state ^{129}Xe atoms ($I = 1/2$) can also have their nuclei oriented. The pumping process must occur at low pressures, but it is then possible to compress the gas for convenient transport of reasonable amounts of gas [891]. The polarized inert gases can keep their orientation for hours (100 h) [892] and thus be brought to the patient, inhaled into the lungs without risk, and kept there for a few seconds during the MRI recording. The high degree of orientation strongly compensates for the low density of spins so that images of diagnostic quality can be obtained. Examples of human lung imaging are shown in Fig. 7.22. Since xenon is absorbed into the blood stream, it is possible to follow the dynamic gas uptake from the lungs, which yields further diagnostic information.

We note that the possibility of creating an ensemble of fully spin-polarized He nuclei opens up very interesting possibilities in nuclear physics, providing polarized beam targets, spin analysis in nuclear reactions, etc. [894, 895].

Optical pumping in solids also provides new possibilities in material research. Relaxation processes can be studied, and optical detection of NMR and ENDOR signals can be obtained [895, 896].

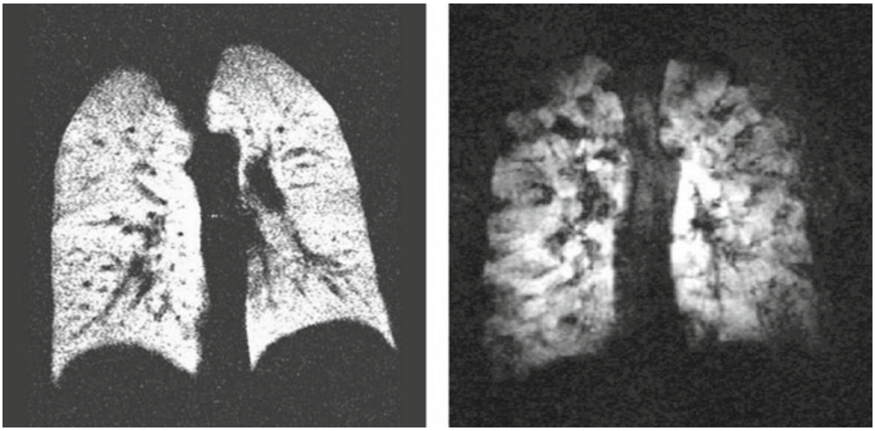

Fig. 7.22 MRI images of human lungs, recorded using spin-polarized helium gas. To the *left* normal lungs are shown, while the lungs of a heavy smoker are shown to the *right* [893]

Electron Spin Resonance. ESR is the counterpart of NMR, corresponding to magnetic splitting due to *electron* spin rather than *nuclear* spin. The projection of the orbital angular momentum $\boldsymbol{L}$ in a given direction is frequently averaged to zero in a crystal field. This is called *quenching* and has the effect that orbital angular momentum does not need to be considered when discussing the energy-level splittings in an external field. Thus, the splitting will be given only by the magnetic moment due to the total electronic spin $\boldsymbol{S}$, as shown in Fig. 7.23. In the simplest case, we have

$$E_{\mathrm{m}} = g_s \mu_B B m_s. \tag{7.40}$$

Since the magnetic moment of the electron is large ($g_s \sim 2$) in comparison with that of the nucleus, much higher resonance frequencies are obtained than for NMR. It is customary to work at 0.34 T in commercial instruments, corresponding to a resonance frequency of about 9.5 GHz. Thus, the experimental technique involves resonant cavities and waveguides for the microwaves used. The position of the resonance in the presence of crystal fields depends on the orientation of the crystal with respect to the magnetic field. The interaction must therefore be described by vectors or tensors rather than by a scalar relation such as (7.40).

Because of the larger energy separations in ESR, the signals are much stronger than in NMR. ESR can be applied in much the same way as NMR for analytical purposes. A prerequisite is that the net spin is non-zero, which is the case for *paramagnetic* substances. In particular, free radicals and molecular ions can frequently be investigated. ESR techniques have been discussed in [897–899].

Electron-Nuclear Double Resonance. In the ENDOR method, NMR and ESR are combined. The technique is illustrated in Fig. 7.24, in which a system with $S = 1/2$

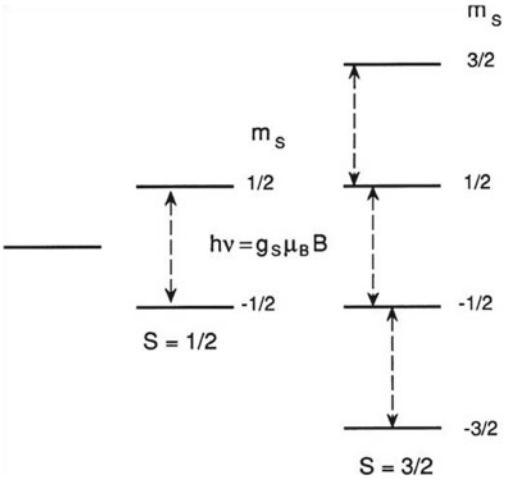

Fig. 7.23 ESR transitions

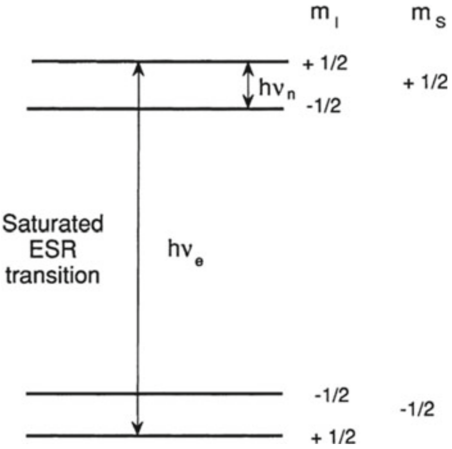

Fig. 7.24 The principle of ENDOR

and $I = 1/2$ is considered. We have two m_I values for each m_S value in the Paschen–Back region. If a microwave field saturates the ESR transition between the states with $m_I = +1/2$, only a weak absorption signal is obtained when an equilibrium situation is reached. The upper level then has a high excess population compared with the Boltzmann distribution. If an NMR transition is then induced in the upper group of levels, the state with $m_I = +1/2$ is depopulated. This results in a strong increase in the ESR resonance. The ESR resonance in an ENDOR experiment in the microwave region is thus constantly driven and a search is made in the radio-frequency region until the NMR resonance occurs, resulting in a strong increase in the ESR amplitude. Using the ENDOR technique, NMR signals with an intensity typical for ESR signals are thus obtained.

We have discussed earlier the high sensitivity achieved in optical pumping, for which a much more complete orientation is achieved than in the thermal case. As mentioned above, certain solids can also be pumped optically and ESR and NMR signals can be detected optically [895, 896, 900]. However, the efficiency is reduced due to competing radiationless transitions. Recently, radio-frequency resonances have been efficiently detected optically in studies of, e.g. nitrogen vacancies in diamond, related to magnetometry and quantum information studies [901–904].

7.2 Microwave Radiometry

Spectroscopy in the microwave region yields valuable information on the rotational structure of molecules [905–909]. Apart from this type of fundamental experiments, important applications of microwave radiometry include atmospheric and ocean monitoring [910–917]. Passive as well as active techniques are used for different types of remote sensing. Active microwave techniques are pursued with radar systems.

The vertical absorption of the atmosphere in the 1–300 GHz region is shown in Fig. 7.25. The absorption bands are due to H_2O and O_2. The 60 GHz O_2 band consists of about 25 lines, which can be resolved in the stratosphere but which overlap in a single band at low altitudes due to pressure broadening. The atmospheric pressure can be measured by studying such pressure-broadening effects. At high altitudes, the broadening is given by the Doppler effect, which yields information on the temperature. The water vapour content can be determined using the strong

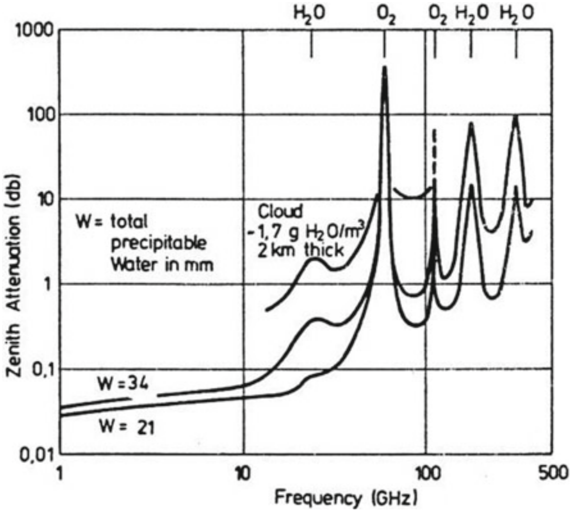

Fig. 7.25 The integrated vertical microwave absorption of the atmosphere with varying water content in the air [918]

absorption at 22 and 183 GHz. Vertical measurements can be performed from the ground (towards *zenith*) or from satellites (towards *nadir*). So-called *limb emission* or *limb absorption* measurements can be made from satellites (see Fig. 6.82). In absorption measurements, radiation through the atmosphere at sunrise and sunset is employed. A deconvolution procedure must be used to obtain the vertical profiles of pressure, temperature, and humidity. Satellites equipped with microwave radiometers can be used to determine temperatures to an accuracy of better than 1 °C.

Active microwave systems (radar) have many applications apart from the normal ranging applications that are used, for example, for navigation. A weather radar station is capable of locating and quantifying rainfall over considerable distances. In order to detect the small particles, a short operating wavelength is necessary to achieve adequate scattering. Radar systems for environmental applications are air- or satellite-borne. In SLAR (*Side Looking Airborne Radar*) systems, the imaging sweep is obtained through the forward movement of the propelling craft. The principle of SLAR is shown in Fig. 7.26. A disc-shaped radiation lobe is transmitted from an elongated antenna. The ground surface is hit at successively later times and the echo from the radar pulse will return to the antenna at different times and a picture line is thus generated after geometrical rectification. Then a new pulse is transmitted and a new picture line, corresponding to the new position of the aeroplane, is obtained. The strength of the return signal depends not only on the distance, which can easily be compensated for, but also on the structure of the surface, water content, etc. Ocean waves, especially, yield echoes whose strength depends on the wavelength of the water waves (sea clutter). A 10 GHz system ($\lambda = 3$ cm) is especially sensitive to the fine capillary waves, which occur at sufficiently large wind speeds (> 8 m/s). If the sea is covered by oil, the capillary waves disappear and the oil slick can be detected as a decrease in the sea clutter. Oil detection with a SLAR system is illustrated in Fig. 7.27. Such a system is also useful for sea ice monitoring.

Because of the long wavelength of the radar waves, a high spatial resolution cannot be obtained for antennas of reasonable size. This is a particular problem for satellite applications, which can, however, be circumvented using so-called SAR (*Synthetic Aperture Radar*) techniques [920–926]. A high lateral resolution is obtained by using short pulses in the same way as in a SLAR system. In order to obtain a high resolution

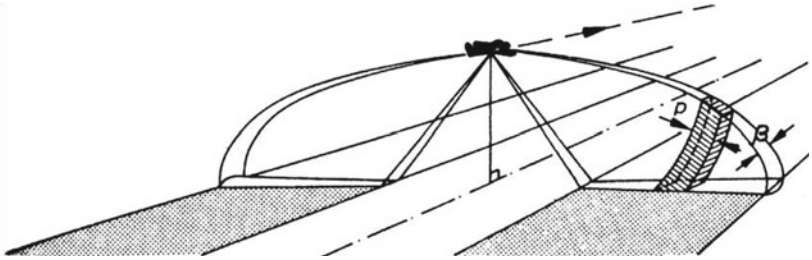

Fig. 7.26 The principle of SLAR [919]

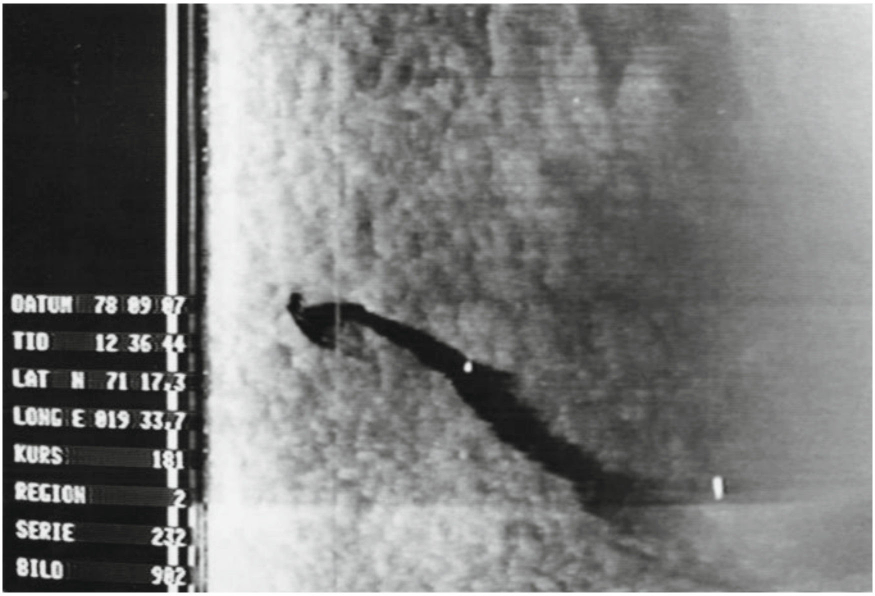

Fig. 7.27 20 × 20 km^2 SLAR image of a marine oil slick and ships. 24 h before the recording 25 tonnes of crude oil had been dumped. Bright echoes are seen from two ships and reduced sea clutter signal from oil-covered parts of the sea (Courtesy: The Swedish Space Corporation)

in the flight line direction, the slightly different Doppler shifts in the backscattered radiation from the diverging antenna lobe are used to sort the return signals into different spatial channels along the flight line. Using powerful computers, all Doppler data for the individual image points can be merged ("focused") to yield a sharper image. This is mathematically equivalent to the utilization of a much larger antennae (a synthetic aperture) with a size in the flight direction corresponding to the distance swept during the Doppler shift collection. Clearly, this heavily relies on the smooth and fully predictable movement of the space vehicle during the data sampling time (in radio astronomy, this corresponds to accurate atomic clock synchronization between the distant telescopes; see Sect. 7.3).

Several active radar satellites were early launched, e.g. the European ERS-1 (1991–1999) and ERS-2 (launched 1995) satellites, which have circular orbits 785 km above the ground.

Radar sensors have the particular advantage of providing data irrespective of the cloud layer. The ERS SAR system operating in the C-band (5.3 GHz, 6 cm) yields a ground resolution of about 20 m. An ERS image from the Arctic during a ship expedition is presented in Fig. 7.28. The radar echoes depend on the dielectric properties of the target materials. For example, different types of sea ice and the water content of snow can be evaluated in this way [927].

Multi-frequency systems and polarization analysis provide spectral fingerprinting at microwave wavelengths and classification of image elements [911, 913, 928].

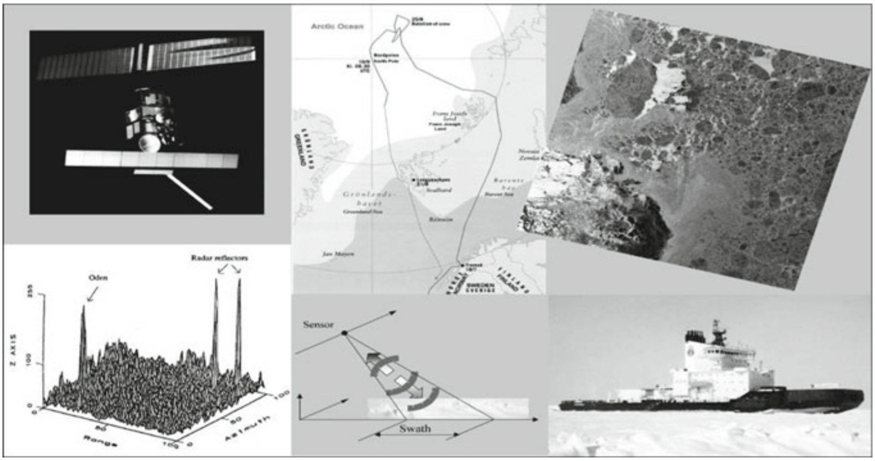

Fig. 7.28 During Arctic expeditions in 1991 and 1996 with the Swedish ice-breaker Oden, data on sea ice and snow were collected, and at the same time, the ESA ESR-1/2 satellites were used to acquire SAR images (an image over 80 × 80 km^2 is included). Radar reflectors for calibration were also used (Courtesy: J. Askne, CTH)

Novel SAR systems include the RADARSAT-2, ENVISAT, and SENTINEL I satellites.

7.3 Radio Astronomy

Continuum radiation and absorption or emission lines due to celestial phenomena are observed in the science of radio astronomy in the frequency region of 1–300 GHz (300 mm > λ > 1 mm). The absorption bands due to the terrestrial atmosphere, as illustrated in Fig. 7.25, will clearly place limitations on such measurements. The diffraction-limited resolution for a telescope is determined by the ratio λ/d, where d is the diameter of the telescope. In a comparison with optical telescopes, it can be noted that a radio telescope has 10^4–10^5 times worse angular resolution for a given value of d. For practical reasons, a telescope diameter of the order of 100 m is an upper limit, especially since a surface precision of about $\lambda/20$ must be maintained. Examples of early radio telescopes are the 100 m telescope near Bonn in Germany, which is used in the frequency region 1–45 GHz, and the 20 m Onsala telescope in Sweden, which can be used for frequencies up to 120 GHz ($\lambda = 2.5$ mm). A diagram of the latter telescope is shown in Fig. 7.29.

To amplify the weak radio signals picked up by the telescopes, travelling-wave masers and superconducting mixers are sometimes used. An example of a maser medium is iron-doped rutile (TiO_2), which can be magnetically tuned in a certain frequency range. Signal analysis is often performed using autocorrelation techniques,

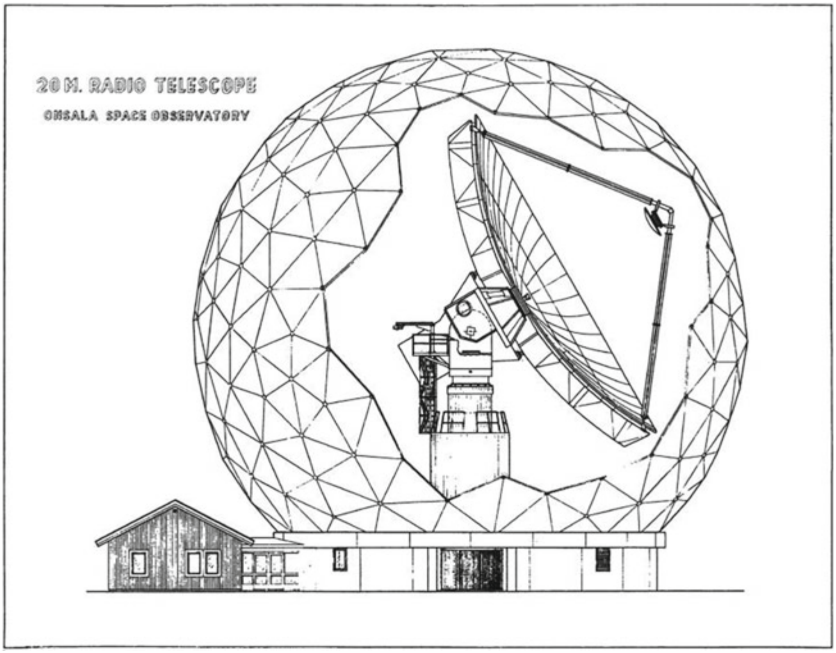

Fig. 7.29 Diagram of the 20 m diameter millimetre-wave telescope at Onsala, Sweden (Courtesy: Onsala Space Observatory)

in which the incoming signal is compared with a replica of itself that has been displaced in time by a variable interval. Other signal analysis techniques employ analogue filter banks.

In order to increase the angular resolution in radio astronomy, the technique of *aperture synthesis* is used, in which signals from spatially separated antennas are combined, monitoring the correct relative phases. An early large such interferometer is the Very Large Array in New Mexico, a Y with 3 arms of length 21 km. The mathematical processing of data from different telescope positions to form a high-resolution radio image includes, as its most critical component, a fast Fourier transform, and the fast development of computers has been a prerequisite for high-resolution radio astronomy. As in optical Fourier transform spectroscopy (Sect. 6.2.4), a multiplex advantage is obtained in radio interferometry: information from a solid angle interval, which is determined by the (wide) diffraction lobe of each individual small telescope, is obtained simultaneously.

An extreme angular resolution (10^{-4} arcseconds) can be obtained in so-called VLBI (*Very Long Baseline Interferometry*) measurements. The first trans-oceanic radio-interferometric measurements were performed in 1968 between telescopes in Sweden, Massachusetts, West Virginia, and California. The largest telescope separation was 8,000 km. Perfect time synchronization using atomic clocks (Sect. 7.1.3) is needed in order to utilize the detailed phase difference information. VLBI can also be used to obtain precise information on the continuing small displacements of continents. From such measurements, it is known that Europe and North America drift apart at a rate of 2 cm/year! Several networks using VLBI are now operating. The Very Long Baseline Array (VLBA) system connects ten 25-m diameter telescopes across the US (including Mauna Kea, Hawaii) with a longest baseline of close to 9,000 km. Precision atomic clocks are used to synchronize the signals into a huge synthetic aperture. The European VLBI network operates telescopes in Europe, China, South Africa, and Puerto Rico, and further networks in Asia and Australia exist. A natural step is to place radio telescopes in space. There could be at least two motivations. Obviously, the baseline length can be very substantially extended, but also observations in new and largely inaccessible wavelength regions could be possible. Radio frequencies below 30 MHz are largely disturbed by the earth's ionospheric layer. As a matter of fact, the Russian-led RadioAstron project explores space techniques for radio astronomy, where a 10-m diameter telescope on board a satellite is complemented with a hydrogen maser for synchronization with earth telescopes. While this system addresses frequencies above 300 MHz, the Dutch-Chinese OLFAR (Orbiting Low-Frequency Antenna for Radio astronomy) project, with a test system launched in 2018, is exploring space technology for frequencies below 30 MHz.

Radio signals are obtained primarily from interstellar gas clouds but also from distinct, localized sources. The gas clouds are observed against the general cosmic background corresponding to black-body radiation of $T_\mathrm{b} = 3$ K. Depending on whether the local radiation temperature T of the cloud is lower or higher than T_b, molecular lines from the cloud are observed as absorption lines in the background radiation or as emission lines, as illustrated in Fig. 7.30. If a population inversion between the molecular levels exists (at least three levels must then be involved), the background radiation can be amplified by maser action. Such action can be recognized through the characteristic line narrowing for stimulated emission [930, 931].

Molecular lines observed in the microwave region are due to pure rotational or hyperfine transitions. Hydrogen is the most abundant element in the universe. The H_2 molecule does not possess a dipole moment and therefore no allowed electric dipole transitions are observed. This molecule can, therefore, not be observed.

However, atomic hydrogen can be observed at the magnetic dipole hyperfine transition ($\nu = 1.42$ GHz) between the hyperfine levels $F = 1$ and $F = 0$ of the ground state (Sect. 7.1.3). For example, using the corresponding 21 cm line, the spiral structure of our galaxy has been investigated.

A large number of interstellar molecules have been detected. The hydroxyl radical OH has a large dipole moment and was observed in 1963 after necessary laboratory measurements had been made. The OH levels and transitions are depicted in Fig. 7.31. The rotational level is split into two levels (Λ-doubling, Sect. 3.2), each with two hyperfine levels. The observations made were absorption measurements with the strong continuum radio-source Cassiopeia A (a supernova remnant) providing the background. Maser action in OH has been observed in many cases and the pumping is normally due to hot star radiation. The CH radical, also featuring Λ-doubling, was observed at Onsala in 1973. The water molecule H_2O, which has an angle of 105°

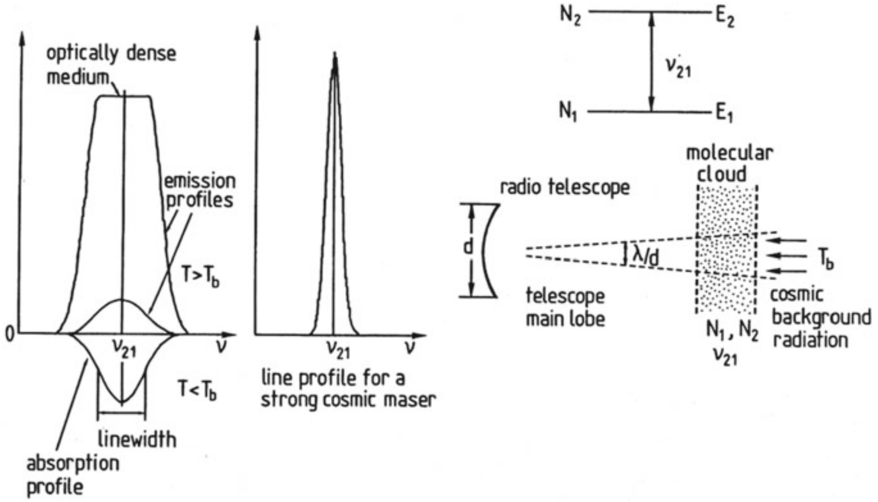
optically dense medium
emission profiles
T>T_b
0
ν_21
ν
T<T_b
linewidth
absorption profile
ν_21
ν
line profile for a strong cosmic maser
N_2
E_2
ν_21
N_1
E_1
molecular cloud
radio telescope
d
λ/d
T_b
telescope main lobe
N_1, N_2
ν_21
cosmic background radiation

Fig. 7.30 Absorption and emission lines in the microwave region. The narrowing of a maser transition is also illustrated [929]

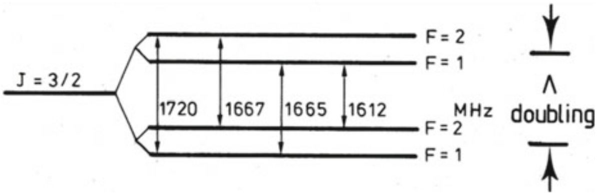
J = 3/2
F = 2
F = 1
1720
1667
1665
1612
MHz
F = 2
F = 1
Λ doubling

Fig. 7.31 OH molecule substructure and microwave transitions [929]

between the H atoms, has a complex rotational spectrum. Intense maser action has been observed for the 22 GHz transition, which is also seen in atmospheric absorption (Fig. 7.25). High-frequency radio astronomy observations have to be performed on dry days. A large number of other molecules, some of them quite complex, have been observed in space. The (very) remote sensing of the physical conditions in the interstellar clouds has been discussed in [932, 933].

As with any other spectral lines, radio lines exhibit the Doppler shifts if the molecular gas is in motion. Velocity distributions are shown in Fig. 7.32 based on the Doppler observations on OH, CH, and HCHO lines observed in the direction of Cassiopeia A. The components around 45 km/s are due to clouds in the Perseus arm of our galaxy, while the components around 0 km/s are due to the Orion arm. While OH and HCHO appear in absorption, CH is seen in (weak maser) emission against the background source.

Apart from the study of interstellar clouds, a large number of “point” sources have also been investigated using radio astronomy. The observation of pulsars (1967) by

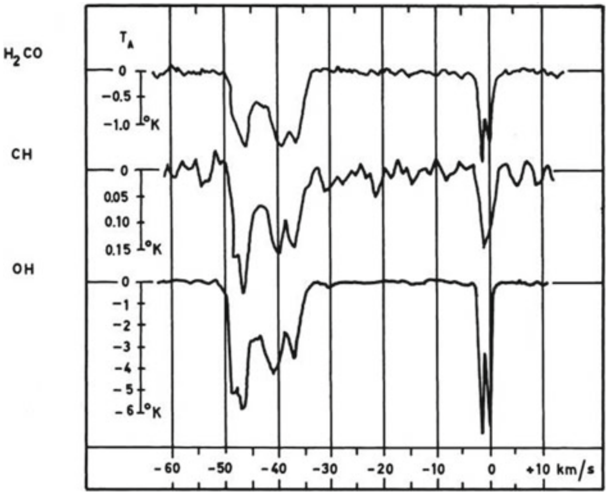

Fig. 7.32 Spiral structure of our galaxy mapped out with Doppler-shifted microwave signals [929]

A. Hewish, J. Bell et al. is one of the more spectacular discoveries [934] (Nobel Prize in Physics to *A. Hewish* in 1994). Pulsars have a pulse period of the order of seconds. They are considered to be rapidly rotating neutron stars, which are very small, dense objects. An example of pulsar signals is given in Fig. 7.33.

The pulsar PSR 1913+16 is particularly interesting since it exhibits small periodic changes in its pulse frequency (which is very high; the period is only 59 ms). This means that it has a companion and they orbit, bound to each other, with a period of 7.8 h, corresponding to a velocity of about $0.001c$. According to the general theory of relativity, an intensely rotating heavy system should emit gravitational radiation, leading to a slow decrease in the orbit period. This has been accurately observed, fully supporting Einstein's theory [935, 936]. The 43 arcsecond per century advancement of the perihelion of Mercury was an early confirmation of the theory. For the double pulsar PSR 1913+16, the corresponding effect is 4 degrees/year! The 1993 Nobel prize in Physics was awarded to *R.A. Hulse* and *J.H. Taylor* for their discovery of

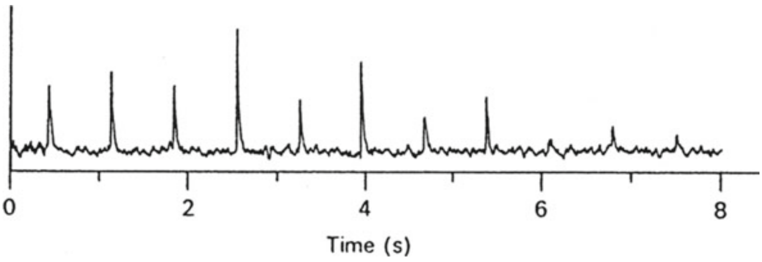

Fig. 7.33 Periodic signals due to a pulsar source (Courtesy: Onsala Space Observatory)

this remarkable double pulsar, which constitutes a precise laboratory for relativity research. In particular, the data show that gravitational radiation must exist and should be of a quadrupolar nature. As noted in Sect. 6.2.4 and Fig. 6.111, the direct observation of gravitational waves from spiralling and coalescing black holes has recently been made using ultra-high precision optical interferometry.

The enormous energy generation in quasars, probably associated with black holes at cosmological distances, is another fascinating discovery due to radio astronomy. Radio astronomy has been covered in [937–941].

A very hot field in radio astronomy is the study of background microwaves with a frequency distribution peaking at about 160 GHz, corresponding to 2.73 K, and generally interpreted as due to a primordial explosion some 13 billion years ago [942–944]. The discovery of this cosmic background radiation was awarded with the Physics Nobel Prize to *A.A. Penzias* and *R.W. Wilson* in 1978. The perfect Planck radiation pattern and small spatial variations (fluctuations) in the radiation distribution were studied with the COBE (Cosmic Background Explorer) satellite and resulted in the 2006 Physics Nobel Prize to *S.C. Mather* and *G.F. Smoot* [945, 946]. Much more accurate data were obtained from the WMAP (Wilkinson Microwave Anisotropy Probe) satellite and even better data from the PLANCK satellite. The latter allowed minute temperature variations (less than 5 μK) to be determined by using nine different microwave bands and fitting the data to a Planck radiation curve. An angular resolution of 0.07 degrees was obtained in studying the minute structures. A map of the background microwave radiation of the full sky as recorded by the PLANCK satellite, with comparison to WMAP data, is shown in Fig. 7.34. The anisotropy (granularity) shows an observed spatial frequency pattern as presented in Fig. 7.35. Such data could be used to refine the standard cosmological model of the universe, and the current interpretation is that the universe consists of 5% normal (baryonic) matter, 27% dark matter of unknown origin, and 68% “dark energy”, a concept related to the cosmological constant defined in Einstein’s early gravitational work and the finding that the universe has an accelerating expansion.

The somewhat controversial field of the search for extraterrestrial intelligence (CETI—Communication with Extraterrestrial Intelligence) has been treated in [947–949]. Radio astronomy tools have been used, but the search has been extended to a search for possible laser flashes from distant objects. The first two spacecraft to leave the solar system (Pioneer 10 and 11, launched in 1972 and 1973, respectively) carried a plaque with, e.g. the periods of the 14 strongest pulsars, expressed in binary notation with the hydrogen hfs period (0.704 ns) as a base, and with indications of their relative directions with regard to our solar system, as signs of our own intelligence [950]! The plaque is shown in Fig. 7.36.

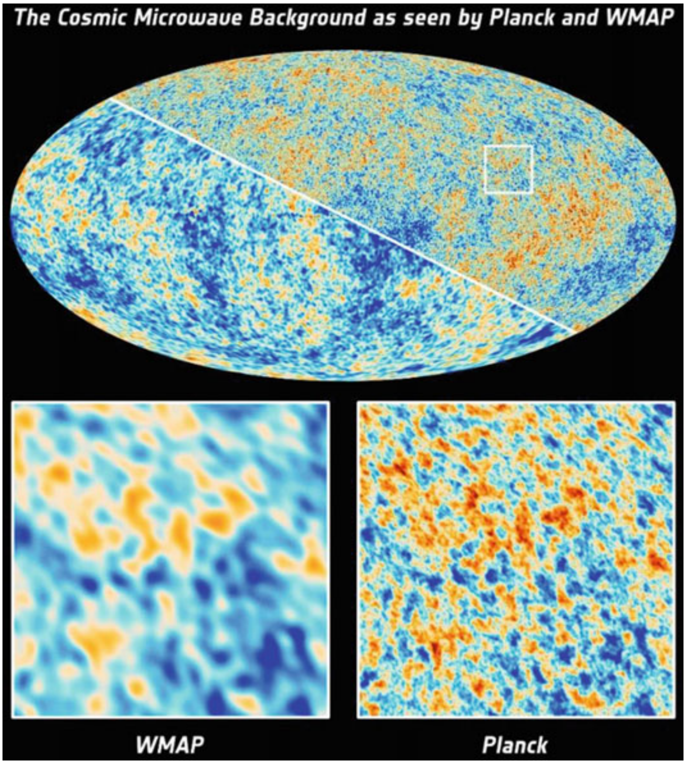
The Cosmic Microwave Background as seen by Planck and WMAP
WMAP
Planck

Fig. 7.34 Temperature fluctuations in the cosmic background radiation as detected by the WMAP and PLANCK satellites (Courtesy: ESA and the Planck Collaboration; NASA/WMAP Science Team)

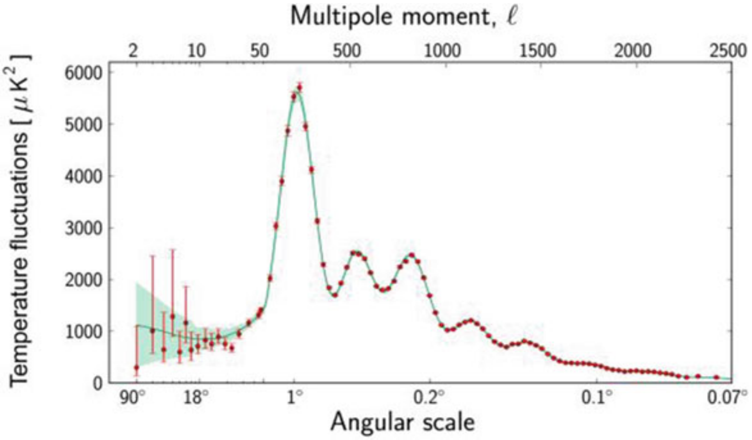

Fig. 7.35 Temperature fluctuation (angular granularity) spectrum as retrieved from PLANCK satellite data (Courtesy: ESA and the PLANCK Collaboration)

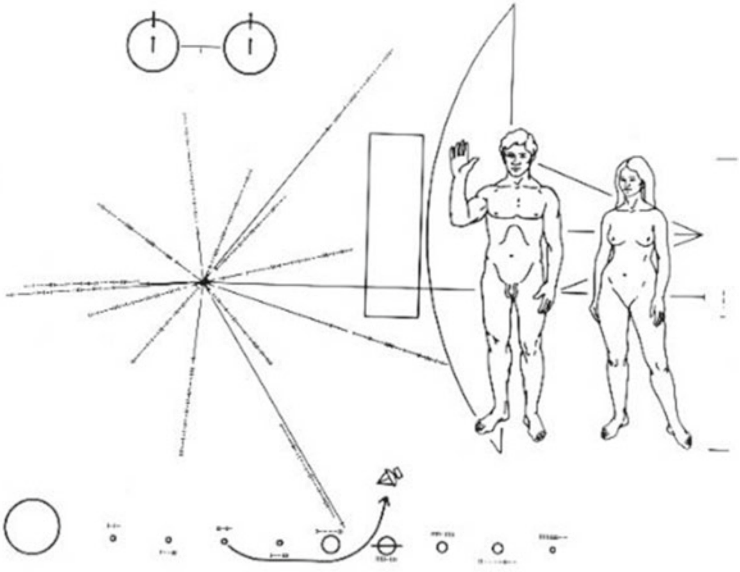

Fig. 7.36 "Interstellar message" on board the NASA Pioneer spacecrafts, the first human-made objects to leave our solar system. The frequencies of the 14 strongest pulsars, binary coded with the hydrogen hyperfine-structure transition as the base are included with directional information as seen from our solar system (Courtesy: NASA)

Chapter 8
Lasers

We will in this chapter discuss the general principles of lasers. Since we mainly consider spectroscopic aspects in this book, we will focus on tunable lasers for laser spectroscopy in the frequency (wavelength) domain and short-pulse lasers for spectroscopy in the time domain. Short-pulse lasers are also required for the generation of ultra-intense laser pulses, the use of which has opened up a new field of spectroscopy: ultra-intense laser/matter interaction. In addition to the many types of spectroscopically interesting lasers, we will also cover a number of the fixed-frequency lasers that are used to pump them. For more detailed accounts of the field of laser physics, frequently also referred to as quantum electronics, we refer the reader to standard textbooks [951–960].

8.1 Basic Principles

The first operating laser, the ruby laser, was constructed in 1960 by *T. H. Maiman* [961]. An important step in the development chain resulting in the laser was a theoretical paper from 1958 by *A. L. Schawlow* and *Ch. H. Townes* [962], who analysed the prerequisites for laser action. The ammonia maser had been introduced as early as 1954 by *Gordon* et al. [963]. This device operated in the microwave region, and the laser is the counterpart in the visible wavelength region. As we will see, it is not trivial to bridge the large frequency gap between the microwave and optical regions. The 1964 Nobel Prize in Physics was awarded to *N. G. Basov*, *A. M. Prokhorov,* and *Ch. H. Townes* for fundamental work in the field of quantum electronics, which has led to the construction of oscillators and amplifiers based on the maser–laser principle [964–966]. Maser and laser are acronyms for "microwave" and "light", respectively, "amplification by stimulated emission of radiation". Stimulated emission is essential for both processes, and we will discuss this phenomenon first. Let us in the same way as in Sect. 4.1 consider a system of atoms with two energy levels E_1 and E_2 (Fig. 8.1). Photons of energy $E_2 - E_1$ are allowed to impinge on the system and we

© The Author(s), under exclusive license to Springer Nature Switzerland AG 2022

S. Svanberg, *Atomic and Molecular Spectroscopy*, Graduate Texts in Physics,
https://doi.org/10.1007/978-3-031-04776-3_8

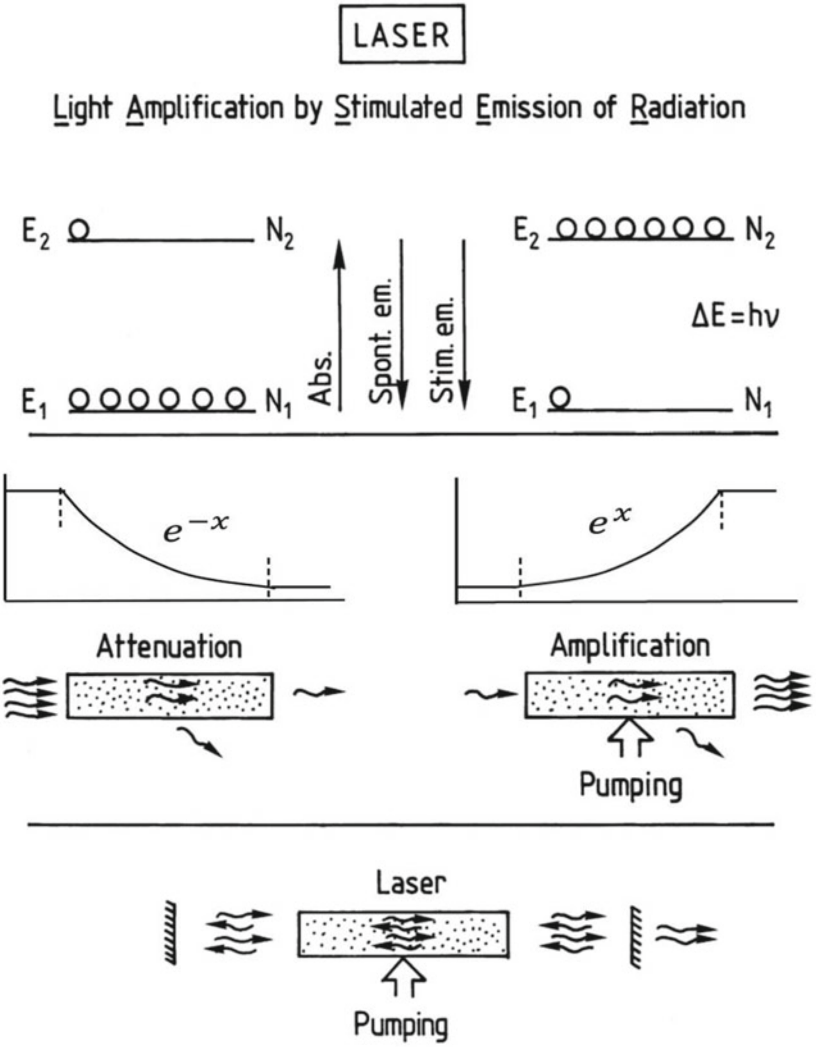
LASER
Light Amplification by Stimulated Emission of Radiation
E2
N2
E1
N1
Abs.
Spont. em.
Stim. em.
E2
N2
ΔE=hν
E1
N1
e^{-x}
e^{x}
Attenuation
Amplification
Pumping
Laser
Pumping

Fig. 8.1 Basic phenomena in laser action

consider which of the two processes, absorption or stimulated emission, is the most probable. In Chap. 4, we showed that $B_{21} = B_{12,}$ and therefore, the relative probability of the two events is only dependent on the populations of the individual levels. In a system in thermodynamical equilibrium (left in the figure), the lower level is strongly overpopulated and therefore the photon is normally absorbed. In order to make the stimulated emission process more probable, we must, in one way or another, create a larger population in the upper level than in the lower level. Then a greater number of photons are obtained than the number impinging on the medium. These stimulated photons have the same frequency, phase, and direction of propagation as the stimulating photons and are described as *coherent*. We have thus shown that *population inversion* is a prerequisite for amplification by stimulated emission of radiation. Note the complete symmetry pertaining to the two processes of absorption and stimulated emission. When a system absorbs like described by the Beer–Lambert law (Eq. 6.44), the exponent in the e-function is negative; when there is amplification, the exponent is instead positive. In the same way as a well-defined laser beam is attenuated in a non-scattering medium while still keeping its well-defined laser beam properties such as directionality, the beam keeps its well-defined properties when it passes the gain medium, but is instead amplified instead of attenuated. By arranging a feedback cavity around the amplifying medium, a self-oscillating laser can be obtained, as will be discussed in more detail later. A complete analysis of the conditions for reaching the threshold for laser oscillation must also include considerations of linewidths.

The construction of a maser or a laser involves the fundamental task of creating a population inversion. Spontaneous emission is not desired in this case, since it reduces the population difference without leading to the emission of coherent photons. Such decays constitute noise in the amplifier that the inverted system constitutes. A good introduction to laser physics is obtained by considering the mechanism of the ammonia maser. The ammonia molecule is drawn schematically in Fig. 8.2. The nitrogen atom oscillates back and forth through the plane defined by the hydrogen atoms. Two eigenstates are possible for this inversion oscillation, corresponding to a symmetric and an anti-symmetric wave function. The energy separation between these eigenstates corresponds to 23.87 GHz or a wavelength of 1.25 cm for absorbed/emitted photons. Townes' set-up is also shown in Fig. 8.2 (see also Fig. 7.9, Sect. 7.1.3). Molecules emerge from the gas reservoir in both energy states. In passing through an inhomogeneous electric field, molecules in the upper energy level will be focused into the cavity, while lower level molecules are defocused and filtered away. The molecular-induced electric dipole moment is active in

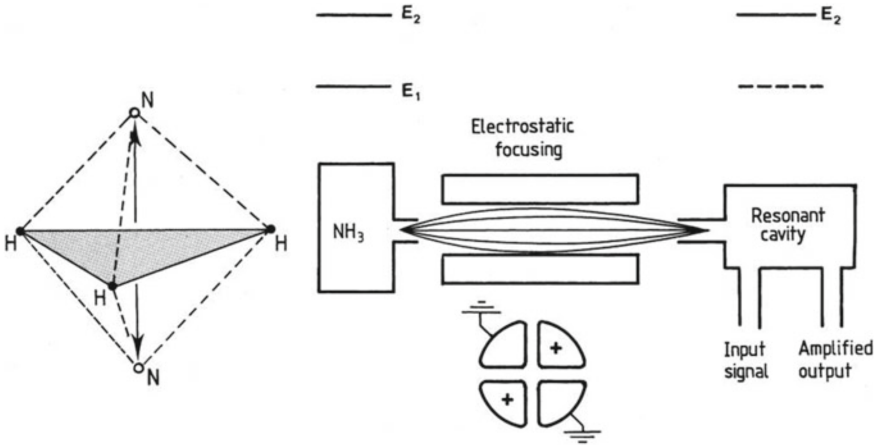

Fig. 8.2 The ammonia molecule and schematics of an ammonia maser [1]

this process (Sect. 7.1.2). The cavity is resonant at the transition frequency between the eigenstates. An inverted population is sustained in the cavity. If a microwave signal of the correct frequency is then fed into the cavity, it will give rise to stimulated emission and the signal will be amplified. If a sufficiently large number of molecules in the upper energy state are fed into the cavity, self-oscillation can be initiated by the noise photons also present in the cavity. The ammonia maser was used as a clock before more accurate atomic clocks were developed. The hydrogen maser, illustrated in Fig. 7.9, is still a very useful atomic clock.

Whereas amplification (oscillation) is obtained comparatively readily at these frequencies, which are of the order of 10^{10} Hz, it is considerably more difficult to achieve a corresponding situation for optical waves with a frequency of 10^{15} Hz. The reason is clear from (4.27)

$$\frac{A_{21}}{B_{21}\rho(\nu)} = 16\pi^2 \frac{\hbar\nu^3}{c^3\rho(\nu)}, \tag{8.1}$$

i.e. the ratio between the number of spontaneous and stimulated decays increases as ν^3. Thus, the upper level will be comparatively rapidly depopulated by spontaneous decays, and a very efficient pumping mechanism for the upper level is necessary to achieve laser action. From this argument, it follows that it is very difficult to construct an X-ray laser.

The first demonstration of X-ray lasing was actually made in 1985 for $3s$-$3p$ transitions at 20.6 and 21.0 nm in neon-like selenium (Se XXV) [967, 968]. Population inversion was created in an elongated plasma created after the impinging of 0.5 ns pulses (0.53 μm) from part of the NOVA Nd: glass laser facility. In subsequent developments, a neon-like zinc system has emerged as particularly useful, as operating at 21.2 nm and up to 10 mJ output power [969]. Through the years, much progress has been made [969–984] facilitated by the development of relatively compact, ultra-intense lasers. These aspects will be covered in Sects. 8.7.2 and 9.6.4.

8.2 Coherence

Lasers are characterized by the light that is highly *coherent* in comparison with light from conventional light sources. There are two types of coherence: *temporal coherence* and *spatial coherence*. The degree of *temporal coherence* of a light source is a measure of the possibility of predicting phase and amplitude for the light at a given location and at a certain time, provided that these quantities were known at an earlier well-defined time, at the same point. As discussed in Chap. 4, there is a time uncertainty τ associated with the spontaneous decay of an excited atom. If the classical wave approach is applied to the light, then the wave will be emitted during ~τ seconds, and therefore, the length ℓ_c, the *coherence length* of the connected wave train, will be

$$\ell_c = \tau c. \tag{8.2}$$

Because of the finite emission time in this picture, the wave train is cut off and a Fourier analysis of the train yields a frequency spread of $\Delta\nu = (2\pi\tau)^{-1}$, as previously discussed. From a quantum–mechanical point of view, the argument should be given the other way around. The time uncertainty yields a frequency spread and a corresponding associated length of the wave train. Wave trains emitted in different decays are completely unrelated. A coherence length of 3 m is obtained for $\tau = 10^{-8}$ s. Practical gaseous light sources have a Doppler broadening, which is considerably larger than the natural radiation width. Because of the increased frequency spread, a prediction of the phase is made more difficult. Line light sources have a typical coherence length of ~10 cm. Sources emitting a Planck distribution clearly have a very short coherence length.

A light wave is considered to be *spatially coherent* if there is a constant phase difference between *different* points of observation. The light that is emitted from different parts of a conventional light source is not phase-related. Therefore, the light from an extended light source will not be spatially coherent at close distances.

A good measure of the coherence of a light source is its ability to produce stable interference fringes. (An incoherent light source may produce momentary interference but the fringes continuously move swiftly and unpredictably.) The two types of coherence can be illustrated by two examples. If the path difference in a Michelson interferometer (Sect. 6.2.4) is 1 m, no fringes are obtained with a conventional light source because of its poor temporal coherence. If the two slits in Young's experiment are illuminated by light from different parts of a fluorescence tube, no fringes are obtained because of the poor spatial coherence of the light source. Lasers have very high temporal and spatial coherence since the photons are produced in chain reactions of stimulated emissions, in which all the generated photons represent waves with a common phase.

8.3 Resonators and Mode Structure

A population-inverted medium will amplify an incoming wave of the correct frequency through stimulated emission. Whereas the maser in the microwave region is an amplifier with a low noise level, finding applications, for example, in radio astronomy (Sect. 7.3), a laser in the visible region is very noisy because of the increasing importance of the spontaneous emission. According to (8.1), the signal-to-background ratio will be reduced by a factor of about 10^{15} for a frequency change of a factor 10^5, from microwaves to visible light. Therefore, lasers are rarely used for light amplification, except for the case of amplifying laser pulses, including the very important use in repeaters (mostly based on Er-doped fibre amplifiers (EDFA) in long-haul fibre-optical communication systems (Sects. 8.4.2 and 8.5.5). Lasers are

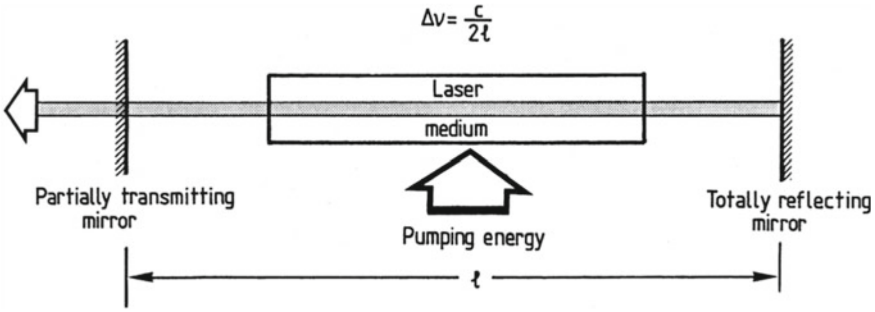
$\Delta\nu = \frac{c}{2\ell}$
Laser
medium
Partially transmitting mirror
Pumping energy
Totally reflecting mirror
ℓ

Fig. 8.3 Principal arrangements for a laser [1]

normally used as *light generators (oscillators)*. An amplifier becomes an oscillator if feedback is introduced. This can be achieved by placing the laser medium in a *resonator* consisting of two mirrors (Figs. 8.1 and 8.3). A spontaneously generated noise photon of the correct frequency and direction of propagation (perpendicular to the end mirror) is amplified and starts the process. The light intensity is substantially increased by reflections back and forth through the laser medium. In order to sustain the laser action, it is necessary to continuously pump to ensure an ongoing population inversion. One of the mirrors is made partially transparent in order to obtain a useful external beam. Clearly, the emerging light represents a loss factor, and the degree of *output coupling* possible without terminating the laser action depends on the gain of the medium. Ideally, the extracted energy would be the only source of loss. By using multiple dielectric layers, the absorption losses due to the mirrors can be kept well below 1%. All optical surfaces inside the cavity must be kept very clean since any absorption is "amplified" by the multiple passes.

The laser mirrors are indicated as plane in the figure. For such a system, the alignment of the resonator is critical if losses are to be prevented. A considerably more stable configuration is obtained if at least one of the mirrors is slightly curved. A number of resonator arrangements are illustrated in Fig. 8.4. The relative merits of different configurations have been discussed, e.g. in [985–989].

As for a microwave cavity, several types of transverse electromagnetic oscillations or *modes* are possible for a laser cavity. Generally, one tries to isolate the mode that has the highest symmetry. This mode is designated TEM_{00}. Other modes (TEM_{pq}, p, q integers) corresponding to more or less asymmetric radiation fields can be suppressed by making the tube containing the laser medium sufficiently narrow or by introducing an axial aperture. A laser beam due to a laser oscillating in the TEM_{00} mode has a symmetric cross-section and the intensity falls off according to a Gaussian distribution. Laser modes were discussed in [985–991].

As a consequence of the coherence, the laser light can be transmitted as an almost parallel bundle. The small divergence is a consequence of the unavoidable influence of diffraction. For radiation in phase and with the same amplitude over a circular aperture of diameter d, the angle θ between the centre of the diffraction pattern and the first dark interference ring is given by

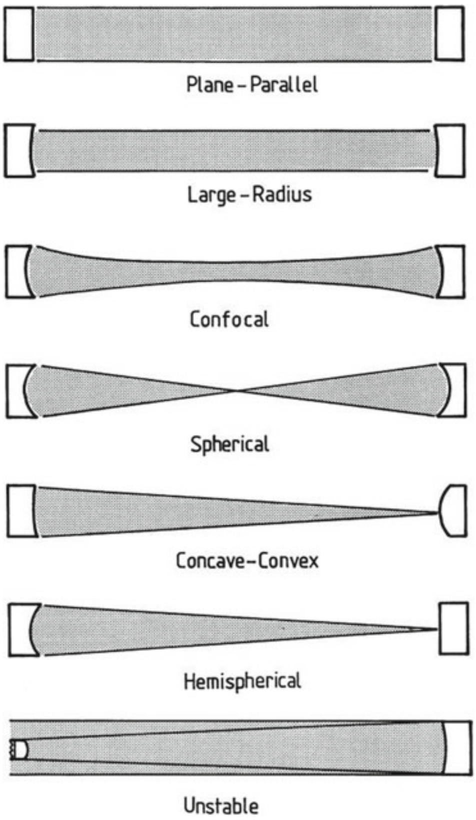

Fig. 8.4 Different resonator arrangements

$$\theta = 1.22\,\lambda/d. \tag{8.3}$$

A visible diffraction-limited laser with an emerging beam of diameter 1 mm will have a divergence of about 0.5 mrad. Many practical systems have a divergence that is limited only by diffraction. The spot at a distance of 1 km has a diameter of about 0.5 m for such a laser. By first expanding the beam to a larger value of *d*, it is possible to achieve a correspondingly smaller divergence. By focusing a parallel TEM_{00} beam, a very small spot diameter δ can be obtained. For a perfect lens of focal length *f*, we obtain

$$\delta = \frac{4}{\pi} f \frac{\lambda}{d}. \tag{8.4}$$

A further useful quantity, related to focused laser beams, is the *confocal parameter* *z*, defined as the distance between the two locations at each side of the focus at which the intensity has fallen to 50% of the maximum value:

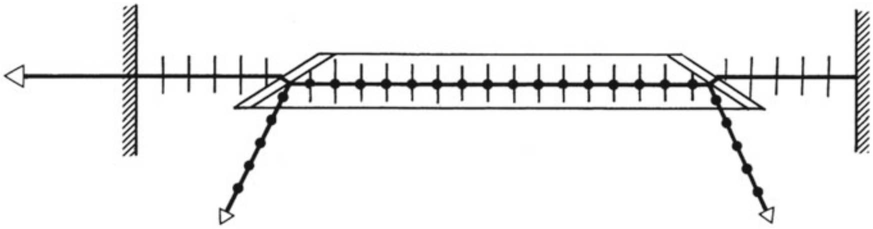

Fig. 8.5 Generation of polarized laser light using intracavity Brewster angle windows [1]

$$z = 2\pi\delta^2/\lambda. \tag{8.5}$$

A very high degree of linear polarization can be obtained for a laser with low losses in one direction of oscillation and high losses in the perpendicular direction. This is accomplished for a laser with gas as the active medium by placing the windows of the gas container at the Brewster angle to the optical axis of the laser (Fig. 8.5). Some other kinds of polarizer can be placed inside the cavity for other laser types.

We have now discussed the different characteristics of laser light without dealing with its frequency distribution in detail. It is evident that a stable oscillation mode can be achieved in the resonator only if there is constant constructive interference, i.e. standing waves. This occurs when an integral number of half-wavelengths fit into the cavity of (optical) path length ℓ. By considering two adjacent modes, we obtain the mode separation $\Delta\nu$:

$$\begin{aligned} &n\frac{\lambda}{2} = n\frac{c}{2\nu} = (n+1)\frac{c}{2(\nu+\Delta\nu)} = \ell \\ &\Delta\nu = c/2\ell. \end{aligned} \tag{8.6}$$

This expression has already been derived; see (6.26). Clearly, the laser cavity is a Fabry–Pérot resonator with a free spectral range given by (8.6). With a cavity length of 1 m, the mode separation is 150 MHz.

Let us now consider a gas laser, for which the stimulated emission occurs for a certain spectral line, determined mostly by Doppler and pressure broadening (Fig. 8.6). Modes not falling within the linewidth are impossible since there is no gain for such modes. As a matter of fact, modes that are not close to the peak of the profile (the gain profile) will have too low a gain to compensate for the losses. Clearly, there is a certain threshold for the pump energy, below which no modes at all have a sufficient gain. When lasing, only the most favourable modes will oscillate because of the regenerative nature of the laser action ("strong become stronger, weak become weaker"). When several modes oscillate simultaneously, we talk about *multi-mode operation*. By introducing a Fabry–Pérot interferometer into the laser cavity with a free spectral range sufficiently large so that only one of its transmission peaks falls in the region for possible laser action, a single cavity mode can be selected (*single-mode operation*). The interferometer is frequently made as a plane-parallel disc with

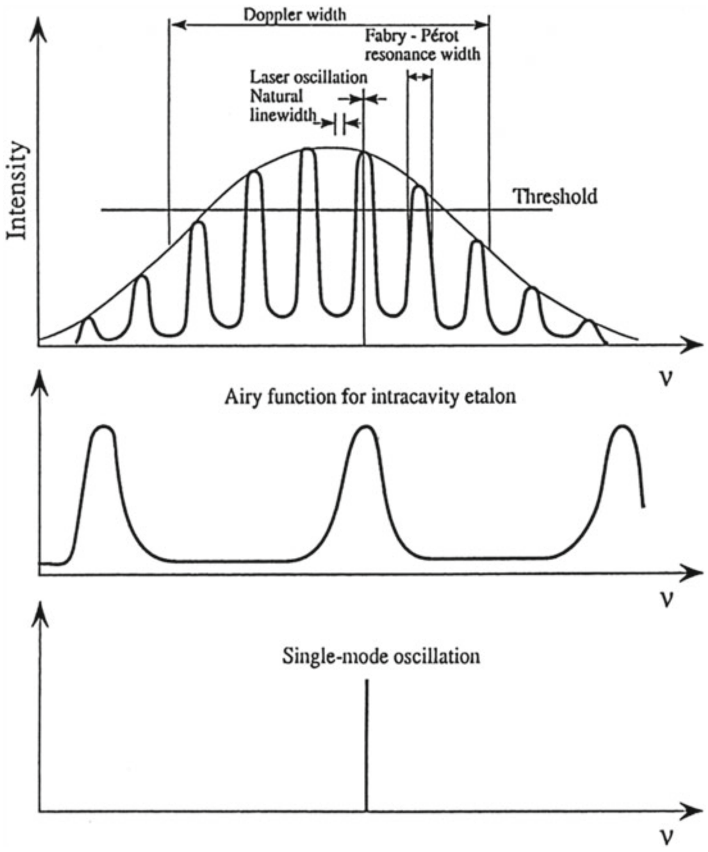
Doppler width
Fabry - Pérot resonance width
Laser oscillation
Natural linewidth
Intensity
Threshold
ν
Airy function for intracavity etalon
ν
Single-mode oscillation
ν

Fig. 8.6 Multi-mode laser action and the generation of single-mode radiation [1]

semi-transparent dielectric coatings (an "etalon"). The choice of mode is made by inclining the etalon. The transmission maxima of the etalon are also influenced by the temperature. In the absence of temperature stabilization, "mode hopping" can occur. It is important to notice that the etalon only needs to transmit the preferred mode slightly better than the ones to be rejected—a 5% difference would because of the regenerative laser action with multiple passes result in a transmission difference of $1.05^{100} = 132$ after 100 passages.

When the laser is oscillating in only one mode, it produces a beam of very sharp frequency. Because of the generation of light by stimulated emission in multiple passes inside the cavity, the linewidth can become much smaller than the width of the Fabry–Pérot resonance (the Airy function) or the natural radiation width. Using indirect measurement techniques, linewidths of the order of 1 Hz have been established for a He–Ne laser, approaching the *Schawlow–Townes limit* [962]. To obtain narrow lines, a careful stabilization of the length of the laser cavity using a servo system is necessary; otherwise, vibrations will cause a considerably larger effective linewidth. Even without such servo stabilization, a single-mode laser has very good temporal coherence. In comparison, the coherence length for a multi-mode laser is very small. A high spatial coherence is still maintained due to phase locking in the stimulated emission. Therefore, sharp interference fringes are obtained in most interference experiments.

Now we will study a number of laser types more closely. We distinguish between *fixed-frequency lasers* and *tunable lasers*. In a limited sense, the former type is also tunable since different modes under the gain curve can be selected. The gain curve can be moved slightly by changing the temperature in lasers for which the active medium is a solid. We will primarily discuss fixed-frequency lasers that are used for the pumping of tunable lasers. By a tunable laser, we here mean a laser whose wavelength can be varied over a large region (at least a few nm). Such lasers, which are of great spectroscopic interest, will be discussed in some detail.

At the end of this section, we will address the question of how the laser action starts. Like for a conventional radio wave oscillator, it is rather easy to conceive its operation once it is up and running. The oscillator always starts because of a perturbation, which could be the influence of noise. For the laser, the spontaneous emission from the excited state will contain a photon, having the correct frequency and direction to pass the laser cavity, and will through the action of amplified stimulated emission create the resulting laser emission in the feedback provided by the cavity mirrors. A parallel from the audio region is acoustic self-sustained oscillation when using a too highly set amplification. Spurious sounds from the environment may be caught and result in oscillation, even in the absence of an intended speaker, due to feedback from the "echoing" wall.

8.4 Fixed-Frequency Lasers

8.4.1 The Ruby Laser

As we have mentioned, laser action was first observed in ruby [961]. Ruby is a red crystal of Al_2O_3 with an addition of about 0.05% Cr_2O_3. Only the Cr^{3+} ions are of interest here since the other ions do not participate in the process. The chromium ion has three d electrons in its unfilled shell and has a ^4F term as the ground-state term. The next higher state is a ^2G term. The ruby crystal has a weakly rhombic structure. Because of the action of the crystal field, the ^4F term will be split into the levels $^4F_1$, $^4F_2$, and $^4A_2$, where the designations are no longer the ordinary ones from atomic spectroscopy but are defined in the group-theory treatment of the crystal field problem. The ^2G term is split into levels designated $^2A_1$, $^2F_1$, $^2F_2$, and ^2E. The $^4F_1$ and $^4F_2$ levels are strongly broadened into energy bands, whereas ^2E has a doublet structure. The energy levels of Cr^{3+} in ruby that are relevant for laser action are indicated in Fig. 8.7. The ruby crystal has strong, broad absorption bands around 550 and 400 nm. Ions that have been pumped to the ^4F bands will fall, within 10^{-7} s,

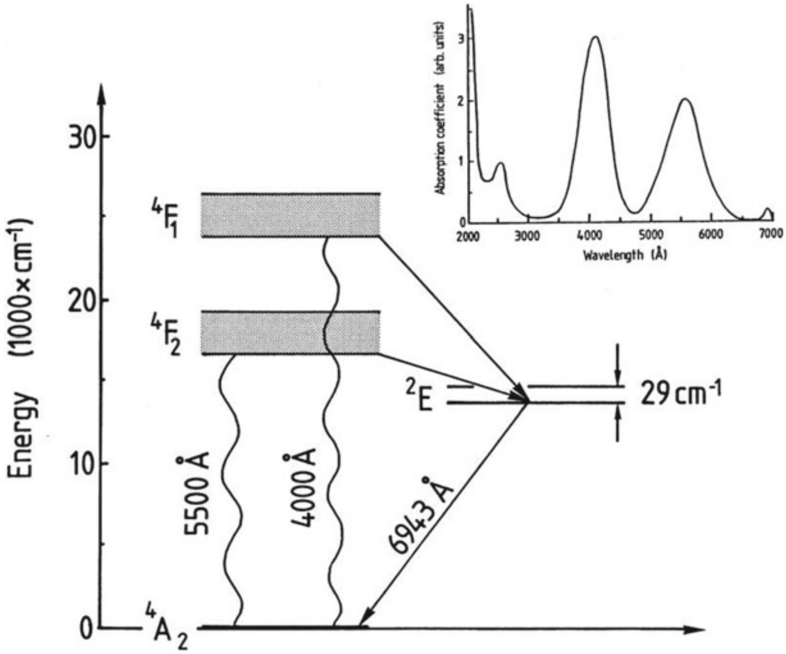

Fig. 8.7 Level diagram and schematic absorption curves for ruby (10 Å = 1 nm) [1]

to the ^2E levels, in which a population is quickly built up because the lifetime of this level is very long, about 5 ms. Population inversion with regard to the ground state is most easily achieved for the lower of the two ^2E levels. Stimulated emission is obtained at 694.3 nm at room temperature. If the crystal is cooled to 77 K (liquid nitrogen temperature), the wavelength is shifted to 693.4 nm.

In the ruby laser, which is an example of a *three-level laser*, population inversion must be achieved with regard to the normally well-populated ground state. It is thus necessary to pump the ions very efficiently from the ground state to the ^4F levels. One possible pumping arrangement (also used by Th. Maiman) is shown in Fig. 8.8. A ruby rod, about 5 cm long and with flat, parallel silvered end surfaces, is placed inside a helical flash-lamp, filled with, for example, xenon at high pressure (Sect. 6.1.2). A capacitor of about 100 μF charged to about 2 kV is discharged through the flash-lamp, which lights up for about 1 ms. Because of the broad absorption bands of ruby, a non-negligible part of the light, emitted as a continuum, is absorbed. After about 0.5 ms, stimulated emission is transmitted through the one semi-transparent end surface of the rod. The light is emitted as a sequence of short spikes of about 1 μs duration. This is due to the disappearance of the population inversion when stimulated emission has occurred. The flash-lamp is still on and needs some time to restore the population inversion, leading to the emission of a new laser spike. This behaviour, which is frequently not wanted, can be eliminated by *Q-switching* [992–996].

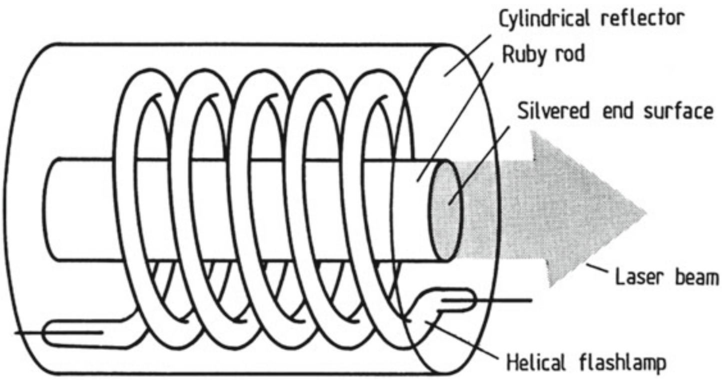

Fig. 8.8 Arrangement for a ruby laser

In this case, laser mirrors, separated from the rod, are used and the light path between the mirrors is initially blocked. The quality factor, or *Q value,* of the cavity is then low, and stimulated emission is not initiated, although a strong inversion has occurred. If the blocking is quickly removed, the cavity can enhance the light field and the emission occurs in a *giant pulse*. In practice, polarized laser light is used and the Kerr or Pockels effect is employed to rapidly switch the plane of polarization. Giant pulses can have a peak power of 10^8 W and a pulse width of about 10 ns. This technique is referred to as *active Q-switching*. By introducing a *saturable absorber*, which is a nonlinear device with a strong absorption for weak intensities but showing a good transparency for high intensities, the same effect can be achieved, although not at an equally well-defined time. Saturable absorbers can be bleachable dyes, such as BDN (4-dimethyl-aminodithiobenzil-nickel) dissolved in 1,2-dichloroethane for switching of the Nd:YAG laser. Modern saturable absorbers are frequently of the SESAM (semiconductor saturable absorber mirror) type [995, 996].

8.4.2 Four-Level Lasers

We have already mentioned the difficulties involved with a three-level laser, in which the laser transition is terminated in the continuously well-populated ground state. The successful operation of the ruby laser relies on the very favourable combination of broad absorption bands and the long upper-state lifetime allowing the storage of energy. In a *four-level laser*, a final level, which is not the ground state, is used. The basic diagram is shown in Fig. 8.9a.

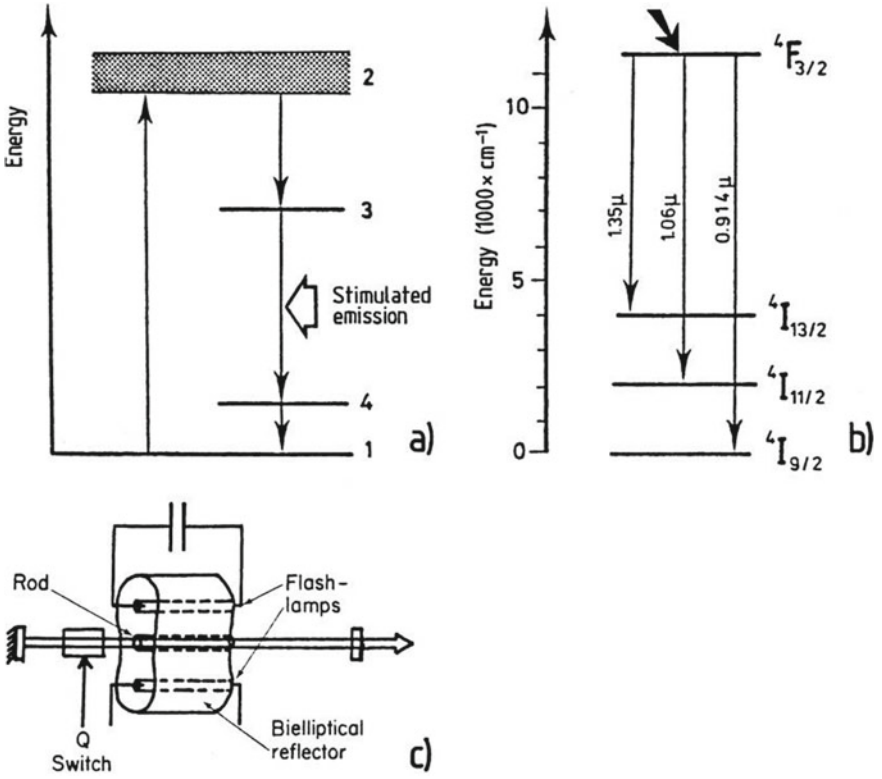

Fig. 8.9 The four-level laser. **a** Basic energy-level diagram; **b** lasing transitions in the Nd^{3+}:YAG laser; **c** typical practical arrangement for a Nd:YAG laser [997]

Suitable energy-level diagrams of this general type can be found, particularly for ions of the rare-earth elements. The ions can be incorporated into certain crystals such as CaF_2 or $CaWO_4$ and also in glass. It is important that level 3 (the storage level) has a comparatively long lifetime so that the ions can be accumulated there. On the other hand, level 4 must be depopulated efficiently. Level 4 is so close to the ground state in many elements, so that cooling is necessary to reduce its thermal population. Laser action has been achieved for most of the rare-earth ions. An especially useful type of four-level laser is the Nd:YAG laser, for which Nd^{3+} ions have been incorporated into an yttrium–aluminium host crystal of garnet type ("Yttrium–Aluminium Garnet", $Y_3Al_5O_{12}$). The lasing transitions for this laser are shown in Fig. 8.9b; in particular, the most commonly used one at 1.064 μm. A frequently used Nd:YAG laser arrangement with two linear flash-lamps in a bi-elliptic pumping cavity for efficient pumping of the rod is shown in Fig. 8.9c.

Nd:YAG lasers with a high output power are constructed with an oscillator followed by one or several amplifier stages. This is a very general construction for pulsed lasers. The oscillator is designed for relatively low power. It is then possible to control the mode structure, linewidth, and pulse length precisely. A sharp frequency, a short pulse length, and a clean TEM_{00} mode can generally only be achieved at the expense of the output power. A laser amplifier, consisting of a larger optically pumped rod, will boost the energy of the pulse without changing the beam quality. The diameter of the amplifying medium is successively increased in the amplifying stages and the laser beam is correspondingly expanded. The technology of solid-state lasers has been discussed in [998–1004]. High-power Nd-glass lasers are used in fusion research based on laser-driven inertial confinement [1005–1008]. The generation of ultra-high peak laser power is addressed in Sect. 8.7.2.

A typical Nd:YAG laboratory laser system for spectroscopic applications is an oscillator–amplifier arrangement yielding 1.06 μm pulses of 10 ns duration and 1 J energy at a repetition rate of 10 Hz. In such systems, a so-called unstable resonator (Fig. 8.4) is sometimes used to allow a more efficient energy extraction from the oscillator rod than that which is possible for a resonator sustaining a TEM_{00} mode. Instead of a semi-transparent output coupler, a very small central feedback mirror is used and the output power is extracted in an annulus around this mirror. In rod arrangements, Nd:glass is limited to very low repetition rates because of the poor thermal properties of glass, leading to strong lens effects. Instead of using amplifying media rods, slabs of the material of suitable thickness can be used, in order to allow more efficient pumping and handling of the thermal load of the material and associated beam distortions. This technique is used in the final stages of amplification for the purpose of inducing fusion. The slabs are then pumped from both sides by linear flash-lamps. Modern high-power Nd-based lasers for industrial applications frequently use thin slabs with reflector and cooling on one side, and are used in multiple reflective beam passes [1009–1013].

The Nd:YAG and glass materials absorb the pumping radiation in certain spectral regions, as shown in Fig. 8.10. New host materials, such as GGG (Gadolinium–Gallium Garnet, $\mathrm{Gd_3Ga_5O_{12}}$) and GSGG (Gadolinium–Scandium–Gallium Garnet), in which Cr^{3+} ions have also been incorporated as sensitizers, utilize the available radiation more efficiently and show great promise.

Another useful laser material is Nd:YLF (Yttrium–Lithium–Fluoride). The upper-state fluorescent lifetime in YLF is about 520 μs as compared with about 230 μs for YAG, which makes Nd:YLF particularly valuable for high-repetition systems (kHz), which can then be efficiently pumped by a CW discharge lamp rather than a flash-lamp. After frequency doubling to 527 nm, such systems can yield 20 mJ/pulse at 1 kHz, averaging a power in the green of 20 W.

Different laser crystals have been described in [999, 1000]. Increased efficiencies (beyond the 2% wall-plug power to laser power-conversion efficiency typical for a Nd:YAG laser) are attainable by pumping a YAG rod with a suitable frequency-matched diode laser (Sect. 8.5.5) [1015–1017]. Frequently, the diode laser is chosen to operate at the 808 nm absorption peak. The pumping of a miniature rod is shown in Fig. 8.11 and results in single-mode output at a wall-plug conversion efficiency of better than 5%. Such a laser is ideal as a high-quality oscillator for subsequent amplification. High pumping powers can be obtained using arrays of diode lasers, where each array can have output powers exceeding 100 W [1019–1023]. The cost of

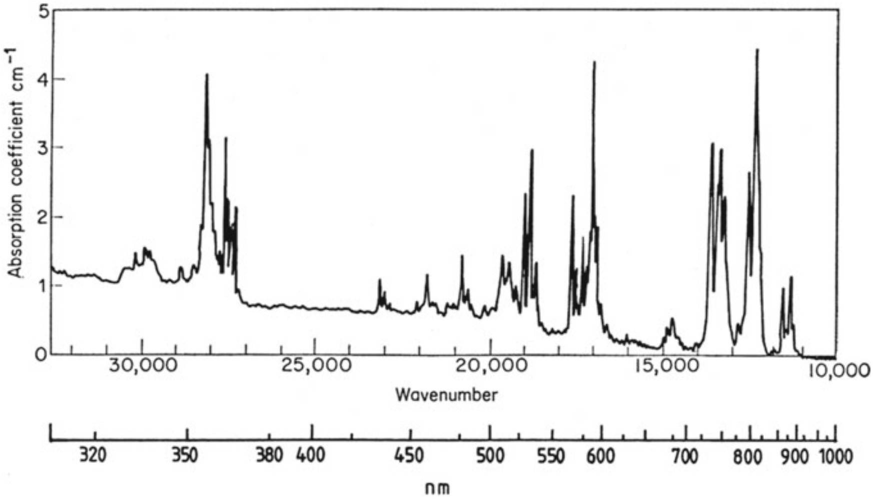

Fig. 8.10 Absorption curve for Nd:YAG [1014]

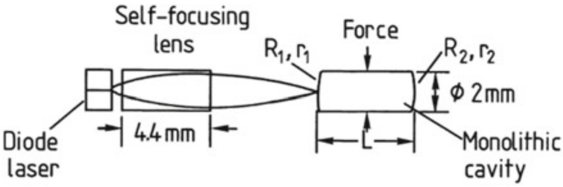

Fig. 8.11 Diode-laser pumping of a miniature Nd:YAG laser [1018]

such lasers is rapidly coming down, and diode-pumped solid-state lasers of considerable output (1 kW or even more) are now quickly emerging, particularly for industrial CW applications, where also the slab amplifier technology discussed above is implemented (see also the end of Sect. 8.4.5).

Sometimes, the weaker 885 nm absorption peak of the Nd:YAG gain medium is used. Since less energy is lost in the thermal relaxation to the upper level involved in the 1064 nm laser transition, a higher efficiency and smaller cooling requirements are achieved.

High average power from solid-state media can be obtained by using a sufficiently long silica fibre, which is doped with a suitable ion and pumped by diode lasers along its full length [1024–1027]. These lasers frequently have Bragg gratings, which are integrated into the fibre, as cavity mirrors. Fibre lasers, with powers up to the kW level, can be seen as an extension of the Er-doped fibre amplifiers (EDFA)s (Sect. 8.5.5) used for amplification at 1.55 μm signals in fibre-optic long-haul optical communication networks.

8.4.3 Pulsed Gas Lasers

The lasers we have considered so far have a solid material as the active medium. Generally, flash-lamp pumping is employed and short pulses are obtained at a repetition rate of typically 10 Hz. High peak powers are obtained in the Q-switched mode (MW–GW). Gaseous media can also be used for the generation of short laser pulses. We shall consider here the nitrogen laser, the excimer laser, and the copper vapour laser.

The relevant parts of the N_2 molecule level diagram and the basic arrangement for the N_2 laser are given in Fig. 8.12. Pumping is achieved using an electrical discharge of short duration, transversely, in a tube through which N_2 at a pressure of about 100 torr (13 kP) is flowing. The transfer probability at electron impact for $X \rightarrow C$ is much larger than for $X \rightarrow B$. Thus, a population inversion occurs at level C with regard to B. However, the lifetime of state C is only about 40 ns, whereas the corresponding value for state B is about 10 μs. A very fast discharge, generated using a *Blumlein circuit*, is utilized, since the upper level cannot store energy (Q-switching is not possible). The population inversion can obviously be achieved only for a short time (self-terminating transition). The pulse length for the nitrogen laser is normally less than 10 ns and emission follows at 337.1 nm. Peak power up to 1 MW can be achieved. Pulse energies are typically a few mJ, and repetition rates exceeding 100 Hz can be obtained. Sealed-off N_2 lasers operating with 0.1 mJ output energy in 3 ns pulses at 10 Hz are also available as very compact units with wide applicability, especially for inducing fluorescence in analytical and diagnostic applications (Chap. 10).

The nitrogen laser has such a high gain that a laser beam can be obtained even without cavity mirrors through *amplified spontaneous emission* (*ASE*; sometimes, the term *super-radiant laser* is used). Normally, a totally reflecting mirror is used at one end of the gain tube while the window at the opposite end has a very high transmission. The divergence of the beam is given by the geometry of the discharge channel and is typically 10 mrad.

The construction of an *excimer laser* [1028–1031] is similar to that of an N_2 laser. Excimer molecules ("excited dimers") are characterized by the absence of a stable ground state, while short-lived, excited states exist. Molecules such as KrF and XeCl

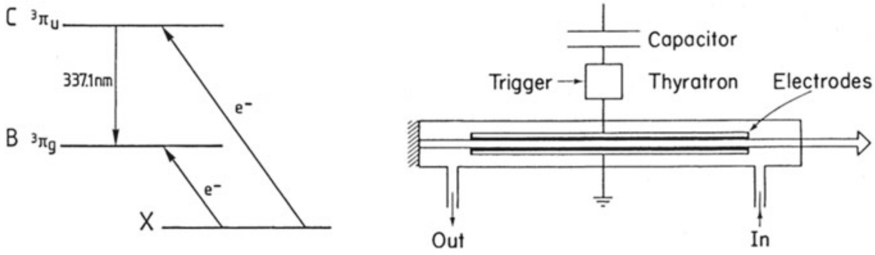

Fig. 8.12 Energy-level diagram and basic arrangements for a nitrogen laser [997]

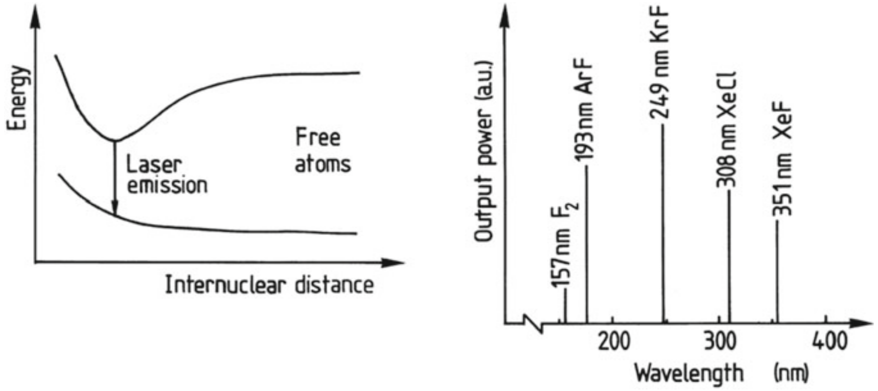

Fig. 8.13 Energy-level diagram for an excimer molecule and laser emission lines from different excimer molecules

are used as the active medium in excimer lasers (named after *exci*ted di*mer,* a dimer being a diatomic molecule). These molecules are formed in the excited state in a fast, electrical discharge in a mixture of the inert gas and F_2 or HCl. The high reactivity of the latter gases makes the material selection, gas handling, etc. critical for this type of laser. An excimer level diagram and laser lines for different excimer molecules are given in Fig. 8.13. Since no ground state exists, excimer molecules constitute the perfect laser medium, with automatic population inversion once a molecule has been created. Important laser emission lines are 249 nm (KrF; yields the highest power), 308 nm (XeCl; best suited for dye laser pumping), and 193 nm (ArF; attractive short wavelength for photochemistry and lithography). Pulse energies of hundreds of mJ can be achieved and average powers of 100 W can be reached. Excimer lasers find many important applications, including in lithography.

Pulsed CO_2 lasers, which were available long before excimer lasers, have a similar construction. These infrared lasers are of great technological importance. CO_2 lasers will be discussed later.

In the *copper vapour laser,* the discharge tube must be heated to high temperatures in order to produce a sufficient Cu vapour pressure. This laser emits at 510 and 578 nm, corresponding to the $(4p\ ^2P_{3/2} \rightarrow 4d\ ^2D_{5/2})$ and $(4p\ ^2P_{1/2} \rightarrow 4d\ ^2D_{3/2})$ transitions, respectively. Since the terminal ^2D states are meta-stable, only pulsed operation is possible. High repetition rates can usually be obtained with this laser, up to 10 kHz. The average power can exceed 10 W. Exchanging copper for gold results in red emission at 628 nm. Metal vapour lasers are discussed in [1032–1034].

Whereas population inversion can often be achieved relatively easily with a pulsed pumping source, it is considerably more difficult, and sometimes impossible, to continuously maintain population inversion while laser action prevails. Clearly, lasing means that excited atoms decay with the emission of stimulated radiation, and thus, the laser action itself will cause the lasing action to stop. Efficient pumping mechanisms are required. We will now study some important types of continuous fixed-frequency lasers which all work with gaseous laser media.

8.4.4 The He–Ne Laser

The helium–neon laser was the first gas laser and it was designed and built by *A. Javan* and co-workers [1035] shortly after the introduction of the ruby laser. Traditionally, the He–Ne laser was one of the most common laser types. The construction can be made comparatively simple and cheap, and continuous laser action is obtained. The active medium is a gas mixture of He and Ne (ratio 5:1) in a glass tube at a total pressure of about 1 torr (133 P). Energy is added through an electric discharge through the gas. In order to understand the principle of the He–Ne laser, the energy-level diagrams of both He and Ne must be considered (Fig. 8.14). In the discharge (1000 V, 10 mA), He atoms are excited to the metastable $2s\ ^3S_1$ and $2s\ ^1S_0$ states through electron impact. The $4s$ and $5s$ level systems in Ne have almost the same energies as the metastable He states. Because of this, the probability of Ne excitation through collisions with metastable He atoms is very large. A population inversion between the s states and the lower lying $3p$ and $4p$ levels is achieved and several laser transitions are possible. Since the lifetimes of the p states are very short ($\sim$10 ns) in comparison with the s-state lifetimes (100 ns), the population inversion can be maintained and continuous lasing is achieved.

The reflection properties of the laser mirrors determine which line will lase. The most frequently used line is the red line at 632.8 nm, but many other visible and IR lines are possible (e.g. 543 nm, 594 nm, 1.15, 1.52, and 3.39 μm), when employing cavity mirrors with high reflectivity at such wavelengths. The Doppler width of the normal red line is about 1700 MHz. With a typical resonator length of 30 cm, a mode

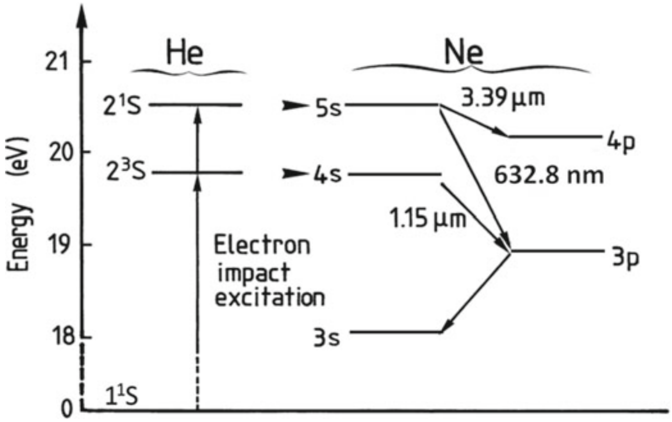

Fig. 8.14 Simplified energy-level diagrams relevant to the He–Ne laser

separation of 500 MHz is obtained. Such a laser will exhibit two or three modes. With a sufficiently short laser (10–15 cm), a single-mode operation can be attained. He–Ne lasers yield low output powers, typically a few mW.

Primary energy storage in He is also used in the *helium–cadmium laser*. Here, a sufficient metal vapour pressure must be achieved by heating. Excited Cd ions are produced by the Penning ionization:

$$A^* + B \rightarrow A + B^+ + \mathrm{e}.$$

Two short-wavelength lines, 441.6 nm ($4d^9 5s^2\ {}^2D_{5/2} \rightarrow 4d^{10} 5p\ {}^2P_{3/2}$) and 325.0 nm ($4d^9 5s^2\ {}^2D_{3/2} \rightarrow 4d^{10} 5p\ {}^2P_{1/2}$), are obtained at power levels of 50 and 5 mW, respectively. An alternative way of producing the excited Cd ions is to use soft X-ray photoionization of ground-state $4d^{10}5s^2$ Cd atoms [1036, 1037]. High-power laser pulses impinging on a high-Z material, such as Ta, can be used for soft X-ray production (Sects. 5.1.3 and 9.6.5). Using soft X-ray pumping, the gain has also been demonstrated in In III (185 nm) [1038] and Xe III (109 nm) [1039, 1040]. As further discussed in Sect. 9.6.4, ultra-high power lasers with sufficient pulse energy can be used for achieving true X-ray lasing.

8.4.5 Gaseous Ion Lasers

In gaseous ion lasers, a population inversion between excited states of ionized argon or krypton is achieved. The pumping is accomplished through a strong dc discharge in low-density gas (~0.2 torr; 27 P). The discharge tube is 1–2 m long and current densities of about 500 A/cm^2 are used. Thus, a high electrical power is needed (~10 kW) and the discharge tube, which is made of beryllium oxide or graphite, must have an efficient water cooling system. Excited ions are produced in collisions between inert gas atoms and electrons. An energy of 15.75 eV is needed for the ionization of an argon atom. The interesting excited ionic states belonging to the configuration $3p^44p$ are located about 20 eV above the ionic $3p^5$ ground state. A partial level scheme for Ar$^+$ is given in Fig. 8.15, with laser lines connecting $3p^44p$ levels and $3p^44s$ levels indicated. Several blue and green laser lines are obtained (514.5, 501.7, 496.5, 488.0, 476.5, 472.7, 465.8, 457.9, and 454.5 nm). The strongest lines are

$$3p^4 4p\,{}^4D_{5/2} \rightarrow 3p^4 4s\,{}^2P_{3/2} \quad 514.5\,\mathrm{nm}$$

and

$$3p^4 4p\,{}^2D_{5/2} \rightarrow 3p^4 4s\,{}^2P_{3/2}. \quad 488.0\,\mathrm{nm}$$

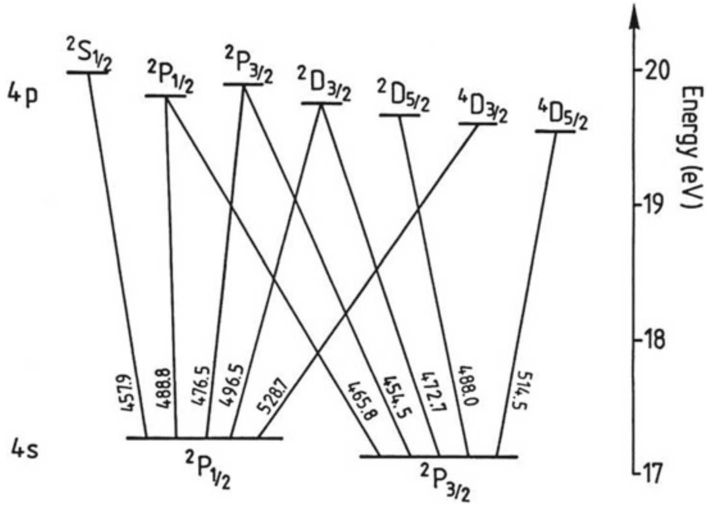
$^2S_{1/2}$
$^2P_{1/2}$
$^2P_{3/2}$
$^2D_{3/2}$
$^2D_{5/2}$
$^4D_{3/2}$
$^4D_{5/2}$
4p
4s
$^2P_{1/2}$
$^2P_{3/2}$
457.9
488.8
476.5
496.5
528.7
465.8
454.5
472.7
488.0
514.5
20
19
18
17
Energy (eV)

Fig. 8.15 Energy-level diagram of the Ar^+ ion, with argon-ion laser lines indicated (wavelengths in nm)

When using laser mirrors with a high reflectivity in the blue–green region, all the lines are produced simultaneously. Argon-ion lasers with a total output power of up to 30 W are commercially available. The principal arrangement of an argon-ion laser is shown in Fig. 8.16.

By using a prism in front of the totally reflecting mirror, the individual spectral lines can be isolated. For a certain position of the prism, only one wavelength is reflected back towards the semi-transparent output coupler, while the other wavelengths are refracted out of the cavity (see how this method can be used to achieve full tunability for dye lasers; Sect. 8.5.1.) By introducing an intracavity solid Fabry–Pérot interferometer (etalon), single-mode oscillation can be obtained.

At very high discharge currents, laser transitions are also obtained in doubly ionized argon. Several UV lines in the wavelength region of 300–386 nm are then obtained with a total power of up to 5 W.

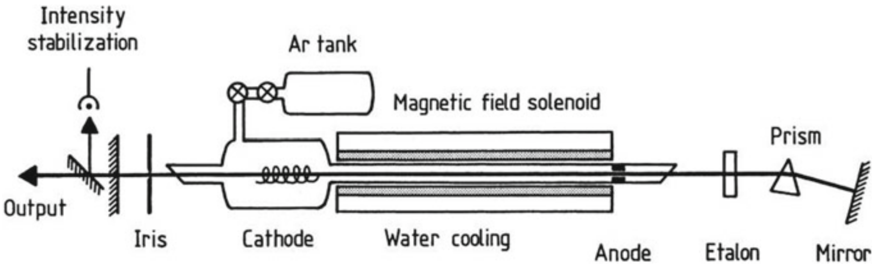
Intensity stabilization
Ar tank
Magnetic field solenoid
Prism
Output
Iris
Cathode
Water cooling
Anode
Etalon
Mirror

Fig. 8.16 Principal arrangement for an argon-ion laser [1]

The *krypton-ion laser* has the same construction as the *argon-ion laser* but the discharge tube is instead filled with krypton. Apart from blue and green lines, several red lines are also obtained with this laser (793.1, 752.5, 676.4, 647.1, 568.2, 530.9, 520.8, 482.5, 476.2, 468.0, 413.1, and 406.7 nm), as well as strong UV lines (356.4, 350.7, and 337.5 nm). Ion lasers are discussed in greater detail in [1041].

Argon-ion lasers are now being replaced by CW solid-state lasers, which can be conveniently pumped by diode-laser arrays, leading to a high efficiency and tractable heat dissipation. Thus, CW Nd:YVO_4 (Yttrium–Vanadate; upper-state lifetime 60 μs) lasers with intracavity frequency doubling in LBO (Lithium triborate) yielding up to 10 W output power at 532 nm are increasingly used as pump sources for tunable lasers and for mode-locked solid-state lasers used as the first unit in a chirped pulse amplification (CPA) chain (see Sect. 8.7.2).

8.5 Tunable Lasers

Whereas fixed-frequency lasers have found important applications in, for example, measurement techniques, information transmission, holography, material processing and medicine, tunable lasers are of greatest interest for atomic and molecular spectroscopy. Using different types of tunable lasers, the wavelength range of 320 nm to tens of μm (and recently even THz frequencies) can be covered by direct laser action, and the tunability region of an individual laser can be considerably extended using nonlinear optical effects. Tunable lasers comprise dye lasers, F-centre lasers, certain solid-state lasers, spin-flip Raman lasers [1043], parametric oscillators, high-pressure CO_2 lasers, and semiconductor lasers. Here, we will discuss the most important ones of these laser types. Overviews of tunable lasers can be found in [1043–1047].

8.5.1 Dye Lasers

Laser action in organic dyes was discovered independently by *Sorokin* et al. [1048] and Schäfer et al. [1049] in 1966. Since then, several hundreds of dyes have been shown to have suitable properties, to greater or lesser degrees, for use as laser media. One of the most common laser dyes is Rhodamine 6G dissolved in methanol or ethylene glycol. The complex structure of organic dyes is illustrated in Fig. 8.17, where the formula for Rhodamine 6G is shown.

The general energy-level structure of an organic dye is shown in Fig. 8.18 The transitions relevant for laser action occur between the two lower electronic singlet states. The ground state, as well as the excited state, is split into a continuous structure of smeared energy sublevels due to the interaction with the solvent. Normally, the molecules are Boltzmann-distributed on the lowest sublevels of the ground state. The molecules can be excited to the next singlet band with light. The molecules relax very quickly ($\sim 10^{-12}$ s) in radiation-less transitions to the lowest level of the excited state,

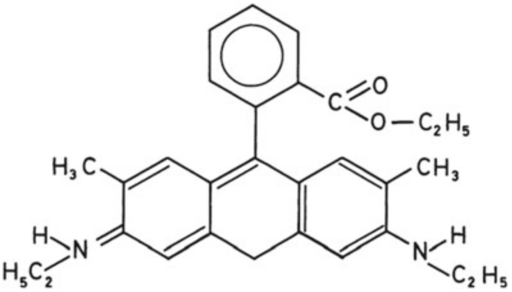

Fig. 8.17 The chemical structure of Rhodamine 6G

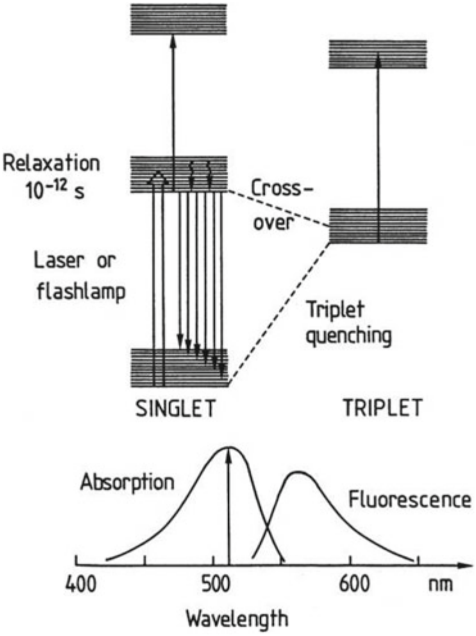
Relaxation
10^{-12} s
Cross-
over
Laser or
flashlamp
Triplet
quenching
SINGLET
TRIPLET
Absorption
Fluorescence
400
500
600
nm
Wavelength

Fig. 8.18 General energy-level structure of an organic dye molecule and resulting absorption and fluorescence curves [1]

from where the molecules return to the sublevels of the ground state with a lifetime of about 10^{-9} s, emitting fluorescent light. The resulting absorption and emission curves for Rhodamine 6G are included in Fig. 8.18. Because of the relaxation in the excited singlet band, the same fluorescence curve is obtained regardless of the spectral distribution of the absorbed light. For example, the curve given in the figure is obtained regardless of whether a flash-lamp or a fixed-frequency laser is used for the excitation.

The usefulness of an organic dye for laser applications much depends on the position of higher lying singlet bands and on the influence of the system of triplet levels that is always present in organic dye molecules. If a higher lying singlet state has an inappropriate energy, a strong absorption of fluorescence light results. Through radiation-less transitions, excited dye molecules can be transferred to the triplet system. If a large number of molecules assemble in the lowest triplet state, the fluorescent light from the singlet system can be strongly absorbed by triplet molecules.

If the organic dye is pumped sufficiently strongly, a population inversion between the lowest sublevel of the upper singlet state and the sublevels of the ground state is obtained. Amplification by stimulated emission can then be achieved. If a dye solution is contained in a cell, placed in a laser cavity, and sufficient pumping power is supplied, laser action will occur (Fig. 8.19). With broadband laser mirrors, stimulated emission is obtained in a wavelength range of a few nm close to the peak of the fluorescence band.

A very important step was taken by *Soffer* and *McFarland* [1050] in 1967 by replacing the totally reflecting mirror with a grating in a Littrow mount (Fig. 6.22). We saw a similar arrangement already in Fig. 8.16, where individual laser lines were selected in the Ar-ion laser by using a prism. A frequency-selective feedback is obtained and the bandwidth of the stimulated radiation is reduced to about 0.05 nm. By turning the grating, the laser can be continuously tuned over the fluorescence band of the dye. An arrangement for flash-lamp-pumping of a tunable dye laser is shown in Fig. 8.19. Here, a tube is used for the dye solution, which is pumped with a linear flash-lamp. Laser pulses with a duration of about 1 μs and a peak power of several kW are obtained. The repetition rate is generally about 1 Hz. Pulsed dye lasers are more

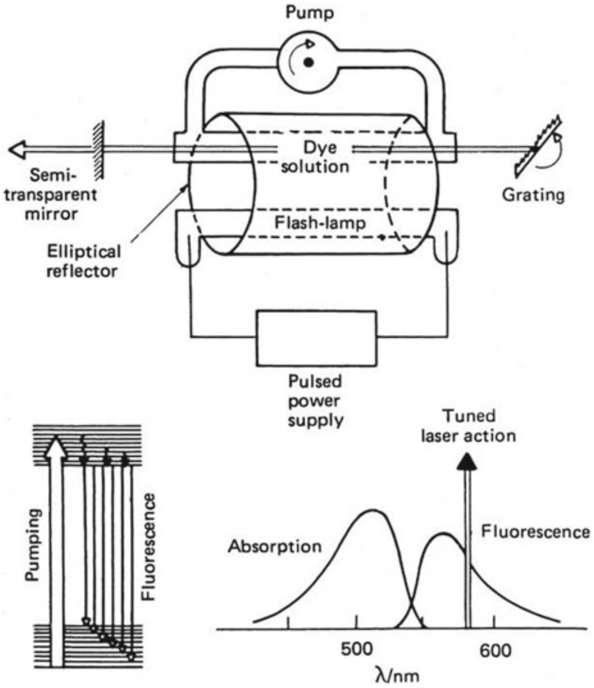
Pump
Dye solution
Semi-transparent mirror
Grating
Flash-lamp
Elliptical reflector
Pulsed power supply
Tuned laser action
Pumping
Fluorescence
Absorption
Fluorescence
500
600
λ/nm

Fig. 8.19 Flash-lamp-pumped dye laser [997]

frequently pumped by a fixed-frequency laser, which can be a nitrogen, an excimer, a copper, or a frequency-doubled Nd:YAG laser. Three different arrangements are shown in Fig. 8.20. An intracavity beam expander is used in the *Hänsch* design [1051], to widen the diameter of the beam so that more lines of the Littrow-mounted grating are illuminated. This leads to an increased resolution (Eq. 6.15; Sect. 6.2.2) at the same time as the grating is protected from local heating. The linewidth with such an arrangement is typically 0.01 nm. Using an intracavity etalon, the linewidth can be reduced by a factor of 10. Instead of using a telescope, a multiple-prism arrangement can be used since expansion *across* the groves is the only consideration from a resolution point of view (Eq. 6.15). Because of the short pumping time (5–10 ns), there is normally no time for a pronounced cavity mode structure to build up in a short-pulse laser. Mode positions are only weakly indicated in the essentially smooth frequency distribution.

An arrangement is shown in Fig. 8.20, in which all the grating lines can be utilized without using any form of beam expansion [1052–1055]. Here, grazing incidence on a fixed grating is employed, which is called a *Littman* arrangement. The laser is tuned

Fig. 8.20 Dye laser cavities of various designs

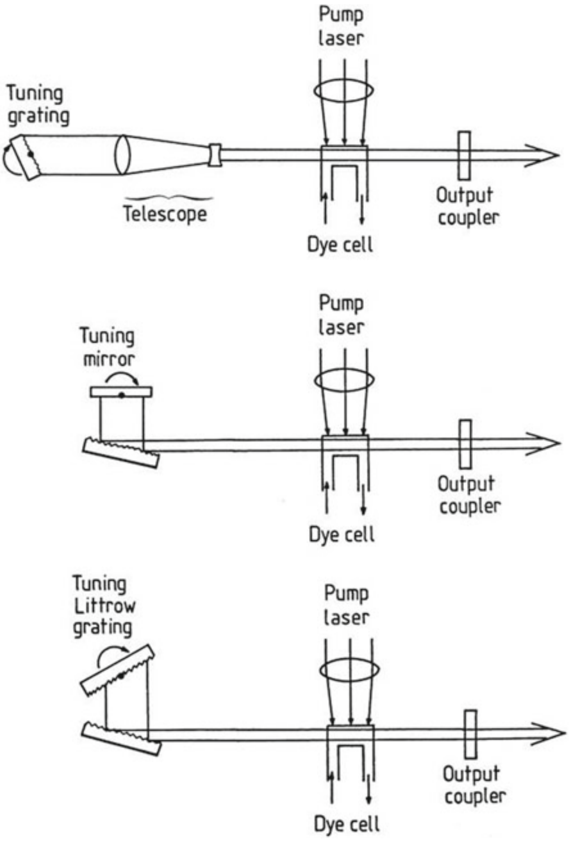
Pump laser
Tuning grating
Telescope
Output coupler
Dye cell
Pump laser
Tuning mirror
Output coupler
Dye cell
Tuning Littrow grating
Pump laser
Output coupler
Dye cell

by turning a mirror reflecting the first-order diffraction of the grating back on itself. The useful laser beam can be taken out as the zeroth-order beam from the grating (reflection) or through a partially transmitting end mirror. The latter arrangement reduces the broadband dye emission. By exchanging the tuning mirror for a grating in a Littrow mount, a still higher resolution can be achieved. By eliminating the telescope, the cavity can be made very short. This leads to many round trips during the pulse, a large free spectral range, and the possibility of single-mode operation.

If a high pulse energy is needed while retaining a small linewidth and a high beam quality, it is advisable to utilize an oscillator/amplifier arrangement, as mentioned in Sect. 8.4.2. Two examples are given in Fig. 8.21. By expanding the laser beam inside the oscillator cavity, a large number of grating lines are illuminated, which increases the spectral sensitivity of the grating. This is done by a lens telescope in the figure upper panel, while multiple prisms (with surfaces close to the Brewster angle, to reduce losses) are used in the figure lower panel. In order to achieve a very small linewidth ($\sim$100 MHz), an external Fabry–Pérot interferometer can be used to filter the oscillation output [1051, 1056, 1057]. The possibility of pressure-scanning the laser is also illustrated in the figure. Since grating, internal, and external Fabry–Pérot interferometer are tuned in the same way when the pressure is changed (the expression nl occurs in all the formulae), all the elements will remain synchronized once they have been correctly adjusted.

Pulsed dye lasers can be operated from 320 to 1000 nm using different dyes. Tuning curves for a dye laser, pumped by an excimer laser or harmonics of the Nd:YAG laser, are shown in Fig. 8.22. An energy conversion of 10–20% is typical for excimer laser pumping. With a frequency-doubled Nd:YAG laser (532 nm), the conversion for Rhodamine dyes can exceed 40%. The frequency range of dye lasers can be extended using nonlinear optics techniques (Sect. 8.6).

In the same way as for fixed-frequency lasers, it is considerably more difficult to achieve continuous laser action than pulsed operation with a dye laser. The first continuous dye laser was designed in 1970 by Peterson et al. [1059]. A special problem associated with organic dyes is the building up of a population of molecules in the lowest triplet state. For pulsed pumping, laser light can be obtained for a short time before triplet absorption dominates. To achieve continuous laser action, absorbing triplet molecules must be removed. Certain chemicals, such as cyclooctatetraene (COT) or even dissolved O_2, are very active in transferring triplet molecules to the ground state without emitting radiation (triplet quenching). An argon or a krypton-ion laser with a power of several watts is used as a pump source for a continuous dye laser. With Rhodamine 6G, a conversion efficiency of 20% can be achieved in the most favourable wavelength region. However, the efficiency is normally lower. It is possible to cover the wavelength range of 375–950 nm with continuous dye lasers. In order to achieve continuous laser action, a certain dye must be pumped at a suitable wavelength, for which good absorption occurs. The green, yellow, and red regions can be covered by dyes that can be pumped by the blue–green lines of the argon-ion laser. Dyes emitting in the near-IR region (NIR) need to be pumped by the red lines from a krypton-ion laser. Alternatively, a mixture of two dyes can be used, where the first one can be pumped by green light and then fluoresce

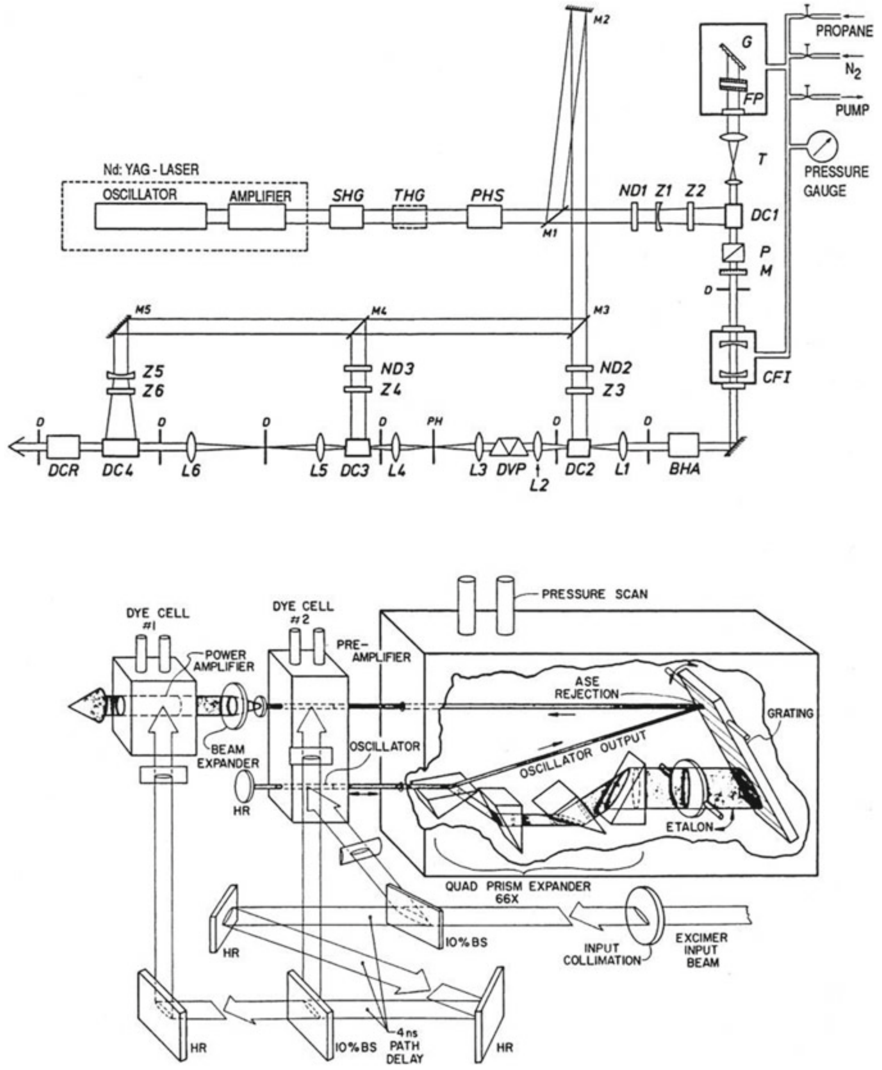
M2
G
FP
PROPANE
N_2
PUMP
T
PRESSURE GAUGE
Nd: YAG - LASER
OSCILLATOR
AMPLIFIER
SHG
THG
PHS
M1
ND1
Z1
Z2
DC1
P
M
D
M5
M4
M3
Z5
Z6
ND3
Z4
ND2
Z3
CFI
D
D
D
D
PH
D
D
DCR
DC4
L6
L5
DC3
L4
L3
DVP
L2
DC2
L1
BHA
DYE CELL #1
DYE CELL #2
PRESSURE SCAN
POWER AMPLIFIER
PRE-AMPLIFIER
ASE REJECTION
GRATING
BEAM EXPANDER
OSCILLATOR
OSCILLATOR OUTPUT
HR
ETALON
QUAD PRISM EXPANDER 66X
HR
10% BS
INPUT COLLIMATION
EXCIMER INPUT BEAM
HR
10% BS
4 ns PATH DELAY
HR

Fig. 8.21 Oscillator/amplifier arrangements for tunable dye lasers ([1057], and courtesy: Lambda Physik)

in the red, providing proper energy transfer for pumping the NIR dye. (In passing we note that a similar strategy is taken in red algae, which can grow deep in the sea, where the only faint green light is present (Fig. 6.61). The algae contain the red accessory pigments phycocyanin and phycoerytrin, which absorb in the green and can fluoresce in the red, where normal chlorophyll, always needed for synthesis, can absorb. The energy transfer mostly occurs radiationless in practice).

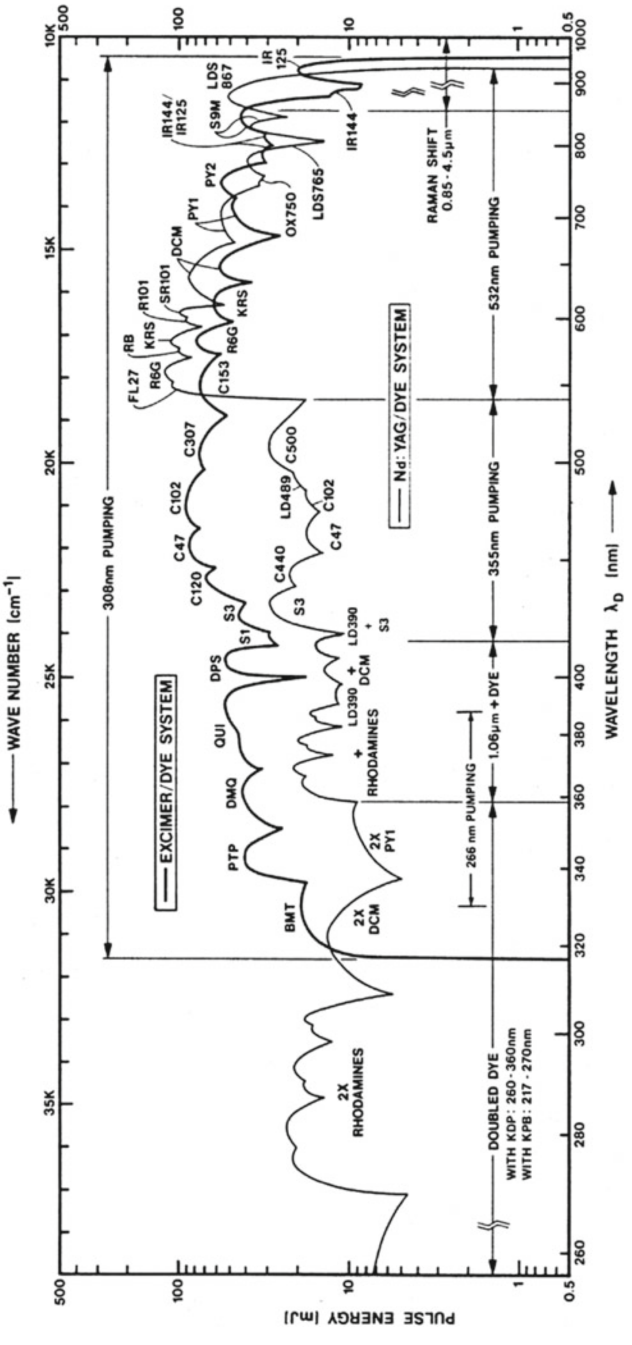

Fig. 8.22 Tuning curves for excimer-pumped and Nd:YAG-pumped dye lasers [1058]

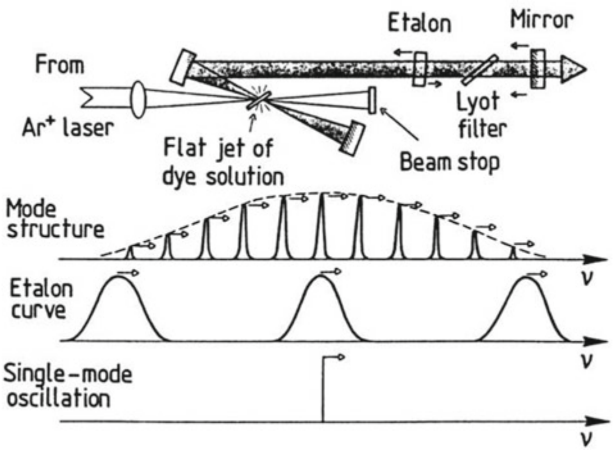

Fig. 8.23 Continuous dye laser using a flat dye-solution jet as the active medium

Blue and violet dyes, e.g. Stilbene, require pumping with the UV lines from an Ar^+ or Kr^+ laser. An example of the arrangement of a continuous, tunable dye laser is given in Fig. 8.23. Using focused argon-ion laser light, a continuous population inversion is maintained at a point on a quickly flowing flat jet of dye that is ejected through a specially designed nozzle. Ethylene glycol is in this case used as the dye solvent, because of its high viscosity. This arrangement ensures an efficient cooling of the dye.

The gain volume is at the focal point of a folded cavity, consisting of two spherical mirrors and a flat output coupler. Tuning is accomplished with a birefringent, so-called *Lyot filter* [1060]. This consists of one or several crystalline quartz plates mounted at the Brewster angle. The dominant transmission maximum of this filter can be moved by turning the optical axis of the filter with respect to the plane of polarization of the light in the cavity.

A bandwidth of about 0.05 nm is obtained from a CW dye laser when only a primary tuning element is used. The width of the filter peak is much larger but the laser will only oscillate close to the transmission peak because of the regenerative nature of laser action ("strong becomes stronger because it is strong, weak becomes weaker because it is weak", or "the winner takes it all"). With a typical cavity length of 30 cm, a mode separation of 500 MHz is obtained, thus permitting several hundreds of modes to oscillate under the gain profile, which is given by the frequency selectivity of the cavity (not by any Doppler broadening as is the case in a gas laser). A single cavity mode can be selected with an intracavity high-finesse etalon (Sect. 6.2.3), but the resulting frequency width for the outgoing light will still be several 10's of MHz, since the frequency stability is limited by vibrations, etc. The linewidth can be reduced to less than 1 MHz with a frequency stabilization system. Such a system is shown in Fig. 8.24. Using more advanced systems with active electro-optic phase control, the linewidth can be reduced to the Hz level.

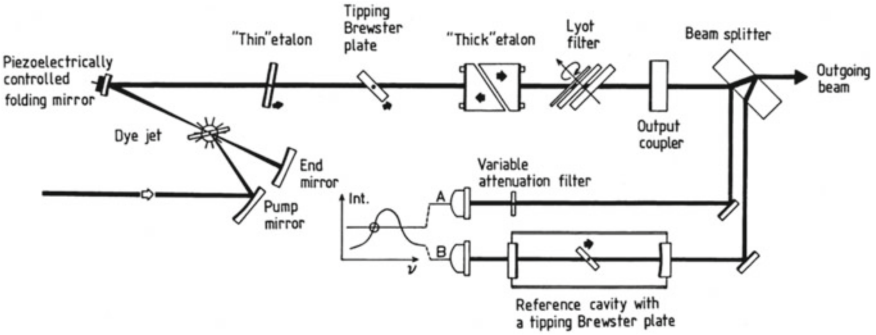
"Thin"etalon
Tipping Brewster plate
"Thick"etalon
Lyot filter
Beam splitter
Piezoelectrically controlled folding mirror
Outgoing beam
Dye jet
Output coupler
End mirror
Variable attenuation filter
Int.
A
B
ν
Pump mirror
Reference cavity with a tipping Brewster plate

Fig. 8.24 Tunable single-mode dye laser with active frequency stabilization (Courtesy: Coherent, Inc.)

In order to be able to make a system with etalons work over a wide wavelength region, two low-finesse etalons (broadband coatings) are used in series. With a 1 mm-thick etalon ($n = 1.5$), a free spectral range of 100 GHz is obtained and, when operated with a transmission maximum close to a maximum of the Lyot filter, some 10 modes may lase. Adjacent etalon maxima occur where the filter has a substantially reduced transmission. If an additional, thicker etalon is introduced, having a substantially reduced free spectral range, say 10 GHz, a single-mode operation can be achieved. The transmission profiles of the different resonator components are shown in Fig. 8.25. In order to achieve a high single-mode power, a ring-laser cavity is frequently used instead of the usual standing-wave linear cavity. This avoids the problem of high non-utilized gain in the standing-wave nodes of the linear cavity. This gain will ultimately be utilized by an unwanted second cavity mode, so that at high pumping power it can no longer be suppressed. A ring-laser arrangement

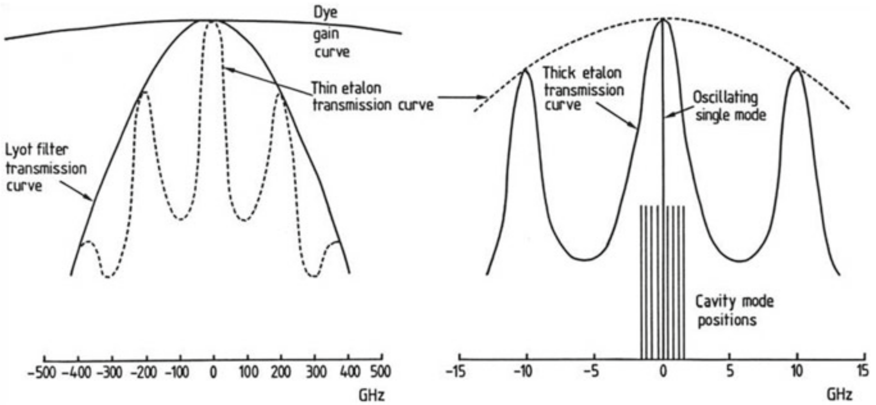

Fig. 8.25 Hierarchic sequence of spectral curves illustrating the narrowing of the frequency domain and the isolation of a single cavity mode for a linear cavity

is shown in Fig. 8.26a. Tuning curves for a single-mode dye laser are shown in Fig. 8.26b. Dye lasers have been discussed in detail in [1061–1065], and laser dyes are covered in [1066–1068].

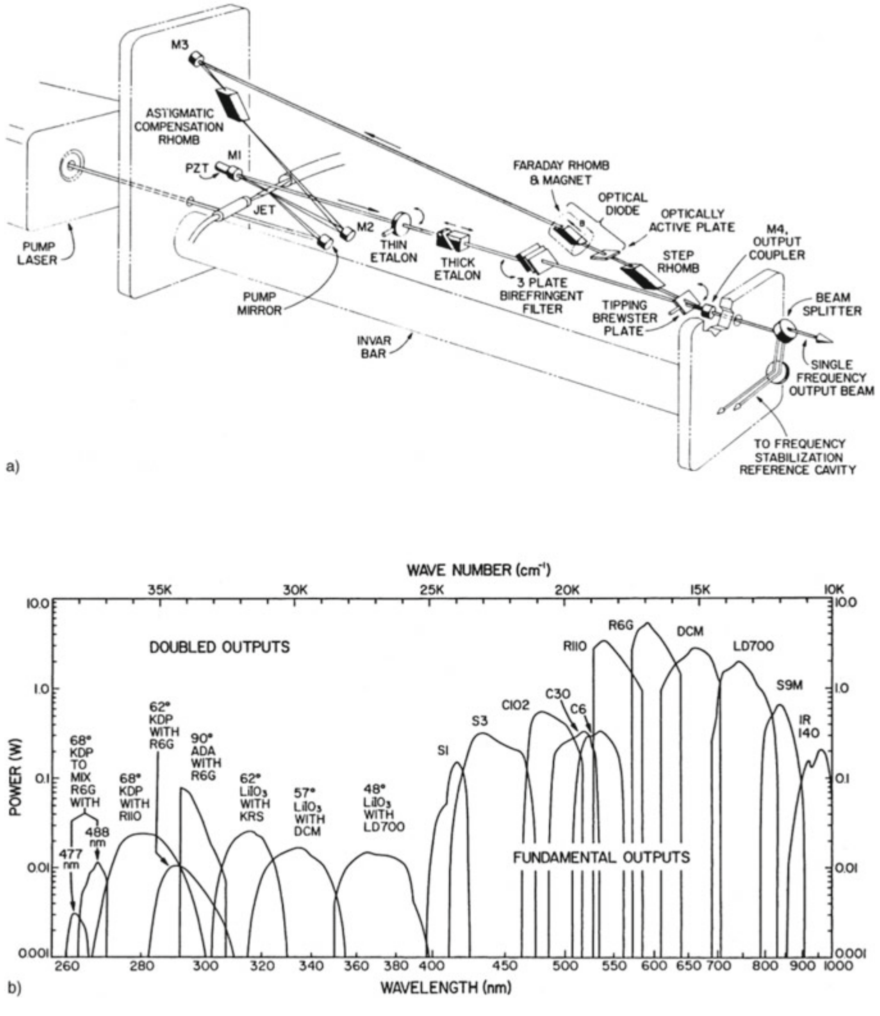
M3
ASTIGMATIC COMPENSATION RHOMB
MI
PZT
JET
PUMP LASER
M2
THIN ETALON
THICK ETALON
PUMP MIRROR
INVAR BAR
3 PLATE BIREFRINGENT FILTER
FARADAY RHOMB & MAGNET
OPTICAL DIODE
OPTICALLY ACTIVE PLATE
STEP RHOMB
TIPPING BREWSTER PLATE
M4, OUTPUT COUPLER
BEAM SPLITTER
SINGLE FREQUENCY OUTPUT BEAM
TO FREQUENCY STABILIZATION REFERENCE CAVITY
a)
WAVE NUMBER (cm⁻¹)
35K
30K
25K
20K
15K
10K
10.0
1.0
0.1
0.01
0.001
POWER (W)
DOUBLED OUTPUTS
68° KDP TO MIX R6G WITH
477 nm
488 nm
68° KDP WITH RIIO
62° KDP WITH R6G
90° ADA WITH R6G
62° LiIO₃ WITH KRS
57° LiIO₃ WITH DCM
48° LiIO₃ WITH LD700
SI
S3
CI02
C30
C6
RIIO
R6G
DCM
LD700
S9M
IR 140
FUNDAMENTAL OUTPUTS
260
280
300
320
340
360
380
400
450
500
550
600
650
700
800
900
1000
WAVELENGTH (nm)
b)

Fig. 8.26 **a** Tunable single-mode dye ring laser (Courtesy: Coherent, Inc.); **b** tuning curves for a CW single-mode dye laser (Courtesy: Coherent, Inc.)

8.5.2 Colour-Centre Lasers

Colour-centre (F-centre) lasers can be used in the near-IR region. These lasers resemble dye lasers with regard to function and construction. Instead of the dye solution, a cooled F-centre crystal is used as the active, laser-pumped medium. The colour centre is a defect in a crystal lattice, e.g. KCl. The defect consists of an ion vacancy that has trapped an electron. If impurity ions are close to the vacancy, the optical properties are changed. F-centre crystals absorb visible radiation and fluorescence in the near-IR (NIR) region. Using different crystals, the range of 1–3.5 μm can be covered. F-centre structures, absorption, and lasing curves are shown in Fig. 8.27 as well as a practical arrangement in a commercial F-centre laser. F-centre lasers have

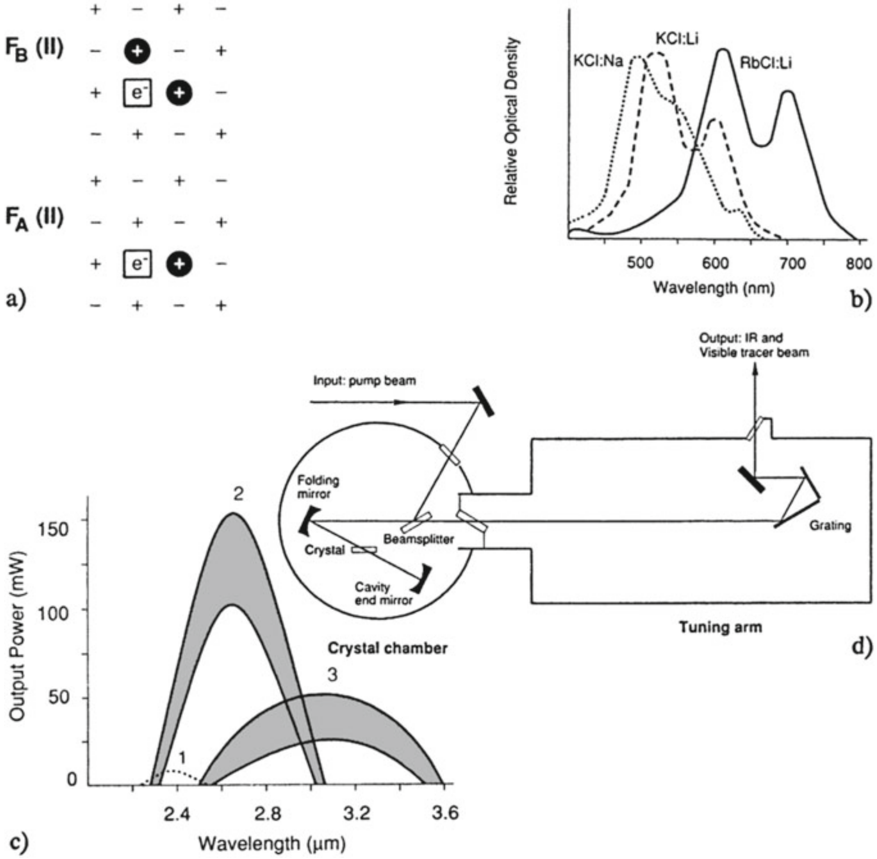

F_B (II)
F_A (II)
e⁻
a)
Relative Optical Density
KCl:Na
KCl:Li
RbCl:Li
500
600
700
800
Wavelength (nm)
b)
Output: IR and
Visible tracer beam
Input: pump beam
Folding mirror
Beamsplitter
Crystal
Cavity end mirror
Crystal chamber
Grating
Tuning arm
d)
Output Power (mW)
150
100
50
0
1
2
3
2.4
2.8
3.2
3.6
Wavelength (μm)
c)

Fig. 8.27 Basics of F-centre lasers. The figure shows **a** F-centre structures, **b** absorption, **c** laser emission curves, and **d** the cavity arrangement for a commercially available unit (Courtesy: Burleigh Instruments, Inc.)

become largely obsolete through the availability of semiconductor lasers working in the same spectral region.

8.5.3 Tunable Solid-State Lasers

Certain solid-state materials with transition-element or rare-earth ions as impurities in a host matrix have rather broad gain curves and can thus be tuned over a certain range. This is the case for the Nd: Glass laser, which can be tuned in the region 1.0–1.1 μm. The *alexandrite* (Cr^{3+}:$BeAl_2O_4$) and *emerald* (Cr^{3+}:$Be_3Al_2Si_6C_{18}$) lasers that bear a close resemblance to ruby lasers can, in the same way, be tuned in the regions of 730–800 nm and 700–850 nm, respectively. Additional chromium-based lasers are LISAF (Cr^{3+}:$LiSrAlF_6$) and Forsterite (Cr^{4+}:Mg_2SiO_4). All these lasers can be pumped directly with a flash-lamp. Finally, some further transition-element lasers should be mentioned. Co:MgF_2 can be pumped by a simple, non-Q-switched Nd:YAG laser and yields tunable radiation in the region of 1.7–2.3 μm. If the material is instead doped with vanadium, it can be tuned in the region of 1.0–1.1 μm.

Titanium-doped sapphire (Ti:S, Ti^{3+}:Al_2O_3) [1069] has emerged as a very important tunable solid-state laser material. It has a particularly large tuning range of 660–1100 nm. This broad gain profile also makes it extremely interesting for the generation of ultrashort pulses by mode-locking, as will be discussed in Sect. 8.7. Ti:S can be directly pumped by flash-lamps (with short pulse lengths because of the upper-state short lifetime of about 3.2 μs), but better by a frequency-doubled Nd:YAG laser (532 nm), and behaves much like a dye laser. The fact that sapphire conducts heat extremely well makes the thermal effects tractable, in spite of it being a solid. CW operation is possible using argon-ion laser pumping, and single-mode tunable laser arrangements similar in construction to what is shown in Fig. 8.26a are available. Fluorescence curves for some tunable solid-state laser materials are given in Fig. 8.28 [1070]. Tunable solid-state lasers have been discussed in [998, 1071–1075].

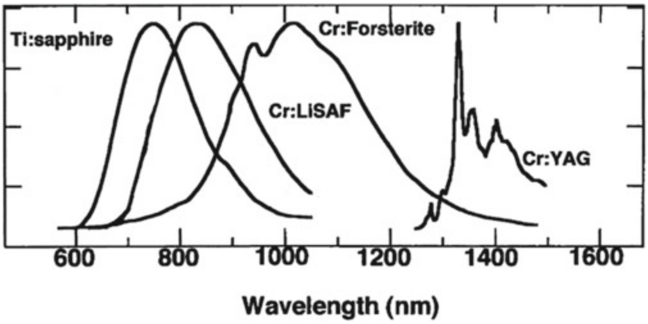

Fig. 8.28 Fluorescence curves for some tunable solid-state laser materials (Adapted from [1070])

8.5.4 Tunable CO_2 Lasers

The carbon dioxide laser is the most efficient gas laser, with a wall-plug efficiency of up to 20%. It works in the IR region at around 10 μm. A non-tuned CO_2 laser is used in numerous applications. However, from a spectroscopic point of view, the fact that it can be line-tuned and continuously tuned at high gas pressures is useful. A level diagram and a practical arrangement for a tuned CO_2 laser are shown in Fig. 8.29, together with a diagram of the available lines. The CO_2 molecule has three fundamental modes of vibration (Sect. 3.4). In the mode that corresponds to symmetric stretching (ν_1), the two oxygen atoms move in opposite directions while the carbon atom is stationary. In the bending mode (ν_2), the molecule is bent back and forth. Finally, in the asymmetric stretching mode (ν_3), the oxygen atoms move together while the carbon atom moves in the opposite direction.

The vibrational state of the molecule is specified by a set of vibrational quantum numbers (ν_1, ν_2, ν_3), one for each vibrational mode. In the CO_2 laser, the level corresponding to asymmetric stretching (001) is populated efficiently by almost-resonant collisions with excited molecules of nitrogen that have been added to the CO_2 gas. An electric discharge populates the first excited vibrational level in nitrogen. A strong population inversion with respect to the lower lying CO_2 states (100) and (020) occurs. In a suitably arranged laser cavity, laser emission can occur in the bands of 10.2–10.8 μm and 9.2–9.7 μm using a large number of rotational lines. If no special precautions are taken, lasing occurs on the strongest line: P(20) at 10.59 μm.

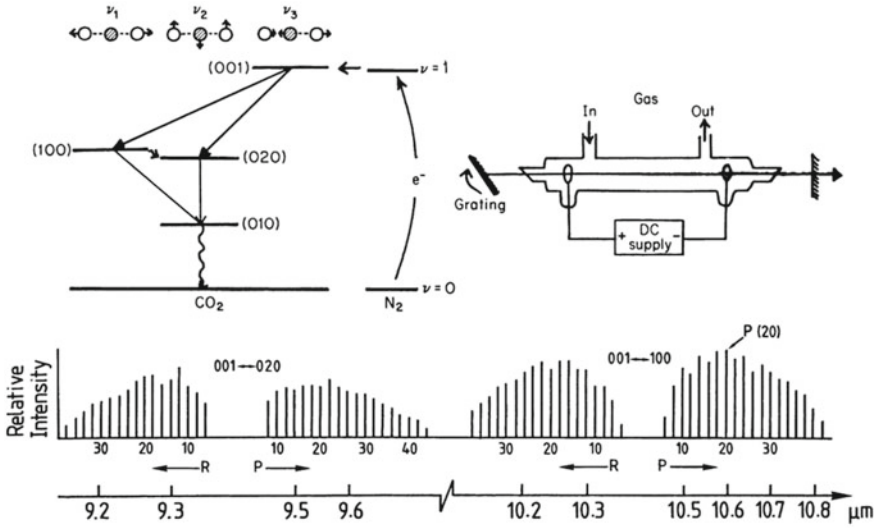

Fig. 8.29 Energy-level diagram relevant to the CO_2 laser with individual vibrational–rotational laser lines and a cavity arrangement illustrated [997]

Using a Littrow-mounted grating, other individual P- and R-branch lines can be chosen. Within every line, finetuning can be accomplished within about 50 MHz, corresponding to the Doppler width at 10 μm for the CO_2 molecules. By utilizing isotopic molecules, like $^{13}CO_2$, further fixed wavelengths can be chosen. A continuous CO_2 laser of this type normally has an electric discharge along the tube. However, it is also possible to work at high gas pressures (at atmospheric pressure and up to 10 atmospheres) if a transverse, pulsed discharge is used (TEA, Transverse Electric Atmospheric laser; see also Sect. 8.4.3). At 10 atmospheres, the pressure broadening is about 2 cm^{-1} (60 GHz) and the individual rotational–vibrational lines that are typically separated by 1–3 cm^{-1} merge. Continuous laser action within the band is then possible. Continuous laser action with a certain tunability can be obtained in *waveguide lasers*, operating at 1 atmosphere pressure.

Non-spectroscopic high-power CO_2 lasers have been constructed with a continuous output of up to tens of kW. Such lasers are used industrially for cutting, welding, hardening, etc. High-power pulsed CO_2 lasers have also been used for fusion research. CO_2 lasers were discussed in [1076–1078].

Carbon dioxide lasers are now being increasingly challenged by high-power fibre lasers [1024–1027], where a sufficiently long suitably doped fibre (frequently Erbium is the dopant) is pumped by high-power diode lasers, and being able to achieve output powers in kW range. Doped fibres can be hundreds of metres long and be coiled and employ distributed feedback mirrors in very compact arrangements. Mode-locking can also be achieved using, e.g. SESAMs (Sect. 8.7.1 [1024, 1027]).

Lasers with CO as an active medium can also be constructed. This type of laser type yields a large number of lines in the region of 5.1–5.6 μm. In order to achieve efficient operation, the discharge tube must be cooled to low temperatures which complicate practical use. It is simpler to use HF or DF lasers, which give lines in the 2.8–4.0 μm region. Such lasers are examples of chemical lasers, for which the active molecules are formed in the discharge tube from the supplied gases H_2/ D_2 and SF_6.

As we have seen above, lasing has been achieved for a very large number of atomic and molecular lines. Listings of these lines can be found in [1079, 1080].

8.5.5 Semiconductor Lasers

Around 1962, several researchers discovered that laser action can be achieved in certain semiconductor diode arrangements [1081–1084]. The physics behind this process is different from that discussed so far. However, the fundamental requirement of the creation of a population inversion still exists. A typical diode-laser material is gallium arsenide (GaAs) that has been strongly doped. Laser action occurs in the transition zone between p- and n-doped material in a diode, which is subject to a voltage applied in the forward direction. The basic energy-level diagrams for the cases of voltage off and on are shown in Fig. 8.30. The voltage forces electrons as well as holes into the transition region. Here, the conduction-band states have an excess population with respect to the empty states of the valence band. Stimulated

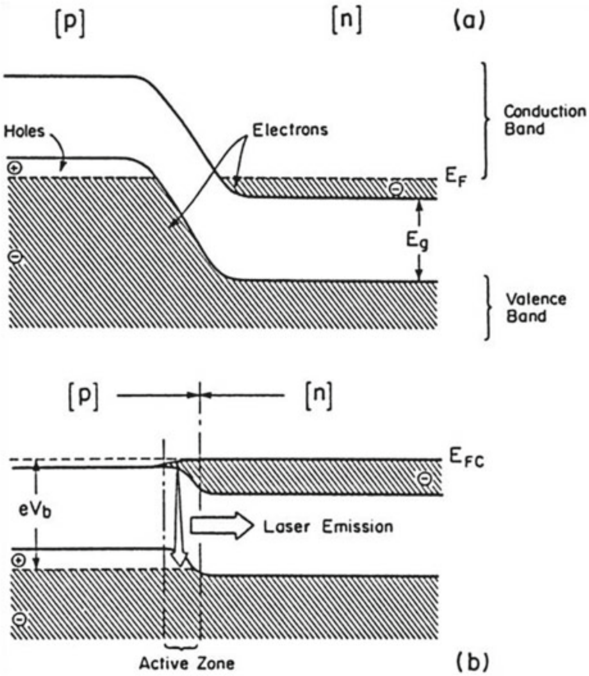
[p]
[n]
(a)
Holes
Electrons
Conduction Band
E_F
E_g
Valence Band
[p]
[n]
E_{FC}
eV_b
Laser Emission
Active Zone
(b)

Fig. 8.30 Energy-level diagram for a semiconductor diode laser **a** without voltage and **b** with an applied voltage [1085]

light emission with a photon energy corresponding to the band gap will result upon the recombination of electrons and holes. Semiconductor lasers are very small, with typical dimensions of less than one mm. The geometry of a typical early laser diode is shown in Fig. 8.31. Two opposite sides are polished and serve as a cavity. Due to the smallness of the cavity, single-mode oscillation is frequently obtained, since the spacing between neighboring modes is very large. Diode lasers with an external cavity can also be used.

The original homojunction systems have successively been replaced by *heterojunction lasers* [1086–1089], which have a complex layered structure (Fig. 8.32), made possible through the development of *MBE* (Molecular Beam Epitaxy) and *MOCVD* (Metal Chemical Vapour Deposition) techniques [1090–1094]. The development of heterojunction systems for high-speed-electronics and opto-electronics

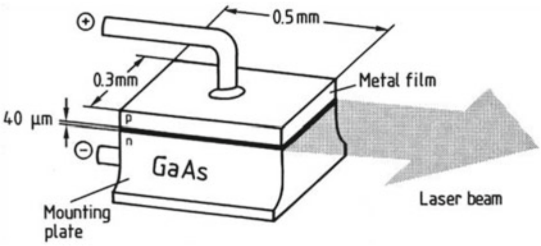
0.5 mm
0.3mm
Metal film
40 µm
p
n
GaAs
Laser beam
Mounting plate

Fig. 8.31 Diode laser

was awarded with the 2000 Physics Nobel Prize to *Zh. I. Alferov* and *H. Kroemer* [1095, 1096].

$Al_xGa_{1-x}As$ diode lasers operating at room temperature around 800 nm have obtained great importance for use in CD players, laser printers, and bar-code readers. Such lasers are also high-quality, narrow-band sources for laser spectroscopy. Coarse tuning is performed by thermo-electric change of the junction temperature, which changes the bandgap and index of refraction, while swift scanning over small spectral regions is achieved by current ramping. The resonance lines of K, Rb, and Cs are readily accessed in this way, as well as lines in molecular oxygen (760 nm) and water vapour (e.g. at ~950 nm). High-power systems, frequently manufactured with many individual units integrated into a "bar" [1019–1023], are now, as already discussed, widely used for efficient solid-state laser pumping (Sect. 8.4.2). The high diode-laser efficiency (electrical-to-optical power) of up to 80% results in low power consumption and easily tractable thermal problems (Fig. 8.32).

Diode-laser development is largely driven by optical telecommunication needs. The usefulness of this type of laser in these contexts stems from the ease with which the output can be electrically modulated at an extremely high bit-rate (up to tens of Gb/s). Since low-loss wavelength regions for optical fibres are around 1.3 and at 1.55 μm (see Fig. 8.33), as governed by the presence of Fe impurities, OH radical absorption, and elastic scattering, the most developed diode lasers are found there. As already mentioned, an important technology employing diode-pumped Er^{3+}-doped fibre amplifiers for 1.55 μm has also been developed for long-haul transmission lines [1027, 1099–1101]. While telecommunication lasers are operated at room temperature, lasers for longer wavelengths need cryogenic cooling. Spectroscopic diode lasers for wavelengths out to 40 μm have been developed as indicated in Fig. 8.34. Material combinations of Pb, S, Sn, Se, and Te are used.

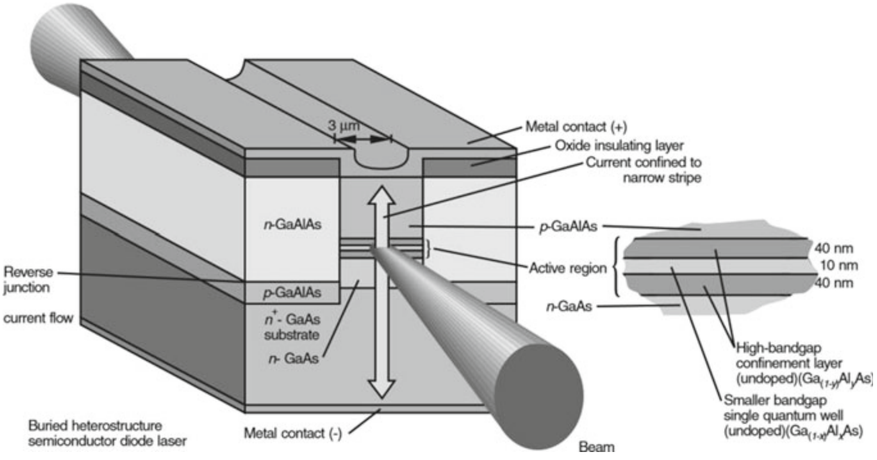
3 μm
Metal contact (+)
Oxide insulating layer
Current confined to narrow stripe
n-GaAlAs
p-GaAlAs
Active region
n-GaAs
40 nm
10 nm
40 nm
Reverse junction
current flow
p-GaAlAs
n⁺- GaAs substrate
n- GaAs
High-bandgap confinement layer (undoped)(Ga(1-y)AlyAs)
Smaller bandgap single quantum well (undoped)(Ga(1-x)AlxAs)
Buried heterostructure semiconductor diode laser
Metal contact (-)
Beam

Fig. 8.32 Heterostructure diode laser [1097]

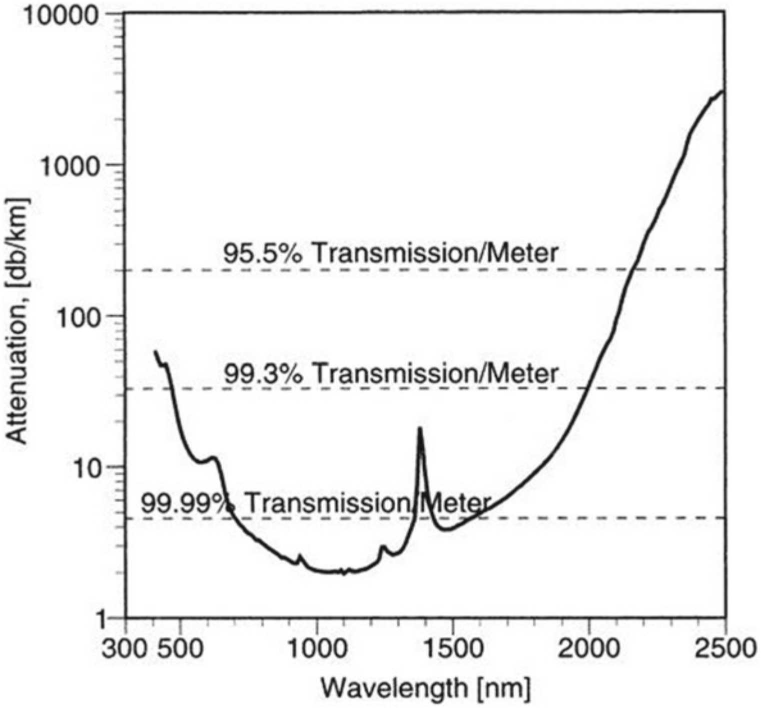

Fig. 8.33 Transmission curve for a quartz optical fibre [1098]

Intense research was invested in extending room-temperature diode-laser emission to visible wavelengths [1102]. Laser pointers at 670 nm and at 633 nm (where the human eye has nine times higher sensitivity) are readily available. Blue and violet CW laser action in GaN and other materials has also been achieved (printing and lithographic applications) [1103, 1104]. Such materials used in very efficient light-emitting diodes (LEDs) combined with an highly fluorescent coating enabled the revolution in efficient lighting (see Fig. 6.9). The Nobel Prize in Physics was given to *I. Akasaki*, *H. Amano,* and *S. Nakamura* in 2014 [495, 496, 1104]. New developments in semiconductor lasers include distributed feedback lasers (DFL) [1105], vertical cavity surface-emitting lasers (VCSEL) [1106–1109], and quantum cascade lasers (QCL) [1110–1115], which all have interesting properties for spectroscopy. DFLs have a periodic structure imprinted in the gain medium, which is responsible for the wavelength-selective lasing action, and tuning becomes very well-controlled by changing the temperature, by external heating, or by changing the driving current. Output powers can reach tens of mW. VCSELs have low cost and are widely tunable, but have inherently low output power (mW). They have multiple thin-film layers as the Bragg-reflecting cavity mirrors outside the gain medium, while the Bragg structure occurs through the gain medium in the DFB lasers. Both these laser types are limited to the visible and near-IR region. For the IR region (3–20 μm), instead the

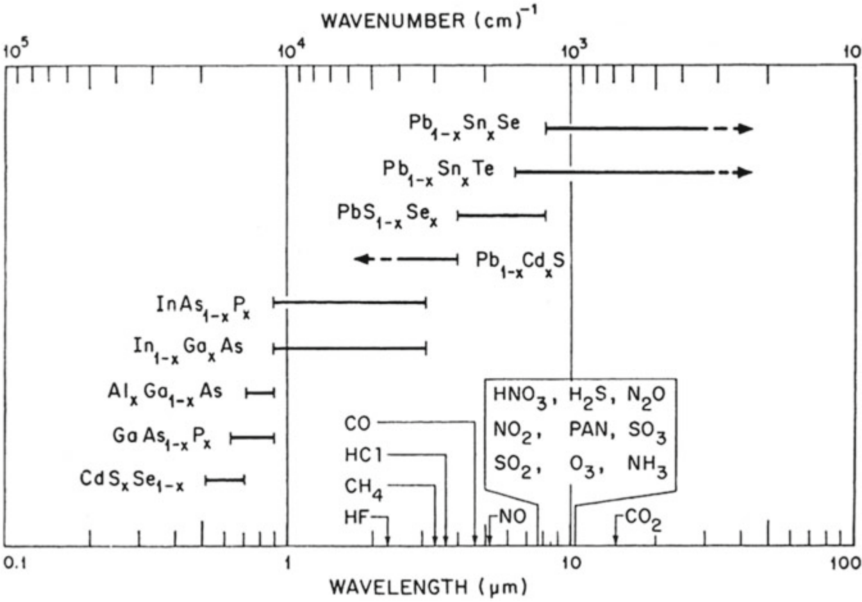

Fig. 8.34 Tuning ranges for different types of semiconductor laser [1085]

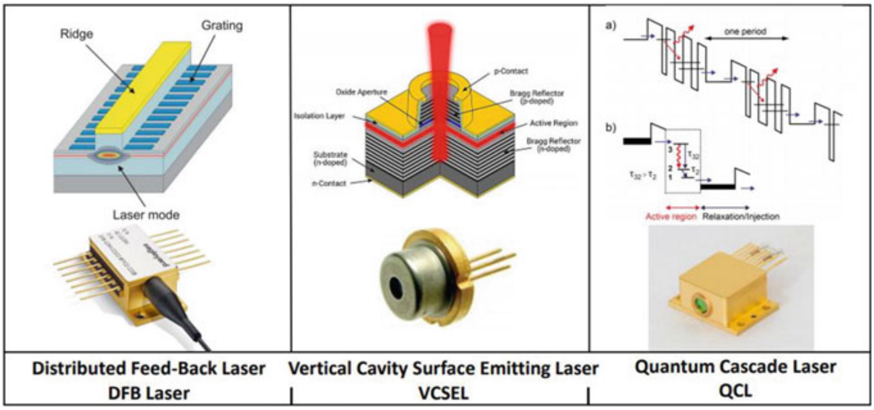
Ridge
Grating
Laser mode
Oxide Aperture
Isolation Layer
Substrate (n-doped)
n-Contact
p-Contact
Bragg Reflector (p-doped)
Active Region
Bragg Reflector (n-doped)
a)
one period
b)
3
2
1
τ_{32}
τ_2
$\tau_{32} > \tau_2$
Active region
Relaxation/Injection
Distributed Feed-Back Laser
DFB Laser
Vertical Cavity Surface Emitting Laser
VCSEL
Quantum Cascade Laser
QCL

Fig. 8.35 Basic arrangements for three types of modern semiconductor lasers: Distributed Feedback (DFB) Laser ([1024] and Courtesy: Eagleyard); Vertical Cavity Surface-Emitting Laser (VCSEL) (Courtesy: 21 Semiconductors; Frankfurt Laser Company); Quantum Cascade Laser (QCL) (Courtesy: Prof. J. Faist, ETH; Alpes Lasers)

QCLs are very convenient. They operate on a fundamentally different principle than the ordinary one used in lasers. Using very advanced epitaxial growth [1116, 1090–1094] of numerous layers in a repetitive manner, laser emission occurs in a chain of emissions when the system decreases its energy like moving down a stair. This leads to high efficiency. CW operation can be achieved at room temperature, but frequently QCLs are cooled. The basic construction of these three types of semiconductor lasers is shown in Fig. 8.35.

Semiconductor lasers are further discussed in [1117–1124], and spectroscopic applications of diode lasers are described in [1125–1132].

8.6 Nonlinear Optical Phenomena

Several nonlinear optical phenomena can be utilized to extend the available wavelength range for a certain laser type. First, we will consider *frequency doubling*. Frequency doubling of an input signal can be achieved by using nonlinear components in an electric circuit. The corresponding optical phenomenon, which is an example of *nonlinear optical effects*, can be observed in certain crystals that are traversed by very intense laser light. Light propagation through a transparent medium can be considered as a process, in which electrical dipoles (electrons bound to a nucleus) are made to oscillate by the radiation field and thus to re-emit the light (Eq. 4.59). The delay in this process can be seen as a reduction in the speed of light, leading to an increased index of refraction n, and the velocity of light inside the medium becomes c/n. Through interference, light in the beam direction only is obtained, although each dipole radiates in many directions. Such defined beam propagation through a medium was discussed also in connection with the Beer–Lambert law (Eq. 6.44).

As long as the oscillation amplitude is small in the light passage of a transparent medium, the dipoles can follow the applied oscillation, but at higher amplitudes, nonlinearities occur when the dipoles can no longer reproduce the applied oscillation. Harmonics then occur. This corresponds to the case in electronics, where an input sinusoidal signal to an amplifier does not produce a pure amplified sinus wave because the amplification curve is not linear, but curved. Clearly, any phenomenon in nature will stop responding linearly when subject to an ever-increasing input stimulus. Nonlinear output behaviour in response to a linear input is illustrated in Fig. 8.36. A pure sinusoidal input signal gives rise to a deformed sinus-wave output. Since a repetitive signal can always be mathematically expanded in a series of harmonics with frequencies being multiples of the fundamental one, and with amplitudes as required, it is easy to see the origin of electronic as well as optical overtones.

If $\mathcal{E}$ is the applied electric field and P is the polarization for the optical medium, we can write

$$P = \chi^{(1)}\mathcal{E} + \chi^{(2)}\mathcal{E}^2 + \chi^{(3)}\mathcal{E}^3 + \dots, \tag{8.7}$$

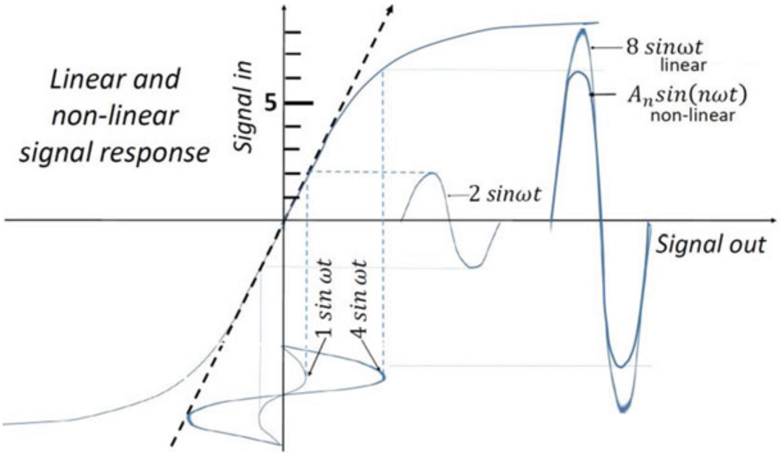

Fig. 8.36 Linear and nonlinear output response to a sinusoidal input signal of increasing intensity. At low intensity, the system responds with a likewise sinusoidal curve (with amplification 2 in the case shown). In contrast, for higher input amplitudes, the system responds nonlinearly, resulting in a distorted curve, which can be mathematically expanded in a series of sinus waves (fundamental ω and overtones $n\omega$ with proper amplitudes A_n)

where $\chi^{(i)}$ are polarizability constants (*susceptibilities*). From the second term in (8.7), we obtain for $\mathcal{E} = \mathcal{E}_0 \sin \omega t$

$$P_2 = \chi^{(2)} \mathcal{E}_0^2 \sin^2 \omega t = \frac{1}{2} \chi^{(2)} \mathcal{E}_0^2 (1 - \cos 2\omega t).$$

This term is responsible for the generation of frequency-doubled light. A prerequisite is that the crystal has a non-central symmetric structure. Using symmetry arguments, it can be shown that for a material with a centre of symmetry, all even coefficients $\chi^{(2)}$, $\chi^{(4)}$, etc. must vanish. Since $\chi^{(2)}$ is always small, it is necessary for $\mathcal{E}_0$ to be sufficiently high. Electric field strengths of a sufficient magnitude ($\sim 10^5$ V/cm) can easily be obtained with pulsed lasers so that the terms $\chi^{(1)}\mathcal{E}$ and $\chi^{(2)}\mathcal{E}^2$ become comparable in magnitude. The generation of frequency-doubled radiation is hampered by wavelength dispersion for the two waves at frequencies ω and 2ω. Since the waves do not normally propagate with the same velocity (because of the wavelength dependence of n; see, e.g. Fig. 6.20b), destructive interference occurs with a resulting low yield. By utilizing doubly refractive materials, for which the velocity of propagation for the "ordinary" ray at ω coalesces with the velocity for the "extraordinary" ray at 2ω, *"phase-matching"* can be obtained. The phase-matching condition also expresses the requirement for conservation of momentum in the particle picture of radiation. By tilting the crystal, and thus selecting the direction of propagation through it, phase-matching can be achieved within a certain, very small, wavelength range. The generation of a frequency-doubled wave and the achievement of phase-matching are illustrated in Fig. 8.37.

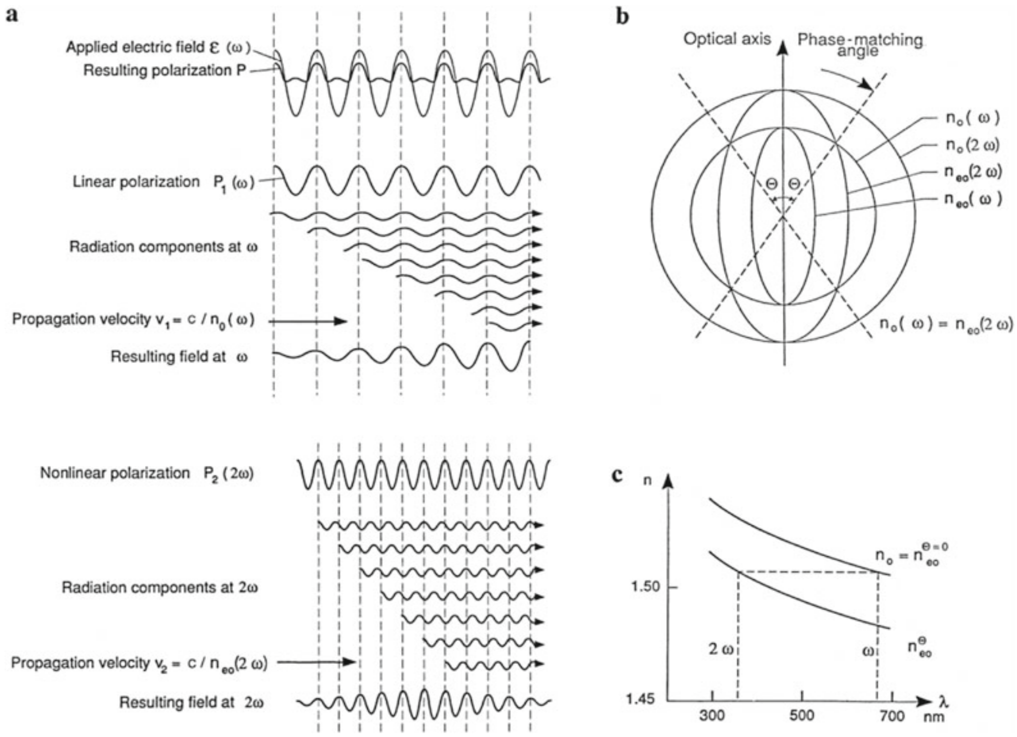
a
Applied electric field $\mathcal{E}$ (ω)
Resulting polarization P
Linear polarization P_1 (ω)
Radiation components at ω
Propagation velocity $v_1 = c / n_0(\omega)$
Resulting field at ω
Nonlinear polarization P_2 (2ω)
Radiation components at 2ω
Propagation velocity $v_2 = c / n_{eo}(2\omega)$
Resulting field at 2ω
b
Optical axis
Phase-matching angle
Θ Θ
$n_o(\omega)$
$n_o(2\omega)$
$n_{eo}(2\omega)$
$n_{eo}(\omega)$
$n_o(\omega) = n_{eo}(2\omega)$
c
n
1.50
1.45
$n_o = n_{eo}^{\Theta=0}$
n_{eo}^{Θ}
2 ω
ω
300
500
700
λ
nm

Fig. 8.37 The generation of frequency-doubled wave in a nonlinear crystal. **a** Fields and polarizations in the crystal. **b** Polar diagram of the indices of refraction for an ordinary and an extraordinary beam. **c** Alternative diagram showing how phase-matching can be achieved

Temperature also influences the phase-matching. It is especially advantageous if phase-matching for a direction at 90° to the optical axis can be achieved by temperature adjustment. Then the extraordinary ray is not displaced with respect to the ordinary ray, which is otherwise the case, reducing the beam overlap. KDP (potassium dihydrogen phosphate) and KPB (potassium pentaborate) are frequently used crystals, which are industrially grown, frequently using the so-called *Czochralski* process. Here, a single-crystal seed is put into the material smelt and is slowly withdrawn while the perfect crystal pattern is multiplying and forming large boules of crystal [1133]. An energy conversion efficiency of tens of per cent can be achieved for KDP, whereas KPB has a substantially smaller efficiency. β-barium-borate (BBO, BaB_20_4) is a newer high-efficiency material, which is replacing KPB. Because of the nonlinear nature of the frequency-doubling process, it is normally used in connection with pulsed lasers. Using tunable dye lasers, doubling down to about 200 nm can be achieved, with the limit set by material absorption. Frequency-doubling curves for a Nd:YAG-pumped dye laser are given in Fig. 8.38.

By using an intracavity frequency-doubling crystal or an external enhancement cavity [1134–1136], continuous frequency doubling and mixing can also be achieved for CW dye laser radiation. Powers of several mW can then be achieved.

Frequency doubling can be seen as a *mixing* of two waves of the same frequency in a nonlinear medium. The more general processes, sum- and difference-frequency generation using different-frequency beams, are also possible and can be used to generate new frequencies using two lasers. The process can be explained by expressing the light field as

$$\mathcal{E} = \mathcal{E}_1 \cos \omega_1 \mathrm{t} + \mathcal{E}_2 \cos \omega_2 \mathrm{t}. \tag{8.8}$$

The quadratic term in (8.7) can then be written.

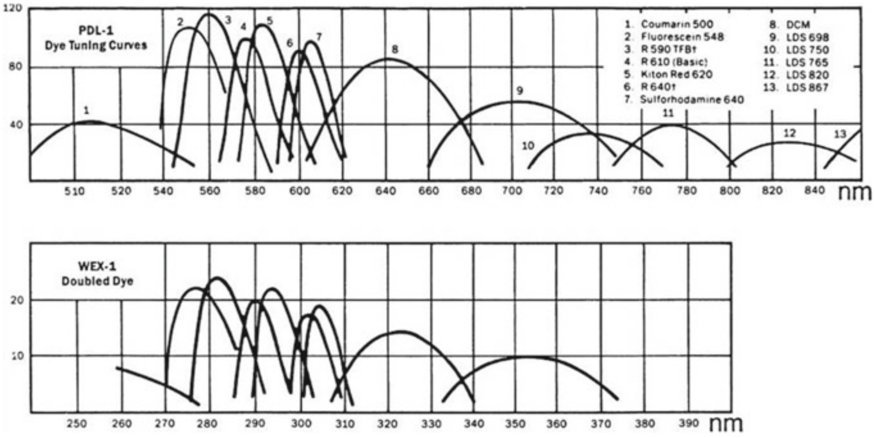

Fig. 8.38 Primary and frequency-doubled tuning curves for a Nd:YAG-pumped dye laser (Courtesy: Spectra Physics, Inc.)

$$\begin{aligned} P_2 &= \chi^{(2)}\left[\mathcal{E}_1^2\cos^2\omega_1 t + \mathcal{E}_2^2\cos^2\omega_2 t + 2\mathcal{E}_1\mathcal{E}_2\cos\omega_1 t\cos\omega_2 t\right] \\ &= \chi^{(2)}\left[\frac{1}{2}(\mathcal{E}_1^2+\mathcal{E}_2^2) + \frac{1}{2}\mathcal{E}_1^2\cos 2\omega_1 t + \frac{1}{2}\mathcal{E}_2^2\cos 2\omega_2 t \right. \\ &\quad \left. + \mathcal{E}_1\mathcal{E}_2\cos(\omega_1+\omega_2)t + \mathcal{E}_1\mathcal{E}_2\cos(\omega_1-\omega_2)t\right]. \end{aligned} \tag{8.9}$$

It can be seen that, apart from the doubled frequencies, sum and difference frequencies are obtained. The phase-matching is chosen to strongly enhance one of the terms. Curves for sum generation employing a dye laser and the fundamental frequency of the Nd:YAG laser are given in Fig. 8.39. We especially note that only one of the lasers needs to be tunable. The mixing process then efficiently displaces the tunability to a new spectral region. Materials that are transparent in the IR region are needed for difference-frequency generation. IR generation in $LiNbO_3$ (lithium niobate) is illustrated in Fig. 8.40, employing single-mode Ar^+ and dye lasers, and output curves for a Nd:YAG-based difference-frequency generator are also given. Crystals of $CdGeAs_2$, $AgGaS_2$, and $AgGaSe_2$ are also available, allowing frequency doubling and sum-frequency generation for pulsed CO_2 lasers. Nonlinear materials for frequency doubling and mixing have been discussed in [1138–1141].

Nonlinear processes require high intensities if they are to be efficient. This limits the applications in the field of diode lasers. However, it is possible to focus the radiation into a narrow waveguide structure of a nonlinear material, such as $LiNbO_3$. Clearly, phase mismatch will occur after some distance of propagation. By the technique of electric-field-induced *periodic poling,* it is possible to regain phase-matching

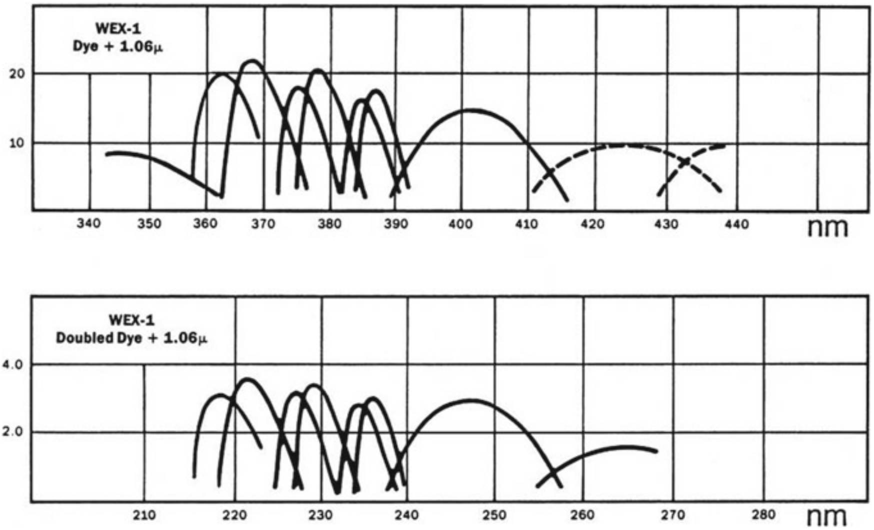

Fig. 8.39 Sum-frequency generation curves for a Nd:YAG-based tunable dye laser (Courtesy: Spectra Physics, Inc.)

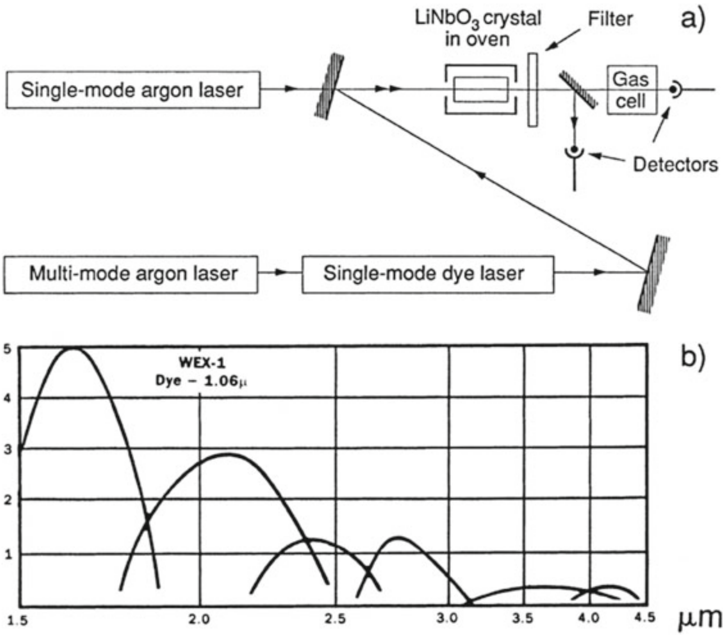

Fig. 8.40 IR radiation by difference-frequency generation in $LiNbO_3$: **a** A set-up for CW generation [1137] and **b** curves for pulsed IR radiation obtained using a Nd:YAG-based tunable laser (Courtesy: Spectra Physics, Inc.)

in this *quasi-phase-matching* scheme by periodically switching the sign of the dispersion. Local ferroelectric domain switching occurs and leads to permanent changes in the crystal structure. In this way, it has become possible to perform frequency doubling to the blue wavelength region [1142] and difference-frequency generation to IR wavelengths [1143], in a similar way to that shown in Fig. 8.40. It has also become possible to perform poling of bulk crystals to allow high-power applications, and in this way, the applicability has been much extended [1144–1146]. The use of the techniques described here has important advantages over conventional phase-matching. The same polarization can be used on all beams, resulting in typically 10 times higher specific nonlinearity and a corresponding increase in efficiency of the conversion. Further, phase-matching can be achieved over the whole transmission range of the material.

The *Optical Parametric Oscillator* (OPO) process is also important in nonlinear optics. Here, a nonlinear crystal in a cavity is used to generate two new frequencies (ω_1 and ω_2) from a single one (ω) that is used to "pump" the crystal (Fig. 8.41). Energy conservation requires $\omega_1 + \omega_2 = \omega$. The frequency division between the two new waves (the *signal* and the *idler*) is chosen by the phase-matching condition. In order to further narrow down the resulting linewidth, one of the cavity mirrors can be replaced by a grating, as indicated in the figure. The crystal and grating are tuned synchronously. The parametric process can also be used in *Optical Parametric*

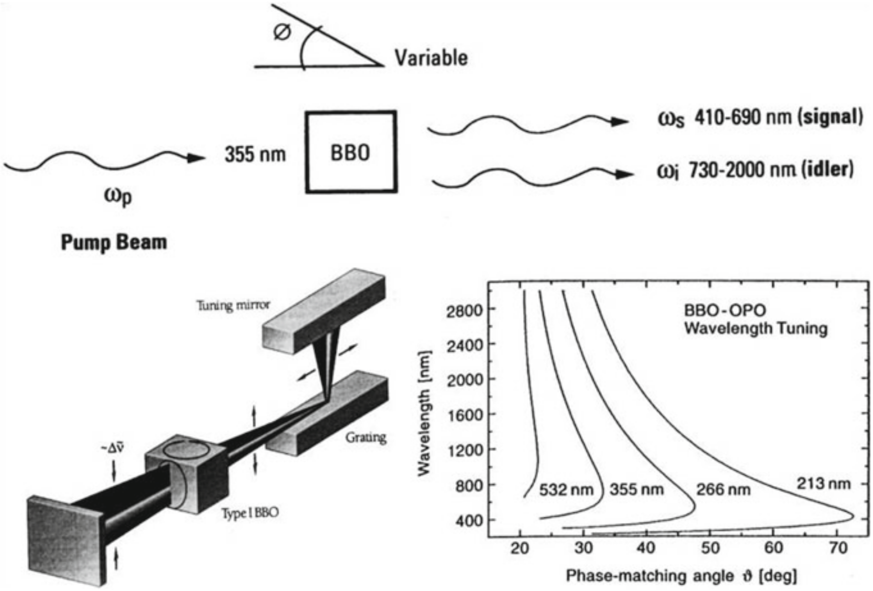
Ø
Variable
ωs 410-690 nm (signal)
355 nm
BBO
ωi 730-2000 nm (idler)
ωp
Pump Beam
Tuning mirror
Grating
~Δν̃
Type I BBO
BBO-OPO
Wavelength Tuning
Wavelength [nm]
2800
2400
2000
1600
1200
800
400
532 nm
355 nm
266 nm
213 nm
20
30
40
50
60
70
Phase-matching angle ϑ [deg]

Fig. 8.41 Principle of an optical parametric oscillator (OPO) (Courtesy: Spectra Physics and Continuum and [1147])

Amplifiers (OPA) to boost the output power. Parametric systems have been refined with regard to linewidth and output power to present a competitive alternative to dye or other tunable lasers. Large wavelength regions can be spanned, especially since the fundamental, doubled, or tripled output of the fixed-frequency pump laser (frequently a Nd:YAG laser) can be employed. Tuning curves for a commercial unit are shown in Fig. 8.42. Parametric light generation is further discussed in [1148–1150].

It should be noted that the OPO process of splitting a pump photon into two lower energy photons is a very powerful and commonly used way to create entangled states, which are critically utilized in the quantum information field (Sect. 4.9).

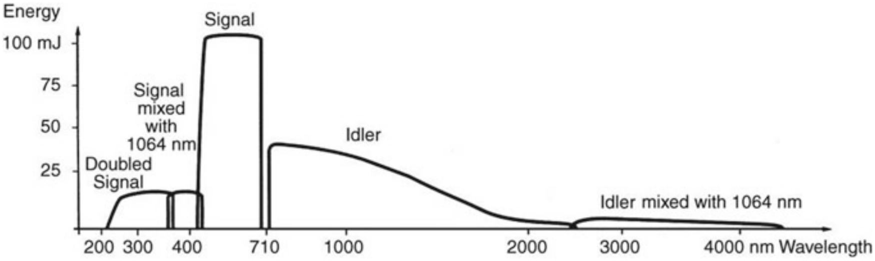

Fig. 8.42 Tuning curves for a commercial pulsed OPO (Courtesy: Spectra Physics)

Frequency mixing can also be achieved in mixtures of metal vapours and inert gases. Since asymmetry is not present in a gas, terms depending on $\chi^{(2)}$ are excluded. Third-order processes $\left(\chi^{(3)} \neq 0\right)$ can be utilized. Direct frequency tripling and four-wave mixing processes are of this type.

In order to access short VUV wavelengths down to the LiF cutoff (110 nm), the resonant four-wave mixing process is quite efficient. This technique is illustrated for the case of Kr gas in Fig. 8.43 [1151]. Basically, two UV photons at 212 nm are subtractively mixed with a third, co-propagating tunable photon to generate a short-wavelength tunable photon in a process involving the frequencies ω_R, $\omega_{L,}$ and ω_{VUV}:

$$\omega_{VUV} = 2\omega_R - \omega_L. \tag{8.10}$$

Since the process is two-photon resonant, it has a high efficiency. Examples of experimental tuning curves in Kr [1152] are shown in Fig. 8.44 for different dyes in the tunable laser, which was used with its fundamental output ω_L, its frequency-doubled output $2\omega_{L,}$ and its IR frequency mixed output $\omega_L + \omega_{IR}$ (see also Fig. 8.38). VUV generation in inert gases and metal vapours and applications of VUV radiation are discussed in [1153–1157]. High-harmonic generation using ultra-intense laser radiation has more recently gained a dominant role in the generation and application of VUV and soft-X-ray generation (Sect. 9.6.2).

If all photons involved in the mixing process have the same wavelength, the process is referred to as *degenerate four-wave mixing* (DFWM). Clearly, the generated photons are then hard to distinguish from the pumping photons and the process is of little interest. However, a different beam geometry, which satisfies the phase-matching condition, can be used, allowing the generated photon beam to be readily distinguished (see Fig. 8.45). Two counter-propagating beams are overlapped in the medium, and a third beam, coming in at an angle, is added. The newly generated beam will then propagate backwards and can be isolated by using a beamsplitter. The process can be seen as the Bragg scattering (Littrow geometry) by the standing-wave grating set up by the counter-propagating beams. The process occurs in gases, with strong resonant enhancement if the frequency is tuned to an atomic or molecular transition. The presence of a particular species in a gas can be detected in this way (see also Sect. 10.1.4). The process also occurs in crystals, where the medium is much denser. The most fascinating aspect of the backward-propagating beam is that it can be shown to be *phase conjugated*, i.e. the wavefront is exactly reversed and in all details retraces the incoming beam. This means that if the incoming beam was first distorted by passing a phase aberrator, such as a turbulent flame or even a piece of ground glass (bathroom window), it will appear undistorted when it reappears through the aberrator again. The result is that a badly distorted image can be reconstructed again.

An example is shown in Fig. 8.46, where an argon laser beam was passed through a photographic film with an image (the Lund University logotype) and then a piece of ground glass before being reflected back. The images were recorded after reflecting off a normal mirror (*left*) and a phase conjugator (*right*; BSO (bismuth silicon oxide; $Bi_{12}SiO_{20}$) self-conjugating crystal). By making one of the mirrors in a laser phase

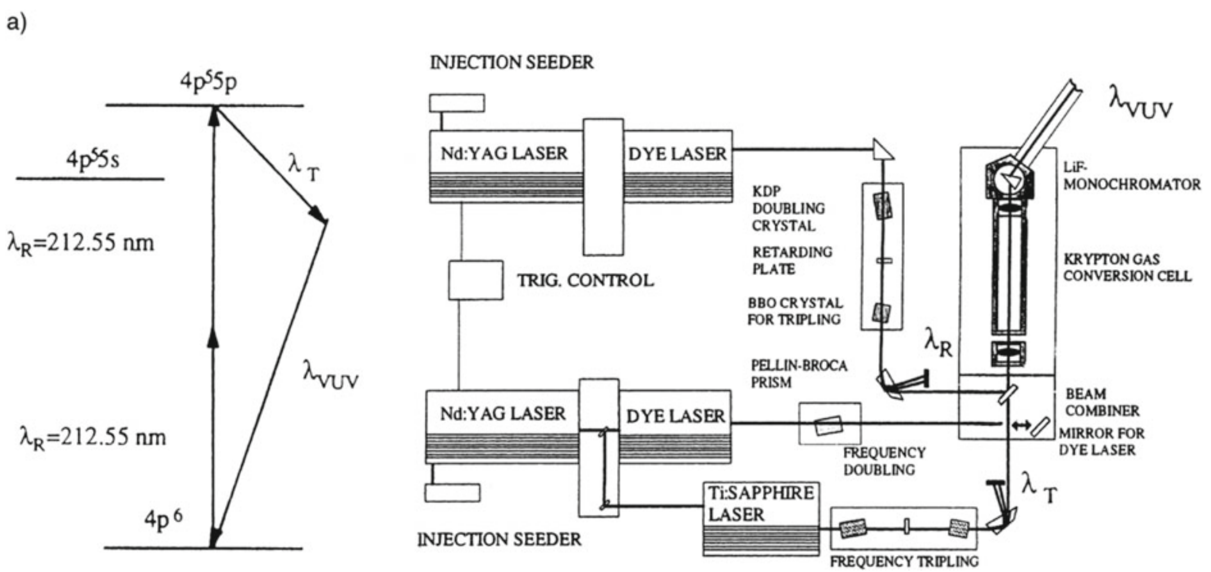
a)
4p^{5}5p
4p^{5}5s
λ_T
λ_R=212.55 nm
λ_{VUV}
λ_R=212.55 nm
4p^6
INJECTION SEEDER
Nd:YAG LASER
DYE LASER
TRIG. CONTROL
Nd:YAG LASER
DYE LASER
INJECTION SEEDER
KDP DOUBLING CRYSTAL
RETARDING PLATE
BBO CRYSTAL FOR TRIPLING
PELLIN-BROCA PRISM
FREQUENCY DOUBLING
Ti:SAPPHIRE LASER
FREQUENCY TRIPLING
λ_R
λ_{VUV}
LiF-MONOCHROMATOR
KRYPTON GAS CONVERSION CELL
BEAM COMBINER
MIRROR FOR DYE LASER
λ_T

Fig. 8.43 Illustration of VUV radiation generation using two laser beams interacting in Kr gas [1151]

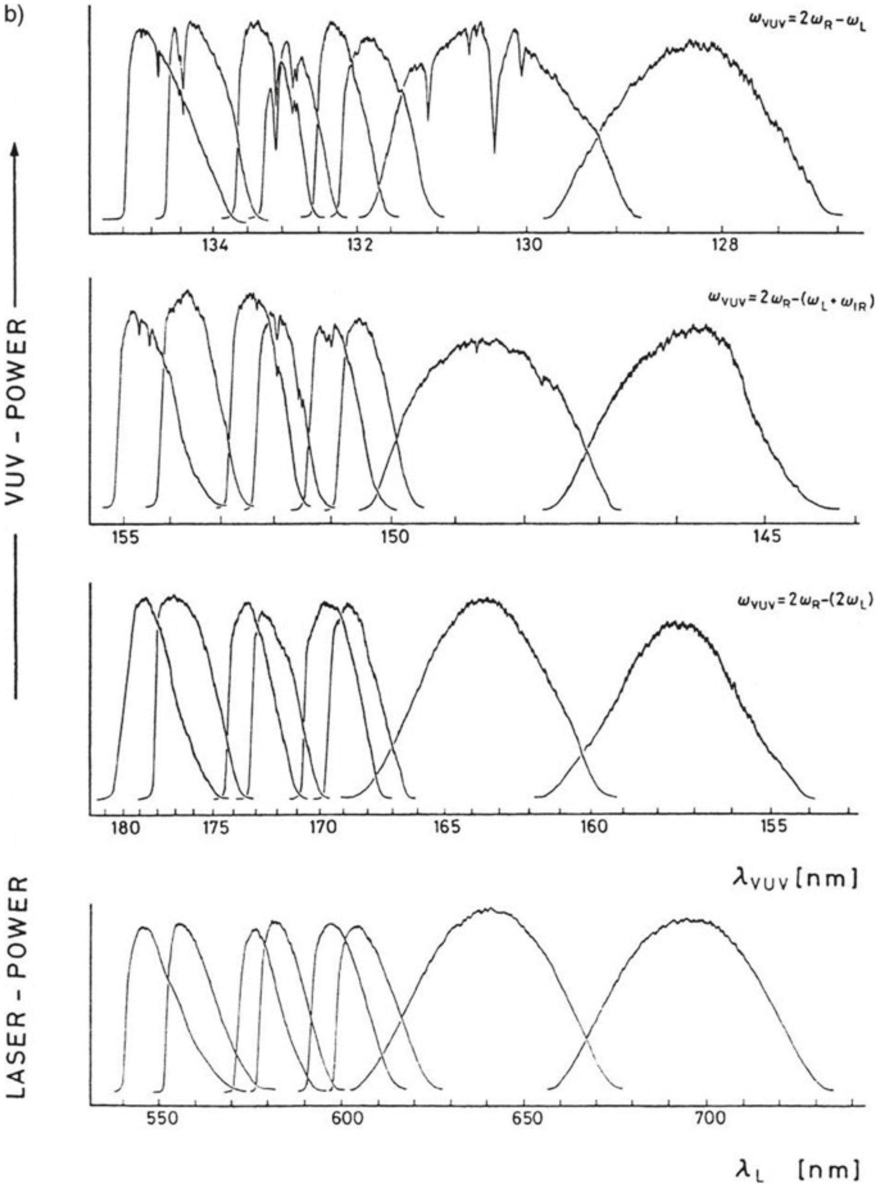

Fig. 8.44 Tuning curves in the vacuum-ultraviolet spectral region obtained using different mixing processes in Kr [1152]

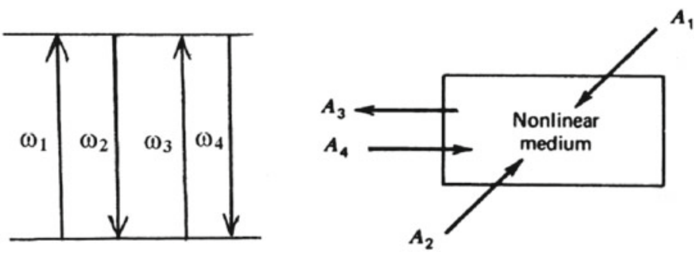
ω_1
ω_2
ω_3
ω_4
A_1
A_2
A_3
A_4
Nonlinear medium

Fig. 8.45 Principle of degenerate four-wave mixing

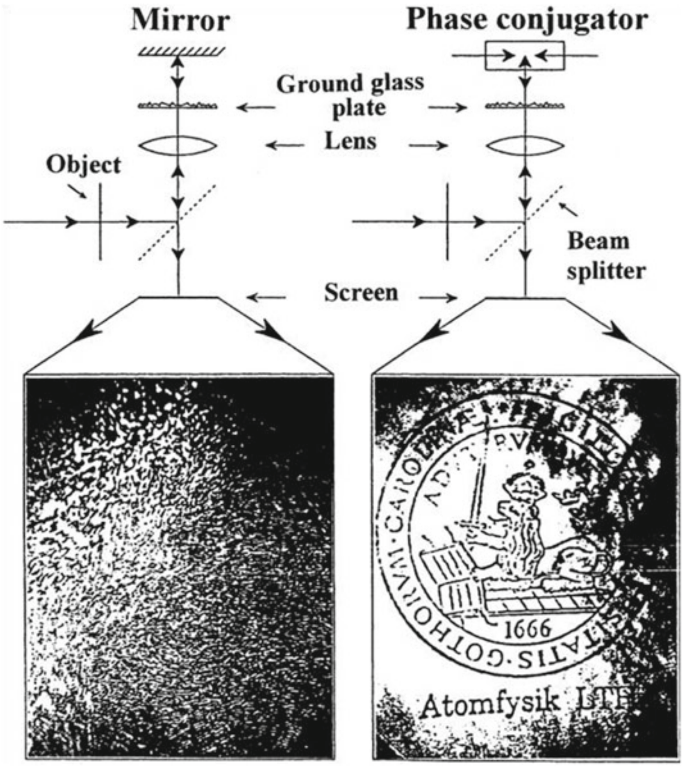
Mirror
Phase conjugator
Ground glass plate
Lens
Object
Beam splitter
Screen
1666
Atomfysik LTH

Fig. 8.46 Demonstration of optical phase conjugation. The experimental arrangement and images with and without a phase conjugator are shown (Courtesy: Sven-Göran Pettersson, LTH)

conjugating, the cavity becomes immune to lensing in the laser medium caused by thermal loads. The technique has been incorporated into commercial lasers.

Optical phase conjugation was first observed in connection with *stimulated Brillouin scattering* (SBS) [1158, 1159] and then in four-wave mixing processes [1160, 1161]. It is further discussed in [1162–1166].

The SBS process has a further interesting property, namely to provide temporal compression of laser pulses [1167, 1168], which can be very useful in time-resolved spectroscopy of short-lived excited states [1151, 1169].

Stimulated Raman scattering processes are particularly convenient for the generation of new tunable wavelengths. If a gas is irradiated with laser light of sufficiently high power, stimulated Raman scattering occurs, which is a third-order nonlinear process. The Stokes-shifted light propagates in the same direction as the pump radiation. In hydrogen gas, a vibrational shift of 4155 cm^{-1} (~0.5 eV) is obtained. The process is illustrated in Fig. 8.47 together with an illustration of how higher Stokes components are obtained by further Stokes shifts. Radiation of shorter wavelength can also be obtained (anti-Stokes components) by four-wave mixing between the pump radiation and Stokes-shifted components. A gas pressure of 10 atmospheres is common. There is no phase-matching condition. By using a small number of very efficient dyes in a pulsed dye laser, wavelengths from the vacuum-ultraviolet to 10 μm can be achieved by the Raman shifting. The efficiency in the conversion to the first Stokes component can exceed 10%, whereas higher order components are much weaker. The relation between the primary radiation and the generated wavelengths is illustrated in Fig. 8.48. Besides H_2, other gases, in particular D_2 (2987 cm^{-1}) and CH_4 (2917 cm^{-1}), can be used in the Raman shifters. The Raman shifting is discussed in [1170–1172].

High harmonics generation in gases as a means to achieve short-wavelength tunable radiation requires very high peak intensities and will be considered in Sect. 9.6.2.

Fig. 8.47 Generation of stimulated Raman scattering

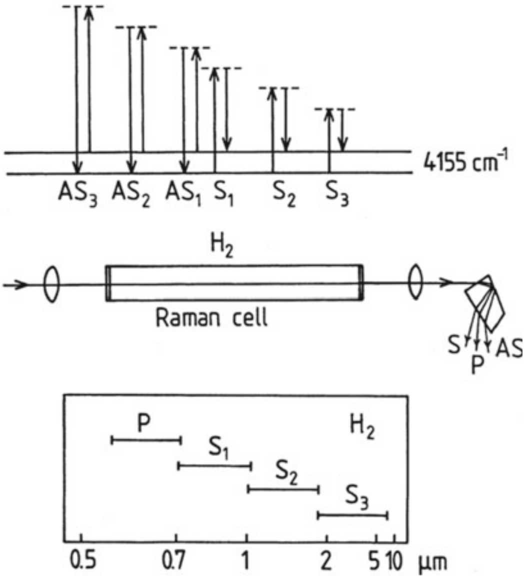

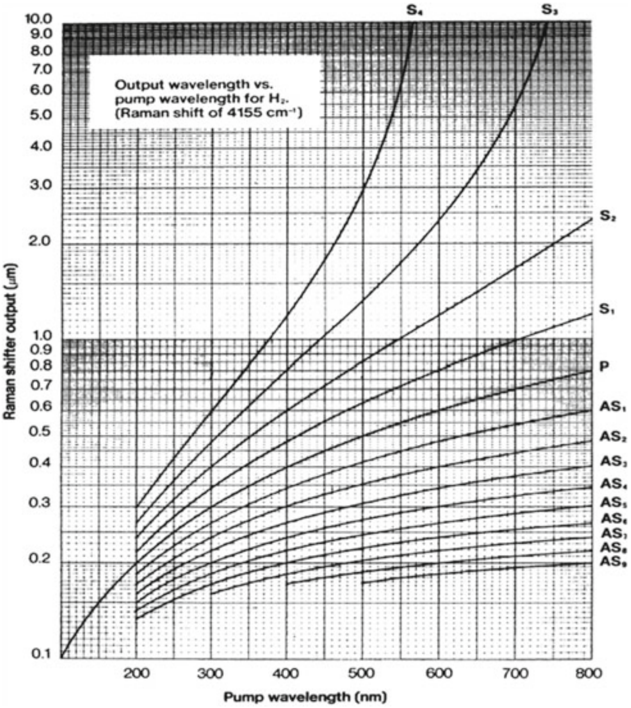

Fig. 8.48 The relation between applied wavelength and generated coherent Raman components using H_2 gas (G. Bjorklund, private communication)

We end this section on frequency extension techniques by discussing the *CARS* (Coherent Anti-Stokes Raman Scattering) process, which is a special case of four-wave mixing [1173]. The process is useful for the generation of new frequencies (c.f., first anti-Stokes component in the stimulated Raman scattering discussed above) and also for powerful spectroscopic applications (Sect. 10.1.4). Basic diagrams for the process are given illustrating energy and linear momentum conservation in Fig. 8.49.

In the CARS process, the sample is irradiated by two laser beams and the frequency difference between the beams is chosen to correspond to the vibrational (rotational) splitting of the irradiated molecules. The beams are denoted by the *pump beam* (at frequency ω_P) and the *Stokes beam* (at frequency ω_S). Two photons of frequency ω_P are mixed with a photon of frequency ω_S, through the third-order susceptibility $\chi^{(3)}$, to generate a stimulated anti-Stokes photon of frequency ω_{AS} (in the anti-Stokes position with regard to the pump beam):

$$\omega_{AS} = 2\omega_P - \omega_S. \tag{8.11}$$

The phase-matching condition can be written as

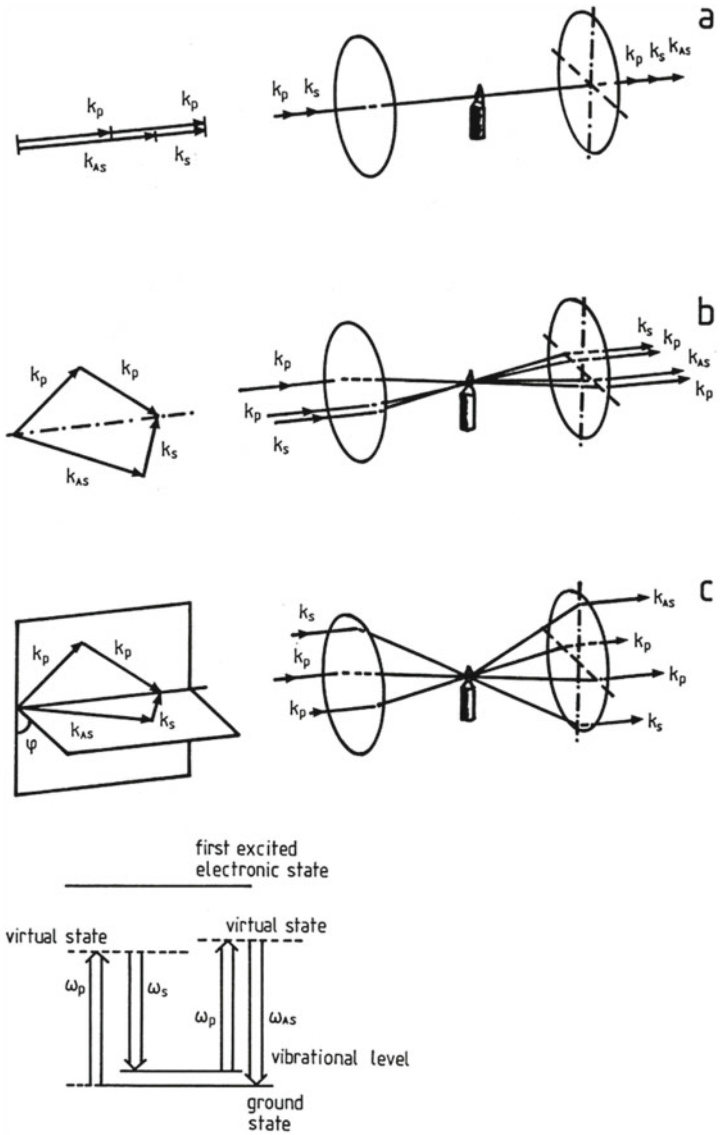
a
k_p
k_p
k_{AS}
k_s
k_p k_s
k_p k_s k_{AS}
b
k_p
k_p
k_s
k_{AS}
k_p
k_p
k_s
k_s k_p
k_{AS}
k_p
c
k_p
k_p
k_{AS}
k_s
φ
k_s
k_p
k_p
k_{AS}
k_p
k_p
k_s
first excited
electronic state
virtual state
virtual state
ω_p
ω_s
ω_p
ω_{AS}
vibrational level
ground
state

Fig. 8.49 Basic diagram and phase-matching schemes for Coherent anti-Stokes Raman Scattering (CARS). **a** Collinear, **b** BOXCARS, and **c** folded BOXCARS phase-matching [1174]

$$\boldsymbol{k}_{\mathrm{AS}} = 2\boldsymbol{k}_{\mathrm{P}} - \boldsymbol{k}_{\mathrm{S}}, \tag{8.12}$$

where $\boldsymbol{k}$ is the wave vector with $|\boldsymbol{k}| = \omega n/c$.

In liquids and solids with a strong wavelength dispersion, the two primary laser beams must be crossed at a small angle and the generated CARS beam will emerge at still another angle to fulfil the phase-matching condition (8.12). In a gas with negligible dispersion (n $\cong$ 1), collinear phase-matching is possible. In diagnostic applications, the so-called BOXCARS geometry is frequently used to achieve improved spatial resolution [1175]. The CARS beam is generated only from the region in which the incoming laser beams cross. In this case, two pump beams and one Stokes beam are used. With the folded BOXCARS variety, the generated CARS is better spatially separated from the other participating beams.

CARS and stimulated Raman scattering are all processes that have been used extensively in not only combustion research (Sect. 10.1) and microscopy, especially of biomedical samples, but also for real-time tissue diagnostics using endoscopically adapted probes (Sect. 10.5).

When the phase-matching condition is fulfilled, the power P_{AS} of the generated beam is related to the powers P_{P} and P_{S} of the pump and Stokes beams, respectively, through the expression

$$P_{\mathrm{AS}} \simeq \left|\chi^{(3)}\right|^2 \cdot P_{\mathrm{P}}^2 P_{\mathrm{S}}. \tag{8.13}$$

Since $\chi^{(3)}$ is proportional to the molecular number density, N, we make the interesting (and unusual) observation that the generated beam strength is proportional to N^2 rather than to N.

The basis for most nonlinear optical processes has been discussed in [1176]. Several monographs cover the field extensively [1177–1182].

8.7 Ultrashort and Ultra-High Power Laser Pulse Generation

During recent years, a particularly fast-developing field has been the generation and application of extremely short laser pulses covering the picosecond (1 ps = 10^{-12} s) range down to a duration of a few femtoseconds (1 fs = 10^{-15} s). Such short pulses can also be amplified to extremely high powers in the terawatt (1 TW = 10^{12} W) range, even entering the petawatt (1 PW = 10^{15} W) regime. We will here describe the laser technology for achieving these extreme levels of performance and will refer a discussion of applications to Sects. 9.5 and 9.6.

8.7.1 Short-Pulse Generation by Mode-Locking

We will here describe the use of *mode-locking* [1183, 1184], where we find, perhaps somewhat surprisingly, that the shortest optical pulses are generated by using continuous laser beams! Interference effects are employed and a particularly clear and beautiful illustration of the action of the Fourier transform from the frequency to the time domain is obtained.

For a short description of the mode-locking phenomenon, we consider a CW laser system with a cavity length of ℓ. If no frequency discriminating element is present in the cavity, laser operation on an atomic or ionic line will yield only a few cavity modes, whereas a corresponding dye laser with a very broad gain medium will feature a large number of modes. The modes are separated by $\Delta\nu = c/2\ell$, or, in angular frequency, $\Delta\omega = 2\pi(c/2\ell) = \pi c/\ell$, where ℓ is the cavity length. The phases of these modes are completely unrelated. If we instead consider an idealized situation in which $2\,N + 1$ modes of equal amplitude $\mathcal{E}_0$ oscillate with a constant phase relation

$$\varphi_k - \varphi_{k-1} = \alpha \tag{8.14}$$

between adjacent modes (mode-locking), the resulting light field $\mathcal{E}(\mathrm{t})$ is given by

$$\mathcal{E}(\mathrm{t}) = \sum_{\mathrm{k}=-\mathrm{N}}^{\mathrm{N}} \mathcal{E}_0 \exp\{\mathrm{i}[(\omega_0 + \mathrm{k}\Delta\omega)\mathrm{t} + \mathrm{k}\alpha]\}. \tag{8.15}$$

Here, ω_0 is the centre angular frequency. The evaluation of this expression involves the same type of mathematics as that used for calculating the spectral intensity distribution from a grating, and we have

$$\mathcal{E}(\mathrm{t}) = A(t)\exp(\mathrm{i}\omega_0\mathrm{t}) \tag{8.16}$$

with

$$A(t) = \mathcal{E}_0 \frac{\sin[(2N+1)(\Delta\omega t + \alpha)/2]}{\sin[(\Delta\omega t + \alpha)/2]}. \tag{8.17}$$

Equation (8.16) represents an optical sinusoidal carrier wave of frequency ω_0, which is amplitude-modulated in time according to (8.17). The light intensity is proportional to $A^2(t)$, and the intensity for the case of seven locked modes is given in Fig. 8.50.

The phase relation (8.14) causes the continuous partial waves to interfere constructively to give short pulses separated in time by

$$\Delta t = 2\ell/c. \tag{8.18}$$

Fig. 8.50 Temporal structure of seven locked modes of equal amplitude

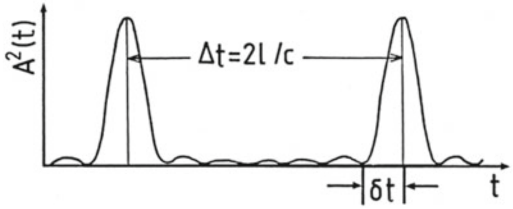

(The maxima occur when the denominator in (8.17) approaches 0.) The pulse separation is the time taken for light to go back and forth in the cavity ("cavity round-trip time") and is typically 5 ns (1 ns ↔ 30 cm). From (8.17), we also obtain the time δt from the pulse maximum to the first zero point

$$\delta t = \frac{2\pi}{(2N+1)\Delta\omega} = \frac{1}{\nu_{\mathrm{osc}}}. \tag{8.19}$$

Thus, δt is the inverse of the oscillation bandwidth ν_{osc} of the laser and we note that a large number of locked modes is needed in order to obtain a short pulse length. Clearly, this is entirely consistent with the uncertainty relation requiring a large frequency uncertainty if the time uncertainty is small. It also reflects the general properties of the Fourier transform between the time and the frequency domains and the need for detailed interference to attain sharp structures, as discussed at the end of Sect. 6.2. In a dye laser with a broad frequency-selective element (e.g. a single-plate Lyot filter), resulting in a bandwidth of $\sim$ 0.5 nm, mode-locking results in pulses of a few picoseconds (1 ps = 10^{-12} s) duration. From (8.17), it follows that the pulse peak intensity $A^2(t)$ is proportional to $(2N+1)^2\mathcal{E}_0^2$, whereas the light intensity for non-locked modes would be proportional to $(2N+l)\mathcal{E}_0^2$. This is consistent with the observation that $\Delta t/\delta t = (2N+1)$. The total time-averaged intensity remains constant but the distribution in time is entirely different. We see the parallel to spatial interference, where the total light intensity also remains the same. We note that very high peak powers can be obtained with a dye laser that has a high N value [1185].

We will now describe how mode-locking according to (8.14) can be accomplished. Several approaches can be used: active or passive mode-locking. *Active* mode-locking is obtained by modulating the gain or loss of the laser at a frequency that matches the mode separation $\Delta\omega$. This can be accomplished using a Bragg cell, as illustrated in Fig. 8.51a. Optical side-bands are then generated for every mode (compare Raman scattering!). These side-bands coalesce with the neighboring mode positions and impose their phase on them. In this way, all modes are successively locked in phase with each other, i.e. mode-locking. In an alternative way of describing the phenomenon, the loss modulation can be seen as a shutter in the cavity. The shutter is only open during certain intervals separated by the cavity round-trip time. Then a multi-mode oscillation with unrelated phases cannot occur since each mode would be strongly attenuated. On the other hand, if the phases are locked as in (8.14), the energy distribution in the resonator is a short pulse that passes the shutter when it is

Fig. 8.51 **a** Active mode-locking by acousto-optic modulation. **b** Synchronous pumping of a dye laser equipped with a cavity dumper. **c** Passive mode-locking using a saturable absorber

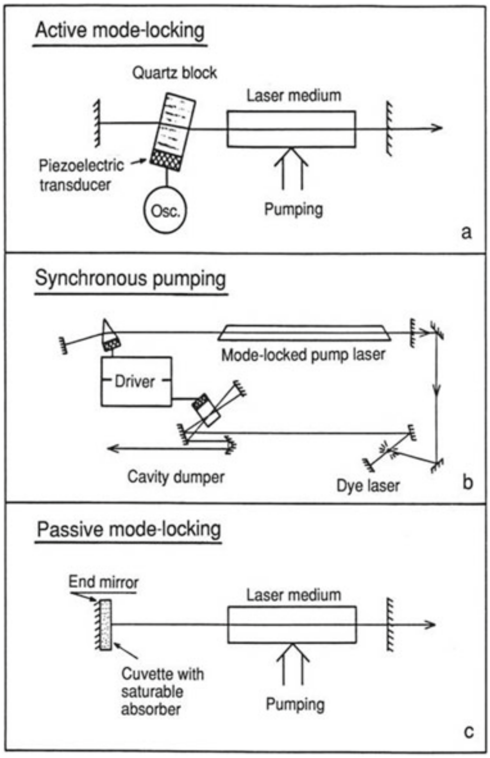
Active mode-locking
Quartz block
Laser medium
Piezoelectric transducer
Osc.
Pumping
a
Synchronous pumping
Mode-locked pump laser
Driver
Cavity dumper
Dye laser
b
Passive mode-locking
End mirror
Laser medium
Cuvette with saturable absorber
Pumping
c

open, which happens at exactly the right times. Because of the “regenerative” nature of the laser action, the phases tend to lock in a way leading to low effective losses (at pulse formation).

One way to mode-lock a dye laser that is pumped by an ion laser is to use *synchronous pumping*. An actively locked ion laser with the same cavity length as the dye laser is then used (the length of the dye-laser cavity is accurately adjusted). Then the laser medium is inverted only during short time intervals, and only a light pulse that bounces back and forth in the cavity passing the gain medium at exactly the right time can be amplified (Fig. 8.51b). By using a second Bragg cell in the dye laser, a bouncing pulse can be deflected out of the resonator when it has gained in intensity in the low-loss cavity. Using this *cavity-dumping* technique, stronger ultrashort pulses at longer time separations than those from normal mode-locking are obtained. Single-picosecond pulses can then be further amplified in successive stages using amplifier cells with a dye that is pumped by a high-power pulsed laser, e.g. a frequency-doubled Nd:YAG laser.

In *passive* mode-locking, a thin (0.1 mm) *saturable absorber* (a special dye, or a semiconductor saturable absorber mirror, SESAM [995, 996]) is used in the cavity. For sufficiently high light intensities, the absorption of the substance is reduced (bleaching). Such intensities are obtained for mode-locking with associated pulse formation, whereas all unrelated cavity modes are strongly absorbed and quenched. The laser modes then tend to arrange themselves so that oscillation and intensity can build up and passive mode-locking is achieved. The best efficiency is obtained if the absorber is placed in direct connection to the high reflector of the cavity (or even integrated in the mirror; SESAM) so that a still higher intensity is obtained in the turning pulse (Fig. 8.51c). In a technique using *"colliding" pulses,* a ring cavity is used with a very thin saturable absorber (e.g. a bleachable dye jet) [1186]. In the ring cavity, light circulates in both directions. Only if extremely short pulses from both directions simultaneously pass the saturation medium, there is sufficient bleaching and thus high transmission is obtained. In this way, pulse lengths of 100 femtoseconds (1 fs $= 10^{-15}$ s), corresponding to a spectral width of about 5 nm, can be achieved. The formal mathematical treatment for active and passive mode-locking is rather complex and we give only the above rather crude phenomenological descriptions.

Further reductions in pulse length can be accomplished by *pulse compression*. A femtosecond pulse is then transmitted through an optical fibre, which has an index of refraction that depends on the intensity (Eq. (8.20)). The spectral distribution of the pulse is then broadened by self-phase modulation and the pulse length is shortened by a subsequent passage of the pulse through a wavelength-dependent optical retarder consisting of two gratings, as illustrated in Fig. 8.52. Pulses of 6 fs duration corresponding to only three optical periods could be obtained in this way [1187], and even better results have been obtained. The initial stretching is also frequently made using a grating pair, with an arrangement opposite to the one used in the compressor. By using a hollow fibre filled with an inert gas, very favourable conditions for pulse compression also for higher pulse energies can be achieved [1188–1190].

Very short laser pulses must, as we have seen, contain a broad frequency (wavelength) distribution. Special attention must then be paid to the pulse propagation, since the index of refraction and thus the speed of light in optical materials depend on the wavelength, resulting in different transit times for different pulse colours through an optical component. The spread would typically be tens of fs for a Fourier-limited 100 fs pulse passing through a 1 mm sample of glass. In order to allow a short pulse to build up, it is necessary to compensate for this *group-velocity dispersion*. It can

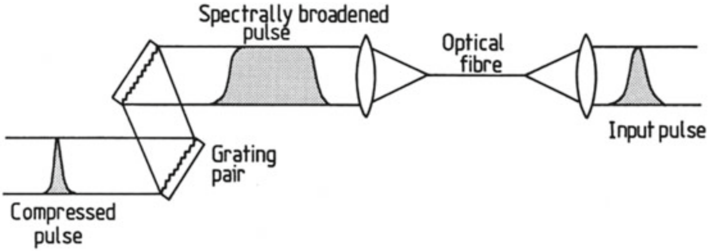

Fig. 8.52 Pulse compression using spectral broadening in an optical fibre and subsequent wavelength-dependent retardation in a grating pair

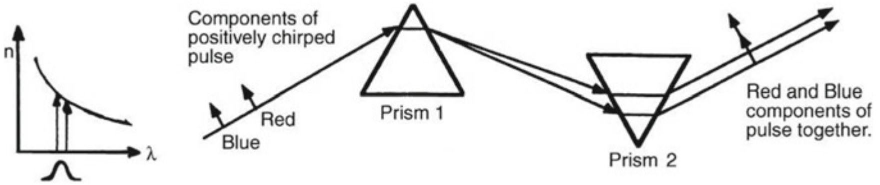
n
λ
Components of
positively chirped
pulse
Red
Blue
Prism 1
Prism 2
Red and Blue
components of
pulse together.

Fig. 8.53 Group-velocity dispersion compensation using a prism pair

conveniently be performed by a pair of prisms, as illustrated in Fig. 8.53. Because of the differential sideways translation of different wavelengths due to the angular dispersion of the prism, the length of the light path in the time-delaying glass is correspondingly different. By proper adjustment of the prisms, it is possible to make light of all wavelengths pass through the intracavity optical components at the same time, resulting in ultrashort pulse generation. (The angular deviation in one prism is compensated for by the other one). As an alternative to the prism pair, it is possible to use chirped mirrors, with multilayer coatings designed to introduce different delays for the different wavelength components building up the pulse [1191]. In this way, group-velocity dispersion compensation can be achieved.

A particularly interesting femtosecond laser in terms of pulse length, output power, and ease of operation is the *self-mode-locked (or Kerr-lens mode-locked) Ti:sapphire laser* [1192]. The mechanism of mode-locking is here different from those discussed above and relies on the nonlinear effects of self-focusing. The layout of such a laser is shown in Fig. 8.54. A key aspect is the presence of an iris aperture which is closed to such a small hole, that laser action is almost quenched by intracavity absorption. However, if because of a statistical fluctuation, the light intensity is high in a temporal spike, there is a slight focusing of the beam, since the index of refraction *n* in a medium

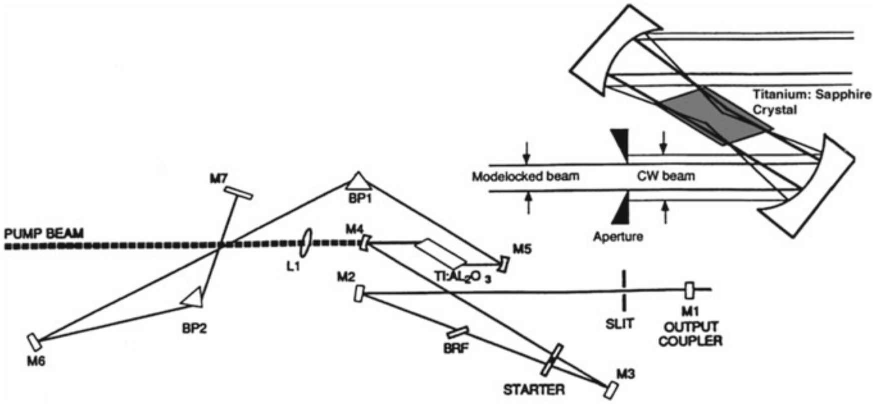
Titanium: Sapphire
Crystal
Modelocked beam
CW beam
Aperture
M7
BP1
PUMP BEAM
M4
L1
M5
Ti:Al$_2$O$_3$
M2
SLIT
M1
OUTPUT
COUPLER
BP2
M6
BRF
STARTER
M3

Fig. 8.54 Schematic layout of a mode-locked titanium-doped sapphire laser. The aperture arrangement critical for the self-(Kerr-lens) mode-locking is illustrated separately. (Courtesy: Coherent, Inc.)

is intensity-dependent and higher for higher intensities I:

$$n = n_0 + n_2 I. \tag{8.20}$$

This is frequently referred to as the optical Kerr effect. Thus, a beam with a Gaussian cross-section will experience the action of a positive lens causing focus on passing through a slab of optical material. The intensity spike will experience less loss and will be further amplified. Since the spike can be seen as formed by interference between phase-related equidistant modes, mode-locking has been achieved spontaneously. The lasing action can only occur when there is mode-locking and intense pulse formation; otherwise, the light is scraped off by the aperture.

The broad gain medium of Ti:S ($\Delta v = 10^{14}$ Hz) allows the build-up of very short pulses with a Fourier limitation of roughly $1/\Delta v = 10\,\mathrm{fs}$. Pulse lengths of about 5.5 fs have been attained directly from a Ti:S laser, corresponding to about two optical cycles [1194, 1195]. Using subsequent compression of pulses, which have first been spectrally broadened by self-phase modulation as already discussed in connection with Fig. 8.52, a pulse length below 5 fs has been attained [1195, 1196]. Techniques for ultrashort laser-pulse generation are discussed in [1197–1200]. We especially note that frequency conversion of ultrashort fixed-frequency pulses to the IR region can conveniently be achieved with the optical parametric oscillator/amplifier (OPO/OPA) approach. Measuring techniques for ultra-fast phenomena will be discussed in Sect. 9.5.

8.7.2 Generation of Ultra-High Power Pulses

Ultrashort pulses can be very useful for attaining very high optical power levels, since the pulse energies can still stay modest. As an example, a mode-locked Ti:S laser of the kind illustrated in Fig. 8.54, running at an average power of 1 W, a pulse repetition rate of 100 MHz, and a pulse length of 100 fs, yields a peak power of about 10^5 W. To reach, e.g. terawatt power levels, very substantial amplification is needed. Using conventional amplifiers would require the diameter of the beam to be increased substantially, since the damage threshold for many optical components is of the order of 100 GW/cm^2. Such systems become very expensive and have a very low repetition rate and availability and found their place mostly in huge inertial confinement fusion installations (NOVA, NIF, etc.) [1005–1008]. However, the technique of *chirped pulse amplification* (CPA) [1201, 1202] offers a very elegant way to circumvent these problems, and its invention resulted in the award of the 2018 Nobel Prize in Physics to *G. Mourou* and *D. Strickland* [1203, 1204]. The basics of the CPA technique can be explained considering Fig. 8.55. An oscillator pulse of typically 100 fs duration and 10 nJ energy derived from a laser of the type shown in Fig. 8.54 is first stretched in time by typically a factor of a few thousand. The pulse is then amplified extensively, while still keeping the peak value reasonably low because of the stretching, so that small-diameter beams (typically 5 mm diameter)

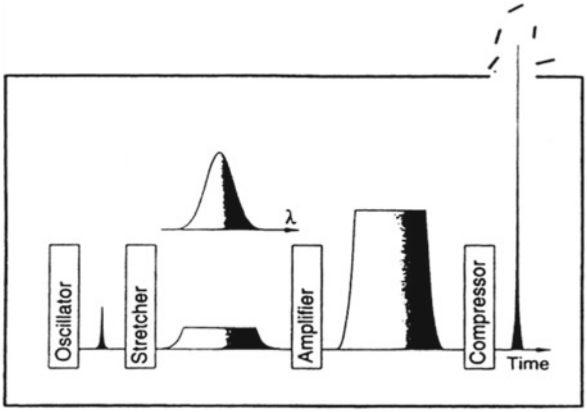

Fig. 8.55 The principle of chirped pulse amplification [1205, 1206]

can be employed without damage to the optical parts. The amplified beam is then expanded to a larger diameter and is temporally compressed back to the original time duration, leading to peak powers in the TW range. The action of the stretcher, which consists of a lens and grating arrangement, is based on different colour components in the Fourier broadened short pulse, as illustrated in Fig. 8.56a. The low-frequency components travel a shorter distance and will come out first after reflection back through the system. The emerging pulse is thus colour-coded in time in a well-defined

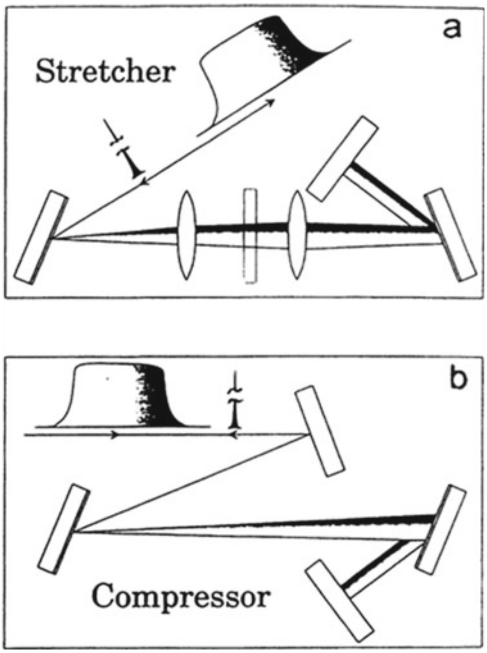

Fig. 8.56 Operational principle of a pulse stretcher (**a**) and a pulse compressor (**b**) [1205, 1206]

way, allowing, in principle, an exact play-back later on. The compressor, handling the strongly amplified pulse, incorporates two gratings (Fig. 8.56b) arranged with tilts in such a way that the high-frequency components are retarded and exit the compressor at the same time as the low-frequency components which entered in the trailing end of the incoming stretched pulse. The situation resembles the conditions in a race between two skaters on a race track, where the “injustice” created in the first lap with one skater taking the inner, shorter course is compensated by interchanging the courses for the second lap, forcing the favoured contestant to now take the longer course. The situation has certain similarities to the case of photon echo formation (Sects. 7.1.6, 9.5.3). At the stage of compression, the diameter of the laser beam has to be expanded to handle the increasing energy impinging on the gratings.

An illustration of the construction of an early terawatt system is given in Fig. 8.57. A 100 fs oscillator pulse, generated in a Ti:S mode-locked laser (Fig. 8.54; Kerr-lens mode-locking), is stretched by a factor of 2500 and is injected into *a regen(erative) amplifier*, where it is trapped bouncing back and forth in a resonator containing a Ti:S amplifier crystal. After 12 passes and an amplification of 10^6, the pulse is ejected from the regen. The switching in and out of the cavity is accomplished by a combination of polarizers and a Pockels cell inside the cavity, which switches the plane of linear polarization of the pulse at the proper times. Further boosting of the energy (now about 10 mJ) is achieved in one or more multi-pass Ti:S amplifiers, which like the regen are pumped by frequency-doubled Nd:YAG radiation (532 nm). After compression, several TW of peak power is available from systems of this kind.

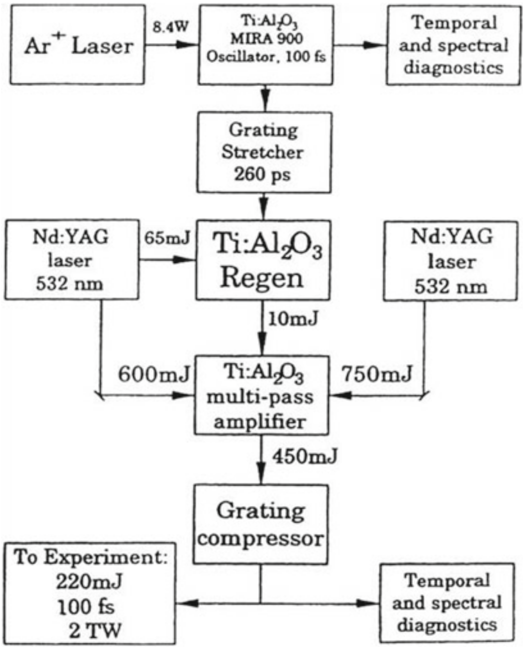
Ar$^+$ Laser
8.4W
Ti:Al$_2$O$_3$ MIRA 900 Oscillator, 100 fs
Temporal and spectral diagnostics
Grating Stretcher 260 ps
Nd:YAG laser 532 nm
65mJ
Ti:Al$_2$O$_3$ Regen
Nd:YAG laser 532 nm
10mJ
600mJ
Ti:Al$_2$O$_3$ multi-pass amplifier
750mJ
450mJ
Grating compressor
To Experiment: 220mJ 100 fs 2 TW
Temporal and spectral diagnostics

Fig. 8.57 Schematics of a high-repetition-rate terawatt laser system based on chirped pulse amplification [1205, 1206]

If a Fourier-limited pulse is amplified, the original pulse length can be obtained after stretching, amplification, and compression, provided that all frequency components of the pulse are handled with the same efficiency in the process. Otherwise, pulse prolongation will occur as well as the formation of a longer-duration pedestal of intensity surrounding the main pulse. Even if the intensity level is 10^6 times lower in the pedestal, the power may still be enough to ionize the target before the arrival of the main pulse, which is supposed to provide an instantaneous ultra-intense interaction with an unperturbed target.

Chirped pulse amplification Ti:S systems with a repetition rate of 10 Hz allow convenient high-power laser/matter interaction experiments on normal laboratory scales. Such experiments are discussed in Sect. 9.6. Systems with 10 Hz repetition rate, 30 fs pulse duration, and tens of TW output powers are commercially available. In CPA systems using large Nd:glass final amplifiers, even PW ($1\ \mathrm{PW} = 10^{15}\ \mathrm{W}$) power levels are available at low repetition rates.

In order to achieve short pulses and high contrasts, the group-velocity dispersion must be compensated to a high precision (to high orders in the mathematical expansion of the dispersion). The build-up of a large accumulated optical phase shift (the so-called “B-integral”)

$$\phi_{\mathrm{nonlinear}} = \int (2\pi/\lambda) n_2 I(l)\,\mathrm{d}l \tag{8.21}$$

in the most intense parts of the beam due to the nonlinear index of refraction n_2 (see (8.20)) in optical components and also in the air must also be avoided. This necessitates air evacuation in the compressor area and in the subsequent beam-transport tubes of high-power systems in order to avoid distortions of the optical pulses. Higher repetition rate CPA lasers operating at 1 kHz or higher and with sub-TW powers can also be constructed. The 1 kHz pump lasers are then normally Nd:YLF units pumped by CW discharge lamps or diode-laser arrays. Lasers based on the CPA technique are discussed in [1207–1215].

A large number of high-power laser facilities are constructed around the world, including the three European Extreme Light Infrastructures (ELI) located in Prague, Szeged, and Bucharest [1216–1218], focusing on versatile spectroscopic applications, attosecond physics (see Sect. 9.6.3), and nuclear physics (Sect. 9.6.7), respectively. Lasers running at 10 Hz at PW powers are even available [1219].

It should be noted that as an alternative to the CPA technique discussed above, the optical parametric chirped pulse amplification (OPCPA) approach, invented by *A. Piskarskas* et al., can be taken [1220–1224] (see also OPO/OPA; Figs. 8.41 and 8.42). Here, nonlinear crystals are used as the gain medium instead of the commonly used Ti:S, avoiding the heat dissipation inherent in the optical absorptive pumping process. This approach is increasingly taken in high-power applications.

Mode-locking of CW lasers and subsequent CPA or OPCPA have been shown to be capable to generate pulses of few optical cycle duration (a single cycle at 800 nm corresponds to 2.7 fs) with extreme powers. However, the position of the optical oscillation with regard to the peak of the pulse envelope, i.e. the phase $\Delta\varphi$ of the oscillation, is unknown and can vary between laser pulses, which has detrimental effects in several contexts. However, the value of $\Delta\varphi$ can be related to the frequency off-set ν_{offset}—the position of the first equidistant modes (see also Fig. 9.70). The mode spacing is ν_{fsr}, which equals the pulse repetition rate. ν_{offset} can be determined by observing, by heterodyne techniques, the beat frequency between a particular laser mode with a frequency-doubled replica of it:

$$2\nu(m) - \nu(2m) = 2\big(m\nu_{fsr} + \nu_{offset}\big) - (2m\nu_{fsr} + \nu_{offset}) = \nu_{offset}. \tag{8.22}$$

By measuring ν_{offset}, it is also possible to determine $\Delta\varphi$:

$$2\pi\nu_{offset} = \Delta\varphi\nu_{fsr}. \tag{8.23}$$

Since the relevant parameters can be measured, it then also becomes possible to opto-electronically stabilize the values. As will be further discussed later (Sect. 9.6.3 and Figs. 9.70, 9.71), this allows optical frequencies to be determined with unprecedented precision and is very important in the generation of reproducible attosecond pulses. Carrier envelope phase stabilization and precision optical frequency measurements are discussed in [1225–1231].

Chapter 9
Laser Spectroscopy

The wide applicability of lasers in spectroscopy is due to several factors. As we have seen, very high intensities can be obtained in a small frequency interval. The favourable spatial properties of laser beams with the possibility of very good focusing are also of great importance. With the advent of tunable lasers, completely new types of experiments have become possible and investigations that were only barely possible with conventional light sources can now be readily performed. It is fair to state that tunable lasers have revolutionized optical spectroscopy. The availability of laser pulses of ultrashort duration has also enabled studies of laser spectroscopy in the femto- and attosecond time domains, and sometimes combined with extreme peak powers. Several monographs and review articles on laser spectroscopy have been published [1232–1251]. A wealth of material is presented in the Proceedings of International Laser Spectroscopy Conferences [1252–1269]. The 1981 Nobel Prize in Physics was awarded to *A.L. Schawlow* and *N. Bloembergen* for laser spectroscopy [1270, 1271], and the prize of 2005 to *J.L. Hall* and *T.W. Hänsch* for high-resolution laser spectroscopy, including the frequency comb technique [1272, 1273]. High power laser-matter interactions are covered in the European Conference on Laser Interaction with Matter (ECLIM) series [1274].

9.1 Basic Principles

9.1.1 Comparison Between Conventional Light Sources and Lasers

A comparison is made in Table 9.1 between a conventional line light source and a continuous single-mode dye laser, with representative data for both sources. A decisive factor in many spectroscopic experiments is by what power per unit area and spectral interval a sample can be irradiated. The designation $I(\nu)$ is used for this

© The Author(s), under exclusive license to Springer Nature Switzerland AG 2022

S. Svanberg, *Atomic and Molecular Spectroscopy*, Graduate Texts in Physics,
https://doi.org/10.1007/978-3-031-04776-3_9

Table 9.1 Comparison between a conventional light source (RF discharge lamp) and a single-mode dye laser

	Conventional Line source (RF discharge lamp)	Dye laser Single-mode Continuous
Linewidth	1000 MHz	1 MHz
Total output of line	10^{-1} W	10^{-1} W
Power within a useful solid angle	10^{-2} W	10^{-1} W
Irradiated area (depends on focusing)	10 cm^2	10^{-4} cm^2
$I(\nu)$ power density per unit frequency	10^{-6} W/($\text{cm}^2 \cdot$ MHz)	10^{3} W/($\text{cm}^2 \cdot$ MHz)

power density/frequency unit. The value of $I(\nu)$ is 10^9 times higher for the laser in the comparison in Table 9.1. $I(\nu)$ may be increased by many more orders of magnitude with a pulsed laser.

9.1.2 Saturation

A very high population in short-lived excited states can be obtained using the high values of $I(\nu)$ that are available with lasers. For a two-level system (Sect. 4.1) with populations N_1 and N_2 in the lower and upper states, respectively, we obtain using (4.21), (4.22), and (4.26) (Hint: Calculate first $(N_1 + N_2)/N_2 = N_1/N_2 + 1 = ...$)

$$\frac{N_2}{N_1 + N_2} = \frac{1/2}{1 + A/2B\rho(\nu)}. \tag{9.1}$$

For $B\rho(\nu) \gg A$ we have

$$\frac{N_2}{N_1 + N_2} \approx \frac{1}{2}, \tag{9.2}$$

i.e., half the number of atoms are found in the excited state and half in the lower state. This situation is called *saturation*. (If statistical weights ($g = 2J + 1$) are taken into account, the expression $g_2/(g_1 + g_2)$ is obtained instead of 1/2.) We will now calculate which values of $I(\nu)$ are required to achieve this situation. $I(\nu)$ is related to the energy density $\rho(\nu)$ through

$$I(\nu) = c\rho(\nu). \tag{9.3}$$

Using this equation and (4.27), we find the following condition for saturation at a chosen wavelength of 600 nm:

$$I(\nu) \gg c\frac{A}{B} = 16\pi^2\frac{\hbar c}{\lambda^3} = \frac{16 \cdot 3.14^2 \cdot 1.05 \times 10^{-34} \cdot 3 \times 10^8}{6^3 \times 10^{-21}}$$
$$= 2 \times 10^{-5}\frac{W}{m^2 \cdot Hz} = 2 \times 10^{-3}\frac{W}{cm^2 \cdot \text{MHz}}. \tag{9.4}$$

Thus, a laser power of the order of $\text{mW}/(\text{cm}^2 \cdot \text{MHz})$ is needed to achieve saturation. As we see from Table 9.1, this condition is easily met, even with a continuous laser.

The first excited $^2P_{1/2}$ state of the sodium atom ($3p$) can only decay back to the $3\,s\,^2S_{1/2}$ ground state (the D_1 line). The natural radiative lifetime of the $3p\,^2P_{1/2}$ state is 16 ns. At saturation $(1/2)\left(1/16 \times 10^{-9}\right) \simeq 3 \times 10^7$ scattered fluorescence photons per second are obtained. This means that it is in principle possible to “see” individual atoms with the naked eye (Sect. 9.8.3, Fig. 9.77a).

Two types of laser spectroscopy can be distinguished. In the first kind, the laser is adjusted to the desired wavelength. The experiment is then performed at this fixed wavelength, either by pulsing the light or influencing the atoms or molecules in other ways. In this kind of measurement, good frequency stability of the laser is desirable. In the second type of spectroscopic experiment, the laser wavelength is varied continuously through the structure to be studied. Most frequently, single-mode operation is required. A continuous sweep without mode hopping must then be achieved.

9.1.3 Excitation Methods

Several different excitation schemes can be used in laser spectroscopy. This is illustrated in Fig. 9.1 for the case of alkali atoms.

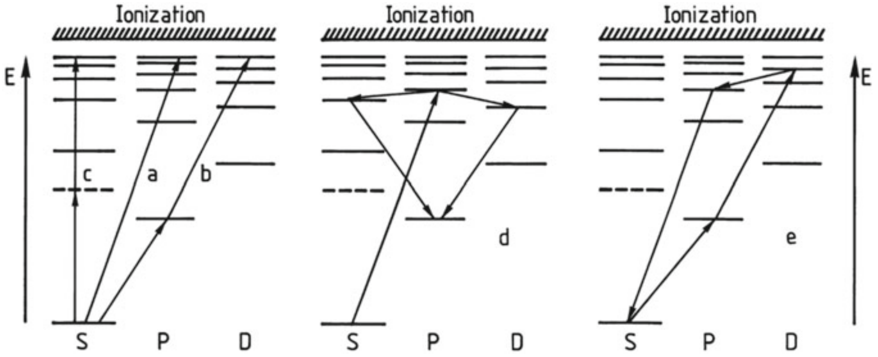

Fig. 9.1 Different schemes for excitation of an alkali atom including **a** single-step, **b** two-step, **c** two-photon, and **d**, **e** cascade excitation

Single-Step Excitation. Atoms are transferred directly from the ground state to the excited state using an allowed electric dipole transition. This means an S-P transition for an alkali atom.

Multi-step Excitation. Since tunable lasers have high output powers enabling the saturation of optical transitions, stepwise excitation via short-lived intermediate states is possible. A two-step process has been indicated in the figure. For an alkali atom this may mean *S-P-D* transitions. Stepwise excitations give access to states that cannot normally be reached.

Multi-photon Absorption. Higher-order optical absorption processes become non-negligible at high laser powers. Thus, it becomes possible for an atom to simultaneously absorb two photons, thus bridging energy differences between two states without utilizing real intermediate states. The theory of two-photon absorption processes was presented by M. Goeppert-Mayer as early as 1931, but only in 1961 such transitions could be observed with lasers. The transition probability R_{gf} from the ground state g to the final state f can be expressed in matrix elements of the electric dipole operator ***er*** involving non-resonant intermediate states i:

$$R_{gf} \propto \sum_i \left| \frac{\langle g|e\mathbf{r}|i\rangle\langle i|e\mathbf{r}|f\rangle}{\delta E_i} \right|^2 P^2, \tag{9.5}$$

where the summation is performed over all allowed intermediate states i. δE_i is the energy difference between the virtual and the real intermediate states i, and P is the laser power. Frequently, a single real state close to the virtual state dominates the expression. A quadratic laser power dependence is obtained. The two-photon absorption method connects states of the same parity. An *S–S* transition is indicated in the figure. Similarly, more than two photons can be absorbed simultaneously. For example, molecules can be made to absorb tens of IR photons in this way. Experiments of this kind will be further discussed in Sects. 9.7.4 and 10.4.2.

In the cascade decay of a laser-excited state, lower-lying states are populated as illustrated in the figure for the case of alkali atoms. This provides further possibilities for laser spectroscopy investigations.

9.1.4 Detection Methods

There are several methods of detecting whether an excited state has been populated. This is particularly true for highly excited states, i.e., *Rydberg states*, that have been the object of many laser spectroscopy investigations. Rydberg atoms are essentially hydrogen-like and some of their properties are given in Table 9.2. The spectroscopy of Rydberg states has been discussed in [1275–1283].

Considering these properties, we will now discuss a number of detection methods.

Table 9.2 Properties of Rydberg atoms [1232] (R: Rydberg constant, a_0: Bohr radius, n: principal quantum number)

Quantity	n dependence	Numerical examples for	
		Na(10d)	H($n = 50$)
Binding energy	$-Rn^{-2}$	0.14 eV	0.0054 eV
Orbital radius	$a_0 n^2$	$147 a_0$	$2500 a_0$
Geometrical cross-section	$\pi {a_0}^2 n^4$	$7 \times 10^4\ {a_0}^2$	$6 \times 10^6\ {a_0}^2$
Polarizability	$\propto n^7$	210 kHzV^{-2}cm^2	
Radiative lifetime	$\propto n^3$	10^{-6} s	10^{-4} s
Stark splitting in electric field $E =$ 1 kV/cm	$\Delta w \propto n(n-1)E$	~15 cm^{-1}	~10^2 cm^{-1}
Critical field strength E_c for field ionization	$E_c = \pi \epsilon_0 R^2 e^{-3} n^{-4}$	3×10^6 V/m	5×10^3 V/m

Fluorescence. The most direct way of detecting whether an atom has been excited to an upper state is to detect that light has been absorbed and that fluorescence light is released when the atom decays. The atom can return to the state from which it was excited via an allowed electric dipole transition. With increasing excitation energy the number of possible decay paths increases corresponding to many spectral lines. Since the detection must frequently be limited to a narrow wavelength band, only a small fraction of the decays will be observed. Further, the lifetime increases as n^3. If pulsed excitation is used, the detection temporal interval must be successively increased in order to be able to detect a reasonable fraction of the photons. This leads to an increase in the background signal. These factors make fluorescence detection of highly excited states less and less attractive as n increases.

Photoionization. An excited atom can be photoionized by absorbing a further photon of sufficient energy to bring the atom above the ionization limit. One way of detecting the excited atom is to detect the released electron with an electron multiplier, which is essentially a photomultiplier tube without a photocathode. For highly excited states, an IR photon, e.g., from a CO_2 laser, can be used (–0.1 eV). If a laser of sufficiently high power is used for the excitation process, ionization can occur using another photon from the laser beam. The cross-section for photoionization is low but is strongly enhanced in the presence of resonant autoionizing states above the ionization limit.

It is also possible to perform mass or energy analysis of the ions generated. This can be accomplished using a *time-of-flight* (TOF) spectrometer, where the ions generated are sent through an evacuated drift tube equipped with ion optics, and the arrival time at an ion detector (electron multiplier tube or a channeltron) is recorded. It is also possible to accelerate low-velocity ions in a well-defined electric field before the passage of the drift tube. Since the velocity attained depends on the mass, species identification can be performed. TOF spectrometers are discussed in [1284–1286].

Collisional Ionization. Highly excited atoms have a high probability of colliding because of their considerable size. Since the thermal energy of the atom (∼kT) may be larger than the energy required to reach the ionization limit, there is a significant probability that a collision results in the formation of an ion. A *thermo-ionic detector* can be used to detect the presence of the ions. This technique is extremely sensitive [1287].

Field Ionization. Highly excited atoms are very sensitive to electrical fields. Field ionization (Sect. 2.5.2) can be brought about by populating a well-defined highly excited state using stepwise, pulsed excitation in the absence of an electric field and then applying an electric field pulse [1288, 1289]. The electrons can be detected with a suitably located electron multiplier. Ionization detection is further illustrated in Sect. 9.2.6.

9.1.5 Laser Wavelength Setting

Before discussing different types of laser spectroscopy experiments, we will consider the question of how the frequency of the laser is made to coincide with the absorption frequency of the atoms or molecules of interest. The problem is not at all trivial considering the sharpness of both the laser and the absorption lines, and the mode structure of both laser resonators and intracavity etalons. A high-resolution grating monochromator can be used for rough wavelength determination, but the use of digital laser wavelength meters is much more powerful and convenient. Two systems are shown in Fig. 9.2. Figure 9.2a shows a wavelength meter for continuous single-mode lasers, and Fig. 9.2b shows a system that can also operate with a pulsed laser beam.

The wavelength meter for continuous light is essentially a double Michelson interferometer (Sect. 6.2.4) in which the light from the "unknown" laser and the light from a reference laser are directed in counter-propagating paths [1290, 1291]. The movable mirror is a retroreflector ("corner cube"; Sect. 6.2.1), which is self-adjusting with regard to the beam direction. It can be mounted on a carriage, which moves on a frictionless air track. Interference fringes from each laser are recorded at different detectors during a certain time. The optical path difference Δ can be expressed in two ways:

$$\Delta = N_\ell \lambda_\ell = N_{ref} \lambda_{ref}, \ i.e., \ \lambda_\ell = \frac{N_{ref}}{N_\ell} \lambda_{ref}, \tag{9.6}$$

where N_{ref} and N_ℓ are the numbers of counted interference fringes for the reference laser and the unknown laser, respectively. Since the laser beams overlap in the instrument, the method is quite insensitive to air turbulence, etc. Normally, a single-mode He–Ne laser is used as the reference source. If this laser is stabilized at a saturation dip (Sect. 9.7.2), very high accuracy and stability can be obtained. It is practical

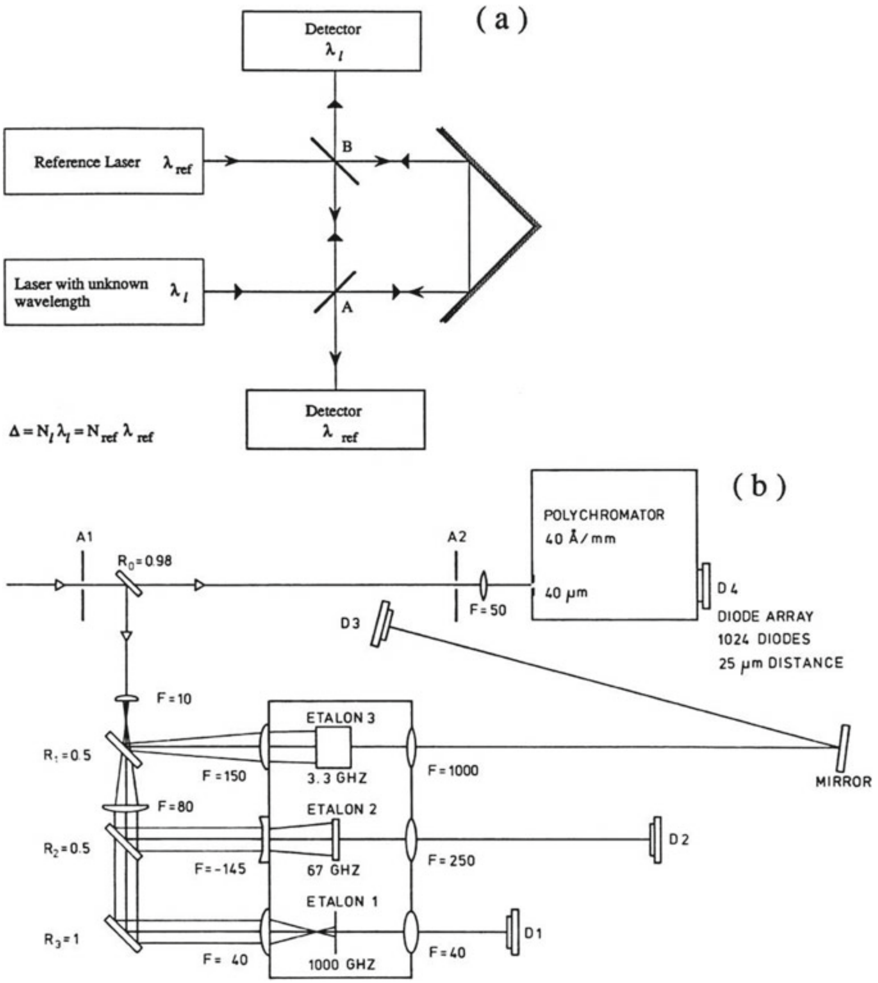
(a)
Detector
λ_l
Reference Laser λ_{ref}
B
Laser with unknown wavelength λ_l
A
Detector
λ_{ref}
$\Delta = N_l \lambda_l = N_{ref} \lambda_{ref}$
(b)
POLYCHROMATOR
40 Å/mm
40 μm
A1
A2
$R_0 = 0.98$
F = 50
D4
DIODE ARRAY
1024 DIODES
25 μm DISTANCE
D3
F = 10
ETALON 3
$R_1 = 0.5$
F = 150
3.3 GHZ
F = 1000
MIRROR
F = 80
ETALON 2
$R_2 = 0.5$
D2
F = -145
67 GHZ
F = 250
ETALON 1
$R_3 = 1$
D1
F = 40
1000 GHZ
F = 40

Fig. 9.2 **a** Wavelength meter for continuous lasers [1290]. **b** Wavelength meter for pulsed or continuous lasers [1292]

to stop the fringe counting in the electronic unit when N equals the stored digital number for the wavelength of the He–Ne laser. Then the corresponding number N_{ref} can be directly displayed as λ; see (9.6). Since only whole fringes can be electronically counted, the accuracy can be considerably increased if the fringe counting frequency is multiplied by a factor (i.e., 10) using a *Phase-Locked Loop* (PLL).

A wavelength meter that also works for pulsed laser light employs a small spectrometer and Fabry–Pérot interferometers with different free spectral ranges [1292]. The image plane of the spectrometer and the ring systems of the interferometers are detected by diode arrays (Sect. 6.3). The information is handled by a microprocessor which calculates the wavelength. A He–Ne laser can be used as a reference. However, if the free spectral ranges of the interferometers are constant and well known, a reference laser is not needed for moderate accuracies. We note that the method just described operates on the principle that based on an earlier crude measurement it is possible to select the correct next digit in the wavelength determination (among a number of "suggestions", since the Fabry-Pérot fringes are repetitive). The process is repeated until a sufficient number of digits have been determined using the successive finer "verniers". The same idea is used in laser CW distance measurement devices employed, e.g., in geological surveys. Rather than using a time-of-flight approach as in pulsed lidar (Sect. 10.2.3.1), a CW laser beam is sinusodially modulated at several frequencies/wavelengths. The phase shift of the longest wavelength, returned from a distant retroreflector, determines the first digit in the distance evaluation, and the phase shifts for the returning waves of shorter wavelengths give the distance with successively increasing precision. Like in CW wavemeters, a Phase-Locked-Loop (PLL) can be used to increase the precision in the phase determination.

Several additional techniques for accurate laser wavelength determination have been developed [1293–1296]. The accuracy of laser wavemeters has been discussed in [1297]. Wavemeters of different constructions are commercially available. Very accurate measurements of CW laser wavelengths can also be done by heterodyne techniques, where the difference frequency ("beat") between two lasers is measured (Sect. 10.2.1), or through using frequency comb techniques (Fig. 9.70).

In spectroscopy using continuous laser tuning it is very important to be able to monitor the change in wavelength. For this purpose, a stable multi-pass interferometer (Sect. 6.2.3) can be used, from which the fringes are recorded together with the spectrum [1298], providing a convenient wavelength "ruler".

We will now consider different laser spectroscopy methods. We will first discuss techniques in which a reasonable resolution is sufficient and where relatively broadband lasers (0.01–0.001 nm) and Doppler-broadened samples are used. We will then describe how resonance techniques (Chap. 7) can be combined with laser excitation. Time-resolved spectroscopy will be considered in the following sections. Lifetime measurements and structure determinations using such techniques will be described. A comprehensive survey of methods for determining the radiative properties of atoms and molecules is made in this context.

Extremely high laser intensities can be achieved with the pulsed systems discussed in Sect. 8.7.2. Experiments using such systems are surveyed in Sect. 9.6. A further aspect of the extreme performance achievable with laser techniques is the ultra-narrow bandwidth achievable in CW single-mode laser systems as discussed in Sect. 8.5.1. In order to benefit from this, the Doppler broadening must be eliminated. The different techniques of Doppler-free laser spectroscopy are discussed in Sect. 9.7. Finally, the extreme resolution achievable by laser cooling and trapping techniques is discussed in Sect. 9.8. The combination with frequency comb techniques enables to achieve the ultimate precisions.

9.2 Doppler-Limited Techniques

We will in this section discuss measurement techniques in which Doppler broadening, caused by the thermal movements of the atoms or molecules, limits the achievable resolution. Lasers with a comparatively large linewidth (0.01–0.001 nm) are therefore normally employed. Experiments within this category are aimed at the determination of primary energy-level structure without regard to finer details, such as hyperfine structure. Several important analytical applications are also discussed.

9.2.1 Absorption Measurements

A tunable laser is very useful for measuring the absorption of a sample as a function of the wavelength as shown in Fig. 9.3a. In this case, the laser replaces the normal light source as well as the monochromator in the set-up (Sect. 6.5.6). Because of the good geometrical properties of the laser beam, it is possible to work with small samples or with long absorption paths and low concentrations. Dual-beam techniques are generally employed. With continuous lasers, lock-in techniques (Fig. 6.68) are used for recording. When pulsed lasers are used, gated integrators (boxcar integrators; see Sect. 9.4.2) are employed. Sample and reference signals are divided for normalizing purposes., A commercial diode spectrometer for the IR region is shown in Fig. 9.3b. A grating monochromator has been included in this particular case to suppress unwanted laser modes.

If gaseous samples of low concentration are to be investigated a *White cell or a Heriott cell* can be used [1299–1301]. These are multi-pass devices, in which a well-defined beam path is obtained by repeated focusing using spherical mirrors of suitable curvature. The number of passes can easily be chosen by adjusting the mirrors: 50–100 double passes can be achieved. The transmitted intensity is largely determined by the mirror reflectivities. By using strongly scattering, nano-porous ceramics, where the gas to be studied can enter the pores, extremely prolonged optical path lengths can be achieved. Thus, it was demonstrated that a physical size of only 7 mm of ceramics can result in a 750 times prolonged path length through the gas [1302]. A prolonged path length can also be obtained by enclosing the gas in an integrating sphere [1303].

For absorption experiments on metal atoms, for which a high temperature is required to obtain a sufficient vapour pressure (Fig. 7.2), a *heat-pipe oven* can be used [1304, 1305]. This consists of an evacuated metal tube, in which the central inner part is covered by a fine metal mesh. The metal is placed in the centre of the tube and a few torrs of inert gas are frequently added. The central part of the tube is resistively heated while the end parts, with optical windows, are water-cooled. A micro-climate develops in the tube and metal atoms evaporate out into the cold zones, where condensation occurs. The liquid metal is then sucked back towards the centre by surface-tension forces between the metal atoms and the mesh. The

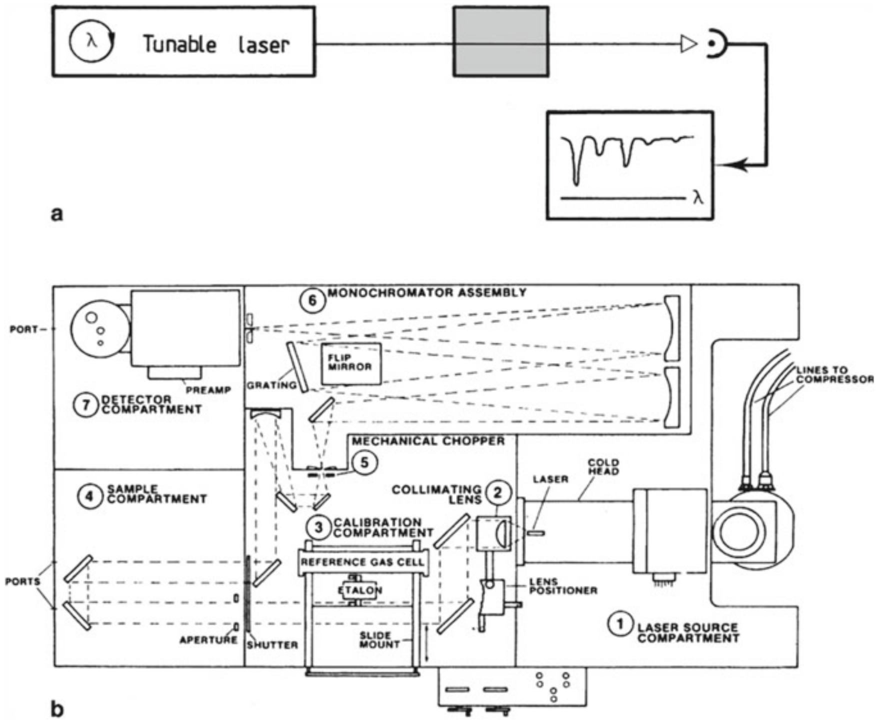
λ
Tunable laser
λ
a
6 MONOCHROMATOR ASSEMBLY
PORT
FLIP MIRROR
LINES TO COMPRESSOR
PREAMP
GRATING
7 DETECTOR COMPARTMENT
MECHANICAL CHOPPER
5
COLD HEAD
LASER
4 SAMPLE COMPARTMENT
COLLIMATING LENS 2
3 CALIBRATION COMPARTMENT
REFERENCE GAS CELL
PORTS
ETALON
LENS POSITIONER
1 LASER SOURCE COMPARTMENT
APERTURE
SHUTTER
SLIDE MOUNT
b

Fig. 9.3 **a** Principle of laser absorption spectroscopy. **b** A diode laser spectrometer (Courtesy: Spectra Physics)

gas is fractioned so that the inner zone contains metal atoms while the windows are protected against deposits, due to metal evaporation, by the inert gas in front of them. Different aspects of laser absorption spectroscopy have been discussed in [1306].

9.2.2 *Intracavity Absorption Measurements*

An external laser beam was used in the absorption measurements described above. A great increase in sensitivity can be achieved if the sample is placed inside the laser cavity [1307–1311]. This is due to the mode competition in a multi-mode laser. The principle of intracavity absorption measurements is given in Fig. 9.4. A multi-mode dye laser is run in the wavelength region where the species under investigation absorbs. As an example, we will consider the case of molecular iodine (I_2). If the intracavity cell is first taken out and the laser is adjusted to the desired wavelength region, laser-induced fluorescence will be observed in an external iodine cell. Normally, several molecular transitions are induced. If the iodine cell is now introduced inside the cavity, the fluorescence light will disappear or be strongly

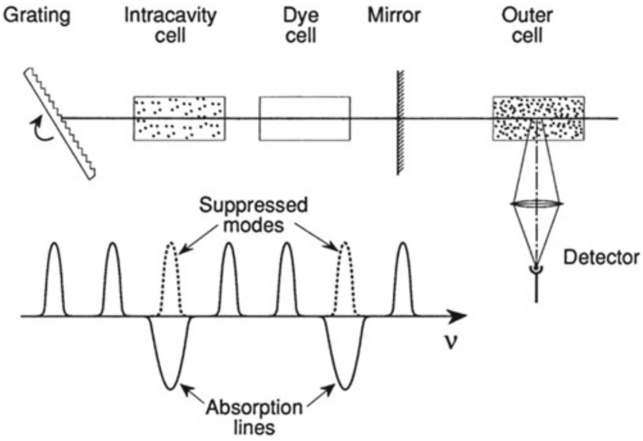

Fig. 9.4 Principle of intracavity absorption measurements [1]

reduced. The reason is that in the cavity the modes that earlier excited the molecules in the external cell will be greatly reduced in intensity compared with other modes due to the intracavity absorption. Since we have multiple passages through the internal sample and the laser is very sensitive to a small imbalance, very few molecules are needed to strongly influence the fluorescence light in the external cell. The sensitivity when using an intracavity sample is about 10^5 times greater than when an external absorption cell is used.

Cavity ring-down spectroscopy is a related technique, where the mode-competition in a multi-mode laser is, however, not utilized [1312–1318]. Here the damping of the laser light inside a cavity (which can also be external to the primary laser), caused by intracavity absorption by the sample, is measured by observing the intensity of a small part of the light leaking through one of the cavity mirrors. If a picosecond pulse is bouncing in the cavity, it is particularly simple to observe the number of passes through the cavity. If losses apart from the sample absorption can be kept low by using highly reflecting cavity mirrors, very long effective absorption lengths can be achieved. By tuning the laser off the absorption, the effects due to the sample can be isolated. If the reflectance of the mirrors in an external multi-pass cavity is known, a CW laser can be used to pump the cavity, and the time constant of the cavity output light decay can be determined following the shut-off of the pumping laser.

9.2.3 Absorption Measurements on Excited States

Classical absorption measurements with a continuum light source and a recording spectrograph with photographic-plate or electronic array detection, only display absorption lines originating in the ground state or in low-lying, thermally well-populated metastable states. Through the possibility of saturating an optical transition with a laser, thus transferring essentially half the number of atoms into a short-lived excited state, it is now possible to extend absorption experiments to spectral series originating in excited states [1319, 1320]. An example for Ba is given in Fig. 9.5. A nitrogen laser is used for synchronous pumping of two dye lasers. One has a narrow bandwidth and is used to saturate the $6s^2\ ^1S_0$–$6s6p\ ^1P_1$ transition at 553.5 nm. The barium vapour is contained in a heat pipe. The second laser has a normal incidence mirror instead of a Littrow-mounted grating, and it yields an intense continuum close to the dye emission peak at the same time as the excited state is populated. As illustrated in the recording, light is absorbed from the continuum at wavelengths corresponding to the $6s6p\ ^1P_1$–$6sns\ ^1S_0$ and $6snd\ ^1D_2$ series. The trace in the figure has been obtained from the photographic plate using a microdensitometer.

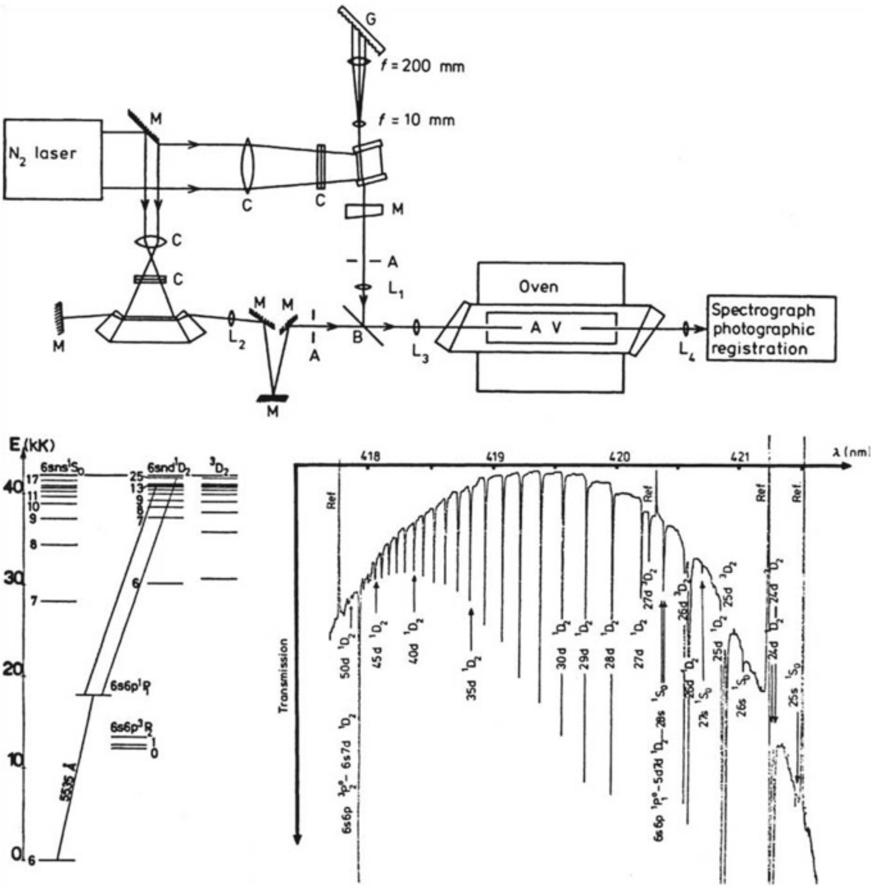
G
f = 200 mm
f = 10 mm
N₂ laser
M
C
C
M
A
L₁
C
C
M
L₂
M M
A
B
L₃
Oven
A V
L₄
Spectrograph photographic registration
M
E (kK)
40
30
20
10
0
6sns ¹S₀
6snd ¹D₂
³D₂
6s6p ¹P₁
6s6p ³P₂ 1 0
5535 Å
418
419
420
421
λ (nm)
Ref
Transmission
50d ¹D₂
45d ¹D₂
40d ¹D₂
35d ¹D₂
30d ¹D₂
29d ¹D₂
28d ¹D₂
27d ¹D₂
26d ¹D₂
25d ¹D₂
24d ¹D₂
28s ¹S₀
27s ¹S₀
26s ¹S₀
25s ¹S₀
6s6p ¹P°₁ – 6s7d ¹D₂
6s6p ¹P°₁ – 5d7d ¹D₂

Fig. 9.5 Illustration of absorption spectroscopy from an excited state. A level scheme for Ba, an experimental set-up, and a resulting absorption spectrum are shown [1320]

9.2.4 Level Labelling

The analysis of molecular spectra is complicated because of the very large number of lines that is obtained simultaneously in normal excitation or absorption experiments. With narrow-band laser excitation, an individual excited rotational-vibrational level can be populated selectively and only the decays originating in the excited state are observed. A similar simplification in absorption measurements is very desirable. Through the possibility of saturating optical transitions, a certain lower level can be "labelled" by depleting the population with a laser (*pump* laser). If this laser is switched on and off repetitively, all absorption lines originating in the labelled level will be modulated when induced with a second (*probe*) laser [1321, 1322]. Lock-in techniques, observing the resulting modulation, are employed (Fig. 6.68). A number of schemes for modulation detection are indicated in Fig. 9.6. Several schemes can be used to ascertain that absorption has occurred, as discussed in Sect. 9.1.4. A still more powerful technique using equipment similar to that described in the preceding section is shown in Fig. 9.7. The probe laser is a broadband laser and normally cannot illuminate the entrance slit of the recording spectrometer since it is blocked by crossed polarizers. The pump laser is circularly polarized and induces an optical anisotropy by molecular orientation of the sample, which is placed between the crossed polarizers [1323]. For lines coupled to the oriented molecules, the plane of polarization is rotated for the probe laser light and the entrance slit is illuminated. On the photographic plate or array detector, all absorption lines originating in the labelled level give rise to bright lines.

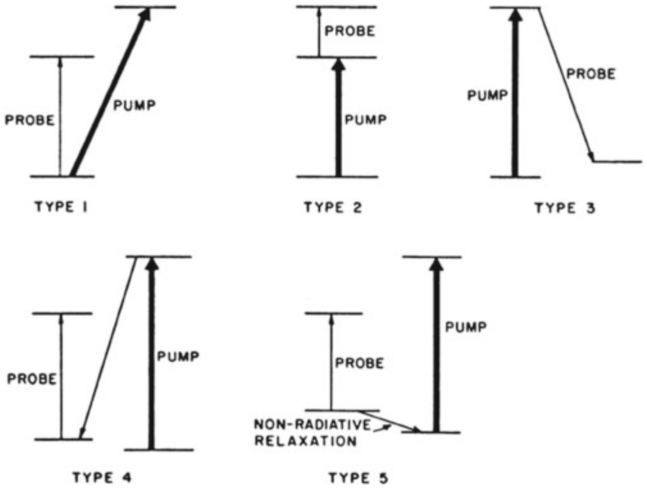

Fig. 9.6 Different schemes for level labelling [1322]

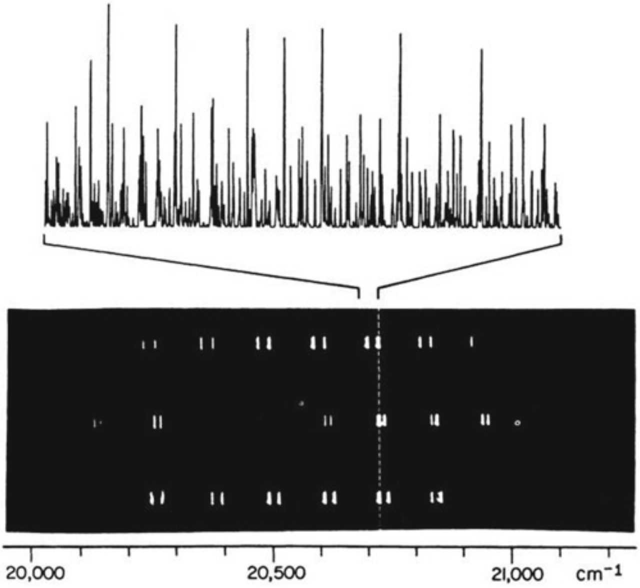

Fig. 9.7 Principles of level polarization labelling. The experimental set-up and a recording for Na_2 molecules displaying $\Delta J = +1$ and $\Delta J = -1$ transitions from the labelled level are shown [1323]

9.2.5 Two-Photon Absorption Measurements

Series of levels of the kind discussed in connection with absorption measurements from excited states (Sect. 9.2.3) can also be investigated in two-photon absorption experiments. Then only a single pulsed dye laser is needed. Amplifier stages may be used to achieve sufficient power (Sect. 8.5.1). When the laser has been tuned to bridge the energy difference between the ground state and an excited state of the same parity by means of two simultaneously absorbed laser photons, this can be detected by using yet another photon to photoionize the excited atoms. The ion current can be detected by electrodes at a low DC voltage inserted into the heat-pipe oven. The ion transients are averaged in a boxcar integrator. Two-photon transitions to $5sns\ {}^1S_0$ and $5snd\ {}^1D_2$ states in Sr are shown in Fig. 9.8. Simultaneous single-photon absorption detection of $5s^2\ {}^1S_0 \rightarrow 5snp\ {}^1P_1$ transitions is illustrated using frequency-doubled laser radiation. The increase in ionization current above the ionization limit of Sr is shown in the figure, as well as a dispersion-shaped broad resonance due to an autoionizing state (*Fano resonance*).

9.2.6 Opto-Galvanic Spectroscopy

In the previous section, we described how *optical* resonance could be detected by direct observation of *electrical* phenomena. From this point of view, we described a special type of *opto-galvanic* spectroscopy. When electrical detection of optical

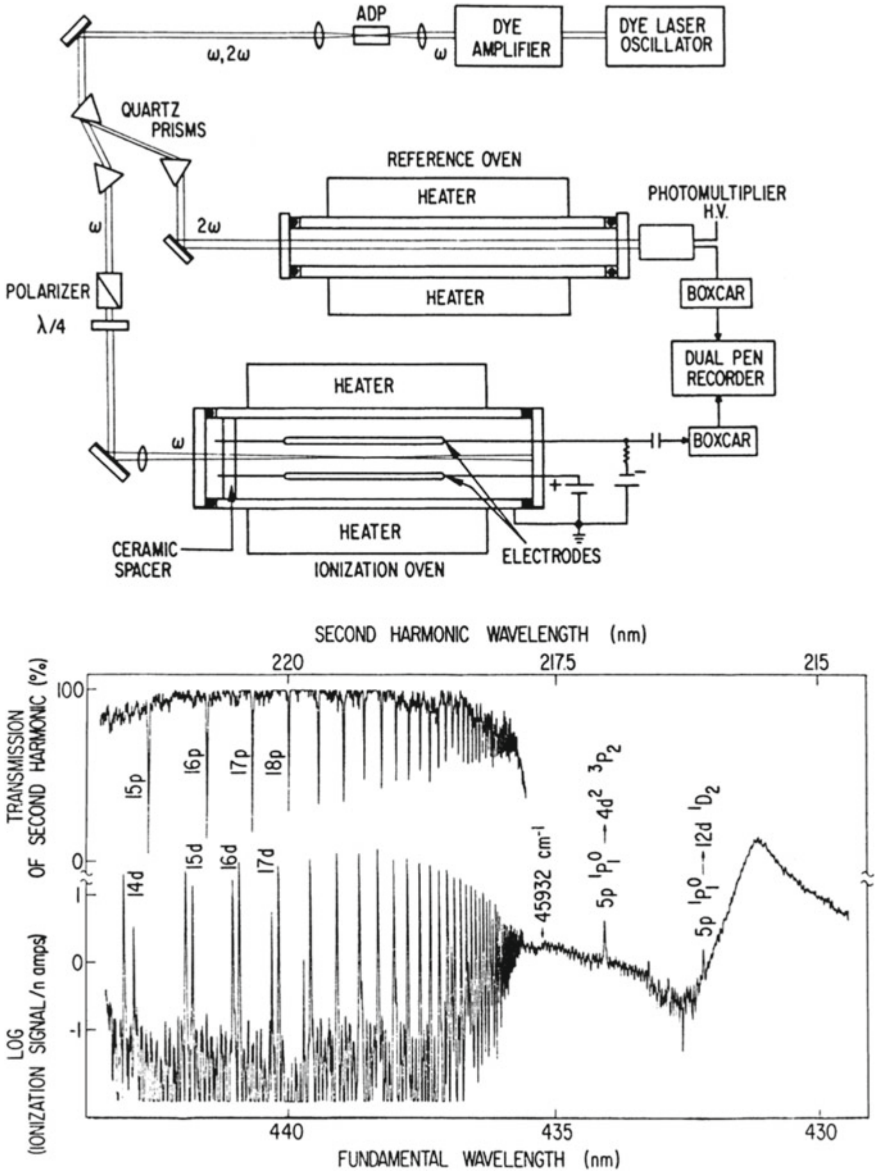
ADP
DYE AMPLIFIER
DYE LASER OSCILLATOR
ω, 2ω
ω
QUARTZ PRISMS
REFERENCE OVEN
HEATER
HEATER
PHOTOMULTIPLIER
H.V.
2ω
ω
POLARIZER
λ/4
BOXCAR
DUAL PEN RECORDER
BOXCAR
HEATER
HEATER
CERAMIC SPACER
IONIZATION OVEN
ELECTRODES
SECOND HARMONIC WAVELENGTH (nm)
220
217.5
215
TRANSMISSION OF SECOND HARMONIC (%)
100
0
15p
16p
17p
18p
14d
15d
16d
17d
45932 cm⁻¹
5p ¹P₁⁰ → 4d² ³P₂
5p ¹P₁⁰ → 12d ¹D₂
LOG (IONIZATION SIGNAL/n amps)
1
0
-1
440
435
430
FUNDAMENTAL WAVELENGTH (nm)

Fig. 9.8 Experimental set-up, ionization recording of two-photon transitions, and absorption recording of single-photon transitions in strontium vapour [1324]

resonance in connection with measurements on electrical discharges or flames is performed the term *Laser-Enhanced Ionization* (LEI) spectroscopy is frequently used. Opto-galvanic spectroscopy (LEI) of a gas discharge is illustrated in Fig. 9.9. The laser beam is directed into the discharge and when it is tuned to an optical transition the discharge current is changed, since the probability of collisional ionization is different for high-lying levels compared with low-lying ones. Current changes ΔI can be detected as a voltage change, $\Delta V = R\Delta I$, over a ballast resistor R in the discharge circuit. An opto-galvanic spectrum of a neon discharge is also given in the figure. The technique can conveniently be used for wavelength calibration of a tunable laser. A small part of the laser light is then directed into a hollow cathode containing, e.g., thorium or uranium, which both have a large number of lines distributed over the visible and ultraviolet spectral regions [1326]. A very simple pure electrical method

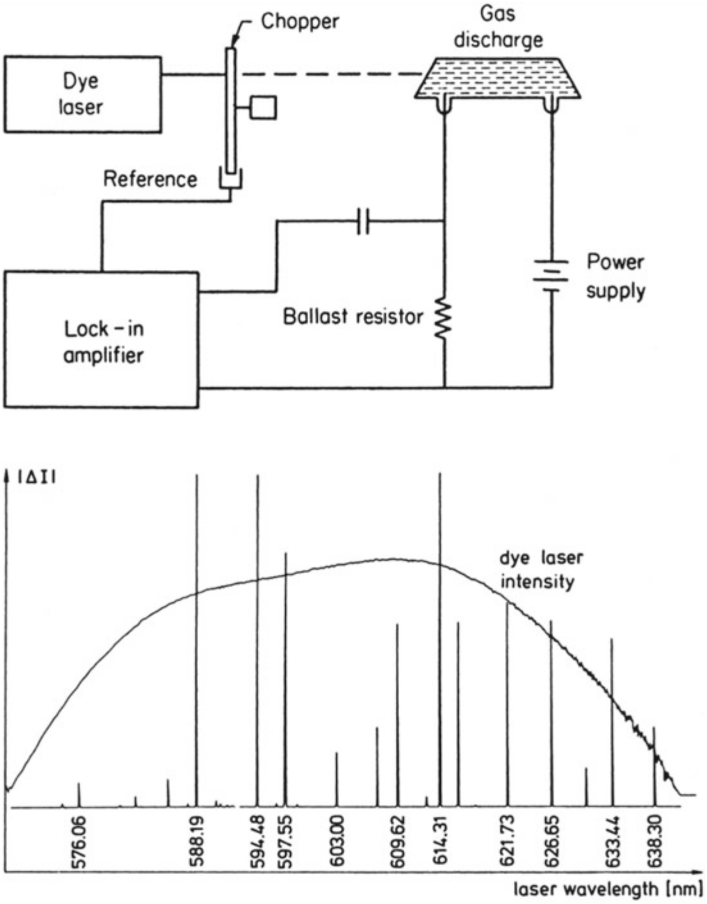
Chopper
Gas discharge
Dye laser
Reference
Power supply
Ballast resistor
Lock-in amplifier
|ΔI|
dye laser intensity
576.06
588.19
594.48
597.55
603.00
609.62
614.31
621.73
626.65
633.44
638.30
laser wavelength [nm]

Fig. 9.9 Experimental arrangement for opto-galvanic spectroscopy on a gas discharge [1325] and a recorded spectrum for a Ne discharge [1232]

of detection of the reference lines can thus be obtained. Optical resonance in radiofrequency discharges can also be detected electrically by observing an imbalance in the RF circuitry used for the oscillator.

Opto-galvanic spectroscopy of flames has important analytical applications. If an atomic absorption flame (Sect. 6.5.3) is irradiated by a tunable laser, a change in the current between two electrodes, placed in the outer parts of the flame, can be detected. A typical arrangement is shown in Fig. 9.10. A sensitivity exceeding that obtainable in atomic absorption spectroscopy (Sect. 6.5.2) can be achieved for elements seeded into the flame. Two-step excitation improves both sensitivity and background rejection [1328, 1329]. A very high sensitivity can be obtained by evaporating the analytical sample in an electrically heated graphite oven (Sect. 6.5.4) [1330–1332]. Laser absorption or fluorescence spectroscopy is frequently used for the detection in this case.

Tunable diode lasers are finding important applications in this context and generally in analytical and fundamental spectroscopy [1131, 1333–1336]; see also Sect. 10.2.2. The opto-galvanic technique can also be used for studying normal flame constituents such as O, H, and OH [1337].

As we have seen, collisions are important for the signal generation in LEI. Photoionization is instead the principal origin of the signal in low-pressure experiments. The term *Resonance Ionization Spectroscopy* (RIS) is then frequently used. Several examples of opto-galvanic detection schemes for different atoms are shown in Fig. 9.11. If multi-photon excitation of the atoms to be studied is used the technique is referred to as REMPI (*REsonance MultiPhoton Ionization*) spectroscopy.

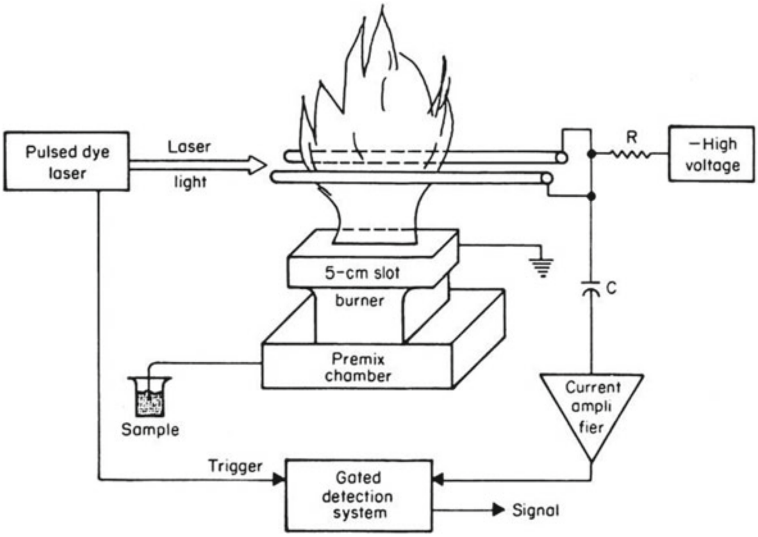

Fig. 9.10 Set-up for opto-galvanic flame spectroscopy [1327]

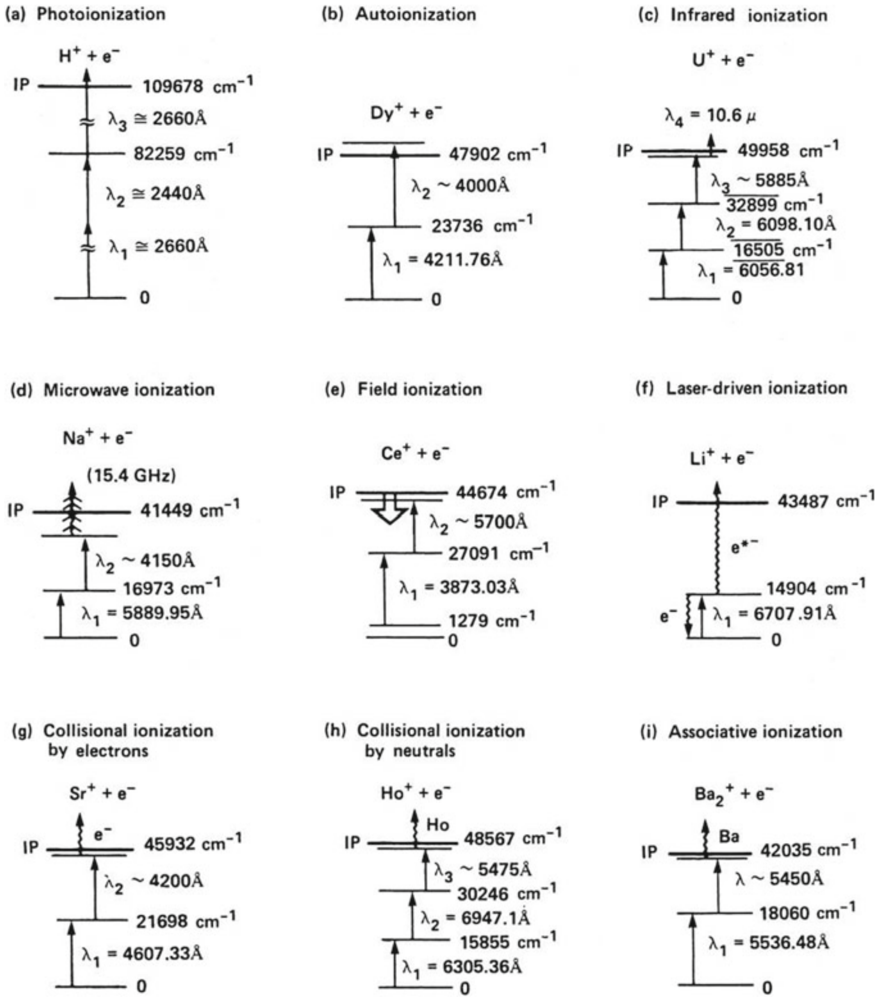
(a) Photoionization
H⁺ + e⁻
IP
109678 cm⁻¹
λ₃ ≅ 2660Å
82259 cm⁻¹
λ₂ ≅ 2440Å
λ₁ ≅ 2660Å
0
(b) Autoionization
Dy⁺ + e⁻
IP
47902 cm⁻¹
λ₂ ~ 4000Å
23736 cm⁻¹
λ₁ = 4211.76Å
0
(c) Infrared ionization
U⁺ + e⁻
λ₄ = 10.6 μ
IP
49958 cm⁻¹
λ₃ ~ 5885Å
32899 cm⁻¹
λ₂ = 6098.10Å
16505 cm⁻¹
λ₁ = 6056.81
0
(d) Microwave ionization
Na⁺ + e⁻
(15.4 GHz)
IP
41449 cm⁻¹
λ₂ ~ 4150Å
16973 cm⁻¹
λ₁ = 5889.95Å
0
(e) Field ionization
Ce⁺ + e⁻
IP
44674 cm⁻¹
λ₂ ~ 5700Å
27091 cm⁻¹
λ₁ = 3873.03Å
1279 cm⁻¹
0
(f) Laser-driven ionization
Li⁺ + e⁻
IP
43487 cm⁻¹
e*⁻
14904 cm⁻¹
e⁻
λ₁ = 6707.91Å
0
(g) Collisional ionization by electrons
Sr⁺ + e⁻
e⁻
IP
45932 cm⁻¹
λ₂ ~ 4200Å
21698 cm⁻¹
λ₁ = 4607.33Å
0
(h) Collisional ionization by neutrals
Ho⁺ + e⁻
Ho
IP
48567 cm⁻¹
λ₃ ~ 5475Å
30246 cm⁻¹
λ₂ = 6947.1Å
15855 cm⁻¹
λ₁ = 6305.36Å
0
(i) Associative ionization
Ba₂⁺ + e⁻
Ba
IP
42035 cm⁻¹
λ ~ 5450Å
18060 cm⁻¹
λ₁ = 5536.48Å
0

Fig. 9.11 Examples of resonance ionization pathways. The element, which is detected, is indicated at the top of each diagram [1338]

The selectivity of RIS and REMPI can be further enhanced by using a mass spectrometer to analyse the produced ions. This technique is referred to as RIMS (*Resonance Ionization Mass Spectroscopy*). The numerous aspects of opto-galvanic spectroscopy are covered in [1338–1346].

9.2.7 Single-Atom and Single-Molecule Detection

We have above seen how the condition of optical resonance can be detected by measuring the absorption of photons out of the interacting laser beam. Sometimes the fact that atoms in this process have been transferred to the excited state can be observed by an accompanying change in associated electrical phenomena—optogalvanic detection. A very common way to observe the transfer of atoms to the excited state is to observe the associated emission of fluorescence light We have already mentioned that single atoms or ions can, in principle, be detected by the emission of a large number of photons per second at saturation. We will come back to this in Sect. 9.8.4. The resonance ionization techniques discussed in the previous section also have the potential for single-atom detection. The energy density of the laser beams is chosen in such a way that the probability of photoionization of an atom in the beam is unity. The released electron can be detected with 100% probability if the atom is located inside a proportional counter. It has been demonstrated that a single Cs atom in a background of 10^{19} Ar atoms can be detected in this way. Single-atom detection is of great interest, e.g., for studying rare reactions such as those induced by neutrinos from the sun: ^{37}Cl (ν,e) ^{37}Ar. Other applications include dating of the polar ice caps, studies of ocean mixing by monitoring of atmospherically produced ^{37}Ar, etc. Single-atom detection using resonant photoionization is reviewed in [1347–1350]. Different techniques for ultra-sensitive atomic laser spectroscopy are discussed in [1351, 1352]. Single-molecule detection has also been achieved using mostly fluorescence detection techniques [1353–1358]. The ultra-sensitive analytical methods are of great interest, e.g., in molecular biology research [1359]. The general field of analytical laser spectroscopy is treated in [1360–1363].

At the end of this section, we would like to describe how super-resolution microscopy can be achieved using single-molecule detection. As discussed at the end of the section of spectroscopic resolution instruments (Sect. 6.2) the angular resolution on an optical instrument, like a telescope, microscope, etc., is given by the λ/d ratio, where λ is the wavelength, and d is the diameter of the objective. This means, that for microscope objects smaller than about $\lambda/2$ cannot be resolved (the Abbe resolution criterion, after *E. Abbe*, a pioneer in "modern" microscopy). This is a clear limitation, e.g., in modern biomedical research. However, recently ways to get around this limitation were found and resulted in the 2014 Nobel Prizes in Chemistry to *E. Betzig, S.W. Hell*, and *W.E. Moerner* [1364–1366].

The *STORM (stochastic optical reconstruction microscopy)* [1367–1369] approach (also called *PALM (photoactivated localization spectroscopy)*) relies on the possibility to observe the fluorescence photons emitted from single molecules. The resulting spot-size from a single molecule is clearly diffraction limited. Special molecules, which can be photoactivated from a dark, non-fluorescent state into a fluorescent one must be used. Then, if a given molecule is made to emit many photons while the neighbouring molecules do not emit, the centre of the emission spot from a single molecule can be determined much more accurately than the position of an individual photon. The other molecules are later in turn switched on to emit. Clearly, this

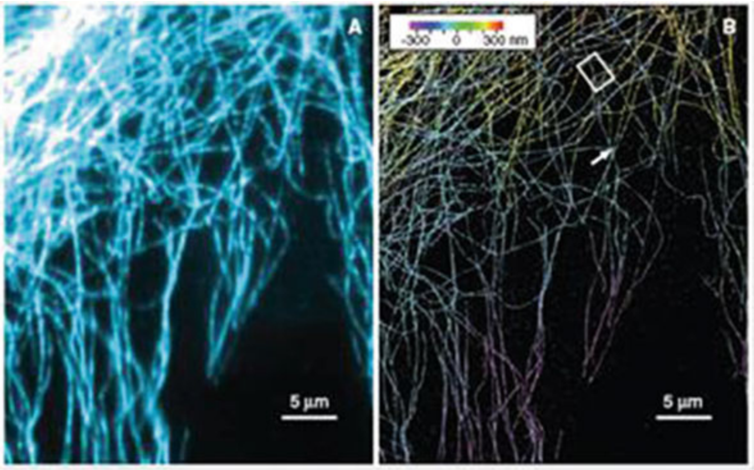

Fig. 9.12 Comparison between confocal (left) and STORM (right) microscopy. The recordings regard cell microtubules ([1369]; reproduced with permisson from AAAS)

only works if bursts of photons from well-separated fluorophores are detected, which means that data have to be collected and read out during a substantial time. Accuracies down to few nm can be achieved. An example is given in Fig. 9.12. If bursts of photons from many molecules overlap temporally clearly the super-resolution is lost. This is in contrast to the *STED (stimulated emission depletion)* approach [1370–1373], where the improved spatial resolution comes from the nonlinear molecular response, also from an ensemble of molecules and which we will discuss in Sect. 9.7.2 (Fig. 9.60).

9.2.8 Opto-Acoustic Spectroscopy

In this section, we will describe another non-optical technique for the detection of optical absorption: *opto-acoustic spectroscopy*, sometimes called *photo-acoustic spectroscopy*. The principle of a laser-based opto-acoustic spectrometer (spectrophone) is given in Fig. 9.13. A molecular sample at relatively high pressure is contained in a closed volume and is irradiated with a chopped CW laser beam tuned to resonance. The excited molecules are mainly de-excited radiationlessly at the prevailing pressure. The excitation energy is converted to translational energy upon collision. Thus, the pressure rises and falls periodically in the cell. The pressure variations can be detected as a sound wave by a microphone mounted in the cell wall. Weak signals can be detected by lock-in techniques (Fig. 6.68). If the cell is shaped as a resonant cavity for the chopping frequency, a very high sensitivity can be achieved, better than 1 ppb (1 part in 10^9) in the measurement of, for example, air pollutants. CO_2 lasers or diode lasers can be used to induce vibrational transitions.

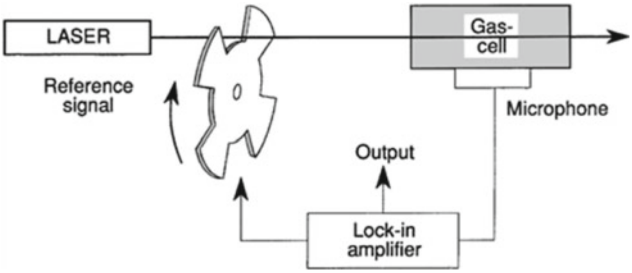

Fig. 9.13 The principle of opto-acoustic spectroscopy [1374]

Since the detector used in photo-acoustic spectroscopy is only sensitive to the absorbed part of the radiation, very small absorptions can be measured. This is not possible in normal optical absorption measurements, where the difference between two almost equally large quantities is to be measured. There is a similar advantage of fluorescence detection over absorption measurements—again only the absorbed part of the light is detected leading to the signal to rise from a basically zero background. A special feature of opto-acoustic spectroscopy is that it is largely insensitive to stray light. Techniques are further discussed in [1375–1384].

A recent development in opto-acoustic spectroscopy is the introduction of the *quartz-enhanced photo-acoustic spectroscopy*, *QEPAS* [1385–1388]. Here, the laser beam is directed to the gap between the arms of a quartz micro tuning fork of the type typically used as the primary oscillator in an electronic clock. If the laser beam is chopped at the resonance frequency of the tuning fork, the minute pressure waves due to the absorption of light in the gas between the fork arms will make them resonate and induce an electric signal, which can be picked up.

The absorption of solid or liquid materials can also be measured using these techniques [1389, 1390]. The laser illuminates the sample and the heat variations are coupled to a non-absorbing gas, which is in contact with the microphone. Piezoelectrical detection can also be used with solid or liquid samples. Elastic waves in the material are then detected. An example of an opto-acoustic spectrum of a powder is given in Fig. 9.14.

Fig. 9.14 Example of an opto-acoustic spectrum from a solid [1389]

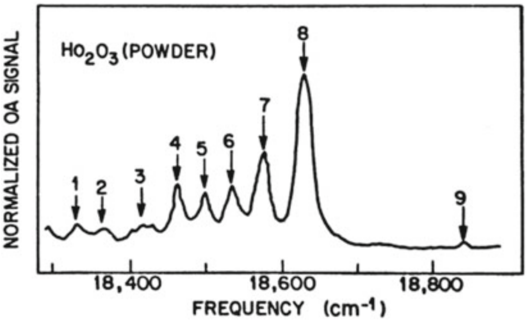

More recently, photo-acoustic spectroscopy of this kind has gained great importance in biophotonics, where laser beam absorption is picked up by ultra-sonic detectors surrounding the biological sample [1391]. Basically, a modified ultra-sound diagnostic machine is used. Such applications will be discussed in Sect. 10.5.4.4 (Fig. 10.72).

9.3 Optical Double-Resonance and Level-Crossing Experiments with Laser Excitation

In this section we will deal with experiments in which, similarly to the conditions in the previous sections, Doppler-broadened media and rather broadband lasers are used. In spite of this fact, a resolution is obtained that is only limited by the Heisenberg uncertainty relation. This is due to the fact that the signals are resonant in nature with half-widths limited essentially only by the lifetime of the excited state, since the Doppler broadening for an rf-transition is negligible. Optical double-resonance and level-crossing experiments (Sects. 7.1.4 and 7.1.5) with laser excitation utilize the high intensity of polarized laser light in order to populate levels that are normally not accessible for investigation for intensity reasons. In particular, experiments employing stepwise excitation become possible [1392, 1393]. A large number of investigations on fine structure, hyperfine structure, and the Stark effect have been performed for the alkali metal atoms, using such techniques [1394–1399]. As an example, the energy-level diagram of Cs is given in Fig. 9.15. Stepwise excitation of S and D levels via the first P-doublet is illustrated in the diagram. At the early stage of development of CW dye lasers, only a narrow wavelength region in the yellow and red spectral ranges was available with Rhodamine dyes. Thus, the spectroscopic applicability for such lasers was quite limited. However, if the laser excitation is initiated from the first P state, many highly excited states become accessible for the given spectral range. This is true not only for Cs but also for the other alkali metals. The P states can be weakly populated using the very strong resonance lines (D_1 and D_2) in the alkali atoms. A sealed RF lamp (Sect. 6.1.1) is very suitable for the efficient generation of these lines. Strong multiple scattering is obtained at a vapour pressure of 10^{-3} torr (133 mP) in the resonance cell for these lines, and thus the average population of the P levels is increased. Re-emitted photons are reused to bring the atoms back into the P state, which has a lifetime of some tens of ns. Still, only about 1 atom in 10^4 is in the P state. The RF lamp cannot, by a long way, saturate the optical transition. A multi-mode dye laser is used to induce the second excitation step. By piezo-electrically vibrating one of the laser mirrors the mode structure can, on average, be washed out and a "white" excitation is obtained. An experimental arrangement for stepwise optical double-resonance and level-crossing spectroscopy is shown in Fig. 9.16.

Lock-in detection (Fig. 6.68) is used for signal detection and the lock-in signals are further averaged using a multichannel analyzer, which has a channel advancement,

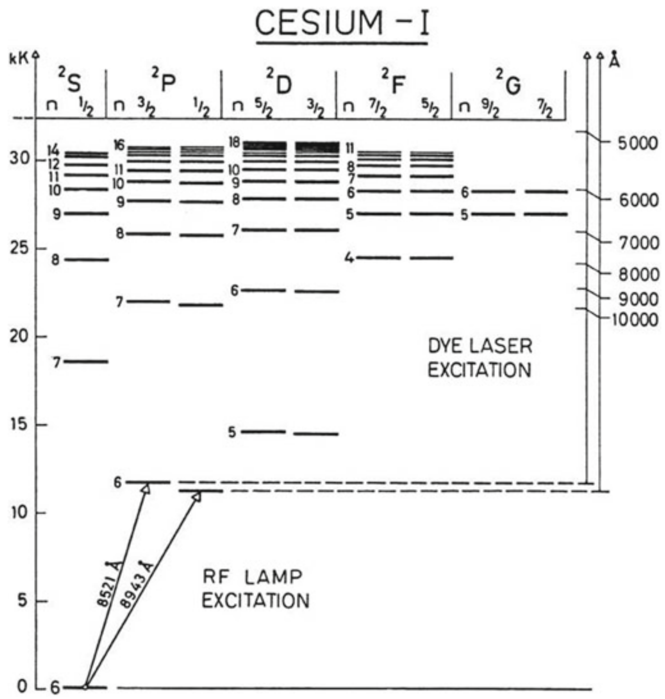

Fig. 9.15 Energy level scheme for Cs. Rf-lamp excitation of the first excited ^2P states is indicated and absorption wavelengths for subsequent ^2S and ^2D state excitation are given [1397]

which is synchronized with a repetitive magnetic field sweep. In ODR experiments the RF transmission is pulse-modulated, while LC signals are detected by recording the fluorescent light intensity through a rotating linear polarizer. Normally, circularly polarized light components are obtained in the direction of the magnetic field (Fig. 4.9). The only occasion for which linearly polarized light can be obtained in the direction of the magnetic field is at a coherently excited and coherently decaying level crossing, where the σ^+ and σ^- light is superimposed and phase-related, resulting in linearly polarized light. This light is then modulated by the rotating linear polarizer and this modulation is detected by the lock-in amplifier. A fluorescence light spectrum for Cs is given in Fig. 9.17 as recorded with the apparatus shown in Fig. 9.16. The 12 $^2D_{5/2}$ state is populated by stepwise excitation. In cascade decays, as illustrated in Fig. 9.1, lower-lying P and F levels are populated and numerous fluorescence lines are obtained in the blue and UV, and in the red spectral regions, respectively.

If the primary excitation is performed, e.g., with π light (Fig. 4.9) the magnetic sublevels of the $^2D_{5/2}$ state will be non-uniformly populated. The fluorescence in the different decay lines will then also be linearly polarized. Radio-frequency transitions, that are induced in the primary state or in cascade states, will give rise to a depolarization and redistribution of the light that can be detected. Thus, the properties of

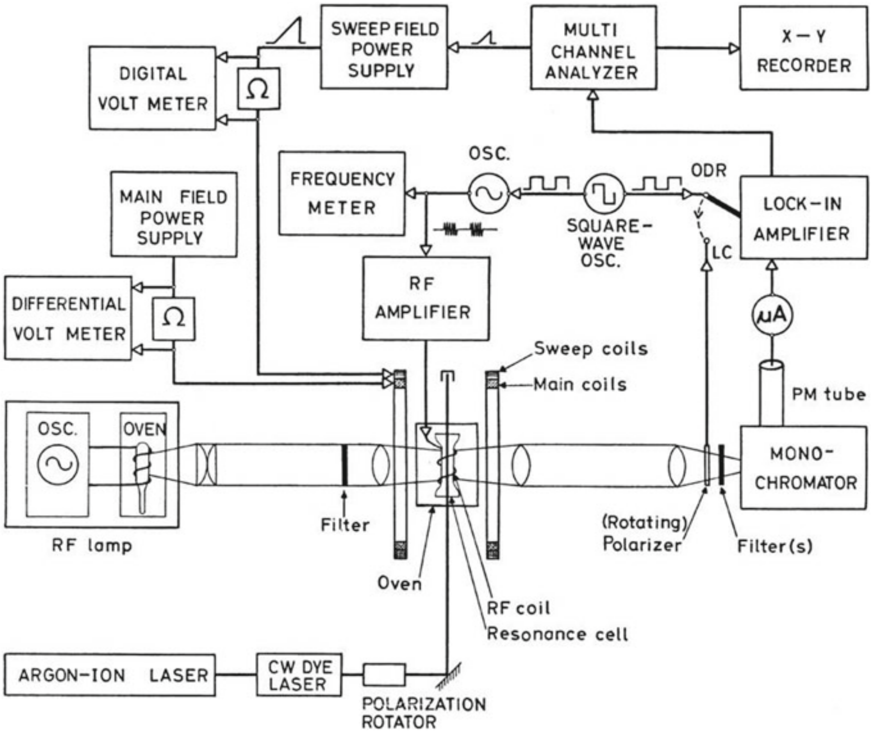
DIGITAL VOLT METER
Ω
SWEEP FIELD POWER SUPPLY
MULTI CHANNEL ANALYZER
X – Y RECORDER
MAIN FIELD POWER SUPPLY
FREQUENCY METER
OSC.
SQUARE-WAVE OSC.
ODR
LC
LOCK-IN AMPLIFIER
DIFFERENTIAL VOLT METER
Ω
RF AMPLIFIER
μA
Sweep coils
Main coils
PM tube
OSC.
OVEN
MONO-CHROMATOR
Filter
RF lamp
(Rotating) Polarizer
Filter(s)
Oven
RF coil
Resonance cell
ARGON-ION LASER
CW DYE LASER
POLARIZATION ROTATOR

Fig. 9.16 Experimental arrangement for LC and ODR spectroscopy of excited alkali metal atom levels, populated using stepwise excitation [1396]

many *P*, *D,* and *F* states can be investigated. Examples of ODR signals in excited *S* states, populated by stepwise excitation, were given in Fig. 7.11.

In Chap. 7, we have discussed how hyperfine structure in $^2P_{3/2}$ states can be determined by level-crossing spectroscopy. Clearly, alkali atom ^2D states can readily be studied using this technique after stepwise excitation. We will here instead choose an example illustrating fine-structure measurements. The example of the inverted (see Fig. 2.5) sodium $4d\ ^2D_{5/2,3/2}$ state is given in Fig. 9.18. From the measured level-crossing positions, the fine-structure splitting can be calculated using the Breit–Rabi formula for the fine structure, (2.31).

We will conclude this section by illustrating how the tensor Stark polarizability constant can be measured using level-crossing spectroscopy. As illustrated in Fig. 9.19, for the case of the potassium $5d\ ^2D_{3/2}$ state, the unknown Stark effect is measured in terms of the well-known Zeeman effect (g_J is well-defined in LS coupling). In the absence of an external electric field, the normal Hanle signal (shown differentiated because of the magnetic field modulation; see Fig. 6.88d) is recorded. If, in addition, a fixed electric field E is applied over the atoms, a high-field level

Fig. 9.17 Fluorescence spectrum from Cs atoms following stepwise excitation to the 12 $^2D_{5/2}$ state [1397]

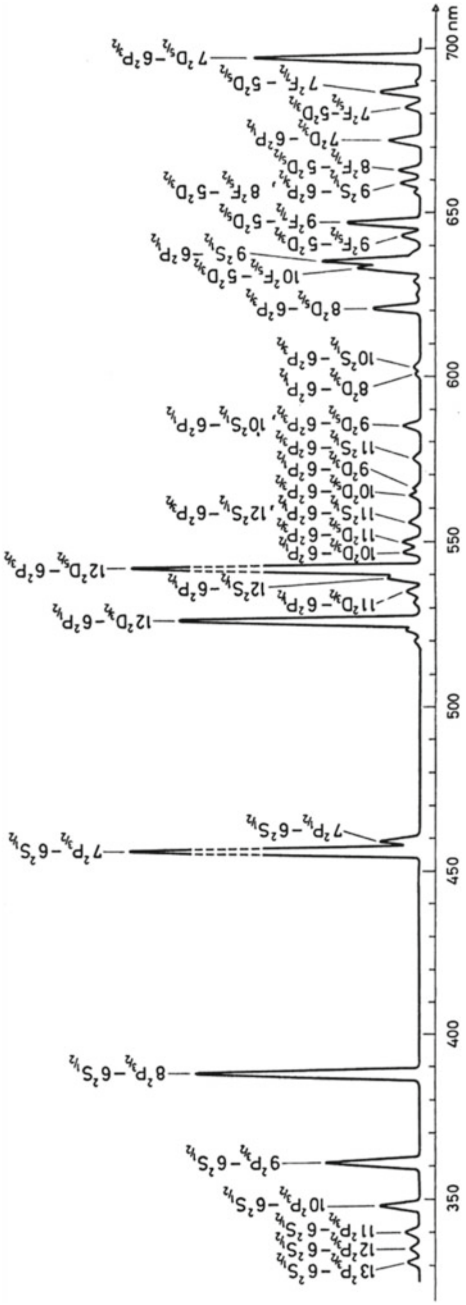

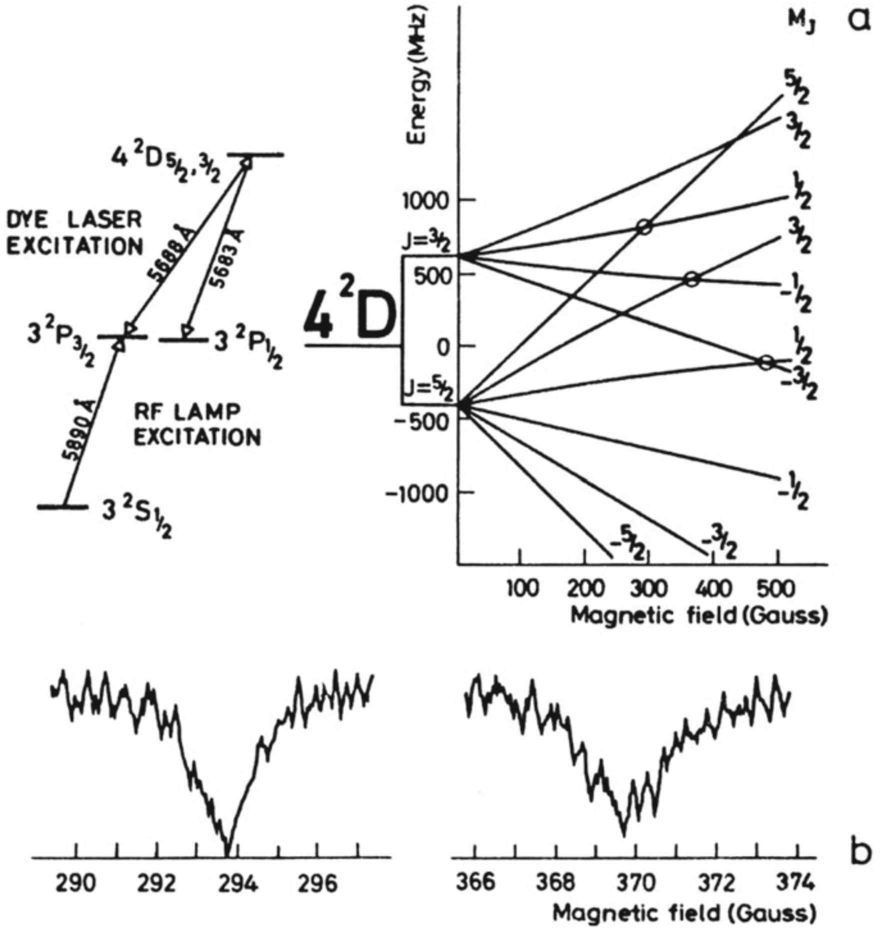
4 ²D5/2,3/2
DYE LASER EXCITATION
5688 Å
5683 Å
3 ²P3/2
3 ²P1/2
5890 Å
RF LAMP EXCITATION
3 ²S1/2
4 ²D
Energy (MHz)
1000
J=3/2
500
0
J=5/2
-500
-1000
M_J
a
5/2
3/2
1/2
3/2
-1/2
1/2
-3/2
-1/2
-5/2
-3/2
100
200
300
400
500
Magnetic field (Gauss)
290
292
294
296
366
368
370
372
374
Magnetic field (Gauss)
b

Fig. 9.18 Illustration of fine-structure measurement for an alkali metal *D* doublet using level-crossing spectroscopy [1395]. We note that the level-crossing signals are here recorded as symmetric curves rather than derivative-like curves, such as those appearing in Fig. 7.16. The reason is that in this latter case the magnetic field was modulated (see Fig. 6.68d), while here a rotating linear polarizer was used. Then the modulated signal is obtained as twice the full intensity change due to the quantum interference, since the signal changes sign for 90° rotation of the polarizer; see discussion after Eq. 7.32

crossing will be produced when scanning the magnetic field. The simple relation given in Fig. 9.19 is easily verified from (2.29) and (2.35).

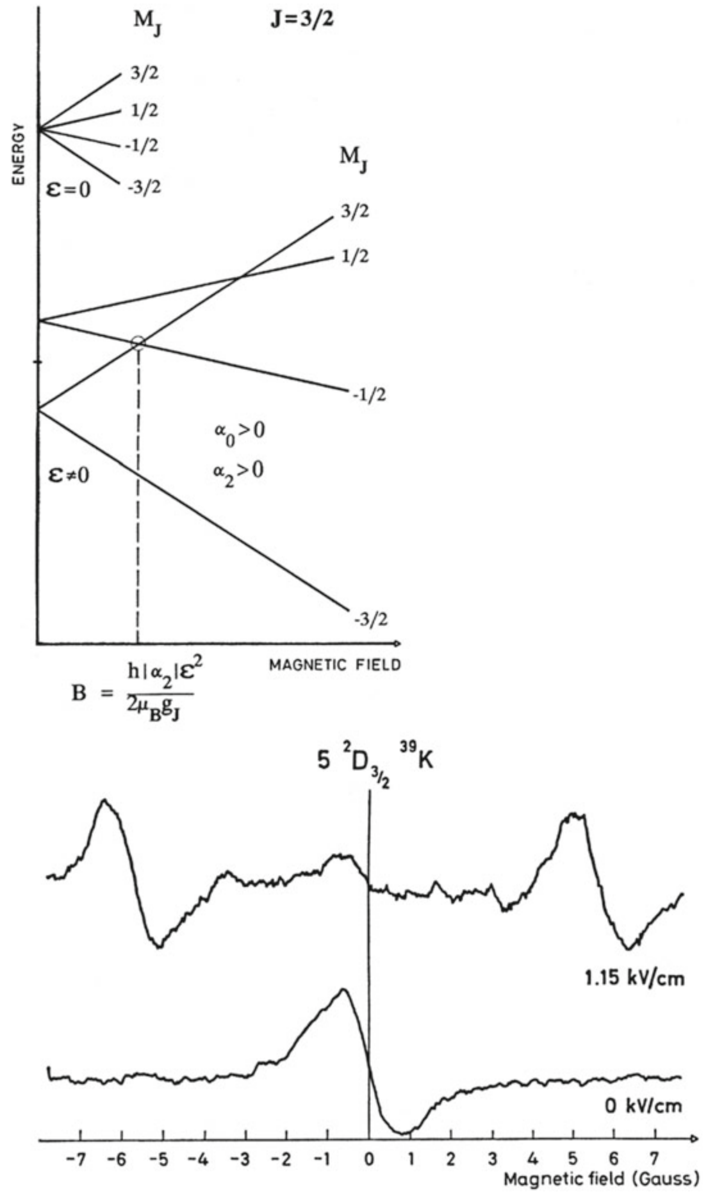

Fig. 9.19 Illustration of the determination of the tensor polarizability of an excited alkali metal *D* state using level-crossing spectroscopy in parallel electric and magnetic fields [1394]. Since fluorescence observation in the magnetic field direction is blocked by the Stark plates, the rotating polarizer technique could not be used for lock-in detection. Instead, the magnetic field was modulated resulting in derivative-like signals

9.4 Time-Resolved Atomic and Molecular Spectroscopy

We will study time-resolved laser spectroscopy in this section and generally discuss radiative properties of atoms and molecules and methods of studying these properties. Since very short laser pulses with a power density sufficient to saturate optical transitions can be obtained, a large fraction of the irradiated ground-state atoms can be transferred to the excited state. Using stepwise excitation with synchronized lasers, a large number of atoms can be excited into very highly excited states. When the laser pulse ceases, the exponential decay of the excited state can be monitored. Note, that primarily the population number $N(t)$ decays exponentially, i.e.,

$$N(t) = N_0\, \mathrm{e}^{-t/\tau}. \tag{9.7}$$

This primary population decay can be monitored by observing the decay of the fluorescence light in an arbitrary spectral line originating in the state. We have for the light intensity $I(t)$

$$I(t) \sim -\frac{\mathrm{d}N(t)}{\mathrm{d}t} = \frac{N_0}{\tau}\mathrm{e}^{-t/\tau} = I_0\mathrm{e}^{-t/\tau}. \tag{9.8}$$

Because of the special properties of the exponential function, the light decays with the same time constant τ as the population decay. The light decay can be followed by a fast detector connected to fast, time-resolving electronics. If the excited state has a substructure, e.g., because of the Zeeman effect or hyperfine structure, and an abrupt, coherent excitation is made, oscillations (quantum beats) in the light intensity will be recorded as discussed later. The oscillation frequencies correspond to the energy level separations and can be used for structure determinations. We will first discuss the generation of short optical pulses and measurement techniques for fast optical transients.

9.4.1 Generation of Short Optical Pulses

Broadband flash-lamps with specially designed driving circuits can be used to produce light pulses, with a pulse length of the order of 1 ns. Synchrotron radiation can be produced as pulses of tens of ps duration, while FEL:s can provide shorter pulses [1400–1402]. A suitable spectral region can be filtered out from the broadband distribution from the synchrotron using a monochromator and can be used for exciting species with broad absorption bands, i.e., liquids and solids. However, the high monochromaticity of lasers is normally needed for efficient excitation of free atoms or molecules absorbing in a very narrow spectral region. We described in Chap. 8 a variety of pulsed lasers with a pulse duration in the 3-20 ns range. The repetition rate of such lasers seldom exceeds a few hundred Hz and is frequently substantially lower (e.g., 10 Hz). Pulses at a higher repetition rate can be obtained by modulating a CW laser beam by means of a Pockels cell or a Bragg diffraction cell (acousto-optic modulation). In the latter device, an RF oscillator coupled to a piezoelectric transducer induces density variations in a crystal causing a deflection of the beam into an aperture because of grating diffraction. While a rise time below 10 ns can be achieved in this way, the peak power of the pulses is, by necessity, minute. A much more efficient way of producing laser pulses of short duration and high peak power is by *mode-locking*, possibly combined with cavity dumping, as discussed in Sect. 8.7.1.

9.4.2 Measurement Techniques for Optical Transients

We will in this subsection discuss techniques for recording a decaying optical signal on a timescale exceeding 0.1 ns, where fast photomultiplier tubes can still be used. The corresponding electrical signal can be handled in different ways, which can conveniently be discussed with reference to Fig. 9.20.

Transient-Digitizer Technique. Historically, the most direct way of capturing the transient signal from the photomultiplier tube was to use a normal fast oscilloscope and take a photograph of the screen with open camera shutter while the electron beam, which is triggered by the laser, sweeps the screen drawing the decay curve. Clearly, it is inconvenient to further process data stored as photographs. A *transient digitizer* instead captures the transient digitally by successively recording the input voltage at given time intervals, e.g., 10 ns, and generating numbers that are proportional to the input voltage. The whole sequence of numbers is stored digitally and the memory can then be read out repetitively as an analogue signal at a low rate. Thus,

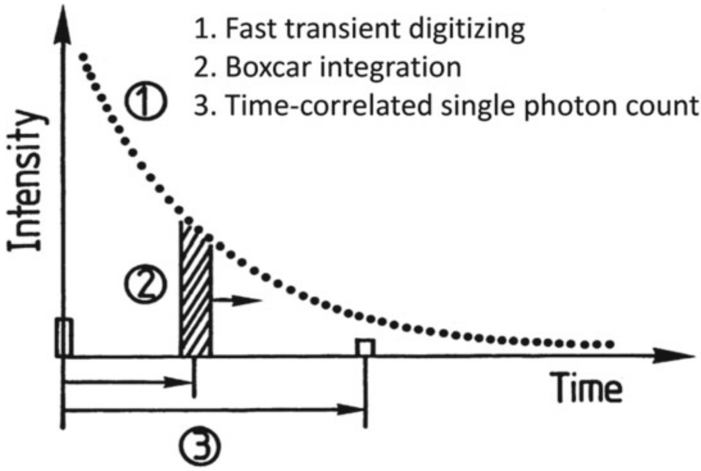
1. Fast transient digitizing
2. Boxcar integration
3. Time-correlated single photon counting
Intensity
①
②
Time
③

Fig. 9.20 Illustration of methods to measure optical transients

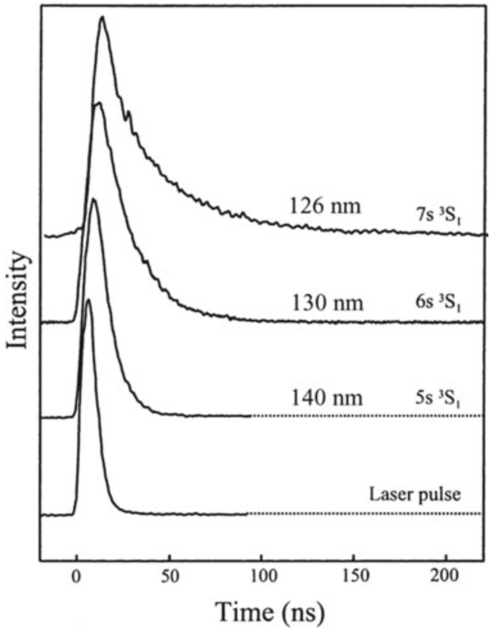

Fig. 9.21 Time-resolved laser-induced fluorescence recordings in a sequence of sulphur, employing the transient digitizer technique [1403]. The VUV excitation wavelengths were obtained by resonant sum-difference four-wave mixing in krypton gas

a permanent oscilloscope trace of high brightness is obtained. Alternatively, the sequence of numbers can be transferred to a computer and an arbitrary number of individual transients can then be averaged. This method of measurement is very efficient since all the signal information from each transient is captured. A time resolution of less than 1 ns can be obtained. As a result of the digitization, the data can easily be processed further. Modern fast oscilloscopes can all be considered to be transient digitizers, which also allow signal averaging.

Examples of atomic excited-state decay curves recorded with the transient digitizer technique for a sequence of states in sulphur are shown in Fig. 9.21. The lifetimes increase with a $\tau \propto n^3$ trend as expected for a Rydberg sequence (Table 9.2). Sulphur and a number of other elements evaporate as molecules, making normally employed thermal atomization techniques (Fig. 7.2) less suitable. A laser-produced plasma source, where pulses of few tens of mJ from a Q-switched laser impinge on a sample of a sulphur compound kept in a vacuum chamber is then very convenient. Other advantages with laser plasma generation are the ease with which refractory elements are vaporized, and singly and doubly ionized atoms are formed. Through the laser ablation a rapidly expanding (several km/s) plume consisting of atoms and also ions is formed, and this dynamic target can be studied by firing the spectroscopic laser after an appropriate delay to ensure unperturbed conditions and correct lifetime determinations. Figure 9.22 shows a time-expanded recording related to Fig. 9.21,

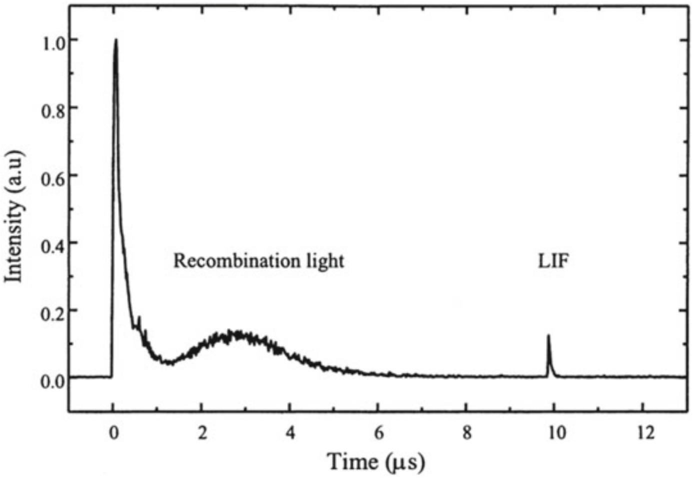

Fig. 9.22 Time-resolved recording of the light emission following laser ablation from a sulphur target. The spike at 10 µs is the laser-induced fluorescence from the 7 $s\,^3S_1$ state [1403]

where the light emission from the recombining plasma is first observed. Then, after a delay of about 10 µs the spectroscopic laser tuned to 126 nm for exciting the 7 $s\,^3S_1$ state is fired and the subsequent laser-induced fluorescence is observed as a spike. This signal, on a higher resolution timescale, is included in Fig. 9.21 [1403]. In the example discussed the sulphur sample was in the form of a lead sulphide powder. It was placed in a container which was shaken to re-prepare the surface [1404]. Alternatively, a rotating disc made out of the element under study can be used to ensure fresh target points for the ablation laser [1405] or a self-healing molten target surface can be employed [1406]. The combination of sample preparation in a laser-produced plasma and generation of UV and VUV laser light (Fig. 8.43) of short pulse duration [1407] has recently allowed the laser techniques to be applied on a broad scale [1408–1416] addressing, for example, the astrophysical needs related to the wealth of new short-wavelength data obtained for atoms and ions employing, e.g., the Hubble Space Telescope. Even ions with three electrons removed from the atomic shell can be studied [1417].

Boxcar Technique. A time window of a certain length is set in a *boxcar integrator (gated integrator)* for the input signal at a certain delay after the trigger signal, and the corresponding electrical charge is stored in a capacitor with a suitable time constant. Transients are repeatedly recorded, and the capacitor is charged to a stationary value. The voltage over the capacitor is read out to a recorder. If the time delay is slowly increased to longer and longer values (with a speed that is compatible with the chosen discharge constant), the exponential decay will be reproduced on the recorder. An ADC (Analogue-to-Digital Converter) at the output of the boxcar integrator can be used to adapt the signal for computer processing. The boxcar technique is relatively simple, but clearly not very efficient, since only photons at a certain time delay are used while the others are discarded. In this respect, the cases of transient digitizer versus boxcar integrator and optical multichannel analyzer versus photoelectrically recording slit monochromator are analogous. The transient digitizer, as well as the boxcar technique, normally requires strong optical transients consisting of a large number of individual photon pulses. Possible nonlinearities in the photomultiplier, which has to record very strong and very weak signals at short time intervals, constitute a limitation to both techniques as regards the recording accuracy.

Time-correlated single-photon counting (TCSPC). This method operates in the extremely low intensity regime, in which single-photon counts are recorded. The principle is illustrated in Fig. 9.23.

A single photon gives rise to an electric pulse (Fig. 1.9b), which in good photomultipliers has a length of only a few nanoseconds. A Time-to-Amplitude pulse-height Converter (TAC) is a critical component when using this technique. A clock is started when the excitation pulse is fired. The clock runs until the photomultiplier records the first fluorescence photon. A standard electronic pulse, the height (= voltage) of which is proportional to the time difference, is generated and is fed to a Multichannel Analyzer (MCA). An ADC at the input of the MCA converts the voltage into a channel address number, which is proportional to the pulse height. One count is then added to the contents of this channel. Since the decay is exponential, it is

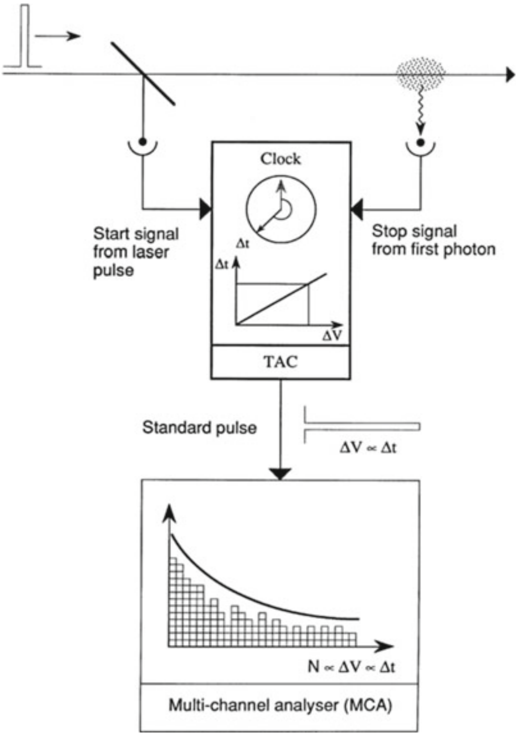
Clock
Start signal from laser pulse
Stop signal from first photon
Δt
Δt
ΔV
TAC
Standard pulse
ΔV ∝ Δt
N ∝ ΔV ∝ Δt
Multi-channel analyser (MCA)

Fig. 9.23 Principle of lifetime measurements using the time-correlated single-photon counting (TCSPC) technique. The arrival time of a photon can be even better defined by adding a *constant-fraction discriminator (CFD),* where the trigging occurs when the photon signal voltage passes a certain fraction of the peak pulse intensity. In this way, the effect of photons being detected with different amplitude (but same half-width) is eliminated

likely that the first photon will arrive early. It is important that the probability of two or more photons reaching the detector is kept low, since later photons cannot be recorded. In such cases small time delays would be strongly overrepresented, giving rise to the so-called *pile-up* effect. If the probability of detecting a single photon is kept below 1: 30 following a laser pulse, the pile-up correction will be negligible [1418]. A histogram is then built up in the multichannel analyzer.

The histogram displays the exponential decay when a sufficient number of counts have been accumulated. The microscopic probability function is then converted into a macroscopic intensity function. Clearly, a high repetition rate is necessary for the excitation source in order to provide an acceptable measurement time. Thus, a pulse-modulated CW laser or a mode-locked laser is normally required. Very accurate results are obtained with this method since there are no linearity problems. It is simply a matter of *when* the photon comes, not how large the corresponding pulse is. When using high-repetition rate sources, it is useful to reverse the role of the start and stop pulses so that the TAC is activated by a fluorescence photon and is stopped by the next excitation pulse. In this way, dead time in the electronics is reduced. Time-correlated single-photon measurements with pulse-modulated or mode-locked CW lasers have been presented in [1419, 1420].

Examples of decay curves recorded using the TCSPC technique with an acousto-optic modulator are shown in Fig. 9.24 for excited Ba states. Two-step excitation is used, and only the second laser is pulse-modulated. Lifetime results are also given for the $6sns\ ^1S_0$ and $6snd\ ^1D_2$ sequences of Ba in the figure. An overall trend of $\tau \propto n^3{}_{\mathrm{eff}}$ is found, but strong localized perturbations are also evident. These are due to admixtures into the wave function of a doubly excited state of the same parity, belonging to the $5d7d$ configuration. Doubly excited states have very short lifetimes in comparison with the highly excited states of the Rydberg sequences. Thus the experimental results can be used to investigate the composition of the atomic wave functions [1421–1424].

While the time-correlated single photon counting (TCSPC) method *(*or *delayed-coincidence technique*, as it is sometimes referred to, remembering its nuclear physics origin) is very fast and convenient in this type of Rydberg-state studies, its inherently high precision is even more valuable in experiments designed to distinguish between accurate theoretical methods for lifetime calculations. Very accurate lifetimes of the first excited states in lithium and sodium are of great interest in this context. Using a mode-locked CW dye laser with a cavity dumper to produce a MHz train of 6 ps-long pulses, it was possible to reach a lifetime precision of about 0.5 percent for short lifetimes around 20 ns [1425–1427].

Single-photon counting techniques are increasingly used in biophotonics for characterizing complex biological molecules and for imaging tissues based on differences in decay times of laser-excited molecules (Sect. 10.5.3, Figs. 10.64, 10.65).

Optical detection methods (streak camera and pump-probe techniques) exist that are even faster than those discussed here. Ultrafast spectroscopy is discussed in Sect. 9.5.

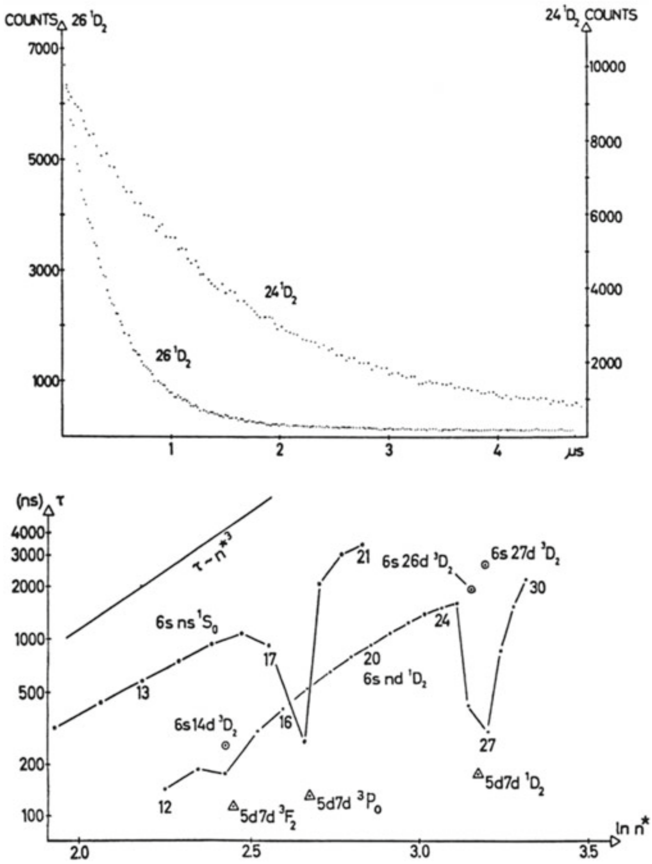

Fig. 9.24 TCSPC recordings of decay curves for excited barium $6snd\ ^1D_2$ states and plot of lifetime results for perturbed barium Rydberg state sequences [1421] and [1422]. An excitation scheme can be found in Fig. 9.5

9.4.3 Background to Lifetime Measurements

On several previous occasions, we have discussed measurement techniques yielding information on natural radiative lifetimes. We now discuss the motivation behind such measurements. Some important relations between radiative properties are presented in Fig. 9.25.

Transition probabilities, A_{ik}, (Sect. 4.1) are the quantities of primary interest in many contexts. As we will see in the next section, relative transition probabilities, a_{ik}, can be determined by several methods. A direct, absolute determination is considerably more difficult. However, lifetimes can be used to determine the relevant constant c, used to normalize relative transition probabilities to absolute ones

Fig. 9.25 Relations between radiative properties

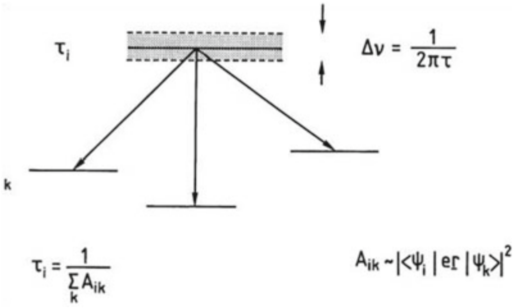
τ_i
$\Delta\nu = \frac{1}{2\pi\tau}$
k
$\tau_i = \frac{1}{\sum_k A_{ik}}$
$A_{ik} \sim |\langle\psi_i|e\mathbf{r}|\psi_k\rangle|^2$

$$\frac{l}{\tau_i} = \sum_k ca_{ik} = \sum_k A_{ik}. \tag{9.9}$$

There are many reasons for studying radiative properties:

1. The natural lifetime determines the *fundamental limit* of resolution $\Delta\nu_N = 1/2\pi\tau$ in spectroscopic investigations.
2. Transition probabilities can be used for sensitive *testing of atomic wave functions*. A_{ik} is related to the matrix element of the electric dipole operator ***er*** between the two wave functions (Sect. 4.1). Note that A_{ik} is especially sensitive to the outer part of the wave function (at larger r values) because of the r weighting.
3. As we have mentioned in Sect. 6.7, transition probabilities and the related *oscillator strengths* f_{ik} are of utmost importance for *astrophysics*, e.g., for calculations of the relative abundances of the elements in the sun and stars.

   The absorption oscillator strength f_{ki} is related to the corresponding transition probability A_{ik} by the following relation:

$$f_{ki} = 1.5\frac{1}{\sigma^2}\frac{g_k}{g_i}A_{ik}, \tag{9.10}$$

   where σ is the wavenumber for the transition and g_i and g_k are the statistical weights for the upper and lower states, respectively.
4. The radiative properties of atoms and ions are also of great importance in *plasma physics*, e.g., for temperature determination and for the calculation of the concentrations of different constituents. Determination of the concentrations of contaminating species that tend to cool the plasma are of great interest in fusion research. The study of the properties of refractory elements that are used for plasma confinement (Mo, Va, etc.) is especially important [1428, 1429].
5. In *laser physics,* lifetimes and transition probabilities are decisive for predictions of potential laser action in specific media.

9.4.4 Survey of Methods of Measurement for Radiative Properties

We will now discuss a number of measurement techniques for radiative properties. We start with methods of lifetime determination and continue with techniques for the measurement of transition probabilities. Detailed descriptions can be found in [1430–1434].

Linewidth Measurements. The natural linewidth of a short-lived state is $\Delta\nu_N = 1/2\pi\tau$. If this constitutes the only broadening mechanism, the measured linewidth yields the lifetime directly. The technique is quite useful for very short lifetimes leading to broad lines. The lifetimes of inner-shell states connected by X-ray transitions can be determined in this way (see discussion in connection with Fig. 5.9). Short-lived states for external electrons can also be determined from the linewidth if the Doppler effect is totally eliminated and a single-mode laser of small linewidth is employed [1435].

ODR (Optical Double Resonance) **and LC** (Level Crossing). Here the natural radiative width is also determined directly. The contribution from Doppler broadening is negligible since the measurement is performed in the radio-frequency regime ($\sim 10^7$ Hz). Thus the Doppler broadening is about 10^8 times smaller than for optical transitions. In radio-frequency measurements, the lifetime is given by $\tau = 1/\pi\Delta\nu$ in the limit of vanishing RF field strengths. At higher field strengths a broadening of the signal occurs, since the perturbation is no longer negligible. In level-crossing experiments the lifetime is directly obtained from high-field crossing signals. If $I = 0$ or $I = J$, the Hanle signal is also easy to analyse, since only signal contributions of the same half-width occur ($\mathrm{d}\nu/\mathrm{d}B$ is the same for all contributing level pairs; $g_F = g_J/2$ for all F if $I = J$; see (7.33) and (2.45)). In the general case a superposition of signal contributions of different intensities and half-widths has to be analysed [1436].

Beam-Foil Techniques. The beam-foil method has been discussed in Sect. 6.1. It is a very general method for measuring lifetimes of atoms and ions. However, the non-selective excitation, leading to cascading decays, places heavy demands on the data analysis and sometimes a detailed study of the different cascade channels is necessary for reliable lifetime evaluations. While the non-selective excitation frequently constitutes a problem, it is also an advantage of the method since a multitude of excited states are populated. The technique provides unique measurement possibilities for measurements of multiply charged ions in particular, where other techniques are not applicable.

Beam-Laser Techniques. By exchanging the exciting foil in the beam-foil technique for a focused laser beam, selective excitation can be obtained and the problem of cascades is eliminated [1437]. By directing the laser beam at a certain angle θ with respect to the ion beam considerable Doppler shifts in the interaction with the fast beam are obtained. The relativistically correct formula for the interaction wavelength

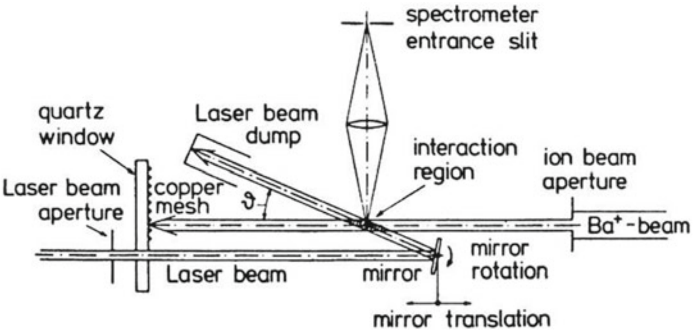

Fig. 9.26 Lifetime measurement with the beam-laser technique using Doppler tuning [1436]

λ_i, experienced by the ions that are illuminated by a laser of wavelength λ_ℓ is given by

$$\lambda_i = \lambda_\ell \frac{\sqrt{1 - \upsilon^2/c^2}}{1 - (\upsilon/c)\cos\theta}. \tag{9.11}$$

For $\upsilon/c = 1/100$ we note that Doppler shifts of several nm (see also Fig. 6.105!) are easily accomplished by varying θ. Measurements of this kind are illustrated in Fig. 9.26. A fixed-frequency laser (e.g., an Ar^+ laser) can be used owing to the possibility of Doppler tuning. The first experiments of this kind were performed for the resonance line of Ba^+ $6\,s\,^2S_{1/2} \rightarrow 6p\,^2P_{3/2}$ at 455.4 nm. The 454.5 nm laser line could be utilized by chosing $\theta = 23°$ for an ion velocity of 0.63×10^6 m/s.

The lithium and sodium transitions discussed above were studied with a precision of a fraction of one percent [1438, 1439]. A charge-exchange cell containing alkali vapour was used in the fast ionic beam to generate the neutral species. Theoretical calculations can accurately reproduce the experimental results [1440, 1441]. Since the transition wavelengths for ions of different charge states rapidly shift into the ultraviolet and VUV regions, due to the electronic shell contraction, and as CW lasers are scarce at such wavelengths, the applicability of this high-precision technique is unfortunately limited.

Time-Resolved Spectroscopy with Pulsed Lasers. We have recently discussed these techniques in the sections above.

Time-Resolved Spectroscopy with Pulsed Electron Beam Excitation. Abrupt excitation of atoms and molecules can be accomplished with a pulsed electron beam. In the same way as for the beam-foil interaction, non-selective excitation is obtained. One of the most efficient variations of this technique is the *high-frequency deflection* method [1442–1445], which is illustrated in Fig. 9.27. An electron beam of high power (~20 keV, 0.5 A) is deflected using RF deflection plates, as in an oscilloscope. The beam is swept over a slit and the repetition rate and pulse length can easily be selected. Time-correlated single-photon counting techniques (Sect. 9.4.2) are used

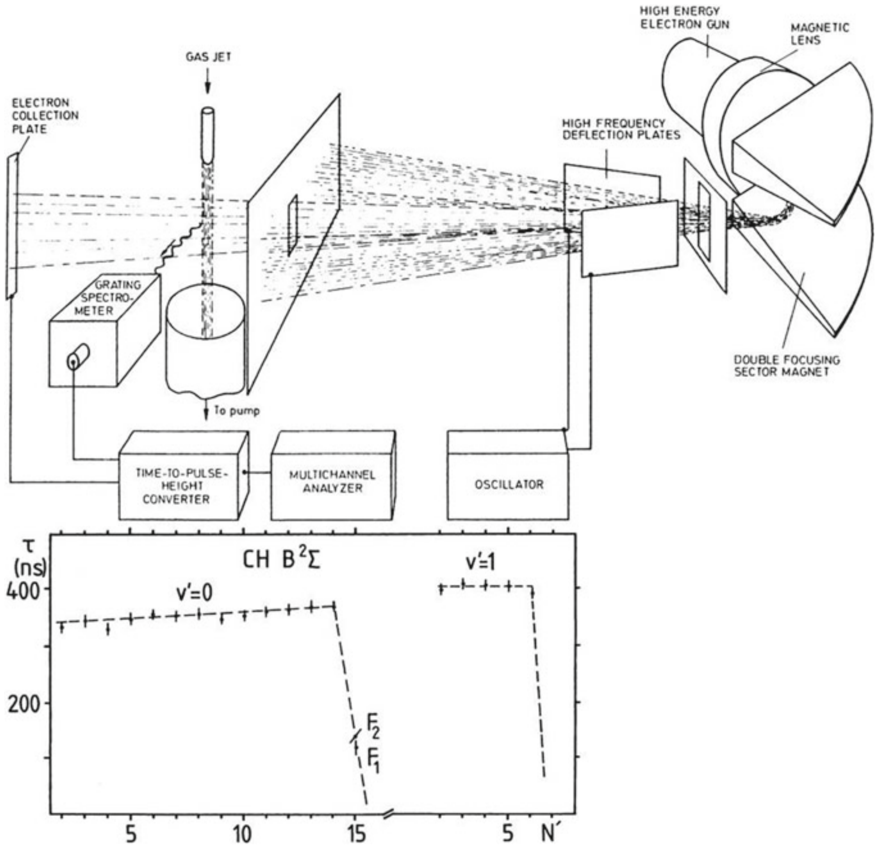
HIGH ENERGY ELECTRON GUN
MAGNETIC LENS
GAS JET
ELECTRON COLLECTION PLATE
HIGH FREQUENCY DEFLECTION PLATES
GRATING SPECTRO-METER
DOUBLE FOCUSING SECTOR MAGNET
To pump
TIME-TO-PULSE-HEIGHT CONVERTER
MULTICHANNEL ANALYZER
OSCILLATOR
τ (ns)
400
200
CH B²Σ
v′=0
v′=1
F2
F1
5
10
15
5
N′

Fig. 9.27 The principle of the high-frequency deflection method for lifetime measurements, and experimental lifetime data for the CH radical [1442, 1445]

to record the decay. Because of the high light intensity obtained with this technique, a high-resolution monochromator (with a narrow slit) can be used for the detection. This is of great importance, particularly in studies of molecules, for which individual rotational-vibrational lines can be isolated without blending., Cascade problems are frequently less severe for molecules than for atoms. Lifetime results for the CH molecule are shown in the figure illustrating the shortening of lifetimes for higher rotational levels due to predissociation at potential curve crossings.

Phase-Shift Method. In the phase-shift method, atoms or molecules are excited by a sinusoidally modulated light or electron beam, as illustrated in Fig. 9.28. Fluorescence light is recorded with a photomultiplier tube. This light will thus also be modulated, but because of the delay in the excited state a phase-shift is introduced [1446–1448]. At the same time, the contrast in the modulation is reduced. If light is used for the excitation, the phase shift can be determined by comparison with the

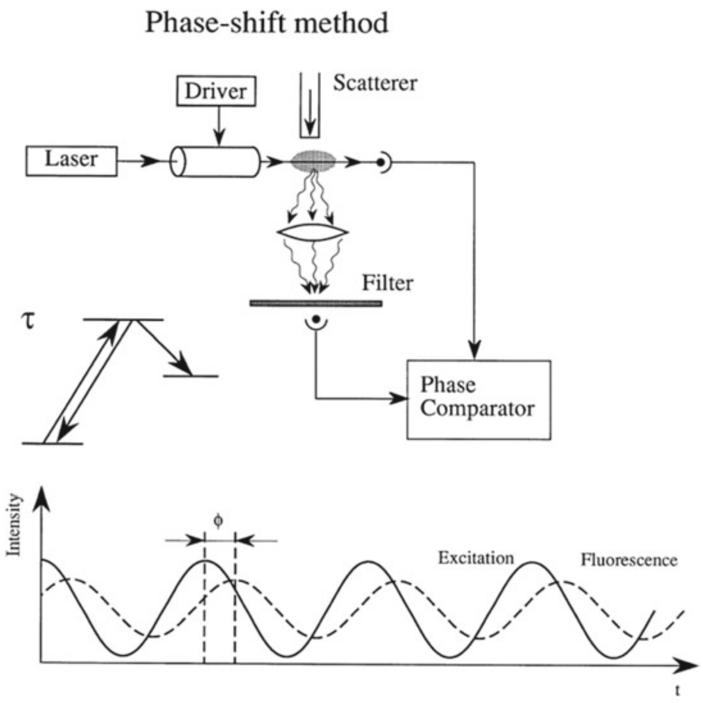
Phase-shift method
Driver
Scatterer
Laser
Filter
τ
Phase Comparator
Intensity
ϕ
Excitation
Fluorescence
t

$$I_{exc} = I_0 (1 + a \sin \Omega t) \cos \omega t$$

$$I_{fl} = bI_0 \left[1 + \frac{a}{\sqrt{1 + \Omega^2 \tau^2}} \sin (\Omega t + \phi) \right] \cos \omega t$$

$$\tan \phi = \Omega \tau$$

Fig. 9.28 The principle of lifetime measurements by the phase-shift method

signal that is obtained when stray light is sent directly into the detector by inserting a small scattering object into the light beam at the point of interaction. If the exciting light is described by the expression

$$I_{\text{exc}} = I_0(1 + a \sin \Omega t) \cos \omega t, \tag{9.12}$$

it can be shown, by integrating the exponential decays from the different excitation function time elements, that the fluorescence light intensity is given by

$$I_{\text{fl}} = bI_0\left(1 + \frac{a}{\sqrt{1 + \Omega^2\tau^2}} \sin(\Omega t + \phi)\right) \cos \omega t \tag{9.13}$$

with

$$\tan \phi = \Omega \tau. \tag{9.14}$$

If multiple-scattering processes occur, an erroneously long lifetime will be obtained, as for several of the above-mentioned methods. The opposite effect is obtained if, in addition to the fluorescence light, non-shifted stray light from the modulated light source is recorded. If the modulation is not perfectly sinusoidal, the first Fourier component can be isolated and the phase shift for this component will still yield the lifetime.

It should be noted that a higher accuracy in the phase-shift method is obtained if recordings are made for many different modulation frequencies. Compared to lifetime evaluations based on time-resolved spectroscopy following pulsed excitation, this corresponds to fitting the whole decay rather than finding the time when the intensity has fallen to 1/e (9.8).

The phase-shift method has more recently been used much in spectroscopy of biological tissue and other strongly scattering media for studying light propagation. Then it is frequently called *photon density wave spectroscopy* (Sect. 10.5.4).

We now turn to the determination of transition probabilities.

The Emission Method. If the effective temperature in local thermodynamic equilibrium is known, the relative strength of spectral lines from a light source can be used to calculate *relative transition probabilities*. Clearly, corrections for the wavelength-dependence of the spectrometer transmission and the photomultiplier sensitivity must be applied. This can be done by replacing the actual light source by a standard tungsten lamp (Planck radiator), which has been accurately spectrally calibrated. A large number of elements have been investigated by *Corliss* and *Bozman* using a standardized arc discharge [1449]. Actually, absolute values are given, but a correction factor of up to 5, as determined from normalizing lifetime measurements, must frequently be applied.

The Hook Method. The hook method is based on the *Kramer–Kronig dispersion relations*, which relate the refractive index of a gas to its absorption properties and thus to transition probabilities [1450, 1451]. The relations have at their base the fact, that a complex index of refraction $n*$ can be defined as consisting of a real part n (the normal index of refraction) and an imaginary part α (describing absorption) as expressed by

$$n^* = n + i\alpha. \tag{9.15}$$

At the same time as atoms in a vapour absorb at the transition frequency, an anomalous dispersion is obtained. (The increase in refractive index of transparent materials towards the UV region is related to the UV absorption of the material; see Figs. 6.20b and 6.54.) The relation between the absorption and dispersion at the sodium D lines is illustrated in Fig. 9.29 (top left). In the hook method, light from a continuum source is sent through a Mach–Zehnder interferometer, where a heat-pipe

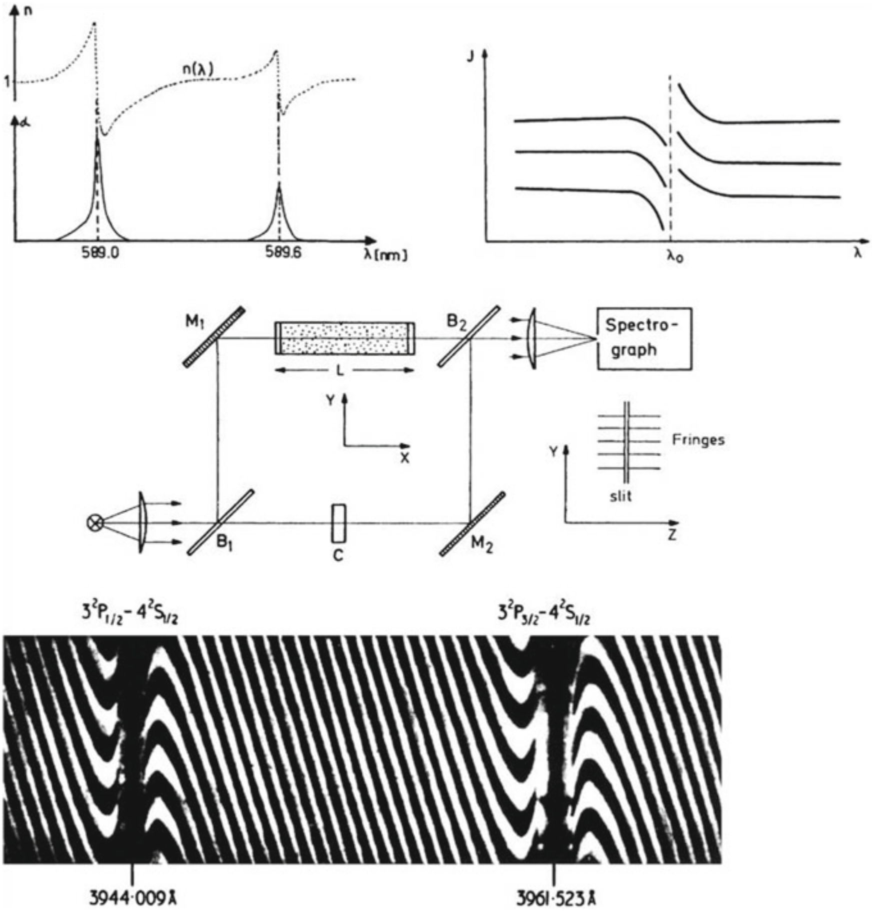

Fig. 9.29 Illustration of oscillator strength measurements. An experimental recording for the Al I resonance doublet is included [1232]

oven containing the metal vapour is inserted in one arm. The interference pattern is imaged as a function of wavelength through a spectrometer on a photographic plate. The abrupt change in refractive index at a line gives rise to the "hooks" in the recording. It can be shown that the product of the atomic density and the transition probability is proportional to Δ^2, where Δ is the hook separation. By measuring absorption as well as dispersion, absolute transition probabilities can in principle be determined.

At first it might seem surprising that transition probabilities related to the natural radiative lifetime and its corresponding small Heisenberg broadening can be measured in the presence of the much larger Doppler broadening. However, the technique is pursued for high atomic densities where the hooks occur some 0.1 nm from the line centre, as seen in Fig. 9.29. At this large distance from the centre the influence of the Doppler broadening, described by a swiftly falling Gaussian function (of type $y = e^{-x^2}$); 6.6) is negligible compared to the influence of the Lorentzian function (of type $y = 1/(1 + x^2)$; 4.40) due to the natural lifetime, although the half-width of the Gaussian is typically 100 times larger than for the Lorentzian. However, a Lorentzian has a much slower fall-off than a Gaussian.

The Hook method yields very accurate, reliable relative transition probabilities. A laser-based related technique, the "inverse Hook method", has also been introduced [1452].

As mentioned, the anomalous dispersion of a material around an absorptive structure is due to the coupling between the index of refraction and the absorption according to the Kramer–Kronig dispersion relations. A change in refractive index leads to a change in the velocity of light propagation through the medium. This velocity which is observed when a pulse propagates through a medium is referred to as the *group velocity,* while individual frequency components, which build up the pulse, propagate at the normal *phase velocity* (*c/n*) but in the resulting interference result in the observed group velocity. Based on the Kramer–Kronig equations the following relation between the group velocity v and the refractive index n and its derivative $dn/d\omega$ (related to the angular frequency of the radiation ω) can be derived:

$$v = \frac{c}{n + \omega \frac{dn}{d\omega}} \tag{9.16}$$

We note, that close to a sharp absorption line, where the slope $dn/d\omega$ can be very large, the (group) velocity can change very drastically, although the value of the index of refraction does not change drastically. The phenomena of *slow-light propagation* have been demonstrated very effectively in several experiments, where light could be almost "stopped". We will discuss such phenomena in Sect. 9.5.3.

9.4.5 Quantum-Beat Spectroscopy

We have already discussed quantum-beat spectroscopy (QBS) in connection with beam-foil excitation (Fig. 6.6). There the case of abrupt excitation upon passage through a foil was discussed. Here we will consider the much more well-defined case of a pulsed optical excitation. If two close-lying levels are populated simultaneously by a short laser pulse, the time-resolved fluorescence intensity will decay exponentially with a superimposed modulation, as illustrated in Fig. 6.6. The modulation, or the quantum beat phenomenon, is due to interference between the transition amplitudes from these coherently excited states. Consider the simultaneous excitation, by a laser pulse, of two eigenstates, *1* and *2,* from a common initial state *i*. In order to achieve coherent excitation of both states by a pulse of duration Δt, the Fourier-limited spectral bandwidth $\Delta\nu \simeq 1/\Delta t$ must be larger than the frequency separation $(E_1 - E_2)/h = \omega_{12}/2\pi$. If the pulsed excitation occurs at time $t = 0$, the wave function of the excited state can be written as a linear superposition of the eigenstates

$$|\psi(0)\rangle = \sum_k a_k |\phi_k(0)\rangle, \tag{9.17}$$

where the coefficients a_k are probability amplitudes for finding the atom in level k. Due to the exponential decay to the final level f, the time-dependent wave function is given by

$$|\psi(t)\rangle = \sum_k a_k |\phi_k(0)\rangle \exp(-\mathrm{i}E_k t/\hbar)\mathrm{e}^{-t/2\tau}. \tag{9.18}$$

The time-dependent fluorescence light intensity from the excited states is determined by the transition matrix element, (see (4.28) and (7.26)).

$$I(t) = C\left|\langle\phi_f\left|\boldsymbol{e_g}\cdot\boldsymbol{r}\right|\psi(t)\rangle\right|^2, \tag{9.19}$$

where $\mathbf{e_g}$ is the polarization vector for the detected light. Inserting (9.18) in (9.19) for the case of two sublevels yields

$$I(t) = Ce^{-t/\tau}(A + B\cos\omega_{12}t), \tag{9.20}$$

with

$$A = a_1^2\left|\langle\phi_f\left|\boldsymbol{e_g}\cdot\boldsymbol{r}\right|\phi_1\rangle\right|^2 + a_2^2\left|\langle\phi_f\left|\boldsymbol{e_g}\cdot\boldsymbol{r}\right|\phi_2\rangle\right|^2, \tag{9.21}$$

$$B = 2a_1a_2\left|\langle\phi_f\left|\boldsymbol{e_g}\cdot\boldsymbol{r}\right|\phi_1\rangle\right|\left|\langle\phi_f\left|\boldsymbol{e_g}\cdot\boldsymbol{r}\right|\phi_2\rangle\right|. \tag{9.22}$$

We note that a modulation is obtained ($B \neq 0$) only if the matrix elements for the transitions $1 \to f$ and $2 \to f$ are non-zero at the same time. A quantum–mechanical interpretation of the beats is based on the observation that it is impossible to determine whether the atom decayed via the transition $1 \to f$ or $2 \to f$. The total probability amplitude is therefore the sum of the two corresponding amplitudes; the observed intensity is the square of this sum and the cross-term gives rise to interference. If it had been possible to detect the transitions separately (spectrally, or by means of the polarizations), then the interference would have been lost. The situation here is analogous to that in Young's double-slit experiment. If attempts are made to determine through which of the slits the photon passes, the interference is lost. Note the very close relationship between quantum-beat spectroscopy and level-crossing spectroscopy. If time integration of the QBS phenomenon is performed, the LC phenomenon is obtained, for which continuous excitation and detection are used. Quantum beats are induced by a tunable laser with a short pulse duration (~5 ns).

If very fast beats are to be studied, the pulse must be correspondingly shorter (in order to obtain Fourier components spectrally overlapping both levels or, expressed differently, to ensure a sufficiently small initial spread in the wave function phase factors). With a mode-locked laser, pulse lengths in the ps and fs domains can be obtained (Sect. 8.7).

An example of Zeeman quantum beats is shown in Fig. 9.30. The geometries for excitation and detection are the same as for a recording of the Hanle effect (Sect. 7.1.5). The signal is also a $\Delta M = 2$ phenomenon. Zeeman quantum beats can also be explained semiclassically using the same model as was used for the Hanle effect (Fig. 7.15). The linearly polarized light (which has a σ^+ as well as a σ^- nature, Fig. 4.9) induces an oscillating *electric dipole* in the electron cloud, which will radiate with a dipole distribution, shrinking with a time constant of τ. Since the atom has a *magnetic dipole moment*, it will Larmor process (Sect. 2.3.1) in the external magnetic field and a radiation lobe will be turned in towards the detector twice every full revolution. The excited atom is a microscopic "light-house". The Hanle effect is the part of the Zeeman quantum beat that "survives" the time integration because of the common initial condition and slow lobe rotation in the field region of the Hanle effect. The situation was illustrated in Fig. 7.15. For high fields, the lobes pass in and out of the detector direction many times during the decay of the dipolar distribution. Thus, the fraction of time the detector is illuminated will become essentially independent of the field strength and the signal levels off.

From the semiclassical picture, it is also evident that the phase of the beat signal is changed by 180° if the linear polarizer for the case of signal detection in the direction of the magnetic field is turned by 90° (this corresponds to a sign change of the Hanle effect; see comments in connection with Fig. 9.18). Because of the phase inversion it is possible to eliminate the primary exponential decay by subtracting two signals of equal unmodulated light intensity but recorded for perpendicular detection polarizer

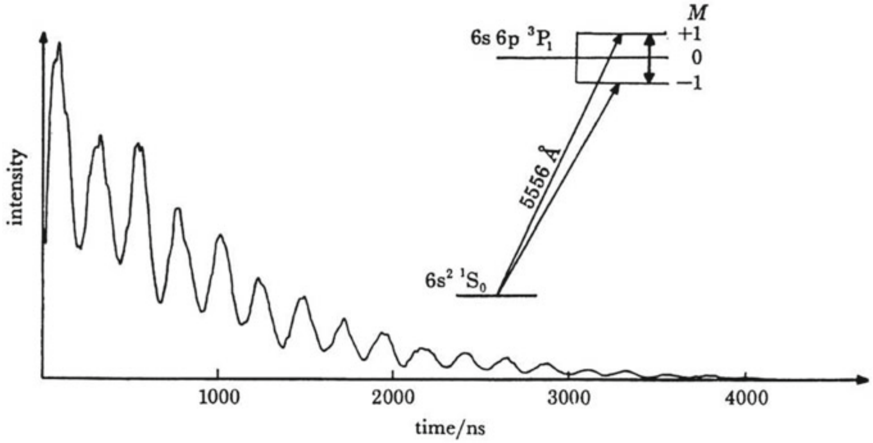

Fig. 9.30 Zeeman quantum beats for the resonance line in ytterbium [1453]

settings. When pure exponentials are desirable for lifetime evaluation, a sufficiently high magnetic field can be applied, corresponding to frequencies well above the cut-off frequency of the detection system, to wash out the quantum beats.

Although the general features of the quantum-beat phenomenon can be understood in a simple semiclassical model, a full quantum–mechanical description is required for calculating the correct relation between B and A in (9.20) to determine the beat contrast in the decay curve. Quantum-beat spectroscopy has been discussed in detail in [1454, 1455]. The phenomenon has also been observed in photo-electron spectroscopy (see; e.g., [1456]).

Fine- and hyperfine splittings also give rise to quantum-beat signals. For example, the hfs beats can be understood semiclassically by considering the radiating electronic shell processing at hyperfine frequency in the internal field due to the nucleus. $\Delta F = 1$ and $\Delta F = 2$ beats can be obtained in zero magnetic field. Hfs quantum-beat signals corresponding to two polarizer settings are given in Fig. 9.31. It can be shown that the beat amplitude is proportional to $3\cos^2\theta - 1$, where θ is the angle between the polarizers in the exciting and detection beams. (Thus, by making $\theta = \arccos(1/\sqrt{3}) \cong 54.7°$ ("magic angle") it is possible to suppress beats all together.) When many beat frequencies occur simultaneously, they can be isolated by a Fourier transformation from the time to the frequency domain. An example of hfs beats from the two stable gallium isotopes is shown in Fig. 9.32, and a corresponding Fourier transform is also given.

Quantum-beat spectroscopy as well as level-crossing and optical double resonance measurements using pulsed lasers are powerful techniques for high-resolution investigation of small energy intervals in a very wide wavelength region [1459–1461]. This is because pulsed lasers can be shifted to UV/VUV or IR wavelengths using nonlinear optical techniques (Sect. 8.6).

As a final point in this section, we discuss the question of increasing the spectral resolution beyond the natural radiation width$\Delta\nu_N = 1/2\pi\tau$. Different experiments have been performed, in which the observation after pulsed excitation is limited to "old" atoms, i.e., the detection system is activated after a certain delay such that only the atoms that have survived longest in the statistical process will contribute to the signal [1462–1467]. Normally, the whole exponential decay is utilized and in the integration from 0 to ∞ a Lorentzian of half-width $1/2\pi\tau$ is obtained in frequency space (Fig. 4.4). The Breit formula (7.25) describing the level-crossing phenomenon has been obtained through such a complete integration. Lorentzian crossing signals are then obtained. If the integration is performed from a delayed time T to infinity, oscillations in the signal wings are obtained but the central peak becomes narrower. The same is true for quantum-beat signals, for which the Fourier transform also narrows when integration is performed after a time delay. Clearly, a very strong loss in intensity is obtained. For example, after 4τ the intensity has been reduced to 1% of the original intensity. Thus, it is not at all clear that the information content has been improved by restricting the observation to "old" atoms. In special cases, e.g., if the signals are non-symmetric or overlapping, reduced systematic errors can be obtained if the linewidth is reduced in spite of the significant loss in intensity.

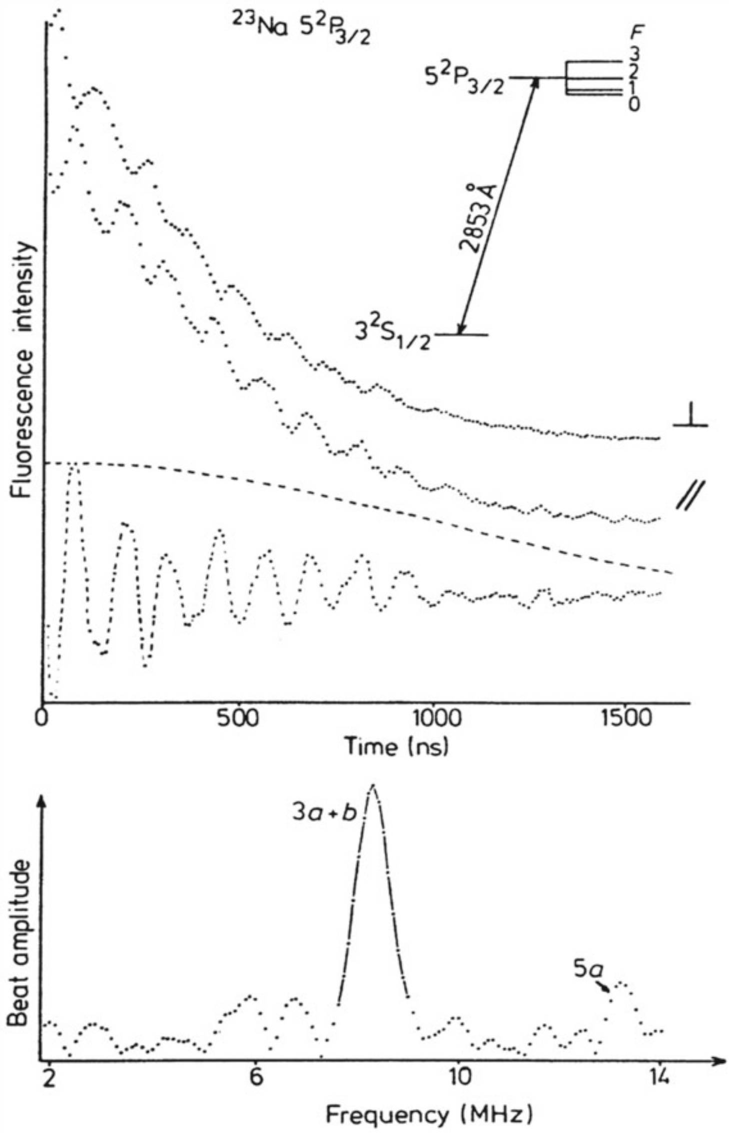

Fig. 9.31 Hyperfine quantum beats for a $^2P_{3/2}$ state in ^{23}Na recorded for two different polarizer settings [1457]

Examples of recordings, where the detection time interval has been manipulated, are shown in Fig. 9.33. In the upper part of the figure, the influence on overlapping level-crossing signals (improved resolution) is seen for the case of the $9d\ ^2D_{3/2}$ state of ^{133}Cs, reached by stepwise excitations [1467]. The sublevel system corresponding to this recording is of the type shown in Fig. 7.16, although the nuclear spin is now

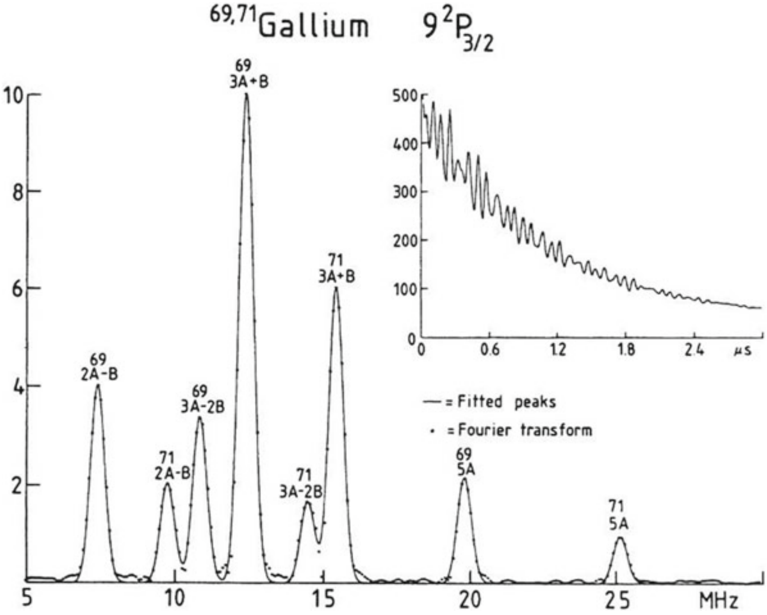

Fig. 9.32 Superimposed hyperfine quantum beats for the two stable gallium isotopes ^{69} Ga (60%) and ^{71} Ga (40%); both with nuclear spins $I = 3/2$, and the corresponding Fourier transform displaying the beat frequencies [1458]

$I = 7/2$. Time-gated recordings of Paschen–Back region optical double-resonance signals are shown in the lower part of the figure for the case of the $4d^{10}6p\ ^2P_{3/2}$ state of silver [1465]. The situation is similar to the one depicted in Fig. 7.11, although now with nuclear spin $I = 1/2$, resulting in $2I + 1 = 2$ RF signals. Since natural silver consists of two spin-1/2 isotopes, ^{107}Ag and ^{109}Ag, of about equal abundance and with magnetic moments differing by only 15 percent, each of the two signals actually consists of two closely overlapping contributions.

9.5 Ultrafast Spectroscopy

While the previous section mostly focused on time-resolved studies on the nanosecond timescale we will now describe how ultrafast processes, occurring on the pico- or femtosecond scale, can be investigated. Such fast phenomena mostly occur in the liquid or solid state and frequently are connected with energy transfer. Important and much-studied processes of this kind include photosynthesis, involving different light-harvesting antenna pigments, and the visual process, involving rhodopsin and other complex molecules. Ultrafast techniques also allow a detailed study of fundamental chemical reactions leading to dissociation or the formation of new molecules.

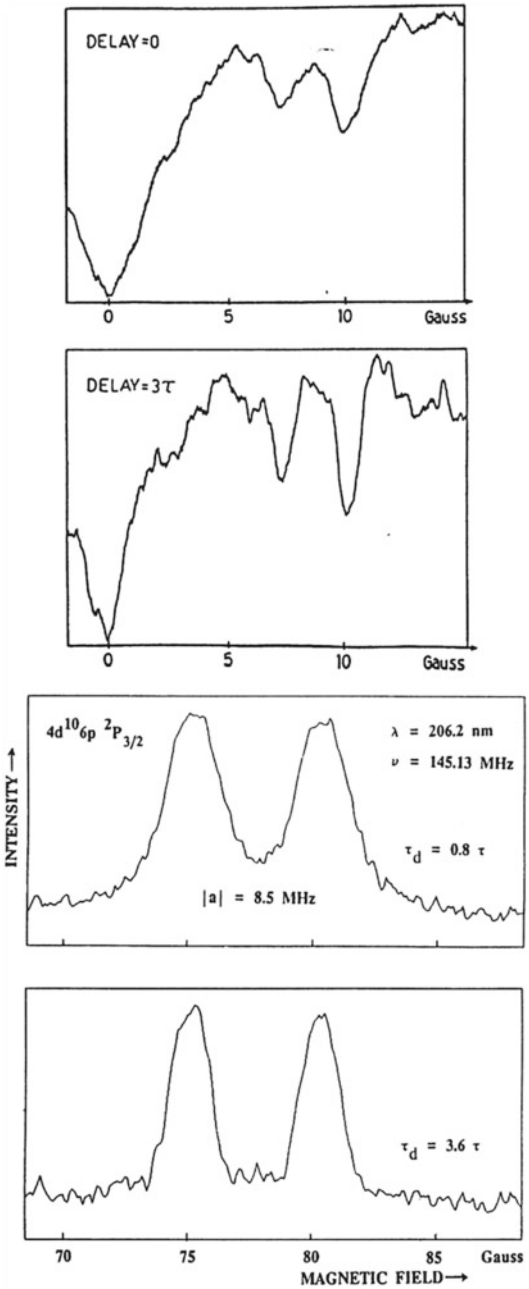

Fig. 9.33 Illustration of the influence on level-crossing (*upper part*) and optical double-resonance signals (*lower part*) due to the restriction of the recording to "old atoms" [1467, 1465]

Mode-locked lasers provide the necessary short pulse lengths (Sect. 8.7). Frequently, more energy than that directly available from mode-locked CW lasers is needed, e.g., for white-light generation (see below). Then the chirped-pulse amplification (CPA) technique can be employed (Sect. 8.7.2). Intermediate pulse-energy systems operating at 1-10 kHz repetition rate (employing Nd:YLF pump lasers) are then preferred to 10 Hz Nd:YAG-pumped high-energy systems, since photochemical decomposition of the samples studied must be avoided. We will now discuss ultrafast measurement techniques and consider some examples of ultrafast chemistry studies. General references to the field are given in [1468–1481].

9.5.1 Ultrafast Measurement Techniques

Boxcar integrators and transient digitizers discussed in Sect. 9.4.2 have a time resolution down to 0.5 ns or slightly better, also matching the rise time of the fastest photomultipliers available for optical measurements. The delayed-coincidence technique can be pushed further, to the tens of ps regime. This is because the clock trigging can be set to occur at a constant fraction of the full amplitude of a single-photon waveform using special *constant-fraction discriminator* electronics to eliminate time jitter due to statistical variations in the amplitude of photomultiplier photon signals. For faster measurements, streak camera or autocorrelation techniques can be employed.

Streak Cameras. For the recording of very fast phenomena, a *streak camera* can be used [1482–1484]. The principle is illustrated in Fig. 9.34. The incoming transient light impinges on a photo-cathode. The released electrons are accelerated, focused, and deflected by plates subjected to a rapidly rising voltage. The deflected electron beam hits a microchannel plate (Sect. 6.3) in which every electron gives rise to an electron burst. The temporal electron distribution gives rise to a streak of light on a phosphor screen. The intensity on the screen is proportional to the time-resolved light intensity. The streak is read off by a sensitive optical multichannel system (Sect. 6.3) and the intensity is displayed on an oscilloscope or relayed to a computer. By proper choice of cathode material, the streak camera can be operated for visible and UV wavelengths (see Fig. 6.40) or even X-ray wavelengths. In the latter case, normally thin cathodes made of CsI are employed. Since no appropriate window materials exist, the interface between the camera and the experiment must be a vacuum. Time resolutions down to 0.2 ps can be achieved [1484].

Autocorrelators. Autocorrelators work on the principle of “probing light by light”. The general idea in these types of measurement is given in Fig. 9.35. First we consider the case of studying the shape of ultrashort laser pulses. The incoming train of pulses is divided up in a beam splitter and part of the light is passed through a fixed delay line, while the other part is passed through a variable delay line. Pulses from the two arms are merged at a certain angle into a thin nonlinear crystal where phase-matching for frequency doubling in the bisectrix direction occurs if the two pulses arrive simultaneously. It can be shown that for Gaussian-shaped pulses the generated

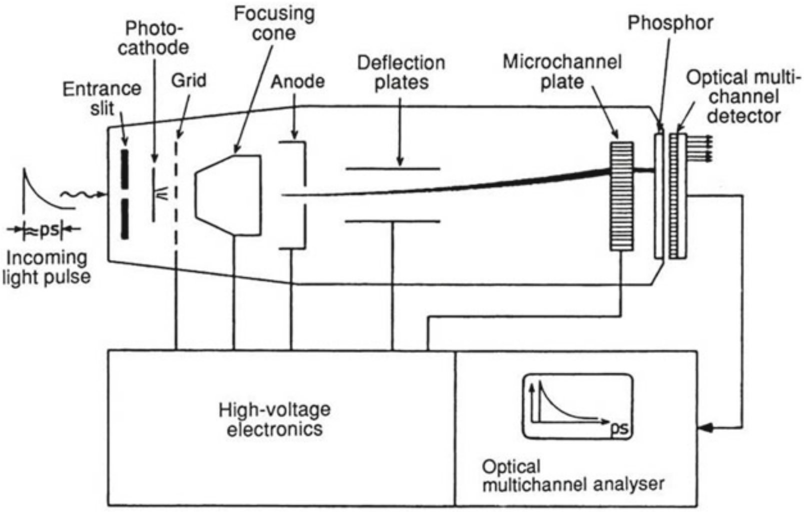

Fig. 9.34 The construction of a streak camera

UV intensity as a function of the temporal delay (the time) follows a curve with a half-width which is a factor of $\sqrt{2}$ broader than that of the incoming pulses. In autocorrelators of this kind, symmetrical curves are always obtained. Thus, it is not possible to separately monitor the leading and the trailing edges of a pulse. If a third-order process is used, e.g., a frequency-doubled pulse is correlated with the pulse itself using frequency tripling, it is possible to unravel the true shape of the pulse. By employing broad beams and an imaging detector it is possible to capture the temporal shape of individual pulses using geometrical delays across the detector.

Autocorrelators are very useful for optimizing the adjustments of ultrafast laser systems. This is particularly necessary when dealing with terawatt laser systems for high-power laser/matter interaction studies. Here the presence of an intensity pedestal around the main short pulse can be very detrimental. Generally speaking, it is very desirable to have *transform-limited* Gaussian-shaped temporal pulses, where the spectral contents are described by the Fourier transform, also a Gaussian. In complex laser amplification systems, the oscillator pulse is frequently distorted temporally by the fact that not all the frequency components building up the short pulse are amplified equally, mainly due to the limited spectral region where the amplification medium has gain (gain narrowing) and due to possible spectral clipping in the wavelength-dispersion arrangement of a CPA system. These modifications in the spectral content by necessity lead to modifications in the amplified pulse temporal behaviour after compression, e.g., the occurrence of an intensity pedestal. To allow a full characterization and manipulation of a pulse, it is necessary to monitor the temporal as well as the spectral contents and their interplay. Several methods have been developed for the purpose, e.g., the *frequency-resolved optical gating (FROG)* technique and the *spectral phase interferometry for direct electric-field reconstruction (SPIDER)*

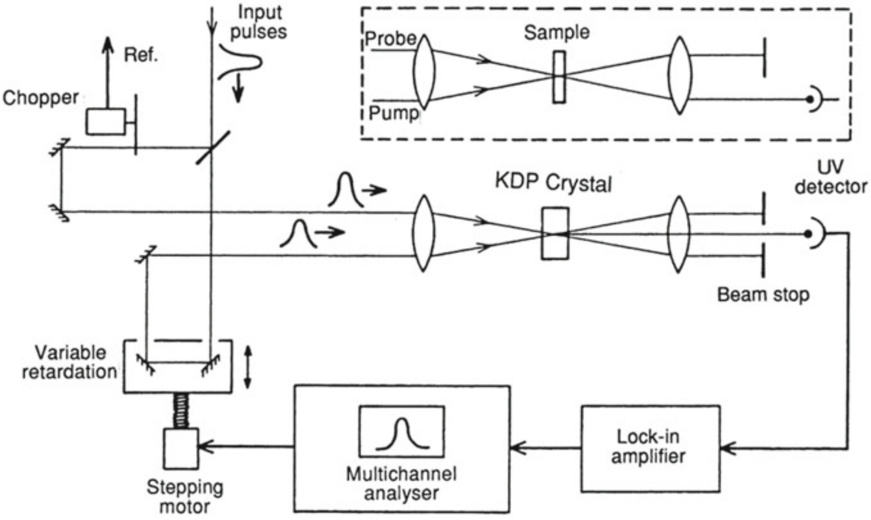

Fig. 9.35 The principle of pump-probe experiments using picosecond pulses (*insert*) and pulse-length determinations using autocorrelation with frequency doubling

technique [1485–1491]. The *d-scan* technique is a further new pulse characterization method [1492].

Many experiments on the femto- and attosecond scales require very high control of the laser pulses produced. Thus, the position of the oscillating field waves under the envelope defining the duration of the pulse needs to be fixed, which can be achieved by *carrier envelope phase (CEP) stabilization* schemes. This can be achieved with the $f-2f$ scheme, discussed in Sects. 8.7.2 and 9.7.5.

Pump-Probe Techniques

Pump-probe techniques are more general schemes, in which the temporal resolution comes from the short pulse duration and the possibility of defining temporal intervals by the corresponding spatial translations in optical delay lines (light travels 0.3 mm in 1 ps). Autocorrelators, as discussed above, operate on these principles, but the concept can be extended to the study of liquid or solid samples as indicated in the insert of Fig. 9.35. A *pump* pulse tuned to a certain frequency provides a partial depletion of the lower level, which is observed as a loss of absorption in the *probe* pulse. The two pulses can be of different frequencies if a primary short-pulse laser pumps a secondary source to generate new wavelengths by nonlinear optical methods or laser action. By delaying the probe pulse progressively, it is possible to see how fast the hole is filled in by *relaxation* processes. Alternatively, the excited-state population can be probed by letting the second pulse ionize or transfer the remaining atoms/molecules and then integrating the resulting signal using detectors and electronics that do not need to be ultrafast.

Optical parametric oscillators (OPOs) (Sect. 8.6) are very useful, widely tunable secondary sources of ultrafast pulses that find a wide applicability in pump-probe experiments. Two independent OPOs, which are pumped by the same laser for automatic synchronization and minimal temporal jitter, are particularly useful.

White-Light generation

In other experiments it is very convenient to monitor the action of a wavelength-selected pump pulse by a *white-light continuum* probe pulse [1493–1495]. If a beam of high-power pulses is focused onto a transparent solid or liquid (water is frequently used), a beam of “white” laser light will emerge. The reason for this white-light generation is self-phase modulation of the optical waves due to the rapid change in the nonlinear refractive index (8.20) of the medium in the rising and falling edges of the intense pulses. This fast refractive index change corresponds to the generation of new wavelength components as evidenced in a Fourier transformation from the time to the frequency domain. A very strong frequency broadening occurs, resulting in intense light covering the whole visible spectrum. The duration of this continuum is about the same as the generating pulse. The probe light can be dispersed by a grating (resulting in some temporal stretching) and imaged by a CCD detector. White light can be very effectively generated by focusing the ultrafast pulses into a photonic bandgap fiber, which contains many air-filled channels. Strong nonlinear effects occur due to the highly focused and confined radiation. Compact white-light sources are finding many applications, e.g., in optical coherence tomography (OCT) (Sect. 10.5.4.3). Intense terawatt pulses transmitted into the atmosphere cause ionization and filamentation associated with strong frequency broadening. White light lidar (light detection and ranging) systems are also being constructed [1496].

Recently, an unrelated mechanism for the generation of white light has emerged using CW infra-red laser sources interacting with certain materials, including semiconductors and graphene [1497].

Terahertz-Radiation Generation

Broadband radiation in the THz frequency region can also be generated using ultrashort laser pulses. *Terahertz time-domain spectroscopy* utilizes pump-probe techniques as well. If charged short antenna rods of a length of typically 50 μm are connected photoconductively by impacts from a train of intense laser pulses of ultrashort duration, broadband bursts of terahertz radiation (5 THz–100 GHz; 60-3000 μm) are generated [1498–1500]. This radiation can be collected by a mirror and sent through a sample, followed by radiation collection and detection in a THz detector, as illustrated in Fig. 9.36. The detector consists of a similar arrangement to the transmitting antenna and generates a signal only when it is made conducting by the impact of a gating pulse derived from the short-pulse laser. By sweeping an optical delay line between transmitter and receiver at a typical velocity υ of 30 cm/s ($\upsilon/c = 10^{-9}$), a time-resolved signal down-converted to the kHz region can be recorded as the beat note between the primary THz radiation and the Doppler-shifted detector-gating radiation. More recently, THz radiation has been generated more conveniently from *quantum-cascade lasers* (Sect. 8.5.5).

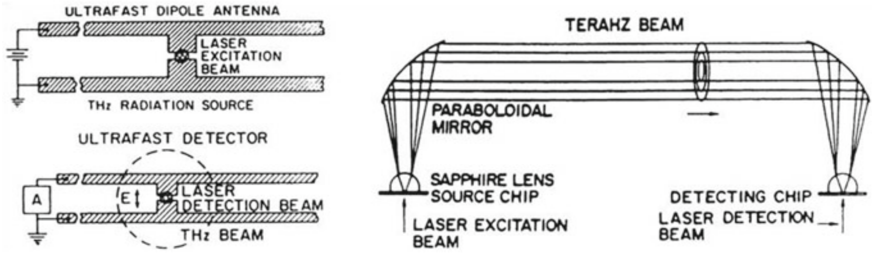

Fig. 9.36 Set-up for terahertz spectroscopy, and transmitter and receiving antennas [1499]

THz radiation penetrates most dry materials such as plastics, paper, and cardboard but is strongly absorbed in water (cf. Fig. 7.25) and other polar solvents, and is totally blocked by metals. Molecules in the gas phase absorb on rotational or vibrational–rotational transitions. Terahertz techniques allow applications such as luggage inspection and spectroscopic gas analysis. THz techniques can also be implemented for object imaging, including regarding passenger body screening at airport, with capacity to reveal, e.g., concealed weapons, including non-metallic ones. THz technology and applications based on the techniques described are discussed in [1501–1508].

9.5.2 Molecular Reaction Dynamics (Femtochemistry)

One of the most exciting possibilities of ultrafast laser techniques is to follow the course of fundamental chemical reactions on the relevant timescale at which they occur. Previously, it was only possible to know the individual states of molecules A and B before reacting and the final state of the compound molecule AB. In contrast, the details of the chemical reaction can now be followed on a femtosecond scale with information on how chemical bonds are formed and broken. In particular, the existence of *transition states* has been demonstrated. This new field of science is frequently referred to as *femtochemistry* [1509–1512], for which *A. Zewail* was awarded a Nobel Prize in chemistry (1999) [1513].

The study of the dissociation of sodium iodide (NaI) into sodium and iodine can serve as an example showing the power of ultrafast spectroscopy. A short pump pulse excites the molecule, which has an equilibrium separation of 0.28 nm, to a higher state as indicated in Fig. 9.37. Here the molecule starts to vibrate. At a nucleus separation of 0.69 nm, there is a large probability that the molecule falls back to the ground state (when the internuclear distance diminishes) or, alternatively, dissociates into free Na and I atoms (when the internuclear distance increases). The molecular dissociation process, depicted in the experimental recordings included in the figure, can be monitored by a femtosecond probe pulse tuned to excite the upper-state molecules from the potential bottom to a still more excited molecular state

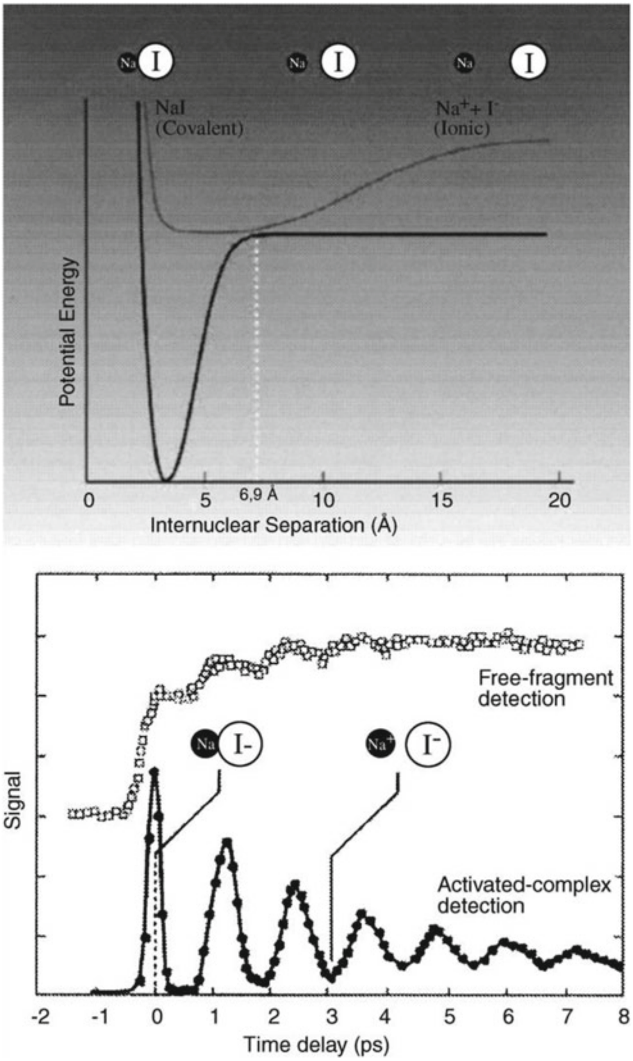

Fig. 9.37 Photodissociation of NaI by a short pulse. The energy-level structure is shown and experimental curves showing excited-state molecular vibration and the periodic release of sodium atoms are shown (Adapted from [1510])

(maximum signal). When the atoms move apart, the energy level moves upward and the molecule tunes out of resonance (minimum signal). The periodic release of dissociation products can be monitored if the probe pulse is tuned instead of the sodium D-line. The build-up in Na atom concentration through periodic additions of Na pulses can also be seen in the figure [1510].

An important question in chemistry is why certain bonds are more reactive than others and what happens if there are two equivalent bonds in a molecule subject to photodissociating light. Will the bonds break simultaneously or sequentially? In a study of tetrafluorodiiodoethane, $C_2I_2F_4$, it was found that the dissociation, freeing I atoms, is sequential; the first stage occurring about 200 fs after the pump pulse and the second one after about 20 ps (100 times longer) [1511].

A further type of reaction, which can be studied by femtosecond spectroscopy, is *photoisomerisation*, i.e., the optically induced transformation of one molecular geometrical structure into another. When *cis*-stilbene is excited by a femtosecond pulse, the central double bond is weakened allowing a rotation of the benzene rings to yield the *trans*-stilbene configuration (Fig. 9.38). The process occurs in 300 fs [1512]. Similar molecular twisting occurs in a timescale of 200 fs in retinal, which is part of the rhodopsin molecule active in the light absorption in the vision process. The schematic construction of a light-harvesting photosynthetic pigment is included in Fig. 9.38.

Ultrafast spectroscopy is now being refined with developments in many directions. One of them is 2D spectroscopy, which is related to *cold target recoil-ion momentum spectroscopy (COLTRIMS)*, where fragments from laser-induced interactions can be imaged with angular resolution and with regard to mass, and energy [1514].

Related to ultrafast spectroscopy is ultrafast imaging, where recently new approaches have been developed [1515–1520].

9.5.3 Coherent Control

Normally, only the frequency and the intensity of a light field are considered in the interaction of radiation with matter. With the availability of short-pulse radiation with well-defined phase properties, it has become possible to interact coherently with matter, opening up new possibilities of controlling chemical reactions and light-matter interactions. We will here consider two aspects of this quickly evolving field: coherent chemistry and interference effects profoundly changing the absorptive properties of matter.

Coherent Chemistry. Short-pulse laser radiation normally leads to broad and rather unspecific excitation of vibrational modes (See also Sect. 10.4). By tailoring the pulses, which typically would have a pulse length of 100 fs, by sending them into a pulse shaper, certain modes can be enhanced and others be suppressed. In particular, discrimination between chiral molecules (right- or left-handed) otherwise performing in an identical way could be considered. A pulse shaper is a stretcher-like arrangement (Sect. 8.7.2) with an electro-optical or liquid–crystal modulator between the gratings to modify the frequency contents. The modulator can be operated in a learning loop to achieve optimum spectral modification for enhancing selected spectral features.

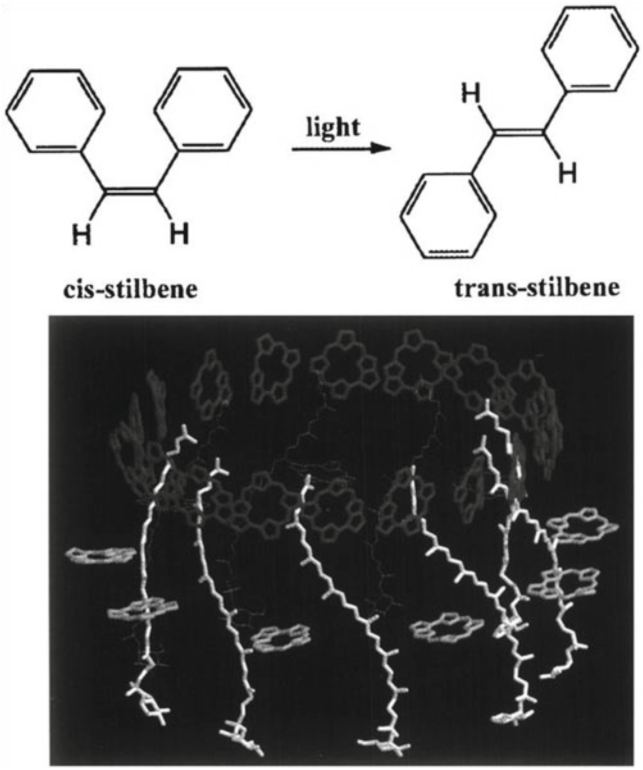

Fig. 9.38 Photoisomerization of stilbene (*upper part*), and the structure of a light-harvesting photosynthetic pigment (including chlorophyll and carotinoid building blocks) (*lower part*; Courtesy: V. Sundström)

By strongly driving certain vibrations, it might become possible to perform selective chemistry (Sect. 10.4) [1521–1525].

Electromagnetically Induced Transparency, Lasing Without Inversion, and Slow Light. The traditional requirement for population inversion in order to achieve gain in a laser has recently been challenged. As a matter of fact, it is possible to eliminate the lower state absorption by simultaneously pumping two suitably chosen transitions, for which a quantum-mechanical interference brings about an elimination of the absorption in a sharp wavelength region. The phenomenon is called *electromagnetically induced transparency* (EIT) [1526–1528] and forms the basis for various theoretical predictions of the *lasing without inversion* phenomenon, which has also been amply experimentally demonstrated [1527, 1529–1537]. The phenomenon is of particular interest for achieving powerful X-ray lasing with lower pulsed-pumping requirements, although a lot of the work in this field actually has been performed with narrow-band CW lasers.

The electromagnetically induced transparency leads to a very steep change in the index of refraction around the nominal transition frequency (see also Fig. 9.29). Still, the value is all the time close to 1, meaning that the phase velocity is very close to the speed of light in vacuum. However, a pulse of light contains different Fourier components which develop slightly different phase velocities and thus get out of phase with each other, leading to the pulse envelope travelling much more slowly than the individual frequency components. The pulse speed, or the group velocity, is basically inversely proportional to the slope of $n(\omega)$ (Eq. (9.16), and light velocities as low as 10 m/s have been observed in certain experiments, while light has been brought to a full stop in others [1538–1543]. In the latter case the photon is "absorbed" with a memory, and can be coherently emitted at a later occasion. Clearly, there is a connection to the concepts of *photon echoes*, mentioned in Sect. 7.1.6.

Using light beams propagating at low velocities means that very long interaction times become possible, ultimately enabling nonlinear optics to be performed at the single-photon level [1544, 1545].

9.6 High-Power Laser-Matter Interactions and Applications

High-power, short-pulse lasers, as described in Sect. 8.7.2, have made possible new types of basic physics experiments, and many applications are also emerging. Extremely high focused intensities can be obtained with the new types of sources. To get a feeling for the numbers involved we note that if 1 TW laser radiation is focused down to a 10 μm diameter spot size, a power density of about 10^{18} W/cm^2 is obtained, corresponding to an optical electric field strength of about 3×10^{10} V/cm. In comparison, it could be noted that an electron in the ground state of hydrogen experiences a Coulomb field of about 5×10^9 V/cm. Thus, instead of being a small perturbation to the atomic potential, as discussed in Chap. 4, the field interaction now becomes the dominant one, posing new challenges to theoretical atomic physics. Progress in this swiftly developing field is presented in [1546–1569].

9.6.1 Above Threshold Ionization (ATI)

The process of regular photoionization was considered in Sects. 5.2 and 9.1.4. The electron released in the photoionization attains a kinetic energy which equals the excess energy of the photon above the ionization limit I_{p}. Frequently, a multi-photon process is needed to attain sufficient energy for ionization. If the power of the ionizing field is increased and the energy of the electrons released is measured, e.g., by a time-of-flight spectrometer, several peaks are separated by the laser photon energy are observed, as shown in Fig. 9.39 [1570, 1546]. The electron can pick up the

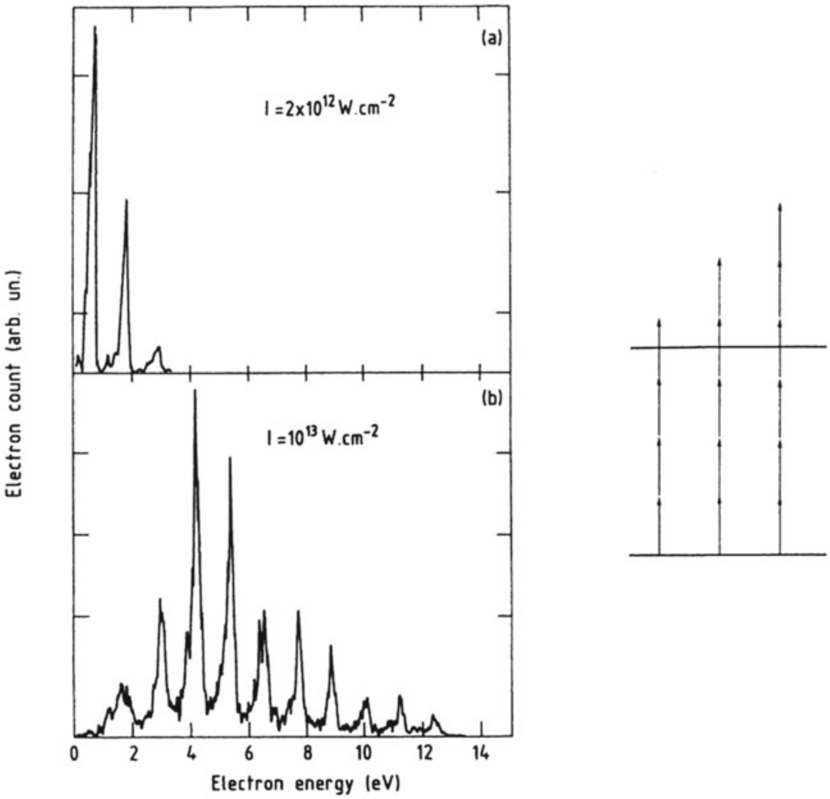

Fig. 9.39 ATI spectra for xenon atoms irradiated with intense pulses from a Nd:YAG laser (1064 nm, 1.1 eV). **a** Electron energy spectrum obtained for $I = 2 \times 10^{12}$ W/cm^2, **b** corresponding spectrum for $I = 10^{13}$ W/cm^2. The insert shows a schematic view of the lower-power process (From [1546])

total energy of several photons up to a maximum number determined by the power of the laser light. The strongly nonlinear process, which is schematically depicted in the insert of Fig. 9.39, is referred to as *Above Threshold Ionization (ATI)*. For not-too-high intensities (Fig. 9.39a), it can be described by perturbation theory and extensions thereof. Each peak corresponds to a certain order of perturbation theory, and the strength of the peaks correspondingly falls off quickly. However, if the intensity is increased (Fig. 9.39b) we see a completely different behaviour, indicating the breakdown of perturbation theory. New theory developments thus became necessary [1571–1577]. The oscillation (*quiver*) energy U_p of the external weakly bound electrons in the oscillating field E becomes non-negligible. U_p is frequently referred to as the *ponderomotive potential*:

$$U_\mathrm{p} = \overline{mv^2}/2 = e^2E^2/4m\omega^2 \tag{9.23}$$

Fig. 9.40 ATI spectrum for Ar atoms recorded for 616 nm (2 eV) pulses with a pulse length of 0.2 ps [1578]

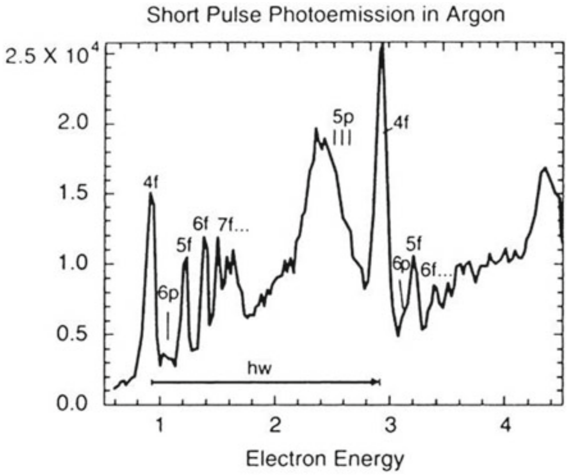

(e and m are the electronic charge and mass, respectively, and ω is the angular frequency of the light field $E\ \sin\omega t$; the mean value of $\cos^2\ \omega t$, occurring in the calculation, is 1/2). To free an electron from the atom, the additional energy of U_p is needed; thus the ionization potential I_p is effectively increased by this amount. Thus, a shift by U_p in the kinetic energy of the released electron is observed.

For even higher intensities and, in particular, when short pulses are employed, a strong AC Stark effect due to the electric field in the pulse is obtained. In the rising electric field of the laser pulse, real atomic energy levels are swept into resonance, temporarily increasing the ionization yield [1578]. This gives a stronger weight to certain energies in the monitored spectrum, which starts to display features related to the atomic bound states, as shown in Fig. 9.40.

When molecules are subjected to high-power laser radiation, ionization occurs, but of course so does also violent photodissociation. When a lot of electrons are removed, the remaining highly charged atoms cannot stay together; a *Coulomb explosion* occurs. High-power dissociation processes are discussed in [1579–1584].

9.6.2 High Harmonic Generation

When a high-power laser beam is focused onto a gas jet of inert gas atoms, odd *high harmonics* are generated [1585, 1586]. Even harmonics are not obtained due to symmetry considerations. The process clearly is in competition with the ATI phenomenon just discussed. High-harmonic generation is now quite well understood [1587–1589] and early overviews are given in, for example, [1590, 1591]. The first step is a tunnelling of an external electron through the barrier due to the Coulomb field combined with the electric field of the laser light. The situation is similar to the one shown in Fig. 2.14. The electron is accelerated in the optical field and is then

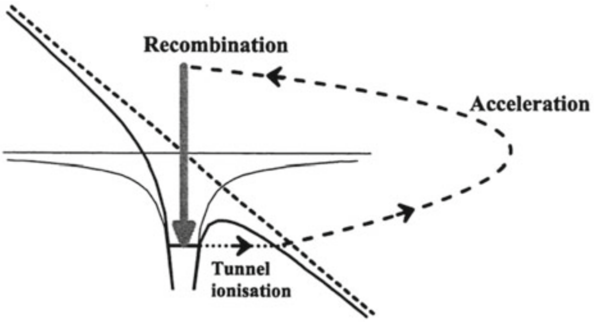

Fig. 9.41 Schematic description of high-harmonic generation in atoms [1592]

forced back towards the nucleus when the field switches direction. Passing in the vicinity of the nucleus, it recombines with the ion and harmonic radiation is emitted, as schematically shown in Fig. 9.41 [1592]. The fact that only odd harmonics are generated in gases is related to that the same situation regarding the potential is occurring twice for every optical cycle. The highest order harmonics are obtained for the light inert gases such as He and Ne, but the most efficient generation of lower harmonics is in the heavy gases such as Kr and Xe. Experimental recordings of high harmonics are shown in Fig. 9.42 [1593]. Among early studies of high-harmonic generation, the 109th harmonic for a titanium sapphire laser at 806 nm, [1594], the 143rd harmonic for a Nd:Glass system at 1053 nm [1595], and the 37th harmonic of a KrF laser at 248 nm [1596] were reported. Using ultrashort pulses with pulse lengths below 10 fs employing titanium sapphire technology, it became possible to reach the water window [1597, 1598] (see also Fig. 5.15), corresponding to harmonic orders of about 200. The reason that the water-window could be reached with short-pulse lasers but not with the longer pulses is that an ultrafast rise time leaves less time for competing ionization. Much effort has been put into understanding the high-frequency cut-off for the harmonics. Considering the single-atom response only, the cut-off is given by [1587–1589].

$$E_{\text{cut-off}} = I_{\text{p}} + 3.2U_p, \tag{9.24}$$

where I_{p} is the ionization potential and U_{p} is the ponderomotive potential. Experimentally an earlier cut-off is observed [1594]. This is because of phase mismatch in the collective generation by an ensemble of atoms. Also this effect is now well understood, and remedies have been implemented. Generally speaking, and maybe counter-intuitive, in order to generate short harmonic wavelengths, it is favourable to use a long wavelength λ for the driving laser field, since according to (9.23) U_p is proportional to λ^2.

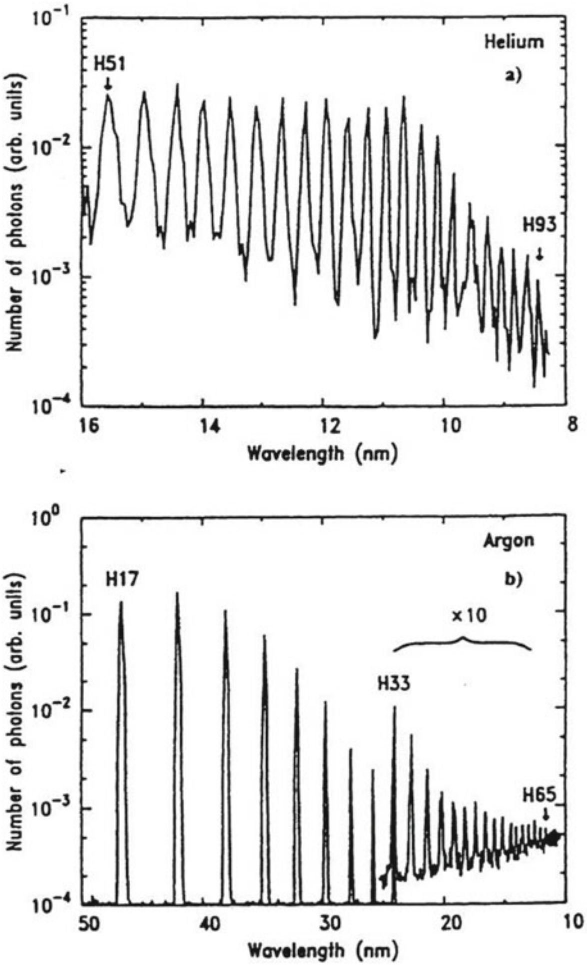

Fig. 9.42 Harmonics from He and Ar pulsed jets when the focused laser intensity was approximately 10^{15} W/cm^2 [1593]

In the process of developing high harmonics into an attractive general-purpose source of spectroscopic radiation much effort has been invested in optimizing the generation efficiency with regard to focus geometry, gas density, etc., and many studies along these lines, as well as for the temporal and spatial characterization, have been performed [1599–1607].

Harmonics can also be obtained from laser-produced plasmas with ionized atoms (which can be selected from large parts of the periodic system) [1608, 1609]. When high-intensity radiation impinges on a solid surface, a plasma with a very strong density gradient is formed and electrons will get a very anharmonic motion, resulting in the generation of even and odd harmonics [1610–1613]. It should be noted that short-pulse harmonics are for Fourier-transform reasons by necessity broad, putting limitations on the spectral resolution.

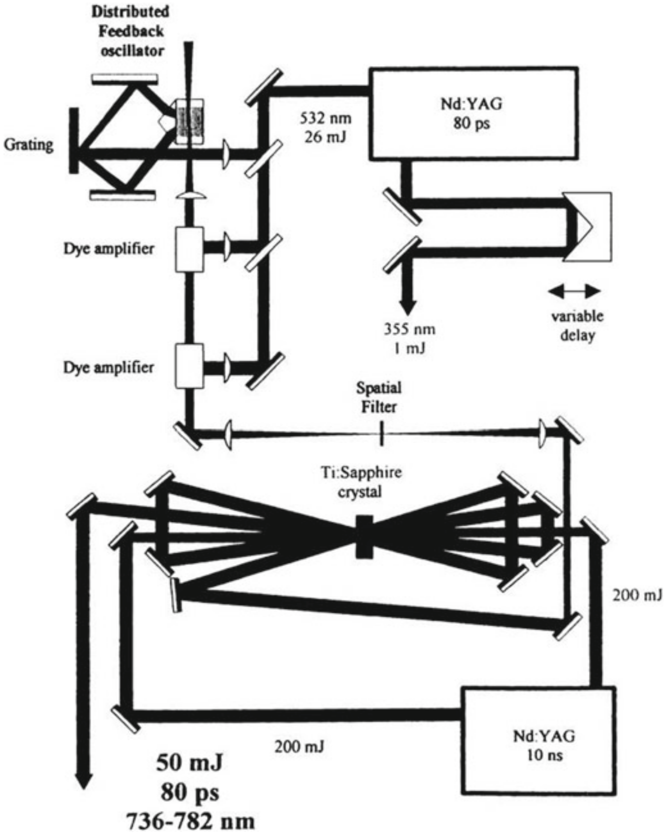
Distributed Feedback oscillator
Grating
532 nm
26 mJ
Nd:YAG
80 ps
Dye amplifier
Dye amplifier
355 nm
1 mJ
variable delay
Spatial Filter
Ti:Sapphire crystal
200 mJ
200 mJ
Nd:YAG
10 ns
50 mJ
80 ps
736-782 nm

Fig. 9.43 Lay-out of a spectroscopic high-peak-power, fully tunable combined dye/Ti:S laser system, suitable for the generation of narrow-band, tunable harmonics [1622, 1623]

The harmonics are particularly attractive in terms of the radiation peak power, which can be many orders of magnitude higher than for synchrotron undulators. Thus, the field of nonlinear laser spectroscopy in the short-wavelength (10 nm) range opens up [1614]. A competing technology, which requires much larger installations, is *Self-Amplified Spontaneous Emission used for Free-Electron Laser* action *(SASE-FEL)* [1615–1620]. (See also Sect. 6.1.3). Here it is of interest to use a well-defined high-harmonic component as the injector for further SASE-FEL amplification (see, e.g. [1621]).

Harmonics are tunable when the primary laser radiation is obtained from a tunable laser, such as a titanium-doped sapphire laser. However, the need for wavelength-dependent adjustments in the CPA chain can make the tuning procedure tedious. The laser system illustrated in Fig. 9.43 is easier to tune [1622, 1623]. A *distributed feedback dye laser* (DFDL) oscillator [1624–1628] is used, where the wavelength selection is performed by changing the angles of the two short-pulse Nd:YAG pumping

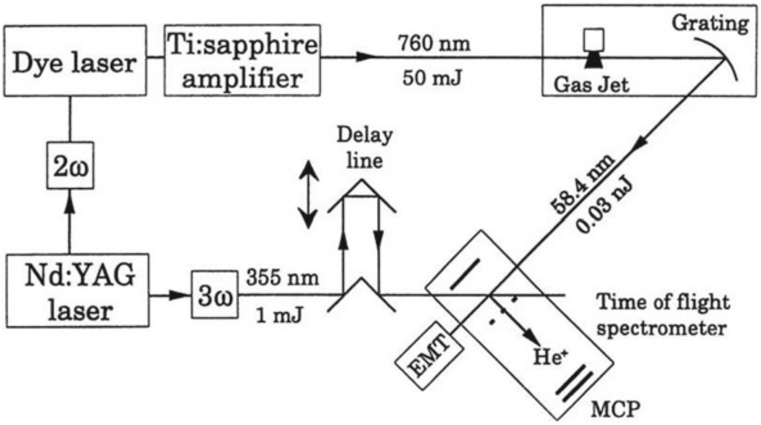

Fig. 9.44 Set-up for delayed photoionization measurements on helium atoms, excited by high-harmonic radiation [1622]

beams, changing the separation of the gain regions set up by constructive light interference in the dye. Fine tuning can be achieved by changing the temperature of the dye. Two dye amplifier cells and a multi-pass titanium-sapphire final amplifier are used to boost the 30 ps pulses to power density levels close to the material damage limit. Since the CPA techniques are not used, the entire system tunes easily together with the DFDL oscillator. The peak power is still enough for this system to generate low harmonics (7th–21st) in a jet of Kr or Xe. In this way a very interesting fully tunable laser source for the XUV region has been achieved, featuring a high spectral resolution feasible with pulse-lengths of tens of ps, rather than tens of fs.

As discussed in Sect. 9.4.3, experimentally determined radiative properties of free atoms and ions are of great interest for testing atomic theories, and more practically, for astrophysics, plasma and laser physics. With the availability of the Hubble Space Telescope, the VUV spectral region, out of reach for terrestrial observation, has become accessible and there is a great need for accurate data in the short-wavelength region. The most straightforward way to measure excited-state lifetimes is to perform a selective laser excitation and then observe the exponential decay of the light intensity from the excited state [1408–1416]. Such measurements are described in Sect. 9.4.2. The VUV region can be assessed by stimulated Raman scattering or by four-wave mixing (Fig. 8.44). Narrow-band harmonic generation as discussed here gives access to even shorter wavelengths (the XUV region). The available energy for the excitation is low, and direct fluorescence light observation is not possible. Instead, a more efficient detection method using a pump/probe scheme (Sect. 9.5.1) can be used to follow the decay. Such a technique using optical delays of the probe beam also eliminates problems with limited time response for the detection system. As an example, a measurement of the radiative lifetime of the $2p\,^1P_1$ states of helium is chosen [1622]. The experimental set-up used is shown in Fig. 9.44. To excite the $2p$ state (with a transition energy of 21 eV, i.e., 58.4 nm), the DFDL in Fig. 9.43

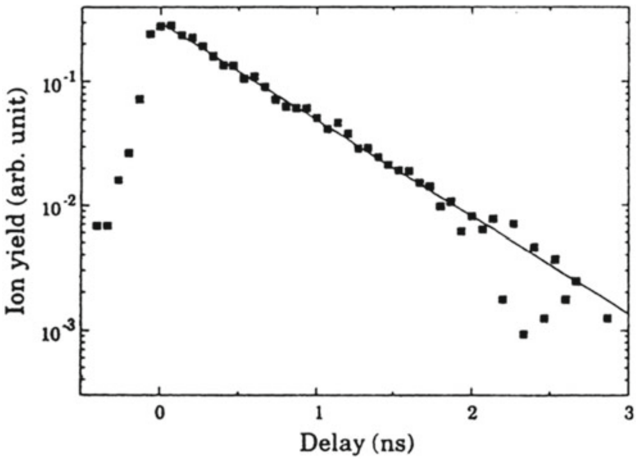

Fig. 9.45 Experimental decay curve for the $2p\ ^1P_1$ state of He [1622]

was tuned to 760 nm and the 13th harmonic was selected with a normal-incidence spherical grating. Helium atoms were excited and the number of excited atoms was probed by photoionization using a temporally delayed pulse, chosen to be the second or the third harmonic of the Nd:YAG pump laser. The resulting ions were detected by a microchannel plate detector after passage through a time-of-flight (TOF) spectrometer that was tuned to the helium mass. An experimental decay curve for the $2p$ state is given in Fig. 9.45. The techniques can also be extended to the study of radiative properties of simple molecules with absorption in the VUV spectral region and also to perform nonlinear laser spectroscopy [1629, 1630].

The tunability of such a system could also be utilized for measuring autoionization widths of Rydberg states of molecules [1631]. More fundamentally, similar techniques, emphasizing a maximal resolution, have been used for studies of the He atom, yielding accurate Lamb-shift data [1632, 1633].

Photoionization experiments are conveniently performed with monochromatized synchrotron radiation. However, if a high temporal resolution is required, harmonics provide unique possibilities [1634–1636].

Harmonics constitute a source of coherent XUV radiation that can be utilized for interferometric measurements of electron densities in plasmas, which cannot be studied with visible radiation because of strong refraction and absorption by the plasma. A very high temporal coherence is obtained using short-pulse high harmonics [1637–1639].

9.6.3 Attosecond Generation and Spectroscopy

An important application of high-order harmonics is their use for generating a train of attosecond pulses [1640], recognizing the conceptual similarity between the energetically equidistant high-order harmonics and the cavity modes in a CW laser, which can be locked together for femtosecond pulse generation (Sect. 8.7.1). The challenge is to assure phase-locking and to isolate individual attosecond pulses, and different approaches have been suggested and demonstrated [1641–1655]. Pulses of a duration of about 10^{-16} s (100 as, corresponding to the classical orbiting time of a ground-state hydrogen electron or the vibrational time period in small molecules) are achievable, opening up a new field of ultrafast spectroscopy. Measuring techniques on this timescale have been developed. It is interesting to note that attosecond pulse generation requires a very wide bandwidth, about 20 eV (see (8.19)), which can be understood from the Heisenberg uncertainty relation or, more technically, from the mathematical properties of the Fourier transform. Such a wide frequency range is only available in the high-frequency domain, well beyond the visible region ($\nu = 5 \times 10^{14}$ Hz).

Molecular dynamics, e.g., regarding vibrational motion and energy transfer within complex molecules occur on the fs scale. In contrast, electron dynamics are much faster. An interesting aspect is to investigate the process of photo-ionization in atoms. Traditionally, such processes, like Raman scattering, were considered to be instantaneous. However, using attosecond spectroscopy it has been shown that this is not the case. While absolute time constants are difficult to measure, it has been shown that photoionization from the $3s^2$ and the $3p^6$ shells of argon occurs with a relative delay of about 100 as [1656]. Subsequently, many detailed studies of photoionization processes have been performed (see, e.g., [1657]). Data from these types of experiments are shown in Fig. 9.46, where a technique denoted *reconstruction of attosecond beating by interference of two-photon transitions (RABBIT)* is used for data recording.

In the quest to achieve short-wavelength harmonics and shortest possible attosecond pulses it is, as mentioned earlier, favourable to start with a mid-IR laser as discussed earlier, because of the wavelength dependence in the generation of very high-order harmonics. This is illustrated in Fig. 9.47a, where different atomic processes, energy, and time scales are indicated.

9.6.4 X-Ray Laser Pumping

Achieving population inversion in the X-ray regime is difficult because of the strong probability of spontaneous emission for such frequencies (8.1). As mentioned in Chap. 8, soft X-ray lasing was first demonstrated in neon-like selenium, yielding emission at about 21 nm [1658]. Since then an intense research activity has been pursued [1658–1675] involving mainly *collisional and recombination schemes.*

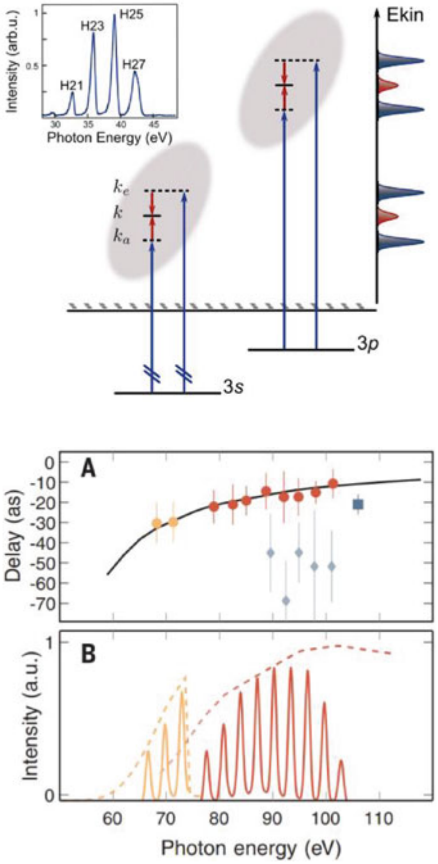

Fig. 9.46 Photoionization delay studies with attosecond time resolution. Photoionization occurs due to absorption of a photons generated from carrier-envelope-locked high-harmonics of an IR short-pulse driver laser. The process is observed with the RABBIT technique, in which interference is observed between one channel, where one harmonic photon is non-linearly subtracted by an IR photon and another one, where an IR photon is instead added to the lower energy neighbouring harmonic. The interference pattern observed in the emitted photoelectrons oscillates with the time delay between the VUV and IR photons, which are derived from the same intense laser. Top: Photoionization pathways from the 3 s and 3p levels in neon ([1656], Creative Commons Attribution 3.0 License, APS). Bottom: Measured photon-energy dependent delays for the case of the 2s and 2p levels in neon, well agreeing with a theoretical calculation. The points below the theory curve relate to shake-up processes (Sect. 5.2.2) ([1657], reproduced with permission from AAAS)

Initially, very large lasers with low repetition rates had to be used for achieving X-ray lasing. A wavelength of 3.5 nm was achieved for collisional pumping of nickel-like gold [1676]. The neon-like zinc laser at 21.2 nm is particularly efficient and easy to operate, and has been employed in applications [1677, 1678].

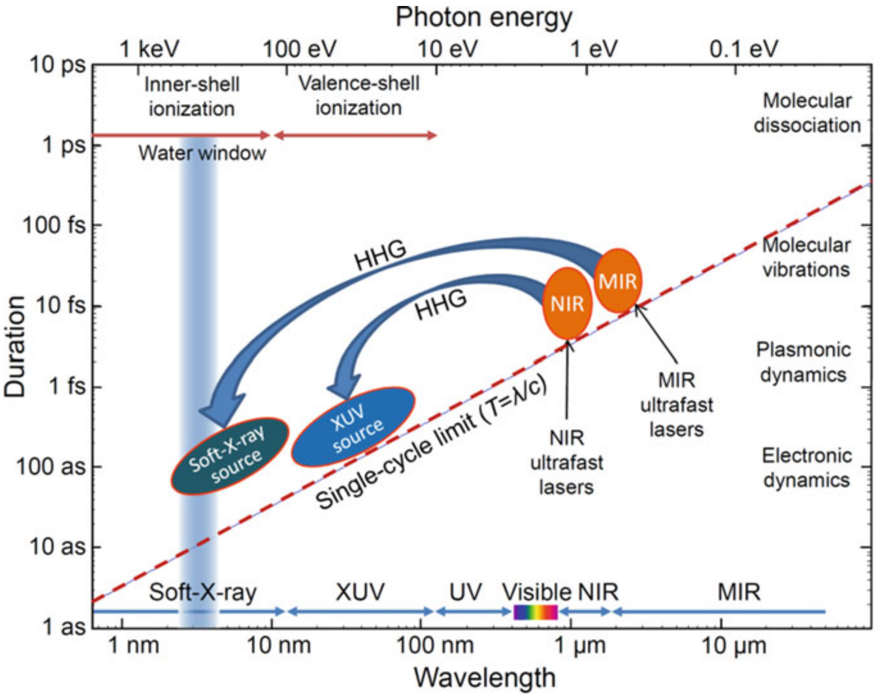
Photon energy
1 keV
100 eV
10 eV
1 eV
0.1 eV
10 ps
1 ps
100 fs
10 fs
1 fs
100 as
10 as
1 as
Duration
Inner-shell ionization
Valence-shell ionization
Water window
Molecular dissociation
Molecular vibrations
Plasmonic dynamics
Electronic dynamics
HHG
HHG
NIR
MIR
Soft-X-ray source
XUV source
Single-cycle limit (T=λ/c)
NIR ultrafast lasers
MIR ultrafast lasers
Soft-X-ray
XUV
UV
Visible
NIR
MIR
1 nm
10 nm
100 nm
1 μm
10 μm
Wavelength

Fig. 9.47a Diagram over laser/matter interactions on different time scales and in different wavelength ranges. Enabling laser technology with the generation of high harmonics and attosecond pulses is included. The diagram shows how XUV harmonics and attosecond pulses can be generated using a near-IR (NIR) laser source, while soft X-ray harmonics and attosecond pulses are best generated from a middle-IR (MIR) source. The position of the "water window" region (see Fig. 5.15) is indicated. (Courtesy: Cord Arnold, Lund University)

The development of high-repetition rate and moderate pulse-energy systems as described in Sect. 8.7.2 has opened the possibility of achieving more practical soft X-ray lasers. Special attention has been given to *optical field ionization* (OFI) schemes [1679] using gaseous media. Detailed spectroscopy of laser-produced plasmas is needed for locating gain line candidates. The experimental set-up is then very similar to the one used in the studies of high-harmonic generation. Search for gain can be performed by observing the emission of the laser-produced gas plasma in the forward direction and in a perpendicular direction. Gain is manifested by stronger forward emission for certain lines and has been identified, e.g., for ionized nitrogen and oxygen [1680, 1681]. Particularly spectacular is the demonstration of strong amplification in Xe^{8+} at about 42 nm [1682], as illustrated in Fig. 9.47b. Efficient soft X-ray laser emission in neon-like argon at 46.9 nm has also been achieved using a strong capillary electrical discharge in argon gas [1683]. A historical account of the development of X-ray lasers is given in [1684].

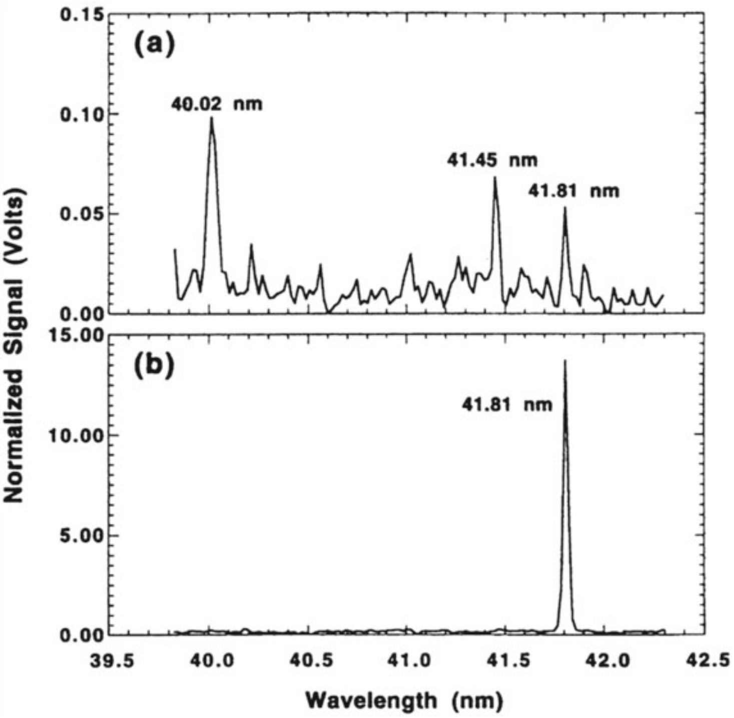

Fig. 9.47b Emission lines of Xe^{8+} for gas pressures of 3 and 12 torr, respectively (note the × 100 change in scale). The strong amplification of spontaneous emission at about 42 nm is clearly demonstrated [1682]

9.6.5 Broadband X-Ray Generation

By focusing sub-picosecond terawatt pulses on solid targets consisting of atoms with a high nuclear charge Z, intense X-ray radiation can be obtained. An experimental set-up for such experiments is shown in Fig. 9.48a. In contrast to the situation when nanosecond pulses are employed, there is no time for the formation of an expanding plasma that would shield off the main part of the impinging pulse. Thus, femtosecond laser pulses may lead to the formation of a solid-density plasma. The plasma radiates at all wavelengths, from microwaves to hard X-rays. It was early shown that photon energies of the order of MeV can be obtained [1685, 1686]. The measurement of the spectrum poses difficult problems since the radiation is produced in ultrashort (10^{-12} s), extremely intense bursts followed by intermissions that are typically 10^{11} times longer. Thus, solid-state detectors, developed for low-intensity conventional X-ray and γ-ray spectroscopy, are hampered by heavy pile-up problems. By using energy-dispersive detectors in Compton-scattering geometry, or specially developed X-ray spectrometers, it is still possible to characterize the spectrum [1687, 1688], which consists of a broad continuum with superimposed characteristic lines. The new

Fig. 9.48a Experimental set-up for the generation of ultrashort broadband hard X-ray radiation [1691]

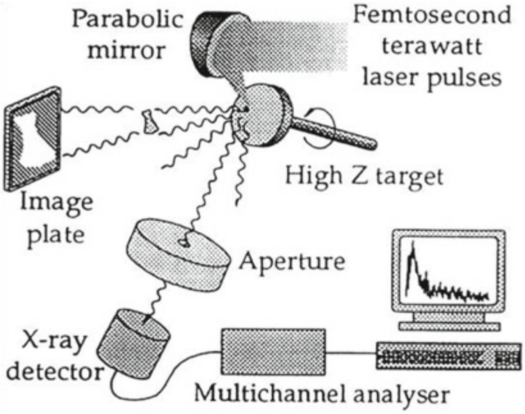

X-ray source has special properties and can have medical applications, as already discussed in Sect. 5.1.3. Imaging on standard radiological image plates using a laser-driven X-ray source was early demonstrated [1686, 1689].

Differential absorption radiography using monochromatic X-rays above and below the K absorption edge of a contrast agent such as iodine (33 keV) has been demonstrated using synchrotron radiation for angiographic applications [1690]. Such measurements using the characteristic lines from Gd and W targets bridging the K-edge (at 50 keV) of gadolinium have also been demonstrated [1691].

The extremely short duration of the X-ray burst can be utilized for gated viewing through tissue in order to eliminate Compton-scattered X-rays blurring the image. While multiple scattering is massive in the optical regime, calling for the development of reduced-scattering methods for optical mammography as will be discussed in Sect. 10.5.4.2, elimination of the less prominent X-ray scattering, particularly for thick tissue imaging, can be advantageous from a dose-reduction point of view [1692]. Monte Carlo simulations on X-ray transport through tissue give insight in the process, and experiments employing an X-ray streak camera for one-dimensional imaging through thick tissue phantoms clearly demonstrate the gating effect [1693]. The shadow of a small lead object is (in Fig. 9.48b) recorded time-resolved through water layers of increasing thickness. It can be clearly seen that a sharp shadow is obtained using the “ballistic” X-rays, even when imaging through 15 cm of water, while the time-integrated images in the lower part of the figure show a strong loss of contrast. Scattering reduction is particularly valuable in volume tomography and the gating principle has also been demonstrated for the tomographic case [1694]. The future of these techniques will be strongly coupled to the potential development of efficient gateable imaging X-ray detectors. The radiotoxic equivalence between a given dose (Grays) of conventionally produced X-rays and a corresponding dose of laser-produced X-rays, having 10^{10} higher peak power, has been established in cell culture experiments [1695, 1696].

Short pulses of X-rays are very attractive for time-resolved X-ray absorption measurements [1697]. Time-resolved X-ray diffraction is a very powerful technique.

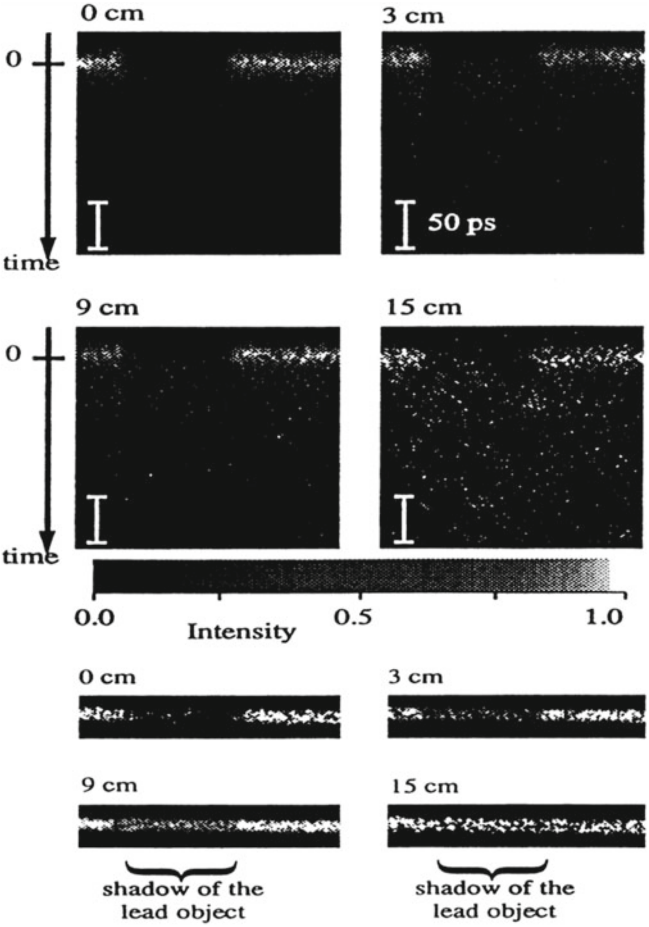

Fig. 9.48b Gated viewing recordings of a small lead object using short-pulse X-ray bursts passing through water layers of different thicknesses. In the lower part of the figure time-integrated representations are shown, clearly demonstrating the loss of contrast for thicker samples [1693]

The duration of laser-produced X-rays is much shorter (1 ps) than what is available from synchrotrons (tens of ps). Diffraction techniques are strongly developing based on ultra-fast laser sources and in approaches where laser plasma sources and synchrotron techniques are being combined [1698–1703]. Of particular interest is to study diffraction patterns of complex molecules in crystal form. Such studies are being pursued at powerful X-ray free-electron laser facilities [1704–1707].

9.6.6 Relativistic Effects and Laser Accelerators

When the ponderomotive energy (9.23) of an electron in a laser field is of the order of 1 MeV, the speed of the electron becomes a substantial fraction of that of light and relativistic effects start to occur [1708]. The relativistic effects cause a self-focusing of a high-power laser beam, which produces a plasma in a gas target. A plasma column can be a useful source of X-ray laser radiation [1709]. A further strongly relativistic effect of high-power laser beams would be the creation of matter (production of electron–positron pairs; the inverse of annihilation radiation, Sect. 5.1.3). The required power density would be of the order of 10^{30} W/cm^2 for production in vacuum. Such powers may not be unrealistic in the future [1710].

The intense fields in the optical pulse can be used in various schemes for laser particle acceleration, including *wake-field acceleration* [1711–1713]. Here, electrons ride like surfers on the enormous electric wave moving forward at a speed very close to the velocity of light and caused by the optical pulse propagating and creating a plasma in a gas jet, onto which the laser beam is focused. The process is schematically shown in Fig. 9.49a. Acceleration of electrons energies beyond 1 GeV in a distance of just 1 mm has been demonstrated, suggesting that laser techniques will find important applications in future accelerator technology [1714–1718]. Laser-accelerated electrons will start to oscillate sidewise in the complex plasma environment with strong interactions with positive ions in the plasma “bubble”, which is created after the propagating laser pulse. The oscillation is similar to the one electrons experience in an undulator at a synchrotron radiation facility and so-called *betatron radiation* in the X-ray regime is created. Such radiation can be used, e.g., for phase contrast microscopy. A schematic set-up for laser acceleration and betatron radiation employed for imaging is shown in Fig. 9.49b. An example of an image of an insect recorded in this way is shown in Fig. 9.49c [1719].

Protons and other light nuclei can also be accelerated by intense laser pulses. Now the mechanism is different: the pulse typically impinges on a thin foil, and electrons are immediately ejected. The negative electron cloud strongly attracts protons at the surface (derived from, e.g., water contamination) and accelerates them out from the foil, as shown in Fig. 9.50a. Energies up to 100 MeV and with a reasonably small energy spread have been reached in this way [1720–1725]. Accelerated protons and light ions, such as He$^+$ and C$^+$, are attractive for tumour irradiation, since they, in contrast to electrons or γ-rays, deposit most of their energy when they are stopped in the tissue; they exhibit a so-called *Bragg peak* (Fig. 9.50b), which is favourable for selective dose delivery, since surrounding tissue can be spared. This fact is being used at oncology centres using conventional accelerators (see, e.g., [1726]. By varying the proton energy, the maximum dose can be distributed through the full tumour mass [1726, 1727]. Laser-based so-called hadron therapy might have advantages over present approaches using conventional accelerators. One important aspect is that the movable beam-stearing gentry, with weights of typically hundreds of tons, might be replaced with mirror arrangements for the intense laser beam.

Recently, the prospects for using laser-accelerated electrons for tumour therapy have been investigated [1728] with the advantage that 100 MeV electrons (readily

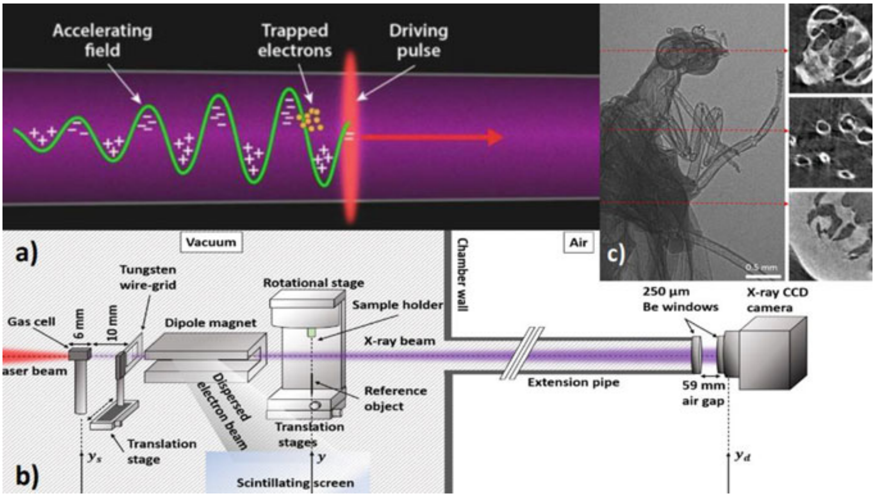
Accelerating field
Trapped electrons
Driving pulse
a)
Vacuum
Air
Chamber wall
c)
0.5 mm
Tungsten wire-grid
Rotational stage
Sample holder
Gas cell
6 mm
10 mm
Dipole magnet
X-ray beam
aser beam
Dispersed electron beam
Reference object
Translation stages
Translation stage
y_s
y
Scintillating screen
b)
250 µm Be windows
X-ray CCD camera
Extension pipe
59 mm air gap
y_d

Fig. 9.49 **a** Wake-field acceleration of electrons (Reproduced from F. Grüner: Shooting ahead with wakefield acceleration, Physics 12, 19 (2019); Creative Commons Attribution 3.0 License, APS). **b** Set-up for phase contrast imaging of small biological samples using wake-field electron acceleration and associated betatron radiation. An example of an image of a *Chrysopa* lace-wing insect is shown in **c**. Included are also tomograhically constructed cross sections along the dotted lines, based on recordings taken for different rotation angles of the insect ([1719]; reproduced with permission from OPTICA)

available from laser acceleration) has a much more favourable depth deposition profile than the few MeV electrons presently used at oncology centres (see Fig. 9.50b).

9.6.7 Laser-Nuclear Interactions and Laser-Driven Fusion

We have seen that intense laser radiation can induce hard X-rays and accelerate particles to high energies. Thus, it is not unexpected that even nuclear reactions can be induced. Such experiments are now being pursued [1729–1733]. In particular, laser-accelerated protons can be used to produce short-lived isotopes of great importance for nuclear medical-imaging techniques such as *Single Photon Emission Computed Tomography* (SPECT), and *Positron Emission Tomography* (PET) (Sect. 5.1.3).

Gamma-ray laser action is a further related field which has attracted much efforts [1734, 1735]. Laser-driven (inertial confinement) deuterium–tritium fusion using the largest laser installations is a huge research field for laser-nuclear interaction (see, e.g., [1736, 1737]). A modified concept, the "*fast igniter*" scheme, where an extremely intense (petawatt) laser pulse is fired into the pre-compressed plasma [1738] is a proposed scheme, which may have advantages. An alternative laser-driven fusion approach using a proton/^{11}B reaction is also being pursued [1739].

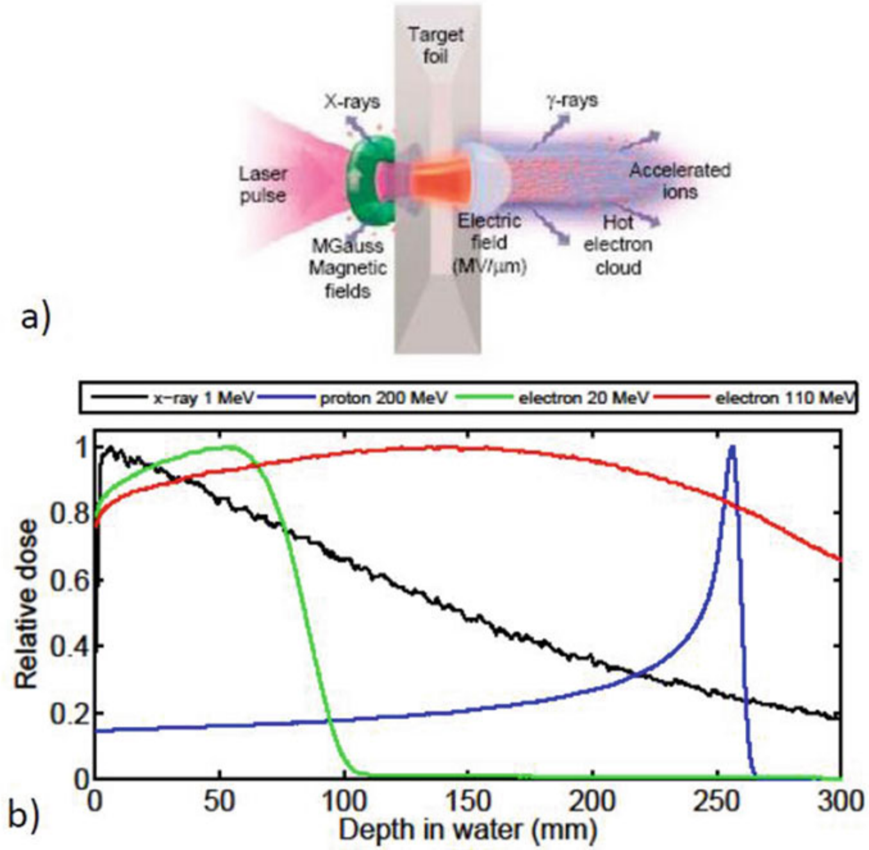

Fig. 9.50 **a** Proton and light-ion acceleration using ultra-intense laser pulses. The laser beam is focused on a thin foil creating a plasma and the shock-wave propagating forward releases an intense burst of electrons moving forward and then creating a very strong electric field that sucks out the positive ions from the foil surface and accelerates them to MeV energies. The process is also accompanied by the generation of super-intense magnetic fields and γ-ray emission (Source: https://www.scapa.ac.uk/?page_id=53, Courtesy: SCAPA and RAL). **b** Interaction of ionizing radiation with human tissue as utilized in radiation oncology (Courtesy: Olle Lundh, Physics Department, Lund University). Electrons used in current therapy have a rather shallow penetration depth, while higher-energy electrons, readily available by laser acceleration penetrate much deeper. X-rays—the normal modality used in tumour treatment—propagate deep, but with a strong and expected attenuation. In contrast, protons deliver most of their therapeutic dose as they are stopped in the tissue—a prominent Bragg peak occurs, at a location, which depends on the energy. Proton therapy is very attractive for treatment of brain tumours (100–200 MeV needed) while for ocular tumours a lower energy of 50–70 MeV provides sufficient penetration

Since no neutrons, which can cause material activation, are produced in this reaction, radioactive waste may be avoided.

In closing, we note that in principle laser spectroscopy on nuclei should be possible. In fact, for the very specific case of ^{229}Th, where a nuclear level has an excitation energy of only 8.1 eV, laser-driven transitions were studied in the VUV spectral region. Nuclear transitions can be expected to be less influenced by environmental effects. This observation, together with the attractiveness of a very high transition frequency, could make the thorium isotope an excellent candidate of a clock with unprecedented precision [1740, 1741].

9.7 High-Resolution Laser Spectroscopy

A number of high-resolution methods, in which the extremely narrow linewidth of single-mode lasers is utilized will be described in this section. Various ways of eliminating Doppler broadening have been investigated leading to the development of *Doppler-free* laser spectroscopic techniques. The effective linewidth that is experimentally obtained is determined by a number of effects:

- The natural radiation width.
- Residual Doppler broadening, in particular the *second-order Doppler effect* (due to the time dilatation effect $1/(1-v^2/c^2)^{1/2}$ in (9.11),which is present irrespective of the direction of motion.
- The laser linewidth.
- The transit time broadening, due to the finite time that an atom dwells in the laser beam because of its motion (see also Sect. 7.1.2).

We will first describe spectroscopy on *collimated atomic beams* and on *kinematically compressed ion beams*. Two groups of nonlinear spectroscopic techniques will be discussed: *saturation techniques* and *two-photon absorption techniques*. We will also deal with the optical analogy to the Ramsey fringe technique (Sect. 7.1.2), and the utilization of *frequency comb techniques* (Sect. 9.7.5). Laser cooling and atom- and ion-trap techniques will be discussed in a subsequent section (Sect. 9.8). Here, the particles are basically brought to rest, eliminating the Doppler as well as the transit broadening effects. The phenomenon of *Bose Einstein condensation (BEC)* will also be described.

9.7.1 Spectroscopy on Collimated Atomic and Ionic Beams

As we have already noted (Sect. 6.1.1), a well-collimated atomic beam displays a very small absorption width perpendicular to the atomic beam. As shown in Fig. 9.51, the collimation ratio C for an atomic beam is defined as

$$C = s/d. \tag{9.25}$$

Fig. 9.51 Definition of the collimation ratio

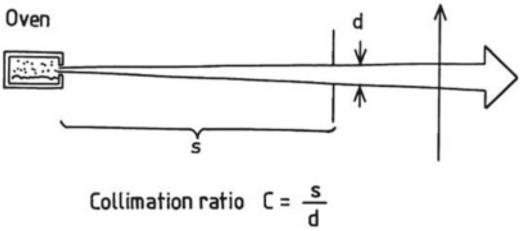

The residual (first-order) Doppler broadening $(\varDelta\nu_{\mathrm{D}})_{\mathrm{res}}$ for a collimated atomic beam is given by

$$(\Delta\nu_{\mathrm{D}})_{\mathrm{res}} \simeq \frac{\Delta\nu_{\mathrm{D}}}{C\sqrt{2}}, \tag{9.26}$$

where $\varDelta\nu_{\mathrm{D}}$ is the normal Doppler broadening. High-resolution spectroscopy can be performed by irradiating such a beam at right angles with a narrowband, single-mode laser. With a collimation ratio of 100, a typical residual Doppler broadening of 5 MHz is obtained.

The atomic-beam technique is a very versatile one. Atomic beams can be produced for essentially any element (Fig. 7.2), whereas conventional cell techniques are limited to a temperature interval up to about 1000 °C. Besides reducing the Doppler width, collisional effects are significantly reduced with the atomic-beam technique compared with cells. The possibility of utilizing spatially separated interaction regions along the beam is also valuable in certain cases. We note that the most probable velocity υ of a thermal atomic beam emerging from an oven is

$$\upsilon = \sqrt{\frac{3RT}{M}}, \tag{9.27}$$

where T is the absolute temperature, M the mass number, and R the gas constant. This formula results in typical thermal velocities of about 300 m/s. Typical mean free paths between collisions with residual gas in the vacuum system are about 10 m at 10^{-5} torr (1.3 mP).

There are several methods for detecting the narrow resonance induced by the laser. A few methods are illustrated in Fig. 9.52, and will be subsequently discussed.

Detection Through Fluorescence. The most direct way to study optical resonance is to observe the *fluorescence light* that is released after the excitation. A schematic spectrum for the D_2 line in ^{23}Na $(3\,s\,^2S_{1/2} \rightarrow 3p\,^2P_{3/2})$ is shown in Fig. 9.53. Two well-separated component groups corresponding to the ground-state hyperfine splitting occur. The components corresponding to the small excited-state splittings are well resolved and the a and b constants for the hyperfine structure can be evaluated. The natural radiation width corresponding to $\tau = 16$ ns for the $3p\ ^2P_{3/2}$ state is

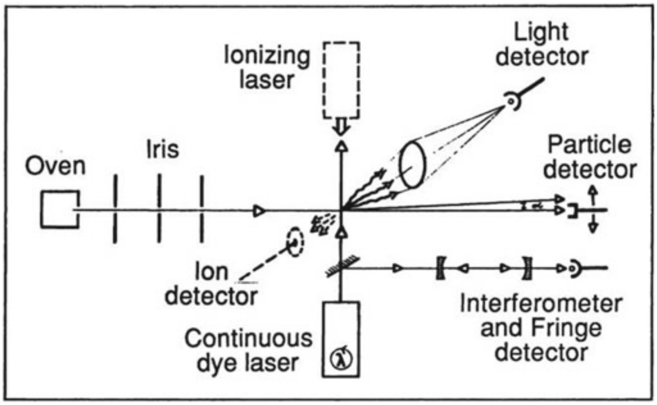

Fig. 9.52 Laser spectroscopy with a collimated atomic beam. Three different detection methods are illustrated

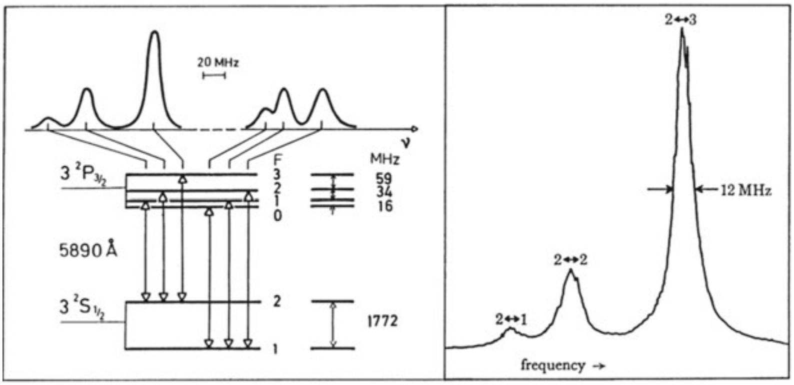

Fig. 9.53 Schematic representation of the hyperfine structure in the sodium D_2 line. An experimental curve from a well-collimated sodium beam is included [1453]

10 MHz. As can be seen from the inserted experimental curve, such a linewidth can be approached. A further example of this type of spectroscopy is given in Fig. 9.54. Here, a broadband CW laser has been used to populate the rather long-lived $5d$ $^2D_{5/2}$ ($\tau \sim 1$ μs) state in ^{133}Cs in the cascade decay of the primary excited $7p$ $^2P_{3/2}$ state. A narrow-band laser is swept through the components of the $5d$ $^2D_{5/2} \rightarrow 10f$ $^2F_{7/2,5/2}$ transition. The inverted hyperfine structure of the lower state and the inverted fine structure (evident from the intensity ratio between the low- and high-frequency groups) of the highly excited state are shown. The hyperfine structure of the F-state is too small to be resolved.

An example of the Stark effect is given in Fig. 9.55. Note, that while only the tensor Stark interaction constant α_2 (Eq. 2.35) can be determined in an LC experiment (Sect. 7.1.5; Fig. 9.19), the scalar interaction constant α_0 can be obtained in this type of experiment as well as α_2. In the same way, isotope shifts can be measured by direct optical high-resolution methods while resonance methods and quantum-beat spectroscopy can only be used for measurements of splittings within the *same atom.*

Detection by Photoionization. The atomic beam is simultaneously irradiated by a narrow-band laser and an intense laser when detection by photoionization is employed. The latter has a sufficient photon energy to photoionize the atoms that are transferred to the excited state, while ground-state atoms cannot be ionized. The photoelectrons are detected in an electron multiplier, which is constructed like a photomultiplier tube but without a photocathode. For the case of very long-lived Rydberg atoms, field ionization can also be applied as an efficient detection method. During a period of 10 μs atoms move several mm, and it is possible to physically separate a field-free laser interaction region from the field-ionization region [1745].

Detection by the Recoil Effect. When an atom absorbs a photon impinging perpendicularly to the direction of flight of the atom the photon momentum

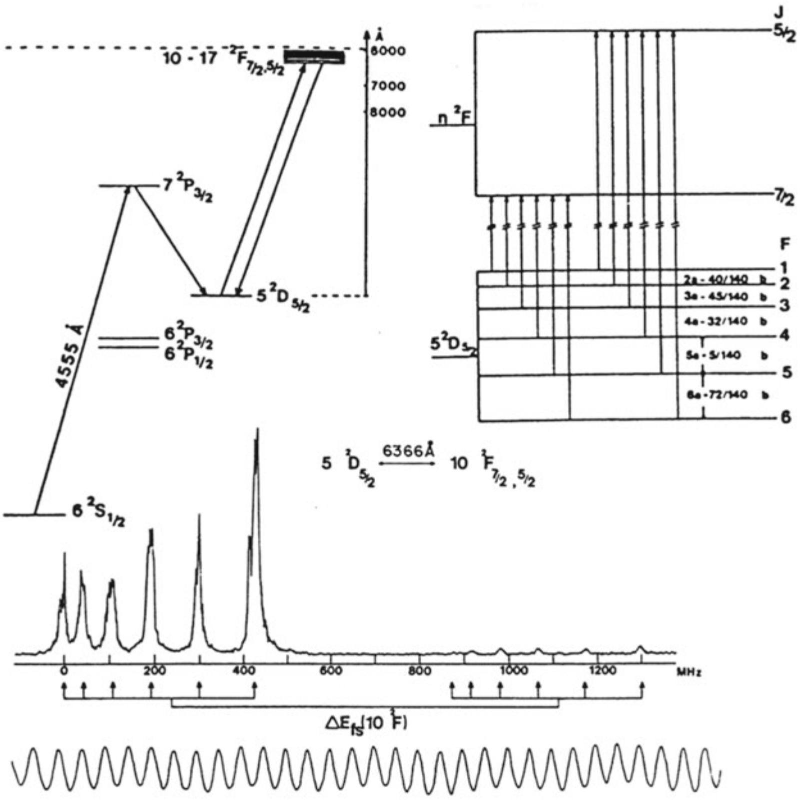

10 - 17 ²F7/2,5/2
Å
6000
7000
8000
7 ²P3/2
5 ²D5/2
6 ²P3/2
6 ²P1/2
4555 Å
6 ²S1/2
J
5/2
n ²F
7/2
F
1
2
3
4
5
6
2a - 40/140 b
3a - 45/140 b
4a - 32/140 b
5a - 5/140 b
6a - 72/140 b
5²D5/2
5 ²D5/2
6366Å
10 ²F7/2 , 5/2
0
200
400
600
800
1000
1200
MHz
ΔEfs(10 ²F)

Fig. 9.54 Recording of a D–F cesium transition obtained in a collimated atomic beam experiment using stepwise excitations [1742]

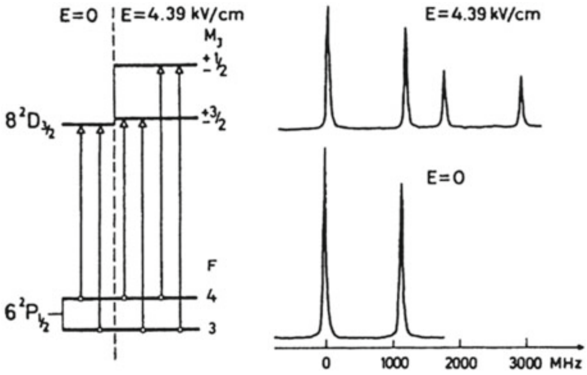

Fig. 9.55 Stark-effect determination in the transition $6\,^2P_{1/2}$–$8\,^2D_{3/2}$ in ^{133}Cs. The lower state has too low a polarizability to be affected by the electric field [1743, 1744]

$$p = h\nu/c \tag{9.28}$$

is transferred to the atom. For a sodium atom absorbing a D-line quantum, the transverse velocity change is about 3 cm/s. The atom is then deflected by an angle given by

$$\alpha \simeq p/mv \simeq 10^{-5}\text{rad}, \tag{9.29}$$

where m and v are the mass and the velocity of the atom, respectively. If the atom is de-excited by stimulated emission, the absorbed perpendicular momentum is cancelled by the recoil of the atom when the stimulated photon is emitted in the same direction as the incoming light. On the other hand, if spontaneous decay occurs, the direction of the recoil will be randomized. Thus, on average, a transverse momentum is transferred to the atomic beam, which is deflected and also broadened. At optical resonance, the intensity at a particle detector placed in the path of the original atomic beam is reduced. The deflection of the beam depends on the intensity of the laser and the length of the interaction region. Deflections are normally small (~1°). In principle, isotopes can be separated in this way by isotope-selective excitation. However, more efficient methods have been developed (Sect. 10.4.2). Beam deflection under the influence of resonance radiation was demonstrated as early as in 1933 using classical lamps [1746]. Beam deflection due to laser radiation is much more efficient [1747, 1748].

The mechanical influence of light on atoms and particles was noticed early on when observing the comet tails pointing away from the sun. Particle acceleration with laser light was also considered early on [1749]. Cooling and trapping with laser light are discussed in Sect. 9.8.

Detection by Magnetic Deflection. In one version of this kind of experiment, the atomic beam in an ABMR apparatus (Sect. 7.1.2) is irradiated by a sharply tuned laser in the C region. At optical resonance, a flop-in signal is obtained due to the pumping of atoms with $\mu_{\text{eff}} < 0$ into states with $\mu_{\text{eff}} > 0$. A single inhomogeneous magnetic field, e.g., from a sextupole magnet, can also be used for non-optical signal detection. The atomic beam emerging from the source is perpendicularly irradiated by the laser beam before it enters the sextupole magnet, which focuses $\mu_{\text{eff}} < 0$ atoms and defocuses $\mu_{\text{eff}} > 0$ atoms. The focused atoms hit the detector, which can be the entrance slit of a mass spectrometer. Such a detection system is particularly valuable when dealing with small amounts of radioactive atoms. When the laser beam pumps atoms from one F-state into another in a field-free region, a flop-in (increase) or a flop-out (decrease) signal is recorded, depending on which Paschen–Back group a particular F-level communicates with. An example of this type of experiment for radioactive alkali metal elements is shown in Fig. 9.56. Extensive measurements of short-lived radioactive isotopes of the alkali metal elements, including francium, have been performed [1750–1753].

As we have seen, magnetic deflection can be used for the detection of optical resonance. However, laser beams can also be used to replace the in-homogeneous A and B magnets in ABMR (Fig. 7.5). The laser is then tuned to substantially reduce the population of a particular F-level while the atoms are in the A region. A beam from

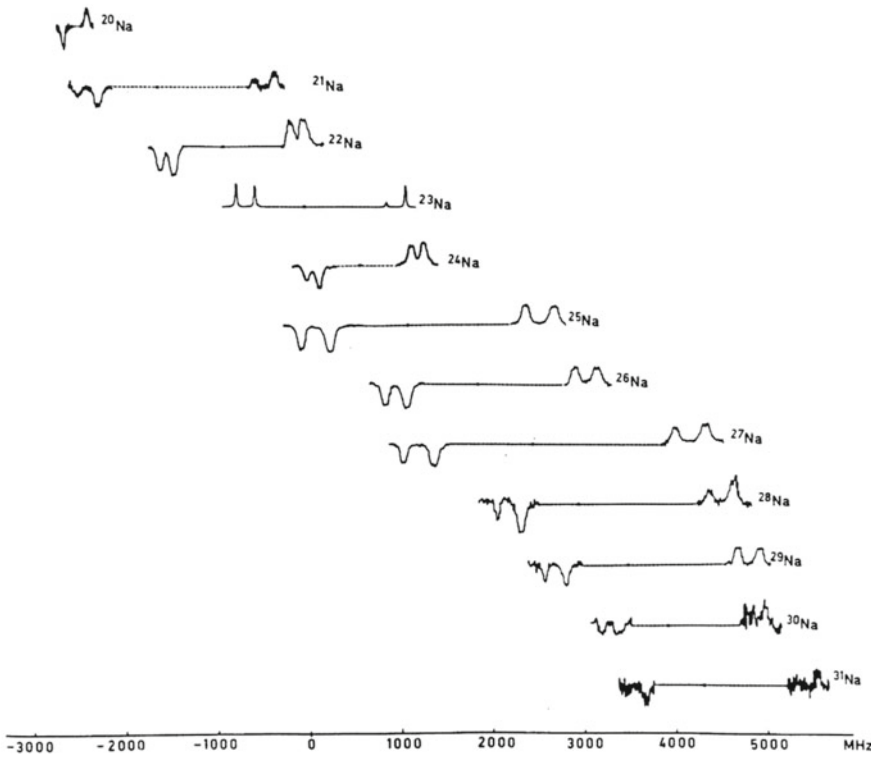

Fig. 9.56 Recordings illustrating hfs and isotopic shifts between different isotopes of sodium. The recordings were made on collimated beams and detection by magnetic deflection was used [1750]

the same laser is used in the B region, where the fluorescence induced by the beam is monitored. Here, the light is reduced as a result of the low F-state population. However, if $\Delta F = \pm 1$ transitions from neighbouring, well-populated levels are induced in the C region, the population of the state initially chosen is increased, which is observed in the B region as an increase in the fluorescence light [1754, 1755]. With the A and B magnets retained, laser-induced fluorescence can be used to detect the transmitted atoms [1756].

We conclude this section by describing the special conditions pertaining to spectroscopy on fast ion beams. As we have noted in connection with beam-foil spectroscopy, the transverse Doppler broadening of an ion beam is substantial due to the high ion velocities. Thus, high-resolution spectroscopy cannot be accomplished by perpendicular laser beam radiation. However, it is possible to obtain a high resolution by directing the laser beam along the ion beam, which at first sight might seem very surprising. The effect is due to a *kinematic compression*, which occurs in the ion acceleration process [1757, 1758]. The non-relativistic kinetic energy for a particle in movement is given by

$$E = \frac{1}{2}mv^2. \tag{9.30}$$

By differentiating, we obtain

$$\Delta E = mv\Delta v. \tag{9.31}$$

For a given energy spread ΔE of the ions, which is mainly due to the thermal velocity spread in the ion source, we obtain, since ΔE is the same after the acceleration,

$$\Delta v \propto 1/v. \tag{9.32}$$

The velocity spread Δv that gives rise to the Doppler broadening is thus inversely proportional to the ion velocity! At $v = 0.001\mathrm{c}$, which should be compared with the thermal value of $v \simeq 300\,\mathrm{m/s}$, we have a reduction of the Doppler width by a factor of 1000. This technique can also be applied to neutral atoms. An ion beam can be neutralized by sending it through a charge-exchange gas. Many studies of isotope shifts and hfs have been performed for longitudinally excited fast beams. In particular, short-lived radioactive nuclei have been studied [1759–1761]. Further results and reviews of determinations of nuclear properties using various laser spectroscopic techniques are given in [1762–1770].

Ion storage rings with high-intensity beams have become available and are used for spectroscopic studies. Lifetime measurements of ions in long-lived metastable states can be performed, taking advantage of the small losses resulting from collisions with the residual gas [1771]. Also, multiply charged ions and molecular ions can be investigated. Many types of collision experiments (ion–atom, ion–ion, ion–electron) of theoretical and astrophysical interest can be performed [1772, 1773]. As one molecular example, the study of dissociative recombination in the astrophysically very important ion $H_3{}^+$ could be mentioned [1774, 1775]. The particle energy spread present in normal storage rings can be strongly reduced by co-linear interaction with a strongly monochromatic electron beam (*electron cooler*), and by laser interaction it is also possible to cool ionic beams, i.e., reduce the energy spread [1776–1778]. If the energy spread between the ions is eliminated, the electrostatic forces between the ions will start to dominate and the ionic beam can be expected to "crystallize" [1779] (*Wigner crystal*; see also Sect. 9.8.3; Fig. 9.77b). The DESIREE facility at Stockholm University features two ion storage rings with electrostatic focusing and beam deflection, where ions of opposite charges are merged in a common straight section and are allowed to interact at extremely low relative energies, down to 10 meV, and under extreme high vacuum. This resembles conditions in interstellar space and relevant reactions under such conditions can be studied. Storage rings, also for heavy ions, are also available, e.g., at the Max Planck Institute for Nuclear Physics in Heidelberg and at GSI, Darmstadt. Further results from storage rings for ions are given in [1780–1786].

It should be noted in connection with the laser spectroscopy of ionic beams that *negative ions* can also be investigated [1787–1789]. Positive ions in an accelerated beam are then subjected to a charge-exchange process in a cell filled with cesium vapour, and electrons can be picked up. Negatively charged systems are weakly bound by forces, which are due to polarization effects and are particularly suited for studying *electron correlation* effects. The shallow boxlike potential can generally only bind a ground state, and for many atomic species not even such a state is formed, i.e., the ion does not exist. Negative ions can only be studied by breaking them up by absorption of photons of sufficiently high energy to remove one of the electrons (*photo-detachment*). The binding energy is thus determined by observing at what wavelength the onset of the photo-detachment process occurs. Thus, it has been found that bound states exist for Li^-, Be^-, O^-, and Rb^-, for example. Ca^- was long believed not to exist, until it was finally found that an extremely weakly bound state (24.55(10) meV) does exist [1790]. A particularly efficient method for detecting the process is to excite the negative ion to an excited state of the neutral atom, followed by a second excitation to a Rydberg state. After field ionization (Sects. 2.5.2 and 9.1.4) the positive ion is detected in a mass spectrometer [1791]. Further results on negative ions are presented, e.g., in [1792, 1793].

9.7.2 Saturation Spectroscopy and Related Techniques

We discussed earlier how a multi-mode laser reacts in the presence of an intracavity absorption cell (Sect. 9.2.2). We now consider the corresponding situation when the laser is forced to run in a single-cavity mode through the action of an intracavity etalon (Fig. 9.57). The atoms or molecules in the intracavity absorption cell have a Doppler broadening of the order of 1000 MHz. Different velocity groups of the atoms are responsible for the absorption in the different parts of the absorption curve. The

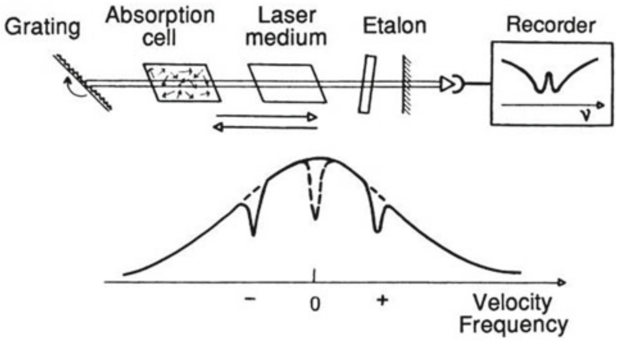

Fig. 9.57 Inverted Lamb-dip spectroscopy [1]

narrow-band laser light will be absorbed at two different positions in the Doppler profile, symmetrically placed around the peak. Light moving to the right is absorbed at one position, while light moving to the left is absorbed at the other position. Through the action of the intense light, essentially half the number of the atoms with the corresponding velocity will leave the ground state; "holes" are burnt in the velocity distribution (saturation, Sect. 9.1.2). If the laser is tuned towards the centre of the Doppler-broadened absorption line, the output power of the laser will drop successively. When the laser is tuned exactly to the peak of the absorption curve, both laser beams will be absorbed at the same position (atoms moving perpendicularly to the laser beam are affected). Since light of *one* direction of propagation can saturate the transition for the particular velocity group, the total absorption will *decrease* when light of *both* directions of propagation interacts with the same atoms. Compared with the situation just before the laser tuning had reached the line centre only half the number of atoms are available as ground-state absorbers. The output power of the laser will be significantly *increased* at the centre of the absorption line. The width of the corresponding signal is no longer limited by the Doppler broadening. We note that the reason why the signal at the line centre is obtained is that the absorption is *nonlinear*, due to the saturation phenomenon. If the laser intensity is weak and we are far from saturation, very weak hole burning occurs and we have the *linear* absorption situation. Then no narrow signal is observed at the line centre, since the absorptions add linearly at the line centre as well as off the line centre. In contrast, the *inverted Lamb-dip* experiment [1794] we have just described constitutes an example of *nonlinear laser* spectroscopy. The *normal Lamb-dip* effect [1795], which is closely related to the above-described process, produces a *decrease* in the output power of a single-mode gas laser (without absorption cell) when the frequency is tuned to the centre of the laser gain profile. The decrease occurs since only one population-inverted velocity group is available at the line centre, whereas two velocity groups contribute to the amplification off the line centre. The sharp Lamb dip or inverted Lamb dip can be used for frequency stabilization of a laser. The output power is sensed and a servo system adjusts the length of the cavity. A small modulation is introduced into the length regulation and the derivative of the light intensity is monitored using lock-in techniques (Fig. 6.68). Thus, the servo system adjustment can be performed with the correct phase. The reason is, that while the primary absorption peak is a symmetric (even) function, the derivative is an odd function, which changes sign when passing the line centre, and thus allowing the servo system to know if to adjust towards higher or lower frequencies. A He–Ne laser can in this way be stabilized on an I_2 absorption line at 632.8 nm or a methane line at 3.39 μm. The frequency of the He–Ne transitions, and some I_2 lines, was early measured directly with the Cs clock as the reference, using a special technique employing ultrafast mixing photodetectors and several intermediate stabilized lasers [1796–1799]. We will describe the newer and much simpler optical frequency comb technique later. Further, the wavelength of the stabilized light has been determined with high precision using interferometric techniques. The orange (Doppler broadened) line at 605.8 nm from ^{86}Kr defined the metre until 1983 as 1,650,763.73 wavelengths of the line. By multiplying frequency and wavelength, a very accurate value for the velocity of light could be calculated. A best value of $c = 299{,}792{,}458$ m/s was established from measurements at different laboratories. An error is associated with this result, mainly reflecting the uncertainty in the definition of the metre, which has posed a significant problem. At the meeting of "Conference Internationale des Poids et des Mesures" in 1983, it was decided that the metre should be directly connected to the much more precise time (second) definition by *defining* the velocity of light as the above-mentioned value (it no longer has an error) resulting in a definition of the metre as the distance light travels in vacuum during 1/299,792,458 s [1800]. Thus, one basic unit definition has effectively been eliminated, and length is now expressed in terms of time. For practical purposes, secondary standards must, of course be used, and obvious ones are the Lamb-dip stabilized laser lines used in the process of establishing the above-mentioned value of *c*. Lamb-dip studies of transitions in gas lasers have been performed for a long time. Authorized data for a few lines are given in Table 9.3.

As noted in Chap. 7, the second is presently defined as 9,192,631,770 oscillations on the hyperfine frequency interval in ^{133}Cs. However, optical clocks operating at

Table 9.3 Secondary length standards based on saturation spectroscopy using He–Ne laser oscillations locked to molecular absorption lines [1800]

Transition	Frequency	Wavelength
CH_4, ν_3, P(7), comp. $F_2^{(2)}$	88,376,181,608 kHz	3,392,231,397.0 fm
$^{127}I_2$, 17-1, P(62), comp. o	520,206,808.51 MHz	576,294,760.27 fm*
$^{127}I_2$, 11-5, R(127), comp. i	473,612,214.8 MHz	632,991,398.1 fm
$^{127}I_2$, 9-2, R(47), comp. o	489,880,355.1 MHz	611,970,769.8 fm

* Frequency-doubled 1.15 μm He–Ne transition

Table 9.4 Optical clock transitions [1802, 1803]

Frequency/Hz	Fractional uncertainty	Transition
9192 631 770	Exact	^{133}Cs ground state hfs
6834 682 610.904 3126	6×10^{-16}	^{87}Rb ground state hfs
429 228 004 229 873.0	4×10^{-16}	^{87}Sr $5s^2\ ^1S_0$–$5s5p\ ^3P_0$
444 779 044 095 486.5	1.5×10^{-15}	^{88}Sr$^+$ $5s\ ^2S_{1/2}$–$4d\ ^2D_{5/2}$
518 295 836 590 863.6	5×10^{-16}	^{171}Yb $6s^2\ ^1S_0$–$6s6p\ ^3P_0$
642 121 496 772 645.0	6×10^{-16}	^{171}Yb$^{+2}S_{1/2}$–$^2F_{7/2}$
688 358 979 309 308.3	6×10^{-16}	^{171}Yb$^+$ $6\ s\ ^2S_{1/2}$–$5d\ ^2D_{3/2}$
1064 721 609 899 145.3	1.9×10^{-15}	^{199}Hg$^+$ $5d^{10}6s\ ^2S_{1/2}$–$5d^96s^2\ ^2D_{5/2}$
1121 015 393 207 857.3	1.9×10^{-15}	^{27}Al$^+$ $3s^2\ ^1S_0$–$3s3p\ ^3P_0$
1128 575 290 808 154.4	5×10^{-16}	^{199}Hg $6s^2\ ^1S_0$–$6s6p\ ^3P_0$

much higher frequencies are much more accurate, and are likely to soon replace the microwave standard [1801]. E.g., a strontium clock operating close to 430 THz would be uncertain with one second during a time span of 15 billion years! With such a stability, the clock notices a relativistic gravitational shift if the clock is moved by 2 cm vertically! Table 9.4 lists a number of more recently accurately determined optical frequencies (and thus wavelengths) [1802, 1803].

The first saturation spectroscopy experiments using a tunable narrow-band laser were performed by *Hänsch, Schawlow* and co-workers [1804, 1805] and by *Bordé* [1806]. With the advent of the dye laser, spectroscopy utilizing saturation effects could evolve quickly. The atomic sample is normally placed outside the cavity for practical reasons. An experimental set-up for studying the sodium D_1 line ($3s\ ^2S_{1/2} \rightarrow 3p\ ^2P_{1/2}$) is shown in Fig. 9.58.

The primary laser beam is divided into two beams using a partially reflecting mirror (beam splitter). The two beams then pass the sodium vapour cell in opposite directions and with overlapping paths. One of the beams, the saturating beam or *pump beam*, has a high intensity while the other one, the detection or *probe beam*, is weak. The intensity of the probe beam is measured after passing through the cell. When the laser is tuned towards the centre of the Doppler-broadened absorption line, the strong laser beam saturates the transition for atoms in a certain velocity group. At the same time, the probe beam experiences an increasing absorption. When the laser is tuned to the line centre, the probe beam "detects" the hole that has been burnt by the saturating beam and thus its transmission is increased. A Doppler-broadened absorption line with a sharp and narrow intensity increase at the line centre occurs, as is also indicated in Fig. 9.58. In order to isolate the part of the signal that depends on the saturation (*the Doppler-free signal*), a lock-in amplifier (Fig. 6.68), which is synchronized with a light-chopper in the saturating beam, is used. The lock-in amplifier records the amplitude of the AC component that can be obtained when the saturating beam is switched on and off. Out in the line wings, the two beams interact with completely different velocity groups and therefore the transmission of the probe

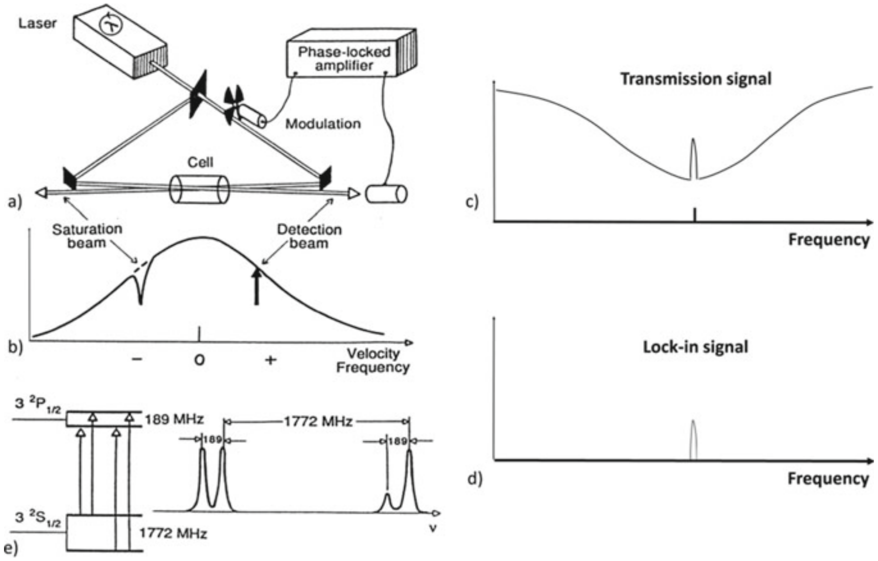
Laser
Phase-locked amplifier
Modulation
Cell
a)
Saturation beam
Detection beam
b)
– 0 +
Velocity Frequency
Transmission signal
c)
Frequency
Lock-in signal
d)
Frequency
3 ²P1/2
189 MHz
1772 MHz
189
189
3 ²S1/2
1772 MHz
v
e)

Fig. 9.58 **a** Set-up for saturation spectroscopy of the sodium D_1 line and **b** Ground state atom population distribution (after [1805]). **c** Transmitted light at the detector when both laser beams are present in the cell. **d** Doppler-free signal, isolated by the lock-in technique. **e** A schematic Doppler-free spectrum of the D_1-line hyperfine components, where “cross-over resonances” (Fig. 9.62) have been omitted

beam does not depend on the presence or not of a saturating beam. However, at the line centre the transmission strongly depends on whether a hole has been burnt or not and therefore an AC signal is obtained at the chopper frequency. Information is then transferred from one beam to the other, counter-propagating one with the atoms as the transfer medium. The Doppler-free structure of the D_1 line is schematically shown Fig. 9.58e, when the laser is tuned through the line. The Doppler-free signal is given by the expression

$$S(\nu) = f(I/I_{\text{sat}})\frac{1}{1+\left[(\omega-\omega_0)/\gamma_s\right]^2}, \tag{9.33}$$

where the signal amplitude f depends on the pump-beam intensity in relation to I_{sat}, which is the intensity required to saturate the transition.

The half-width γ_s of the signal increases with pump beam intensity according to

$$\gamma_s = \frac{1}{2}\gamma_0\left(1+\sqrt{1+I/I_{\text{sat}}}\right), \tag{9.34}$$

where

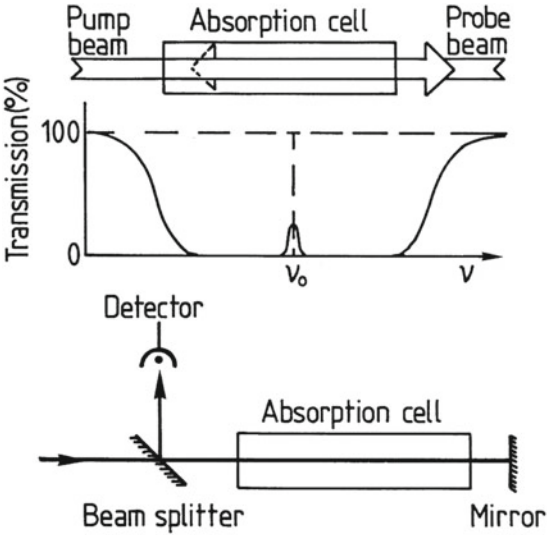

Fig. 9.59 High-contrast transmission spectroscopy [1807]

$$\gamma_0 = \pi \Delta\nu_N. \tag{9.35}$$

A particularly simple form of saturation spectroscopy is obtained if a sample that is sufficiently dense to completely block a probe beam is used. Only at the line centre, the bleached path induced by a strong counter-propagating pump beam allows the probe beam to emerge from the cell and hit the detector. A simple set-up and a schematic curve are shown in Fig. 9.59 for this type of high-contrast transmission spectroscopy [1807]. Interestingly, because of the saturation effect, a line narrowing even beyond the limit given by the natural radiation width can be achieved [1808]. Our observations also relate to the discussion regarding appropriate thicknesses of coloured-glass filters, presented in Sect. 6.4.2.

A much more important case of increase of resolution, which is also related to saturation, can be achieved in microscopy beyond the *Abbe diffraction limit* for spatial resolution: *stimulated emission depletion microscopy (STED)*. The method, which was first presented by *Hell and Wichmann* in 1994 [1370], relies on the strong non-linearity that can be achieved when a donut-shaped beam is used to deplete the population in the excited state created in a fluorescent molecule by a primary focused laser beam. Only a small area around the zero-intensity centre of the donut-shaped beam is not depleted and still emits fluorescence, now from a spot much smaller than corresponding to the normal diffraction limit. This spot is scanned across the image field and a high-resolution image is formed. The principle is illustrated in Fig. 9.60 [1809, 1810] and further discussed in [1373, 1810]. We have earlier, in Sect. 9.2.7, discussed a further method to achieve such super-resolution, the *STORM* method, relying on single-molecule detection. As earlier mentioned, *Hell* was together with

Betzig, and *Moerner* awarded the 2014 Nobel Prize in chemistry for these developments [1364–1366]. Different super-resolution microscopy techniques are discussed in [1811–1813].

Returning to Doppler-free spectroscopy, we note, that in normal saturation spectroscopy the detector essentially "looks" straight into the laser and a substantial absorption is needed in order to observe a signal. This means that only strong spectral lines, originating in well-populated states, can be investigated by this method. In cases where less favourable conditions prevail, the so-called *polarization spectroscopy* method can instead be used [1814]. The experimental set-up is shown in Fig. 9.61.

The set-up is similar to the one used in normal saturation spectroscopy but the probe beam is now blocked by crossed polarizers that are placed at opposite sides of the absorption cell. The polarizer in front of the cell is used to increase the degree of

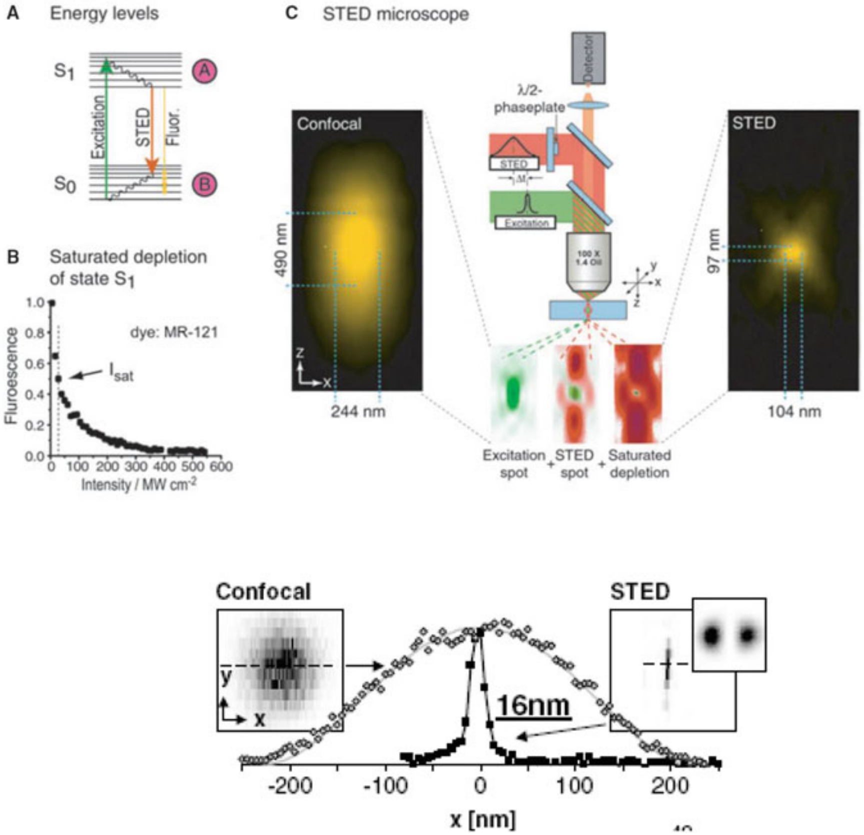
A Energy levels
S1
S0
Excitation
STED
Fluor.
A
B
B Saturated depletion of state S1
Fluroescence
1.0
0.8
0.6
0.4
0.2
0.0
dye: MR-121
I_sat
0 100 200 300 400 500 600
Intensity / MW cm-2
C STED microscope
Detector
λ/2-phaseplate
STED
Excitation
100 X 1.4 Oil
Confocal
490 nm
244 nm
STED
97 nm
104 nm
Excitation spot
STED spot
Saturated depletion
Confocal
STED
y
x
16nm
-200
-100
0
100
200
x [nm]

Fig. 9.60 Principle of stimulated emission depletion (STED) microscopy ([1809], reproduced with permission from Springer-Nature) and example of a super-resolution image ([1810], Creative Commons Attribution 3.0 License; APS)

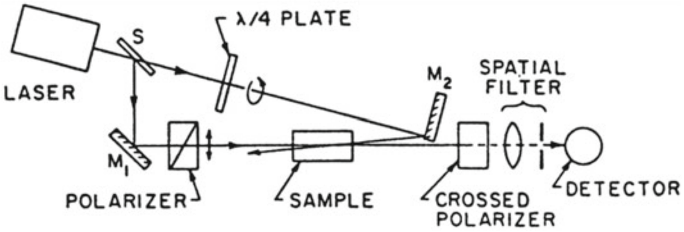

Fig. 9.61 Arrangement for polarization spectroscopy [1814]

linear polarization of the laser beam, which is frequently already well polarized. A matched pair of polarizers (frequently Glan–Thompson prisms, Fig. 6.52) can have a rejection ratio of 10^6 to 10^7 in the crossed position. The pump beam is circularly polarized and induces an anisotropy in the gas for the affected velocity group. At the line centre these atoms can, considered as an optically active medium, turn the plane of polarization so that probe beam light can pass the analysing polarizer (Sect. 9.2.4). The same effect is active when the concentration of chiral molecules, such as sucrose, is measured by observing the rotation of the plane of linear polarization, when light is passed through the sample. If the relative orientation of the polarizer is off-set by a small angle θ, a constant background results, but at the same time signal amplification is also obtained. It can be shown that the intensity of the polarization spectroscopy signal is given by

$$I = I_0\left(\theta^2 + \frac{1}{2}\theta s \frac{x}{1+x^2} + \frac{1}{16}s^2\frac{1}{1+x^2}\right), \tag{9.36}$$

where s is a factor that depends on the degree of saturation, which in turn is determined by the transition probability and the laser spectral power density. The variable x is proportional to the laser frequency detuning from the line centre. For completely crossed polarizers ($\theta = 0$) the signal is a Lorentzian, while the admixture of a dispersion-shaped curve increases with θ. The amplitude of the dispersion curve increases but so does the background θ^2. Thus, there exists a small angle θ, for which the signal-to-noise ratio has an optimum value. The dispersion-shaped signal can be very useful for locking a laser onto an atomic transition. A change in signal sign is obtained close to the line centre without a need for frequency modulation of the laser, which is used in normal saturation spectroscopy. One interesting application of Doppler-free laser spectroscopy is precision determination of the Rydberg constant, which was first performed by *Hänsch*, *Schawlow* and co-workers [1815–1818], and others [1819–1821]. The Rydberg constant can be evaluated if an accurate wavelength determination is performed for a suitable line in hydrogen [1822–1825]. A large number of evaluations have historically been performed by conventional spectroscopy on the red Balmer line H_α at 656.3 nm [1821]. The very large Doppler broadening (~6000 MHz) of the very light element hydrogen presents a significant problem because of the wide overlap of the fine structure components. The fine

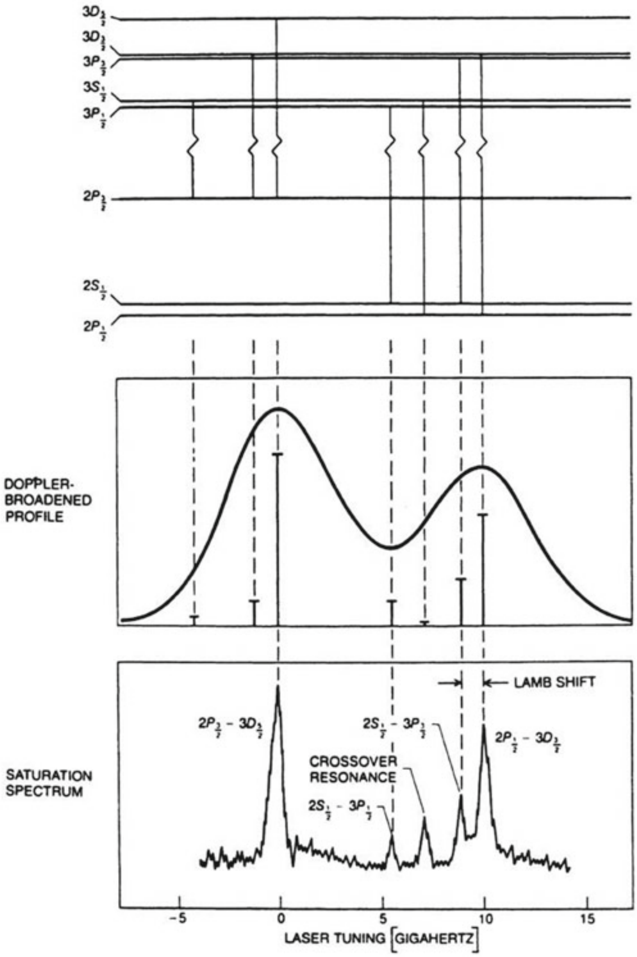
$3D_{5/2}$
$3D_{3/2}$
$3P_{3/2}$
$3S_{1/2}$
$3P_{1/2}$
$2P_{3/2}$
$2S_{1/2}$
$2P_{1/2}$
DOPPLER-BROADENED PROFILE
SATURATION SPECTRUM
$2P_{3/2}$ - $3D_{5/2}$
$2S_{1/2}$ - $3P_{3/2}$
CROSSOVER RESONANCE
$2S_{1/2}$ - $3P_{1/2}$
$2P_{1/2}$ - $3D_{3/2}$
LAMB SHIFT
-5
0
5
10
15
LASER TUNING [GIGAHERTZ]

Fig. 9.62 Saturation spectroscopy recording of the H_α line of hydrogen [1815]

structure of the H_α line and a theoretically calculated Doppler-broadened line are shown in Fig. 9.62. The Doppler-free structure obtained by saturation spectroscopy is shown in the lower part of the figure. The Lamb shift can be directly observed. The individual positions of the components can now be well established and the uncertain deconvolution procedure that previously had to be used can now be eliminated. The Rydberg constant can in this way be determined much more accurately than before. The presently recommended value for the Rydberg constant obtained is $R_y = 10{,}973{,}731.568\,160(21)\ \text{m}^{-1}$.

A fascinating aspect of precision spectroscopy is that the constancy of the natural constants is being challenged, to be further discussed later.

A so-called *cross-over resonance* is shown in Fig. 9.62. This is an inherent phenomenon in saturation spectroscopy and occurs when two lower- or upper-state sublevels have transitions to a common level in the other state. The two oppositely propagating laser beams can then interact at frequencies half-way between the normal resonances. Then atoms moving with a certain velocity projection along the laser beams are utilized [1826, 1827].

An experimental set-up similar to the one used in polarization spectroscopy is employed in experiments testing atomic manifestations of *parity violation* in the electro-weak interaction [1828, 1829]. The experiments are important for testing the *Standard Model* in elementary particle physics. Right-left asymmetries in atomic physics are of the order of $1{:}10^6$. A small optical rotation detectable using crossed polarizers is induced by interference between neutral weak and electromagnetic interactions in atoms. The most accurate experiments deal with heavy elements such as mercury, thallium, lead, and bismuth [1830, 1831]. Another way of probing the parity violation is to observe the strength of certain forbidden transitions, notably the $7\ {}^2S$ – $6\ {}^2S$ transition in cesium [1829, 1832]. The interaction between the neutral intermediate vector boson Z^0 with the electron violates parity and mixes a tiny amount (10^{-11}) of the P state into the S state, making the highly forbidden transition slightly allowed by electric dipole interaction. By applying a weak electric field the transition can be made more probable through the induced state mixing. A multiplicative interference term occurring between the two interactions amplifies the electro-weak interaction term of interest. For the interpretation of the nuclear effect, an accurate atomic physics calculation has to be performed. This is more feasible for the alkali metal element cesium than for the heavier atoms [1833, 1834]. The strength of the parity violation is now accurately measured in terms of the "weak charge" parameter Q with the result $Q = -72.2(3)$, in good agreement with the theoretical value of -73.2. By attaining an even higher accuracy, experimentally and theoretically, manifestations of further neutral vector bosons or of a nuclear *anapole moment* could be detectable [1832]. Further studies of parity violations are reported in [1835–1837].

In connection with this discussion of fundamental interactions we note that, besides hydrogen, there are numerous simple systems for which precision spectroscopic measurements can provide accurate tests of the QED theory and reveal effects beyond the Standard Model. *Positronium* (e^+–e^-) and *muonium* (μ^+–e^-) are hydrogen-like systems for which precise Lamb-shift and g-2 experiments (Eq. 2.23) have been performed [1838–1842]. Precision spectroscopic studies on *anti-hydrogen (antiproton–positron)* are extremely interesting in revealing possible asymmetries between the "world" and an "anti-world" [1843–1847].

Returning to the field of saturation spectroscopy we note that it is also possible to observe Doppler-free saturation signals in cell experiments without detecting the intensities of the transmitted beams. Fluorescence, opto-galvanic, and opto-acoustic detection can all be used. However, since the signal information is no longer carried by a well-defined probe beam, which is coupled to the pump beam only at the line centre, a double-modulation technique must generally be employed in order to isolate the Doppler-free signal from the Doppler-broadened one. This is because a modulation of the pump beam at frequency f_1 clearly causes a huge Doppler-broadened

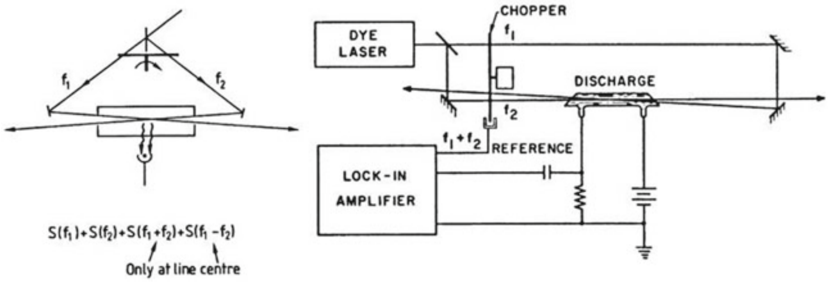

Fig. 9.63 Experimental arrangements for intermodulated fluorescence spectroscopy (*left*) and intermodulated opto-galvanic spectroscopy (*right*) [1849]

signal at frequency f_1 in these alternative detection schemes. If the oppositely directed beam (which in this case has an intensity similar to that of the pump beam) is modulated at a different frequency f_2, a modulation of the signal will also occur at this frequency. Clearly, these modulations are normally quite independent of each other since they are coupled to different velocity groups. However, at the line centre the two modulations interact due to the nonlinear response of the medium resulting from the saturation. Thus, for the same reason that frequency sum- and difference generation occurs in nonlinear crystals (Sect. 8.6), signals at the frequencies ($f_1 + f_2$) and ($f_1 - f_2$) will arise at the line centre in these *intermodulated* experiments. Arrangements for intermodulated fluorescence [1848] and intermodulated opto-galvanic spectroscopy [1849] are shown in Fig. 9.63. Doppler-free signals can also be obtained using RF opto-galvanic spectroscopy [1850] where amplitude variations in the RF oscillator driving a discharge in the sample are utilized. Doppler-free acousto-optic intermodulated spectroscopy is described in [1851].

The need for intermodulation in the experiments discussed above arises from the fact that the beams are amplitude modulated. By instead utilizing beam overlap modulation, e.g., by reflecting the laser beam back through the cell from a vibrating mirror, both beams are present at all times and no modulation is normally obtained. However, when one beam is swept to overlap the other, the nonlinear interaction at the line centre changes the total signal at the vibration frequency f or $2f$, depending on the sweep geometry [1852]. By combining the saturation spectroscopy techniques discussed above with rotating polarizers instead of choppers in the laser beams, problems due to ($f_1 + f_2$) and ($f_1 - f_2$) frequency generation caused by nonlinearities in the detectors, rather than true signals, can be eliminated. The technique is then called POLINEX (POLarization INtermodulated EXcitation) spectroscopy [1853]. The polarization methods also have an additional advantage of being largely insensitive to velocity-changing collisions, which can cause broad signal pedestals under the narrow signals even if lock-in detection at the frequencies ($f_1 + f_2$) or ($f_1 - f_2$) is performed. (The collisions tend to spread the "hole" over a larger frequency range). Since the orientation of the atoms induced by the polarized light is normally changed by collisions, the POLINEX signal, which is sensitive to polarization rather than to light intensity, will essentially only exhibit the narrow signal contribution.

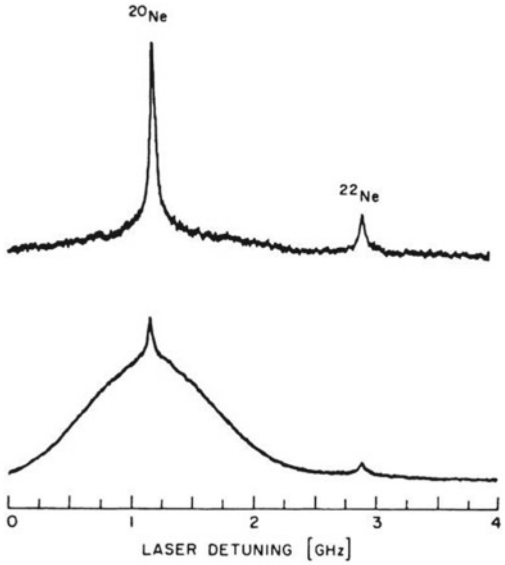

Fig. 9.64 Comparing recordings of the 588.2 nm Ne line using POLINEX (*upper curve*) and intermodulated fluorescence spectroscopy [1853]

The effect is illustrated in Fig. 9.64, in which the reduction in collisional effects is shown for a Ne transition.

9.7.3 Doppler-Free Two-Photon Absorption

We have already discussed the two-photon absorption process [1854] (Sect. 9.1.3). Normally, the signals are Doppler broadened, and high resolution is not obtained even if narrow-band lasers are used. However, a very important observation was made as early as 1970 by *Chebotayev* and coworkers [1855]. The Doppler broadening can be eliminated if the two photons are extracted in such a way that one is supplied from one of two counter-propagating laser beams and one from the other beam. For a certain atom with a velocity component v along one direction of propagation, the energy interval ΔE can be bridged by two Doppler-shifted contributions

$$\Delta E = h\nu(1 + v/c) + h\nu(1 - v/c) = 2h\nu. \tag{9.37}$$

Thus, the first-order Doppler shift in one absorption is exactly cancelled by the corresponding shift in the second absorption. Since the velocity is eliminated in the expression, *all* irradiated atoms can contribute to the signal and not just a certain group, as in saturation techniques. In S–S transitions, we have the selection rules $\Delta F = 0$, $\Delta M = 0$ for the two-photon transition between the two states of equal parity. By making both laser beams either right-hand circularly polarized or left-hand circularly polarized, it is possible to ensure that the two photons come from

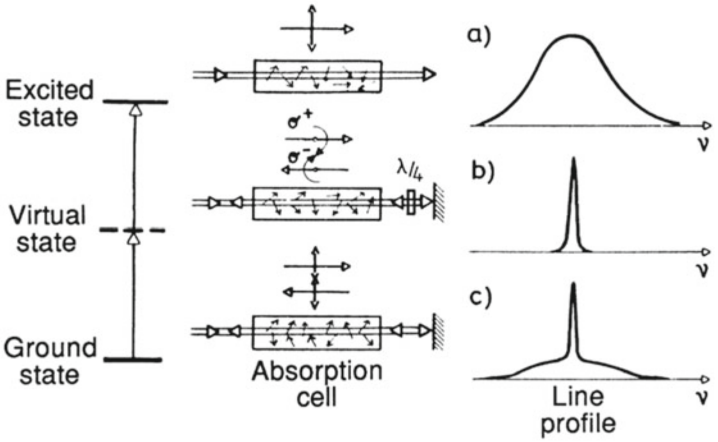

Fig. 9.65 Two-photon absorption spectroscopy signals for different laser beam arrangements

different laser beams ($\Delta M = +1$ and $\Delta M = -1$ make effectively$\Delta M = 0$). This case is shown in Fig. 9.65 as well as the case of a Doppler-broadened signal, which is obtained if only one laser beam (unpolarized or linearly polarized) is used. If two such oppositely propagating beams are used, a Doppler-free as well as a Doppler-broadened contribution will be obtained (Fig. 9.65c). Early experimental observations of Doppler-free signals were made by several groups [1856–1859]. Doppler-free two-photon absorption has been used in a large number of atomic level investigations. For highly excited states, thermionic diode detection is frequently employed. States up to $n = 500$ have been reached in stepwise excitations [1860]. As an example, a recording is shown in Fig. 9.66. Systematic studies of alkali metal atoms [1861–1863] and alkaline earth atoms have been performed. Data obtained in two-photon and stepwise excitation experiments on sequences of Rydberg states in the alkaline earth atoms have been analysed using multichannel quantum defect theory [1864–1867].

9.7.4 Precision Laser Spectroscopy on Hydrogen

We will also discuss another series of investigations on hydrogen initiated by *Hänsch* and co-workers, which is of fundamental importance [1868–1873, 1818]. The experiments include the determination of the Lamb shift in the ground state ($n = 1$) (Fig. 9.67). In contrast to the situation for the $n = 2$ state, in which the position of the $2\,s\ ^2S_{1/2}$ state can easily be related to the $2p\ ^2P_{1/2}$ state position, there is no neighbouring state for the ground state. However, its energy position is still affected by QED effects, and in order to measure these, reference to the $n = 2 \leftrightarrow n = 4$

Fig. 9.66 Doppler-free spectrum for high-lying Rydberg states in Ba [1860]

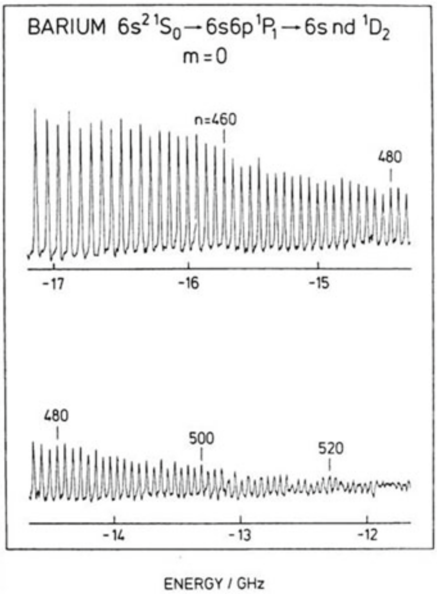

transition (H_β) can be made. The simple Balmer formula (4.42) states that the $n = 2 \leftrightarrow n = 4$ interval should be 1/4 of the $n = 1 \leftrightarrow n = 2$ interval.

Because of fine structure, relativistic, and QED effects (the Lamb shift is the ground state QED effect, which is to be determined), the simple energy interval relation does not hold exactly. Starting from a primary narrow-band laser at 486.0 nm it is possible to simultaneously measure the H_β-line using polarization spectroscopy and the $n = 1 \leftrightarrow n = 2$ transition with two-photon spectroscopy, and compare the signal positions for the Lamb-shift determination. Sometimes well-known lines from Te_2 molecules are used as reference lines. These molecules have many transitions in the blue spectral region which can be used as wavelength standards [1874] in the same way as I_2 lines are used at longer wavelengths [1875]. Light from the 486.0 nm laser is amplified with pulsed amplifier stages pumped by a pulsed excimer laser and the pulses are frequency-doubled to 243.0 nm in a nonlinear crystal. The two-photon transitions between $n = 1$ and $n = 2$ are monitored using the Lyman-α line at 121.6 nm, which is obtained after collisional transfer in the discharge from the $2s\ ^2S_{1/2}$ to the $2p\ ^2P_{1/2}$ state. The two-photon signals have a larger linewidth than the polarization spectroscopy signals because of the Fourier broadening of the pulsed amplification (pulse length 10 ns $\rightarrow\ \Delta\nu \cong 1/10^{-8}$ Hz $=$ 100 MHz). The measurement yields a Lamb shift of the 1s state of about 8170 MHz (a precise value is 8172.876(29) MHz [1878]), which is in close agreement with the theoretical predictions. Since the natural lifetime of the 2s state is about 10^{-1} s, extremely narrow lines should, in principle, be attainable. Narrow-band 243 nm radiation has been generated using CW frequency-mixing techniques, yielding a resolution of 1: 10^{10}, or better [1870, 1876, 1877].

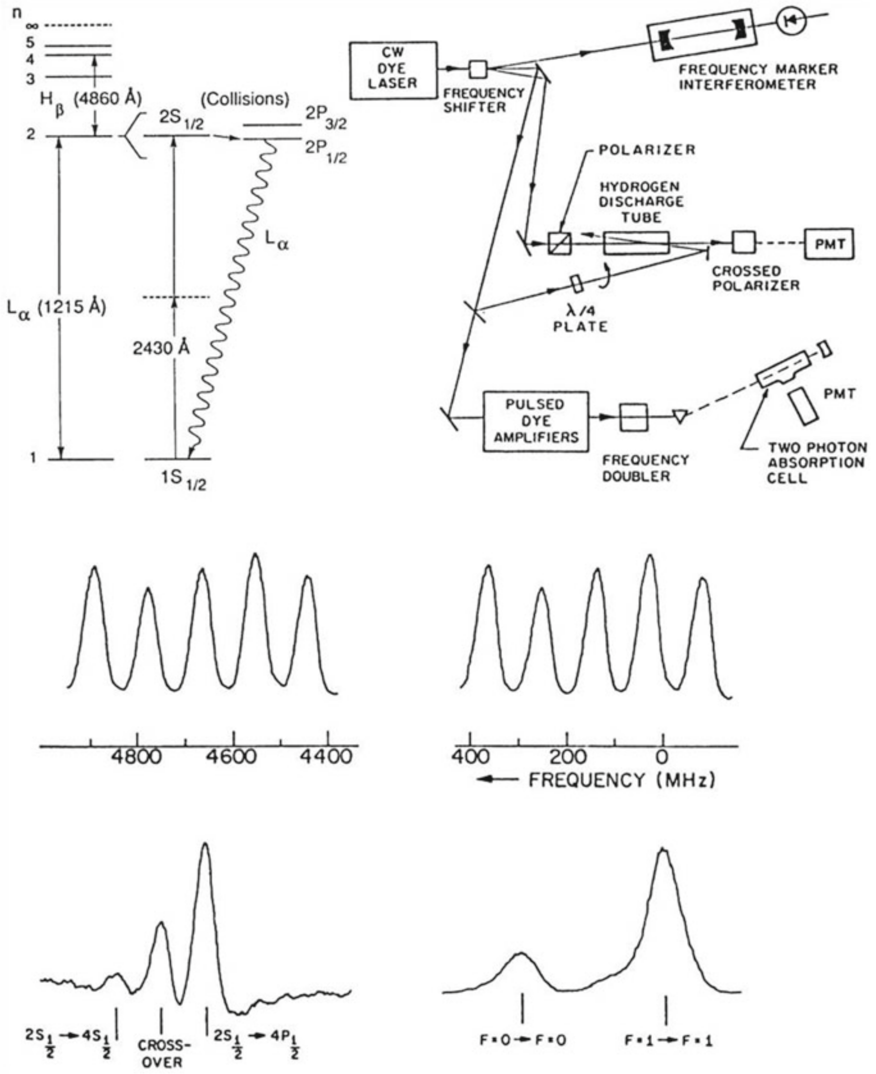
n
∞
5
4
3
H_β (4860 Å)
(Collisions)
2
2S_1/2
2P_3/2
2P_1/2
L_α
L_α (1215 Å)
2430 Å
1
1S_1/2
CW DYE LASER
FREQUENCY SHIFTER
FREQUENCY MARKER INTERFEROMETER
POLARIZER
HYDROGEN DISCHARGE TUBE
PMT
CROSSED POLARIZER
λ/4 PLATE
PULSED DYE AMPLIFIERS
FREQUENCY DOUBLER
PMT
TWO PHOTON ABSORPTION CELL
4800
4600
4400
400
200
0
← FREQUENCY (MHz)
2S_1/2 → 4S_1/2
CROSS-OVER
2S_1/2 → 4P_1/2
F=0→F=0
F=1→F=1

Fig. 9.67 Experimental arrangement and recorded signals for simultaneous saturation spectroscopy (2*s*-4*p*) and two-photon absorption spectroscopy (1*s*-2*s*) in atomic hydrogen [1868]

An example of high-resolution spectroscopy for hydrogen and deuterium is given in Fig. 9.68, where isotope shifts are determined and the absolute frequencies of the two-photon transitions are related to Doppler-free saturation spectroscopy reference transitions in a tellurium molecular frequency standard, by observing the beat frequency between the two lasers when mixed in a common detector. Many

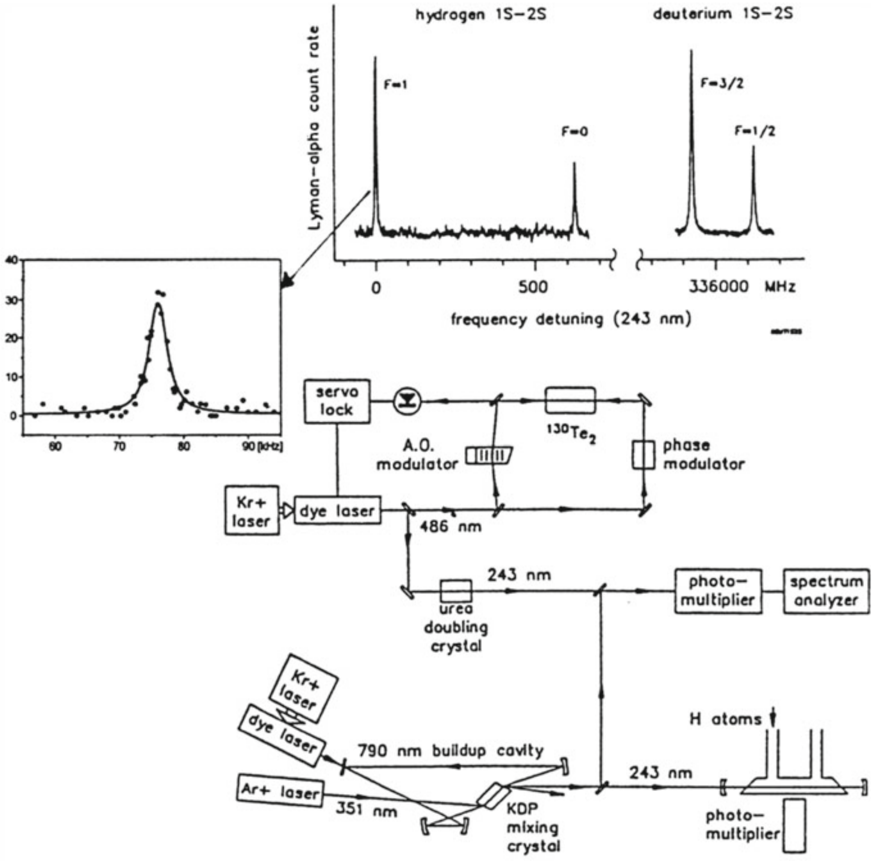
hydrogen 1S–2S
deuterium 1S–2S
Lyman-alpha count rate
F=1
F=0
F=3/2
F=1/2
0
500
336000 MHz
frequency detuning (243 nm)
40
30
20
10
0
60
70
80
90 [kHz]
servo lock
A.O. modulator
$^{130}Te_2$
phase modulator
Kr+ laser
dye laser
486 nm
243 nm
urea doubling crystal
photo-multiplier
spectrum analyzer
Kr+ laser
dye laser
790 nm buildup cavity
Ar+ laser
351 nm
KDP mixing crystal
243 nm
H atoms
photo-multiplier

Fig. 9.68 Recording of the 1*s*-2*s* transition in atomic hydrogen and deuterium using CW high-resolution lasers [1870, 1871]. As an insert a narrow-linewidth recording of one of the hyperfine transitions is shown [1878]

groups have been very active in the field of precision hydrogen spectroscopy [1879–1881]. Frequently, combinations of atomic states and utilization of simple relationships between transition frequencies as given by the Balmer formula (4.42), and its extensions, have been utilized [1817].

Relating optical frequencies to the cesium time standard has been a very important issue in precision metrology. In this context, the development of the optical-frequency comb technique using mode-locked lasers has been very important.

9.7.5 Emergence of the Laser Frequency Comb Technique

The laser frequency comb technique has brought about a further revolution in precision spectroscopy and metrology. Historically, there is a connection to the Ramsey fringe technique, first introduced for the RF region (Sect. 7.1.2), but now applied to the optical region. We first consider the case of two-photon spectroscopy with a pulsed laser. The inevitable Fourier broadening of a short pulse is illustrated in Fig. 9.69 (*top*).

However, by applying a further pulse after a delay T, a sharp interference pattern in the two-photon signal can be obtained. It is important that the signal is Doppler-free so that the phase memory from the first pulse is not lost through the velocity spread. Ordinary signals and Ramsey fringes for the two-photon transitions $3\,s\ {}^2S_{1/2} \rightarrow 4d\ {}^2D_{3/2,5/2}$ in ^{23}Na are shown in the figure [1882]. The signals display the hyperfine structure of the ground state (1772 MHz, Fig. 9.58) and the inverted fine structure of the excited state (1028.8 MHz, see also Fig. 9.18). The sharpness in the interference pattern can be increased using multiple pulses [1883]. An analogy with the interference from a double slit and from a grating illuminates this effect.

A similar technique was also demonstrated using a train of femtosecond pulses [1884]. The possibility of using multi-pulse interference effects of the Ramsey type for high-resolution laser spectroscopy is particularly interesting for the VUV, XUV, and soft X-ray regions, where narrow-band CW coherent sources are absent. High-harmonic generation (Sect. 9.6.2) is of particular interest in this context, especially since the radiation has been shown to have a high degree of coherence [1638]. As discussed earlier, high-resolution spectroscopy of internal structures over difficult wavelength ranges can also be performed using quantum-beat spectroscopy or optical double resonance and level-crossing spectroscopy using pulsed sources, for which nonlinear conversion can readily be performed [1459–1461].

The optical Ramsey effect has also been demonstrated for the case of saturation spectroscopy with CW laser beams [1885]. An atomic beam is crossed by counter-propagating laser beams at three different locations along the atomic beam. In this way the transit-time broadening can be strongly reduced, which was the original reason for introducing the technique in the RF regime. The technique has primary importance in connection with the establishment of ultra-stable laser secondary wavelength standards. A special variety of the Ramsey fringe technique using a "fountain" of very slow atoms has also been proposed and demonstrated [1886–1888].

As we have noted, hydrogen is a very fundamental system which is well suited for precision studies. Hydrogen-like ions, i.e., heavier atoms, where all but one electron have been stripped off, are also very interesting to study, since relativistic and QED effects scale very favourable with the nuclear charge Z. Precision spectroscopy on such ions, frequently held in traps (see Sect. 9.8), have been pursued [1889, 1890]. Another fundamental system, encompassing three particles, is the helium atom, which has also been much studied by precision laser spectroscopy [1891–1893].

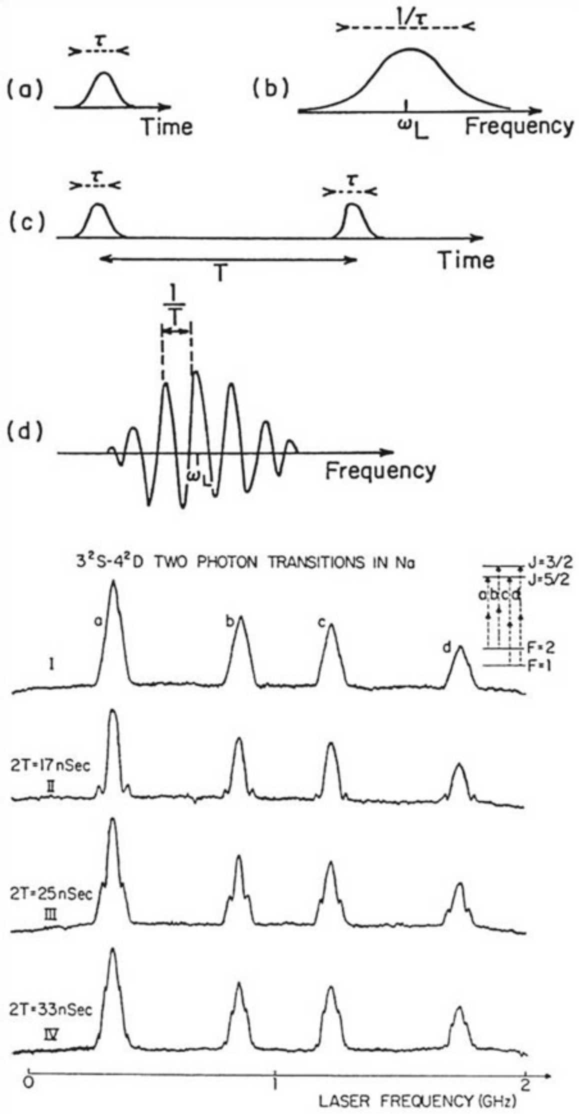

Fig. 9.69 Illustration of the optical Ramsey fringe technique in the time domain [1882]

An extremely important aspect for precision spectroscopy as well as for frequency metrology related, e.g., to the definition of the second, is the development of *frequency comb spectroscopy*. As we know, a CW laser exhibits sharp, equidistant laser modes, which by mode-locking can be made to be related to each other (Sect. 8.7.1) and then producing a train of ultra-short laser pulses. We have here a strong dualism: individual laser modes are present at all times, but their interference leads to the formation of extremely intense, short pulses, separated by very "long" times of total darkness. The individual sharp laser modes can be used for precision spectroscopy, as was early demonstrated by filtering dye laser pulses by an external, piezo-electrically scanned Fabry-Pérot interferometer [1051, 1894], and then clearly subject to overlapping orders, like in classical Fabry-Pérot spectroscopy (See, e.g., Fig. 6.32).

We have already discussed the corresponding phenomenon above in the time doman, and then related to the Ramsey fringe technique. A narrowing of signals occurs if the atoms are illuminated by two laser pulses [1882] and further narrowing occurs when a train of pulses is employed [1883]. Frequency comb spectroscopy emerged from such observations and the demonstration, that the spacing between the modes in a femtosecond laser is stable to a precision on the 1: 10^{19} level [1895–1897]. Important aspects in terms of this precision metrology came by the realization, that a very short femtosecond pulse has a very broad spectral distribution of modes (Eq. 8.19) and that the corresponding intense pulses can efficiently be frequency doubled (with all its individual modes). If the mode distribution is wide enough, or can be widened enough, the high-frequency modes of the fundamental pulse can fall close to the low-frequency modes of the frequency doubled pulse. Since mode-spacings f_{fsr} are typically of the order of 100 MHz this means, that a beat-frequency (difference frequency) can be picked up by heterodyne techniques (Sect. 10.2.1). This will allow further stabilization of the laser cavity, but also the determination of the zero-off-set for the first of the equidistant laser mode positions. This was also early noted in [1898]. This is illustrated in Fig. 9.70 [1899] and expressed in (9.38) (actually presented already as Eq. (8.22) in the laser chapter, but now with symbols according to Fig. 9.70).

$$2f(n) - f(2n) = 2\left(nf_{fsr} + f_o\right) - \left(2nf_{fsr} + f_o\right) = f_o. \tag{9.38}$$

The sufficient spectral broadening required is normally achieved by focusing the pulses into a structured photonic bandgap fibre, in a process closely related to white-light generation (Sect. 9.5.1). The highest accuracy in precision laser spectroscopy has been achieved with frequency comb laser systems (See, e.g., [1900–1903]). As mentioned earlier, the 2005 Nobel Prize in Physics was awarded to *J.L. Hall* and *T.W. Hänsch* for their contributions to the development of lasers-based precision spectroscopy, including the frequency comb technique [1272, 1273].

The reduction in complexity in relating optical frequencies to the current microwave standard for the second unit is illustrated in Fig. 9.71. The same approach to stabilization of the frequency in a frequency comb laser system related to spectroscopy and metrology pertains regarding the carrier-envelope phase stabilization of systems relevant to attosecond pulse generation (Sect. 8.7.2). This is the case, since the accumulated phase slip $\Delta\varphi$ in the carrier-envelope relative position during one second is corresponding to the frequency off-set f_0 according to (8.39) (presented in Chap. 8 as (8.23):

$$f_0 = f_{\text{rep}}\Delta\varphi/2\pi \tag{9.39}$$

where $f_{rep} = f_{fsr}$ (see Eq. (8.18)).

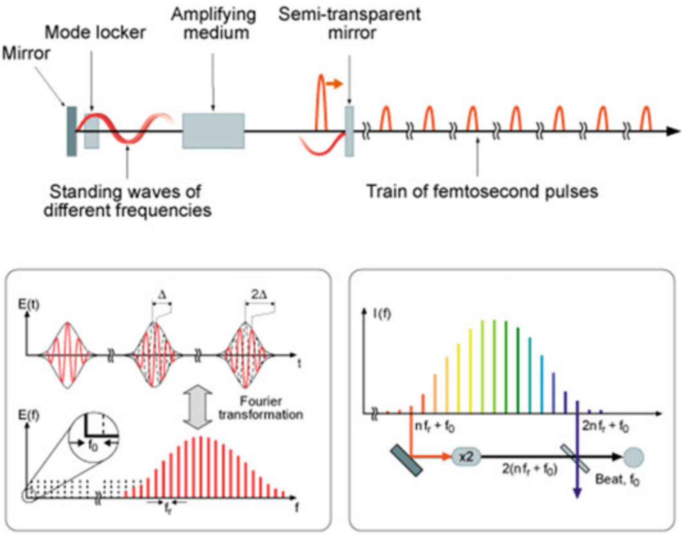

Fig. 9.70 Frequency combs derived from a femtosecond laser and its frequency doubled output, allowing the determination of the zero-offset frequency of the cavity modes [1899]

The frequency comb technique has allowed an extreme precision in the measurement of optical frequencies. An uncertainty of about 1: 10^{18} has been attained, but the absolute frequency in terms of the best cesium fountain atomic clocks, which define the second, is clearly limited by the current definition, and there is a clear need to change the definition and make it be based on an optical frequency. The very fundamental 1-2s transition in hydrogen atoms has been measured to a precision of 5×10^{-15} [1905], which is close to what is feasible with the current second definition.

The frequency comb laser techniques have also found many applications in practical gas analysis [1906–1909]. Figure 9.72 shows the general idea of an absorption measurement with frequency comb techniques. Instead of using a normal white-light source together with a dispersive spectrometer, the comb provides discrete lines with well-defined frequency. However, the technique has several further advantages, e.g., if a Michelson (FTS) interferometer is used. Instead of seeing the interferogram as a result of the interference of frequency components as the moving arm length is changed, it is now more fruitful to consider the Doppler shift in the light, which bounces off the moving mirror. At the detector, beats (falling in the audio domain) are then formed between the shifted and unshifted frequency components. In the case of a comb, such beats are formed corresponding to each mode, and a frequency comb at low frequencies is formed by the down-converted optical radiation.

By simultaneously operating two different frequency comb with slightly different free spectral range, one comb can be seen as acting as a local oscillator creating beat signals with the corresponding modes of the other comb. Effectively, the generated signal (the interferogram) becomes equivalent to that obtained in a normal Michelson

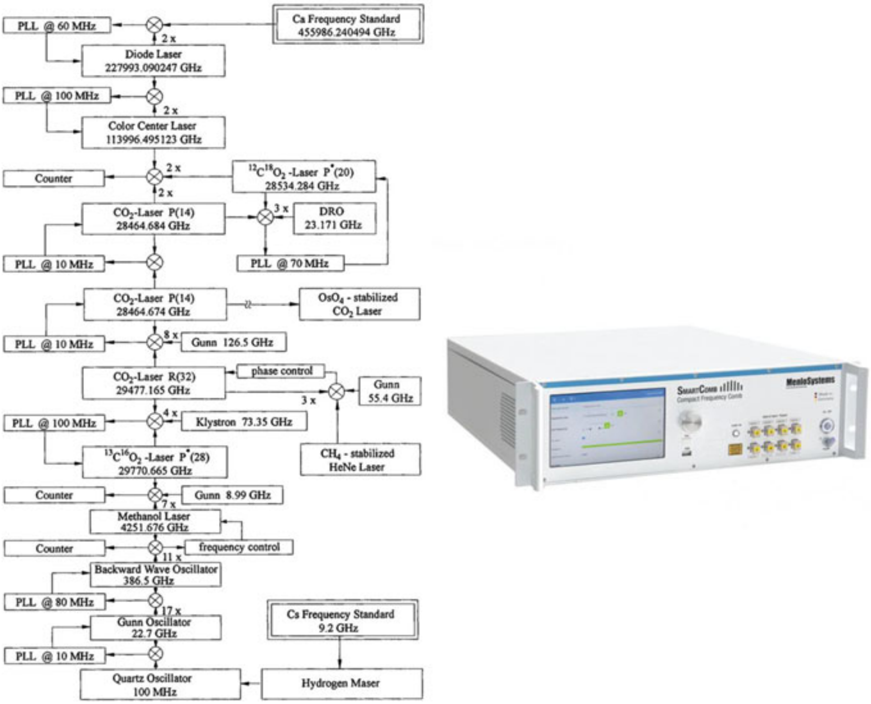
PLL @ 60 MHz
Ca Frequency Standard 455986.240494 GHz
2 x
Diode Laser 227993.090247 GHz
PLL @ 100 MHz
2 x
Color Center Laser 113996.495123 GHz
Counter
2 x
$^{12}C^{18}O_2$ -Laser P*(20) 28534.284 GHz
2 x
CO_2-Laser P(14) 28464.684 GHz
3 x
DRO 23.171 GHz
PLL @ 10 MHz
PLL @ 70 MHz
CO_2-Laser P(14) 28464.674 GHz
OsO_4 - stabilized CO_2 Laser
PLL @ 10 MHz
8 x
Gunn 126.5 GHz
CO_2-Laser R(32) 29477.165 GHz
phase control
Gunn 55.4 GHz
3 x
PLL @ 100 MHz
4 x
Klystron 73.35 GHz
$^{13}C^{16}O_2$ -Laser P*(28) 29770.665 GHz
CH_4 - stabilized HeNe Laser
Counter
Gunn 8.99 GHz
7 x
Methanol Laser 4251.676 GHz
Counter
frequency control
11 x
Backward Wave Oscillator 386.5 GHz
PLL @ 80 MHz
17 x
Gunn Oscillator 22.7 GHz
Cs Frequency Standard 9.2 GHz
PLL @ 10 MHz
Quartz Oscillator 100 MHz
Hydrogen Maser
SmartComb
MenloSystems

Fig. 9.71 Comparison of complexity in relating an optical laser wavelength to the present microwave time standard of the second. (**a**) laser chain at PTB Braunschweig ([1904], reproduced under the Creative Commons Licence CC BY 4.0, APS) and (**b**) stabilized compact frequency comb laser (Courtesy: Menlo Systems)

interferometer, but now without the need for any moving parts. Different approaches of frequency comb spectroscopy are shown in Fig. 9.73.

9.8 Cooling and Trapping of Ions and Atoms

9.8.1 Introduction

In principle, lasers can be stabilized to a linewidth in the sub-Hz region. If transitions between the ground state and long-lived metastable states with a lifetime of the order of 1 ms are utilized, the natural radiation width will be very small (100 Hz). On the other hand, transit-time broadening can be substantial. The transit time of a thermal atom through a 3 mm laser beam is about 10^{-5} s, which corresponds to a broadening of about 10 kHz. As we have seen, this effect can be reduced by employing the Ramsey fringe technique. A remaining fundamental broadening is the second-order

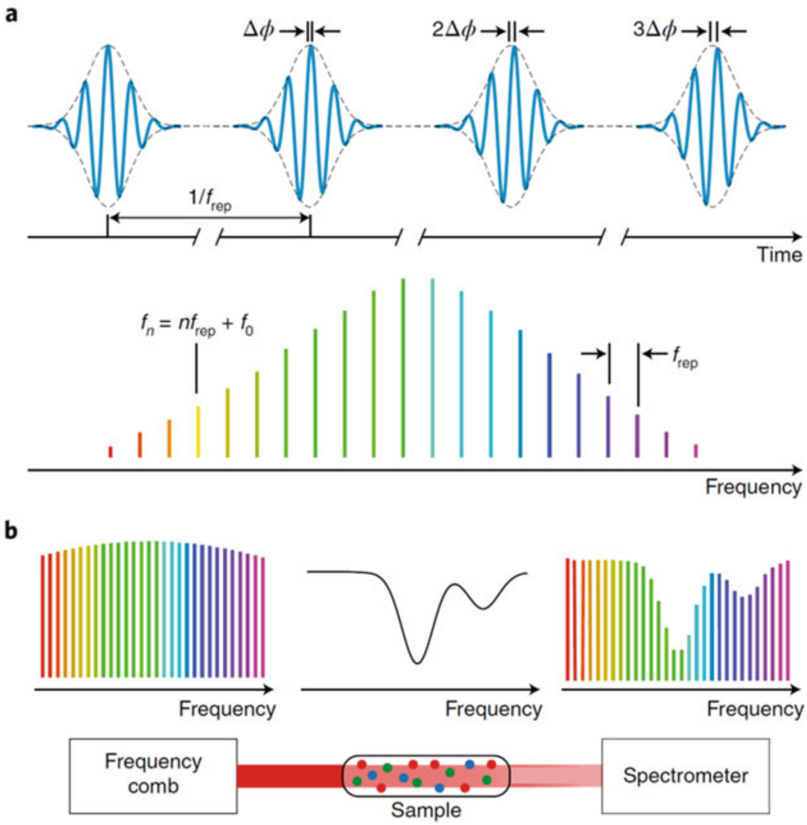

Fig. 9.72 **a** Illustration of carrier envelope slip and basic principle of frequency comb spectroscopy. By stabilizing the comb, which is the same thing as measuring and stabilizing the frequency offset, a high-precision frequency scale is automatically established without the need for any well-characterized molecular reference lines, when pursuing frequency comb absorption spectroscopy, as illustrated in **b** ([1909], reproduced with permission from Springer-Nature)

Doppler effect (see Eq. 9.11), related to the relativistic Lorenz contraction. The effect amounts to about 100 Hz in the visible region. Obviously, in order to achieve an optimal resolution the atoms must be brought to rest. Spectroscopy on a sample of ultracold atoms or ions can provide extremely small linewidths and extreme precision in measurements of fundamental nature (Rydberg constant, Lamb shift, fine-structure constant, isotropy of space, etc.). New types of atomic clocks with unprecedented precision (fractions of a Hz on a visible transition at about 10^{15} Hz) are also possible. Finally, at very low temperatures, sufficiently dense atomic samples can “condense” into a new state of matter, a *Bose condensate*.

Slowing down the velocity of atoms, ions or molecules thermodynamically corresponds to cooling. Cooling can be achieved using laser light. Basically, the transfer of the momentum of the photon ($p = h\nu/c$; Eq. (9.28)) is utilized as suggested in 1975

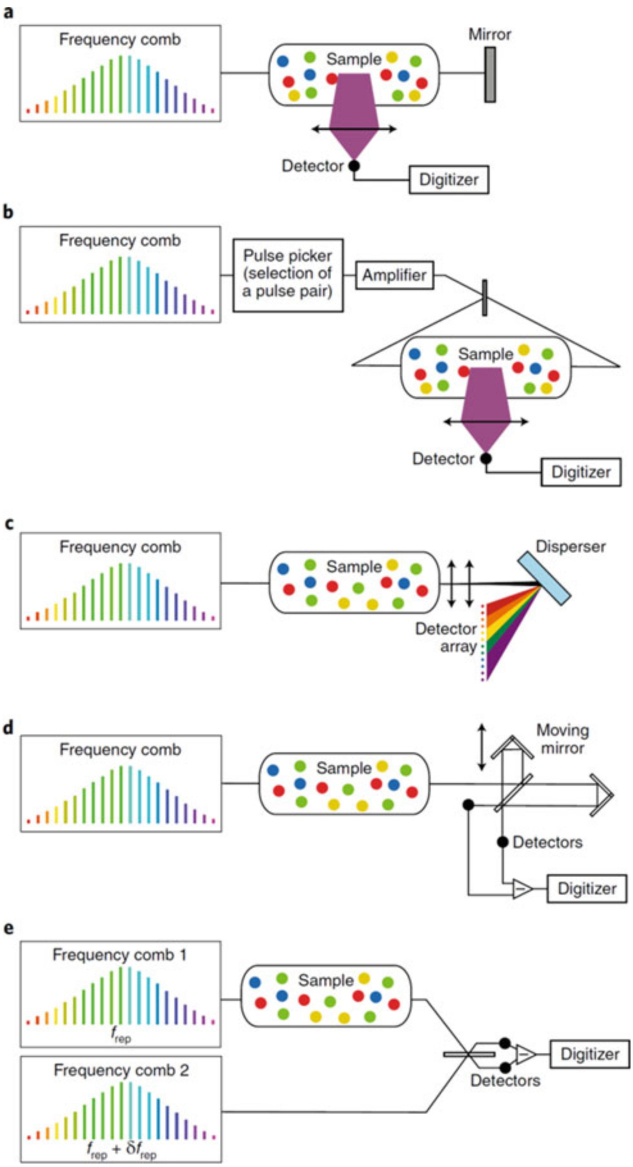
a
Frequency comb
Sample
Mirror
Detector
Digitizer
b
Frequency comb
Pulse picker (selection of a pulse pair)
Amplifier
Sample
Detector
Digitizer
c
Frequency comb
Sample
Disperser
Detector array
d
Frequency comb
Sample
Moving mirror
Detectors
Digitizer
e
Frequency comb 1
f_{rep}
Frequency comb 2
$f_{rep} + \delta f_{rep}$
Sample
Detectors
Digitizer

Fig. 9.73 Different varieties of frequency comb spectroscopy. **a** Doppler-free two-photon spectroscopy with fluorescence detection. **b** Ramsey-fringe detection using a pulse-picker isolating two pulses from the train generated by the mode-locked laser. Again, two-photon excitation and fluorescence detection is used. **c** Frequency comb absorption spectroscopy with wavelength dispersion using a grating. **d** Frequency comb Fourier transform spectroscopy employing a scanning Michelson interferometer. **e** Dual-comb spectroscopy with one comb interacting with the sample and the other one serving as a local oscillator ([1909], reproduced with permission from Springer-Nature)

by *Hänsch and Schawlow* [1910] and *Wineland and Dehmelt* [1911]. The mechanical influence of light on atoms and other particles was demonstrated early on (Sect. 9.7.1). The motion of atoms in a beam can be decreased by directing a laser beam against the atoms. For each head-on absorption process, the velocity of a sodium atom is reduced by 3 cm/s. By absorbing (and emitting) photons some 20,000 times they can be brought to rest. Clearly, the fact that the atoms shift out of resonance with the counter-propagating single-mode laser beam as they slow down is a problem. *Letokhov* and co-workers suggested that the laser frequency be shifted downwards to counteract the Doppler shift [1912–1914]. A small "package" of atoms could be cooled down to 1.5 K without shifting the frequency [1915, 1916]. A more efficient way was proposed and demonstrated by *Phillips* and co-workers [1917–1921]. By using the combined effect of optical pumping into the highest m quantum state (Sect. 7.1.3) and Zeeman tuning in a magnetic field of decreasing strength along the beam path, the atoms can be kept in resonance (Fig. 9.74). The techniques described above only affect the longitudinal velocity of the beam. In order to bring atoms or ions to a "complete" rest all velocity components must be removed. This can be achieved if the atoms or ions are confined in a trap. An electrically charged particle can be trapped in a potential generated by static or oscillating electromagnetic fields, while the trapping of neutrals is more complicated.

9.8.2 Ion Traps

Many different types of ion trap exist. Already in the 1930´s the *Penning* trap had been developed, basically as a means of making more sensitive ionization gauges for vacuum measurements [1922]. In a discharge through a low-pressure gas, the electron paths can be considerably prolonged by applying a strong magnetic field, in which the charged particles spiral. An optimized Penning trap consists of two hyperbolically shaped pole caps held at the same potential and a hyperbolically shaped ring forming the other electrode placed symmetrically between the caps. (See Fig. 9.75a). The potential field tends to stabilize the charged particles between the caps in the z-direction but they are unstable in the x–y plane. The magnetic field in the z-direction makes them spiral back and forth between the end caps with a given rotation frequency, which is close to the *cyclotron resonance* frequency

$$\omega_c = qB/m, \tag{9.40}$$

where q is the particle charge, m its mass, and B the applied magnetic field. This equation suggests that the mass of an ion can be measured very exactly in an ion trap [1923, 1924].

Of particular interest is to study highly charged ions kept in a trap. Such systems exhibit, compared to singly ionized atoms, effects due to relativity and quantum

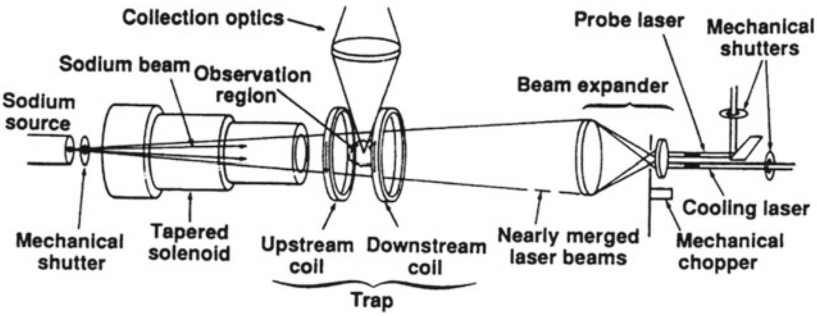
Collection optics
Sodium beam
Observation region
Sodium source
Probe laser
Mechanical shutters
Beam expander
Cooling laser
Mechanical shutter
Tapered solenoid
Upstream coil
Downstream coil
Trap
Nearly merged laser beams
Mechanical chopper

Fig. 9.74 Arrangement for cooling atoms in a beam using a Zeeman slower. In the middle of the figure a magnetic trap is shown [1921]

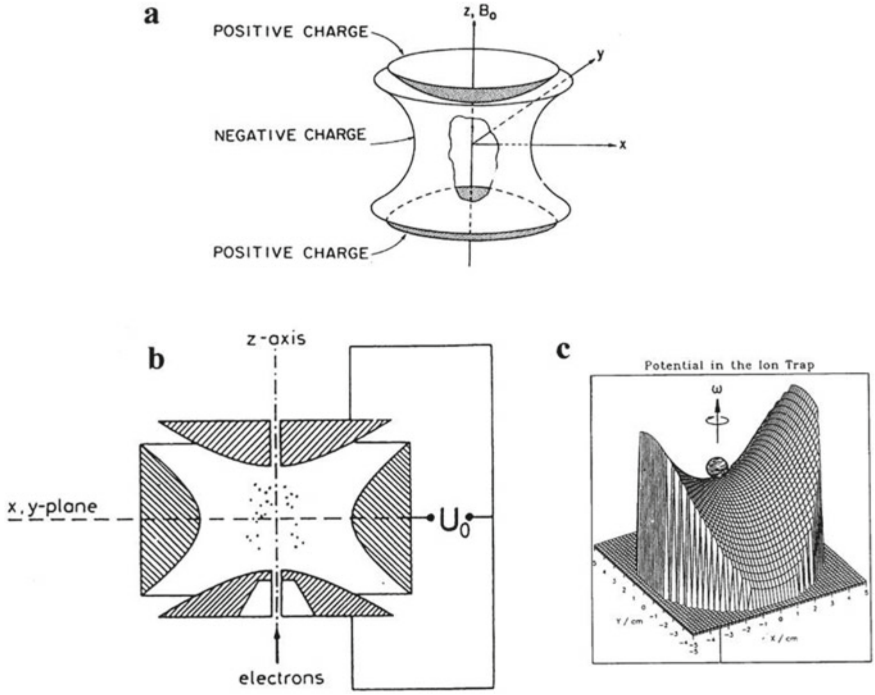
a
z, B₀
POSITIVE CHARGE
y
NEGATIVE CHARGE
x
POSITIVE CHARGE
b
z-axis
x, y-plane
U₀
electrons
c
Potential in the Ion Trap
ω
Y / cm
X / cm

Fig. 9.75 **a** Penning and **b** Paul traps for ions. A mechanical analogue of the Paul trap is also included **c** [1932, 1933]

electrodynamics, which are enhanced by orders of magnitude [1925]. Such systems have also allowed precise measurements of the electron mass and magnetic moment. Possible changes in fundamental constants, such as the fine-structure constant can also be investigated using such systems [1926].

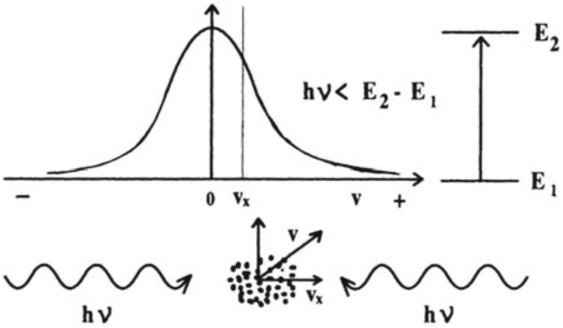

Fig. 9.76 The principle of laser cooling

In the *Paul trap* (the RF quadrupole trap), the static magnetic field is removed and the DC electric supply for the Penning trap is replaced by an RF electric field (Fig. 9.75b), which brings about a dynamic stabilization [1927]. This can be seen in a mechanical analogue (Fig. 9.75c). The trap forms a saddle-shaped surface on which a small steel ball is placed. The ball is stabilized in one dimension but will slide down in the other dimension. If now the saddle surface is rotated around a vertical axis, the ball is prevented from falling down. The depth of the trapping potential is substantial ($\approx$eV).

Further examples on the powerful technique of using traps are given in [1928–1931]. The Nobel Prize in Physics of 1989 was given to *W. Paul* and *H.G. Dehmelt* for developments of trapping techniques for ions [1932, 1933].

9.8.3 Basic Laser Cooling in Traps

By irradiating an ion or atom in a trap with laser radiation tuned to the low-frequency side of the Doppler curve of the transition, the velocity of the ion will be successively slowed down [1910, 1911] (Fig. 9.76). Because of the detuning of the laser, a photon can only be absorbed when the ion is moving against the laser beam. The absorption of the momentum of the photon will slow down the ion. The decay photon can be emitted in any direction. After some time, the ion will have been brought to a very low velocity. Two counter-propagating beams of the same frequency can be used for simultaneously cooling particles moving in opposite directions. The intuitive velocity limit would correspond to the atomic recoil energy due to a photon emission, which in thermodynamical language corresponds to the *recoil limit temperature* T_R:

$$T_R = p^2/4mk, \qquad (9.41)$$

where p is the photon momentum (9.28).

The recoil velocity for a sodium atom is, as mentioned above, about 0.03 m/s, which would in thermodynamic language correspond to a temperature of about 2

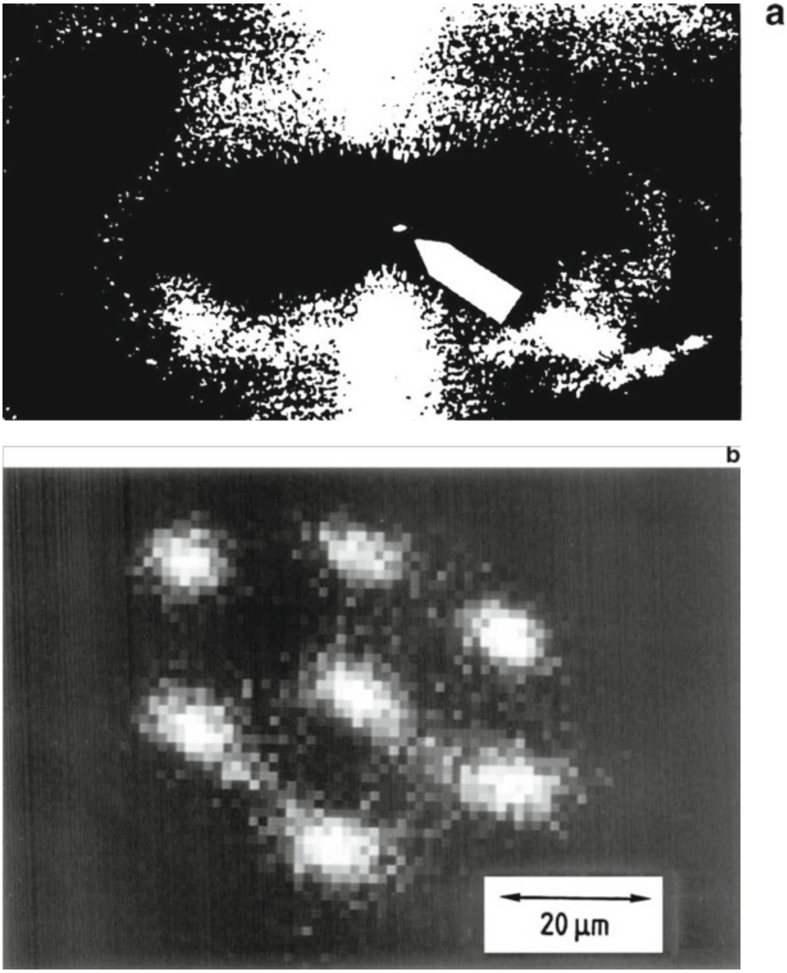

Fig. 9.77 **a** Photograph of the fluorescence light from a single barium ion kept in an RF trap [1937]. **b** Recording of the fluorescence of seven stored magnesium ions exhibiting "crystallization" behaviour [1939]

μK. However, the statistical nature of absorption and emission in a gas of atoms or ions leads to a certain heating of the gas and a corresponding Doppler width, which is of the order of few hundred μK. This is referred to as the *Doppler limit* for the cooling temperature T_{D}, which is related to the excited state lifetime τ and can be expressed as

$$T_{\mathrm{D}} = \hbar/2\tau k. \tag{9.42}$$

Efficient cooling of ions was first achieved in 1978 [1934–1937]. A photograph of a single Ba^+ ion is shown in Fig. 9.77a. The “crystallization” of a few Mg^+ ions in a trap is illustrated in Fig. 9.77b. The ions are cooled to such a low velocity that the electrostatic forces between them dominate and an ordered arrangement (“Wigner crystal”, [1938]) is obtained [1939]. Arrangements of cooled ions exhibit interesting properties that are discussed in [1940–1942]. Linear arrangements of ions are being used in connection with *quantum computing* [1943–1948] (Sect. 4.9). Studies of excited state lifetimes and collisional processes are described in [1949].

Cooled and trapped single ions allow measurements of frequencies with unprecedented precision, and can serve for establishing an optical clock (for possible transition candidates, see Table 9.4) and for investigating possible changes in fundamental constants over time.

9.8.4 Trapped Ion Spectroscopy

Laser spectroscopy on a trapped and cooled ion can yield an extreme spectral resolution in transitions to long-lived (metastable) upper states. A new problem then has to be dealt with, connected with the low fluorescence yield of such highly forbidden transitions. A technique in which a strong transition is used for the detection of the forbidden transition has been proposed and demonstrated [1950–1954]. The technique, which is applicable to a single atom or ion, is illustrated in Fig. 9.78 for the case of a Hg ion. “Strong” fluorescence light induced by a laser tuned to the strong $5d^{10}6p\,^2P_{1/2}$ - $5d^{10}6s\,^2S_{1/2}$ fully allowed transition at 194 nm is normally detected. If another laser is tuned through the extremely narrow resonance of the (electric-dipole) “forbidden” $5d^{10}6s\,^2S_{1/2} - 5d^9 6s^2\,^2D_{5/2}$ transition, a resonant transfer of the ion to the metastable state(“*shelving*”) is detected through the abrupt disappearance of the fluorescent light in the strong transition (“quantum jump”). Experimental recordings of this phenomenon are included in Fig. 9.78, as are ultra-high-resolution scans of the “forbidden” transition.

A recent example on how the observations of shelving signals can be used to measure the lifetime of metastable states is given in [1955]. Spectroscopy on single laser-cooled ions in traps provides an extreme spectral resolution in the sharp transitions between metastable states and the ground state in many types of ions (examples of transitions are given in Table 9.4). This forms the foundation for optical atomic clocks as well as for searches of possible changes in fundamental constants, such as the Rydberg and fine-structure constants [1956, 1957]. An alternative way to search for possible changes is to observe the spectra of extremely distant galaxies, where the much lower spectral resolution is compensated by very long time lapses, compared to the few years of separation in precision laboratory studies [1958].

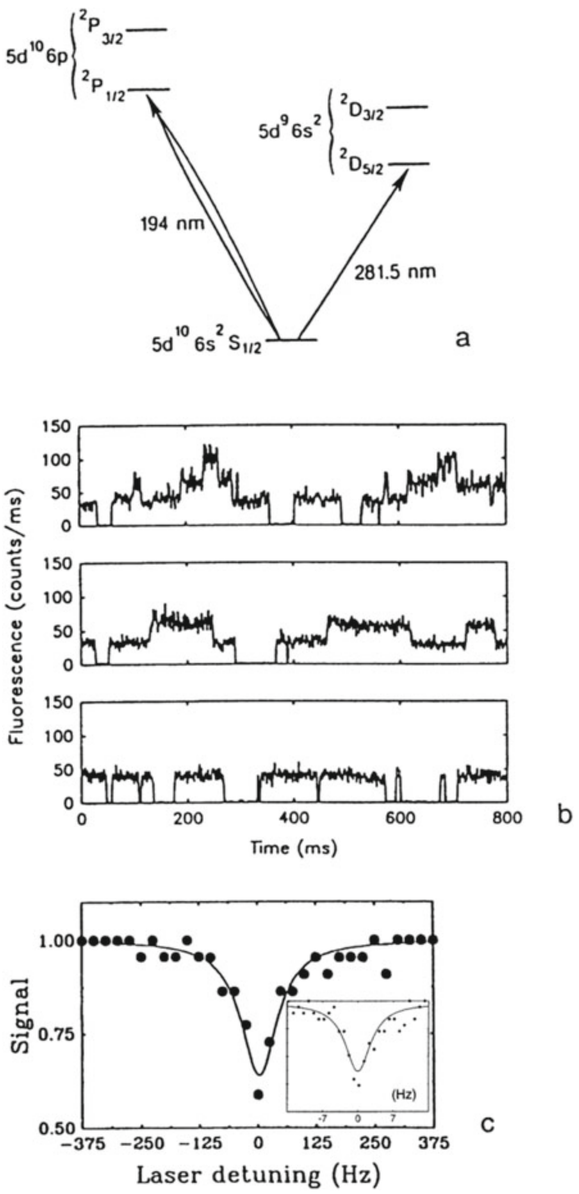

Fig. 9.78 **a** Energy levels for Hg^+, with the "strong" transition at 194 nm and the "weak" transition at 281.5 nm indicated. **b** Fluorescence light recording at 194 nm illustrating quantum jumps in 3 ions (*top*), two ions (*middle*), and one ion (*bottom*). **c** An experimental scan of the "weak" transition using an electrooptically stabilized laser is shown, featuring a linewidth of 86 Hz. This corresponds to a spectroscopic resolution of 1: 10^{15}. The insert shows an even narrower linewidth [1953, 1954]

9.8.5 Atom Cooling and Trapping

Since atoms are neutral it is obviously much more difficult to trap them. One way to prepare an ensemble of cold atoms in a small volume is to use six laser beams, pairwise in opposite directions and along three orthogonal directions. With the laser beams all derived from the same laser, tuned to the low-frequency side of the atomic transitions, the movement in all three directions can be cooled. The atoms experience a viscous force in the opposite direction to their flight direction, leading to a confinement of slow atoms in the region where the laser beams overlap ("optical molasses"). It is not a true trap, since the forces are not position-dependent. Using this technique sodium atoms were cooled to about 240 μK by *Chu* and collaborators [1959], corresponding to the Doppler limit, (9.42). Further cooling was thought to be impossible until *Phillips* and collaborators showed (using different methods to determine the temperature, including studying the expansion of the cooled cloud) that the actual temperature was much lower, only about 40 μK [1960]. This surprising phenomenon was soon explained by *Cohen-Tannoudji and Dalibard* as the result of a combination of spatially varying energy level shifts due to the laser light (dynamic Stark effect; Sect. 9.6.1) and optical repumping [1961, 1962]. Light shifts are naturally explained in the *dressed atom* theory developed by Cohen-Tannoudji since the 1960s [1963–1965]. The atom loses energy by climbing the energy hill, and is then repumped to the valley without gaining velocity. Then the atom starts a new climb slowing down further (See Fig. 9.79). The mechanism is called *Sisyphos cooling*, with reference to an unrewarded stone-roller in Greek mythology, who experienced that the stone he had rolled up to the mountain top always rolled down again. In a more detailed explanation, two counter-propagating and perpendicularly polarized laser beams are seen to result in a light field, the polarization of which changes spatially from right-hand circularly polarized to linearly polarized to left-hand circularly polarized for movements of $\lambda/8$. Since the selection rules between ground- and excited-state sublevels depend on the polarization, the atoms will be repumped between ground-state sublevels with different light shifts. It can be shown that the repumping is most probable from an energetically up-shifted level to a down-shifted level. The same effect can be described in terms of *Raman cooling*, formulated and demonstrated by *Chu* and co-workers [1966]. A common feature in laser cooling is that the energy is dissipated in emissions of blue-shifted photons. In order to truly trap atoms, different techniques have been suggested. Unfortunately, atomic traps are always shallow (the potential depth is only a few meV). In order to trap atoms they have to be precooled, e.g., by using a Zeeman slower as discussed above. The simplest form of a trap is just a focused laser beam, as proposed by *Ashkin* [1967, 1968] and illustrated in Fig. 9.80a). Optical forces for confining had already been suggested by *Letokhov* [1969]. An atom feels a force directed towards the volume of highest light intensity because of a dipole force (the light-induced electric dipole feels the electric force gradient).

Pure magnetic traps were developed by *Paul* and collaborators [1970] and by *Phillips* and collaborators, following a suggestion by *Pritchard* [1971, 1972]. Basically, two magnetic coils acting with the fields against each other were used, creating a strong magnetic gradient, which is felt by the magnetic atoms (see Fig. 9.80b). It became the first atomic trap to be realized [1972], and it was performed on a Zeeman-slowed sample of sodium atoms, as indicated in Fig. 9.74. In both the electric and magnetic traps, the gradient forces expressed in ((7.10), (7.11)) and discussed in connection with Figs.7.4, 7.5, 7.7, and 8.2 are at work. In order to obtain a deeper trap

Fig. 9.79 Illustration of the principles of Sisyphos cooling (Adapted from [1962])

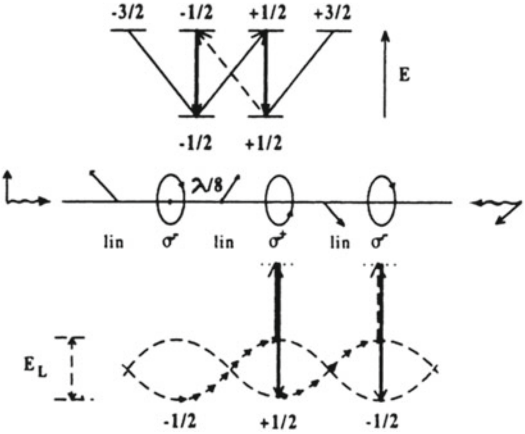

Fig. 9.80 Atomic traps based in a focused laser beam (**a**) and magnetic confinement (**b**)

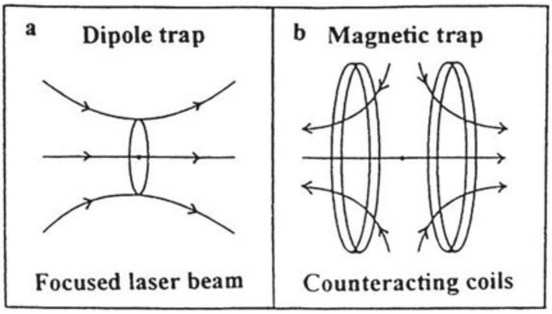

for neutral atoms a combination of magnetic field coils and laser beams, the so-called *magneto-optical trap* (MOT) was developed [1973]. The MOT uses a combination of a weak magnetic field, growing from the centre outwards, and circularly polarized light, as shown in Fig. 9.81. Polarization considerations and selection rules in combination with the position-dependent energy level tuning act in such a way that atoms, which move away from the centre of the trap, feel on the average a recoil-based force directed towards the centre.

Emission processes always lead to a photon-related recoil velocity for an atom. Thus, in the quest for still lower temperatures it is necessary to ascertain that an atom, which for some reason is brought to a standstill, can be exempt from further interaction with the light. This is possible if the atom is placed in a so-called *dark state* [1974, 1975]. If the atom is in a coherent superposition of two ground-state sublevels, from which the transition amplitudes exhibit a total destructive interference, a dark state is achieved (See also Sect. 9.5.3).

It can be shown that for counter-propagating beams with circular polarization only atoms with zero velocity are exempt from the absorption/emission process. Using this type of phenomenon, cooling even below the recoil limit has also been achieved by

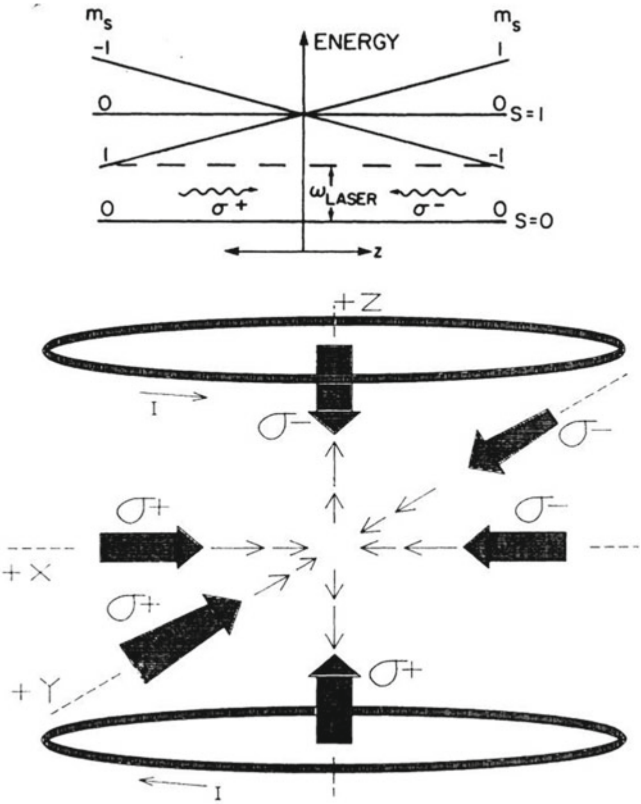

Fig. 9.81 Principle of a magneto-optical trap (MOT) [1973]

so-called *velocity selective coherent population trapping* (VSCPT) [1976]. Temperatures as low as 5 nK have been achieved by *Cohen-Tannoudji* and collaborators for metastable helium atoms, for which $T_D = 23$ μK and $T_\mathrm{R} = 4$ μK. Two- and three-dimensional VSCPT cooling was also achieved [1977, 1978]. The dark state can be seen as a superposition of quantum–mechanical wave packets, describing an atom which simultaneously moves in six perpendicular directions with speeds corresponding to a single-photon recoil. When the laser beams are shut off and the position of the atom is measured, the wave function collapses and the atom is found in one of six possible positions. Raman cooling is a further method of achieving sub-recoil temperatures [1979, 1980].

The 1997 Nobel prize in physics was awarded to *S. Chu*, *C. Cohen-Tannoudji* and *W.D. Phillips* for their contributions to the development of cooling and trapping of neutral atoms [1981–1983]. Laser cooling and trapping are further discussed in [1984–1990].

9.8.6 Atom Optics

A beam of slow atoms can be manipulated in many ways. This is performed within the field of atom optics [1991–1994]. An atomic beam can be bent or focused using laser fields. An atomic beam can also be reflected at an optical surface using the evanescent optical field from a laser beam reflected from the other side of the surface. The atom version of the Young double-slit experiment has been performed with monochromatic thermal atoms, showing clearly the existence of matter waves, even for particles as heavy as an antibiotic polypeptide [1995–2000]. Beam splitters for slow atomic beams can be optically achieved to build atomic interferometers based on de Broglie wave interference. The thermal de Broglie wavelength

$$\lambda_{dB} = h/p_{\mathrm{th}} = h/(2\pi mkT)^{1/2} \tag{9.43}$$

attains considerable values for slow atoms. Atom interferometers with slow atoms allow very accurate measurement of gravity (down to few parts in a billion) and possible space–time fluctuations [2001–2006]. Even atom holography has been achieved [2007].

By using oppositely directed pairs of laser beams with carefully controlled relative phases, it is possible to set up an optical lattice using the light shifts present in Sisyphos cooling. Atoms are cooled and confined into the periodic lattice points [2008–2017]. Optical lattices form the basis for the most precise optical clocks [2012, 2013]. The advantage is taken from the strong signal intensities available from the large number of trapped particles in the lattice wells, in sharp contrast to the case of studies on a single trapped ion. An optical lattice constitutes an ideal testing ground for simulations of solid-state structures, which are also periodic. A lattice, with a period corresponding to optical wavelengths, can scatter laser beams in the same way as a normal crystal lattice (with typically 0.3 nm spacing) scatters X-rays (Bragg and Laue diffraction) (see Sect. 5.1.1).

Cooled atoms enable fundamental experiments in collision physics [2018, 2019]. When the particles move very slowly, scattering can be described accurately by theory. The study of collisions is also important since they constitute a loss mechanism in laser cooling. On the other hand, collisions are necessary to achieve the evaporative cooling needed for Bose–Einstein condensation (see below).

Cooling has also been achieved for molecules without laser techniques, but employing interaction with cold helium gas or by using a pulsed electric field [2020, 2021]. Clearly, many fundamental studies can be performed on well-prepared samples of cooled molecules.

Laser cooling and trapping, and atomic optics constitute important aspects of the mechanical effects of light on atoms. Several other such effects exist and have been explored. Studied phenomena include light diffusive pulling [2022], light-induced drift and the optical piston [2023–2025].

9.8.7 Bose–Einstein Condensation and "Atom Lasers"

So-called *Bose–Einstein condensation* (BEC) can occur in sufficiently cold and dense atomic samples, where the thermal de Broglie wavelength becomes comparable to the mean separation between the atoms. In this case, the atomic matter waves overlap and the indistinguishability of atoms becomes important. Then a gas of bosonic particles will condense into the lowest energy level, in a phase-transition process as predicted by Einstein, based on earlier work by the Indian physicist S.N. Bose [2026, 2027]. A coherent matter wave is obtained with obvious fundamental interest. The condensation is a macroscopic quantum phenomenon like superfluidity or superconductivity, where electrons (fermions) couple to Cooper pairs, which behave like bosons. Photons are also bosons, and their "Bose–Einstein condensation" is the normal laser action, where all photons are in the same coherent state.

A crucial step for achieving BEC for free atoms was to combine laser cooling with *evaporative cooling* [2028–2030]. Such non-optical cooling by evaporation just means that the most energetic (fastest) atoms will escape from the trap more quickly than the colder ones, effectively lowering the temperature through thermalizing collisions. It was developed for the cooling of hydrogen, which cannot easily be optically cooled since the resonance line (Lyman-α) is at 121.6 nm. By a combination of very efficient laser cooling in a MOT with evaporative cooling, BEC was achieved in 1995 by *E. Cornell*, *C. Wieman* and collaborators [2031] and by *W. Ketterle* and collaborators [2032] for the case of ^{87}Rb and ^{23}Na, respectively. The final requirement was to tighten a final leak in a trap due to spin flips into a repelled state occurring around zero magnetic field. The stored atoms could be kept away from such field regions either by a blue-detuned focused beam repelling the atoms or by a rotating magnetic field moving the hole away from the atoms. Evaporative cooling removes the fastest atoms from the trap. An RF field is used to flip the atoms by Zeeman-level transitions into a state in which they are repelled out of the trap. In this way, "warm" atoms are "skimmed off". The magnetic field is zero at the trap centre and increases outwards. By properly adjusting the RF frequency the flip region can be moved. Sufficiently fast atoms can only reach the higher field region, where they are flipped. The condensate is imaged by laser-induced fluorescence or absorption imaging using a CCD camera (in a similar way as used in combustion diagnostics; Fig. 10.8). The process is illustrated for the case of ^{87}Rb in Fig. 9.82. The images show clouds of atoms 6 ms after the trap has been switched off. Clouds just before condensation, at the beginning of condensation and at full condensation are shown. The temperature of the Bose condensate is of the order of 10^{-9} K. Images can also be formed through the dispersive scattering of off-resonant light. The primary laser light is blocked in a Fourier plane of the imaging system. This latter method is non-intrusive and does not heat or influence the condensate.

A Bose condensate can be seen as a coherent matter wave with a very long de Broglie wavelength. The coherence can be observed by letting two expanding Bose condensates interfere, producing sharp fringes [2034]. By switching out part of a condensate repeatedly using RF pulses and letting the atoms fall by gravity, pulses

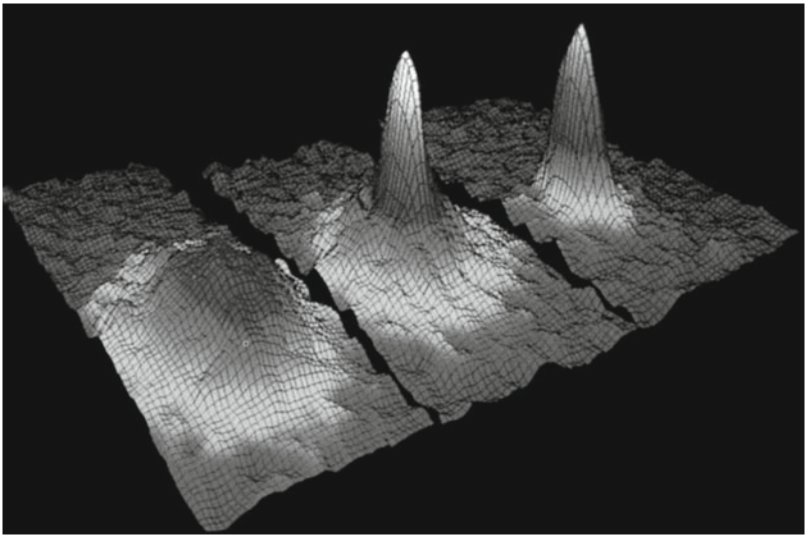

Fig. 9.82 Illustration of Bose–Einstein condensation in rubidium atoms [2033]

of coherent matter, a pulsed atom laser ("boser"), can be attained (see Fig. 9.83 [2035]). Quasi-CW boser waves have also been achieved, and atom "amplification" has been observed [2036–2039]. The applications of such sources in atomic engineering and nano-fabrication could be numerous. The field of BEC has attracted very high scientific interest with numerous theoretical and experimental activities [2040–2055]. Among the achievements the demonstration of the corresponding phenomena for coherent matter waves as observed in normal nonlinear optics could be mentioned (degenerate four-wave mixing, sum-frequency generation, etc.) [2056, 2057].

BEC in spin-polarized hydrogen, the most long-running candidate, was achieved in 1998 [2058] using an efficient combination of magnetic trapping and evaporative cooling [2028–2030].

The 2001 Nobel Prize in Physics was awarded to *E.A. Cornell*, *W. Ketterle*, and *C.E. Wieman* for the achievement of BEC in dilute gases of alkali atoms [2059, 2060].

9.8.8 Ultracold Fermionic Gases

Whereas integer-spin atoms can be made to pile up in the lowest energy state, resulting in Bose–Einstein condensation, half-integer spin atoms *(fermions)* cannot do so because of the *Pauli exclusion principle*. Instead the atoms can be brought to fill all the lowest energy states up to the Fermi level, in the same way that electrons do in a solid. While the transition into the BEC region is abrupt, as discussed

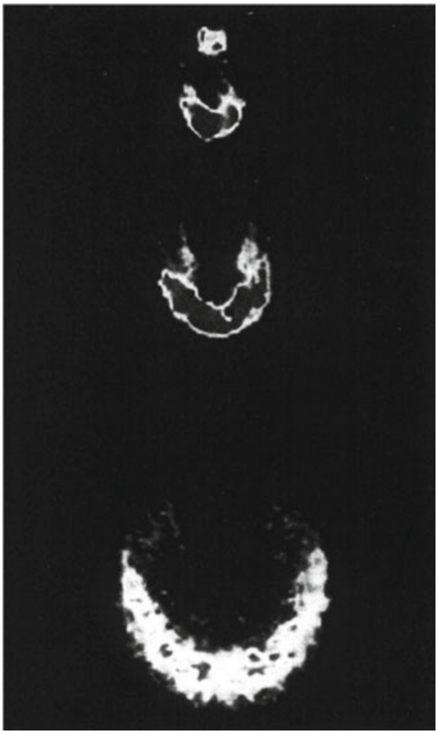

Fig. 9.83 Pulses of coherent matter waves generated from a Bose–Einstein condensate [2035]

above, the crossover into the *fermionic degenerate state* is more gradual. However, the phenomenon in strongly cooled fermionic gases has been clearly demonstrated by *Debbie Jin* and collaborators [2061]. It manifests itself in the suppression of inelastic collisions and spontaneous emission rates, both caused by the full occupancy of the lowest-lying energy states. A major problem to be overcome was that normal evaporative cooling and subsequent rethermalization are ineffective due to the inelastic-collision suppression discussed above. This could be overcome by using a cold mixture of ^{40}K ($I = 4$) atoms in different magnetic substates of the $F = 9/2$ ground-state hyperfine level. The formation by fermions of Cooper pairs (bosons) just as for normal superfluidity, resulting in the condensation of the original fermionic gas into a superfluid, was also demonstrated [2062].

Ultracold fermions have now been much studied, as documented, e.g., in [2063–2071].

Chapter 10
Applications of Laser Spectroscopy

We have in the previous chapter seen how lasers can be used in a multitude of ways to gain basic information on atomic and molecular systems. Thus, the laser has had a major impact on basic research, and its utility within the field of applied spectroscopy is just as great. We will here discuss some applications of considerable interest. Previously, we have mainly chosen examples of atomic rather than molecular spectroscopy, but in this chapter, we shall mainly discuss applied molecular spectroscopy. First, we will describe *diagnostics of combustion processes* and then discuss *atmospheric monitoring* by laser techniques. Such monitoring can regard air pollutants, but another field of application is ecological studies of flying insects and birds. Different aspects of *laser-induced fluorescence and Raman spectroscopy* in liquids and solids will be considered with examples from the environmental, industrial, and medical fields. We will also describe *laser-induced chemical processes* and *isotope separation with lasers*. Finally, *spectroscopic aspects of lasers in medicine* will be discussed. Applied aspects of laser spectroscopy are discussed, e.g. in [2072–2077].

10.1 Diagnostics of Combustion Processes

10.1.1 Background

Research in the field of combustion has been strong during the latest decades because of the appreciation of the need for efficient combustion combined with low pollution. In spite of strong global efforts to introduce green alternatives to the combustion of fossil fuels, these will remain very important over considerable time [2078]. The use of alternative fuels, such as biomass, hydrogen, and metals is also a growing trend. In order to obtain a deeper understanding of combustion processes, it is necessary to perform the study at a molecular level. Laser spectroscopic techniques provide unique possibilities for non-intrusive measurements on the extremely aggressive media that burning or exploding gases constitute. Because of the unique properties

© The Author(s), under exclusive license to Springer Nature Switzerland AG 2022

S. Svanberg, *Atomic and Molecular Spectroscopy*, Graduate Texts in Physics,
https://doi.org/10.1007/978-3-031-04776-3_10

Table 10.1 Some effective chemical reactions in fuel combustion

Flame	Effective reactions	Temperature (K)	Energy release (J/g)
H_2/O_2	$2H_2 + O_2 \rightarrow 2H_2O$	3100	24,000
CH_4/O_2	$CH_4 + 2O_2 \rightarrow CO_2 + 2H_2O$	3000	10,000
C_2H_2/O_2	$2C_2H_2 + 5O_2 \rightarrow 4CO_2 + 2H_2O$	3300	12,000

of laser beams, both high spatial and temporal resolution can be achieved. Before we describe some measurement techniques, we will give an elementary background to combustion processes [2079–2085].

A detailed understanding of combustion must start with simple processes such as hydrogen, methane or acetylene combustion in oxygen or air. Normal liquid hydrocarbons are considerably more complex, and wood or coal combustion can hardly be attacked at a molecular level. Table 10.1 presents some "effective" chemical reactions leading to the transformation of fuel and oxidant into carbon dioxide and water. The processes are strongly exothermic, which, of course, is a common feature of combustion processes.

Combustion occurs with a large number of intermediate steps, and even simple processes, such as the ones listed in Table 10.1, occur through dozens of coupled elementary reactions. It is possible to describe the interaction between the reactions with computer modelling, and concentration profiles can be calculated. In order to perform the computer calculations, it is necessary to know the rate constants for the individual elementary reactions. Comparisons between theory and experiments are best made for a flat, premixed flame, which in its central part can be considered to have only one-dimensional (vertical) variation, allowing computer calculations to be performed comparatively easily. The most important reactions are included in the model. Experimental and theoretically calculated concentration curves are given in Fig. 10.1 for the case of low-pressure ethane/oxygen combustion. As examples of important elementary processes, we give the following reactions:

$$\begin{aligned} CO + OH &\rightarrow CO_2 + H \\ H + O_2 &\rightarrow O + OH. \end{aligned}$$

Reactive molecular fragments or radicals, such as OH, H, and O, are very important for combustion. The combustion zone of a stoichiometric CH_4/O_2 flame contains about 10% OH, and 5% each of H and O. The number of radicals is doubled in the second one of the two reactions given above. A fast increase in radical formation frequently leads to explosive combustion. Because of the high reactivity of radicals, they cannot be measured by probe (extraction tube) techniques since wall reactions immediately eliminate them. Thus, laser techniques are particularly valuable for radical monitoring. Pollution formation in flames is an important aspect. Nitrogen and sulphur oxides, incompletely burnt hydrocarbons, and soot particles form important pollutants. It is of the utmost importance to understand which elementary reactions form and eliminate pollutants. The formation of nitric oxide is reasonably well

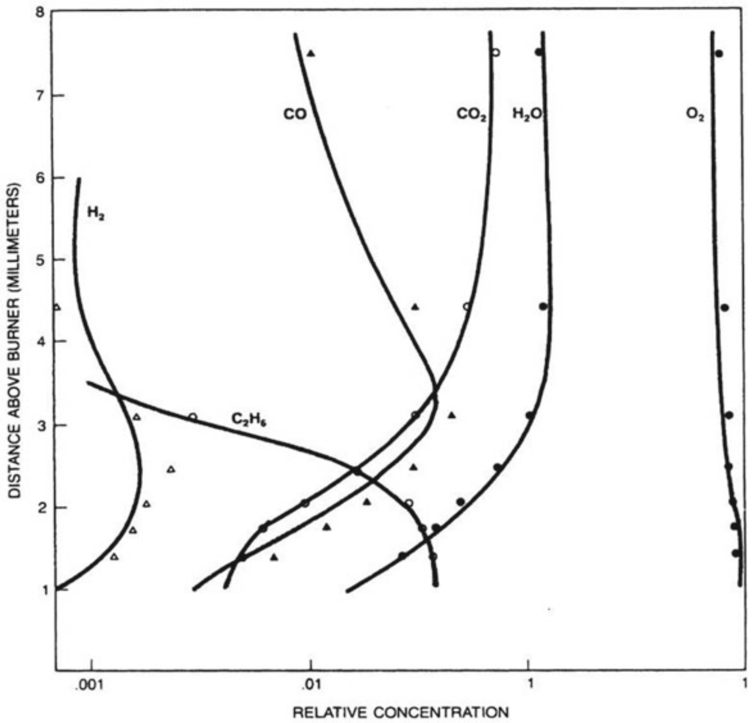

Fig. 10.1 Experimental and theoretical concentration profiles for an ethane/oxygen flame [2079]. (Copyright 1982 by Scientific American, Inc. All rights reserved)

understood. At temperatures above 2000 K, the nitrogen in the air is attacked

$$O + N_2 \rightarrow NO + N$$
$$N + O_2 \rightarrow NO + O.$$

The two reactions constitute the so-called *Zeldovich mechanism*. NO is then oxidized to the toxic NO_2 by oxygen in the air. NO can be eliminated from the post flame gases by the addition of NH_3. The following reactions occur [2086]:

$$NH_3 + OH \rightarrow NH_2 + H_2O$$
$$NO + NH_2 \rightarrow N_2 + H_2O.$$

In the case of sulphur oxide, SO, it is immediately further oxidized to SO_2 in the flame. It seems that a reduction of SO_2 can only be obtained by using low-sulphur fuels. SO_2 and NO_2 are further oxidized to H_2SO_4 and HNO_3 in the atmosphere with subsequent acid rain formation.

Soot formation is the subject of many studies [2087-2091]. Soot formation is enhanced at high fuel/air mixing ratios (rich flames) when using hydrocarbons with comparatively little hydrogen, and for bad mixing conditions. Since available fuels will become successively poorer in hydrogen, soot formation will become an increasing problem. The chemistry of soot formation is not well understood. Many processes, including polymerization of simple hydrocarbons to heavier ones and reactions with polyaromatic hydrocarbons, may be important. Basic flame combustion has been described in [2079–2085, 2092, 2093], and early emission and absorption spectroscopy of flames is discussed in [2094].

Laser techniques have a great potential for studies of microscopic as well as macroscopic combustion in flames and engines. Combustion diagnostics with lasers has been discussed in several books and reviews [2095–2102]. We will here give examples of measurements of concentrations and temperature (flame kinetics) using fluorescence, Raman, and coherent Raman techniques. Turbulence is extremely important in practical combustion systems [2103] and we will also briefly discuss laser techniques for flow and turbulence measurements.

10.1.2 Laser-Induced Fluorescence and Related Techniques

In *laser-induced fluorescence (LIF)* experiments, a laser is normally tuned to an allowed dipole transition from a lower to an upper state of the species under consideration, and the fluorescence light that is emitted during the subsequent decay is observed. We will start this section by considering the corresponding spontaneous emission process. At the high temperatures in a flame, upper levels become thermally populated and a natural emission giving the flame its colour occurs. The emission spectrum from a C_3H_8/air Bunsen burner flame is shown in Fig. 10.2, featuring strong bands due to the radical C_2. This emission was described by Swan as early as 1857 in one of the earliest molecular spectroscopy experiments. (Compare with the similar spectral emission from the tail of Halley´s comet, shown in Fig. 6.109!) C_2 is responsible for the blue-green light from the lower parts of hydrocarbon flames. Schematic energy-level diagrams for C_2 and OH with the wavelengths of the individual bandheads are depicted in Fig. 10.3. Hydrocarbon flames also exhibit strong bands due to the CH ($\sim$390 and 430 nm, especially in the flame front) and the OH radicals ($\sim$300 nm). In sooty flames, the strong yellow light is due to the incandescence of soot particles.

LIF yields a much more well-defined emission situation than the one pertaining to thermal emission. The reason is that the strength of the fluorescence is related to the ground-state population rather than to the very temperature-dependent excited-state population. Different aspects of the use of LIF for combustion studies are treated in [2106–2109]. For quantitative LIF measurements, it is necessary to consider and control the quenching of the fluorescence due to collisional and radiationless transitions. The quenching can be represented by a term Q to be accounted for on equal footing with A (describing spontaneous emission). The observed light intensity will

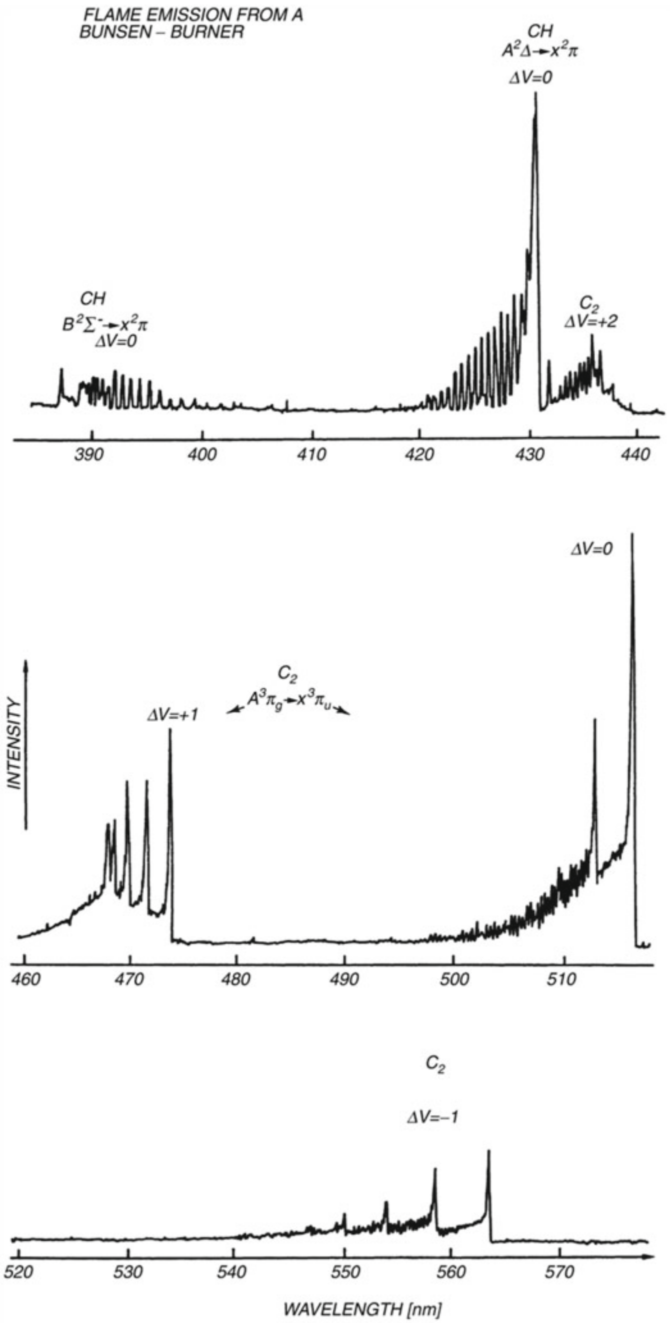

Fig. 10.2 Emission from a propane/air Bunsen burner flame [2104]

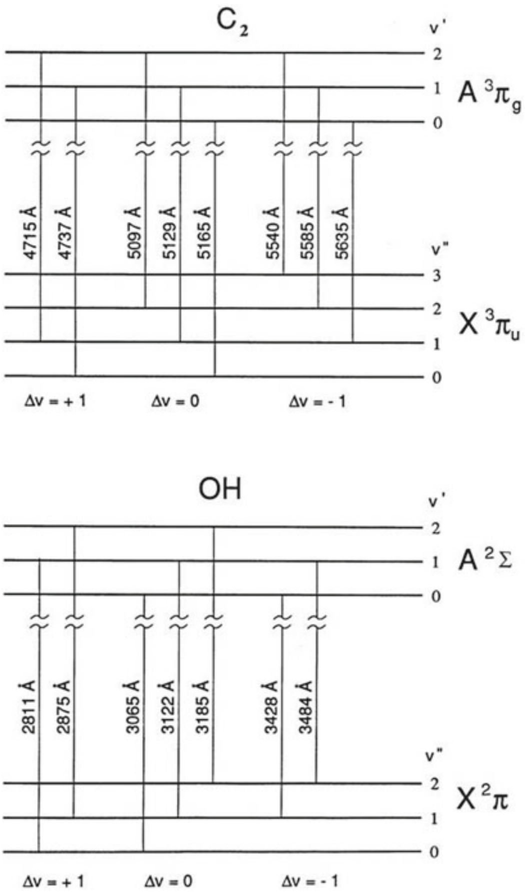
C2
v'
2
1
0
A 3πg
4715 Å
4737 Å
5097 Å
5129 Å
5165 Å
5540 Å
5585 Å
5635 Å
v"
3
2
1
0
X 3πu
Δv = + 1
Δv = 0
Δv = - 1
OH
v'
2
1
0
A 2Σ
2811 Å
2875 Å
3065 Å
3122 Å
3185 Å
3428 Å
3484 Å
v"
2
1
0
X 2π
Δv = + 1
Δv = 0
Δv = - 1

Fig. 10.3 Energy level schemes for the C_2 and OH molecules (10 Å = 1 nm) [2105]

be strongly reduced due to the strong but rather unpredictable degree of quenching. Equation (9.1), describing saturation must now be written as

$$\frac{N_2}{N_1 + N_2} = \frac{1/2}{1 + \frac{A+Q}{2B\rho(\nu)}} . \tag{10.1}$$

Since Q is frequently 10^3 times larger than A, a very high spectral energy density $\rho(\nu)$ is needed to obtain saturation with a laser beam. However, this can often be achieved and then the maximum fluorescence intensity is obtained despite the quenching, which no longer influences the measurement. Alternatively, the degree of quenching can be measured directly using time-resolved fluorescence spectroscopy (Sect. 9.4). This is possible since the lifetime τ is shortened from its natural value $1/A$ to $1/(A + Q)$. With prior knowledge of the low-pressure "true" lifetime, the observed value immediately yields the quenching at the particular pressure. Clearly, the quenched lifetimes are normally very short and have to be measured with picosecond laser techniques (Sect. 9.5) [2110–2116].

An experimental set-up for studying LIF in flames is shown in Fig. 10.4. The output of a Nd:YAG-pumped dye laser can be frequency doubled and, if needed, the doubled output can be mixed with residual 1.06 μm radiation to achieve still shorter wavelengths (Figs. 8.38 and 8.39). The beam is directed through the flame and the fluorescence can be spectrally analyzed with the spectrometer shown in the upper part of the figure. The figure also shows how a diode-array detector can be used to obtain a one-dimensional image of the distribution of a radical across a flame [2118]. The streak of LIF is imaged onto the detector, which is gated by the laser firing. Figure 10.5 shows distributions of OH fluorescence at various heights in a CH_4/O_2 flame. A single 10 ns pulse is used for each recording.

Using two-dimensional CCD detectors, LIF imaging of full sections through flames can be performed [2119–2123]. Then a thin sheet of laser light is formed by employing a combination of cylindrical and spherical lenses, and the cross-section with the flame is imaged at right angles on the gated and intensified imaging detector. Many flame species, including OH, C, CN, CH, and NO have been studied using single-photon LIF. Several important flame species (such as H, C, N, and O) have their single-photon excitation in the VUV region, where the flame gases absorb and tunable lasers are not readily available (see, e.g. [2124, 2125]). It is then possible to use two-photon or even three-photon excitation (Sect. 9.1.3). An excitation scheme

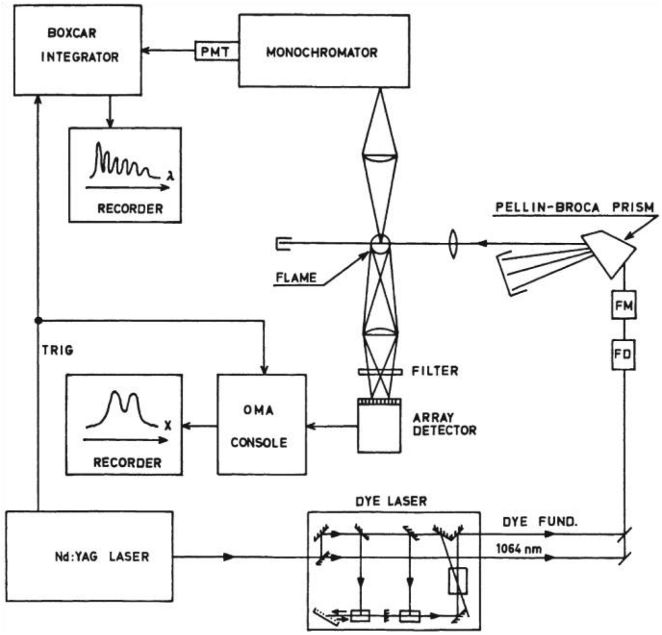

Fig. 10.4 Set-up for spectrally resolved and imaging laser-induced fluorescence studies [2117]

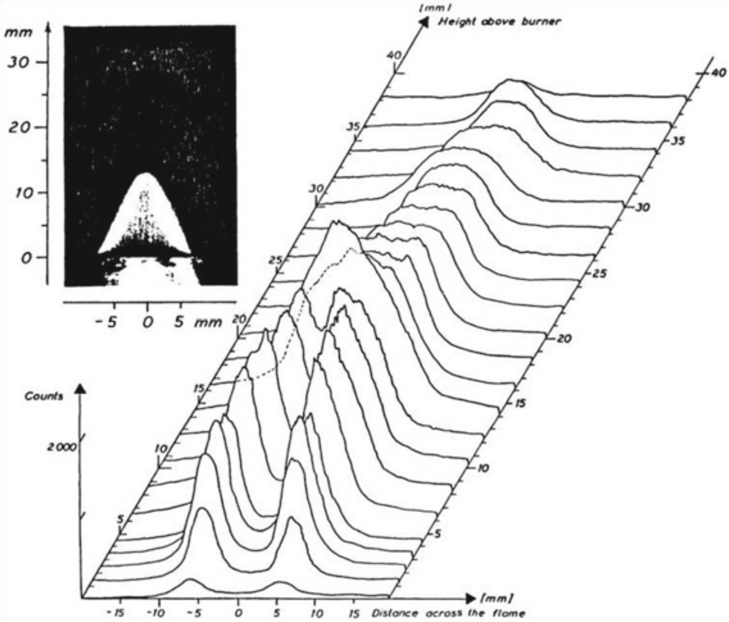

Fig. 10.5 Spatial distributions of the OH radicals in a CH_4/O_2 flame [2118]. The excitation wavelength was 281 nm and the detection wavelength was 307 nm

is shown in Fig. 10.6 and in Fig. 10.7 (trace a) a 2-photon LIF spectrum for oxygen atoms in a C_2H_2/O_2 welding torch is shown. The collisional transfer from the triplet to the quintet system in O should be especially noted. (The absence of free oxygen atoms in room air is illustrated in Fig. 10.7 (trace b)).

If the two-photon transition is pumped sufficiently hard, strong amplified spontaneous emission is obtained in the forward direction [2126]. (The spectra in Fig. 10.7 are recorded in the perpendicular direction). The laser-like emission can also be used for diagnostics purposes, although quantitative information is more difficult to extract.

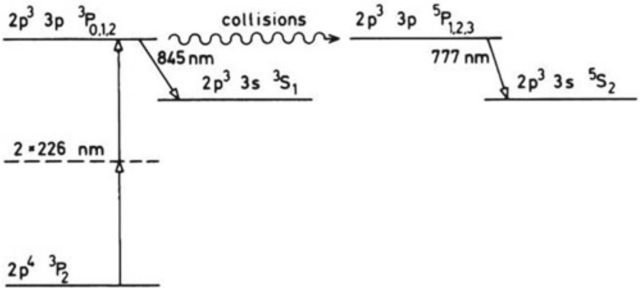

Fig. 10.6 Two-photon excitation scheme for oxygen atoms [2124]

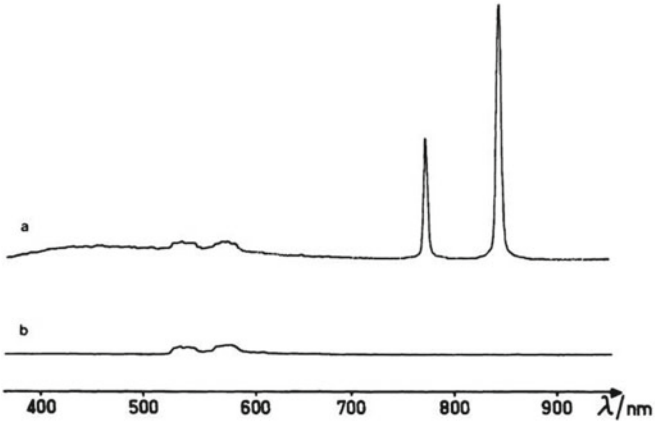

Fig. 10.7 **a** Laser-induced fluorescence spectrum for oxygen atoms in a C_2H_2 welding torch and **b** Recording for normal air (no free oxygen atoms) [2124]

Hydrogen atoms can be detected by observing H_α or H_β emission from the $n = 3$ or 4 levels following two-photon excitation [2127], three-photon excitation [2128], or stepwise excitation [2129]. CO and NH_3 molecules are also best detected using two-photon excitation [2130, 2131]. Examples of 2-D monitoring of flame radicals using single- and two-photon excitation are given in Fig. 10.8 [2132]. Using a 287 nm and 226 nm radiation obtained in nonlinear mixing processes employing a common laser system, these images could be captured simultaneously.

It has also become possible to record the temporal evolution of the radical concentrations following engine ignition by using special cameras, which can be gated to record fluorescence at different delays following, e.g. spark-plug ignition and/or for studying the details of turbulence [2133, 2134].

The excitation of flame species to an upper level can also be detected by other means. Optogalvanic spectroscopy (Sect. 9.2.6) [2135, 2136] and photoacoustic spectroscopy (Sect. 9.2.8) [2137] employing pulsed lasers have been used. The former method is not non-intrusive in nature because of the need for electrodes.

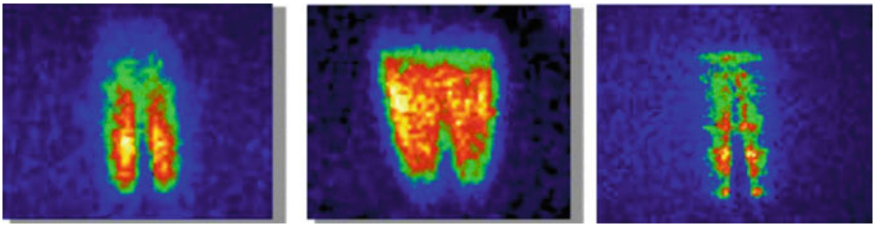

Fig. 10.8 Simultaneous recordings of 2-D images of different flame radicals: OH (single-photon excitation at 287 nm), NO (single-photon excitation at 226 nm), and O (two-photon excitation at 226 nm) ([2132]; reproduced with permission from Elsevier)

The latter technique utilizes the local pressure increase following excitation, and a microphone close to the flame is used for detection. Spatial resolution is limited since the signal is collected along the laser beam. Ordinary absorption measurements clearly constitute the best examples of such line-of-sight measurements. Diode lasers, as well as dye lasers, have been used successfully in flame absorption measurements [2138]. Polarization spectroscopy (Sect. 9.7.2), which is a special kind of absorption technique, has also been used for combustion diagnostics [2139, 2140]. With tomographic techniques, similar to those used in medical X-ray imaging [see Fig. 5.13a], spatially resolved information can be obtained from integrated absorption measurements in different directions through a gas flow or a flame [2141, 2142]. By using tomography, three-dimensional information can also be obtained utilizing thermal flame emission [2143] and interferometry [2144].

Laser beam deflection can also be used to detect optical resonance. The index of refraction of the gas changes in the region of optical excitation and a probing laser beam (frequently a He−Ne laser beam) crossing the excited region will be deflected [2145, 2146].

10.1.3 Raman Spectroscopy

The laser combustion diagnostics techniques discussed so far utilized resonant processes, whether it be single- or multi-photon excitation, fluorescence or stimulated emission. We will now consider non-resonant processes of Raman nature. Because of its insensitivity to quenching (the lifetime of the virtual state is $\sim 10^{-15}$ s or less, making it so fuzzy in energy that it overlaps the ground state, and the Heisenberg uncertainty principle remains valid), Raman spectroscopy is of considerable interest for quantitative measurements of combustion processes. Further, important flame species such as O_2, N_2, and H_2 that do not exhibit IR transitions (they lack a permanent dipole moment; Sect. 4.2.2) can be readily studied with the Raman technique. However, because of the inherent weakness of the Raman scattering process (Sect. 4.3), only non-luminous (non-sooting) flames can be studied.

Extractive Raman measurements on stable flame species can readily be performed. Here gases are transferred from the flame through a thin tube to the scattering cell of a laser Raman gas analyzing system. Stokes Raman spectra, obtained using an Ar^+ laser operating on the 488 nm line are shown in Fig. 10.9 for the lower and upper part of a C_3H_8/air Bunsen burner flame. The conversion of fuel and O_2 into CO_2 and H_2O, constituting the overall combustion process, is clearly demonstrated. The H_2O signal is prevented from increasing by a water vapour condenser in the gas extraction line. Soot particles, which give rise to a broadband LIF background, are also filtered away. The lower trace also displays signals due to CO and H_2, gases that will mostly burn up higher up in the flame. The weak signals in the shoulder of the strong Rayleigh line in the lower trace are due to pure rotational Raman transitions in the H_2 molecule, which, because of its small mass, has an exceptionally large rotation constant B (Sect. 3.2; Eqs. (3.6) and (3.4)). The main hydrocarbon signal at

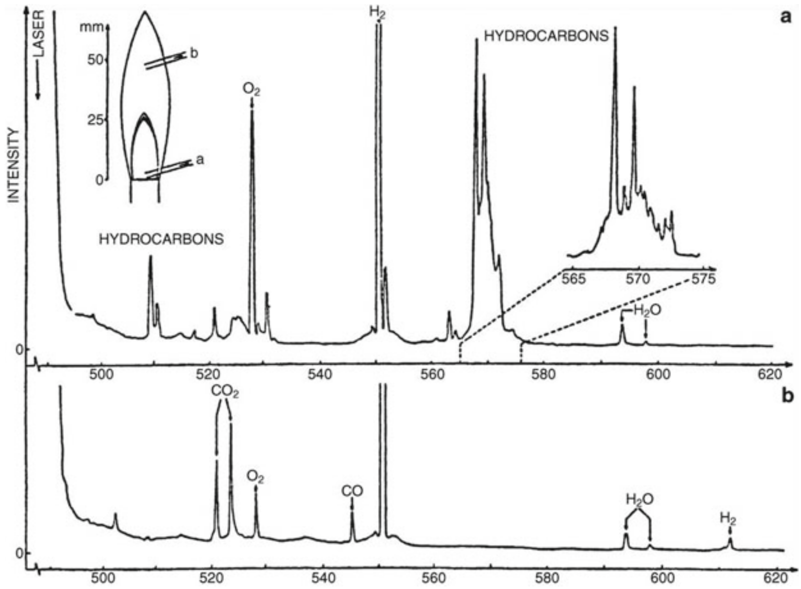

Fig. 10.9 Raman spectra of extracted flame gases at two different heights **a** and **b** in a Bunsen burner flame [2104]

about 570 nm has many components corresponding to slightly different C—H stretch vibrational frequencies. They occur at a Raman shift around 2960 cm^{-1} (Table 6.5). The corresponding IR transitions occur around 3.4 μm. Overtone and combination bands are also observed at smaller Raman shifts.

Using pulsed lasers and gated detection electronics, Raman measurements can also be performed for major species in flames that do not contain too many particles. When using very short pulses and fast time gating, the thermal emission, and also the fluorescence background, which has a distinct lifetime, can be suppressed. Temperature measurements can then also be made using the Stokes/anti-Stokes signal asymmetry or the occurrence of slightly displaced Stokes hot bands as discussed in Sect. 4.4.1 (Fig. 4.18). Flame Raman Spectroscopy is discussed further in detail in [2147–2151].

10.1.4 Coherent Anti-Stokes Raman Scattering

The CARS process has been described previously (Sect. 8.6; Fig. 8.49). CARS spectroscopy is of particular interest for combustion diagnostics because of the strong signal available as a new laser beam emerging from the irradiated gas sample. Thus, CARS is largely insensitive to the strong background light that characterizes practical combustion systems such as industrial flames and internal combustion engines. We recall that the spectroscopic information is contained in the third-order susceptibility term $\chi^{(3)}$. This term is given by the sum of a complex resonant term (proportional to the concentration of the studied molecule) and a non-resonant background term. Thus, when the expression $|\chi^{(3)}|^2$ governing the signal strength is formed (8.13), interference between the resonant signal and the background occurs, resulting in asymmetric signals, very much like the case of polarization spectroscopy; see (9.36).

For a molecule with vibrational and rotational levels, whose populations are temperature dependent, there are many close-lying resonances and the signal shape has to be calculated with a computer program. Theoretical curves for the N_2 molecule are shown in Fig. 10.10 for different temperatures. The occurrence of the first hot band (related to the first excited vibrational level of the ground state) and the gradual widening of the vibration-related peaks due to increasing rotational level population can clearly be seen for increasing temperatures. Figure 10.11 shows experimental spectra for a CH_4/air flame and for room-temperature air recorded with a set-up of the type shown in Fig. 10.12.

The BOXCARS phase-matching scheme (Fig. 8.49) is implemented for the pump beams at ω_p and the Stokes beam at ω_s in the arrangement shown in Fig. 10.12. After frequency doubling, the main part of the Nd:YAG laser output is used to pump the dye laser that generates the tunable ω_s Stokes beam, while the rest is used for the pump beam. The anti-Stokes beam at $\omega_{AS} = 2\omega_p - \omega_{s,}$ which emerges when $\omega = \omega_p - \omega_s$

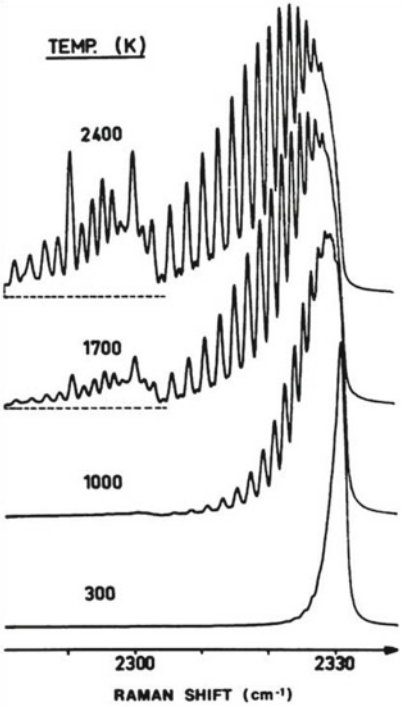

Fig. 10.10 Theoretically calculated CARS curves for N_2 molecules at different temperatures [2152]

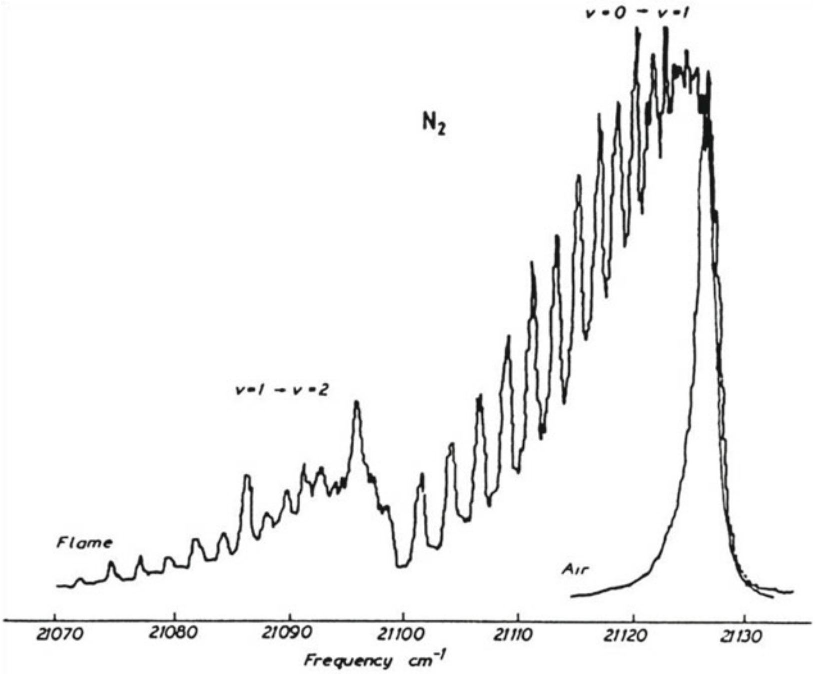

Fig. 10.11 Experimental CARS recordings for room-temperature N_2 molecules and for N_2 molecules in a flame [2152]

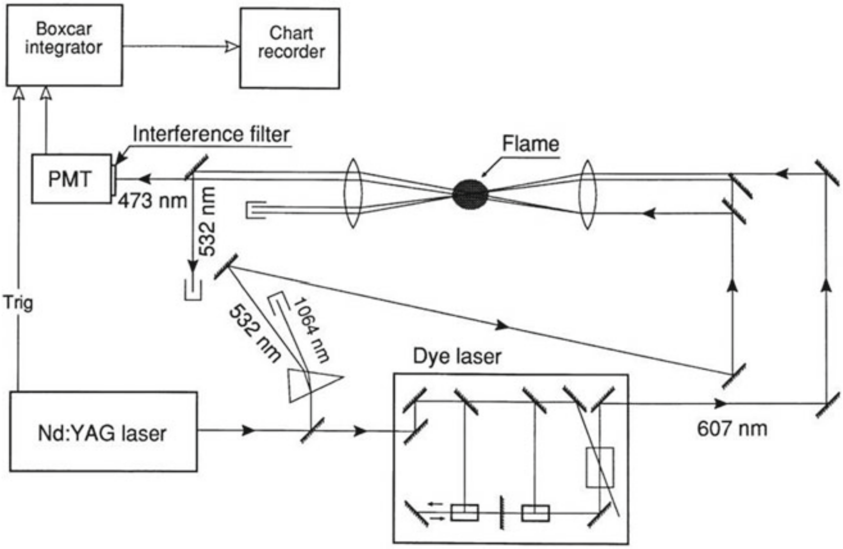
Boxcar integrator
Chart recorder
Interference filter
Flame
PMT
473 nm
532 nm
Trig
532 nm
1064 nm
Dye laser
Nd:YAG laser
607 nm

Fig. 10.12 Experimental set-up for CARS spectroscopy using the BOXCARS phase-matching scheme [2105]

matches a rotational–vibrational transition for the molecule, is detected after proper spectral/spatial isolation from the strong pump beam. When the dye laser is slowly tuned through the signal region with the laser continuously firing, curves such as the ones shown in Fig. 10.11 are recorded using a gated boxcar integrator (Fig. 9.20). The resolution in the spectrum is given by the (small) laser linewidths and not by the resolution of a spectrometer, as in normal spontaneous Raman spectroscopy.

Because of the highly nonlinear nature of the CARS process (the signal is proportional to the square of the molecular number density and to $P_p{}^2P_s$; see (8.13)), signal averaging does not yield a true value for rapidly varying, turbulent media. It is thus desirable to be able to perform the measurement using a single laser pulse. This is possible using an amplified broadband dye laser (Sect. 9.2.3) for the Stokes beam, which, in conjunction with a narrow-band pump-laser beam, will cover all the difference frequencies $\omega_p - \omega_s$ of interest for a specific molecular spectrum. The anti-Stokes signal frequency components are then all generated simultaneously through the action of the third-order susceptibility $\chi^{(3)}$. A gated and intensified linear diode array (Fig. 6.42) is used to capture the single-pulse spectrum. The technique can be used for measurements in specially adapted internal combustion engines. The laser firing can be strobed on a particular crank angle and the temperature at various time intervals can then be determined [2153-2157]. Experimental CARS spectra from N_2 molecules in an internal combustion engine, shown in Fig. 10.13, are exhibiting a strong temperature increase for larger crank angles (piston moving downwards). CARS techniques have also been applied to full-scale coal furnaces [2158] and other practical combustors [2159, 2160]. CARS is especially useful for remote thermometry, but species concentrations can also be determined, especially for major species. Pure rotational CARS can also be pursued, with the special advantage of yielding stronger signals and allowing multi-species monitoring using a single dye laser [2157]. CARS techniques have been discussed in more detail in [2147, 2152, 2161, 2162].

For minor species, LIF is frequently the most suitable technique. Since the LIF signals also depend on the temperature-dependent distribution of the population on

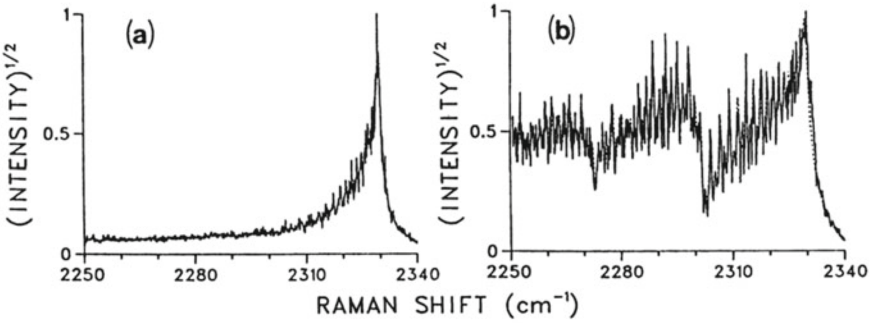

Fig. 10.13 N_2 CARS spectrum from a firing engine [2156]: **a** 10 degrees after ignition, 7.1 atm; **b** 40 degrees after ignition, 15.6 atm

levels (Eq. 4.24), the temperature can also be determined in such experiments if excitations from two metastable levels with different energies are used (two-line fluorescence method [2163–2171]). Indium, which like the alkali atoms, has one electron outside closed shells, but now a p electron rather than an *s* electron, is particularly suitable, since it has its ground ^{2}P ground state split up in two fine-structure components ($^2P_{3/2}$ and $^2P_{1/2}$), with an energy separation ΔE of 0.3 eV, making it suitable for temperature assessments in the 1000–2000 °C range ($kT \cong 0.1 - 0.2$ eV). The two fine-structure components are both connected to the first excited $^2S_{1/2}$ state with spectral lines at 410 and 451 nm, respectively. From measured fluorescence light intensities – F_{21}, as observed in the decay of level 2 to level 1 following excitation from the well-populated ground state 0, and F_{20}, as measured in the decay of level 2 to level 0 following excitation from the metastable state 1 – the temperature can be calculated using Eq. 4.24, noting that the Einstein transition coefficients for excitation and emission occur symmetrically for the two schemes

$$T = const \cdot \Delta E / \big(ln(F_{21}/F_{20}) \cdot Const \big) \tag{10.2}$$

Here, the constants can be determined by calculation or calibration.

An example of a flame temperature determination is given in Fig. 10.14, where sheets of laser light were used in combination with a 2-D detector [2172].

Degenerate four-wave mixing (Sect. 8.6, Fig. 8.45) can also be applied to combustion studies [2173–2178]. The sensitivity of LIF is in this technique combined with the advantages of a coherent signal beam characteristic of CARS.

The techniques discussed here in connection with combustion diagnostics can clearly also be used for the monitoring of other reactive media. The techniques have been found to be valuable in the characterization of *chemical vapour deposition (CVD)* processes for semiconductor fabrication [2179–2184]. The methods are also equally useful for studies of plasmas, which have many fields of utilization, including etching, surface coating, etc. [2185, 2186]. The examples mentioned here illustrate the power of laser spectroscopic techniques in studying industrial processes. Applications of laser spectroscopy in chemistry are discussed in [2073, 2187–2191].

10.1.5 Velocity Measurements

Laser Doppler Velocimetry (LDV) is an important non-spectroscopic laser technique for intrusion-free measurements of velocities in liquid or gaseous flows, including combustion flows. When using this technique, two laser beams (frequently from an Ar^+ laser) are crossed at a small angle in the medium to be studied, as shown in Fig. 10.15. A standing interference pattern with bright and dark fringes is then formed. If a small particle being carried by the flow passes the interference pattern, it will produce periodic glimpses of light that can be detected by a photomultiplier tube. The frequency f_D of the periodic signal (the *Doppler burst*) can be analyzed by

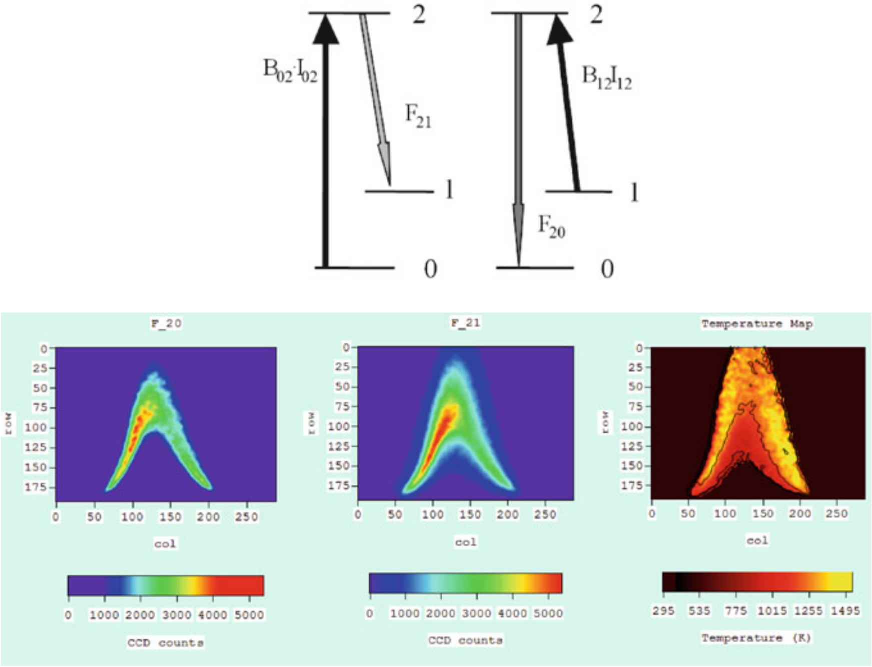

Fig. 10.14 Two-dimensional imaging of temperature in a methanol/air flame seeded with atomic indium. To the left and middle, the planar laser-induced fluorescence recordings for emissions excited from the ground state and the metastable indium states, respectively, are shown, enabling the reconstruction of the temperature image (right) ([2172]; reproduced with permission from VDI)

Fig. 10.15 Principle of Laser Doppler Velocimetry (LDV)

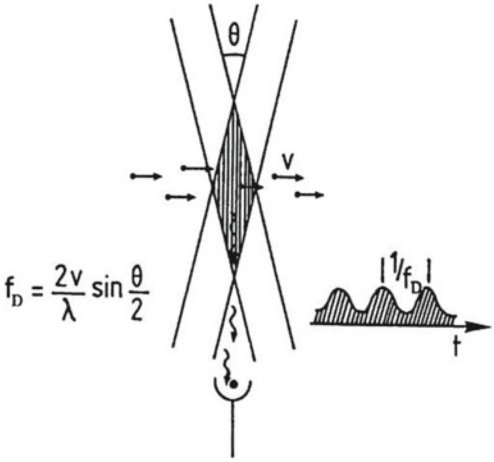

Fourier transformation, and the velocity v can then be determined since the fringe separation d is given by the laser wavelength λ and the beam-crossing angle θ. We have

$$v = \frac{\lambda f_{\mathrm{D}}}{2\sin(\theta/2)}. \tag{10.3}$$

Clearly, if the particle is larger than the fringe separation, the contrast is reduced and thus LDV measurements also provide information on the particle sizes.

With one pair of crossing laser beams, only one velocity component in the flow field can be determined. Furthermore, it is not possible to determine the sign of that velocity component since either flow direction produces the same Doppler burst. However, by frequency shifting one of the crossing beams with a Bragg cell (acousto-optic modulator), moving interference fringes are produced. It is then possible to decide from which direction a particle passed the interference pattern, by noting whether the burst frequency was shifted upwards or downwards from the frequency of a fixed object. A second velocity component can be measured by using two additional laser beams propagating in a plane perpendicular to the first laser beam plane and crossing at the same point. In order to be able to distinguish the Doppler burst from this interference pattern, different wavelengths are used for the laser beams. Thus, it is customary to use the 514.5 nm line of an Ar^{+} laser for one velocity component and the 488.0 nm line for the other. The elastically scattered light is then detected through sharp interference filters in front of individual photomultiplier tubes. The third velocity component (in the direction of the bisectrix of the crossing laser beams) is harder to measure. However, by using three crossing beams in the same plane and extracting the information pair-wise from the central beam and one or other of the external beams, the third velocity component can be projected out, although at lower accuracy. When the scattered intensity is low, e.g. because of small particles, it is still possible to extract velocity information from the time correlation of the recorded individual photons. Special autocorrelation techniques have been developed for optimum information extraction [2192]. It is frequently necessary to seed the flow with small particles. These particles do not necessarily truly follow the gas flow, which constitutes a complication with this technique.

We should conclude this description of LDV techniques with a comment on its common name. In our description of the technique, we have not used "Doppler language" at all but rather expressed the observed phenomena in terms of a spatial interference pattern. However, we can alternatively consider the Doppler shift in the scattered light frequency caused by the motion of the particle. This shift is detected as a beat frequency against the light scattered from the other crossing beam. The beat frequency corresponds exactly to the frequency produced by a particle crossing the fringe pattern, so the two pictures are actually equivalent! LDV techniques have been discussed in detail in the monographs [2193–2195].

A further class of velocity measurement techniques uses molecular "*tagging*". A "package" of molecules is first tagged with a pump pulse, and the movement of the molecules is then monitored with a second laser beam [2196, 2197].

We will also consider a technique for velocity measurements, which is based on the Doppler shifting of absorption lines of atoms or molecules in the flow [2198, 2199]. The principle of the technique is illustrated in Fig. 10.16. A narrow-band CW laser is tuned to a frequency ν in the shoulder of a Doppler-broadened absorption line, where fluorescence light of half the maximum intensity can be induced. If the gas molecules are displaced by a flow, the whole Doppler-broadened profile will shift in frequency. Depending on the direction of this flow, the fluorescence light intensity will increase or decrease. In order to measure the presence of a net flow, two alternating laser beams are sent through the medium in opposite directions. The fluorescence intensities are balanced out for a static gas, by adjusting the relative powers in the two beams. If the gas is moving, a modulation will be observed at the frequency of the beam direction shifting. By normalizing the signal, it becomes independent of the number density of the molecules. We have

$$v = \frac{c}{\nu} \frac{I_{\text{left}} - I_{\text{right}}}{I_{\text{left}} + I_{\text{right}}} \frac{g(\nu)}{\mathrm{d}g/\mathrm{d}\nu}, \tag{10.4}$$

where I_{left} and I_{right} are the two detected fluorescence intensities and $g(\nu)$ is the value of the line-shape function at the chosen frequency ν.

A single-mode CW dye laser can be used for measurements of this kind. The experimental set-up is similar to the one used in Doppler-free intermodulated fluorescence measurements (Sect. 9.7.2), but now the beams are presented to the atoms/molecules one at a time. For measurements of this kind, the flow can be seeded with sodium atoms or I_2 molecules. Imaging measurements along a line can be performed using a CCD detector as illustrated in Fig. 10.16.

Laser techniques for flow measurements are discussed in [2200–2202].

10.2 Laser Remote Sensing of the Atmosphere

Different aspects of remote sensing have been discussed in Sects. 6.6 and 7.2. We will, in this section, now describe how laser techniques can be used for monitoring of the atmosphere and its pollutants. General information on the atmosphere and its optical properties is given in [2203–2207]. Laser beams are particularly useful for monitoring over large distances because of the low divergence of the beam. Typically, a divergence of 0.5 mrad is obtained, corresponding to a spot diameter of 0.5 m at a distance of 1 km. Dry air contains 78.1% N_2 and 20.9% O_2. The rare gases Ar, Ne, and He are present at levels of 9300, 18, and 5 ppm (parts per million), respectively. The CO_2 content is presently (2021) about 420 ppm (parts per million), a value that increases annually by 0.5%. Superimposed on the long-term trend, there is a

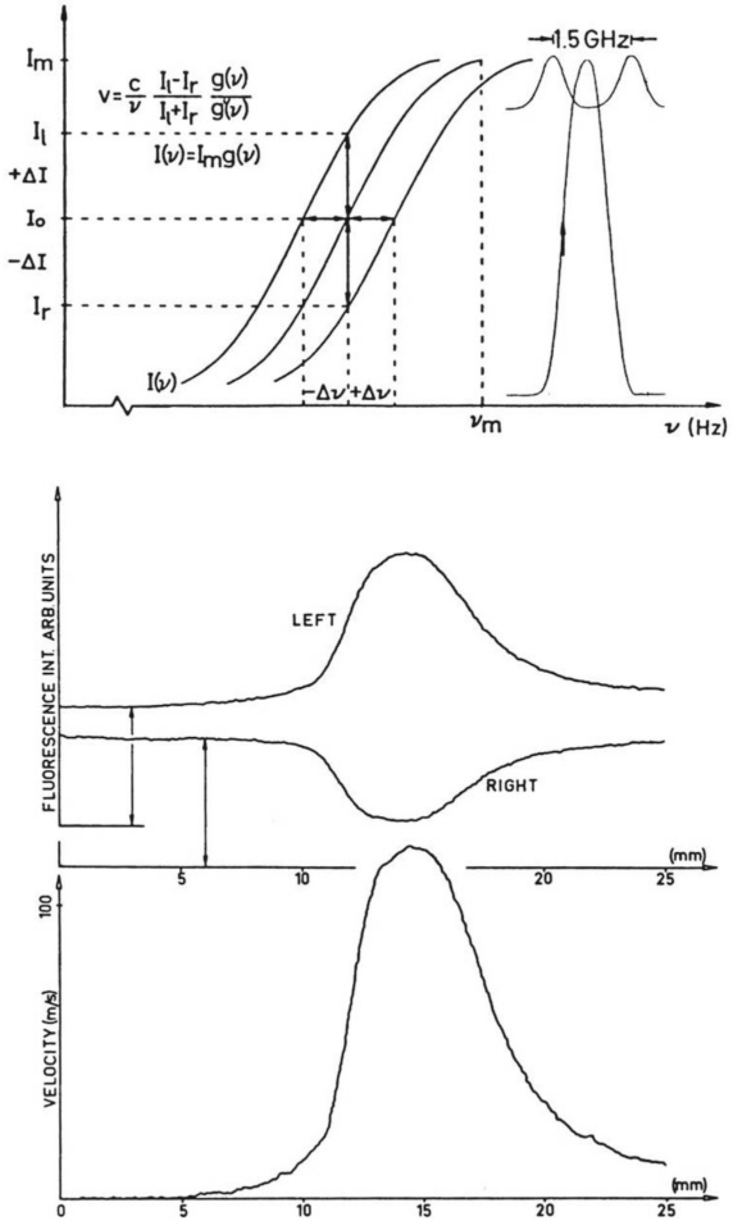

Fig. 10.16 Spectroscopic flow imaging for an I_2 seeded gas jet [2199]

variation of about 5 ppm between summer and winter due to the seasoned vegetation growth. The increase in carbon dioxide and certain other gases has been shown to give rise to an increase in the average global temperature because of the change in the atmospheric radiation budget, the so-called extended *greenhouse effect* [2208–2210], which was discussed extensively in connection with Fig. 6.59. Extensive modelling is needed to understand and predict climate change. The 2021 Nobel Prize in Physics was awarded to *S. Manabe* and *K. Hasselmann* for their work related to the climate change [2211].

Ordinary air also contains widely varying amounts of water vapour. As an example, it can be noted that air at 20 °C and 37 °C contains 2.3% and 6.2% water vapour, respectively, at full saturation (relative humidity 100%), as given by the Arden-Buck relation [2212]. Such data for water vapour are the corresponding ones to those given for the elements in Fig. 7.2 and can be readily calculated using an online program [2213]. The gases N_2O, H_2, CH_4, NO_2, O_3, SO_2, CO, NH_3, etc. are also naturally present in the atmosphere in concentrations that vary from several ppm to fractions of ppb (parts per billion). If such gases are found in higher concentrations in the air because of human activities, they are considered as pollutants [2214–2218]. Measurements in the troposphere (1–15 km), as well as in the stratosphere (15–50 km), are of great interest. In the troposphere, monitoring of industrial emissions, as well as ambient air quality, is needed for environmental protection purposes. Stratospheric measurements are important, e.g. for assessing possible long-term changes in the absorption characteristics that could result in an altered radiation environment at the earth's surface (see the discussion of ozone destruction in Sect. 6.4.5). Further, laser techniques also provide powerful means of remotely measuring meteorological conditions such as temperature, pressure, humidity, visibility, and wind speed.

We will discuss two active remote-sensing techniques for the atmosphere—the *long-path absorption technique* and the *lidar technique*. However, we will first consider a passive technique, in which lasers play an important part in the detection scheme. This *optical heterodyne technique* is even more frequently used for signal recovery in connection with the active optical remote sensing methods. The field of laser monitoring of the atmosphere is covered in several monographs and articles [2219–2225].

10.2.1 Optical Heterodyne Detection

Heterodyne detection is an important technique for low-noise signal recovery. Well-known in the radio-frequency regime, it also has its counterpart in the optical regime. The principle of optical heterodyne detection is illustrated in Fig. 10.17. The incoming radiation is mixed in the detector with the radiation from a local oscillator, which could be a CW diode laser, or a CO_2 laser. Beats are generated in the detector at the difference frequency between the signal frequency ν_s and the local oscillator frequency ν_ℓ. A narrow-band electronic filter, which only transmits a

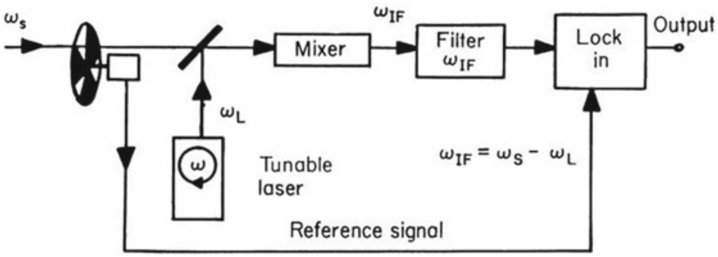

Fig. 10.17 Optical heterodyne detection ($\omega = 2\pi\nu$)[2226]

fixed frequency ν_{if}, the *intermediate* frequency, selects the beat frequency $\nu_{\mathrm{s}} - \nu_{\ell} = \nu_{\mathrm{if}}$. ν_{if} is chosen in the radio-frequency region in which amplification can easily be performed. When the frequency of the local oscillator is swept, the frequency of the recorded external signal is also swept and the spectrum will be recorded successively. The mixing of the signals can be described as

$$\begin{aligned} I &= [A_{\mathrm{s}} \sin(2\pi \nu_{\mathrm{s}} t) + A_{\ell} \sin(2\pi \nu_{\ell} t)]^2 \\ &= A_{\mathrm{s}} A_{\ell} \sin[2\pi(\nu_{\mathrm{s}} - \nu_{\ell})t] + \text{terms oscillating at high frequencies} \end{aligned} \tag{10.5}$$

As we can see, the amplitude of the recorded signal is proportional to that of the incoming signal A_{s} as well as to that of the local oscillator A_{ℓ}. By increasing the amplitude of the local oscillator, noise-free amplification can be achieved. Heterodyne detection is frequently referred to as *coherent detection* in contrast to *direct* detection of the incoming radiation. It is sometimes also convenient to use phase-sensitive (lock-in) detection (Fig. 6.68) at the frequency of a beam chopper to obtain a further increase in the signal-to-noise ratio and background rejection. An example of heterodyne detection is shown in Fig. 10.18. The sundisc is used as a radiation source and the absorption of the earth's atmosphere is monitored. The sun disc is tracked with a heliostat. By tuning the local diode laser oscillator through the spectral region of an ozone infrared absorption line (see also Fig. 6.58), a signal with a pressure-broadened component (Sect. 6.1.1) from tropospheric ozone and a narrow component from the stratospheric layer is recorded. The vertical ozone concentration profile can then be calculated using a mathematical deconvolution procedure.

We note that the occurrence of difference- and sum frequencies have earlier been encountered in connection with Raman scattering (Stokes, and anti-Stokes components, nonlinear optics, etc.), and are always related to having two sinusoidal oscillations simultaneously, being coupled through a quadratic term. Frequency mixing in the same way as utilized in heterodyne detection can clearly also occur when both signals are strong. Then also the difference frequency is generated at the detector, and the "beat" frequency can be measured. This is the approach taken in the calibration and stabilization of frequency combs, discussed in Sect. 9.7.5; Fig. 9.70.

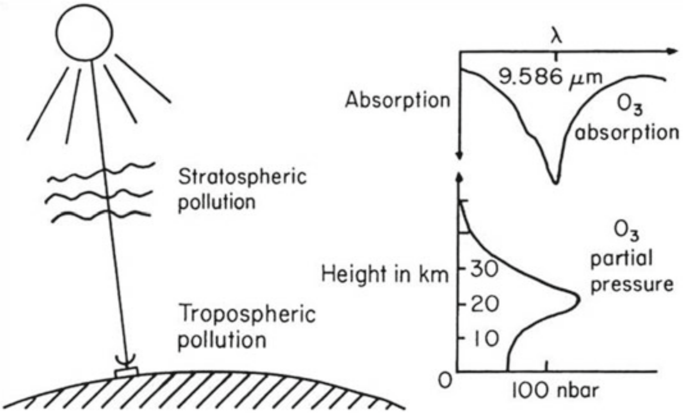
λ
9.586 μm
Absorption
O_3 absorption
Stratospheric pollution
O_3 partial pressure
Height in km
30
20
10
0
Tropospheric pollution
100 nbar

Fig. 10.18 Vertical ozone profiling using the heterodyne technique. A weak, overlapping line explains the asymmetry in the recorded line profile (Adapted from [2227])

10.2.2 Long-Path Absorption Techniques

The principle of long-path absorption techniques is illustrated in Fig. 10.19. A laser beam is transmitted continuously into the atmosphere against a corner cube retroreflector (Fig. 6.23) that is placed at a distance of up to 10 km. The reflected beam is received by an optical telescope that is placed at the site of the laser and is directed towards the retroreflector. The received light intensity is measured photoelectrically as a function of the laser wavelength. The absorption spectrum of the atmosphere between the laser and the retroreflector is then recorded and the mean concentrations N_i, of pollutant molecules can be determined using the Beer–Lambert relation

$$\ln \frac{P_0(\nu)}{P_t(\nu)} = 2R\left(\sum_{i=1}^{n} \sigma_i(\nu) N_i + K_{\text{ext}}\right). \tag{10.6}$$

Here $P_t(\nu)$ is the received light intensity and $P_0(\nu)$ is the intensity that would have been received in the absence of atmospheric absorption. $\sigma_i(\nu)$ is the absorption cross-section for the molecules of type i. $\sigma_i(\nu)$ normally varies strongly with the

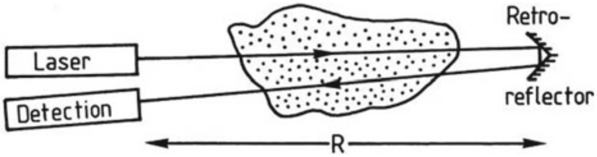
Laser
Detection
Retro-
reflector
R

Fig. 10.19 Long-path absorption measurement of atmospheric pollutants

wavelength while K_{ext} represents particle extinction, which is largely wavelength independent in a small wavelength region. If several molecules absorb in the same wavelength range, it is necessary to perform the measurements in a sufficiently large wavelength interval, preferably with a continuously tunable laser to allow unambiguous determination of the individual molecular species. Frequently, one tries to work in a wavelength region where the gas of interest is the dominant absorber. When using pulsed lasers, which was common at an early stage of this technique, the measurement can conveniently be performed by rapidly switching the laser wavelength from the line centre to a nearby off-line wavelength. Clearly, it is necessary to work in a wavelength region where the dominant atmospheric absorbers CO_2 and H_2O have a low absorption (Sect. 6.4.5). Such regions can be found where the CO_2 and DF lasers emit around 10 and 4 µm, respectively. These gas lasers are normally only line-tunable, and accidental wavelength coincidences are utilized. Sometimes, two lasers tuned to an on-resonance and an off-resonance frequency, respectively, are used, and rapid switching between transmission from the two lasers is performed. High-pressure CO_2 lasers and semiconductor lasers are continuously tunable. The latter laser type is now the strongly dominant one in these types of measurements. Quantum-cascade lasers (Sect. 8.5.5) are particularly convenient to use [2228–2230]. Several lasers addressing different wavelengths can here be arranged on the same chip [2231]. The long-path absorption technique is being used for monitoring many gases, including C_2H_4 (ethylene), C_2H_3Cl (vinyl chloride) O_3, and CO. Early results from a measurement of NO across a major road are shown in Fig. 10.20. Clearly, these kinds of long-path absorption measurements are closely related to those performed using classical light sources (*differential optical absorption spectroscopy*, *doas*, Fig. 6.84). It should be noted, that the long-path absorption technique has numerous applications in the monitoring of gases across smoke stacks with diameters of typically 1–5 m. Commercial equipment is available from several companies. Semiconductor laser spectroscopy for atmospheric measurements is discussed in [2228–2238].

The IR region can also be reached by difference-frequency generation between two diode lasers operating in the red and near-IR regions [2239–2241]. For increased efficiency, a periodically poled lithium niobate (PPLN) crystal (Sect. 8.6) can be used. A set-up for such measurements is shown in Fig. 10.21, where the three available frequencies ω_1, ω_2, and $\omega_1-\omega_2$ are each resonant with an atmospheric specie, O_2 at 760 nm, H_2O at 980 nm, and CH_4 at 3.4 µm [2241]. The three species are simultaneously monitored over a 15 m open-air path through the laboratory. Included in the figure is a demonstration of the evacuation by the room ventilation system down to ambient levels following a methane release from a pressurized tank. An isolated CH_4 line at 2928 cm^{-1} belonging to the *P*-branch of the ν_3 fundamental band was monitored in the measurements (Table 6.5). We note that methane is remaining after evacuation, reflecting the ambient air contents of 1.9 ppm of methane.

By sum-frequency mixing of the outputs from a blue and a red diode laser, the UV region can be reached as illustrated in Fig. 10.22. Measurements on the 254 nm mercury line are demonstrated for a low-pressure cell containing a mercury droplet and after letting atmospheric pressure air into the cell. Individual isotopic lines exhibiting only Doppler broadening merge together under the influence of pressure

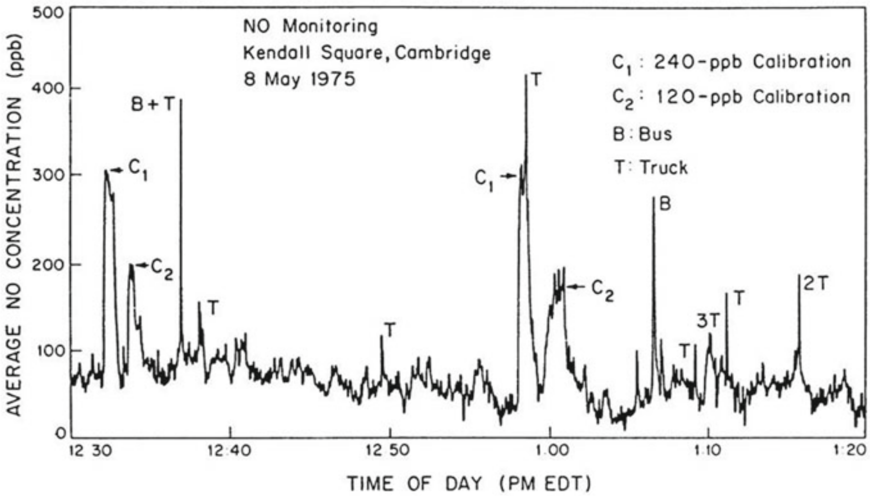

Fig. 10.20 Long-path absorption measurement of the NO concentration across a major road [2232]

broadening [2242]. The UV region can also be reached by frequency quadrupling a high-power near-IR laser in two successive frequency-doubling stages with nonlinear crystals in enhancement cavities [2243].

The recordings in Figs. 10.21 and 10.22 were obtained by averaging a large number of fast sweeps. In this way, the detrimental influence of atmospheric turbulence, etc. can be eliminated, as in *doas* measurements. Also, if the sweep repetition rate is high, the frequently dominant 1/f noise can be suppressed (Sect. 6.5.2). Generally speaking, if the optical absorption is very small, an increased signal-to-noise ratio can be obtained if a modulation technique is employed combined with lock-in detection (Fig. 6.68). If the modulation frequency imposed on the diode-laser drive current is low compared to the absorption linewidth, the driver wavelength is slightly modulated and the signal can be picked up by the lock-in amplifier as illustrated in Fig. 10.23a. The technique is referred to as *wavelength modulation spectroscopy* (WMS). If the modulation frequency is increased to be of the order of one MHz, the lock-in amplifier is replaced by a combination of a mixer and a phase shifter (Fig. 10.23b). The phase-sensitive detection can be performed at the modulation frequency (ν_m) and a signal resembling the derivative is obtained, or at $2\nu_\mathrm{m}$, where the signal resembles the second derivative (see Fig. 6.68d, e). An example of a recording where the modulation frequency was 5 MHz is included in Fig. 10.22 (curve (d) in the right part of the figure). If the modulation frequency is comparable to the pressure-broadened linewidth (few GHz) a more natural view of the modulation process is to consider the occurrence of an upper and a lower sideband around the single-frequency optical carrier. The phases of the sidebands are locked to the carrier, and there is a 180 degree phase shift between the two sidebands. The beat notes (at the modulation frequency) between the upper sideband and the carrier, on the one hand, and the lower sideband and the carrier, on the other hand, will normally cancel out at the detector because

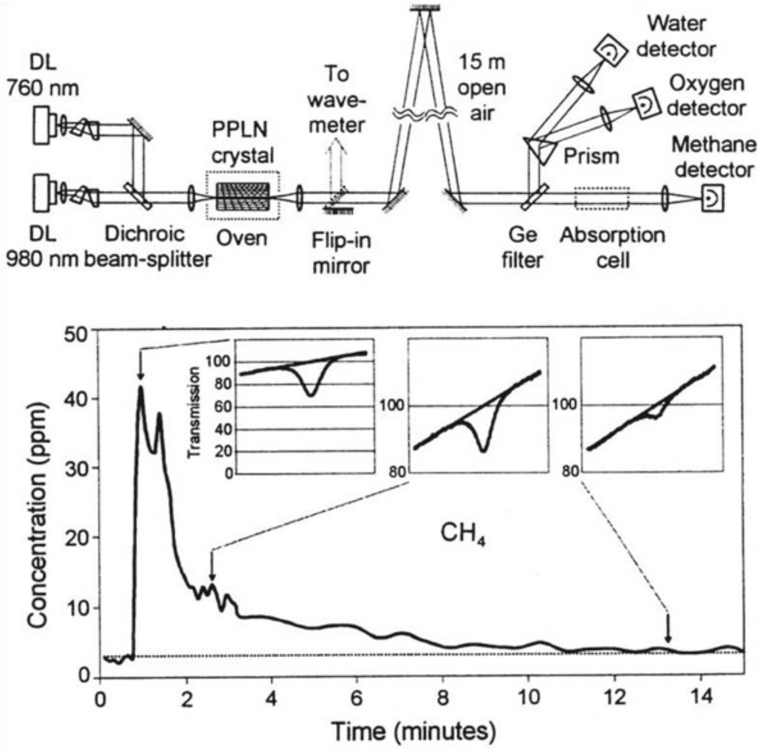
DL
760 nm
DL
980 nm
Dichroic
beam-splitter
PPLN
crystal
Oven
To
wave-
meter
Flip-in
mirror
15 m
open
air
Water
detector
Oxygen
detector
Prism
Methane
detector
Ge
filter
Absorption
cell
Concentration (ppm)
0
10
20
30
40
50
Time (minutes)
0
2
4
6
8
10
12
14
Transmission
0
20
40
60
80
100
100
80
100
80
CH₄

Fig. 10.21 Set-up for difference frequency generation using two diode lasers. Arrangements for simultaneous long-path absorption monitoring of water vapour, molecular oxygen, and methane are shown. Included in the figure are also the dynamics of the evacuation of a methane release into the laboratory [2241]

of the phase shift. If, however, one of the sidebands is attenuated by the presence of an absorbing species, a high-frequency beat is obtained. It is demodulated down to DC in a mixer, which can be seen to have the role of a high-frequency lock-in amplifier. The technique is referred to as *frequency modulation spectroscopy* (FMS) and is illustrated in Fig. 10.24. In a variety of this technique, *two-tone frequency modulation spectroscopy* (TTFMS), the diode laser is simultaneously modulated at two high frequencies, separated by, for example, 10 MHz. It can be shown that the absorptive signal can be picked up at the 10 MHz frequency, which is electronically more convenient for detection.

It has been shown that FM techniques are capable of measuring absorption signals down to the *shot-noise limit* (caused by the number fluctuations for the discrete photons), which frequently means, that absorptive signals of 1 part in 10^6 or 10^7 are detectable. Frequency modulation spectroscopy is described and discussed in [2245–2252].

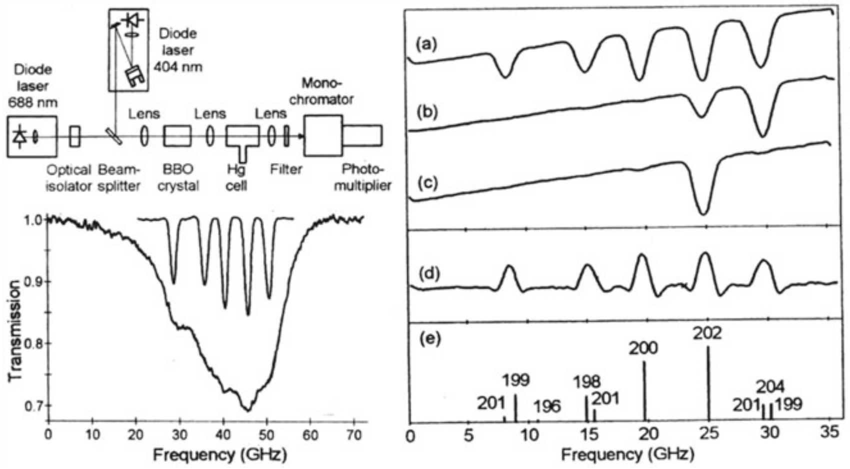

Fig. 10.22 Set-up for sum-frequency generation between a blue and a red diode laser to achieve the 254 nm mercury line (*upper left*). The mercury absorption spectra recorded at low pressure for natural isotopic mixture (**a**) and isotopically enriched samples; ^{204}Hg in (**b**) and ^{202}Hg in (**c**), are also included in the *right part* of the figure, together with designations and relative strengths of natural Hg line components (**e**). A recording obtained using wavelength modulation spectroscopy is shown in (**d**). Finally, in the *lower left part* of the figure, the pressure-broadened line of mercury in atmospheric air is shown together with a low-pressure spectrum [2242]

In a variant of the long-path absorption technique, radiation from a diode laser or a light-emitting diode is transmitted fibre-optically to remotely located multi-pass absorption cells (Sects. 6.5.6, 9.2.1) and the partially absorbed beam is sent back to the measurement system also using fibre optics.

Using such a system, which operates at short IR wavelengths (1 to 2 μm) at which optical fibres transmit well (Fig. 8.33), many points can be monitored from a central system with laser and computer facilities [2253].

10.2.3 Lidar Techniques

Lidar, which is an acronym for *Li*ght *d*etection *a*nd *r*anging, is a measurement technique, where in its most common variety pulsed laser radiation is transmitted into the atmosphere and backscattered light is detected at a certain time delay in a radar-like fashion. However, CW lidar systems, where the range resolution is based on triangulation, rather than photon *time-of-flight (TOF)*, have been developed and applied in expanding areas of application. We will discuss these types of lidar systems in the following two sub-sections.

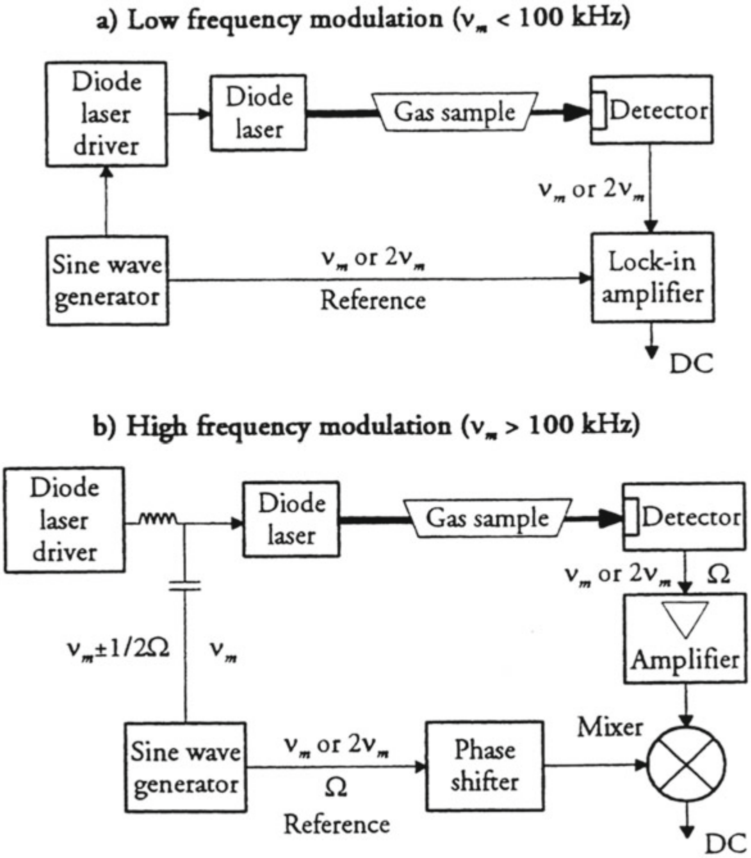
a) Low frequency modulation (ν_m < 100 kHz)
Diode laser driver
Diode laser
Gas sample
Detector
ν_m or 2ν_m
Sine wave generator
ν_m or 2ν_m
Reference
Lock-in amplifier
DC
b) High frequency modulation (ν_m > 100 kHz)
Diode laser driver
Diode laser
Gas sample
Detector
ν_m or 2ν_m
Ω
Amplifier
ν_m±1/2Ω
ν_m
Mixer
Sine wave generator
ν_m or 2ν_m
Ω
Reference
Phase shifter
DC

Fig. 10.23 Arrangements for frequency modulation spectroscopy with diode lasers. In (**a**), low frequencies are employed and the term wavelength modulation spectroscopy pertains. In (**b**), high frequencies are used and discrete components replace the lock-in amplifier [2244]

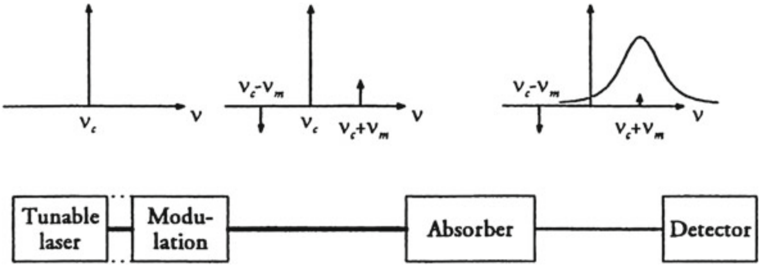
ν_c
ν
ν_c-ν_m
ν_c
ν_c+ν_m
ν
ν_c-ν_m
ν_c+ν_m
ν
Tunable laser
Modu-lation
Absorber
Detector

Fig. 10.24 Sideband generation in high-frequency modulation spectroscopy and resulting imbalance when one of the sidebands is absorbed by a gas [2244]

10.2.3.1 Pulsed Lidar Systems

The principle of lidar (also called laser radar) is illustrated in Fig. 10.25. Laser light that is back scattered from a distance R arrives at the lidar receiver at a time $t = 2R/c$ after the transmission of the pulse. The velocity of light, c, is 300 m/μs. Range-resolved information can be obtained from the time delay and the range resolution ΔR is given by the duration of the laser pulse $t_p : \Delta R = t_p c/2$. (The range resolution may be further impaired due to the finite electronic response of the detection system).

The most common use of the lidar techniques is for ranging, where the distance to a target is measured. Laser *range finders* have many applications, many of which were originally of a military nature. However, the technique is also used in land surveillance and in a number of interesting scientific contexts. A distinction is made between *cooperative and non-cooperative targets*, the former being equipped with reflectors to ease the procedure. (We note that a target can be made more or less invisible, especially to a radar system, if *stealth* technology is employed, where sections are flat and edges are sharp). Using high-repetition rate systems employing mirror scanning, it is possible to map out the geometry of complex volumes such as grottoes, underground storage rooms, and mines, e.g. for volume assessment.

A strongly expanding application is the use of airborne laser scanning of the surface topography, e.g. over cities and canopies of trees [2254–2259]. Remotely operated vehicles (ROVs), such as drones, are useful in these contexts [2260, 2261], and many commercial systems are available. The technique has also been used for discovering ancient temples in the Central American jungle [2262–2264]. An application, which is now being strongly developed is the use of compact lidar systems for allowing autonomous car driving, where all the necessary information about the environment is obtained to allow the car to drive itself, ultimately without human intervention [2265]. An already widely implemented feature is automatic distance adjustment to a vehicle moving in front of the lidar-equipped car.

Satellite ranging is performed from a global network of stations equipped with picosecond laser transmitters and moderate-size receiving telescopes, observing signals from small retroreflectors. Satellite ranging is important for orbit tracking, but a large number of very interesting geodetic results are also obtained. The technique allows establishing a very accurate reference frame for the surface definition. Precision data from the network include the following findings: there are tidal effects in the solid earth crust amounting to a few cm, the average sea surface is changing by 2 mm/y, and the motion of the centre of gravity of the earth is constrained within a

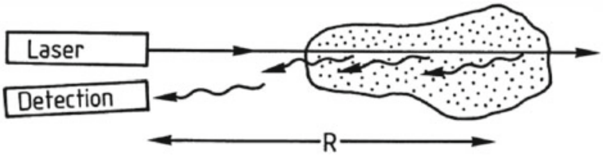

Fig. 10.25 The principle of lidar

roughly 1 cm diameter sphere relative to the fixed network of stations, tectonic plates are moving relative to each other at speeds ranging from a few mm to several cm/y, the length of the day varies, but on average is getting longer by about 2 ms/century, and the poles (instantaneous spin axis) wander within a 14 m diameter circle about its nominal position. Lunar ranging measurements using retroreflectors left on the lunar surface by astronauts or placed on unmanned moon landers have a precision of about 2 cm and reveal that the moon is moving away from the earth at a rate of 3.9 cm/y. Finally, in a laser time-transfer experiment involving ground-based and airborne atomic clocks and precision satellite ranging to the aircraft over a period of approximately 30 hrs, a 47 ns time differential was observed in agreement with general relativistic predictions of the effect of gravity and aircraft velocity on the rate of atomic clocks [2266–2268].

Referring to light bouncing off satellites, it should be noted that sun-reflections (there are thousands of satellites operating) is an increasing problem for astronomy. It is easy to conceive that an accidental reflection from a satellite would completely destroy a long-time recording of the type shown in Fig. 6.102.

Lidar backscattering is not only obtained from solid targets, but also from particles and molecules in the atmosphere. The scattering is of the same kind as the common one involving the sun's radiation (Fig. 4.22). We obtain continuous laser ranging from small targets distributed along the path of the laser beam as illustrated in Fig. 10.25. The intensity of the received lidar signal is given by the general lidar equation

$$P(R, \Delta R) = C W N_{\mathrm{b}}(R) \sigma_{\mathrm{b}}(R) \frac{\Delta R}{R^2} \exp\left\{ -2 \int_0^R [\sigma(\nu) N(r) + K_{\mathrm{ext}}(r)] \mathrm{d}r \right\}. \quad (10.7)$$

where C is a system constant, W is the transmitted pulse energy and $N_{\mathrm{b}}(R)$ is the number density of scattering objects with backscattering cross-section σ_{b}. The exponential factor describes the attenuation of the laser beam and the backscattered radiation due to the presence of absorbing molecules of concentration $N(r)$ and absorption cross-section $\sigma(\nu)$, and due to attenuating particles with wavelength-independent extinction coefficient K_{ext}. A single absorbing molecular species is assumed. The product $N_{\mathrm{b}}(R)\sigma_{\mathrm{b}}$ in the lidar equation determines the strength of the backscattering, which can be caused by several processes. It can be due to *fluorescence* from atoms or molecules that are resonantly excited by the laser light. At high pressures, i.e. in the troposphere, radiationless transitions due to collisions strongly quench the fluorescence light (Sect. 10.1.2). On the other hand, fluorescence detection is very efficient for the monitoring of mesospheric constituents. There are layers of Li, Na, K, Ca, Ni, and Fe atoms in the upper layers of the mesosphere at a height of about 100 km (mesosphere 50–85 km; the mesopause is the point of lowest temperature (−100 °C), which is found at a height of 85–100 km, followed by the thermosphere, where the temperature is again rising). These layers of atoms, which are produced mainly through evaporation of meteorites impinging on the thin atmosphere, have been mapped out very successfully with ground-based fluorescence lidar systems operating with tunable dye lasers [2269–2275] or with radiation obtained by sum-frequency mixing of 1064 nm and 1319 nm radiation from Nd:YAG lasers, which for the case of Na accidentally coincides with the strong 589 nm yellow line [2276–2278]. An alternative approach is to use frequency doubling of radiation at 1178 nm, produced by amplification of semiconductor laser radiation in a fibre-based stimulated Raman scattering amplifier [2279].

As discussed in connection with astronomical imaging (Sect. 6.7), sodium fluorescence lidars have found important applications for providing *laser guide stars* for allowing effective use of adaptive optics to enhance image quality through the turbulent atmosphere [2280–2283].

The backscattering can also be caused by the *Raman* process. Because of the weakness of this kind of scattering, high-power laser beams are normally required even for the monitoring of major atmospheric species. Here light, which is back scattered with a characteristic Stokes frequency shift, is detected. The technique has been used for vertical monitoring of water vapour profiles and for temperature measurements. Temperature can be retrieved by observing the pure rotational or the rotational–vibrational lines from the major constituents N_2 and O_2 [2284–2287] using two narrow-band filters located at different positions in the line distributions. The line intensities are affected by the temperature as discussed in connection with Figs. 4.15, 4.18, and 4.20, and from the intensity ratio of the two detection channels, the temperature can be obtained after calibration. Clearly, pure rotational Raman is much more sensitive to moderate temperatures than vibrational Raman, where the levels are further separated. The water vapour Raman signal [2288] is normally referenced to the well predictable N_2 signal to get the mixing ratio. Atmospheric visibility can also be assessed by measuring signals from N_2 molecules that are recorded with reduced intensity because of mist and fog particles. Slant visibility measurements are of great importance, e.g. at airports.

The strongest backscattering process in the atmosphere is Mie scattering from particles (see Sect. 4.5). Since this form of scattering is elastic, no information is obtained on the chemical composition of the particles, but Doppler shifts in the Mie scattered light can be used for remote wind velocity measurements (see below). Particle composition information can be obtained using very high-power ns laser pulses which, through focusing, can induce air breakdown (laser sparks) at distances up to 100 m. The emission spectrum from the spark carries information on vaporized particles. LIBS (*Laser-Induced Breakdown Spectroscopy*) is also a powerful laboratory technique for surface elemental analysis [2289–2296]. A hot plasma is formed, also emitting a broadband background. Sharp emission lines emerge in the recombination in the cooling plasma, as observed in a delayed detection time window, accomplished with a gated image intensifier (Fig. 6.42). LIBS can also be performed in remote sensing [2297], including imaging and remote cleaning capability [2298, 2299]. LIBS at a distance was even used early for analysis of Martian rocks from dispatched rovers. Remote LIBS is reviewed in [2300]. A specialized conference series on LIBS is being arranged.

In recent years, terawatt laser pulses have been used to create long, ionized channels through air (filamentation) accompanied by white light generation due to self-phase modulation and other nonlinear processes. The high intensity causes Kerr self-focussing (Eq. 8.20) followed by break down, beam diverging, and again refocusing. The distributed white light source allows lidar monitoring of numerous molecular absorption lines [1496, 2301, 2302].

Intense radiation with filamentation can also lead to population inversion and the possibility for lasing, also backwards towards the receiver, which then defeats the normal $1/R^2$ range dependence [2303, 2304].

Returning to conventional lidar systems for atmospheric particle monitoring, the intensity of the Mie scattered light depends on the number density, size, shape, refractive index, and absorption properties of the particles (Sect. 4.5). Evaluating particle properties and size distributions are challenging since the lidar equation contains several parameters, which cannot be evaluated independently. Operating at several wavelengths (frequently with harmonics of a Nd:YAG laser) improves the situation. Different inversion algorithms, operating on certain assumptions have been developed, i.e. by *Klett, Fernald,* and others [2305–2309]. A quantitative analysis is facilitated by calibration on well-characterized particles, whereas relative particle spatial distributions can be obtained more directly. Since particle backscattering frequently dominates strongly over particle extinction K_{ext}, the range-resolved lidar signal maps the particle distribution $N_{\mathrm{b}}(r)$. Lidar stations for monitoring aerosol particles are distributed around the world, collaborating, e.g. in the EARLINET network [2310, 2311]. Data are especially important in view of modelling *climate forcing* (Fig. 6.59).

The construction of a lidar system is illustrated in Fig. 10.26 [2312]. A Nd:YAG laser is used, either directly or after frequency conversion in a dye laser, to produce pulses that are transmitted into the atmosphere via a planar first-surface aluminized mirror. The same mirror is used for directing backscattered light down into a fixed Newtonian telescope. In the focal plane of the telescope, there is a polished metal mirror with a small hole, which defines the field of view of the telescope. For a telescope with a focal length of 1 m, a 1 mm hole corresponds to a telescope field of view of 1 mrad, which matches typical laser beam divergences. In order to suppress background light, it is essential that the telescope only observes regions from which laser photons can be backscattered. The light passing the aperture is detected by a photomultiplier tube, while all the other light is directed into a digital camera which produces a picture of the target area, except for the laser beam region, which is seen as a black spot. The detected lidar signal is transferred to a transient digitizer (Sect. 9.4.2) and is read out to a computer system. The computer is used for controlling the planar mirror, the laser wavelength, etc. and also performs signal averaging and the necessary processing of the lidar signals. Particle monitoring with lidar techniques is illustrated in Fig. 10.27. Increased backscattering is monitored from particle plumes while a smoothly falling $1/R^2$ intensity is obtained from the otherwise uniform background particle distribution in the atmosphere. A modern version of a dye laser-based mobile lidar system is described in [2314], while a system operating with an OPO transmitter, also with near-IR capability, is described in [2315].

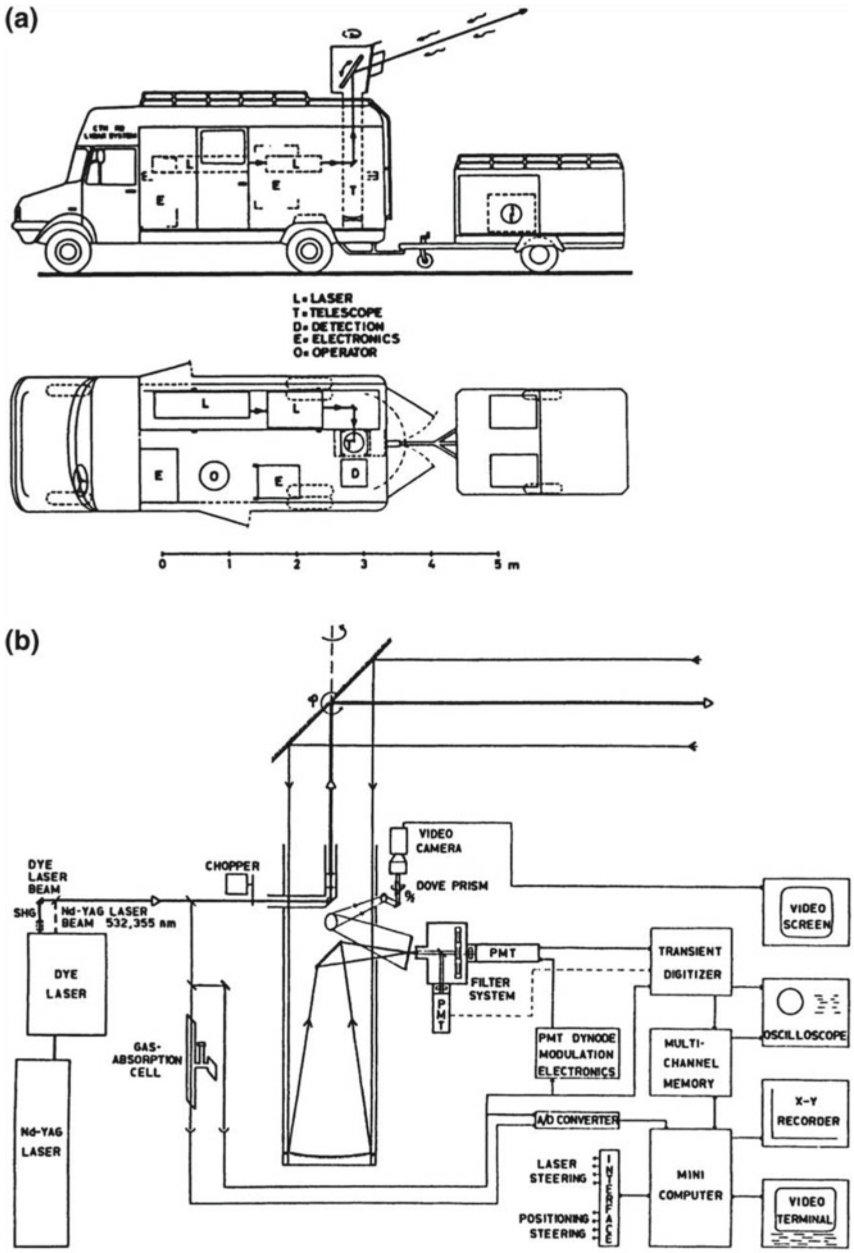
(a)
L = LASER
T = TELESCOPE
D = DETECTION
E = ELECTRONICS
O = OPERATOR
0
1
2
3
4
5 m
(b)
DYE LASER BEAM
SHG
Nd-YAG LASER BEAM 532,355 nm
DYE LASER
Nd-YAG LASER
CHOPPER
GAS-ABSORPTION CELL
VIDEO CAMERA
DOVE PRISM
PMT
FILTER SYSTEM
PMT
PMT DYNODE MODULATION ELECTRONICS
A/D CONVERTER
LASER STEERING
POSITIONING STEERING
INTERFACE
TRANSIENT DIGITIZER
MULTI-CHANNEL MEMORY
MINI COMPUTER
VIDEO SCREEN
OSCILLOSCOPE
X-Y RECORDER
VIDEO TERMINAL

Fig. 10.26 Construction of a mobile lidar system. **a** General lay-out; **b** optical and electronic systems [2312]

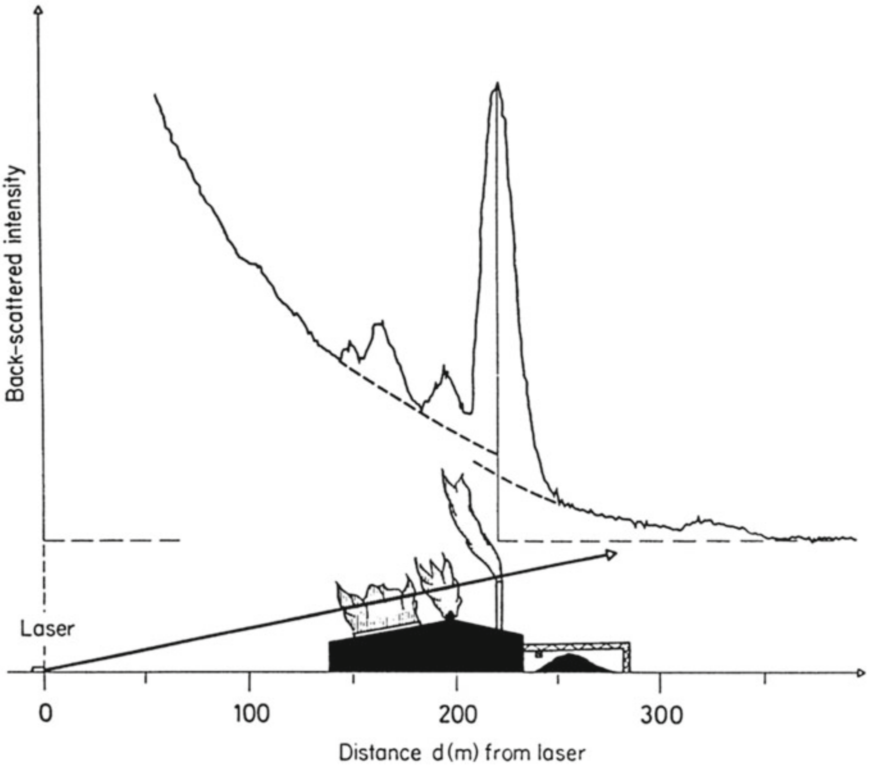

Fig. 10.27 Lidar particle monitoring. Diffuse emissions from roof openings of a smelting plant are observed together with a strong signal from the smokestack emission. It can be clearly seen how particles also attenuate the laser beam, causing a step-down in the smooth $1/R^2$ fall-off curve. The far away signal is due to dust stirred by vehicles [2313]

In order to measure the concentration of gaseous pollutants with lidar techniques, resonance absorption can be used in a similar way to the long-path absorption method that was described above. However, in the lidar technique, no retroreflector is required and the scattering from particles is utilized to generate a reflected signal. The particles serve as a "distributed mirror". The differential absorption at close-lying wavelengths of molecules in the atmosphere is used. The method, which is called DIAL (*DIfferential Absorption Lidar*), is useful for qualitative as well as quantitative range-resolved measurements of air pollutants. The principles are illustrated in Fig. 10.28. For the sake of argument, we consider an atmosphere with a uniform particle distribution and with two localized clouds of absorbing gas molecules. Lidar curves are recorded at a frequency ν_1 of strong specific absorption and at a nearby reference frequency ν_2. For atmospheres with typical particle size distributions, σ_b and K_{ext} will not change in the small frequency range, since the oscillatory behaviour that is characteristic of uniform particles will be washed out. If the particle extinction K_{ext} is small, the recorded curves for both frequencies will have a simple $1/R^2$ dependence for the

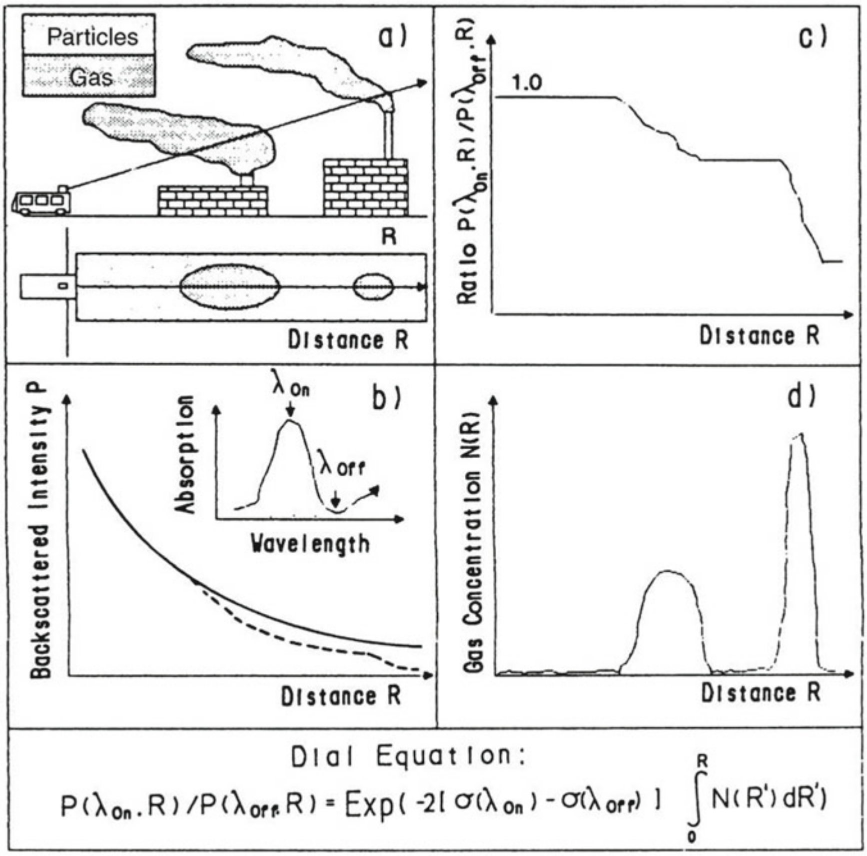
Particles
Gas
a)
R
Distance R
c)
Ratio P(λon.R)/P(λoff.R)
1.0
Distance R
b)
Backscattered Intensity P
Absorption
λ On
λ off
Wavelength
Distance R
d)
Gas Concentration N(R)
Distance R
Dial Equation:
P(λon.R)/P(λoff.R) = Exp(-2[σ(λon) - σ(λoff)] ∫₀ᴿ N(R')dR')

Fig. 10.28 Illustration of the DIAL principle [2316]

region preceding the first gas cloud. For the non-absorbing frequency, the lidar curve continues with a 1/R^2 intensity fall-off even through the gas clouds, while intensity reductions occur in the on-resonance lidar curve at the site of the gas clouds. If no gas had been present, both curves would have had the same appearance. The presence of an absorbing gas is best illustrated if the two curves are divided by each other, as illustrated in the figure. Mathematically, this ratio can be formed by dividing the expressions for the lidar equation (10.7) for the two frequencies ν_1 and ν_2:

$$\frac{P_{\nu_1}(R,\Delta R)}{P_{\nu_2}(R,\Delta R)} = \exp\left\{-2[\sigma(\nu_1)-\sigma(\nu_2)]\int_0^R N(r)\mathrm{d}r\right\}. \tag{10.8}$$

As can be seen, all unknown parameters such as $N_\mathrm{b}(r)$, σ_b and $K_\mathrm{ext}(r)$ are eliminated upon division and only the absorption cross-sections at the two frequencies have to be known from laboratory measurements for an evaluation of the gas concentration $N(r)$ as a function of the distance R. It can also be seen that the method does not even require a uniform particle distribution (assumed above for pedagogical reasons), since any bumps in the curves due to particle clouds would be cancelled out. This is important since gaseous pollutants and particles frequently occur together. The divided (DIAL) curve in fact describes a *dimensionless quantity*, which has many attractive properties in terms of insensitivity to unknown parameters, as discussed in Sect. 1.1 and in connection with Fig. 10.61.

The absorption spectrum for SO_2 in the wavelength region around 300 nm is shown in Fig. 10.29. Similar spectra have already been illustrated in the *doas* recordings shown in Figs. 6.84 and 6.85. In practical DIAL measurements, the wavelength is changed between 300.0 nm and 299.3 nm every other laser pulse and the corresponding lidar curves are added in separate computer registers to attain a sufficient signal-to-noise ratio. SO_2 monitoring of an industrial plume, also containing particulate emissions, is illustrated in Fig. 10.30a. The effective elimination of the extended particle backscattering in the plume is clearly seen in the divided signal curve, where only the step due to the SO_2 contents is observed, surrounded by horizontal portions of the curve corresponding to no SO_2 contents. By combining evaluated range-resolved concentration curves, a plume concentration cross-section can be obtained (Fig. 10.30b). The concentration values (g/m^3) are multiplied by the area elements (m^2) over the cross-sectional area to yield the integrated value (g/m). Finally, by multiplying with the perpendicular wind velocity component (m/s), the total flux of SO_2 (g/s) is obtained as the environmentally most relevant parameter [2319]. We note how the simple analysis of appropriate units leads us to the correct multiplicative expression for flux. This is an example of how considerations of units can guide in the recollection of expressions describing phenomena.

Sulphur dioxide emissions from volcanoes can be measured by performing traverses with a vertically sounding lidar [2320–2323]. Such shipborne measurements are illustrated for the Italian volcano Stromboli in Fig. 10.31. Lidar measurements can be used for comparisons with more commonly employed passive measurements with *doas* or correlation techniques (Figs. 6.85 and 6.86). The passive measurements on high-lying plumes require corrections due to sunlight scattering inside and below the plume. For low-altitude plumes with few scattering particles, e.g. Mt. Stromboli (920 m), the downwelling sky radiation mostly originates above the plume, and a simple evaluation of the gas contents using the Beer–Lambert law can be performed. This is to be contrasted with the complicated situation pertaining to Mt. Etna (3340 m) [2322]. An interplay between absorption and scattering occurs, and becomes very prominent in connection with light propagation in strongly scattering biological tissue, to be discussed in Sect. 10.5.4.

Also mercury is a gas which can have a geophysical origin apart from anthropogenic ones. It is the only pollutant that is present in the atmosphere in atomic form. Compared to molecules with a multitude of rotational–vibrational transitions, mercury in contrast exhibits only a single pressure-broadened resonance line at about 254 nm (built up from a number of isotopic and hyperfine components; see Fig. 10.22)

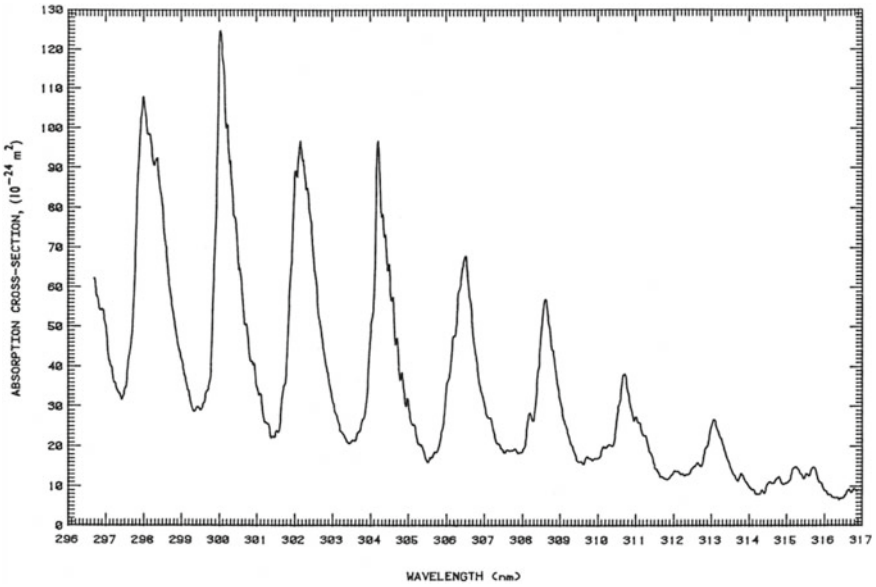

Fig. 10.29 SO_2 absorption spectrum [2317, 2318]

with a high transition probability. This means that very low atmospheric concentrations (ppt:s; parts per trillion, instead of ppb:s or ppm:s) can be detected [2324]. Mercury can, because of its high vapour pressure (Fig. 7.2), be used as a geophysical tracer gas with certain relations to geothermal energy [2325, 2326], ore deposits, and mining [2327–2330], and possibly to seismic activities. A DIAL mapping of the mercury concentration around a cooling tower at a geothermal power station is shown in Fig. 10.32.

Mercury is a very serious neurotoxic pollutant, especially when converted to methyl mercury, $CH_3\ Hg^+$, a process that occurs in nature. This compound, when industrially produced, was widely used as an anti-fungal agent for major crop seeds, to ensure high seed germination probability. Accidents with the use of such grain in human consumption have led to very serious consequences. Environmental mercury pollution is discussed in [2331, 2332]. A total ban on the use of mercury has been agreed on in 2013 between a large number of countries (the *Minamata convention*, named after the Minamata Bay in Japan, where many people died from methyl mercury poisoning, due to intake of contaminated seafood due to industrial discharges).

Recently, a mercury lidar system was used in a study at the "terracotta army" emperor Qin's mausoleum in Xi'an, China. According to 2200-year-old chronicles, large amounts of liquid mercury (being considered as an elixir of life) were introduced into the underground burial chamber. Over time, cracks in the sealed enclosure could have developed allowing volatile mercury fumes to escape. Actually, excess

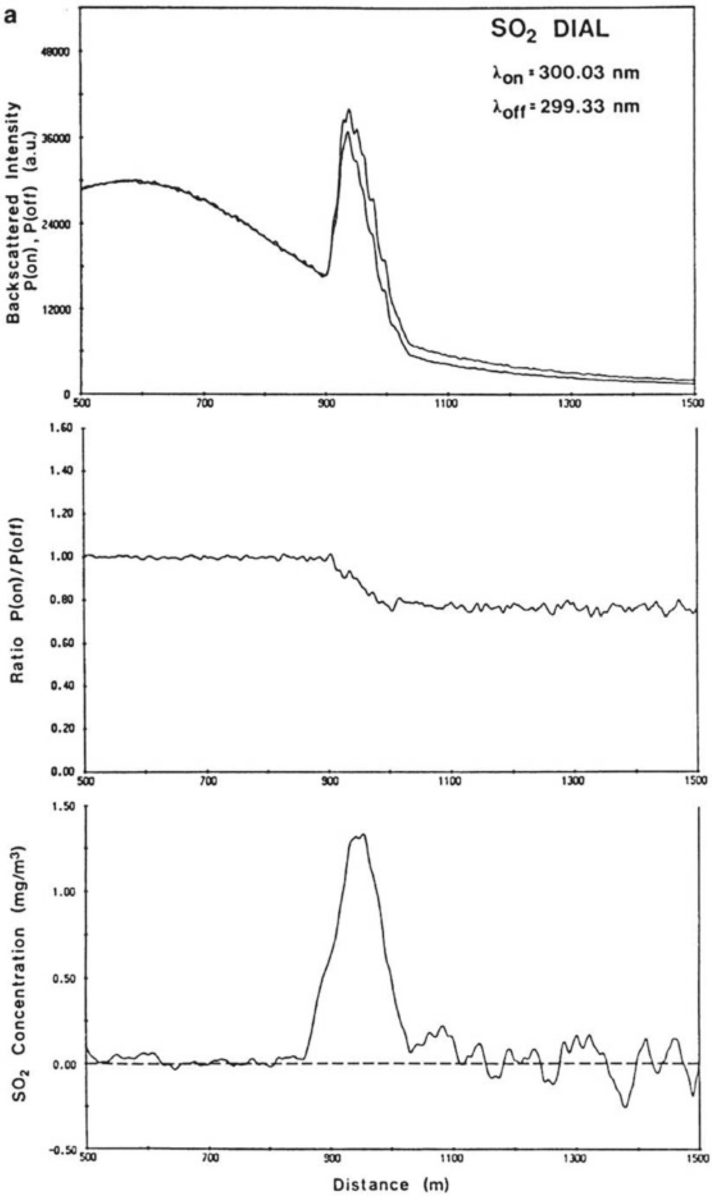

Fig. 10.30 **a** SO_2 DIAL measurement. The R^{-2} dependence has been suppressed by using a reduced photomultiplier tube amplification at short ranges [2316].

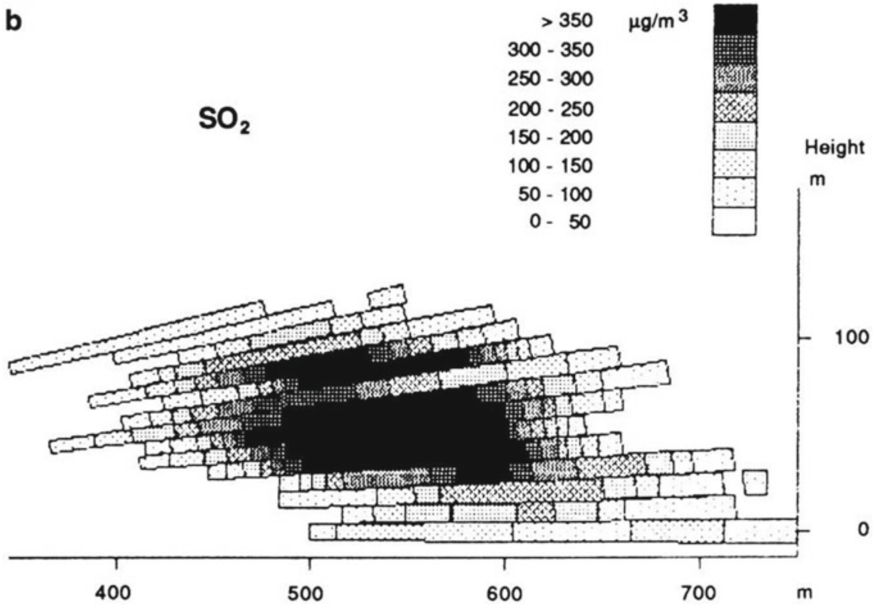

Fig. 10.30 **b** Mapping of a cross-section of an SO_2 plume from a paper mill obtained by DIAL measurements. By multiplying the integrated SO_2 content by the wind velocity, normal to the vertical section, a total flow of 230 kg/h of SO_2 was found [2316]

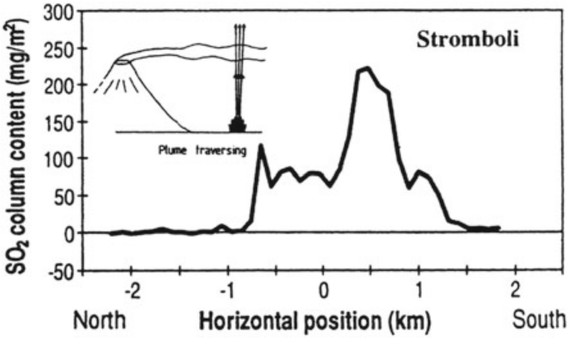

Fig. 10.31 Illustration of shipborne DIAL monitoring of the SO_2 emission of Mt. Stromboli. By multiplying the integrated overhead SO_2 burden by the wind velocity, a flux of 6 metric tonnes per hour was obtained [2320]

mercury in the atmosphere above the mausoleum was observed [2333], supporting the historical account of the tomb (Fig. 10.33), which was never opened.

Nitrogen oxide (NO) is, as discussed in Sect. 10.1.1, formed by the Zeldovich mechanism at high combustion temperatures, and is mostly due to automotive traffic. Nitric oxide (NO) and the subsequently formed nitrogen dioxide (NO_2) can both readily be measured by DIAL techniques [2334–2337]. A sharp bandhead around 226 nm is utilized for attaining the characteristic differential absorption for NO [2334, 2335], while NO_2 which was the gas studied in the first demonstrations of

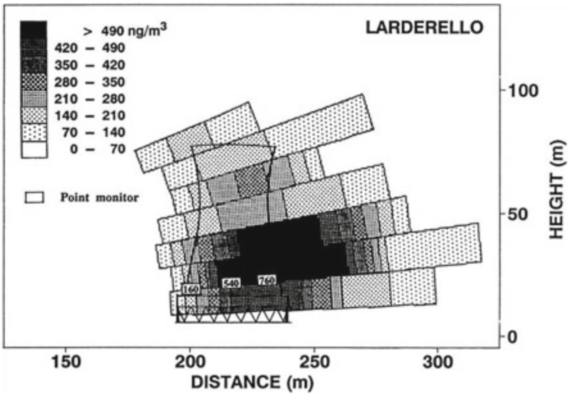

Fig. 10.32 Atomic mercury distribution around a cooling tower of an Italian geothermal power plant. The numbers given at certain locations are reference values measured with the standard gold amalgamation technique [2326]

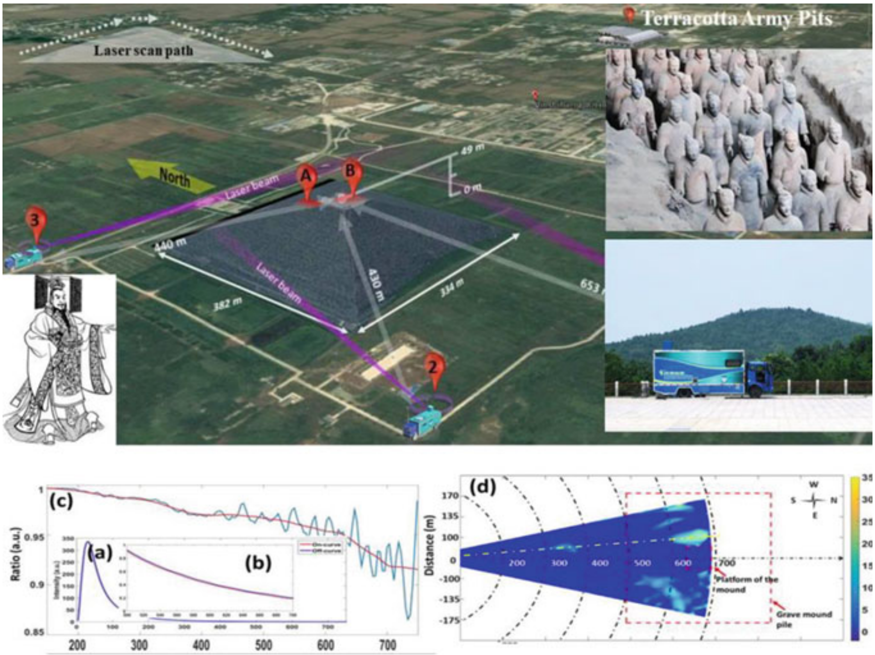
Laser scan path
Terracotta Army Pits
North
Laser beam
A
B
3
2
49 m
0 m
440 m
430 m
382 m
334 m
Laser beam
653
(c)
(a)
(b)
Ratio (a.u.)
1
0.95
0.9
0.85
200
300
400
500
600
700
On-curve
Off-curve
(d)
Distance (m)
170
135
100
0
-100
-135
-175
700
Platform of the mound
Grave mound pile
W
S
N
E
35
30
25
20
15
10
5
0

Fig. 10.33 Measurements of atomic mercury emission from the Emperor Qin mausoleum in Xi'an, China. Inserted figures in the upper part show part of the Terracotta army, the DIAL system in measurement position at the tomb mound, and an ancient drawing of the emperor. Lower part diagrams show raw lidar returns (**a**) and (**b**), the resulting DIAL curve (**c**), and measured atomic mercury concentrations close to the top of the mound (**d**) [2333], published under the Creative Commons Attribution 4.0 License, CC BY 4.0, Springer-Nature

the DIAL technique, can be measured in a wide range of blue wavelengths [2336, 2337]. Actually, blue laser radiation can be frequency doubled, so that a lidar system conveniently can monitor NO, as well as NO_2, using the same primary blue wavelength region [2338]. The monitoring of hydrocarbons and carbon monoxide (CO) requires IR wavelengths (see, e.g., Figs. 6.77, 10.21, and Table 6.5). Emissions from petrochemical industries and leaks from natural gas pipelines are important targets for hydrocarbon monitoring around 3.4 μm [2339, 2315]. Here, gas correlation imaging, as discussed in connection with Fig. 6.87 is a complementary technique.

The requirements for very sharp and well-defined laser frequencies when using the DIAL technique can be relaxed by using a gas correlation lidar technique [2340], where the backscattered radiation from a broadband transmitter is split up into two channels; one supplied with a cell filled with optically thick gas, which only passes the off-resonance components for the signal, and one channel where the total signal (on and off) is detected. If the cell gas is present in the atmosphere, a differential lidar effect is obtained using many absorption lines simultaneously (compare with Fig. 6.87). This technique has been demonstrated for Hg [2340] and CH_4 [2341] lidar detection.

Industrial emission control using lidar techniques is discussed in [2342].

Ozone is a particularly important gas in relation to global environmental issues. It can be monitored by DIAL around 300 nm. Water vapour vertical profiles can also be measured. Ground-based and airborne lidar systems are being used in extensive studies of these gases [2343–2349]. Furthermore, many lidar stations monitor the stratospheric dust layers due to volcanic eruptions (e.g. Mt. Helens 1980, El Chichon 1982, Pinatubo 1991, Eyafjallajökull 2010) [2350–2354]. The dust cloud movements provide an important insight into upper atmosphere dynamics. Dust particles, water vapour, ozone, carbon dioxide, and other greenhouse gases all influence the global heat balance. (The year 1816 is frequently referred to as "the year without a summer", due to heavy emissions from Mt. Tambora, Indonesia, which blew up on April 5, 1815.) Actually, the detailed influence of atmospheric aerosol particle represents the largest uncertainties in the modelling of "*climate forcing*", i.e. global warming [634].

Atmospheric wind velocities can also be measured by lidar techniques. Apart from the obvious interests in meteorology, there are important air-traffic applications. Clear-air turbulence causes unexpected problems for airliners in flight, and a minute of early warning from an onboard forward-looking wind lidar system is useful. Shear winds resulting in a sudden height drop along projected landing approach lines are dangerous and have caused accidents. The appearance of a pair of strongly rotating swirls persisting for minutes in the wake behind a landing airliner can cause problems to smaller aeroplanes. The Doppler shift in the backscattered radiation is used in a similar way to that discussed in connection with the velocity measurements in Sect. 10.1.5. Recently, a technique for reducing the swirl is to angle the end of the aeroplane wings upwards, in this way counteracting the vortex formation and reducing the drag to achieve better fuel economy [2355].

If a narrow-band lidar transmitter is used, it is possible to distinguish between a sharp Mie scattering peak, which moves corresponding to the particle flow, and a Doppler-broadened Rayleigh scattering component due to the fast thermal motion of the molecules. The envelope (a few GHz broad) also shifts corresponding to the wind displacement in a similar way to that discussed in connection with Fig. 10.16. In order to detect the movement, sharp transmission Fabry–Pérot transmission filters are placed around the Mie and/or Rayleigh distributions to observe the increase or decrease in the intensity in split detection channels. This is the so-called *edge technique* [2356–2358]. Clearly, the etalons used for the interferometer must be very accurately temperature stabilized to avoid drifts. It can then be an advantage to use atomic or molecular absorption filters [2358] and observe the Doppler distribution slide up or down the sharp absorption edges. A related technique for velocity measurements in combustion flows utilizing thermal emission lines that are more or less absorbed by blocking atomic line gas filters has been proposed [2359].

A different approach to atmospheric wind velocity measurements is to utilize *coherent detection* in narrow-bandwidth IR lidar systems. If the scattering aerosol particles in the atmosphere are moving, a Doppler shift in the received signal leads to a corresponding difference frequency beat when mixed with a CW local oscillator signal (see Sect. 10.2.1). Frequently, the local oscillator also seeds the pulsed lidar transmitter to give it a sharp and well-defined frequency. The beat-frequency spectrum yields information on radial wind speed and turbulence. Ranges of tens of kilometres have been attained with coherent wind lidar systems [2360–2364]. In order to obtain all wind vector components, the laser beam is frequently scanned over the surface of a cone. This scenario is particularly relevant for airborne or space-borne large-area coverage. Lidar systems are also being deployed to space, with initial testing utilizing the Shuttle vehicle, followed by the CALIPSO system [2365–2370]. First applications were Mie scattering lidar measurements of particles and cloud structures. Global wind mapping is the single most important task for a continuously monitoring space system. Doppler wind lidar is also efficiently used in connection with the presently very quickly expanding use of wind turbines for electricity generation [2371, 2372].

Developments in lidar research and applications are covered in the biennial series of International Laser Radar Conferences (ILRC) with a recent event arranged in 2019 in Hefei, China [2373]. Coherent lidar techniques are likewise the subject of a series of International Coherent Lidar Conferences (ICLC), with a recent event in 2018 in Okinawa, Japan [2374]. The strongly expanding field of automotive lidar applications is also subject to specialized conferences [2375].

Overviews of pulsed lidar technology and applications can be found, e.g. in [2376–2379].

10.2.3.2 CW Lidar Systems

While range resolution can be achieved by time-of-flight (TOF) lidars operating with pulsed lasers, it can also be accomplished when using continuous-wave lasers.

In this case, the transmitter and receiver are separated in space, and the receiver sequentially observes the atmosphere along the laser beam, e.g. by scanning (*bi-static lidars*, in contrast to mono-static lidars, discussed in the previous section)

[2380, 2381]. Recently, a particularly powerful implementation of this principle has been accomplished by the introduction of CW Scheimpflug lidars [2382] relating to the Austrian *Theodor Scheimpflug* (1865–1911), who showed that simultaneous focusing at short and long ranges in areal photography could be achieved by tilting the photographic plate. In the lidar implementation, the corresponding geometrical arrangements must be made [2383]. A very small separation between the transmitter and receiver is chosen (normally less than 1 m), allowing a long section along the laser beam to be sharply imaged on a tilted linear array detector; as shown in Fig. 10.34. The compact arrangement allows the whole internally adjusted system, which can be based on readily available and low-cost amateur astronomy tubes, to be mounted on an amateur-telescope pivotal stand, and it can be freely adjusted to appropriate directions. The proper tilting of the detector ensures that objects far away, are focused at a shorter distance from the main mirror/lens than objects at close range, reflecting a common observation for old-fashion manual camera focusing. In contrast to the common pulsed lidar systems with the backscattered intensity falling with a $1/R^2$ dependence (Eq. 10.7), the recorded signal intensity stays constant with the range. This occurs because, at a large range, the intensity from a long sector along the laser beam is falling on the same detector pixel, whereas for short ranges, the intensity received at a specific pixel corresponds to a short range. Expressed differently, the range resolution is good at short ranges and poor far away.

Systems of the Scheimpflug type are frequently used for elastic backscattering monitoring employing fixed frequency, multi-mode lasers, with monitoring of flying insects (which we could consider as large atmospheric particles…) as the first application. Using lasers of perpendicular linear polarization, the depolarization of light in interaction with the insect can reveal if it is hairy or shiny [2384]. Scattering against spherical raindrops keeps full linear polarization according to Mie theory,

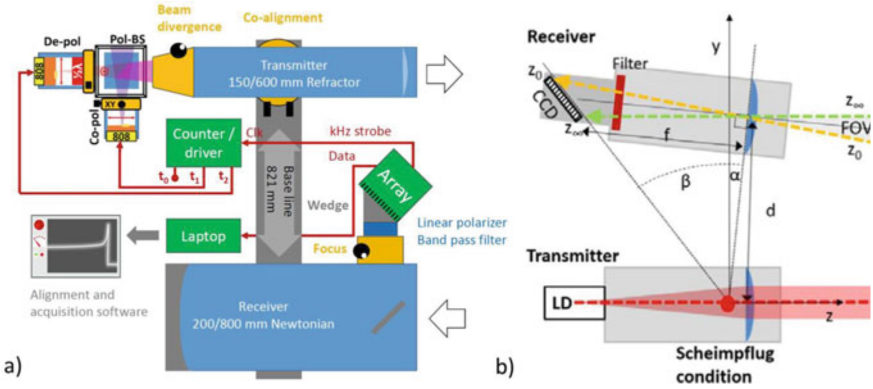
Beam divergence
Co-alignment
De-pol
Pol-BS
808
λ/4
XY
Co-pol
808
Transmitter
150/600 mm Refractor
Counter / driver
Clk
kHz strobe
Data
t_0
t_1
t_2
Base line
821 mm
Wedge
Array
Linear polarizer
Band pass filter
Laptop
Focus
Alignment and acquisition software
Receiver
200/800 mm Newtonian
a)
Receiver
y
Filter
z_0
CCD
z_∞
f
z_∞
FOV
z_0
β
α
d
Transmitter
LD
z
b)
Scheimpflug condition

Fig. 10.34 **a** Principle of a Scheimpflug lidar system, with two lasers with perpendicular linear polarizations being transmitted, and a reflector telescope being used for receiving the backscattered signal ([2384], reproduced with permission from Springer-Nature) **b** Geometric arrangement pertaining to such a system, shown for the case of a receiving refractor telescope ([2382], reproduced with permission from PIERS, The Electromagnetic Academy) and also allows the discrimination of insects from raindrops. By using two lasers with different wavelengths, the differential reflectance can be assessed, which gives some information on the insect coloration [2385, 2386]. By reading out the detector at high rates (kHz), which is possible with modern CMOS detectors, it is feasible to capture the insect wing beats as an oscillating backscattering intensity, which provides further characterization.

Different aspects of aerial fauna monitoring with a Scheimpflug CW lidar system are shown in Fig. 10.35 [2387], which illustrates signals during a 24 hour timespan from insects and bats flying over Chinese rice fields. Wing-beat signals with corresponding Fourier transform showing the frequency contents are included. Further aspects of insect monitoring with CW lidar systems are discussed, e.g. in [2388–2393].

Lasers with moderate requirements on linewidth can be used in Scheimpflug CW lidars for studies on insects and much smaller aerosol particles, the latter aspect being of considerable interest in pollution management and related to climate change issues. Also for particles, the use of more than one laser wavelength is beneficial [2394]. By exchanging the broadband (multi-mode) laser for a tuneable single-mode CW

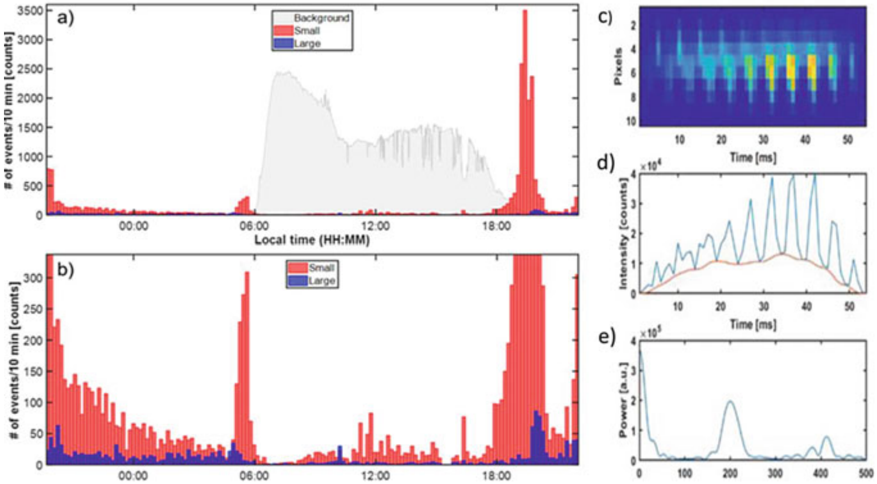

Fig. 10.35 Monitoring of insects and bats flying over a Chinese rice field. A CW Scheimpflug lidar system, as shown in Fig. 10.34a) was utilized. **a** 24 hour histogram of the number of insect echoes (Small) and bat echoes (Large) in 10 minutes intervals, as well as the general daylight background level. It is observed that activities peak at dawn and especially at dusk. The more intense activity at dusk may be related to the longer duration of the low-light intensity transition due to particles accumulated during the day causing sky scattering even when the sun is well below the horizon (**b**) With 10x magnification it is clearly seen how the bats peak their hunting activity towards the night side of the insect peaks, to themselves avoid flying predators, such as hawks needing daylight to hunt. **c** Raw backscattering data of an individual insect flying through the laser beam, flapping the wings, as digitized in (**d**), where also the static body background is indicated. Finally, (**e**) shows the Fourier transform, featuring 200 Hz as the wing-beat frequency, typical of a rice pest insect ([2387], reproduced under the CC BY 4.0 licence, Royal Society, London)

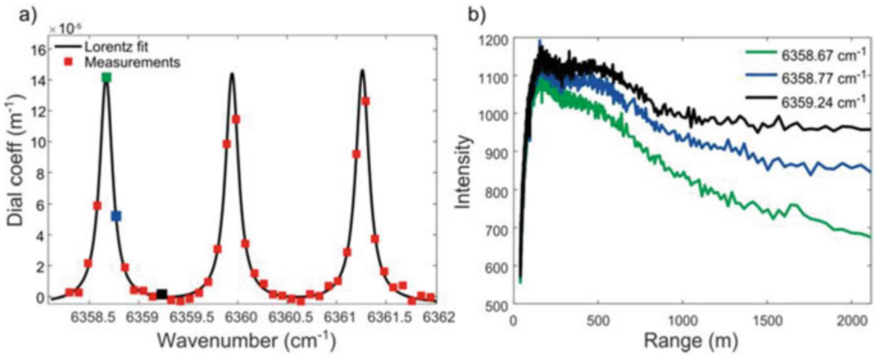

Fig. 10.36 Illustration of DIAL measurements for atmospheric carbon dioxide using a single-mode CW lidar system operating in the 1.57 μm spectral region. **a** CO_2 absorption spectrum recorded over a 2000 m path length. **b** Range-resolved atmospheric backscattering recordings, when the laser is tuned to an absorption peak, halfway down, and off the peak, as indicated by dark points in the left part of the (**a**) panel ([2396]; reproduced with permission from OPTICA)

laser, it is also possible to perform CW DIAL measurements on molecular gases, such as H_2O, CO_2, and NO_2 [2395–2397]. This important development is illustrated in Fig. 10.36.

10.3 Laser-Induced Fluorescence and Raman Spectroscopy in Liquids and Solids

Laser-induced fluorescence (LIF) in liquids and solids can be used for diagnostic purposes in many contexts. Most substances have broad absorption bands in the UV region and a pulsed UV laser is frequently most useful for inducing fluorescence. The nitrogen laser ($\lambda = 337$ nm) is a simple and practical source for such measurements. Other useful laser systems are tripled Nd:YAG lasers ($\lambda = 355$ nm), excimer lasers (XeCl, $\lambda = 308$ nm; KrF, $\lambda = 249$ nm) or blue diode lasers. Liquids and solids exhibit broad fluorescence emission bands [2398, 2399]. As already discussed for dyes, sharp emission features are lost because of rotational quenching and mutual interactions between the molecules. Vibrational Raman spectra, on the other hand, exhibit quite sharp lines. Raman spectroscopy is a powerful tool for studying liquids and surface layers on solids. We shall describe a few applications of LIF and Raman spectroscopy of liquids and solids in this section. We will first consider hydrospheric remote sensing, vegetation monitoring, and monitoring of fauna, and will then discuss monitoring of surface layers.

10.3.1 Hydrospheric Remote Sensing

The increasing pollution of seas and inland waters calls for efficient methods of aquatic pollution monitoring. Oil spills cause drastic damage to the environment. Plastics are being introduced into the ocean to such an extent that, by 2050, the amount by weight will be higher than that of fish [2400]. For marine monitoring, airborne surveillance systems are the most useful ones. All-weather capability generally calls for a microwave-based system. Fluorescence can be monitored at a distance with a modified lidar set-up and an airborne laser fluorosensor can be a valuable complement to a SLAR or SAR system (Sect. 7.2) for characterizing detected oil slicks. Clearly, it is necessary to perform laboratory measurements on the substances of interest in order to obtain the basic information necessary for a field system. An early laboratory set-up for LIF studies is shown in Fig. 10.37. Either a scanning monochromator connected to a boxcar integrator is used, or better, an optical multichannel analyzer (Fig. 6.42). LIF spectra for different substances in the aquatic environment are shown in Fig. 10.38 for N_2-laser excitation. A crude-oil spectrum is shown featuring a broad and strong fluorescence distribution. Oil products fluoresce quite strongly because of their aromatic hydrocarbon content, e.g. anthracene and naphthalene. Refined products fluoresce even more strongly with the peak fluorescence shifted to shorter wavelengths, while heavy residual oils, such as asphalt, fluoresce weakly and mainly towards longer wavelengths. A spectrum of sea water is also shown in the figure with a prominent sharp signal due to the OH stretch Raman mode of H_2O, corresponding to a Raman shift of about 3400 cm^{-1}. The broad blue fluorescence is due to organic water pollution, sometimes referred to as *dissolved organic matter (DOM)*. The spectrum also shows a fluorescence peak from a tracer dye that has been added to the water. Such dyes can be used to tag a “package” of water allowing studies of flow patterns in aquatic systems.

A concentration as low as 1 μg/l is sufficient for such fluorescence tracing. Included in Fig. 10.38 is a spectrum from river water, polluted by lignin sulphonate from a pulp mill and a spectrum of water containing microscopic green algae. The prominent peak at 685 nm is due to the chlorophyll-*a* pigment that is present in all plants to mediate photosynthesis [2402–2404]. LIF can be used to study algal blooms, induced by eutrophication in seas and lakes [2405–2409]. Airborne oil monitoring

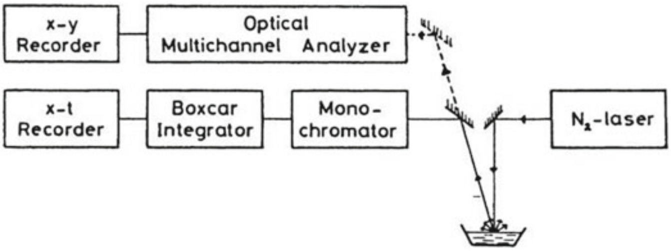

Fig. 10.37 Laboratory set-up for LIF measurements [2401]

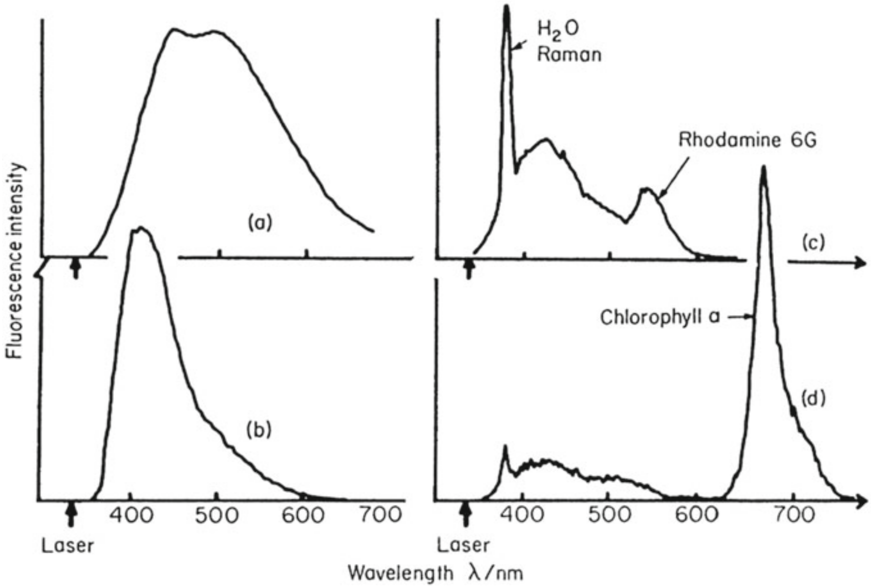

Fig. 10.38 LIF spectra for aquatic substances. **a** Crude oil, Abu Dhabi; **b** river water downstream from a sulphite pulp mill; **c** sea water containing 3μg/l Rhodamine 6G dye. The Raman peak from water is exhibited, too; **d** the green algae *Chlorella ovalis* Butcher in sea water [2401]

systems can efficiently detect and characterize oil slicks [2410–2415]. Oil slicks are detected by an increase in the blue fluorescence at the same time as the water Raman signal disappears because of full absorption in the oil layer. Recently, a low-weight fluorosensor system, which was lifted by a drone, has been employed for remote aquatic fluorescence monitoring [2416]. The system used a blue CW laser and a compact spectrometer, such as the one shown in Fig. 6.28a. The same technology was used in an earlier much heavier land-based system [2417]. Systems based on CW lasers are clearly much more sensitive to the daylight background compared to pulsed systems, for which gated detection can be employed.

An airborne lidar system operating in the blue-green transmission window of water (Fig. 6.61) can be used for measurements of water depth [2418–2423]. The principle of such measurements is given in Fig. 10.39. The speed of light in water is about 0.75 *c*. A laser with a short pulse length must be used. Water is strongly attenuating, and in order to enhance the weak bottom echo with respect to the strong surface echo, a polarization scheme can be used. If the laser pulse is linearly polarized, the surface echo remains largely polarized, whereas the bottom echo is almost completely depolarized. Thus, by using a crossed linear polarizer in front of the detector, a more reasonable relative strength of the two echoes is obtained. Depths down to several tens of metres can be measured by laser bathymeters of this construction. A frequency-doubled Nd:YAG laser (λ = 532 nm), a copper vapour laser (λ = 510 and 578 nm) or a Hg−Br laser (λ = 520 nm) are candidates for laser bathymeters. Such

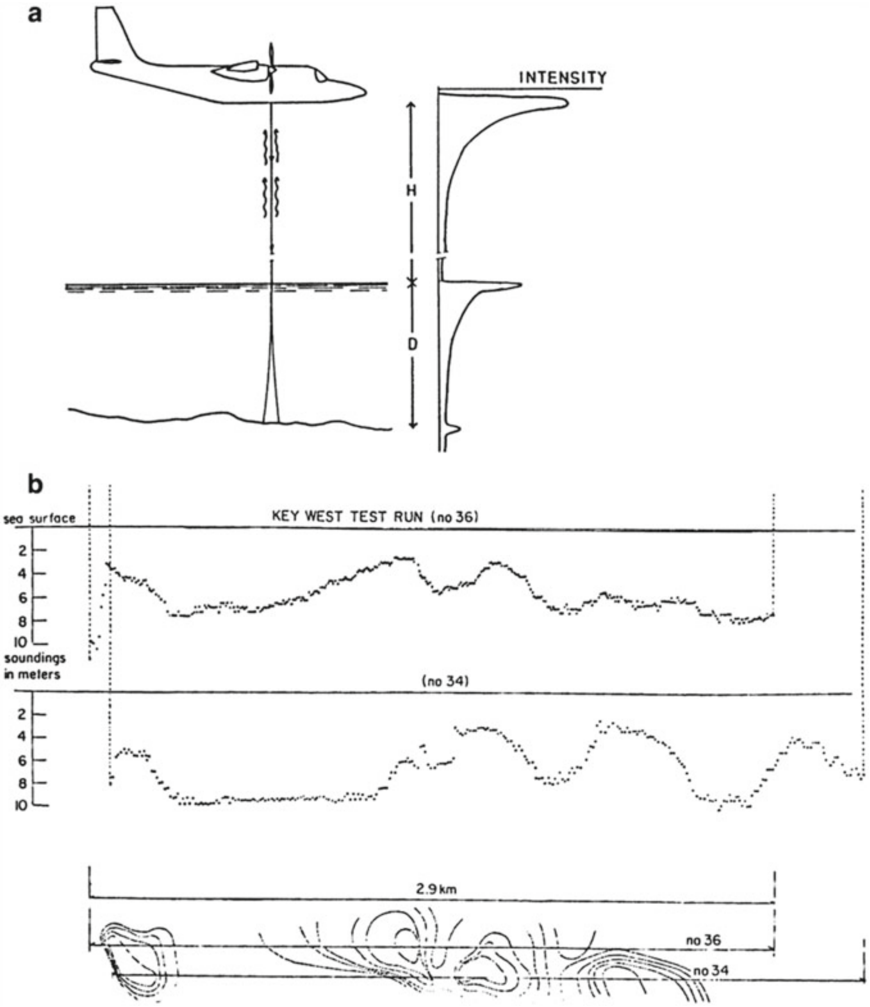
a
INTENSITY
H
D
b
sea surface
KEY WEST TEST RUN (no 36)
2
4
6
8
10
soundings in meters
(no 34)
2
4
6
8
10
2.9km
no 36
no 34

Fig. 10.39 **a** Principle of airborne laser bathymetry [2420]. **b** Results from lidar bathymetry in shallow waters [2418]

airborne systems can also be used for the detection of fish schools and submarines. Space-borne green lasers are being employed for communication with submarines, since the green spectral region is the only practical one where penetration of the atmosphere, as well as water, is possible. Further aspects of hydrospheric probing by lasers are included in [2418–2423]. Spectroscopic Scheimpflug lidar systems can also be constructed for underwater monitoring of fluorescence [2424, 2425]. Here a 2-D detector is used, with one axis corresponding to range, and the other one to fluorescence recording. We note the similarity to airborne pushbroom sensors

(Fig. 6.92). Fluorescence spectral recording with range resolution can be achieved up to a distance of about 10 m.

10.3.2 *Vegetation, Cultural Heritage, and Fauna Monitoring*

10.3.2.1 Vegetation

In the same way, as a UV laser beam can be directed into the water to induce fluorescence for diagnostic purposes, the beam from the fluorescence lidar system can be directed onto the leaves and needles of vegetation. A measurement scenario is shown in Fig. 10.40. Frequency-tripled Nd:YAG radiation at 355 nm is directed onto the foliage of a beech tree and fluorescence is collected by the lidar system receiving telescope. After dispersion in a spectrometer, the spectrum is recorded on a gated and image-intensified detector. The microchannel plate of the intensifier is activated at a delay after the laser is fired, corresponding to the time-of-flight from the system to the target and back. In this way, the background radiation can be suppressed, and measurements in full daylight become possible. Fluorescence spectra, captured at a 60 m distance, are included in the figure. In addition to the 690 nm chlorophyll peak already discussed above, a second peak at 735 nm is observed in terrestrial vegetation. When the concentration of chlorophyll in the leaves increases both peaks grow, but since the 690 nm peak occurs at a wavelength where chlorophyll absorbs (see Fig. 6.89), the continuing growth of this peak is suppressed. Thus, the ratio between the two peak intensities is related to the chlorophyll concentration, which can be determined after calibration. The blue-green fluorescence observed is due to accessory pigments and the leaf wax layer. The vegetation's spectral shape depends on the excitation wavelength. Thus, with 405 nm violet excitation, which is centred on the Soret absorption band of chlorophyll, very prominent near-IR chlorophyll signals are obtained. In contrast, if instead UV excitation is used, e.g. by employing a nitrogen laser at 337 nm, only blue-green fluorescence is effectively observed, while

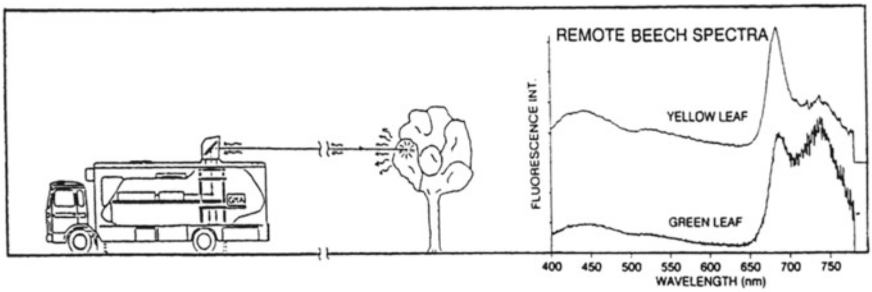

Fig. 10.40 Fluorescence lidar monitoring of vegetation. Remote fluorescence spectra from green and yellow leaves of a beech tree are included [2426]

the chlorophyll signals at 690 and 735 nm are absent since the light does not penetrate the wax layer (cf. the skin protection by sunscreens). Environmental stress can influence the shape of the fluorescence spectrum [2402] and provide complementary information to data obtained in reflectance measurements (Sect. 6.6.2). Vegetation studies using fluorescence lidar techniques are discussed, e.g. in [2426–2434].

The systems discussed so far are quite heavy and complex. Recently, a drone-based low-weight remote-sensing system based on the Scheimpflug principle was demonstrated [2435]. A blue CW semiconductor laser is used to induce fluorescence, which can be recorded range-resolved from the tree canopy to the ground. Such a system operated under GPS control can be much more cost-effective than a helicopter or fixed-wing aircraft system.

Clearly, it would be of considerable interest to be able to monitor vegetation fluorescence globally, as is done for reflectance using earth-resource satellites, operating in a passive mode using sunlight. Fluorescence gives information on the dynamics in photosynthesis and thus provides important complementary information to reflectance spectra. In order to provide a remedy for the complexity and challenges of an active, laser-based satellite-installed scanning fluorosensor, a passive method, using *sun-induced vegetation fluorescence* has been proposed and implemented. After proof-of-principle demonstrations and aeroplane tests, the technique has also become satellite-based with global coverage. Chlorophyll fluorescence is induced by the blue light present in sunlight, but the resulting fluorescence is very weak and superimposed on the much stronger reflected light from the vegetation. However, this is not the case at the locations of the black Fraunhofer absorption lines in the sun spectrum. In particular, the molecular oxygen A-absorption line at about 760 nm can be utilized (see Figs. 1.5 and 6.57). Fluorescence causes the contrast in the black Fraunhofer line to be reduced as observed with a high-resolution spectrometer [2436–2439]. The technique was actually first used for the detection of oil floating on water, where the short-wavelength parts of the solar spectrum induced a strong bluish fluorescence.

10.3.2.2 Cultural Heritage Monitoring

A fluorescence lidar system can also be used for studies of the facades of historical buildings and monuments [2299, 2440–2443]. Different stone materials used have different spectral signatures, which are related to the contents of different trace elements, e.g. in marbles. The stone surface might be corroded due to environmental pollutants and the surface may also be invaded by algae, lichen or microorganisms. Data from an investigation of the gate area of a cathedral are shown in Fig. 10.41. An area of 8 x 8 m was sequentially scanned, point by point, line by line, with a fluorescence lidar system placed 60 m away (*whiskbroom imaging*). The beam interacts with the sandstone wall, which at some places has some algae, exhibiting the characteristic chlorophyll fluorescence. At other places, fluorescence is strongly quenched due to ions from rusting iron clamps. Famous buildings, such as the Coliseum and Lateran Baptistery/Rome, and the Parma and Lund cathedrals have been studied in

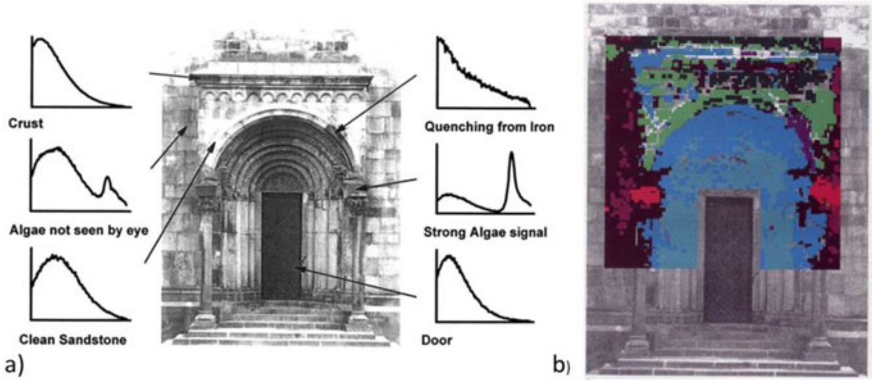

Fig. 10.41 Remote fluorescence monitoring at the Lund Cathedral with a lidar system placed 60 meters from the building. **a** Fluorescence spectra from different surfaces, and **b** false colour imaging of areas with similar spectral properties, as evaluated with principal component analysis ([2441]; reproduced with permission from OPTICA)

this way, with typical measurement distances of 50–100 m. LIF lidar applications to the cultural heritage sector have been reviewed in [2444]. The related field of LIBS remote sensing, including remote statue cleaning by laser ablation, was included in Sect. 10.2.3.1.

Generally speaking, optics and lasers have found important applications in the management of cultural heritage. Raman spectroscopy is a powerful technique to characterize pigments used in paintings, and can together with methods such as X-ray fluorescence (Sect. 5.1.1) be used for determining if a painting is authentic or a falsification/copy. Pigments have very specific elemental contents, which can differ considerably even if two colours are perceived as being the same [2445]. Multi-spectral imaging including the UV and IR regions may reveal invisible restorations, and even primary images which were overpainted [2446]. Fluorescence imaging can also provide much information on paintings [2447]. Short-range LIBS is much being used for surface cleaning, e.g. removing old varnish from paintings [2448], and for cleaning objects as large as cathedrals (e.g. the Stefan-Dom in Vienna). Aspects of lasers in the management of the cultural heritage are discussed in [2449–2451].

10.3.2.3 Insect and Bird Monitoring

We have above illustrated how Scheimpflug systems can be used to study aerial and aquatic fauna, mostly employing elastic backscattering. We will here describe how flying animals can be characterized by LIF using pulsed lidar systems. Systems would typically use frequency-tripled or quadrupled Nd:YAG radiation at 355 or 266 nm to induce fluorescence, which can be recorded by a spectrometer, equipped with a gated and intensified array detector for full spectral coverage at a set range (Fig. 6.42). Alternatively, a beam-splitted range-resolving detector arrangement, where target

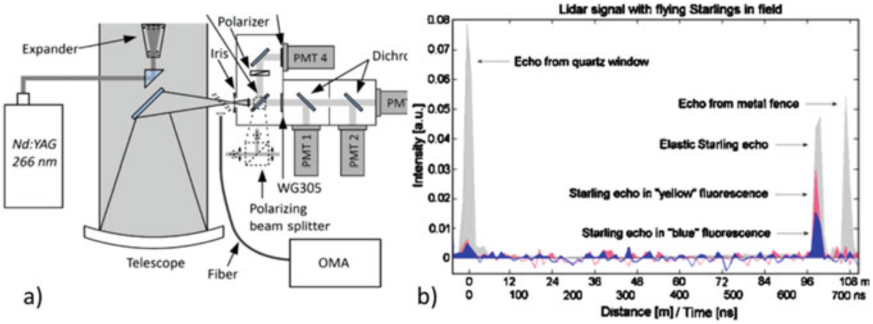

Fig. 10.42 Pulsed lidar recording of flying bird fluorescence **a** A four-colour range-resolved fluorescence lidar system [2453] **b** Echo of a flying starling recorded at about 100 m range in elastic backscattering and two fluorescence channels [2452] (Figures reproduced with permission from OPTICA)

echoes can be detected in a low number of spectral bands, isolated by filters, can be used [2452, 2453]. Such a system is shown in Fig. 10.42a and in b a flying bird (starling) is captured at about 100 m distance in elastic backscattering, and blue and yellow fluorescence, yielding some useful object identification. Different types of birds have been characterized by fluorescence properties [2452]. Long-term recordings of bird elastic echoes in three wavelength bands and one Raman band [2454] have been obtained at one of the EARLINET aerosol lidar stations [2311]. Passing birds can also be recorded by moon or sky occultation [2453], in a similar way as exoplanets are recorded when passing in front of the illumination source (Sect. 6.7). The infrared spectral region can be used for obtaining valuable spectral and wing movement information [2455].

Flying insects can also be studied by pulsed lidar systems observing elastic backscattering. Insect lidar work was first reported by Shaw et al. [2456–2458], where the interest was the localization of hidden land mines, which could be detected by the release of bees, trained to be attracted to a mixture of honey and TNT vapour smells, and recorded by lidar when swarming above the hidden explosive. Laser-induced fluorescence from insects can also be recorded. Further, by first catching insects and dusting them with fluorescent dye powders (separating species and/or sexes, by different fluorescent dye colours), their later whereabouts can be followed based on lidar encounters. Such work is reported in [2459, 2460]. Insects can also be studied by a passive spectroscopic technique, which can be characterized as an inverse occultation method. Here, a telescope connected to a compact spectrometer is directed towards a black background, and sun-illuminated insects occasionally passing the field of view are recorded as fast intensity spikes which can be analyzed with regard to spectral distribution and wing-beat frequency [2461, 2462].

Optical techniques, which have spectroscopic features, can complement the more common and well-established utilization of high-frequency radar systems for insect and bird studies [2463].

The general field of studying aerial and aquatic fauna by photonics technique is reviewed in [2464].

10.3.3 Food and Pharmaceutical Spectroscopy

Food quality assessment is an important aspect, also related to the fact that huge volumes of food are wasted due to inadequate handling and storage. Spectroscopic techniques; in particular, IR spectroscopy, have wide applications in monitoring food stuffs and food [2465–2467]. Fruits are particularly sensitive, and assessment of maturity and ripeness is of great interest. This can be achieved by reflectance (colour) recording as well as by LIF studies (see, e.g., [2468, 2469]). Of particular interest is the possibility to construct small, hand-held devices for quality assessment. Another aspect regards gases associated with fruit maturing. It is well known that the processes are strongly influenced by ethylene, the concentration of which in store houses can control the appropriate time of consumption. Gas analysis for foods is discussed in Sect. 10.5.4.5.

The pharmaceutical industry has very strict quality control requirements, especially what regards to the amount of active substance present, e.g. in one tablet. Again, spectroscopy, frequently in the IR region, and combined with multivariate analysis methods are very useful [2470]. Tablets are strongly scattering, and time-resolved techniques can, like for biomedical applications (Sect. 10.5.4), provide proper decoupling of absorptive and scattering properties [2471, 2472].

10.3.4 Monitoring of Surface Layers

We have already mentioned that oils strongly absorb UV light. Thus, LIF can be used for detecting very thin surface layers of oil [2473, 2474]. Industrially, it can be of interest to be able to establish that sheet metal components are free from oil before entering a painting shop. It is also interesting to monitor the presence of surface layers, e.g. corrosion-protective agents. Examples of spectra of this kind are given in Fig. 10.43. Monitoring of the application of oil for rust protection during sheet metal coiling in a steel rolling mill using an industrial fluorosensor is illustrated in Fig. 10.44.

The penetration depth in organic liquids rapidly increases for longer wavelengths. By choosing a suitable excitation wavelength, sensitive measurements of film thickness can be performed in different thickness ranges. The fluorescence of organic substances can also be used for the sensitive detection of signals in liquid chromatography and electrophoresis [2475–2478]. A UV laser or blue laser beam can be used for exciting fluorescence at the outlet of the column, or can be used to illuminate the whole column. In the latter case, the fluorescence from the different constituents moving forward in the column under the influence of an electric field can be imaged

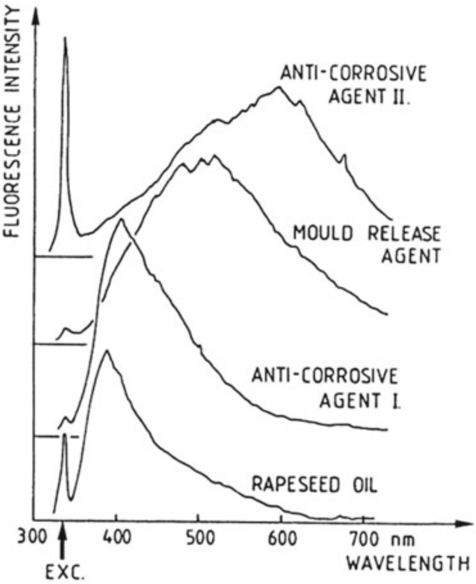

Fig. 10.43 LIF spectra of industrial surface layers. A nitrogen laser was used for the excitation [2473]

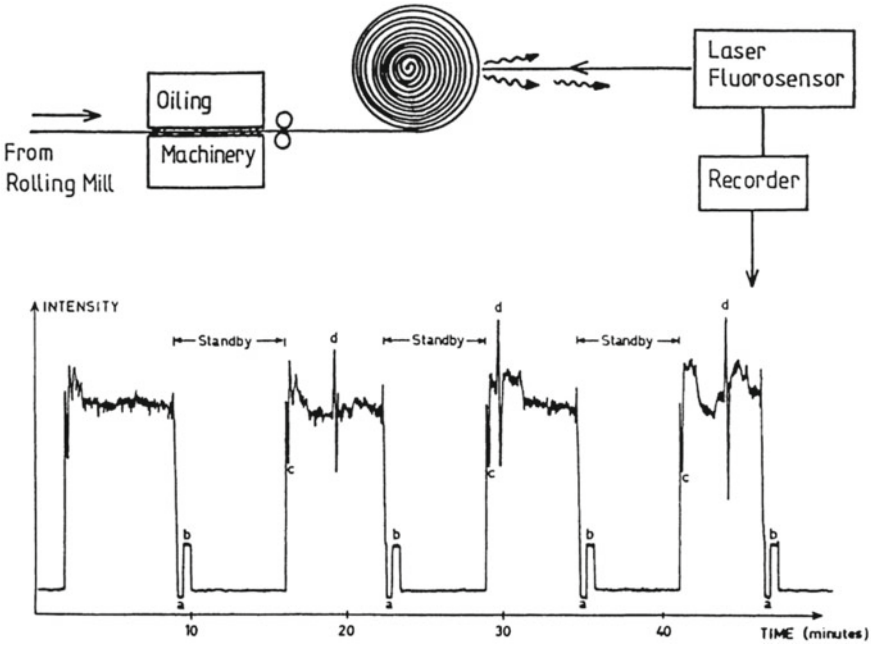
Oiling
Machinery
From
Rolling Mill
Laser
Fluorosensor
Recorder
INTENSITY
Standby
Standby
Standby
a
b
c
d
10
20
30
40
TIME (minutes)

Fig. 10.44 Anti-rust oil application monitoring in a steel rolling mill [2473]

simultaneously onto a CCD detector, as illustrated in Fig. 10.45. By spectral analysis of the fluorescence from the different components, further selectivity in the identification of individual components in complicated chromatography and electrophoresis separations can be obtained.

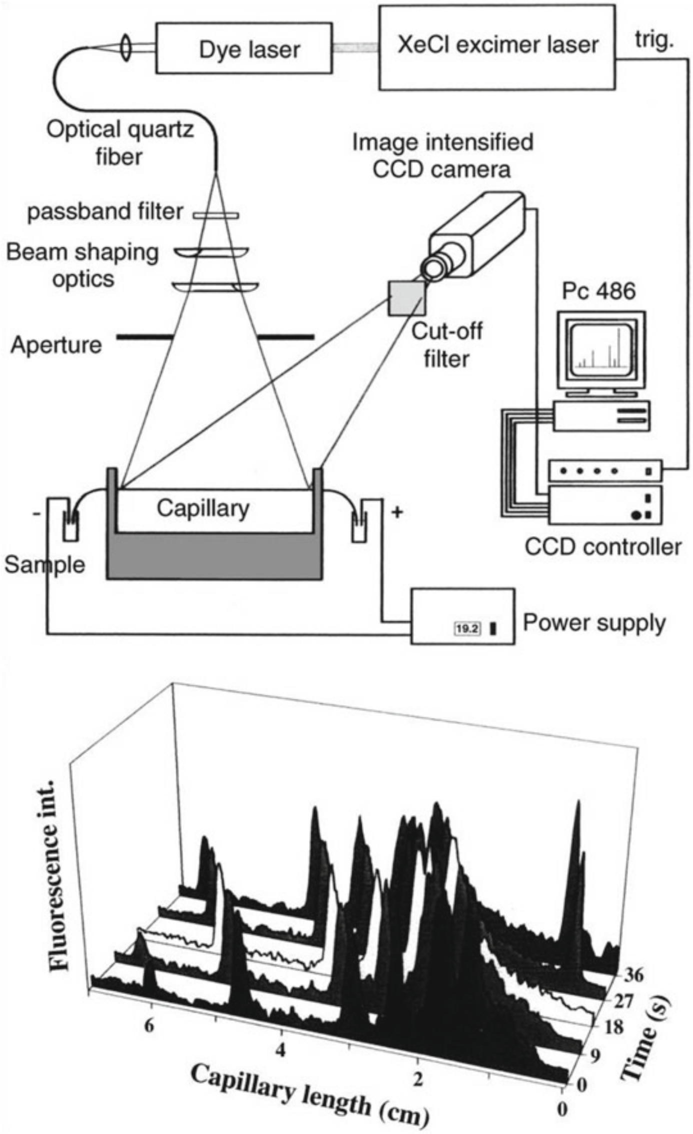
Dye laser
XeCl excimer laser
trig.
Optical quartz fiber
Image intensified CCD camera
passband filter
Beam shaping optics
Aperture
Cut-off filter
Pc 486
Capillary
-
+
Sample
CCD controller
19.2
Power supply
Fluorescence int.
6
4
2
0
Capillary length (cm)
36
27
18
9
0
Time (s)

Fig. 10.45 Set-up for imaging detection of capillary electrophoretic separation. Blue light from an excimer-pumped dye laser is used to induce fluorescence from DNA fragments, which are separating in the column as visualized in read-outs (*bottom*) from an intensified CCD camera [2478]

Fluorescence can be used in many additional analytical applications. As discussed in Sect. 10.5, it is a powerful tool in medical diagnostics of tissue. It is also used in forensic sciences, e.g. for visualization of latent fingerprints [2479–2482]. More everyday applications include fluorescence "hidden" codes on bank notes, credit cards, and driving licences.

Certain salts of rare earth exhibit sharp fluorescence lines when excited by UV light. This occurs because of the shielding of the optically active inner 4f electrons by electrons in outer shells (Table 2.2). It has been shown that the relative strengths of different lines, and also the decay time of the fluorescence at a certain fluorescence wavelength vary strongly with temperature [2483–2485]. This reflects the fact that the measured fluorescence lines originate in levels that are excited from different low-lying metastable states, which have populations determined by the Boltzmann distribution. Fibre thermometers with a rare-earth-salt fibre tip have been developed. By applying thin layers of such salts to surfaces, it is possible to remotely measure the temperature by LIF. This technique could be particularly valuable for hot rotating machine parts. Remote-sensing thermometry related to combustion is reviewed in [2486].

Surfaces of solids can also be investigated by Raman spectroscopy, which has a higher specificity than LIF. Thus, this method is well suited for studying chemical processes such as corrosion, electrochemical processes, etc. Frequently, an Ar^+ laser is used in conjunction with a double or triple monochromator for isolating the Raman signals from the very strong elastic scattering from the surface. A Raman spectrum illustrating surface oxidation is shown in Fig. 10.46. The Raman scattering from a surface can be strongly enhanced compared with the bulk material scattering. The enhancement is connected with periodic structures on the surface. Surface-enhanced Raman scattering has been discussed in [2488–2494]. This field is related to the growing area of *plasmonics* [2495–2497]. In plasmonics, *surface plasmon polaritons* are utilized. They are surface optical waves moving along the interface between a dielectric and a metal surface, and are accompanied by coherent electron oscillations in the metal. Plasmonics operates in the twilight zone between electronics and photonics and has great potential, e.g. for sensors. Surfaces can also be studied by other optical techniques. A method in which the strength of surface frequency doubling of impinging laser light is investigated has been established [2498–2502]. An example of surface studies using frequency doubling is shown in Fig. 10.47.

The general field of laser spectroscopy of solids was covered in [2503–2505].

10.4 Laser-Induced Chemical Processes

Laser light can be used for inducing or controlling chemical processes in different ways. Photons of suitable energy can greatly increase the speed of certain reactions, leading to a significant increase in the yield of the desired substance. In this section, we will discuss *laser-induced chemical processes* in general and also

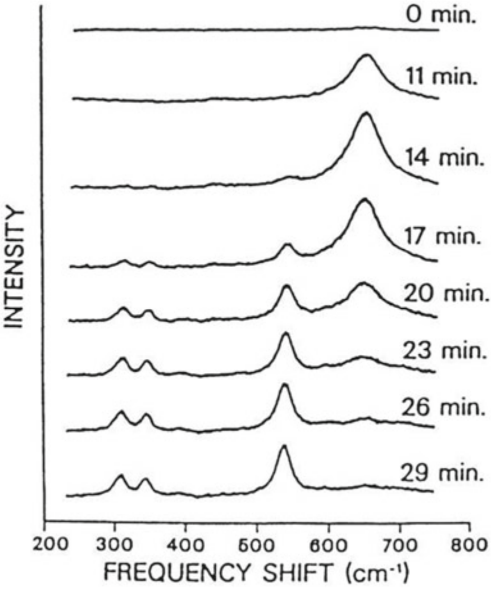

Fig. 10.46 Surface Raman spectra showing an oxidation process on a surface of a Fe/Cr/Mo alloy. Initially, an Fe/Cr double oxide (spinel) is formed which is successively transformed into Cr_2O_3 [2487]

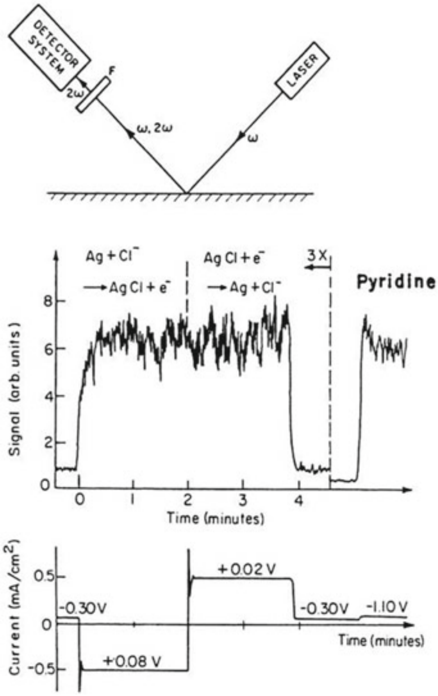

Fig. 10.47 Surface monitoring by observing the generation of frequency-doubled light. The *top* figure depicts the experimental arrangement in this type of measurement. *Below*, the electrolytic build up and removal of AgCl on an Ag electrode in a cell with KCl solution are illustrated. The second-harmonic signal saturates for a single monolayer. When the last monolayer is removed following voltage reversal, the voltage changes and the signal disappears [2498]

consider processes in which strong isotopic selectivity is obtained leading to *laser isotope separation*. The field of laser-induced processes is discussed in [2506–2523].

10.4.1 Laser-Induced Chemistry

A primary question in connection with laser-induced chemistry is whether it could be possible to selectively break chemical bonds in large molecules by irradiating the molecules at a frequency corresponding to the vibrational mode associated with that particular bond. It has been found that the energy absorbed in a particular vibrational mode is very quickly distributed over the whole molecule, resulting in an essentially thermal and unselective excitation. In order to achieve selectivity, a great deal of energy must be deposited in a bond in a time shorter than 1 ps. This can be achieved using the techniques of femtochemistry (Sect. 9.5.2) and coherent control (Sect. 9.5.3). We will here consider other techniques to influence chemical reactions using laser light. By exciting a molecule to a higher vibrational level, it can be made to react much faster (*chemical activation*). One such example is the following reaction:

$$\mathrm{K} + \mathrm{HCl} \rightarrow \mathrm{KCl} + \mathrm{H}.$$

This reaction occurs 100 times faster if the HCl molecules are excited to $\nu = 1$ compared with $\nu = 0$. Laser radiation can also act as a catalyst in certain reactions, e.g. in the production of vinyl chloride, C_2H_3Cl, for the plastic industry. The process, which is basically the thermal break up of dichloroethane $C_2H_4Cl_2$ into C_2H_3Cl and HCl, can be run at considerably lower temperatures in the presence of laser light. With an XeCl excimer laser (308 nm), free Cl radicals are formed that open up new reaction paths. Only one laser photon is needed to produce 10^4 vinyl chloride molecules since a chain reaction is utilized [2506]. Laser radiation is also very effective in many *pyrolysis reactions*. Here local heating of the reacting gases is accomplished by the laser light. As an example, the cracking of heavy hydrocarbons into lighter ones can be mentioned. In the petrochemical industry, it is frequently desirable to increase the yield of ethylene C_2H_4 over methane CH_4, since ethylene is a more desirable starting material for many petrochemical processes. Laser pyrolysis results in a higher yield than that possible with thermal heating. Laser pyrolysis also has good potential in the production of ceramic materials. Using silane (SiH_4) as a starting product, powders of Si, Si_3N_4 or SiC can be produced, and later be sintered into ceramics.

Laser chemistry can also be used for *purifying* certain chemicals. The production of ultrapure silicon for the semiconductor industry and for producing solar cells is of special interest. For optical fibres, the purest possible SiO_2 is desirable. A suitable starting material is silane gas. Arsine (AsH_3) and phosphine (PH_3) are typical impurities. On irradiation of the natural gas mixture with an ArF excimer laser ($\lambda =$ 193 nm), the impurities are quickly dissociated. The technique has a good production potential and the cost for purification could be quite reasonable. Since the cost of the laser photons will always be an important factor, it is likely that laser-induced chemical processes will be advantageous, especially for producing specialized and expensive chemicals, e.g. pharmaceuticals. Photo-assisted production of vitamin D and prostaglandin has also been considered.

10.4.2 Laser Isotope Separation

Using narrow-band laser light, it is possible to induce isotope-selective processes leading to isotopic separation by utilizing optical isotopic shifts [2515–2523]. Enriched or separated isotopes are of great interest in many contexts. Pure radioisotopes are used in medicine. Also, stable elements, such as ^{13}C, can be used for the study of metabolism and other biological processes. In NMR spectroscopy, signals are only obtained from isotopes with a nuclear spin. For sulphur and calcium, the useful isotopes ^{33}S and ^{43}Ca are naturally present only in very small concentrations. By using enriched isotopes in the building up of organic materials, completely new possibilities arise. Enrichment of ^{14}C from organic objects that are to be dated would mean a much higher sensitivity since the tracer element could be concentrated into a small volume allowing small detectors to be used with a resulting low background count rate. In this way, the time span when dealing with the ^{14}C method could be considerably increased.

However, the greatest interest in isotope separation historically comes from the nuclear energy sector. Production of heavy water for heavy-water reactors and separation of highly active components from the burnt-out uranium fuel are two applications. The most important aspect by far is, however, the isotope separation of ^{235}U. Natural uranium contains only 0.7% ^{235}U and enrichment to about 3% is needed for use in light-water reactors. The normal separation method is the diffusion of uranium hexafluoride UF_6 through porous filters. This process, which relies on the slightly different mobilities of $^{235}UF_6$ and $^{238}UF_6$, is very inefficient and the separation costs are very high and correspond to about 10% of the resulting price of the produced electricity. A technique based on high-speed gas centrifugation is now pursued as an alternative. Laser techniques for uranium isotope separation have been investigated. Clearly, any technique that could reduce the separation costs would be of interest.

Laser techniques can lead to a high degree of enrichment and may also be useful in processing uranium tailings from which most of the fissile material has already been removed. Laser isotope separation schemes based on free atoms or on UF_6 are possible. In both cases, the presence of an isotopic shift is utilized. We will first consider free atoms. For heavy elements, such as uranium, the isotopic shift is only due to the volume effect (Sect. 2.8). The different isotopically separated components of a uranium emission line are shown in Fig. 10.48 for an enriched sample. The broadening in the ^{235}U line is due to an unresolved hyperfine structure. The basic principle for atomic uranium separation is illustrated in Fig. 10.49. A narrow-band tunable laser selectively transfers ^{235}U atoms to an excited state. Since atomic transitions can be saturated with laser pulses (Sect. 9.1.2), a large fraction of the ^{235}U atoms is transferred to the higher state, from which they can be photoionized using a second

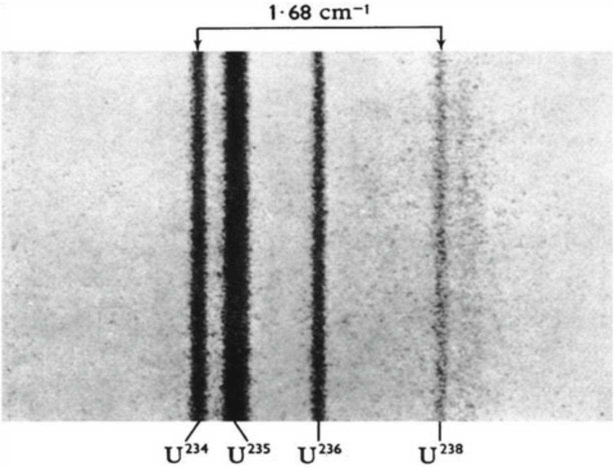

Fig. 10.48 Isotope shifts in a uranium emission line [2524]

Fig. 10.49 A schematic uranium isotope separation scheme

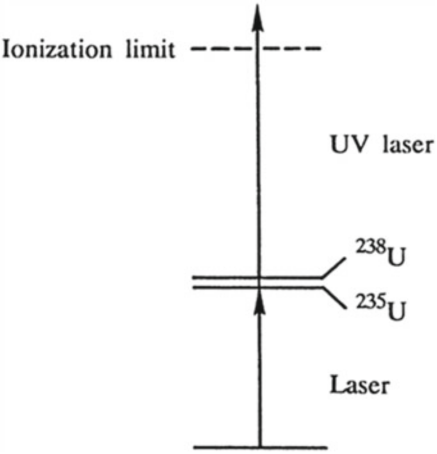

laser pulse. The photon energy for this laser is not sufficient to photoionize ground-state atoms. The ^{235}U ions that are formed in this way are extracted to a collector plate using an electric field. A separation scheme with two selective excitation steps induced by dye lasers that are pumped by powerful copper vapour lasers has been explored for practical separation purposes [2515, 2516]. A powerful excimer laser is used for the photoionizing step. The properties of uranium call for special evaporation techniques. It is necessary to heat the uranium to 2300 K to achieve substantial evaporation. However, molten uranium metal is extremely reactive and attacks most furnace materials. One technique that can be used to overcome this problem is local surface heating with electron guns.

Uranium isotope separation using a molecular approach is based on selective multi-photon dissociation of UF_6. The relevant vibrational isotope shift is 0.6 cm^{-1} in the primary vibrational transition at 628 cm^{-1} (16 μm). In the development of the technique, experiments on SF_6 have been very important. The conditions are much more favourable for SF_6 than for UF_6. The isotope shift is 17 cm^{-1} between ^{32}S and ^{34}S in the IR active vibrational mode that involves asymmetric stretching of two *S–F* bonds. The spectrum has a typical *P*, *Q,* and *R* branch structure and the whole region of absorption for the rotational level population distribution that is obtained at room temperature is 15 cm^{-1}. Thus, the isotopic molecules are spectroscopically totally separated. Furthermore, the vibrational transition in $^{32}SF_6$ well matches the emission of a free-running pulsed CO_2 laser.

The multi-photon dissociation process is illustrated in Fig. 10.50. Because of the anharmonicity of the vibrational potential, photon energy that is resonant in the first vibrational step will successively pull out of resonance higher up in the vibrational energy-level ladder. However, the molecule can be excited in a multi-photon process (Sect. 9.1.3) until it is dissociated. SF_6 then disintegrates into SF_5 and F. By making the first step resonant for one isotopic molecule, the probability of subsequent dissociation for this molecular species is significantly increased.

To carry out the corresponding process for UF_6, the availability of efficient lasers in the 16 μm region is a necessity. This has resulted in the considerable effort being put into producing such lasers. An efficient way of generating laser radiation at 16

Fig. 10.50 Multi-photon dissociation process [2525]

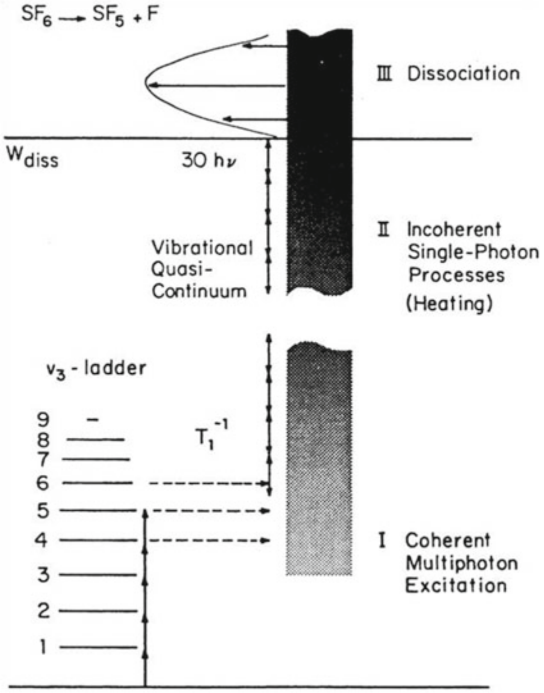
$SF_6 \rightarrow SF_5 + F$
III Dissociation
W_{diss}
30 hν
Vibrational Quasi-Continuum
II Incoherent Single-Photon Processes (Heating)
v_3 - ladder
9
8
7
6
5
4
3
2
1
T_1^{-1}
I Coherent Multiphoton Excitation

μm is to Raman shift a pulsed CO_2 laser at 10.6 μm. A 16 μm beam can be produced at a 50% efficiency by stimulated Raman scattering a multi-pass cell filled with para-H_2 (hydrogen with the two nuclear spins anti-parallel). Rotational transitions in this molecule with parallel nuclear spins are used. A problem with UF_6 is that the width of the sharpest feature in the spectrum (the *Q* branch) is 5 cm^{-1} at room temperature, which greatly exceeds the isotope shift.

Thus, the selectivity is poor. The selectivity can be increased by using two laser wavelengths in the 16 μm region. By dynamic cooling of the UF_6 gas through expansion from a supersonic nozzle, the number of populated rotational levels can be drastically reduced, leading to a much better resolution of the Q branches of the two isotopic molecules. Even then, two separate 16 μm wavelengths are advantageous and further efficiency is gained by adding excimer laser UV photons for more efficient photo-dissociation of molecules that are excited in the multi-photon process. Upon UF_6 dissociation, UF_5 molecules are formed in the form of a powder that can be collected. Separation of uranium always involves the important ethic issue of the dual-use of uranium for reactors and atomic bombs.

For the separation of ^{13}C, multi-photon dissociation of Freon-22 (CF_2HCl) or CF_3I can be used, and macroscopic quantities are produced utilizing CO_2 TEA lasers. Heavy water (D_2O) can also be enriched with a multi-photon process utilizing CO_2 laser radiation acting on CF_3D molecules

$$\mathrm{CF_3D} + nh\nu \rightarrow \mathrm{CF_2} + \mathrm{DF},$$

$$\mathrm{2DF} + \mathrm{CaO} \rightarrow \mathrm{D_2O} + \mathrm{CaF_2}.$$

The isotope shift between CF_3D and CF_3H is large and the cross-sections for multi-photon absorption differ by a factor of 6000 between the two molecules.

Formaldehyde, HCHO, has also been much studied. Using multi-photon processes this molecule can be used for the separation of hydrogen and carbon as well as oxygen.

Stepwise processes involving a few photons can also be used for molecules. As a matter of fact, one of the first laser separations was performed in this way [2526]. This experiment on NH_3 molecules is illustrated in Fig. 10.51. A mixture of $^{14}NH_3$ and $^{15}NH_3$ is kept in a cell and is irradiated by a pulsed CO_2 laser, which can only excite $^{14}NH_3$ vibrationally because of the isotope shift. At the same time, a strong UV source, consisting of a spark discharge in the air, is fired. The UV photons dissociate the vibrationally excited molecules, but thanks to suitable filtering, no photons with sufficient energy to dissociate ground-state molecules are available. The following reactions occur, but only for $^{14}NH_3$:

$$\begin{aligned}
&\mathrm{NH_3} + h\nu \rightarrow \mathrm{NH_2} + \mathrm{H},\\
&\mathrm{NH_2} + \mathrm{NH_2} \rightarrow \mathrm{N_2H_4},\\
&\mathrm{N_2H_4} + \mathrm{H} \rightarrow \mathrm{N_2H_3} + \mathrm{H_2},\\
&\mathrm{2N_2H_3} \rightarrow \mathrm{2NH_3} + \mathrm{N_2}.
\end{aligned}$$

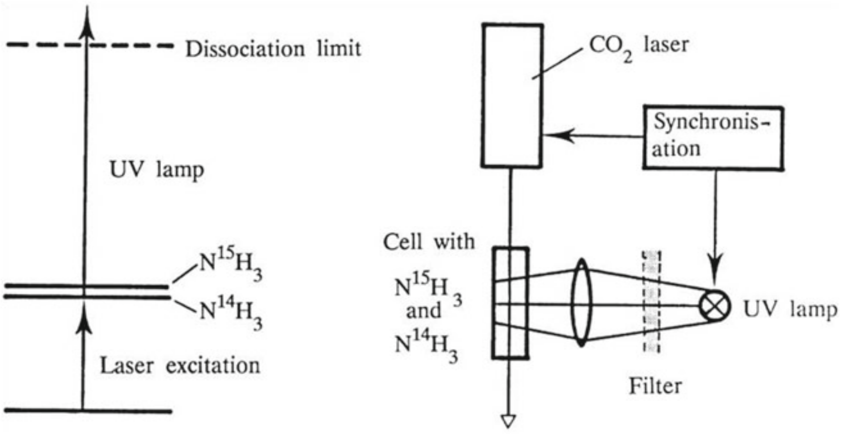
Dissociation limit
UV lamp
$N^{15}H_3$
$N^{14}H_3$
Laser excitation
CO_2 laser
Synchronis-ation
Cell with $N^{15}H_3$ and $N^{14}H_3$
UV lamp
Filter

Fig. 10.51 Ammonia separation scheme [1]

Thus, isotopically enriched $^{14}N_2$ gas has been formed in the cell. Similar processes can be used for boron and chlorine separation.

For the production of pure radioisotopes for medical use, it is advantageous to induce the nuclear reactions in suitably chosen isotopically pure elements. Examples of such processes are

$$^{203}\mathrm{Tl} \rightarrow ^{201}\mathrm{Tl},$$
$$^{124}\mathrm{Te} \rightarrow ^{123}\mathrm{I},$$
$$^{68}\mathrm{Zn} \rightarrow ^{67}\mathrm{Ga},$$

and

$$^{109}\mathrm{Os} \rightarrow ^{191}\mathrm{Ir}.$$

The annual world demand for such isotopes may only be of the order of 100 grams, but since conventional production methods are extremely costly, laser isotope separation might here be an attractive possibility.

10.5 Spectroscopic Aspects of Lasers in Medicine

10.5.1 Thermal Interaction of Laser Light with Tissue

Lasers are finding ever-increasing applications in the field of medicine. Frequently, the heating effect of laser beams is utilized. Raising the temperature from 37° to 44 °C causes disruptions in the enzymatic and electrical activities of the cells. At 60 °C, protein denaturation occurs, and at 100 °C, the cells rupture due to the boiling of the cellular fluid. Carbonization occurs at temperatures above 200 °C. The laser power densities required to attain a certain temperature rise clearly depend on the absorption properties of the tissue, which are governed by the properties of water and haemoglobin, but also by the blood flow, which carries away heat. Skin absorption is largely due to the presence of melanin. The corresponding absorption curves are included in Fig. 10.52. Beams from three important medical laser types, the CO_2, the Nd:YAG, and the Ar^+ laser, have a surgical penetration depth of about 0.1, 4, and 1 mm, respectively, in normal tissue. Short-wavelength excimer lasers have a very low penetration depth and tissue removal is caused by ablation. Under pulsed irradiation, the tissue is lifted off layer by layer. These lasers are extensively used for medical use, e.g. for corneal refractive surgery and opening of clogged blood vessels (angioplasty). Different regimes of laser interaction with tissue are illustrated in Fig. 10.53 [2528], where, for a total delivered energy of 0.1–100 J/cm^2, the interrelation between laser power and interaction time is shown.

An important feature of laser beams in surgery is their ability to cut tissue and small vessels, and at the same time coagulate the blood, which strongly reduces the need for blood transfusions (“the bloodless knife”). The thickness of the coagulated zone varies with the laser wavelength used. Other advantages are the sterile, contactless nature of the cutting, and the minimum mechanical strain on the tissue. The last point is particularly important in neurosurgery. Lasers are also used to vaporize tumours. The laser radiation from Nd:YAG and Ar^+ lasers can conveniently be delivered through flexible optical fibres that are highly transparent to the corresponding wavelengths. For CO_2 radiation, special fibres made of ZnSe (Fig. 6.55), or hollow fibres, can be used. Such radiation can also be delivered through a specially designed multi-joint arm that is terminated with a handpiece.

The strong absorption of green Ar^+ radiation in the blood is the basis for selective coagulation of blood in small blood vessels. This is utilized in the treatment of port-wine stains. This dermatological disease is caused by the excessive growth of a network of tiny blood vessels close to the skin. The laser light penetrates the skin but is absorbed in the blood, eliminating the cause of skin discolouration.

Ar^+ lasers are also used for photo-coagulation treatment of excessive blood vessel growth (retinopathy) in the retina of diabetes patients. In addition, this type of laser is used for “spot welding” of the retina in cases of retinal detachment. Because of the relatively easy optical access to the interior of the eye, this organ is well suited for laser treatment. The retina consists of many layers with different absorption properties

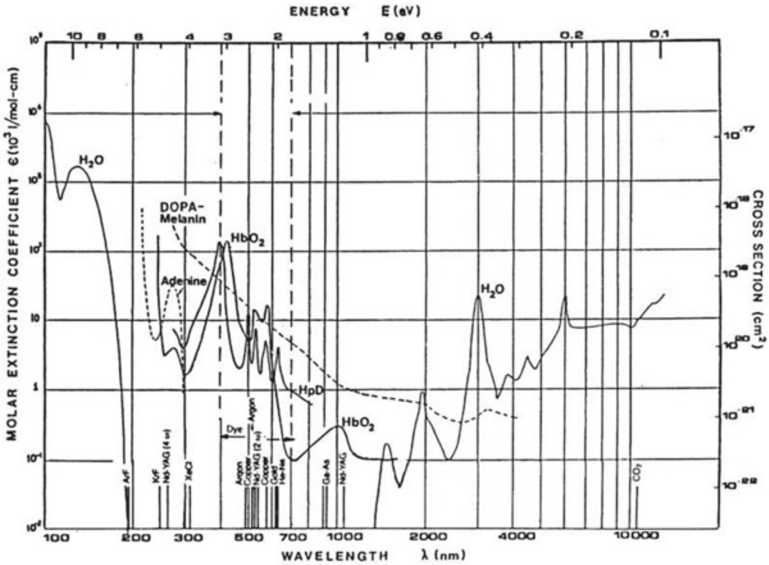

Fig. 10.52 Absorption curves for tissue constituents [2527]

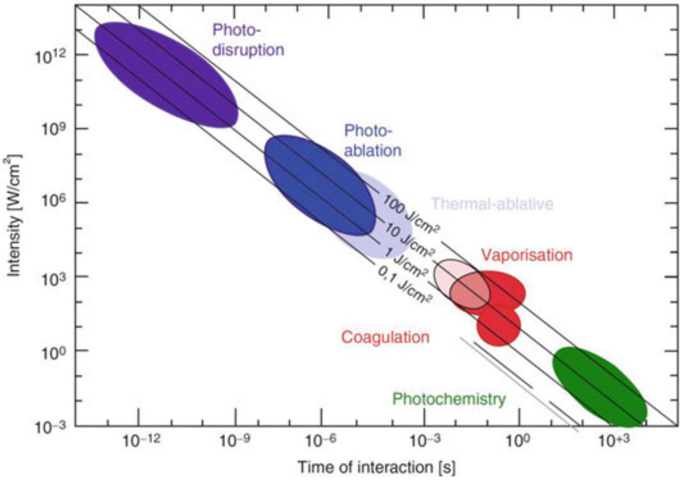

Fig. 10.53 Diagram showing different types of laser/tissue interactions depending on the time duration of the interaction. A constant energy dose of 0.1–100 J/cm^2 is indicated by the straight lines in the log-log diagram of power versus time ([2528, 2527], reproduced with permission from Springer Nature)

(see also Fig. 10.71). Thus, by choosing a certain wavelength, an energy dose can be delivered to a particular layer with a certain selectivity. One area in the retina has very special absorption properties because of its high content of xanthophyll. The optical and spectroscopic properties of the eye largely determine the criteria for safe utilization of lasers and form the basis for the legal classification of lasers. American regulations [2529] are frequently used as a starting point in setting up national rules. European regulations are defined in [2530], and the general area is treated, e.g. in [2531–2534]. The maximum permissible dose of laser light for eye exposure obviously varies strongly with wavelength. The strictest regulations are applied to the wavelength region of 400 to 1400 nm, in which the retina is fully exposed to the radiation. The Nd:YAG laser operating at 1.06 μm is one of the most dangerous lasers from an eye safety point of view since it penetrates into the eye, yet the presence of beams is not revealed, since the wavelength falls in the invisible region. For wavelengths below 400 nm, absorption occurs in the cornea. However, high doses of UV absorbed in the cornea cause cataracts.

The most relaxed regulations pertain to the wavelength region above 1.4 μm, where only the heat deposition in the cornea sets the limit. As a rule of thumb, safety limits are relaxed by at least a factor of 1000 when operating outside the 400–1.4 μm window. For detailed accounts of the medical use of lasers, we refer the reader to [2527, 2535–2541]. The somewhat related field of material processing with laser is covered extensively in [2542–2547].

10.5.2 Photodynamic Tumour Therapy

Apart from the surgical application of laser beams discussed above, another field of laser utilization, in tumour localization and treatment, is now expanding. The techniques take advantage of the special properties of certain agents (called sensitizers), e.g. hematoporphyrin derivative (HPD), which was much used in early work [2548–2553]. After intravenous injection (typically 3 mg/kg body weight), the HPD molecules are distributed all over the body. However, after a few days, the material is excreted from the body, but less from tumours, where it is selectively retained, as illustrated in Fig. 10.54. The HPD molecules themselves have no therapeutic effect but they have two important properties that can be used in connection with the selective retention just mentioned. These properties are set on a spectroscopic foundation in Fig. 10.55. The molecules have a very characteristic dual-peaked fluorescence in the red spectral region, as shown in the figure. The excitation is most efficiently performed in the Soret band peaking at 405 nm. Originally, the violet lines of a Kr^+ laser (Sect. 8.4.5), conveniently falling in this region, and Ar^+ laser lines or the N_2 laser emission could be used, but today readily available diode lasers in the violet or blue (405, or 445 nm) region are normally employed. The fluorescence can be utilized for localizing tumors, e.g. in the lung or bladder, that would otherwise not be visible in normal endoscopic investigations with viewing devices based on fibre optics. For early references; see [2554–2564].

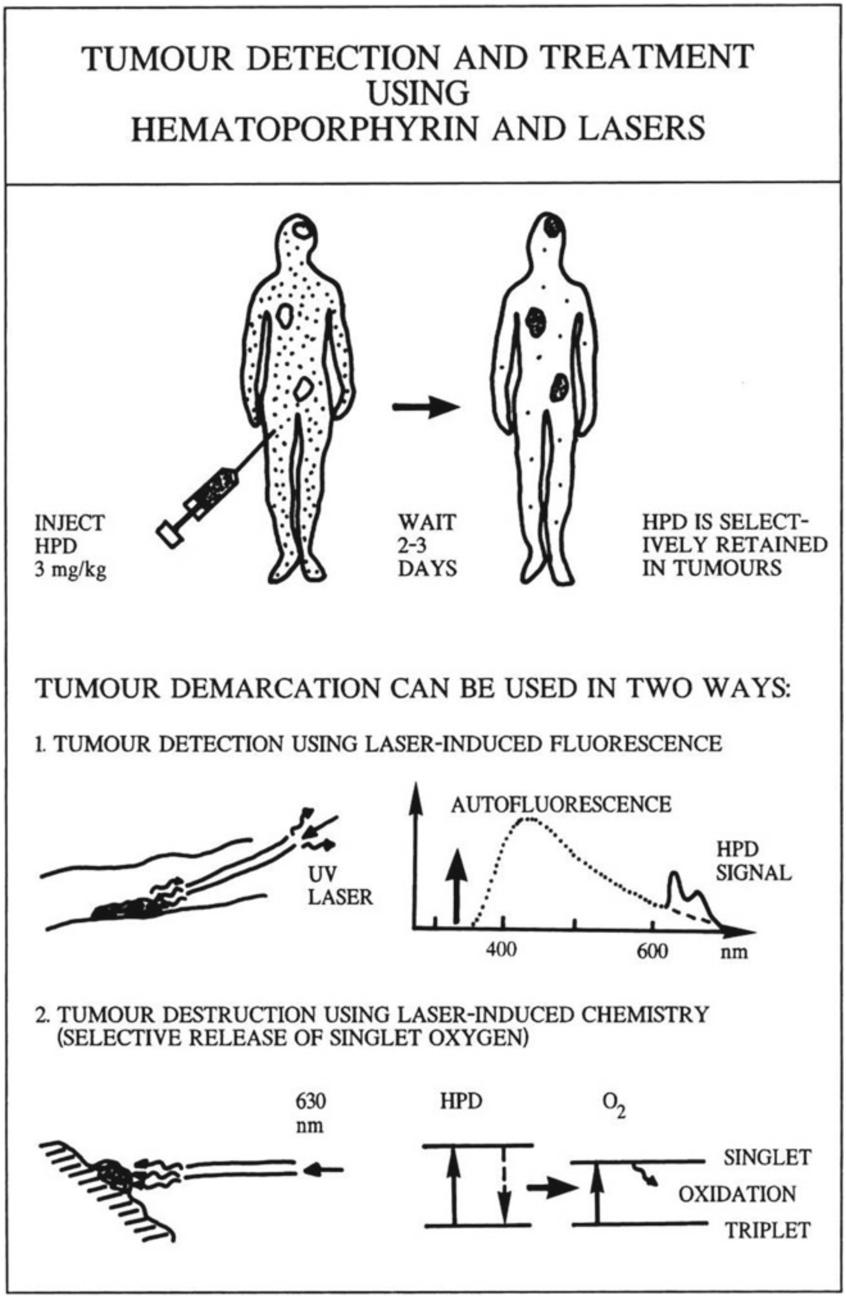
TUMOUR DETECTION AND TREATMENT USING HEMATOPORPHYRIN AND LASERS
INJECT HPD 3 mg/kg
WAIT 2-3 DAYS
HPD IS SELECTIVELY RETAINED IN TUMOURS
TUMOUR DEMARCATION CAN BE USED IN TWO WAYS:
1. TUMOUR DETECTION USING LASER-INDUCED FLUORESCENCE
UV LASER
AUTOFLUORESCENCE
HPD SIGNAL
400
600
nm
2. TUMOUR DESTRUCTION USING LASER-INDUCED CHEMISTRY (SELECTIVE RELEASE OF SINGLET OXYGEN)
630 nm
HPD
O2
SINGLET
OXIDATION
TRIPLET

Fig. 10.54 Principle of HPD–PDT and tumour fluorescence detection [2554]

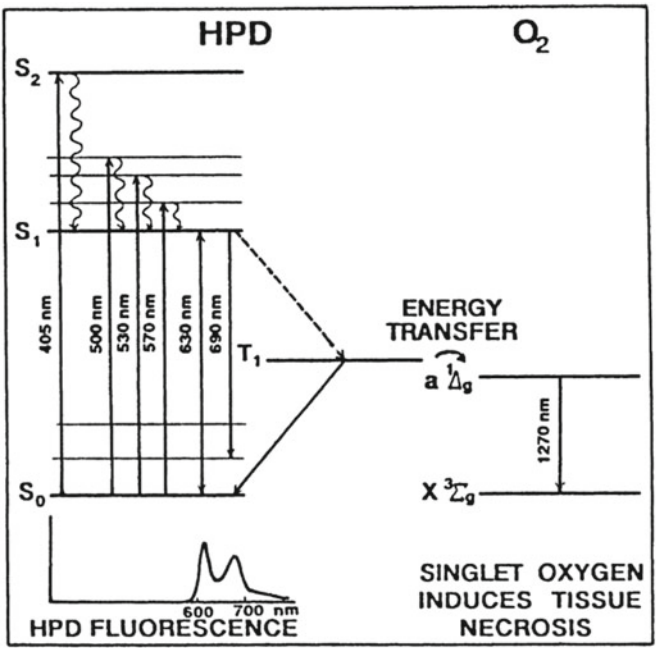

Fig. 10.55 Energy level diagrams for HPD and oxygen molecules [2555]

The other important property of HPD is that upon excitation and subsequent transfer to its triplet state, the HPD molecules can transfer their excitation energy to ground-state $X\,^3\Sigma_g$ oxygen molecules that are present in the tissue, as indicated in Figs. 10.54 and 10.55. The oxygen molecules are then excited from the triplet state to a singlet state, $a\,^1\Delta_g$. Singlet oxygen is a free radical known to strongly react with tissue through rapid oxidation and the tissue becomes necrotic. The process is thus of the laser-induced chemistry type (Sect. 10.4.1) and involves heating of the tissue only as a weak secondary effect. (Disregarding the quite different molecular mechanisms, photodynamic therapy can be seen as the "inverse" of photosynthesis, where also a specific molecule, chlorophyll, is activated by light, and in a cold, photochemistry process builds biomass out of CO_2 and H_2O while producing oxygen. Now, instead, biomass is broken down, mediated by a sensitizer and added oxygen in a cold process). Since the action only occurs in the presence of HPD, and since HPD is accumulated in tumours, selective therapy (called *photodynamic therapy, PDT*) is obtained. Again, the HPD excitation most efficiently takes place in the Soret band. However, normally the absorption peak of HPD at 630 nm is preferred since tissue transmits this radiation much better as the wavelength falls outside the region of strong haemoglobin absorption (Fig. 10.52). An effective penetration depth of a few millimeters is achieved. CW argon-ion or pulsed copper vapour laser pumping of a dye laser was initially used to generate the 630 nm radiation, but also the 628 nm emission from a pulsed gold vapour laser could also be utilized. Presently, diode

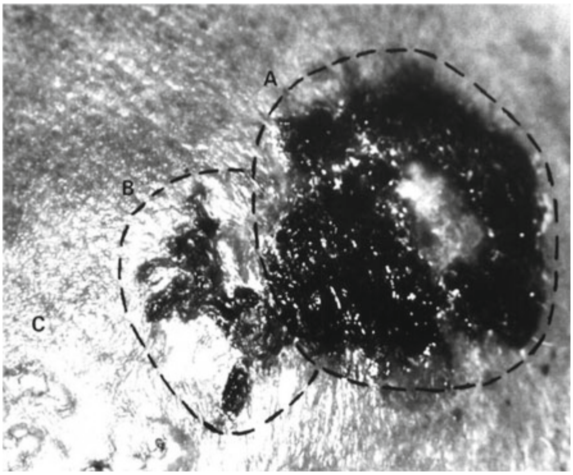

Fig. 10.56 Photograph of human basal cell cancer lesions one week after HPD-PDT. The area *A* received a uniform light dose of 60 J/cm^2. The strong demarcation of destructed tissue from undamaged tissue due to the selective uptake of HPD in tumour cells only is evident. Area *B* received only 30 J/cm^2. In area *C*, untreated tumour parts are visible

lasers with sufficient powers ($\sim$2 W) are available also in the 630 nm region and provide unprecedented convenience in this type of therapy. The laser radiation can conveniently be delivered through quartz optical fibres. For superficial tumours, the radiation is applied directly to the surface and doses of tens of J/cm^2 are normally used. An example of tumour treatment is shown in Fig. 10.56, for the case of basal cell carcinoma. The radiation can also be fibre-optically delivered through a bronchoscope or a cystoscope for lung and bladder applications, respectively. A remarkable rate of success has been reported for this new type of treatment.

For deep-lying lesions, the laser light can be transmitted fibre-optically through the lumen of a syringe needle that is inserted into the tumour mass [2565–2574]. This modality is referred to as Interstitial PDT (IPDT) and is illustrated in Fig. 10.57. The same fibres can be used for the treatment of light delivery, as well as for monitoring of treatment parameters such as light fluence through the tissue, sensitizer concentration, and the blood oxygenation level [2568].

The increasing interest in PDT is related to the development of new, improved sensitizers. Attractive properties of a PDT substance are a high selectivity for tumour tissue versus normal ones, a well-defined chemical structure, a fast clearance from the body, and absorption at deeper red wavelengths than for HPD in order to allow thicker lesions to be treated. Additional sensitizers (with absorption wavelength) now being tested include verteporfin, (690 nm), mono aspartyl chlorin e6, MACE (670 nm), tetra hydrophenylchlorin, THPC (650 nm), zinc phthalocyanine, ZnPC (675 nm), and tin ethyl etiopurpurin, SnET2 (660 nm). Recently, nanoparticles, which have been functionalized to attach to tumour cells, have also been tested. Pandeliporfin (WST11, Tookad), activated at 753 nm, has a different working mechanism, where vessels are blocked by radical formation, leading to tumour necrosis [2575–2577].

Of special interest is δ-amino levulinic acid, ALA, which occurs naturally in the human body. It is the building stone, out of which the red blood pigment, haem, is synthesized in the haem cycle, illustrated in Fig. 10.58. In an enzymatically controlled

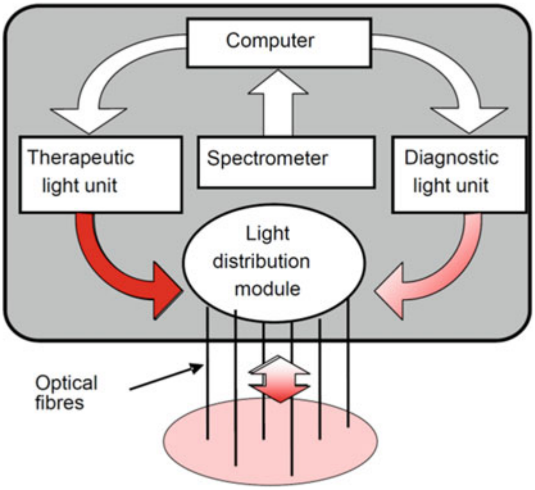
Computer
Therapeutic light unit
Spectrometer
Diagnostic light unit
Light distribution module
Optical fibres

Fig. 10.57 Equipment for interstitial photodynamic therapy (IPDT), with combined treatment light delivery and diagnostic spectroscopy (for light flow, oxygen- and sensitizer concentrations) applied through the same optical fibres ([2568]; reproduced with permission from OPTICA)

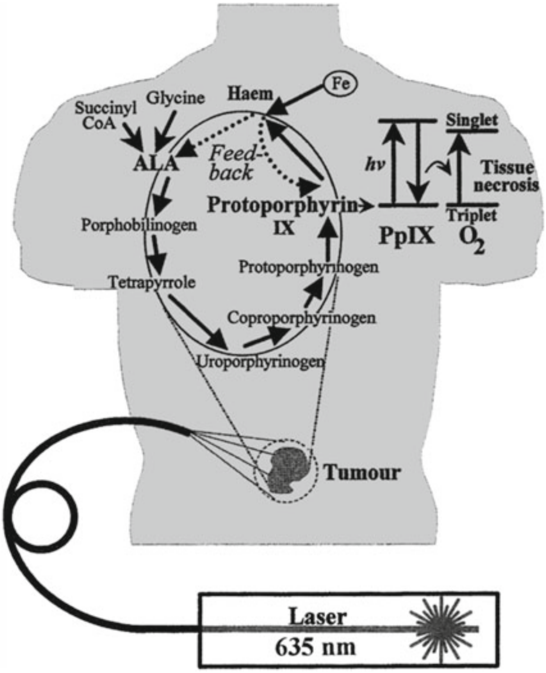
Succinyl CoA
Glycine
Haem
Fe
ALA
Feed-back
Protoporphyrin IX
Porphobilinogen
Tetrapyrrole
Protoporphyrinogen
Coproporphyrinogen
Uroporphyrinogen
hν
Singlet
Tissue necrosis
Triplet
PpIX
O2
Tumour
Laser
635 nm

Fig. 10.58 Schematic diagram of the haem cycle, in which the haem pigment is produced from ALA (δ-amino levulinic acid). The photodynamic action of protoporphyrin IX leading to tissue necrosis is also indicated [2580]

process, the strongly fluorescent and photodynamically active substance protoporphyrin IX (PpIX) is produced. After the incorporation of an iron atom, haem is obtained. If ALA is administered orally or intravenously to the body in elevated concentrations, an excess concentration of PpIX is produced with selectivity to tumour tissue because of differences in enzymatic concentrations. A special feature of ALA is that it can also be administered topically, e.g. in a cream applied over skin tumours. After a few hours, PpIX is built up in the skin tumours, also related to stronger permeability of the damaged keratin layer. The generated substance is clearly seen in fluorescence, and treatment can be performed using 635 nm radiation.

ALA-PDT is a very convenient treatment modality, which is now widely being used [2578–2584].

10.5.3 Tissue Diagnostics with Laser-Induced Fluorescence

We will now discuss tumour diagnostics using laser-induced fluorescence. As mentioned above, the tumour-seeking agents exhibit characteristic peaks in the red spectral region. Also, the natural tissue fluorescence from the various organic compounds in the tissue, such as elastin, collagen, amino acids, etc. gives rise to a broad fluorescence distribution in the blue-green spectral region (the *autofluorescence*), and often this natural signal is also useful for tumour detection and demarcation. Tissue fluorescence can be recorded using a fibre-optic fluorosensor of the type shown in Fig. 10.59. A sealed-off nitrogen laser, emitting at 337 nm, is a very convenient excitation source. This laser typically generates 3 ns long pulses at 10 Hz, and can also be employed to pump a compact dye laser, converting the pump radiation to a longer, selectable wavelength. Fluorescence is best analyzed with an

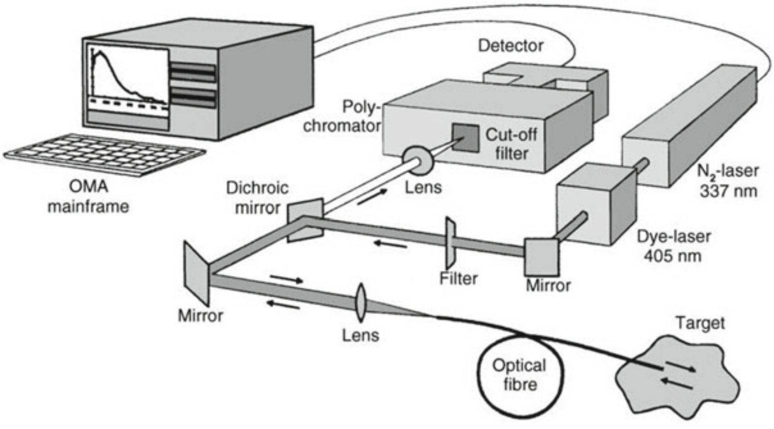

Fig. 10.59 Diagram of a laser fluorosensor based on a pulsed short-wavelength laser, fibre-optic fluorescence sampling, and an optical multichannel analyzer [2585]

optical multichannel analyzer system consisting of a spectrometer equipped with an intensified CCD detector in the focal plane (see Fig. 6.42). For each exciting laser pulse, the whole fluorescence spectrum is captured and can be directly displayed on a monitor and stored in a computer. The image intensifier, providing amplification of the weak light signals, is gated synchronously with the laser pulses. In this way, background radiation due to daylight or operation lamps can be suppressed in the recordings. In the body interior, where background light is absent, a CW laser, e.g. a semiconductor laser at 405 nm, can conveniently be used.

Typical tissue spectra recorded with a fluorosensor are shown in Fig. 10.60. The sample chosen is a rat tumour in a muscle environment and spectra for tumour as well as for surrounding normal tissue are shown for two excitation wavelengths, 337 and 405 nm. The rat had been injected with a dose of HPD two days earlier. For both excitation wavelengths, a broad intensity distribution extending from the blue to the near-IR region is obtained. In the measurements, the strong elastically scattered light from the primary laser excitation light is suppressed by a suitable filter, blocking completely towards shorter wavelengths but letting all longer wavelengths through, basically unattenuated (see Fig. 6.49, upper panel).

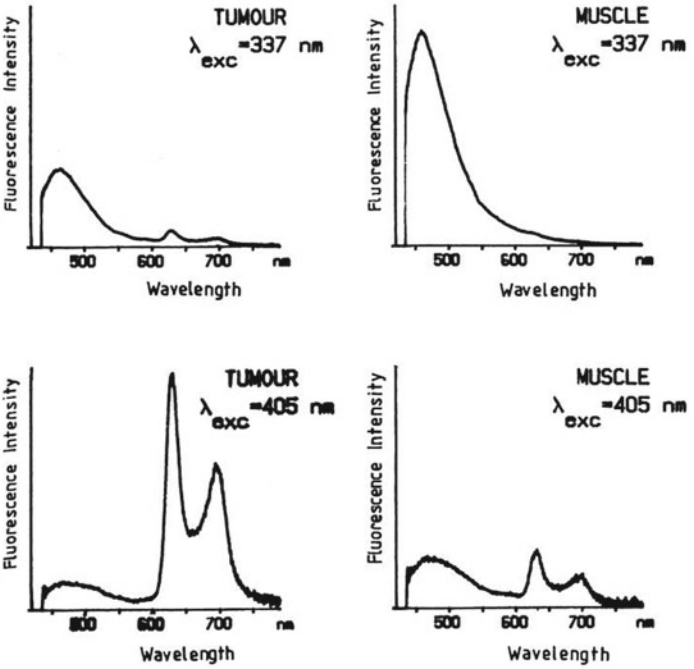

Fig. 10.60 Laser-induced fluorescence spectra for an experimental tumour (a human colon adenocarcinoma inoculated in rat muscle) and normal surrounding tissue. The rat had been injected with a dose of hematoporphyrin derivative about two days before the investigation. Two excitation wavelengths, 337 and 405 nm, are chosen to illustrate the influence of the wavelength choice [2587]

In the tumour spectra, we can see the characteristic dual-peaked fluorescence signal from HPD in the red wavelength region (see also Figs. 10.54 and 10.55). This signal is more prominent in the tumour than in the normal tissue because of the selective retention of the drug in tumour tissue. The blue-green autofluorescence peaks at about 470 nm. We notice that the autofluorescence is much stronger and the red HPD signal much weaker when 337 nm is chosen as the excitation wavelength. This can be understood from the absorption curves in Fig. 10.52. 405 nm corresponds to the absorption maximum (the Soret band) of the HPD molecules, and excitation here is more efficient than at 337 nm. Many chromophores contribute to the signal in the blue-green wavelength region. The absorption for most of these molecules increases for shorter wavelengths. An interesting observation relating to Fig. 10.60 is that the intensity of the autofluorescence signal is reduced in tumour tissue as compared to the normal one. This might be due to a transformation of strongly fluorescing NADH in normal tissue to NAD^+ with a much weaker fluorescence. These observations form the basis for efficient tumour detection and demarcation using laser-induced fluorescence after injection of a tumour-seeking drug: the red fluorescence increases and the blue-green fluorescence decreases in a tumour. Both effects can be utilized in a convenient way by dividing the red signal intensity by the blue intensity. This is illustrated in Fig. 10.61 for the case of a scan through a tumour inoculated in a rat brain. The rat had been injected with HPD (1 mg/kg body weight) 24 hours before the animal was sacrificed and the fluorescence investigation was performed. Typical spectra for normal and tumour regions are included in the figure, with the red intensity at 630 nm denoted by A´ and the blue intensity at 480 denoted by B. The background-free HPD signal at 630 nm is denoted by A. In the scan, the red increase and the blue decrease in the tumour are very evident. Contrast enhancement is obtained by forming the ratio A/B. It is a dimensionless quantity (a well-known dimensionless quantity is π, the ratio of the circle circumference and its diameter, both expressed in, e.g. [m], which cancels out in the division). As pointed out already in Sect. 1.1 in connection with Figs. 1.6 and 1.7, the use of such a quantity has important advantages in practical clinical work, since dimensionless quantities are immune to many factors which may be hard to control in practical measurement. Clearly, these observations about dimensionless quantities pertain to many other measurement situations in physics unrelated to medicine, in particular, in the imaging of objects which have complex topology [2589].

As already mentioned, laser-induced fluorescence has proven to have a considerable potential for early tumour detection and demarcation in many clinical specialties [2585–2593]. Since the fluorosensor fibre can be brought through the biopsy channel on clinical endoscopes, access to the surface of organs like the bronchi, the bladder, the gastrointestinal, and the gynaecological tracts can be obtained.

We have noticed that the use of tumour-seeking fluorescing substances as well as the natural autofluorescence emission can be used to detect and delineate tumours, sometimes also achieving contrast enhancement. However, in certain cases, it is favourable to be able to observe specific fluorescence undisturbed by autofluorescence. The latter type is induced by UV light. By using stepwise excitation of the marker molecules using visible light, as illustrated for the case of atoms, e.g. in

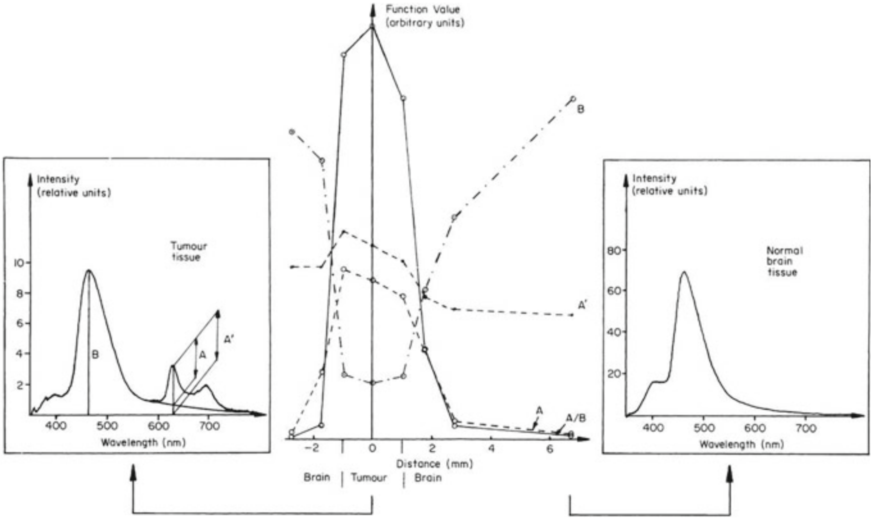

Fig. 10.61 Fluorescence spectra for a rat-brain tumour and normal brain following HPD injection. Demonstration of contrast enhancement by ratio formation [2588]

Figs. 9.1 and 9.54, it is possible to eliminate the background light. The field of up-converting nanoparticles containing rare-earth ions featuring sharp absorption lines has attracted considerable attention [2594–2597]. However, achieving sufficient light levels in the light diffuse scattering regime can be challenging for stepwise excitation.

Laser-induced fluorescence can also be used for characterization of arteriosclerosis in blood vessels. A scenario for combined diagnosis and treatment of cardiovascular disease is shown in Fig. 10.62. A fibre-optic fluorosensor characterizes the vessel wall by its fluorescence, which has been found to be different for normal wall and atherosclerotic plaques [2598–2604]. The reason is different molecular compositions, e.g. the balance between elastin and collagen. Depending on the outcome of the spectral analysis following a diagnostic pulse, a high-energy ablation pulse from an excimer laser is released through the fibre to remove material and clear a clogged vessel (cf. *corneal refractive surgery*; Sect. 10.5.1). Laser ablative intervention in cardiac vessels has been studied and found to be problematic [2605], while diagnostics are being further developed (see also below).

Differences in the spectral properties of various organic substances can be used for different kinds of diagnostics in biology and medicine [2606, 2607]. Fluorescence properties can be used for assessing the status of fruits including their degree of maturity [2608–2610]. Fluorescence and reflectance spectra of two types of ripe fruits are shown in Fig. 10.63, and a discussion of human perception of colour is included in the figure caption. Fluorescence can also be used for the identification of as different substances such as teas and narcotics [2611, 2612].

Autofluorescence only has been used for tumour characterization [2613–2620] as well as for the detection of caries in teeth [2621–2623]. Raman, near-IR and polarized

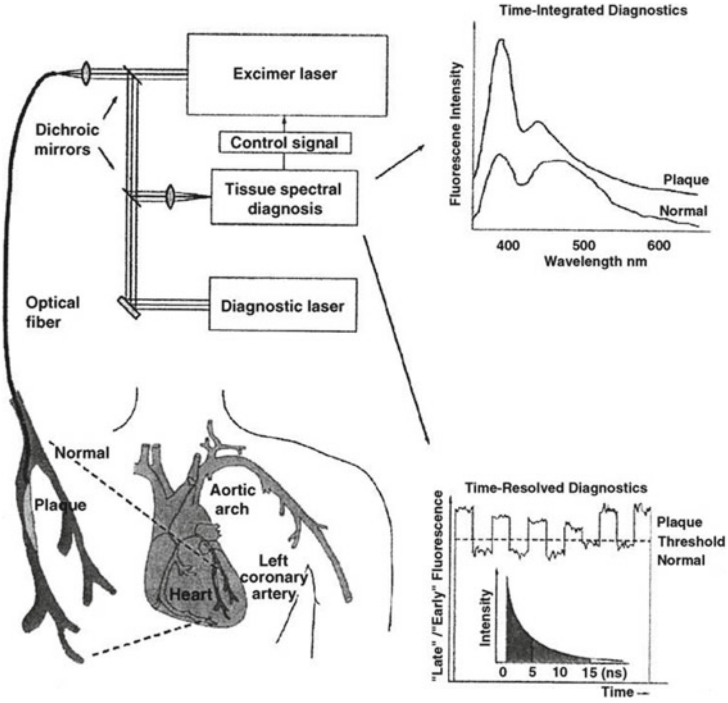
Excimer laser
Control signal
Tissue spectral diagnosis
Diagnostic laser
Dichroic mirrors
Optical fiber
Normal
Plaque
Aortic arch
Left coronary artery
Heart
Time-Integrated Diagnostics
Fluorescene Intensity
Plaque
Normal
400
500
600
Wavelength nm
Time-Resolved Diagnostics
"Late" /"Early" Fluorescence
Plaque
Threshold
Normal
Intensity
0
5
10
15 (ns)
Time

Fig. 10.62 Conceptual schematic diagram of fluorescence diagnostics and interactive laser ablation to remove plaque in clogged vessels. Fast spectral characterization of the material in front of the fibre end allows a decision on whether an ablation pulse should be fired or not [2598]

light reflectance spectroscopy also shows substantial promise for medical diagnostics [2624–2630]. In particular, Raman spectroscopy has been strongly developed during recent years [2631–2634]. One important area of a successful application is the early detection of the life-threatening condition of sepsis [2635].

So far, only the spectral distribution of the fluorescence light has been utilized for diagnostics. However, as discussed extensively in Sect. 9.4, the fluorescence decay time following a pulsed excitation is also a characteristic property of molecules. Differences in decay times can thus be exploited for cancer and cardiovascular disease diagnostics, as illustrated in Fig. 10.64. This type of measurement is also illustrated in Fig. 10.62, where a simple ratio between the intensity of "late" fluorescence to "early" fluorescence is shown to demarcate between normal tissue walls and plaque. Time-resolved fluorescence spectroscopy is generally speaking a valuable tool in biological and medical research [2636–2643]. In particular, fluorescence lifetime imaging microscopy (*FLIM*) has been developed into a powerful technique for demarcating different tissue compartments. Early surveys of the use of laser-induced fluorescence for medical diagnostics can be found in [2644, 2645].

The point-monitoring techniques discussed above can be extended to tissue imaging, and sometimes include time-resolved detection [2646–2653]. A larger area

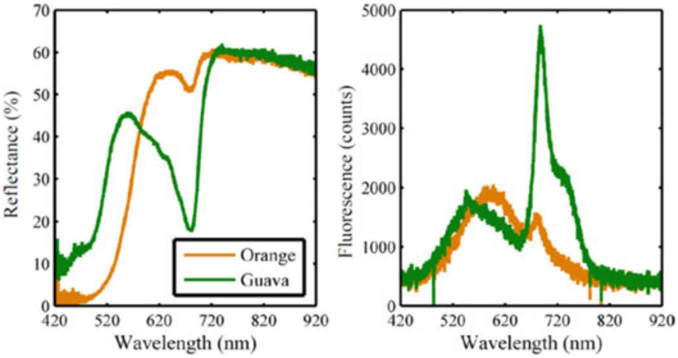

Fig. 10.63 Reflectance and fluorescence spectra of ripe guava (green lines) and orange (orange lines). It can be clearly seen how "warm" colours (orange, red) are strong in reflectance from the orange fruit compared to the green guava (peaking in green), while the 690 nm chlorophyll fluorescence peak is strong in guava and almost absent in the orange fruit ([2076], reproduced with permission from OPTICA). Regarding the visual apprehension of colour, the sensitivity curves $S_i(\lambda)$for the three types of cones ($i = 1 - 3$) in the human retina (Fig. 6.44) have to be integrated $\int S_i(\lambda)R(\lambda)d\lambda$ with the reflectance curve $R(\lambda)$ to yield three numerical values V_1, V_2, and V_3, which are interpreted by the brain as colours with assigned words (depending on the language) by training at an early age of childhood (See also Fig. 1.4 for a discussion of "objective" colours (reflectance values) and "agreed on", subjective ones)

is then illuminated with exciting light and fluorescence images are then recorded in selected spectral bands using a gated and image-intensified two-dimensional CCD detector. Alternatively, time-correlated single-photon counting (TCSPC) (Sect. 9.4.2) in a scanning mode (whisk-broom scanning, Sect. 6.6.2) can be employed. Contrast-enhancement mathematical operations are then performed for spatially corresponding points in the images, e.g. a ratio is formed as discussed in connection with Fig. 10.61 (and Figs. 1.6, 1.7) Alternatively, the fluorescence image for a selected wavelength band is recorded for different delays after the exciting pulse and spatial mapping of the lifetimes can be made, discriminating certain types of tissue. Images of both types are shown in Fig. 10.65 for the case of a human basal cell carcinoma tumour.

Similar spectral techniques as discussed for macroscopic tumour imaging can be employed for fluorescence microscopy [2655]. *Confocal laser microscopy* uses small pin-holes to define the location of interrogation, and is efficient to suppress out-of-focus scattering or fluorescence [2656, 2657]. *Two-photon-induced fluorescence* [2658, 2659] *and CARS microscopy* [2660–2662] are likewise scanning (whisk-broom) techniques with well-defined interrogation volumes, which are reduced due to the nonlinear processes favouring the highest intensity locations. A comparison of several techniques is made in [2663]. Imaging Fourier transform spectroscopy allows the recording of the full spectrum at all locations simultaneously, but needs a certain scanning time for the spectral recordings [2664, 2665]. Further novel multispectral techniques are presented, e.g. in [2666, 2667].

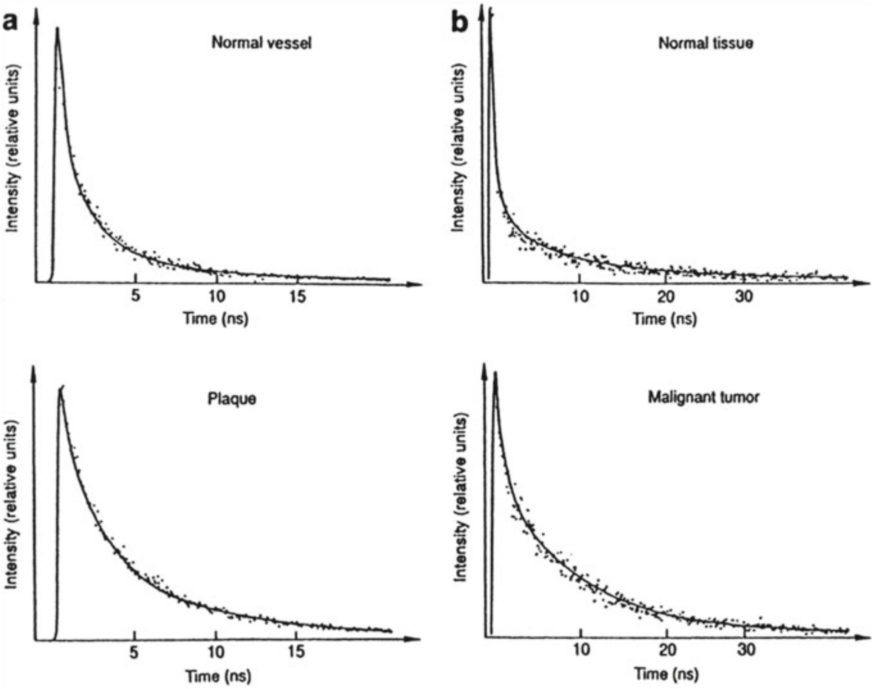

Fig. 10.64 Fluorescence-decay curves showing demarcations between the normal vessel and atherosclerotic plaque (*left*), and normal tissue and malignant tumour (*right*) [2638]

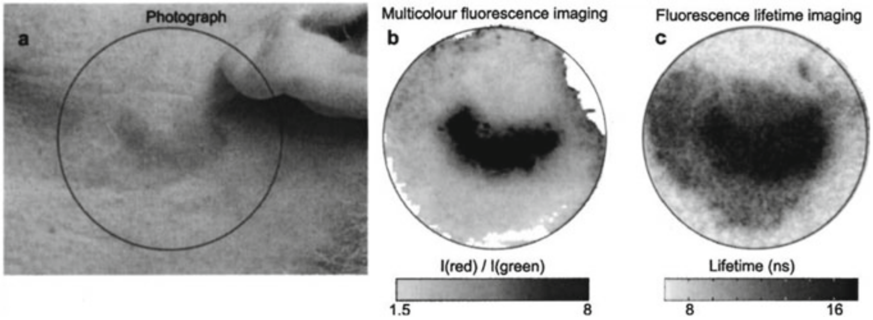
Photograph
a
Multicolour fluorescence imaging
b
Fluorescence lifetime imaging
c
I(red) / I(green)
1.5
8
Lifetime (ns)
8
16

Fig. 10.65 Fluorescence imaging of a basal cell carcinoma below the ear. The photograph **a** shows the measurement site, **b** is a multi-colour image obtained by dividing two images, recorded in the red region of sensitizer peak and for the blue autofluorescence, and **c** is a lifetime image, where the fluorescence decay time of red fluorescence light has been evaluated in each image point from gated recordings made at different time delays after the excitation [2650]

A field that is related to microscopy is the one of optical trapping of cells with focused laser beams (*optical tweezers*), which relies on gradient forces of the same kind as discussed in Sect. 9.8.5. Trapped cells and polymer strings can be manipulated in many ways to enable fundamental studies [2668–2674]. The 2018 Nobel prize in Physics was awarded to *A. Ashkin* for these developments [2675]. Further, such trapping and manipulation techniques are also very useful in the expanding field of micro-machines [2676, 2677]. Related is the strongly developing area of molecular motors, rewarded with the 2016 Nobel Prize of Chemistry to *J.P. Sauvage, J.F. Stoddart, and B.L. Feringa* [2678, 2679].

10.5.4 Scattering Spectroscopy

10.5.4.1 Basic Considerations

Atmospheric light scattering has been discussed in Sects. 4.5, 4.6, and 10.2.3. If the density of scatterers is high, multiple scattering can occur, as in clouds or in dense fog. Light can also be scattered in turbid liquids and in solids. Examples of strongly scattering media are milk and human tissue. Cases of light scattering occurring on different length scales are shown in Fig. 10.66 [2680].

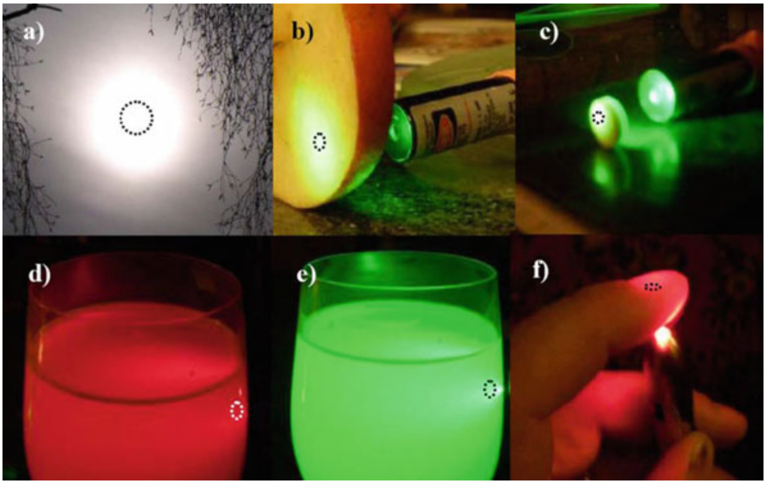

Fig. 10.66 Light scattering in different contexts: **a** sunlight scattering in a thin cloud; **b** laser light scattered in a slice of apple, and **c** in a tablet; **d** and **e** show light scattering in turbid liquids, and **f** light propagation through a human fingertip. In each case, the expected beam profile for the case of a non-scattering medium is indicated ([2680], reproduced with permission from Springer Nature)

In order to understand light propagation in the tissue, it is necessary to treat absorption and scattering simultaneously and on an equal footing. Both processes contribute to the reduction of light passing a sample. Clearly, no simple Beer–Lambert law (6.44) is valid in scattering media, since the path length is undefined.

In the same way as the absorption coefficient $\mu_a = \sigma c$, as defined in (6.44), implies that photons travel on the average a distance $1/\mu_a$ (mean free path) before they are removed and do not contribute to a signal at the detector, it is possible to define a scattering coefficient μ_s, where photons would typically travel a distance of $1/\mu_s$ before they are scattered away from the original direction (and missing the detector). If scattering strongly dominates over absorption, it is practical to introduce the concept of a *reduced scattering coefficient* $\mu_s{}'$, defined as

$$\mu_s' = \mu_s(1 - g), \tag{10.9}$$

where

$$g = <\cos\theta> \tag{10.10}$$

with g being the average of the resulting scattering angle (see also Fig. 4.21). For completely isotropic scattering, $g = 0$, while for $g = 0.9$ the average deflection angle $<\theta>$is 26°. Complete forward scattering corresponds to $g = 1$.

Basically, many anisotropic scattering events are replaced by a single, isotropic scattering event with a virtual mean free path length, which is $1/(1-g)$ times larger. It can also be shown [2681] that the combined action of scattering and absorption can be handled by introducing an *effective attenuation coefficient*

$$\mu_{eff} = \sqrt{3\mu_a(\mu_a + \mu_s')}. \tag{10.11}$$

Much effort has been invested in describing the optics of scattering media [2682–2693]. Analytical descriptions based on transport equations can be used or differential equations can be solved numerically. The most general way to treat the problem is by *Monte Carlo simulations*, where individual photons released by the source are followed on their way through the medium controlled by probabilistic laws for absorption and scattering at certain angles [2694–2696]. A good understanding of human tissue optics is important for light dosimetry for PDT [2574], for spectroscopy for the determination of the oxygenation [2697–2699] or the concentration of constituents such as glucose (diabetic applications) or urea (dialysis applications) in blood, or photosensitizers in tissue [2700–2703]. It is also important for the development of optical mammography and similar applications [2704–2712]. Using time-resolved spectroscopy, it is possible to follow the photon paths through the tissue. Two basic geometries are illustrated in Fig. 10.67. In transillumination, there is the shortest path corresponding to the very unlikely event of non-scattered radiation, giving rise to a distinct signal (*ballistic photons*). Most photons arriving at the detector come much later and only after several scattering events. If the transmitter and the detector

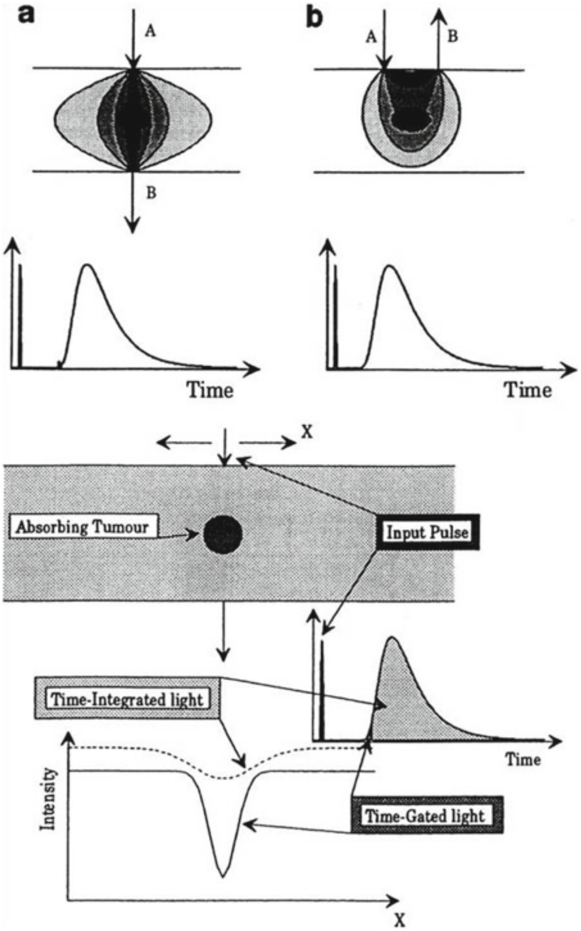

Fig. 10.67 *Top*: Geometries for time-resolved measurements on turbid media. **a** Transillumination **b** Backscattering. *Bottom*: Gated viewing through tissue. An enhanced spatial resolution is obtained by selecting the "early" light only [2690]

are on the same side of the sample, all photons received must have been scattered. If the position of transmitter and receiver coalesce (laser-radar geometry), a histogram of arrival times for photons that have sampled a certain volume below the measurement point is obtained. This mode of operation is common in Doppler measurements of superficial blood flow, which we will discuss first.

A measure of the blood perfusion in tissue can be obtained by analyzing the signal due to slightly Doppler-shifted photons that encountered scattering against moving red blood cells. Originally, a CW helium–neon laser operating at 633 nm was used, while presently a dark red/near-IR diode laser is normally used in such measurements. The shift is governed by the Doppler formula (6.1). Light (at about 10^{14} Hz), which is scattered from capillary blood cells moving with a velocity of 3 mm/s is shifted by about 1 kHz. Such small shifts can only be detected by optical heterodyne techniques (Sect. 10.2.1), where the beat signal between the light scattered from the moving objects and from the fixed tissue cells is picked up. Obviously, an objective full quantification is difficult to obtain, since a complex averaging is performed over photons scattered at different depths. Still, valuable information can be obtained, in particular, for assessing reperfusion in connection with transplant surgery and for the monitoring of wound healing, e.g. after burns. By performing sequential measurements with a system where the laser beam is scanned in a matrix pattern over the tissue it is possible to generate images of the superficial blood flow. Laser Doppler techniques for blood perfusion monitoring are discussed in [2713–2717].

10.5.4.2 Optical Mammography and Related Techniques

Complete image blurring occurs in the transillumination of strongly scattering media. It is well known that red light penetrates a human finger (due to the strongly reduced absorption of haem above 600 nm; see Fig. 10.52). Nevertheless, it is impossible to see the shadows of the bones because of strong multiple scattering. *Optical mammography* (breast transillumination) would be attractive because of the absence of mutagenic ionizing radiation, but obviously, a straightforward approach has little chance of success because of the massive scattering. However, the problems can be reduced by using a pulsed transmitter and time-resolving detection electronics for the transmitted light, as illustrated in the lower part of Fig. 10.67. Because of the multiple scattering, most of the photons penetrating the tissue have spent a long time in the tissue, while only very few photons arrive at the detector at the nominal propagation time without disruptions. By selecting a small detection time window and recording the very first photons, it is possible to look at just the "fastest" photons coming out of the tissue. *Gated viewing* or *conditional sampling* is performed. If an obstacle, such as a bone [2708] or a tumour [2709], blocks the passage, a "shadow" will be created for the selected subgroup of very early photons. For thicker samples, there are no unscattered photons. Still, the first photons have been minimally scattered and produce a clearer image, as schematically shown in Fig. 10.67. By performing a scan of the tissue under investigation, a transillumination image can be created. An example of ductal carcinoma in a newly resected human breast shown in Fig. 10.68, where the transmitting and receiving fibres were scanned together under computer control over the tissue, which was compressed between glass plates [2709]. A diode laser operating at 815 nm and producing 30 ps long pulses at a repetition rate of 10 MHz was used in these recordings. An example of a time dispersion curve is shown, recorded by the time-correlated single- photon counting technique (TCSPC; Fig. 9.23). By restricting the detection to a narrow time window around the nominal ballistic flight time, it was possible to see the tumour (lower diagram), which disappears in a total light image (upper diagram). A streak camera can also be used for detecting the early photons [2710, 2718].

It should be noted that different types of photons detected in time-resolved tissue transillumination recordings (ballistic or prompt photons with minimum transit time, minimally scattered photons (strong forward scattering; Fig. 4.21), and completely diffusely scattered, "late" photons) have their counterparts in spatially resolved

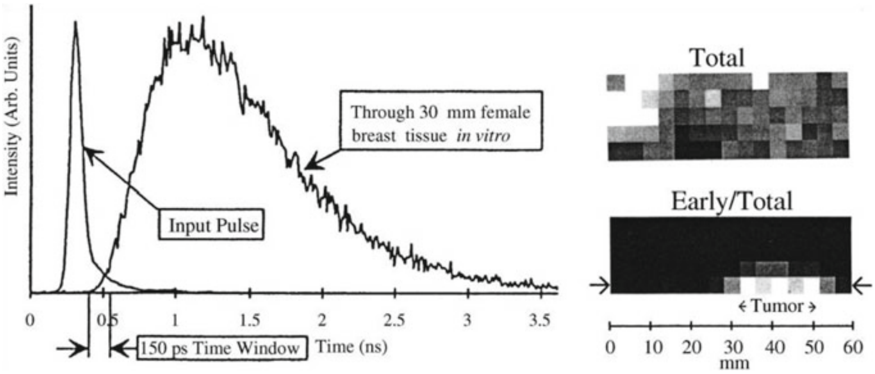

Fig. 10.68 Transillumination images of breast tissue in vitro, show the presence of a tumour when the first part of the time dispersion signal is utilized. Integration of the whole signal does not yield a tumour image. The early light signal has been normalized to the integrated light [2709]

imaging, also on a large scale, such as shown in Fig. 10.66a). The sun is imaged on a foggy day, and the slightly scattered light, propagating in the forward direction gives rise to a light halo around the marked sun disc. The disc with sharp edges would be emerging if the scattering had been just a little less, and some ballistic photons could reach the camera. On the other hand, on a cloudy day, the sky is more or less uniformly emitting, with no indication whatsoever where the sun is located (massive multiple scattering).

In addition to the electronic gating techniques that we have discussed above for suppressing the influence of excessive scattering in tissue, nonlinear optical phenomena can be utilized for the gating. Three techniques are illustrated in Fig. 10.69. When using an optical Kerr gate, a Kerr-active medium is utilized and, by employing a strong laser pulse, birefringence is induced to rotate the plane of polarization of the probing light, which is normally blocked out by crossed polarizers (compare also with Figs. 9.7 and 9.61). By proper delay between the two pulses, derived from the same laser, it is possible to strobe on the early light [2719]. The same result can be obtained using a Raman amplifier, which is activated by a fast pump light arriving at the proper time [2720]. Finally, using the second-harmonic cross-correlation technique (see also Fig. 9.35), the desired temporal part of the probe light can be selected [2721].

By studying the shape of the whole time-dispersed photon distribution from a scattering medium the absorption and scattering coefficients of the medium can be evaluated, as earlier mentioned in connection with pharmaceutical tablet monitoring [2471, 2472]. While the full temporal shape of the time dispersion curve (such as the one shown in Fig. 10.68) is used in a fit of μ_a and μ_s to a set of model curves, calculated using diffusion equations or by Monte Carlo techniques, it can be intuitively conceived that the scattering coefficient μ_s is strongly related to the position of the curve maximum, while the rate of intensity fall-off at long-time delays mostly reflects the value of the absorption coefficient μ_a. The same experimental

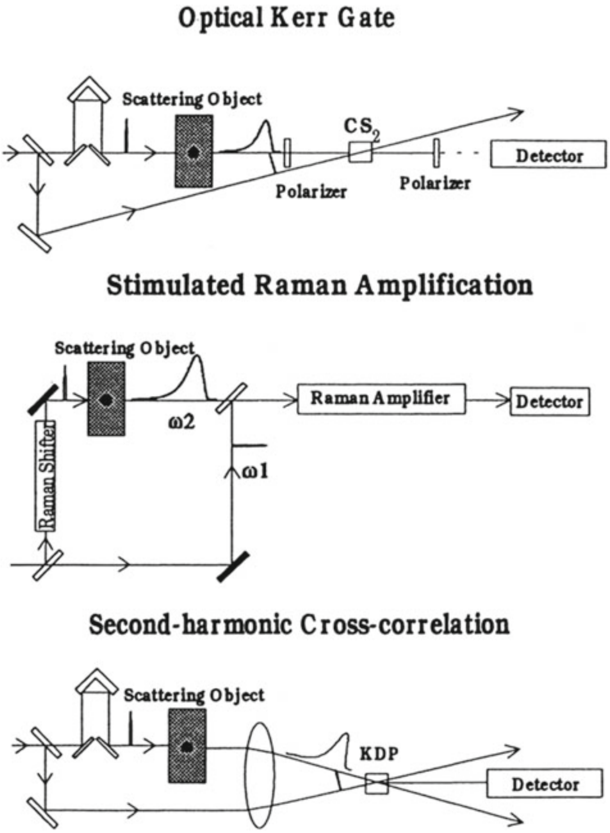
Optical Kerr Gate
Scattering Object
CS$_2$
Polarizer
Polarizer
Detector
Stimulated Raman Amplification
Scattering Object
ω2
ω1
Raman Shifter
Raman Amplifier
Detector
Second-harmonic Cross-correlation
Scattering Object
KDP
Detector

Fig. 10.69 Gated-viewing techniques using nonlinear optical phenomena [2690]

information on photon delays can be obtained by employing a sinusoidally modulated CW laser beam and studying the phase-shift and the modulation contrast reduction in the scattered light [2722–2725]. This is basically the phase-shift method discussed previously in Sect. 9.4.4. Several modulation frequencies are needed to obtain the same information as in the conceptually simpler pulsed techniques.

A further technique to assess the propagation of light through turbid media is based on heterodyne detection using a swiftly frequency-ramped laser, employing beat-frequency detection in a Mach-Zehnder interferometer [2726, 2727].

The non-scattered part of the transmitted radiation can be detected by *coherent* techniques, as illustrated in Fig. 10.70. Using heterodyne detection [2728], a signal with a well-defined phase is only obtained at the intermediate frequency ($\Delta\omega$) if the probe light has not been scattered. *Light-in-flight holography* [2729–2732] is a technique, that also relies on the presence of a fixed phase relation between the probe and the reference beam, only available for the non-scattered part of the radiation [2730].

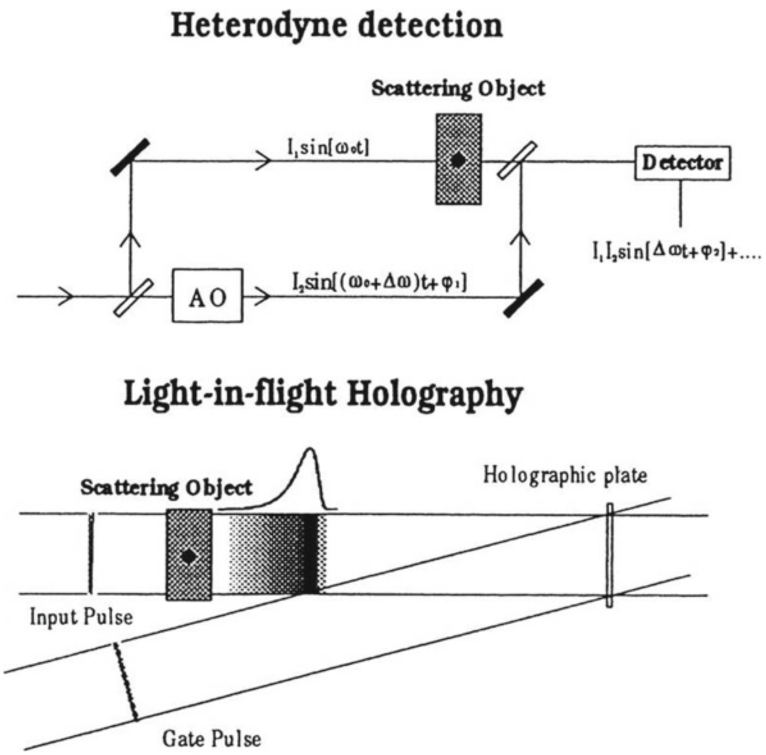
Heterodyne detection
Scattering Object
$I_1 \sin[\omega_0 t]$
Detector
$I_1 I_2 \sin[\Delta\omega t+\varphi_2]+\ldots$
AO
$I_2 \sin[(\omega_0+\Delta\omega)t+\varphi_1]$
Light-in-flight Holography
Scattering Object
Holographic plate
Input Pulse
Gate Pulse

Fig. 10.70 Detection of the non-scattered part of the probe light by coherent techniques [2690]

All the techniques discussed can be used in multiple beam/detector applications to allow tomographic reconstruction of the interior of a scattering medium. Then more complex objects can be studied, such as uncompressed breasts [2733, 2734, 2710–2712] or human sculls (for detection of bleeding, e.g., after accidents) [2735]. A similar situation pertains when the amount of light in different parts of tissue containing a tumour is to be calculated in interstitial photodynamic therapy with multiple transmitting and receiving fibres (Fig. 10.57) [2571].

10.5.4.3 Optical Coherence Tomography (OCT)

For thin objects a further, particularly simple and powerful, coherent technique can be utilized, *optical coherence tomography* [2736–2749]. As illustrated in Fig. 10.71, a Michelson interferometer (Sect. 6.2.4; Fig. 6.35), frequently arranged with fibre-optic arms, is used. The technique relies on the fact that all frequency components from a broadband CW light source interfere constructively when the interferometer arms have the same length. Thus, by scanning the length of the reference arm, light scattered at different depths in the tissue can be isolated to map out a depth profile.

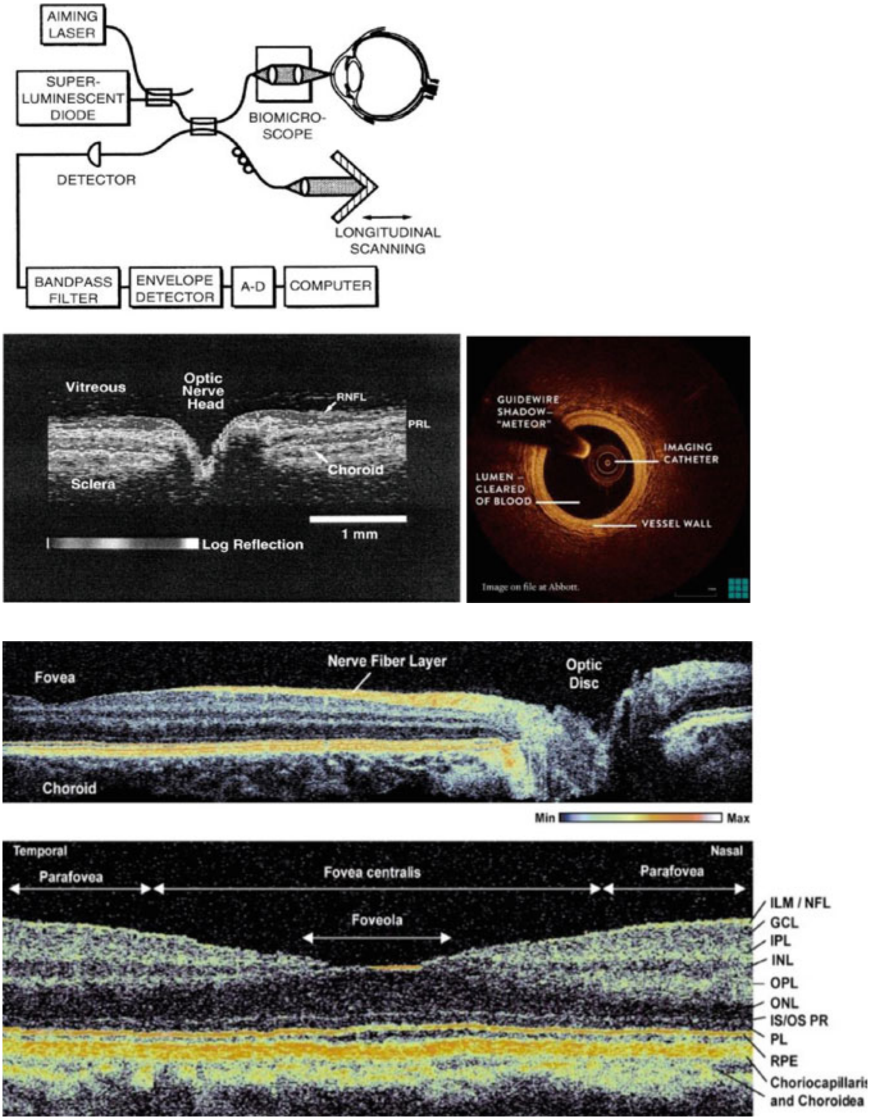
AIMING LASER
SUPER-LUMINESCENT DIODE
BIOMICRO-SCOPE
DETECTOR
LONGITUDINAL SCANNING
BANDPASS FILTER
ENVELOPE DETECTOR
A-D
COMPUTER
Vitreous
Optic Nerve Head
RNFL
PRL
Choroid
Sclera
1 mm
Log Reflection
GUIDEWIRE SHADOW– "METEOR"
IMAGING CATHETER
LUMEN – CLEARED OF BLOOD
VESSEL WALL
Image on file at Abbott.
Fovea
Nerve Fiber Layer
Optic Disc
Choroid
Min
Max
Temporal
Nasal
Parafovea
Fovea centralis
Parafovea
Foveola
ILM / NFL
GCL
IPL
INL
OPL
ONL
IS/OS PR
PL
RPE
Choriocapillaris and Choroidea

Fig. 10.71 *Top*: Set-up for *in vivo* eye optical coherence tomography using a fibre-optic Michelson interferometer. *Below, left*, a scan of the region around the position of the optical nerve is shown, featuring many details including the photoreceptor layer [2737], and right, a cross-section through a blood vessel (Courtesy: Abbott Lightwave Initiative). *Bottom*: High-resolution OCT images of human retina ([2738], reproduced with permission from Springer-Nature)

The broader the spectral distribution of the light source, the higher the depth resolution of the system will be. The technique has proved very successful for probing the structures of the eye (Fig. 10.71) and OCT is now routinely used at many eye clinics with millions of procedures pursued so far. OCT is also very effective in mapping out cross-sections of blood vessels [2746, 2747]. Besides the original implementation of OCT, called *Time-Domain OCT* (TD-OCT) as illustrated in Fig. 10.71 (top left), alternative approaches such as *Fourier Domain OCT* (FD-OCT) and *Spectral Domain OCT* (SD-OCT), which allow spectrally resolved recordings and a very high sampling speed, have been developed. The field is characterized by fast innovation and adaption of powerful monitoring techniques [2748, 2749]. Among the clinical applications of biophotonics, the OCT technique is probably the one with the greatest impact. Numerous companies manufacture and sell OCT scanners.

A novel way to handle scattering problems leading to image blurring in biophotonics is to use various types of *wavefront engineering*, basically to undo the detrimental effects of scattering and allow sharp focusing inside the scattering medium [2750–2755]. The area relates to adaptive optics (Sects. 6.7 and 10.2.3.1), coherent control (Sect. 9.5.3) and high-power laser pulse optimization using wavefront manipulations (Sect. 8.7.2). A further method to allow focusing in scattering media is to generate a focused ultrasound “guide star”, at the location of which impinging light is guided, again by wavefront engineering [2756].

10.5.4.4 Photoacoustic Tomography

Photoacoustic tomography (PAT), sometimes denoted *photoacoustic imaging (PAI),* is a new technique in biophotonics, which has developed tremendously in recent years. Photoacoustics for gases and solids were introduced in Sect. 9.2.8. Early work on condensed matter and tissue was presented in the mid-90’s [2757], and many advanced techniques were later developed for tissue by many groups [2758–2767]. Basically, a pulsed laser is directed towards the tissue to be studied and by absorption and heating, a pressure wave is generated, which is picked up by a conventional ultrasound imager. The light propagates diffusely in tissue, but the absorption, e.g. by blood in the vessels, leads to localized heating. Thus, the ultrasound waves emerge from well-defined points, and since ultrasound is little scattered, sharp images through the tissue are obtained. By using tunable pulsed radiation, differential absorption imaging can be performed (similar to in DIAL, Sect. 10.2.3) and, e.g. oxygenated and deoxygenated blood can be mapped out. The two types of blood show equal optical absorption at 808 nm (the isobestic point), while absorption is quite different at shorter or longer wavelengths. A schematic diagram of the photoacoustic imaging process is shown in Fig. 10.72, where also examples of recorded images are shown. The techniques have great potential for the identification of malignancies. It could also be mentioned that the specific blood vessel patterns in human hands might be used as a very secure human identification method.

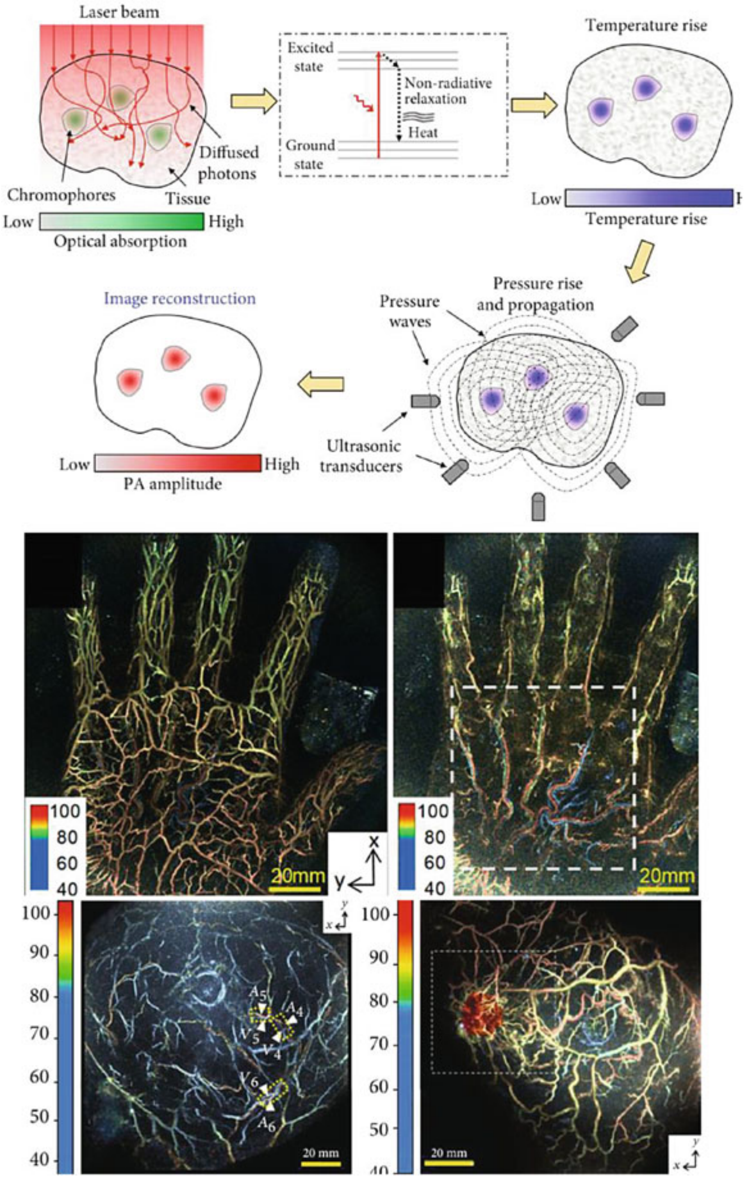
Laser beam
Chromophores
Tissue
Diffused photons
Low
High
Optical absorption
Excited state
Non-radiative relaxation
Heat
Ground state
Temperature rise
Low
Temperature rise
Pressure rise and propagation
Pressure waves
Ultrasonic transducers
Image reconstruction
Low
High
PA amplitude
100
80
60
40
20mm
x
y
100
80
60
40
20mm
100
90
80
70
60
50
40
A5
A4
V5
V4
V6
A6
20 mm
y
x
100
90
80
70
60
50
40
20 mm
y
x

Fig. 10.72 (Top) Set-up for medical photoacoustic recordings. Pulsed laser radiation diffuses through the tissue and is absorbed, resulting in transient heating, depending on the local absorption. Pressure waves emerge from specific locations and are picked up by multiple ultrasound receivers, which are arranged around the object. An image can then be formed by time-of-flight tomography, as in conventional ultrasound imaging ([2765], reproduced under the Creative Commons Attribution 4.0 License, CC BY 4.0). (Bottom) Photoacoustic images of hand palms and female breasts ([2763], Creative Commons CC BY, Springer-Nature)

Since pulsed radiation is used, and ultrasound waves are attenuated much less than light, imaging of deep-lying structures (up to 10 cm) can be achieved photoacoustically. However, the technique can also be used on small scales, such as in microscopy.

Recently, a further technique, where ultrasound and light are combined, is emerging. In the *ultrasound optical tomography (UOT)* approach [2768, 2769], focused ultrasound of frequency f_{us} around 1 MHz interacts with laser radiation with a frequency f_l to generate side bands at $f_l \pm f_{us}$ from the overlap region. "Tagged" frequency photons are generated and are detected optically. Thus, in contrast to PAT, the UOT approach generates images by optical detection of ultrasound. While in UOT, strongly scattered and attenuated optical radiation is used on the illumination as well as on the detection side, PAT in contrast only uses light for illumination, but the very sensitive detection of optical photons outperforms the capabilities of ultrasound detection [2769]. However, the UOT approach only works if the information-carrying photons (which are extremely little shifted from the carrier laser light, which, in turn, is many order-of-magnitudes stronger) can be effectively isolated. Actually, this can be done with extremely sharp optical filters, generated by spectral hole-burning in a rare-earth-ion crystal of the kind now extensively used in the quest to achieve efficient quantum information handling systems (Sect. 4.9). Since the holes burnt are very sharp, they can be placed very close to the sharp laser probing wavelength to isolate the tagged sideband. The fact that the narrow absorption profile, according to the Kramer–Kronig's dispersion relations (Sect. 9.4.4), is characterized by very strong gradients in the refraction index, leads to the phenomenon of slow light to occur (Eq. 9.16). Because of this, the frequency-shifted response following focused ultrasound irradiation is observed strongly time delayed, and an even stronger background light rejection is obtained, when suitably long slices of laser light from a CW narrow-band laser are used for the irradiation [2768, 2769]. The general phenomenon of slow light was earlier discussed with relevant references [1538–1543].

In a more trivial and widespread application, *pulse oximetry,* the differential absorption between oxygenated and deoxygenated blood is monitored in diffuse light transmission (for two different wavelengths) through a fingertip or an earlobe in order to routinely evaluate the blood oxygen saturation, e.g. during surgical operations. The scattering problems are here handled by calibration. Pulse oximeters only observe the part of the signal, which is varying with the heartbeat (the *pulsating* part), in this way recording arterial blood, which is the medically important aspect. Because of its way of operating, the heart beat frequency is automatically measured and displayed on these devices, which are cheap and extremely common in health care.

Techniques developed primarily for medical applications can also find many other biological and technical applications. Thus, the time-resolved techniques using time-correlated single-photon counting TCSPC have been used for studying the scattering properties and light propagation in plant leaves [2770], paper sheets [2771], and pharmaceutical preparations [2471, 2472].

10.5.4.5 Gas in Scattering Media Absorption Spectroscopy (GASMAS)

All the laser-based techniques developed for biomedical applications as discussed above have the bound constituents in the tissue as the targets. Thus, with regards to the spectroscopic equipment used we here technically deal with condensed matter physics, where sharp spectroscopic features are rare (See, e.g., Fig. 10.52). However, the human body also contains free gas compartments, and a new technique for studying such gas in scattering solids and liquids has been introduced [2772, 2773]. In *gas in scattering media absorption spectroscopy (GASMAS)*, single-mode laser radiation is injected into the scattering object and sharp absorptive signals in detected scattered light are observed. Free gas typically exhibits a linewidth of 0.01 nm or less, which is typically 10^4 times smaller than absorptive features in the condensed matter matrix material. By wavelength modulation spectroscopy (Sect. 10.2.2), which is conveniently performed with diode lasers, the gas absorption imprints can be observed even in weak light, which has travelled a long distance. A basic diagram of GASMAS is shown in Fig. 10.73 [2774], illustrating measurements in transillumination of a porous material (e.g., a lung) as well as measurements in larger gas volumes in backscattering (e.g., in a sinus cavity).

By performing time-resolved measurements with a pulsed laser in a similar way as discussed in connection with Figs. 10.67 and 10.68, it is possible to track the time history of the emerging photons and determine the mean path length. Thus, by combining CW and pulsed measurements performed at the same wavelength, it is possible to calculate the absolute gas concentration in the medium, if light dominantly travels through gas, which is the case, e.g. for polystyrene foam [2775]. For the general case, most often encountered in medical applications, this is clearly not true, and only the product of the concentration and mean pathlength in gas can be obtained from the absorptive imprint in the light which diffusely emerges from the surface

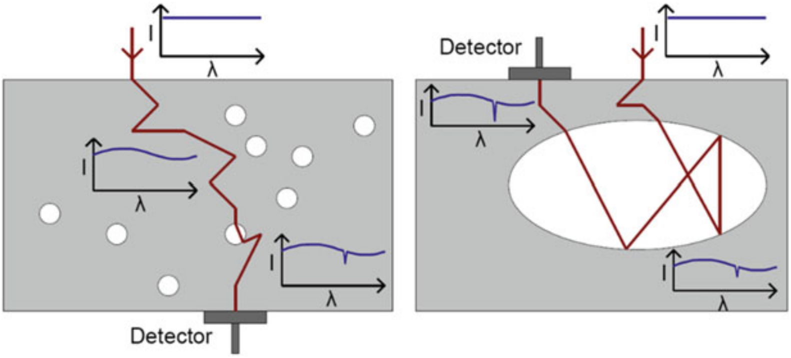

Fig. 10.73 Principle of GASMAS is applied in a transmissive mode on a sample with distributed pores and in a reflective mode on a larger cavity, surrounded by a scattering medium. Note the difference in linewidth for the absorptive imprints of the gas and the matrix medium ([2774], reproduced with permission)

(see Eq. (6.44). Molecular oxygen, featuring lines around 760 nm, is well adapted for GASMAS studies. The transition corresponds to the terrestrial Fraunhofer A-line (Figs. 1.5, 6.57). The internal pressure in gas pores can be assessed from the linewidth observed [2772, 2776]. It is also possible to readily study gas diffusion through the porous medium by first subjecting the sample to, e.g. pure nitrogen gas, which penetrates the sample and displaces the oxygen. By then performing GASMAS measurements in the normal ambient atmosphere, the oxygen reinvasion of the sample can be followed. The technique has many applications, e.g. in studying building materials [2775], surface coatings, ceramics [2777], wood [2778, 2779], fruits [2780, 2781], food packaging [2782–2784], and pharmaceutical preparations [2785, 2786]. It should be noted that in many food or pharmaceutical contexts, a modified atmosphere, void of oxygen, is used to increase shelf storing time, and the efficiency of the protective gas filling (nitrogen or carbon dioxide) and the sealing integrity can be readily assessed non-invasively by GASMAS. However, the most profound impact may be found in the biomedical field. Clearly, oxygen is the most important gas in human physiology, and its absorption of around 760 nm falls conveniently in the tissue optical window of low blood and liquid water absorption (Fig. 10.52). Clearly, it is of major interest to determine not only the presence of oxygen, but also its concentration. This is, however, challenging because of the normally unknown pathlength through gas, eliminating the direct use of the Beer-Lambert law (Eq. 6.44). However, there is a way to get around this problem. Living matter and many natural products contain liquid water. The concentration of water vapour is, as already discussed in connection with the description of the atmospheric constituents, determined by the temperature through the Arden-Buck relation [2212]. That means, that the concentration is known in the enclosed cavities, where 100% relative humidity pertains. Water vapour exhibits many absorption bands and some quite close to the oxygen A band. Then the scattering and absorption properties of the matrix material are similar to those pertaining to oxygen, and by normalization the unknown pathlength can be eliminated. Expressed differently, the effective pathlength is determined by the absorptive imprint by the gas of known concentration, and the same pathlength is inserted for oxygen to yield its concentration [2787].

The GASMAS technique provides an opportunity to monitor the human sinus cavities and the middle ear, which are the locations of very common infections. While the majority of these infections are due to virii, which are insensitive to antibiotics, treatment with such medication is applied, as if the infections were of bacterial origin. This fact, and severe abuse in animal raising for meat production, has lead to an alarming worldwide development of bacterial resistance, while few new antibiotics are being developed. The presence of sharp GASMAS signals from the cavities ensure that they are not filled with liquid/pus, and the presence of oxygen indicates that draining channels are open for ventilation. Initial studies suggest that GASMAS monitoring may help doctors in better diagnostics and treatment of sinusitis [2788–2791] and otitis [2792, 2793].

Lung function is very crucial to humans. Prematurely born infants are particularly vulnerable since the lungs are then not fully developed. Such infants are then frequently influenced by respiratory distress syndrome (RDS). In a quest to reduce the use of ionizing radiation for lung surveillance, GASMAS is being developed for 24 hour non-intrusive lung surveillance of air filling and oxygen contents [2794, 2795]. Again, normalization of water vapour is being pursued. Extension to adult lung monitoring and the possibility of ventilator feedback control is a highly motivated endevour and challenge in times of pandemics, such as SARS-CoV-2, and initial considerations have been made [2796].

As a final application example for GASMAS, the monitoring of decaying bone is chosen. Following a femoral neck fracture, the femoral head may degrade due to inadequate blood supply. Then gas-filled pores would develop and signal the ongoing condition. It has been shown that such pores can be detected by water vapour monitoring in the strongly scattering decaying bone [2797]. Different medical applications are illustrated in Fig. 10.74.

More basic studies utilizing the GASMAS technique include the use of nanoporous ceramics to achieve a long-pass absorption cell based on multiple scattering rather than highly reflecting mirrors in a multi-pass cell [660]. Also, since such nanoporous, translucent materials have pore sizes smaller than the typical free mean path of the molecules, line broadening from wall collisions occurs, a phenomenon that has potential for determining pore size [2772, 2798, 2799].

The strongly expanding field of biophotonics and medical uses of laser techniques is covered in a number of monographs (see, e.g. [2800–2805]).

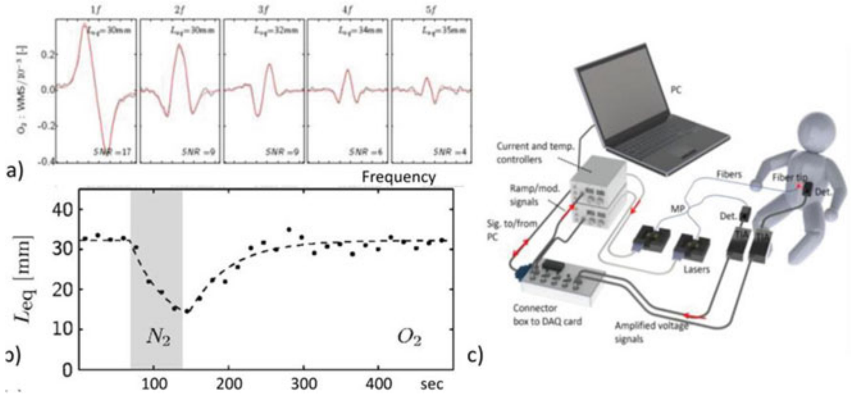

Fig. 10.74 **a** Signals from a human sinus cavity were recorded by GASMAS. By means of lock-in detection with modulation of the laser wavelength, 1f–5f harmonic modulation signals are produced, and resemble the 1st-5th derivative of the primary absorption signal ([2789], reproduced with permission from OPTICA). **b** oxygen signal amplitude for a human sinus cavity when the nasal cavity is flushed with nitrogen gas, while the volunteer is breathing normally through the mouth. The channel connecting the sinus with the nasal cavity is shown to be open, since nitrogen displaces the normal oxygen-containing air ([2788], reproduced with permission from SPIE) (**c**) Set-up for simultaneous monitoring of oxygen and water vapour signals from the lungs of a new-born child ([2894], reproduced with permission from SPIE)

10.6 Closing Remarks

It is the author's hope that by this broad review of basic and applied spectroscopy the reader has got a firm grasp of the many possibilities offered by spectroscopy, and also how it fits in the larger picture of understanding our world. The relations and similarities between processes and phenomena have been stressed, and the need for strong interdisciplinarity has also been emphasized. Spectroscopy can be seen as a toolbox filled with sharp tools, which when properly used can serve many tasks. The somewhat unexpected interrelation between seemingly widely separated topics and methods can be illustrated in Figs. 10.75 and 10.76. The connection between environmental monitoring and medicine is demonstrated in Fig. 10.75, where, e.g., pollution gas probing over km range is shown, as well as probing of the oxygen contents in the human frontal sinuses, where everything is the same, except the size of the optics. Likewise, in Fig. 10.76 the connection between large-scale DIAL and small-scale GASMAS is illustrated, where scattering in both cases provides the signal to be analyzed; in the first case regarding the gas between particles and in the second case regarding the gas inside the pores. Again, scales change from km to cm.

Another observation is the re-occurrence of basically the same physical principles in widely different contexts, and frequently using different terminology for describing very similar things. Examples, which we have encountered in this book include:

Optical resolution (spatial/spectral/temporal): High resolution in a general sense is obtained when many partial optical waves are allowed to interfere to create sharp features: Lens and telescope (large diameter helps), prism (large size helps), grating (many rules help), Fabry-Pérot-interferometer (high reflectivity helps), hologram (large area helps), mode locking (many modes help).

Diffuse light scattering and absorption: The interplay between the two phenomena occurs in the atmosphere (global warming), as well as in tissue optics (light propagation).

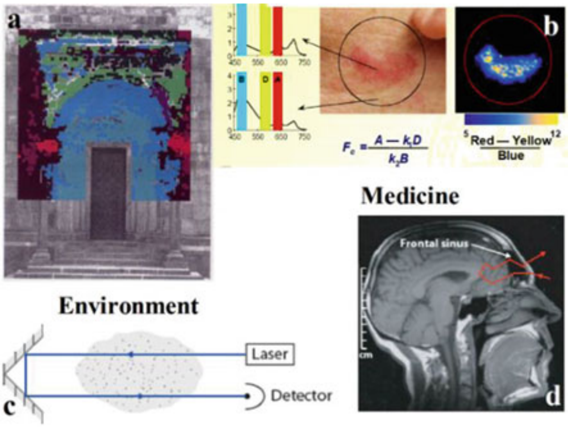

Fig. 10.75 Relation between biomedical and environmental monitoring—very similar—only the geometrical dimensions are different

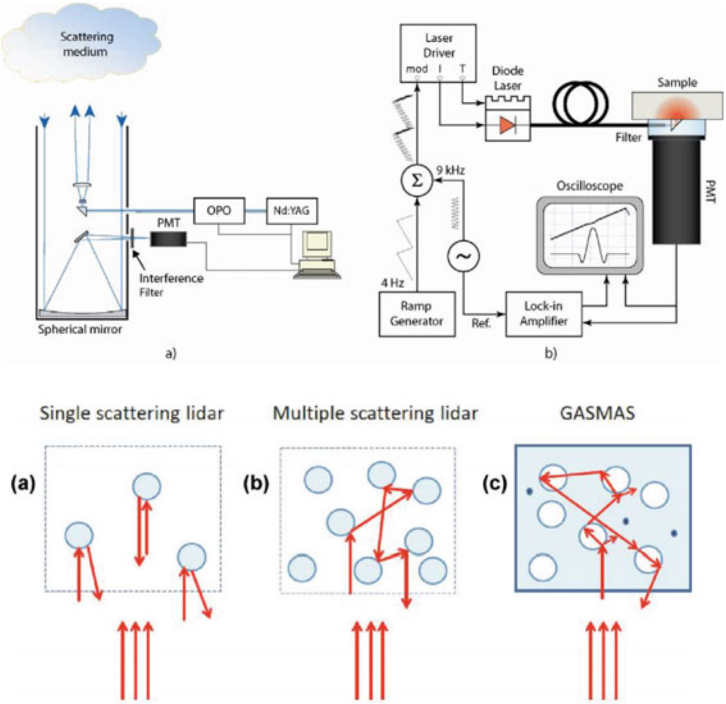
Scattering medium
OPO
Nd:YAG
PMT
Interference Filter
Spherical mirror
a)
Laser Driver
mod I T
Diode Laser
Sample
Filter
9 kHz
Σ
Oscilloscope
PMT
~
4 Hz
Ramp Generator
Ref.
Lock-in Amplifier
b)
Single scattering lidar
Multiple scattering lidar
GASMAS
(a)
(b)
(c)

Fig. 10.76 Relation between DIAL and GASMAS ([2806], reproduced with permission from Springer Nature), and ([2773], reproduced with permission from Wiley)

The "turning-around" phenomenon: The Fortrat parabola manifested in molecular spectroscopy creates intense bandheads, the rainbow is created by taking light from certain angles and heaping it at a special one, days are equally long for quite some time at summer and winter solstice seasons, the preferred position of a classical swinging pendulum is at the end-points where it spends most of its time, and the value of the quantum-mechanical wavefunction is highest at the turning points in the harmonic oscillator description of molecular vibration.

Heterodyne/beat detection: Sensitive detection of weak signals, wind speed measurements, laser Doppler blood perfusion assessment, precision frequency measurements by comb spectroscopy, Raman upconversion to visible region of IR transitions, quantum beats to measure small energy splittings.

Sum/Difference frequency generation: Nonlinear optics enables the generation of new laser frequencies, Raman scattering couples the internal molecular oscillation to the oscillation of the driving field, laser- and ultrasound frequencies couple enabling photon "tagging".

Magnetic orientational energy: Same mathematical expression pertains to the orientational energy of a compass needle, for atomic fine structure, hyperfine structure, and the Zeeman effect.

Representations: A state or condition can be expressed as a combination of orthogonal coordinate values. Geometric Cartesian coordinates define the position in space, and a wavefunction describing a state can be expanded in a set of eigenfunctions in quantum mechanics, Complex spectroscopic data can be analyzed and simplified by using multivariate methods, e.g. expansion in orthogonal principal components.

Harmonics of a fundamental frequency: High-harmonics generation in intense laser-matter interaction, complex wing-beat movements of flying insects can be expressed in a series of frequencies, lock-in detection can be performed on the fundamental or on higher harmonics yielding different line shapes.

Spherical harmonics: Their specific mathematical properties "allow" the description of electronic probability functions, which together can form a closed atomic electronic shell; the correct and "natural" combination of π and σ radiation distribution functions from atoms gives rise to isotropic radiation patterns without specific polarization.

Fourier transform: Extracts data from spectroscopic interferometers, analyzes quantum-beat data, analyzes insect wing beats, produces 3D images from tomographic data, analyzes cosmic microwave background radiation, ……

Synthetic aperture: A higher spatial resolution can be achieved by arranging a larger-size telescope/antenna. A large "synthetic aperture" can be achieved in radio astronomy by temporally synchronizing distant, individual telescopes (VLBI) by atomic clocks. Likewise, close-lying optical telescopes can be synthetized electronically, or interferometrically, to a larger, effective array surface (VLT, ELT). Here there is a strong connection to the early Hanbury Brown – Twiss experiment. If only, say, three parts at the rims of a normal lens are exposed by a mask covering the rest of the lens, a good resolution image can still be achieved, since the three parts, through the smooth and predictable curvature of the lens, allow a well-defined phase relation between the Huygens´ partial waves forming the image. By induction, all parts of a normally exposed lens can be seen as "synchronized" in the same way. In synthetic aperture radar (SAR), a higher resolution is achieved by co-processing Doppler shifts from terrain structures during some flight time of the satellite, yielding an apparent larger antenna.

The "magic" of nonlinearity: The utilization of nonlinearity has been amply demonstrated in this book. One example is how the suppression by a coloured-glass filter of one of two initially equally strong spectral lines can be strongly improved by just increasing the thickness of the filter by two (along the philosophy that $0.9 \times 0.9 = 0.81$, while $0.1 \times 0.1 = 0.01$). Other examples are the sub-natural line creation in high-contrast transmission spectroscopy, and the much more important case of sub-diffraction-limit STED microscopy. Much relies on the specific properties of the exponential function (the fact that its derivative has the same shape as the function itself also helps in many spectroscopic contexts). The Beer-Lambert law, featuring an exponential function, basically reflects the trivial fact, that while light intensities may become almost unlimited strong, nothing can become more black than black!

Questions and Exercises

Chapter 1

1. Discuss some methodology for extracting useful information from multi-spectral images.
2. Why is it useful to use contrast functions without any unit when processing multi-spectral data?
3. What is the basic reason for systems of atomic size to exhibit quantized energy levels?

Chapter 2

4. A closed electronic shell of an atom becomes spherically symmetric. Why?
5. Discuss the two angular momentum coupling schemes, *LS* and *jj* coupling. How can it be determined experimentally which coupling scheme is relevant for a particular atomic configuration?
6. Why do rare-earth elements (lanthanides) have similar chemical properties and sharp spectral lines even when incorporated into a crystal matrix?
7. What can be learned from measurements of

   (a) Landé g_J factors,
   (b) Stark effect constants (polarizabilities),
   (c) Magnetic hyperfine structure constants,
   (d) Isotopic shifts,
   (e) Radiative lifetimes?

8. What characterizes the Zeeman and the Paschen–Back effects, respectively? What is the meaning of the non-crossing rule?
9. Explain why the Zeeman effect is linear in the applied magnetic field B while the (non-hydrogenic) Stark effect is quadratic in the electric field E.
10. Why are there magnetic sublevels which always progress with a linear energy displacement as a function of the magnetic field? Discuss the fine-structure and the hyperfine-structure cases.

© The Editor(s) (if applicable) and The Author(s), under exclusive license
to Springer Nature Switzerland AG 2022

S. Svanberg, *Atomic and Molecular Spectroscopy*, Graduate Texts in Physics,
https://doi.org/10.1007/978-3-031-04776-3

11. The Stark effect:
    (a) Write down the expression for the Stark shift of a fine-structure level with quantum numbers J and m_J.
    (b) Explain the particular dependence on the electric field strength for non-hydrogenic states.
    (c) Can you see any practical application of measurements of the Stark effect?
12. In a strong electric field, an atom can be ionized. Discuss this phenomenon and under what conditions it can most easily be studied.
13. The atomic hyperfine structure is due to the interaction between the nucleus and the electronic shell. Discuss the origin of the interactions and what nuclear and electronic properties are being tested. Give some examples of hyperfine splitting (e.g. for a state with electronic spin $J = 3/2$ and nuclear spin $I = 3/2$) with reference to the mathematics governing the structure.
14. Discuss electrical hyperfine structure. What is its origin? What can be learned from it? Under what circumstances (quantum numbers, etc.) can it be observed?
15. Hyperfine structure:
    (a) What is the typical size of atomic hyperfine structures?
    (b) Which hyperfine structure quantum numbers F are possible for a $J = 3/2$ state in an $I = 5/2$ atom?
    (c) For what types of electrons does the Fermi contact interaction yield a large contribution to the hyperfine structure?
    (d) How can an inverted hyperfine-structure level sequence occur?
    (e) How does the electric hyperfine structure show up in high-resolution spectra?
    (f) What are the requirements for the I and J quantum numbers to make an electric quadrupole interaction possible?
16. When do the normal mass isotopic shift and the volume shift dominate?

Chapter 3

17. What is the essence of the Born–Oppenheimer approximation?
18. Discuss the vibrational energy of a diatomic molecule. How can the simplest quantum-mechanical model be extended for realistic molecules? Explain how observed deviations from the simplest model can be utilized for temperature measurements in molecular gases.
19. What information about a diatomic molecule can be obtained from the rotational constant B?
20. Discuss how the vibrational spectrum is influenced by electronic transitions in diatomic molecules considering the Franck–Condon principle.
21. Why are electronic molecular transitions necessary in order to be able to observe bandheads (bent-over Fortrat parabolas)? What determines if a band is shaded to the red or to the violet?

Chapter 4

22. Discuss the energy-level diagram and the spectrum of the helium atom. Which types of emission lines are seen in the spectrum? The calcium atom also has two electrons outside its closed shells. Discuss the differences between the calcium and helium spectra!
23. What is phosphorescence?
24. Discuss Rayleigh and Raman scattering.
25. When the sublevels of an excited state are statistically populated, the emitted light becomes isotropic and non-polarized. What does this mean in terms of the relation between π and σ radiation?
26. Discuss the wavelength and angular dependence of Rayleigh and Mie scattering.
27. Explain the basics of the formation of the rainbow.
28. What is the origin of the "green flash"? The Aurora Borealis?
29. Mention some aspects of quantum optics and quantum information. What is the origin of the particularities of these fields compared to classical aspects?

Chapter 5

30. Describe the physics behind the X-ray absorption spectroscopy method and discuss its refinement, EXAFS.
31. Discuss the PIXE method for chemical analysis.
32. What is common to XPS (ESCA) and Auger spectroscopy, and what is different? Discuss how the techniques can be used for identifying chemical compounds.
33. Discuss Auger electron spectroscopy. Why are the requirements for energy sharpness of the exciting X-ray radiation more relaxed than for normal electron spectroscopy (XPS)?
34. Explain the basic ideas behind X-ray absorption tomography.
35. Which are common and different aspects of SPECT and PET in nuclear medicine?

Chapter 6

36. What is the meaning of the two concepts homogeneous and inhomogeneous linewidths?
37. Electron synchrotrons provide radiation of great importance for spectroscopy. Describe briefly the generation process and the properties of the radiation.
38. What factors determine the resolution of the following spectroscopic instruments:

    (a) Grating spectrometer;
    (b) Fabry–Pérot interferometer;
    (c) Fourier transform spectrometer.

39. What is the difference between an Ebert and a Czerny–Turner spectrometer?
40. Mention three different types of detectors for IR radiation.
41. Describe the construction and use of an optical multichannel analyser system with time-gating possibility.

42. How short-lived would an excited level have to be to exhibit a natural radiative width of the same order of magnitude as the Doppler width (visible light)? How does the Doppler broadening depend on the temperature and the mass of the gas particles?
43. What is the use of neutral density filters?
44. Transmission of media:
    (a) What window material is transparent at the shortest possible optical wavelengths, and what is the wavelength cut-off?
    (b) Below what wavelength can spectroscopic investigations not be performed without evacuating the air from the apparatus?
    (c) Below what wavelength can ground-based astronomers not observe the stars using optical techniques?
    (d) How far out into the IR spectral region can quartz be used as a lens material?
    (e) At what wavelength towards the UV region does the atmosphere cut off sunlight, and what molecule is responsible for the absorption?
    (f) Discuss the transmission of seawater.
45. Discuss the problems that occur when one wants to push optical spectroscopy from the visible region down towards shorter wavelengths (transmission in optical components, air, etc.).
46. What practical problems might be encountered when performing satellite-based measurements of the reflectance of the Earth's surface in order to do Earth-resource inventories?
47. Spectroscopic lineshapes:
    (a) How does pressure influence the linewidth of a spectral absorption line?
    (b) Discuss briefly how a vertical atmospheric concentration profile can be obtained by satellite limb absorption measurements for a particular species.
48. Why are hollow-cathode lamps used in connection with atomic absorption spectrometry?
49. Describe the calibration procedure for atomic absorption spectrometry (establishing a calibration curve, or using the standard addition method).
50. Discuss satellite remote sensing of land and water areas using passive optical techniques.
51. Discuss colour vision of the human eye. Is there any way to achieve night colour vision?
52. Discuss the spectroscopic background to the enhanced greenhouse effect.
53. Describe the function and application of a lock-in amplifier.
54. Describe some gas detection techniques which rely on spectral correlation principles.
55. Discuss satellite launching and different types of orbits.
56. Why is it advantageous to perform astronomical observations from space?
57. Describe some evidence for the existence of black holes.

Chapter 7

58. Precession:
    - (a) Show that a quantum–mechanical magnetic moment precesses around a magnetic field.
    - (b) Are there any clear manifestations of such a precession in any laser spectroscopic experiment?
    - (c) The precession of a magnetic moment can be used for the detection of nuclear magnetic resonance signals. How?
59. Briefly explain the Atomic Beam Magnetic Resonance (ABMR) technique according to Rabi. Why can only certain types of magnetic resonance transitions be seen? What determines the linewidth of the transitions?
60. Briefly discuss the level-crossing spectroscopic method. The zero-field level-crossing effect is understandable also classically. How?
61. Level-crossing signals at certain magnetic fields can be used for determining hyperfine structure constants of excited states. Why is the number of detectable signals quite limited? Describe in general terms how hyperfine structure information can be deduced from the experimental data.
62. When is it advantageous to use the level-crossing method instead of the optical double resonance technique?
63. What is the advantage of using the Fourier Transform NMR method instead of a scanning technique?
64. Discuss microwave radiometry, applied to environmental monitoring and to astronomy.
65. Discuss radio astronomy paying special attention to telescope resolution, aperture synthesis, and microwave lineshapes.
66. How can a reasonable spatial resolution still be obtained when imaging in the microwave region (radar, radio astronomy)?
67. What can be learned from precision measurements of cosmic background radiation?

Chapter 8

68. Why is it easier to achieve a maser than an X-ray laser?
69. How does the laser process start?
70. Why is a combination of an oscillator and an amplifier preferred to a strongly pumped laser oscillator only?
71. Discuss the CO_2 laser: molecular basis, arrangement, and spectroscopic possibilities.
72. The dye laser and the titanium-doped sapphire (Ti: Al_2O_3) laser are both capable of generating pulsed or continuous tuneable radiation. Discuss the advantages (possibilities) and disadvantages (limitations) of the two different types.
73. Mode-locking:
    - (a) Describe the generation of short laser pulses by mode-locking.

(b) What is the relation between mode-locking and a spectroscopic grating in terms of interference?

74. Describe the general idea of chirped pulse amplification.
75. Describe different types of semiconductor lasers and their characteristics.
76. What is the difference between chirped pulse amplification and parametric chirped pulse amplification?
77. What does the concept of carrier envelope stabilization mean?

Chapter 9

78. Give some characteristics of Rydberg atoms.
79. Indicate some advantages of laser spectroscopic analytical techniques.
80. Laboratory trace gas monitoring: Discuss and compare the following methods: optoacoustic spectroscopy, cavity ring-down spectroscopy, and frequency modulation spectroscopy.
81. Describe the Zeeman quantum-beat method using laser excitation. If a Landé g factor of 1.500 is determined for an atomic state designated $^3P_1$, how would you comment on such a result?
82. Discuss the relation between the Zeeman quantum beats and the Hanle effect.
83. In a Zeeman quantum-beat experiment of the $4p^35s\ ^5S_2$ state in the selenium atom, the excitation was performed at 207 nm from the ground state $4p^4\,^3P_2$ using linearly polarized light from a pulsed laser. In the decay, a signal curve in an external magnetic field as illustrated below was obtained.

    (a) Comment on the fact that the selected transition can be used for the excitation. Is this expected?
    (b) Evaluate the natural radiative lifetime τ and the Landé g_J factor for the state from the recording.
    (c) Comment on the g_J factor result. Is the result expected?

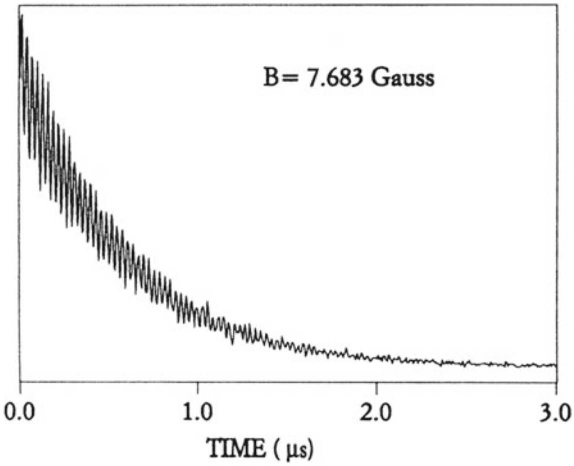

84. In Zeeman quantum-beat measurements, oscillations superimposed on exponential decay of the fluorescence light intensity are observed. In experiments on ytterbium atoms with zero nuclear spin, the beat frequency for the $6s19d\ {}^1D_2$ state was 31.52 MHz for a fixed magnetic field, in which the beat frequency for the signal from the $6s6p\ {}^3P_1$ state (with known g_J value = 1.493) was 46.05 MHz. What is the g_J value of the $6s19d\ {}^1D_2$ state? Is the result expected? Discuss what can be learned from measurements of Landé g_J factors.
85. The spectrum below is recorded in fluorescence from a collimated cesium atomic beam, excited on the D–F transition by a single-mode tunable dye laser. The D level is populated in cascade decay from the P state, which is excited with a broadband CW dye laser. The Fabry–Pérot fringes at the bottom correspond to a free spectral range of 50 MHz.

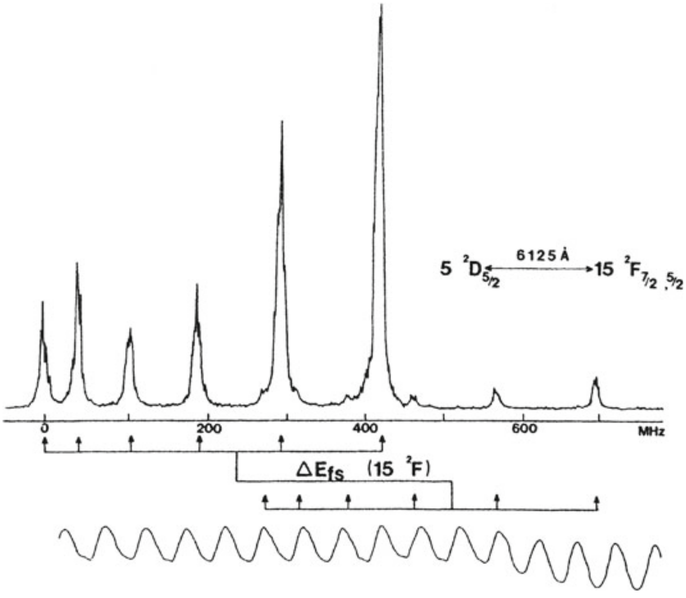

(a) How can it be seen from the spectrum that the magnetic dipole interaction constant (a) of the D-state is negative?
(b) Give an approximate value for the a constant.
(c) What is the nuclear spin of the single cesium isotope in the beam?
(d) What is the fine-structure splitting of the F doublet (which has a negligible hyperfine structure)? Could this splitting be resolved using conventional Doppler-broadened spectroscopy?

86. Describe the saturation spectroscopy method. Why is the polarization spectroscopy version of the technique attractive? How can the technique be used to create a secondary standard for the metre unit?

87. Describe the basic physics behind high-harmonic generation in gases. Discuss some applications of such radiation.
88. Why is it interesting to study chemical reactions on the femtosecond timescale? How can such studies be achieved?
89. Discuss how fundamental information on the hydrogen atom and basic atomic theories can be obtained by simultaneously performing two Doppler-free laser spectroscopic investigations on two different energy splittings in the atom.
90. Why is it interesting from a spectroscopic point of view to be able to cool down atoms to very low translation energies (temperatures)?
91. Discuss techniques to achieve laser cooling of atoms.
92. How can a strongly forbidden atomic transition be used as a frequency standard with a strong spectroscopic signal in spite of the low transition probability (the shelving phenomenon)?
93. What is the general idea behind Bose–Einstein condensation experiments?
94. Discuss atomic optics and the concept of an atomic laser.
95. How can attosecond pulses be generated? Can an attosecond pulse be generated in the visible spectral region? What can attosecond pulse be used for?
96. Describe approaches for electron and proton acceleration using intense laser pulses.
97. Describe two methods for achieving sub-diffraction-limit microscopy using laser techniques.
98. Describe frequency combs and how they can be used in precision metrology and spectroscopy.

Chapter 10

99. Describe some methods for non-intrusive measurements of temperature in flames.
100. Describe the CARS method and its application to combustion diagnostics.
101. How can the laser Doppler velocimetric method be used to measure flow velocities in particle-rich gas flows?
102. How does optical heterodyne spectroscopy/coherent detection work?
103. Describe air pollution measurements using the lidar method.
104. Why is it possible to obtain information on atmospheric gaseous pollutants using laser radar although elastic backscattering from particles is primarily observed?
105. How can range resolution be achieved when using a CW lidar system?
106. How can insects be studied with a CW lidar system? What properties can be investigated?
107. Discuss the principles that allow laser-induced chemistry to be performed.
108. Discuss the penetration of laser light of different wavelengths into tissue and how this governs the medical applications of lasers.
109. Discuss the fluorescence diagnostics and photodynamic treatment of cancer tumours using tumour-seeking drugs and laser light.
110. Describe the principles of optical coherence tomography (OCT). What can be studied?

111. Describe the principles of photoacoustic tomography (PAT). What can be studied?
112. Describe the principles of gas in scattering absorption spectroscopy (GASMAS). What is it good for?

Questions Not Pertaining to Any Special Chapter

113. What spectroscopic method would you choose for the following tasks (explain)?

    (a) Determine the amount of cadmium in a blood sample from a patient.
    (b) Determine the amount of vanadium in a steel alloy.
    (c) Determine the average concentration of sulphur dioxide 5 m above street level.
    (d) Determine the amount of organic oil admixed in a sample of seawater after a tanker accident.
    (e) Determine the temperature of a welding torch flame.
    (f) Determine the water contents in newly harvested grain.

114. What spectroscopic method would you choose for the following tasks (explain)?

    (a) Determine the average concentration of atomic mercury in the smoke from a coal-fired power plant.
    (b) Determine the concentration of chlorophyll in leaves from a maple tree.
    (c) Monitor the growth of an oxide layer on a metal surface.
    (d) Determine the content of CO_2 in respiration air from a patient's lungs.
    (e) Determine if the ozone hole over Antarctica is increasing.
    (f) Determine if the red light from a piece of fireworks is due to strontium.

115. Suggest and explain (in a few words) a suitable spectroscopic method for the following tasks:

    (a) Determination of the absorption spectrum of a powder such as flour.
    (b) Measurement of the magnetic field in a Helmholtz coil system capable of producing a field strength of 0.1 T.
    (c) Monitoring of thin oil films on metal surfaces.
    (d) Precision determination of the Rydberg constant.
    (e) Determination of the content of CO in the exhaust gases from a car at the car inspection station.
    (f) Determination of whether the black paints in two paintings, said to be by Rubens, are really of the same type.

116. What spectroscopic method would you choose for the following tasks (explain)?

    (a) Determine the amount of mercury in the pikes in a lake in an industrial area.

(b) Determine the concentration of sulphur dioxide 100 m above the top of the Big Ben Tower in London.
(c) Determine if a sheet metal surface is really clean from press oil before it enters the painting stage at a car assembly plant.
(d) Determine the amount of lead in the leaves of a tree standing close to a highway.
(e) Determine if a metallic surface, prepared for fundamental surface physics research in an ultra-high vacuum system, is really clean.
(f) Determine the concentration of carbon dioxide in indoor air.

117. Suggest, with a short explanation, a suitable spectroscopic method for the following tasks:

(a) Determination of the CO contents in car engine exhausts.
(b) Determination of the total flux of SO_2 from a volcano.
(c) Study of the start of corrosion/oxidation on a metal surface.
(d) Determination of the Li contents in blood serum (this relates to certain psychiatric diseases).
(e) Determination of the oil contents in sunflower seeds.
(f) Determination of the average concentration of ozone in the stratosphere.

118. Suggest, with a short explanation, a suitable spectroscopic method for the following tasks:

(a) Calibration of the magnetic field in a coil designed for fields up to 0.001 Tesla (10 Gauss).
(b) Determination of the gas temperature in the hot gas stream of a jet engine.
(c) Detection of a major oil spill at sea.
(d) Precision determination of the mass of an ion.
(e) Study of the details of a molecular dissociation process.
(f) Efficient detection of gas leaks in the petrochemical industry.

119. What factors determine the resolution obtainable using the following spectroscopic methods?

(a) Optical double resonance.
(b) Optical pumping.
(c) Laser saturation spectroscopy.

120. Discuss atomic clocks operating at microwave and optical frequencies (brief operating principles). Give examples of applications where a very high time precision is required.

121. Electron synchrotrons provide radiation of great importance for spectroscopy.

(a) Describe briefly the generation process and the properties of the radiation.
(b) Compare synchrotron radiation with laser radiation and give some hints when one or the other is to be preferred.

122. Discuss the medical applications of X-rays. Recently, laser-produced X-rays have been generated. What are the possible future advantages in medicine using such X-rays?
123. In certain cases, the energy levels of an atom are slightly modified by the environment, which can be utilized for chemical analysis and chemical structure determinations. Discuss the following cases:

    (a) Electron spectroscopy.
    (b) Nuclear magnetic resonance spectroscopy.

124. How are picosecond laser pulses generated using mode-locking? What parallels do you see between this process and the conditions for a diffraction grating, a Fabry–Pérot interferometer, or a hologram?
125. Discuss the hyperfine structure and isotopic shifts. What are the origins of these effects? What can be learned from these phenomena? Certain experimental techniques can be used for measuring hyperfine structures as well as isotopic shifts, while others are only useful for hyperfine-structure measurements. How does this arise?
126. Give approximate values for the following quantities (numbers without calculations are OK; numbers derived after calculations are also OK, but take more time!):

    (a) Doppler broadening of spectral lines in the visible wavelength region.
    (b) Thermal velocities of free atoms/molecules at room temperature.
    (c) kT at room temperature.
    (d) Frequency of visible light.
    (e) Energy in eV for visible light.
    (f) Number of atoms/molecules per cm^3 of gas at atmospheric pressure.
    (g) Distance light travels in 1 ns.
    (h) Size in eV of vibrational splittings in simple diatomic molecules.
    (i) Energy of X-rays in eV.
    (j) Cavity mode spacing in a normal laboratory He–Ne laser.

127. Laser mode-locking:

    (a) Describe the generation of short laser pulses by mode-locking.
    (b) What is the relation between mode-locking and spectroscopic grating in terms of interference?
    (c) Is it possible to generate a 100 attosecond pulse (10^{-16} s) in the visible part of the spectrum?

128. Discuss the relation between the Hanle effect and Zeeman quantum beats following short laser light excitation of an ensemble of free atoms.
129. Mark with an (x) in the table below if the method listed is useful for the determination of the atomic physics properties indicated:

	Hyperfine coupling constants a, b	Scalar polarizability α_0	Natural lifetime τ
Level-crossing spectroscopy			
Doppler-free two-photon abs.			
Quantum-beat spectroscopy			
Saturation spectroscopy			

130. How can population differences be created between atomic sublevels to be used in resonance investigations of structures? Discuss three principally different methods.
131. Fourier transformation is a useful mathematical tool in many spectroscopic contexts. Mention a few and describe their utility in specific cases.
132. Explain briefly why the optical Doppler effect is eliminated in the following types of experiments:

    (a) Collimated thermal atomic-beam spectroscopy.
    (b) Accelerated ion-beam spectroscopy (irradiation along the beam).
    (c) Saturation spectroscopy.
    (d) Two-photon absorption spectroscopy.
    (e) Optical double resonance.
    (f) Spectroscopy on a sample of laser-cooled atoms.

133. Describe in a few words the meaning of the following concepts:

    (a) Core polarization.
    (b) Bragg relation.
    (c) Hyperfine anomaly.
    (d) Equivalent width.
    (e) Magic angle.
    (f) Coherent detection.

134. Explain the meaning of the following abbreviations, and write one sentence describing each concept:

(a) QED	(h) NMR
(b) EXAFS	(i) MRI
(c) ESR	(j) DOAS
(d) SAR	(k) BEC
(e) CARS	(l) CPA
(f) DIAL	(m) VLBI
(g) PET	(n) OCT

References

Chapter 1

1. Adapted/modified from I. Lindgren, S. Svanberg, *Atomfysik* (Universitets-förlaget, Uppsala 1974), in Swedish
2. F. Cardarelli, *Scientific Unit Conversion* (Springer, Heidelberg, 1998)
3. K.S. Butcher, L.D. Crown, E.J. Gentry, C. Hockert (eds.), NIST Special Publication 1038, *The International System of Units (SI) – Conversion Factors for General Use* (NIST, Gaithersburg, 2014)
4. P.J. Mohr, D.B. Newell, B.N. Taylor, CODATA recommended values of the fundamental physical constants: 2014. J. Phys. Chem. Ref. Data **45**, 043102 (2016)
5. The International System of Units (SI), 9th edn. (Bureau International des Poids et Mesures 2019)
6. M. Brydegaard, Z.G. Guan, S. Svanberg, Broad-band multi-spectral microscope for imaging transmission spectroscopy employing an array of Light-Emitting Diodes (LEDs). Am. J. Phys. **77**, 104 (2009)
7. K. Esbensen, *Multivariate Data Analysis in Practice* (CAMO ASA, Oslo, 2006)
8. H.F. Grahn, P. Geladi (eds.), *Hyperspectral Image Analysis* (Wiley, Chichester UK, 2007)
9. F.D. van der Meer, S.M. de Jong, *Imaging Spectrometry* (Springer, Heidelberg, 2014)
10. M. Petrou, C. Petrou, *Image Processing: The Fundamentals*, 2nd edn. (Wiley, 2010)
11. R.C. Gonzales, R.E. Woods, *Digital Image Processing*, 4th edn. (Pearson, 2018)
12. L. de Broglie, Waves and quanta. Nature **112**, 540 (1923)
13. M. Arndt, O. Nairz, J. Vos-Andreae, C. Keller, G. van der Zouw, A. Zeilinger, Wave–particle duality of C_{60} molecules. Nature **401**, 680–682 (1999)
14. S. Eibenberger, S. Gerlich, M. Arndt, M. Mayor, J. Tüxen, Matter-wave interference of particles selected from a molecular library with masses exceeding 10,000 amu. Phys. Chem. Chem. Phys. **15**, 14696 (2013)
15. W. Rueckner, J. Peidle, Young's double-slit experiment with single photons and quantum eraser. Am. J. Phys. **81**, 951 (2013)

Chapter 2

16. H. Haken, H.C. Wolf, *The Physics of Atoms and Quanta*, 5th edn. (Springer, Berlin, Heidelberg, 1996)

© The Editor(s) (if applicable) and The Author(s), under exclusive license
to Springer Nature Switzerland AG 2022

S. Svanberg, *Atomic and Molecular Spectroscopy*, Graduate Texts in Physics,
https://doi.org/10.1007/978-3-031-04776-3

17. B. Cagnac, J.C. Pebay-Peyroula, *Modern Atomic Physics: I Fundamental Principles, II Quantum Theory and its Applications* (Wiley, New York, 1975)
18. E.U. Condon, G.H. Shortley, *The Theory of Atomic Spectra* (Cambridge University Press, Cambridge, 1964)
19. E.U. Condon, H. Odabasi, *Atomic Structure* (Cambridge University Press, Cambridge, 1980)
20. I.I. Sobelman: *Atomic Spectra and Radiative Transitions*, 2nd edn., Springer Ser. Atoms and Plasmas, vol.12 (Springer, Berlin, Heidelberg 1996)
21. G. Herzberg, *Atomic Spectra and Atomic Structure* (Dover, New York, 1944)
22. R.D. Cowan, *The Theory of Atomic Structure and Spectra* (University of California Press, Berkeley, 1981)
23. H.A. Bethe, E.E. Salpeter, *Quantum Mechanics of One- and Two-Electron Atoms (Springer, Berlin, Heidelberg 1957*) (Plenum/Rosetta, New York, 1977)
24. C. Cohen-Tannoudji, B. Diu, F. Laloe, *Quantum Mechanics*, vol. 1. Basic Concepts, Tools, and Applications, 2nd ed. (Wiley-VCH 2019) *Vol. 2: Angular Momentum, Spin, and Approximation Methods, 2*nd ed. (Wiley-VCH 2019) *vol. 3: Fermions, Bosons, Photons, Correlations and Entanglements,* 2nd ed. (Wiley-VCH 2019)
25. L.I. Schiff, *Quantum Mechanics* (McGraw-Hill, New York, 1968)
26. A. Messiah, *Quantum Mechanics* (Wiley, New York, 1962)
27. E. Merzbacher, *Quantum Mechanics*, 2nd edn. (Wiley, Orlando, FL, 1970)
28. B.H. Bransden, J.C. Joachain, *Physics of Atoms and Molecules*, 2nd edn. (Longman, Essex, 1990)
29. W. Greiner, *Quantum Mechanics - An Introduction*, 3rd edn. (Springer, Berlin, Heidelberg, 1994)
30. Z.B. Rudzikas, *Theoretical Atomic Spectroscopy* (Cambridge University Press, Cambridge, 1997)
31. C.J. Foot, *Atomic Physics* (Oxford University Press, Oxford, 2004)
32. C.E. Burkhardt, J.J. Leventhal, *Topics in Atomic Physics* (Springer, New York, 2006)
33. G. Drake (ed.), *Springer Handbook of Atomic, Molecular, and Optical Physics* (Springer, New York, 2007)
34. R.L. Brooks, *The Fundamentals of Atomic and Molecular Physics* (Springer, 2013)
35. L. Susskind, A. Friedman, *Quantum Mechanics: The Theoretical Minimum* (Penguin Books 2014)
36. V. Natarajan, *Modern Atomic Physics* (CRC Press, 2015)
37. R. Kakkar, *Atomic and Molecular Spectroscopy* (Cambridge University Press, Cambridge, 2015)
38. J. House: *Fundamentals of Quantum Mechanics*, 3rd edn. (Academic Press 2017)
39. J.J. Sakurai, J. Napolitano, *Modern Quantum Mechanics*, 2nd edn. (Cambridge University Press, Cambridge, 2017)
40. H. Friedrich, *Theoretical Atomic Physics* (Springer, Heidelberg, 2017)
41. D.J. Griffiths, D.F. Schroeter, *Introduction to Quantum Mechanics*, 3rd edn. (Cambridge University Press, Cambridge, 2018)
42. L. Colombo, *Atomic and Molecular Physics* (AIP Publishing 2019)
43. J.A. Barrett, *The Conceptual Foundations of Quantum Mechanics* (Oxford University Press, Oxford, 2019)
44. M. Fox, *A Student´s Guide to Atomic Physics* (Cambridge University Press, Cambridge, 2019)
45. J. Baggott, *The Quantum Cookbook* (Oxford University Press, Oxford, 2020)
46. P.H. Manning, *Atoms, Molecules and Compounds* (Chelsey House Publishers, 2020)
47. I. Lindgren, I. Martinson, R. Schuch (eds.), Heavy-ion spectroscopy and QED effects in atomic systems, Phys. Scripta **T46**, (1993)
48. V.W. Hughes, High-precision spectroscopy of positronium and muonium. Adv. Quantum Chem. **30**, 99 (1998)
49. S.G. Karshenboim, Positronium, antihydrogen, light and the equivalence principle. J. Phys. B **49**, 144001 (2016)

50. T. Tanaka et al., High precision measurement of muonium hyperfine structure. IOP Conf. Ser.: J. Phys. Series **1138**, 012008 (2018)
51. C.E. Moore, *Atomic Energy Levels as Derived from Optical Spectra*, Circular 467, National Bureau of Standards, Volumes I–III, Reissued 1971 as NSRDS-NBS 35 Vol.I 1H–23V, Vol.II 24Cr–41Nb, Vol.III 42Mo–57La (NBS, Washington, DC 1971)
52. W.C. Martin, R. Zalubas, L. Hagan, *Atomic Energy Levels – The Rare Earth Elements, NSRDS-NBS 60* (US Govt. Printing Office, Washington, DC, 1978)
53. S. Bashkin, J.O. Stoner, *Atomic Energy Levels and Grotrian Diagrams*, Vol. I H I – P XV (1975), Vol.I Addenda (1978), Vol. II S I – Ti XXII (1978), Vol. III V I – Cr XXIV (1981), Vol. IV Mn I–XXV (North-Holland, Amsterdam 1982)
54. B. Edlén, Atomic spectra, in *Handbuch der Physik*, Vol. XXVII, ed. by S. Flügge (Springer, Berlin, Heidelberg 1964)
55. B. Edlén, Energy structure of highly ionized atoms (See [127], Pt.D, p. 271)
56. P.J. Mohr, W.L. Wiese (eds.), *Atomic and Molecular Data and their Applications* (AIP Press, New York, 1998)
57. V.A. Boiko, V.G. Pal'chikov, I. Yu. Skobelev, A. Ya. Faenov, *The Spectroscopic Constants of Atoms and Ions* (CRC, Boca Raton, CA 1994)
58. G.W.F. Drake (ed.), *Atomic, Molecular and Optical Physics Reference Book* (AIP Press, New York 1996) Atomic Spectra Database, NIST Standard Reference Version 5.8, Database, 78OI, https://doi.org/10.18434/T4W30F (NIST, Gaithersburg 2019)
59. N.H. March, *Self-consistent Fields in Atoms* (Pergamon, Oxford, 1978)
60. C. Froese-Fisher, *The Hartree-Fock Method for Atoms* (Wiley, New York, 1977)
61. C. Froese-Fisher, *Multi-configuration Hartree-Fock calculations for complex atoms.* (See [2.77], Pt.C, p.29)
62. C.F. Froese Fischer, T. Brage, P. Jönsson, *Computational Atomic Structure – An MCHF Approach* (IOP Publishing, Bristol 1997)
63. B.G. Wybourne, *Spectroscopic Properties of Rare Earths* (Wiley, New York, 1965)
64. B.R. Judd, Complex atomic spectra. Rep. Prog. Phys. **48**, 907 (1985)
65. A.A. Svinarenko, A.V. Glushkov, O. Yu. Khetselius, V.B. Ternovsky, Y.V. Dubrovskaya, A.A. Kuznetsova, V.V. Buyadzhi, *Theoretical Spectroscopy of Rare-Earth Elements: Spectra and Autoionization Resonances* (2017). https://doi.org/10.5772/intechopen.69314
66. M.J. Seaton, Quantum defect theory. I. General formulation. Proc. Phys. Soc. London **88**, 801 (1966); II. Illustrative one-channel and two-channel problems. Proc. Phys. Soc. London **88**, 815 (1966)
67. U. Fano, Unified treatment of perturbed series, continuous spectra and collisions. J. Opt. Soc. Am. **65**, 979 (1975)
68. J.A. Armstrong, P. Esherick, J.J. Wynne, Bound, even parity $J = 0$ and 2 spectra of Ca: A multichannel quantum-defect theory analysis. Phys. Rev. A **15**, 180 (1977)
69. P. Esherick, Bound, even parity $J = 0$ and $J = 2$ spectra of Sr. Phys. Rev. A **15**, 1920 (1977)
70. M. Aymar, O. Robaux, Multichannel quantum defect analysis of the bound, even parity $J = 2$ spectra of neutral barium. J. Phys. B **12**, 531 (1979)
71. M. Aymar, Ch.H. Greene, E. Luc-Koenig, Multichannel Rydberg spectroscopy of complex atoms. Rev. Mod. Phys. **68**, 1015 (1996)
72. N. Ryde, *Atoms and Molecules in Electric Fields* (Almquist & Wiksell International, Stockholm 1976)
73. J.-P. Connerade, *Highly Excited Atoms* (Cambridge University Press, Cambridge, 1997)
74. T.F. Gallagher, *Rydberg Atoms* (Cambridge University Press, Cambridge 1994). Paperback version 2005
75. N. Sibalic, C.S. Adams, *Rydberg Physics* (IOP Publishing, Bristol, 2018)
76. A. Browaeys, D. Barredo, T. Lahaye, Experimental investigations of dipole–dipole interactions between a few Rydberg atoms. J. Physics B: Atomic, Molecular and Optical Physics **49**, 152001 (2016)
77. R.G. Cortiñas, M. Favier, B. Ravon, P. Méhaignerie, Y. Machu, J.M. Raimond, C. Sayrin, M. Brune, Laser trapping of circular Rydberg atoms. Phys. Rev. Lett. **124**, 123201 (2020)

78. T.W. Ducas, M.G. Littman, R.R. Freeman, D. Kleppner, Stark ionization of high-lying states of sodium. Phys. Rev. Lett. **35**, 366 (1975)
79. T.F. Gallagher, L.M. Humphrey, R.M. Hill, S.A. Edelstein, Resolution of [m_l] and [m_j] levels in the electric field ionization of highly excited states of Na. Phys. Rev. Lett. **37**, 1465 (1976)
80. T.F. Gallagher, L.M. Humphrey, R.M. Hill, W. Cooke, S.A. Edelstein, Fine structure intervals and polarizabilities of highly excited p and d states of sodium. Phys. Rev. A **15**, 1937 (1977)
81. D. Kleppner, M.G. Littman, M.L. Zimmerman, Highly excited atoms. Sci. Am. **244**(5), 108 (1981)
82. H. Kopfermann, *Nuclear Moments* (Academic Press, New York, 1958)
83. W.A. Nierenberg, I. Lindgren, in *Alpha-, Beta-, and Gamma-Ray Spectroscopy*, ed. by K. Siegbahn (North-Holland, Amsterdam 1965) p.1263
84. G.H. Fuller, V.W. Cohen, Nuclear spins and moments. Nuclear Data Tables A **5**, 433 (1969)
85. M. Allegrini, E. Arimondo, L.A. Orozco, Survey of hyperfine structure measurements in alkali atoms. J. Phys. Chem. Ref. Data **51**, 043102 (2022)
86. I. Lindgren, A. Rosén, Relativistic self-consistent field calculations with application to hyperfine interaction. Pt.I Relativistic self-consistent fields, Pt.II Relativistic theory of atomic hyperfine interaction. Case Stud. Atom. Phys. **4**, 93 (1974), Pt.III Comparison between theoretical and experimental hyperfine structure results. Case Stud. Atom. Phys. **4**, 197 (1974)
87. S. Büttgenbach, *Hyperfine Structure in 4d- and 5d-Shell Atoms*, Springer Tracts Mod. Phys., Vol.96 (Springer, Berlin, Heidelberg 1982)
88. I. Lindgren, Effective operators in the atomic hyperfine interaction. Rep. Prog. Phys. **47**, 345 (1984)
89. I. Lindgren, J. Morrison, *Atomic Many-Body Theory*, 2nd edn., Springer Ser. Atoms and Plasmas, Vol.3 (Springer, Berlin, Heidelberg 1987)
90. A.V. Andreev, *Atomic Spectroscopy - Introduction to the Theory of Hyperfine Structure* (Springer, New York, 2006)
91. J. Schirmer, *Many-Body Methods for Atoms, Molecules and Clusters* (Springer, Heidelberg, 2018)
92. J.R.P. Angel, P.G.H. Sandars, The hyperfine structure Stark effect. I. Theory. Proc. Roy. Soc. A **305**, 125 (1968)
93. A. Khadjavi, A. Lurio, W. Happer, Stark effect in the excited states of Rb, Cs, Cd, and Hg. Phys. Rev. **167**, 128 (1968)
94. K. Heilig, A. Steudel, Changes in mean square nuclear charge radii from optical isotope shifts. At. Data Nucl. Data Tables **14**, 613 (1974)
95. K. Heilig, A. Steudel: New developments in classical optical spectroscopy. (See [126], Pt.A, p.263)
96. W.H. King, *Isotope Shifts in Atomic Spectra* (Plenum, New York, 1984)
97. U.D. Jentschura, A. Matveev, C.G. Parthey, J. Alnis, R. Pohl, Th. Udem, N. Kolachevsky, T.W. Hänsch, Hydrogen-deuterium isotope shift: From the 1S–2S-transition frequency to the proton-deuteron charge-radius difference. Phys. Rev. A **83**, 042505 (2011)
98. M. Witkowski, G. Kowzan, R. Nunoz-Rodrigues, R. Ciurylo, P.S. Z´Uchowski, P. Maslowski, M. Zawada, Absolute frequency and isotope shift measurements of mercury $^1S_0 - {}^3P_1$ transition. Opt. Express **27**, 11069 (2019)
99. V.W. Hughes, B. Bederson, V.W. Cohen, F.M.J. Pichanick (eds.), *Atomic Physics, New York 1968* (Plenum, New York, 1969)
100. G.K. Woodgate, P.G.H. Sandars (eds.), *Atomic Physics 2, Oxford 1970* (Plenum, New York, 1971)
101. S.J. Smith, G.K. Walters (eds.), *Atomic Physics 3*, Boulder, Colo. 1972 (Plenum, New York 1973)
102. G. zu Putlitz, E.W. Weber, A. Winnacker (eds.), *Atomic Physics 4*, Heidelberg 1974 (Plenum, New York 1975)
103. R. Marrus, M. Prior, H. Shugart (eds.), *Atomic Physics 5, Berkeley 1976* (Plenum, New York, 1977)

104. A.M. Prokhorov, R. Damburg (eds.), *Atomic Physics 6, Riga 1978* (Plenum, New York, 1979)
105. D. Kleppner, F.M. Pipkin (eds.), *Atomic Physics 7, Cambridge, MA 1980* (Plenum, New York, 1981)
106. I. Lindgren, A. Rosén, S. Svanberg (eds.), *Atomic Physics 8, Göteborg 1982* (Plenum, New York, 1983)
107. R.S. Van Dyck, Jr., E.N. Fortson, (eds.), *Atomic Physics 9, Seattle 1984* (World Scientific, Singapore, 1985)
108. H. Narumi, I. Shimamura (eds.), *Atomic Physics 10, Tokyo 1986* (NorthHolland, Amsterdam, 1987)
109. S. Haroche, J.C. Gay, G. Grynberg (eds.), *Atomic Physics 11, Paris 1988* (World Scientific, Singapore, 1989)
110. J. Zorn, R. Lewis (eds.), *Atomic Physics 12, Ann Arbor 1990* (Plenum, New York, 1990)
111. H. Walther, T.W. Hänsch, B. Neizert (eds.), *Atomic Physics 13, Munich 1992* (AIP Press, New York, 1993)
112. D.J. Wineland, C.E. Wieman, S.J. Smith (eds.), *Atomic Physics 14, Boulder 1994* (AIP Press, New York, 1995)
113. H.B. van Linden, J.T.M. van den Heuvell, M.W.R. Walraven (eds.), *Atomic Physics 15, Amsterdam 1996* (World Scientific, Singapore, 1997)
114. W.E. Baylis, G.W.F. Drake (eds.), *Atomic Physics 16*, Windsor 1998, AIP Conference Proceedings **16** (1999)
115. E. Arimondo, P. De Natale, M. Inguscio (eds.), *Atomic Physics 17*, Firenze 2000 (AIP Conference Proceedings, Melville, NY 2001)
116. H.R. Sagdepour, D.E. Pritchard, E.J. Heller (eds.), *Atomic Physics 18, Cambridge* (World Scientific, Singapore, 2003)
117. L.G. Marcassa, K. Helmerson, S. Bagnato (eds.), *Atomic Physics 19*, Rio de Janeiro 2004 (AIP Conf. Proceedings **770**, 2005)
118. C. Ross, H. Häffner, R. Blatt (eds.), *Atomic Physics 20*, 2006 Innsbruck (AIP Conf. Proc. 869, 2006)
119. R. Côté, P.L. Gould M. Rozman, W.W. Smith (eds.), *Atomic Physics 21*, Storrs, Ct. 2008 (World Scientific, Singapore 2009)
120. H. Bachor, P. Drummond, P. Hannaford (eds.), *Atomic Physics 22*, 2010, Cairns, Australia, Journal of Physics, Conf. Series **264** (2011)
121. O. Delieu, P. Grangier, M. Leduc, H. Perrin (eds.), *Atomic Physics 23*, Palaiseau 2012, EPJ Web of Conferences (EDP Sciences 2012)
122. G. Cambell, T. Porto (eds.), *Atomic Physics 24*, Washington DC 2014, http://www.icap2014.org/sites/icap2014.org/files/icap_all_no_ads-compressed.pdf
123. D. Cho, Y. Kim (eds.), *Atomic Physics 25*, 2016 Soeul, Korea; jhe.snu.ackr/icap2016/en/index.html
124. M. Lewenstein et al. (eds.), *Atomic Physics 26,* 2018 Barcelona, Spain; icap2018.eu
125. *Atomic Physics 27,* 2022 Toronto https://ucan.physics.utoronto.ca/conferences/icap-2020-27th-international-conference-atomic-physics/
126. W. Hanle, H. Kleinpoppen (eds.), *Progress in Atomic Spectroscopy*, Pts.A and B (Plenum, New York 1978 and 1979)
127. H.J. Beyer, H. Kleinpoppen (eds.), *Progress in Atomic Spectroscopy*, Pts.C and D (Plenum, New York 1984 and 1987)

Chapter 3

128. R.W.B. Pearse, A.G. Gaydon, *The Identification of Molecular Spectra* (Chapman and Hall, London, 1950)

129. C.E. Banwell, E.M. McCash, *Fundamentals of Molecular Spectroscopy*, 4th edn. (McGraw-Hill, London, 1983)
130. J.I. Steinfeld, *Molecules and Radiation*, 2nd edn. (MIT Press, Cambridge, MA, 1985)
131. W.G. Richards, P.R. Scott, *Structure and Spectra of Molecules* (Wiley, Chichester, 1985)
132. G. Herzberg, *Molecular Spectra and Molecular Structure. I. The Spectra of Diatomic Molecules* (Krieger Publ., Malabar, FL 1991)
133. G. Herzberg, *Molecular Spectra and Molecular Structure, II. Infrared and Raman Spectra of Polyatomic Molecules* (Krieger Publ., Malabar, FL 1991)
134. G. Herzberg, *Molecular Spectra and Molecular Structure. III. Electronic Spectra and Electronic Structure of Polyatomic Molecules* (Krieger Publ., Malabar, FL 1991)
135. G. Herzberg, *The Spectra and Structures of Simple Free Radicals – An Introduction to Molecular Spectroscopy* (Dover, New York 1971, 1988)
136. K.P. Huber, G. Herzberg, *Molecular Spectra and Molecular Structure* (IV Constants of Diatomic Molecules (Van Nostrand Reinhold, New York, 1979)
137. H. Lefebre-Brion, R.W. Field, *Perturbations in the Spectra of Diatomic Molecules* (Academic, Orlando, 1986)
138. L.M. Sverdlov, M.A. Kovner, E.P. Krainov, *Vibrational Spectra of Polyatomic Molecules* (Israel Program for Scientific Translations, Jerusalem 1974)
139. P.J. Mohr, W.L. Wiese (eds.), *Atomic and Molecular Data and their Applications* (AIP Press, New York, 1998)
140. J.L. McHale, *Molecular Spectroscopy* (Goodreads, 1998)
141. M.C. Gupta, *Atomic and Molecular Spectroscopy* (New Age International, 2001)
142. G. Drake (ed.), *Springer Handbook of Atomic, Molecular, and Optical Physics* (Springer, New York, 2007)
143. S. Chandra, *Molecular Spectroscopy* (Alpha Science International, 2009)
144. R.L. Brooks, *The Fundamentals of Atomic and Molecular Physics* (Springer, 2013)
145. D.L. Andrews, *Molecular Photophysics and Spectroscopy* (IOP Publishing, Bristol, 2014)
146. P. Atkins, *Atkin´s Molecules,* 2nd revised ed. (Cambridge University Press, Cambridge 2014)
147. R. Kakkar, *Atomic and Molecular Spectroscopy* (Cambridge University Press, Cambridge, 2015)
148. B. Stuart: *Infrared Spectroscopy.* https://doi.org/10.1002/0471238961.0914061810151405.a01.pub3 (Wiley Online Library, 2015)
149. L. Colombo: *Atomic and Molecular Physics* (AIP Publishing 2019)
150. C. Johnson (ed.), *Spectroscopy and Dynamics of Single Molecules : Methods and Applications* (Elsevier, US, 2019)
151. P.H. Manning, *Atoms, Molecules and Compounds* (Chelsey House Publishers, 2020)
152. R. Marquardt, M. Quack (eds), *Molecular Spectroscopy and Quantum Dynamics* (Elservier, US 2020)
153. B.S. Tsukerblat, *Group Theory in Chemistry and Spectroscopy* (Academic Press, London, 1994)
154. D.C. Harris, M.D. Bertolucci, *Symmetry and Spectroscopy* (Dover, New York, 1990)
155. D.M. Bishop, *Group Theory and Chemistry* (Dover, New York, 1993)
156. K. Veera Reddy, *Symmetry and Spectroscopy of Molecules* (New Age Science, 2010)
157. D.A. McQuarrie, *Quantum Chemistry* (Oxford University Press, Oxford 1983) Chap.10
158. R. McWeeny, B.T. Pickup, Quantum theory of molecular electronic structure. Rep. Prog. Phys. **43**, 1065 (1980)
159. A. Hinchliffe, *Ab Initio Determination of Molecular Electronic Structure* (Hilger, Bristol, 1987)
160. R.G. Parr, W.T. Yang, *Density Functional Theory of Atoms and Molecules* (Oxford Science, Oxford, 1989)
161. R.M. Dreizler, E.K.U. Gross, *Density Functional Theory* (Springer, Berlin, Heidelberg, 1990)
162. W.J. Hehre, L. Radom, P.V.R. Schleyer, J.A. Pople, *Ab Initio Molecular Orbital Theory* (Wiley, New York, 1996)

163. Ch. Jungen, *Molecular Applications of Quantum Defect Theory* (IOP Publishing, Bristol, 1996)
164. D.A. McQuarrie, *Quantum Chemistry*, 2nd edn. (University Science Books, Sausalito, 2007)
165. Y. Ozaki, M.J. Wójcik, J. Popp (eds.), *Molecular Spectroscopy: A Quantum Chemistry Approach, Vol. 1 and 2* (Wiley-VCH, 2019)
166. T. Engel, P. Reid, *Quantum Chemistry and Spectroscopy, 4th Edition* (Pearson, 2019)
167. R.F. Curl, R.E. Smalley, Probing C_{60}. Science **242**, 1017 (1988)
168. H. Kroto, Space, stars, C_{60}, and soot. Science **242**, 1139 (1988)
169. H. Haberland, *Clusters of Atoms and Molecules I, Springer Series in Chemical Physics*, vol. 52 (Springer, Berlin, Heidelberg, 1994)
170. H. Haberland, *Clusters of Atoms and Molecules II (Springer Series in Chemical Physics*, vol. 56 (Springer, Berlin, Heidelberg, 1994)
171. P.W. Fowler, D.E. Manolopoulos, *An Atlas of Fullerenes* (Dover Publications, 2007)
172. F. Langa De La Puente, J.-F. Nierengarten (eds.), *Fullerenes: Principles and Applications: 2* nd edition (Roy. Soc. Chemistry, 2011)
173. R.E. Smalley, Self-assembly of the fullerenes. Acc. Chem. Res. **25**, 98 (1992)
174. S. Ijima, Helical microtubules of graphitic carbon. Nature **354**, 56 (1991)
175. P.M. Ajayan, T.W. Ebbesen, Nanometer size tubes of carbon. Rep. Prog. Phys. **60**, 1025 (1997)
176. T.W. Ebbesen, *Carbon Nanotubes* (CRC Press, Boca Raton, 1997)
177. A. Rosén, A periodic table in three dimensions: A sightseeing tour in the nanometer world. In: *Modern Trends in Atomic Physics*, Adv. Quantum Chem. **30**, 235 (1998)
178. R. Saito, G. Dresselhaus, M.S. Dresselhaus, *Physical Properties of Carbon Nanotubes* (Imperial College Press, London, 1998)
179. K. Tanaka, S. Iijima (eds.), *Carbon Nanotubes and Graphene* (Elsevier, 2014)
180. M. Miao (ed.), *Carbon Nanotube Fibres and Yarns: Production, Properties and Applications in Smart Textiles* (Elsevier Science, 2019)
181. M. Schulz, V. Shanov, Z.Z. Yin, M. Cahay (eds.), *Nanotube Superfiber Materials, 2^{nd} Edition* (Elsevier 2019)
182. M. Arndt, O. Nairz, J. Vos-Andreae, C. Keller, G. van der Zouw, A. Zeilinger, Wave–particle duality of C_{60} molecules. Nature **401**, 680–682 (1999)
183. M.J. Allen, V.C. Tung, R.B. Kaner, Honeycomb carbon: A review of graphene. Chem Rev. **110**, 132 (2010)
184. M.Q. Chen, R.N. Guan, S.F. Yang: Hybrids of fullerenes and 2D nanomaterials. Adv. Sci. **6**, doi.org/https://doi.org/10.1002/advs.201800941 (2018)
185. A. Nag, A. Mitra, S.C. Mukhopadhyay, Graphene and its sensor-based applications: A review. Sensors and Actuators A **270**, 177 (2018)
186. D. Akinwande, C. Huyghebaert, C.H. Wang, M.I. Serna, S. Goossens, L.J. Li, H.S.P. Worg, F.H.L. Koppens, Graphene and two-dimensional materials for silicon technology. Nature **573**, 507 (2019)
187. E.L. Wolf, *Graphene* (Oxford University Press, 2016)
188. E. Celasco, A.N. Chaika (eds.), *Handbook of Graphene, Volume 1: Growth, Synthesis, and Functionalization* (Wiley, 2019).
189. M.I. Katsnelson, *The Physics of Graphene, 2^{nd} edition* (Cambridge University Press, 2019)
190. K.S. Novoselov, Graphene: Nobel Lecture: Materials in the flatland. Rev. Mod. Physics **83**, 837 (2011)
191. A.K. Geim, Nobel Lecture: Random walk to graphene. Rev. Mod. Phys. **83**, 851 (2011)

Chapter 4

192. D.J. Jackson, *Classical Electrodynamics*, 2nd edn. (Wiley, New York, 1975)

193. P. Lorraine, D. Corson, *Electromagnetic Fields and Waves*, 2nd edn. (Freeman, New York, 1970)
194. F.A. Hopf, G.I. Stegeman, *Applied Classical Electrodynamics, Vol.1: Linear Optics, Vol.2: Non-Linear Optics* (Wiley, New York 1986)
195. W. Heitler, *The Quantum Theory of Radiation*, 2nd edn. (Oxford University Press, Oxford, 1944)
196. R. Loudon, *The Quantum Theory of Light*, 3rd edn. (Oxford Univ. Press, New York, 2000)
197. J.N. Dodd, *Atoms and Light Interactions* (Plenum, New York, 1991)
198. F.H.M. Faisal, *Theory of Multiphoton Processes* (Plenum, New York, 1987)
199. H.C. van de Hulst, *Light Scattering by Small Particles* (Wiley, New York, 1957)
200. H.C. van de Hulst, *Multiple Light Scattering*, Vols.1 and 2 (Academic Press, Orlando 1980)
201. B. Chu, *Laser Light Scattering*, 2nd edn. (Academic Press, New York, 1991)
202. C.F. Bohren, D.R. Huffman, *Absorption and Scattering of Light by Small Particles* (Wiley, New York, 1983)
203. M.I. Mishchenko, L.D. Travis, J.W. Hovenier (eds.), *Conference on Light Scattering by Nonspherical Particles: Theory, Measurements, and Applications* (American Meteorological Society, Boston, 1998)
204. A.A. Kokanovsky (ed.), *Light Scattering Review 5* (Springer, 2013)
205. D.A. Long, *Raman Spectroscopy* (McGraw-Hill, New York, 1977)
206. Anderson (ed.), *The Raman Effect, Principles* and *The Raman Effect,* (Dekker, New York 1971 and 1973)
207. J.F. Ferraro, K. Nakamoto, *Introductory Raman Spectroscopy* (Academic Press, London, 1994)
208. J. Javier Laserna, *An Introduction to Raman Spectroscopy: Introduction and Basic Principles* (Wiley Analytical Science, 2001)
209. S. Schlucker, W. Kiefer, *Surface Enhanced Raman Spectroscopy* (Wiley Analytical Science, 2010)
210. H.J. Butler, L. Ashton, B. Bird, G. Cinque, K. Curtis, J. Dorney, K. Esmonde-White, N.J. Fullwood, B. Gardner, P.L. Martin-Hirsch, M.J. Walsh, M.R. McAinsh, N. Stone, F.L. Martin, Using Raman spectroscopy to characterize biological materials. Nat. Protoc. **11**, 664 (2016)
211. D.W. Shipp, F. Sinjab, I. Notingher, Raman spectroscopy: techniques and applications in the life sciences. Adv. Opt. Phot. **9**, 315 (2017)
212. A. Einstein, On the quantum theory of radiation. Phys. Z. **18**, 124 (1917)
213. T.F. Gallagher, W.E. Cooke, Interaction of blackbody radiation with atoms. Phys. Rev. Lett. **42**, 835 (1979)
214. J. Farley, W.H. Wing, Accurate calculation of dynamic Stark shifts and depopulation rates of Rydberg energy levels induced by blackbody radiation. Hydrogen, helium and alkali-metal atoms. Phys. Rev. A **23**, 2397 (1981)
215. K. Bhatia, P. Grafström, C. Levinson, H. Lundberg, L. Nilsson, S. Svanberg, Natural radiative lifetimes in the perturbed 6snd $^1D_2$ Sequence of Barium. Z. Physik A **303**, 1 (1981)
216. D. Kleppner, Turning off the vacuum. Phys. Rev. Lett. **47**, 233 (1981)
217. R.G. Hulet, E.S. Hilfer, D. Kleppner, Inhibited spontaneous emission by a Rydberg atom. Phys. Rev. Lett. **55**, 2137 (1985)
218. W. Jhe, A. Anderson, E.A. Hinds, O. Meschede, L. Moi, S. Haroche, Suppression of spontaneous decay at optical frequencies: Test of vacuum-field anisotropy in confined space. Phys. Rev. Lett. **58**, 666 (1987)
219. S. Haroche, J.M. Raimond, *Advances in Atomic and Molecular Physics 20, 350* (Academic, New York, 1985)
220. P. Goy, J.M. Raimond, M. Gross, S. Haroche, Observation of cavity-enhanced single-atom spontaneous emission. Phys. Rev. Lett. **50**, 1903 (1983)
221. G. Herzberg, *Molecular Spectra and Molecular Structure, I.* (*The Spectra of Diatomic Molecules* (Van Nostrand, Princeton, NJ, 1963)
222. H. Inaba, In *Laser Monitoring of the Atmosphere*, ed. by E.D. Hinkley, Topics Appl. Phys., Vol.14 (Springer, Berlin, Heidelberg 1976)

223. C.K. Sloan, Angular dependence light scattering studies of the aging of precipitates. J. Phys. Chem. **59**, 834 (1955)
224. D'Alessio, A. Di Lorenzo, A.F. Serafim, F. Beretta, S. Masi, C. Venitozzi, Soot formation in methane-oxygen flames. 15th Int. Symp. on Combustion (The Combustion Institute, Pittsburgh 1975) p.1427
225. D'Alessio, A. Di Lorenzo, A. Borghese, F. Beretta, S. Masi, Study of the soot nucleation zone of rich methane-oxygen combustion. 16th Int. Symp. on Combustion (The Combustion Institute, Pittsburgh 1977) p.695
226. H.M. Nussenzveig, The theory of the rainbow. Sci. Am**. 236/**4, 116 (1977)
227. A.B. Fraser, W.H. Mach, Mirages. Sci. Am. **234**(1), 102 (1976)
228. D.K. Lynch, Atmospheric haloes. Sci. Am. **238**(4), 144 (1978)
229. W. Tape, The topology of mirages. Sci. Am. **252**(6), 100 (1985)
230. D.J.K. O'Connel, The green flash. Sci. Am. **202**(1), 112 (1960)
231. H.C. Bryant, N. Jarmie, The glory. Sci. Am. **231**(1), 60 (1974)
232. J. Walker (ed.), *Light from the Sky, Reprint collection (Scientific American)* (Freeman, San Francisco, 1980)
233. R. Greenler, *Rainbows, Haloes and Glories* (Cambridge University Press, Cambridge, 1980)
234. D.K. Lynch, W. Livingstone, *Color and Light in Nature* (Cambridge University Press, Cambridge, 1995)
235. M. Mimaert, *Light and Color in the Outdoors* (Springer, Berlin, Heidelberg, 1995)
236. C.F. Bohren, *Atmospheric Optics* (Wiley, 2007) https://doi.org/10.1002/9783527600441.oe004
237. M. Vollmer, R. Greenler, Halo and mirage demonstrations in atmospheric optics. Appl. Optics **42**, 394 (2003)
238. Yu.M. Timofeyev, A.V. Vasil′ev, *Theoretical Fundamentals of Atmospheric Optics* (International Science Publishing, Cambridge, 2008)
239. S.G. Lipson, ´Atmospheric Optics´, Chap. 8 in *Optics Experiments and Demonstrations for Student Laboratories* (IOP Publishing, 2020)
240. D. Lummerzheim, Modeling and forecasting aurora. Computing in Science and Engineering **9**, 53 (2007)
241. H. Falck-Ytter, T. Lövgren, *Aurora: the Northern Lights in Mythology, History and Science* (Floris, Edinburgh, 1999)
242. E. Salanave, The optical spectrum of lightning. Science **134**, 1395 (1961)
243. H.D. Betz, U. Schumann, P. Laroche (eds.), *Lightning: Principles, Instruments and Applications* (Springer, 2009)
244. U. Fano, A.R.P. Rau, *Atomic Collisions and Spectra* (Academic Press, New York, 1986)
245. P. Schattschneider, *Fundamentals of Inelastic Electron Scattering* (Springer, Wien, 1986)
246. C.F. Barnett, M.F.A. Harrison (eds.), *Plasmas: Applied Atomic Collision Physics*, Vol. 2 (Academic Press, 2013)
247. M. Vinodkumar (ed.), *Electron Collision Processes in Atomic and Molecular Physics* (Narosa Publishing House, 2014)
248. K. Bartschat, M.J. Kushner, Electron collisions with atoms, ions, molecules, and surfaces: Fundamental science empowering advances in technology. Proc. Natl. Acad. Sci. **113**, 7026 (2016)
249. E.W. McDaniel, W.L. Nighan, *Gas Lasers: Applied Atomic Collision Physics, Vol. 3 (*Academic Press, 2017)
250. J.F. Clauser, M.A. Horne, A. Shimony, R.A. Holt, Proposed Experiment to Test Local Hidden-Variable Theories. Phys. Rev. Lett. **23**, 880 (1969)
251. S.J. Freedman, J.F. Clauser, Experimental test of local hidden-variable theories. Phys. Rev. Lett. **28**, 938 (1972)
252. J.F. Clauser, M.A. Horne, Experimental consequences of objective local theories. Phys. Rev. D. **10**, 526 (1974)
253. A. Aspect, P. Grangier, G. Roger, Experimental tests of realistic local theories via Bell's theorem. Phys. Rev. Lett. **47**, 460 (1981)

254. A. Aspect, P. Grangier, G. Roger, Experimental realization of Einstein-Podolsky-Rosen-Bohm Gedankenexperiment: A new violation of Bell's inequalities. Phys. Rev. Lett. **49**, 91 (1982)
255. A. Aspect, J. Dalibard, G. Roger, Experimental test of Bell's inequalities using time-varying analyzers. Phys. Rev. Lett. **49**, 1804 (1982)
256. D. Rauch, J. Handsteiner, A. Hochrainer, J. Gallicchio, A.S. Friedman, C. Leung, B. Liu, L. Bulla, S. Ecker, F. Steinlechner, R. Ursin, B. Hu, D. Leon, C. Benn, A. Ghedina, M. Cecconi, A.H. Guth, D.I. Kaiser, T. Scheidl, A. Zeilinger, Cosmic Bell Test using random measurement settings from high-redshift quasars. Phys. Rev. Lett. **121**, 080403 (2018)
257. J.S. Bell, On the Einstein-Podolsky-Rosen paradox. Physics **1**, 195 (1964)
258. J.S. Bell, On the problem of hidden variables in quantum mechanics. Rev. Mod. Phys. **38**, 447 (1966)
259. A. Einstein, B. Podolsky, N. Rosen, Can quantum-mechanical description of physical reality be considered complete? Phys. Rev. **47**, 777 (1935)
260. J. Yin, J.-G. Ren, H. Lu, Y. Cao, H.-L. Yong, Y.-P. Wu, C. Liu, S.-K. Liao, F. Zhou, Y. Jiang, X.-D. Cai, P. Xu, G.-S. Pan, J.-J. Jia, Y.-M. Huang, H. Yin, J.-Y. Wang, Y.-A. Chen, C.-Z. Peng, J.-W. Pan, Quantum teleportation and entanglement distribution over 100-kilometre free-space channels. Nature **488**, 185 (2012)
261. J. Yin, Y. Cao, Y.H. Li, S.K. Liao, L. Zhang, J.G. Ren, W.Q.iCai, W.Y. Liu, B. Li, H. Dai, G.B. Li, Q.M. Lu, Y.H. Gong, Y. Xu, S.L. Li, F.Z. Li, Y.Y. Yin, Z.Q. Jiang, M. Li, J.J. Jia, G. Ren, D. He, Y.L. Zhou, X.X. Zhang, N. Wang, X. Chang, Z.C. Zhu, N.L. Liu, Y.A. Chen, C.Y. Lu, R. Shu, C.Z.Peng, J.Y. Wang, J.W. Pan, Satellite-based entanglement distribution over 1200 kilometers. Science **356**, 1140 8 (2017)
262. P.W. Shor, Algorithms for quantum computation: discrete logarithms and factoring. In *Proceedings 35th Annual Symposium on Foundations of Computer Science*. IEEE Comput. Soc. Press, p. 124 (1994).
263. F. Arute, K. Arya, J.M. Martinis, Quantum supremacy using a programmable superconducting processor. Nature **574**, 505 (2019)
264. D. Kielpinski, V. Meyer, M.A. Rowe, C.A. Sackett, W.M. Itano, C. Monroe, D.J. Wineland, A decoherence-free quantum memory using trapped ions. Science **291**, 1013 (2001)
265. H. Häffner, C.F. Roos, R. Blatt, Quantum computing with trapped ions. Phys. Reports **469**, 155 (2008)
266. C.R. Monroe, D.J. Wineland, Computing with ions. Sci. Am., August 2008, p. 6
267. L. Henriet, L. Beguin, A. Signoles, T. Lahaye, A. Browaeys, G.O. Reymond, C. Jurczak, Quantum computing with neutral atoms. Quantum **4**, 327 (2020)
268. J.H. Wesenberg, K. Molmer, L. Rippe, S. Kröll, Scalable designs for quantum computing with rare-earth-ion-doped crystals. Phys. Rev. A**75** (2007)
269. A. Walther, L. Rippe, Y. Yan, J. Karlsson, D. Serrano, A.N. Nilsson, S. Bengtsson, S. Kröll, High-fidelity readout scheme for rare-earth solid-state quantum computing. Phys. Rev. A **92**, 022319 (2015)
270. R. Bedington, J.M. Arrazola, A. Ling, Progress in satellite quantum key distribution. Quant. Inf. **3**, 30 (2017)
271. M. Pereira, M. Curty, K. Tamaki, Quantum key distribution with flawed and leaky sources. Quant. Inf. **5**, 62 (2019)
272. A.B. Al-Ghamdi, A. Al-Sulami, A.O. Aljahdali, On the security and confidentiality of quantum key distribution. Security and Privacy https://doi.org/10.1002/spy2.111 (2020)
273. F.H. Xu, X.F. Ma, Q. Zhang, H.K. Lo, J.W. Pan, Secure quantum key distribution with realistic devices. Rev. Mod. Phys. **92**, 025002 (2020)
274. B.Z. Zhao, Xiaoming Zha, Z.Y. Chen, R. Shi, D. Wang, T.L. Peng, L.C. Yan, Performance analysis of quantum key distribution technology for power business. Appl. Sci. **10**, 2906 (2020)
275. B. Julsgaard, A. Kozhekin, E.S. Polzik, Experimental long-lived entanglement of two macroscopic objects. Nature **413**, 400–403 (2001)

276. C.H. Bennett, G. Brassard, C. Crépeau, R. Jozsa, A. Peres, W.K. Wootters, Teleporting an unknown quantum state via dual classical and Einstein–Podolsky–Rosen channels. Phys. Rev. Lett. **70**, 1895 (1993)
277. J.G. Ren, P. Xu, H.L. Yong, L. Zhang, S.K. Liao, J. Yin, W.Y. Liu, W.Q. Cai, M. Yang, Ground-to-satellite quantum teleportation. Nature **549**, 70 (2017)
278. R. Hanbury-Brown, R.Q. Twiss, Correlation between photons in two coherent beams of light. Nature **177**, 27 (1956)
279. L. Mandel, Fluctuations of photon beams and their correlations. Proc. Phys. Soc. **72**, 1037 (1958)
280. R. Glauber, The quantum theory of optical coherence. Phys. Rev. **130**, 2529 (1963)
281. R. Glauber, Coherent and incoherent states of the electromagnetic field. Phys. Rev. **131**, 2766 (1963)
282. H.J. Kimble, M. Dagenais, L. Mandel, Photon anti-bunching in resonance fluorescence. Phys. Rev. Lett. **39**, 691 (1976)
283. D.F. Walls, Evidence for the quantum nature of light. Nature **280**, 451 (1979)
284. R. Loudon, Non-classical effects in the statistical properties of light. Rep. Prog. Phys. **43**, 913 (1980)
285. R. Glauber, One hundred years of light quanta (Nobel Lecture). Chem Phys. Chem. **7**, 1618 (2006)
286. P. Meschede, H. Walther, G. Müller, One-atom maser. Phys. Rev. Lett. **54**, 551 (1985)
287. S. Haroche, J.-M. Raimond, Cavity quantum electrodynamics. Sci. Am. **268**(4), 26 (1993)
288. G. Raitel, Ch. Wagner, H. Walther, L.M. Narducci, M.O. Scully, 'The micromaser: A proving ground for quantum physics.' In*: Cavity Quantum Electrodynamics* ed. by P.R. Berman (Academic Press, Boston 1994) p.57
289. P.R. Berman (ed.), *Cavity Quantum Electrodynamics* (Academic Press, Boston, 1994)
290. P. Meschede, Radiating atoms in confined space: From spontaneous emission to micromasers. Phys. Rep. **211**, 201 (1992)
291. H. Walther, Atoms in cavities and traps. Adv. At. Mol. Opt. Phys. **32**, 379 (1994)
292. K. An, J.J. Childs, R.R. Dasari, M.S. Feld, Microlaser: A laser with one atom in an optical resonator. Phys. Rev. Lett. **73**, 3375 (1994)
293. M.S. Feld, K.W. An, The single-atom laser. Sci. Am. **279**(1), 40 (1998)
294. S. Haroche, Controlling photons in a box and exploring the quantum to classical boundary (Nobel lecture). Angew. Chem. Int. Ed. **52**, 10158 (2013)
295. D.J. Wineland, Superposition, entanglement, and raising Schrödinger's cat (Nobel lecture). Angew. Chem. Int. Ed. **52**, 10179 (2013)
296. C.M. Caves, Quantum-mechanical noise in an interferometer. Phys. Rev. D **23**, 1693 (1981)
297. D.F. Walls, Squeezed states of light. Nature **306**, 141 (1983)
298. G. Leuchs, Squeezing the quantum fluctuations of light. Contemp. Phys. **29**, 299 (1988)
299. R.E. Slusher, B. Yurke, Squeezed light. Sci. Am. **258**(5), 50 (1988)
300. R.E. Slusher, L.W. Hollberg, B. Yurke, J.C. Mertz, J.F. Valley, Observation of squeezed states generated by four-wave mixing in an optical cavity. Phys. Rev. Lett. **55**, 2409 (1985)
301. L.-A. Wu, H.J. Kimble, J.L. Hall, H. Wu, Generation of squeezed states by parametric down-conversion. Phys. Rev. Lett. **57**, 2520 (1986)
302. H.J. Kimble, D.F. Walls (eds.), Squeezed states of the electromagnetic field. J. Opt. Soc. Am. **4**, 1450 (1987) (Feature Issue)
303. C. Fabre, Squeezed states of light. Phys. Rep. **219**, 215 (1992)
304. F. Acernese et al., (Virgo Collaboration): Increasing the astrophysical reach of the Advanced Virgo Detector via the application of squeezed vacuum states of light. Phys. Rev. Lett. **123**, 231108 (2019)
305. M. Tse et al., (LIGO Collaboration): Quantum-Enhanced Advanced LIGO Detectors in the era of gravitational-wave astronomy. Phys. Rev. Lett. **123**, 231107 (2019)
306. J. Dietrich, Realizing LIGO. Eng. Sci. **64**(2), 8 (1998)
307. B.P. Abbott et al., (LIGO Scientific and Virgo Collaborations): Observation of gravitational waves from a binary black hole merger. Phys. Rev. Lett. **116**, 061102 (2016)

308. B.P. Abbott et al., (LIGO Scientific and Virgo Collaborations): GWTC-1: A gravitational-wave transient catalog of compact binary mergers observed by LIGO and Virgo during the first and second observing runs. Phys. Rev. X **9**, 031040 (2019)
309. D.F. Walls, G.J. Milburn, *Quantum Optics* (Springer, Berlin, Heidelberg, 1994)
310. L. Mandel, E. Wolf, *Optical Coherence and Quantum Optics* (Cambridge University Press, Cambridge, 1995)
311. M.O. Scully, M.S. Zubairy, *Quantum Optics* (Cambridge University Press, Cambridge, 1997)
312. C.C. Gerry, P.L. Knight, *Introductory Quantum Optics* (Cambridge University Press, Cambridge, 2004)
313. M. Fox, *Quantum Optics: An Introduction* (Oxford University Press, 2006)
314. P. Lambropoulos, D. Petrosyan, *Fundamentals of Quantum Optics and Quantum Information* (Springer, 2007)
315. D.F. Walls, G.J. Milburn, *Quantum Optics, 2nd ed.* (Springer, 2007)
316. M.A. Nielsen, I.L. Chuang, *Quantum Computation and Quantum Information* (Cambridge University Press, Cambridge, 2010)
317. G. Grynberg, A. Aspect, C. Fabre, *Introduction to Quantum Optics: From the Semi-classical Approach to Quantized Light* (Cambridge University Press, 2010)
318. E.G. Rieffel, W.H. Polak, *Quantum Computing – A Gentle Introduction* (MIT Press, Cambridge, 2011)
319. G.S. Agarwal, *Quantum Optics* (Cambridge University Press, Cambridge, 2012)
320. Z. Ficek, M.R. Wahiddin, *Quantum Optics for Beginners* (Taylor and Francis, 2014)
321. P.W. Milonni, *An Introduction to Quantum Optics and Quantum Fluctuations* (Oxford University Press, Oxford, 2019)
322. J.D. Hidary, *Quantum Computing – An Applied Approach* (Springer 2019)
323. P. Rice, *An Introduction to Quantum Optics - An open systems approach* (IOP Publishing, 2020)

Chapter 5

324. R. Karazija, *Introduction to the Theory of X-Ray and Electronic Spectra of Free Atoms* (Plenum, New York, 1992)
325. R.W. Dunford, D.S. Gemmell, E.P. Kanter, B. Krassig, S.H. Southworth, L. Young, *X-Ray and Inner Shell Processes* (AIP, Melville, NY, 2000)
326. J. Als-Nielsen, D. McMorrow, *Elements of Modern X-ray Physics* (John Wiley & Sons, 2011)
327. C.A. MacDonald, *An Introduction to X-Ray Physics, Optics, and Applications* (Princeton, 2017)
328. W.C. Röntgen, Sitzungsbericht der Physikal.-Medicin. Gesellschaft 132 (Würzburg 1895): Engl. Translation: Nature **53**, 274 (1896)
329. G. Farmelo, The discovery of X-rays. Sci. Am. **273**(5), 68 (1995)
330. G.L. Clark, *Applied X-Rays* (McGraw-Hill, New York, 1955)
331. K. Siegbahn (ed.), *Alpha-, Beta-, and Gamma-Ray Spectroscopy* (North Holland, Amsterdam, 1965)
332. E. Förster, E.E. Fill, K. Göbel, H. He, Th. Missalla, O. Renner, I. Ushmann, J. Wark, X-ray emission spectroscopy. J. Quant. Spectrosc. Radiat. Transf. **51**, 101 (1994)
333. G. Hölzer, E. Förster, M. Grätz, C. Tillman, S. Svanberg, X-ray crystal spectroscopy of sub-picosecond laser-produced plasmas beyond 50 keV. J. XRay Sci. Technol. **7**, 50 (1997)
334. P. Suortti, U. Lienert, C. Schulze, 'Bent crystal optics for high energy synchrotron radiation.' In: *X-Ray and Inner Shell Processes*, AIP Conference Proceedings Vol.389, ed. by R.L. Johnson, H. Schmidt-Böcking, B.F. Sonntag (AIP, Woodbury 1997), p.175A

335. J.Y. Liu D.M. Shu, Y.J. Wang S. Narayanan, A. Mashayekhi, J. Qian J. Wang, A sagittally focusing double-multilayer monochromator for ultrafast X-ray imaging applications. J. Synchr. Rad. **14**, 138 (2007)
336. P. Willmot, *An Introduction to Synchrotron Radiation: Techniques and Applications* (John Wiley, 2019)
337. J.E. Rubensson, *Synchrotron Radiation - An Everyday Application of Special Relativity* (Morgan & Claypool Publishers, 2016)
338. B. Agarwal, *X-Ray Spectroscopy*, 2nd edn., Springer Ser. Opt. Sci., Vol.15 (Springer, Berlin, Heidelberg 1990)
339. R. Jenkins, R.W. Gould, D. Gedcke, *Quantitative X-Ray Spectrometry* (Dekker, New York, 1981)
340. J.V. Gilfrich et al. (eds.), *Advances in X-Ray Analysis* (Plenum, New York, several publishing years for series of books)
341. B. Beckhoff, B. Kanngießer, N. Langhoff, R. Wedell, H. Wolff, *Handbook of Practical X-Ray Fluorescence Analysis* (Springer, 2007)
342. J.A. van Bokhoven, C. Lamberti (eds.), *X-Ray Absorption and X-Ray Emission Spectroscopy: Theory and Applications* (Wiley, 2016)
343. H.E. Martz, C.M. Logan, D.J. Schneberk, P.J. Schull, *X-Ray Imaging: Fundamentals, Industrial Techniques and Applications* (CRC Press, 2017)
344. A. Olivo, P.R.T. Munro, *X-Ray Phase Contrast Imaging* (World Scientific, 2021)
345. S.A.E. Johansson, Proton-induced X-ray emission spectrometry – state of the art. Fresenius Z. Anal. Chem. **324**, 635 (1986)
346. H. van Rinsvelt, S. Bauman, J.W. Nelson, J.W. Winchester (eds.). Proc. 4th Int. PIXE Conf., Nucl. Instrum. Methods B **22**, 1 (1987)
347. S.A.E. Johansson, J.L. Campbell, K.G. Malmqvist (eds.), *Particle-Induced X-Ray Emission Spectroscopy (PIXE)* (Wiley, New York, 1996)
348. P.K. Nayak, T.R. Rautray, V. Vijayan, External proton-induced X-ray emission: A simple method for multi-elemental analysis of water. Ind. J. Chem. **45**, 2233 (2006)
349. M. Kurosawa, Particle-Induced X-ray Emission (PIXE). In: W. White W. (ed.) *Encyclopedia of Geochemistry. Encyclopedia of Earth Sciences Series* (Springer, 2017)
350. Courtesy, J. Pallon, Department of Physics, Lund University
351. R.W. Shaw, Air pollution by particles. Sci. Am. **257**(2), 84 (1987)
352. T.G. Dzubiey (ed.), *X-Ray Fluorescence Analysis of Environmental Samples* (Ann Arbor Science Publ, Ann Arbor, 1977)
353. J. Boman, Trace element analysis of urban aerosol particles using X-ray fluorescence spectrometry. Spectrosc. Eur. **21**(6), 11 (2009)
354. J. Nordgren, L. Selander, L. Pettersson, C. Nordling, K. Siegbahn, H. Ågren, Core state vibrational excitations and symmetry breaking in the CK and OK emission spectra of CO_2. J. Chem. Phys. **76**, 3928 (1982)
355. A. Meisel, G. Leonhardt, R. Szargon, *X-Ray Spectra and Chemical Bonding*, Springer Ser. Chem. Phys., Vol.37 (Springer, Berlin, Heidelberg 1989)
356. J. Nordgren, C. Nordling, Ultrasoft X-ray emission from atoms and molecules. Comments At. Mol. Phys. **13**, 229 (1983)
357. J. Nordgren, H. Ågren, Interpretation of ultra-soft X-ray emission spectra. Comments At. Mol. Phys. **14**, 203 (1984)
358. F. de Groot, High-resolution X-ray emission and X-ray absorption spectroscopy. Chem. Rev. **101**, 1779 (2001)
359. J. Kaastra, F. Paerels, *High-Resolution X-Ray Spectroscopy: Past, Present and Future* (Springer, 2014)
360. E.A. Stern, Structure determination by X-ray absorption. Contemp. Phys. **19**, 289 (1978)
361. B.K. Teo, *EXAFS: Basic Principles and Data Analysis, Inorganic Chemistry Concept*, vol. 9 (Springer, Berlin, Heidelberg, 1986)
362. J. Stöhr, *NEXAFS Spectroscopy* (Springer, New York, 1992)

363. G.S. Henderson, F.M.F. de Groot, B.J.A. Moulton, X-ray Absorption Near-Edge Structure (XANES) Spectroscopy. Rev. Mineral. Geochem. **78**, 75 (2014)
364. T.S. Curry III., J.E. Dowdey, R.C. Murry Jr., *Christensen's Physics of Diagnostic Radiology*, 4th edn. (Lea & Febiger, Philadelphia, 1990)
365. P. Butler, A. Mitchell, J.C. Healy, *Applied Radiological Anatomy* (Cambridge University Press, 2012)
366. P. Russo, *Handbook of X-ray Imaging: Physics and Technology* (CRC Press, 2017)
367. General Electric Co., Medical Systems Operations, Milwaukee, WI (1980)
368. R. Lewis, Medical applications of synchrotron radiation X-rays. Phys. Med. Biol. **42**, 1213 (1997)
369. F.A. Dilmanian, X.Y. Wu, E.C. Parsons, B. Ren, J. Kress, T.M. Button, L.D. Chapman, J.A. Coderre, P. Giron, D. Greenberg, D.J. Krus, Z. Liang, D. Marcovici, M.J. Petersen, C.T. Roque, M. Shleifer, D.N. Slatkin, W.C. Tomlinson, K. Yamamoto, J. Zhou, Single- and dual-energy CT with monochromatic synchrotron X-rays. Phys. Med. Biol. **42**, 371 (1997)
370. P. Suortti, W. Thomlinson, Medical application of synchrotron radiation. Phys. Med. Biol. **48**, R1 (2003)
371. W. Thomlinson, H. Elleaume, L. Porraa, P. Suortti, K-edge subtraction imaging in biomedical research. Physica Med. **49**, 58 (2018)
372. R.K. Jain, T. Vokes, Dual-energy X-ray absorptiometry. J. Clin. Densitom. **20**, 291 (2017)
373. R.A. Robb, *Three-Dimensional Biomedical Imaging – Principles and Practice* (VCH, New York, 1994)
374. D. Stromer, V. Christlein, C. Martindale, P. Zippert, E. Haltenberger, T. Hausotte, A. Maier, Browsing through sealed historical manuscripts by using 3-D computed tomography with low-brilliance X-ray sources. Sci. Rep. **8**, 15335 (2018)
375. M.T. Madsen, Recent advances in SPECT imaging. J. Nucl. Med. **48**(4), 661–673 (2007)
376. B. Barrios-Lopez, K. Bergstrom, Radiolabeled sugars used for PET and SPECT imaging. Current Radiopharm. **9**, 180 (2016)
377. O. Israel, O. Pellet, L. Biassoni, D. De Palma, E. Estrada-Lobato, G. Gnanasegaran, T. Kuwert, C. la Fougère, G. Mariani, S. Massalha, D. Paez, F. Giammarile, Two decades of SPECT/CT – the coming of age of a technology: An updated review of literature evidence. Eur. J. Nucl. Med. Molec. Imaging **46**, 1990 (2019)
378. R.A. Powsner, M.R. Palmer, E.R. Powsner, *Essentials of Nuclear Medicine Physics and Instrumentation, 3rd Ed.* (Wiley Blackwell, 2013)
379. M. Dahlbom (ed.), Physics of PET and SPECT Imaging (CRC Press, 2017)
380. J.J. Vaquero, P. Kinahan, Positron Emission Tomography: Current challenges and opportunities for technological advances in clinical and preclinical imaging systems. Annu. Rev. Biomed. Eng. **17**, 385 (2015)
381. M. Unterrainer, C. Eze, H. Ilhan, S. Marschner, O. Roengvoraphoj, N.S. Schmidt-Hegemann, F. Walter, W.G. Kunz, P. Munck af Rosenschöld, R. Jeraj, N.L. Albert, A.L. Grosu, M. Niyazi, P. Bartenstein, C. Belka, Recent advances of PET imaging in clinical radiation oncology. Rad. Oncology **15**, 88 (2020)
382. M. Murnane, H.C. Kapteyn, M.D. Rosen, R.W. Falcone, Ultrafast X-ray pulses from laser-produced plasmas. Science **251**, 531 (1991)
383. J.D. Kmetec, C.L. Gordon III., J.J. Macklin, B.E. Lemoff, G.S. Brown, S.E. Harris, MeV X-ray generation with a femtosecond laser. Phys. Rev. Lett. **68**, 1527 (1992)
384. K. Herrlin, G. Svahn, C. Olsson, H. Pettersson, C. Tillman, A. Persson, C.-G. Wahlström, S. Svanberg, Generation of X-rays for medical imaging by high-power lasers: Preliminary results. Radiology **189**, 65 (1993)
385. C. Tillman, A. Persson, C.-G. Wahlström, S. Svanberg, K. Herrlin, Imaging using hard X-rays from a laser-produced plasma. Appl. Phys. B **61**, 333 (1995)
386. A. Sjögren, M. Harbst, C.-G. Wahlström, S. Svanberg, High-repetition-rate, hard x-ray radiation from a laser-produced plasma: Photon yield and application considerations. Rev. Sci. Instr. **74**, 2300 (2003)
387. L.T. Hudson, J.F. Seely, Laser-produced X-ray sources. Rad. Phys. Chem. **79**, 132 (2010)

388. F. Girard, Review of laser produced multi-keV X-ray sources from metallic foils, cylinders with liner, and low density aerogels. Phys. Plasmas **23**, 040501 (2016)
389. C. Tillman, I. Mercer, S. Svanberg, K. Herrlin, Elemental biological imaging by differential absorption using a laser-produced X-ray source. J. Opt. Soc. Am. B **13**, 209 (1996)
390. C.L. Gordon III., G.Y. Yin, B.E. Lemoff, P.E. Bell, C.P.J. Barty, Timegated imaging with an ultrashort-pulse laser-produced-plasma X-ray source. Opt. Lett. **20**, 1056 (1995)
391. M. Grätz, A. Pifferi, C.-G. Wahlström, S. Svanberg, Time-gated imaging in radiology: Theoretical and experimental studies. IEEE J. Sel. Topics Quantum Electron. **2**, 1041 (1996)
392. M.F.C. Ladd, R.A. Palmer, *Structure Determination by X-Ray Crystallography* (Plenum, New York, 1993)
393. D.R. Powell, Review of X-ray crystallography. J. Chem. Educ. **93**, 59 (2016)
394. E.S. Ameh, A review of basic crystallography and x-ray diffraction applications. Int. J. Adv. Manufact. Tech. **105**, 3289 (2019)
395. M. Wulff, F. Schotte, G. Naylor, D. Bourgeois, K. Moffat, G. Mourou, Time-resolved structures of macromolecules at the ESRF: Single-pulse Laue diffraction, stroboscopic data collection and femtosecond flash photolysis. Nucl. Instrum. Methods Phys. Res. A **398**, 69 (1997)
396. J. Greenberg, *X-Ray Diffraction Imaging: Technology and Applications* (CRC Press, 2018)
397. S. Werin, S. Thorin, M. Eriksson, J. Larsson, Short pulse facility for MAX-lab. Nucl. Instr. Meth. A **601**, 98 (2009)
398. R. Neutze, K. Moffat, Time-resolved structural studies at synchrotrons and X-ray free electron lasers: opportunities and challenges. Curr. Opin. Struct. Biol. **22**, 651 (2012)
399. M.R. Howells, J. Kirz, W. Sayre, X-ray microscopes. Sci. Am. **264**(2), 42 (1991)
400. A.G. Michette, X-ray Microscopy. Rep. Prog. Phys. **51**, 1525 (1988)
401. G. Schmahl, D. Rudolph, J. Thieme, E. Umbach (eds.), *X-ray Microscopy V* (Springer, Heidelberg, 1998)
402. H. Riegler, Laser produced x-ray by high brightness and power diode pumped Nd:YAG laser for compact x-ray lithography and microscopy. Proc. SPIE **6261**, 62610W (2006)
403. C. Jacobsen, *X-ray Microscopy* (Cambridge University Press, 2019)
404. M. Kördel, A. Dehlinger, C. Seim, U. Vogt, E. Fogelqvist, J.A. Sellberg, H. Stiel, H.M. Hertz, Laboratory water-window x-ray microscopy. Optica **7**, 658 (2020)
405. L. Rymell, H.M. Hertz, Droplet target for low-debris laser-plasma soft X-ray generation. Opt. Commun. **103**, 105 (1993)
406. L. Malmqvist, L. Rymell, H.M. Hertz, Droplet-target laser-plasma source for proximity X-ray lithography. Appl. Phys. Lett. **68**, 2627 (1996)
407. Ł Węgrzyński, A. Bartnika, P. Wachulak, T. Fok, H. Fiedorowicz, Laser-produced plasma soft x-ray source based on an aerosol target. Phys. Plasmas **27**, 073102 (2020)
408. M.J. Dykstra, *Biological Electron Microscopy* (Plenum, New York, 1992)
409. J. Kuo (ed.), *Electron Microscopy: Methods and Protocols*, 2nd edn. (Humana Press, NJ, 2007)
410. N. Brodusch, H. Demers, R. Gauvin, *Field Emission Scanning Electron Microscopy: New Perspectives for Materials Characterization* (Springer, Singapore, 2018)
411. K. Svendsen I. Gallardo Gonzales, M. Hansson, J. Björklund Svensson, H. Ekerfeldt, A. Persson, and O. Lundh, Optimization of soft X-ray phase-contrast tomography using a laser wakefield accelerator, Opt. Express **26**, 33930 (2018)
412. J.C. Wood, D.J. Chapman, K. Poder, N.C. Lopes, M.E. Rutherford, T.G. White, F. Albert, K.T. Behm, N. Booth, J.S.J. Bryant, P.S. Foster, S. Glenzer, E. Hill, K. Krushelnick, Z. Najmudin, B.B. Pollock, S. Rose, W. Schumaker, R.H.H. Scott, M. Sherlock, A.G.R. Thomas, Z. Zhao, D.E. Eakins, S.P.D. Mangles, Ultrafast imaging of laser driven shock waves using betatron X-rays from a laser wakefield accelerator. Sci. Rep. **8**, 11010 (2018)
413. G.D. Kubiak, D.R. Kania (eds.), *Extreme Ultraviolet Lithography, OSA Trends in Optics and Photonics*, vol. 4 (OSA, Washington, DC, 1996)
414. V. Bakshi (ed.), *EUV Lithography*, 2nd edn. (SPIE, Bellingham, 2018)

415. S.M. Sze, M.K. Lee, *Semiconductor Devices - Physics and Technology, 3^rd^ Edition (John Wiley, 2012)*
416. T. Tomie, Tin laser-produced plasma as the light source for extreme ultraviolet lithography high-volume manufacturing: History, ideal plasma, present status, and prospects. J. Micro/Nanolith. MEMS MOEMS **11**, 021109 (2012)
417. I. Fomenkov, D. Brandt, A. Ershov, A. Schafgans, Y.Z. Tao, G. Vaschenko, S. Rokitski, M. Kats, M. Vargas, M. Purvis, R. Rafac, B. La Fontaine, S. De Dea, A. LaForge, J. Stewart, S. Chang, M. Graham, D. Riggs, M. Abraham, D. Brown, Light sources for high-volume manufacturing EUV lithography: Technology, performance, and power scaling. Adv. Opt. Techn. **6**, 173 (2017)
418. K. Siegbahn, Electron spectroscopy for atoms, molecules and condensed matter, *in Nobel Lectures, Physics 1981–1990*, Editor G. Ekspong (World Scientific Publishing Co., Singapore, 1993)
419. B. Lindberg, R. Maripuu, K. Siegbahn, R. Larsson, C.G. Gölander, J.C. Eriksson, ESCA studies of heparinized and related surfaces. J. Colloid Interface Sci. **95**, 308 (1983)
420. H. Siegbahn, L. Karlsson, 'Photoelectron Spectroscopy.' In: *Handbuch der Physik*, Vol.31, ed. by E. Mehlhorn (Springer, Berlin, Heidelberg 1982)
421. U. Becker, D.A. Shirley (eds.), *VUV and Soft X-Ray Photoionization* (Plenum, New York, 1995)
422. S. Hüfner, *Photoelectron Spectroscopy*, 3rd edn. (Springer, Heidelberg, 2003)
423. A.M. Ellis, M. Feher, T.G. Wright, *Electronic and Photoelectron Spectroscopy: Fundamentals and Case Studies* (Cambridge University Press, Cambridge, 2005)
424. P. van der Heide, *X-Ray Photoelectron Spectroscopy – An Introduction to Principles and Practices* (Wiley, 2012)
425. S. Suga, A. Sekiyama, *Photoelectron Spectroscopy* (Springer, Berlin, 2014)
426. J.C. Woicik (ed.), *Hard X-ray Photoelectron Spectroscopy (HAXPES)* (Springer, 2016)
427. S. Shigemasa, A. Sekiyama, C. Tusche, *Photoelectron Spectroscopy - Bulk and Surface Electronic Structures* (Springer, 2021)
428. K. Siegbahn, 'Some Current Problems in Electron Spectroscopy.' In: *Atomic Physics 8*, ed. by I. Lindgren, A. Rosén, S. Svanberg (Plenum, New York 1983) p.243
429. N.V. Smith, F.J. Himpsel, 'Photoelectron Spectroscopy.' In: *Handbook of Synchrotron Radiation*, ed. by E.E. Koch (North-Holland, Amsterdam 1983)
430. J.W. Rabalais, *Principles of Ultraviolet Photoelectron Spectroscopy* (Wiley-Interscience, New York, 1977)
431. S. Svensson, N. Mårtensson, E. Basilier, P.Å. Mamquist, U. Gelius, K. Siegbahn, Core and valence orbitals in solid and gaseous mercury by means of ESCA. J. Electron. Spectrosc. Rel. Phenom. **9**, 51 (1976)
432. K. Siegbahn, Electron Spectroscopy and molecular structure. J. Pure Appl. Chem. **48**, 77 (1976)
433. H. Siegbahn, Electron Spectroscopy for chemical analysis of liquids and solutions. J. Phys. Chem. **89**, 897 (1985)
434. L.-G. Petersson, S.-E. Karlsson, Clean and oxygen-exposed potassium studied by photoelectron Spectroscopy. Phys. Scr. **16**, 425 (1977)
435. R.H. Williams, Electron spectroscopy of surfaces. Contemp. Phys. **19**, 389 (1978)
436. K. Siegbahn, 'Electron Spectroscopy for solids, surfaces, liquids and free molecules.' In: *Molecular Spectroscopy*, ed. by A.R. West (Heyden, London 1977) Chap.15
437. K. Siegbahn, PES: Retrospects and prospects. Phil. Trans. Roy. Soc. London **A318**, 3 (1986)
438. D. Briggs, M.P. Seah (eds.), *Practical Surface Analysis by Auger and X-Ray Photoelectron Spectroscopy* (Wiley, Chichester, 1983)
439. S. Hofmann, *Auger- and X-Ray Photoelectron Spectroscopy in Materials Science - A User-Oriented Guide* (Springer, 2013)

Chapter 6

440. G.R. Harrison (ed.), *MIT Wavelength Tables* (Wiley, New York, 1969)
441. F.M. Phelps III, *MIT Wavelength Tables*, Vol.2: *Wavelengths by Element* (MIT Press, Cambridge, MA 1982)
442. R.L. Kelly, L.J. Palumbo, Atomic and ionic emission lines below 2000 Angstroms, hydrogen through krypton. NRL Report 7599 (Naval Research Laboratory, Washington, DC 1973)
443. R.L. Kelly, Atomic and ionic spectral lines below 2000 Angstroms, hydrogen through krypton. J. Phys. Chem. Ref. Data, Suppl. No.l to Vol.16 (1987)
444. J. Reader, C.H. Corliss, W.L. Wiese, G.A. Martin, *Wavelengths and Transition Probabilities for Atoms and Atomic Ions*. NSRDS-NBS 68 (US Govt. Prtg. Off., Washington, DC 1980)
445. A.R. Striganov, N.S. Sventitskii, *Tables of Spectral Lines in Neutral and Ionized Atoms* (IFI/Plenum, New York, 1968)
446. https://physics.nist.gov/PhysRefData/ASD/lines_form.html
447. A. Thorne, U. Litzén, S. Johansson, *Spectrophysics* (Springer, Berlin, Heidelberg, 1999)
448. N.V. Tkachenko, *Optical Spectroscopy – Methods and Instrumentation* (Elsevier, 2006)
449. M. Quack, F. Merkt (eds.), *Handbook of High-Resolution Spectroscopy* (Wiley, Chichester, 2011)
450. E. Rodhuner, *Optical Spectroscopy - Fundamentals and Advanced Applications* (World Scientific, 2018)
451. J. Kuba, L. Kucera, F. Plzak, M. Dvorak, J. Mraz, *Coincidence Tables for Atomic Spectroscopy* (Elsevier, Amsterdam, 1965)
452. R. Beck, W. Englisch, K. Gürs, *Tables of Laser Lines in Gases and Vapors*, 3rd edn., Springer Ser. Opt. Sci., Vol.2 (Springer, Berlin, Heidelberg 1980)
453. M.J. Weber, *Handbook of Laser Wavelengths* (CRC Press, Boca Raton, 1999)
454. A.C.G. Mitchell, M.W. Zemansky, *Resonance Radiation and Excited Atoms* (Cambridge University Press, Cambridge, 1961)
455. K. Burnett (ed.), *Spectral Line Shapes* (de Gruyter, Berlin, 1983)
456. I.I. Sobelmann, L.A. Vainshtein, E.A. Yukov, *Excitation of Atoms and Broadening of Spectral Lines*, 2nd edn., Springer Ser. Chem. Phys., Vol.7 (Springer, Berlin, Heidelberg 1995)
457. G.W.F. Drake (ed.), *Atomic, Molecular, & Optical Physics Handbook, Chaps. 19 and 57* (AIP, Woodbury, NY, 1996)
458. J.M. Hartmann, V. Sironneau, C. Boulet, T. Svensson, J.T. Hodges, C. Xu, Collisional broadening and spectral shapes of absorption lines of free and nanopore-confined O_2 gas. Phys. Rev. A **83**, 032510 (2013)
459. C.H. Corliss, W.R. Bozman, *Experimental Transition Probabilities for Spectral Lines of Seventy Elements, NBS Monograph 53* (National Bureau of Standards, Washington, DC, 1962)
460. C.H. Corliss, J.L. Tech, Revised lifetimes of energy levels in neutral iron. J. Res. Natl. Bur. Stand. Sect. A **80**, 787 (1976)
461. E.T. Kennedy, Plasmas and intense laser light. Contemp. Phys. **25**, 31 (1984)
462. M.N. Rosenbluth, R.Z. Sagdeev (eds.), *Physics of Laser Plasma* (North-Holland, Elsevier, Amsterdam, 1991)
463. F.J. Wuilleumier, Y. Petroff, I. Nenner (eds.), *Vacuum Ultraviolet Radiation Physics* (World Scientific, Singapore, 1993)
464. E. Oks, *Plasma Spectroscopy, Springer Series on Atoms and Plasmas*, vol. 9 (Springer, Berlin, Heidelberg, 1995)
465. M. Richardson, Laser-Produced Plasmas, in J.A.R. Samson, D.L. Ederer (eds): *Vacuum Ultraviolet Spectroscopy* (Elsevier, 1998)
466. G. O'Sullivan, A. Cummings, C.Z. Dong, P. Dunne, P. Hayden, O. Morris, E. Sokell, F. O'Reilly, M.G. Su, J. White, Emission and absorption in laser produced plasmas: processes and applications. J. Physics Conf. Ser. **163**, 012003 (2009)

467. N.G. Basov, Yu.A. Zakharenkov, N.N. Zorev, G.V. Sklizkov, A.A. Rupasov, A.S. Shikanov, *Heating and Compression of Thermonuclear Targets by Laser Beams* (Cambridge University Press, Cambridge, 1986)
468. S.E. Bodner, A.J. Schmitt, J.D. Sethian, Laser requirements for a laser fusion energy power plant. High Power Laser Sci. Eng. **1**, 2 (2013)
469. R.S. Craxton et al., Direct-drive inertial confinement fusion: A review. Phys. Plasmas **22**, 110501 (2015)
470. H. Hora, S. Eliezer, G.J. Kirchhoff, N. Nissim, J.X. Wang, P. Lalousis, Y.X. Xu, G.H. Miley, J.M. Martinez-Val, W. McKenzie, J. Kirchhoff, Road map to clean energy using laser beam ignition of boron-hydrogen fusion. Laser Part. Beams **35**, 730 (2017)
471. R.D. Cowan, Progress in the spectroscopy of highly ionized atoms and its use in plasma diagnostics. Phys. Scr. **24**, 615 (1981)
472. C. de Michelis, M. Mattioli, Spectroscopy and impurity behaviour in fusion plasmas. Rep. Prog. Phys. **47**, 1233 (1984)
473. E. Källne, J. Källne, X-ray spectroscopy in fusion research. Phys. Scr. **T17**, 152 (1987)
474. R.J.E. Jaspers, Plasma spectroscopy. Fusion Sci. Tech. **57**, 421 (2010)
475. W. Gonzalez, W. Biel, Ph. Mertens, M. Tokar, O. Marchuk, Ch. Linsmeier, Conceptual studies on spectroscopy and radiation diagnostic systems for plasma control on DEMO. Fusion Eng. Design **146**, 2297 (2019)
476. L. Kay, A van de Graaff beam as a source of atomic emission spectra. Phys. Lett. **5**, 36 (1963)
477. S. Bashkin, Optical spectroscopy with van de Graaff accelerators. Nucl. Instrum. Methods **28**, 88 (1964)
478. J.O. Stoner, J.A. Leavitt, Reduction in Doppler broadening of spectral lines in fast-beam spectroscopy. Appl. Phys. Lett. **18**, 477 (1971)
479. R. Hutton, L. Engström, E. Träbert, Nucl. Instrum. Methods Phys. Res. B **31**, 294 (1988)
480. L.J. Curtis, H.J. Berry, J. Bromander, A meanlife measurement of the $3d\ ^2D$ resonance doublet in SiII by a technique which exactly accounts for cascading. Phys. Lett. A **34**, 169 (1971)
481. L. Engström, CANDY, a computer program to perform ANDC analysis of cascade corrected decay curves. Nucl. Instrum. Methods **202**, 369 (1982)
482. I. Martinson, A. Gaupp, Atomic physics with ion accelerators – beam-foil spectroscopy. Phys. Rep. **15**, 113 (1974)
483. H.G. Berry, L.J. Curtis, D.G. Ellis, R.M. Schectman, Hyperfine quantum beats in oriented ^{14}N IV. Phys. Rev. Lett. **35**, 274 (1975)
484. U. Fano, J.H. Macek, Impact excitation and polarization of the emitted light. Rev. Mod. Phys. **45**, 553 (1973)
485. W. Wittmann, K. Tillmann, H.J. Andrä, P. Dobberstein, Fine-structure measurement of ^{4}He by zero-field quantum beats. Z. Physik **257**, 279 (1972)
486. O. Poulsen, J.L. Subtil, Hyperfine structure measurement in Be III. J. Phys. B **7**, 31 (1974)
487. S. Bashkin (ed.), *Beam-Foil Spectroscopy*, Topics Current Phys., Vol.1 (Springer, Berlin, Heidelberg 1976)
488. I.A. Sellin, D.J. Pegg (eds.), *Beam-Foil Spectroscopy*, Vols.1,2 (Plenum, New York 1976)
489. E.J. Knystautas, R. Drouin (eds.), Proc. 6th Int. Conf. on Fast Ion Beam Spectroscopy. Nucl. Instrum. Methods **202** (1982)
490. I. Martinson, Recent progress in the studies of atomic spectra and transition probabilities by beam-foil spectroscopy. Nucl. Instrum. Methods **202**, 1 (1982)
491. H.G. Berry, M. Mass, Beam-foil spectroscopy. Ann. Rev. Nucl. Part. Sci. **32**, 1 (1982)
492. J.D. Silver, N.J. Peacock (eds.), The Physics of Highly Ionized Atoms. Nucl. Instrum. Methods Phys. Res. B **9**, 359 (1985)
493. I. Martinson, The spectroscopy of highly ionized atoms. Rep. Prog. Phys. **52**, 157 (1989)
494. S.M. Schafroth, J.C. Austin (eds.), *Accelerator-Based Atomic Physics – Techniques and Applications* (AIP Press, New York, 1997)
495. I. Akasaki, Fascinating journeys into blue light (Nobel Lecture). Ann. Physik **527**, 311 (2015)

496. H. Amano, Growth of GaN on sapphire via low-temperature deposited buffer layer and realization of p-type GaN by Mg doping followed by low-energy electron beam irradiation (Nobel Lecture). Ann. Physik **527**, 327 (2015)
497. S. Nakamura, Background story of the invention of efficient blue InGaN light emitting diodes (Nobel Lecture). Ann. Physik **527**, 335 (2015)
498. L.N. Hu, W.S. Li, H.Y. Lin, Y. Li, H. Zhang, K. Svanberg, S. Svanberg, Towards an optical diagnostic system for otitis media using a combination of otoscopy and spectroscopy, J. Biophotonics, Doi.org/https://doi.org/10.1002/jbio.201800305 (2019)
499. E.F. Schubert, J.K. Kim, Solid-state light sources getting smart. Science **308**, 1274 (2005)
500. N. Zheludev, The life and times of the LED – a 100-year history. Nature Photonics **1**, (2007)
501. V.K. Khanna, *Fundamentals of Solid State Lighting: LEDs, OLEDs, and Their Application in Illumination and Displays* (CRC Press 2014)
502. M. Brydegaard, A. Merdasa, H. Jayaweera, J. Ålebring, S. Svanberg, Versatile multispectral microscope based on light emitting diodes. Rev. Sci. Instr. **82**, 123106 (2011)
503. J. Schwinger, On the classical radiation of accelerated electrons. Phys. Rev. **75**, 1912 (1949)
504. D.H. Tomboulian, P.L. Hartman, Spectral and angular distribution of ultraviolet radiation from the 300 MeV Cornell synchrotron. Phys. Rev. **102**, 1423 (1956)
505. R.P. Madden, K. Codling, Phys. Rev. Lett. **10**, 516 (1963)
506. O.J. Jackson, *Classical Electrodynamics*, 2nd edn. (Wiley, New York, 1975)
507. E. Matthias, R.A. Rosenberg, E.D. Poliakoff, M.G. White, S.-T. Lee, D.A. Shirley, Time-resolved VUV spectroscopy using synchrotron radiation: Fluorescent lifetimes of atomic Kr and Xe. Chem. Phys. Lett. **52**, 239 (1977)
508. T. Müller, G. Zimmerer, Time-resolved spectroscopy with synchrotron radiation in the vacuum ultraviolet. Phys. Scr. **T17**, 177 (1987)
509. R. Rigler, O. Kristensen, J. Roslund, P. Thyberg, K. Oba, M. Eriksson, Molecular structures and dynamics: Beamline for time-resolved spectroscopy at the MAX synchrotron in Lund. Phys. Scr. **T17**, 204 (1987)
510. R.P.S.M. Lobo, J.D, Laveigne, D.H. Reitze, D.B. Tanner, G.L. Carr, Subnanosecond, time-resolved, broadband infrared spectroscopy using synchrotron radiation. Rev. Sci. Instr. **73**, 1 (2002)
511. L. Stebel, M. Malvestuto, V. Capogrosso, P. Sigalotti, B. Ressel, F. Bondino, E. Magnano, G. Cautero, F. Parmigiani, Time-resolved soft x-ray absorption setup using multi-bunch operation modes at synchrotrons. Rev. Sci. Instr. **82**, 123109 (2011)
512. H. Motz, Undulators and free-electron lasers. Contemp. Phys. **20**, 547 (1979)
513. V.V. Mikhailin, Synchrotron and undulator radiations and their applications in spectroscopy. Phys. Usp. **56**, 412 (2013)
514. J.A. Clarke, *The Science and Technology of Unulators and Wigglers* (Oxford University Press, Oxford, 2004)
515. J.M.J. Madey, Stimulated emission of Bremsstrahlung in a periodic magnetic field. J. Appl. Phys. **42**, 1906 (1971)
516. D.A.G. Deacon, L.R. Elias, J.M.J. Madey, G.J. Ramian, H.A. Schwettman, T.I. Smith, First operation of free electron laser. Phys. Rev. Lett. **38**, 892 (1977)
517. H.P. Freund, R.K. Parker, Free-electron lasers. Sci. Am. **260**(4), 56 (1989)
518. E.L. Saldin, E.A. Schneidmiller, M.V. Yurkov, The physics of free electron lasers: An Introduction. Phys. Rep. **260**, 187 (1995)
519. J. Feldhaus, FLASH—the first soft x-ray free electron laser (FEL) user facility. J. Phys. B **43** (2010)
520. E.A. Seddon, J.A. Clarke, D.J. Dunning, C. Masciovecchio, C. J. Milne, F. Parmigiani, D. Rugg, J.C.H. Spence, N.R. Thompson, K. Ueda, S.M. Vinko, J. S. Wark, W. Wurth, Short-wavelength free-electron laser sources and science: A review. Reports on Progr. Phys. **80** (2017)
521. K. Ueda (ed.), *X-Ray Free Electron Laser* (MPDI Books, 2018)
522. J.M. Ortega, Y. Lapierre, B. Girard, M. Billardon, P. Elleaume, C. Baziin, M. Bergher, M. Velghe, Y. Petroff, Ultraviolet coherent generation from an optical klystron. IEEE J. Quantum Electron. **QE-21**, 909 (1985)

523. S. Werin, M. Eriksson, J. Larsson, A. Persson, S. Svanberg, First results in coherent harmonic generation using the undulator at the MAX-Lab electron storage ring. Nucl. Instrum. Methods Phys. Res. A **290**, 589 (1990)
524. R. Bonifacio, C. Pellegrini, I.M. Narducci, Collective instabilities and high-gain regime in a free electron laser. Opt. Commun. **50**, 373 (1984)
525. J.R. Schneider, Properties and scientific perspectives of a single-pass X-ray free- electron laser. Nucl. Instrum. Methods Phys. Res. A **388**, 41 (1997)
526. E.B. Szarmes, *Classical Theory of Free-Electron Lasers* (IOP Science, 2014)
527. C. Joshi, T. Katsouleas (eds.), *Laser Accelerators of Particles*, AIP Conf. Proc. Vol.130 (Am. Inst. Physics, New York 1985)
528. K. Siegbahn, 'Electron spectroscopy for solids, surfaces, liquids and free molecules.' In: *Molecular Spectroscopy* (Heyden & Son, London 1983) Chap.15, p.227
529. H.N. Chapman et al., Femtosecond diffractive imaging with a soft-X-ray free-electron laser. Nat. Phys. **2**, 839 (2006)
530. E.E. Koch (ed.), *Handbook on Synchrotron Radiation*, Vols.1–3, (NorthHolland, Amsterdam 1983, 1986, 1987)
531. M. Altarelli, F. Schachter, J. Cross, Making ultrabright X-rays. Sci. Am. **279**(6), 36 (1998)
532. H. Winick, *Synchrotron Radiation Sources – A Technical Primer* (World Scientific, River Edge, 1994)
533. H. Wiedemann, *Synchrotron Radiation* (Springer, 2003)
534. J.E. Rubensson, *Synchrotron Radiation – An Everyday Applications of Special Relativity* (Morgan & Claypool, 2016)
535. X.Y. Zhang, *Synchrotron Radiation Applications* (World Scientific, 2018)
536. Ph. Willmott, *An Introduction to Synchrotron Radiation: Techniques and Applications, 2nd* Ed. (John Wiley, 2019)
537. H.H. Malitson, The solar energy spectrum. Sky and Telescope **29**(4), 162 (1965)
538. W.K. Pratt, *Laser Communication Systems* (Wiley, New York, 1969)
539. S.P. Davis, *Diffraction Grating Spectrometers* (Holt, Rinehard, Winston, New York, 1970)
540. J.M. Lerner and A. Thevenon, The optics of spectroscopy. https://web.mit.edu/8.13/8.13d/manuals/Hydrogenic/jy-theory-optics-spectroscopy.pdf (2002)
541. D.J. Brady, *Optical Imaging and Spectroscopy* (Wiley, 2008)
542. D.A. Skoog et al., Principles of Instrumental Analysis (Holt-Saunders. Philadelphia **1980**, 1997 (2017)
543. *Handbook of Diffraction Gratings, Ruled and Holographic* (Jobin-Yvon Optical Systems, Metuchen, NJ 1970)
544. M.C. Hutley, *Diffraction Gratings* (Academic Press, London, 1982)
545. E. Kristensson, J. Bood, M. Aldén, E. Nordström, J.J. Zhu, S. Huldt, P.-E. Bengtsson, H. Nilsson, E. Berrocal, A. Ehn, Stray light suppression in spectroscopy using periodic shadowing. Opt. Express **22**, 7711 (2014)
546. M. Linne, Imaging in the optically dense regions of a spray: A review of developing techniques. Prog. Energ. Combust. **39**, 403 (2013)
547. E. Kristensson, E. Berrocal, Crossed patterned structured illumination for the analysis and velocimetry of transient turbid media. Sci. Reports **8**, 11751 (2018)
548. E. Kristensson, M. Richter, S.-G. Pettersson, M. Aldén, S. Andersson-Engels, Spatially resolved, single-ended two-dimensional visualization of gas flow phenomena using structured illumination. Appl. Opt. **47**, 3927 (2008)
549. A. Ehn, J. Bood, Z.M. Li, E. Berrocal, M. Aldén, E. Kristensson, FRAME: femtosecond videography for atomic and molecular dynamics. Light: Science & Applications **6**, e17045 (2017)
550. Y.Y. Lin, S. Svanberg, Foreground scattering elimination by inverse lock-in-like spatial modulation. Vision **4**, 37 (2020)
551. H. Walther, Das Kernquadrupolmoment des ^{55}Mn. Z. Physik **170**, 507 (1962)
552. J.M. Vaughan, *The Fabry-Pérot Interferometer* (Hilger, Bristol, 1989)

553. N. Ismail, C. Calil Kores, D. Geskus, M. Pollnau, Fabry-Pérot resonator: spectral line shapes, generic and related Airy distributions, linewidths, finesses, and performance at low or frequency-dependent reflectivity. Opt. Express **24**, 16366 (2016)
554. W. Demtröder, *Laser Spectroscopy*, *Vol. 1: Basic Principles, and Vol. 2: Experimental Techniques* (Springer, Berlin, Heidelberg, 2008)
555. R.W. Ramirez, *The FFT: Fundamentals and Concepts* (Prentice Hall, Englewood Cliffs, NJ, 1985)
556. J.F. James, *A Student's Guide to Fourier Transforms* (Cambridge University Press, Cambridge, 1995)
557. J.S. Walker, *Fast Fourier Transforms*, 2nd edn. (CRC Press, Boca Raton, 1996)
558. G. Guelachvili, High accuracy Doppler-limited 10^6 samples Fourier transform spectroscopy. Appl. Opt. **17**, 1322 (1978)
559. S. Tolansky, *An Introduction to Interferometry* (Longmans, London, 1973)
560. P. Hariharan, *Basics of Interferometry* (Academic Press, London, 1992)
561. D.B. Chase, J.F. Rabold (eds.), *Fourier Transform Raman Spectroscopy* (Academic Press, London, 1994)
562. Th. Kreis, *Holographic Interferometry – Principles and Methods* (Akademie Verlag, Berlin, 1996)
563. B.C. Smith, *Advanced Fourier Transform Infrared Spectroscopy* (Springer, Berlin, Heidelberg, 1997)
564. B.P. Abbott et al., (LIGO Scientific Collaboration and Virgo Collaboration): Observation of gravitational waves from a binary black hole merger. Phys. Rev. Lett. **116**, 061102 (2016)
565. R. Weiss, LIGO and the discovery of gravitational waves, I: Nobel Lecture. Ann. Phys. **531**, 1800349 (2019)
566. B.C. Barish, Nobel lecture: LIGO and gravitational waves II. Rev. Mod. Phys. **90**, 040502 (2018)
567. K.S. Thorne, LIGO and gravitational waves, III: Nobel Lecture. Ann. Phys **531**, 1800350 (2019)
568. F. Antonucci et al., and the LISA International Team: LISA Pathfinder: mission and status. Class. Quant. Grav. **28**, 094001 (2011)
569. A. Sutton, K. McKenzie, B. Ware, D.A. Shaddock, Laser ranging and communications for LISA. Opt. Express **18**, 20759 (2010)
570. *Optical Industry & Systems Purchasing Directory*, 26th edn. (Laurin Publ. Co., Pittsfield, MA 1980) p.B-114
571. S.A. Kalogirou, *Solar Energy Engineering: Processes and Systems* (Academic Press, 2014)
572. A.A. Bayod-Rújula, Solar Photovoltaics (PV), Chap. 8 in *Solar Hydrogen Production* (Academic Press, 2019)
573. R. Wang, M. Mujahid Y. Duan Z.K. Wang, J.L Xue, Y. Yang, A review of perovskites solar cell stability. Adv. Funct. Mat. **29**, 1808843 (2019)
574. J.Y. Kim, J.W. Lee, H.S. Jung, H.J. Shin, N.G. Park, High-efficiency perovskite solar cells. Chem. Rev. **120**, 7867 (2020)
575. D. Bronzi, F. Villa, S. Tisa, A. Tosi, F. Zappa, SPAD figures of merit for photon-counting, photon-timing and imaging applications: A review. IEEE Sensor J. **16**(1), 3 (2016)
576. C. Bruschini, H. Homulle, I.M. Antolovic, S. Burri, E. Charbon, Single-photon avalanche diode imagers in biophotonics: Review and outlook. Light: Sci. Appl. **8**, 1 (2019)
577. R.W. Boyd, *Radiometry and the Detection of Optical Radiation* (Wiley, New York, 1983)
578. E.L. Dereniak, D.G. Crowe, *Optical Radiation Detectors* (Wiley, New York, 1984)
579. G.H. Rieke, *Detection of Light from the Ultraviolet to the Submillimeter Region* (Cambridge University Press, Cambridge, 1994)
580. R.H. Kingston, *Optical Sources, Detectors and Systems – Fundamentals and Applications* (Academic Press, New York, 1995)
581. E.L. Dereniak, G.D. Boreman, *Infrared Detectors and Systems* (Wiley, New York, 1996)
582. J. Fraden, *Handbook of Modern Sensors: Physics, Designs, and Applications, 5th ed.* (Springer, 2016)

583. M. Lampton, The microchannel image intensifier. Sci. Am. **245**(5), 46 (1981)
584. W.S. Boyle, CCD – An extention of man´s view. Rev. Mod. Phys. **82**, 2305 (2010)
585. G.E. Smith, The invention and early history of the CCD. Rev. Mod. Phys. **82**, 2307 (2010)
586. C.N. Anagnostopolous, M.M. Blouke, M.P. Lesser (eds.), *Solid State Sensor Arrays and CCD Cameras.* SPIE **2654** (1996)
587. G.C. Holst, T.S. Lomheim, *CMOS/CCD Sensors and Camera Systems*, 2nd edn. (SPIE, Bellingham, 2011)
588. D. Durini, *High Performance Silicon Imaging. Fundamentals and Applications of CMOS and CCD Sensors* (Elsevier – Woodhead, 2014)
589. T. Kuroda, *Essential Principles of Image Sensors* (CRC Press, 2015)
590. A. Boukhayma, *Ultra Low Noise CMOS Image Sensors* (Springer, 2018)
591. R. Navarro, The optical design of the human eye: a critical review. J. Optometry **2**, 3 (2009)
592. K. Rogers, *The Eye: The Physiology of Human Perception* (Rosen Publ. Group, 2010)
593. M.A. Stern, A. Kaiser, H.W. Mahler, E. DiBenedetto, Low-light-level image-amplifying device with full color capability. Journal of the SMPTE **83**, 185 (1974)
594. S. Svanberg, J. Johansson, Image registering in color at low light intensity. US Patent 5,483,379 (1996)
595. G. Blasse, B.C. Grabmaier, *Luminescent Materials* (Springer, New York, 1994)
596. A. Kitai, *Luminescent Materials and Applications* (Wiley, 2008)
597. J. Miyahara, The imaging plate: A new radiation image sensor. Chem. Today **223**, 29 (1989)
598. J.D. Cox, D.S. Langford, D.W. Williams, 'Electronic intraoral dental imaging system employing a direct sensing CCD array.' In: *X-ray Detector Physics and Applications II*, ed. by V.J. Orphan, SPIE **2009** (1993)
599. B. Vandenberghe, R. Jacobs, H. Bosmans, Modern dental imaging: A review of the current technology and clinical applications in dental practice. Review Eur. Radiol. **20**, 2637 (2010)
600. H.A. Macleod, *Thin-Film Optical Filters , 5th Ed.* (CRC Press, 2017)
601. *The Photonics Design & Application Handbook* (Laurin Publ. Comp., Pittsfield, MA 1990)
602. G.A. Kopp, Liquid crystal tunable birefringent filters. Proc. SPIE **2830**, 345 (1996)
603. L. Driencourt, F. Federspiel, D. Kazazis, L.T. Tseng, R. Frantz, Y. Ekinci, R. Ferrini, B. Gallinet, Electrically tunable multicolored filter using birefringent plasmonic resonators and liquid crystals. ACS Photonics **7**, 444 (2020)
604. G.R. Fowles, *Introduction to Modern Optics* (Holt, Rinehart and Winston, New York, 1968)
605. J. Strong, *Procedures in Experimental Physics* (Prentice Hall, New York, 1945)
606. M. Kasha, Transmission filters for the ultraviolet. J. Opt. Soc. Am. **38**, 929 (1948)
607. K. Bennett, R.L. Byer, Computer controllable wedge-plate optical variable attenuator. Appl. Opt. **19**, 2408 (1980)
608. C.G. Granqvist, *Handbook of Inorganic Electrochromic Materials* (Elsevier, Amsterdam, 1995)
609. C.G. Granqvist, A. Azens, A. Hjelm, L. Kullman, G.A. Niklasson, D. Ronnow, M. Stromme Mattsson, M. Veszelei, G. Vaivars, Recent advances in electrochromics for smart windows applications. Solar Energy **63**, 199 (1998)
610. P.M.S. Monk, R.J. Mortimer, D.R. Rosseinsky, *Electrochromism: Fundamentals and Applications* (John Wiley & Sons, 2008)
611. R.J. Mortimer, D.R. Rosseinsky, P.M.S. Monk (eds.), *Electrochromic Materials and Devices* (John Wiley & Sons, 2015)
612. M. Hagedon, S. Yang, A. Russell, J. Heikenfeld, Bright e-paper by transport of ink through a white electrofluidic imaging film. Nature Commun. **3**, 1173 (2012)
613. J. Heikenfeld, A critical review of the present and future prospects for electronic paper. J. Soc. Inf. Display. **19**, 129 (2011)
614. H. Bach, N. Neuroth (eds.), *The Properties of Optical Glass* (Springer, Berlin, Heidelberg, 1995)
615. B. Edlén, The refractive index of air. Metrologia **2**, 71 (1966)
616. J.C. Farman, B.G. Gardiner, J.D. Shanklin, Large losses of total ozone in Antarctica reveal seasonal ClO_x/ NO_2 interaction. Nature **315**, 207 (1985)

617. R.S. Stolarski, The Antarctic ozone hole. Sci. Am. **258**(1), 20 (1988)
618. O.B. Toon, R.P. Turco, Polar stratospheric clouds and ozone depletion. Sci. Am. **264**(6), 40 (1991)
619. J.H. Seinfeld, *Atmospheric Chemistry and Physics of Air Pollution* (Wiley, New York, 1986)
620. T.E. Graedel, D.T. Hawkins, L.D. Claxton, *Atmospheric Chemical Compounds: Sources, Ocurrence, Bioassay* (Academic Press, Orlando, 1986)
621. B.A. Thrush, The chemistry of the stratosphere. Rep. Prog. Phys. **51**, 1341 (1988)
622. T.H. Graedel, P.J. Crutzen, The changing atmosphere. Sci. Am. **261**(3), 28 (1989)
623. R.W. Baubel, D.B. Turner, A.C. Stern, *Fundamentals of Air Pollution*, 3rd edn. (Academic Press, London, 1994)
624. C.S. Zeregos, A.F. Bais, *Solar Ultraviolet Radiation, Modelling, Measurements and Effects* (Springer, Berlin, Heidelberg, 1997)
625. W. Michaelis, *Air Pollution* (Springer, Berlin, Heidelberg, 1997)
626. S.L. Valley (ed.), *Handbook of Geophysics and Space Environments* (McGraw-Hill, New York, 1965)
627. M. Vergez-Deloncle, Absorption des radiations infrarouges par les gas atmosphériques. J. Physique **25**, 773 (1964)
628. R.A. Houghton, G.W. Woodwell, Global climatic change. Sci. Am. **260**(4), 18 (1989)
629. B.J. Mason, The greenhouse effect. Contemp. Phys. **30**, 417 (1989)
630. A. Wiin-Nielsen, The increased greenhouse effect - A general review. Proc. Indian Acad. Sci. - Earth and Planetary Sciences **102**, 3 (1993)
631. B.J. Mason, Predictions of climate changes caused by manmade emissions of greenhouse gases: A critical assessment. Contemp. Phys. **36**, 299 (1995)
632. A. Gore, *An Inconvenient Truth: The Planetary Emergency of Global Warming and What We Can Do About It* (Rodale Books, 2006)
633. C. Rosenzweig, D. Rind, A. Lacis, D. Manley (Eds.), *Our Warming Planet - Topics in Climate Dynamics* (World Scientific, 2018)
634. S. Manabe, A.J. Broccoli, *Beyond Global Warming – How Numerical Models Reveiled the Secrets of Climate Change* (Princeton University Press, Princeton, 2020)
635. Hudson and Hudson (1975), quoted in [642]
636. B.A. Thompson, P. Harteck, R.R. Reeves Jr., Ultraviolet absorption coefficients of CO_2, CO, O_2, H_2O, N_2O, NH_3, NO, SO_2, and CH_4 between 1850 and 4000 A. J. Geophys. Res. **68**, 6431 (1963)
637. P.L. Hanst, *QA Soft '96, Database and quantitative analysis program for measurements of gases* (Infrared Analysis Inc., Anaheim, CA, 1996)
638. E. Gordon, L.S. Rothman et al., The HITRAN2016 molecular spectroscopic database. J. Quant. Spectr. Rad. Transf. **203**, 3 (2017)
639. N.G. Jerlov, *Optical Oceanography* (Elsevier, Amsterdam, 1968)
640. T. Stefanick, The nonacoustic detection of submarines. Sci. Am. **258**(3), 25 (1988)
641. C.D. Mobley, *Light and Water – Radiative Transfer in Natural Waters* (Academic Press, London, 1994)
642. R.M. Measures, *Laser Remote Sensing* (Wiley-Interscience, New York, 1984)
643. D.B. Northam, M.A. Guerra, M.E. Mock, I. Itzkan, C. Deradourian, High repetition rate frequency-doubled Nd:YAG laser for airborne bathymetry. Appl. Opt. **20**, 968 (1981)
644. P. Armbruster, F.P. Hessberger, Making new elements. Sci Am. **279**(5), 50 (1998)
645. S. Hofman, New elements – approaching $Z = 114$. Rep. Prog. Phys. **61**, 639 (1998)
646. Yu. Ts. Oganessian *et al.*, Experimental studies of the ^{249}Bk + ^{48}Ca reaction including decay properties and excitation function for isotopes of element 117, and discovery of the new isotope ^{277}Mt. Phys. Rev. C **87**, 054621 (2013)
647. Ch.E. Düllmann, 118 and counting … The Periodic Table on its 150th anniversary. Angew. Chemie Int. Ed. **58**, 4070 (2019)
648. B. Welz, *Atomic Absorption Spectroscopy* (VCH, Weinheim, 1985)
649. Flame Atomic Absorption Spectroscopy https://www.agilent.com/cs/library/brochures/AA-5991-8145EN-methods-primer.pdf

650. D.A. Skoog, *Principles of Instrumental Analysis*, 3rd edn. (Saunders, Philadelphia, 1985)
651. D.A. Skoog, M.D. West, *Fundamentals of Analytical Chemistry*, 4th edn. (Saunders, Philadelphia, 1986)
652. S.E. Sholupov, A.A. Ganeev, Zeeman atomic absorption spectrometry using high frequency modulated light polarization. Spectrochim. Acta B **50**, 1227 (1995)
653. H.H. Willard, L.L. Merritt Jr., J.A. Dean, F.A. Settle Jr., *Instrumental Methods of Analysis*, 6th edn. (Wadsworth, Belmont, CA, 1981)
654. G.D. Christian, J.E. O'Reilly (eds.), *Instrumental Analysis*, 2nd edn. (Allyn and Bacon, Boston, 1986)
655. J.U. White, Long optical paths of large aperture. J. Opt. Soc. Am. **32**, 285 (1942)
656. J.U. White, Very long paths in air. J. Opt. Soc. Am. **66**, 411 (1976)
657. H. Edner, A. Sunesson, S. Svanberg, L. Unéus, S. Wallin, Differential optical absorption spectroscopy system used for atmospheric mercury monitoring. Appl. Opt. **25**, 403 (1986)
658. J. Hodgkinson, D. Masiyano, R.P. Tatam, Using integrating spheres as absorption cells: path-length distribution and application of Beer's law. Appl. Optics **48**, 5748 (2009)
659. S. Bergin, J. Hodgkinson, D. Francis, R. Tatam, Ratiometric pathlength calibration of integrating sphere-based absorption cells. Opt. Express **28**, 19574 (2020)
660. T. Svensson, E. Adolfsson, M. Lewander, C.T. Xu, S. Svanberg, Disordered, strongly scattering porous materials as miniature multi-pass gas cells. Phys. Rev. Lett. **107**, 143901 (2011)
661. J. Larsson, L. Mei, P. Lundin, J. Bood, S. Svanberg, Development of a compact multipass oxygen sensor used for gas diffusion studies in opaque media. Appl. Optics **54**, 9772 (2015)
662. H.A. Szymanski, *Interpreted Infrared Spectra*, Vols.1–3 (Plenum, New York 1964–67)
663. H.A. Szymanski, R.E. Erickson, *Infrared Band Handbook*, Vols.1, 2 (IFI/Plenum, New York 1970)
664. S. Hüfner, *Optical Spectra of Transparent Rare Earth Compounds* (Academic Press, New York, 1978)
665. A.P.B. Lever, *Inorganic Electronic Spectroscopy*, 2nd edn. (Elsevier, Amsterdam, 1984)
666. B. Smith, *Infrared Spectral Interpretation* (Springer, Berlin, Heidelberg, 1997)
667. T. Jolliffe*, Principal Component Analysis, 2nd ed.* (Springer, 2002)
668. K. Esbensen, *Multivariate Data Analysis in Practice* (CAMO ASA, Oslo, 2006)
669. *IUPAP Tables of Wavenumbers for the Calibration of Infrared Spectrometers* (Butterworths, London 1961) p.560
670. R.J. Pressley (ed.), *Handbook of Lasers (with Selected Data on Optical Technology* (CRC Press, Cleveland, Ohio 1971) p.407
671. M.M. Sushchinskii, *Raman Spectra of Molecules and Crystals* (Israel Progr. for Sci. Transl., Jerusalem 1972)
672. A. Weber (ed.), *Raman Spectroscopy of Gases and Liquids*, Topics Current Phys., Vol.11 (Springer, Berlin, Heidelberg 1979)
673. D.P. Strommen, K. Nakamoto, *Laboratory Raman Spectroscopy* (Wiley, New York, 1984)
674. J.F. Ferraro, K. Nakamoto, *Introductory Raman Spectroscopy* (Academic Press, London, 1994)
675. D.W. Shipp, F. Sinjab, I. Notingher, Raman spectroscopy: techniques and applications in the life sciences. Adv. Opt. Phot. **9**, 315 (2017)
676. R.R. Jones, D.C. Hooper, L.W. Zhang, D. Wolverson, V.K. Valev, Raman techniques: Fundamentals and frontiers. Nanoscale Res. Lett. **14**, 231 (2019)
677. H. Bergström, Lund Institute of Technology (unpublished)
678. G.L. Eesley, *Coherent Raman Spectroscopy* (Pergamon, Oxford, 1981)
679. S. Svanberg, Lasers as probes for air and sea. Contemp. Phys. **21**, 541 (1980)
680. E. Schanda, *Physical Fundamentals of Remote Sensing* (Springer, Berlin, Heidelberg, 1986)
681. S. Svanberg, 'Fundamentals of atmospheric spectroscopy.' In: *Surveillance of Electromagnetic Pollution and Resources by Electromagnetic Waves*, ed. by T. Lund (Reidel, Dordrecht 1978)

682. C.B. Ludwig, M. Griggs, W. Malkmus, E.R. Bartle, Measurements of air pollutants from satellites, 1: Feasibility considerations. Appl. Opt. **13**, 1494 (1974)
683. E.J. McCartney, *Absorption and Emission by Gases: Physical Processes* (Wiley, New York, 1983)
684. Ph.L. Hanst, S.T. Hanst: 'Gas measurement in the fundamental infrared region.' In: *Air Monitoring by Spectroscopic Techniques* ed. by M.W. Sigrist (Wiley, New York 1994)
685. S. Beirle, U. Platt, M. Wenig, T. Wagner, Weekly cycle of NO_2 by GOME measurements. Atmos. Chem. Phys. **3**, 2225 (2003)
686. T. Wagner, S. Beirle, T. Deutchmann, E. Eigemeier, C. Frankenberg, M. Grzegorski, C. Liu, T. Marbach, U. Platt, M. Penning de Vries, Monitoring of atmospheric t race gases, clouds, aerosols and surface properties from UV/Vis/NIR satellite instruments. J. Opt. A: Pure Appl. Opt. **10**, 104019 (2008)
687. U. Platt, D. Perner, H.W. Pätz, Simultaneous measurement of atmospheric CH_2O, O_3, and NO_2 by differential optical absorption. J. Geophys. Res. **84**, 6329 (1979)
688. U. Platt, D. Perner, 'Measurements of atmospheric trace gases by long path differential UV/visible absorption Spectroscopy.' In: *Optical and Laser Remote Sensing*, ed. by D.K. Killinger, A. Mooradian, Springer Ser. Opt. Sci., Vol.39 (Springer, Berlin, Heidelberg 1983)
689. U. Platt, 'Differential optical absorption spectroscopy (DOAS).' In: *Air Monitoring by Spectroscopic Techniques*, ed. by M.W. Sigrist (Wiley, New York 1994)
690. H. Edner, A. Amer, P. Ragnarson, M. Rudin, S. Svanberg, Atmospheric NH_3 Monitoring by Long-Path UV Absorption Spectroscopy. Proc. SPIE **1269**, 14 (1990)
691. H. Edner, P. Ragnarson, S. Spännare, S. Svanberg, A differential optical absorption spectroscopy (DOAS) system for urban atmospheric pollution monitoring. Appl. Opt. **32**, 327 (1993)
692. H. Axelsson, H. Edner, A. Eilard, A. Emanuelsson, B. Galle, H. Kloo, P. Ragnarson, Measurements of aromatic hydrocarbons with the DOAS technique. Appl. Spectr. **49**, 1254 (1995)
693. U. Platt, J. Stutz, *Differential Optical Absorption Spectroscopy - Principles and Applications* (Springer, 2008)
694. P.V. Johnston, R.L. McKenzie, Long-path absorption measurements of tropospheric NO_2 in rural New Zealand. Geophys. Lett. **11**, 69 (1984)
695. P. Weibring, H. Edner, S. Svanberg, G. Cecchi, L. Pantani, R. Ferrara, T. Caltabiano, Monitoring of volcanic sulphur dioxide emissions using differential absorption lidar (DIAL), differential optical absorption spectroscopy (DOAS), and correlation spectroscopy (COSPEC). Appl. Phys. B **67**, 419 (1998)
696. M.M. Millan, R.M. Hoff, Dispersive correlation spectroscopy: A study of mask optimization procedures. Appl. Opt. **16**, 1609 (1977)
697. D.M. Hamilton, H.R. Varey, M.M. Millan, Remote sensing of atmospheric sulphur dioxide. Atmos. Environ. **12**, 127 (1978)
698. J.A. Hodgeson, W.A. McClenney, P.L. Hanst, Air pollution monitoring by advanced spectroscopic techniques. Science **182**, 248 (1973)
699. T.V. Ward, H.H. Zwick, Gas cell correlation spectrometer: GASPEC. Appl. Opt. **14**, 2896 (1975)
700. H.S. Lee, H.H. Zwick, Gas filter correlation instrument for the remote sensing of gas leaks. Rev. Sci. Instrum. **56**, 1812 (1985)
701. J. Sandsten, H. Edner, S. Svanberg, Gas imaging using infrared gas correlation spectrometry. Opt. Lett. **21**, 1945 (1996)
702. J. Sandsten, P. Weibring, H. Edner, S. Svanberg, Real-time gas-correlation imaging employing thermal background radiation. Opt. Express **6**, 92 (2000)
703. J. Sandsten, H. Edner, S. Svanberg, Gas Visualization of industrial hydrocarbon emissions. Opt. Express **12**, 1443 (2004)
704. U.N. Rao, A. Weber (eds.), *Spectroscopy of the Earth's Atmosphere and Interstellar Medium* (Academic Press, London, 1992)

705. G. Gibson, B. van Well, J. Hodgkinson, R. Pride, R. Strzoda, S. Murray, S. Bishton, M. Padgett, Imaging of methane gas using a scanning, open-path laser system. New J. Physics **8**, 26 (2006)
706. J.P. Dakin, H.O. Edwards, Gas sensor using correlation spectrosopy, compatible with fibre-optic operation. Sens. Actuators B **11**, 9 (1993)
707. J.P. Dakin, H.O. Edwards, B.H. Weigl, Progress with gas sensors using correlation spectroscopy. Sens. Actuators B **29** (1995)
708. P. Dakin, M.J. Gunning, P. Chambers, Z.J. Xin, Detection of gases by correlation spectroscopy. Sens. Actu. B **90**, 124 (2003)
709. Z.G. Guan, M. Lewander, S. Svanberg, Quasi zero-background tuneable diode laser spectroscopy by using a balanced Michelson interferometer. Opt. Express **16**, 21714 (2008)
710. J. Deans, J. Gerhard, L.J. Carter, Analysis of a thermal imaging method for landmine detection, using infrared heating of the sand surface. Infrared Phys. Tech. **48**, 202 (2006)
711. N.T. Thành, D.N. Hào, H. Sahli, Infrared thermography for land mine detection, in *Augmented Vision Perception in Infrared* (Springer, 2009) p. 3
712. R. Bello, Literature review on landmines and detection methods. Frontiers in Science **3**, 27 (2013)
713. J. Goldberg, *Earth Imaging Satellites* (Rosen Publ., 2003)
714. M. Worboys, M. Duckham, *GIS – A Computing Perspective*, 2nd edn. (CRC Press, Boca Raton, 2004)
715. C.H. Chen (ed.), *Signal and Image Processing in Remote Sensing* (CRC Press, Boca Raton, 2007)
716. A.P. Cracknell, L. Hayes, *Introduction to Remote Sensing* (CRC Press, Boca Raton, 2007)
717. M. Borengasser, W.S. Hungate, R. Watkins, *Hyperspectral Remote Sensing* (CRC Press, Boca Raton, 2007)
718. M. Moorkamp, P.G. Lelièvre, N. Linde, A. Khan (eds.), *Integrated Imaging of the Earth: Theory and Applications* (Amer. Geophys. Union, 2016)
719. S. Foerster, L. Guanter, T. Lopez, J. Moreno, M. Rast, M.E. Schaepman, (eds.), *Exploring the Earth System with Imaging Spectroscopy* (Springer, 2019)
720. S.Q. Kidder, T.H. von der Haar, *Satellite Meteorology* (Academic Press, London, 1995)
721. D. Emerson, *Interpreting Astronomical Spectra* (Wiley, Chichester, 1996)
722. K. Robinson, *Spectroscopy: The Key to the Stars - Reading the Lines in Stellar Spectra* (Springer, 2007)
723. J.B. Hearnshow, *The Analysis of Starlight: Two Centuries of Astronomical Spectroscopy* (Cambridge University Press, 2014)
724. R. Bacon, G. Monnet, *Optical 3D-Spectroscopy for Astronomy* (Wiley-VCH Verlag, 2017)
725. J. Tennyson, Astronomical Spectroscopy (World Scientific, 2019)
726. J. Tennyson, *Astronomical Spectroscopy: An Introduction to the Atomic and Molecular Physics of Astronomical Spectroscopy, 3rd edition* (Blackwell, 2019)
727. R.H. Baker, *Astronomy* (Van Nostrand, Princeton, NJ, 1964)
728. R.F. Griffin, *A Photometric Atlas of the Spectrum of Arcturus* (Cambridge Phil. Soc, Cambridge, 1968)
729. J.M. Beckers, C.A. Bridges, L.B. Gilliam, *A High Resolution Atlas of the Solar Irradiance from 380–700nm* (Sacramento Peak Observatory, 1983)
730. D. Dravins, In: *KOSMOS 1980* (Swedish Phys. Soc., Stockholm 1980)
731. B. Edlén, Z. Astrophysik **22**, 30 (1942)
732. B. Edlén, Forbidden lines in hot plasmas. Phys. Scr. **T8**, 5 (1984)
733. E. Biémont, P. Quinet, A database of astrophysical interest covering the UV region. J. Electron Spectr. Rel. Phen. **144–147**, 23 (2005)
734. A. Vidal-Madjar, Th. Encrenaz, R. Ferlet, J.C. Henoux, R. Lallement, G. Vaudair, Galactic ultraviolet astronomy. Rep. Prog. Phys. **50**, 65 (1987)
735. R. Giacconi, X-ray astronomy: Past achievements and future prospects. Phys. Scr. **T61**, 9 (1996)

736. K. Arnaud, R. Smith, A. Siemiginowska (eds.), *Handbook of X-Ray Astronomy* (Cambridge University Press, 2011)
737. C. Bambi, *Tutorial Guide to X-ray and Gamma-ray Astronomy - Data Reduction and Analysis* (Springer, 2020)
738. H.J. Habing, G. Neugebauer, The infrared sky. Sci. Am. **251**(5), 42 (1984)
739. C. Collins Peterson, J.C. Brandt, *Hubble Vision, Astronomy with the Hubble Space Telescope* (Cambridge University Press, Cambridge 1995)
740. D. Fischer, H. Duerbeck, *Hubble – A New Window to the Universe* (Copernicus-Springer, New York, 1996)
741. P. Benvenuti, F.D. Machetto, E.J. Schreier (eds.), *Science with the Hubble Space Telescope-II* (Space Telescope Science Institute, Baltimore, 1996)
742. T. Dickinson, *Hubble's Universe: Greatest Discoveries and Latest Images, 2^{nd} Ed.* (Firefly, 2017)
743. J. Bell, *Hubble Legacy: 30 Years of Discoveries and Images* (Sterling, 2020)
744. D.S. Leckrone, S. Johansson, G.M. Wahlgren, S.J. Adelman, High resolution UV stellar spectroscopy with the HST/GHRS, challenges and opportunities for atomic physics. Phys. Scr. **T47**, 149 (1993)
745. http://oposite.stsci.edu/ Material created with support to AURA/STScI from NASA contract NAS5–26555
746. P. Gardner, J.C. Mather, M. Clampin, R. Doyon, The James Webb Space Telescope. Space Sci. Rev. **123**, 485 (2009)
747. R.D. Gehrz, T.L. Roellig, M.W. Werner, G.G. Faziod, J.R. Houcke, F.J. Low, G.H. Rieke, B.T. Soifer, D.A. Levine, The NASA Spitzer Space Telescope. Rev. Sci. Instr. **78**, 011302 (2007)
748. J.M. Beckers, Adaptive optics for astronomy: Principles, performance and applications. Am. Rev. Astron. Astrophys. **31**, 13 (1993)
749. F. Roddier, *Adaptive Optics for Astronomy* (Cambridge University Press, 1999)
750. N. Ageorges, C. Dainty (eds.), *Laser Guide Star Adaptive Optics for Astronomy* (Springer NATO ASI Series, 2000)
751. I.S. Bowen, The spectrum and composition of the gaseous nebulae. Astrophys. J. **81**, 1 (1935)
752. S. Johansson, Strong Fe II fluorescence lines in RR Tel and V1016 Cyg excited by C IV in a Bowen mechanism. Mon. Not. R. Astr. Soc. **205**, 71P (1983)
753. S. Johansson, V.S. Letokhov, Radiative cycle with stimulated emission from atoms and ions in an astrophysical plasma. Phys. Rev. Lett. **90**, 011101 (2003)
754. D.W. Weedman, *Quasar Astronomy* (Cambridge University Press, Cambridge, 1986)
755. T.J.-L. Courvoisier, E.I. Robson, The Quasar 3C 273. Sci. Am. **264**(6), 24 (1991)
756. P.S. Osmer, Quasars as probes of the distant and early universe. Sci. Am. **246**(2), 96 (1982)
757. P. Murdin, The supernova in the Large Magellanic Cloud. Contemp. Phys. **28**, 441 (1987)
758. W. Hillebrandt, P. Höflich, The supernova 1987A in the Large Magellanic Cloud. Rep. Prog. Phys. **52**, 1421 (1989)
759. D.N. Schramm, J.W. Truran, New physics from supernova 1987A. Phys. Rep. **189**, 89 (1990)
760. P. Murdin, *End of Fire: The Supernova in the Large Magellanic Cloud* (Cambridge University Press, Cambridge, 1990)
761. A. Ray, IAUS 331: Supernova 1987A thirty years later. Nature Astron. **1**, 0100 (2017)
762. R. Fosburg, The spectrum of supernova 1987A. ESO Messenger **47**, 32 (1987)
763. P. Connes, G. Michel, Astronomical Fourier spectrometer. Appl. Opt. **14**, 2067 (1975)
764. T. Oen, Titan. Sci. Am. **246**(2), 76 (1982)
765. L.A. Soderblom, T.V. Johnson, The moons of Saturn. Sci. Am. **246**(1), 72 (1982)
766. R.P. Laeser, W.I. McLaughlin, D.M. Wolff, Engineering Voyager 2's encounter with Uranus. Sci. Am. **255**(5), 34 (1986)
767. A.P. Ingersoll, Uranus. Sci. Am. **256**(1), 30 (1987)
768. T.J. Johnson, R.H. Brown, L.A. Soderblom, The moons of Uranus. Sci. Am. **256**(4), 40 (1987)
769. J. Kinoshita, Neptune. Sci. Am. **261**(5), 60 (1989)

770. J.N. Cuzzi, L.W. Esposito, The rings of Uranus. Sci. Am. **257**(1), 42 (1987)
771. A.P. Ingersoll, Cassini exploration of the planet Saturn: A comprehensive review. Space Sci. Rev. **216**, 122 (2020)
772. Sky and Telescope **73**, No.3 (1987) (Feature issue)
773. Nature **321**, No.6067 (1987) (Feature issue)
774. H. Balsiger, H. Fechtig, J. Geiss, A close look at Halley's comet. Sci. Am. **259**(3), 62 (1988)
775. C. Arpigny, F. Dossin, J. Manfroid, P. Magain, A.C. Danks, D.L. Lambert, C. Sterken, Spectroscopy, photometry and direct filter imagery of comet P/Halley. ESO Messenger **45**, 10 (1986)
776. M.R. El-Maarry, O. Groussin, H.U. Keller, N. Thomas, J.-B. Vincent, S. Mottola, M. Pajola, K. Otto, C. Herny, S. Krasilnikov, Surface morphology of comets and associated evolutionary processes: A review of Rosetta's observations of 67P/Churyumov–Gerasimenko. Space Sci. Rev. **215**, 36 (2019)
777. M. Gassner, *Mission Rosetta: Exploration of the comet Churyumov-Gerasimenko* (Kindle, 2020)
778. M. Mayor, D. Queloz, A Jupiter-mass companion to a solar-type star. Nature **378**, 355 (1995)
779. M. Mayor, Nobel Lecture: Plurality of worlds in the cosmos: A dream of antiquity, a modern reality of astrophysics. Rev. Mod. Phys. **92**, 030502 (2020)
780. D. Queloz, Nobel Lecture: 51 Pegasi b and the exoplanet revolution. Rev. Mod. Phys. **92**, 030503 (2020)
781. E. Tasker, *The Planet Factory: Exoplanets and the Search for a Second Earth* (Bloomsbury Publishing, 2017)
782. S. Seager, D. Deming, Exoplanet Atmospheres. Ann. Rev. Astronomy Astrophys. **48**, 631 (2010)
783. N. Madhusudhan, M. Agúndez, J.I. Moses, Y.Y. Hu, Exoplanetary Atmospheres—Chemistry, Formation Conditions, and Habitability. Space Sci. Rev. **205**, 285 (2016)
784. H.R. Wakeford, D.K. Sing, D. Deming, N.K. Lewis, J. Goyal, T.J. Wilson, J. Barstow, T. Kataria, B. Drummond, T.M. Evans, A.L. Carter, N. Nikolov, H.A. Knutson, G.E. Ballester, A.M. Mandell, The complete transmission spectrum of WASP-39b with a precise water constraint. Astronom. J. **155**, 14 (2018)
785. https://www.miragenews.com/scientists-detect-39-new-gravitational-wave-events/
786. R. Schödel et al., A star in a 15.2 year orbit around the supermassive black hole at the center of the Milky Way. Nature **419**, 694 (2002).

Chapter 7

787. N. Ramsey, *Molecular Beams* (Clarendon, Oxford 1956; Paperback 1985)
788. J.M. Pendlebury, K.F. Smith, Molecular beams. Contemp. Phys. **28**, 3 (1987)
789. J.M. Lafferty, *Foundations of Vacuum Science and Technology* (Wiley, New York, 1998)
790. N. Harris, *Modern Vacuum Technology, 3^{rd} edn.* (www.modernvacuumpractice.com, 2007)
791. K. Jousten (ed.), *Handbook of Vacuum Technology* (Wiley-VCH Verlag, 2016)
792. A.N. Nesmeyanov, *Vapor Pressure of the Elements* (Academic Press, New York, 1963)
793. R.E. Honig, D.A. Kramer, RCA Rev. **30**, 285 (1969)
794. E.R. Cohen, D.R. Lide, G.L. Trigg (eds.), *AIP Physics Desk Reference*, 3rd edn. (Springer-Verlag, New York, 2003)
795. O. Stern, W. Gerlach, Der experimentelle Nachweis der Richtungsquantelung im Magnetfeld. Das magnetische Moment des Silberatoms. Z. Physik **9**, 349, 353 (1922)
796. I.I. Rabi, J.R. Zacharias, S. Millman, P. Kusch, A new method of measuring nuclear magnetic moment. Phys. Rev. **53**, 318 (1938)
797. N.F. Ramsey, A new molecular beam resonance method. Phys. Rev. **76**, 996 (1949); A molecular beam resonance method with separated oscillating fields. Phys. Rev. **78**, 695 (1950); Phase shifts in the molecular beam method of separated oscillating fields. Phys. Rev. **84**, 506 (1951)

798. N.F. Ramsey, Experiments with separated oscillatory fields and hydrogen masers (Nobel Lecture). Angew. Phys. **29**, 725 (1990)
799. M.G.H. Gustavsson, A.-M. Mårtensson-Pendrill, Four decades of hyperfine anomaly. Adv. Quantum Chem. **30**, 343 (1998)
800. J.R. Persson, Table of hyperfine anomaly in atomic systems. At. Data Nucl. Data Tables **99**, 62 (2013)
801. J.R. Persson, Hyperfine structure and hyperfine anomaly in Pb. J. Phys. Commun. **2**, 055028 (2018)
802. C. Ekström, I. Lindgren, 'Atomic beam experiments at the ISOLDE facility at CERN.' In: *Atomic Physics 5*, ed. by R. Marrus, M. Prior, H. Shugart (Plenum, New York 1977) p.201
803. C. Ekström, Spins and moments of nuclei far from stability determined by on-line atomic-beam techniques. Adv. Quantum Chem. **30**, 361 (1998)
804. M. Lindroos, Review of ISOL-type radioactive beam facilities. Proc. EPAC 2004, Lucerne, Switzerland
805. W.J. Childs, Case Studies. Atomic Phys. **3**, 215 (1973)
806. S. Büttgenbach, G. Meisel, S. Penselin, K.H. Schneider, A new method for the production of atomic beams of highly refractory elements and first atomic beam magnetic resonances in Ta^{181}. Z. Physik **230**, 329 (1970)
807. H. Rubinsztein, I. Lindgren, L. Lindström, H. Riedl, A. Rosén, Atomic beam measurements on refractory elements. Nucl. Instrum. Methods **119**, 269 (1974)
808. M. Heiblum, J. Bloch, J.J. O'Sullivan, Electron-gun evaporators of refractory metals compatible with molecular beam epitaxy. J. Vacuum Sci. Tech. **A3**, 1885 (1985)
809. U. Brinkmann, J. Goschler, A. Steudel, H. Walther, Experimente mit Erdalkaliatomen in Metastabilen Zuständen. Z. Physik **228**, 427 (1969)
810. S. Garpman, G. Lidö, S. Rydberg, S. Svanberg, Lifetimes of some highly excited levels in the Pb-I spectrum measured by the Hanle method. Z. Physik **241**, 217 (1971)
811. S. Penselin, 'Recent developments and results of the atomic beam magnetic resonance method.' In: *Progress in Atomic Spectroscopy*, Pt.A, ed. by W. Hanle, H. Kleinpoppen (Plenum, New York 1979) p.463
812. W.J. Childs, Overview of laser-radiofrequency double-resonance studies of atomic, molecular and ionic beams. Phys. Rep. **211**, 113 (1992)
813. A. Kastler, Quelques suggestions concernant la production optique et la détection optique d'une inégalité de population des niveaux de quantification spatiale des atomes. Application á l'expérience de Stern et Gerlach et á la résonance magnétique. J. Phys. Radium **11**, 255 (1950); Méthodes optiques d'étude de la résonance magnétique, Physica **17**, 191 (1951); Optical methods of atomic orientation and of magnetic resonance. J. Opt. Soc. Am. **47**, 460 (1957); A. Kastler, Optical methods for studying Hertzian resoances. Science **158**, 214(1967)
814. H.J. Besch, U. Köpf, E.W. Otten, Optical pumping of short-lived beta emitters. Phys. Lett. B **25**, 120 (1967)
815. E.W. Otten, 'Hyperfine and isotope shift measurements far from stability by optical pumping.' In: *Atomic Physics 5*, ed. by R. Marrus, M. Prior, H. Shugart (Plenum, New York 1977) p.239
816. J. Bonn, G. Huber, H.J. Kluge, U. Köpf, L. Kugler, E.W. Otten, J. Rodrigues, 'Orientation of short-lived mercury isotopes by means of optical pumping detected by β and γ radiation.' In: *Atomic Physics 3*, ed. By S.J. Smith, G.K. Walters (Plenum, New York 1973) p.471
817. S.A. Ahmad, Optical pumping for investigation of nuclear properties of short-lived isotopes/isomers: A review. Hyperfine Interact. **74**, 241 (1992)
818. H.-J. Kluge, W. Nörtershäuser, Lasers for nuclear physics. Spectrochim. Acta **B58**, 1031 (2003)
819. R. Bernheim, *Optical Pumping* (Benjamin, New York, 1965)
820. W. Happer, Optical pumping. Rev. Mod. Phys. **44**, 169 (1972)
821. G.W. Series, Thirty years of optical pumping. Contemp. Phys. **22**, 487 (1981)
822. M. Arditi, T.R. Carver, Optical detection of zero-field hyperfine structure in Na^{23}. Phys. Rev. **109**, 1012 (1958); Frequency shift of the zero-field hyperfine splitting of Cs^{133} produced by various buffer gases. Phys. Rev. **112**, 449 (1958)

823. H.M. Goldenberg, D. Kleppner, N.F. Ramsey, Atomic hydrogen maser. Phys. Rev. Lett. **5**, 361 (1960)
824. D. Kleppner, H.M. Goldenberg, N.F. Ramsey, Properties of the hydrogen maser. Appl. Opt. **1**, 55 (1962)
825. S.B. Crampton, D. Kleppner, N.F. Ramsey, Hyperfine structure of ground state atomic hydrogen. Phys. Rev. Lett. **11**, 338 (1963)
826. F.L. Walls, Frequency standards based on atomic hydrogen. Proc. IEEE **74**, 142 (1986)
827. D.J. Wineland, Frequency standards based on stored ions. Proc. IEEE **74**, 147 (1986)
828. J. Vanier, C. Audoin, *The Quantum Physics of Atomic Frequency Standards* (Hilger, Bristol, 1989)
829. Time and Frequency. Special issue of Proc. IEEE **79**(7) (1991)
830. W.M. Itano, N.F. Ramsey, Accurate measurement of time. Sci. Am. **269**(1), 56 (1993)
831. P.F. Fisk, Trapped-ion and trapped-atom microwave frequency standards. Rep. Prog. Phys. **60**, 761 (1997)
832. F.G. Mayor, *The Quantum Beat – The Physical Principles of Atomic Clocks* (Springer, Berlin, Heidelberg, 1998)
833. S.T. Cundiff, L. Hollberg, 'Spectroscopy - Absolute Optical Frequency Metrology' in *Encyclopedia of Modern Optics*, (Elsevier, 2005) p. 82
834. A.D. Ludlow, M.M. Boyd, J. Ye, E. Peik, P.O. Schmidt, Optical atomic clocks. Rev. Mod. Phys. **87**, 637 (2015)
835. I. Ushijima, M. Takamoto, M. Das, T. Ohkubo, H. Katori, Cryogenic optical lattice clocks. Nat. Photon. **9**, 185 (2015)
836. E. Oelker, et al., Demonstration of 4.8×10^{-17} stability at 1 s for two independent optical clocks. Nat. Photon. **13**, 714 (2019)
837. E. Pedrozo-Peñafiel, S. Colombo, C. Shu, F. Adiyatullin, Z.Y. Li, E. Mendez, B. Braverman, A. Kawasaki, D. Akamatsu, Y.H. Xiao, V. Vuletić, Entanglement on an optical atomic-clock transition. Nature **588**, 414 (2020)
838. Th.A. Herring, The global positioning system. Sci. Am. **274**(2), 32 (1996)
839. B. Hofmann-Wellenhof, H. Lichtenegger, *GPS Theory and Practice*, 4th edn. (Springer, Berlin, Heidelberg, 1997)
840. B. Hofmann-Wellenhof, H. Lichtenegger, E. Wasle, *GNSS – Global Navigation Satellite Systems - GPS, GLONASS, Galileo, and more* (Springer, 2008)
841. G.S. Rao, *Global Navigation Satellite Navigation* (Tata McGraw-Hill, 2010)
842. B. Levitan, L. Harte, *GPS Systems -Technology, Operation, and Applications* (Discovernet, 2016)
843. G. Elgered, J.M. Johansson, B.O. Rönnäng, J.L. Davis, Measuring regional atmospheric water vapor using the Swedish permanent GPS network. Geophys. Res. Lett. **24**, 2663 (1997)
844. P. Benevides, J. Catalao, P.M.A. Miranda, On the inclusion of GPS precipitable water vapour in the nowcasting of rainfall. Nat. Hazards Earth Syst. Sci. **15**, 2605 (2015)
845. A. Kastler, J. Brossel, La détection de la résonance magnétique des niveaux excités: L'effet de dépolarisation des radiations de résonance optique et de fluorescence. Comp. Rend. **229**, 1213 (1949)
846. J. Brossel, F. Bitter, A new "double resonance" method for investigating atomic energy levels. Application to Hg $^3P_1$. Phys. Rev. **86**, 308 (1952)
847. G. Belin, I. Lindgren, L. Holmgren, S. Svanberg, Hyperfine interaction, Zeeman and Stark effects for excited states in potassium. Phys. Scr. **12**, 287 (1975)
848. W. Hanle, Ûber magnetische Beeinflussung der Polarisation der Resonanzfluoreszenz. Z. Physik **30**, 93 (1924); Erg. Ex. Naturwiss. **4**, 214 (1925)
849. F.D. Colgrove, P.A. Franken, R.R. Lewis, R.H. Sands, Novel method of spectroscopy with applications to precision fine structure measurements. Phys. Rev. Lett. **3**, 420 (1959)
850. G. Breit, Quantum theory of dispersion (continued). Pts. VI and VII. Rev. Mod. Phys. **5**, 91 (1933)

851. P. Franken, Interference effects in the resonance fluorescence of “crossed” excited states. Phys. Rev. **121**, 508 (1961)
852. T.G. Eck, L.L. Foldy, H. Wiedner, Observation of “anticrossings” in optical resonance fluorescence. Phys. Rev. Lett. **10**, 239 (1963)
853. H. Wiedner, T.G. Eck, “Anticrossing” signals in resonance fluorescence. Phys. Rev. **153**, 103 (1967)
854. H.J. Beyer, H. Kleinpoppen, ‘Anticrossing spectroscopy.’ In: *Progress in Atomic Spectroscopy*, Pt.A, ed. by W. Hanle, H. Kleinpoppen (Plenum, New York 1979) p.607
855. G. Belin, S. Svanberg, Electronic g_J factors, natural lifetimes and electric quadrupole interaction in the np $^2P_{3/2}$ series of the Rb I spectrum. Phys. Scr. **4**, 269 (1971)
856. R. Gupta, S. Chang, C. Tai, W. Happer, Cascade radio-frequency spectroscopy of excited *S* and *D* states of rubidium; anomalous *D*-state hyperfine structure. Phys. Rev. Lett. **29**, 695 (1972)
857. R. Gupta, W. Happer, L. Lam, S. Svanberg, Hyperfine structure measurements of excited *S* states of the stable isotopes of potassium, rubidium and cesium by cascade radio-frequency spectroscopy. Phys. Rev. A **8**, 2792 (1973)
858. M.E. Rose, R.L. Carovillano, Coherence effects in resonance fluorescence. Phys. Rev. **122**, 1185 (1961)
859. G. zu Putlitz, ‘Double resonance and level-crossing spectroscopy.’ In: *Atomic Physics*, ed. by V.W. Hughes, B. Bederson, V.W. Cohen, F.M.J. Pichanick (Plenum, New York 1969)
860. G. Moruzzi, F. Strumia (eds.), *The Hanle Effect and Level-Crossing Spectroscopy* (Plenum, New York, 1991)
861. B. Budick, In: *Advances in Atomic and Molecular Physics*, ed. by R.D. Bates, I. Esterman (Academic Press, New York 1967)
862. W. Happer, R. Gupta, ‘Perturbed fluorescence spectroscopy.’ In: *Progress in Atomic Spectroscopy*, Pt.A, ed. by W. Hanle, H. Kleinpoppen (Plenum, New York 1979) p.391
863. E. Arimondo, M. Inguscio, P. Violino, Experimental determinations of the hyperfine structure in the alkali atoms. Rev. Mod. Phys. **49**, 31 (1977); updated version; M. Allegrini, E. Arimondo, L.A. Orozco, Survey of hyperfine structure measurements in alkali atoms. J. Phys. Chem. Ref. Data **51**, 043102 (2022)
864. D.A.R. Williams, *Nuclear Magnetic Resonance Spectroscopy* (Wiley, Chichester, 1986)
865. W. Kemp, *NMR in Chemistry* (McMillan, London, 1986)
866. C.P. Slichter, *Principles of Magnetic Resonance*, 3rd edn. Springer Ser. Solid-State Sci., Vol.1 (Springer, Berlin, Heidelberg 1990)
867. A.U. Rahman, M. Iqbal, *Solving Problems with NMR* (Academic Press, London, 1995)
868. T.N. Mitchell, B. Costicella, *NMR – From Spectra to Structures, 2nd edn.* (Springer, 2006)
869. J. Keeler: *Understanding NMR Spectroscopy*, *2^{nd} edn.* (Wiley, 2010)
870. H. Gunther, *NMR Spectroscopy – An Introduction*, 3rd edn. (Wiley, Chichester, 2013)
871. G. Webb (ed.), *Annual Reports on NMR Spectroscopy*, *Volume 102* (Elsevier, 2021)
872. D.A. Skoog, D.M. West, *Principles of Instrumental Analysis* (Saunders, Philadelphia, 1980)
873. R. Brewer, E.L. Hahn, Atomic memory. Sci. Am. **251**(6), 42 (1984)
874. B.A. Jung, M. Weigel, Spin echo magnetic resonance imaging. J. Magn. Res. Imag. **27**, 805 (2013)
875. K. Wüthrich, NMR studies of structure and function of biological macromolecules (Nobel lecture). Angew. Chemie **42**, 3340 (2003)
876. D.R. Bailes, D.J. Bryant, NMR imaging. Contemp. Phys. **25**, 441 (1984)
877. R.S. MacKay, *Medical Images and Displays: Comparison of Nuclear Magnetic Resonance. Ultrasound, X-Rays and Other Modalities* (Wiley, New York 1984)
878. R.A. Robb, *Three-Dimensional Biomedical Imaging – Principles and Practice* (VCH, New York, 1994)
879. C.N. Guy, The second revolution in medical imaging. Contemp. Phys. **37**, 15 (1996)
880. C. Westbrook, *Handbook of MRI Technique, 4^{th} edn.* (Wiley-Blackwell, 2014)
881. L.L. Kelly, C.M. Petersen: *Sectional Anatomy, 4^{th} edn.* (Elsevier, 2018)

882. R. Kimmich, *NMR-Tomography, Diffusometry, Relaxometry* (Springer, Berlin, Heidelberg, 1997)
883. M.S. Albert, G. Driehuys, W. Happer, B. Saam, C.S. Springer Jr., A. Wishnia, Biological magnetic resonanace imaging using laser-polarized Xe-129. Nature **370**, 199 (1994)
884. W. Happer, 'Medical NMR sensing with laser polarized ^{3}He and ^{129}Xe.' In: *Atomic Physics Methods in Modern Research*, ed. by K. Jungmann et al. (Springer, Berlin, Heidelberg 1997) p.121
885. M. Ebert, T. Grossmann, W. Heil, E.W. Otten, R. Surkau, M. Leduc, P. Bachert, M.V. Knopp, L.R. Schad, M. Thelen, MRI-imaging with hyperpolarized ^{3}He. Lancet **347**, 9011 (1996)
886. M.S. Albert, F.T. Hane (eds.), *Hyperpolarized and inert gas MRI - From technology to application in research and medicine* (Academic Press, 2017)
887. C.G. Aminoff, C. Larat, M. Leduc, B. Viana, D. Vivien, A powerful infrared laser for optical pumping of ^{3}He. J. Lumin. **50**, 21 (1991)
888. M. Bouchiat, T.-R. Carver, C.M. Varnum, Nuclear polarization in ^{3}He gas induced by optical pumping and dipolar exch[ange. Phys. Rev. Lett. **5**, 373 (1960)
889. F.D. Colgrove, L.D. Schearer, G.K. Walters, Polarization of ^{3}He gas by optical pumping. Phys. Rev. **132**, 2561 (1963)
890. T.G. Walker, W. Happer, Spin-exchange optical pumping of noble-gas nuclei. Rev. Mod. Phys. **69**, 629 (1997)
891. J. Becker, W. Heil, B. Krug, M. Leduc, M. Meyerhoff, P.J. Nacher, E.W. Otten, Th. Prokscha, L.D. Schearer, R. Surkau, Study of mechanical compression of spin-polarized ^{3}He gas. Nucl. Instrum. Methods A **346**, 45 (1994)
892. W. Heil, H. Humblot, E.W. Otten, M. Schfer, R. Surkau, M. Leduc, Very long relaxation times of spin-polarized ^{3}He in metal coated cells. Phys. Lett. A **201**, 337 (1995)
893. E.W. Otten, 'Interdisciplinary experiments with polarized noble gases.' In: *Atomic Physics 15*, ed. by H.B. van Linden van den Heuvell, J.T.M. Walraven, M.W. Reynolds, Amsterdam 1996 (World Scientific, Singapore 1997), p.113
894. E. Otten, 'Polarized, compressed ^{3}He gas and its applications.' In: *Atomic Physics Methods in Modern Research*, ed. by K. Jungmann et al. (Springer, Berlin, Heidelberg 1997) p.105
895. P.D. Perry, Th.R. Carver, S.O. Sari, S.E. Schnatterly, Optically pumped and monitored electron-nuclear double resonance in alkali halides. Phys. Rev. Lett. **22**, 326 (1969)
896. B.M. Goodson, Applications of optical pumping and polarization techniques in NMR: I. Optical nuclear polarization in molecular crystals. Ann. Rep. NMR Spectr. **55**, 299 (2005)
897. R.S. Alger, *Electron Paramagnetic Resonance* (Wiley, New York, 1968)
898. J.E. Wertz, *Electron Spin Resonance: Elementary Theory and Practical Applications* (Chapman and Hall, New York, 1986)
899. T.K. Ishii (ed.), *Handbook of Microwave Technology*, Vols.1, 2 (Academic Press, London 1995)
900. J.J. Davies, Optically detected magnetic resonance and its applications. Contemp. Phys. **17**, 275 (1976)
901. S. Choi, J. Choi, R. Landig, G. Kucsko, H.Y. Zhou, J. Isoya, F. Jelezko, S. Onoda, H. Sumiya, V. Khemani, C. von Keyserlingk, N.Y. Yao, E. Demler, M.D. Lukin, Observation of discrete time-crystalline order in a disordered dipolar many-body system. Nature **543**, 221 (2017)
902. H.A.R. El-Ella, S. Ahmadi, A.M. Wojciechowski, A. Huck, U.L. Andersen, Optimised frequency modulation for continuous-wave optical magnetic resonance sensing using nitrogen-vacancy ensembles. Opt. Express **25**, 14809 (2017)
903. D.R. Glenn, D.B. Bucher, J. Lee, M.D. Lukin, H. Park, R.L. Walsworth, High-resolution magnetic resonance spectroscopy using a solid-state spin sensor. Nature **555**, 351 (2018)
904. F.M. Stürner, A. Brenneis, J. Kassel, U. Wostradowski, R. Rölver, T. Fuchs, K. Nakamura, H. Sumiya, S. Onoda, J. Osoya, F. Jelezko, Compact integrated magnetometer based on nitrogen-vacancy centres in diamond. Diam. Relat. Mater. **93**, 59 (2019)
905. C.H. Townes, A.L. Schawlow, *Microwave Spectroscopy* (Dover, New York, 1975)
906. H.W. Kroto, *Molecular Rotation Spectra* (Wiley, London, 1975)

907. W. Gordy, R.L. Cook, *Microwave Molecular Spectra*, 3rd edn., Techniques of Chemistry, Vol.XVIII (Wiley, New York 1984)
908. H. Møllendal, 'Microwave Spectroscopy', In *Strength from Weakness: Structural Consequences of Weak Interactions in Molecules, Supermolecules, and Crystals*, ed. by A. Domenicano, I. Hargittai. *NATO Science Series (Series II: Mathematics, Physics and Chemistry)*, vol 68. (Springer, Dordrecht 2002)
909. W. Caminati, J.-U. Grabow, 'Microwave Spectroscopy', in J. Laane (Ed.): *Frontiers in Molecular Spectroscopy,* (Elsevier, 2009)
910. T. Lund (ed.), Surveillance of environmental pollution and resources by electromagnetic waves. NATO Adv. St. Inst. Ser. (Reidel, Dordrecht 1978)
911. E. Schanda, *Physical Fundamentals of Remote Sensing* (Springer, Berlin, Heidelberg, 1986)
912. K.A. Browning, Uses of radar in metrology. Contemp. Phys. **27**, 499 (1986)
913. Ch.G. Collier, *Applications of Weather Radar Systems*, 2nd edn. (Wiley, New York, 1996)
914. I.H. Woodhouse, *Introduction to Microwave Remote Sensing* (Taylor and Francis, Informa, 2005)
915. F.Z. Weng, *Passive Microwave Remote Sensing of the Earth: for Meteorological* Applications (Wiley-VCH Verlag, 2017)
916. V. Raizer, Advances in Passive Microwave Remote Sensing of Oceans (CRC Press, 2017)
917. C.A. Varotsos, V.F. Krapivin, *Microwave Remote Sensing Tools in Environmental Science* (Springer, 2020)
918. E. Schanda, Microwave radiometry applications to remote sensing. In: [910]
919. E.P.W. Attema, The radar signature of natural surfaces and its application in active microwave remote sensing. In: [910]
920. D.L. Evans, E.R. Stofan, T.J. Jones, L.M. Godwin, Earth from sky. Sci. Am. **271**(6), 44 (1994)
921. W. Noack (ed.), *X-SAR Picture Book* (Springer, Berlin, Heidelberg, 1996)
922. J.A. Richards, *Remote Sensing by Imaging Radar* (Springer, 2009)
923. R. Yang, H. Li, S. Li, P. Zhang, L. Tan, X. Gao, X. Kang, *High-Resolution Microwave Imaging* (Springer, 2018)
924. A. Alonso-González, I. Hajnsek, *Radar Remote Sensing of Land Surface Parameters* (Springer, 2019)
925. D.-J. Kim (ed.), Special Issue "*InSAR in Remote Sensing",* MPDI Journal *Remote Sensing* (MPDI, Basel 2021)
926. S. Tebaldini (ed.), *"SAR Tomography of Natural Media",* MPDI Journal *Remote Sensing* (MPDI, Basel 2021)
927. S. Haykin, E.O. Lewis, R.K. Raney, J.R. Rossiter, *Remote Sensing of Sea Ice and Icebergs* (Wiley, New York, 1994)
928. Gustavsson, P.O. Frölind, H. Hellsten, T. Jonsson, B. Larsson, G. Stenström: *The airborne VHF SAR system CARABAS.* Proc. IEEE Geoscience Remote Sensing Symp., IGARSS'93, Tokyo, Japan, Vol.2, pp.558–562, August 1993
929. O.E.H. Rydbeck, 'Interstellar molecules.' In: *Kosmos 1974*, ed. by N.R. Nilsson (Swedish Phys. Soc., Stockholm 1975)
930. A.W. Clegg, G.E. Nedoluka (eds.), *Astrophysical Masers* (Springer, Berlin, Heidelberg, 1993)
931. M. Elitzar, Masers in the sky. Sci. Am. **272**(2), 52 (1995)
932. J. Lequeux, E. Roueff, Interstellar molecules. Phys. Rep. **200**, 241 (1991)
933. G. Winnewisser, G.C. Pelz, *The Physics and Chemistry of Interstellar Molecular Clouds, Springer Lecture Notes on Physics*, vol. 459 (Springer, Berlin, Heidelberg, 1995)
934. A. Hewish, S.J. Bell, J.D.H. Pilkington, P.F. Scott, R.A. Collins, Observation of a rapidly pulsating radio source. Nature **217**, 709 (1968)
935. R.A. Hulse, J.H. Taylor, Discovery of a pulsar in a binary system. Astrophys. J. **195**, L51 (1975)
936. J.H. Taylor, L.A. Fowler, P.M. McCulloch, Measurements of general relativistic effects in the binary pulsar PSR 1913+16. Nature **277**, 437 (1979)

937. A.R. Thompson, J. Moran, G.W. Swenson Jr., *Interferometry and Synthesis in Radio Astronomy* (Wiley, New York, 1986)
938. T. Wilson, K. Rohlfs, S. Huettemeister, *Tools of Radio Astronomy* (Springer, 2013)
939. S. Joardar, J.R. Claycomb, *Radio Astronomy – An Introduction* (Mercury, 2014)
940. R.L. Snell, S. Kurtz, J. Marr, *Fundamentals of Radio Astronomy - Astrophysics* (CRC Press, 2019)
941. M.J. Bentum et al., A roadmap towards a space-based radio telescope for ultra-low frequency radio astronomy. Adv. Space. Res. **65**, 859–867 (2020)
942. P.D. Naselsky, D.I. Novikov, I.D. Novikov, *The Physics of the Cosmic Microwave Background* (Cambridge University Press, 2009)
943. D. Scott, G.F. Smoot, Cosmic microwave background, https://pdg.lbl.gov/2018/reviews/rpp2018-rev-cosmic-microwave-background.pdf (2017)
944. Planck Collaboration, Planck 2018 results. Astron. Astrophys. **641**, A6 (2018)
945. J.C. Mather, Nobel lecture: From the Big Bang to the Nobel Prize and beyond. Rev. Mod. Phys. **79**, 1331 (2007)
946. G.F. Smoot, Nobel lecture: Cosmic microwave background radiation anisotropies: Their discovery and utilization. Rev. Mod. Phys. **79**, 1349 (2007)
947. P. Morrison, J. Billingham, J. Wolfe, *The Search for Extraterrestial Intelligence (prepared by NASA) (Dover, New York 1979* (Academic Press, New York, 1986)
948. P. Horowitz, C. Sagan, Five year of project META: An all-sky narrow-band radio search for extraterrestrial signals. Astrophys. J. **415**, 218 (1993)
949. D.A. Vakoch (ed.), *Communication with Extraterrestrial Intelligence* (SUNY Press, New York, 2011)
950. C. Sagan, L.S. Sagan, F.D. Drake, Message from Earth. Science **175**, 881 (1972) http://www.nauts.com/vehicles/70s/pioneer10-11.html

Chapter 8

951. A.E. Siegman, *Lasers* (University Science Books, Mill Valley, CA, 1986)
952. Ch.C. Davis, *Lasers and Electro-Optics* (Cambridge University Press, Cambridge, 1996)
953. W.T. Silfvast, *Laser Fundamentals*, 2nd edn. (Cambridge University Press, Cambridge, 2004)
954. O. Svelto, *Principles of Lasers*, 5th edn. (Springer, 2010)
955. H. Haken, *Laser Theory* (Springer, Berlin, Heidelberg 1983, 2012)
956. K. Thyagarajan, A. Ghatak, *Lasers: Fundamentals and Applications* (Springer, 2010)
957. P.W Milonni, J.H. Eberly, *Laser Physics* (Wiley, 2010) K.F. Renk: *Basics of Laser Physics* (Springer, 2012)
958. C.B. Hitz, J. Ewing, J. Hecht, *Introduction to Laser Technology, 4th edn.* (Wiley, 2012)
959. A. Yariv, *Introduction to Optical Electronics*, 3rd edn. (Dover Books, 2013)
960. O. Shulika, I. Sukhoivanov (eds.), *Advanced Lasers - Laser Physics and Technology for Applied and Fundamental Science* (Springer, 2015)
961. T.H. Maiman, Stimulated optical radiation in ruby. Nature **187**, 493 (1960)
962. A.L. Schawlow, C.H. Townes, Infrared and optical masers. Phys. Rev. **112**, 1940 (1958)
963. J.P. Gordon, H.J. Zeiger, Ch.H. Townes, The maser – new type of microwave amplifier, frequency standard and spectrometer. Phys. Rev. **99**, 1264 (1955)
964. C.H. Townes, *In: Nobel Lectures in Physics*, vol. 4 (Elsevier, Amsterdam, 1972)
965. N.G. Basov, *In: Nobel Lectures in Physics*, vol. 4 (Elsevier, Amsterdam, 1972)
966. A.M. Prokhorov, *In: Nobel Lectures in Physics*, vol. 4 (Elsevier, Amsterdam, 1972)
967. D.L. Matthews, P.L. Hagelstein, M.D. Rosen, M.J. Eckart, N.H. Ceglio, A.U. Hazi, H. Medicki, B.J. MacGowan, J.E. Trebes, B.L. Witten, E.M. Campbell, C.W. Hatcher, A.H. Hawryluk, R.L. Kaufmann, L.D. Pleasance, G. Rambach, J.H. Scoefield, G. Stone, T.A. Weaver, Demonstration of a soft X-ray amplifier. Phys. Rev. Lett. **54**, 110 (1985)

968. D.L. Matthews, M.D. Rosen, Soft X-ray lasers. Sci. Am. **256**(6), 60 (1988)
969. T. Mocek et al., Plasma-based X-ray laser at 21 nm for multidisciplinary applications. Eur. Phys. J. D **54**, 439 (2009)
970. G. Tallents (ed.), *X-Ray Lasers*, IOP Conf. Ser. 116 (Institute of Physics Publ., Bristol 1990)
971. E.E. Fill (ed.), *X-Ray Lasers 1992*, IOP Conf. Ser. 125 (Institute of Physics Publ., Bristol 1992)
972. D.C. Eder, D.L. Matthews (eds.), *X-Ray Lasers 1994*, AIP Conf. Proc. Vol.332 (AIP Press, New York 1994)
973. S. Svanberg, C.-G. Wahlström (eds.), *X-Ray Lasers 1996*, IOP Conf. Ser. Vol.151 (Institute of Physics Publ., Bristol 1996)
974. Y. Kato, H. Takuma, H. Daido (eds.), *X-Ray Lasers 1998*, IOP Conf. Ser. 159 (Institute of Physics Publ., Bristol 1999)
975. G. Jamelot, C. Möller, A. Klishnik (eds.), *X-Ray Lasers 2000*, J. Physique **11** (2000)
976. J.J. Rocca, J. Dunn, S. Suchewer (eds.), *X-Ray Lasers 2002* (AIP, 2002)
977. J. Zhang (ed.), *X-Ray Laser 2004* (CRC Press, 2005)
978. P.V. Nickles, K.A. Janulewicz (eds.), *X-Ray Lasers 2006* (Springer, 2008)
979. C.L.S. Lewis, D. Riley (eds.), *X-Ray Lasers 2008* (Springer, 2010)
980. J. Lee, C.H. Nam, K.A. Janulewicz (eds.), *X-Ray Lasers 2010* (Springer, 2011)
981. S. Sebban, J. Gauthier, D. Ros, P. Zeitoun (eds.), *X-Ray Lasers 2012* (Springer, 2013)
982. J. Rocca, C. Menoni, M. Marconi (eds.), *X-Ray Lasers 2014* (Springer, 2015)
983. T. Kawachi, S.V. Bulanov, H. Daido, Y. Kato (eds.), *X-Ray Lasers 2016* (Springer, 2017)
984. M. Kozlová, Michaela, J. Nejdl (eds.), *X-Ray Lasers 2018* (Springer, 2020)
985. H. Kogelnik, T. Li, Laser beams and resonators. Proc. IEEE **54**, 1312 (1966)
986. H.K.V. Lotsch, The confocal resonator system. Optik **30**, 1, 181, 217, 563 (1969/70)
987. N. Hodgson, H. Weber, *Optical Resonators* (Springer, Berlin, Heidelberg, 1997)
988. M. Eichhorn, *Laser Physics,* Chapter on Laser Resonators (Springer, 2014)
989. R. Pachotta, Laser design: Understanding and optimizing laser resonator designs: An overview. Laser FocusWorld, July 31 2019)
990. G.D. Boyd, J.P. Gordon, Confocal multimode resonator for millimeter through optical wavelength masers. Bell Syst. Tech. J. **40**, 489 (1961)
991. G.D. Boyd, H. Kogelnik, Generalized confocal resonator theory. Bell Syst. Tech. J. **41**, 1347 (1962)
992. R.W. Hellwarth, 'Control of fluorescent pulsations.' In: *Advances in Quantum Electronics*, ed. by J.R. Singer (Columbia University Press, New York 1961) p.334
993. F.J. McClung, R.W. Hellwarth, Giant Optical Pulsations from Ruby. J. Appl. Phys. **33**, 828 (1962)
994. A. Szabo, R.A. Stein, Theory of laser giant pulsing by a saturable absorber. J. Appl. Phys. **36**, 1562 (1965)
995. U. Keller, K. J. Weingarten, F. X. Kärtner, D. Kopf, B. Braun, I. D. Jung, R. Fluck, C. Hönninger, N. Matuschek, J. aus der Au: Semiconductor saturable absorber mirrors (SESAMs) for femtosecond to nanosecond pulse generation in solid-state lasers. IEEE J. Selected Topics in Quantum Electronics **2**, 435 (1996)
996. U. Keller, Recent developments in compact ultrafast lasers. Nature **424**, 831 (2003)
997. S. Svanberg, Lasers as probes for air and sea. Contemp. Phys. **21**, 541 (1980)
998. W. Koechner, *Solid-State Laser Engineering*, 6th edn. Springer Ser. Opt. Sci., Vol.1 (Springer, Berlin, Heidelberg 2006)
999. A.A. Kaminskii, *Laser Crystals*, 2nd edn. Springer Ser. Opt. Sci., Vol.14 (Springer, Berlin, Heidelberg 1990)
1000. A.A. Kaminskii, Laser crystals and ceramics: recent advances. Lasers Phot. Rev. **1**, 93 (2007)
1001. D.N. Nikogosyan, *Properties of Optical and Laser Related Materials: A Handbook* (Wiley, New York, 1997)
1002. N. Hodgeson, R. Wallenstein (eds.), *Solid State Lasers – New Developments and Applications* (Plenum, New York, 1993)
1003. W. Koechner, M. Bass, *Solid-State Lasers* (Springer, New York, NY., 2003)

1004. B. Denker, E. Shklovsky (eds.), *Handbook of Solid-State Lasers - Materials, Systems and Applications* (Woodhead, 2013)
1005. A.F. Gibson, Lasers for compression and fusion. Contemp. Phys. **23**, 285 (1982)
1006. S.E. Bodner, A.J. Schmitt, J.D. Sethian, Laser requirements for a laser fusion energy power plant. High Power Laser Sci. Eng. **1**, 2 (2013)
1007. D. Biello, High-powered lasers deliver fusion energy breakthrough. Sci. Am. December 31 (2014)
1008. S. Le Pape et al., Fusion energy output greater than the kinetic energy of an imploding shell at the National Ignition Facility. Phys. Rev. Lett. **120**, 245003 (2018)
1009. J.E. Eggleston, T.J. Kane, K. Kuhn, J. Unternahrer, R.L. Byer, The slab geometry laser. IEEE J. Quantum Electron. **QE-20**, 289 (1984)
1010. A. Dergachev, J. Flint, Y. Isyanova, B. Pati, E. Slobodtchikov, K. Wall, P. Moulton, Review of multipass slab laser systems. IEEE Sel. Topics Quant. Electr. **13**, 647 (2007)
1011. A.K. Sridharan, S. Saraf, S. Sinha, R.L. Byer, Zigzag slabs for solid-state laser amplifiers: batch fabrication and parasitic oscillation suppression. Appl. Opt. **45**, 3340 (2006)
1012. R.-A. Lorbeer, B. Ewers, C. Santek, D. Beisecker, J. Speiser, T. Dekorsy, Monolithic thin-disk laser and amplifier concept. Optica **7**, 1409 (2020)
1013. N. Peyghambarian, A. Chavez-Pirson (eds.), Special Issue on Laser Amplifiers, MPDI Photonics, 2021
1014. D. Findlay, D.W. Goodwin, ‘The neodymium in YAG laser.’ In: *Advances in Quantum Electronics*, Vol.1, ed. by D.W. Goodwin (Academic Press, London 1970)
1015. B. Zhou, T.J. Kane, G.J. Dixon, R.L. Byer, Efficient, frequency-stable laser-diode-pumped Nd:YAG laser. Opt. Lett. **10**, 62 (1985)
1016. W.R. Trutna, D.K. Donald, M. Nazarathy, Unidirectional diode-laserpumped Nd:YAG ring laser with a small magnetic field. Opt. Lett. **12**, 248 (1987)
1017. G.P.A. Malcolm, A.I. Ferguson, Diode-pumped solid-state lasers. Contemp. Phys. **32**, 305 (1991)
1018. R.L. Byer, G.J. Dixon, T.J. Kane, W. Kozlovsky, B. Zhou, ‘Frequency-doubled, laser diode pumped, miniature Nd:YAG oscillator – progress toward an all-solid state sub-kilohertz linewidth coherent source.’ In: *Laser Spectroscopy VII*, ed. by T.W. Hänsch, Y.R. Shen, Springer Ser. Opt. Sci., Vol.49 (Springer, Berlin, Heidelberg 1985) p.350
1019. D. Botez, D.R. Scifres (eds.), *Diode Laser Arrays* (Cambridge University Press, Cambridge 1994, 2005)
1020. N.W. Carlson, *Monolithic Diode-Laser Arrays* (Springer, Berlin, Heidelberg, 1994)
1021. N.W. Carlson, *Diode Laser Arrays* (Springer Verlag, Heidelberg, 1998)
1022. H. Li et al., Near 1 kW of continuous-wave power from a single high-efficiency diode-laser bar. IEEE Photon. Technol. Lett. **19**(13), 960 (2007)
1023. P. Crump, G. Tränkle, A brief history of kilowatt-class diode-laser bars. SPIE **11301**, 113011D (2020)
1024. R.A. Motes, R.W. Berdine, *Introduction to High Power Fiber Lasers* (Directed Energy Professional Society, 2009)
1025. M.N. Zervas, C.A. Codemard, High Power Fiber Lasers: A Review. IEEE J. Sel. Topics. Quant. Electr. **20**, 219 (2014)
1026. D.J. Richardson, J. Nilsson, W.A. Clarkson, High power fiber lasers: current status and future perspectives. J. Opt. Soc. Amer. **B27**, B63 (2010)
1027. V.V. Ter-Mikirtychev, *Fundamentals of Fiber Lasers and Fiber Amplifiers* (Springer, 2019)
1028. C.K. Rhodes (ed.), *Excimer Lasers*, 2nd edn. Topics Appl. Phys., Vol.30 (Springer, Berlin, Heidelberg 1984)
1029. M.H.R. Hutchinson, Excimers and excimer lasers. Appl. Phys. **21**, 15 (1980)
1030. D. Basting, G. Marowsky (eds.), *Excimer Laser Technology* (Springer, Heidelberg, 2005)
1031. V. Bakshi (ed.), *EUV Sources for Lithography* (SPIE Press, Burlington, 2006)
1032. Ch.E. Little, *Metal Vapour Lasers* (Wiley, New York, 1998)
1033. I.G. Ivanov, E.L. Latush, M.F. Sem, *Metal Vapour Ion Lasers* (Wiley, New York, 1996)

1034. V.M. Batenin, V.V. Buchanov, A.M. Boichenko, M.A. Kazaryan, *High-Brightness Metal Vapour Lasers* (CRC Press, 2020)
1035. W.R.B. Javan, Jr., D.R., Herriott, Population inversion and continous optical maser oscillation in a gas discharge containing a He-Ne mixture. Phys. Rev. Lett. **6**, 106 (1961)
1036. W.T. Silfvast, J.J. Macklin, O.R. Wood II., High-gain inner-shell photoionization laser in Cd vapor pumped by soft X-ray radiation from a laser produced plasma source. Opt. Lett. **8**, 551 (1983)
1037. W.T. Silfvast, O.R. Wood II., Photoionization lasers pumped by broadband soft-X-ray flux from laser-produced plasmas. J. Opt. Soc. Am. **4**, 609 (1987)
1038. R.A. Lacy, A.C. Nilsson, R.L. Byer, W.T. Silfvast, O.R. Wood II., S. Svanberg, Photoionization-pumped gain at 185 nm in a laser-ablated indium plasma. J. Opt. Soc. Am. B **6**, 1209 (1989)
1039. H.C. Kapteyn, R.W. Lee, R.W. Falcone, Observation of a short-wavelength laser pumped by Auger decay. Phys. Rev. Lett. **57**, 2939 (1986)
1040. M.H. Sher, J.J. Macklin, J.F. Young, S.E. Harris, Saturation of the Xe III -109 nm laser using traveling-wave laser-produced-plasma excitation. Opt. Lett. **12**, 891 (1987)
1041. C.C. Davis, T.A. King, 'Gaseous ion lasers.' In: *Advances in Quantum Electronics*, ed. by D.W. Goodwin (Academic Press, London 1975)
1042. S.D. Smith, R.B. Dennis, R.G. Harrison, The spin-flip Raman laser. Prog. Quantum Electron. **5**, 205 (1977)
1043. M.J. Colles, C.R. Pigeon, Tunable lasers. Rep. Prog. Phys. **38**, 329 (1975)
1044. A. Mooradian, Tunable infrared lasers. Rep. Prog. Phys. **42**, 1533 (1979)
1045. F.J. Duarte, *Tunable Lasers Handbook* (Academic Press, New York, 1996)
1046. F.J. Duarte (ed.), *Tunable Laser Optics* (Academic Press, 2013)
1047. F.J. Duarte (ed.), *Tunable Laser Applications, 3rd ed.* (CRC Press, 2016)
1048. P.P. Sorokin, J.R. Lankard, Stimulated emission observed from an organic dye, chloro-aluminium phthalocyanine. IBM J. Res. Dev. **10**, 162 (1966)
1049. F.P. Schäfer, W. Schmidt, J. Volze, Organic dye solution laser. Appl. Phys. Lett. **9**, 306 (1966)
1050. B.H. Soffer, B.B. McFarland, Continously tunable narrow-band organic dye laser. Appl. Phys. Lett. **10**, 266 (1967)
1051. T.W. Hänsch, Repetitively pulsed tunable dye laser for high resolution spectroscopy. Appl. Opt. **11**, 895 (1972)
1052. M.G. Littman, H.J. Metcalf, Spectrally narrow pulsed dye laser without beam expander. Appl. Opt. **25**, 375 (1978)
1053. I. Shoshan, U. Oppenheim, The use of a diffraction grating as a beam expander in a dye laser cavity. Opt. Commun. **25**, 375 (1978)
1054. M.G. Littman, Single-mode operation of grazing incidence pulsed dye laser. Opt. Lett. **3**, 138 (1978)
1055. M.G. Littman, Single-mode pulsed tunable dye laser. Appl. Opt. **23**, 4465 (1984)
1056. P. Grundevik, M. Gustavsson, A. Rosén, S. Svanberg, High resolution laser fluorescence spectroscopy in the deep blue spectral region. Z. Physik A **283**, 127 (1977)
1057. R. Wallenstein, T.W. Hänsch, Powerful dye laser oscillator-amplifier system for high-resolution spectroscopy. Opt. Commun. **14**, 353 (1975); R. Wallenstein, H. Zacharias: High-power narrowband pulsed dye laser oscillator-amplifier system. Opt. Commun. **32**, 429 (1980)
1058. T.F. Johnston, 'Tunable dye lasers.' In: *Encyclopedia of Physical Science and Technology*, Vol.14 (Academic Press, New York 1987)
1059. O.G. Peterson, S.A. Tuccio, B.B. Snavely, CW operation of an organic dye solution laser. Appl. Phys. Lett. **17**, 245 (1970)
1060. J. Evans, The birefringent filter. J. Opt. Soc. Am. **39**, 229 (1949)
1061. F.P. Schäfer (ed.), *Dye Lasers*, 3rd edn., Topics Appl. Phys., Vol.1 (Springer, Berlin, Heidelberg 1990)
1062. T.F. Johnston, R.H. Brady, W. Proffitt, Powerful single-frequency ring dye laser spanning the visible spectrum. Appl. Opt. **21**, 2307 (1982)

1063. F.J. Duarte, L.W. Hillman (eds.), *Dye Lasers Principles and Applications* (Academic Press, 1990)
1064. M. Stuke (ed.), *Dye Lasers: 25 Years* (Springer Verlag, Berlin, Heidelberg, 1992)
1065. R. Bornemann, E. Thiel, P.H. Bolívar, High-power solid-state CW dye laser. Opt. Express **19**, 26382 (2011)
1066. M. Maeda, *Laser Dyes* (Academic Press, Orlando, 1984)
1067. U. Brackmann, Lambdachrome Laser Dyes (Lambda Physik, Göttingen 1986)
1068. G.S. Shankarling, K.J. Jarag, Laser dyes. Resonance **15**, 804 (2010)
1069. P.F. Moulton, Spectroscopic and laser characteristics of Ti: Al_2O_3. J. Opt. Soc. Am. B **3**, 125 (1986)
1070. Courtesy: D.T. Reid and W. Sibbett, University of St. Andrews
1071. R.L. Byer (ed.), Special issue on tunable solid state lasers. IEEE J. Quantum Electron. **QE-21**, 1567–1636 (1985)
1072. B. Henderson, G.F. Imbusch, Optical processes in tunable transition-metal-ion lasers. Contemp. Phys. **29**, 235 (1988)
1073. P. Moulton, Tunable solid-state lasers. Proc. IEEE **80**, 348 (1992)
1074. S. Forget, S. Chenais, *Organic Solid-State Lasers* (Springer, 2013)
1075. Y.Y. Kaliski, *Solid State Lasers: Tunable Sources and Passive Q-Switching Elements* (SPIE, Bellingham, 2014)
1076. W.J. Witteman, *The* CO_2 *Laser*, Springer Ser. Opt. Sci., Vol.53 (Springer, Berlin, Heidelberg 1987)
1077. D.C Dumitras, (ed.), CO_2 *Laser – Optimization and Application* (Intech Open, 2012)
1078. F. O'Neill, W.T. Whitney, A high-power tunable laser for the 9 – 12.5 μm spectral range. Appl. Phys. Lett. **31**, 271 (1977)
1079. R. Beck, W. Englisch, K. Gürs, *Table of Laser Lines in Gases and Vapors*, 3rd edn., Springer Ser. Opt. Sci., Vol.2 (Springer, Berlin, Heidelberg 1978)
1080. M.J. Weber, *Handbook of Laser Wavelengths* (CRC Press, Boca Raton, 1999)
1081. N.G. Basov, O.N. Krokhin, Y.M. Popov, Production of negative temperature states in *p-n* junctions of degenerate semiconductors. JETP **13**, 1320 (1961)
1082. R.N. Hall, G.E. Fenner, J.D. Kingsley, T.S. Soltys, E.O. Carlson, Coherent light emission from GaAs junctions. Phys. Rev. Lett. **9**, 366 (1962)
1083. M.I. Nathan, W.P. Dumke, G. Burns, F.D. Hill Jr., G.J. Lasher, Stimulated emission of radiation from GaAs *p-n* junctions. Appl. Phys. Lett. **1**, 62 (1962)
1084. T.M. Quist, R.H. Rediker, R.J. Keyes, W.E. Krag, B. Lax, A.L. McWhorter, H.J. Zeiger, Semiconductor maser of GaAs. Appl. Phys. Lett. **1**, 91 (1962)
1085. R.M. Measures, *Laser Remote Sensing: Fundamentals and Applications* (Wiley, New York, 1984)
1086. Zh.I. Alferov, R.F. Kazarinov, Semiconductor laser with electric pumping. Sov. patent appl. **950**, 840 (1963)
1087. Zh.I. Alferov et al., AlAs-GaAs heterojunction lasers with a low room-temperature threshold. Sov. Phys. Semicond. **3**, 1107 (1969)
1088. H. Kroemer, A proposed class of heterojunction injection lasers. Proc. IEEE **51**, 1782 (1963)
1089. H.G. Grimmeiss (ed.), Heterostructures in Semiconductors. Phys. Scr. **T68**, Nr. 4 (1996)
1090. J. Coleman, Metalorganic Chemical Vapor Deposition for Optoelectronic Devices. Proc. IEEE **85**, 1715 (1997)
1091. P. Shamba, *MOCVD Growth and Electrical Characterisation of InAs Thin Films* (Lambert Academic Publ., 2011)
1092. M. Henini, *Molecular Beam Epitaxy - From Research to Mass Production,* 2^{nd} *edn.* (Elsevier, 2018)
1093. H. Asahi, Y. Horikoshi, *Molecular Beam Epitaxy: Materials and Applications for Electronics and* Optoelectronics (Wiley, 2019)
1094. S. Irvine, P. Capper (eds.), *Metalorganic Vapor Phase Epitaxy (MOVPE): Growth, Materials Properties, and Applications* (Wiley, 2020)

1095. Zh.I. Alferov, Nobel Lecture: The double heterostructure concept and its applications in physics, electronics, and technology. Rev. Mod. Phys. **73**, 767 (2001)
1096. H. Kroemer, Nobel Lecture: Quasielectric fields and band offsets: teaching electrons new tricks. Rev. Mod. Phys. **73**, 783 (2001)
1097. J. Hecht, Laser Focus World, May 1992
1098. Courtesy: Fiberguide Industries, Stirling, NJ, USA
1099. J. Mears, L. Reekie, I.M. Jauncey, D.N. Payne, Low-noise erbium-doped fibre amplifier operating at 1.54 µm. Electronics Letters **23**, 1026 (1987)
1100. E. Desurvire, *Erbium-Doped Fiber Amplifiers* (Wiley, New York, 1994)
1101. P.M. Becker, A.A. Olsson, J.R. Simpson, Erbium-Doped Fiber Amplifiers: Fundamentals and Applications (Academic Press, 1999)
1102. N. Holonyak Jr., S.F. Bevacqua, Coherent visible light emission from Ga($As_{1-x}P_x$) junctions. Appl. Phys. Lett. **1**, 82 (1982)
1103. S. Nakamura, G. Fasol, *The Blue Laser Diode* (Springer, Heidelberg, 1997)
1104. S. Nakamura, Background story of the invention of efficient InGaN blue-light-emitting diodes (Nobel lecture). Angew. Chemie Int. Ed. **54**, 7770 (2015)
1105. R.G. Hunsperger, 'Distributed-Feedback Lasers', in: *Integrated Optics* (Springer, New York, 2009
1106. K. Iga, F. Koyama, S. Kinoshita, Surface emitting semiconductor lasers. IEEE J. Quantum Electron. **QE-24**, 1845 (1988)
1107. M. Grabherr, R. Jager, R. Michalzik, B. Weigl, G. Reiner, K.J. Ebeling, Efficient single-mode oxide-confined GaAs VCSELs emitting in the 850 nm wavelength regime. IEEE Photonics Technol. Lett. **9**, 1304 (1997)
1108. R. Michalzik (ed.), *VCSELs - Fundamentals, Technology and Applications of Vertical-Cavity Surface-Emitting Lasers* (Springer, Berlin, Heidelberg, 2013)
1109. K. Iga, Forty years of vertical-cavity surface-emitting laser: Invention and innovation. Jpn. J. Appl. Phys. **57**, 08PA01 (2018)
1110. J. Faist, F. Capasso, D.L. Sivco, C. Sirtori, A.L. Hutchinson, A.Y. Cho, Quantum cascade laser. Science **264**, 553 (1994)
1111. F. Capasso, J. Faist, C. Sirtori, A.Y. Cho, Infrared (4 – 11 µm) quantum cascade lasers. Solid State Commun. **102**, 231 (1997)
1112. K. Namjou, S. Cai, E.A. Whittaker, J. Faist, F. Capasso, C. Gmachl, D.L. Sivco, A.Y. Cho, Sensitive absorption spectroscopy using room temperature distributed-feedback quantum cascade lasers. Opt. Lett. **23**, 219 (1998)
1113. P. Rauter, F. Capasso, Multi-wavelength quantum cascade laser arrays. Lasers Phot. Rev. **9**. 452 (2015)
1114. M.S. Vitiello, G. Scalari, B. Williams, P. De Natale, Quantum cascade lasers: 20 years of challenges. Opt. Express **23**, 5167 (2015)
1115. K. Isensee, N. Kröger-Lui, W. Petrich, Biomedical applications of mid-infrared quantum cascade lasers - a review. Analyst **143**, 5888 (2018)
1116. J. W. Orton, T. Foxon, *Molecular Beam Epitaxy: A Short History* (Oxford University Press, 2015)
1117. W.W. Chow, S.W. Koch, M. Sargent III., *Semiconductor Laser Physics* (Springer, Berlin, Heidelberg, 1994)
1118. G.P. Agarwal (ed.), *Semiconductor Lasers* (AIP Press, Melville, NY, 1995)
1119. J. Buus, M.-C. Amann, D.J. Blumenthal, *Tunable Laser Diodes and Related Optical Sources, 2nd edn.* (Wiley, 2005)
1120. A. Baranov, E. Tournié, *Semiconductor Lasers* (Woodhead Publishing, 2013)
1121. G.P. Agrawal, *Semiconductor Lasers* (Springer, 2013)
1122. J. Ohtsubo, *Semiconductor Lasers, 4^{th} edn.* (Springer, 2017)
1123. A.F.J. Levi, *Essential Semiconductor Laser Device Physics* (IOP Science, 2018)
1124. J. Seufert, M. Fischer, M. Legge, K. Roessner, R. Werner, J. Hildenbrand, J. Herbst, A. Lambrecht, J. Koeth, DFB Laser Diodes and Quantum Cascade Lasers for sensors in safeguard applications. Proc. SPIE **7114**, 71140K-K71149 (2008)

1125. J.C. Camparo, The diode laser in atomic physics. Contemp. Phys. **26**, 443 (1985)
1126. C.E. Wieman, L. Hollberg, Using diode lasers for atomic physics. Rev. Sci. Instrum. **62**, 1 (1991)
1127. L. Ricci, M. Weidemüller, T. Esslinger, A. Herrerich, C. Zimmermann, V. Vuletic, W. Knig, T.W. Hänsch, A compact grating-stabilized diode laser system for atomic physics. Opt. Commun. **117**, 541 (1995)
1128. U. Gustafsson, J. Alnis, S. Svanberg, Atomic spectroscopy with violet laser diodes. Am. J. Phys. **68**, 660 (2000)
1129. A.W. Mantz, A review of spectroscopic applications of tunable semiconductor lasers. Spectrochim. Acta A **51**, 221 (1995)
1130. P. Werle, Spectroscopic trace gas analysis using semiconductor diode lasers. Spectrochim. Acta A **52**, 805 (1996)
1131. M. Lackner, Tunable diode laser spectroscopy in the process industries: a review. Rev. Chem. Eng. **23**, 65 (2007)
1132. M.A. Bolshov, Yu.A. Kuritsyn, Yu.V. Romanovskii, Tunable diode laser spectroscopy as a technique for combustion diagnostics. Spectrochim. Acta B **106**, 45 (2015)
1133. J. Friedrich, 'Methods for bulk growth of inorganic crystals: Crystal growth' in *Encyclopedia of Condensed Matter Physics* (Elsevier, 2005) pp. 262–274
1134. B. Couillaud, L.A. Bloomfield, T.W. Hänsch, Generation of continuous-wave radiation near 243 nm by sum frequency mixing in an external ring cavity. Opt. Lett. **8**, 259 (1983)
1135. W.H. Yang, Y.J. Wang, Y.H. Zheng, H.D. Lu, Comparative study of the frequency-doubling performance on ring and linear cavity at short wavelength region. Opt. Express **23**, 19624 (2015)
1136. P. Nilaya, D.J. Biswas, Towards enhancing the efficiency of nonlinear optical generation. IntechOpen, DOI: https://doi.org/10.5772/intechopen.80816 (2018)
1137. A.S. Pine, 'IR Spectroscopy via difference-frequency generation.' In: *Laser Spectroscopy III*, ed. by J.L. Hall, J.L. Carlsten, Springer Ser. Opt. Ser., Vol.7 (Springer, Berlin, Heidelberg 1977) p.376
1138. D.S. Chemla, J. Zyss (eds.), *Nonlinear Optical Properties of Organic Molecules and Crystals*, Vols.1, 2 (Academic Press, Orlando 1987)
1139. V.G. Dmitriev, G.G. Gurzadyan, D.N. Nikogosyan, *Handbook of Nonlinear Optical Crystals*, Springer Ser. Opt. Sci., Vol.64 (Springer, Berlin, Heidelberg 1991)
1140. D.N. Nikogosyan, *Nonlinear Optical Crystals: A Complete Survey* (Springer, 2005)
1141. R.A. Kumar, Borate crystals for nonlinear optical and laser applications: A review. J. Chemistry **2013**, 154862 (2013)
1142. J. Webjörn, F. Laurell, G. Arvidsson, Blue light generated by frequency doubling of laser diode light in a lithium niobate channel waveguide. IEEE Photonics Technol. Lett. **1**, 316 (1989)
1143. U. Simon, S. Waltman, I. Loa, L. Hollberg, F. Tittel, External-cavity difference-frequency source near 3.2 μm, based on combining a tunable diode laser with a diode-pumped Nd:YAG laser in $AgGaS_2$. J. Opt. Soc. Am. B **12**, 323 (1995)
1144. M. Yamada, N. Nata, M. Saitoh, K. Watanabe, First-order quasi-phase matched $LiNbO_3$ waveguide. Appl. Phys. Lett. **62**, 435 (1993)
1145. D.S. Hum, M.M. Fejer, Quasi-phasematching. C. R. Physique **8**, 180 (2007)
1146. Y. Petit, A. Peña, P. Segonds, J. Debray, S. Joly, A. Zukauskas, F. Laurell, V. Pasiskevicius, C. Canalias, B. Boulanger, Development and experimental demonstration of negative first-order quasi-phase matching in a periodically poled Rb-doped $KTiOPO_4$ crystal. Opt. Letters **45**, 6026 (2020)
1147. W. Demtröder, *Laser Spectroscopy, Vol. 1: Basic Principles, and Vol. 2: Experimental Techniques* (Springer, Berlin, Heidelberg, 2008)
1148. S.E. Harris, Tunable optical parametric oscillators. Proc. IEEE **57**, 2096 (1969)
1149. Y.X. Fan, R.L. Byer, Progress in optical parametric oscillators. SPIE Int. Soc. Opt. Eng. **461**, 27 (1984)

1150. M.E. Marhic, *Fiber Optical Parametric Amplifiers, Oscillators and Related Devices: Theory, Applications, and Related Devices* (Cambridge University Press, 2007)

1151. R. Zerne, J. Larsson, S. Svanberg, Determination of radiative lifetimes in the $3d^{10}np\ ^2P$ sequence of neutral copper by time-resolved VUV laser spectroscopy. Phys. Rev. A **49**, 128 (1994)

1152. R. Hilbig, G. Hilber, A. Lago, B. Wolff, R. Wallenstein, Tunable coherent VUV radiation generated by nonlinear optical frequency conversion in gases. Comments At. Mol. Phys. **18**, 157 (1986)

1153. J.F. Rentjes, *Nonlinear Optical Parametric Processes in Liquids and Gases* (Academic Press, New York, 1984)

1154. R.W. Falcone, J. Kirz (eds.), *Short Wavelength Coherent Radiation: Generation and Applications* (Opt. Soc. Am, Washington, DC, 1988)

1155. C. Yamanaka (ed.), *Short-Wavelength Lasers*, Springer Proc. Phys., Vol.30 (Springer, Berlin, Heidelberg 1988)

1156. S. Svanberg, A. L'Huillier, C.-G. Wahlström, Atomic physics using short-wavelength coherent radiation. Nucl. Instrum. Methods Phys. Res. A **398**, 55 (1997)

1157. U. Berzinsh, S. Svanberg, Atomic radiative lifetimes measured by pulsed laser spectroscopy in the UV/VUV spectral region. Adv. Quantum Chem. **30**, 283 (1998)

1158. B. Ya Zeldovich, V.I. Popovichev, V.V. Ragulsky, F.S. Faizullov, Connection between the wavefronts of the reflected and exciting light in stimulated Mandelshtam–Brillouin scattering. ZhETF Pis. Red. **15**, 160 (1972); JETP Lett. **15**, 109 (1972)

1159. O.Yu. Nosach, V.I. Popovichev, V.V. Ragulsky, F.S. Faizullov: Cancellation of phase distortions in an amplifying medium with a Brillouin mirror. ZhETF Pis. Red. **16**, 617 (1972); JETP Lett. **16**, 435 (1972)

1160. R.W. Hellwarth, Generation of time-reversed wave fronts by nonlinear refraction. J. Opt. Soc. Am. **67**, 1 (1977)

1161. A. Yariv, On transmission and recovery of three-dimensional image information in optical waveguides. J. Opt. Soc. Am. **66**, 301 (1976)[

1162. B.Ya. Zel'dovich, N.F. Pilipetsky, V.V. Shkunov, *Principles of Phase Conjugation*, Springer Ser. Opt. Sci., Vol.42 (Springer, Berlin, Heidelberg 1985)

1163. V.V. Shkunov, B. Ya, Zel'dovich, Optical phase conjugation. Sci. Am. **253**(6), 40 (1985)

1164. D.M. Pepper, Applications of optical phase conjugation. Sci. Am. **254**(1), 56 (1986)

1165. H.J. Eichler, P. Gunther, D.W. Pohl, *Laser Induced Dynamic Gratings*, Springer Ser. Opt. Sci., Vol.50 (Springer, Berlin, Heidelberg 1986)

1166. M.C. Gower, D. Proch (eds.), *Optical Phase Conjugation* (Springer, Berlin, Heidelberg, 1994)

1167. D.T. Hon, Pulse compression by stimulated Brioullin scattering. Opt. Lett. **5**, 516 (1980)

1168. S. Schiemann, W. Ubachs, W. Hogervorst, Efficient temporal compression of coherent ns-pulses in a compact SBS generator-amplifier setup. IEEE J. Quantum Electron. **33**, 358 (1997)

1169. Z.-S. Li, J. Norin, A. Persson, C.-G. Wahlström, S. Svanberg, P.S. Doidge, E. Biemont, Radiative properties of neutral germanium obtained from excited state lifetime and branching ratio measurements and comparison with theoretical calculations. Phys. Rev. A **60**, 198 (1999)

1170. V. Wilke, W. Smidt, Tunable coherent radiation source covering a spectral range from 185–880 nm. Appl. Phys. **18**, 177 (1979)

1171. J. Paisner, S. Hargrove, 'A tunable laser system for UV, visible, and IR regions.' In: Energy and Technology Review (Lawrence Livermore Nat'l Lab., Livermore 1979)

1172. A.P. Hickman, J.A. Paisner, W.K. Bishel, Theory of multiwave propagation and frequency conversion in a Raman medium. Phys. Rev. A **33**, 1788 (1986)

1173. F. Moya, S.A.J. Druet, J.P. Taran, 'Rotation-vibration spectroscopy of gases by coherent anti-Stokes Raman scattering: Application to concentration and temperature measurements.' In: *Laser Spectroscopy*, ed. by S. Haroche, J.C. Pebay Peyroula, T.W. Hänsch, S.E. Harris (Springer, Berlin, Heidelberg 1975)

1174. M. Aldén, H. Edner, S. Svanberg, Coherent anti-Stokes Raman spectroscopy (CARS) applied to combustion probing. Phys. Scr. **27**, 29 (1983)
1175. A.C. Eckbreth, BOXCARS: Crossed beam phase-matched CARS generation in gases. Appl. Phys. Lett. **32**, 421 (1978)
1176. N. Bloembergen, *Nonlinear Optics* (Benjamin, New York, 1977)
1177. V.S. Letokhov, V.P. Chebotayev, *Nonlinear Laser Spectroscopy*, Springer Ser. Opt. Sci., Vol.4 (Springer, Berlin, Heidelberg 1977)
1178. Y.R. Shen, *The Principles of Nonlinear Optics* (Wiley, New York, 1984)
1179. E.G. Sauter, *Nonlinear Optics* (Wiley, New York, 1996)
1180. R.W. Boyd, *Nonlinear Optics*, 3rd edn. (Academic Press, San Diego, 2008)
1181. J.Q. Yao, *Nonlinear Optics and Solid State Lasers* (Springer, 2012)
1182. J.W. Haus, *Fundamentals of Nonlinear Optics, 2^{nd} ed.* (Taylor and Francis, 2017)
1183. H. Mocker, R.J. Collins, Mode competition and self-locking effects in a Q-switched ruby laser. Appl. Phys. Lett. **7**, 270 (1965)
1184. A.J. De Maria, D.A. Stetser, H. Heynau, Self mode-locking of lasers with saturable absorbers. Appl. Phys. Lett. **8**, 174 (1966)
1185. E.P. Ippen, C.V. Shank, A. Dienes, Passive mode-locking of the CW dye laser. Appl. Phys. Lett. **21**, 348 (1972)
1186. R.L. Fork, B.I. Greene, C.V. Shank, Generation of optical pulses shorter than 0.1 ps by colliding pulse mode-locking, Appl. Phys. Lett. **38**, 671 (1981)
1187. R.L. Fork, C.H. Brito Cruz, P.C. Becker, C.V. Shank, Compression of optical pulses to six fs by using cubic phase compression, Opt. Lett. **12**, 483 (1987)
1188. M. Nisoli, S. De Silvestri, O. Svelto, Generation of high energy 10 fs pulses by a new pulse compression technique. Appl. Phys. Lett. **68**, 2793 (1996)
1189. G. Fan, T. Balčiūnas, T. Kanai, T. Flory, G. Andriukaitis, B. E. Schmidt, F. Légaré, A. Baltuška, Hollow-core-waveguide compression of multi-millijoule CEP-stable 3.2 μm pulses. Optica **3**, 1308 (2016)
1190. P. Balla, A.B. Wahid, I. Sytcevich, C. Guo, A.-L. Viotti, L. Silletti, A. Cartella, S. Alisauskas, H. Tavakol, U. Grosse-Wortmann, A. Schönberg, M. Seidel, A. Trabattoni, B. Manschwetus, T. Lang, F. Calegari, A. Couairon, A. L'Huillier, C.L. Arnold, I. Hartl, C.M. Heyl, Postcompression of picosecond pulses into the few-cycle regime. Opt. Letters **45**, 2572 (2020)
1191. L. Xu, C. Spielmann, F. Krausz, R. Szipöcs, Ultra-broadband ring oscillator for sub-10-fs pulse generation. Opt. Lett. **21**, 1259 (1996)
1192. D.E. Spence, P.N. Kean, W. Sibbett, 60 fs pulse generation from a selfmode-locked Ti:sapphire laser. Opt. Lett. **16**, 42 (1991)
1193. U. Morgner, F.X. Kärtner, S.H. Cho, Y. Shen, H.A. Haus, J.G. Fujimoto, E.P. Ippen, V. Scheuer, G. Angelow, T. Tshudi, Sub-two-cycle pulses from a Kerr-lens mode-locked Ti:sapphire laser. Opt. Lett. **24**, 411 (1999)
1194. D.H. Sutter, G. Steinmeyer, L. Gallman, N. Matuschek, F. Morier-Genoud, U. Keller, V. Scheuer, G. Angelow, T. Tschudi, Semiconductor saturable absorber mirror-assisted Kerr-lens mode-locked Ti:sapphire laser producing pulses in the two-cycle regime. Opt. Lett. **24**, 631 (1999)
1195. A. Baltuska, Z. Wei, M.S. Pshenichnikov, D.A. Wiersma, Optical pulse compression to 5 fs at a -1 MHz repetition rate. Opt. Lett. **22**, 102 (1997)
1196. M. Nisoli, S. De Silvresti, O. Svelto, R. Szipcs, F. Ferencz, Ch. Spielmann, S. Sartania, F. Krausz, Compression of high-energy laser pulses below 5 fs. Opt. Lett. **22**, 522 (1997)
1197. P.M.W. French, The generation of ultrashort laser pulses. Rep. Prog. Phys. **58**, 169 (1995)
1198. I.N. Duling (ed.), *Compact Sources of Ultrashort Pulses* (Cambridge University Press, Cambridge, 1995)
1199. J.-C. Diels, W. Rudolph, *Ultrashort Laser Pulse Phenomena* (Academic Press, San Diego, 1996)
1200. C. Rullires (ed.), *Femtosecond Laser Pulses* (Springer, Berlin, Heidelberg, 1998)

1201. D. Strickland, G. Mourou, Compression of amplified chirped optical pulses. Opt. Commun. **56**, 219 (1985)
1202. P. Maine, D. Strickland, P. Bado, M. Pessot, G. Mourou, Generation of ultrahigh peak power pulses by chirped pulse amplification. IEEE J. Quantum Electron. **QE-24**, 398 (1988)
1203. G. Mourou, Nobel Lecture: Extreme light physics and applications. Rev. Mod. Phys. **91**, 030501 (2019)
1204. D. Strickland, Nobel Lecture: Generating high-intensity ultrashort optical pulses. Rev. Mod. Phys. **91**, 030502 (2019)
1205. S. Svanberg, J. Larsson, A. Persson, C.-G. Wahlström, Lund High-Power Laser Facility - Systems and first results. Phys. Scr. **49**, 187 (1994)
1206. S. Svanberg, High-power lasers and their applications. Adv. Quantum Chem. **30**, 209 (1998)
1207. M.D. Perry, G. Mourou, Terawatt to petawatt subpicosecond lasers. Science **264**, 917 (1994)
1208. M.D. Perry, D. Pennington, B.C. Stuart, G. Tietbohl, J.A. Britten, C. Brown, S. Herman, B. Golick, M. Kartz, J. Miller, H.T. Powell, M. Vergino, V. Yanovsky, Petawatt laser pulses. Opt. Lett. **24**, 160 (1999)
1209. S. Backus, Ch.G. Durfee III., M.M. Murnane, H.C. Kapteyn, High power ultrafast lasers. Rev. Sci. Instrum. **69**, 1207 (1998)
1210. C.P.J. Barty, W. White, W. Sibbett, R. Trebino (eds.), *Ultrafast Optics*. IEEE J. Sel. Top. Quantum Electron. **4**, No.2 (1998)
1211. I. Jovanovic, Chirped-Pulse Amplification ultrahigh peak power production from compact short-pulse laser systems. Optik & Photonik December 2010 (Nr. 4)
1212. A.M. Weiner, *Ultrafast Optics* (Wiley, 2009)
1213. H. Injeyan, G.D. Goodny, *High Power Laser Handbook* (McGraw-Hill, 2011
1214. V.V. Apollonov, *High-Power Optics - Lasers and Applications* (Springer, 2015)
1215. S. Nolte, F. Schrempel, F. Dausinger (eds.), *Ultrashort Pulse Laser Technology - Laser Sources and Applications* (Springer, 2016)
1216. www.eli-beams.eu B. Le Garrec, S. Sebban, D. Margarone, M. Precek, S. Weber, O. Klimo, G. Korn, B. Rus, ELI-beamlines: Extreme light infrastructure science and technology with ultra-intense lasers. SPIE **8962**, 89620I (2014)
1217. www.eli-alps.hu S. Kühn et al., The ELI-ALPS facility: the next generation of attosecond sources. J. Phys. B: At. Mol. Opt. Phys. **50**, 132002 (2017)
1218. http://www.eli-np.ro D. Ursescu et al., Extreme Light Infrastructure Nuclear Physics (ELI-NP): Present status and perspectives. Proc. SPIE **8780** (2013)
1219. C. Danson, C. Haefner, J. Bromage, T. Butcher, J.F. Chanteloup, E.A. Chowdhury, A. Galvanauskas, L.A. Gizzi, J. Hein, D.I. Hillier, N.W. Hopps, Y. Kato, E.A. Khazanov, R. Kodama, G. Korn, R. Li, Y. Li, J. Limpert, J. Ma, C.H. Nam, D. Neely, D. Papadopoulos, R.R. Penman, L. Qian, J.J. Rocca, A.A. Shaykin, C.W. Siders, C. Spindloe, S. Szatmári, R.M.G.M. Trines, J. Zhu, P. Zhu, J.D. Zuegel, Petawatt and exawatt class lasers worldwide. High Power Laser Sci. Eng. **7**, e54 (2019)
1220. A. Dubietis, G. Jonusauskas, A. Piskarskas, Powerful femtosecond pulse generation by chirped and stretched pulse parametric amplification in BBO crystal. Opt. Commun. **88**, 437 (1992)
1221. A. Dubietis, R. Butkus, A. Piskarskas, Trends in chirped pulse optical parametric amplification. IEEE J. Sel. Top. Quantum Electron. **12**, 163 (2006)
1222. A. Vaupel, N. Bodnar, B. Webb, L. Shah, M.C. Richardson, Concepts, performance review, and prospects of table-top, few-cycle optical parametric chirped-pulse amplification. Opt. Eng. **53**, 051507 (2013)
1223. H.W. Lee, Y.G. Kim, J.Y. Yoo, S.K. Lee, J.M. Yang, Y.J. Son, J.H. Sung, Broadband nanosecond optical parametric chirped-pulse amplification with a double-sliced pump pulse. Opt. Commun. **460**, 125125 (2020)
1224. J. Rothhardt, S. Hädrich, J.C. Delagnes, E. Cormier, J. Limpert, Technology development for ultra-intense all-OPCPA systems. High Power Laser Sci. Eng. **7**, e4 (2019)
1225. H.R. Telle, G. Steinmeyer, A.E. Dunlop, J. Stenger, D.H. Sutter, U. Keller, Carrier-envelope offset phase control: A novel concept for absolute optical frequency measurement and ultrashort pulse generation. Appl. Phys. B **69**, 327 (1999)

1226. J. Reichert, R. Holzwarth, T. Udem, T.W. Hänsch, Measuring the frequency of light with mode-locked lasers. Opt. Com. **172**, 59 (1999)
1227. D.J. Jones, S.A. Diddams, J.K. Ranka, A. Stentz, R.S. Windeler, J.L. Hall, S.T. Cundiff, Carrier-envelope phase control of femtosecond mode-locked lasers and direct optical frequency synthesis. Science **288**, 635 (2000)
1228. S.T. Cundiff, Phase stabilization of ultrashort optical pulses. J. Phys. D: Appl. Phys. **35**, R43 (2002)
1229. Z. Chang, Carrier-envelope phase shift caused by grating-based stretchers and compressors. Appl. Opt. **45**, 8350 (2006)
1230. E. Moon, H. Wang, S. Gilbertson, H. Mashiko, M. Chini, Z. Chang, Advances in carrier-envelope phase stabilization of grating-based chirped-pulse amplifiers. Lasers Phot. Rev. **4**, 160 (2010)
1231. G. Gademann, F. Plé, P.-M. Paul, M.J.J. Vrakking, Carrier-envelope phase stabilization of a terawatt level chirped pulse amplifier for generation of intense isolated attosecond pulses. Opt. Express **19**, 24922 (2011)

Chapter 9

1232. W. Demtröder, *Laser Spectroscopy*, 4th edn. Volume 1: Basic Principles; Volume 2: Experimental Techniques (Springer, Berlin, Heidelberg 2008)
1233. V.S. Letokhov, V.P. Chebotayev, *Nonlinear Laser Spectroscopy*, Springer Ser. Opt. Sciences, Vol.4 (Springer, Berlin, Heidelberg 1977)
1234. R.C. Thompson, High-resolution laser spectroscopy of atomic systems. Rep. Prog. Phys. **48**, 531 (1985)
1235. Y. Prior, A. Ben-Reuven, M. Rosenbluh, *Methods of Laser Spectroscopy* (Plenum, New York, 1986)
1236. L.J. Radziemski, R.W. Solarz, J.A. Paisner (eds.), *Laser Spectroscopy and its Applications* (Dekker, New York, 1987)
1237. M.D. Levenson, W.H. Yen (eds.), Lasers, Spectroscopy and New Ideas. A Tribute to A.L. Schawlow, Springer Ser. Opt. Sci., Vol.54 (Springer, Berlin, Heidelberg 1987)
1238. M.D. Levenson, S. Kano, *Introduction to Nonlinear Spectroscopy*, revised. (Academic Press, New York, 1988)
1239. B.W. Shore, *The Theory of Coherent Atomic Excitation. Vol.1: Simple Atoms and Fields, Vol.2: Multilevel Atoms and Incoherence* (Wiley, New York, 1990)
1240. M.H. Mittelman, *Introduction to the Theory of Laser-Atom Interactions* (Plenum, New York, 1993)
1241. R. Gupta, Resource letter LS-1: Laser Spectroscopy. Am. J. Phys. **59**, 874 (1991)
1242. A.P. Roy (ed.), *Spectroscopy – Perspectives and Frontiers* (Narosa, New Delhi 1997)
1243. S. Mukamel, *Principles of Nonlinear Optical Spectroscopy* (Oxford University Press, Oxford, 1998)
1244. C. Cohen-Tannoudji, J. Dupont-Roc, G. Grynberg, *Atom-Photon Interactions – Basic Processes and Applications* (Wiley, New York, 1998)
1245. T.W. Hänsch, H. Walther, Laser spectroscopy and quantum optics. Rev. Mod. Phys. **71**, S242 (1999)
1246. H. Abramzsyk, *Introduction to Laser Spectroscopy* (Elsevier, 2005)
1247. D.L. Andrews, A.A. Demidov, *Introduction to Laser Spectroscopy, 2nd ed.* (Springer, 2012)
1248. M. Baudelet (ed.), *Laser Spectroscopy for Sensing - Fundamentals, Techniques and Applications* (Elsevier 2014)
1249. H.H. Telle, Á. González Ureña, *Laser Spectroscopy and Laser Imaging – An Introduction* (CRC Press, 2018)
1250. P.N. Ghosh, *Laser Physics and Spectroscopy* (Taylor and Francis, 2018)

1251. V.P. Gupta, Y. Ozaki (eds.), *Molecular and Laser Spectroscopy - Advances and Applications: Volume 2* (Elsevier, 2020)
1252. T.W. Hänsch, Y.R. Shen (eds.), *Laser Spectroscopy VII*, Proc. 7th Int. Conf., Maui 1985, Springer Ser. Opt. Sci., Vol.49 (Springer, Berlin, Heidelberg 1985)
1253. W. Persson, S. Svanberg (eds.), *Laser Spectroscopy VIII*, Proc. 8th Int. Conf., Åre 1987, Springer Ser. Opt. Sci., Vol.55 (Springer, Berlin, Heidelberg 1987)
1254. M.S. Feld, J.E. Thomas, A. Mooradian (eds.), *Laser Spectroscopy IX* (Academic Press, Boston, 1989)
1255. M. Ducloy, E. Giacobino, G. Camy (eds.), *Laser Spectroscopy X* (World Scientific, Singapore, 1992)
1256. L. Bloomfield, Th. Gallagher, D. Larson (eds.), *Laser Spectroscopy XI* (AIP, New York, 1994)
1257. M. Inguscio, M. Allegrini, A. Sasso (eds.), *Laser Spectroscopy XII* (World Scientific, Singapore, 1996)
1258. Z.-J. Wang, Y.-Z. Wang, Z.-M. Zhang (eds.), *Laser Spectroscopy XIII* (World Scientific, Singapore, 1998)
1259. R. Blatt, J. Eschner, D. Leibfried, F. Schmidt-Kaler (eds.), *Laser Spectroscopy XIV* (World Scientific, Singapore, 1999)
1260. S. Chu, V. Vutelic, A.J. Kerman, C. Chin (eds.), *Laser Spectroscopy 15* (World Scientific, Singapore, 2002)
1261. P. Hannaford, A. Siderov, H. Bachor, K. Baldwin (eds.), *Laser Spectroscopy 16* (World Scientific, Singapore, 2004)
1262. E.A. Hinds, A. Ferguson, E,. Riis (eds.), *Laser Spectroscopy 17* (World Scienfitic. 2005)
1263. L.W. Hollberg, J.C. Bergquist, M. Kasevich (eds.), *Laser Spectroscopy 18* (World Scientific, Singapore, 2007)
1264. H. Katori, H. Yoneda, K. Nakagawa, F. Shimizu (eds.), *Laser Spectroscopy XIX* (World Scientific, 2010)
1265. W. Ertmer, R. Schultz (eds.), *Laser Spectroscopy 20* (Logos Verlag, Berlin, 2011)
1266. S. Budker, H. Höffner, H. Müller (eds.), *Laser Spectroscopy 21.* J. Phys. Conf. Ser. **467** (2013)
1267. K. Diekmann (ed.), *Laser Spectroscopy XXII* (World Scientific, 2016)
1268. *Laser Spectroscopy 23* (Arcachon, France)
1269. *Laser Spectroscopy 24* (Queenstown, New Zeeland)
1270. A.L. Schawlow, Spectroscopy in a new light. Rev. Mod. Phys. **54**, 697 (1982)
1271. N. Bloembergen, Nonlinear optics and spectroscopy. Rev. Mod. Phys. **54**, 685 (1982)
1272. J.L. Hall, Nobel Lecture: Defining and measuring optical frequencies. Rev. Mod. Phys. **78**, 1278 (2006)
1273. T.W. Hänsch, Nobel Lecture: Passion for precision. Rev. Mod. Phys. **78**, 1297 (2006)
1274. Proceedings of European Conference on Laser Interaction with Matter (ECLIM), with a recent conference, ECLIM XXXV, arranged in Rethymno, Crete in 2018. Selected papers from the ECLIM conferences are published in the journal Laser and Particle Beams.
1275. D. Kleppner, M.G. Littman, M.L. Zimmerman, Highly excited atoms. Sci. Am. **244**, 130 (1981)
1276. T.F. Gallagher, Rydberg atoms. Rep. Prog. Phys. **51**, 143 (1988)
1277. T.F. Gallagher, *Rydberg Atoms* (Cambridge University Press, Cambridge, 1994)
1278. J.-P. Connerade, *Highly Excited Atoms* (Cambridge University Press, Cambridge, 1997)
1279. R.R. Jones, L.D. Noordam, 'Electronic wavepackets.' In: *Progress in Atomic, Molecular, and Optical Physics*, Vol.38, ed. by B. Bederson, H. Walther (Academic Press, San Diego 1998) p.1
1280. G.M. Lankhuijzen, L.D. Noordam, 'Rydberg ionization: From field to photon.' In: *Progress in Atomic, Molecular, and Optical Physics*, Vol.38, ed. by B. Bederson, H. Walther (Academic Press, San Diego 1998) p.121
1281. M.P.A. Jones, L.G. Marcassa, J. Shaffer, Special Issue on Rydberg atom physics. J. Phys. B: At. Mol. Opt. Phys. **50,** 060202 (2017)

1282. A.A. Morgan, S.D. Hogan, Coupling Rydberg atoms to microwave fields in a superconducting coplanar waveguide resonator. Phys. Rev. Lett. **124**, 193604 (2020)
1283. F. Ripka, H. Kübler, R. Löw, T. Pfau, A room-temperature single-photon source based on strongly interacting Rydberg atoms. Science **362**, 446 (2018)
1284. D.J. Trevor, L.D. van Woerkom, R.R. Freeman, A parabolic mirror time-of-flight electron energy analyzer. Rev. Sci. Instrum. **60**, 1051 (1989)
1285. J. Spickermann, K. Martin, H.J. Rüder, K. Müllen, R.-P. Krüger, H. Schlaad, A.H.E. Müller, Quantitative analysis of broad molecular weight distributions obtained by matrix-assisted laser desorption/ionisation time-of-flight mass spectrometry. Eur. Mass Spectrom. **2**, 161 (1996)
1286. I. Jordan, M. Huppert, M.A. Brown, J.A. van Bokhoven, H.J. Wörner, Photoelectron spectrometer for attosecond spectroscopy of liquids and gases. Rev. Sci. Instr. **86**, 123905 (2015)
1287. V.K. Saini, P. Kumar, S. Shaikh, S.K. Dixit, Development of a thermionic diode detector for laser spectroscopy. Meas. Sci. Techn. **30**, 065501 (2019)
1288. T.W. Ducas, M.G. Littman, R.R. Freeman, D. Kleppner, Stark ionization of high-lying states of sodium. Phys. Rev. Lett. **35**, 366 (1975)
1289. T.F. Gallagher, L.M. Humphrey, R.M. Hill, S.A. Edelstein, Resolution of $[m_l]$ and $[m_j]$ levels in the electric field ionization of highly excited d-states of Na. Phys. Rev. Lett. **37**, 1465 (1976)
1290. F.V. Kowalski, R.T. Hawkins, A.L. Schawlow, Digital wavemeter for CW lasers. J. Opt. Soc. Am. **66**, 965 (1976)
1291. J.L. Hall, S.A. Lee, Interferometric real time display of **CW** dye laser wavelengths with sub-Doppler accuracy. Appl. Phys. Lett. **29**, 367 (1976)
1292. A. Fischer, K. Kullmer, W. Demtröder, Computer-controlled Fabry-Pérot wavemeter. Opt. Commun. **39**, 277 (1981)
1293. L.S. Lee, A.L. Schawlow, Multi-wedge wavemeter for pulsed lasers. Opt. Lett. **6**, 610 (1981)
1294. P. Juncar, J. Pinard, A new method for frequency calibration and laser control. Opt. Commun **14**, 438 (1975)
1295. T.W. Hänsch, J.J. Snyder, *Wavemeters, Dye Lasers*, 3rd edn., ed. by
1296. F.P. Schäfer, Topics Appl. Phys., Vol.1 (Springer, Berlin, Heidelberg 1990)
1297. R. Castell, W. Demtröder, A. Fischer, R. Kullmer, H. Weickenmeier, K. Wikkert, The accuracy of laser wavelength meters. Appl Phys. B **38**, 1 (1985)
1298. M. Herscher, The spherical mirror Fabry-Pérot interferometer. Appl. Opt. **7**, 951 (1968)
1299. J.U. White, Long optical paths of large aperture. J. Opt. Soc. Am. **32**, 285 (1942)
1300. J.U. White, Very long paths in air. J. Opt. Soc. Am. **66**, 411 (1976)
1301. M. Graf, L. Emmenegger, B. Tuzson, Compact, circular, and optically stable multipass cell for mobile laser absorption spectroscopy. Opt. Lett. **43**, 2434 (2018)
1302. T. Svensson, E. Adolfsson, M. Lewander, C.T. Xu, S. Svanberg, Disordered, strongly scattering porous materials as miniature multi-pass gas cells. Phys. Rev. Lett. **107**, 143901 (2011)
1303. S. Bergin, J. Hodgkinson, D. Francis, R.P. Tatam, Ratiometric pathlength calibration of integrating sphere-based absorption cells. Opt. Express **28**, 19574 (2020)
1304. G. Yale Eastman, The heat pipe. Sci. Am. **218**, 38 (1968)
1305. C.R. Vidal, J. Cooper, Heat pipe oven. A new well-defined metal vapor device for spectroscopic measurements. J. Appl. Phys. **40**, 3370 (1969)
1306. H.-L. Chen, Applications of laser absorption spectroscopy. In: [1236] p.261
1307. T.W. Hänsch, A.L. Schawlow, P. Toschek, Ultrasensitive response of a CW dye laser to selective extinction. IEEE J. Quantum Electron. **QE-8**, 802 (1972)
1308. V.M. Baev, J. Eschner, E. Paeth, R. Schüler, P.E. Toschek, Intra-cavity spectroscopy with diode lasers. Appl. Phys. B **55**, 463 (1992)
1309. W. Gurlit, J.P. Burrows, H. Burkhard, R. Bohm, V.M. Baev, P.E. Toschek, Intracavity diode laser for atmospheric field measurements. Infrared Phys. Technol. **37**, 95 (1996)

1310. P. Malara, C.E. Campanella, A. Giorgini, S. Avino, P. De Natale, G. Gagliardi, Super-resonant intracavity coherent absorption. Sci. Reports **6**, 28947 (2016)
1311. P. Fjodorow, O. Hellmig, V.M. Baev, H.B. Levinsky, A.V. Mokhov, Intracavity absorption spectroscopy of formaldehyde from 6230 to 6420 cm^{-1}. Appl. Physics B **123**, 147 (2017)
1312. A. O'Keefe, D.A.G. Deacon, Cavity ring-down spectrometer for absorption measurements using pulsed laser sources. Rev. Sci. Instrum. **59**, 2544 (1988)
1313. R.T. Jongma, M.G.H. Boogaarts, I. Holleman, G. Meijer, Trace gas detection with cavity ring down spectroscopy. Rev. Sci. Instrum. **66**, 2821 (1995)
1314. G. Berden, R. Engeln (eds.), *Cavity Ring-Down Spectroscopy: Techniques and Applications* (Wiley Blackwell, 2009)
1315. T. Stacewicz, J. Wojtas, Z. Bielecki, M. Nowakowski, J. Mikołajczyk, R. Mędrzycki, B. Rutecka, Cavity ring down spectroscopy: detection of trace amounts of substance. Opto-Electr. Rev. **20**, 53 (2011)
1316. A. Karpf, Y. Qiao, G.N. Rao, Ultrasensitive, real-time trace gas detection using a high-power, multimode diode laser and cavity ringdown spectroscopy. Appl. Optics **55**, 4497 (2016)
1317. L. Yang, H. Lin, M. Plimmer, X.J. Feng, H.W. Chu, Y.J Ma, J.T. Luo, H.B. Sun, and J.T. Zhang, Possible two-photon absorption in the near-infrared region observed by cavity ring-down spectroscopy. Opt. Express **28**, 39128 (2020)
1318. S. Maithani, M. Pradhan, Cavity ring-down spectroscopy and its applications to environmental, chemical and biomedical systems. J. Chem. Sci. **132**, 114 (2020)
1319. D.J. Bradley, P. Ewart, J.V. Nicholas, J.R.D. Shaw, Excited state absorption spectroscopy of alkaline earths selectively pumped by tunable dye lasers. I. Barium arc spectra. J. Phys. B **6**, 1594 (1973)
1320. J.R. Rubbmark, S.A. Borgström, K. Bockasten, Absorption spectroscopy of laser-excited barium. J. Phys. B **10**, 421 (1977)
1321. M.E. Kaminsky, R.T. Hawkins, F.V. Kowalski, A.L. Schawlow, Identification of absorption lines by modulated lower-level population: Spectrum of Na. Phys. Rev. Lett. **36**, 671 (1976)
1322. A.L. Schawlow, Simplifying spectra by laser level labeling. Phys. Scr. **25**, 333 (1982)
1323. R. Teets, R. Feinberg, T.W. Hänsch, A.L. Schawlow, Simplification of spectra by polarization labeling. Phys. Rev. Lett. **37**, 683 (1976)
1324. P. Esherick, Bound, even-parity $J = 0$ and $J = 2$ states of Sr. Phys. Rev. A **15**, 1920 (1977)
1325. J.E.M. Goldsmith, J.E. Lawler, Optogalvanic spectroscopy. Contemp. Phys. **22**, 235 (1981)
1326. C.J. Sansonetti, K.-H. Weber, Reference lines for dye-laser wavenumber calibration in the optogalvanic spectra of uranium and thorium. J. Opt. Soc. Am. **131**, 361 (1984)
1327. O. Axner, I. Lindgren, I. Magnusson, H. Rubinsztein-Dunlop, Trace element determination in flames by laser-enhanced ionization spectrometry. Anal. Chem. **57**, 773 (1985)
1328. O. Axner, H. Rubinsztein-Dunlop, Detection of trace amounts of Cr by two laser-based spectroscopic techniques: Laser-enhanced ionization in flames and laser-induced fluorescence in graphite furnace. Appl. Opt. [**32**, 867 (1993)
1329. J. Travis, G. Turk (eds.), *Laser-Enhanced Ionization Spectrometry* (Wiley, New York, 1996)
1330. P. Ljung, E. Nyström, J. Enger, P. Ljungberg, O. Axner, Detection of titanium in electrothermal atomizers by laser-induced fluorescence. Spectrochim. Acta B **52**, 675 (1997); B **52**, 703 (1997)
1331. P. Ljung, O. Axner, Measurements of rubidium in standard reference samples by wavelength-modulation diode laser absorption spectrometry in a graphite furnace. Spectrochim. Acta B **52**, 305 (1997)
1332. X. Hou, S.-J.J. Tsai, J.X. Zhou, K.X. Yang, R.F. Leonardo, R.G. Michel, 'Laser-excited atomic fluorescence spectrometry: Principle, instrumentation and applications.' In: *Lasers in Analytical Spectroscopy*, ed. by J. Sneddon, T.L. Thiem, Y.-I. Lee (VCH Publishers, New York 1997)
1333. C.E. Wieman, L. Hollberg, Using diode lasers for atomic physics. Rev. Sci. Instrum. **62**, 1 (1991)
1334. T. Imasaka, Analytical molecular spectroscopy with diode lasers. Spectrochim. Acta Rev. **15**, 329 (1993)

1335. A.W. Mantz, A review of spectroscopic applications of tunable semiconductor lasers. Spectrochim. Acta A **51**, 221 (1995)
1336. A. Zybin, C. Schnürer-Patschan, M.A. Bolshov, K. Niemax, Elemental analysis by diode laser spectroscopy. Trends Anal. Chem. **17**, 513 (1998)
1337. J.E.M. Goldsmith, Recent advances in flame diagnostics using fluorescence and ionization techniques. In: [1253] p.337
1338. J.A. Paisner, R.W. Solarz, Resonance photoionization spectroscopy. In: [1236] p.175
1339. P. Camus (ed.), Optogalvanic Spectroscopy and its Applications. J. Physique Coll. C7, Suppl. no.11, Tome 44 (1983)
1340. P. Hannaford, Spectroscopy with sputtered atoms. Contemp. Phys. **24**, 251 (1983)
1341. V.S. Letokhov, *Laser Photoionization Spectroscopy* (Academic Press, Orlando, 1987)
1342. N. Omenetto, 'The impact of several atomic and molecular laser spectroscopic techniques for chemical analysis.' In: *Laser Technology in Chemistry*, Special issue, ed. by H. Medin, S. Svanberg, Appl. Phys. B **46**, No.3 (1988)
1343. G.S. Hurst, M.G. Payne (eds.), *Principles and Applications of Resonance Ionization Spectroscopy* (Adam Hilger, Bristol, 1988)
1344. H.-J. Kluge, B.A. Bushaw, G. Passler, K. Wendt, N. Trautmann, Resonance ionization spectroscopy for trace analysis and fundamental research. Fresenius Z. Anal. Chem. **350**, 78 (1994)
1345. G. Eilers, A. Persson C. Gustavsson, L. Ryderfors, E. Mukhtar, G. Possnert, M. Salehpour, The radiocarbon intracavity optogalvanic spectroscopy setup at Uppsala. Radiocarbon **55**, 237(2013)
1346. S. Olmschenk, P.R. Banner, J. Hankes, A.M. Nelson, Optogalvanic spectroscopy of the hyperfine structure of the $5p^6 5d\ ^2D_{3/2,5/2}$ and $5p^6 4f\ ^2F_{5/2,7/2}$ levels of La III. Phys. Rev. A **96**, 032502 (2017)
1347. G.S. Hurst, M.G. Payne, S.D. Kramer, C.H. Chen, R.C. Phillips, S.L. Allman, G.D. Alton, J.W.T. Dabbs, Rd. Willis, B.E. Lehman, Method for counting noble gas atoms with isotopic selectivity. Rep. Prog. Phys. **48**, 1333 (1985)
1348. V.S. Letokhov, Detecting individual atoms and molecules with lasers. Sci. Am. **259**(3), 44 (1988)
1349. J.T. Höffges, H.W. Baldauf, T. Eichler, S.R. Helmfrid, H. Walther, 'Resonance fluorescence of a single ion.' In: *Atomic Physics Methods in Modern Research*, ed. by K. Jungmann, J. Kowalski, I. Reinhard, F. Träger (Springer, Berlin, Heidelberg 1997)
1350. R. Zimmermann, L. Hanley, *Photoionization and Photo-Induced Processes in Mass Spectrometry: Fundamentals and Applications* (Wiley-VCH Verlag, 2021)
1351. D. Kliger (ed.), *Ultrasensitive Laser Spectroscopy* (Academic Press, New York, 1983)
1352. J.J. Snyder, R.A. Keller (eds.), *Ultrasensitive Laser Spectroscopy*, Special issue, J. Opt. Soc. Am. B **2**, No9 (1985)
1353. Th. Basche, W.E. Moerner, M. Orritt, U.P. Wild (eds.), *Single Molecule Optical Detection, Imaging and Spectroscopy* (Wiley-VCH, Munich, 1997)
1354. D.R. Walt, Optical methods for single molecule detection and analysis. Anal. Chem. **85**, 1258 (2013)
1355. K. Kneipp, Y. Wang, H. Kneipp, L.T. Perelman, I. Itzkan, R.R. Dasari, M.S. Feld, Single molecule detection using surface-enhanced Raman scattering (SERS). Phys. Rev. Lett. **78**, 1667 (1997)
1356. S. Weiss, Fluorescence spectroscopy of single biomolecules. Science **283**, 1676 (1999) (Special Issue, March 12, 1999)
1357. X. Sunney Xie, J.K. Trautman, Single-molecule optical studies at room temperature. Ann. Rev. Phys. Chem. **49**, 441 (1998)
1358. W.E. Moerner, M. Orrit, Illuminating single molecules in condensed matter. Science **283**, 1670 (1999)
1359. E. Betzig, G.H. Patterson, R. Sougrat, O. Wolf Lindwasser, S. Olenych, J.S. Bonifacino, M.W. Davidson, J. Lippincott Schwartz, H.F. Hess, Imaging intracellular fluorescent proteins at nanometer resolution. Science **313**, 1642 (2006)

1360. N. Omenetto (ed.), *Analytical Laser Spectroscopy* (Wiley, New York, 1979)
1361. E.H. Piepmeier (ed.), *Analytical Applications of Lasers* (Wiley, New York, 1986)
1362. V.S. Letokhov (ed.), *Laser Analytical Spectrochemistry* (Hilger, Bristol, 1986)
1363. N. Omenetto, The role of lasers in analytical atomic spectroscopy – Where, when and why. J. Anal. At. Spectrom. **13**, 385 (1998)
1364. E. Betzig, Single molecules, cells, and super-resolution optics. Rev. Mod. Phys. **87**, 1153 (2015)
1365. S. Hell, Nanoscopy with focused light. Angew. Chem. Int. Ed. **54**, 8054 (2015)
1366. W.E. Moerner, Single-molecule spectroscopy, imaging, and photocontrol: Foundations for super-resolution microscopy. Angew. Chem. Int. Ed. **54**, 8069 (2015)
1367. Z. Liu, L.D. Lavis, E. Betzig, Imaging live-cell dynamics and structure at the single-molecule level. Mol. Cell **58**, 644 (2015)
1368. M.J. Rust, M. Bates, X. Zhuang, Sub-diffraction-limit imaging by stochastic optical reconstruction microscopy (STORM). Nat. Meth. **3**, 793 (2006)
1369. B. Huang, W. Wang, M. Bates, X. Zhuang, Three-dimensional super-resolution imaging by stochastic optical reconstruction microscopy. Science **319**, 810 (2008)
1370. S.W. Hell, J. Wichmann, Breaking the diffraction resolution limit by stimulated emission: Stimulated emission-depletion fluorescence microscopy. Opt. Lett. **19**, 780 (1994)
1371. W. Westphal, S.W. Hell, Nanoscale resolution in the focal plane of an optical microscope. Phys. Rev. Lett. **94**, 143903 (2005)
1372. S.W. Hell, K.I. Willig, M. Dyba, S. Jakobs, L. Kastrup, V. Westphal, Nanoscale resolution with focused light: STED and other RESOLFT microscopy concepts, in J.B. Pawley (ed.), *Handbook of Biological Confocal Microscopy*, 3rd edition (Springer Science, New York 2006)
1373. S. Hell, Far-field optical nanoscopy. Science **316**, 1153 (2007)
1374. S. Svanberg, 'Fundamentals of atmospheric spectroscopy.' In: *Surveillance of Electromagnetic Pollution and Resources by Electromagnetic Waves*, ed. by T. Lund (Reidel, Dordrecht 1978)
1375. L.B. Kreutzer, Laser optoacoustic spectroscopy. A new technique of gas analysis. Anal. Chem. **46**, 239A (1974)
1376. A. Rosencwaig, *Photoacoustics and Photoacoustic Spectroscopy* (Wiley, New York, 1980)
1377. V. Zharov, V. Letokhov, *Laser Opto-Acoustic Spectroscopy*, Springer Ser. Opt. Sci., Vol.37 (Springer, Berlin, Heidelberg 1986)
1378. A.C. Tam, Applications of photoacoustic sensing techniques. Rev. Mod. Phys. **58**, 381 (1986)
1379. P. Hess (ed.), *Photoacoustics* (Springer, Berlin, Heidelberg, 1990)
1380. M.W. Sigrist, 'Air monitoring by laser photoacoustic spectroscopy.' In: *Air Monitoring by Spectroscopic Techniques*, ed. by M.W. Sigrist (Wiley, New York 1994)
1381. F.J.M. Harren, 'Photoacoustic spectroscopy in trace gas monitoring.' In: *Encyclopedia of Analytical Chemistry: Applications, Theory and Instrumentation*, ed. by R.A. Meyers (Wiley, New York 2000) p.2203
1382. T. Schmid, Photoacoustic spectroscopy for process analysis. Anal. Bioanalyt. Chem. **384**, 1071 (2006)
1383. M.W. Sigrist, Photoacoustic Spectroscopy, Methods and Instrumentation', in *Encyclopedia of Spectroscopy and Spectrometry, 3rd edn.,* (Elsevier, 2017)
1384. D.C. Dumitras, M. Petrus, A.-M. Bratu, C. Popa, Applications of near infrared photoacoustic spectroscopy for analysis of human respiration: A review. Molecules **25**, 1728 (2020)
1385. A.A. Kosterev, Y.A. Bakhirkin, R.F. Curl, F.K. Tittel, Quartz-enhanced photoacoustic spectroscopy. Opt. Lett. **27**, 1902 (2002)
1386. Y.F. Ma, R. Lewicki, M. Razeghi, F.K. Tittel, QEPAS based ppb-level detection of CO and N_2O using a high power CW DFB-QCL. Opt. Express **21**, 1008 (2013)
1387. P. Patimisco, G. Scamarcio, F.K. Tittel, V. Spagnolo, Quartz-enhanced photoacoustic spectroscopy: A review. Sensors **14**, 6165 (2014)
1388. H.P. Wu, L. Dong, H.D. Zheng, Y.J. Yu, W.G. Ma, L. Zhang, W.B. Yin, L.T. Xiao, S.T. Jia, F.K. Tittel, Beat frequency quartz-enhanced photoacoustic spectroscopy for fast and calibration-free continuous trace-gas monitoring. Nature Com **8**, 15331 (2017)

1389. C.K.N. Patel, A.C. Tam, Pulsed optoacoustic spectroscopy of condensed matter. Rev. Mod. Phys. **53**, 517 (1981)

1390. C. Hernández-Aguilar, A. Domínguez-Pacheco, A. Cruz-Orea, R. Ivanov, Photoacoustic spectroscopy in the optical characterization of foodstuff: A Review. J. Spectroscopy **2019**, 5920948 (2019)

1391. L.V. Wang (ed.), *Photoacoustic Imaging and Spectroscopy* (CRC Press, 2009)

1392. S. Svanberg, P. Tsekeris, W. Happer, Hyperfine structure studies of highly excited D and F levels in alkali atoms using a CW dye laser. Phys. Rev. Lett. **30**, 817 (1973)

1393. S. Svanberg, P. Tsekeris, Hyperfine-structure investigation of highly excited ^{2}D levels in ^{87}Rb and ^{133}Cs using a CW tunable laser in a two-step excitation scheme. Phys. Rev. A **11**, 1125 (1975)

1394. G. Belin, I. Lindgren, L. Holmgren, S. Svanberg, Hyperfine interaction, Zeeman and Stark effects for excited states in potassium. Phys. Scr. **12**, 287 (1975)

1395. K. Fredriksson, S. Svanberg, Precision determination of the fine structure of the $4d$ state in sodium using level crossing spectroscopy. Phys. Lett. A **53**, 61 (1975)

1396. G. Belin, L. Holmgren, S. Svanberg, Hyperfine interaction, Zeeman and Stark effects for excited states in rubidium. Phys. Scr. **13**, 351 (1976)

1397. G. Belin, L. Holmgren, S. Svanberg, Hyperfine interaction, Zeeman and Stark effects for excited states in cesium. Phys. Scr. **14**, 39 (1976)

1398. R. Neumann, F. Träger, G. zu Putlitz, 'Laser-microwave spectroscopy.' In: *Progress in Atomic Spectroscopy*, Pt.D, ed. by H.K. Beyer, H. Kleinpoppen (Plenum, New York 1987) p.1

1399. T.F. Gallagher, 'Radiofrequency spectroscopy of Rydberg atoms.' In: *Progress in Atomic Spectroscopy*, Pt.D, ed. by H.K. Beyer, H. Kleinpoppen (Plenum, New York 1987) p.12

1400. E. Matthias, R.A. Rosenberg, E.D. Poliakoff, M.G. White, S.-T. Lee, D.A. Shirley, Time-resolved VUV spectroscopy using synchrotron radiation: Fluorescent lifetimes of atomic Kr and Xe. Chem. Phys. Lett. **52**, 239 (1977)

1401. R. Rigler, O. Kristensen, R. Roslund, P. Thyberg, K. Oba, M. Eriksson, Molecular structure and dynamics: Beamline for time-resolved spectroscopy at the MAX synchrotron in Lund. Phys. Scr. **T17**, 204 (1987)

1402. J. Jaeschke, S. Kahn, J.R. Schneider, J.B. Hastings (eds.), *Synchrotron Light Sources and Free-Electron Lasers* (Springer, 2016)

1403. U. Berzinsh, Luo Caiyan, R. Zerne, S. Svanberg, Determination of radiative lifetimes of neutral sulphur by time-resolved VUV laser spectroscopy. Phys. Rev. A **55**, 1836 (1997)

1404. Se. Johansson, A. Joueizadeh, U. Litzén, J. Larsson, A. Persson, C.-G. Wahlström, S. Svanberg, D.S. Leckrone, G.M. Wahlgren, Comparison of new experimental and astrophysical f-values for some Ru II lines, observed in HST spectra of χ Lupi. Astrophys. J. **421**, 809 (1994)

1405. H. Bergström, G.W. Faris, H. Hallstadius, H. Lundberg, A. Persson, C.-G. Wahlström, Radiative lifetime and hyperfine-structure studies on laser-evaporated boron. Z. Phys. D **8**, 17 (1988)

1406. R.A. Lacy, A.C. Nilsson, R.L. Byer, W.T. Silvfast, O.R. Wood II, S. Svanberg, 'Photoionization-pumped gain at 185 nm in a laser-ablated Indium plasma.' In: *Short Wavelength Coherent Radiation: Generation and Applications*, AIP Conference Proceedings No.147, ed. by D.T. Attwood, J. Bokor (AIP, New York 1986); and J. Opt. Soc. Am. B **6**, 1209 (1989)

1407. Z.-S. Li, J. Norin, A. Persson, C.-G. Wahlström, S. Svanberg, P.S. Doidge, E. Bimont, Radiative properties of neutral germanium obtained from excited state lifetime and branching ratio measurements and comparison with theoretical calculations. Phys. Rev. A **60**, 198 (1999)

1408. M.B. Gaarde, R. Zerne, C. Luo, Z. Jiang, J. Larsson, S. Svanberg, Determination of radiative lifetimes of excited states in neutral gold using time-resolved VUV laser spectroscopy. Phys. Rev. A **50**, 209 (1994)

1409. R. Zerne, J. Larsson, S. Svanberg, Determination of radiative lifetimes in the $3d^{10}np\ ^2P$ sequence of neutral copper by time-resolved VUV laser spectroscopy. Phys. Rev. A **49**, 128 (1994)

1410. U. Berzinsh, S. Svanberg, Atomic radiative lifetimes measured by pulsed laser spectroscopy in the UV/VUV spectral region. Adv. Quantum Chem. **30**, 283 (1998)
1411. J.C. Cooper, N.D. Gibson, J.E. Lawler, Radiative lifetimes in Cr I by laserinduced fluorescence. J. Quant. Spectrosc. Radiat. Transfer **58**, 85 (1997)
1412. G.M. Wahlgren, S.G. Johansson, U. Litzén, N.D. Gibson, J.C. Cooper, J.E. Lawler, D.S. Leckrone, R. Engleman Jr., Atomic data for the Re II resonance multiplet and its application to astrophysics. Astrophys. J. **475**, 380 (1997)
1413. P. Quinet, P. Palmeri, E. Biemont, Z.S. Li, Z.G. Zhang, S. Svanberg, Radiative lifetime measurements and transition probability calculations in lanthanide ions. J. of Alloys and Compounds **344**, 255 (2002)
1414. H.L. Xu, S. Svanberg, P. Quinet, P. Palmeri, E. Biémont, Improved Atomic Data for Iridium Atom (Ir I) and Ion (Ir II) and the Solar Content of Iridium. J. Quant. Spectr. Rad. Transf. **104**, 52 (2007)
1415. H. Nilsson, J. Andersson, L. Engström, H. Lundberg, H. Hartman, Experimental transition probabilities for 4p–4d spectral lines in V II. Astr. Astrophys. **622**, 201834795 (2019)
1416. H. Nilsson, L. Engström, H. Lundberg, H. Hartman, P. Palmeri, P. Quinet, Experimental and theoretical lifetimes and transition probabilities for spectral lines in NbII. Astr. Astrophys. **627**, A112 (2019)
1417. Z.G. Zhang, S. Svanberg, P. Quinet, P. Palmeri, E. Biemont, Time-resolved spectroscopy of multiply ionized atoms – Natural radiative lifetimes in Ce IV. Phys. Rev. Lett. **87**, 273001 (2001)
1418. P.B. Coates, The correction for photon ”pile-up” in the measurement of radiative lifetimes. J. Phys. E **1**, 878 (1968)
1419. M. Gustavsson, H. Lundberg, L. Nilsson, S. Svanberg, Lifetime measurements for excited states of rare-earth atoms using pulse-modulation of a CW dye laser beam. J. Opt. Soc. Am. **69**, 984 (1979)
1420. J. Carlsson, Accurate time-resolved laser spectroscopy on sodium and bismuth atoms. Z. Phys. D **9**, 147 (1988)
1421. K. Bhatia, P. Grafström, C. Levinson, H. Lundberg, L. Nilsson, S. Svanberg, Natural radiative lifetimes in the perturbed $6snd\ ^1D_2$ sequence of barium. Z. Physik A **303**, 1 (1981)
1422. S. Svanberg, Perturbations in Rydberg sequences probed by lifetime, Zeeman-and hyperfine structure measurements. In: A.R.W. McKellar, T. Oka, B.P. Stoicheff (Eds.), *Laser Spectroscopy V* (Springer, 1981) p. 301
1423. T.F. Gallagher, W. Sandner, K.A. Safinya, Probing configuration interaction of the Ba $5d7d\ ^1D_2$ state using radiofrequency spectroscopy and lifetime measurements. Phys. Rev. A **23**, 2969 (1981)
1424. M. Aymar, R.-J. Champeau, C. Delsart, J.C. Keller, Lifetimes of Rydberg levels in the perturbed $6snd\ ^{1,3}D_2$ series of barium I. J. Phys. B **14**, 4489 (1981)
1425. J. Carlsson, L. Sturesson, Accurate time-resolved laser spectroscopy on lithium atoms. Z. Phys. D **14**, 281 (1989)
1426. J. Carlsson, Accurate time-resolved laser spectroscopy on sodium and bismuth atoms. Z. Phys. D **9**, 147 (1988)
1427. J. Carlsson, P. Jönsson, L. Sturesson, C. Froese Fischer, Multi-configuration Hartree-Fock calculations and time-resolved laser spectroscopy studies of hyperfine structure constants in sodium. Phys. Scr. **46**, 394 (1992)
1428. C. De Michelis, M. Mattioli, Spectroscopy and impurity behaviour in fusion plasmas. Rep. Prog. Phys. **47**, 1233 (1984)
1429. R.C. Isler, Impurities in Tokomaks. Nucl. Fusion **24**, 1599 (1984)
1430. R.E. Imhof, F.H. Read, Measurements of lifetimes of atoms, molecules and ions. Rep. Prog. Phys. **40**, 1 (1977)
1431. P. Erman, ‘Time-resolved spectroscopy of small molecules.’ In: Specialists Periodical Reports, *Molecular Spectroscopy*, Vol.6, Chap.5 (The Chemical Society, London 1979) p.174
1432. J.N. Dodd, G.W. Series, ‘Time-resolved fluorescence spectroscopy.’ In: *Progress in Atomic Spectroscopy*, Pt.A, ed. by W. Hanle, H. Kleinpoppen (Plenum, New York 1978) p.639

1433. W.L. Wiese, 'Atomic transition probabilities and lifetimes.' In: *Progress in Atomic Spectroscopy*, Pt.B, ed. by W. Hanle, H. Kleinpoppen (Plenum, New York 1979) p.1101
1434. M.C.E. Huber, R.J. Sandeman, The measurement of oscillator strengths. Rep. Prog. Phys. **49**, 397 (1986)
1435. O. Poulsen, J.L. Hall, Spectroscopic investigation in ^{209}Bi I using tunable CW-dye-laser spectroscopy. Phys. Rev. A **18**, 1089 (1978)
1436. S. Svanberg, Natural radiative lifetimes of some excited Bi I levels belonging to the $6p^2 7s$ and the $6p^2 6d$ configurations measured by the Hanle method. Phys. Scr. **5**, 73 (1972)
1437. H.J. Andrä, A. Gaupp, W. Wittmann, New method for precision lifetime measurements by laser excitation of fast-moving atoms. Phys. Rev. Lett. **31**, 501 (1973)
1438. A. Gaupp, P. Kuske, H.J. Andrä, Accurate lifetime measurements of the lowest $^2P_{1/2}$ states in neutral lithium and sodium. Phys. Rev. A **26**, 3351 (1982)
1439. C.E. Tanner, A.E. Livingston, R.C. Rafac, F.G. Serpa, K.W. Kukla, H.G. Berry, L. Young, C.A. Kurtz, Phys. Rev. Lett. **69**, 2765 (1992)
1440. T. Brage, C. Froese Fischer, P. Jönsson, Effects of core-valence and core-core correlation on the line strength of the resonance lines in Li I and Na I. Phys. Rev. A **49**, 2181 (1994)
1441. C.E. Tanner, 'Precision measurements of atomic lifetimes.' In: *Atomic Physics XIV*, ed. by D.J. Wineland, C.E. Wieman, S.J. Smith (AIP Publ., New York 1995) p.150
1442. P. Erman, J. Brzozowski, B. Sigfridsson, Gas excitations using highfrequency deflected electron beams: A convenient method for determinations of atomic and molecular lifetimes. Nucl. Instrum. Methods **110**, 471 (1973)
1443. P. Erman, High-resolution measurements of atomic and molecular lifetimes using the high-frequency deflection technique. Phys. Scr. **11**, 65 (1975)
1444. P. Erman, Astrophysical applications of time-resolved molecular spectroscopy. Phys. Scr. **20**, 575 (1979); Studies of perturbations using time resolved techniques. Phys. Scr. **25**, 365 (1982)
1445. J. Brzozowski, P. Bunker, N. Elander, P. Erman, Predissociation effects in the A, B, and C states of CN and the interstellar formation rate of CH via inverse predissociation. Astrophys. J. **207**, 414 (1976)
1446. J.K. Link, Measurement of the radiative lifetimes of the first excited states of Na, K, Rb, and Cs by means of the phase-shift method. J. Opt. Soc. Am. **56**, 1195 (1966)
1447. P.T. Cunningham, J.K. Link, Measurement of lifetimes of excited states of Na, Tl, In, Ga, Cu, Ag, Pb, and Bi by the phase-shift method. J. Opt. Soc. Am. **57**, 1000 (1967)
1448. L. Armstrong Jr., S. Ferneuille, Theoretical analysis of the phase shift measurement of lifetimes using monochromatic light. J. Phys. B **8**, 546 (1975)
1449. C.H. Corliss, W.R. Bozman, Experimental transition probabilities for spectral lines of seventy elements. NBS Monograph 53 (National Bureau of Standards, Washington, DC 1962)
1450. W. Marlow, Hakenmethode. Appl. Opt. **6**, 1715 (1967)
1451. N.P. Penkin, 'Experimental determination of electronic transition probabilities and the lifetimes of the excited atomic and ionic states.' In: *Atomic Physics 6*, ed. by R. Damburg (Plenum, New York 1979) p.33
1452. W.A. van Wijngaarden, K.D. Bonin, W. Happer, Inverse hook method for measuring oscillator strengths for transitions between excited atomic states. Hyperfine Interact. **38**, 471 (1987)
1453. S. Svanberg, Atomic spectroscopy by resonance scattering. Philos. Trans. R. Soc. London A **293**, 215 (1979)
1454. J.N. Dodd, G.W. Series, 'Time-resolved fluorescence spectroscopy.' In: *Progress in Atomic Spectroscopy*, Pt.A, ed. by W. Hanle, H. Kleinpoppen (Plenum, New York 1978) p.639
1455. S. Haroche, Quantum beats and time-resolved fluorescence spectroscopy. In: K. Shimoda (ed.): *High-Resolution Laser Spectroscopy,* Topics Appl. Phys. Vol. 13 (Springer, Berlin Heidelberg 1976) p.253
1456. R. Forbes, V. Makhija, J.G. Underwood, A. Stolow, I. Wilkinson, P. Hockett, R. Lausten, Quantum-beat photoelectron-imaging spectroscopy of Xe in the VUV. Phys. Rev. A **97**, 063417 (2018)

1457. P. Grundevik, H. Lundberg, A.-M. Mårtensson, K. Nyström, S. Svanberg, Hyperfine-structure study in the *P* sequence of ^{23}Na using quantum-beat spectroscopy. J. Phys. B **12**, 2645 (1979)
1458. G. Jönsson, C. Levinson, L. Lindgren, A. Persson, C.G. Wahlström, Experimental and theoretical studies of the $4s^2np\ ^2P$ sequence in neutral gallium. Z. Phys. A **322**, 351 (1985)
1459. J. Bengtsson, J. Larsson, S. Svanberg, C.-G. Wahlström, Hyperfine-structure study of the $3d^{10}5p\ ^2P_{3/2}$ level of neutral copper using pulsed level-crossing spectroscopy at short wavelengths. Phys. Rev. A **41**, 233 (1990)
1460. G.J. Bengtsson, P. Jönsson, J. Larsson, S. Svanberg, Time-resolved spectroscopic studies of the $7p\ ^2P$ states of neutral silver following VUV excitation. Z. Physik D **22**, 437 (1991)
1461. J. Larsson, S. Svanberg, High-resolution VUV spectroscopy using pulsed laser sources. Appl. Phys. B **59**, 433 (1994)
1462. H. Figger, H. Walther, Optical resolution beyond the natural linewidth: A level-crossing experiment on the $3\ ^2P_{3/2}$ level of sodium using a tunable dye laser. Z. Phys. **267**, 1 (1974)
1463. P. Schenk, R.C. Hilborn, H. Metcalf, Time-resolved fluorescence from Ba and Ca excited by a pulsed tunable dye laser. Phys. Rev. Lett. **31**, 189 (1974)
1464. D.P. O'Brien, P. Meystre, H. Walther, 'Subnatural linewidths in atomic spectroscopy.' In: *Advanced Atomic and Molecular Physics*, Vol.21, ed. by D.R. Bates, B. Bederson (Academic Press, Orlando 1985)
1465. J. Bengtsson, J. Larsson, S. Svanberg, Hyperfine structure and radiative lifetime determination for the $4d^{10}6s\ ^2P$ states of neutral silver using pulsed laser spectroscopy. Phys. Rev. A **42**, 545 (1990)
1466. F. Shimizu, K. Shimuiu, Y. Gomi, H. Takuma, Direct observation of hyperfine splittings of the ^{7}Li $^2P_{3/2}$ state by subnatural linewidth spectroscopy. Phys. Rev. A **35**, 3149 (1987)
1467. J. Larsson, L. Sturesson, S. Svanberg, Manipulation of level-crossing signals using narrow-band or pulsed laser excitation. Phys. Scr. **40**, 165 (1989)
1468. G.D. Billings, K.V. Mikkelsen, *Introduction to Molecular Dynamics and Chemical Kinetics* (Wiley, London, 1996)
1469. O. Svelto, S. De Silvresti, G. Denardo (eds.), *Ultrafast Processes in Spectroscopy* (Plenum, New York, 1996)
1470. J. Hoff, J. Deisenhofer, Photophysics of photosynthesis. Phys. Rep. **287**, 1 (1997)
1471. E. Schreiber, *Femtosecond Real-Time Spectroscopy of Small Molecules and Clusters* (Springer, Berlin, Heidelberg, 1998)
1472. Th. Elsaesser, M. Woerner, Femtosecond infrared spectroscopy of semiconductors and semiconductor nanostructures. Phys. Rep. **321**, 253 (1999)
1473. A.M. Weiner, *Ultrafast Optics* (John Wiley, 2008)
1474. M.D. Fayer (ed.), *Ultrafast Infrared Vibrational Spectroscopy* (CRC Press, 2013)
1475. J. Yuen-Zhou, J.J. Krich, I. Kassal, A.S. Johnson, A. Aspuru-Guzik, *Ultrafast Spectroscopy - Quantum information and wavepackets* (IOP Publishing 2014)
1476. T. Schultz, M. Vrakking (eds.), *Attosecond and XUV Physics: Ultrafast Dynamics and Spectroscopy* (Wiley, 2014
1477. K. Yamanouchi, S. Cundiff, R. de Vivie-Riedle, M. Kuwata-Gonokami, L. DiMauro (eds.), *Ultrafast Phenomena XIX* (Springer 2015)
1478. D. Zigmantas, T. Polivka, Advanced Ultrafast Spectroscopy Methods, in *Light Harvesting in Photosynthesis*. ed. by R. Croce, R. van Grondelle, H. van Amerongen, I. van Stokkum (CRC Press, 2018), pp. 427–446
1479. A. Bhattacharya, *Ultrafast Optics and Spectroscopy in Physical Chemistry* (World Scientific, 2018)
1480. A. Leitenstorfer, K.A. Nelson, K. Tanaka, Special issue on ultrafast spectroscopy: Fundamentals. J. Phys. B: At. Mol. Opt. Phys. **52**, 010201 (2019)
1481. M. Maiuri, M. Garavelli, G. Cerullo, Ultrafast spectroscopy: State of the art and open challenges. J. Am. Chem. Soc. **142**, 3 (2020)
1482. S. Letzring, Buying and using a streak camera. Lasers & Appl. (March 1983) p.49

1483. G.H. Kassier, K. Haupt, N. Erasmus, E.G. Rohwer, H.M. von Bergmann, H. Schwoerer, S.M.M. Coelho, F.D. Auret, A compact streak camera for 150 fs time resolved measurement of bright pulses in ultrafast electron diffraction. Rev. Sci. Instr. **81**, 105103 (2010)
1484. Guide to Streak Cameras, https://www.hamamatsu.com/resources/pdf/sys/SHSS0006E_STREAK.pdf (Hamamatsu Corp., Hamamatsu City, Japan, 2008)
1485. R. Trebino, D.J. Kane, Using phase retrieval to measure the intensity and phase of ultra-short pulses: Frequency-resolved optical gating. J. Opt. Soc. Am. A **10**, 1101 (1993)
1486. R. Trebino, K.W. DeLong, D.N. Fittinghoff, D.N. Sweetser, M.A. Krumbugel, B.A. Richman, D.J. Kane, Measuring ultra-short laser pulses in the time-frequency domain using frequency-resolved optical gating. Rev. Sci. Instrum. **68**, 3277 (1997)
1487. A. Baltuska, M. Pshenichnikov, D.A. Wiersma, Amplitude and phase characterization of 4.5 fs pulses by frequency-resolved optical gating. Opt. Lett. **23**, 1474 (1998)
1488. S. Linden, H. Giessen, J. Kuhl, XFROG, A new method for amplitude and phase characterization of weak ultrashort pulses. Phys. Status Solidi **206**, 119 (1998)
1489. C. Iaconis, I.A. Walmsley, Spectral phase interferometry for direct electric field reconstruction of ultrashort optical pulses. Opt. Lett. **23**, 792 (1998)
1490. C. Iaconis, I.A. Walmsley, Self-referencing spectral interferometry for measuring ultrashort optical pulses. IEEE J. Quant. Electr. **35**, 501 (1999)
1491. A. Monmayrant, S. Weber, B. Chatel, A newcomer's guide to ultrashort pulse shaping and characterization. J. Phys. B: At. Mol. Opt. Phys. **43**, 103001 (2010)
1492. M. Miranda, M. Kotur, P. Rudawski, C. Guo, A. Harth, A. L'Huillier, C. Arnold, Spatiotemporal characterization of ultrashort laser pulses using spatially resolved Fourier transform spectrometry. Opt. Letters **39**, 5142 (2014)
1493. R.R. Alfano (ed.), *The Supercontinuum Laser Source* (Springer-Verlag, New York, 1989)
1494. J.M. Dudley, G. Genty, S. Coen, Supercontinuum generation in photonic crystal fiber. Rev. Mod. Phys. **78**, 1135 (2006)
1495. J.W. Wang, P.A. Tanner, Upconversion for white light generation by a single compound. J. Am. Chem. Soc. **132**, 947 (2010)
1496. H. Wille, M. Rodriguez, J. Kasparian, D. Mondelain, J. Yu, A. Mysyrowicz, R. Sauerbrey, J.P. Wolf, L. Wöste, Teramobile: A mobile femtosecond terawatt laser and detection system. Eur. Phys. J. AP **20**, 183 (2002)
1497. J.H. Wu, G.J. Zheng, X.F. Liu, J.R. Qiu, Near-infrared laser driven white light continuum generation: materials, photophysical behaviours and applications. Chem. Soc. Rev. **49**, 3461 (2020)
1498. P.R. Smith, D.A. Auston, M.C. Nuss, Subpicosecond photoconducting dipole antennas. IEEE J. Quantum Electron. **QE-24**, 255 (1988)
1499. M. van Exter, Ch. Fattiger, D. Grischkowsky, High-brightness terahertz beams characterized with an ultrafast detector. Appl. Phys. Lett. **55**, 337 (1989)
1500. D. Grischkowsky, S. Keiding, M. van Exter, Ch. Fattiger, Far-infrared time-domain spectroscopy with terahertz beams of dielectrics and semiconductors. J. Opt. Soc. Am. B **7**, 2006 (1990)
1501. R.A. Cheville, D. Grischkowsky, Far-infrared terahertz time-domain spectroscopy of flames. Opt. Lett. **20**, 1646 (1995)
1502. D.M. Mittleman, R.H. Jacobsen, M.C. Nuss, T-ray imaging. IEEE J. Sel. Topics Quantum Electron. **2**, 679 (1996)
1503. P.Y. Han, G.C. Cho, X.C. Zhang, Time-domain transillumination of biological tissues with terahertz pulses. Opt. Lett. **24**, 242 (2000)
1504. R.M. Woodward, W.P. Wallace, R.J. Pye, B.E. Cole, D.D. Arnone, E.H. Linfield, M. Pepper, Terahertz pulse imaging of ex vivo basal cell carcinoma. J. Invest. Derm. **120**, 72 (2003)
1505. B.S. Williams, Terahertz quantum-cascade lasers. Nat. Photonics **1**, 717 (2007)
1506. P. Dean, A. Valavanis, J. Keeley, K. Bertling, Y.L. Lim, R. Alhathlool, A.D. Burnett, L.H. Li, S.P. Khanna, D. Indjin, T. Taimre, A.D. Rakić, E.H. Linfield, A.G. Davies, Terahertz imaging using quantum cascade lasers—a review of systems and applications. J. Phys. D: Appl. Phys. **47**, 374008 (2014)

1507. B.S. Williams, Q. Hu, ‘Terahertz Lasers,’ *In Encyclopedia of Modern Optics (2nd edn.)* (Elsevier, 2018) Vol. 1, pp. 379–386
1508. M.S. Vitiello, L. Consolino, M. Inguscio, P. De Natale, Toward new frontiers for terahertz quantum cascade laser frequency combs. Nanophotonics **10**, 187 (2021)
1509. A.H. Zewail, Laser femtochemistry. Science **242**, 1645 (1988)
1510. M.J. Rosker, T.S. Rose, A.H. Zewail, Real-time dynamics of photofragment-trapping resonances on dissociative potential energy surfaces. Chem. Phys. Lett. **146**, 175 (1988)
1511. L.R. Khundkar, A.H. Zewail, Picosecond photofragment spectroscopy. IV. Dynamics of consecutive bond breakage in the reaction $C_2F_4I_2 \rightarrow C_2F_4 + 2I$. J. Chem. Phys. **92**, 231 (1990)
1512. S. Pedersen, L. Banares, A.H. Zewail, Femtosecond vibrational transition state dynamics in a chemical reaction. J. Chem. Phys. **97**, 8801 (1992)
1513. A. Zewail, Femtochemistry: Atomic-scale dynamics of the chemical bond using ultrafast lasers (Nobel lecture). Angew. Chemie **39**, 2596 (2000)
1514. J. Ullrich, R. Moshammer, A. Dorn, R. Dorner, LPh.H. Schmidt, H. Schmidt-Böcking, Recoil-ion and electron momentum spectroscopy: reaction-microscopes. Rep. Prog. Phys. **66**, 1463 (2003)
1515. A. Ehn, J. Bood, Z.M. Li, E. Berrocal, M. Aldén, E. Kristensson, FRAME: femtosecond videography for atomic and molecular dynamics. Light Sci. Appl. **6**, 17045 (2017)
1516. V. Kornienko, E. Kristensson, A. Ehn, A. Fourriere, E. Berrocal, Beyond MHz image recordings using LEDs and the FRAME concept. Sci. Rep. **10**, 16650 (2020)
1517. J. Liang, L.V. Wang, Single-shot ultrafast optical imaging. Optica **5**, 1113 (2018)
1518. P. Wang, J.Y. Liang, L.V. Wang, Single-shot ultrafast imaging attaining 70 trillion frames per second. Nature Com. **11**, 2091 (2020)
1519. Y. Zheng et al., Computational 4D imaging of light-in-flight with relativistic effects. Photonics Res. **8**, 1072 (2020)
1520. K. Morimoto et al., Superluminal motion-assisted four-dimensional light-in-flight imaging. Phys. Rev. X **11**, 011005 (2021)
1521. M. Shapiro, P. Brumer, Coherent and incoherent laser control of photochemical reactions. Int. Rev. Phys. Chem. **13**, 187 (1994)
1522. T.C. Weinacht, J. Ahn, P.H. Bucksbaum, Controlling the shape of a quantum wavefunction. Nature **397**, 233 (1999)]
1523. M. Dantus, V.V. Lozovoy, Experimental coherent laser control of physicochemical processes. Chem. Rev. **104**, 1813 (2004)
1524. M. Shapiro, P. Brumer, *Quantum Control of Molecular Processes* (Wiley-VCH, 2012)
1525. L. Levin, W. Skomorowski, L. Rybak, R. Kosloff, Ch. Koch, Z. Amitay, Coherent control of bond making. Phys. Rev. Lett. **114**, 233003 (2015)
1526. S.E. Harris, Electromagnetically induced transparancy. Phys. Today **50**(7), 36 (1997)
1527. O. Kocharovskaya, Amplification and lasing without inversion. Phys. Rep. **219**, 175 (1992)
1528. M. Fleischhauer, A. Imamoglu, J.P. Marangos, Electromagnetically induced transparency: Optics in coherent media. Rev. Mod. Phys. **77**, 633 (2005)
1529. O.A. Kocharovskaya, Y.I. Khanin, Coherent amplification of ultrashort pulse in the three-level medium without population inversion. JETP Lett. **48**, 630 (1988)
1530. S.E. Harris, Lasers without inversion: Interference of lifetime-broadened resonances. Phys. Rev. Lett. **62**, 1033 (1989)
1531. M.O. Scully, S.-Y. Zhu, A. Gavridiles, Degenerate quantum-beat laser: Lasing without inversion and inversion without lasing. Phys. Rev. Lett. **62**, 2813 (1989)
1532. O. Kocharovskaya, From lasers without inversion to gamma lasers? Laser Phys. **5**, 284 (1995)
1533. O. Kocharovskaya, R. Kolesov, Yu. Rostovtsev, Lasing without inversion: a new path to gamma-ray laser. Laser Phys. **9**, 745 (1999)
1534. E.S. Fry, X. Li, D. Nikonov, G.G. Padmabandu, M.O. Scully, A.V. Smith, F.K. Tittel, C. Wang, S.R. Wilkinson, S.-Y. Zhu, Atomic coherence effect within the sodium D line: Lasing without inversion via population trapping. Phys. Rev. Lett. **70**, 3235 (1993)

1535. W.E. van der Veer, R.J.J. van Dienst, A. Dönszelmann, H.B. van Linden van den Heuvell, Experimental demonstration of light amplification without population inversion. Phys. Rev. Lett. **70**, 3243 (1993)
1536. A.S. Zibrov, M.D. Lukin, D.E. Nikonov, L. Hollberg, M.O. Scully, V.L. Velichansky, H.G. Robinson, Experimental demonstration of laser oscillation without population inversion via quantum interference in Rb. Phys. Rev. Lett. **75**, 1499 (1995)
1537. C. Fort, F.S. Cataliotti, T.W. Hänsch, M. Inguscio, M. Prevedelli, Gain without inversion on the cesium D_1 line. Opt. Commun. **139**, 31 (1997)
1538. A. Kaspari, M. Jain, G.Y. Jin, S.E. Harris, Electromagnetically induced transparancy: Propagation dynamics. Phys. Rev. Lett. **74**, 2447 (1995)
1539. L. Vestergaard Hau, S.E. Harris, Z. Dutton, C.H. Behroozi, Light speed reduction to 17 metres per second in an ultracold atomic gas. Nature **397**, 594 (1999)
1540. M.M. Kash, V.A. Sautenkov, A.S. Zibrov, L. Hollberg, G.R. Welch, M.D. Lukin, Y. Rostovtsev, E.S. Fry, M.O. Scully, Ultraslow group velocity and enhanced nonlinear optical effects in a coherently driven hot atomic gas. Phys. Rev. Lett. **82**, 5229 (1999)
1541. D.-F. Phillips, A. Fleischhauer, A. Mair, R.L. Walsworth, M.D. Lukin, Storage of light in atomic vapor. Phys. Rev. Lett. **86**, 783 (2001)
1542. C. Liu, Z. Dutton, C.H. Behroozi, L.V. Hau, Observation of coherent optical information storage in an atomic medium using halted light pulses. Nature **409**, 490 (2001)
1543. M. Ossiander, Y.-W. Huang, W.T. Chen, Z. Wang, X. Yin, Y.A. Ibrahim, M. Schultze, F. Capasso, Slow light nanocoatings for ultrashort pulse. Compression. Nature Commun. **12**, 6518 (2021)
1544. S.E. Harris, L. Vestergaard Hau, Nonlinear optics at low light levels. Phys. Rev. Lett. **82**, 4611 (1999)
1545. M.D. Lukin, A. Imamoglu, Nonlinear optics and quantum entanglement of ultraslow single photons. Phys. Rev. Lett. **84**, 1419 (2000)
1546. G. Mainfrey, P. Agostini (eds.), *Multiphoton Processes* (CEA, Paris 1991)
1547. M. Gavrila (ed.), *Atoms in Intense Laser Fields* (Academic Press, Boston, 1992)
1548. N.B. Delone, V.P. Krainov, *Multiphoton Processes in Atoms*, vol. 13 (Springer Verlag, Heidelberg, 1994)
1549. S. Svanberg, J. Larsson, A. Persson, C.-G. Wahlström, Lund high power laser facility - Systems and first results. Phys. Scr. **49**, 187 (1994)
1550. P. Lambropoulos, H. Walther (eds.), *Multiphoton Physics*, IOP Conf. Ser., Vol.154 (IOP Publishing, Bristol 1997)
1551. S. Svanberg, A. L'Huillier, C.-G. Wahlström, Atomic physics using short-wavelength coherent radiation. Nucl. Instrum. Methods A **398**, 55 (1997)
1552. M. Protopapas, C.H. Keitel, P.L. Knight, Atomic physics with super-high intensity lasers. Rep. Prog. Phys. **60**, 389 (1997)
1553. N.H. March, *Atoms and Molecules in Intense Fields* (Springer Verlag, Heidelberg, 1997)
1554. L. Di Mauro, M. Murnane, A. L'Huillier (eds.), *Applications of ol.Highfield and Short Wavelength Sources* (Plenum, New York 1998)
1555. P. Mulser, *High Power Laser-Matter Interaction* (Springer, Berlin, Heidelberg, 1999)
1556. P. Gibbon, *Short Pulse Laser Interactions with Matter - An Introduction* (World Scientific, 2005)
1557. P. Mulser, D. Bauer, *High Power Laser-Matter Interaction* (Springer, 2010)
1558. C.J. Joachain, N.J. Kylstra, R.M. Potvliege, *Atoms in Intense Laser Fields* (Cambridge University Press, 2012)
1559. K. Yamanouchi, K. Midorikawa (eds.), *Multiphoton Processes and Attosecond Physics* (Springer, 2012)
1560. L.A. Gizzi, R. Assmann, P.M. Koester, A. Giulietti (eds.), *Laser-Driven Sources of High Energy Particles and Radiation* (Springer, 2019)
1561. P. Mulser, *Hot Matter from High-Power Lasers - Fundamentals and Phenomena* (Springer, 2020)

1562. H. Takabe, *The Physics of Laser Plasmas and Applications - Physics of Laser Matter Interaction* (Springer, 2020)
1563. K. Yamanouchi, S.L. Chin, P. Agostini, G. Ferrante (eds.), *Progress in Ultrafast Intense Laser Science I* (Springer, 2006)
1564. K. Yamanouchi, S.L. Chin, P. Agostini, G. Ferrante (eds.), *Progress in Ultrafast Intense Laser Science II* (Springer, 2007)
1565. K. Yamanouchi, S.L. Chin, P. Agostini, G. Ferrante (eds.), *Progress in Ultrafast Intense Laser Science III* (Springer, 2008)
1566. K. Yamanouchi, A. Becker, R. Li, S.L. Chin (eds.), *Progress in Ultrafast Intense Laser Science IV* (Springer, 2008)
1567. K. Yamanouchi, Kaoru, K. Midorikawa (eds.), *Progress in Ultrafast Intense Laser Science IX* (Springer, 2013)
1568. K. Yamanouchi, P. Martin, M. Sentis, L. Ruxin, D. Normand (eds.), *Progress in Ultrafast Intense Laser Science XIV* (Springer, 2018)
1569. K. Yamanouchi, D. Charalambidis (eds.), *Progress in Ultrafast Intense Laser Science XV* (Springer, 2020)
1570. P. Agostini, F. Fabre, G. Mainfray, G. Petite, N. Rahman, Free-free transitions following six-photon ionization of xenon atoms. Phys. Rev. Lett. **42**, 1127 (1979)
1571. K.C. Kulander, Time-dependent theory of multiphoton ionization of xenon. Phys. Rev. A **38**, 778 (1988)
1572. H.B. van Linden van den Heuvel, H.G. Muller, In: *Multiphoton Processes*, Studies in Modern Optics, Vol. 8, ed. by S.J. Smith, P.L. Knight (Cambridge University Press, Cambridge 1988)
1573. P.B. Corkum, N.H. Burnett, F. Brunel, Above-threshold ionization in the long-wavelength limit. Phys. Rev. Lett. **62**, 1259 (1989)
1574. J.H. Eberly, J. Javanainen, K. Rzazewski, Above-threshold ionization. Phys. Rep. **204**, 331 (1991)
1575. L.F. DiMauro, P. Agostini, Ionization dynamics in strong laser fields. Adv. At. Mol. Opt. Phys. **35**, 79 (1995)
1576. D.B. Miloševic´, G.G. Paulus, D. Bauer, W. Becker, Above-threshold ionization by few-cycle pulses –Topical Review. J. Phys. B: At. Mol. Opt. Phys. **39**, R203 (2006)
1577. C. Cheng, R. Forbes, A.J. Howard, M. Spanner, P.H. Bucksbaum, T. Weinacht, Momentum-resolved above-threshold ionization of deuterated water. Phys. Rev. A **102**, 052813 (2020)
1578. R.R. Freeman, P.H. Bucksbaum, H. Milchberg, S. Darack, D. Schumacher, M. Geusic, Above-threshold ionization with subpicosecond laser pulses. Phys. Rev. Lett. **59**, 1092 (1987)
1579. L.J. Fransinski, K. Codling, P.A. Hatherly, Covariance mapping: A correlation method applied to multiphoton multiple ionization. Science **246**, 973 (1989)
1580. R. Schinke, *Photodissociation Dynamics* (Cambridge University Press, Cambridge, 1993)
1581. K. Codling, L.J. Frasinski, Coulomb explosion of simple molecules in intense laser fields. Contemp. Phys. **35**, 243 (1994)
1582. L.J. Fransinski, P.A. Hatherly, K. Codling, M. Larsson, A. Persson, C.-G. Wahlström, Multielectron dissociative ionization of CO_2 in intense laser fields. J. Phys. B **27**, L109 (1994)
1583. S. Hunsche, T. Starczewski, A. L'Huillier, A. Persson, C.-G. Wahlström, H.B. van Linden van den Heuvell, S. Svanberg, Ionization and fragmentation of C_{60} via multiphoton-multiplasmon excitation. Phys. Rev. Lett. **77**, 1966 (1996)
1584. T. Yatsuhashi, N. Nakashima, Multiple ionization and Coulomb explosion of molecules, molecular complexes, clusters and solid surfaces. J. Photochem. Photobiol. C - Photochemistry Reviews **34**, 52 (2018)
1585. A. McPherson, G. Gibson, H. Jara, U. Johann, T.S. Luk, I.A. McIntyre, K. Boyer, C.K. Rhodes, Studies of multi-photon production of vacuum ultraviolet radiation in rare gases. J. Opt. Soc. Am. B **4**, 595 (1987)
1586. M. Ferrey, A. L'Huillier, X.F. Li, L.A. Lompre, G. Mainfray, C. Manus, Multiple-harmonic conversion of 1064 nm radiation in rare gases. J. Phys. B **21**, L31 (1988)

1587. J.L. Krause, K.J. Schaefer, K.C. Kulander, High-harmonic generation from atoms and ions in the high intensity regime. Phys. Rev. Lett. **68**, 3535 (1992)
1588. P.B. Corkum, Plasma perspective on strong field multiphoton ionization. Phys. Rev. Lett. **71**, 1994 (1993)
1589. M. Lewenstein, Ph. Balcou, MYu. Ivanov, A. L'Huillier, P.B. Corkum, Theory of high-harmonic generation by low-frequency laser fields. Phys. Rev. A **49**, 2117 (1994)
1590. A. L'Huillier, T. Auguste, Ph. Balcou, B. Carr, P. Monot, P. Salières, C. Altucci, M. Gaarde, J. Larsson, E. Mevel, T. Starczewski, S. Svanberg, C.-G. Wahlström, R. Zerne, K.S. Budil, T. Ditmire, M.D. Perry, High-order harmonics: a coherent source in the XUV range. J. Nonlinear Opt. Phys. Mater. **4**, 647 (1995)
1591. A. L'Huillier, Generation and application of high-order harmonics: An alternative coherent short-pulse XUV source. In: *X-Ray Lasers 1996*, IOP Conference Series **151**, ed. by. S. Svanberg, C.-G. Wahlström (IOP Publishing, Bristol 1996)
1592. C. Lyngå, PhD Dissertation (Lund Institute of Technology, Lund 1999)
1593. C.-G. Wahlström, J. Larsson, A. Persson, T. Starczewski, S. Svanberg, P. Salières, P. Balcou, A. L'Huillier, High-order harmonic generation in rare gases with an intense short-pulse low-frequency laser. Phys. Rev. A **48**, 4709 (1993)
1594. J.J. Macklin, J.M. Kmetec, C.L. Gordon III, High-order harmonic generation using intense femtosecond pulses. Phys. Rev. Lett. **70**, 766 (1993)
1595. A. L'Huillier, Ph. Balcou, High-order harmonic generation in rare gases with a 1 ps 1053 nm laser. Phys. Rev. Lett. **70**, 774 (1993)
1596. S.G. Preston, A. Sanpera, M. Zepf, W.J. Blyth, C.G. Smith, J.S. Wark, M.H. Key, K. Burnett, M. Nakai, D. Neely, A.A. Offenberger, High-order harmonics of 248.6 nm KrF laser from helium and neon ions. Phys. Rev. A **53**, 31 (1996)
1597. Z. Chang, A. Rundquist, H. Wang, M.M. Murnane, H. Kapteyn, Generation of coherent soft X-rays at 2.7 nm using high harmonics. Phys. Rev. Lett. **79**, 2967 (1997)
1598. Ch. Spielmann, N.H. Burnett, S. Sartarnia, R. Koppnitsch, M. Schnürer, C. Kan, M. Lenzner, P. Wobrauschek, F. Krausz, Generation of coherent X-rays in the water window using 5 femtosecond laser pulses. Science **278**, 661 (1997)
1599. C. Altucci, T. Starczewski, C.-G. Wahlström, E. Mevel, B. Carr, A. L'Huillier, Influence of atomic density in high-order harmonic generation. J. Opt. Soc. Am. B **13**, 148 (1996)
1600. T. Starczewski, J. Larsson, C.-G. Wahlström, M.H.R. Hutchinson, J.E. Muffett, R.A. Smith, J.W.G. Tisch, Time-resolved harmonic generation in an ionizing gas. J. Phys. B **27**, 3291 (1994)
1601. T. Brabec (ed.), *Strong-Field Laser Physics* (Springer, 2009)
1602. K. Varjú, Y. Mairesse, B. Carre, M.B. Gaarde, P. Johnsson, S. Kazamias, R. Lopez-Martens, J. Mauritsson, K.J. Schafer, Ph. Balcou, A. L'Huillier, P. Salières, Frequency chirp of harmonic and attosecond pulses. J. Mod. Opt. **52**, 379 (2005)
1603. P. Salires, A. L'Huillier, Ph. Antoine, M. Lewenstein, 'Study of the spatial and temporal coherence of high-order harmonics.' In: *Progress in Atomic, Molecular, and Optical Physics*, Vol.41, ed. by B. Bederson, H. Walther (Academic Press, San Diego 1999)
1604. J.M. Schins, P. Breger, P. Agostini, R.C. Constantinescu, H.G. Muller, A. Bouhal, G. Grillon, A. Antonetti, A. Mysyrowicz, Cross-correlation measurements of femtosecond extreme-ultraviolet high-order harmonics. J. Opt. Soc. Am. B **13**, 197 (1996)
1605. X. Lavocat-Dubuis, F. Vidal, J.-P. Matte, C. Popovici, T. Ozaki, J.-C. Kieffer, Effects of chirp and pulse shape on high harmonic generation and absorption in overdense plasmas. Lasers Part. Beams **29**, 95 (2011)
1606. K. Midorikawa, High-order harmonic generation and attosecond science. Jap. J. Appl. Physics **50**, 090001 (2011)
1607. L. Roos, M.B. Gaarde, A. L'Huillier, Tailoring harmonic radiation to different applications using a genetic algorithm. J. Phys. B. **34**, 5041 (2001)
1608. R. Ganeev, *High-Order Harmonic Generation in Laser Plasma Plumes.* (World Scientific, 2012)
1609. R. Ganeev, *Resonance Enhancement in Laser-Produced Plasmas* (Wiley-Blackwell 2018)

1610. D. von der Linde, Generation of high order optical harmonics from solid surfaces. Appl. Phys. B **68**, 315 (1999)
1611. G. Ndabashimiye, S. Ghimire, M.X. Wu, D.A. Browne, K.J. Schafer, M.B. Gaarde, D.A. Reis, Solid-state harmonics beyond the atomic limit. Nature **532**, 520 (2016)
1612. J.-G. Fan, X.Y. Miao, X.F. Jia, Control of the high-order harmonic generation by sculpting waveforms with chirp in solids. Chem. Phys. Lett. **762**, 138136 (2021)
1613. M.R. Shcherbakov, H.Z. Zhang, M. Tripepi, G. Sartorello, N. Talisa, A. AlShafey, Z.Y. Fan, J. Twardowski, L.A. Krivitsky, A.I. Kuznetsov, E. Chowdhury, G. Shvets, Generation of even and odd high harmonics in resonant metasurfaces using single and multiple ultra-intense laser pulses. Nature Commun. **12**, 4185 (2021)
1614. S. Kazamias, D. Douillet, C. Valentin, Th. Lefrou, G. Grillon, G. Mullot, F. Augé, P. Mercère, Ph. Zeitoun, Ph. Balcou, Optimization of the focused flux of high harmonics. Eur. Phys. D. **26**, 47 (2003)
1615. R. Bonifacio, C. Pellegrini, I.M. Narducci, Collective instabilities and high-gain regime in a free electron laser. Opt. Commun. **50**, 373 (1984)
1616. K. Tiedtke, A. Azima, N. von Bargen, L. Bittner, S. Bonfigt, S. Düsterer, B. Faatz, U. Frühling, M. Gensch, Ch. Gerth, The soft x-ray free-electron laser FLASH at DESY: beamlines, diagnostics and end-stations. New J. Phys. **11**, (2009)
1617. J. Feldhaus, FLASH—the first soft x-ray free electron laser (FEL) user facility. J. Phys. B: At. Mol. Opt. Phys. **43**, 194002 (2010)
1618. H.P. Freund, *Principles of Free-Electron Lasers* (Springer, 2012)
1619. S. Schreiber, B. Faatz, The free-electron laser FLASH. High Power Laser Sci. Eng. **3**, e20 (2015)
1620. C. Pellegrini, A. Marinelli, S. Reiche, The physics of x-ray free-electron lasers. Rev. Mod. Phys. **88**, 015006 (2016)
1621. J. Rossbach, J.R. Schneider, W. Wurth, 10 years of pioneering X-ray science at the Free-Electron Laser FLASH at DESY. Phys. Rep. **808**, 1 (2019)
1622. J. Larsson, E. Mevel, R. Zerne, A. L'Huillier, C.-G. Wahlström, S. Svanberg, Two-colour time-resolved spectroscopy of helium using high-order harmonics. J. Phys. B **28**, L53 (1995)
1623. C. Lyngå, F. Ossler, T. Metz, J. Larsson, A laser system providing radiation tunable from 35 nm to 2 μm. Appl. Phys. B **72**, 913 (2001)
1624. C.V. Shank, J.E. Bjorkholm, H. Kogelnik, Distributed feedback dye laser. Appl. Phys. Lett. **18**, 395 (1972)
1625. F. Schäfer, W. Schade, B. Garbe, V. Helbig, Temperature-tuned distributed feedback dye laser with high repetition rate. Appl. Opt. **29**, 3950 (1990)
1626. G.J. Bengtsson, K. Hansen, J. Larsson, W. Schade, S. Svanberg, Determination of radiative lifetimes in neutral nitrogen using short laser pulses from a distributed feedback dye laser. Z. Physik D **22**, 397 (1991)
1627. M.I. Skvortsov, A.A. Wolf, A.V. Dostovalov, A.A. Vlasov, V.A. Akulov, S.A. Babin, Distributed feedback fiber laser based on a fiber Bragg grating inscribed using the femtosecond point-by-point technique. Laser Phys. Lett. **15**, 035103 (2018)
1628. Y.L. Fu, T.R. Zhai, Distributed feedback organic lasing in photonic crystals. Front. Optoelectr. **13**, 18 (2020)
1629. P. Cacchiani, W. Ubachs, P.C. Hinnen, C. Lyngå, A. L'Huillier, C.-G. Wahlström, Lifetime measurements of the $E^1\Pi$, $v = 0$ and $v = 1$ states of $^{12}C^{16}O$, $^{13}C^{16}O$ and $^{13}C^{18}O$. Astrophys. J. **499**, L223 (1998)
1630. D. Dechamps, L. Roos, C. Delfin, A. L'Huillier, C.-G. Wahlström, Two- and three-photon ionization of rare gases using femtosecond harmonic pulses generated in a gas medium. Phys. Rev. A**64**, 031404/1–4 (2001)
1631. P. Erman, A. Karawajcyk, E. Rachlew-Källne, E. Mevel, R. Zerne, A. L'Huillier, C.-G. Wahlström, Autoionization width of the NO Rydberg valence state complex in the 11–12 eV region. Chem. Phys. Lett. **239**, 6 (1995)
1632. K.S.E. Eikema, W. Ubachs, W. Wassen, W. Hogervorst, First laser excitation of the ^{4}He 1 ^{1}S–2 ^{1}P resonance line at 58 nm. Phys. Rev. Lett. **71**, 1690 (1993)

1633. K.S.E. Eikema, W. Ubachs, W. Vassen, W. Hogervorst, Precision spectroscopy on the Lyman-α transitions of H and He. In *Laser Physics at the limit*; eds. H. Figger, D. Meschede, C. Zimmerman (Springer Verlag, Berlin, Heidelberg 2002) p.107

1634. R. Haight, J. Bokor, J. Stark, R.H. Storz, R.R. Freeman, P.H. Bucksbaum, Picosecond time-resolved photoemission study of the InP (110) surface. Phys. Rev. Lett. **54**, 1302 (1985)

1635. H.S. Karlsson, G. Ghiaia, U.O. Karlsson, A system for time- and angle-resolved photoelectron spectroscopy based on an amplified titanium:sapphire laser system. Rev. Sci. Instrum. **67**, 3610 (1996)

1636. S. Sorensen, O. Björneholm, S. Buil, D. Deschamps, T. Kihlgren, A. L'Huillier, J. Norin, G. Öhrwall, S. Sundin, S. Svensson, C.-G. Wahlström, Femtosecond pump-probe photoelectron spectroscopy of predissociative Rydberg states in acetylene. J. Chem. Phys. **112**, 8038 (2000)

1637. R. Zerne, C. Altucci, M. Bellini, M.B. Gaarde, T.W. Hänsch, A. L'Huillier, C.-G. Wahlström, Phase-locked high-order harmonic sources. Phys. Rev. Lett. **79**, 1006 (1997)

1638. M. Bellini, C. Lyngå, A. Tozzi, M.B. Gaarde, T.W. Hänsch, A. L'Huillier, C.-G. Wahlström, Temporal coherence of ultrashort high-order harmonic pulses. Phys. Rev. Lett. **81**, 297 (1998)

1639. D. Deschamps, C. Lyngå, J. Norin, A. L'Huillier, C.-G. Wahlström, J.-F. Hergott, H. Merdji, P. Salières, M. Bellini, T.W. Hänsch, Extreme ultraviolet interferometry measurements with high-order harmonics. Opt. Lett. **25**, 135 (2000)

1640. G. Farkas, C. Toth, Proposal for attosecond light pulse generation using laser-induced multiple-harmonic conversion processes in rare gases. Phys. Lett. A **168**, 447 (1992)

1641. S.E. Harris, J.J. Macklin, T.W. Hänsch, Atomic scale temporal structure inherent to high-order harmonic generation. Opt. Commun. **100**, 487 (1993)

1642. P.B. Corkum, N.H. Burnett, M.Y. Ivanov, Subfemtosecond pulses. Opt. Lett. **19**, 1870 (1994)

1643. P. Antoine, A. L'Huillier, M. Lewenstein, Attosecond pulse trains using high-order harmonics. Phys. Rev. Lett. **77**, 1234 (1996)

1644. I.P. Christov, N.H. Murnane, H.C. Kapteyn, High-harmonic generation of attosecond pulses in the "single-cycle" regime. Phys. Rev. Lett. **78**, 1251 (1997)

1645. E. Constant, V.D. Tatanukhin, A. Stolow, P.B. Corkum, Methods for the measurement of the duration of high-harmonic pulses. Phys. Rev. A **56**, 3870 (1997)

1646. N.A. Papadogiannis, B. Witzel, C. Kalpouzos, D. Charalambidis, Observation of attosecond light localization in higher order harmonic generation. Phys. Rev. Lett. **83**, 4289 (1999)

1647. P.M. Paul, E.S. Toma, P. Breger, G. Mullot, F. Aug, Ph. Balcou, H.G. Muller, P. Agostini, Observation of a train of attosecond pulses from high harmonic generation. Science **292**, 1689 (2001)

1648. M. Drescher, M. Hentschel, R. Kienberger, G. Tempea, C. Spielmann, G.A. Reider, P.B. Corkum, F. Krausz, X-ray pulses approaching the attosecond frontier. Science **291**, 1923 (2001)

1649. M. Hentschel, R. Kienberger, Ch. Spielmann, G.A. Reider, N. Milosevic, T. Brabec, P.B. Corkum, U. Heinzmann, M. Drescher, F. Krausz, Attosecond metrology. Nature **414**, 511 (2001)

1650. M. Drescher, M. Hentschel, R. Kienberger, M. Uiberacker, V. Yakovlev, A. Scrinzi, Th. Westerwalbesloh, U. Kleineberg, U. Heinzmann, F. Krausz, Time resolved atomic inner-shell spectroscopy. Nature **419**, 803 (2002)

1651. D. Charalambidis, N.A. Papadogiannis, P. Tzallas, G.D. Tsakiris, K. Witte, Recent developments in attosecond pulse train metrology. Phys. Scr. **T105**, 23 (2003)

1652. R. López-Martens, K. Varjú, P. Johnsson, J. Mauritsson, Y. Mairesse, P. Salières, M.B. Gaarde, K.J. Schafer, A. Persson, S. Svanberg, C.G. Wahlström, A. L'Huillier, Amplitude and phase control of attosecond light pulses. Phys. Rev. Lett. **94**, 033001 (2005)

1653. F. Krausz, M. Ivanov, Attosecond physics. Rev. Mod. Phys. **81**, 163 (2009)

1654. F. Krausz, *Electrons in Motion: Attosecond Physics Explores Fastest Dynamics* (World Scientific, 2019)

1655. Z.Y. Wei (ed.), *Proceedings of the 6th International Conference on Attosecond Physics* (Springer 2020)

1656. K. Klünder, J.M. Dahlström, M. Gisselbrecht, T. Fordell, M. Swoboda, D. Guénot, P. Johnsson, J. Caillat, J. Mauritsson, A. Maquet, R. Taïeb, A. L'Huillier, Probing single-photon ionization on the attosecond time scale. Phys. Rev. Lett. **106**, 143002 (2011)
1657. M. Isinger, R.J. Squibb, D. Busto, S. Zhong, A. Harth, D. Kroon, S. Nandi, C.L. Arnold, M. Miranda, J.M. Dahlström, E. Lindroth, R. Feifel, M. Gisselbrecht, A. L'Huillier, Photoionization in the time and frequency domain. Science **358**, 6365 (2017)
1658. D.L. Matthews, P.L. Hagelstein, M.D. Rosen, M.J. Eckart, N.M. Ceglio, A.U. Hazi, H. Medecki, B.J. MacGowan, J.E. Trebes, B.L. Whitten, E.M. Campbell, C.W. Hatcher, A.M. Hawryluk, R.L. Kauffman, L.D. Pleasance, G. Rambach, J.H. Scofield, G. Stone, T.A. Weaver, Demonstration of a soft X-ray amplifier. Phys. Rev. Lett. **54**, 110 (1985)
1659. R.C. Elton, *The Physics of X-Ray Lasers* (Academic Press, New York, 1990)
1660. J.J. Rocca, L.B. Da Silva (eds.), *Soft X-Ray Lasers and Applications II*, Proc. SPIE Int. Soc. Opt. Eng. **3156** (SPIE, Bellingham 1997)
1661. E. G. Tallents (ed.), *X-Ray Lasers*, IOP Conf. Ser. Vol.116 (Institute of Physics Publ., Bristol 1990)
1662. E. Fill (ed.), *X-Ray Lasers 1992*, IOP Conf. Ser. Vol.125 (Institute of Physics Publ., Bristol 1992)
1663. D.C. Eder, D.L. Matthews (eds.), *X-Ray Lasers 1994*, AIP Conf. Proc. Vol.332 (AIP Press, New York 1994)
1664. S. Svanberg, C.-G. Wahlström (eds.), *X-Ray Lasers 1996*, IOP Conf. Ser. Vol.151 (Institute of Physics Publ., Bristol 1996)
1665. Y. Kato, H. Takuma, H. Daido (eds.), *X-Ray Lasers 1998*, IOP Conf. Ser. Vol.159 (Institute of Physics Publ., Bristol 1999)
1666. G. Jamelot, C. Möller, A. Klisnick (eds.), *X-Ray Lasers 2000* (EDP Sciences, Les Ulis 2001)
1667. J.J. Rocca, J. Dunn, S. Suckewer (eds.), *X-Ray Lasers 2002*, AIP Conf. Proc. Vol. 641 (AIP Press, New York 2002)
1668. J. Zhang (ed.), *X-Ray Laser 2004* (CRC Press, 2005)
1669. P.V. Nickles, K.A. Janulewicz (eds.), *X-Ray Lasers 2006* (Springer, 2008)
1670. C.L.S. Lewis, D. Riley (eds.), *X-Ray Lasers 2008* (Springer, 2010)
1671. J. Lee, C.H. Nam, K.A. Janulewicz (eds.), *X-Ray Lasers 2010* (Springer, 2011)
1672. S. Sebban, J. Gauthier, D. Ros, P. Zeitoun (eds.), *X-Ray Lasers 2012* (Springer, 2013)
1673. J. Rocca, C. Menoni, M. Marconi (eds.), *X-Ray Lasers 2014* (Springer, 2015)
1674. T. Kawachi, S.V. Bulanov, H. Daido, Y. Kato (eds.), *X-Ray Lasers 2016* (Springer, 2017)
1675. M. Kozlová, Michaela, J. Nejdl (eds.), *X-Ray Lasers 2018* (Springer, 2020)
1676. B.J. MacGowan, L.B. Da Silva, D.J. Fields, C.J. Keane, J.A. Koch, R.A. London, D.L. Matthews, S. Maxon, S. Mrowka, A.L. Osterheld, J.H. Scofield, G. Smimkaveg, J.E. Trebes, R.S. Walling, Short wavelength X-ray laser research at the Lawrence Livermore National Laboratory. Phys. Fluids B **4**, 2326 (1992)
1677. B. Rus, A. Clarillon, B. Gauth, P. Goedtkindt, P. Jaeglé, G. Jamelot, A. Klisnick, A. Sureau, P. Zeitoun, Observation of intense soft-X-ray lasing at the $J = 0$ to $J = 1$ transition in neon-like zinc. J. Opt. Soc. Am. B **11**, 564 (1994)
1678. F. Albert, Ph. Zeitoun, P. Jaeglé, D. Joyeux, M. Boussoukaya, A. Clarillon, S. Hubert, G. Jamelot, A. Klisnick, D. Phalippou, D. Ros, A. Zeitoun-Fakiris, Metal-surface mapping by means of soft-x-ray interferometry. Phys. Rev. B **60**, 11,089 (1999)
1679. Y. Nagata, K. Midorikawa, M. Obara, H. Tashiro, K. Toyoda, Soft-X-ray amplification of the Lyman-α transition by optical-field-induced ionization. Phys. Rev. Lett. **71**, 3774 (1993)
1680. B.N. Chichkov, A. Egbert, H. Eichmann, C. Momma, S. Nolte, B. Wellegehausen, Soft-x-ray lasing to the ground states in low-charged oxygen ions. Phys. Rev. A **52**, 1629 (1995)
1681. E. Fill, S. Borgström, J. Larsson, T. Starczewski, C.-G. Wahlström, S. Svanberg, XUV spectra of optical-field ionized plasmas. Phys. Rev. E **51**, 6016 (1995)
1682. B.E. Lemoff, G.Y. Yin, C.L. Gordon III, C.P.J. Barty, S.E. Harris, Demonstration of a 10 Hz femtosecond-pulse-driven XUV laser at 41.8 nm in Xe IX. Phys. Rev. Lett. **74**, 1574 (1995)
1683. J.J. Rocha, V.N. Shlyapstev, F.G. Tomasel, O.D. Cortazar, D. Hartshorn, J.L.A. Chilla, Demonstration of a discharge-pumped table-top soft-X-ray laser. Phys. Rev. Lett. **73**, 2192 (1994)

1684. J. Hecht, The history of the X-ray laser. Optics and Photonics News, May 2008, p. 27
1685. J.D. Kmetec, C.L. Gordon III., J.J. Macklin, B.E. Lemoff, G.S. Brown, S.E. Harris, MeV X-ray generation with a femtosecond laser. Phys. Rev. Lett. **68**, 1527 (1992)
1686. K. Herrlin, G. Svahn, C. Olsson, H. Pettersson, C. Tillman, A. Persson, C.-G. Wahlström, S. Svanberg, Generation of X-rays for medical imaging by high-power lasers: Preliminary results. Radiology **189**, 65 (1993)
1687. C. Tillman, S. Johansson, B. Erlandsson, M. Grätz, B. Hemdal, A. Almén, S. Mattson, S. Svanberg, High-resolution spectroscopy of laser-produced plasmas in the photon energy range above 10 keV. Nucl. Instrum. Methods A **394**, 387 (1997)
1688. G. Hölzer, E. Förster, M. Grätz, C. Tillman, S. Svanberg, X-ray crystal spectroscopy of sub-picosecond laser-produced plasmas beyond 50 keV. J. X-Ray Sci. Technol. **7**, 50 (1997)
1689. C. Tillman, A. Persson, C.-G. Wahlström, S. Svanberg, K. Herrlin, Imaging using hard X-rays from a laser-produced plasma. Appl. Phys. B **61**, 333 (1995)
1690. R. Lewis, Medical applications of synchrotron radiation X-rays. Phys. Med. Biol. **42**, 1213 (1997)
1691. C. Tillman, I. Mercer, S. Svanberg, K. Herrlin, Elemental biological imaging by differential absorption using a laser-produced X-ray source. J. Opt. Soc. Am. B **13**, 209 (1996)
1692. C.L. Gordon III., G.Y. Yin, B.E. Lemoff, P.E. Bell, C.P.J. Barty, Timegated imaging with an ultrashort-pulse laser-produced-plasma X-ray source. Opt. Lett. **20**, 1056 (1995)
1693. M. Grätz, A. Pifferi, C.-G. Wahlström, S. Svanberg, Time-gated imaging in radiology: Theoretical and experimental studies. IEEE J. Sel. Topics Quantum Electron. **2**, 1041 (1996)
1694. M. Grätz, L. Kiernan, C.-G. Wahlström, S. Svanberg, Time-gated X-ray tomography. Appl. Phys. Lett. **73**, 2899 (1998)
1695. C. Tillman, G. Grafström, A.-C. Jonsson, B.-A. Jnsson, I. Mercer, S. Mattson, S.-E. Strandh, S. Svanberg, Survival of mammalian cells exposed to ultrahigh dose rates from a laser-produced plasma X-ray source. Radiology **213**, 860 (1999)
1696. K. Shinohara, H. Nakano, N. Miyazaki, M. Tago, R. Kodama, Effects of single-pulse ($<$ or $=$ 1 ps) X-rays from laser-produced plasmas on mammalian cells. J. Radiat. Res. **45**, 509 (2004)
1697. L. Miaja-Avila, G.C. O'Neil, J. Uhlig, C.L. Cromer, M.L. Dowell, R. Jimenez, A.S. Hoover, K.L. Silverman, J.N. Ullom, Laser plasma x-ray source for ultrafast time-resolved x-ray absorption spectroscopy. Struct. Dynamics **2**, 024301 (2015)
1698. J. Wark, Time-resolved X-ray diffraction. Contemp. Phys. **37**, 205 (1996)
1699. C. Rischel, A. Rousse, I. Uschmann, O.-A. Albouy, J.-P. Geindre, P. Audebert, J.C. Gauthier, E. Förster, J.-L. Martin, A. Antonetti, Femtosecond time-resolved X-ray diffraction from laser-heated organic films. Nature **370**, 480 (1997)
1700. J. Hajdu, The challenge offered by X-ray lasers. Nature **417**, 15 (2002)
1701. J. Larsson, A. Allen, P.H. Bucksbaum, R.W. Falcone, A. Lindenberg, G. Naylor, T. Misalla, D.A. Reis, K. Scheidt, A. Sjögren, P. Sondhauss, M. Wulff, J.S. Wark, Pico-second X-ray diffraction studies in laser-excited acoustic phonons in InSb. App. Phys. **A75**, 467 (2002)
1702. R. Neutze, K. Moffat, Time-resolved structural studies at synchrotrons and X-ray free electron lasers: opportunities and challenges. Curr. Opin. Struct. Biol. **22**, 651 (2012)
1703. A.L. Calendron, J. Meier, M. Hemmer, L.E. Zapata, F. Reichert, H. Cankaya, D.N. Schimpf, Y. Hua, G.Q. Chang, A. Kalaydzhyan, A. Fallahi, N.H. Matlis, F.X. Kärtner, Laser system design for table-top X-ray light source. High Power Laser Sci. Eng. **6**, e12 (2018)
1704. R. Neutze, R. Wouts, D. van der Spoel, E. Weckert, J. Hajdu, Potential for biomolecular imaging with femtosecond X-ray pulses. Nature **406**, 752 (2000)
1705. H.N. Chapman et al., Femtosecond X-ray protein nanocrystallography. Nature **470**, 73 (2011)
1706. A. Aquila et al., Time-resolved protein nanocrystallography using an X-ray free-electron laser. Opt. Express **20**, 2706 (2012)
1707. K. Ueda (ed.), *X-Ray Free Electron Laser* (MPDI Books, 2018)
1708. D. Umstadter, T.B. Norris (eds.), *Feature Issue on Optics of Relativistic Electrons.* IEEE J. Quantum Electron. **33**, 1877 (1997)

1709. J. Fan, T.R. Clark, H.M. Milchberg, Generation of a plasma waveguide in an elongated, high repetition rate gas jet. Appl. Phys. Lett. **73**, 3064 (1998)

1710. T. Tajima, G. Mourou, Zettawatt-exawatt lasers and their applications in ultrastrong-field physics. Phys. Rev. Spec. Topics – Accel. Beams **5**, 031301 (2002)

1711. T. Tajima, J.M. Dawson, Laser electron accelerator. Phys. Rev. Lett. **43**, 267 (1979)

1712. R. Wagner, S.-Y. Chen, A. Maksimchuk, D. Umstadter, Electron acceleration by a laser wakefield in a relativistically self-guided channel. Phys. Rev. Lett. **78**, 3125 (1997)

1713. T. Tajima, X.Q. Yan, T. Ebisuzaki, Wakefield acceleration. Rev. Mod. Plasma Phys. **4**, 7 (2020)

1714. J. Faure et al., A laser–plasma accelerator producing monoenergetic electron beams. Nature **431**, 541 (2004)

1715. S. Mangles et al., Monoenergetic beams of relativistic electrons from intense laser–plasma interactions. Nature **431**, 535 (2004)

1716. C. Geddes et al., High-quality electron beams from a laser wakefield accelerator using plasma-channel guiding. Nature **431**, 538 (2004)

1717. W.P. Leemans, B. Nagler, A.J. Gonsalves, Cs. Tóth, K. Nakamura, C.G.R. Geddes, E. Esarey, C.B. Schroeder, S.M. Hooker, GeV electron beams from a centimetre-scale accelerator. Nature Phys. **2**, 696 (2006)

1718. O. Lundh, J. Lim, C. Rechatin, L. Ammoura, A. Ben-Ismaïl, X. Davoine, G. Gallot, J.-P. Goddet, E. Lefebvre, V. Malka, J. Faure, Few femtosecond, few kiloampere electron bunch produced by a laser–plasma accelerator. Nature Phys. **7**, 219 (2011)

1719. K. Svendsen, I. Gallardo Gonzalez, M. Hansson, J. Björklund Svensson, H. Ekerfelt, A. Persson, O. Lundh, Optimization of soft X-ray phase-contrast tomography using a laser wakefield accelerator. Optics Exp. **26**, 33930 (2018)

1720. H. Daido, M. Nishiuchi, A.S. Pirozhkov, Review of laser-driven ion sources and their applications. Rep. Prog. Phys. **75**, 056401 (2012)

1721. A. Macchi, M. Borghesi, M. Passoni, Ion acceleration by superintense laser-plasma interaction. Rev. Mod. Phys. **85**, 751 (2013)

1722. J. Schreiber, P.R. Bolton, K. Parodi, "Hands-on" laser-driven ion acceleration: A primer for laser-driven source development and potential applications. Rev. Sci. Instrum. **87**, 071101 (2016)

1723. A. Higginson, R.J. Gray, R.J. Dance, S.D.R. Williamson, N.M.H. Butler, R. Wilson, R. Capdessus, C. Armstrong, J.S. Green, S.J. Hawkes, P. Martin, W.Q. Wei, S.R. Mirfayzi, X.H. Yuan, M. Borghesi, R.J. Clarke, D. Neely, P. McKenna, Near-100 MeV protons via a laser-driven transparency-enhanced hybrid acceleration scheme. Nat. Commun. **9**, 724 (2018)

1724. L. Volpe, R. Fedosejevs, G. Gatti, J. A. Pérez-Hernández, C. Méndez, J. Apiñaniz, X. Vaisseau, C. Salgado, M. Huault, S. Malko, G. Zeraouli, V. Ospina, A. Longman, D. De Luis, K. Li, O. Varela, E. García, I. Hernández, J. D. Pisonero, J. García Ajates, J. M. Alvarez, C. García, M. Rico, D. Arana, J. Hernández-Toro, L. Roso, Generation of high energy laser-driven electron and proton sources with the 200 TW system VEGA 2 at the Centro de Laseres Pulsados. High Power Laser Sci. Eng. **7** e25 (2019)

1725. S. Vallières, M. Salvadori, A. Permogorov, G. Cantono, K. Svendsen, Z. Chen, S. Sun, F. Consoli, E. d'Humières, C.-G. Wahlström, P. Antici, Enhanced laser-driven proton acceleration using nanowire targets. Sci. Reports **11**, 2226 (2021)

1726. A. Hoffmann, B. Oborn, M. Moteabbed, S. Yan, T. Bortfeld, A. Knopf, H. Fuchs, D. Georg, J. Seco, M.F. Spadea, O. Jäkel, C. Kurz, K. Parodi, MR-guided proton therapy: a review and a preview. Radiat. Oncol. **14**, 129 (2020)

1727. K.W.D. Ledingham, W. Galster, R. Sauerbrey, Laser-driven proton oncology — a unique new cancer therapy? Brit. J. Radiology https://doi.org/10.1259/bjr/29504942 (2007)

1728. K. Svendsen, D. Guénot, J. Björklund Svensson, K. Petersson, A. Persson, O. Lundh, A focused very high energy electron beam for fractionated stereotactic radiotherapy. Scientific Rep. **11**, 5844 (2021)

1729. S. Matinyan, Lasers as a bridge between atomic and nuclear physics. Phys. Rep. **298**, 199 (1998)
1730. K. Ledingham, P.A. Norreys, Nuclear physics merely using a light source. Contemp. Phys. **40**, 367 (1999)
1731. G. Gahn, G.D. Tsakiris, G. Pretzler, K.J. Witte, C. Delfin, C.G. Wahlström, D. Habs, Generating positrons with femtosecond-laser pulses. Appl. Phys. Lett. **77**, 2662 (2000)
1732. H. Schwoerer, F. Ewald, R. Sauerbrey, J. Galy, J. Magill, V. Rondinella, R. Schenkel, T. Butz, Fission of actinides using a tabletop laser. Europhys. Lett. **66**, 47 (2003)
1733. K.W.D. Ledingham, Laser induced nuclear physics and applications. Nucl. Phys. A **752**, 633c (2005)
1734. O. Kocharovskaya, R. Kolesov, Yu. Rostovtsev, Lasing without inversion: a new path to gamma-ray laser. Laser Phys. **9**, 745 (1999)
1735. A.P. Mills, Positronium Bose-Einstein condensation in liquid ^{4}He bubbles. Phys. Rev. A **100**, 063615 (2019)
1736. F. Hannachi et al., Prospects for nuclear fusion with lasers. Plasma Phys. Contr. Fusion **49**, B79 (2007)
1737. S. Le Pape et al., Fusion energy output greater than the kinetic energy of an imploding shell at the National Ignition Facility. Phys. Rev. Lett. **120**, 245003 (2018)
1738. M. Tabak, J. Hammer, M.E. Glinsky, W.L. Kruer, S.C. Wilks, J. Woodsworth, E.M. Campbell, M.D. Perry, Ignition and high gain with ultrapowerful lasers. Phys. Plasmas **1**, 1626 (1994)
1739. H. Hora, S. Eliezer, G.H. Miley, J. Wang, Y. Xu, N. Nissim, Extreme laserpulses for non-thermal fusion ignition of hydrogen–boron for clean and low-cost energy. Laser Part. Beams **36**, 335 (2018)
1740. J. Thielking, M.V. Okhapkin, G. Przemyslaw, D.M. Meier, L. von der Wense, B. Seiferle, C.E. Düllmann, P.G. Thirolf, E. Peik, Laser spectroscopic characterization of the nuclear-clock isomer $^{229\mathrm{m}}$Th. Nature **556**, 321 (2018)
1741. L. von der Wense, Ticking toward a nuclear clock. Physics **13**, 152 (2020). https://doi.org/10.1103/Physics.13.152
1742. K. Fredriksson, H. Lundberg, S. Svanberg, Fine- and hyperfine structure investigation in the $5D$ - nF series of cesium. Phys. Rev. A **21**, 241 (1980)
1743. K. Fredriksson, L. Nilsson, S. Svanberg, Stark interaction for alkali atoms (unpublished report, 1980)
1744. S. Svanberg, Measurements and calculations of excited alkali hyperfine and Stark parameters. In: J.L Hall, J.L. Carlsten: Laser Spectroscopy III, Springer Ser. Opt. Sci. Vol. 7 (Springer, Berlin, Heidelberg 1977)
1745. M.A. Zaki Ewiss, W. Hogervorst, W. Vassen, B.H. Post, The Stark effect in the $6snf$ Rydberg series of barium. Z. Phys. A **322**, 211 (1985)
1746. R. Frisch, Experimenteller Nachweis des Einsteinschen Strahlungs-Rückstosses. Z. Physik **86**, 42 (1933)
1747. J.-L. Piqué, J.-L. Vialle, Atomic-beam deflection and broadening by recoils due to photon absorption or emission. Opt. Commun. **5**, 402 (1972)
1748. R. Schieder, H. Walther, L. Wöste, Atomic beam deflection by the light of a tunable dye laser. Opt. Commun. **5**, 337 (1972)
1749. A.P. Kazantzev, Acceleration of atoms by a resonant field. Sov. Phys. JETP **36**, 1628 (1973)
1750. F. Touchard, J.M. Serre, S. Büttgenbach, P. Guimbal, R. Klapisch, M. de Saint Simon, C. Thibault, H.T. Duong, P. Juncar, S. Liberman, J. Pinard, J.-L. Vialle, Electric quadrupole moments and isotopic shifts of radioactive sodium isotopes. Phys. Rev. C **25**, 2756 (1982)
1751. H.T. Duong, P. Juncar, S. Liberman et al., First observation of the blue optical lines of francium. Europhys. Lett. **3**, 175 (1987)
1752. S.V. Andreev, V.S. Letokhov, V.I. Mishin, Laser resonance photoionization spectroscopy of Rydberg levels in Fr. Phys. Rev. Lett. **59**, 1274 (1987)
1753. A. Voss, M.R. Pearson, J. Billowes, F. Buchinger, B. Cheal, J.E. Crawford, A.A. Kwiatkowski, C.D.P. Levy, O. Shelbaya, First use of high-frequency intensity modulation of narrow-linewidth laser light and its application in determination of Fr ground-state properties. Phys. Rev. Lett. **111**, 122501 (2013)

1754. S.D. Rosner, R.A. Holt, T.D. Gaily, Measurement of the zero-field hyperfine structure of a single vibration-rotation level of Na_2 by a laser fluorescence molecular-beam-resonance technique. Phys. Rev. Lett. **35**, 785 (1975)
1755. W. Ertmer, B. Hofer, Zero-field hyperfine structure measurements of metastable states $3d^2 4s$ $^4F_{3/2,9/2}$ of ^{45}Sc using laser fluorescence atomic-beam-magnetic-resonance technique. Z. Phys. A **276**, 9 (1976)
1756. P. Grundevik, M. Gustavsson, I. Lindgren, G. Olsson, L. Robertsson, A. Rosén, S. Svanberg, Precision method for hyperfine structure studies in low-abundance isotopes: The quadrupole moment of ^{43}Ca. Phys. Rev. Lett. **42**, 1528 (1979)
1757. W.H. Wing, G.A. Ruff, W.E. Lamb, J.J. Spezeski, Observation of the infrared spectrum of the hydrogen molecular ion HD^+. Phys. Rev. Lett. **36**, 1488 (1976)
1758. S.L. Kaufmann, High resolution laser spectroscopy in fast beams. Opt. Commun. **17**, 309 (1976)
1759. K.T. Flanagan et al., Collinear resonance ionization spectroscopy of neutron-deficient francium isotopes Phys. Rev. Lett. **111**, 212501 (2013)
1760. A. Voss, M.R. Pearson, J. Billowes, F. Buchinger, B. Cheal, J.E. Crawford, A.A. Kwiatkowski, C.D.P. Levy, O. Shelbaya, First use of high-frequency intensity modulation of narrow-linewidth laser light and its application in determination of Fr ground-state properties. Phys. Rev. Lett. **111**, 122501 (2013)
1761. R. Neugart, J. Billowes, M.L. Bissell, K. Blaum, B. Cheal, K.T. Flanagan, G. Neyens, W. Nörtershäuser, D.T. Yordanov, Collinear laser spectroscopy at ISOLDE: new methods and highlights. J. Phys. G: Nucl. Part. Phys. **44**, 064002 (2017)
1762. P. Jaquinot, R. Klapisch, Hyperfine spectroscopy of radioactive atoms. Rep. Prog. Phys. **42**, 773 (1979)
1763. S. Svanberg, Laser spectroscopy applied to the study of hyperfine interactions. Hyperfine Interact. **15/16**, 111 (1983)
1764. R. Neugart, Nuclear moments from laser spectroscopy. Hyperfine Interact. **43**, 441 (1988)
1765. T. Kuehl, Nuclear properties by laser spectroscopy in beams and rings. Phys. Scr. **22**, 144 (1988)
1766. D.T. Yordanov et al., Structural trends in atomic nuclei from laser spectroscopy of tin. Commun. Phys. **3**, 107 (2020)
1767. D. Müll, F. Grussie, K. Blaum, S. George, J. Göck, M. Grieser, R. von Hahn, Z. Harman, Á. Kálosi, C. H. Keitel, C. Krantz, C. Lyu, O. Novotný, F. Nuesslein, D. Paul, V. C. Schmidt, S. Singh, S. Sunil Kumar, X. Urbain, A. Wolf, H. Kreckel, Metastable states of Si^- observed in a cryogenic storage ring. Phys. Rev. A **104**, 032811 (2021)
1768. T. Day Goodacre, A.V. Afanasjev, A.E. Barzakh, B.A. Marsh, S. Sels, P. Ring, H. Nakada, A.N. Andreyev, P. Van Duppen, N. A. Althubiti, B. Andel, D. Atanasov, J. Billowes, K. Blaum, T.E. Cocolios, J.G. Cubiss, G.J. Farooq-Smith, D.V. Fedorov, V.N. Fedosseev, K.T. Flanagan, L.P. Gaffney, L. Ghys, M. Huyse, S. Kreim, D. Lunney, K.M. Lynch, V. Manea, Y. Martinez Palenzuela, P.L. Molkanov, M. Rosenbusch, R.E. Rossel, S. Rothe, L. Schweikhard, M.D. Seliverstov, P. Spagnoletti, C. Van Beveren, M. Veinhard, E. Verstraelen, A. Welker, K. Wendt, F. Wienholtz, R.N. Wolf, A. Zadvornaya, K. Zuber, Laser spectroscopy of neutron-rich ^{207,208}Hg Isotopes: Illuminating the kink and odd-even staggering in charge radii across the N=126 shell closure. Phys. Rev. Lett. **126**, 032502 (2021)
1769. H. Heylen, C.S. Devlin, W. Gins, M.L. Bissell, K. Blaum, B. Cheal, L. Filippin, R.F. Garcia Ruiz, M. Godefroid, C. Gorges, J.D. Holt, A. Kanellakopoulos, S. Kaufmann, Á. Koszorús, K. König, S. Malbrunot-Ettanauer, T. Miyagi, R. Neugart, G. Neyens, W. Nörtershäuser, R. Sánchez, F. Sommer, L.V. Rodríguez, L. Xie, Z.Y. Xu, X. F. Yang, D.T. Yordanov, High-resolution laser spectroscopy of $^{27-32}$Al. Phys. Rev. **C 103**, 014318 (2021)
1770. V. Fedosseev, K. Chrysalidis, T.D. Goodacre, B. Marsh, S. Rothe, Ch. Seiffert, K. Wendt, Ion beam production and study of radioactive isotopes with the laser ion source at ISOLDE. J. Phys. G: Nucl. Part. Phys. **44**, 084006 (2017)
1771. J. Lidberg, A. Al-Khalidi, L.-O. Norlin, P. Royen, X. Tordoir, S. Mannervik, Lifetime of the metastable $3d\ ^2D_{3/2}$ and $3d\ ^2D_{5/2}$ levels in Ca^+ measured by laser probing of a stored ion beam. J. Phys. B **32**, 757 (1999)

1772. M. Larsson, Atomic and molecular physics with ion storage rings. Rep. Prog. Phys. **58**, 1267 (1995)

1773. Th.U. Kühl, ‘Storage ring laser spectroscopy.’ In: *Progress in Atomic, Molecular, and Optical Physics*, Vol.40, ed. by B. Bederson, H. Walther (Academic Press, San Diego 1999) p.114

1774. M. Larsson, H. Danared, J.R. Mowat, P. Sigray, G. Sundström, L. Broström, A. Filevich, A. Kilberg, S. Mannervik, K.G. Rensfelt, S. Datz, Direct high-energy neutral-channel dissociative recombination of cold $H^+{}_3$ in an ion storage ring. Phys. Rev. Lett. **70**, 430 (1993)

1775. S. Datz, G. Sundström, Ch. Biedermann, L. Broström, H. Danared, S. Mannervik, J.R. Mowat, M. Larsson, Branching processes in the dissociative recombination of $H^+{}_3$. Phys. Rev. Lett. **74**, 896 (1995)

1776. G. Budker, In: *Proc. Int. Symp. on Electron and Positron Storage Rings*, ed. by H. Zyngier, E. Cremieux-Alcan (Presses Universitaire, Saclay 1966)

1777. G. Budker et al., in *Proc. IV All-Union Meeting on Accelerators of Charged Particles*, IEEE Trans. Nucl. Sci. **VS-22**, 2093 (1975)

1778. H. Danared, G. Andler, L. Bagge, C.J. Herrlander, J. Hilke, J. Jeansson, A. Källberg, A. Nilsson, A. Pal, K.-G. Rensfelt, U. Rosengård, J. Starker, M. af Ugglas, Electron cooling with an ultracold electron beam. Phys. Rev. Lett. **72**, 3775 (1994)

1779. D.M. Maletic, A.G. Ruggiero (eds.), *Crystalline Beams and Related Issues* (World Scientific, Singapore, 1996)

1780. R.D. Thomas et al., The double electrostatic ion ring experiment: A unique cryogenic electrostatic storage ring for merged ion-beams studies. Rev. Sci. Instr. **82**, 065112 (2011)

1781. M. Gatchell, H.T. Schmidt, R.D. Thomas, S. Rosén, P. Reinhed, P. Löfgren, L. Brännholm, M. Blom, M. Björkhage, E. Bäckström et al., Commissioning of the DESIREE storage rings – a new facility for cold ion-ion collisions. J. Phys. Conf. Ser. **488**, 01204 (2014)

1782. H. Zettergren, A summary of results obtained with the cryogenic electrostatic storage ring DESIREE. Can. J. Phys. **95**, 817 (2017)

1783. C. Meyer et al., Radiative rotational lifetimes and state-resolved relative detachment cross sections from photodetachment thermometry of molecular anions in a cryogenic storage ring. Phys. Rev. Lett. **119**, 023202 (2017)

1784. H. Kreckel, O. Novotný, A. Wolf, Astrochemical studies at the Cryogenic Storage Ring. Phil. Trans. Roy. Soc. A doi.org/https://doi.org/10.1098/rsta.2018.0412 (2019)

1785. M.H. Stockett, J.N. Bull, J.T. Buntine, E. Carrascosa, M. Ji, N. Kono, H.T. Schmidt, H. Zettergren, Unimolecular fragmentation and radiative cooling of isolated PAH ions: A quantitative study. J. Chem. Phys. **153**, 154303 (2020)

1786. M. Steck, Y.A. Litvinov, Heavy-ion storage rings and their use in precision experiments with highly charged ions. Prog. Part. Nucl. Phys. **115**, 103811 (2020)

1787. L.H. Andersen, T. Andersen, P. Hvelplund, Studies of negative ions in storage rings. Adv. At. Mol. Opt. Phys. **38**, 155 (1998)

1788. D. Hanstorp, An ion beam apparatus for collinear photodetachment experiments. Nucl. Instrum. Methods B **100**, 165 (1995)

1789. D. Hanstorp. G. Haeffler, A.E. Klinkmüller, U. Ljungblad, U. Berzinsh, I.Yu. Kiyan, D.J. Pegg: ‘Two-electron dynamics in photodetachment.’ In: *Modern Trends in Atomic Physics*, Adv. Quantum Chem. **30**, 311 (1998)

1790. D. Hanstorp, P. Devynck, W.G. Graham, J.R. Peterson, Observation of metastable autodetaching Ca^-. Phys. Rev. Lett. **63**, 368 (1989)

1791. V.V. Petrunin, J.D. Voldstad, P. Balling, P. Kristensen, T. Andersen, H.K. Haugen, Resonant ionization spectroscopy of Ba^- metastable and stable ions. Phys. Rev. Lett. **75**, 1911 (1995)

1792. U. Warring, M. Amoretti, C. Canali, A. Fischer, R. Heyne, J.O. Meier, Ch. Morhard, A. Kellerbauer, High-resolution laser spectroscopy on the negative osmium ion. Phys. Rev. Lett. **102**, (2009)

1793. D. Müll, F. Grussie, K. Blaum, S. George, J. Göck, M. Grieser, R. von Hahn, Z. Harman, Á. Kálosi, C. H. Keitel, C. Krantz, C. Lyu, O. Novotný, F. Nuesslein, D. Paul, V. C. Schmidt, S. Singh, S. Sunil Kumar, X. Urbain, A. Wolf, H. Kreckel, Metastable states of Si^- observed in a cryogenic storage ring. Phys. Rev. A **104**, 032811 (2021)

1794. P.H. Lee, M.L. Skolnick, Saturated neon absorption inside a 6328 Å laser. Appl. Phys. Lett. **10**, 303 (1967)

1795. W.E. Lamb Jr., Theory of an optical maser. Phys. Rev. A **134**, 1429 (1964)

1796. W.R. Rowley, B.W. Jolliffe, K.C. Schotton, A.J. Wallard, P.T. Woods, Laser wavelength measurements and the speed of light. Opt. Quantum Electron. **8**, 1 (1976)

1797. J.L. Hall, Stabilized lasers and precision measurements. Science **202**, 147 (1978)

1798. D.A. Jennings, C.R. Pollock, F.R. Petersen, R.E. Drullinger, K.M. Evenson, J.S. Wells, Direct frequency measurement of the I_2 stabilized He-Ne 473 THz (633 nm) laser. Opt. Lett. **8**, 136 (1983)

1799. R.G. DeVoe, R.G. Brewer, Laser frequency division and frequency stabilization. Phys. Rev. A **30**, 2827 (1984)

1800. Documents concerning the new definition of the metre, Metrologia **19**, 163 (1984)

1801. J. Yao et al., Optical-clock-based time scale. Phys. Rev. Appl. **12**, 044069 (2019)

1802. F. Riehle, P. Gill, F. Arias, L. Robertsson, The CIPM list of recommended frequency standard values: Guidelines and procedures. Metrologia **55**, 188380 (2018)

1803. J. Lodewyck, On a definition of the SI second with a set of optical clock transitions. Metrologia **56**, 055009 (2019)

1804. M.D. Levenson, A.L. Schawlow, Hyperfine interactions in molecular iodine. Phys. Rev. A **6**, 10 (1972)

1805. T.W. Hänsch, I.S. Shahin, A.L. Schawlow, High resolution saturation spectroscopy of the sodium *D* line with a pulsed tunable dye laser. Phys. Rev. Lett. **27**, 707 (1971)

1806. C. Bordé, Spectroscopie d'absorption saturée de diverses molécules au moyen des lasers á gas carbonique et á prooxyde d'azote. C. R. Acad. Sci. B **271**, 371 (1970)

1807. S. Svanberg, G.-Y. Yan, T.P. Duffey, A.L. Schawlow, High-contrast Doppler-free transmission spectroscopy. Opt. Lett. **11**, 138 (1986)

1808. C. Luo, S. Kröll, L. Sturesson, S. Svanberg, The observation of strongly sub-homogeneous linewidths using high contrast transmission spectroscopy: Experiment and theory. Phys. Rev. A **53**, 1 (1996)

1809. S.W. Hell, K.I. Willig, M. Dyba, S. Jakobs, L. Kastrup, V. Westphal, Nanoscale resolution with focused light: STED and other RESOLFT microscopy concepts, in J.B. Pawley (ed.), *Handbook of Biological Confocal Microscopy, 3rd edition* (Springer Science, New York 2006)

1810. W. Westphal, S.W. Hell, Nanoscale resolution in the focal plane of an optical microscope. Phys. Rev. Lett. **94**, 143903 (2005)

1811. U.J. Birk, *Super-Resolution Microscopy*: A Practical Guide (Wiley-VCH, 2017)

1812. H. Erfle (ed.), *Super-Resolution Microscopy: Methods and Protocols* (Humana Press, 2017)

1813. V. Astratov, (ed.): *Label-Free Super-Resolution Microscopy* (Springer, 2019)

1814. C. Wieman, T.W. Hänsch, Doppler-free laser polarization spectroscopy. Phys. Rev. Lett. **36**, 1170 (1976)

1815. T.W. Hänsch, I.S. Shahin, A.L. Schawlow, Optical resolution of the Lamb shift in atomic hydrogen. Nature **235**, 56 (1972)

1816. T.W. Hänsch, M.H. Nayfeh, S.A. Lee, S.M. Curry, I.S. Shahin, Precision measurement of the Rydberg constant by laser saturation spectroscopy of the Balmer-α line in hydrogen and deuterium. Phys. Rev. Lett. **32**, 1336 (1974)

1817. K. Pachucki, D. Leibfried, M. Weitz, A. Huber, W. Knig, T.W. Hänsch, Theory of the energy levels and precise two-photon spectroscopy of atomic hydrogen and deuterium. J. Phys. B **29**, 177 (1996)

1818. A. Beyer, L. Maisenbacher, A. Matveev, R. Pohl, K. Khabarova, A. Grinin, T. Lamour, D.C. Yost, T.W. Hänsch, N. Kolachevsky, T. Udem, The Rydberg constant and proton size from atomic hydrogen. Science **358**, 79 (2017)

1819. P. Zhao, W. Lichten, H. Layer, J. Bergquist, New value for the Rydberg constant from the hydrogen Balmer-β transition. Phys. Rev. Lett. **58**, 1293 (1987)

1820. F. Biraben, J.C. Garreau, L. Julien, Determination of the Rydberg constant by Doppler-free two-photon spectroscopy of hydrogen Rydberg states. Europhys. Lett. **2**, 925 (1986)

1821. G.W. Series (ed.), *The Spectrum of Atomic Hydrogen: Advances* (World, Scientific, Singapore 1988)
1822. G.F. Bassani, M. Inguscio, T.W. Hänsch (eds.), *The Hydrogen Atom* (Springer, Berlin, Heidelberg, 1989)
1823. B. Cagnac, M.D. Plimmer. L. Julien, F. Biraben, The hydrogen atom, a tool for metrology. Rep. Prog. Phys. **57**, 853 (1995)
1824. A.E. Kramida, A critical compilation of experimental data on spectral lines and energy levels of hydrogen, deuterium, and tritium. At. Data Nucl. Data Tables **96**, 586 (2010)
1825. N. Bezginov, T. Valdez, M. Horbatsch, A. Marsman, A.C. Vutha, E.A. Hessels, A measurement of the atomic hydrogen Lamb shift and the proton charge radius. Science **365**, 1053 (2019)
1826. H.R. Schlossberg, A. Javan, Saturation behaviour of a Doppler-broadened transition involving levels with closely spaced structure. Phys. Rev. **150**, 267 (1966)
1827. T.W. Hänsch, P. Toschek, Theory of a three-level gas laser amplifier. Z. Physik **236**, 213 (1970)
1828. D.N. Stacey, 'Parity non-conservation in atoms.' In: *Atomic Physics 13*, ed. by H. Walther, T.W. Hänsch, B. Neizert (AIP Publishing, New York 1993) p.46
1829. M.-A. Bouchiat, C. Bouchiat, Parity violation in atoms. Rep. Prog. Phys. **60**, 1352 (1997)
1830. M.J.D. MacPherson, K.P. Zetie, R.B. Warrington, D.N. Stacey, J.P. Hoare, Precise measurement of parity non-conserving optical rotation at 876 nm in atomic bismuth. Phys. Rev. Lett. **67**, 2784 (1991)
1831. P.A. Vetter, D.M. Meekhof, P.K. Majumder, S.K. Lamoreaus, E.N. Fortson, Precise test of electroweak theory from a new measurement of parity nonconservation in atomic thallium. Phys. Rev. Lett. **74**, 2658 (1995)
1832. C.S. Wood, S.C. Bennett, D. Cho, B.P. Masterson, J.L. Roberts, C.E. Tanner, C.E. Wieman, Measurement of parity nonconservation and an anapole moment in cesium. Science **275**, 1759 (1997)
1833. S.A. Blundell, W.R. Johnson, J. Sapirstein, High-accuracy calculation of the 6 $S_{1/2}$ - 7 $S_{1/2}$ parity-nonconserving transition in atomic cesium and implications for the standard model. Phys. Rev. Lett. **65**, 1411 (1990); Phys. Rev. A **43**, 3407 (1991)
1834. A.C. Hartley, E. Lindroth, A. Mårtensson-Pendrill, Parity nonconservation and electric dipole moments in caesium and thallium. J. Phys. B **23**, 3417 (1990)
1835. B.M. Roberts, V.A. Dzuba, V.V. Flambaum, Parity and time-reversal violation in atomic systems. Annu. Rev. Nucl. Part. Sci. **65**, 63 (2015)
1836. M.S. Safronova et al., Search for new physics with atoms and molecules. Rev. Mod. Phys. **90**, 025008 (2018)
1837. K. Tsigutkin, D. Dounas-Frazer, A. Family, J.E. Stalnaker, V.V. Yashchuk, D.D. Antypas, A. Fabricant, J.E. Stalnaker, K. Tsigutkin, V.V. Flambaum, D. Budker, Isotopic variation of parity violation in atomic ytterbium. Nature Phys. **15**, 120 (2019)
1838. V.W. Hughes, High-precision spectroscopy of positronium and muonium. Adv. Quantum Chem. **30**, 99 (1998)
1839. D. Taqqu, F. Biraben, C.A.N. Conde, T.W. Hänsch, F.J. Hartmann, P. Hauser, P. Indelicato, P. Knowles, F. Kottmann, F. Mulhauser, C. Petitjean, R. Pohl, P. Rabinowitz, R. Rosenfelder, J.M.F. Santos, W. Scott, L.M. Simons, J.F.C.A. Veloso, Laser spectroscopy of the Lamb shift in muonic hydrogen. Hyperfine Interact. **119**, 317 (1999)
1840. C. Pizzolotto et al., The FAMU experiment: muonic hydrogen high precision spectroscopy studies. Eur. Phys. J. A **56**, 185 (2020)
1841. L. Gurung, T.J. Babij, S.D. Hogan, D.B. Cassidy, Precision microwave spectroscopy of the positronium n=2 fine structure. Phys. Rev. Lett. **125**, 073002 (2020)
1842. J.L. Miller, Laser spectroscopy: A new way to study pions. Physics Today **73**, https://doi.org/10.1063/PT.3.4516 (2020)
1843. G. Gabrielse, N.S. Bowen, P. Oxley, A. Speck, C.H. Storry, J.N. Tan, M. Wessels, D. Grzonka, W. Oelert, G. Schepers, T. Sefxick, J. Walz, H. Pittner, T.W. Hänsch, E.A. Hessels, Background-free observation of cold antihydrogen with field-ionization analysis of its states. Phys. Rev. Lett. **89**, 213,401 (2002)

1844. M. Ahmadi et al., Observation of the hyperfine spectrum of antihydrogen. Nature **548**, 66 (2017)

1845. M. Ahmadi et al., Observation of the 1S–2P Lyman-α transition in antihydrogen. Nature **561**, 211 (2018)

1846. ALPHA Collaboration, Investigation of the fine structure of antihydrogen. Nature **578**, 375 (2020)

1847. M. Hori, Recent progress of laser spectroscopy experiments on antiprotonic helium. Phil. Trans. Royal Soc. London **3 76**, 20170270 (2018)

1848. M.S. Sorem, A.L. Schawlow, Saturation spectroscopy in molecular iodine by intermodulated fluorescence. Opt. Commun. **5**, 148 (1972)

1849. J.E. Lawler, A.I. Ferguson, J.E.M. Goldsmith, D.J. Jackson, A.L. Schawlow, Doppler-free intermodulated optogalvanic spectroscopy. Phys. Rev. Lett. **42**, 1046 (1979)

1850. D.R. Lyons, A.L. Schawlow, G.-Y. Yan, Doppler-free radiofrequency optogalvanic spectroscopy. Opt. Commun. **38**, 35 (1981)

1851. E.E. Marinero, M. Stuke, Doppler-free optoacoustic spectroscopy. Opt. Commun. **30**, 349 (1979)

1852. T.P. Duffey, D. Kammen, A.L. Schawlow, S. Svanberg, H.-R. Xia, G.-G. Xiao, G.-Y. Yan, Laser spectroscopy using beam overlap modulation. Opt. Lett. **10**, 597 (1986)

1853. T.W. Hänsch, D.R. Lyons, A.L. Schawlow, A. Siegel, Z.-Y. Wang, G.-Y. Yan, Polarization intermodulated excitation (POLINEX) spectroscopy of helium and neon. Opt. Commun. **37**, 87 (1981)

1854. M. Goeppert-Mayer, Ûber Elementarakte mit zwei Quantensprüngen. Ann. Phys. **9**, 273 (1931)

1855. L.S. Vasilenko, V.P. Chebotayev, A.V. Shishaev, Line shape of a two-photon absorption in a standing-wave field in a gas. JETP Lett. **12**, 113 (1970)

1856. F. Biraben, B. Cagnac, G. Grynberg, Experimental evidence of two-photon transition without Doppler broadening. Phys. Rev. Lett. **32**, 643 (1974)

1857. G. Grynberg, B. Cagnac, Doppler-free multiphoton spectroscopy. Rep. Prog. Phys. **40**, 791 (1977)

1858. N. Bloembergen, M.D. Levenson, Dopplerfree two-photon absorption spectroscopy. Phys. Rev. Lett. **31**, 645 (1974)

1859. T.W. Hänsch, K.C. Harvey, G. Meisel, A.L. Schawlow, Two-photon spectroscopy of Na 3s–4d without Doppler broadening using a CW dye laser. Opt. Commun. **11**, 50 (1974)

1860. J. Neukammer, H. Rinneberg, K. Vietzke, A. König, H. Hieronymus, M. Kohl, H.-J. Grabka, Spectroscopy of Rydberg atoms at $n \cong 500$: Observation of quasi-Landau resonances in low magnetic fields. Phys. Rev. Lett. **59**, 2947 (1987)

1861. B.P. Stoicheff, E. Wineberger, Doppler-free two-photon absorption spectrum of rubidium. Can. J. Phys. **57**, 2143 (1979)

1862. C.-J. Lorenzen, K. Niemax, L.R. Pendrill, Precise measurements of ^{39}K *nS* and *nD* energy levels with an evacuated wavemeter. Opt. Commun. **39**, 370 (1981)

1863. K.-H. Weber, C.J. Sansonetti, Accurate energies of *nS*, *nP*, *nF* and *nG* levels of neutral cesium. Phys. Rev. A **35**, 4650 (1987)

1864. M.J. Seaton, Quantum defect theory. Rep. Prog. Phys. **46**, 167 (1983)

1865. W. Hogervorst, Laser spectroscopy of Rydberg states of two-electron atoms. Comments At. Mol. Phys. **13**, 69 (1983)

1866. M. Aymar, Rydberg series of alkaline-earth atoms Ca through Ba. The interplay of laser spectroscopy and multi-channel quantum defect theory. Phys. Rep. **110**, 163 (1984)

1867. C.L. Vaillant, M.P.A. Jones, R.M. Potvliege, Multichannel quantum defect theory of strontium bound Rydberg states. Phys. B: At. Mol. Opt. Phys. **47**, 155001 (2014)

1868. C. Wieman, T.W. Hänsch, Precision measurement of the 1*S* Lamb shift and the 1*S*–2*S* isotope shift of hydrogen and deuterium. Phys. Rev. A **22**, 192 (1980)

1869. E.A. Hildum, U. Boesl, D.H. McIntyre, R.G. Beausoleil, T.W. Hänsch, Measurements of the 1s–2s frequency in atomic hydrogen. Phys. Rev. Lett. **56**, 576 (1986)

1870. R.G. Beausoleil, D.H. McIntyre, C.J. Foot, E.A. Hildum, B. Couillaud, T.W. Hänsch, Continous wave measurement of the 1*S* Lamb shift in atomic hydrogen. Phys. Rev. A **35**, 4878 (1987); ibid. A **39**, 4591 (1989)

1871. T.W. Hänsch, R.G. Beausoleil, B. Couillaud, C. Foot, E.A. Hildum, D.H. McIntyre, High resolution laser spectroscopy of atomic hydrogen. In: [1253] p.2

1872. M. Niering, R. Holzwarth, R. Reichert, P. Pokasov, Th. Udem, M. Weitz, T.W. Hänsch, P. Lemonde, G. Santarelli, M. Abgrall, P. Laurent, C. Salomon, A. Clairon, Measurement of the hydrogen 1*S*–2*S* transition frequency by phase coherent comparison with a microwave cesium fountain clock. Phys. Rev. Lett. **84**, 5496 (2000)

1873. A. Matveev, C.G. Parthey, K. Predehl, J. Alnis, A. Beyer, R. Holzwarth, T. Udem, T. Wilken, N. Kolachevsky, M. Abgrall, D. Rovera, C. Salomon, P. Laurent, G. Grosche, O. Terra, T. Legero, H. Schnatz, S. Weyers, B. Altschul, T.W. Hänsch, Precision measurement of the hydrogen 1S–2S frequency via a 920-km fiber link. Phys. Rev. Lett. **110**, 230801 (2013)

1874. J. Cariou, P. Luc, *Atlas du Spectre d'Absorption de la Molécule de Tellure* (Laboratoire Aimé Cotton, CNRS II, Orsay 1980)

1875. S. Gersternkorn, P. Luc, *Atlas du Spectre d'Absorption de la Molecule d'Iode 14,800–20,000 cm−1* (Editions du CNRS, Paris, 1978)

1876. C.J. Foot, B. Couillaud, R.G. Beausoleil, T.W. Hänsch, Continous two-photon spectroscopy of hydrogen 1s–2s. Phys. Rev. Lett. **54**, 1913 (1985)

1877. M.G. Boshier, P.E.G. Baird, C.J. Foot, E.A. Hinds, M.D. Plimmer, D.N. Stacey, J.B. Swan, D.A. Tate, D.M. Warrington, G.K. Woodgate, Precision CW laser spectroscopy of hydrogen and deuterium. In: [1253] p.18

1878. Th. Udem, A. Huber, B. Gross, J. Reichert, M. Prevedelli, M. Weitz, T.W. Hänsch, Phase-coherent measurement of the hydrogen 1*S*–2*S* transition frequency with an optical frequency interval divider chain. Phys. Rev. Lett. **79**, 2646 (1997)

1879. B. de Beauvoir, F. Nez, L. Juilien, B. Cagnac, F. Biraben, D. Touahri, L. Hilico, O. Acef, A. Clarion, J.J. Zondy, Absolute frequency measurement of the 2*S*–8*S/D* transitions in hydrogen and deuterium: New determination of the Rydberg constant. Phys. Rev. Lett. **78**, 440 (1997)

1880. P. Zhao, W. Lichten, H.P. Layer, J.C. Bergquist, Absolute wavelength measurements and fundamental atomic physics. In: [1253] p.12

1881. S. Bourzeix, B. de Beauvoir, F. Nez, M.D. Plimmer, F. de Tomasi, L. Julien, F. Biraben, High resolution spectroscopy of the hydrogen atom: Determination of the 1*S* Lamb shift. Phys. Rev. Lett. **76**, 384 (1996)

1882. M.M. Salour, C. Cohen-Tannoudji, Observation of Ramsey's interference fringes in the profile of Doppler-free two-photon resonances. Phys. Rev. Lett. **38**, 757 (1977)

1883. R. Teets, J. Eckstein, T.W. Hänsch, Coherent two-photon excitation by multiple light pulses. Phys. Rev. Lett. **38**, 760 (1977)

1884. M. Bellini, A. Bartoli, T.W. Hänsch, Two-photon Fourier spectroscopy with femtosecond light pulses. Opt. Lett. **22**, 540 (1997)

1885. J.C. Bergquist, S.A. Lee, J.L. Hall, Saturated absorption with spatially separated laser fields: Observation of optical "Ramsey" fringes. Phys. Rev. Lett. **38**, 159 (1977)

1886. R.G. Beausoleil, T.W. Hänsch, Ultra-high-resolution two-photon optical Ramsey spectroscopy of an atomic fountain. Phys. Rev. A **33**, 1661 (1986)

1887. M.A. Kasevich, E. Riis, S. Chu, R.G. DeVoe, RF spectroscopy in an atomic fountain. Phys. Rev. Lett. **63**, 612 (1989)

1888. A. Beyer, Ch.G. Parthey, N. Kolachevsky, J. Alnis, K. Khabarova, R. Pohl, E. Peters, D.C. Yost, A. Matveev, K. Predehl, S. Droste, T. Wilken, R. Holzwarth, T. W. Hänsch, M. Abgrall, D. Rovera, Ch. Salomon, Ph. Laurent, Th. Udem, Precision spectroscopy of atomic hydrogen. J. Phys.: Conf. Series **467**, 012003 (2013)

1889. Th. Stöhlker, H. Beyer, A. Gumberidze, A. Kumar, D. Liesen, R. Reuschl, U. Spillmann, M. Trassinelli, Ground state Lamb-shift of heavy hydrogen-like ions: status and perspectives. Hyperfine Inter. **172**, 135 (2007)

1890. K. Blaum, S. Eliseev, S. Sturm, Perspectives on testing fundamental physics with highly charged ions in Penning traps. Quant. Sci. Techn. **6**, 014002 (2021)

1891. R.J. Rengelink, Y. van der Werf, R.P.M.J.W. Notermans, R. Jannin, K.S.E. Eikema, M.D. Hoogerland, W. Vassen, Precision spectroscopy of helium in a magic wavelength optical dipole trap. Nature Physics **14**, 1132 (2018)
1892. Y.R. Sun, S.M. Hu, Precision spectroscopy of atomic helium. National Sci. Rev. **7**, 1818 (2020)
1893. M. Hori, H. Aghai-Khozani, A. Soter, A. Dax, D. Barna, Laser spectroscopy of pionic helium atoms. Nature **581**, 37 (2020)
1894. P. Grundevik, M. Gustavsson, A. Rosén, S. Svanberg, High resolution laser fluorescence spectroscopy in the deep blue spectral region. Z. Physik A **283**, 127 (1977)
1895. Th. Udem, J.Reichert, R. Holzwarth, T.W. Hänsch, Accurate measurement of large optical frequency differences with a mode-locked laser. Opt. Lett. **24**, 881(1999]
1896. J. Reichert, R. Holzwarth, T. Udem, T.W. Hänsch, Measuring the frequency of light with mode-locked lasers. Opt. Com. **172**, 59 (1999)
1897. S.A. Diddams, D.J. Jones, L.S. Ma, S.T. Cundiff, J.L. Hall, Optical frequency measurement across a 104-THz gap with a femtosecond laser frequency comb. Opt. Lett. **25**, 186 (2000)
1898. H.R. Telle, G. Steinmeyer, A.E. Dunlop, J. Stenger, D.H. Sutter, U. Keller, Carrier-envelope offset phase control: A novel concept for absolute optical frequency measurement and ultrashort pulse generation. Appl. Phys. B. **69**, 327 (1999)
1899. https://www.nobelprize.org/uploads/2018/06/popular-physicsprize2005.pdf
1900. T.W Hänsch, J. Alnis, P. Fendel, M. Fischer, C. Gohle, M. Herrmann, R. Holzwarth, N. Kolachevsky, Th. Udem, M. Zimmermann, Precision spectroscopy of hydrogen and femtosecond laser frequency combs. Phil. Trans. Roy. Soc. A **363** (2005) doi.org/https://doi.org/10.1098/rsta.2005.1639
1901. G.E. Marti, R.B. Hutson, A. Goban, S.L. Campbell, N. Poli, J. Ye, Imaging optical frequencies with 100 μHz precision and 1.1 μm resolution. Phys. Rev. Lett. **120**, 103201 (2018)
1902. C.W. Chou, A.L. Collopy, C. Kurz, Y. Lin, M.E. Harding, P.N. Plessow, T. Fortier, S. Diddams, D. Leibfried, D.R. Leibrandt, Frequency-comb spectroscopy on pure quantum states of a single molecular ion. Science **367**, 1458 (2020)
1903. A. Grinin, A. Matveev, D.C. Yost, L. Maisenbacher, V. Wirthl, R. Pohl, T.W. Hänsch, T. Udem, Two-photon frequency comb spectroscopy of atomic hydrogen. Science **370**, 1061 (2020)
1904. H. Schnatz, B. Lipphardt, J. Helmcke, F. Riehle, G. Zinner, First phase-coherent frequency measurement of visible radiation. Phys. Rev. Lett. **76**, 18 (1996)
1905. S.A. Diddams, L. Hollberg, V. Mbele, Molecular fingerprinting with the resolved modes of a femtosecond laser frequency comb. Nature **445**, 627–630 (2007)
1906. A. Foltynowicz et al., Quantum-noise-limited optical frequency comb spectroscopy. Phys. Rev. Lett. **107**, 233002 (2011)
1907. G. Millot et al., Frequency-agile dual-comb spectroscopy. Nat. Photon. **10**, 27–30 (2016)
1908. M. Vainio, M., L. Halonen, Mid-infrared optical parametric oscillators and frequency combs for molecular spectroscopy. Phys. Chem. Chem. Phys. **18**, 4266 (2016)
1909. N. Picqué, T.W. Hänsch, Frequency comb spectroscopy. Nature Phot. **13**, 146 (2019)
1910. T.W. Hänsch, A.L. Schawlow, Cooling of gases by laser radiation. Opt. Commun. **13**, 68 (1975)
1911. D. Wineland, H. Dehmelt, Proposed $10^{14}\Delta\nu < \nu$ laser fluorescence spectroscopy on Tl^+ mono-ion oscillator III. Bull. Am. Phys. Soc. **20**, 637 (1975)
1912. V.S. Letokhov, V.G. Minogin, B.D. Pavlik, Cooling and trapping of atoms and molecules by a resonant laser field. Opt. Commun. **19**, 72 (1976)
1913. V.S. Letokhov, Laser control of atomic motion: Velocity selection, cooling and trapping. Comments At. Mol. Phys. **6**, 119 (1977)
1914. V.S. Letokhov, V.G. Minogin, B.D. Pavlik, Cooling and capture of atoms and molecules by a resonant light field. Sov. Phys. JETP **45**, 698 (1977)
1915. V.I. Balykin, V.S. Letokhov, V.I. Mishin, Cooling of sodium atoms by resonant laser emission. JETP Lett. **29**, 560 (1979)

1916. S.V. Andreev, V.I. Balykin, V.S. Letokhov, V.G. Minogin, Radiative slowing and reduction of the energy spread of a beam of sodium atoms to 1.5 K in an oppositely directed laser beam. JETP Lett. **34**, 442 (1982)
1917. J. Prodan, A. Migdal, W.D. Phillips, I. So, H. Metcalf, J. Dalibard, Stopping atoms with laser light. Phys. Rev. Lett. **54**, 992 (1985)
1918. W. Phillips, J. Prodan, H. Metcalf, Laser cooling and electromagnetic trapping of neutral atoms. J. Opt. Soc. Am. B **2**, 1751 (1985)
1919. W.D. Phillips, H. Metcalf, Laser deceleration of an atomic beam. Phys. Rev. Lett. **48**, 596 (1982)
1920. J.V. Prodan, W.D. Phillips, H. Metcalf, Laser production of very slow mono-energetic atomic beam. Phys. Rev. Lett. **49**, 1149 (1982)
1921. W.D. Phillips, P.L. Gould, P.D. Lett, Cooling, stopping and trapping atoms. Science **239**, 877 (1988)
1922. F.M. Penning, Die Glimmentladung bei niedrigem Druck zwischen koaxialen Zylindern in einem axialen Magnetfeld. Physica **3**, 873 (1936)
1923. G. Bollen et al., ISOLTRAP: A Penning trap system for accurate on-line mass determinations of short-lived isotopes. Nucl. Instrum. Methods A **368**, 675 (1996)
1924. A. Rischka, H. Cakir, M. Door, P. Filianin, Z. Harman, W.J. Huang, P. Indelicato, C.H. Keitel, C.M. König, K. Kromer, M. Müller, Y.N. Novikov, R.X. Schüssler, Ch. Schweiger, S. Eliseev, K. Blaum, Mass-difference measurements on heavy nuclides with an eV/c^2 accuracy in the PENTATRAP spectrometer. Phys. Rev. Lett. **124**, 113001 (2020)
1925. H.-J. Kluge, K. Blaum, F. Herfurth, W. Quint, Atomic and nuclear physics with stored particles in ion traps. Phys. Scr. **2003**, 167 (2003)
1926. K. Blaum, S. Eliseev, S. Sturm, Perspectives on testing fundamental physics with highly charged ions in Penning traps. Quantum Sci. Technol. **6**, 014002 (2021)
1927. W. Paul, H.P. Reinhard, U. von Zahn, Das elektrische Massenfilter als Massenspektrometer und Isotopentrenner. Z. Physik **152**, 143 (1958)
1928. I. Bergström, C. Carlberg, R. Schuch (eds.), *Trapped Charged Particles and Related Fundamental Physics*. Phys. Scr. **T59** (1995)
1929. C. Carlberg et al., SMILETRAP – A wide range high-precision mass spectrometer. IEEE Trans. Instrum. Meas. **44**, 553 (1995)
1930. K. Blaum, Sz. Nagy, G. Werth, High-accuracy Penning trap mass measurements with stored and cooled exotic ions. J. Physics B: Atomic, Molecular and Optical Physics **42**, 154015 (2009)
1931. P. Micke, S. Kühn, L. Buchauer, J.R. Harries, T.M. Bücking, K. Blaum, A. Cieluch, A. Egl, D. Hollain, S. Kraemer, T. Pfeifer, P.O. Schmidt, R.X. Schüssler, Ch. Schweiger, T. Stöhlker, S. Sturm, R.N. Wolf, S. Bernitt, J. R. Crespo López-Urrutia, The Heidelberg compact electron beam ion traps. Rev. Sci. Instr. **89**, 063109 (2018)
1932. W. Paul, 'Electromagnetic traps for charged and neutral particles.' In: *Nobel Lectures in Physics 1981–1990*, ed. by G. Ekspong (World Scientific, Singapore 1993), p.601
1933. H.G. Dehmelt, 'Experiments with an isolated subatomic particle at rest.' In: *Nobel Lectures in Physics 1981–1990*, ed. by G. Ekspong (World Scientific, Singapore 1993), p.583
1934. D.J. Wineland, R.E. Drullinger, F.L. Walls, Radiation pressure cooling of bound resonant absorbers. Phys. Rev. Lett. **40**, 1638 (1978)
1935. W. Neuhauser, M. Hohenstatt, P. Toschek, H. Dehmelt, Optical-sideband cooling of visible atom cloud confined in parabolic well. Phys. Rev. Lett. **41**, 233 (1978)
1936. D.J. Wineland, W.M. Itano, Spectroscopy of a single Mg$^+$ ion. Phys. Lett. A **82**, 75 (1981)
1937. W. Neuhauser, M. Hohenstatt, P. Toschek, H. Dehmelt, Localized visible Ba$^+$ mono-ion oscillator. Phys. Rev. A **22**, 1137 (1980)
1938. E.P. Wigner, Effects of the electron interaction on the energy levels of electrons in metals. Trans. Faraday Soc. **34**, 678 (1938)
1939. F. Diedrich, E. Peik, J.M. Chen, W. Quint, H. Walther, Observation of a phase transition of stored laser-cooled ions. Phys. Rev. Lett. **59**, 2931(1987); and Phys. Blätter **44**, 12 (1988); Nature **334**, 309 (1988)

1940. D.J. Wineland, J.C. Bergquist, W.M. Itano, J.J. Bollinger, C.H. Manney, Atomic-ion Coulomb cluster in an ion trap. Phys. Rev. Lett. **59**, 2935 (1987)
1941. J. Hoffnagle, R.V. DeVoe, L. Reyna, R.G. Brewer, Order-chaos transition of two trapped ions. Phys. Rev. Lett. **61**, 255 (1988)
1942. R.G. Brewer, J. Hoffnagle, R.G. DeVoe, L. Reyna, W. Henshaw, Collision-induced two-ion chaos. Nature **344**, 305 (1990)
1943. D.J. Wineland, C. Monroe, D.M. Meekhof, B.E. King, D. Leibfried, W.M. Itano, J.C. Bergquist, D. Berkeland, J.J. Bollinger, J. Miller, Coherent quantum state manipulation of trapped atomic ions. Adv. Quantum Chem. **30**, 41 (1998)
1944. A. Steane, Quantum computing. Rep. Prog. Phys. **61**, 117 (1998)
1945. H. Häffner, C.F. Roos, R. Blatt, Quantum computing with trapped ions. Phys. Rep. **469**, 155 (2008)
1946. B.P. Lanyon, P. Jurcevic, M. Zwerger, C. Hempel, E.A. Martinez, W. Dür, H.J. Briegel, R. Blatt, C.F. Roos, Measurement-based quantum computation with trapped ions. Phys. Rev. Lett. **111**, 210501 (2013)
1947. K. Brown, J. Kim, C. Monroe, Co-designing a scalable quantum computer with trapped atomic ions. npj Quantum Inf. **2**, 16034 (2016)
1948. C.D. Bruzewicza, J. Chiaverini, R. McConnell, J.M. Sage, Trapped-ion quantum computing: Progress and challenges featured. Appl. Phys. Rev. **6**, 021314 (2019)
1949. D.A. Church, Collision measurements and excited-level lifetime measurements on ions stored in Paul, Penning and Kingdon ion traps. Phys. Rep. **228**, 253 (1993)
1950. H.G. Dehmelt, Proposed $10^{14}\Delta\nu > \nu$ laser fluorescence spectroscopy on Tl^+ mono-ion oscillator II. Bull. Am. Phys. Soc. **20**, 60 (1975)
1951. Th. Sauter, W. Neuhauser, R. Blatt, P.E. Toschek, Observation of quantum jumps. Phys. Rev. Lett. **57**, 1696 (1986); see also Phys. Scr. **T22**, 129 (1988) and [1253] p.121
1952. W. Nagourney, The mono-ion oscillator: An approach to an ideal atomic spectrometer. Comments At. Mol. Phys. **21**, 321 (1988)
1953. J.C. Bergquist, F. Diedrich, W.M. Itano, D.J. Wineland, Hg^+ single ion spectroscopy. In: [1253] p.274
1954. B.C. Young, R.J. Rafac, J.A. Beall, F.C. Cruz, W.M. Itano, D.J. Wineland, J.C. Bergquist, Hg^+ optical frequency standard: Recent progress. In: [1253] p.61; Physics Today **3**, 37 (2001)
1955. E.A. Dijck, A. Mohanty, N. Valappol, M. Nuñez Portela, L. Willmann, K. Jungmann, Lifetime of the 5d $^2D_{5/2}$ level of $^{138}Ba^+$ from quantum jumps with single and multiple Ba+ ions. Phys. Rev. A **97**, 032508 (2018)
1956. T. Rosenband, D.B. Hume, P.O. Schmidt, C.W. Chou, A. Brusch, L. Lorini, W.H. Oskay, R.E. Drullinger, T.M. Fortier, J.E. Stalnaker, S.A. Diddams, W.C. Swann, N.R. Newbury, W.M. Itano, D.J. Wineland, J.C. Bergquist, Frequency ratio of Al^+ and Hg^+ single-ion optical clocks; Metrology at the 17th decimal place. Science **319**, 1808 (2008)
1957. L. Morel, Z.B. Yao, P. Cladé, S. Guellati-Khélifa, Determination of the fine-structure constant with an accuracy of 81 parts per trillion. Nature **588**, 61 (2020)
1958. M.R. Wilczynska, J.K. Webb, M. Bainbridge, J.D. Barrow, S.E.I. Bosman, R.F. Carswell, M.P. Dąbrowski, V. Dumont, C.C. Lee, A.C. Leite, K. Leszczyńska, J. Liske, K. Marosek, C.J.A.P. Martins, D. Milaković, P. Molaro, L. Pasquini, Four direct measurements of the fine-structure constant 13 billion years ago. Science Adv. **24** , eaay9672 (2020)
1959. S. Chu, L. Hollberg, J.E. Bjorkholm, A. Cable, A. Ashkin, Three-dimensional viscous confinement and cooling of atoms by resonance radiation pressure. Phys. Rev. Lett. **55**, 48 (1985)
1960. P.D. Lett, R.N. Walls, Ch.I. Westbrook, W.D. Phillips, P.L. Gould, H.J. Metcalf, Observation of atoms laser cooled below the Doppler limit. Phys. Rev. Lett. **61**, 169 (1988)
1961. J. Dalibard, C. Cohen-Tannoudji, Dressed-atom approach to atomic motion in laser light: the dipole force revisited. J. Opt. Soc. Am. B **2**, 1707 (1986)
1962. J. Dalibard, C. Cohen-Tannoudji, Laser cooling below the Doppler limit by polarization gradients: simple theoretical models. J. Opt. Soc. Am. B **6**, 2023 (1989)
1963. C. Cohen-Tannoudji, Thesis (Paris 1962); Ann. Phys. **7**, 423 and 469 (1962)

1964. C. Cohen-Tannoudji, in *Cargese Lectures in Physics*, ed. by Levy (Gordon & Breach, 1968)
1965. C. Cohen-Tannoudji, J. Dupont-Roc, G. Grynberg, *Atom-Photon Interactions – Basic Processes and Applications*, Chap.VI (Wiley, New York 1992)
1966. P.J. Ungar, D.S. Weiss, E. Riis, S. Chu, Optical molasses and multilevel atoms: Theory. J. Opt. Soc. Am. **6**, 2058 (1989)
1967. A. Ashkin, Trapping of atoms by resonance radiation pressure. Phys. Rev. Lett. **40**, 729 (1978)
1968. S. Chu, J.E. Bjorkholm, A. Ashkin, A. Cable, Experimental observation of optically trapped atoms. Phys. Rev. Lett. **57**, 314 (1986)
1969. V.S. Letokhov, Narrowing of the Doppler width in a standing light wave. JETP Lett. **7**, 272 (1968)
1970. K.-J. Kugler, W. Paul, U. Trinks, A magnetic storage ring for neutrons. Phys. Lett. B **72**, 422 (1978)
1971. D.E. Pritchard, Cooling neutral atoms in a magnetic trap for precision spectroscopy. Phys. Rev. Lett. **51**, 1336 (1983)
1972. A.L. Migdall, J.V. Prodan, W.D. Phillips, T.H. Bergemann, H.J. Metcalf, First observation of magnetically trapped neutral atoms. Phys. Rev. Lett. **54**, 2596 (1985)
1973. E.L. Raab, M.G. Prentiss, A.E. Cable, S. Chu, D.E. Pritchard, Trapping of neutral sodium atoms with radiation pressure. Phys. Rev. Lett. **59**, 2631 (1987)
1974. G. Alzetta, A. Gozzini, L. Moi, G. Orriols, An experimental method for the observation of r.f. transitions and laser beat resonances in oriented Na vapour. Nuovo Cimento B **36**, 5 (1976)
1975. E. Arimondo, G. Orriols, Nonabsorbing atomic coherences by coherent two-photon transitions in a three-level optical pumping. Lett. Nuovo Cimento **17**, 333 (1976)
1976. A. Aspect, E. Arimondo, R. Kaiser, N. Vansteenkiste, C. CohenTannoudji, Laser cooling below the one-photon recoil energy by velocityselective coherent population trapping. Phys. Rev. Lett. **61**, 826 (1988)
1977. J. Lawall, F. Bardou, B. Saubamea, K. Shimizu, M. Leduc, A. Aspect, C. Cohen-Tannoudji, Two-dimensional subrecoil laser cooling. Phys. Rev. Lett. **73**, 1915 (1994)
1978. J. Lawall, S. Kulin, B. Saubamea, N. Bigelow, M. Leduc, C. CohenTannoudji, Three-dimensional laser cooling of helium beyond the single-photon recoil limit. Phys. Rev. Lett. **75**, 4194 (1995)
1979. M. Kasevich, S. Chu, Laser cooling below a photon recoil with three-level atoms. Phys. Rev. Lett. **69**, 1741 (1992)
1980. H.J. Lee, C.S. Adams, M. Kasevich, S. Chu, Raman cooling of atoms in an optical dipole trap. Phys. Rev. Lett. **76**, 2658 (1996)
1981. S. Chu, Nobel Lecture: The manipulation of neutral particles. Rev. Mod. Phys. **70**, 685 (1998)
1982. C.N. Cohen-Tannoudji, Nobel Lecture: Manipulating atoms with photons. Rev. Mod. Phys. **70**, 707 (1998)
1983. W.D. Phillips, Nobel Lecture: Laser cooling and trapping of neutral atoms. Rev. Mod. Phys. **70**, 721 (1998)
1984. S. Stenholm, Light forces put a handle on the atom: To cool and trap atoms by laser light. Contemp. Phys. **29**, 105 (1988)
1985. C.J. Foot, Laser cooling and trapping of atoms. Contemp. Phys. **32**, 369 (1991)
1986. C. Cohen-Tannoudji, Laser cooling and trapping of neutral atoms: Theory. Phys. Rep. **219**, 153 (1992)
1987. A. Ashkin, Optical trapping and manipulation of neutral particles using lasers. Proc. Natl. Acad. Sci. USA **94**, 4853 (1997)
1988. M. Metcalf, P. van der Straten, *Laser Cooling and Trapping* (Springer, Berlin, Heidelberg, 1999)
1989. I. Georgescu, From trapping to laser-cooling antihydrogen. Nature Rev. Physics **3**, 237 (2021)
1990. H. Zhai, *Ultracold Atomic Physics* (Cambridge Univ, Press, 2021)
1991. V.I. Balykin, V.S. Letokhov, Yu.B. Ovchinnikov, A.I. Sidorov, Focusing of an atomic beam and imaging of atomic sources by means of a laser lens based on resonance-radiation pressure. J. Mod. Opt. **35**, 17 (1988)

1992. V.I. Balykin, V.S. Letokhov, V.G. Minogin, Laser control of the motion of neutral atoms and optical atomic traps. Phys. Scr. **T22**, 119 (1988)
1993. K. Cloppenburg, G. Hennig, A. Mihm, H. Wallis, W. Ertmer, Optical elements for manipulating atoms. In: [1253] p.87
1994. C.S. Adams, M. Sigel, J. Mlynek, Atom optics. Phys. Rep. **240**, 143 (1994)
1995. P.E. Moskowitz, P.L. Gould, S.R. Atlas, D.E. Pritchard, Diffraction of an atomic beam by standing-wave radiation. Phys. Rev. Lett. **51**, 370 (1983)
1996. O. Carnal, J. Mlynek, Young's double-slit experiment with atoms: A simple atom interferometer. Phys. Rev. Lett. **66**, 2689 (1991)
1997. D.K. Keith, C.E. Ekstrom, Q.A. Turchette, D.E. Pritchard, An interferometer for atoms. Phys. Rev. Lett. **66**, 2693 (1991)
1998. C.S. Adams, O. Carnal, J. Mlynek, Atom interferometry. Adv. At. Mol. Opt. Phys. **34**, 1 (1994)
1999. M. Arndt, O. Nairz, J. Vos-Andreae, C. Keller, G. van der Zouw, A. Zeilinger, Wave-particle duality of C_{60} molecules. Nature **401**, 680 (1999)
2000. A. Shayeghi, P. Rieser, G. Richter, U. Sezer, J. Rodewald, P. Geyer, T.J. Martinez, M. Arndt, Matter-wave interference of a native polypeptide. Nat. Commun. **11**, 1447 (2020)
2001. K. Hornberger, S. Gerlich, P. Haslinger, S. Nimmrichter, M. Arndt, Colloquium: Quantum interference of clusters and molecules. Rev. Mod. Phys. **84**, 157 (2012)
2002. A. Peters, K.Y. Chung, S. Chu, Measurement of gravitational acceleration by dropping atoms. Nature **400**, 849 (1999)
2003. G. Rosi G, F. Sorrentino, L. Cacciapuoti, M. Prevedelli, G.M. Tino, Precision measurement of the Newtonian gravitational constant using cold atoms. Nature **510**, 518 (2014)
2004. T. Kovachy, P. Asenbaum, C. Overstreet, C.A. Donnelly, S.M. Dickerson, A. Sugarbaker, J.M. Hogan, M.A. Kasevich, Quantum superposition at the half-metre scale. Nature **528**, 530 (2015)
2005. B. Stray et al., Quantum sensing for gravity cartography. Nature **602**, 590 (2022)
2006. P. Asenbaum, Ch. Overstreet, T. Kovachy, D.D. Brown, J.M. Hogan, M.A. Kasevich, Phase shift in an atom interferometer due to spacetime curvature across its wave function. Phys. Rev. Lett. **118**, 183602 (2017)
2007. M. Morinaga, M. Yasuda, T. Kishimoto, F. Shimizu, Holographic manipulation of a cold atomic beam. Phys. Rev. Lett. **77**, 802 (1996)
2008. C.I. Westbrook, R.N. Watts, C.E. Tanner, S.L. Rolston, W.D. Phillips, P.D. Lett, P.L. Gould, Localization of atoms in a three-dimensional standing wave. Phys. Rev. Lett. **65**, 33 (1990)
2009. A. Hemmerich, T.W. Hänsch, Two-dimensional atomic crystal bound by light. Phys. Rev. Lett. **70**, 410 (1993)
2010. D. Grynberg, B. Lounis, P. Verkerk, J.-Y. Courtois, C. Salomon, Quantized motion of cold cesium atoms in two- and three-di[mensional optical potentials. Phys. Rev. Lett. **70**, 2249 (1993)
2011. A. Kastberg, W.D. Phillips, W.S.L. Rolston, R.J.C. Spreeuw, P.S. Jessen, Adiabatic cooling of cesium to 700 nK in an optical lattice. Phys. Rev. Lett. **74**, 1542 (1995)
2012. M. Takamoto, F.l. Hong, R. Higashi, H. Katori, An optical lattice clock. Nature **435**, 321 (2005)
2013. X.B. Zhang, J. Ye, Precision measurement and frequency metrology using ultracold atoms. Nat. Sci. Rev. **3**, 189 (2016)
2014. I. Bloch, Ultracold quantum gases in optical lattices. Nat. Phys. **1**, 23 (2005)
2015. M. Greiner, S. Fölling, Optical lattices. Nature **453**, 736 (2008)
2016. M. Lewenstein, A. Sanpera, V. Ahufinger, *Ultracold Atoms in Optical Lattices: Simulating quantum many-body systems* (Oxford Univ, Press, 2012)
2017. B. Yang, H. Sun, C.J. Huang, H.Y. Wang, Y.J. Deng, H.N. Dai, Z.S. Yuan, J.W. Pan, Cooling and entangling ultracold atoms in optical lattices. Science **369**, 550 (2020)
2018. P.D. Lett, P.S. Jessen, W.D. Phillips, S.L. Rolston, C.I. Westbrook, P.L. Gould, Laser modification of ultracold collisions: Experiment. Phys. Rev. Lett. **67**, 2139 (1991)

2019. J. Weiner, Advances in ultracold collisions: Experimentation and theory. Adv. At. Mol. Opt. Phys. **35**, 45 (1995)
2020. J.D. Weinstein, R. deCarvalho, T. Guillet, B. Friedrich, J.M. Doyle, Magnetic trapping of calcium monohydride molecules at millikelvin temperatures. Nature **395**, 148 (1998)
2021. H.L. Bethlem, G. Berden, G. Meijer, Decelerating neutral dipolar molecules. Phys. Rev. Lett. **83**, 1558 (1999)
2022. S.N. Atutov, S.P. Podjachev, A.M. Shalagin, Diffusion pulling of Na vapor into the light beam. Opt. Commun. **57**, 236 (1986)
2023. E.R. Eliel, Light-induced drift. Adv. At. Mol. Opt. Phys. **31**, 199 (1993)
2024. H.G.C. Werij, J.P. Woerdman, J.J.M. Beenakker, I. Kuscer, Demonstration of a semipermeable optical piston. Phys. Rev. Lett. **52**, 2237 (1984)
2025. G. Nienhuis, Theory of light-induced drift and the optical piston. Phys. Rev. A **31**, 1636 (1985)
2026. S.N. Bose, Plancks Gesetz und Lichtquantenhypothese. Z. Phys. **26**, 178 (1924)
2027. A. Einstein, Quantentheorie des einatomigen idealen Gas. Sitzungsber. Preuss. Akad. Wiss. **1924**, 261 (1924); Quantentheorie des einatomigen idealen Gases. 2. Abhandlung. ibid. **1925**, 3 (1925)
2028. H.F. Hess, Evaporative cooling of magnetically trapped and compressed spin-polarized hydrogen. Phys. Rev. B **34**, 3476 (1986)
2029. H.F. Hess, G.P. Kochanski, J.M. Doyle, N. Masuhara, D. Kleppner, T.J. Greytak, Magnetic trapping of spin-polarized atomic hydrogen. Phys. Rev. Lett. **59**, 672 (1987)
2030. N. Masuhara, J.M. Doyle, J.C. Sandberg, D. Kleppner, T.J. Greytak, H.F. Hess, G.P. Kochanski, Evaporative cooling of spin-polarized atomic hydrogen. Phys. Rev. Lett. **61**, 935 (1988)
2031. M.H. Anderson, J.R. Ensher, M.R. Matthews, C.E. Wieman, E.A. Cornell, Observation of Bose-Einstein condensation in a dilute atomic vapor. Science **269**, 198 (1995)
2032. K.B. Davies, M.O. Mewes, M.R. Andrews, N.J. van Druten, D.S. Durfee, D.N. Kurn, W. Ketterle, Bose-Einstein condensation in a gas of sodium atoms. Phys. Rev. Lett. **75**, 3969 (1995)
2033. Physics Today (August 1995) p.17
2034. M.R. Andrews, C.G. Townsend, H.-J. Miesner, D.S. Durfee, D.M. Kurn, W. Ketterle, Observation of interference between two Bose condensates. Science **275**, 637 (1997)
2035. M.-O. Mewes, M.R. Andrews, D.M. Kurn, D.S. Durfee, C.G. Townsend, W. Ketterle, Output coupler for Bose-Einstein condensed atoms. Phys. Rev. Lett. **78**, 582 (1997)
2036. I. Bloch, T.W. Hänsch, T. Esslinger, Atom laser with a CW output coupler. Phys. Rev. Lett. **82**, 3008 (1999)
2037. W. Hagley, L. Deng, M. Kozuma, J. Wen, M.A. Edwards, K. Helmersson, S.L. Rolston, W.D. Phillips, A well-collimated quasi-continuous atom laser. Science **283**, 1706 (1999)
2038. S. Inouye, T. Pfau, S. Gupta, A.P. Chikkatur, A. Gorlitz, D.E. Pritchard, W. Ketterle, Phase-coherent amplification of atomic matter waves. Nature **402**, 641 (1999)
2039. A.P. Chikkatur, Y. Shin, A.E. Leanhardt, D. Kielpinski, E. Tsikata, T.L. Gustavson, D.E. Pritchard, W. Ketterle, A continuous source of Bose-Einstein condensed atoms. Science **296**, 2193 (2002)
2040. W. Ketterle, M.R. Andrews, K.B. Davies, D.S. Durfee, D.M. Korn, M.-O. Mewes, N.J. van Druten, Bose-Einstein condensation of ultra-cold atomic gases. Phys. Scr. **T66**, 31 (1996)
2041. K. Burnett, Bose-Einstein condensation with evaporatively cooled atoms. Contemp. Phys. **37**, 1 (1996)
2042. W. Ketterle, N.J. Druten, Evaporative cooling of trapped atoms. Adv. At. Mol. Opt. Phys. **37**, 181 (1996)
2043. E.A. Cornell, C.E. Wieman, The Bose-Einstein condensate. Sci. Am. **278**(3), 26 (1998)
2044. G. Modugno, G. Ferrari, G. Roati, R. Brecha, A. Simoni, M. Inguscio, Bose-Einstein condensation of potassium by sympathetic cooling. Science **294**, 1320 (2001)
2045. M. Greiner, O. Mandel, T. Esslinger, T.W. Hänsch, I. Bloch, Quantum phase transition from a superfluid to a Mott insulator in a gas of ultracold atoms. Nature **415**, 39 (2002)

2046. M. Greiner, O. Mandel, T.W. Hänsch, I. Bloch, Collapse and revival of the matter wave field of a Bose-Einstein condensate. Nature **419**, 51 (2002)
2047. J.R. Anglin, W. Ketterle, Bose-Einstein condensation of atomic gases. Nature **416**, 211 (2002)
2048. P. Engels, I. Coddington, P.C. Haljan, V. Schweikhard, E.A. Cornell, Observation of long-lived vortex aggregates in rapidly rotating Bose–Einstein condensates. Phys. Rev. Lett. **90**, 170,405/1–4 (2003)
2049. A.E. Leanhardt, Y. Shin, A.P. Chikkatur, D. Kielpinski, W. Ketterle, D.E. Pritchard, Bose–Einstein condensates near a microfabricated surface. Phys. Rev. Lett. **90**, 100,404 (2003)
2050. A. Griffin, D.W. Snoke, S. Stringari (eds.), *Bose-Einstein Condensation* (Cambridge Univ. Press, 2009)
2051. B.J. Pethick, H. Smith, *Bose–Einstein Condensation in Dilute Gases, 2nd Ed.* (Cambridge Univ. Press, 2011)
2052. L. Pitaevskii, S. Stringari, *Bose-Einstein Condensation and Superfluidity* (Oxford Scholarship Online, 2016)
2053. N.P. Proukakis, D.W. Snoke, P.B. Littlewood (eds.), *Universal Themes of Bose-Einstein Condensation* (Cambridge Univ. Press, 2017)
2054. D.C. Aveline, J.R. Williams, E.R. Elliott, C. Dutenhoffer, J.R. Kellogg, J.M. Kohel, A. Urvoy, Z. Vendeiro, J. Ramette, A. Adiyatullin, V. Vuletić, Direct laser cooling to Bose-Einstein condensation in a dipole trap. Phys. Rev. Lett. **122**, 203202 (2019)
2055. N.E. Lay, K. Oudrhiri, R.F. Shotwell, N. Yu, R.J. Thompson, Observation of Bose-Einstein condensates in an Earth-orbiting research lab. Nature **582**, 193 (2020)
2056. L. Deng, E.W. Hagley, J. Wen, M. Trippenbach, Y. Band, P.S. Julienne, J.E. Simsarian, K. Helmersson, S.L. Rolston, W.D. Phillips, Four-wave mixing with matter waves. Nature **398**, 218 (1999)
2057. J.R. Abo-Shaeer, D.E. Miller, J.K. Chin, K. Xu, T. Mukaiyama, W. Ketterle, Coherent molecular optics using ultracold sodium dimers. Phys. Rev. Lett. **94**, 040405 (2005)
2058. D.G. Fried, T.C. Killian, L. Willmann, D. Landhuis, S.C. Moss, D. Kleppner, T.J. Greytak, Bose-Einstein condensation of atomic hydrogen. Phys. Rev. Lett. **81**, 3811 (1999)
2059. E.A. Cornell, C.E. Wieman, Nobel Lecture: Bose-Einstein condensation in a dilute gas, the first 70 years and some recent experiments. Rev. Mod. Phys. **74**, 875 (2002)
2060. W. Ketterle, Nobel Lecture: When atoms behave like waves: Bose-Einstein condensation and the atom laser. Rev. Mod. Phys. **74**, 1131 (2002)
2061. B. DeMarco, D.S. Jin, Onset of Fermi degeneracy in a trapped atomic gas. Science **285**, 1703 (1999)
2062. M. Greiner, C. Regal, D.S. Jin, Emergence of a molecular Bose-Einstein condensate from a Fermi gas. Nature **426**, 537 (2003)
2063. G. Modugno. G. Roati, F. Riboli, F. Ferlaino, R. Brecha, M. Inguscio, Collapse of a degenerate Fermi gas, Science **297**, 2240 (2002)
2064. E.G.M. van Kempen, B.J. Verhaar, W. Ketterle, Rf spectroscopy of ultracold fermions. Science **300**, 1723 (2003)
2065. M. Inguscio, W. Ketterle, C. Salomon (eds.), *Ultracold Fermi Gases.* Proceedings of the International School of Physics "Enrico Fermi" 164 (IOS Press, 2007)
2066. J.T. Stewart, J.P. Gaebler, D.S. Jin, Using photoemission spectroscopy to probe a strongly interacting Fermi gas. Nature **454**, 744 (2008)
2067. J.P. Gaebler, J.T. Stewart, T.E. Drake, D.S. Jin, A. Perali, P. Pieri, G.C. Strinati, Observation of pseudogap behaviour in a strongly interacting Fermi gas. Nat. Phys. **6**, 569 (2010)
2068. S. Gupta, Z. Hadzibabic, M.W. Zwierlein, C.A. Stan, K. Dieckmann, C.H. Schunck, C. Gardiner, P. Zoller, *The Quantum World of Ultra-Cold Atoms and Light Book III: Ultra-Cold Atoms* (World Scientific, Singapore, 2017)
2069. M. Inguscio, L. Fallani, *Atomic Physics – Precise Measurement and Ultracold Matter* (Oxford University Press, Oxford, 2018)
2070. L. De Marco, G. Valtolina, K. Matsuda, W.G. Tobias, J.P. Covey, J. Ye, A degenerate Fermi gas of polar molecules. Science **363**, 853 (2019)
2071. H. Zhai, 'Degenerate Fermi Gases', in [1990], pp.155–200

Chapter 10

2072. L.J. Radziemski, R.W. Solarz, J.A. Paisner (eds.), *Laser Spectroscopy and its Applications* (Dekker, New York, 1987)
2073. H. Medin, S. Svanberg (eds.), Laser Technology in Chemistry, Special issue. Appl. Phys. B **46**, No.3 (1988)
2074. D.L. Andrews (ed.), Applied Laser Spectroscopy: Techniques, Instrumentation and Applications (VCH, 1992)
2075. S. Svanberg, Laser based diagnostics - from cultural heritage to human health. Appl. Phys. B **92**, 351 (2008)
2076. S. Svanberg, G.Y. Zhao, H. Zhang, J. Huang, M. Lian, T.Q. Li, S.M. Zhu, Y.Y. Li, Z. Duan, H.Y. Lin, K. Svanberg, Laser spectroscopy applied to environmental, ecological, food safety and biomedical research. Opt. Express **24**, A515 (2016)
2077. R.P. Lucht, *Applied Laser Spectroscopy* (CRC Press, 2021)
2078. International Energy Agency, *World Energy Outlook 2020* (IEA, Paris, 2020)
2079. W.C. Gardiner Jr., The chemistry of flames. Sci. Am. **246**(2), 86 (1982)
2080. W.C. Gardiner (ed.), *Combustion Chemistry* (Springer, Berlin, Heidelberg, 1984)
2081. J. Walker, The physics and chemistry underlying the infinite charm of a candle flame. Sci. Am. **238**(4), 154 (1978)
2082. W.C. Strahle, *An Introduction to Combustion* (Gordon and Breach, Langhorne, 1993)
2083. G. Cox, *Combustion Fundamentals of Fire* (Academic Press, London, 1995)
2084. J.F. Griffiths, J.A. Barnard, J.N. Bradley, *Flame and Combustion,* 3rd ed. (Chapman & Hall, 2009)
2085. I. Glassman, R.A. Yetter, N.G. Glumac, *Combustion,* 5th Ed. (Elsevier, 2014)
2086. M. Gehring, K. Hoyermann, H. Schacke, J. Wolfrum, Direct studies of some elementary steps for the formation and destruction of nitric oxide in the $H - N - 0$ system. 14th Symp. on Combustion (Combustion Institute, Pittsburgh, PA 1973)
2087. H. Bockhorn (ed.), *Soot Formation in Combustion Mechanisms and Models, Springer Series in Chemical Physics*, vol. 59 (Springer-Verlag, Berlin, Heidelberg, 1994)
2088. B.S. Haynes, ‘Soot and hydrocarbons in combustion.’ In: *Fossil Fuel Combustion*, ed. by W. Bartok, A.F. Sarofim (Wiley, New York 1991) Chap.4.
2089. H. Bladh, J. Johnsson, P.E. Bengtsson, On the dependence of the laser-induced incandescence (LII) signal on soot volume fraction for variations in particle size. Appl. Phys. B **90**, 109 (2008)
2090. M. Mannazhi, S. Török, J.L. Gao, P.E. Bengtsson, Soot maturity studies in methane-air diffusion flames at elevated pressures using laser-induced incandescence. Proc. Comb. Inst. **38**, 1217 (2021)
2091. A. Karlsson, S. Török, A. Roth, P.E. Bengtsson, Numerical scattering simulations for estimating soot aggregate morphology from nephelometer scattering measurements. J. Aerosol Science. **159**, 105828 (2022)
2092. A.G. Gaydon, H.G. Wolfhard, *Flames, their Structure, Radiation and Temperature* (Chapman and Hall, New York, 1979)
2093. J. Wolfrum, Chemical kinetics in combustion systems: The specific effect of energy, collisions, and transport processes. 20th Symp. on Combustion (Combustion Institute, Pittsburgh, PA 1985)
2094. A.C. Gaydon, *The Spectroscopy of Flames* (Chapman and Hall, New York, 1974)
2095. D.R. Crosley (ed.), *Laser Probes for Combustion Chemistry*, ACS Symp. Ser. Vol.134 (Am. Chem. Soc., Washington 1980)
2096. A.C. Eckbreth, P.A. Bonczyk, J.F. Verdiek, Combustion Diagnostics by Laser Raman and Fluorescence Techniques. Prog. Energy Comb. Sci. **5**, 253 (1979)
2097. J.H. Bechtel, C.J. Dasch, R.E. Teets, ‘Combustion research with lasers.’ In: *Laser Applications*, ed. by R.K. Erf, J.F. Ready (Academic Press, New York 1984)
2098. T.D. McCay, J.A. Roux (eds.), Combustion diagnostics by nonintrusive methods. Progr. Astronautics and Aeronautics, Vol.**92** (1983)

2099. A.C. Eckbreth, *Laser Diagnostics for Combustion Temperature and Species* (Gordon & Breach, Amsterdam, 1996)

2100. K. Iinuma, T. Asanuma, T. Ohsawa, J. Doi (eds.), *Laser Diagnostics and Modelling of Combustion* (Springer, Berlin, Heidelberg, 1987)

2102. K. Kohse-Höinghaus, R.S. Barlow, M. Aldén, J. Wolfrum, Combustion at the focus: laser diagnostics and control. Proc. Combustion Institute **30**, 89–123 (2005)

2102. A. Ehn, J. Zhu, X. Li, J. Kiefer, Advanced laser-based techniques for gas-phase diagnostics in combustion and aerospace engineering. Appl. Spectr. **71**, 341 (2017)

2103. N. Peters, *Turbulent Combustion* (Cambridge Univ, Press, 2001)

2104. M. Aldén, H. Edner, S. Svanberg, T. Högberg, Combustion studies with laser techniques, Göteborg Institute of Physics Reports GIPR-206 (Chalmers University of Technology, Göteborg, 1980)

2105. M. Aldén, H. Edner, G. Holmstedt, T. Högberg, H. Lundberg, S. Svanberg, Relative distribution of radicals and temperature in flat flames, studied by laser-induced fluorescence and BOXCARS spectroscopy. Lund Reports on Atomic Physics LRAP-1 (Lund Institute of Technology, Lund 1981)

2106. D.R. Crosley, G.P. Smith, Laser-induced fluorescence spectroscopy for combustion diagnostics. Opt. Eng. **22**, 545 (1983)

2107. R. Lucht, Applications of laser-induced fluorescence spectroscopy for combustion and plasma diagnostics. In: [2072] p.623

2108. J.W. Daily, Laser induced fluorescence spectroscopy in flames. Progr. Energy Combust. Sci. **23**, 133 (1997)

2109. S. Bejaou, X. Mercier, P. Desgroux, E. Therssen, Laser induced fluorescence spectroscopy of aromatic species produced in atmospheric sooting flames using UV and visible excitation wavelengths. Combust. Flame **161**, 2479 (2014)

2110. N.S. Bergano, P.A. Janimaagi, M.M. Salour, J.H. Bechtel, Picosecond laser spectroscopy measurement of hydroxyl fluorescence lifetime in flames. Opt. Lett. **8**, 443 (1983)

2111. S. Agrup, F. Ossler, M. Aldén, Measurement of collisional quenching of hydrogen atoms in an atmospheric pressure hydrogen/oxygen flame by picosecond laser-induced fluorescence. Appl. Phys. B **61**, 479 (1995)

2112. F. Ossler, J. Larsson, M. Aldén, Measurement of the effective lifetime of O atoms in atmospheric premixed flames. Chem. Phys. Lett. **250**, 287 (1996)

2113. F.C. Bormann, T. Nielsen, M. Burrows, P. Andresen, Single-pulse, collision-insensitive picosecond planar laser-induced fluorescence of OH $A^2\ \Sigma^+(v^{'}=2)$ in atmospheric pressure flames. Appl. Phys. B **62**, 601 (1996)

2114. A. Brockhinke, W. Kreutner, U. Rahmann, K. Kohse-Höinghaus, T.B. Settersten, M.A. Linne, Time-, wavelength-, and polarization-resolved measurements of OH $(A^2\Sigma^+$ picosecond laser-induced fluorescence in atmospheric-pressure flames. Appl. Phys. B **69**, 477 (1999)

2115. Ch. Brackmann, J. Bood, J.D. Naucler, A.A. Konnov, M. Aldén, Quantitative picosecond laser-induced fluorescence measurements of nitric oxide in flames. Proc. Combust. Inst. **36**, DOI: https://doi.org/10.1016/j.proci.2016.07.012 (2016)

2116. X. Liu, M. Bertsch, A.A. Subash, S.B. Yu, R.Z. Szasz, Z.S. Li, P. Petersson, X.S. Bai, M. Aldén, D. Lörstad, Investigation of turbulent premixed methane/air and hydrogen-enriched methane/air flames in a laboratory-scale gas turbine model combustor. Int. J. Hydrogen Energy **46**, 13377 (2021)

2117. M. Aldén, H. Edner, P. Grafström, H.M. Hertz, G. Holmstedt, T. Högberg, H. Lundberg, S. Svanberg, S. Wallin, W. Wendt, U. Westblom, 'Imaging measurements of species concentrations, temperatures and velocities in reactive flows using laser-induced fluorescence.' In: *Lasers 86*, ed. by K.M. Corcoran, D.M. Sullivan, W.C. Stwalley (STS Press, McLean, VA. 1985) p.209

2118. M. Aldén, H. Edner, G. Holmstedt, S. Svanberg, T. Högberg, Single-pulse laser-induced OH fluorescence in an atmospheric flame, spatially resolved with a diode array detector. Appl. Opt. **21**, 1236 (1982)

2119. M.J. Dyer, D.R. Crosley, Two-dimensional imaging of OH laser-induced fluorescence in a flame. Opt. Lett. **7**, 382 (1982)

2120. G. Kychakoff, R.D. Howe, R.K. Hanson, Quantitative flow visualization technique for measurements in combustion gases. Appl. Opt. **23**, 704 (1984)

2121. G. Kychakoff, R.D. Howe, R.K. Hanson, M.C. Drake, R.W. Pitz, M. Lapp, C.M. Penney, Visualization of turbulent flame fronts with planar laserinduced fluorescence. Science **224**, 382 (1984)

2122. B. Hiller, R.K. Hanson, Simultaneous planar measurements of velocity and pressure fields in gas flows using laser-induced fluorescence. Appl. Opt. **27**, 33 (1988)

2123. U. Westblom, M. Aldén, Simultaneous multiple-species detection in a flame using laser-induced fluorescence. Appl. Opt. **28**, 2592 (1989)

2124. M. Aldén, H. Edner, P. Grafström, S. Svanberg, Two-photon excitation of atomic oxygen in a flame. Opt. Commun. **42**, 244 (1982)

2125. M. Aldén, H.M. Hertz, S. Svanberg, S. Wallin, Imaging laser-induced fluorescence of oxygen atoms in a flame. Appl. Opt. **23**, 3255 (1984)

2126. M. Aldén, U. Westblom, J.E.M. Goldsmith, Two-photon-excited stimulated emission from atomic oxygen in flames and cold gases. Opt. Lett. **14**, 305 (1989)

2127. R.P. Lucht, J.P. Salmon, G.B. King, D.W. Sweeney, N.M. Laurendeau, Two-photon-excited fluorescence measurement of hydrogen atoms in flames. Opt. Lett. **8**, 365 (1983)

2128. M. Aldén, A.L. Schawlow, S. Svanberg, W. Wendt, P.-L. Zhang, Three-photon excited fluorescence detection of atomic hydrogen in an atmospheric pressure flame. Opt. Lett. **9**, 211 (1984)

2129. J.E.M. Goldsmith, R.J.M. Anderson, Imaging of atomic hydrogen in flames with two-step saturated fluorescence detection. Opt. Lett. **11**, 67 (1985)

2130. M. Aldén, S. Wallin, W. Wendt, Applications of two-photon absorption for detection of CO in combustion gases. Appl. Phys. B **33**, 205 (1984)

2131. U. Westblom, M. Aldén, Laser-induced fluorecence detection of NH_3 in flames with the use of two-photon excitation. Appl. Spectrosc. **44**, 881 (1990)

2132. N. Georgiev, M. Aldén, Developments of laser-induced fluorescence for two-dimensional multi-species imaging in flames. Spectrochem. Acta B **52**, 1105 (1997)

2133. J. Olofsson, H. Seyfried, M. Richter, M. Aldén, A. Vressner, A. Hultqvist, B. Johansson, K. Lombaert, High-speed LIF imaging for cycle-resolved formaldehyde visualization in HCCI combustion. SAE Transactions, J. Engines **114**, 645 (2005)

2134. M. Aldén, M. Richter, 'Development and Application of High-Speed Laser Visualization Techniques in Combustion Research', in *Micro-World Observed by Ultra High-Speed Cameras,* pp 241–259 (Springer, 2018)

2135. J.E.M. Goldsmith, Resonant multiphoton optogalvanic detection of atomic hydrogen in flames. Opt. Lett. **7**, 437 (1982)

2136. P.J.H. Tjossem, T.A. Cool, Detection of atomic hydrogen in flames by resonance four-photon ionization at 365 nm. Chem. Phys. Lett. **100**, 479 (1983)

2137. K. Tennal, G.J. Salomo, R. Gupta, Minority species concentration measurements in flames by the photoacoustic technique. Appl. Opt. **21**, 2133 (1982)

2138. M.P. Arroya, S. Langlois, R.K. Hanson, Diode-laser absorption technique for simultaneous measurements of multiple gasdynamic parameters in high-speed flows containing water vapor. Appl. Opt. **33**, 3296 (1994)

2139. K. Nyholm, R. Maier, C.G. Aminoff, M. Kaivola, Detection of OH in flames by polarization spectroscopy. Appl. Opt. **32**, 919 (1993)

2140. B. Löfstedt, R. Fritzon, M. Aldén, Investigation of NO detection in flames by the use of polarization spectroscopy. Appl. Opt. **35**, 2140 (1996)

2141. K.E. Bennett, G.W. Faris, R.L. Byer, Experimental optical fan beam tomography. Appl. Opt. **23**, 2678 (1984)

2142. P. Kauranen, H.M. Hertz, S. Svanberg, Tomographic imaging of fluid flows by the use of two-tone frequency modulation spectroscopy. Opt. Lett. **19**, 1489 (1994)

2143. H.M. Hertz, G.W. Faris, Emission tomography of flame radicals. Opt. Lett. **13**, 351 (1988)

2144. H.M. Hertz, Experimental determination of 2-D flame temperature fields by interferometric tomography. Opt. Commun. **54**, 131 (1985)

2145. A. Rose, G.J. Salamo, R. Gupta, Photoacoustic deflection spectroscopy: A new species-specific method for combustion diagnostics. Appl. Opt. **23**, 781 (1984)

2146. G.W. Faris, R.L. Byer, Beam-deflection optical tomography of a flame. Opt. Lett. **12**, 155 (1987)

2147. M. Lapp, C.M. Penney, 'Raman measurements on flames.' In: *Advances in Infrared and Raman Spectroscopy*, ed. by R.J.H. Clark, R.E. Hester (Heyden, London 1977)

2148. R.W. Dibble, A.R. Masri, R.W. Bilger, The spontaneous Raman technique applied to premixed flames of methane. Combust. Flame **67**, 189 (1987)

2149. W. Reckers, L. Huwel, G. Grunewald, P. Andresen, Spatially resolved multispecies and temperature analysis in hydrogen flames. Appl. Opt. **32**, 907 (1993)

2150. J. Kojima. Q.V. Nguyen, Measurement and simulation of spontaneous Raman scattering in high-pressure fuel-rich H_2–air flames. Meas. Sci. Technol. **15** , 565 (2004)

2151. M. Commodo, A.E. Karataş, G.L. De Falco, P. Minutolo, A. D'Anna, Ö.L. Gülder, On the effect of pressure on soot nanostructure: A Raman spectroscopy investigation. Comb. Flame **219**, 13 (2020)

2152. M. Aldén, H. Edner, S. Svanberg, Coherent anti-Stokes Raman spectroscopy (CARS) applied in combustion probing. Phys. Scr. **27**, 29 (1983)

2153. D. Klick, K.A. Marko, L. Rimai, Broadband single-shot CARS spectra in a fired internal combustion engine. Appl. Opt. **20**, 1178 (1981)

2154. G.C. Alessandretti, P. Violino, Thermometry by CARS in an automobile engine. J. Phys. D **16**, 1583 (1983)

2155. M. Richter, B. Axelsson, M. Aldén, G. Josefsson, L.-O. Carlsson, M. Dahlberg, J. Nisbet, H. Simonsen, Investigation of the fuel distribution and the in-cylinder flow field in a stratified charge engine using laser techniques and comparison with CFD-Modelling. SAE Technical Paper Series 1999–01–3540 (SAE International, Warrendale, PA 1999)

2156. L.A. Rahn, S.S. Johnston, R.L. Farrow, P.L. Mattern, 'CARS thermometry in an internal combustion engine.' In: *Temperature*, Vol.5, ed. by J.F. Schooley (AIP, New York 1982)

2157. C. Brackmann, J. Bood, M. Afzelius, P.E. Bengtsson, Thermometry in internal combustion engines via dual-broadband rotational coherent anti-Stokes Raman spectroscopy. Meas. Sci. Tech. **15**, 15 R13 (2004)

2158. M. Aldén, S. Wallin, CARS experiment in a full-scale (10×10 m^2) industrial coal furnace. Appl. Opt. **24**, 3434 (1985)

2159. B. Attal, M. Pealat, J.P. Taran, CARS Diagnostics of combustion. J. Energy **4**, 135 (1980)

2160. A.C. Eckbreth, CARS thermometry in practical combustors. Combust. Flame **39**, 133 (1980)

2161. R.J. Hall, A.C. Eckbreth, 'Coherent anti-Stokes Raman Spectroscopy (CARS): Application to combustion diagnostics.' In: *Laser Applications*, Vol.5, ed. by J.F. Ready, R.K. Erf (Academic Press. New York 1984)

2162. S. Roy, J.R. Gord, A.K. Patnaik, Recent advances in coherent anti-Stokes Raman scattering spectroscopy: Fundamental developments and applications in reacting flows. Progr. Energy. Comb. Sci. **36**, 280 (2010)

2163. H. Haragushi, B. Smith, S. Weeks, D.J. Johnson, J.D. Wineforder, Measurement of small volume flame temperature by the two-line atomic fluorescence method. Appl. Spectrosc. **31**, 156 (1977)

2164. R.G. Jolik, J.W. Daily, Two-line atomic fluorescence temperature measurements in flames: An experimental study. Appl. Opt. **21**, 4158 (1982)

2165. M. Aldén, P. Grafström, H. Lundberg, S. Svanberg, Spatially resolved temperature measurements in a flame using laser-excited two-line atomic fluorescence and diode-array detection. Opt. Lett. **8**, 241 (1983)

2166. J. Hult, S. Burns, C.F. Kaminski, Two-line atomic fluorescence flame thermometry using diode lasers. Proc. Comb. Inst. **30**, 1535 (2005)

2167. P.R. Medwell, Q.N. Chan, P.A.M. Kalt, Z.T. Alwahabi, B. Dally, G.J. Nathan, Instantaneous temperature imaging of diffusion flames using two-line atomic fluorescence. Appl. Spectr. **64**, 173 (2010)

2168. A. Manteghi, Y. Shoshin, N.J. Dam, L.P.H. de Goey, Two-line atomic fluorescence thermometry in the saturation regime. Appl. Phys. B **118**, 281 (2015)
2169. J. Borggren, I. Burns, A.L. Sahlberg, M. Aldén, Z.S. Li, Temperature imaging in low-pressure flames using diode laser two-line atomic fluorescence employing a novel indium seeding technique. Appl. Phys. B **122**, 58 (2016)
2170. J. Borggren, W. Weng, A. Hosseinnia, P.E. Bengtsson, M. Aldén, Z.S. Li, Diode laser-based thermometry using two-line atomic fluorescence of indium and gallium. Appl. Phys. B **123**, 278 (2017)
2171. Z.W. Sun, Z. Alwahabi, B. Dally, G. Nathan, Simultaneously calibrated two-line atomic fluorescence for high-precision temperature imaging in sooting flames. Proc. Comb. Inst. **37**, 1417 (2019)
2172. C. Kaminski, J. Engström, M. Aldén, Quasi instantaneous 2D temperature measurements in combustion by atomic laser-induced fluorescence, VDI Berichte **1313**, 555 (1997), and J. Engström, PhD Thesis, Lund University, 2001
2173. J. Pender, L. Hesselink, Phase conjugation in a flame. Opt. Lett. **10**, 264 (1985)
2174. G. Hall, B.J. Whitaker, Laser-induced grating spectroscopy. J. Chem. Soc. Faraday Trans. **90**, 1 (1994)
2175. B. Yip, P.M. Danehy, R.K. Hanson, Degenerate four-wave mixing temperature measurements in a flame. Opt. Lett. **17**, 751 (199[2)
2176. P. Ewart, P.G.R. Smith, R.G. Williams, Imaging of trace species distributions by degenerate four-wave mixing: Diffraction effects, spatial resolution, and image referencing. Appl. Opt. **36**, 5959 (1997)
2177. J. Kiefer, P. Ewart, Laser diagnostics and minor species detection in combustion using resonant four-wave mixing. Progr. Energy Combust. Sci. **37**, 525e564 (2011)
2178. A.-L. Sahlberg, J. Zhou, M. Aldén, Z. S. Li, Non-intrusive in situ detection of methyl chloride in hot gas flows using infrared degenerate four-wave mixing. J. Raman Spectr. DOI https://doi.org/10.1002/jrs.4651 (2015)
2179. R.M. Osgood, S.R.I. Brueck, H.R. Schlossberg (eds.), *Laser Diagnostics and Photochemical Processing for Semiconductor Devices* (North-Holland, Amsterdam, 1983)
2180. W.G. Breiland, M.E. Coltrin, P. Ho (eds.), *Laser-Based Studies of Chemical Vapor Deposition*, Proc. SPIE-Int. Soc. Opt. Eng. **385**, 146 (1983)
2181. D. Bäuerle (ed.), *Laser Processing and Diagnostics*, Springer Ser. Chem. Phys., Vol.39 (Springer, Berlin, Heidelberg 1984)
2182. D. Bäuerle, K.L. Kompa, L.D. Laudé (eds.), *Laser Processing and Diagnostics II* (Physique, Les Ulis 1986)
2183. D. Bäuerle, *Laser Processing and Chemistry*, 2nd edn. (Springer, Berlin, Heidelberg, 1996)
2184. P. Samuelsson, Towards optical diagnostics and control in aerotaxy semiconductor nanowire growth, PhD thesis (Lund University, Lund 2021)
2185. R. Lober, J. Mazumder, Spectroscopic diagnostics of plasma during laser processing of aluminium. J. Phys. D: Appl. Phys. **40**, 5917 (2007)
2186. Y.P. Bao, K. Dorozynska, P. Stamatoglou, C.D. Kong, T. Hurtig, S. Pfaff, J. Zetterberg, M. Richter, E. Kristensson, A. Ehn, Single-shot 3D imaging of hydroxyl radicals in the vicinity of a gliding arc discharge. Plasma Sources Tech. **30**, 04LT04 (2021)
2187. K.L. Kompa, J. Wanner, *Laser Applications in Chemistry* (Plenum, New York, 1984)
2188. V.S. Letokhov (ed.), *Laser Analytical Spectrochemistry* (Hilger, Bristol, 1986)
2189. D.L. Andrews, *Lasers in Chemistry* (Springer, 1997)
2190. H.H. Telle, A. González Ureña, R.J. Donovan, *Laser Chemistry: Spectroscopy, Dynamics and* Applications (Wiley, 2007)
2191. M. Lackner (ed.), *Lasers in Chemistry* (Wiley, 2008)
2192. E.R. Pike, H.Z. Cummins (eds.), *Photon Correlation and Light Beating Spectroscopy* (Plenum, New York, 1974)
2193. L.E. Drain, *The Laser Doppler Technique* (Wiley, Chichester, 1980)
2194. E. Durst, A. Melling, J.H. Whitelaw, *Principles and Practice of LaserDoppler Anemometry*, 2nd edn. (Academic Press, London, 1981)

2195. Z. Zhang, *LDA Application Methods; Laser Doppler Anemometry for Fluid Dynamics* (Springer Science and Business Media, 2010)
2196. C.J. Dasch, J.A. Sell, Velocimetry in laminar and turbulent flows using the photothermal deflection effect with a transient grating. Opt. Lett. **11**, 603 (1986), (and references therein)
2197. R. Miles, C. Cohen, J. Connors, P. Howard, S. Huang, E. Markovitz, G. Russel, Velocity measurements by vibrational tagging and fluorescent probing of oxygen. Opt. Lett. **12**, 861 (1987)
2198. B. Hiller, J.C. McDaniel, E.C. Rea Jr., R.K. Hanson, Laser-induced fluorescence technique for velocity field measurements in subsonic gas flows. Opt. Lett. **8**, 474 (1983)
2199. U. Westblom, S. Svanberg, Imaging measurements of flow velocitites using laser-induced fluorescence. Phys. Scr. **31**, 402 (1985)
2200. A.M.P.K. Taylor, *Instrumentation for Flows with Combustion* (Academic Press, London, 1993)
2201. L. Laching, G. Wigley, *Optical Diagnostics for Flow Processes* (Plenum, New York, 1995)
2202. R.J. Adrian, D.F.G. Durao, F. Durst, M.V. Heitor, M. Maeda, J.H. Whitelaw (eds.), *Developments in Laser Techniques and Fluid Mechanics* (Springer, Berlin, Heidelberg, 1997)
2203. E.J. McCartney, *Absorption and Emission by Atmospheric Gases* (Wiley, New York, 1983)
2204. L.S. Rothman, C.P. Rinsland, A. Goldman, S.T. Massie, D.P. Edwards, J.-M. Edwards, J.-M. Flaud, A. Perrin, C. Camy-Peyret, V. Dana, J.Y. Mandin, J. Schroeder, A. McCann, R.R. Gamache, R.B. Eattson, K. Yoshino, K.V. Chance, K.W. Jucks, L.R. Brown, V. Nemtshinov, P. Varanasi, The HITRAN molecular database and HAWKS (HITRAN Atmospheric Workstation): 1996 edition. J. Quant. Spectrosc. Radiat. Transfer **60**, 665 (1998)R
2205. M. Kahnert, T. Nousiainen, H. Lindqvist, Review: Model particles in atmospheric optics. J. Quant. Spectr. Rad. Transf. **146**, 41 (2014)
2206. I.E. Gordon, L.S. Rothman et al., The HITRAN2016 molecular spectroscopic database. J. Quant. Spectr. Rad. Transf. **203**, 3 (2017)
2207. L.C. Andrews, *Field Guide to Atmospheric Optics*, 2nd edn. (SPIE, Bellingham, 2019)
2208. B.J. Mason, The greenhouse effect. Contemp. Phys. **30**, 417 (1989)
2209. B.J. Mason, Predictions of climate changes caused by manmade emissions of greenhouse gases: A critical assessment. Contemp. Phys. **36**, 299 (1995)
2210. Intergovernmental Panel on Climate Change (IPCC), *Climate Change 2021: The Physical Science Basis.* www.un.org/en/climatechange/reports (United Nations, 2021)
2211. https://www.nobelprize.org/prizes/physics/2021/popular-information/
2212. A.L. Buck, New equations for computing vapor pressure and enhancement factor. J. Appl. Meteorol. Climatol. **20**, 1527 (1981)
2213. http://www.respirometry.org/calculator/water-vapor-calculators
2214. R.W. Baubel, D.B. Turner, A.C. Stem, *Fundamentals of Air Pollution*, 3rd edn. (Academic Press, London, 1994)
2215. W. Michaelis, *Air Pollution* (Springer, Berlin, Heidelberg, 1997)
2216. B.R. Gurjar, L.T. Molina, C.S.P. Ojha (eds.), Air Pollution - Health and Environmental Impacts (CRC Press, 2010)
2217. D. Vallero, *Fundamentals of Air Pollution, 5th Edition* (Elsevier, 2014)
2218. C. Seigneur, *Air Pollution - Concepts, Theory, and Applications* (Cambridge Univ, Press, 2019)
2219. R.M. Measures, *Laser Remote Sensing - Fundamentals and Applications* (Wiley, New York, 1984)
2220. R.M. Measures (ed.), *Laser Remote Chemical Analysis* (WileyInterscience, New York, 1988)
2221. E. Zanzottera, Differential absorption lidar techniques in the determination of trace pollutants and physical parameters of the atmosphere. Crit. Rev. Anal. Chem. **21**, 279 (1990)
2222. S. Svanberg, 'Differential absorption lidar (DIAL).' In: *Air Monitoring by Spectroscopic Techniques*, ed. by M. Sigrist, (Wiley, New York 1994)
2223. M.W. Sigrist (ed.), *Air Monitoring by Spectroscopic Techniques* (Wiley, New York, 1994)
2224. A. Ansmann, R. Neuber, P. Rairoux, U. Wandinger (eds.), *Advances in Atmospheric Remote Sensing with Lidar* (Springer, Heidelberg, 1997)

2225. M.N. Fiddler, I. Begashaw, M.A. Mickens, M.S. Collingwood, Z. Assefa, S. Bililign, Laser spectroscopy for atmospheric and environmental sensing. Sensors **2009**, 10477 (2009)

2226. S. Svanberg, 'Fundamentals of atmospheric spectroscopy.' In: *Surveillance of Environmental Pollution and Resources by Electromagnetic Waves*, ed. by T. Lund (Reidel, Dordrecht 1978)

2227. R.T. Menzies, R.K. Seals Jr., Ozone monitoring with an IR heterodyne radiometer. Science **197**, 1275 (1977)

2228. A.A. Kosterov, R.F. Curl, F.K. Tittel, G. Gmachl, F. Capasso, D.L. Sivco, J.N. Baillargeon, A.L. Hutchinson, A.Y. Cho, Methane concentration and isotopic composition measurements with a quantum-cascade laser. Opt. Lett. **24**, 1762 (1999)

2229. F.K. Tittel, Y. Bakhirkin, R.F. Curl, A. Kosterev, R. Lewicki, S. So, G. Wysocki, Quantum cascade laser based trace gas sensor technology: Recent advances and applications. IEEE Sensors https://doi.org/10.1109/ICSENS.2007.4388657 (2007)

2230. X.J. Cui, R.Q. Yu, W.D. Chen, Z.R. Zhang, T. Pang, P.S. Sun, H. Xia, B. Wu, F.Z. Dong, Development of a Quantum Cascade Laser-Based Sensor for Environmental HONO Monitoring in the Mid-Infrared at 8 μm. J. Lightwave Tech. **37**, 2784 (2018)

2231. P. Rauter, F. Capasso, Multi-wavelength quantum cascade laser arrays. Lasers Phot. Rev. **9**, 452 (2015)

2232. E.D Hinkley, Laser spectroscopic instrumentation and techniques: Long monitoring by resonance absorption. Opt. Quantum Electron. 8, 155 (1976)

2233. H.I. Schiff, G.I. Macay, J. Bechara, 'The use of tunable diode laser absorption spectroscopy for atmospheric measurements.' In: *Air Monitoring by Spectroscopic Techniques*, ed. by M.W. Sigrist, Chemical Physics Series Vol.127 (John Wiley, New York 1994) p.239

2234. P. Werle, Spectroscopic trace gas analysis using semiconductor diode lasers. Spectrochim. Acta A **52**, 805 (1996)

2235. Th. Töpfer, K.P. Petrov, Y. Mine, D. Jundt, R.F. Curl, F.K. Tittel, Room temperature mid-infrared laser sensor for trace gas detection. Appl. Opt. **36**, 8042 (1997)

2236. I. Linnerud, P. Kaspersen, T. Jaeger, Gas monitoring in the process industry using diode lasers. Appl. Phys. B **67**, 297 (1998)

2237. M. Lackner, Tunable diode laser spectroscopy in the process industries: a review. Rev. Chem. Eng. **23**, 65 (2007)

2238. M.A. Bolshov, Yu.A. Kuritsyn, Yu.V. Romanovskii, Tunable diode laser spectroscopy as a technique for combustion diagnostics. Spectrochim. Acta B **106**, 45 (2015)

2239. U. Simon, C.E. Miller, C.C. Bradley, R.G. Hulet, R.F. Curl, F.K. Tittel, Difference frequency generation in $AgGaS_2$ using single-mode diode laser pump sources. Opt. Lett. **18**, 1062 (1993)

2240. M. Seiter, M.W. Sigrist, Compact gas sensor using a pulsed difference frequency laser spectrometer. Opt. Lett. **24**, 110 (1999)

2241. U. Gustafsson, J. Sandsten, S. Svanberg, Simultaneous detection of methane, oxygen and water vapour utilizing near-infrared diode lasers in conjunction with difference-frequency generation. Appl. Phys. B **71**, 853 (2000)

2242. J. Alnis, U. Gustafsson, G. Somesfalean, S. Svanberg, Sum-frequency generation with a blue diode laser for mercury spectroscopy at 254 nm. Appl. Phys. Lett. **76**, 1234 (2000)

2243. C. Zimmermann, V. Vuletic, A. Hemmerich, T.W. Hänsch, All solid state laser source for tunable blue and ultraviolet radiation. Appl. Phys. Lett. **66**, 238 (1995)

2244. U. Gustafsson, PhD Thesis (Lund Institute of Technology, Lund 2000)

2245. G.C. Bjorklund, Frequency modulation spectroscopy: a new method for measuring weak absorptions and dispersions. Opt. Lett. **6**, 15 (1980)

2246. M. Gehrtz, G.C. Bjorklund, E.A. Whittaker, Quantum-limited laser frequency modulation spectroscopy. J. Opt. Soc. Am. B **2**, 1810 (1985)

2247. G.R. Janik, C.B. Carlisle, T.F. Gallagher, Two-tone frequency modulation spectroscopy. J. Opt. Soc. Am. B **3**, 1070 (1986)

2248. C.B. Carlisle, D.E. Cooper, Tunable-diode-laser frequency modulation spectroscopy using balanced homodyne detection. Opt. Lett. **14**, 1306 (1989)

2249. F.S. Pavone, M. Inguscio, Frequency- and wavelength-modulation spectroscopies: comparison of experimental methods using an AlGaAs diode laser. Appl. Phys. B **56**, 118 (1993)

2250. V.G. Avetisov, P. Kauranen, High-resolution absorption measurements using two-tone frequency-modulation spectroscopy with diode lasers. Appl. Opt. **36**, 4043 (1997)

2251. U. Gustafsson, G. Somesfalean, J. Alnis, S. Svanberg, Frequency modulation spectroscopy with blue diode lasers. Appl. Opt. **39**, 3774 (2000)

2252. L. Mei, S. Svanberg, Wavelength modulation spectroscopy – Digital detection of gas absorption harmonics based on Fourier analysis. Appl. Opt. **54**, 2254 (2015)

2253. M.C. Alarcon, H. Ito, H. Inaba, All-optical remote sensing of city gas through CH_4 gas absorption employing a low-loss optical fibre link and an InGaAsP light emitting diode in the near-infrared region. Appl. Phys. B **43**, 79 (1987)

2254. M.A. Lefsky, W.B. Cohen, G.G. Parker, D.J. Harding, Lidar remote sensing for ecosystem studies: Lidar, an emerging remote sensing technology that directly measures the three-dimensional distribution of plant canopies, can accurately estimate vegetation structural attributes and should be of particular interest to forest, landscape, and global ecologists. Bioscience **52**, 19 (2002)

2255. J. Cuesta, P. Chazette, T. Allouis, P.H. Flamant, S. Durrieu, J. Sanak, P. Genau, D. Guyon, D. Loustau, C. Flamant, Observing the forest canopy with a new ultra-violet compact airborne lidar. Sensors **10**, 7386 (2010)

2256. M.A. Wulder, J.C. White, R.F. Nelson, E. Næsset, H.O. Ørka, N.C. Coops, T. Hilker, C.W. Bater, T. Gobakken, Lidar sampling for large-area forest characterization: A review: Rem. Sens. Env. **121**, 196 (2012)

2257. M. Maltamo, E. Næsset, J. Vauhkonen, Forestry applications of airborne laser scanning. Concepts and case studies. Managing Ecosyst. **27**, 2014 (2014)

2258. Bh. Lohani, S, Ghosh, Airborne LiDAR technology: A review of data collection and processing systems. Proc. Nat. Acad. Sci. India, Section A: Physical Sciences **87**, 567 (2017)

2259. M.N. Bazezew, Y.A. Hussin, E.H. Kloosterman, Integrating airborne LiDAR and terrestrial laser scanner forest parameters for accurate above-ground biomass/carbon estimation in Ayer Hitam tropical forest, Malaysia. Int. J. Appl. Earth Obs. Geoinf. **73**, 638 (2018)

2260. K. Whitehead, C.H. Hugenholtz, Remote sensing of the environment with small unmanned aircraft systems (UASs), part 1: A review of progress and challenges. J. Unmanned Vehic. Syst. **2**, 69 (2014)

2261. L. Tang, G.F. Shao, Drone remote sensing for forestry research and practices. J. Forest Res. **26**, 791 (2015)

2262. A.F. Chase, D.Z. Chase, J.F. Weishampel, J.B. Drake, R.L. Shrestha, K.C. Slatton, J.J. Awe, W.E. Carter, Airborne LiDAR, archaeology, and the ancient Maya landscape at Caracol. Belize. J. Archae. Sci. **38**, 387 (2011)

2263. J.C. Fernandez-Diaz, W.E. Carter, C. Glennie, R.L. Shrestha, Z.G. Pan, N. Ekhtari, A. Singhania, D. Hauser, M. Sartori, Capability assessment and performance metrics for the Titan multispectral mapping lidar. Remote Sens. **8**, 936 (2016)

2264. M.A. Canuto, F. Estrada-Belli, T.G. Garrison, S.D. Houston, MJ. Acuña, M. Kováč, D. Marken, Ph. Nondédéo, L. Auld-Thomas, C. Castanet, D. Chatelain, C.R. Chiriboga, T. Drápela, T.Lieskovský, A. Tokovinine, A. Velasquez, J.C. Fernández-Díaz, R. Shrestha, Ancient lowland Maya complexity as revealed by airborne laser scanning of northern Guatemala. Science **361**, eaau0137 (2018)

2265. Ch. Domke, Q. Potts, LiDARs for self-driving vehicles: a technological arms race. Automotive World, August 2020 issue

2266. J.J. Degnan, 'Satellite laser ranging and very long baseline interferometry.' In: *Encyclopedia of Earth Sciences*, Vol.2, ed. by M. Kauffman (Simon and Schuster Macmillan, New York 1996) p.935

2267. J. Degnan, Asynchronic laser transponders: A new tool for improved fundamental physics experiments. Int. J. Modern Physics D **16**, 1 (2007)

2268. M. Wilkinson, U. Schreiber, I. Procházka, Ch. Moore, J. Degnan, G. Kirchner, Z.P. Zhang, P. Dunn, V. Shargorodskiy, M. Sadovnikov, C. Courde, H. Kunimori, The next generation of satellite laser ranging systems. J. Geodesy **93**, 2227 (2019)
2269. C. Granier, G. Megie, Daytime lidar measurement of the mesospheric sodium layer. Planet. Space Sci. **30**, 169 (1982)
2270. C.Y. She, J.R. Yu, Simultaneous three-frequency Na lidar measurements of radial wind and temperature in the mesopause region. Geophys. Res. Lett. **21**, 1771 (1994)
2271. M. Alpers, J. Hoffner, U. von Zahn, Upper atmosphere Ca and Ca^+ at mid-latitudes. Geophys. Res. Lett. **22**, 263 (1995)
2272. U. von Zahn, J. Hoffner, Mesopause temperature profiling by potassium lidar. Geophys. Res. Lett. **23**, 141 (1996)
2273. M. Gerding, S. Daly, J.M.C. Plane, Lidar soundings of the mesospheric nickel layer using $Ni(^3F)$ and $Ni(^3D)$ transitions. Geophys. Res. Lett. doi.org/https://doi.org/10.1029/2018GL080701 (2018)
2274. X.C. Yue, Q.H. Zhou, S. Raizada, C. Tepley, J. Friedman, Relationship between mesospheric Na and Fe layers from simultaneous and common-volume lidar observations at Arecibo. J. Geophys. Res.: Atmospheres **118**, 905 (2013)
2275. L.F. Du, J. Jiao, F.Q. Li, X. Lin, Z.K. Liu, P.P. Batista, A.A. Pimenta, V.F. Andriolic, J.H. Wang, X.W. Chen, Y. Xia, F.J. Wu, G.T. Yang, The technical optimization of Na-K lidar and to measure mesospheric Na and K over Brazil. J. Quant. Spectr. Rad. Transf. **259**, 107383 (2021)
2276. T.H. Jeys, A.A. Brailove, A. Mooradian, Sum frequency generation of sodium resonance radiation. Appl. Opt. **28**, 2588 (1989)
2277. T. Nishikawa, A. Ozawa, Y. Nishida, M. Asobe, F.-L. Hong, T.W. Hänsch, Efficient 494 mW sum-frequency generation of sodium resonance radiation at 589 nm by using a periodically poled $Zn:LiNbO_3$ ridge waveguide. Opt. Express **17**, 17792 (2009)
2278. T.D. Kawahara, T. Kitahara, F. Kobayashi, Y. Saito, A. Nomura, Sodium temperature lidar based on injection seeded Nd:YAG pulse lasers using a sum-frequency generation technique. Opt. Express **19**, 3553 (2011)
2279. S.H. Huang, Y. Feng, A. Shirakawa, K.I. Ueda, Generation of 10.5 W, 1178 nm laser based on phosphosilicate Raman fiber laser. Jpn J. Appl. Phys. **42**, L1439 (2003)
2280. W. Happer, G. MacDonald, C. Max, F.J. Dyson, Atmospheric-turbulence compensation by resonant optical backscattering from the sodium layer in the upper atmosphere. J. Opt. Soc. Am. A **11**, 263 (1994)
2281. N. Ageorges, C. Dainty (eds.), *Laser Guide Star Adaptive Optics for Astronomy* (Springer NATO ASI Series, 2000)
2282. D. Gavel, Laser technology for astronomical adaptive optics. Proc. SPIE **7015**, 70150 (2008)
2283. C. D'Orgeville, G.J. Fetzer, Four generations of sodium guide star lasers for adaptive optics in astronomy and space situational awareness. Proc. SPIE **9909**, doi:https://doi.org/10.1117/12.2234298 (2016)
2284. Y.F. Arshinov, S.M. Bobrovnikov, V.E. Zuev, V.M. Mitev, Atmospheric temperature measurements using a pure rotational Raman lidar. Appl. Opt. **22**, 2984 (1983)
2285. D. Nedeljkovic, A. Hauchecorne, M.L. Chanin, Rotational Raman lidar to measure the atmospheric temperature from the ground to 30 km. IEEE Trans. Geosci. Remote Sens. **31**, 90 (1993)
2286. A. Behrendt, J. Reichart, Atmospheric temperature profiling in the presence of clouds with a pure rotational Raman lidar by use of an interferencefilter-based polychromator. Appl. Opt. **39**, 1372 (2000)
2287. P. Di Girolamo, R. Marchese, D.N. Whiteman, B.B. Demoz, Rotational Raman Lidar measurements of atmospheric temperature in the UV. Geophys. Res. Lett. **31**, L01106 (2004)
2288. J. Reichardt, U. Wandinger, M. Serwasi, C. Weitkamp, Combined Raman lidar for aerosol, ozone and moisture measurements. Opt. Eng. **35**, 1457 (1996)
2289. L.J. Radziemski, T.R. Loree, D.A. Cremers, N.M. Hoffman, Time-resolved laser-induced breakdown spectrometry of aerosols. Anal. Chem. **55**, 1246 (1983)

2290. D.W. Hahn, N. Omenetto, Laser-induced breakdown spectroscopy (LIBS), Part I: Review of basic diagnostics and plasma-particle interactions: Still-challenging issues within the analytical plasma community. Appl. Spectrosc. A. **64**, 335 (2010)
2291. D.W. Hahn, N. Omenetto, Laser-Induced Breakdown Spectroscopy (LIBS), Part II: Review of instrumental and methodological approaches to material analysis and applications to different fields. Appl. Spectr. Spect. **66**, 347 (2012)
2292. D.A. Cremers, L.J. Radziemski, *Handbook of Laser-Induced Breakdown Spectroscopy, 2nd Ed.* (Wiley, 2013)
2293. J. El Haddad, L. Canioni, B. Bousquet, Good practices in LIBS analysis: Review and advices. Spectrochim. Acta B **101**, 171 (2014)
2294. H.W. Ji, Y. Ding, L.W. Zhang, Y.W. Hu, X.C. Zhong, Review of aerosol analysis by laser-induced breakdown spectroscopy. Appl. Spectr. Rev. **56**, Doi.org/https://doi.org/10.1080/05704928.2020.1780604 (2020]
2295. J. Singh S. Thakur (eds.), *Laser-Induced Breakdown Spectroscopy, 2nd edn.* (Elsevier Science, 2020)
2296. A. Matsumoto, T. Sakka, A review of underwater laser-induced breakdown spectroscopy of submerged solids. Anal. Sciences **37**, 1061 (2021)
2297. S. Palanco, J. M. Baena, and J. J. Laserna, Open-path laser-induced plasma spectrometry for remote analytical measurements on solid surfaces. Spectrochim. Acta, Part B 57, 591 (2002).
2298. R. Grönlund, M. Lundqvist, S. Svanberg, Remote imaging laser-induced break-down spectroscopy and remote cultural heritage ablative cleaning. Opt. Lett. **30**, 2882 (2005)
2299. R. Grönlund, M. Lundquist, S. Svanberg, Remote imaging laser-induced breakdown spectroscopy and laser-induced fluorescence spectroscopy using nanosecond pulses from a mobile lidar system. Appl. Spectr. **60**, 853 (2006)
2300. W.T. Li, X.Y. Li, X. Li, Z.Q. Hao, Y.F. Lu, X.Y. Zeng, A review of remote laser-induced breakdown spectroscopy. Appl. Spectr Rev. **55**, Doi.org/https://doi.org/10.1080/05704928.2018.1472102 (2020)
2301. J. Kasparian, M. Rodriguez, G. Méjean, J. Yu, E. Salmon, H. Wille, R. Bourayou, S. Frey, Y.-B. André, A. Mysyrowicz, R. Sauerbrey, J.-P. Wolf, L. Wöste, White-light filaments for atmospheric analysis. Science **301**, 61–64 (2003)
2302. M. Petrarca et al., White-light femtosecond Lidar at 100 TW power level. Appl. Phys. B **114**, DOI: https://doi.org/10.1007/s00340-013-5741-6 (2014)
2303. P.R. Hemmer, R.B. Miles, P. Polynkin, T. Siebert, A.V. Sokolov, P. Sprangle, M.O. Scully, Standoff spectroscopy via remote generation of a backward-propagating laser beam. Proc. Natl. Acad. Sci. U.S.A. **108**, 3130 (2011)
2304. M. Ruchkina, P.J. Ding, A. Ehn, M. Aldén, J. Bood, Single-shot, spatially-resolved stand-off detection of atomic hydrogen via backward lasing in flames. Proc. Comb. Inst. **37**, 1281 (2019)
2305. J.D. Klett, Stable analytical inversion solution for processing lidar returns. Appl. Optics **20**, 211 (1981)
2306. J.D. Klett, Lidar inversion with variable backscatter/extinction ratios. Appl. Opt. **24**, 1638 (1985)
2307. F.G. Fernald, Analysis of atmospheric lidar observations: some comments. Appl. Optics **23**, 652 (1984)
2308. W.J. Lentz, A.W. Cooper, M.M. Regush, Improved Klett lidar inversion techniques. Proc. SPIE **2222**, 119 (1994)
2309. F. Gaudfrin, O. Pujol, R. Ceolato, G. Huss, N. Riviere, A new lidar inversion method using a surface reference target applied to the backscattering coefficient and lidar ratio retrievals of a fog-oil plume at short range. Atmos. Meas. Tech. **13**, 1921 (2020)
2310. https://www.earlinet.org/
2311. G. Pappalardo, A. Amodeo, A. Apituley, A. Comeron, V. Freudenthaler, H. Linné, A. Ansmann, J. Bösenberg, G. D'Amico, I. Mattis, L. Mona, U. Wandinger, V. Amiridis, L. Alados-Arboledas, D. Nicolae, M. Wiegner, EARLINET: towards an advanced sustainable European aerosol lidar network. Atmos. Meas. Tech. Discuss. **7**, 2929 (2014)

2312. K. Fredriksson, B. Galle, K. Nyström, S. Svanberg, Mobile lidar system for environmental probing. Appl. Opt. **20**, 4181 (1981)

2313. K. Fredriksson, I. Lindgren, S. Svanberg, G. Weibull, Measurements of the emission from industrial smoke stacks using laser radar techniques. Göteborg Institute of Physics Reports GIPR-121 (CTH, Göteborg 1976)

2314. G.Y. Zhao, M. Lian, Y.Y. Li, Z. Duan, S.M. Zhu, L. Mei, S. Svanberg, Mobile lidar system for environmental monitoring. Appl. Opt. **65**, 1506 (2017)

2315. P. Weibring, H. Edner, S. Svanberg, Versatile mobile lidar system for environmental monitoring. Appl. Opt. **42**, 3583 (2003)

2316. H. Edner, K. Fredriksson. A. Sunesson, S. Svanberg, L. Unéus, W. Wendt, Mobile remote sensing system for atmospheric monitoring. Appl. Opt. **26**, 4330 (1987)

2317. D.J. Brassington, Measurement of the SO_2 absorption spectrum between 297 and 316 nm using a tunable dye laser. Lab. Note No. RD/L/N 184/79 (Central Electricity Res. Labs., Leatherhead 1979)

2318. D.J. Brassington, Sulphur dioxide absorption cross-section measurement from 290 nm to 317 nm. Appl. Opt. **20**, 3774 (1981)

2319. P. Weibring, M. Andersson, H. Edner, S. Svanberg, Remote monitoring of industrial emissions by combination of lidar and plume velocity measurements. Appl. Phys. B **66**, 383 (1998)

2320. H. Edner, P. Ragnarson, S. Svanberg, E. Wallinder, R. Ferrara, R. Cioni, B. Raco, G. Taddeucci, Total fluxes of sulphur dioxide from the Italian volcanoes Etna, Stromboli and Vulcano measured by differential absorption lidar and passive differential optical absorption spectroscopy. J. Geophys. Res. **99**, 18,827 (1994)

2321. P. Weibring, H. Edner, S. Svanberg, G. Cecchi, L. Pantani, R. Ferrara, T. Caltabiano, Monitoring of volcanic sulphur dioxide emissions using differential absorption lidar (DIAL), differential optical absorption spectroscopy (DOAS), and correlation spectroscopy (COSPEC). Appl. Phys. B **67**, 419 (1998)

2322. P. Weibring, J. Swartling, H. Edner, S. Svanberg, T. Caltabiano, D. Condarelli, G. Cecchi, L. Pantani, Optical monitoring of volcanic sulphur dioxide emissions – Comparison between four different remote sensing techniques. Opt. Lasers Eng. **37**, 267 (2002)

2323. S. Svanberg, Geophysical gas monitoring using optical techniques: Volcanoes, geothermal fields and mines. Opt. Lasers Eng. **37**, 245 (2002)

2324. H. Edner, G.W. Faris, A. Sunesson, S. Svanberg, Atmospheric atomic mercury monitoring using differential absorption lidar techniques. Appl. Opt. **28**, 921 (1989)

2325. H. Edner, G.W. Faris, A. Sunesson, S. Svanberg, J. Bjarnason, K.H. Sigurdsson, H. Kristmansdottir, Lidar search for atomic mercury in Icelandic geothermal fields. J. Geophys. Res. **96**, 2977 (1991)

2326. H. Edner, P. Ragnarson, S. Svanberg, E. Wallinder, A. De Liso, R. Ferrara, B.E. Maserti, Differential absorption lidar mapping of atmospheric atomic mercury in Italian geothermal fields. J. Geophys. Res. **97**, 3779 (1992)

2327. H. Edner, P. Ragnarson, S. Svanberg, E. Wallinder, R. Ferrara, B.E. Maserti, R. Bargagli, Atmospheric mercury mapping in a cinnabar mining area. Sci. Total Environ. **133**, 1 (1993)

2328. R. Ferrari, B.M. Maserti, M. Andersson, H. Edner, P. Ragnarson, S. Svanberg, A. Hernandez, Atmospheric mercury concentration and fluxes in the Almaden district (Spain). Atmos. Environ. **32**, 3897 (1998)

2329. R. Grönlund, H. Edner, S. Svanberg, J. Kotnik, M. Horvat, Lidar measurements of mercury emissions from the Idrija mercury mine. RMZ - Materials and Geoenvironment **51**, 1581 (2004)

2330. M. Lian, L.H. Shang, Z. Duan, G.Y. Zhao, Y.Y. Li, S.M. Zhu, G.L. Qiu, B. Meng, J. Sommar, X.B. Feng, S. Svanberg, Lidar Mapping of Atmospheric Atomic Mercury in the Wanshan Area. China, Environmental Pollution **240**, 353 (2018)

2331. R. Ebinghaus, R.R. Turner, L.D. de Lacerda, O. Vasiliev, W. Salomons (eds.), *Mercury Contaminated Sites* (Springer, Berlin, Heidelberg, 1999)

2332. F. Beckers, J. Rinklebe, Cycling of mercury in the environment: Sources, fate, and human health implications: A review. Crit. Rev. Envir. Sci. Tech. **47**, 693 (2017)
2333. G.Y. Zhao, W.X. Zhang, Z. Duan, M. Lian, N.B. Hou, Y.Y. Li, S.M. Zhu, S. Svanberg, Mercury as a geophysical tracer gas - Emissions from the Emperor Qin tomb in Xi´an studied by laser radar. Sci. Rep. **10**, 10414 (2020)
2334. M. Aldén, H. Edner, S. Svanberg, Laser monitoring of atmospheric NO using ultraviolet differential-absorption techniques. Opt. Lett. **7**, 543 (1982)
2335. Z.G. Guan, P. Lundin, L. Mei, G. Somesfalean, S. Svanberg, Vertical Lidar Sounding of Air Pollutants in a Major Chinese City. Appl. Phys. B **101**, 465 (2010)
2336. K.W. Rothe, U. Brinkmann, H. Walther, Applications of tunable dye lasers to air pollution detection: Measurements of atmospheric NO_2 concentrations by differential absorption. Appl. Phys. **3**, 115 (1974)
2337. W.R. Grant, R.D. Hake Jr., E.M. Liston, R.C. Robbins, E.K. Proctor Jr., Calibrated remote measurement of NO_2 using the differential absorption backscatter technique. Appl. Phys. Lett. **24**, 550 (1974)
2338. H.J. Kölsch, P. Rairoux, J.P. Wolf, L. Wöste, Simultaneous NO and NO_2 DIAL measurement using BBO crystals. Appl. Optics **28**, 2052 (1989)
2339. T.D. Gardiner, R.A. Robinson, M.J.T. Milton, P.T. Woods, Infrared differential absorption lidar for trace gas measurement. Proc. Int. Laser Sensing Symposium, Fukui, Japan, September 6–8 1999, p.173
2340. H. Edner, S. Svanberg, L. Unéus, W. Wendt, Gas correlation lidar. Opt. Lett. **9**, 493 (1984)
2341. A. Minato, T. Kobayashi, N. Sugimoto, Laser long-path absorption technique for measuring methane using gas correlation method. J. Appl. Phys. **37**, 3610 (1998)
2342. H. Edner, P. Ragnarson, E. Wallinder, Industrial emission control using lidar techniques. Environ. Sci. Technol. **29**, 330 (1995)
2343. J. Werner, K.W. Rothe, H. Walther, Monitoring of the stratospheric ozone layer by laser radar. Appl. Phys. B **32**, 113 (1983)
2344. G.J. Megie, G. Ancellet, J. Pelon, Lidar, measurements of ozone vertical profiles. Appl. Opt. **24**, 3454 (1985)
2345. E.V. Browell et al., Ozone and aerosol distributions and air mass characteristics over the south Atlantic basin during the burning season. J. Geophys. Res. **101**, 24,043 (1996)
2346. R.J. Alvarez, C.J. Senff, A.O. Langford, A.M. Weickmann, D.C. Law, J.L. Machol, D.A. Merritt, R.D. Marchbanks, S.P. Sandberg, W.A. Brewer, R.M. Hardesty, R.M. Banta, Development and application of a compact, tunable, solid-state airborne ozone lidar system for boundary layer profiling. J. Atmos. Oceanic Techn. **28**, 1258 (2011)
2347. R. De Young, W. Carrion, R. Ganoe, D. Pliutau, G. Gronoff, T. Berkoff, S. Kuang, Langley mobile ozone lidar: ozone and aerosol atmospheric profiling for air quality research. Appl. Opt. **56**, 721 (2017)
2348. K.M. Strawbridge, M.S. Travis, B.J. Firanski, J.R. Brook, R. Staebler, T. Leblanc, A fully autonomous ozone, aerosol and night time water vapor LIDAR: a synergistic approach to profiling the atmosphere in the Canadian oil sands region, Atmospheric Measurement Techniques Discussions, 1–56, doi:https://doi.org/10.5194/amt-2018-108 (2018)
2349. A.O. Langford et al., Intercomparison of lidar, aircraft, and surface ozone measurements in the San Joaquin Valley during the California Baseline Ozone Transport Study (CABOTS). Atmos. Meas. Tech. **12**, 1889 (2019)
2350. M.P. McCormick, Lidar measurements of Mount St. Helens effluents. Opt. Eng. **21**, 340 (1982)
2351. M.P. McCormick, T.J. Swisser, W.H. Fuller. W.H. Hunt, M.T. Osborn, Airborne and ground-based lidar measurements of the El Chichon stratospheric aerosol from 90° N to 56° S. Geofisica Internacional **23–2**, 187 (1984)
2352. G. Fiocco, D. Fua, G. Visconti (eds.), *The Mount Pinatubo Eruption – Effects on the Atmosphere and Climate.* NATO ASI Series, Vol.142 (Springer, Heidelberg 1996)
2353. M. Sicard, J.L. Guerrero-Rascado, F. Navas-Guzman, J. Preißler, F. Molero, S. Tomas, J.A. Bravo-Aranda, A. Comeron, F. Rocadenbosch, F. Wagner, M. Pujadas, L. Alados-Arboledas,

Monitoring of the Eyjafjallajokull volcanic aerosol plume over the Iberian Peninsula by means of four EARLINET lidar stations. Atmos. Chem. Phys. **12**, 3115 (2012)

2354. E.J. Hughes, J. Yorks, N.A. Krotkov, A.M. da Silva, M. McGill, Using CATS near-real-time lidar observations to monitor and constrain volcanic sulfur dioxide (SO_2) forecasts. Geophys. Res. Lett. **43**, 11,089 (2016)
2355. D. McLean, Wingtip devices: What they do and how they do it. Boeing Performance and Flight Operations Engineering Conference, Article 4 (2005)
2356. C.L. Korb, B.M. Gentry, C.Y. Weng, Edge technique: Theory and application to the lidar measurement of atmospheric wind. Appl. Opt. **31**, 4202 (1992)
2357. C. Flesia, C.L. Korb, Theory of the double-edge molecular technique for Doppler lidar wind measurement. Appl. Opt. **38**, 432 (1999)
2358. J.S. Friedman, C.A. Tepley, P.A. Catleberg, H. Roe, Middle-atmospheric Doppler lidar using an iodine-vapour edge filter. Opt. Lett. **22**, 1648 (1997)
2359. P. Kauranen, S. Andersson-Engels, S. Svanberg, Spatial mapping of flame radical emission using a spectroscopic multi-colour imaging system. Appl. Phys. B **53**, 260 (1991)
2360. R.M. Huffaker, R.M. Hardesty, Remote sensing of atmospheric wind velocities using solid-state and CO_2 coherent laser systems. Proc. IEEE **84**, 181 (1996)
2361. J.M. Vaughan, Coherent laser spectroscopy and Doppler LIDAR sensing in the atmosphere. Phys. Scr. **T78**, 73 (1998)
2362. V. Banakh, I. Smalikho, *Coherent Doppler Wind Lidars in a Turbulent Atmosphere* (Artech House, 2013)
2363. M.J. Kavaya, J.Y. Beyon, G.J. Koch, M. Petros, P.J. Petzar, U.N. Singh, B.C. Trieu, J.R. Yu, The Doppler aerosol wind (DAWN) airborne, wind-profiling coherent-detection lidar system: Overview and preliminary flight results. J. Atmosph. Oceanic Techn. **31**, b826 (2014)
2364. L. Lombard, M. Valla, C. Planchat, D. Goular, B. Augère, P. Bourdon, G. Canat, Eyesafe coherent detection wind lidar based on a beam-combined pulsed laser source. Opt. Lett. **40**, 1030 (2015)
2365. D.M. Winkler, R.C. Couch, M.P. McCormick, An overview of LITE: NASA's Lidar In-space Technology Experiment. Proc. IEEE **84**, 164 (1996)
2366. E.V. Browell, S. Ismail, W.B. Grant, Differential absorption lidar (DIAL) measurements from air and space. Appl. Phys. B **67**, 399 (1998)
2367. Y. Sasano, K. Asai, N. Sugimoto, Y. Kawamura, K. Tatsumi, T. Imai, NASDA mission demonstration satellite lidar project and science. Proc. SPIE **3504**, 2 (1998)
2368. Z. Wang, M. Menenti, Challenges and opportunities in lidar remote sensing. Front. Rem. Sens. 04 March 2021 | https://doi.org/10.3389/frsen.2021.641723
2369. D.M. Winker, M.A. Vaughan, A. Omar, Y.X. Hu, K.A. Powell, Z.Y. Liu, W.H. Hunt, S.A. Young, Overview of the CALIPSO Mission and CALIOP data processing algorithms. J. Atmosph. Oceanic Techn. **26**, 2310 (2009)
2370. D. Winker, W. Hunt, C. Weimer, The on-orbit performance of the CALIOP LIDAR on CALIPSO Proc. SPIE **10566**, 105661H-H105671 (2017)
2371. S.H. Wu, B.Y. Liu, J.T. Liu, X.C. Zhai, C.Z. Feng, G.N. Wang, H.W. Zhang, J.P. Yin, X.T. Wang, R.Z. Li, Wind turbine wake visualization and characteristics analysis by Doppler lidar. Opt. Express **24**, A762 (2016)
2372. T. Mikkelsen, M. Sjöholm, N. Angelou, J. Mann, 3D wind scanner lidar measurements of wind and turbulence around wind turbines, buildings and bridges. IOP Conf. Series: Materials Science and Engineering **276**, 012004 (2017)
2373. D. Liu et al. (eds.), Proceedings of the 29th International Laser Radar Conference, Hefei, 2019. EPJ Web of Conferences **237** (2020)
2374. Proceedings of the 19th Coherent Laser Radar Conference (CLRC 2018) Okinawa (Curran Assoc., 2018)
2375. www.automotivelidar.com Microtech Ventures, Inc. 2021
2376. T. Fujii, T. Fukuchi (eds.), *Laser Remote Sensing* (CRC Press, 2005)
2377. C. Weitkamp, *Lidar: Range-Resolved Optical Remote Sensing of the Atmosphere: Springer Science & Business*, vol. 102 (Springer, Heidelberg, 2006)

2378. S. Svanberg, LIDAR, in F. Träger, Ed., *Springer Handbook of Lasers and Optics, 2nd Edition* (Springer, Heidelberg 2012), pp 1146

2379. P.F. McManamon, *Lidar Technologies and Systems* (SPIE Bellingham, 2019)

2380. P.C.S. Devara, P.E. Raj, G. Pandithurai, Aerosol-pofile measurements in the lower troposphere with four-wavelength bistatic argon–ion lidar. Appl. Opt. **34**, 4416 (1995)

2381. N. Sharma, J.E. Barnes, T. Kaplan, An imaging bistatic lidar system for boundary layer monitoring. Appl. Opt. **46**, 2922 (2006)

2382. M. Brydegaard, A. Gebru, S. Svanberg, Super resolution laser radar with blinking atmospheric particles – Application to interacting flying insects. Progress Electromagnetic Res. **147**, 141 (2014)

2383. M. Brydegaard, E. Malmqvist, S. Jansson, J. Larsson, S. Török, G.Y. Zhao, The Scheimpflug lidar method. Proc. SPIE **10406**, 104060I (2017)

2384. S.M. Zhu, E. Malmqvist, W.S. Li, S. Jansson, Y.Y. Li, Z. Duan, K. Svanberg, H.Q. Feng, Z.W. Song, G.Y. Zhao, M. Brydegaard, S. Svanberg, Insect abundance over Chinese rice fields in relation to environmental parameters, studied with a polarization-sensitive CW near-IR lidar system. Appl. Phys. B **123**, 211 (2017)

2385. A. Gebru, S. Jansson, R. Ignell, C. Kirkeby, J.C. Prangsma, M. Brydegaard, Multiband modulation spectroscopy for the determination of sex and species of mosquitoes in flight. J. Biophotonics **11**, e201800014 (2018)

2386. J.C. Lu, Y. Li, Y. Yuan, S.M. Zhu, Z. Duan, G.Y. Zhao, S. Svanberg, Monitoring of flying insects using a dual-wavelength CW lidar system. Proc. 2019 ACP Conference, Chengdu: M4A.4 (2019)

2387. E. Malmqvist, S. Jansson, S.M. Zhu, W.S Li, K. Svanberg, S. Svanberg, J. Rydell, Z.W. Song, J. Bood, M. Brydegaard, S. Åkesson, The bat-bird-bug battle: Daily flight activity of insects and their predators over a rice field revealed by high resolution Scheimpflug lidar. Roy. Soc. Open Sci. **5**, 172303 (2018)

2388. M. Brydegaard, Towards quantitative optical cross sections in entomological laser radar–potential of temporal and spherical parameterizations for identifying atmospheric fauna. PLoS ONE **10**, e0135231 (2015)

2389. Z.W. Song, B.X. Zhang, H.Q. Feng, S.M. Zhu, L.N. Hu, M. Brydegaard, Y.Y. Li, S. Jansson, K. Svanberg, G.Y. Zhao, J. Bood, S. Svanberg, D.S. Li, Application of lidar remote sensing of insects in agricultural entomology on the Chinese scene. J. Appl. Entomology **144**, 161 (2020)

2390. A.P. Genoud, R. Basistyy, G.M. Williams, B.P. Thomas, Optical remote sensing for monitoring flying mosquitoes, gender identification and discussion on species identification. Appl. Phys. B **124**, 46 (2018)

2391. Y.Y. Li, K. Wang, R. Quintero-Torres, R. Brick, A.V. Sokolov, M.O. Scully, Insect flight velocity measurement with a CW near-IR Scheimpflug lidar system. Opt. Express **28**, 21891 (2020)

2392. M. Brydegaard, S. Jansson, E. Malmqvist, Y.P. Mlacha, A. Gebru, F. Okumu, G.F. Killeen, C. Kirkeby, Lidar reveals activity anomaly of malaria vectors during pan-African eclipse. Sci Adv. **6**, eaay5487 (2020)

2393. C. Kirkeby, K. Rydhmer, S.M. Cook, A. Strand, M.T. Torrance, J.L. Swain, J. Prangsma, A. Johnen, M. Jensen, M. Brydegaard, K, Græsbøll, Advances in automatic identification of flying insects using optical sensors and machine learning. Sci. Reports **11**, 1555 (2021)

2394. G.Y. Zhao, E. Malmqvist, S. Török, P.-E. Bengtsson, S. Svanberg, J. Bood, M. Brydegaard, Particle measurements by a novel dual-band continuous-wave lidar system. Appl. Optics **57**, 10164 (2018)

2395. L. Mei, M. Brydegaard, Continuous-wave differential absorption lidar. Laser Photonics Rev. **9**, 629 (2015)

2396. J. Larsson, J. Bood, C.T. Xu, X. Yang, R. Lindberg, F. Laurell, M. Brydegaard, Atmospheric CO_2 sensing using Scheimpfluglidar based on a 1.57-μm fiber source. Opt. Express **27**, 17348 (2019)

2397. L. Mei, P. Guan, Z. Kong, Remote sensing of atmospheric NO_2 by employing the continuous-wave differential absorption lidar technique. Opt. Express **25**, A953 (2017)
2398. J.R. Lakowicz (ed.), *Topics in Fluorescence Spectroscopy, Vol.1: Techniques, Vol.2: Principles, Vol.3: Biochemical Applications, Vol.4: Probe Design and Chemical Sensing, Vol.5: Nonlinear and Two-Photon-Induced Fluorescence* (Plenum, New York 1991–1997)
2399. J.R. Lakowizc, *Principles of Fluorescence Spectroscopy*, 3rd edn. (Springer-Verlag, US, 2006)
2400. Ellen MacArthur Foundation, The new plastic economy: Rethinking the future of plastics & catalyzing action. www.ellenmacarthurfoundation.org/assets/downloads/publications/NPEC-Hybrid_English_22-11-17_Digital.pdf (2017)
2401. L. Celander, K. Fredriksson, B. Galle, S. Svanberg, Investigation of laser-induced fluorescence with application to remote sensing of environmental parameters. Göteborg Institute of Physics Reports GIPR-149 (CTH, Göteborg 1978)
2402. H.K. Lichtenthaler, U. Rinderle, The role of chlorophyll fluorescence in the detection of stress conditions in plants. CRC Crit. Rev. Anal. Chem. 19 Suppl.1, S29 (1988)
2403. A.J. Hoff, J. Deisenhofer, Photophysics of photosynthesis. Phys. Rep. **287**, 1 (1997)
2404. L.O. Björn, *Photobiology - The Science of Light and Light* (Springer, 2015)
2405. F.E. Hoge, R.N. Swift, Airborne simultaneous spectroscopic detection of laser-induced water Raman backscatter and fluorescence from chlorophyll a and other naturally occuring pigments. Appl. Opt. **20**, 3197 (1981)
2406. F.E. Hoge, R.N. Swift, J.K. Yungel, Active-passive airborne ocean color measurement 2: Applications. Appl. Opt. **25**, 48 (1986)
2407. Y. Saito, K. Takano, F. Kobayashi, K. Kobayashi, H.D. Park, Development of a UV laser-induced fluorescence lidar for monitoring blue-green algae in Lake Suwa. Appl. Optics **53**, 7030 (2014)
2408. M.A. Sundermayer, E.A. Terray, J.R. Ledwell, A.G. Cunningham, P.E. Larocque, J. Banic, W.J. Lillycrop, Three-dimensional mapping of fluorescent dye using a scanning, depth-resolving airborne lidar. J. Atmos. Oceanic Tech. **24**, 1050 (2007)
2409. V. Drozdowska, Seasonal and spatial variability of surface seawater fluorescence properties in the Baltic and Nordic Seas: results of lidar experiments. Oceanologia **49**, (2007)
2410. R.A. O'Neill, L. Buja-Bijunas, D.M. Rayner, Field performance of a laser fluorosensor for the detection of oil spills. Appl. Opt. **19**, 863 (1980)
2411. H. Amann, Laser spectroscopy for monitoring and research in the ocean. Phys. Scr. **T78**, 68 (1998)
2412. A.B. Utkin, A. Lavrov, R. Vilar, Evaluation of oil spills by laser induced fluorescence spectra. Proc. SPIE **7994**, 48 (2010)
2413. C.E. Brown, Laser fluorosensors. in *Oil Spill Science and Technology*, M. Fingas (ed.), (2011), Chap. 7
2414. M.D.C. Martín, N.V. Yarovenko, C.P. Gómez, J.L.L. Soto, J.M.T. Palenzuela, Oil pollution detection using spectral fluorescent signatures (SFS). Environmental Earth Sciences **73**, 2909 (2015)
2415. V. Raimondi, L. Palombi, D. Lognoli, A. Masini, E. Simeone, Experimental tests and radiometric calculations for the feasibility of fluorescence LIDAR-based discrimination of oil spills from UAV. Int. J. Appl. Earth. Obs. Geoinformation **61**, 46 (2017)
2416. Z. Duan, Y. Li, J.L. Wang, G.Y. Zhao, S. Svanberg, Aquatic environment monitoring using a drone-based fluorosensor. Appl. Phys. **B125**, 08 https://doi.org/10.1007/s00340-019-7215-y (2019)
2417. M. Brydegaard, A. Merdasa, A. Gebru, H. Jayaweera, S. Svanberg, Realistic instrumentation platform for active and passive optical remote sensing. Appl. Spectroscopy **70**, 372 (2016)
2418. H.H. Kim, Airborne laser bathymetry. Appl. Opt. **16**, 45 (1977)
2419. J. Banic, S. Sizgoric, R. O'Neill, Airborne scanning lidar bathymeter measures water depth. Laser Focus **23**(2), 40 (1987)
2420. K. Fredriksson, B. Galle, K. Nyström, S. Svanberg, B. Öström, Under-water laser-radar experiments for bathymetry and fish-school detection. Göteborg Institute of Physics Reports GIPR-162 (CTH, Göteborg 1978)

2421. J. H. Churnside, R. E. Thorne, Comparison of airborne lidar measurements with 420 kHz echo-sounder measurements of zooplankton: Applied Optics **44**, 5504–5511 (2005)

2422. J.H. Churnside, P.L. Donaghay, Thin scattering layers observed by airborne lidar. ICES J. Mar. Sci. **66**, 778 (2009)

2423. J.H. Churnside, Review of profiling oceanographic lidar. Opt. Eng. **53**, 051405–051405 (2014)

2424. G.Y. Zhao, M. Ljungholm, E. Malmqvist, G. Bianco, L.A. Hansson, S. Svanberg, M. Brydegaard, Inelastic hyperspectral lidar for profiling aquatic ecosystems. Lasers Phot. Rev. **10**, 807 (2016)

2425. Z. Duan, Y. Yuan, J.C. Lu, J.L. Wang, Y. Li, S. Svanberg, G.Y. Zhao, Under-water spatially, spectrally, and temporally resolved optical monitoring of aquatic fauna. Opt. Express **28**, 2600 (2020)

2426. H. Edner, J. Johansson, S. Svanberg, E. Wallinder, Fluorescence lidar multicolor imaging of vegetation. Appl. Opt. **33**, 2471 (1994)

2427. S. Svanberg, Fluorescence lidar monitoring of vegetation status. Phys. Scr. **T58**, 79 (1995)

2428. J. Johansson, M. Andersson, H. Edner, J. Mattsson, S. Svanberg, Remote fluorescence measurements of vegetation spectrally resolved and by multicolour fluorescence imaging. J. Plant Physiology **148**, 632 (1996)

2429. T. Fujii (ed.), *Recent Advances in Laser Remote Sensing* (Marcel Dekker 2003)

2430. Y. Saito et al., Laser-induced fluorescence (LIF) imaging lidar with range resolution for vegetation monitoring. In: A. Ansmann, R. Neuber, P. Rairoux, U. Wandinger (eds.), *Advances in Atmospheric Remote Sensing with Lidar* (Springer, Berlin, Heidelberg 1997)

2431. G. Matvienko, V. Timofeev, A. Grishin, N. Fateyeva, Fluorescence lidar method for remote monitoring of effects on vegetation. Proc. SPIE **6367**, 63670Fb (2006)

2432. K.F. Cao, B. Zhao, X. Fang, S.L. Wang, M. Wang, S.X. Hu, Fluorescence lidar for remote monitoring of plant. Chin. Opt. Lett. **8**, 130 (2010)

2433. L. Mei, Z.G. Guan, G. Somesfalean and S. Svanberg, Laser-Induced Fluorescence Monitoring of Chinese Longjing tea. Proc. SPIE **8531**, 85311T-85311T-5 (2012)

2434. H. Zhang, Z. Duan, Y.Y. Li, G.Y. Zhao, S.M. Zhu, W. Fu, T. Peng, Q.Z. Zhao, S. Svanberg, J.D. Hu, Vis/NIR reflectance spectroscopy for hybrid rice variety identification and chlorophyll content evaluation for different nitrogen fertilizer levels. Roy. Soc. Open Sci. **6**, 191132 (2019)

2435. X. Wang, Z. Duan, M. Brydegaard, S. Svanberg, G.Y. Zhao, Drone-based area scanning of vegetation fluorescence height profiles using a miniaturized hyperspectral lidar system. Appl. Phys. B **124**, 207 (2018)

2436. I. Moya, A new instrument for passive remote sensing. 1. Measurements of sunlight induced fluorescence. Remote Sensing of Environment **91**, 196 (2004)

2437. M. Meroni, M. Rossini, L. Guanter, L. Alonso, U. Rascher, R. Colombo, J. Moreno, Remote sensing of solar-induced chlorophyll fluorescence: Review of methods and applications. Remote Sensing Environ. **113**, 2037 (2009)

2438. U. Rascher, L. Alonso, A. Burkart, C. Cilia, S. Cogliati, R. Colombo, A. Damm, M. Drusch, L. Guanter, J. Hanus, Sun-induced fluorescence – a new probe of photosynthesis: First maps from the imaging spectrometer HyPlant. Glob. Change Biol. **21**, 4673–4684 (2015)

2439. L. Guanter, C. Bacour, A. Schneider, I. Aben, T.A. van Kempen, F. Maignan, C. Retscher, P. Köhler, C. Frankenberg, J. Joiner, Y. Zhang, The TROPOSIF global sun-induced fluorescence dataset from the Sentinel-5P TROPOMI mission, Earth Syst. Sci. Data Discuss. https://doi.org/10.5194/essd-2021-199 (2021)

2440. V. Raimondi, G. Cecchi, L. Pantani, R. Chiari, Fluorescence lidar monitoring of historical buildings. Appl. Opt. **37**, 1089 (1996)

2441. P. Weibring, Th. Johansson, H. Edner, S. Svanberg, B. Sundnér, V. Raimondi, G. Cecchi, L. Pantani, Fluorescence lidar imaging of historical monuments. Appl. Opt. **40**, 6111 (2001)

2442. D. Lognoli, G. Cecchi, L. Pantani, V. Raimondi, R. Chiari, Th. Johansson, P. Weibring, H. Edner, S. Svanberg, Fluorescence lidar imaging of the Parma Cathedral and Batistery. Appl. Physics B **76**, 1 (2003)

2443. L. Palombi, D. Lognoli, V. Raimondi, G. Cecchi, C. Conti, J. Hällström, K. Barup, R. Grönlund, A. Johansson, S. Svanberg, Hyperspectral fluorescence lidar imaging at the Coliseum, Rome: Elucidating past conservation interventions. Opt. Express **16**, 6794 (2008)

2444. V. Raimondi, G. Cecchi, D. Lognoli, L. Palombi, R. Grönlund, A. Johansson, S. Svanberg, K. Barup, J. Hällström, The fluorescence LIDAR technique for the remote sensing of photoautotrophic biodeteriogens on outdoor cultural heritage: A decade of in situ experiments. Int. Biodeterior. Biodegradation **63**, 823 (2010)

2445. A.Rousaki, P. Vandenabeele, In situ Raman spectroscopy for cultural heritage studies. J. Raman Spectr. https://doi.org/10.1002/jrs.6166 (2021)

2446. M. Picollo, C. Cucci, A. Casini, L. Stefani, Hyper-spectral imaging technique in the cultural heritage field: New possible scenarios. Sensors **20**, 2843 (2020)

2447. R. Fantoni, L. Caneve, F. Colao, L. Fiorani, A. Palucci, R. Dell'Erba, V. Fassina, Laser-induced fluorescence study of medieval frescoes by Giusto de' Menabuoi. J. Cult. Heritage **14**, S59 (2013)

2448. A. Botto, B. Campanella, S. Legnaioli, M. Lezzerini, G. Lorenzetti, S. Pagnotta, F. Poggialini, V. Palleschi, Applications of laser-induced breakdown spectroscopy in cultural heritage and archaeology: a critical review. J. Analyt. Atomic Spectrom. https://doi.org/10.1039/C8JA00319J (2019)

2449. C. Fotakis, D. Anglos, V. Zafiropulos, S. Georgiou, V. Tornari, *Lasers in the Preservation of Cultural Heritage - Principles and Applications* (CRC Press, Boca Raton, 2006)

2450. W. Kautek, Lasers in Cultural Heritage: The Non-Contact Intervention, in A. Miotello, P.M. Ossi (eds.), *Laser-Surface Interactions for New Materials Production* (Springer, 2009), p. 331

2451. D. Anglos, S. Georgiou, C. Fotakis, Lasers in the analysis of cultural heritage materials. J. Nano Res. **8**, 47 (2009)

2452. M. Brydegaard, P. Lundin, Z.G. Guan, A. Runemark, S. Åkesson, S. Svanberg, Feasibility study: Fluorescence LIDAR for remote bird classification. Appl. Optics **49**, 4531 (2010)

2453. P. Lundin, P. Samuelsson, S. Svanberg, A. Runemark, S. Åkesson, M. Brydegaard, Remote nocturnal bird classification by spectroscopy in extended wavelength ranges. Appl. Optics **50**, 3396 (2011)

2454. S. Jansson, M. Brydegaard, A. Papayannis, G. Tsaknakis, S. Åkesson, Exploitation of an atmospheric lidar network node in single-shot mode for the classification of aerofauna. J. Applied Remote Sensing **11**, 036009 (2017)

2455. M. Brydegaard, P. Samuelsson, M.V. Kudenov, S. Svanberg, On the exploitation of mid-infrared iridescence of plumage for remote classification of nocturnal migrating birds. App. Spectr. **67**, 477 (2013)

2456. K.S. Repasky, J.A. Shaw et al., Optical detection of honeybees by use of wing-beat modulation of scattered laser light for locating explosives and land mines. Appl. Opt. **45**, 1839–1843 (2006)

2457. D.S. Hoffman, A.R. Nehrir et al., Range-resolved optical detection of honeybees by use of wing-beat modulation of scattered light for locating land mines. Appl. Opt. **46**, 3009–3012 (2007)

2458. E.S. Carlsten, G.R. Wicks et al., Field demonstration of a scanning lidar and detection algorithm for spatially mapping honeybees for biological detection of land mines. Appl. Opt. **50**, 2112 (2011)

2459. M. Brydegaard, Z.G. Guan, M. Wellenreuther, S. Svanberg, Insect monitoring with fluorescence lidar techniques: Feasibility study. Appl. Opt. **48**, 5668 (2009)

2460. Z.G. Guan, M. Brydegaard, P. Lundin, M. Wellenreuther, E. Svensson, S. Svanberg, Insect monitoring with fluorescence LIDAR techniques - Field experiments. Appl. Optics **48**, 5668 (2010)

2461. A. Runemark, M. Wellenreuther, H. Jayaweera, S. Svanberg, M. Brydegaard, Rare events in remote dark field spectroscopy: An ecological case study of insects. IEEE JSTQE **18**, 1573 (2012)

2462. S.M. Zhu, Y.Y. Li, L.N. Gao, T.Q. Li, G.Y. Zhao, S. Svanberg, C.H. Lu, J.D. Hu, J.R. Huang, H.Q. Feng, Optical remote detection of flying Chinese agricultural pest insects using dark-field reflectance measurements. Acta Sinica Entymologica **59**, 1376 (2016)

2463. A. Drake, D. Reynolds, *Radar Entomology - Observing Insect Flight and Migration* (CABI, Wallingford, 2012)

2464. M. Brydegaard, S. Svanberg, Photonic monitoring of atmospheric and aquatic fauna. Lasers Phot. Rev. **12**, 1800135 (2018)

2465. B.M. Nicolaï, K. Beullens, E. Bobelyn, A. Peirs, W. Saeys, K.I. Theron, J. Lammertyn, Nondestructive measurement of fruit and vegetable quality by means of NIR spectroscopy: A review. Postharvest Biol. Techn. **46**, 99 (2007)

2466. A.S. Franca, L.M.L. Nollet (eds.), *Spectroscopic Methods in Food Analysis* (CRC Press, 2017)

2467. A. Hassoun et al., Use of spectroscopic techniques to monitor changes in food quality during application of natural preservatives: A review. Antioxidants **9**, 882 (2020)

2468. H. Zhang, J. Huang, T.Q. Li, X.X. Wu, S. Svanberg, K. Svanberg, Studies for tropical fruit ripening using three different spectroscopic techniques. J. Biomed. Opt. **19**, 067001 (2014)

2469. X.B. Lin, H. Zhang, L.N. Hu, G.Y. Zhao, S. Svanberg, K. Svanberg, Ripening of avocado fruits studied by spectroscopic techniques. J. Biophoton. https://doi.org/10.102.jbio.202000076 (2020)

2470. N. Ornelas-Soto, O. Barbosa-García, M. Meneses-Nava, G. Ramos-Ortíz, J. Pichardo-Molina, J.L. Maldonado, U. Contreras, L. López-Martínez, P. López-de-Alba, F. López-Barajas, Spectroscopic analysis of pharmaceutical formulations through the use of chemometric tools. Proc. SPIE **7499**, 74990Z (2009)

2471. J. Johansson, S. Folestad, M. Josefson, A. Sparén, C. Abrahamsson, S. Andersson-Engels, S. Svanberg, Time-Resolved NIR/VIS Spectroscopy for Analysis of Solids: Pharmaceutical Tablets. Appl. Spectrosc. **56**, 725 (2002)

2472. C. Abrahamsson, J. Johansson, S. Andersson-Engels, S. Svanberg, S. Folestad, Time-resolved NIR spectroscopy for quantitative analysis of intact pharmaceutical tablets. Anal. Chemistry **77**, 1055 (2005)

2473. S. Montán, S. Svanberg, A system for industrial surface monitoring utilizing laser-induced fluorescence. Appl. Phys. B **38**, 241 (1985)

2474. P.S. Andersson, S. Montán, S. Svanberg, Remote sample characterization based on fluorescence monitoring. Appl. Phys. B **44**, 19 (1987)

2475. F. Ramos, *Liquid Chromatography – Principles, Technology and Applications* (Nova Science Publisher, 2013)

2476. S. Fanali, P.R. Haddad C. Poole, M.-L. Riekkola (eds.), *Liquid Chromatgraphy – Principles and Applications, 2nd ed.* (Elsevier, 2017)

2477. Ph. Schmitt-Kopplin (ed.), *Capillary Electrophoresis – Methods and Protocols*, 2nd ed. (Springer, 2017)

2478. S. Nilsson, J. Johansson, M. Mecklenburg, S. Birnbaum, S. Svanberg, K.-G. Wahlund, K. Mosbach, A. Miyabayashi, P.-O. Larsson, Real-time fluorescence imaging of capillary electrophoresis: Separation of nucleic acids. J. Cap. Elec. **22**, 46 (1995)

2479. E.R. Menzel, *Laser Detection of Fingerprints*, 2nd edn. (Marcel Dekker, New York, 1999)

2480. E.R. Menzel, 'Fluorescence in forensic science.' In: *Encyclopedia of Analytical Chemistry* (Wiley, New York 2006)

2481. M. Wang, M. Li, A. Yu, Y. Zhu, M.Y. Yang, C.B. Mao, Fluorescent nanomaterials for the development of latent fingerprints in forensic sciences. Adv. Functional Materials **27**, 1606243 (2017)

2482. C. Worawong, W. Phutdawong, S. Jirasirisuk, W. Phutdhawong, The study of fluorescent chemicals for fingerprint development. J. Luminescence **203**, 696 (2018)

2483. J.S. McCormack, Remote optical measurements of temperature using fluorescent materials. Electron. Lett. **17**, 630 (1981)

2484. K.T.V. Grattan, Z.Y. Zhang, *Fibre-Optic Fluorescence Thermometry* (Chapman & Hall, London, 1995)

2485. J. Lindén, Ch. Knappe, M. Richter, M. Aldén, Precision in 2D temperature measurements using the thermographic phosphor BAM 085205. Meas. Sci. Technol. **23**, 085205 (2012)
2486. M. Aldén, A. Omrane, M. Richter, G. Särner, Thermographic phosphors for thermometry: A survey of combustion applications. Progr. Energy Combust. Sci. **37**, 422 (2011)
2487. J.C. Hamilton, R.J.Anderson, In situ Raman spectroscopy of Fe−18Cr−3Mo(100) surface oxidation. Sandia Combustion Research Program Annual Rept. (Sandia, Livermore, CA 1984)
2488. W. Suetaka, *Surface Infrared and Raman Spectroscopy* (Plenum, New York, 1995)
2489. R.K. Chang, T.E. Furtak, *Surface-Enhanced Raman Scattering* (Plenum, New York, 1982)
2490. M. Moskovits, Surface-enhanced spectroscopy. Rev. Mod. Phys. **57**, 783 (1985)
2491. A. Otto, I. Mrozek, H. Grabhorn, W. Akemann, Surface-enhanced Raman scattering. J. Phys. Cond. Matter **4**, 1143 (1992)
2492. K. Kneipp, H. Kneipp, I. Itzkan, R. Dasari, M.S. Feld, Surface-enhanced Raman scattering: A new tool for biomedical spectroscopy. Curr. Sci. **77**, 915 (1999)
2493. P.L. Stiles, J.A. Dieringer, N.C. Shah, R.P. van Duyne, Surface-enhanced Raman spectroscopy. Ann. Rev. Analyt. Chem. **1**, 601 (2008)
2494. R. Pilot, R. Signorini, C. Durante, L. Orian, M. Bhamidipati, L. Fabris, A review on surface-enhanced Raman scattering. Biosensors **9**, 57 (2019)
2495. E. Ozbay, Plasmonics, Merging Photonics and Electronics at Nanoscale Dimensions. Science **311**, 189 (2007)
2496. S.A. Maier, Plasmonics: *Fundamentals and Applications – Fundamentals and Applications* (Springer, 2007)
2497. A.G. Brolo, Plasmonics for future biosensors. Nat. Photonics **6**, 709 (2012)
2498. Y.R. Shen, Applications of optical second-harmonic generation in surface science.' In: *Chemistry and Structure at Interfaces*, ed. by R.B. Hall, A.B. Ellis (Verlag-Chemie, Weinheim 1986) p.151
2499. Y.R. Shen, Surface properties probed by second-harmonic and sum-frequency generation. Nature **337**, 519 (1989)
2500. Y.R. Shen, Optical second harmonic generation at interfaces. Annu. Rev. Phys. Chem. **40**, 327 (1989)
2501. R.K. Lam, S.L. Raj, T.A. Pascal, C.D. Pemmaraju, L. Foglia, A. Simoncig, N. Fabris, P. Miotti, C.J. Hull, A.M. Rizzuto, J.W. Smith, R. Mincigrucci, C. Masciovecchio, A. Gessini, E. Allaria, G. DeNinno, B. Diviacco, E. Roussel, S. Spampinati, G. Penco, S. Di Mitri, M. Trovò, M. Danailov, S.T. Christensen, D. Sokaras, T.-C. Weng, M. Coreno, L. Poletto, W.S. Drisdell, D. Prendergast, L. Giannessi, E. Principi, D. Nordlund, R.J. Saykally, C.P. Schwartz, Soft x-ray second harmonic generation as an interfacial probe. Phys. Rev. Lett. **120**, 023901 (2018)
2502. T. Helk, E. Berger, S. Jamnuch, L. Hoffmann, A. Kabacinski, J. Gautier, F. Tissandier, J.P. Goddet, H.-T. Chang, J. Oh, C. Das Pemmaraju, T.A. Pascal, S. Sebban, Ch. Spielmann, M. Zuerch, Table-top extreme ultraviolet second-harmonic generation. Sci. Adv. **7**, eabe2265 (2021)
2503. W. Yen, P.M. Selzer (eds.), *Laser Spectroscopy of Solids*, 2nd edn. Topics Appl. Phys., Vol.49 (Springer, Berlin, Heidelberg 1989)
2504. W.M. Yen (ed.), *Laser Spectroscopy II*, Topics Appl. Phys., Vol.65 (Springer, Berlin, Heidelberg 1989)
2505. H. Kuzmany, *Solid-State Spectroscopy - An Introduction* (Springer, 2009)
2506. K. Kleinermanns, J. Wolfrum, Laser Chemistry – What is Its Current Status? Angew. Chem. Int. Ed. Engl. **26**, 38 (1987)
2507. P. Brumer, M. Shapiro, Laser control of chemical reactions. Sci. Am. **272**(3), 34 (1995)
2508. S. Svanberg, Chemical sensing with laser spectroscopy. Sensors and Actuators B **33**, 1 (1996)
2509. D.L. Andrews, *Lasers in Chemistry*, 3rd edn. (Springer, Berlin, Heidelberg, 1997)
2510. V.S. Letokhov, *Nonlinear Laser Chemistry*, Springer Ser. Chem. Phys., Vol. 22 (Springer, Berlin, Heidelberg 1983)

2511. V.S. Letokhov, Laser-induced chemistry – basic nonlinear processes and applications, in [2073] p. 237
2512. H.H. Telle, A. González Ureña, R.J. Donovan, *Laser Chemistry: Spectroscopy, Dynamics and Applications* (Wiley, Chicester 2007)
2513. J. I. Steinfeld (ed.), *Laser-Induced Chemical Processes* (Springer, 2012)
2514. Yu.S. Tveryanovich, A.V. Stolyarov, Laser-induced processes in chemistry and material sciences. Russ. Chem. Rev. **84**, E01 (2015)
2515. J.A. Paisner, R.W. Solarz, Resonance photoionization spectroscopy, in [2072] p. 175
2516. J.A. Paisner, Atomic vapor laser isotope separation, in [2073] p. 253
2517. V.S. Letokhov, Laser separation of isotopes. Annu. Rev. Phys. Chem. **28**, 133 (1977)
2518. V.S. Letokhov, Laser isotope separation. Nature **277**, 605 (1979)
2519. P.T. Greenland, Laser isotope separation. Contemp. Phys. **31**, 405 (1990)
2520. P.A. Bokhan, V.V. Buchanov, N.V. Fateev, M.M. Kalugin, M.A. Kazaryan, A.M. Prokhorov, D.E. Zakrevskii, *Laser isotope separation in atomic vapour* (Wiley, 2006)
2521. P. Mathi, V. Parthasarathy, A.K. Nayak, J.P. Mittal, S.K. Sarkar, Laser isotope separation: science and technology, in Proc. National Acad. Sci. India Section A: https://doi.org/10.1007/s40010-015-0249-6 (2015)
2522. V.K. Saini, S. Talwar, V.V.V. Subrahmanyam, R.K. Mishra, P.K. Saini, S.K. Dixit, Laser isotope separation scheme of lithium by three-color photoionization. Phys. Scripta **95**, 075403 (2020)
2523. M.V. Suryanarayana, Isotope separation of ^{176}Lu a precursor to ^{177}Lu medical isotope using broadband lasers. Sci. Rep. **11**, 6118 (2021)
2524. H.G. Kuhn, *Atomic Spectra* (Longmans, London, 1962)
2525. N. Bloembergen, E. Yablonovitch, Collisionless multiphoton dissociation of SF_6: a statistical thermodynamic process.' In: *Laser Spectroscopy III*, ed. by J.L. Hall, J.L. Carlsten, Springer Ser. Opt. Sci., Vol.7 (Springer, Berlin, Heidelberg 1977)
2526. R.V. Ambartzumian, V.S. Letokhov, G.N. Makarov, A.A. Puretsky, Laser separation of nitrogen isotopes. JETP Lett. **17**, 63 (1973); JETP Lett. **15**, 501 (1972)
2527. J.-L. Boulnois, Photophysical processes in recent medical laser developments: A review. Lasers Med. Sci. **1**, 47 (1986)
2528. R. Steiner, Laser-tissue interactions, in C. Raulin, S. Karsai (eds.), Laser and IPL Technology in Dermatology and Aesthetic Medicine (Springer-Verlag, Berlin, Heidelberg 2011) p. 23
2529. ANSI: Laser Standards designed Z 136.1 - 2014 (American National Standards Institute, Washington 2014)
2530. IEC 60825–1:2014 European and International Laser Safety Standard - Safety of laser products Part 1: Equipment classification and requirements (IEC, 2014)
2531. R. Henderson, K. Schulmeister, *Laser Safety* (CRC Press, 2003)
2532. K. Barat (ed.), *Laser Safety – Tools and Training, 2nd Ed.* (CRC Press, 2017)
2533. K. Barat (ed.), *Laser Safety – Practical Knowledge and Solutions* (IOP Publishing Ltd, 2019)
2534. K. Barat (ed.), *Manual of Laser Safety* (AIP Publishing, 2020)
2535. S.L. Jacques, Laser-tissue interactions: Photochemical, photothermal, and photomechanical. Surg. Clin. North Amer. **72**, 531 (1992)
2536. A. Katzir, *Lasers and Optical Fibers in Medicine* (Academic Press, San Diego, 1993)
2537. A.J. Welch, M. van Gemert, *Optical-Thermal Response of Laser-Irradiated Tissue* (Plenum, New York, 1995)
2538. M. Niemz, *Laser-Tissue Interactions* (Springer, Berlin, Heidelberg, 1996)
2539. T. Karu, *The Science of Low Power Laser Therapy* (Gordon & Breach/IPD 1998)
2540. J. Rawlins, J. Din, S. Talwar, P. O'Kane, Coronary intervention with the excimer laser: Review of the technology and outcome data. Interv. Card. Rev. **11**, 27 (2016)
2541. L.R. Stival, M.N. Figueiredo, M.R. Santhiago, Excimer laser ablation: A review. J. Refract. Surg. **34**, 698 (2018)
2542. M. v. Allmen, A. Blatter, *Laser-Beam Interactions with Materials*, 2nd edn. (Springer, Berlin, Heidelberg 1995)

2543. J. Mazumder, A. Kar, *Theory and Application of Laser Chemical Vapor Deposition* (Plenum, New York, 1995)
2544. D. Bäuerle, *Laser Processing and Chemistry*, 2nd edn. (Springer, Berlin, Heidelberg, 1996)
2545. J.C. Miller, R.F. Haglund, *Laser Ablation and Desorption* (Academic Press, San Diego, 1998)
2546. W. Steen, I. Mazumder, *Laser Material Processing* (Springer, 2010)
2547. D. Hoffmann, J. Limpert, A. Thoss, Ultrashort-pulse lasers: Ultrashort-pulsed laser sources with kilowatt power for industrial applications, in Laser Focus World, January 28 (2020)
2548. J.A. Parrish, T.F. Deutsch, Laser photomedicine. IEEE J. Quantum Electron. **QE-20**, 1386 (1984)
2549. T.J. Dougherty, in *CRC Critical Reviews in Oncology/Hematology*, ed. by S. Davis (CRC, Boca Raton, FL 1984)
2550. Ch.J. Gomer (ed.), Proc. Clayton Foundation Conf. on Photodynamic Therapy (Childrens Hospital, Los Angeles 1987)
2551. S.L. Marcus, Photodynamic therapy: clinical status, potential and needs, in *Photodynamic Therapy of Human Cancer*, ed. by C. Gomer (SPIE Press, Bellingham 1990) p.1
2552. L.I. Grossweiner, *The Science of Phototherapy* (CRC Press, Boca Raton, 1994)
2553. T.J. Dougherty, C.J. Gomer, B.W. Henderson, G. Jori, D. Kessel, M. Korbelik, J. Moan, Q. Peng, Photodynamic therapy. J. Nat. Cancer Inst. **90**, 889 (1998)
2554. S. Svanberg, Medical diagnostics using laser-induced fluorescence. Phys. Scr. **T17**, 469 (1987)
2555. S. Svanberg, Medical applications of laser spectroscopy. Phys. Scr. **T26**, 90 (1989)
2556. A.E. Profio, D.R. Doiron, O.J. Balchum, G.C. Huth, Fluorescence bronchoscopy for localization of carcinoma in Situ. Med. Phys. **10**, 35 (1983)
2557. H. Kato, D.A. Cortese, Early detection of lung cancer by means of hematoporphyrin derivative fluorescence and laser photoradiation. Clin. Chest Med. **6**, 237 (1985)
2558. L. Baert, R. Berg, B. Van Damme, M.A. d´Hallewin, J. Johansson, K. Svanberg, S. Svanberg, Clinical fluorescence diagnosis of human bladder carcinoma following low-dose photofrin injection. J. Urol. **41**, 322 (1993)
2559. S. Andersson-Engels, J. Johansson, U. Stenram, K. Svanberg, S. Svanberg, Malignant tumor and atherosclerotic plaque diagnosis using laser-induced fluorescence. IEEE J. Quant. Electron. **QE-26**, 2207 (1990)
2560. C. Eker, S. Montán, E. Jamarillo, K. Koizumi, C. Rubio, S. Andersson-Engels, K. Svanberg, S. Svanberg, P. Slezak, Clinical spectral characterization of colonic mucosial lesions using autofluorescence and δ-aminolevulinic acid sensitization. Gut **44**, 511 (1999)
2561. A.E. Profio, 'Endoscopic fluorescence detection of early lung cancer, in *Optical Methods for Tumor Treatment and Early Diagnosis: Mechanisms and Techniques*, ed. by. T.J. Dougherty, Proc. SPIE-Int. Soc. Opt. Eng. **1426**, 44 (1991)
2562. S. Andersson-Engels, J. Johansson, S. Svanberg, Medical diagnostic system based on simultaneous multi-spectral fluorescence imaging. Appl. Opt. **33**, 8022 (1994)
2563. G.A. Wagnires, W.M. Star, B.C. Wilson, In vivo fluorescence spectroscopy and imaging for oncological applications. Photochem. Photobiol. **68**, 603 (1998)
2564. S. Andersson-Engels, G. Canti, R. Cubeddu, C. Eker, C. af Klinteberg, A. Pifferi, K. Svanberg, S. Svanberg, P. Taroni, G. Valentini, I. Wang: Spectroscopic characterization of basal cell carcinomas of the skin with multi-colour and lifetime fluorescence imaging. Lasers in Surg. Med. **26**, 76 (2000)
2565. T.J. Dougherty, R.E. Thoma, D.G. Boyle, K.R. Weishaupt, Interstitial photoradiation therapy for primary solid tumors in pet cats and dogs. Can. Res. **41**, 401 (1981)
2566. C.P. Lowell, D.V. Ash, I. Driver, S.B. Brown, Interstitial photodynamic therapy. Clinical experience with diffusing fibres in the treatment of cutaneous and subcutaneous tumours. Br. J. Cancer **67**, 1398 (1993)
2567. P.J. Lou et al., Interstitial photodynamic therapy as salvage treatment for recurrent head and neck cancer. British J. Cancer **91**, 441 (2004)

2568. M. Soto Thompson, A. Johansson, T. Johansson, S. Andersson-Engels, S. Svanberg, N. Bendsöe, K. Svanberg, Clinical system for interstitial photodynamic therapy with combined on-line dosimetry measurements. Appl. Optics **44**, 4023 (2005)
2569. M. Soto Thompson, T. Johansson, S. Pålsson, S. Andersson-Engels, S. Svanberg, N. Bendsoe, U. Stenram, K. Svanberg, J. Spigulis, A. Derjabo, J. Kapostins, Photodynamic therapy of basal cell carcinoma with multi-fibre contact light delivery. J. Envir. Path. Toxic. Onc. **25**, 411 (2006)
2570. K. Svanberg, N. Bendsoe, J. Axelsson, S. Andersson-Engels, S. Svanberg, Photodynamic therapy: superficial and interstitial illumination. J. Biomed. Optics **15**, 041502 (2010)
2571. J. Swartling, J. Axelsson, S. Svanberg, S. Andersson-Engels, K. Svanberg, G. Ahlgren, K.M. Källkner, S. Nilsson, System for interstitial photodynamic therapy with on-line dosimetry – First clinical experiences of prostate cancer. J. Biomed. Optics **15**, 058003 (2010)
2572. G. Shafirstein et al., Interstitial photodynamic therapy—a focused review. Cancers **9**, 12 (2017)
2573. S. Lietke et al., Interstitial photodynamic therapy using 5-ALA for malignant glioma recurrences. Cancers **13**, 1767 (2021)
2574. K. Komolibus, C. Fisher, J. Swartling, S. Svanberg, K. Svanberg, S. Andersson-Engels, Perspectives on interstitial photodynamic therapy for malignant tumors. J. Biomed. Optics **26**, 070604 (2021)
2575. R.A. Weersink et al., Techniques for delivery and monitoring of TOOKAD (WST09)-mediated photodynamic therapy of the prostate: Clinical experience and practicalities. J. Photochem. Photobiol. B: Biol. **79**, 211 (2005)
2576. N. Betrouni, S. Boukris, F. Benzaghou, Vascular targeted photodynamic therapy with TOOKAD® Soluble (WST11) in localized prostate cancer: efficiency of automatic pre-treatment planning. Lasers in Medical Science **32**, (2017)
2577. A.R. Azzouzi et al., Padeliporfin vascular-targeted photodynamic therapy versus active surveillance in men with low-risk prostate cancer (CLIN1001 PCM301): an open-label, phase 3, randomised controlled trial. Lancet Oncol. **18**, 181 (2017)
2578. J.C. Kennedy, R.H. Potter, D.C. Pross, Photodynamic therapy with endogenous protoporphyrin IX: Basic principles and present clinical experience. J. Photochem Photobiol. **6**, 143 (1990)
2579. J.C. Kennedy, R. Pottier, Endogenous protoporphyrin IX, a clinically useful photosensitizer for photodynamic therapy. J. Photochem. Photobiol. B **14**, 275 (1992)
2580. K. Svanberg, T. Andersson, D. Killander, I. Wang, U. Stenram, S. Andersson-Engels, R. Berg, J. Johansson, S. Svanberg, Photodynamic therapy of non-melanoma malignant tumours of the skin utilizing topical δ-amino levulinic acid sensitization and laser irradiation. British J. of Dermatology **130**, 743 (1994)
2581. Q. Peng, T. Warloe, K. Berg, J. Moan, M. Kongshaug, K.-E. Giercksky, J.M. Nesland, 5-aminolevulinic acid-based photodynamic therapy: clinical research and future challenges. Cancer **79**, 2282 (1997)
2582. I. Wang, B. Bauer, S. Andersson-Engels, S. Svanberg, K. Svanberg, Photodynamic therapy utilizing topical δ-amino levulinic acid sensitization and laser irradiation. Acta Ophtal. Scand. **77**, 182 (1999)
2583. I. Wang, N. Bendsoe, C. af Klinteberg, A.M.K. Enejder, S. Anderson-Engels, S. Svanberg, K. Svanberg, Photodynamic therapy versus cryosurgery of basal cell carcinomas; Results of a Phase III clinical trial. Brit. J. Derm. **144**, 832 (2001)
2584. M.B. Ericson, A.-M. Wennberg, O. Larkö, Review of photodynamic therapy in actinic keratosis and basal cell carcinoma. Ther. Clin Risk Manag. **4**, 1 (2008)
2585. S. Andersson-Engels, Å. Elner, J. Johansson, S.-E. Karlsson, L.G. Salford, L.-G. Strömblad, K. Svanberg, S. Svanberg, Clinical recordings of laser-induced fluorescence spectra for evaluation of tumour demarcation feasibility in selected clinical specialities. Lasers Med. Sci. **6**, 415 (1991)
2586. C. af Klinteberg, A.M.K. Nilsson, I. Wang, S. Andersson-Engels, S. Svanberg, K. Svanberg, Laser-induced fluorescence diagnostics of basal cell carcinomas of the skin following topical ALA application. Proc. SPIE-Int. Soc. Opt. Eng. **2926** (1996)

2587. S. Montán, On the use of laser-induced fluorescence in medical and industrial applications, PhD dissertation, Lund Reports on Atomic Physics LRAP-75 (Lund Institute of Technology, 1987)

2588. S. Andersson-Engels, A. Brun, E. Kjellén, L.G. Salford, L.-G. Strömblad, K. Svanberg, S. Svanberg, Identification of brain tumours in rats using laser-induced fluorescence and haematoporphyrin derivative. Laser Med. Sci. **4**, 241 (1989)

2589. P.S. Andersson, S. Montán, S. Svanberg, Multi-spectral system for medical fluorescence imaging. IEEE J. Quantum Electron. **QE-23**, 1798 (1987)

2590. D. Shin, N. Vigneswaran, A. Gillenwater, R. Richards-Kortum, Advances in fluorescence imaging techniques to detect oral cancer and its precursors. Future Oncol. **6**, 1143 (2010)

2591. J.C.O. Richter, N. Haj-Hosseini, S. Andersson-Engels, K. Wårdell, Fluorescence spectroscopy measurements in ultrasonic navigated resection of malignant brain tumors. Lasers Surg. Med. **43**, 8 (2011)

2592. W. Stummer, J.C. Tonn, C. Goetz, W. Ullrich, H. Stepp, A. Bink, T. Pietsch, U. Pichlmeier, 5-Aminolevulinic acid-derived tumor fluorescence: the diagnostic accuracy of visible fluorescence qualities as corroborated by spectrometry and histology and postoperative imaging. Neurosurgery **74**, 310 (2014)

2593. Z.P. She, W.X. Wang, W.L. Jiang, Z.Q. Wang, G.J. Mao, J.J. Fei, Y.F. Li, C.Y. Li, Accurate fluorescence diagnosis of cancer based on sequential detection of hydrogen sulfide and pH. Anal. Chem. **93**, 11826 (2021)

2594. T. Zako, H. Hyodo, K. Tsuji, K. Tokuzen, H. Kishimoto, M. Ito, K. Kaneko, M. Maeda, K. Soga, Development of near infrared-fluorescent nanophosphors and applications for cancer diagnosis and therapy. J. Nanomaterials **2010**, 491471 (2010)

2595. Q. Zhan, J. Qian, H. Liang, G. Somesfalean, D. Wang, S. He, Z. Zhang, S. Andersson-Engels, Using 915 nm laser excited $Tm^{3+}Er^{3+}Ho^{3+}$Doped $NaYbF_4$ upconversion nanoparticles for in vitro and deeper in vivo bioimaging without overheating irradiation. ACS Nano **5**, 3744 (2011)

2596. J.Y. He, C.C. Li, L. Ding, Y.N. Huang, X.L. Yin, J.F. Zhang, J. Zhang, C.J. Yao, M.M. Liang, R.P. Pirraco, J. Chen, Q. Lu, R. Baldridge, Y. Zhang, M.H. Wu, R.L. Reis, Y.L. Wang, Tumor targeting strategies of smart fluorescent nanoparticles and their applications in cancer diagnosis and treatment. Adv. Materials **31**, 1902409 (2017)

2597. M. Osuchowski, F. Osuchowski, W. Latos, A. Kawczyk-Krupka, The use of upconversion nanoparticles in prostate cancer photodynamic therapy. Life **11**, 360 (2021)

2598. S. Svanberg, New developments in laser medicine. Phys. Scr. **T72**, 69 (1997)

2599. C. Kittrell, R.L. Willett, C. de los Santon-Pacheo, N.B. Ratliff, J.R. Kramer, E.G. Malk, M.S. Feld, Diagnosis of fibrous arterial atherosclerosis using fluorescence. Appl. Opt. **24**, 2280 (1985)

2600. P.S. Andersson, A. Gustafson, U. Stenram, K. Svanberg, S. Svanberg, Monitoring of human atherosclerotic plaque using laser-induced fluorescence. Lasers Med. Sci. **2**, 261 (1987)

2601. S. Andersson-Engels, J. Johansson, S. Svanberg, The use of time-resolved fluorescence for diagnosis of atherosclerotic plaque and malignant tumours. Spectrochim. Acta A **46**, 1203 (1990)

2602. S. Andersson-Engels, A. Gustafson, J. Johansson, U. Stenram, K. Svanberg, S. Svanberg, An investigation of possible fluorophores in human atherosclerotic plaque. Lasers Life Sci. **5**, 1 (1992)

2603. J.M. Isner, P.G. Steg, R.H. Clarke, Current status of cardiovascular laser therapy. IEEE J. Quantum Electron. **QE-23**, 1756 (1987)

2604. G.O. Angheloiu, J.T. Arendt, M.G. Müller, A.S. Haka, I. Georgakoudi, J.T. Motz, O.R. Scepanovi, B.D. Kuban, J. Myles, F. Miller, E.A. Podrez, M. Fitzmaurice, J.R. Kramer, M.S. Feld, Intrinsic fluorescence and diffuse reflectance spectroscopy identify superficial foam cells in coronary plaques prone to erosion. Arterioscler. Thromb. Vasc. Biol. **26**, 1594 (2006)

2605. E. Briones, J.R. Lacalle, I. Marin-Leon, J.R. Rueda, Transmyocardial laser revascularization versus medical therapy for refractory angina. Cochrane Database Syst. Rev. doi: https://doi.org/10.1002/14651858.CD003712.pub3 (2015)

2606. D.M. Kirschenbaum (ed.), *Atlas of Protein Spectra in the Ultraviolet and Visible Regions*, vol. 2 (IFI/Plenum, New York, 1974)

2607. K.P. Mahler, J.F. Malone, Digital fluorescopy: A new development in medical imaging. Contemp. Phys. **27**, 533 (1986)

2608. N. Kondo, M. Kuramoto, H. Shimizu, Y. Ogawa, M. Kurita, T. Nischizu, V.K. Chong, K. Yamamoto, Identification of fluorescent substance in mandarin orange skin for machine vision system to detect rotten citrus fruits. Eng. Agri. Env. Food **2**, 54 (2009)

2609. H. Zhang, J. Huang, T.Q. Li, X.X. Wu, S. Svanberg, K. Svanberg, Studies for tropical fruit ripening using three different spectroscopic techniques. J. Biomed. Opt. **19**, 067001 (2014)

2610. X.B. Lin, H. Zhang, L.N. Hu, G.Y. Zhao, S. Svanberg, K. Svanberg, Ripening of avocado fruits studied by spectroscopic techniques. J. Biophot. (2020)

2611. L. Mei, P. Lundin, M. Brydegaard, S.Y. Gong, D.S. Tang, G. Somesfalean, S. He, S. Svanberg, Tea classification and quality assessment using laser induced fluorescence combined with singular value decomposition. Appl. Optics **51**, 803 (2012)

2612. S. Mittal, K. Laishram, S. Inamdar, N.R. Das, A.K. Razdan, Narcotic drug detection and identification through synchronous fluorescence technique. Defence Sci. J. **70**, 534 (2020)

2613. R.R. Alfano, B.T. Darayash, J. Cordero, P. Tomashefsky, F.W. Longo, M.A. Alfano, Laser-induced fluorescence spectroscopy from native cancerous and normal tissue. IEEE J. Quantum Electron. **QE-20**, 1507 (1984)

2614. R.R. Alfano, G.C. Tang, A. Pradhan, W. Lam, D.S.J. Choy, E. Opher, Fluorescence spectra from cancerous and normal human breast and lung tissues. IEEE J. Quantum Electron. **QE-23**, 1806 (1987)

2615. R. Richards-Kortum, R.P. Rava, R.E. Petras, M. Fitzmaurice, M.V. Sivak, M.S. Feld, Spectroscopic diagnosis of colonic dysplasia. Photochem. Photobiol. **53**, 777 (1991)

2616. S. Montán, Diploma paper, Lund Reports on Atomic Physics LRAP-19 (Lund University, Lund, 1982)

2617. P.S. Andersson, E. Kjellén, S. Montán, K. Svanberg, S. Svanberg, Autofluorescence of various rodent tissues and human skin tumour samples. Lasers Med. Sci. **2**, 41 (1987)

2618. B. Palcic, S. Lam, J. Hung, C. Mac Aulay, Detection and localization of early lung cancer by imaging techniques. Chest **99**, 742 (1991)

2619. M. Ranaa, A. Zapf, M. Kuehlea, N.-C. Gellricha, A.M. Eckardt, Clinical evaluation of an autofluorescence diagnostic device for oral cancer detection: a prospective randomized diagnostic study. Eur. J. Cancer Prevent. **21**, 460 (2012)

2620. H. Takizawa, K. Kondo, N. Kawakita, M. Tsuboi, H. Toba, K. Kajiura, Y. Kawakami, S. Sakiyama, A. Tangoku, A. Morishita, Y. Nakagawa, T. Hirose, Autofluorescence for the diagnosis of visceral pleural invasion in non-small-cell lung cancer. Eur. J. Cardiothorac. Surg. **53**, 987 (2018)

2621. R.R. Alfano, W. Lam, H.J. Zarrabi, M.A. Alfano, J. Cordero, D.B. Tata, C.E. Swenberg, Human teeth with and without caries studied by laser scattering, fluorescence and absorption spectroscopy. IEEE J. Quantum Electron. **QE-20**, 1512 (1984)

2622. F. Sundström, K. Fredriksson, S. Montán, U. Hafström-Björkman, J. Ström, Laser-induced fluorescence from sound and carious tooth substance: Spectroscopic studies. Swed. Dent. J. **9**, 71 (1985)

2623. A. Cardoso, J. Terra Fernandes, S. Kalil Bussadoria, A.C. Ratto Tempestini Horliana, K. Porta Santos, F.M. Leticia LealGonçalves, L. Jansiski Motta, Use of optical fluorescence for the diagnosis of dental biofilm in young permanent molars - A case series. Photodiag. Photodyn. Therapy **34**, 102216 (2021)

2624. J.J. Baraga, M.S. Feld, R.P. Rava, Rapid near-infrared Raman spectroscopy of human tissue with a spectrograph and CCD detector. Appl. Spectrosc. **46**, 187 (1992)

2625. T.J. Römer, J.F. Brennan III., M. Fitzmaurice, M.F. Feinstein, G. Deinum, J.L. Myles, J.R. Kramer, R.S. Lees, M.S. Feld, Histopathology of human coronary atherosclerosis by quantifying its composition with Raman spectroscopy. Circulation **97**, 878 (1998)

2626. A.M.K. Nilsson, D. Heinrich, J. Olajos, S. Andersson-Engels, Near-infrared diffuse reflection and laser-induced fluorescence spectroscopy for myocardial tissue characterisation. Spectrochim. Acta A **53**, 1901 (1997)

2627. J.J. Baraga, M.S. Feld, R.P. Rava, Infrared attenuated total reflectance of human arthery: a new modality for diagnosing atherosclerosis. Lasers Life Sci. **5**, 13 (1992)
2628. I.J. Bigio, T.R. Loree, T. Shimada, K. Story-Held, R.D. Glickman, R. Conn: Optical diagnostics based on elastic scattering: recent clinical demonstrations with the Los Alamos Biopsy System. Proc. SPIE-Int. Soc. Opt. Eng. **2081** (1994)
2629. V. Backman, R. Gurjar, K. Badizadegan, I. Itzkan, R. Dasari, L.T. Perelman, M.S. Feld, Polarized light scattering spectroscopy for quantitative measurements of epithelial cellular structure in situ. IEEE JSTQE Las. Med. Biol. **5** (1999)
2630. L.T. Perelman, V. Backman, M. Wallace, G. Zonios, R. Manoharan, A. Nusrat, S. Shields, M. Seiler, C. Lima, T. Hamano, I. Itzkan, J. Van Dam, J.M. Crawford, M.S. Feld, Observation of periodic structure in reflectance from biological tissue: A new technique for measuring nuclear size distributions. Phys. Rev. Lett. **80**, 627 (1998)
2631. Ch. Krafft, B. Dietzek, J. Popp, Raman and CARS microspectroscopy of cells and tissues. Analyst **134**, 1046 (2009)
2632. C. Krafft, J. Popp, The many facets of Raman spectroscopy for biomedical analysis. Analyt. Bioanalyt. Chem. **407**, 699 (2015)
2633. C.S. Ho, N. Jean, C.A. Hogan, L. Blackmon, S.S. Jeffrey, M. Holodniy, N. Banaei, A.A.E. Saleh, S. Ermon, J. Dionne, Rapid identification of pathogenic bacteria using Raman spectroscopy and deep learning. Nature Commun. **10**, 4927 (2019)
2634. L. Wang, W. Liu, J.W. Tang, J.J. Wang, Q.H. Liu, P.B. Wen, M.M. Wang, Y.C. Pan, B. Gu, X. Zhang, Applications of Raman spectroscopy in bacterial infections: Principles, advantages, and shortcomings. Front. Microbiol. **12** https://doi.org/10.3389/fmicb.2021.683580 (2021)
2635. A. Tannert, A. Ramoji, U. Neugebauer, J. Popp, Photonic monitoring of treatment during infection and sepsis: development of new detection strategies and potential clinical applications. Analyt. Bioanalyt. Chem. **410**, 773 (2018)
2636. S.R. Meech, C.D. Stubbs, D. Phillips, The application of fluorescence decay measurements in studies of biological systems. IEEE J. Quantum Electron. **QE-20**, 1343 (1984)
2637. D.B. Tata, M. Foresti, J. Cardero, P. Thomachefsky, M.A. Alfano, R.R. Alfano, Fluorescence polarization spectroscopy and time-resolved fluorescence kinetics of native cancerous and normal rat kidney tissues. Biophys. J. **50**, 463 (1986)
2638. S. Andersson-Engels, J. Johansson, S. Svanberg, The use of time-resolved fluorescence for diagnosis of atherosclerotic plaque and malignant tumours. Spectrochim. Acta A **46**, 1203 (1990)
2639. A. Rück, F. Dolp, Ch. Hülshoff, C. Hauser, C. Scalfi-Happ, Fluorescence lifetime imaging in PDT. An overview. Med. Laser Applic. **20**, 125 (2005)
2640. E. Dimitrow, I. Riemann, A. Ehlers, M.J. Koehler, J. Norgauer, P. Elsner, K. König, M. Kaatz, Spectral fluorescence lifetime detection and selective melanin imaging by multiphoton laser tomography for melanoma diagnosis. Exp. Dermatol. **18**, 509 (2009)
2641. L. Marcu, Fluorescence lifetime in cardiovascular diagnostics. J. Biomed. Optics **15**, 011106 (2010)
2642. V. Sharma, S. Shivalingaiah, Y. Peng, D. Euhus, Z. Gryczynski, H.L. Liu, Auto-fluorescence lifetime and light reflectance spectroscopy for breast cancer diagnosis: potential tools for intraoperative margin detection. Biomed. Optics Express **3**, 1825 (2012)
2643. L. Marcu, P.M.W. French, D.S. Elson (eds.), *Fluorescence Lifetime Spectroscopy and Imaging - Principles and Applications in Biomedical Diagnostics* (CRC Press, 2015)
2644. S. Andersson-Engels, J. Johansson, K. Svanberg, S. Svanberg, Fluorescence diagnostics and photochemical treatment of diseased tissue using lasers. Pt. I, Anal. Chem. **61**, 1367A (1989); Pt.II, ibid. **62**, 19A (1990)
2645. S. Andersson-Engels, J. Johansson, U. Stenram, K. Svanberg, S. Svanberg, Malignant tumor and atherosclerotic plaque diagnostics using laserinduced fluorescence. IEEE J. Quantum Electron. **QE-26**, 2207 (1990)
2646. R. Cubeddu, P. Taroni, G. Valentini, G. Canti, Use of time-gated fluorescence imaging for diagnosis in biomedicine. J. Photochem. Photobiol. B **12**, 109 (1992)

2647. R. Cubeddu, A. Pifferi, P. Taroni, G. Valentini, G. Canti, Tumor detectionin mice by measurment of fluorescence decay time matrices. Opt. Lett. **20**, 2553 (1995)

2648. S. Andersson-Engels, C. af Klinteberg, K. Svanberg, S. Svanberg, In vivo fluorescence imaging for tissue diagnosis. Phys. Med. Biol. **42**, 815 (1997)

2649. K. Svanberg, I. Wang, S. Colleen, I. Idvall, C. Ingvar, R. Rydell, D. Jocham, H. Diddens, S. Bown, G. Gregory, S. Montán, S. Andersson-Engels, S. Svanberg, Clinical multi-colour fluorescence imaging of malignant tumours – Initial experience. Acta Radiol. **38**, 2 (1998)

2650. S. Andersson-Engels, G. Canti, R. Cubeddu, Ch. Eker, C. af Klinteberg, A. Pifferi, K. Svanberg, S. Svanberg, P. Taroni, G. Valentini, I. Wang, Preliminary evaluation of two fluorescence imaging methods for the detection and the delineation of basal cell carcinomas of the skin. Lasers Surg. Med. **26**, 76 (2000)

2651. C.S.L. Ho, T. Horiuchi, H. Taniguchi, A. Umetsu, K. Hagisawa, K. Iwaya, K. Nakai, A. Azmi, N. Zulaziz, A. Azhim, N. Shinomiya, Y. Morimoto, Fluorescence multispectral imaging-based diagnostic system for atherosclerosis. BioMed. Eng. OnLine **15**, 98 (2016)

2652. J.L. Lagarto, F. Villa, S. Tisa, F. Zappa, V. Shcheslavskiy, F.S. Pavone, R. Cicchi, Real-time multispectral fluorescence lifetime imaging using single photon avalanche diode arrays. Sci. Reports **10**, 8116 (2020)

2653. M. Lukina, K. Yashin, E.E. Kiseleva, A. Alekseeva, V. Dudenkova, E.V. Zagaynova, E. Bederina, I. Medyanic, W. Becker, D. Mishra, M. Berezin, V.I. Shcheslavskiy, M. Shirmanova, Label-free macroscopic fluorescence lifetime imaging of brain tumors. Front. Oncol. https://doi.org/10.3389/fonc.2021.66605924 (2021)

2654. C. af Klinteberg, I. Wang, I. Karu, Th. Johansson, N. Bendsoe, K. Svanberg, S. Andersson-Engels, S. Svanberg, G. Canti, R. Cubeddu, A. Pifferi, P. Taroni, G. Valentini, Diode laser-mediated ALA-PDT guided by laserinduced fluorescence imaging. Unpublished.

2655. B. Herman, J.J. Lemasters (eds.), *Optical Microscopy – Emerging Methods and Applications* (Academic Press, San Diego, 1993)

2656. R.H. Webb, Confocal optical microscopy. Rep. Prog. Phys. **59**, 427 (1996)

2657. A.D. Elliott, Confocal microscopy: Principles and modern practices. Curr. Protoc. Cytom. **92**, e68 (2020)

2658. P.T.C. So, C.Y. Dong, B.R. Masters, K.M. Berland, Two-photon excitation fluorescence microscopy. Ann. Rev. Biomed. Eng. **2**, 399 (2000)

2659. T. Yoshitake, M.G. Giacomelli, L.C. Cahill, D.B. Schmolze, H. Vardeh, B.E. Faulkner-Jones, J.L. Connolly, J.G. Fujimoto, Direct comparison between confocal and multiphoton microscopy for rapid histopathological evaluation of unfixed human breast tissue. J. Biomed. Optics **21**, 126021 (2016)

2660. M. Müller, A. Zumbusch, Coherent anti-Stokes Raman scattering microscopy. Chem. Phys. Chem. **8**, 2156 (2007)

2661. J.X. Cheng, X.L.S. Xie (eds.), *Coherent Raman Scattering Microscopy* (Taylor & Francis, 2012)

2662. S.W. Li, Y.P. Li, R.X. Yi, L.W. Liu, J.L. Qu, Coherent anti-Stokes Raman scattering microscopy and its applications. Front. Phys. https://doi.org/10.3389/fphy.2020.598420 (2020)

2663. Z.Y. He, P. Wang, X.S. Ye, Novel endoscopic optical diagnostic technologies in medical trial research: recent advancements and future prospects. BioMedical Eng. OnLine **20**, 5 (2021)

2664. Z. Malik, D. Cabib, R.A. Buckwald, Y. Garini, D. Soenkeson, A novel spectral imaging system combining spectroscopy with imaging – Applications for biology. Proc. SPIE-Int. Soc. Opt. Int. **2329**, 180 (1994)

2665. Z. Malik, G. Kostenich, C. Rothmann, I. Barshack, A. Orenstein, Imaging of human skin lesions using multipixel Fourier transform spectroscopy. Lasers Med. Sci. **13**, 12 (1998)

2666. L.H. Bian, J.L. Suo, G.H. Situ, Z.W. Li, J.T. Fan, F. Chen, Q.H. Dai, Multispectral imaging using a single bucket detector. Sci. Reports **6**, 24752 (2016)

2667. Z.M. Li, J. Borggren, E. Berrocal, A. Ehn, M. Aldén, M. Richter, E. Kristensson, Simultaneous multispectral imaging of flame species using Frequency Recognition Algorithm for Multiple Exposures (FRAME). Combust. Flame **192**, 160 (2018)

2668. A. Ashkin, J.M. Dziedzic, J.E. Bjorkholm, S. Chu, Observation of a singlebeam gradient force optical trap for dielectric particles. Opt. Lett. **11**, 288 (1986)

2669. K. Svoboda, S. Block, Biological applications of optical forces. Ann. Rev. Biophys. Biomol. Struct. **23**, 247 (1994)

2670. K. Visscher, S.P. Gross, S.M. Block, Construction of multiple-beam optical traps with nanometer resolution position sensing. IEEE J. Sel. Top. Quantum Electron. **2**, 1066 (1996)

2671. A. Ashkin, Optical trapping and manipulation of neutral particles using lasers. Proc. Natl. Acad. Sci. USA **94**, 4853 (1997)

2672. M.E.J. Friese, T.A. Nieminen, N.R. Heckenberg, H. Rubinsztein-Dunlop, Alignment and spinning of laser-trapped microscopic particles. Nature **394**, 348 (1998)

2673. M.D. Koch, J.W. Shaevitz, Introduction to optical tweezers. Methods. Mol. Biol. **1486**, 3 (2017)

2674. G. Pesce, P.H. Jones, O.M. Maragò, G. Volpe, Optical tweezers: theory and practice. Eur. Phys. J. Plus **135**, 949 (2020)

2675. A. Ashkin, Optical tweezers and their application to biological systems - Nobel Lecture (Royal Academy of Sciences, Stockholm 2018) https://www.nobelprize.org/uploads/2018/10/ashkin-lecture.pdf

2676. V. Loke, T. Nieminen, T. Asavei, Theodor Asavei, H. Rubinsztein-Dunlop, Optically driven micromachines: Design and fabrication. DOI: https://doi.org/10.1615/ICHMT.2007.ConfElectromagLigScat.300 (2007)

2677. G.K. Knopf, K. Uchino, *Light Driven Micromachines* (CRC Press, 2018) S. Kassem, T. van Leeuwen, A.S. Lubbe, M.R. Wilson, B.L. Feringa, D.A. Leigh: Artificial molecular motors. Chem. Soc. Rev. **46**, 2592 (2017)

2678. https://www.nobelprize.org/uploads/2018/06/popular-chemistryprize2016-1.pdf (2016)

2679. M. Peplow, The tiniest Lego: a tale of nanoscale motors, rotors, switches and pumps. Nature **525**, 18 (2015)

2680. S. Svanberg, Optical analysis of trapped gas - Gas in scattering media absorption spectroscopy. Laser Phys. **19**, 1 (2009)

2681. J.B. Fishkin, E. Gratton, Propagation of photon-density waves in strongly scattering media containing an absorbing semi-infinite plane bounded by a straight edge. J. Opt. Soc. Am. A. **10**, 127 (1993)

2682. B. Chance, J.S. Leigh, H. Miyake, D.S. Smith, S. Nioka, R. Greenfeld, M. Finander, K. Kaufmann, W. Levy, M. Young, P. Cohen, H. Yoshioka, R. Boretsky, Comparison of time-resolved and -unresolved measurements of deoxyhemoglobin in the brain. Proc. Natl. Acad. Sci. USA **85**, 4971 (1988)

2683. M.S. Patterson, B.C. Wilson, D.R. Wyman, The propagation of optical radiation in tissue. Models for radiation transport and their application. Lasers Med. Sci. **6**, 155 (1991)

2684. S.L. Jacques, Time-resolved propagation of ultrashort pulses within turbid tissues. Appl. Opt. **28**, 2223 (1989)

2685. B. Chance, G. Müller (eds.), *Optical Tomography*, (SPIE, Bellingham 1993); G. Müller, B. Chance, R. Alfano, S. Arridge, J. Beuthan, E. Gratton, M. Kaschke, B. Masters, S. Svanberg, P. van der Zee (eds.), *Medical Optical Tomography, Functional Imaging and Monitoring*, SPIE Institute Series, Vol.**11** (SPIE, Bellingham 1993)

2686. B.J. Tromberg, L.O. Svaasand, T.-T. Tsay, R.C. Haskell, Properties of optical density waves in multiple-scattering media. Appl. Opt. **32**, 607 (1993)

2687. S. Andersson-Engels, R. Berg, S. Svanberg, Effects of optical constants on time-gated transillumination of tissue and tissue-like media. J. Photochem. Photobiol. **16**, 155 (1992)

2688. C. Lindquist, A. Pifferi, R. Berg, S. Andersson-Engels, S. Svanberg, Reconstruction of diffuse photon-density wave interference in turbid media from time-resolved transmittance measurements. Appl. Phys. Lett. **69**, 1674 (1996)

2689. J.C. Hebden, S.R. Arridge, D.T. Delpy, Optical imaging in medicine: I. Experimental techniques. Phys. Med. Biol. **42**, 825 (1997)

2690. R. Berg, S. Andersson-Engels, S. Svanberg, 'Time-resolved transillumination imaging.' In: G. Müller, B. Chance, R. Alfano, S. Arridge, J. Beuthan, E. Gratton, M. Kaschke, B. Masters,

S. Svanberg, P. van der Zee (eds.), *Medical Optical Tomography, Functional Imaging and Monitoring*, SPIE Institute Series, Vol.**11** (SPIE, Bellingham 1993) p.397

2691. S.L. Jacques, Optical properties of biological tissues: a review. Phys. Med. Biol. **58**, R37 (2013)
2692. V.V. Tuchin, Tissue optics and photonics: Biological tissue structures. J. Biomed. Phot. Eng. **1**, 3 (2015)
2693. V.V. Tuchin, *Tissue Optics: Light Scattering Methods and Instruments for Medical Diagnostics*, 3rd edn. (SPIE, Bellingham, 2015)
2694. S.L. Jacques, Modeling tissue optics using Monte Carlo modeling: a tutorial. Proc. SPIE **6854**, 68540T (2008)
2695. E. Alerstam, T. Svensson, S. Andersson-Engels, Parallel computing with graphics processing units for high-speed Monte Carlo simulation of photon migration. J. Biomed. Opt. **13**, 060504 (2008)
2696. J. Jönsson, E. Berrocal, Multi-scattering software: part I: online accelerated Monto Carlo simulation of light transport through scattering media. Opt. Express **28**, 37612 (2020)
2697. J.P. Payne, J.W. Severinghaus (eds.), *Pulse Oximetry* (Springer, Heidelberg, 1986)
2698. M. Cope, D.T. Delpy, System for long-term measurement of cerebral blood and tissue oxygenation on newborn infants by near-infrared transillumination. Med. Biol. Eng. Comp. **26**, 289 (1988)
2699. E.D. Chan, M.M. Chan, M.M. Chan, Pulse oximetry: Understanding its basic principles facilitates appreciation of its limitations. Resp. Med. **107**, 789 (2013)
2700. J.W. Hall, A. Pollard, Near-infrared spectroscopic determination of serum total proteins, albumin, globulins and urea. Clin. Biochem. **26**, 483 (1993)
2701. S. Andersson-Engels, R. Berg, A. Persson, S. Svanberg, Multispectral tissue characterization using time-resolved detection of diffusely scattered white light. Opt. Lett. **18**, 1697 (1993)
2702. S. Delbeck, T. Vahlsing, S. Leonhardt, G. Steiner, H.M. Heise, Non-invasive monitoring of blood glucose using optical methods for skin spectroscopy -opportunities and recent advances. Anal. Bioanal. Chem. **411**, 63 (2019)
2703. L. Tang, S.J. Chang, C.J. Chen, J.T. Liu, Non-invasive blood glucose monitoring technology: A review. Sensors **20**, 6925 (2020)
2704. J.C. Hebden, R.A. Kruger, K.S. Wong, Time-resolved imaging through a highly scattering medium. Appl. Opt. **30**, 788 (1991)
2705. K.M. Yoo, B.B. Das, R.R. Alfano, Imaging of a translucent object hidden in highly scattering medium from the early portion of the diffuse component of a transmitted ultrafast laser pulse. Opt. Lett. **17**, 958 (1992)
2706. B. Chance, K. Kang, L. He, J. Weng, E. Sevick, Highly sensitive object location in tissue models with linear in-phase and anti-phase multi-element optical arrays in one and two dimensions. Proc. Natl. Acad. Sci. USA **90**, 3423 (1995)
2707. K. Michielsen, H. De Raedt, J. Przeslawski, N. Garcia, Computer simulation of time-resolved optical imaging of objects hidden in turbid media. Phys. Rep. **304**, 89 (1998)
2708. S. Andersson-Engels, R. Berg, S. Svanberg, O. Jarlman, Time-resolved transillumination for medical diagnostics. Opt. Lett. **15**, 1179 (1990)
2709. R. Berg, O. Jarlman, S. Svanberg, Medical transillumination imaging using short pulse diode lasers. Appl. Opt. **32**, 574 (1993)
2710. P. Taroni, L. Spinelli, A. Torricelli, A. Pifferi, G.M. Danesini, R. Cubeddu, Multi-wavelength time domain optical mammography. Technol. Cancer Res. Treat. **4**, 527 (2005)
2711. P. Taroni, A. Pifferi, E. Salvagnini, L. Spinelli, A. Torricelli, R. Cubeddu, Seven-wavelength time-resolved optical mammography extending beyond 1000 nm for breast collagen quantification. Opt. Express **17**, 15932 (2009)
2712. G. Di Leo, R.M. Trimboli, T. Sella, F. Sardanelli, Optical imaging of the breast: Basic principles and clinical applications. Am. J. Roentgenology **209**, 230 (2017)
2713. P. Öberg, Laser-Doppler flowmetry. Crit. Rev. Biomed. Eng. **18**, 125 (1990)
2714. K. Wårdell, A. Jacobsson, G.E. Nilsson, Laser Doppler perfusion imaging by dynamic light scattering. IEEE Trans. Biomed. Eng. **40**, 309 (1993)

2715. M.L. Arildsson, K. Wårdell, G.E. Nilsson, Higher order moment processing of laser Doppler perfusion signals. J. Biomed. Opt. **2**, 358 (1997)

2716. A. Serov, B. Steinacher, T. Lasser, Full-field laser Doppler perfusion imaging and monitoring with an intelligent CMOS camera. Opt. Express **13**, 3681 (2005)

2717. A. Humeau, W. Steenbergen, H. Nilsson, T. Strömberg, Laser Doppler perfusion monitoring and imaging: novel approaches. Med. Biol. Eng. Comput. **45**, 421 (2007)

2718. R.R. Alfano, P.P. Ho, K.M. Yoo, Photons for prompt tumour detection. Phys. World **5**, 37 (1992)

2719. L. Wang, Y. Liu, P.P. Ho, R.R. Alfano, Photons for prompt tumour detection. Proc. SPIE-Int. Soc. Opt. Eng. **1431**, 97 (1991)

2720. M.D. Duncan, R. Mahon, L.L. Tankersley, R. Reintjes, Time-gated imaging through scattering media using stimulated Raman amplification. Opt. Lett. **16**, 1868 (1991)

2721. K.M. Yoo, Q. Xing, R.R. Alfano, Imaging objects hidden in highly scattering media using femtosecond second-harmonic-generation cross-correlation time gating. Opt. Lett. **16**, 1019 (1991)

2722. J.R. Lakowicz, G. Laczo, I. Gryczynski, H. Szmacinski, W. Wiczk, M.L. Johnson, Frequency-domain fluorescence spectroscopy: Principles, biochemical applications and future developments. Ber. Bunsenges. Phys. Chem. **93**, 316 (1989)

2723. J. Fishkin, E. Gratton, M.J. van de Ven, W.W. Mantulin, Diffusion of intensity-modulated near-infrared light in turbid media. Proc. SPIE-Int. Soc. Opt. Eng. **1431**, 122 (1991)

2724. M. Kaschke, H. Jess, G. Gaida, J.-M. Kaltenbach, W. Wrobel, 'Transillumination imaging of tissue by phase-modulation techniques.' In: *Advances in Optical Imaging and Photon Migration*, ed. by R.R. Alfano. Proc. OSA **21**, 88 (1994)

2725. L. Mei, S. Svanberg, G. Somesfalean, Combined optical porosimetry and gas absorption spectroscopy in gas-filled porous media using diode-laser-based frequency domain photon migration. Opt. Express **20**, 16942 (2012)

2726. Z.G. Guan, P. Lundin, S. Svanberg, Assessment of photon migration in scattering media using heterodyning techniques with a frequency modulated diode laser. Opt. Express **17**, 16291 (2009)

2727. L. Mei, G. Somesfalean, S. Svanberg, Frequency-modulated light scattering interferometry employed for optical properties and dynamic studies of turbid media. Biomed. Optics Express **5**, 2810 (2014)

2728. M. Toida, T. Ichimura, H. Inaba, The first demonstration of laser computed tomography achieved by coherent detection imaging method for biomedical applications. IEICE Trans. **E74**, 1692 (1991)

2729. N. Abramson, Light-in-flight recording: High-speed holographic motion pictures of ultrafast phenomena. Appl. Opt. **22**, 215 (1983)

2730. K.G. Spears, J. Serafin, N.H. Abramson, X. Zhu, H. Bjelkhagen, Chronocoherent imaging for medicine. IEEE Trans. Biomed. Eng. **36**, 1210 (1989)

2731. H. Chen, Y. Chen, D. Dilworth, E. Leith, J. Lopez, J. Valdmanis, Two-dimensional imaging through diffusing media using 150 fs gated electronic holography techniques. Opt. Lett. **16**, 487 (1991)

2732. T. Kakue, K. Tosa, J.P. Yuasa, T. Tahara, Y. Awatsuji, K. Nishio, S. Ura, T. Kubota, Digital light-in-flight recording by holography by use of a femtosecond pulsed laser. IEEE J. Sel. Top. Quant. Electr**.** **18**, https://doi.org/10.1109/JSTQE.2011.2147281 (2012)

2733. J.H. Hoogenraad, M.B. van der Mark, S.B. Colak, G.W. t'Hooft, E.S. van der Linden, 'First results from the Phillips optical mammoscope.' In: *Photon Propagation in Tissue*, ed. by D.A. Benaron, B. Chance, M. Ferrari. Proc. SPIE-Int. Soc. Opt. Eng. **3194**, 184 (1998)

2734. B.W. Pogue, M. Testorf, U.L. Osterberg, K.D. Paulsen, Instrumentation and design of a frequency-domain diffuse optical tomography imager for breast cancer detection. Opt. Express **1**, 391 (1997). http://epubs.osa.org/oearchive/source/2827.htm

2735. J.P. van Houten, D.A. Benaron, S. Spilman, D.K. Stevenson, Imaging brain injury using time-resolved near infrared light scanning. Pediat. Res. **39**, 470 (1996)

2736. D. Huang, E.A. Swanson, C.P. Lin, J.S. Schuman, W.G. Stinton, W. Chang, M.R. Hee, T. Flotte, K. Gregory, C.A. Puliafito, J.G. Fujimoto, Optical coherence tomography. Science **254**, 1178 (1991)

2737. C.A. Puliafito, J.G. Fujimoto, In vivo retinal imaging by optical coherence tomography. Opt. Lett. **18**, 1864 (1993)

2738. W. Drexler, U. Morgner, R.K. Ghanta, F.X. Kärtner, J.S. Schuman, J.G. Fujimoto, Ultrahigh-resolution ophthalmic optical coherence tomography. Nat. Med. **7**, 502 (2001)

2739. G.J. Tearny, M.E. Brezinski, B.M. Bouma, S.A. Boppart, C. Pitris, J.F. Southern, J.G. Fujimoto, In vivo endoscopical optical biopsy with optical coherence tomography. Science **276**, 2037 (1997)

2740. A.M. Kowalievicz, T. Ko, I. Hartl, J.G. Fujimoto, M. Pollnau, R.P. Salath, Ultrahigh resolution optical coherence tomography using a superluminescent light source. Opt. Express **10**, 349 (2002)

2741. W. Drexler et al., Enhanced visualization of macular pathology with the use of ultra-high resolution optical coherence tomography. Arch. Ophtalmol. **121**, 695 (2003)

2742. R. Bernardes, J. Cunha-Vaz (eds.), *Optical Coherence Tomography - A Clinical and Technical Update* (Springer, 2012)

2743 W. Drexler, J.G. Fujimoto (eds.), *Optical Coherence Tomography - Technology and Applications,* 2nd Edition (Springer, 2015)

2744. J.S. Schuman, J.G. Fujimoto, J.S. Duker, H. Ishikawa, G. Wollstein, *Optical Coherence Tomography of Ocular Diseases, Fourth Edition* (Slack Inc., 2021)

2745. T.E. de Carlo, A. Romano, N.K. Waheed, J.S. Duker, A review of optical coherence tomography angiography (OCTA). Int. J. Retina Vitr. **1**, 5 (2015)

2746. A. Kini, J. Narula, Y. Vengrenyuk, V. Sharma, *Atlas of Coronary Intravascular Optical Coherence Tomography* (Springer, 2019)

2747. Z. Varga, S.N. Gowda, P. Sethi, A. Stys, Optical coherence tomography in intracoronary diagnostics. S .D. Med. **73**, 202 (2020)

2748. E.A. Swanson, J.A. Izatt, H.M. Hee, D. Huang, C.P. Lin, J.S. Schuman J.F. de Boer, R. Leitgeb, M. Wojtkowski, Twenty-five years of optical coherence tomography: the paradigm shift in sensitivity and speed provided by Fourier domain OCT. Biomed. Opt. Express **8**, 3248 (2017)

2749. R.A. Leitgeb, F. Placzek, E.A. Rank, L. Krainz, R. Haindl, Q. Li, M.Y. Liu, A. Unterhuber, T. Schmoll, W. Drexler, Enhanced medical diagnosis for dOCTors: a perspective of optical coherence tomography. J. Biomed. Opt. **26**, 100601 (2021)

2750. I.M. Vellekoop, A.P. Mosk, Phase control algorithms for focusing light through turbid media. Opt. Commun. **281**, 3071 (2008)

2751. I.M. Vellekoop, A. Lagendijk, A.P. Mosk, Exploiting disorder for perfect focusing. Nat. Photonics **4**, 320 (2010)

2752. O. Katz, E. Small, Y. Bromberg, Y. Silberberg, Focusing and compression of ultrashort pulses through scattering media. Nat. Photon. **5**, 372 (2011)

2753. I.M. Vellekoop, Feed-back based wavefront sensing. Opt. Express **23**, 12189 (2015)

2754. H. Yu, J.P. Lee, K. Lee, J. Jang, J. Lim, W. Yang, Y. Jeong, Y. Park, In vivo deep tissue imaging using wavefront shaping optical coherence tomography. J. Biomed. Opt. **21**, 101406 (2016)

2755. H.B. de Aguiar, S. Gigan, S. Brasselet, Enhanced nonlinear imaging through scattering media using transmission-matrix-based wave-front shaping. Phys. Rev. A **94**, 043830 (2016)

2756. P.X. Lai, L.D. Wang, J.W. Tay, L.V. Wang, Photoacoustically guided wavefront shaping for enhanced optical focusing in scattering media. Nat. Phot. **9**, 126 (2015)

2757. A.A. Oraevsky, S.L. Jacques, F.K. Tittel, Measurement of tissue optical properties by time-resolved detection of laser-induced transient stress. Appl. Opt. **36**, 402 (1997)

2758. V. Ntziachristos, J. Ripoll, L.V. Wang, R. Weissleder, Looking and listening to light: the evolution of whole-body photonic imaging. Nat. Biotech. **23**, 313 (2005)

2759. L.V. Wang, *Photoacoustic Imaging and Spectroscopy* (CRC Press, 2009)

2760. A. Taruttis, V. Ntziachristos, Advances in real-time multispectral optoacoustic imaging and its applications. Nature Phot. **9**, 219 (2015)

2761. L.V. Wang, J. Yao, A practical guide to photoacoustic tomography in the life sciences. Nature Meth. **13**, 627 (2016)
2762. Y. Zhou, J. Yao, L.V. Wang, Tutorial on photoacoustic tomography. J. Biomed. Opt. **21**, 061007 (2016)
2763. Y. Matsumoto, Y. Asao, H. Sekiguchi et al., Visualising peripheral arterioles and venules through high-resolution and large-area photoacoustic imaging. Sci. Rep. **8**, 1 (2018)
2764. A. Binte, E. Attia, G. Balasundaram, M. Moothanchery, U.S. Dinish, R.Z. Bi, V. Ntziachristos, M. Olivo, A review of clinical photoacoustic imaging: current and future trends. Photoacoustics **16**, 100144 (2019)
2765. L. Li, L.V. Wang, Recent advances in photoacoustic tomography. AAAS BME Front. **2021**, 9823268 (2021)
2766. A. Merdasa, J. Bunke, M. Naumovska, J. Albinsson, T. Erlöv, M. Cinthio, N. Reistad, R. Sheikh, M. Malmsjö, Photoacoustic imaging of the spatial distribution of oxygen saturation in an ischemia-reperfusion model in humans. Biomed. Opt. Express **12**, 2484 (2021)
2767. S. Na, L.V. Wang, Photoacoustic computed tomography for functional human brain imaging. Biomed. Opt. Express **12**, 4056 (2021)
2768. H.L. Zhang, M. Sabooni, L. Rippe, C.H. Kim, S. Kröll, L.V. Wang, P.R. Hemmer, Slow light for deep tissue imaging with ultrasound modulation. Appl. Phys. Lett. **100**, 131102 (2012)
2769. A. Walther, L. Rippe, L.V. Wang, S. Andersson-Engels, S. Kröll, Analysis of the potential for non-invasive imaging of oxygenation at heart depth, using ultrasound optical tomography (UOT) or photo-acoustic tomography (PAT). Biomed. Opt. Expr. **8**, 4523 (2017)
2770. J. Johansson, R. Berg, A. Pifferi, S. Svanberg, L.O. Björn, Time-resolved studies of light propagation in *Crassula* and *Phaseolus* leaves. Photochem. Photobiol. **69**, 242 (1999)
2771. J. Carlsson, P. Hellentin, L. Malmqvist, A. Persson, W. Persson, C.-G. Wahlström, Time-resolved studies of light propagation in paper. Appl. Opt. **34**, 1528 (1995)
2772. M. Sjöholm, G. Somesfalean, J. Alnis, S. Andersson-Engels, S. Svanberg, Analysis of gas dispersed in scattering media. Opt. Lett. **26**, 16 (2001)
2773. S. Svanberg, Gas in scattering media absorption spectroscopy – from basic studies to biomedical applications. Lasers Phot. Rev. **7**, 779 (2013)
2774. M. Lewander, PhD Thesis, Lund University (2010)
2775. G. Somesfalean, M. Sjöholm, J. Alnis, C. af Klinteberg, S. Andersson-Engels, S. Svanberg, Concentration measurement of gas imbedded in scattering media by employing absorption and time-resolved laser spectroscopy. Appl. Opt. **41**, 3538 (2003)
2776. U. Tylewicz, P. Lundin, L. Cocola, P. Rocculi, S. Svanberg, P. Dejmek, F. Gómez Galindo, Gas in scattering media absorption spectroscopy (GASMAS) detected persistent vacuum in apple tissue after vacuum impregnation. Food Biophys. **10**, 1483–011–9239–7 (2011)
2777. H. Zhang, S. Svanberg, Laser spectroscopic studies of gas diffusion in alumina ceramics. Opt. Express **24**, 1986 (2016)
2778. J. Alnis, B. Anderson, M. Sjöholm, G. Somesfalean, S. Svanberg, Laser spectroscopy on free molecular oxygen dispersed in wood materials. Appl. Phys. B **77**, 691 (2003)
2779. M. Andersson, L. Persson, M. Sjöholm, S. Svanberg, Spectroscopic studies of wood-drying processes. Opt. Express **14**, 3641 (2006)
2780. L. Persson, H. Gao, M. Sjöholm, S. Svanberg, Diode laser absorption spectroscopy for studies of gas exchange in fruits. Lasers Opt. Engineering **44**, 687 (2006)
2781. J. Huang, H. Zhang, H.Y. Lin, T.Q. Li, L. Mei, K. Svanberg, S. Svanberg, Gas exchange in fruits related to skin condition and fruit ripening. J. Biomed. Opt. **21**(12), 127007 (2016)
2782. M. Lewander, Z.G. Guan, L. Persson, A. Olsson, S. Svanberg, Food monitoring based on diode laser gas spectroscopy. Appl. Phys. B **93**, 619 (2008)
2783. T.Q. Li, H.Y. Lin, H. Zhang, K. Svanberg, S. Svanberg, Application of tunable diode laser spectroscopy in assessment of food quality. Appl. Spectroscopy **71**, 929 (2017)
2784. Y. Li, W.S. Li, L.N. Hu, K. Svanberg, S. Svanberg, Non-intrusive studies of gas contents and gas diffusion in hen eggs. Biomed. Optics Express **10**, 83 (2018)
2785. T. Svensson, L. Persson, M. Andersson, S. Svanberg, S. Andersson-Engels, J. Johansson, S. Folestad, Noninvasive characterization of pharmaceutical solids by diode laser oxygen spectroscopy. Appl. Spectr. **61**, 784 (2007)

2786. T. Svensson, M. Andersson, L. Rippe, S. Svanberg, S. Andersson-Engels, J. Johansson, S. Folestad, VCSEL-based oxygen spectroscopy for structural analysis of pharmaceutical solids. Appl. Phys. B **90**, 345 (2008)
2787. L. Persson, M. Lewander, M. Andersson, K. Svanberg, S. Svanberg, Simultaneous detection of molecular oxygen and water vapor in the tissue optical window using tunable diode laser spectroscopy. Appl. Opt. **47**, 2028 (2008)
2788. L. Persson, M. Andersson, M. Cassel-Engquist, K. Svanberg, S. Svanberg, Gas monitoring in human sinuses using tunable diode laser spectroscopy. J. Biomed. Optics **12**, 2028 (2007)
2789. M. Lewander, Z.G. Guan, K. Svanberg, S. Svanberg, T. Svensson, Clinical system for non-invasive in situ monitoring of gases in the human paranasal sinuses. Opt. Express **13**, 10849 (2009)
2790. M. Lewander, S. Lindberg, T. Svensson, R. Siemund, K. Svanberg, S. Svanberg, Noninvasive diagnostics of the maxillary and frontal sinuses based on diode laser gas spectroscopy. Rhinology **50**, 28–32 (2012)
2791. H. Zhang, N. Han, Y.Y. Lin, J.W. Huang, S. Svanberg, K. Svanberg, Gas monitoring in human frontal sinuses – Stability considerations and gas exchange studies. Sensors **21**, 4413 (2021)
2792. H. Zhang, J. Huang, T.Q. Li, S. Svanberg, K. Svanberg, Optical detection of middle ear infection using spectroscopic techniques - Phantom experiments. J. Biomedical Optics **20**, 057001 (2015). https://doi.org/10.1117/1.JBO.20.5.057001
2793. L.N. Hu, W.S. Li, H.Y. Lin, Y. Li, H. Zhang, K. Svanberg, S. Svanberg, Towards an optical diagnostic system for otitis media using a combination of otoscopy and spectroscopy. J. Biophotonics (2019). https://doi.org/10.1002/jbio.201800305
2794. P. Lundin, E. Krite Svanberg, L. Cocola, M. Lewander Xu, G. Somesfalean, S. Andersson-Engels, J. Jahr, V. Fellman, K. Svanberg, S. Svanberg: Non-invasive monitoring of gas in the lungs and intestines of newborn infants using diode lasers: feasibility study. J. Biomed. Opt. **18**, 127005 (2013)
2795. E. Krite Svanberg, P. Lundin, M. Larsson, J. Åkesson, K. Svanberg, S. Svanberg, S. Andersson-Engels, V. Fellman, Noninvasive monitoring of oxygen in the lungs of newborn infants by diode laser spectroscopy. Pediatric Res. **79**, 621 (2016)
2796. Y.Y. Lin, P. Lundin, E. Krite Svanberg, K. Svanberg, S. Svanberg, A.-L. Sahlberg, Gas in scattering media absorption spectroscopy on small and large scales – Towards the extension of lung spectroscopic monitoring to adults. Transl. Biophot. **3**, e202100003 (2021)
2797. D.L. Chen, W.S. Li, W. He, H. Zhang, Q.W. Zhang, H.Y. Lin, S. Svanberg, K. Svanberg, P. Chen, Laser-based gas absorption spectroscopy in decaying hip bone: Water vapor as a predictor of osteonecrosis. J. Biomed. Opt. **24**, 065001 (2019)
2798. C.T. Xu, M. Lewander, S. Andersson-Engels, E. Adolfsson, T. Svensson, S. Svanberg, Wall collision line broadening at reduced pressures: Towards non-destructive characterization of nanoporous materials. Phys. Rev. A **84**, 042705 (2011)
2799. T. Svensson, E. Adolfsson, M. Burresi, R. Savo, C.T. Xu, D.S. Wiersma, S. Svanberg, Pore size assessment by high-resolution laser spectroscopy of wall collision line roadening of confined gases: experiments of strongly scattering nanoporous zirconia ceramics with fine-tuned pore sizes. Appl. Phys. B. https://doi.org/10.1007/s00340-012-5011-z (2012)
2800. P.N. Prasad, *Introduction to Biophotonics* (John Wiley, 2003)
2801. L.V. Wang, H.I. Wu, *Biomedical Optics: Principles and Imaging* (Wiley, Hoboken, NJ, 2007)
2802. J. Popp, V.V. Tuchin, A. Chiou, S.H. Heinemann (eds), *Handbook of Biophotonics* (Wiley-VCH, 2012)
2803. R.K. Wang, V.V. Tuchin, *Advanced Biophotonics - Tissue Optical Sectioning* (Taylor & Francis, 2013)
2804. M. Olivo, U.S. Dinish (eds.), *Frontiers in Biophotonics for Translational Medicine* (Springer, 2015)
2805. Y. Yeh, V.V. Krishnan, *Biophotonics Science and Technology* (World Scientific, 2018)
2806. M. Andersson, R. Grönlund, L. Persson, M. Sjöholm, K. Svanberg, S. Svanberg, Laser spectroscopy of gas in scattering media at scales ranging from kilometers to millimeters. Laser Phys. **17**, 893 (2007)

Index

A
Ablation, 527
Above Threshold Ionization (ATI), 395, 396
Absolute binding energies, 101
Absorbance, 183
Absorption, 58, 59, 66, 169, 184, 185, 192, 194
  coefficient, 102, 104, 178, 180, 183
  intracavity, 348, 419
  long-path, 474
Absorption coefficient, 201, 532
Absorption cross-section, 476
Absorption edge, 101, 102
Abundances, 216, 373
Accessory pigments, 502
Accidental coincidences, 122, 222
Acid rain, 176, 457
Acousto-optic modulator, 371, 471
AC Stark effect, 397
Adaptive optics, 221, 484
Advantage
  Felgett, 155
  Jaquinot, 155
Air, 175, 176, 472
Air pollution, 99, 177
  particulate, 99
Airy distribution, 150, 283
ALA, 522
Alexander’s dark band, 85
Algae, 500, 503
Alignment, 128
Alkali atoms, 16, 360
Alkaline-earth atoms, 25
Alveoles, 99
Ammonia maser, 277
Amplified spontaneous emission, 290
Analogue-to-Digital Converter (ADC), 98, 369
Anapole moment, 428
Angiography, 407
Angioplasty, 517
Angular distributions, 69, 70, 243, 245
Angular frequency, 19
Anisotropy, 243, 426
Annihilation radiation, 106, 409
Anomalous dispersion, 378
Antenna, 265
Antenna pigments, 385
Anti-crossing, 251
Anti-glare, 172
Anti-hydrogen, 428
Anti-reflection layers, 166
Anti-Stokes, 78, 324, 325
Anti-Stokes component, 79, 325
Aperture synthesis, 268
Apodization, 155
Archaeology, 99
Arden-Buck relation, 474, 543
Assessory pigment, 300
Astronomical observations, 177, 216
Astrophysical spectroscopy, 216, 373
Astrophysics, 373
Atherosclerotic plaques, 527
Atmosphere, 176, 472
Atmospheric absorption, 176, 178, 179, 201, 245, 264
Atmospheric chemistry, 177
Atomic absorption method, 185
Atomic beam, 233
  collimated, 412
  lamp, 126

© The Editor(s) (if applicable) and The Author(s), under exclusive license
to Springer Nature Switzerland AG 2022

S. Svanberg, *Atomic and Molecular Spectroscopy*, Graduate Texts in Physics,
https://doi.org/10.1007/978-3-031-04776-3

Atomic-Beam Magnetic Resonance (ABMR), 233
Atomic clocks, 244, 268, 278, 421, 448, 483
Atom optics, 451
Attosecond pulse generation, 403, 437
Attosecond pulses, 403
Auger effect, 118
Auger electron spectroscopy, 116
Aurora australis, 88
Aurora borealis, 88
Autocorrelation, 267
Autocorrelation technique, 471
Autocorrelator, 387
Autofluorescence, 524
Avalanche diodes, 160

B
Back-projection, 259
Ballast resistor, 354
Ballistic photons, 532
Balmer formula, 432, 434
Bandar Aceh, 212, 215
Band head, 73
Bands, 75
Bathymeters, 500
Bathymetry, 178
Bayer colour filter, 163
B-barium-borate (BBO), 316
Beam-foil light source, 127
Beam-foil method, 127, 374
Beam-laser technique, 374
Beam overlap modulation, 429
Beer–Lambert law, 181, 182, 201, 476, 489
Bell inequality, 89
Betatron radiation, 108, 409, 410
Binding energy, 109, 110
B-integral, 336
Biophotonics, 164, 360, 371, 539, 544
Bird, 455, 504, 505
Birefringence, 166, 535
Birefringent Lyot filter, 302
Black-body emitter, 131
Black-body radiation, 65, 269
Black holes, 272
Blaze angle, 144
Bloch equations, 255
Blood flow, 259, 517, 533, 534
Blood perfusion, 533, 534
Blood vessels, 527, 539
Blumlein circuit, 290
Bohr atomic model, 95
Bohr magneton, 19
Bolometer, 160
Boltzmann constant, 61
Boltzmann distribution, 73, 255, 263
Boltzmann law, 61, 185
Born–Oppenheimer approximation, 46
Bose condensate, 440
Bose–Einstein condensation, 451
Boser, 453
Bowen mechanism, 222
Boxcar integrator, 347, 369, 468
BOXCARS, 327, 466
Bragg cell, 329, 330
Bragg diffraction, 96, 367, 451
Bragg geometry, 97
Bragg peak, 409, 411
Bragg relation, 96, 111
Bragg scattering, 320
Breit formula, 249, 383
Breit–Rabi formula, 31, 40
Bremsstrahlung, 93
Brewster angle, 85, 172, 282, 302
Broadening
  Doppler, 122, 123
  Holtsmark, 124
  homogeneous, 122
  inhomogeneous, 122
  Lorentz, 124
  pressure, 124, 202, 264
  Stark, 124
  transit time, 412, 435
Buckminster fullerene, 54
Buffer gas, 243, 244
Burners, 190

C
CaF_2, 174
Calcium, 27
CALIPSO, 495
Capillary waves, 265
Caries, 527
Carrier, 478
Carrier envelope phase stabilization, 337, 404, 437
CARS microscopy, 529
Cascade impactors, 99
Cavity, 65, 90, 280
Cavity-dumping, 330
Cavity round-trip time, 329
Central field, 15
Central-field approximation, 22
Ceramic materials, 511

Channeltron, 343
Charge Coupled Device (CCD), 163
Charge-exchange process, 419
Chemical activation, 511
Chemical analysis, 181
  Electron Spectroscopy for Chemical Analysis (ESCA), 113, 116
  laser methods, 348, 357, 390, 391, 458, 472, 495, 506, 509
  Nuclear magnetic resonance (NMR), 256
  optical methods, 181
  X-ray methods, 99
Chemical shift, 102, 113, 114
Chemical vapour deposition (CVD), 469
Chernobyl reactor accident, 212
Chiral molecules, 393, 426
Chirped-pulse amplification (CPA), 333
Chlorinated fluorocarbons, 176
Chlorofluoro-carbons, 176
Chlorophyll, 502
Chlorophyll-a, 499
Chromatography, 506
Chromophores, 526
Clear-air turbulence, 494
Clear sky, 139
Climate forcing, 177, 485, 494
Clusters, 53
CMOS detector, 133, 145, 497
Co:MgF$_2$, 306
Czochralski process, 316
Coherence, 279
  spatial, 278, 279
  temporal, 278
Coherence length, 278
Coherent, 277
Coherent Anti-Stokes Raman scattering (CARS), 325, 465
Coherent chemistry, 393
Coherent control, 393, 511
Coherent detection, 475, 495
Coherent excitation, 249
Coherent superposition, 128
Coherent technique, 536
Cold atoms, 447
Cold target recoil-ion momentum spectroscopy (COLTRIMS), 393
Colliding pulse, 331
Collimation ratio, 412
Collisional effects, 413
Collisions, 67, 89, 124, 242, 243, 358, 451, 452
  velocity-changing, 429
Colour night vision, 164
Combustion, 455
Combustion diagnostics, 1, 452, 458, 464, 465, 469
Combustion engines, 468
Comet, 224, 225, 416
Comparator, 157
Complex index of refraction, 82
Compressor, 334, 335
Computer-Aided Tomography (CAT), 259
Computerized Tomography (CT), 105, 106, 133, 174, 175
Cone, 164
Configuration, 22, 253
Confocal microscopy, 529
Confocal parameter, 281
Constant-fraction discriminator, 387
Continuum light source, 195, 203
Contrast agents, 104, 259
Contrast enhancement, 526
Contrast function, 6–8
Conversion factors, 2
Cooling, 439, 440
  evaporative, 452
  Raman, 448
  Sisyphos, 448
  sub-recoil, 449
Cooper pairs, 452, 454
Core, 16
Core polarization, 21
Correlations, 42
Correlation spectrometers, 205
Corrosion, 506
Cosmic Background Explorer, 272
Coulomb explosion, 397
Coulomb field, 42
Covalent bonds, 45
Cross-correlation technique, 535
Cross-over resonance, 428
Cross-section, 82, 88
Cryptation key, 90
Crystal, 313, 314, 317, 318
Crystal field, 262, 284
Crystallization, 445
Curve of growth, 217
Cyclo-octatetraene (COT), 299
Cyclotron resonance, 442
Cylindrical symmetry, 45, 47
Czerny–Turner, 146

D
Dark current, 158

Dark energy, 223, 272
Dark matter, 224, 272
Dark state, 449
De Broglie wavelength, 451, 452
Deconvolution, 202, 427
Deforestation, 212
Degenerate Four-Wave Mixing (DFWM), 320
Delayed coincidence technique, 371, 387
Delay line, 387
δ-amino levulinic acid, 522
Delves cup, 192
Dephasing time, 258
Depolarization, 361, 496
Derivative, 189, 190, 253, 364, 365, 380, 420, 421, 478, 525, 544
Desertification, 212
Detectors, 157
  array, 161
  mercury cadmium telluride (HgCdTe), 160
  thermo-ionic, 344
Deuterium lamp, 195
Diagnostic radiology, 103
Diagonalization, 41, 239
Diatomic molecules, 45
Dielectric layers, 165, 166
Dielectric properties, 266
Difference-frequency generation, 316, 317, 477
Differential Absorption Lidar (DIAL), 487
Differential imaging, 107
Differential optical absorption spectroscopy, 203
Differential Optical Absorption Spectroscopy (DOAS), 477
Diffraction, 107, 108, 137, 141, 143–145, 267, 268, 280, 281, 299, 357, 367, 407, 424, 451
Dimensionless quantities, 526
Diode array, 112
Dipole transitions, 66
Discharge
  channel, 290
  electrical, 291
  gas, 125
  lamp, 126
  spark, 126
Discrimination index, 8
Dispersion, 140, 141, 378
Dispersion curve, 251, 426
Dissociation, 391
Dissociation energy, 51, 52
Distributed Feed-back Laser (DFL), 311
Diurnal cycle, 212
Divergence, 281
Doas, 203, 205, 477
Dobson instruments, 177
Doppler
  effect, 123, 440
  width, 124, 292
Doppler broadening, 124, 347, 413
Doppler burst, 469
Doppler limit, 445
Doppler measurements, 533
Doppler shift, 266, 270, 374, 494
Double Fresnel rhomb, 174
Doubly refractive materials, 314
Dressed atom, 448
Drift tube, 343
Dry ice, 160
Dual X-ray energy Absorptiometry (DXA), 104
Dyes, 295
  bleachable, 286
Dynamic Stark effect, 448
Dynodes, 158

E
EARLINET, 485, 505
Eavesdropper, 90
Ebert–Fastie, 146
Edge technique, 495
Effective attenuation coefficient, 532
Effective charges, 115
Effective magnetic moment, 237
Effective pathlength, 197, 543
Einstein coefficients, 61
Elastic rotator, 50
Electric dipole moment, 33, 76
Electric dipole operator, 60
Electric dipole transitions, 66
Electric field gradient, 38
Electric Hyperfine Structure, 37
Electrochromic films, 171
Electromagnetically Induced Transparency (EIT), 394
Electron configuration, 22
Electron cooler, 419
Electron correlation, 419
Electronic magnetic moment, 40
Electronic wall paper, 172
Electron microscopy, 107
Electron multiplier, 415
Electron-Nuclear Double-Resonance (ENDOR), 262

Electrons
  equivalent, 25
  non-equivalent, 25
Electron Spectroscopy for Chemical Analysis (ESCA), 93, 109, 116, 136
Electron Spin Resonance (ESR), 262
Electron synchrotrons, 133
Electron tunnelling, 34, 397
Electrophoresis, 506
Electrostatic analyser, 110
Electrostatic velocity analyser, 127
Electro-weak interaction, 428
Elementary reactions, 456
Endohedral fullerenes, 54
Energy-dispersive system, 96, 98
Enhanced greenhouse effect, 177, 180
Entangled states, 89, 90, 319
Environmental applications, 99, 265, 455, 474, 499
ENVISAT, 267
Epitaxial growth, 313
Equivalent electrons, 26
Equivalent width, 216, 217
Er-Doped Fiber Amplifiers (EDFA), 279, 289
Etalon, 283, 294, 298
Ether, 154
Eulerian formulae, 58
European Southern Observatory (ESO), 221
Evaporative cooling, 451–454
Exchange interaction, 21
Exoplanet, 225, 227, 228, 505
Extended X-ray Absorption Fine Structure spectroscopy (EXAFS), 102, 103, 137
External fields, 28
Extraordinary beam, 172
Extraterrestrial intelligence, 272
Extreme Light Infrastructures (ELI), 336
Extremely Large Telescope (ELT), 222
Extreme Ultraviolet (EUV), 108, 135
Eye exposure, 519
Eye safety, 519

F
Facades, 503
Fano resonance, 352
Fast igniter, 410
F-centre, 305
Femtochemistry, 391, 511
Fermat principle, 148
Fermi contact interaction, 37
Fermi Golden Rule, 59
Fermi level, 102
Fermionic degenerate state, 454
Fibre amplifier, 310
Fibre laser, 308
Field ionization, 34, 35, 344, 419
Filters
  absorption, 169, 170
  atomic absorption, 495
  coloured glass, 166
  gas, 495
  interference, 165
  liquid, 169
  neutral-density, 170
Fine-focusing, 111
Finesse, 151, 153
Fine structure, 4, 31, 35, 37, 39, 40, 94, 102, 103, 111, 112, 137, 236, 360, 362, 414, 427, 432, 435, 469, 546
Fine-structure constant, 31
Fine-structure splitting, 21
Fingerprints, 509
First-order perturbation theory, 21
Flame, 186, 355, 456
Flash-lamp, 285, 296, 297
Flop-in, 237, 238
Flop-out, 238
Fluorescence, 343
  intermodulated, 429
Fluorescence Life-time Imaging Microscopy (FLIM), 528
Fluorescence light, 66, 413
Fluorescence microscopy, 529
Fluorescent lamp, 165
Fluorosensor, 526
Flux, 489
Food, 506, 543
Forbidden transition, 68, 218, 428, 446
Forensic science, 99, 509
Fortrat parabola, 73, 74
Fountain, 435
4f electrons, 198, 509
Fourier analysis, 64, 279
Fourier broadening, 435
Fourier components, 395
Fourier transform, 64, 154, 155, 257, 268, 328, 329, 399, 403
Fourier transformation, 383, 390, 471
Fourier transform NMR (FT-NMR), 257
Four-wave mixing, 320, 401, 469
Fovea, 164
Franck–Condon principle, 75, 76
Fraunhofer line, 205

Free-Electron Laser (FEL), 135
  Self-Amplified Spontaneous Emission (SASE), 135, 400
Free Induction Decay (FID), 257
Free spectral range, 150
Freons, 176, 177
Frequency-comb spectroscopy, 440, 441
Frequency-comb technique, 434
Frequency doubling, 313
Frequency mixing, 316, 320
Frequency Modulation Spectroscopy (FMS), 479
Frequency off-set, 437, 440
Frequency Recognition Algorithm for Multiple Exposures (FRAME), 147
Frequency-Resolved Optical Gating (FROG), 388
Frequency stabilization, 302, 303, 420
Frequency standard, 241, 244, 434
Fresnel reflection, 171
Fundamental constants, 2
Fundamental frequencies, 52
Fundamental modes, 307

G
GALILEO, 245
Garnet, 287
Gas centrifugation, 512
Gas correlation
  spectrometer, 205
Gas correlation imaging, 206
Gas in scattering media absorption spectroscopy (GASMAS), 197, 261, 542–544
Gated viewing, 534
Gaussian, 124, 280, 333, 380, 387
Geiger counter, 97
Geiger–Muller detector, 240
Geophysical tracer gas, 490
Geostationary orbit, 215
Geothermal energy, 490
Ghost lines, 145
Giant pulse, 286
Giotto, 224
g_J factor, 36, 246
Glass, 174
Global Positioning System (GPS), 245
GLONASS, 245
Glucose, 532
GOES, 215
GOME, 203
Granularity, 272, 273
Graphene, 45, 54
Graphite oven, 191, 355
Grating, 143, 331
  concave, 100, 145
  echelle, 145
  holographic, 144
  replica, 144
Grating spectrometers, 143
Gravitational microlensing, 227
Gravitational radiation, 271
Gravitational wave, 91, 156, 228, 272
Gravity-wave detection, 91
Grays, 407
Gray wedge, 205
Grazing incidence, 145, 298
Green flash, 87
Greenhouse effect, 474
Greenhouse gas, 177, 494
Ground configurations, 23
Ground truth, 211
Group theory, 52, 284
Group velocity, 332, 380, 395
Group velocity dispersion, 331, 332
GSI, 419
Gyro, 19, 215

H
Haloes, 87
Hamiltonian, 15, 21, 57
Hanle effect, 251, 382
Hanle signal, 374
Harmonic oscillator, 51, 63
Heat-pipe, 352
Heat-pipe oven, 347, 379
Heisenberg relation, 91
Heisenberg uncertainty principle, 243
Heisenberg uncertainty relation, 63, 111, 231, 238, 360, 403
Helium, 26
Hematoporphyrin Derivative (HPD), 519
Heriott cell, 347
Hermitian, 60
Heterodyne detection, 161, 474, 536
Hetero-nuclear, 48
High-frequency deflection, 375
High harmonic generation, 397
Highly ionized atoms, 126, 218
Highly ionized spectra, 127
High-power decoupling, 258
Hollow cathode, 126, 185, 186
Hologram, 155
Holography, 295, 451

Homogeneous
  broadening, 65
Homo-nuclear molecules, 46, 72
Hook method, 378
Hot band, 79, 465
Hubble Space Telescope (HST), 219, 369, 401
Human eye, 164, 311, 519, 537
Human vision, 164
Hund coupling cases, 50
Huygen´s partial waves, 140, 143
Huygen´s principle, 11, 156
Hydrogen, 15, 269
Hydrogen maser, 244
Hydrospheric remote sensing, 264, 499
Hyperfine anomaly, 240
Hyperfine structure, 35, 129, 130, 152, 244, 246, 253, 362, 384, 414, 434
Hyperspectral
  imaging, 211

I
Ice crystal, 87
Idler, 318
Image intensifier, 161, 162, 502, 525
Image plates, 104, 165, 407
Image processing, 211
Imaging
  astronomical, 484
  lung, 261
  medical, 103, 407, 410, 530
  spectrometer, 211
  tissue, 528
Imaging spectrometers, 163
Independent particle model, 22
Indium antimonide, 160
Indium arsenide, 160
Inductively Coupled Plasma (ICP), 194
Inelastic scattering, 78
Inertial confinement, 410
Inhomogeneous
  broadening, 65
Inhomogeneous electric field, 277
Inhomogeneous magnetic field, 235, 237
Inner electrons, 93
Insect, 83, 410, 455, 496, 497, 504, 505, 547
Integrating sphere, 196, 347
Interaction constant
  electric quadrupole, 38
  magnetic dipoole, 36
Intercombination lines, 68
Interference, 147, 165, 393, 394, 428, 435, 466
Interferogram, 155
Interferometer, 268
  atom, 451
  confocal, 152
  Fabry–Pérot, 147, 299, 345
  Mach–Zehnder, 378
  Michelson, 279, 344, 537
  multi-pass, 152
Intermediate coupling, 26, 32
Intermediate fields, 40
Intermediate frequency, 475
Intermediate vector boson, 428
Intermodulated, 429
Internal combustion engines, 465, 468
International Ultraviolet Explorer (IUE), 219
Interstellar gas, 269
Interstellar molecules, 269
Interstitial Photodynamic Therapy (IPDT), 522, 523
Interval rule, 26
  Landé, 36, 38
Intracavity, 316, 419
Invar spacers, 151
Inverse Free-Electron Laser (IFEL), 135
Inverse Hook method, 380
Inversion, 73
Inversion layer, 201
Inverted fine structure, 21, 364, 414
Inverted hyperfine structure, 36, 414
Iodine, 104, 472
Ionic bonds, 45
Ionization
  collisional, 344
  field, 34, 344
  Penning, 293
  photo-, 343
Isoelectronic sequence, 218
Isotope shift, 42, 514
Isotopic selectivity, 511

J
James Webb Space Telescope, 220
jj coupling, 26, 32
JWST, 220

K
K-absorption edge, 104, 407
Kayser, 3
Kerr effect, 286, 333

Kerr gate, 535
Kinematic compression, 418
Kramer–Kronig dispersion relation, 378, 541

L
Lamb dip, 420
  inverted, 420
  normal, 420
Lamb shift, 65, 402, 427, 431, 432
Λ doubling, 50, 269
Lamp, 126
  deuterium, 132
  discharge, 126, 340
  hollow cathode, 125, 185
  RF, 126, 360
  xenon and mercury, 132
Landé formula, 32
Landé g_J factor, 30, 246
Landé interval rule, 25, 36
Land mine, 212
LANDSAT, 200, 209
Langmuir–Taylor detector, 240
Laplace operator, 16
Larmor frequency, 252
Larmor precession, 257
Laser, 275
  4-level, 286
  ablation, 368
  accelerators, 409
  alexandrite, 306
  amplifier, 288
  argon-ion, 294
  chemical, 308
  CO, 308
  CO_2, 307
  colour-centre, 305
  continuum, 122, 131, 349
  cooling, 444
  copper vapour, 291
  crystals, 288
  diffraction-limited, 281
  diode, 310, 313
  distributed feedback dye, 400
  dye, 295, 296
  emerald, 306
  excimer, 290, 291
  femtosecond, 332
  fibre, 308
  fixed-frequency, 284
  forsterite, 306
  free-electron, 135
  helium–cadmium, 293
  He–Ne, 292
  heterojunction, 309
  HF, 308
  krypton-ion, 295
  $LiNbO_3$, 317
  line, 121, 122, 279
  LISAF, 306
  Littrow, 297
  LNA, 261
  mount, 141, 145, 297
  Nd-glass, 288
  Nd:YAG, 287
  $Nd:YVO_4$, 295
  nitrogen, 290, 524
  prism, 141
  quantum cascade, 311
  ring, 303
  ruby, 284
  semiconductor, 308, 309
  spin-flip Raman, 295
  super-radiant, 290
  three-level, 285
  $Ti^{3+}:Al_2O_3$, 306
  Ti:sapphire, 332
  tunable, 295
  vertical cavity surface emitting, 311
  waveguide, 308
  X-ray, 278, 403
Laser beam deflection, 464, 479
Laser Doppler Velocimetry (LDV), 469
Laser-driven fusion, 127, 410
Laser-Enhanced Ionization (LEI), 354
Laser guide star, 221, 484
Laser Induced Breakdown Spectroscopy (LIBS), 484
Laser-induced chemical processes, 509
Laser-induced chemistry, 511, 521
Laser-Induced Fluorescence (LIF), 458, 498, 524
Laser isotope separation, 511, 512
Laser-nuclear interactions, 410
Laser-produced plasma, 368
Laser radar, 480
Lasers in medicine, 517
Laser-spectroscopic applications, 455
Lasing without inversion, 394
Lattice, 451
Laue diffraction, 451
Laue geometry, 97
LCAO method, 46
Lead sulphide (PbS) cell, 160
LED lamp, 132

Level crossing, 248, 360
Level inversion, 21
Level labelling, 351
Lidar, 480
Lidar equation, 488
LiF, 174
Lifetime, 63, 248, 371, 401
Lifetime measurements, 372
Light diffusive pulling, 451
Light emitting diode (LED), 5, 6, 131–133, 311, 480
Light-induced drift, 451
Lightning, 88
Light shift, 244, 448
Light sources, 121
LIGO, 91, 156, 228, 230
Limb absorption, 202, 265
Limb emission, 265
Liquid crystal, 166
Liquid-crystal modulator, 393
Liquid nitrogen, 160, 285
Liquids, 255
LISA, 156
Lithium niobate ($LiNbO_3$), 317
Lithium triborate (LBO), 295
Lithographic applications, 311
Lithography, 108, 127, 291
Local oscillator, 474, 495
Lock-in amplifier, 186, 422, 478
Lock-in detection, 253, 360, 475
Lock-in detector, 206
Lock-in techniques, 347
Longitudinal relaxation time, 255
Loop hole, 89
Lorentz condition, 57
Lorentzian, 64, 124, 251, 253, 255, 380, 383, 426
LS coupling, 25, 32, 68
Luggage inspection, 391
Lunar ranging, 483

M
Magic angle, 258, 383
Magnetic dipole interaction constant, 37
Magnetic dipole moment, 35
Magnetic dipole transitions, 233
Magnetic field measurements, 244, 259
Magnetic hyperfine structure, 35, 36
Magnetic moment, 18, 29, 256
Magnetic resonance, 231–233
  atomic-beam, 233
Magnetic Resonance Imaging (MRI), 259
Magnetization, 256
Magnetometers, 244
Magneto-Optical Trap (MOT), 449
Magnification radiography, 107
Mammography, 103, 532
Maser, 269, 270, 277
Mass effect, 42
Mass spectra, 53
Mass spectrometric studies, 53
Maxwell distribution, 123
Mechanical moment, 18
Medical imaging, 103, 407, 410, 530
Mercury, 132, 490
Mesosphere, 483
Metal Chemical Vapour Deposition (MOCVD), 309
Metal coatings, 168
Metastable, 350, 469
Metastable levels, 240
Metastable states, 104, 418, 446
Metastases, 106, 107
Meteorites, 483
Meteorological conditions, 200
METEOSAT, 215
Michelson
  interferometer, 208, 279, 344, 537
Microbeam, 99
Microchannel plate, 111, 161, 162, 387, 502
Microdensitometer, 126, 157, 350
Microwave radiometry, 264
Microphone, 358, 464
Microzone plate, 107
Mie scattering, 82, 484
Minamata convention, 490
Mirages, 87
Mirrors, 166
  chirped, 332
Mixer, 475, 478
Mixing ratios, 458
Mode hopping, 283
Mode-locking, 328
Modes, 52, 280
Molecular Beam Epitaxy (MBE), 309
Molecular structure, 45
Moment
  electric quadrupole, 38
  magnetic dipole, 35
Moment of inertia, 48
Monochromator, 136, 140
  double, 145
Monopole interaction, 38
Monte Carlo simulations, 407, 532
Montreal protocol, 177

Moon, 139, 483
Morse potential, 51
Moseley’s law, 95
Multichannel Analyzer (MCA), 98, 370
Multichannel Quantum Defect Theory (MQDT), 27, 431
Multi-element analysis, 99, 194
Multilayer techniques, 153, 165
Multi-mode operation, 282
Multi-pass cell, 196, 515
Multi-photon absorption, 342
Multi-photon process, 395, 514
Multiplicity, 25, 48
Multipole fields, 62
Multi-spectral aerial photography, 209
Multi-spectral imaging, 4–6, 8, 9
Multi-Spectral Scanning (MSS), 209
Multivariate analysis, 506
Muonium, 16, 428

N
Nadir, 265
Nanoparticles, 522
Nanoporous ceramics, 347, 544
Natural lifetime, 59, 63, 100, 373
Natural linewidth, 374
Natural radiation width, 63, 122, 246, 249, 383, 412
Nd:YAG, 288
Nd:YLF, 288
Near-Edge X-ray Absorption Fine Structure (NEXAFS), 102
Negative ions, 419
Nephelometry, 83
Nernst glower, 131, 195
Neutron stars, 271
NIF, 333
Night vision, 164
Non-crossing rule, 32, 251
Nonharmonicity, 79
Nonlinear index of refraction, 336
Nonlinear optical effects, 313
Nonlinear optics, 313, 395
Normal structure, 36
Nuclear Magnetic Resonance (NMR), 256
Nuclear magneton, 35
Nuclear moments, 37, 38, 240, 256
Nuclear orientation, 243
Nuclear physics, 109, 410
Nuclear spin, 38, 237, 240, 243, 256

O
Oblate shape, 38
O branch, 81
Oil, 265
Oil slicks, 500
Oil spills, 499
Old atoms, 383
1/f noise, 188, 189, 478
Optical clock, 241, 421, 422, 446, 451
Optical Coherence Tomography (OCT), 154, 208, 390, 537–539
Optical components, 165
Optical density, 171, 183
Optical double resonance, 245, 360
Optical fibre, 310, 311, 480, 522
Optical Field Ionization (OFI), 405
Optical klystron, 135
Optical lattice, 451
Optical mammography, 534
Optical materials, 174
Optical molasses, 448
Optical Multichannel Analyser (OMA), 161, 162
Optical Parametric Amplifier (OPA), 319
Optical parametric chirped pulse amplification (OPCPA), 336
Optical Parametric Oscillator (OPO), 318
Optical phase conjugation, 323
Optical piston, 451
Optical pumping, 241, 242, 261
Optical remote sensing, 199
Optical retarder plates, 174
Optical spectroscopy, 121
Optical tweezers, 531
Ordinary beam, 172
Organic dye, 295
Orientational energy, 28, 30, 35, 37
Oscillator strengths, 373
Osteoporosis, 105
Otitis, 543
Overlapping orders, 145, 151
Overtones, 72
Ozone depletion, 176
Ozone hole, 177
Ozone layer, 176

P
Paramagnetic ions, 259
Paramagnetic substances, 262
Parity, 66
Parity violation, 428
Particle, 82, 83, 471, 487

Particle-Induced X-ray Emission (PIXE), 99
Particles, 471
Particle–wave dualism, 11
Parts per billion (ppb), 181
Parts per million (ppm), 181
Parts per trillion (ppt), 181
Paschen–Back effect, 31, 40, 238
Paschen–Back region, 32, 41, 263, 385
Pattern recognition, 9
Pauli principle, 22, 25, 46, 453
P branch, 72, 73
Pedestal, 336, 429
Perihelion, 225, 227, 271
Periodically Poled Lithium Niobate (PPLN), 477
Periodic poling, 317
Periodic table, 181
Petrochemical industries, 494
Pharmaceutical, 181, 506, 512, 535, 541, 543
Phase contrast imaging, 410
Phase control, 302
Phase-Locked Loop (PLL), 345
Phase matching, 314, 316, 327, 387
Phase memory, 249
Phase shift, 149, 336
Phase shifter, 478
Phase-shift method, 376, 536
Phase velocity, 380, 395
Phosphorescence, 66, 67
Phosphor screen, 112
Photoacoustic Imaging (PAI), 539
Photoacoustic spectroscopy, 358
Photoacoustic Tomography (PAT), 539
Photoactivated localization spectroscopy (PALM), 357
Photocell, 158
Photochemistry, 291
Photochromism, 172
Photoconducting detectors, 160
Photoconductive mode, 157
Photo-detachment, 419
Photodissociation, 397
Photodynamic Tumour Therapy (PDT), 519
Photoelectric effect, 96, 158
Photoelectric recording, 126
Photoelectron spectroscopy, 93, 109
Photographic plate, 157
Photoionization, 355, 402, 415, 512
Photoisomerisation, 393
Photomultiplier Tube (PMT), 158, 160
Photon anti-bunching, 90
Photon echoes, 258
Photonic bandgap fibre, 437
Photon momentum, 415
Photosynthetic pigment, 393
Photovoltaic mode, 157
Photovoltaic solar energy, 139
Phycocyanin, 300
Phycoerythrin, 300
Picosecond pulses, 330
Pile-up effect, 371
Pioneer spacecraft, 274
Planck, 2, 5, 6, 10, 131, 137, 272, 273, 378, 419
Planck distribution, 279
Planck radiation law, 61
Planck radiator, 378
Planetary atmospheres, 224
Plant leaves, 541
Plasma, 373
  laser-produced, 126, 127, 369
  solid-density, 406
Plasmons, 118
Pockels cell, 335, 367
Pockels effect, 286
Point groups, 52
Polariton, 509
Polarizability constants, 314
  scalar, 34
  tensor, 34
Polarization, 70, 172, 173, 282
POLarization INtermodulated EXcitation (POLINEX), 429
Polarization spectroscopy, 466
Polarization tensor, 77
Polarized, 85
Polarizers, 172
  Glan–Taylor, 172
  Glan–Thompson, 172
  polyvinyl film, 174
Polarizing beam-splitter, 173
Polar orbit, 214, 215
Pollutants, 487
Pollution, 456
Polyatomic molecules, 52
Poly-Methyl-Meth-Acrylate (PMMA), 108
Ponderomotive potential, 396
Population inversion, 277
Portwine stains, 517
Positron, 409
Positron Emission Tomography (PET), 106, 410
Positronium, 16, 428

Potassium Dihydrogen Phosphate (KDP), 316
Potassium pentaborate (KPB), 316
Powder, 359
Precess, 39, 47, 232
Precession, 31
Precessional motion, 18
Pressure shifts, 244
Primary rainbow, 84
Principal Component Analysis (PCA), 9, 504
Prism, 140, 141, 332
  Amici (roof), 141
  corner-cube, 143
  dove, 143
  Glan-Thompson, 172, 426
  Pellin–Broca, 142
  penta, 142
  right-angle, 141
  straight-view, 142
Prism spectrometers, 140
Probe, 351, 389, 422
Prolate shape, 38
Proton therapy, 411
Protoporphyrin IX, 524
Pulsars, 270, 271
Pulse compression, 331
Pulse oximetry, 541
Pulse shaper, 393
Pump, 351, 389, 422
Pump-probe technique, 389
Purification, 511
Push-broom, 164
Pyroelectric, 160
Pyrolysis, 511

Q
Q branch, 76, 81
Q-switching, 285, 286
Quadrupole interaction, 38
Quantum-Beat Spectroscopy (QBS), 380
Quantum Cascade Lasers (QCL), 311, 312
Quantum chemistry, 53
Quantum computing, 65, 446
Quantum cryptography, 65
Quantum defect, 16
Quantum efficiency, 158
Quantum Electrodynamics (QED), 16, 29, 60, 65, 431
Quantum jump, 446
Quantum-mechanical squares, 21, 30
Quantum mechanics, 2, 9, 15, 52, 55, 62, 64, 89, 547
Quantum number
  azimuthal, 16
  computing, 2, 65
  effective, 16
  principal, 16
Quantum optics, 65
Quartz, 174
Quartz-Enhanced Photo-Acoustic Spectroscopy (QEPAS), 359
Quasars, 223, 272
Quasi-phase-matching, 318
Qubits, 90
Quenching, 88, 262, 458
Quiver energy, 396
Q-value, 90

R
Radar, 265
RADARSAT, 267
Radar systems, 264, 265
Radiation
  resonance, 55
Radiation process, 55
Radiation source
  natural, 137
  Planck, 137
Radicals, 262, 456
Radioactive atoms, 243, 417
Radioactive isotopes, 240, 417
Radioactive nuclei, 418
Radio astronomy, 267
Radio-frequency spectroscopy, 231
Radio-frequency transition, 361
Radiography, 103, 104
Radio telescopes, 267
Radon transform, 105
Rainbow, 84
Rainbow angle, 84
Rainfall, 265
Raman cooling, 450
Raman effect, 78
Raman scattering, 76
  surface-enhanced, 509
Raman shifting, 324
Raman spectroscopy, 198, 199, 465
Ramsey fringe method, 238, 241, 435
Range finders, 482
Ranging, 482
Rayleigh scattering, 77, 494
R branch, 72, 73
Reaction dynamics, 391
Recoil effect, 415

Recoil energy, 110
Recoil limit, 444
Recombination, 403
Reconstruction of Attosecond Beating By Interference of two-photon Transitions (RABBIT), 403
Red-Green-Blue (RGB), 164
Red shifts, 223
Reduced mass, 42, 49, 51
Reduced scattering coefficient, 532
Reflective remote sensing, 209
Refocusing, 127
Refractive surgery, 517
Refractory elements, 241, 368
Regen(erative) amplifier, 335
Relative humidity, 474, 543
Relativistic, 409, 483
Relativistically, 374
Relativistic effects, 134
Relativistic Lorenz contraction, 440
Relativity, 271, 272
Relaxation, 112, 243, 296, 389
Relaxation processes, 244
Remotely Operated Vehicles (ROVs), 482
Remote sensing, 264, 472
  atmospheric, 178
  hydrospheric, 499
Resolution, 267
Resolving power, 140, 141
Resonance, 59
Resonance Ionization Mass Spectroscopy (RIMS), 356
REsonance MultiPhoton Ionization (REMPI), 355
Resonance radiation, 66
Resonance Raman effect, 199
Resonator, 279, 280
Retardation, 148, 149
Retina, 164, 517
Retinopathy, 517
Retroreflector, 143, 344, 476
Rhodopsin, 385, 393
Rigid rotator, 50
Ring-laser cavity, 303
RIS, 355
Rod, 164
Rotational CARS, 468
Rotational constant, 72
Rotational energy, 48
Rotational quantum number, 71
Rotational transitions, 71
Rowland circle, 100, 111, 145
Rydberg atoms, 34, 415
Rydberg constant, 16, 426, 427
Rydberg formula, 67
Rydberg sequences, 371
Rydberg states, 90, 342, 431

S
Sample boat, 192
SARS-CoV-2, 544
Satellite launch, 213
Satellites, 200, 219, 245, 265, 266, 482
Saturable absorber, 286, 330
Saturation, 340
Saturation technique, 412
S branch, 81
Scattering coefficient, 532, 535
Scenes, 211
Schawlow–Townes limit, 283
Scheimpflug, 496, 497, 501, 503–505
Schrödinger cat paradox, 89
Schödinger equation, 15, 46, 55
Scintillation counter, 97, 98
Scintography, 106
Sea clutter, 265
Sea ice, 265
Secondary rainbow, 84
Second-order Doppler effect, 412, 439
Selection rules, 62, 66, 67, 69, 72, 238
Self Amplified Spontaneous Emission-Free-Electron Laser (SASE-FEL), 135, 400
Self-conjugating crystal, 320
Self-consistent field, 27, 115
Self-phase modulation, 331, 333, 390
Self-terminating, 290
Semiconductor saturable absorber mirror (SESAM), 286, 308, 330, 331
Sensitizers, 522
Sensor, 200
SENTINEL, 213, 267
Separation plant, 512
Servo system, 283, 420, 421
Sextupole magnet, 240, 417
Seya–Namioka, 146
Shake-up lines, 112
Shear winds, 494
Shelving, 90, 446
Shielding, 256
Shift register, 163
Side Looking Airborne Radar (SLAR), 265, 499
Si(Li) detector, 99
Single-atom detection, 357

Single-mode dye laser, 304
Single-mode operation, 282
Single-mode oscillation, 294
Single-molecule detection, 357
Single-Photon Avalanche Diode (SPAD), 160
Single-photon counting, 317
Single Photon Emission Computed Tomography (SPECT), 106, 410
Singlet oxygen, 521
Singlet system, 297
Sinus cavity, 542, 544
Sinusitis, 543
Slab, 288
Slab amplifier, 289
Slant visibility, 484
Sliding spark, 126
Slow-light propagation, 380, 541
Smart-window technology, 171
Snell refraction law, 84, 140
Solar corona, 218
Solids, 255
Solvation energy, 116
Solvents, 196
Soot, 458
Soot particles, 456
Soret band, 519
Space quantization, 30, 235
Specific mass effect, 42
Spectral Phase Interferometry for Direct Electric-field Reconstruction (SPIDER), 388
Spectral resolution instruments, 140
Spectrometer
  Fourier transform, 154
  mass, 356
  time-of-flight, 395, 402
Spectroscopy
  atomic absorption, 185
  attosecond, 339, 389, 403–405
  cavity ring-down, 349
  coherent raman, 199
  differential optical absorption, 477
  flame emission, 185
  fluorescence lifetime imaging, 528
  frequency-modulation, 479
  γ-ray, 406
  high-contrast transmission, 424
  laser, 339
  laser induced breakdown, 484
  level crossing, 248
  opto-acoustic, 358
  opto-galvanic, 352, 429, 463
  photoacoustic, 463
  polarization, 425
  quantum-beat, 129, 380
  resonance ionization, 355
  saturation, 419
  time-resolved, 366
  two-tone frequency modulation, 479
  ultrafast, 385
  ultra-sensitive, 357
  vacuum, 175
  wavelength modulation, 478, 480, 481
  X-ray, 406
  X-Ray Absorption, 101
Spectrum
  beam-foil, 127
  photoelectron, 112
  X-ray emission, 94
  X-ray fluorescence, 96
Speed of light, 395, 500
Spherical harmonics, 66, 71, 547
Spherically symmetric, 16
Spin echo, 258
Spin-exchange collisions, 261
Spin-orbit interaction, 20, 26, 112
Spin-spin interactions, 256
Spitzer Space Telescope, 220
Spontaneous emission, 60
SPOT, 200, 211
Sputtering, 125
Squeezed state, 90
Standard addition method, 191
Standard model, 428
Standard solutions, 191
Stark effect, 33
  linear, 33
  scalar, 34
  tensor, 34
Star spectra, 216
Stellar atmosphere, 217
Stern–Gerlach experiment, 236, 237
Stimulated Brillouin Scattering (SBS), 323
Stimulated emission, 59, 275
Stimulated Emission Depletion (STED), 358, 424, 425
Stimulated Raman scattering, 324, 401, 515
Stochastic Optical Reconstruction Microscopy (STORM), 357, 358, 424
Stokes, 78, 324
Stokes component, 79
Stokes shifting, 76
Storage rings, 134, 418
Straggling, 127

Stratosphere, 264
Stratospheric dust, 494
Stratospheric ozone destruction, 474
Stray light, 145
Streak camera, 164, 387, 407, 534
Stretcher, 334
Structured Light Illumination Planar Imaging (SLIPI), 147
Submarines, 178
Sum-frequency mixing, 477
Sun, 137, 139
Sunstone, 83
Sun synchronous, 215
Supercavity, 153
Superconducting coils, 256
Superconductivity, 452
Superfluidity, 452, 454
Supernova, 223
Superresolution microscopy, 357, 425
Supersonic nozzle, 515
Supersonic Transport (SST), 176
Surface, 116–118, 498, 503, 506
Surface plasmon, 509
Surface spectroscopy, 116, 117, 506
Susceptibilities, 314
Swath, 209
Swirls, 494
Symmetry properties, 52
Synchronous pumping, 330
Synchrotron radiation, 102, 133, 134, 366
Synthetic Aperture Radar (SAR), 265

T
Tag, 499
Tagging, 472
TEA laser, 308, 515
Telecommunication, 310
Telescopes, 216
TEM_{00}, 280
Temperature, 79, 80, 212, 223, 484, 509
Temperature measurements, 75, 79, 465, 509
Tensor Stark interaction, 34, 414
Terahertz-radiation generation, 390
Terms, 22
Texture, 211
Thermal interaction, 517
Thermal velocities, 126
Thermocouple, 160
Thermodynamic equilibrium, 61, 276, 378
Thermometers, 509
Thermometry, 468
Thermovision, 206, 212
Theta pinch, 127
Time-correlated single-photon counting (TCSPC), 370–372, 529, 541
Time dilatation, 412
Time-of-flight spectrometer, 343
Time-resolved diffraction studies, 107
Time-resolved experiments, 135, 407
Time-resolved X-ray diffraction, 407
Time-to-Amplitude pulse-height Converter (TAC), 370
Tissue diagnostics, 524
Tokamak, 127
Tomographic, 259, 464
Tomographic reconstruction, 105
Tracer dye, 499
Transform-limited, 388
Transient digitizer, 367, 485
Transillumination, 105, 531–535, 542
Transition
  radiationless, 296
Transition probabilities, 34, 57, 125, 372, 378
Transition states, 391
Transit-time broadening, 435
Transmission medium, 175
Transverse relaxation time, 255
Trap
  ion, 442
  magneto-optical, 449
  Paul, 444
  Penning, 442
  quadrupole, 444
Trapping, 439
Triangulation, 245, 480
Triplet molecules, 299
Triplet state, 299
Tsunami, 212, 215
Tumour, 259, 519
  localization, 212
Tungsten
  lamps, 131, 195
Tuning fork, 258, 359
Turbidimetry, 83
Turbulence, 203, 220–222, 478, 495
Turbulent, 468
Two-photon absorption, 342, 412, 430
Two-photon fluroscence, 529
Two-photon transitions, 57
Two-Tone Frequency Modulation Spectroscopy (TTFMS), 479

U
Ultracold fermionic gases, 454
Ultrasound, 539–541, 546
Ultrasound Optical Tomography (UOT), 541
Undulators, 135
Unit conversion, 2
Universal distribution function, 134
Unpaired electron, 37
Unstable resonator, 288
Up-converting nanoparticles, 527

V
Vacuum state, 60, 65
Vacuum techniques, 233
Vacuum Ultraviolet (VUV), 219, 320, 402
Vacuum wavelengths, 175
Valence orbitals, 113
Van der Waals molecules, 45
Vapour pressure, 233, 242
Variance, 63
Vector potential, 57
Vegetation monitoring, 209, 498, 502
Velocity, 533
Velocity measurements, 469
Velocity of light, 421
Velocity Selective Coherent Population Trapping (VSCPT), 450
Vertical Cavity Surface Emitting Lasers (VCSEL), 311
Very Large Telescope (VLT), 221
Very Long Base line Interferometry (VLBI), 268
Very Long Wavelength (VLW), 178
Vibrational–rotational Raman spectra, 81
Vibrational energy, 51
Vibrational transitions, 71
VIRGO, 91, 156, 228, 230
Virtual levels, 78, 342
Voigt profile, 124
Volcanic plume, 206
Volcanoes, 489
Volume effect, 42
Volume plasmon, 118, 119
Voyager missions, 224

W
Wake-field acceleration, 409
Water depth, 500
Water pollution, 499
Water window, 107, 398
Wavefunction, 13, 16, 46, 546, 547
Wavelength-dispersive, 96
Wavelength Modulation Spectroscopy (WMS), 478
Wavemeter, 346
Weather radar station, 265
Whisk-broom, 209
White cell, 196, 347
White excitation, 360
White-light continuum, 390
White-light generation, 387, 390
Wien displacement law, 131
Wigglers, 135
Wigner crystal, 419, 446
Wilkinson Microwave Anisotropy Probe (WMAP), 272, 273
Wind velocities, 494
Wolf–Rayet stars, 218

X
X-ray
  continuum, 101
  laser-produced, 407
  laser pumping, 403
  lithography, 108
  microscopy, 107
  photoionization, 293
X-ray Absorption, Near-Edge Structure (XANES), 103
X-ray fluorescence, 96
X-ray imaging, 165
X-ray microscopy, 107
X-ray monochromatization, 111
X-ray Photoemission Spectroscopy (XPS), 93, 109
X-ray spectroscopy, 93
XUV, 401

Y
Young's double-slit experiment, 85, 249, 279, 381, 451

Z
Zeeman effect, 30, 36, 39, 40, 224, 238, 362
Zeeman modulation technique, 193
Zeeman quantum beats, 382
Zeeman region, 32
Zeeman slower, 443
Zeldovich mechanism, 457
Zenith, 265
Zero-point energy, 52
Zodiacal light, 139